

LEVEL II

AGARD-CP-301

AGARD-CP-301

AGARD

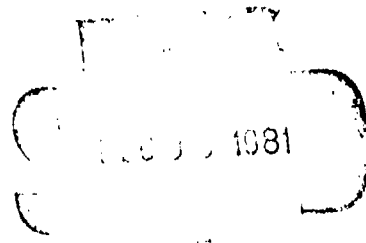
ADVISORY GROUP FOR AEROSPACE RESEARCH & DEVELOPMENT

7 RUE ANCELLE 92200 NEUILLY SUR SEINE FRANCE

AD A108300

AGARD CONFERENCE PROCEEDINGS No. 301

Aerodynamics of Power Plant Installation



NORTH ATLANTIC TREATY ORGANIZATION



DISTRIBUTION AND AVAILABILITY
ON BACK COVER

proved
ita

81 12 08 18 9

DTIC FILE COPY

THE MISSION OF AGARD

The mission of AGARD is to bring together the leading personalities of the NATO nations in the fields of science and technology relating to aerospace for the following purposes:

- Exchanging of scientific and technical information;
- Continuously stimulating advances in the aerospace sciences relevant to strengthening the common defence posture;
- Improving the co-operation among member nations in aerospace research and development;
- Providing scientific and technical advice and assistance to the North Atlantic Military Committee in the field of aerospace research and development;
- Rendering scientific and technical assistance, as requested, to other NATO bodies to member nations in connection with research and development problems in the aerospace field;
- Providing assistance to member nations for the purpose of increasing their scientific and technical potential;
- Recommending effective ways for the member nations to use their research and development capabilities for the common benefit of the NATO community.

The highest authority within AGARD is the National Delegates Board consisting of officially appointed senior representatives from each member nation. The mission of AGARD is carried out through the Panels which are composed of experts appointed by the National Delegates, the Consultant and Exchange Programme and the Aerospace Applications Studies Programme. The results of AGARD work are reported to the member nations and the NATO Authorities through the AGARD series of publications of which this is one.

Participation in AGARD activities is by invitation only and is normally limited to citizens of the NATO nations.

The content of this publication has been reproduced directly from material supplied by AGARD or the authors.

Published September 1981

Copyright © AGARD 1981

All Rights Reserved

ISBN 92-835-0301-5



Printed by Technical Editing and Reproduction Ltd
Harford House, 7-9 Charlotte St, London, W1P 1HD

EXECUTIVE SUMMARY

DR. J.E. GREEN, Co-Chairman, Programme Committee

Powerplant installations involve complex flows, strongly influenced by viscous effects and often with important aerodynamic interactions between the airframe and the propulsion system. The introduction of new vehicle propulsion concepts, and new points of emphasis in aircraft and missile design requirements, provide an expanding range of aerodynamic problems which call for both experimental and theoretical study.

It was the purpose of the symposium to survey the current and foreseeable aerodynamic problems in powerplant installation and to review recent work which has improved basic understanding or has enhanced prediction and design methods in this field. Since the last AGARD symposium on the subject, in September 1974, there have been many significant developments. The present symposium was organised by FDP with the active support of PEP, in order to draw in contributions from both the airframe and the engine communities and also to provide a forum in which workers in these two communities could exchange ideas and debate interface problems.

The presentations were grouped into four sessions under the headings: Combat Aircraft Intakes; Afterbodies and Nozzles; Testing and Analysis Techniques; Installation Aerodynamics of Transport Aircraft. On the final afternoon the symposium concluded with a Round Table Discussion in which progress under each of the four headings was reviewed. Some of the main points to emerge from the symposium are given below.

1. Theoretical methods employing computational fluid dynamics techniques will play an increasingly important role in aerodynamic design and a high level of effort to develop these methods is justified. For transport aircraft, some impressive results obtained by such methods were presented at the symposium. For combat aircraft, with intake and afterbody flow fields of greater complexity, applications are at present more restricted, but the need and the opportunity exists for major advances in the longer term provided effort on method development is sustained.
2. Understanding of the problems of engine/intake compatibility has improved largely as a result of more advanced experimental techniques and increased emphasis on dynamic measurements. Several noteworthy developments were reported at the symposium. Instantaneous distortion is generally agreed to be the most reliable indicator of the acceptability of the intake flow to the compressor, but some unexpected engine surges still occur occasionally during flight test. The need was voiced for work to deepen scientific understanding of the interactions between unsteady intake flow and the engine.
3. In the session on Afterbodies and Nozzles, a number of papers highlighted the need for aerodynamic studies of advanced nozzle concepts to be integrated with weight and cost studies. The complexity of the external flow, particularly for twin-engine configurations and at high angles of attack, means that wind tunnel testing will remain the only reliable means of predicting the external aerodynamics for some time to come: in extrapolating from wind tunnel data to flight, the need to distinguish in the wind tunnel data between true Reynolds number effects and other spurious phenomena was emphasised.
4. A range of engine simulation techniques, including through-flow nacelles, blown nacelles, ejector nacelles and turbine-powered simulators, are in current use, and their application is being progressively extended and refined. For transport aircraft the turbine-powered simulator is in general use and, with the refined calibration techniques now developed for it, high standards of accuracy and repeatability are claimed (though further improvements are still sought). The differences in the simulation requirements for transport and combat aircraft were noted during the Round Table Discussion and the need for improved simulators for combat aircraft was stressed.
5. For transport aircraft, the main priority remains aerodynamic efficiency. The potential for reducing drag by careful tailoring of nacelle, pylon and airframe was well demonstrated in the fourth session of the symposium, and the value of theoretical methods in providing a rational basis for such tailoring was highlighted.

Overall, the symposium lived up to the hopes of its organisers. It brought forward a number of important new technical contributions, it provided a valuable opportunity for engine and airframe specialists to meet and argue, and it enabled the AGARD community to review present knowledge, identify opportunities and assess priorities for future work. From the papers presented and from the Round Table Discussion it is evident that the future will see increasing emphasis on engine-airframe integration. The driving factors are seen to be, for combat aircraft, the requirement for high manoeuvrability, good supersonic performance and low detectability, and for civil aircraft the continued search for improved efficiency. To support future developments, two of the most important needs currently are for improved wind tunnel testing techniques and for a substantial effort to apply computational fluid dynamics methods to engine-airframe combinations.

J.E. Green
J. Dunham
Co-Chairmen,
Programme Committee

AGARD FLUID DYNAMICS PANEL

Chairman: Dr K.J.Orlik-Rückemann
National Aeronautical Establishment
National Research Council
Montreal Road
Ottawa, Ontario K1A 0R6, Canada

Deputy Chairman: M. l'Ing. en Chef B.Monnerie
Chef de la Division d'Aérodynamique Appliquée
ONERA
29 Avenue de la Division Leclerc
92320 Châtillon, France

PROGRAM COMMITTEE MEMBERS

FDP Panel Members

Dr J.E.Green (Co-Chairman)
Head, Aerodynamics Department
Royal Aircraft Establishment
Farnborough
Hants GU14 6TD, UK

M. l'Ing. de l'Armement A.Coursimault
Section "Etudes Générales"
Service Technique de l'Aéronautique
4 Avenue de la Porte d'Issy
75996 Paris Armées, France

Prof. Dr Ing. K.Gersten
Institut für Thermo-und Fluidodynamik
Ruhr Universität Bochum
Postfach 10 21 48
D-4630 Bochum 1, FRG

Dr G.K.Richey
Chief Scientist, Air Force Wright
Aeronautical Laboratories/FS
Wright-Patterson, AFB
Ohio 45433, USA

Dr Ing. U.Sacerdote
v. Direttore
Gruppo Attività Spaziali
ED Energie Alternative
Aeritalia SPA
Corso Marche 41
10146 Torino, Italy

PEP Panel Members

Dr J.Dunham (Co-Chairman)
National Gas Turbine Establishment
Pyestock
Farnborough
Hants GU14 0LS, UK

Mr H.I.Bush
Deputy Director, Turbine Engine Div./TB
AFWAL/POT
Wright-Patterson AFB
OH 45433, USA

Prof. D.Dini
Universita degli Studi
Istituto di Macchine
Via Diotisalvi 3
56100 Pisa, Italy

Dr D.K.Hennecke
Motoren and Turbinen Union GmbH (MTU)
Abt. EW
Dachauerstrasse 665
D-8000 München 50, FRG

PANEL EXECUTIVE

Robert H.Rollins II

	Page
EXECUTIVE SUMMARY	iii
PANEL OFFICERS AND PROGRAM COMMITTEE MEMBERS	iv
	Reference

SESSION I - COMBAT AIRCRAFT INTAKES

PERFORMANCE OF HIGHLY INTEGRATED INLETS FOR SUPERSONIC AIRCRAFT by L.Surber, J.Syberg and J.Konczel	1
TOP-MOUNTED INLET SYSTEM FEASIBILITY FOR TRANSONIC-SUPERSONIC FIGHTER AIRCRAFT APPLICATIONS by T.L.Williams, B.L.Hunt, D.B.Smeltzer and W.P.Nelms	2
SOME RAE RESEARCH ON SHIELDED AND UNSHIELDED FUSELAGE MOUNTED AIR INTAKES AT SUBSONIC AND SUPERSONIC SPEEDS by J.A.Ross, I.McGregor and A.J.Priest	3
PREDICTION AND MEASUREMENT OF TIME-VARIANT, THREE-DIMENSIONAL FLOWS IN MILITARY AIRCRAFT INTAKES by D.E.Colbourne and J.E.Flittcroft	4
EFFECTS OF INTAKE GEOMETRY ON CIRCULAR PITOT INTAKE PERFORMANCE AT ZERO AND LOW FORWARD SPEEDS by A.C.Willmer, T.W.Brown and E.L.Goldsmith	5
ECOULEMENTS TRANSSONIQUES DANS UNE PRISE D'AIR EN GRANDE INCIDENCE ET EFFET DE TRAPPE DE SOUFFLAGE par A.Dyment, P.Gryson et J.P.Flodrops	6
CALCULATION OF TRANSONIC AIR-INTAKES USING A COMPUTER PACKAGE FOR INVISCID AND BOUNDARY LAYER FLOWS by C.W.Lucchi	7
SUBSONIC MILITARY AIRCRAFT ENGINE INTAKE: AN INTEGRATED THEORETICAL - EXPERIMENTAL DESIGN by G.Bertolone and L.Fornasier	8
A PROGRAM TO DEVELOP PERFORMANCE OF THE A-7 INLET SYSTEM CONVERTED TO A TWIN ENGINE APPLICATION *	9
THE DESIGN AND DEVELOPMENT OF THE TORNADO ENGINE AIR INTAKE by C.P.Stocks and N.C.Bissinger	10

SESSION II - AFTERBODIES AND NOZZLES

INTEGRATION OF ADVANCED EXHAUST NOZZLES by D.L.Bowers and J.A.Laughrey	11
THE SUBSONIC PERFORMANCE OF PRACTICAL MILITARY VARIABLE AREA CONVERGENT NOZZLES by L.R.Harper	12

* Not available at time of printing.

COMPARISON OF DIFFERENT NOZZLE CONCEPTS FOR A REHEATED TURBOFAN by P.Grieb, R.Vedova, H.Enderle and H.Nagel	13
ADVANCED EXHAUST NOZZLE TECHNOLOGY by R.J.Glidewell and R.E.Warburton	14
A NUMERICAL INVESTIGATION OF EXHAUST PLUME TEMPERATURE EFFECTS ON NON AXISYMMETRIC NOZZLE/AFTERBODY PERFORMANCE by K.M.Peery and D.L.Russell	15
A REVIEW OF THE EFFECT OF REYNOLDS NUMBER ON AFTERBODY DRAG by O.M.Pozniak	16
 <u>SESSION III – TESTING AND ANALYSIS TECHNIQUES</u>	
DISPOSITIF DE SIMULATION AU BANC COMPRESSEUR D'UNE PRISE D'AIR A GRANDE INCIDENCE par B.Delahaye et G.Laruelle	17
SYSTEME D'ACQUISITION ET D'ANALYSE POUR ESSAIS DYNAMIQUES D'ENTREES D'AIR par P.Perrier, B.Delahaye et G.Laruelle	18
A SYNTHESIS METHOD FOR ESTIMATING MAXIMUM INSTANTANEOUS INLET DISTORTION BASED ON MEASURED INLET STEADY STATE AND RMS PRESSURES by R.Borg	19
MODEL TESTING TECHNIQUES FOR MEASURING INLET DRAG by J.S.Holdhusen and J.L.Grunnet	20
COMPRESSOR STALL INDUCING INSTALLATION EFFECTS OF AN ENGINE CONTROL PARAMETER FOR THE CF-5 AIRCRAFT by W.L.Macmillan, D.M.Rudnitski and W.Grabe	21
THE ROLE AND IMPLEMENTATION OF DIFFERENT NACELLE/ENGINE SIMULATION CONCEPTS FOR WIND-TUNNEL TESTING IN RESEARCH AND DEVELOPMENT WORK ON TRANSPORT AIRCRAFT by B.Ewald and R.Smyth	22
ESSAIS EN SOUFFLERIE DE MAQUETTES MOTORISEES – COMPARAISON DE DEUX METHODES DE SIMULATION DES JETS DES REACTEURS par JP.Becle et R.Perin	23
WIND TUNNEL TEST AND ANALYSIS TECHNIQUES USING POWERED SIMULATORS FOR CIVIL NACELLE INSTALLATION DRAG ASSESSMENT by A.E.Harris and E.C.Carter	24
ESTABLISHMENT OF AN EXPERIMENTAL TECHNIQUE TO PROVIDE ACCURATE MEASUREMENT OF THE INSTALLED DRAG OF CLOSE COUPLED CIVIL NACELLE/ AIRFRAME CONFIGURATIONS, USING A FULL SPAN MODEL WITH TURBINE POWERED ENGINE SIMULATORS by G.Pugh and A.E.Harris	25
EVALUATION OF AN EXPERIMENTAL TECHNIQUE TO INVESTIGATE THE EFFECTS OF THE ENGINE POSITION ON ENGINE/PYLON/WING INTERFERENCE by J.A.J. van Engelen, B.Munniksma and A.Elsenaar	26

SESSION IV – INSTALLATION AERODYNAMICS OF TRANSPORT AIRCRAFT

ESSAIS DE PRISES D'AIR A DES NOMBRES DE REYNOLDS COMPARABLES AU VOL DANS LES SOUFFLERIES F1 ET SIMA DE L'ONERA par J.Leynaert	27
THE INFLUENCE OF CLOSE-COUPLED, REAR FUSELAGE MOUNTED NACELLES ON THE DESIGN OF AN ADVANCED HIGH SPEED WING by R.D.Laughner	28
AERODYNAMIC ASPECTS OF A HIGH BYPASS RATIO ENGINE INSTALLATION ON A FUSELAGE AFTERBODY by N.Voogt, J. van Hengst and J.Th. v. d.Kolk	29
UNE METHODE NUMERIQUE POUR L'ETUDE DE L'INTERACTION NACELLE-JET- VOILURE EN ECOULEMENT TRIDIMENSIONNEL NON VISQUEUX par G.LeGall, J.Bousquet et M.Yermia	30
CALCULATION OF WING-BODY-NACELLE INTERFERENCE IN SUBSONIC AND TRANSONIC POTENTIAL FLOW by K.D.Klevenhusen, H.Jakob and H.Struck	31
PREDICTION OF SUBSONIC AIRCRAFT FLOWS WITH JET EXHAUST INTERACTIONS by D.W.Roberts	32
PROP-FAN INTEGRATION AT CRUISE SPEEDS by H.R.Welge	33
Paper 34 cancelled	
AIRFRAME-PROPULSION SYSTEM AERODYNAMIC INTERFERENCE PREDICTIONS AT HIGH TRANSONIC MACH NUMBERS INCLUDING OFF-DESIGN ENGINE AIRFLOW EFFECTS by R.M.Kulfan and A.Sigalla	35

SESSION V – ROUND TABLE DISCUSSION

TRANSCRIPT OF DISCUSSION	RTD
---------------------------------	------------

PERFORMANCE OF HIGHLY INTEGRATED INLETS FOR SUPERSONIC AIRCRAFT

Lewis Surber
Air Force Wright Aeronautical Laboratories
Wright-Patterson AFB, Ohio

Jan Syberg and Joseph Koncsek
Boeing Military Airplane Company
Seattle, Washington

SUMMARY

Performance data obtained on several subsonic diffusers applicable to advanced supersonic tactical aircraft configurations have been used to select a forebody-inlet model for proof-of-concept wind tunnel performance evaluation. Three of the diffusers were designed for high aspect ratio inlets having throat aspect ratios greater than seven. A fourth design incorporated a low aspect ratio inlet. Two of the high aspect ratio diffusers and the low aspect ratio diffuser incorporated duct bends typical of inlets substantially offset from the engine centerline. Preliminary tests of the high aspect ratio diffuser produced high total pressure recovery coupled with relatively low flow distortion. Furthermore, the use of longitudinal vanes in one high aspect ratio diffuser provided reductions in engine face flow distortion with very little performance degradation. Proof-of-concept tests further investigated the performance of a high aspect ratio, side-mounted external compression supersonic inlet. Tests were performed in a 16-foot supersonic propulsion wind tunnel at Mach numbers of 1.6 to 2.2 over a -5° to 12° angle of attack range and sideslip angles from -8° to $+8^\circ$. The results of these tests support the use of high aspect ratio inlets with sharp duct bends as a viable design option in future supersonic aircraft designs.

NOMENCLATURE

A_o/A_c	Ratio of engine mass flow to mass flow based on free stream conditions and inlet capture area at $\alpha_o = 0^\circ$
D_2	Diffuser exit diameter
F_t	Feet
H_D	Height of diffuser entrance
In	Inches
L_D	Diffuser length
O_N	Diffuser offset perpendicular to plane defined by engine centerline and O_R
O_R	Diffuser offset in supersonic compression plane
P	Static pressure
psi	Pounds per square inch
P_T	Total pressure
P_{TAV}	Engine face average total pressure
P_{TMAX}	Engine face maximum total pressure
P_{TMIN}	Engine face minimum total pressure
$\Delta P/P$	Engine face flow distortion $(P_{TMAX} - P_{TMIN})/P_{TAV}$
W_o	Engine mass flow
W_c	Mass flow through inlet simulator capture area at supply-nozzle exit (includes bleed, bypass and some spillage)
W_D	Width of diffuser entrance
α_o	Angle-of-Attack
β_o	Angle-of-Sideslip

INTRODUCTION

Typical missions for future tactical aircraft will force preliminary designers to consider a broadening array of performance standards. Designing such aircraft to accomplish tactical interdiction missions against defenses of the 1990's may well require some improved combination of speed, agility and short takeoff/landing (STOL) capabilities - all at a reduced level of detectability. Combining supersonic persistence with reduced detectability would in itself necessitate careful integration of advanced technology into the airframe-propulsion system design.

The work described here has been accomplished by the Boeing Military Airplane Company in a combination of independent R&D and a program contracted with the USAF Wright Aeronautical Laboratories. As a part of this work, several airframe-inlet configurations incorporating two-dimensional external compression inlets of unconventional shapes were selected for investigation. This paper discusses the development of various air intake concepts by means of carefully devised subsonic diffuser tests and validation of the diffuser tests by means of forebody-inlet supersonic wind tunnel tests.

Concept Selection

A design study was conducted during the initial phase of the contracted effort to define a series of advanced tactical aircraft configurations with carefully integrated propulsion systems. These configurations were sized to fly an interdiction mission profile which included a high-altitude penetration at a Mach number of 2.20. Thus, all inlets considered in the present study are designed for this Mach number.

Performance and survivability analysis of a number of concepts were used to select the three configurations depicted in Figure 1 for further study. Concept 1 features high-aspect-ratio, two-dimensional, horizontal-ramp, external compression inlets mounted at the wing leading edge. The inlet diffusers are long with an offset in the horizontal plane, and the engines are buried in the fuselage near the airframe centerline. Concept 2 has two topmounted, high-aspect-ratio, horizontal-ramp inlets with long, vertically-offset diffusers. Concept 3 has two sidemounted, low-aspect-ratio, vertical-ramp inlets with relatively short and highly curved diffusers. Another unique feature of concept 3 is the swept top sideplate which extends forward of the inlet to help align the flow with the inlet during aircraft maneuvers.

DIFFUSER TEST PROGRAM

Each of the three inlet concepts described above included features that, from an aerodynamic standpoint, were new and unproven. In particular, the performance potentials of the long, curved subsonic diffusers with the high aspect-ratio entrances of concepts 1 and 2 and the relatively short, highly curved diffuser of concept 3 needed to be verified before such configurations could be considered viable options for future aircraft. An experimental program was therefore devised and conducted to evaluate the performance of subsonic diffusers representative of the three inlet configurations illustrated in Figure 1.

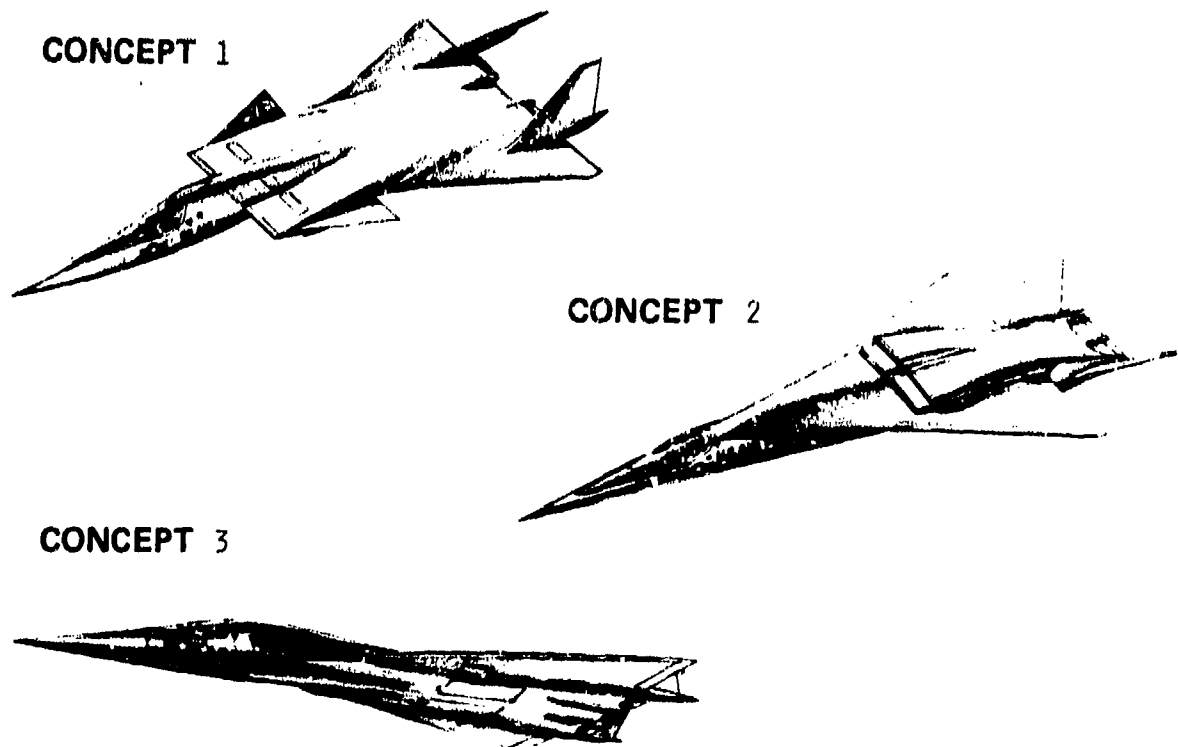
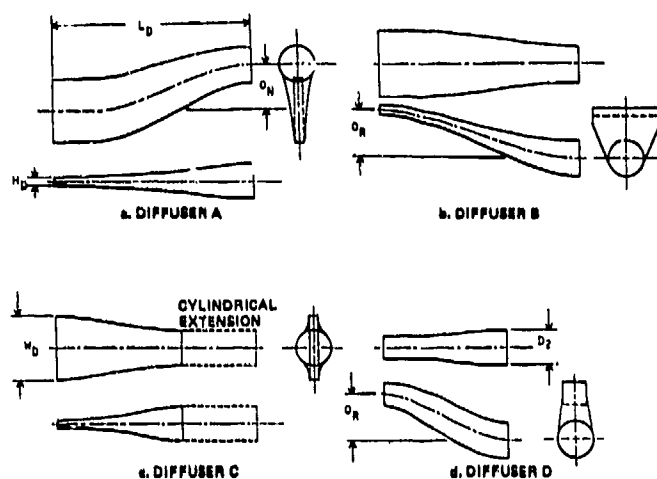


Fig. 1 Airframe-Inlet Concepts Selected for Investigation

Diffuser Test Models

Four diffuser configurations were selected for testing. These configurations are illustrated in Figure 2. Diffusers A, B, and D simulate the diffusers of inlet concepts 1, 2 and 3, respectively. Diffuser C, a short, straight duct, serves as a baseline for the high-aspect-ratio diffusers A and B. An optional cylindrical extension is provided for diffuser C such that its length can be varied from that of diffuser D to that of diffusers A and B.

The main geometric parameters of the four diffusers are shown in Table 1. All configurations have a diffuser area ratio of 1.84 (1.55 when the reduction in diffuser exit area due to the engine hub is considered).



Configuration	L_D/D_2	W_D/H_D	O_R/D_2	O_N/D_2
A	5.5	7.725	0	1.3
B	5.5	7.725	1.3	0
C	3.4	7.725	0	0
D	3.4	1.0	1.3	0

• Diffuser area ratio (without spinner) = 1.836 for all models

Fig. 2 Configurations for Aerodynamic Performance Testing

Table 1 Test Configurations

A duct geometry computer code has been used to generate diffuser contours for the entry geometry, area ratio, area progression and centerline offset design constraints associated with each diffuser. It also provides for inclusion of a section with parallel sidewalls in the forward part of the diffuser to simulate the presence of a movable aft inlet ramp. The length of this section is determined by the engine airflow characteristics and by the diffuser area progression. For the present diffusers and engine cycle, the length of this section is equal to approximately one engine face diameter. Super-elliptic cross-sectional shapes are used to transform the rectangular entrance to a circular exit such that flow separation due to rapid changes in wall slope or discontinuities in wall curvature are avoided. Computer-drawn diffuser contours are presented in Figure 3. Details of the diffuser design work are discussed in Reference 1.

To alleviate potential secondary flow problems caused by the diffuser offsets, diffusers A and D are provided with optional flow guide vanes. In diffuser A the guide vanes consist of three longitudinal vanes located just downstream of the trailing edge of the simulated aft ramp. The three vanes divide the duct into four equal-area ducts. Cruciform vanes have been used in diffuser D to guide the flow through the highly curved part of the duct. The leading edge of this set of vanes is also located just downstream of the trailing edge of the simulated aft ramp. Figure 4 illustrates the optional guide vanes.

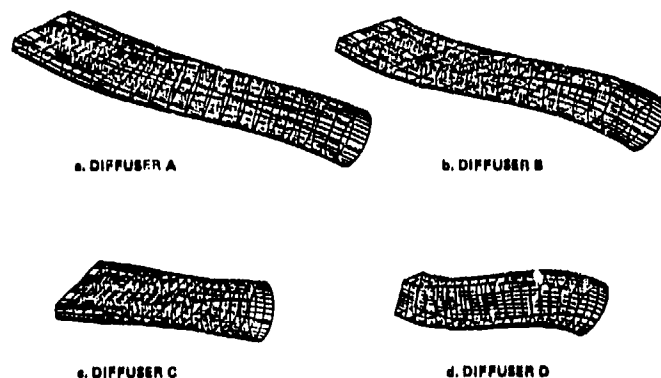


Fig. 3 Isometric Drawings of Diffusers A, B, C, and D

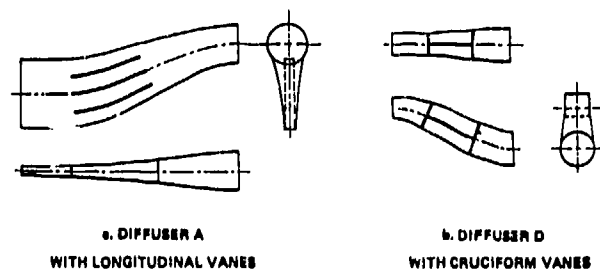


Fig. 4 Guide Vanes for Diffusers A and D

Diffuser Test Facility

Since the performance of a given diffuser is strongly influenced by its entrance flow properties, proper assessment of the performance of the above diffuser configurations necessitates provision of diffuser entrance flows representative of an external compression supersonic inlet. This has been accomplished by using the specialized test apparatus presented in Figure 5. A high-pressure plenum supplies air to a two-dimensional (2-D) nozzle which expands the flow to a uniform Mach number of 1.3. A two-dimensional "inlet simulator" section is installed just downstream of the nozzle. The inlet simulator is designed just like the lip and throat section of a 2-D external compression inlet. Critical flow features, such as the normal shock/boundary layer interaction on the ramp and the sideplates, flow spillage around the cowl lip, flow removal through the throat slot, sideplate bleed in the vicinity of the normal shock, and the flow turning through the forward part of the inlet are simulated with this test setup. Three separate vacuum lines are provided to allow individual control of normal shock position, throat slot bleed and sideplate bleed.

The test diffuser is installed just downstream of the inlet simulator as it would be on an actual inlet. Flow straighteners, flow metering devices, and a hydraulically actuated mass flow plug are connected to the downstream end of the diffuser. The only appreciable losses for an isolated two-dimensional external compression supersonic inlet at $\alpha_0 = 0^\circ$ not simulated with the test apparatus are the oblique shock losses upstream of the normal shock. Since these losses can be reasonably well predicted, the performance results from this diffuser test can be applied to an actual supersonic inlet with a higher degree of confidence than would be possible with simpler diffuser test methods. Photographs of the test apparatus are presented in Figures 6 and 7.

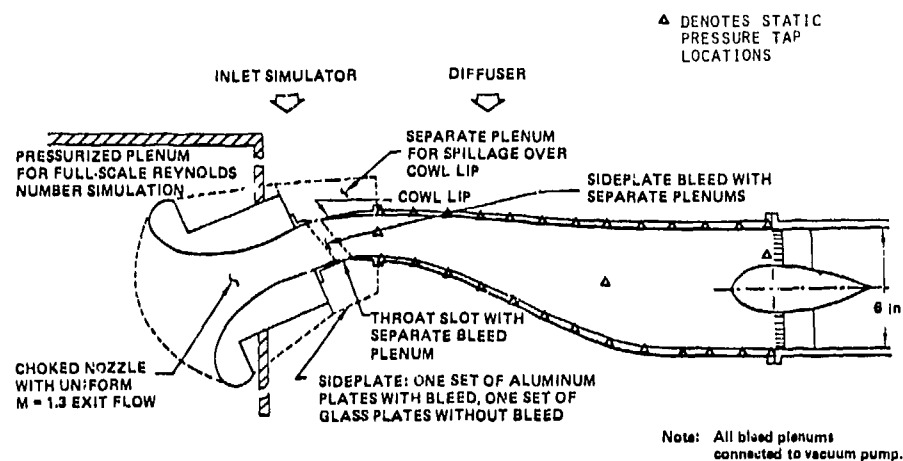


Fig. 5 Diffuser Test Apparatus

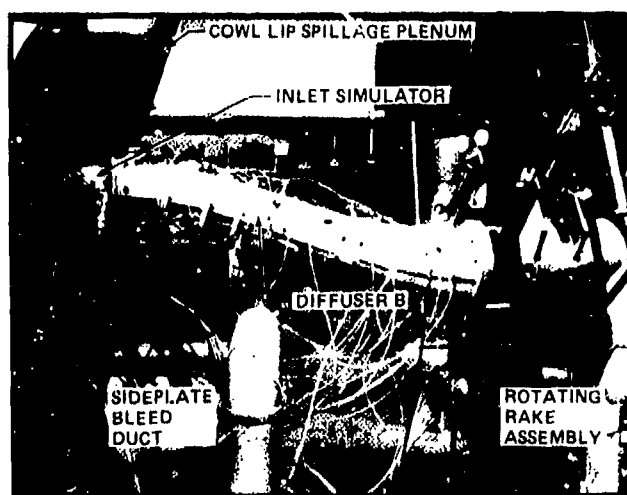


Fig. 6 High-Aspect-Ratio Diffuser B Installed Test Apparatus

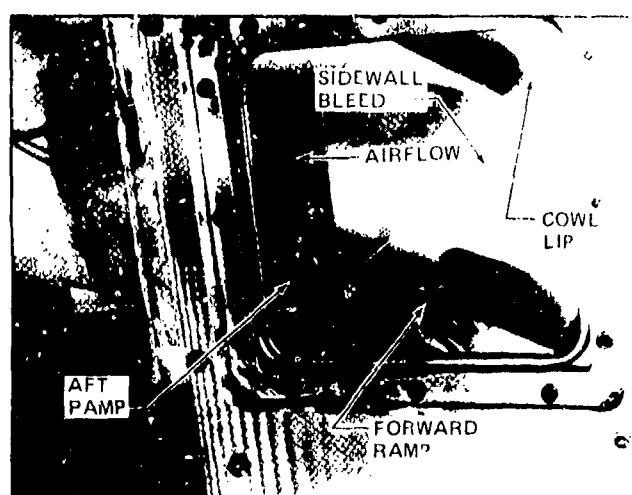


Fig. 7 Low-Aspect-Ratio Inlet Simulator

Diffuser Model Instrumentation

The inlet simulators (one for the high aspect ratio diffusers and one for the low aspect ratio diffuser) are provided with a number of static pressure taps to ensure that proper flow conditions are established in this part of the test apparatus. In addition, pressure measurements are monitored in each bleed/spillage plenum to facilitate proper inlet simulation.

Total pressure measurements are made at the diffuser entrance with a traversing probe and at the diffuser exit with a 28-probe (four rakes, seven probes per rake) rotating rake assembly. Between the entrance and exit planes, wall static pressure measurements are made using approximately 30 static pressure taps in each diffuser model.

The mass flow passing through the individual flow channels (primary duct, throat slot duct, lip spillage duct, sideplate bleed duct) are measured with standard flow meters.

Details of the instrumentation used in the diffuser test are given in Reference 2.

Diffuser Test Conditions and Procedures

The diffuser test was conducted using a supply plenum pressure of approximately 35 psf and local test site plenum temperature (approximately 500°R to 520°R). At Mach 2.2, these conditions produce an inlet Reynolds number of 4.4×10^6 (based on the model engine face diameter). This value corresponds to the Reynolds number for a full scale inlet at 60,000 ft. and Mach 2.2.

The test procedure followed during this program was to move the normal shock in small increments from a supercritical position to a subcritical position by means of the primary duct flow control plug. Figure 8 shows a shadowgraph picture of the inlet simulator taken during a typical test sequence.

At a given test condition data was typically recorded with the rotating rake in three positions. This procedure provides 84 equal-area measurements of the diffuser exit total pressure, which is sufficient to assure accurate measurement of average total pressure recovery and distortion.



a. 6.5% SUPERCRITICAL OPERATION



b. 1.5% SUBCRITICAL OPERATION

Fig. 8 Shadowgraph Pictures of Inlet Simulator Flow Conditions

Diffuser Test Results

Average total pressure recovery is plotted versus engine airflow in Figure 9 for each of the seven test configurations. Since the recovery is referenced to the supply plenum total pressure, measured losses include the normal shock losses and the additional viscous losses associated with the turning of the flow into the diffuser. In Figure 9, the "knee" on the recovery curves corresponds to the point where the normal shock starts spilling over the cowl lip. Five of the seven configurations have recovery curves that fall within a one percent band. Only the two low-aspect-ratio configurations (diffuser D with and without vanes) fall below this band. For a typical operating condition (i.e., just to the left of the "knee" in Figure 9) the throat slot and sideplate bleed flow rates were about 3.0% and 0.4% of the captured flow, respectively.

The engine face total pressure distortion, $(P_{TMAX} - P_{TMIN})/P_{TAV}$, is shown in Figure 10. All of the high-recovery configurations except diffuser C without extension have distortion values below 10%. The distortion for diffuser A with longitudinal vanes is exceptionally low, indicating that the vanes are helping to maintain uniform flow through the horizontal bend in the diffuser.

At the operating condition, the total pressure losses of offset diffusers A and B are relative to C are approximately 0.5% and 0.3% P_{T0} , respectively. An additional 0.7% P_{T0} is lost when the longitudinal vanes are installed in diffuser A but, as observed, a noteworthy improvement in compressor face distortion is obtained with this configuration. The performance of diffuser D is significantly lower than that of the high-aspect-ratio diffusers. The deficiencies of diffuser D will be discussed later.

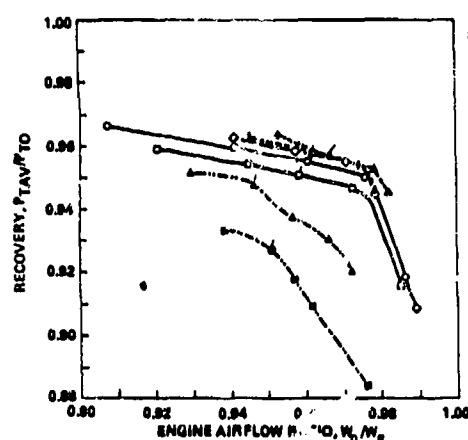


Fig. 9 Performance Summary - Recovery Versus Engine Airflow

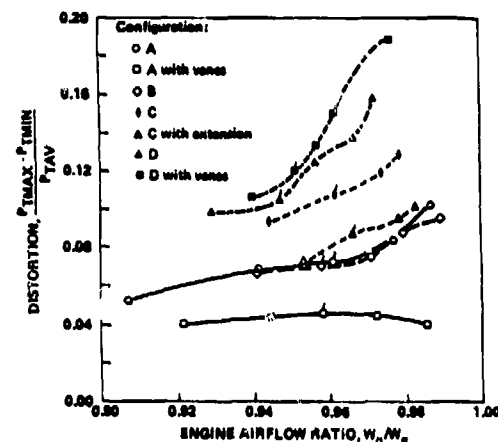


Fig. 10 Performance Summary - Distortion Versus Engine Airflow

Compressor face total pressure maps for diffuser A with and without vanes are shown in Figure 11. These data points were recorded close to a typical operating condition. The guide vanes have clearly accomplished the desired objective of reducing the distortion caused by the duct bend. The redistribution of the duct flow performed by the vanes is also evident from Figure 12, which shows the diffuser static pressure distributions. The vanes provide narrower flow channels, redistributing centrifugal forces and reducing the associated lateral static pressure differences. Therefore, the tendency for generation of large secondary flows and duct flow separation is reduced. For a more comprehensive discussion of this phenomenon, see Reference 3.

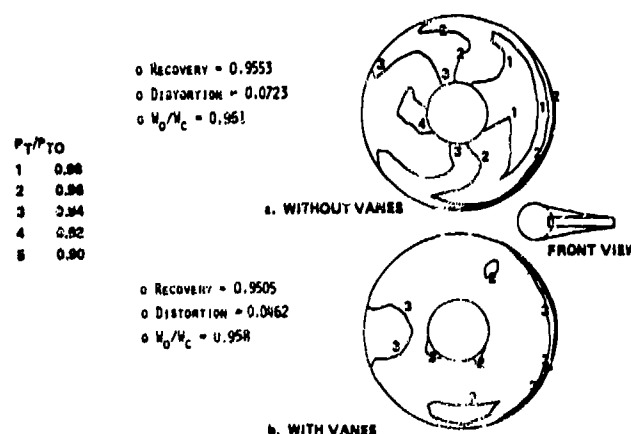


Fig. 11 Compressor Face Total Pressure Maps - Diffuser A

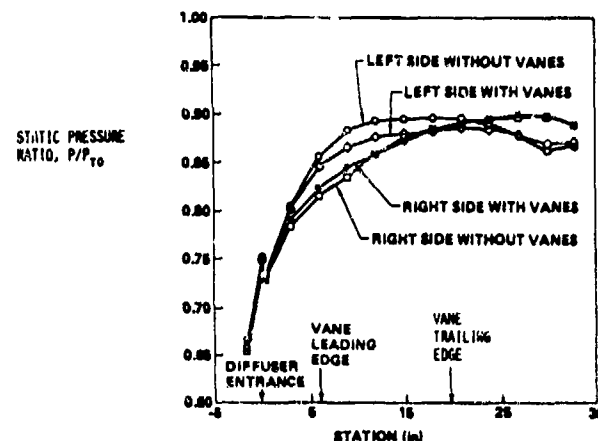


Fig. 12 Static Pressure Distribution - Diffuser A With and Without Vanes

The total pressure map for diffuser B at the operating condition is illustrated in Figure 13. As expected, the depressed total pressure region is larger on the ramp side (lower wall) of the diffuser.

Figure 14 shows typical compressor face maps for diffuser C with and without extension. The improvement in engine face distortion obtained by adding the extension is demonstrated in this figure. The total pressure gradients near the top and bottom diffusing walls have clearly been reduced.

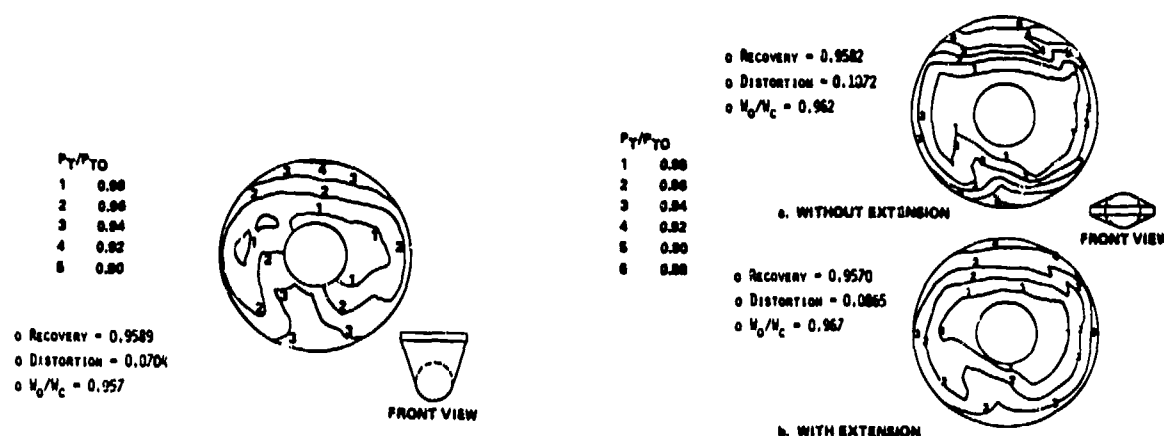


Fig. 13 Compressor Face Total Pressure Map - Diffuser B

Fig. 14 Compressor Face Total Pressure Maps - Diffuser C With and Without Extension

The compressor face maps for diffuser D are presented in Figure 15. The performance of this diffuser is significantly lower than that of the three high-aspect-ratio diffusers. A large low-pressure region is present in the bottom half of the diffuser. The length and area ratio of diffuser D are such that the pressure gradient in a corresponding straight, two-dimensional duct would be close to local boundary layer separation levels. The addition of the duct offset, with the associated secondary flows along the sidewalls, has apparently been sufficient to promote massive flow separation in the lower half of the duct. It is evident from Figure 15 that the cruciform vanes aggravate - rather than alleviate - the flow problems. These vanes are apparently introduced too far downstream in the duct where a fully three-dimensional flow field is already established. Separation off the leading edges of the vanes, due to local high angles of attack, is the probable cause of the added performance losses measured with this device. The bottom half of the duct flow is very low in energy, both with and without vanes. When the cruciform vanes are added, however, the new low energy region behind the upper vane effectively reduces the aerodynamic flow area in the top half of the duct, promoting acceleration of the remaining high energy flow in that region. This theory is supported by the static pressure profiles in Figure 16.

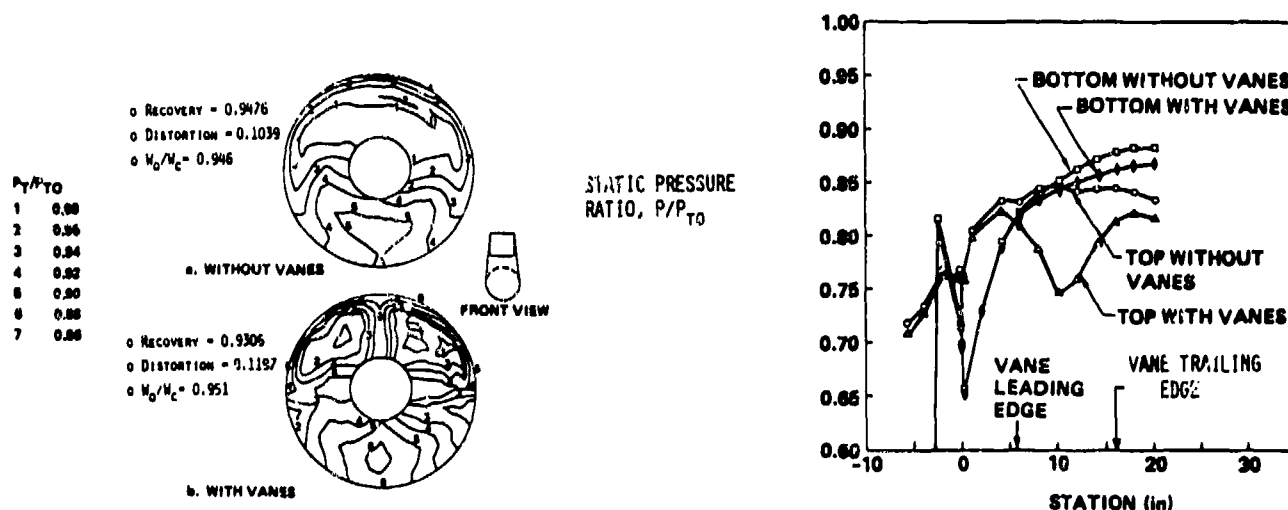


Fig. 15 Compressor Face Total Pressure Maps - Diffuser D

Fig. 16 Static Pressure Distribution - Diffuser D With and Without Vanes

INLET TEST PROGRAM

The use of relatively simple subsonic diffuser models provided a means of exploring the performance potential of a number of inlet design variations, but the weaknesses in such a test program were also recognized. It can be seen, for instance, that the test apparatus does not simulate those upstream flow field irregularities which can alter supersonic flow structure associated with the inlet compression ramps. Therefore, the question concerning validity of these preliminary direct-connect diffuser tests has been addressed by a more detailed proof-of-concept supersonic forebody-inlet wind tunnel test.

Supersonic Inlet Model

The proof-of-concept test selected for this program makes use of the Concept 1 (Figure 1) airframe-inlet configuration which incorporates diffuser A (Fig. 2). In order to reduce possible effects of model scale, the Mach 2.2 design forebody-inlet model has been designed to be tested in approximately 1/4-scale in the Arnold Engineering Development Center (AEDC) 16-Foot Propulsion Wind Tunnel (PWT). Figure 17 is a schematic illustration of the forebody-inlet model installed in the AEDC facility. The model installation provides for testing of the inlet with or without the presence of the forebody. This installation makes use of model hardware from a previous supersonic inlet investigation (References 4 and 5). Specifically, the model generated under this program makes use of primary and secondary flow metering plugs, engine face total pressure rakes, support beams and angle-of-attack sideslip mechanisms from that program. The similarity of inlet flow ranges, instrumentation and test variables invites a data comparison which is accomplished later in the paper.

The inlet itself is designed for operation up to the design Mach number of 2.2. It is a high aspect ratio, external compression two-dimensional, horizontal-ramp, side-mounted inlet. The first compression ramp is a fixed wedge, but the second and third ramps are hydraulically actuated, the second ramp being slaved to the third ramp. The aft ramp, as well, is variable, and can be actuated independently in order to vary inlet throat slot offset. Distributed bleed is provided on the inlet side walls and ramps. These regions of distributed bleed are located at shock-wave boundary layer interaction regions and, coupled with the large throat slot, are designed to control boundary layer growth and the effects of shock wave boundary layer interactions in the inlet prior to subsonic diffuser entry.

The inlet model includes configuration variations for the addition of diffuser vanes and/or cut back inlet sideplates. With the test system available at PWT and appropriate design of the model hardware, many test variations can be accomplished remotely without shutting down the tunnel. Accordingly, the ramp geometries, main inlet flow control, throat slot flow control, model angle-of-attack and model angle-of-sideslip have all been varied remotely by means of hydraulic actuators during the test program. Figure 18 is a photograph of the supersonic inlet installed in the PWT 16S (Propulsion Wind Tunnel 16-Foot Supersonic) facility.

Instrumentation in the supersonic inlet model is largely a reflection of instrumentation used in the subsonic diffuser models. Accordingly, the inlet model has extensive static pressure instrumentation on the subsonic diffuser walls. Forty total pressures are recorded at the compressor face with twelve of these probes having the capability to measure both steady state and dynamic total pressure. Thus, an estimate of compressor face turbulence can be determined for each test condition. In addition to the diffuser and compressor face instrumentation, surface static pressure measurements have been made on the supersonic compression ramps and throat pitot rakes have been used to assess uniformity of flow entering the subsonic diffuser. Details of the instrumentation used in the supersonic inlet test are given in Reference 6.

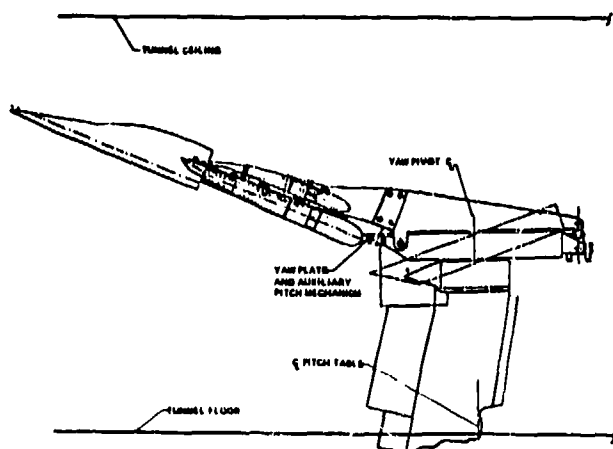


Fig. 17 Proof-of-Concept Model Installation



Fig. 18 High-Aspect-Ratio Inlet Test Installation

Testing in PWT 16S has been accomplished at Mach numbers 2.2, 2.1, 1.8 and 1.6 with angle-of-attack varying from $\alpha_0 = -5^\circ$ to $\alpha_0 = 12^\circ$ and angle-of-sideslip from $\beta_0 = -8^\circ$ to $\beta_0 = 8^\circ$ (negative β_0 indicates inlet in windward flow). Variations of compression ramp geometry, ramp and slot bleed flow and sideplate geometry have been examined both with the isolated inlet and installed with the aircraft forebody. Also, both the isolated inlet and forebody-inlet configurations have been tested with and without the installation of longitudinal vanes in the subsonic diffuser. Representative data will be presented on model configurations employing the cut-back sideplates with the best compression ramp geometry and bleed flow at Mach numbers 2.2 and 2.1.

Average total pressure recovery is plotted versus engine mass flow ratio for the isolated inlet in Figures 19 and 20 for several angles-of-attack. The inlet configuration in both of these cases incorporates a cutback sideplate, but does not make use of the longitudinal diffuser vanes. A very small difference in Mach number (Mach 2.2 in Figure 19 and Mach 2.1 in Figure 20) is seen to have a significant effect on the $\alpha_0 = 0^\circ$ inlet total pressure recovery and stable mass flow range. This Mach number effect suggests that the inlet ramp system design would require additional development for optimum Mach 2.2 performance.

Also, Figure 21 compares the Mach 2.2 $\alpha_0 = 0^\circ$ performance of the isolated proof-of-concept supersonic inlet with performance predicted from the diffuser tests. Here it is seen that the difference in pressure recovery between the two tests is significantly greater than would be accounted for by the oblique shocks necessary to decelerate the flow from Mach 2.2 to Mach 1.3 (entrance Mach number in the diffuser test). Failure to provide adequate stability margin in shock wave positioning at $\alpha_0 = 0^\circ$ apparently resulted in significantly higher shock wave losses than anticipated in the idealized case represented by the diffuser tests. Note that inlet total pressure recovery at the higher angles-of-attack is much closer to predicted levels. Figures 19, 20 and 21 indicate that pressure recovery rises or remains high up to $\alpha_0 = 4^\circ$ (representative of cruise conditions), begins to diminish at $\alpha_0 = 8^\circ$ and is sharply reduced at $\alpha_0 = 12^\circ$, as predicted. Compressor face average distortion level falls between 5% and 10% over the mass flow range for all these cases.

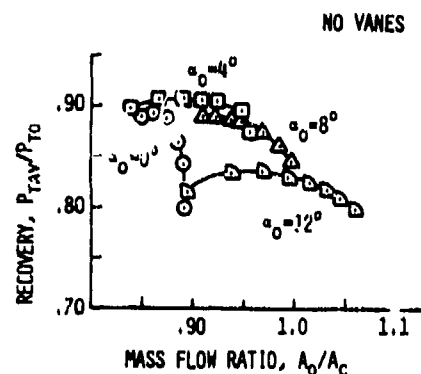


Fig. 19 Isolated Inlet Performance, $M_0 = 2.2$

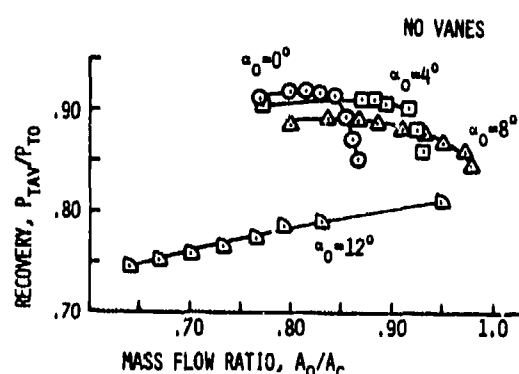


Fig. 20 Isolated Inlet Performance, $M_0 = 2.1$

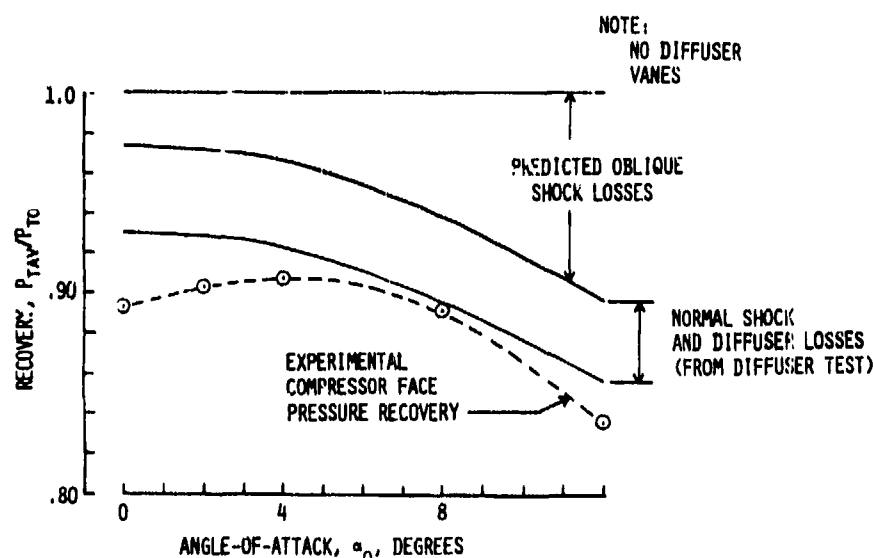


Fig. 21 Comparison of Isolated Inlet Pressure Recovery Measurements Versus Predictions

Making use of the improved $\alpha_0=0^\circ$ performance at $M_0=2.1$, Figure 22 depicts the basic pressure recovery and distortion performance of the isolated Concept 1 two-dimensional inlet with and without the incorporation of longitudinal vanes. Comparing this data with the diffuser data of Figure 10 (near the knees of both curves), it is seen that the overall level of distortion is clearly higher in the vaneless supersonic inlet ($\Delta P/P \approx 11\%$) than in the corresponding diffuser test ($\Delta P/P \approx 7\%$). In both tests, however, the vanes proved to be quite effective in distortion reduction, paying less than 1/2 percent pressure recovery for significant reductions in distortion. In the configurations with vanes, the supersonic inlet distortion ($\Delta P/P \approx 5\%$) was much closer to the comparable diffuser distortion ($\Delta P/P \approx 4\%$).

Effects of the vanes on compressor face distortion maps are seen in Figure 23. Redistribution of the flow in the diffuser with vanes has greatly reduced the level of circumferential total pressure distortion. Comparing this result with that depicted in Figure 11, it is seen that the basic characteristics of the flow improvement with addition of the diffuser vanes have been predicted adequately by the carefully devised subsonic diffuser tests.

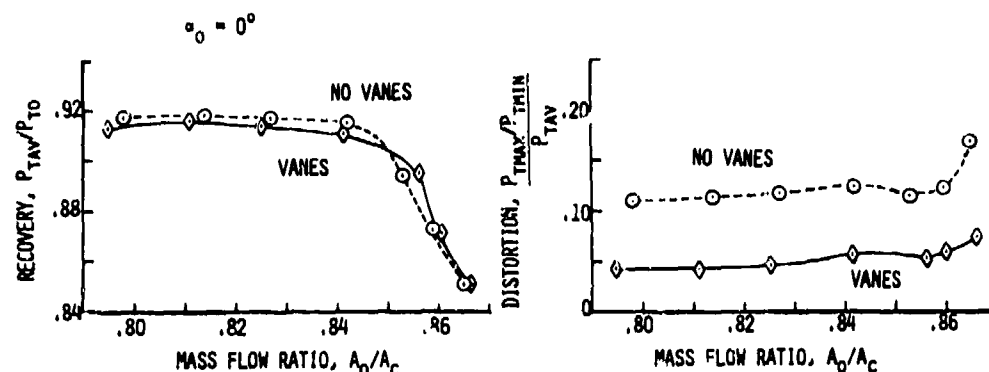


Fig. 22 Effect of Vanes on Isolated Inlet Performance, $M_0=2.1$

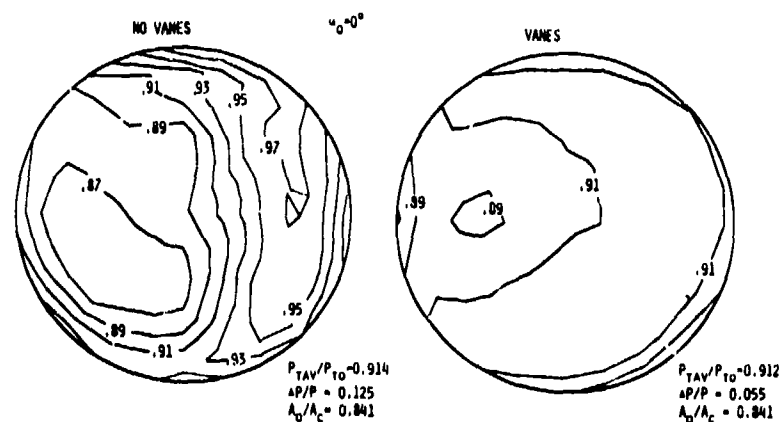
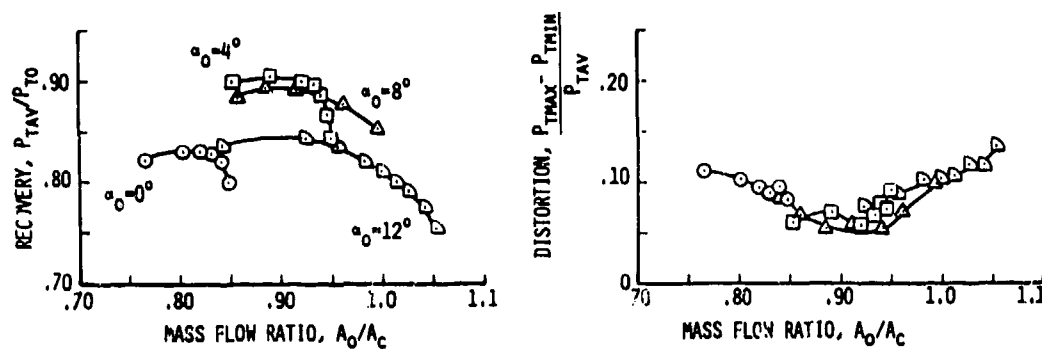
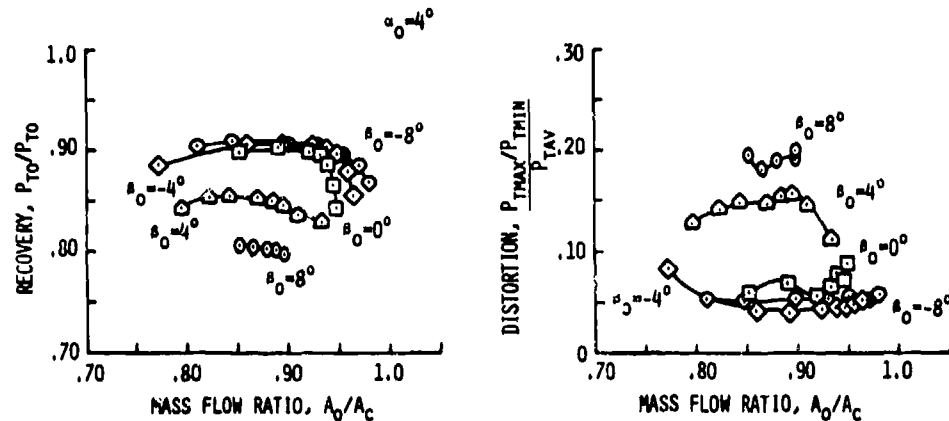


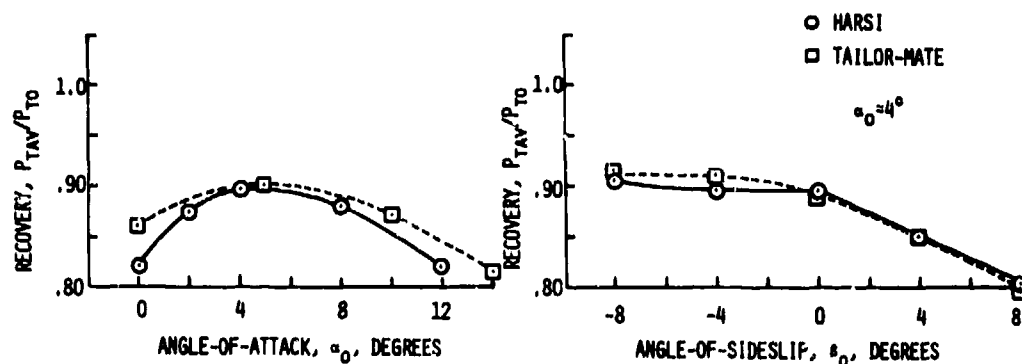
Fig. 23 Effect of Vanes on Isolated Inlet Compressor Face Maps, $M_0=2.1$

Next, the final realism factor is added by integrating the vehicle forebody with the inlet to produce a fully representative test configuration. Data shown in Figure 24 suggests a detrimental effect of the vehicle forebody presence on total pressure recovery at $\alpha_0=0^\circ$ when compared to Figure 19 (presence of vanes has little effect on pressure recovery). Normally, the vehicle forebody presence is observed to produce harmful effects at the higher angles-of-attack and at angles-of-sideslip (leeward inlet). In this case, however, the inlet pressure recovery and stable mass flow range are reduced at the lower angles-of-attack. That is, low α_0 flowfield downwash introduced by the forebody at the inlet is sufficient to alter compression ramp shock wave patterns adversely. Data from this case also reveals that the presence of the forebody is sufficient to increase inlet distortion from $\Delta P/P \approx 7\%$ (isolated) to $\Delta P/P \approx 10\%$ (forebody-inlet). The fact that total pressure recovery is not reduced at the higher angles of attack suggests that the forebody belly shape has been well designed.

Figure 25 shows performance sensitivity to angle-of-sideslip at $M_0=2.2$, $\alpha_0=4^\circ$, revealing that there is a slightly positive effect of windward (negative) sideslip, but that leeward (positive) sideslip causes a significant performance deterioration at $\beta=+4^\circ$ and what would probably be an unacceptable condition at $\beta=+8^\circ$.

Fig. 24 Effect of Angle-of-Attack on Forebody-Inlet Performance, $M_o = 2.2$ Fig. 25 Effect of Angle-of-Sideslip of Forebody-Inlet Performance, $M_o = 2.2$

While the high aspect ratio supersonic inlet (HARSI) performance fell somewhat short of expectations near the design condition (based on the diffuser tests), this is not judged to be indicative of a major development problem. Figure 26 shows a comparison of the HARSI performance with another side-mounted two-dimensional supersonic inlet from a previous investigation (References 4 and 5). In this limited comparison it is seen that the HARSI performance near cruise conditions ($2^\circ < \alpha_o < 4^\circ$) is not inconsistent with the level demonstrated by the more typical design. It is believed that there are two sources which contribute to the performance differences at low and high α_o . First, the Reference 4/5 inlet geometry allowed greater freedom to arrive at optimum ramp positions, and second, the high aspect ratio inlet may be reacting adversely to a broader range of external flow angularities entering the inlet aperture.

Fig. 26 Comparison of High-Aspect-Ratio Inlet Performance with Tailor-Mate Inlet Data, $M_o = 2.2$

CONCLUSIONS

Recent studies have indicated that geometric constraints in future supersonic tactical aircraft inlet installations may lead to the development of inlets with unconventional design features such as high or low aspect ratio apertures and long, highly curved diffusers. A unique apparatus has been used to evaluate the performance potential of such diffusers and a supersonic inlet wind tunnel test has, in turn, been used to validate the basic diffuser test results and to explore one diffuser concept in greater depth. The following conclusions are made with respect to the investigation.

1. The utility of a unique subsonic diffuser test apparatus to duplicate diffuser entrance flow conditions and provide realistic pressure recovery and flow distortion results has been demonstrated.
2. Reasonably high supersonic inlet performance has been demonstrated in a high aspect ratio two-dimensional side-mounted external compression forebody-inlet design.
3. Total pressure recovery penalties associated with long, highly curved subsonic diffusers can be small in a properly designed and integrated supersonic inlet.
4. Properly designed flow guide vanes can be effective in suppressing flow distortion in subsonic diffusers having high aspect ratio entrances without significant pressure recovery loss.
5. Precise design of supersonic inlet compression ramps and variable geometry systems to provide for adequate stability margin in shock wave positioning at the design condition is critical to the generation of high inlet performance.

REFERENCES

1. Koncsek, J. L., "An Approach to Conformal Inlet Diffuser Design for Integrated Propulsion Systems", Paper given at AIAA 17th Joint Propulsion Conference, Colorado Springs, Colorado, 27-29 July 1981.
2. Koncsek, J. L., "Test and Evaluation Report, Aerodynamic Performance Tests. Task 2.2 USAF Contract No. F33615-79-C-3013", D180-25396-8, May 1980.
3. Miller, Donald Stuart, Internal Flow Systems, BHRA Fluid Engineering, 290 pp. (1978).
4. Richey, G. K., Surber, L. E., & Laughrey, J. A., "Airframe/Propulsion Systems Flow Field Interference and the Effect of Air Intake and Exhaust Nozzle Performance", AGARD-CP-150, Paper No. 23, Airframe/Propulsion Interference, September 1974.
5. Surber, L. E., "Effect of Forebody Shape and Shielding Technique on 2-D Supersonic Inlet Performance", AIAA Paper No. 75-1183, September 1975.
6. Syberg, J., "Test and Evaluation Report, First Proof-of-Concept Wind Tunnel Test. Task 3.2 USAF Contract No. F33615-79-C-3013", D180-25396-11, December 1980.

**TOP-MOUNTED INLET SYSTEM FEASIBILITY FOR
TRANSONIC-SUPERSONIC FIGHTER AIRCRAFT APPLICATIONS**

T.L. Williams and B.L. Hunt

Northrop Corporation, Aircraft Division
One Northrop Avenue
Hawthorne, California 90250, USA

D.B. Smeltzer and W.P. Nalms

NASA Ames Research Center
Moffett Field, California 94035, USA

SUMMARY

Top inlet flow field and engine-inlet performance data for an advanced fighter aircraft configuration were obtained over the Mach 0.6 to 2.0 range. These studies not only provided extensive data for the baseline arrangement, but also evaluated the effects of key aircraft configuration variables - inlet location, canopy-dorsal integration, wing leading-edge extension (LEX) planform area, and variable incidence canards - on top inlet performance. In order to set these data in the context of practical aircraft systems top inlet performance is compared with that of more conventional inlet/airframe integration.

The results of these evaluations show that, for the top inlet configuration tested, relatively good inlet performance and compatibility characteristics are maintained during subsonic and transonic maneuver. However, at supersonic speeds, flow expansion over the forebody and wings causes an increase in local inlet Mach number which subsequently reduces inlet performance levels. These characteristics infer that although top inlet may not pose a viable design option for aircraft requiring a high-degree of supersonic maneuverability, they have distinct promise for vehicles with subsonic and transonic maneuver capabilities.

NOMENCLATURE

AZ	Wing aspect ratio	\bar{P}_{T2}	Average total pressure at engine compressor face
FRP	Fuselage reference plane	ΔP_{T2}	Maximum total pressure variation at Engine compressor face
FS	Fuselage station (inches)	\bar{P}_{TRMS}	Average root-mean-square of total pressure fluctuation (turbulence)
IDC	Engine fan instantaneous circumferential distortion index	α	Angle of attack
IDC _{limit}	Maximum allowable instantaneous circumferential distortion index for a typical low-bypass fighter aircraft engine	β	Angle of sideslip
M_L	Local inlet Mach number	δ_c	Canard deflection angle
M_0	Free-stream Mach number	δ_f	Trailing-edge flap angle
\bar{P}_{T1}	Average total pressure at inlet highlight	δ_n	Leading-edge flap angle
ΔP_{T1}	Maximum total pressure variation at inlet highlight	Λ	Leading-edge sweep angle
		Γ	Dihedral angle

1.0 INTRODUCTION

Recent advanced fighter aircraft technology studies have shown that mounting the engine-inlet above the fuselage can afford a variety of potential advantages relative to more conventional inlet locations. These advantages include:

- Unobstructed lower-fuselage for weapons integration (inlet isolated from weapons, thereby eliminating engine-inlet compatibility problems during weapons carriage and delivery)
- Virtual elimination of hot gas reingestion problem associated with VSTOL aircraft
- Reduced incidence of engine foreign object damage (FOD) problems during takeoff and landing
- Superior ground-level access to most aircraft sub-systems
- Reduced aircraft structural weight due to characteristically short inlet duct length
- Reduced frontal aspect radar cross-section (RCS) due to the inherent forebody/wing shielding of the inlet system from low-altitude and ground-based radars.

Despite this attractive list of advantages, top inlet systems have not yet been applied to production fighter aircraft, primarily because of concerns over inlet flow field quality at angle of attack. However, several recent experimental studies (References 1-5) have shown that the upper-fuselage region poses a potentially favorable inlet location for fighter aircraft configurations employing vortex lift enhancement. This is due to the action of the strong, counter-rotating vortex pair produced by the wing leading-edge extensions (LEX's) which effectively inhibits upper-fuselage flow separation. These vortices inhibit separation by entraining high-energy free-stream air into the upper-fuselage region and sweeping low-energy boundary layer air outwards.

Past top inlet studies have been limited to subsonic flow field and engine-inlet performance evaluations (References 1, 2 and 3) and transonic and supersonic upper-fuselage flow field surveys (References 4 and 5). These programs have established a valuable initial data base, but have left a need for inlet performance measurements at higher speeds to provide a firmer data base for aircraft design studies. In addition, previous work has identified several potential problem areas on which further information is needed. First, ingestion of wake flow from the canopy can occur, so that the integration of the canopy with the fuselage appears to be important to top inlet performance. Second, sharply degraded inlet performance can be produced by ingestion of vortex flow into the inlet, either because of vortex bursting or because, in sideslip, the vortex migrates into the inlet. Third, at supersonic flight speeds, expansion of the flow field over the forebody and wings at angle of attack produces local elevations in Mach number and consequent increases in inlet shock losses. The objectives of the study reported on herein are to meet the need for high-speed performance data and to shed further light on the known problem areas.

The test program on which this paper reports was conducted under contract by Northrop Corporation to NASA's Ames Research Center and the David Taylor Naval Ship Research and Development Center*. Top inlet flow field and engine-inlet performance data were obtained for an advanced top-inlet fighter aircraft configuration over the Mach 0.6 to 2.0 range and for angles of attack and sideslip up to 27° and 12°, respectively. In addition to extensive evaluation of the baseline configuration performance characteristics, these tests also investigated the influence of several key aircraft configuration variables.

This paper provides a summary and evaluation of significant test results from this program and, in addition, compares selected top inlet performance data with those of more conventional inlet/airframe arrangements.

2.0 TEST PROGRAM

2.1 Test Vehicle

Top inlet performance evaluations were conducted utilizing a 0.095-scale model based on Northrop's Vertical Attitude Takeoff and Landing (VATOL) configuration. This vehicle, depicted in Figure 1, was designed as an advanced, supersonic, air-to-air fighter with operational capability from ship-board platforms. The vehicle is launched and retrieved utilizing an unusual tail-sitting takeoff and landing procedure from a vertical platform. This launch and retrieval technique imposed special constraints on the design of the inlet which ultimately played a major role in the selection of a top inlet configuration. The inlet employed on this configuration is a two-dimensional fixed geometry design with a 7° external compression ramp, and was sized for shock-on-lip at Mach 2.0. The wing is a clipped delta planform with a 50° leading-edge sweep angle and includes an integral wing leading-edge extension (LEX). Further details concerning the design of this configuration may be obtained in Reference 6.



FIGURE 1. VATOL 0.095-SCALE INLET PERFORMANCE MODEL

* NASA Study Contract NAS2-10584, "Study of Top Inlet Technology"

The subsonic diffuser utilized in the inlet/airframe performance model was modified from the original VATOL design to enable fore and aft movement of the inlet. By eliminating almost all diffuser offset in the diffusion plane (profile view), as is shown in Figure 2, the entire inlet assembly, consisting of the inlet, diffuser and mass flow control plug assemblies, could be positioned at any one of three predetermined locations. Although duct offset was not accurately simulated, other diffuser parameters such as duct aspect ratio and diffusion ratio were retained relative to the initial VATOL design. Inlet mass flow was regulated through the use of two remotely controlled plugs located in the duct exits (see Figure 2).

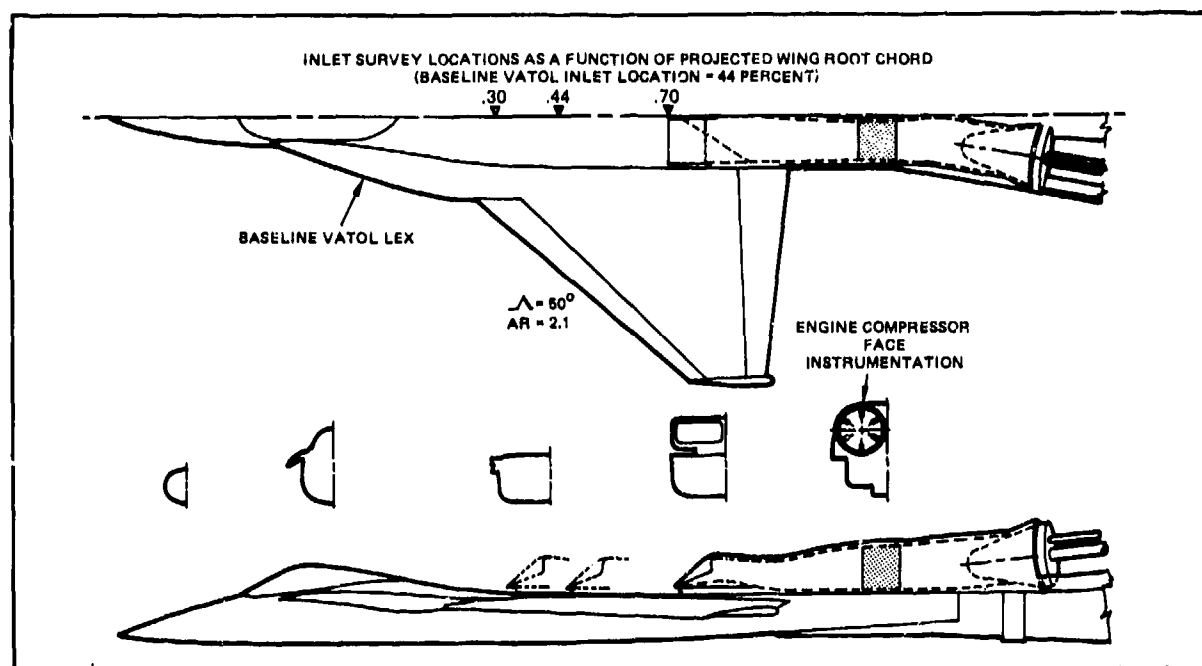


FIGURE 2. VATOL INLET/AIRFRAME PERFORMANCE MODEL LAYOUT

The model was also designed to enable evaluation of the effects of other key aircraft configuration variables, in addition to inlet location, on top inlet performance. Details concerning these configuration options, which included changes in canopy-dorsal integration, wing leading-edge extension (LEX) planform area variations, and replacement of the LEX by a variable incidence canard, are given in Section 3.2.

2.2 Instrumentation

The model was instrumented to enable evaluation of the ingested inlet flow field and engine-inlet performance parameters. Flow field instrumentation spanned both the left and right inlets systems and was located immediately upstream of the compression ramp leading-edge, as is shown in Figure 3. This instrumentation package included an array of pitot and 5-hole cone probes from which local inlet flow field parameters including total pressure, Mach number, and flow angularity were determined. To eliminate interference effects during acquisition of engine-inlet performance data the entire inlet flow field rake assembly was removeable. Unfortunately, cone probe flow angularity and Mach number data were not available at the time of printing of this paper; however, cone probe pitot pressure measurements are included in the flow field total pressure data presented herein.

Determination of engine-inlet performance parameters over the Mach 0.6 to 2.0 range required the use of two different instrumentation systems, one applicable to the subsonic and transonic range and another for supersonic speeds. For free-stream Mach numbers less than 1.4, inlet performance parameters were evaluated at the engine compressor face station (see Figure 2). Due to the small scale of the model [7.3cm (2.9in) compressor face diameter] instrumentation at the engine face was limited to 12 total head pressure probes, 6 "Kulite" transducers (capable of measuring both steady-state and dynamic pressures), and 4 wall static taps. This arrangement can be seen in Figure 4. The 18 probes were mounted in 3 circumferential rings, each containing 6 probes. The spacing corresponded to the centroids of equal areas. This instrumentation package enabled evaluation of inlet total pressure recovery, steady-state distortion, and turbulence.

At supersonic speeds above Mach 1.4, evaluation of inlet performance characteristics at the engine compressor face posed a problem. The small scale of the model did not allow for incorporation of an active boundary layer control system. Thus, there was no means of controlling the shock induced boundary layer separation which results from the interaction of the inlet terminal shock and ramp boundary layer. Inlet performance parameters measured at the engine compressor face are thus masked by the resulting separation region. To counteract this problem "quasi" inlet performance parameters were measured at the inlet entrance plane using a "clipped-cowl" inlet, shown in Figure 5. The rationale behind this arrangement is as follows: Clipping the inlet cowl moves the terminal shock downstream of the true inlet lip location. An array of pitot probes can then be mounted in the inlet entrance plane, upstream of the terminal shock and the resultant separation region. The probes give readings of local pitot pressure which are assumed equal to the corresponding total pressures at the true inlet face. Hence, the mean total pressure recovery and steady-state distortion levels at the

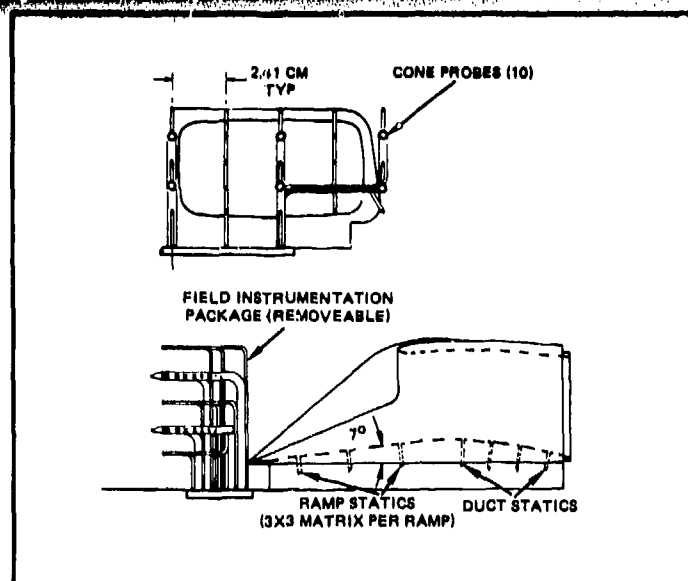


FIGURE 3. EXTERNAL FLOW FIELD INSTRUMENTATION

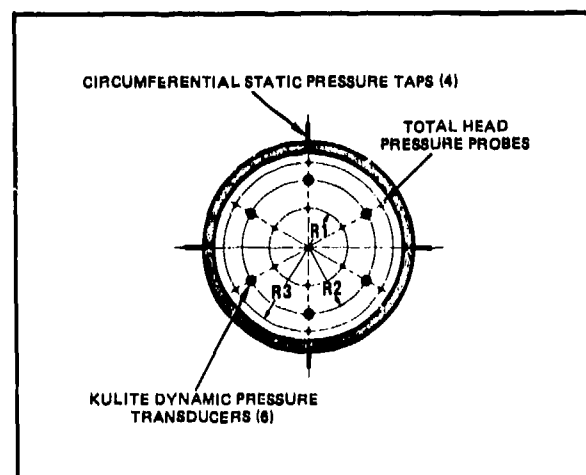


FIGURE 4. ENGINE COMPRESSOR-FACE INSTRUMENTATION

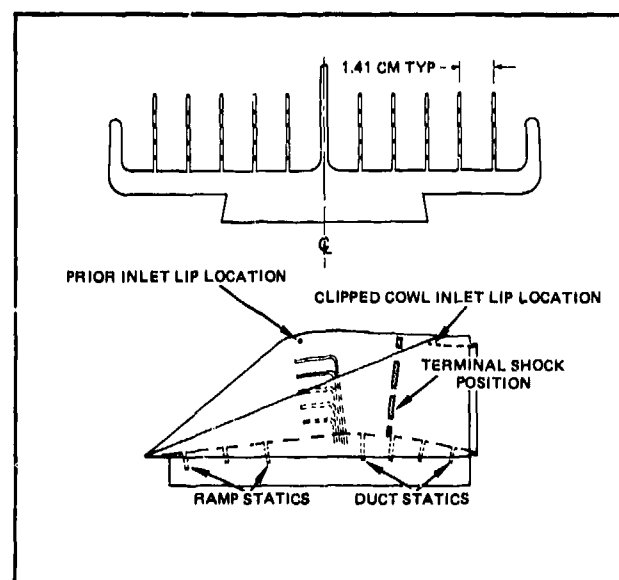


FIGURE 5. CLIPPED COWL INLET SYSTEM

inlet entrance plane can be determined. Diffuser loss characteristics can then be used to estimate the mean compressor face total pressure recovery levels.

The inlet was also instrumented with surface static pressure taps on the ramp and along the upper- and lower-centerlines of the duct for diagnostic purposes (see Figure 5).

2.3 Test Particulars

Top inlet flow field and engine-inlet performance evaluations were conducted in the 11-Foot (3.4m) Transonic and 9-by 7-Foot (2.7m x 2.1m) Supersonic Unitary Plan Wind Tunnel Facilities at NASA's Ames Research Center.

Testing in the 11-Foot Wind Tunnel was conducted at the primary test Mach numbers of 0.6, 0.9 and 1.2 at a fixed Reynolds number of $9.8 \times 10^6/m$ ($3 \times 10^6/ft$). Maximum angle of attack was limited to 27° by sting divergence criteria. The support system enabled survey of a $\pm 15^\circ$ circular angle of attack and sideslip envelope, which was centered at 12.5° angle of attack and 0° sideslip. This gave an angle of attack capability -3° to 27° at zero sideslip and correspondingly reduced ranges of angle of attack at non-zero sideslip angles. Testing was conducted at fixed sideslip angles of 0° , 4° , 8° and 12° . Limited testing was also conducted at negative sideslip angles to determine the effect of possible model asymmetries on inlet performance. The test envelope surveyed can be seen by looking ahead to Figure 14.

In the 9-by 7-Foot Wind Tunnel, the primary test Mach numbers were 1.6 and 2.0, again at a Reynolds number of $9.8 \times 10^6/m$ ($3 \times 10^6/ft$). An angle of attack range of -4° to 15° was surveyed at fixed sideslip angles of 0° , 4° and 8° .

In both tunnels, the influence of inlet mass flow ratio on inlet performance was examined at predetermined angle of attack and sideslip conditions, however, all data presented in this paper are for the maximum engine airflow condition. To ensure turbulent boundary layers on the model, transition strips were fixed to the aircraft nose, wing leading-edges, and canard leading-edges during all testing.

3.0 DISCUSSION OF RESULTS

The following sections present and discuss some of the more significant results from this test program. First, selected results obtained for the baseline configuration will be described. Then, in Section 3.2, the influence of certain configuration variables on inlet performance will be considered. Finally, in Section 3.3, the inlet performance characteristics obtained for the baseline configuration are compared to those of more conventional inlet installations.

3.1 Baseline Configuration Inlet Performance Characteristics

Screening tests were initially conducted to determine the impact of inlet location on engine-inlet performance, and to aid in the selection of a baseline inlet arrangement for future comparative purposes. The results of these tests, however, showed little discernable difference in inlet performance as a function of inlet location over the entire test envelope surveyed. In the absence of any decided preference, based on engine-inlet performance data, the mid-inlet location was selected as the baseline arrangement since it corresponded with the VATOL inlet design location. Similar screening tests were also conducted to assess the influence of leading-edge flap deflections ($0^\circ \leq \alpha \leq 30^\circ$) on inlet performance. Test data showed that only marginal improvements in inlet performance were obtained with leading-edge flaps deployed, thus for all ensuing performance evaluations the zero degree leading-edge flap setting was used. In addition to incorporating a mid-inlet arrangement and zero degree leading-edge flaps, the baseline configuration as defined employed the baseline VATOL LEX, shown in Figure 2, and was tested with trailing-edge flaps undeflected.

Performance characteristics associated with the VATOL inlet/airframe model diffuser system were evaluated during subsonic and transonic wind tunnel testing. The results of these studies show that there is a marked thickening of the boundary layer along the upper- and lower-centerlines of the duct, which adversely effects inlet recovery and distortion. Surface static pressure instrumentation located along the upper-centerline of the duct indicates that this growth is not attributable to boundary layer separation, but rather to the adverse pressure gradient created by the high local wall angles (7° maximum diffuser half-angle as opposed to accepted optimum value for an ideal diffuser of 2.5° to 3.5°). Conversely, surface static pressure instrumentation along the lower-centerline of the duct indicates that there may be a zone of separation and re-attachment immediately downstream of the inlet throat (high turning region shown in Figure 3). Comparison of these data with Northrop experimental data for a similar top inlet diffuser with offset indicates, that VATOL inlet performance levels could have been improved by 0.5 to 0.8 percent had the model diffuser design not been constrained by a fore and aft movement requirement.

3.1.1 Subsonic-Transonic Performance

Subsonic and transonic inlet performance characteristics for the baseline arrangement are presented in Figure 6 in terms of average total pressure recovery, distortion, and turbulence, which is a measure of the total pressure fluctuation. Each of these parameters is presented as a function of angle of attack at zero sideslip for Mach 0.6, 0.9, and 1.2. In addition to the typical maximum minus minimum total pressure, steady-state distortion parameter ($\Delta P_{T2}/P_{T2}$), an estimate of maximum instantaneous fan distortion has been provided to enable a preliminary assessment of engine-inlet compatibility. The instantaneous distortion parameter presented (IDC/IDC_{limit}) is an estimate, based on steady state distortion and root-mean-square turbulence data, of the maximum instantaneous circumferential fan distortion normalized by a representative maximum allowable (limiting) value for a typical low-bypass ratio fighter aircraft engine (this value has not been quoted due to its proprietary nature).

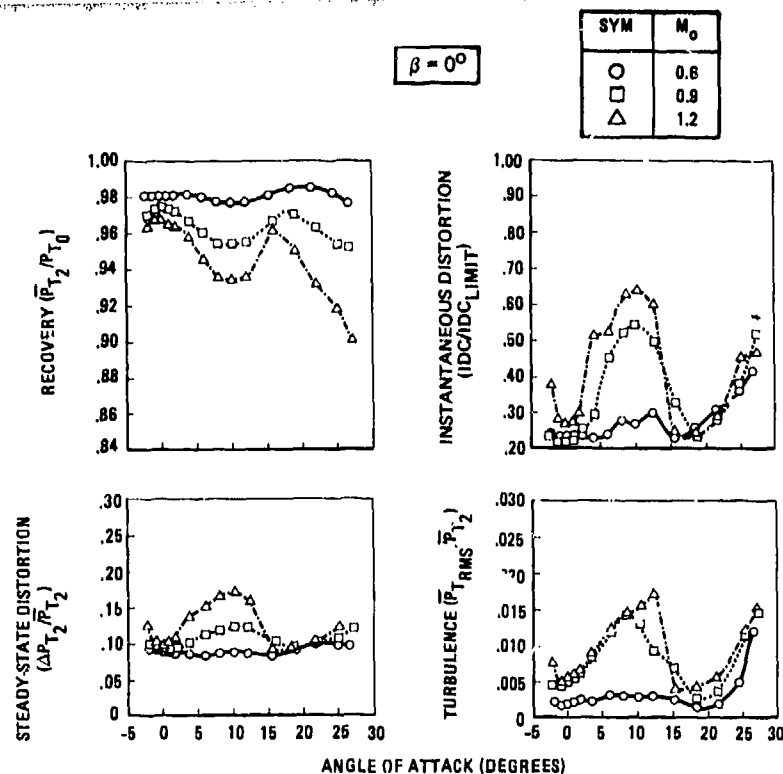


FIGURE 6 SUBSONIC AND TRANSONIC INLET PERFORMANCE CHARACTERISTICS AT ANGLE OF ATTACK ($\beta = 0^\circ$)

It can be seen from Figure 6 that in the lg level flight domain, $1^\circ < \alpha < 3^\circ$, the top inlet system exhibits high total pressure recovery levels, notwithstanding decreases in performance with increasing Mach number. These decreases in performance with Mach number, at low to moderate angles of attack, are attributable to increased incidence of canopy-dorsal separation. This highlights the importance of careful canopy-dorsal integration for top-mounted inlet installations. As angle of attack is increased from 0° to 10° a general deterioration in inlet recovery, distortion, and turbulence is experienced, independent of Mach number. This performance degradation is not the result of increased canopy-dorsal separation, but rather is traceable to ingestion of low-energy flow emanating from the juncture of the wing leading-edge extension and forebody. This is illustrated in Figure 7, where Mach 0.9 inlet flow field total pressure contours are presented in conjunction with corresponding water tunnel flow visualization photographs for a similar top inlet configuration. In fact, Figure 7 shows that at 10° angle of attack the wake shed from the canopy-dorsal is no longer evident, due to the entrainment action of the LEX vortex system. Above 10° angle of attack, a general improvement in inlet performance is noted to levels near those obtained at 0° angle of attack. This effect is ascribed to the increased sweeping action of the LEX vortex with angle of attack, which entrains the low-energy, LEX/body juncture flow out of the inlet flow field. Improvements in recovery are realized until α exceeds 15° to 20° , dependent on free-stream Mach number. Above this angle of attack range there is a reduction in inlet recovery accompanied by increases in distortion and turbulence. This is caused by the movement of the LEX vortex system burst point ahead of the inlet entrance plane. The burst phenomenon on described results in a rapid expansion in the diameter of the low-energy turbulent core of the vortex, which is subsequently ingested by the inlet (see Figure 7, $\alpha = 27^\circ$). It can also be seen in Figure 6 that the burst point moves ahead of the inlet at progressively lower angles of attack with increasing Mach number. This phenomenon is believed to be attributable to changes in the strength of the wing leading-edge vortex system and the magnitude of the LEX/body juncture low-pressure region with Mach number. As Mach number increases the wing leading-edge vortex system strength decreases, while the magnitude of LEX/body juncture flow region increases, thus having a resultant destabilizing action on the wing LEX vortices.

In sideslip, the top-mounted inlet system exhibits performance trends which are diametrically opposed to those of most conventional twin-inlet installations for low to moderate angles of sideslip ($\beta < 12^\circ$). For top-mounted inlet installations, as is shown in Figure 8, it is the windward inlet which experiences the most noticeable degradation in inlet performance. Although Figure 8 presents data only for the Mach 0.9 condition, the trends shown are indicative of those exhibited over the entire Mach 0.6 to 1.2 test envelope.

The leeward inlet initially experiences an improvement in recovery and distortion characteristics, over most of the positive angle of attack spectrum, at low sideslip angles ($\beta = 4^\circ$). This improvement is due to migration of the LEX/body wake out of the inlet flow field, as is illustrated in the total pressure contours of Figure 9. At higher sideslip angles, leeward inlet performance deteriorates as a result of ingestion of low-energy flow from the windward LEX/body juncture. Only a small amount of this low-energy flow is ingested at 8° sideslip, whereas at 12° the entirety of the low-pressure region is ingested, thus accounting for the marked differences in performance shown. The dramatic improvement in inlet performance which occurs at 12° sideslip and 21° angle of attack, shown in Figure 8, is believed attributable to the favorable influence of the LEX vortex entrainment mechanism.

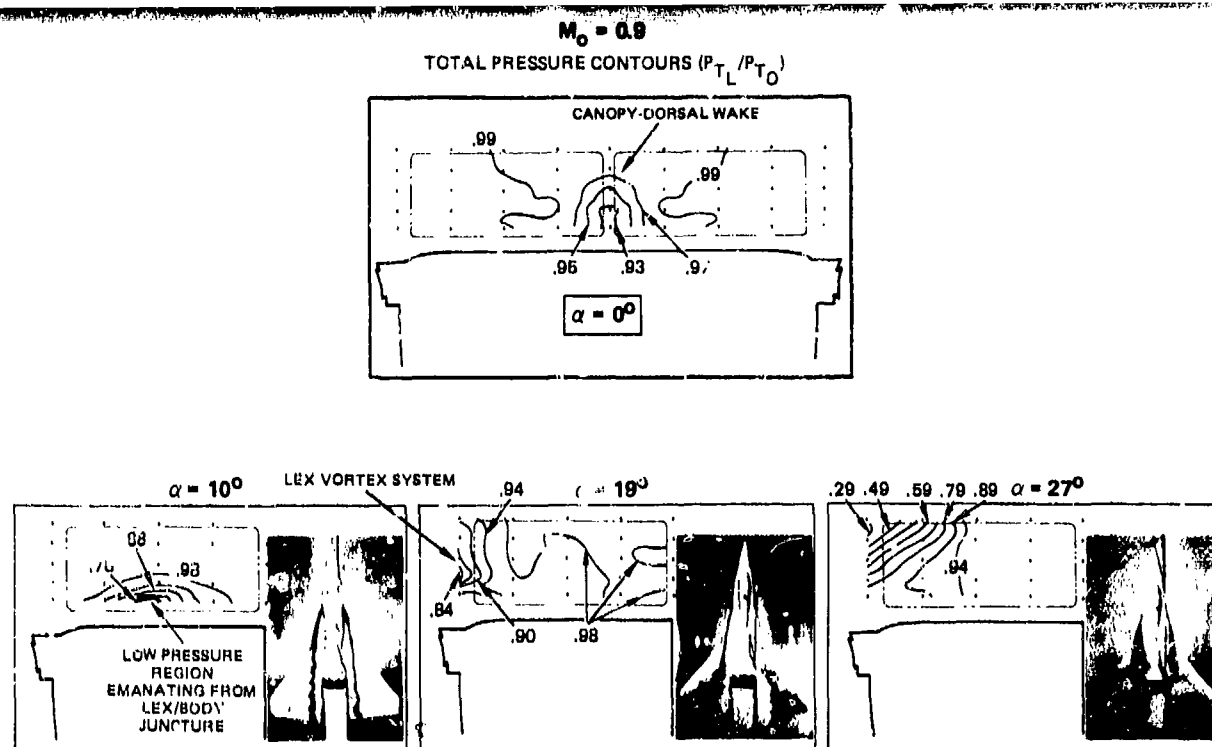


FIGURE 7. TRANSONIC INGESTED INLET FLOW FIELD CHARACTERISTICS AS A FUNCTION OF ANGLE OF ATTACK ($\beta = 0^\circ$)

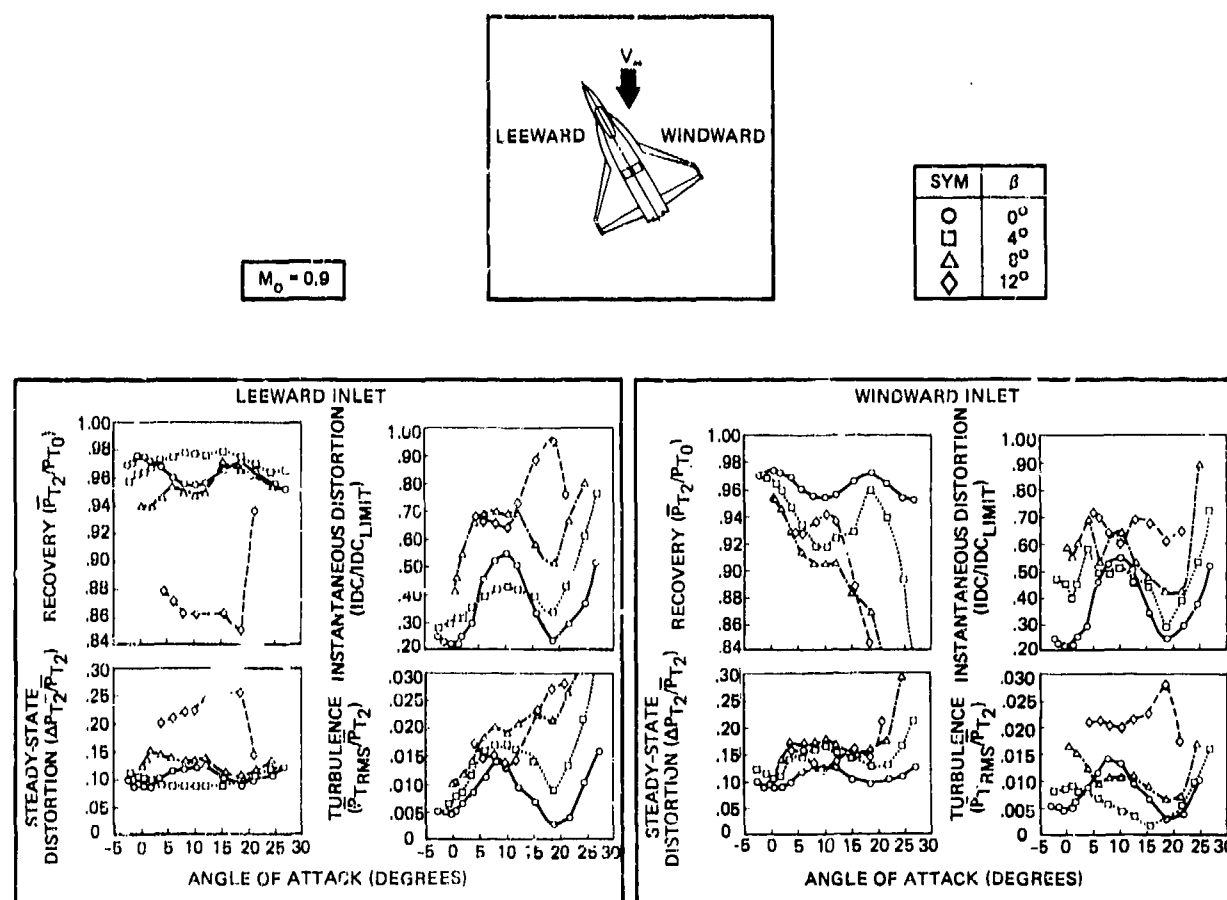


FIGURE 8. EFFECT OF SIDESLIP ON TRANSONIC INLET PERFORMANCE ($M_0 = 0.9$)

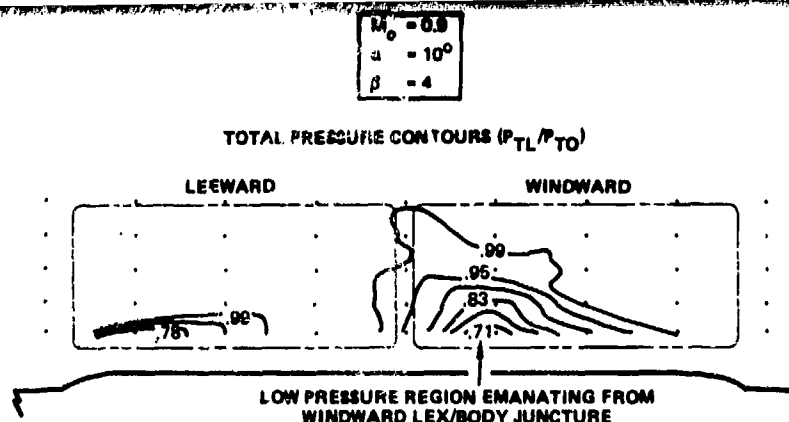


FIGURE 9. IMPACT OF SIDESLIP ON INGESTED INLET FLOW FIELD

In general, windward inlet performance decreases with increasing sideslip. This can be related to increased low-energy flow buildup from the windward LEX/body juncture at low angles of attack, and to migration of the windward LEX vortex system into the inlet flow field at higher angles of attack. An anomaly in this trend is exhibited at 12° sideslip. At this angle, low-pressure flow from the windward LEX/body juncture migrates out of the windward inlet flow field, thereby explaining the improvement in performance observed in Figure 8, relative to the 8° sideslip condition, at low to moderate angles of attack.

3.1.2 Supersonic Characteristics

During supersonic testing, ingested inlet flow field quantities were again evaluated, however, as commented in Section 2.2 "quasi" inlet performance parameters were measured at the inlet entrance plane. The inlet aperture total pressure data were used to estimate average compressor face recovery levels (P_{T2}/P_{T0})_{EST} and to determine steady-state, maximum minus minimum, distortion levels ($\Delta P_{T1}/P_{T1}$) measured at the inlet entrance plane. Estimated compressor face recovery levels were obtained by subtracting an allowance for the diffuser losses from the measured inlet aperture recovery levels. The total pressure loss attributed to the diffuser was 1.9 percent; this value was computed from subsonic test data for the baseline configuration. No attempt was made to estimate compressor face distortion levels from the inlet aperture data as the impact of the diffuser on distortion varies (it can increase or decrease distortion) dependent on the inlet entrance profile.

Values of estimated recovery and measured distortion are presented in Figure 10 as a function of angle of attack at zero sideslip for Mach 1.6 and 2.0. A comparison of the estimated recovery levels in Figure 10 with corresponding transonic values in Figure 6 shows the same initial fall in recovery levels but without the leveling off and subsequent increase seen above 10° at transonic speeds. A direct cause of this difference in behavior is the larger scale and reduced pressures of the low-energy region generated by the LEX/body juncture at supersonic speeds as compared to transonic speeds. This effect can be seen by comparing the pitot pressure contours of Figure 11, which are for Mach 2.0 and 10° angle of attack, with the 10° angle of attack, Mach 0.9 total pressure contours of Figure 7. It can be seen that based on the pitot pressure contours at Mach 2.0 the low-energy region from the LEX/body juncture is more extensive and contains lower total pressures in Figure 11 than in Figure 7. This is reflected in the inlet aperture (total pressure) distortion values presented in Figure 10, which show a marked increase with angle of attack. The reason for this increased effect of flow from the LEX/body juncture is believed to be due to a loss in strength and effectiveness of the LEX vortices at supersonic speeds. Such a loss in strength at supersonic speeds is characteristic of leading-edge vortices, as is discussed in (Reference 7).

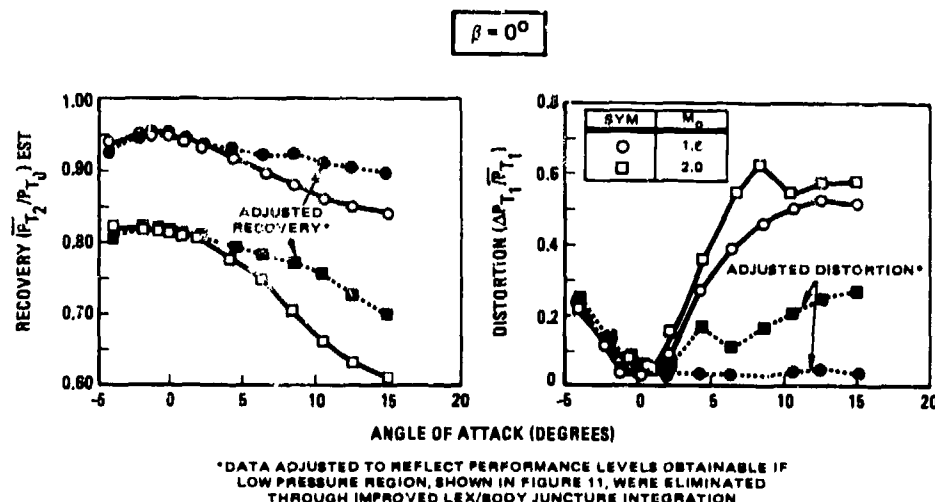


FIGURE 10. SUPERSONIC INLET PERFORMANCE CHARACTERISTICS AS FUNCTION OF ANGLE OF ATTACK

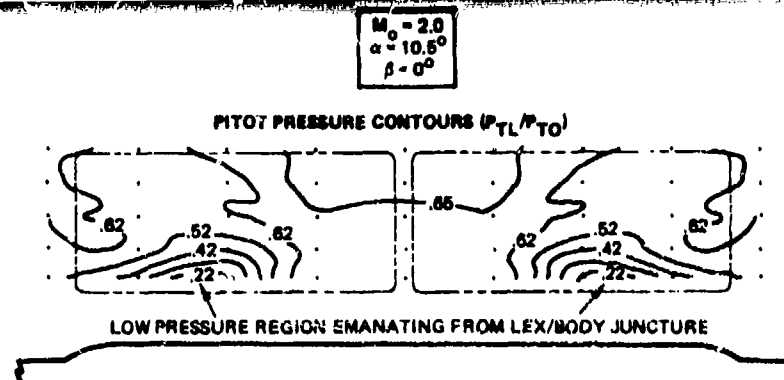


FIGURE 11. SUPERSONIC INGESTED INLET FLOW FIELD AT ANGLE OF ATTACK

The magnitude of the wake generated by the intersection of the wing leading-edge extension with the forebody is believed to be directly related to the shaping of this region*. Hence, it is possible that this low-pressure region could be reduced or eliminated and inlet performance improved by suitable design change. To estimate the relative levels of improvement possible, inlet recovery and distortion levels were recomputed from inlet entrance plane data with the region affected by the wake removed. These values are presented in Figure 10 where they are denoted as "adjusted" recovery and distortion. Significant improvements in recovery and distortion over the unadjusted values are realized over most of the positive angle of attack range tested. These data further highlight the importance of careful LEX/forebody integration with respect to top inlet vehicles.

The adjusted curves of Figure 10 show that there is still a reduction in recovery with increasing angle of attack, even in the absence of the low-pressure region. This is due to supersonic flow expansion over the forebody and wings, which increases the local inlet Mach number and hence increases shock losses. The variation in average local inlet Mach number with angle of attack for zero sideslip at Mach 2.0 is presented in Figure 12. These data have been computed from total head pressure measurements made at the inlet entrance plane and assume that the inlet shock system is purely two-dimensional. Also shown for comparison are corresponding values derived from the data of Reference 5 and the local Mach number for flow over an infinite flat plate, derived from Prandtl-Meyer theory. The VATOL data presented and those of Reference 5 are in generally good agreement, and both give substantially lower local Mach numbers than would be found for a flat plate at angle of attack. Nonetheless, the local inlet Mach number is elevated by approximately 13 percent at 15° angle of attack.

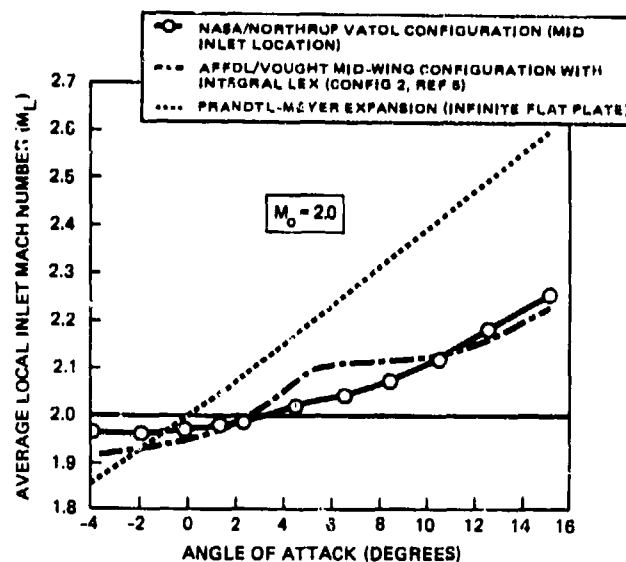


FIGURE 12. EFFECT OF ANGLE OF ATTACK ON LOCAL INLET MACH NUMBER
($\beta = 0^\circ$)

The impact of sideslip on inlet performance at Mach 2.0 is examined in Figure 13. These data show trends which are similar in nature to those exhibited transonically in Figure 8. Supersonically, leeward inlet performance improves in sideslip over most of the positive angles of attack range (note the dramatic improvement in distortion at 4° sideslip). This is due to the migration of the LEX/body juncture wake out of the inlet flow field. The windward inlet, as is shown in Figure 13, experiences marked deteriorations in performance, particularly at higher angles of attack. This performance reduction is attributable to the increased ingestion of low-energy flow from the LEX/body juncture and the eventual migration of the windward LEX vortex system into the inlet.

* Evidence supporting this contention is given in Section 3.2.1

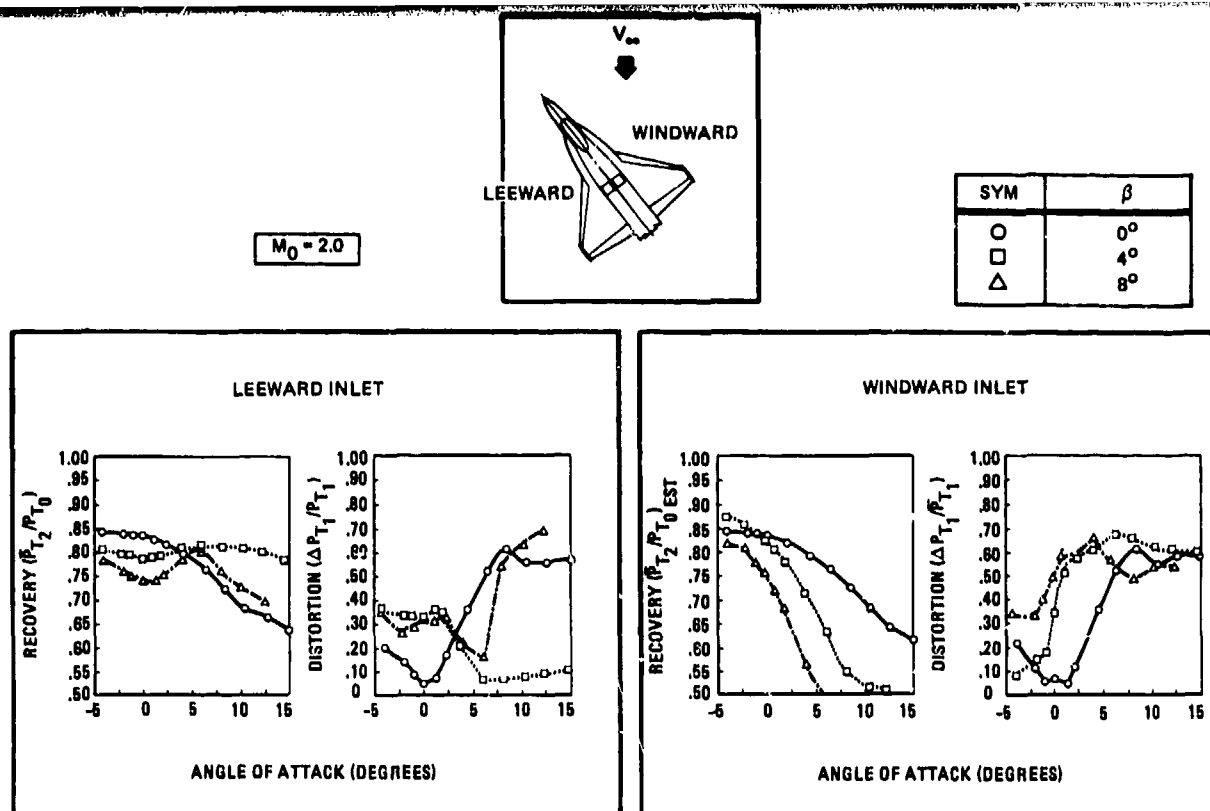


FIGURE 13. EFFECT OF SIDESLIP ON SUPERSONIC INLET PERFORMANCE

3.1.3 Engine-Inlet Compatibility

Compatibility of an aircraft inlet with the engine is crucial since it defines the functional limits over which the engine will operate. Indeed, for instantaneous maneuver, the thrust levels are relatively unimportant and the requirement for the inlet is that it should deliver flow to the engine at sufficiently low distortion levels to prevent engine stall. Normally, engine-inlet compatibility is defined in terms of both instantaneous circumferential and radial distortion. However, prior studies have shown that instantaneous circumferential distortion used alone serves as a good preliminary indicator of engine-inlet compatibility.

Utilizing the estimated instantaneous circumferential distortion parameter defined in Section 3.1.1, Figure 14 shows the conditions at which the estimated instantaneous distortion levels exceed a typical engine stall-free limit over the subsonic and transonic test envelope surveyed. Also shown are fixed-throttle maneuver envelopes characteristic of an air-to-air tactical fighter over the Mach 0.6 to 0.9 range and at Mach 1.2. It can be seen that the compatibility limit was exceeded for only three test conditions: these were all at Mach 1.2 and well outside the corresponding maneuver envelope. A complete assessment of engine-inlet compatibility over the entire $0.6 \leq M_0 \leq 0.9$ maneuver envelope was not possible since the test envelope was limited to 27° angle of attack (see Section 2.3).

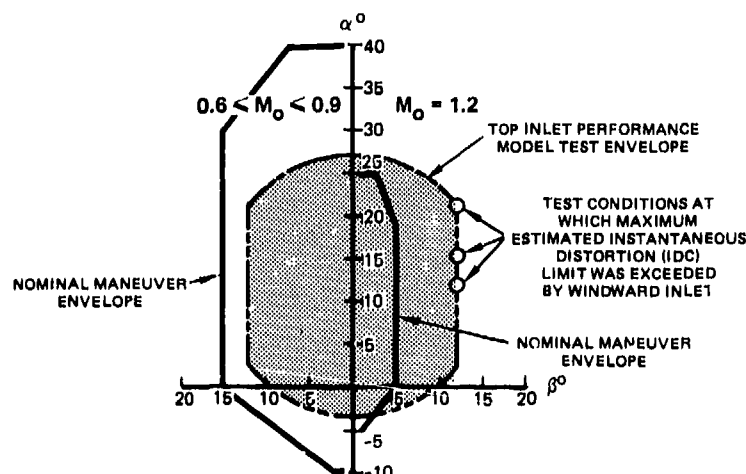


FIGURE 14. TRANSONIC TEST ENVELOPE AND TYPICAL FIXED THROTTLE MANEUVER ENVELOPES

Although no compressor face measurements or dynamic data were obtained at supersonic speeds, some indication of engine-inlet compatibility can be obtained from the steady-state distortion data measured at the inlet entrance plane (Figure 10). Using an allowable total pressure distortion limit of 30 percent, which is the typical compressor face value ($\Delta P_{T1}/P_{T2}$) at which instantaneous distortion limits are exceeded ($IDC/IDC_{limit} > 1$)*, the "unadjusted" values exceed the compatibility bounds at a rather modest 4° angle of attack. However, these high distortion levels are directly related to degraded flow from the LEX/body juncture: thus, if this low-pressure region could be reduced or eliminated, the "adjusted" values shown in Figure 10 indicate that the inlet would not experience any compatibility problems over the entire -5° to 15° angle of attack range at zero sideslip.

3.2 IMPACT OF KEY AIRCRAFT CONFIGURATION VARIABLES ON TOP INLET PERFORMANCE

In order to establish guidelines for the design of future fighter aircraft incorporating top-mounted inlet systems, the impact of several key aircraft configuration variables on top inlet performance was examined. A summary of the variables investigated is presented in Table 1.

TABLE 1. CONFIGURATION VARIABLES

- INLET LOCATION (FORE-MID-AFT)
- LEX PLANFORM AREA
 - BASELINE LEX
 - REDUCED PLANFORM AREA LEX
 - LEX-OFF
- CANOPY-DORSAL INTEGRATION (CANOPY ON-OFF)
- VARIABLE INCIDENCE CANARDS
- LEADING AND TRAILING-EDGE FLAPS
($0^\circ \leq \delta_n \leq 30^\circ$, $0^\circ \leq \delta_f \leq 30^\circ$)

As described in Section 3.1, the influences of inlet location and leading-edge flap deflections was investigated during screening tests and found to have limited impact on inlet-performance. Subsequent tests evaluated the influence of trailing-edge flap deflections and also showed little or no impact. This section presents results for configuration variables which were found to have a more significant influence on inlet performance. These parametric evaluations were conducted with the inlet mounted in the mid location and leading- and trailing-edge flap deflections held fixed at zero degrees.

Only inlet total pressure recovery data are presented for the comparisons which follow. This parameter was selected as it serves as a good general indicator of inlet performance trends (typically losses in recovery are accompanied by increases in inlet distortion and turbulence).

3.2.1 Canopy-Dorsal Effects

The integration of the canopy with the fuselage takes on a new importance in the case of a top inlet aircraft since low-energy flow shed from the canopy-dorsal region may now be ingested by the inlet. This leads to a reduction in inlet recovery and increases the potential for engine-inlet compatibility problems.

The baseline VATOL configuration tested in this study highlights this problem. Since the vehicle was designed for an air-to-air mission, a full 360° field-of-visibility was required, causing the crew module to be elevated. This results in a high canopy-dorsal aft slope, which is responsible at low angles of attack for the low-pressure region and consequent reductions in inlet performance, which have already been pointed out in connection with Figures 6 and 7.

To examine the effects of reducing the canopy-dorsal aft slope, a "canopy-off" block, shown in Figure 15, was fitted in place of the baseline canopy. To limit the extent of the modifications, the dorsal, which comprises part of the center-fuselage, was retained and the canopy-off block faired to it. Thus, even with the canopy-off block in place, some aft slope remains and the resultant configuration is perhaps more indicative of a canopy-dorsal integration which might be employed on an Air-to-Surface aircraft, with its reduced rearward visibility requirement.

The impact of re-configuring the canopy-dorsal on inlet performance can be seen in Figure 16. At Mach 0.9, significant improvements can be seen in the recoveries at low to moderate angles of attack. This improvement is related to two different effects. At low angles of attack ($\alpha < 5^\circ$) corresponding flow field total pressure contour data confirm that there is a considerable reduction (but not elimination) of the wake from the canopy-dorsal. For moderate angles of attack, the baseline performance is degraded by the low-energy flow associated with the LEX/body juncture (see Figure 7), but the canopy-off block reduces the severity of the corner created by the junction of the LEX with the forebody(canopy), thus reducing or eliminating the low-pressure region. As the angle of attack is increased to approximately 20°, the benefit of the improved canopy integration is lost because the increasingly powerful LEX vortices become more effective in sweeping away the LEX/body juncture low-pressure region even from the baseline arrangement. At Mach 1.6, Figure 16 shows that inlet

* This correlation is based on subsonic and transonic inlet performance data.

total pressure recovery continues to improve relative to the baseline configuration with angle of attack. Indeed, comparison with Figure 10 shows that the canopy-off results are almost identical with those of the "adjusted recovery" values obtained for the baseline arrangement. This indicates, that the wake from the LEX/body juncture (see Figure 11) has been significantly reduced or eliminated from the ingested inlet flow field via the smoother blending of the LEX and forebody which results from the use of the canopy-off block.

The reduced effect of the low-pressure region from the LEX/body juncture with canopy-off block confirms that the problems experienced with the baseline arrangement due to this flow phenomenon are configuration-dependent and can be significantly reduced or eliminated by appropriate LEX/body integration.

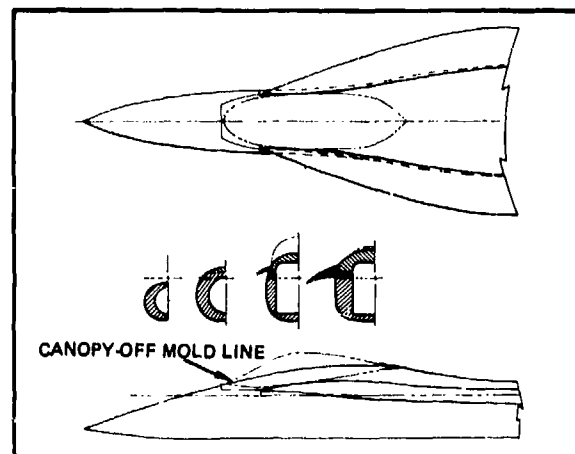


FIGURE 15. CANOPY-OFF BLOCK

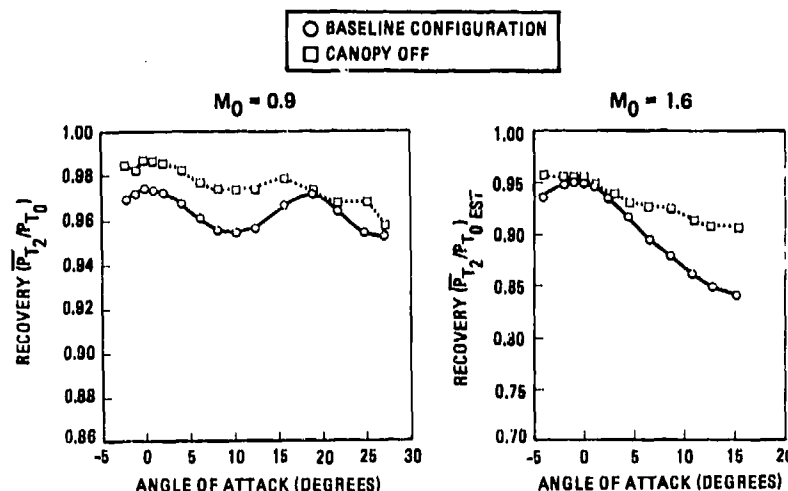


FIGURE 16. IMPACT OF CANOPY-DORSAL ON INLET RECOVERY AT ANGLE OF ATTACK ($\beta = 0^\circ$)

3.2.2 Wing Planform Effects

Earlier top inlet studies (e.g. References 1 and 4) have shown the importance of the LEX vortex system in counteracting the effects of upper-fuselage flow separation. These studies have also shown a direct correlation between LEX vortex system effectiveness and LEX planform area (size) and shape. A further examination of the effects of LEX planform area variation was conducted during this study. This was achieved by testing the model, as is illustrated in Figure 17, with the baseline LEX, a reduced planform area (alternate) LEX, and with wing leading-edge extensions removed. The alternate LEX retains the baseline LEX shape but has a 40 percent reduction in exposed planform area.

Comparisons of inlet pressure recovery for these three wing leading-edge extension arrangements at transonic and supersonic speeds are presented in Figure 18. It can be seen that the alternate LEX performs nearly as well as (and in some instances better than) the baseline LEX, despite a 40 percent reduction in planform area. This result differs from the findings of Reference 1 which shows a direct correlation between improved inlet performance and increased LEX planform area. A possible explanation for this behavior is that the alternate LEX forms a more favorable junction with the body, thus reducing the amount of low-energy flow buildup. In addition, this low-pressure region may be positioned further outboard on the upper-fuselage, since the intersection of the LEX and forebody moves farther out on the fuselage (see Figure 17). Thus, the consequent reduction in the extent of the low-pressure region entering the inlet would compensate for the reduced LEX vortex strength. Verification of this explanation will be possible when the inlet flow field contours become available for the alternate LEX configuration.

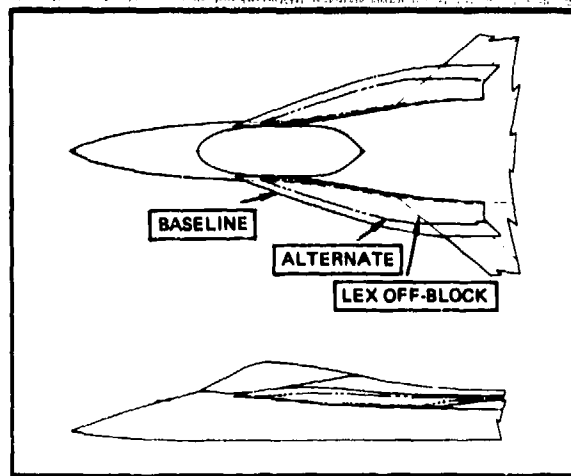


FIGURE 17. WING LEADING-EDGE EXTENSION (LEX) PLANFORM OPTIONS

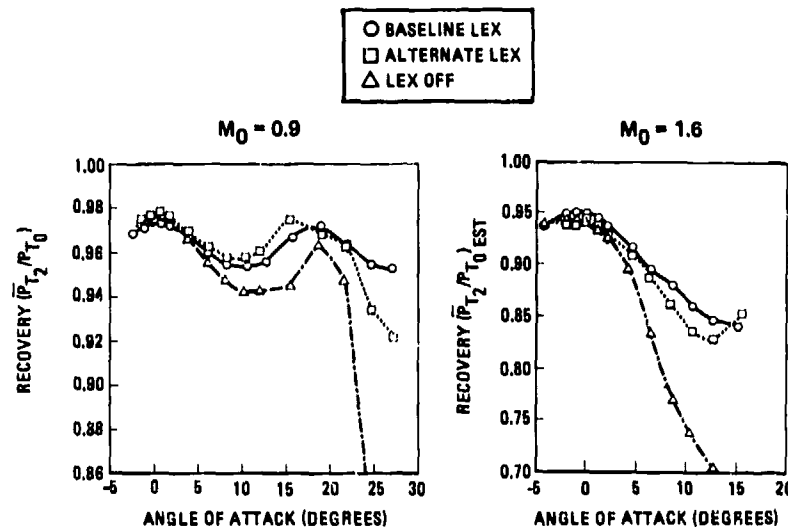


FIGURE 18. EFFECT OF WING PLANFORM VARIATIONS ON INLET RECOVERY AT ANGLE OF ATTACK ($\beta = 0^\circ$)

The LEX-off results of Figure 18 show a number of interesting features. First, at Mach 0.9 the LEX-off recoveries are lower, but not drastically so, than the LEX-on values, except above about 20° of angle of attack. This is due to the strong wing leading-edge vortex system, generated by the 50° swept wing, which is nearly as effective as the LEX vortices in controlling the upper-fuselage flow. However, above 20° angle of attack, the wing is stalled and the LEX-off recoveries fall rapidly. Another striking feature of Figure 18 is that at Mach 1.6 the LEX-off recovery levels continue to decrease relative to the baseline configuration with angle of attack, despite the elimination of the low-pressure region from the LEX-body juncture. Thus, the wing vortices must be much less effective in controlling upper-fuselage separation than the LEX vortices at supersonic speeds. A possible explanation for this is that, while the strengths of both vortex systems are reduced supersonically, the wing leading-edge vortex system experiences a greater reduction in strength as the wing has a lower sweep angle and hence a higher effective leading-edge normal Mach number.

At Mach 0.9 and 4° sideslip, the LEX planform has a strong effect on the windward inlet recovery, as can be seen in Figure 19, but relatively little impact on the leeward inlet performance, until 20° angle of attack, when the wing without LEX stalls. At this sideslip angle, low-energy flow from the LEX-body juncture is ingested by the windward inlet but migrates outboard of the leeward inlet, thus explaining the resultant trends in inlet performance. It should also be noted, that on the windward side of the vehicle the boundary layer buildup from the LEX-body juncture is more severe in sideslip while the effective leading-edge sweep angles of the windward LEX and wing are reduced, resulting in weaker vortices and lower inlet total pressure recoveries. It can be seen that at this sideslip angle the windward vortex generated by the wing alone (LEX-off) becomes almost totally ineffective.

As sideslip angle was increased, the larger vortex from the baseline LEX was found to enter the windward inlet first, hence diminishing the advantage of the baseline LEX. Thus, in the integration of the wing planform with the inlet, it is critically important that the design achieve maximum entrainment with minimum vortex ingestion.

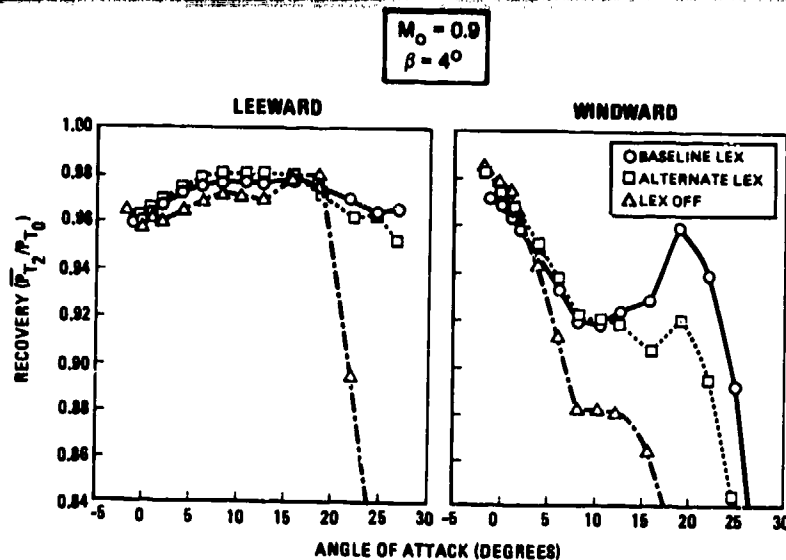


FIGURE 19. WING PLANFORM EFFECTS AT SIDESLIP

The test model did not provide the capability of examining the effect of wing planform variations. However, an indirect evaluation of this parameter is possible by making use of the flow field data of Reference 5 (AFFDL/Vought test program). These data were acquired utilizing a 35° leading-edge swept wing model with a 3.8 wing aspect ratio, which is depicted in Figure 20. Figure 21 compares inlet flow field total pressure recovery values calculated from the AFFDL/Vought data with similar values obtained for the VATOL model, which has a wing leading-edge sweep of 50° and an aspect ratio of 2.1. Data derived for the aft-survey location on the VATOL model were used, in order to obtain the closest correspondence with the flow field survey location used in Reference 5 (see Figure 20). The most important point of difference between the two curves of Figure 21 is the greater angle of attack capability exhibited by the VATOL configuration: The AFFDL/Vought model experiences a rapid decrease in recovery near 15° angle of attack whereas the VATOL configuration gives only a moderate reduction at 25° angle of attack. This difference is ascribed to the following: The VATOL wing has a significantly lower aspect ratio than the AFFDL/Vought Configuration but a similar LEX to wing planform area ratio. Thus, at given angle of attack the adverse pressure gradient associated with the VATOL wing is less than that of AFFDL/Vought configuration. This results in increased LEX vortex system stability for the VATOL configuration and, hence, increases the angle of attack at which the burst point moves ahead of the inlet.

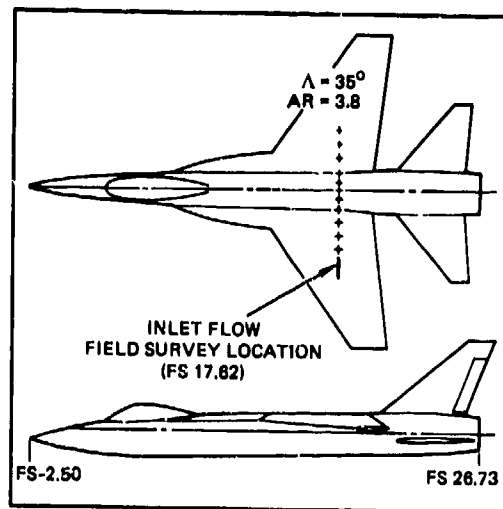


FIGURE 20. AFFDL/VOUGHT TEST CONFIGURATION

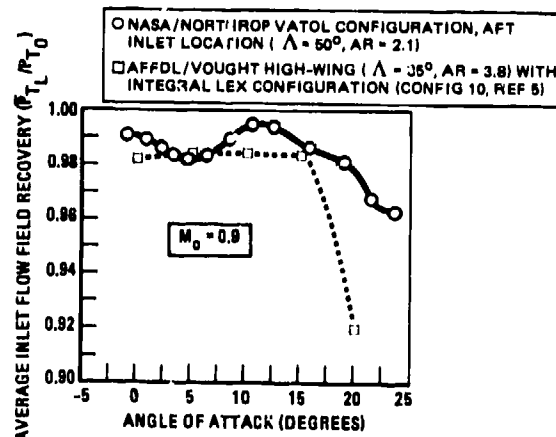


FIGURE 21. WING LEADING-EDGE SWEEP EFFECTS ON INGESTED INLET FLOW FIELD RECOVERY ($\beta = 0^\circ$)

3.2.3 The Effect of Canards

Canards are a configuration option which are employed on a number of advanced fighter aircraft concepts, therefore, it was of interest to determine the impact canards would have on inlet performance if integrated into a top inlet configuration. Variable incidence canards were integrated into the VATOL model by replacing the wing leading-edge extensions with canards having a leading-edge sweep of 60° and a dihedral of 20° , see Figure 22. Although not typical of most canard integrations, this arrangement was selected so as to couple the canard leading-edge vortex system with the wing flow field, thus providing for vortex lift enhancement. In addition, it was desired to create a strong vortex system above the wing in order to establish a similar sweeping action to that provided by the wing leading-edge extensions.

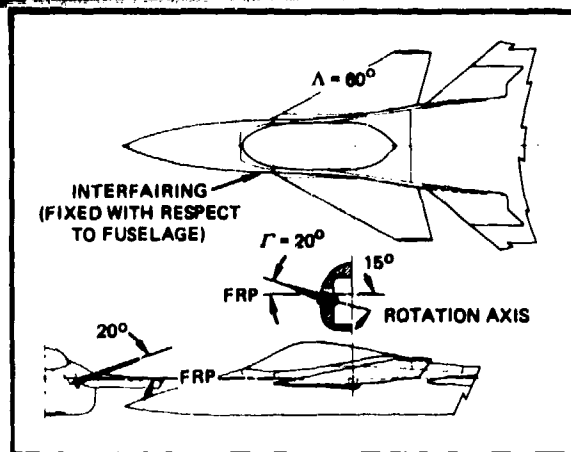


FIGURE 22. CLOSE-COUPLED VARIABLE INCIDENCE CANARDS

Figure 23 compares inlet total pressure recovery characteristics for the canard and baseline configurations at Mach 0.9 and 1.6. Curves are only shown for the undeflected canard condition ($\delta_c = 0^\circ$). At Mach 1.6, a zero degree canard deflection approximates the angle required for trim; but at Mach 0.9, where the aircraft has a negative static margin, quite large negative deflections are required for trim. Inlet recovery levels which would be obtained if the canards were scheduled are shown in Figure 23 for the Mach 0.9 condition at three different angles of attack.

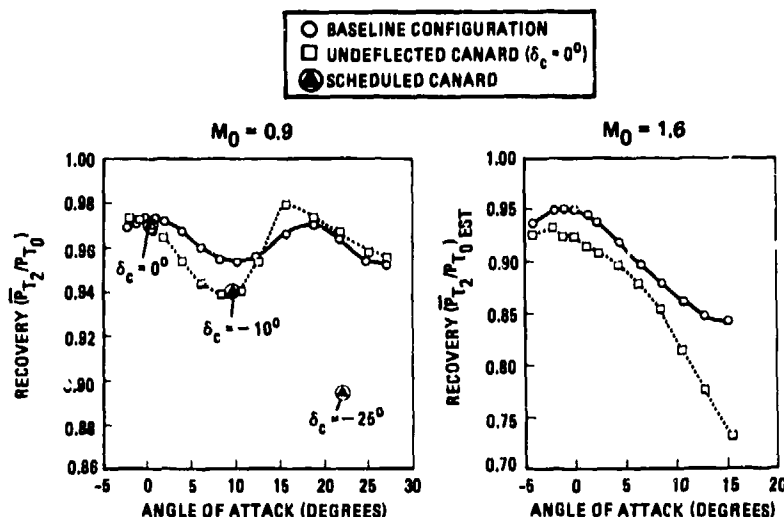


FIGURE 23. EFFECT OF CANARDS ON INLET RECOVERY AT ANGLE OF ATTACK ($\beta = 0^\circ$)

The Mach 0.9 data, shown in Figure 23, indicate that the canards are not effective, over the 0° to 10° angle of attack range, in controlling the upper-fuselage flow field, but at higher angles of attack, the vortex from the fixed canard improves inlet recovery, yielding values higher than those obtained with the baseline configuration. However, the scheduled canard at 22° angle of attack ($\delta_c = -25^\circ$) experiences a large loss in inlet performance, down to the level of the plain wing (compare Figure 18). At Mach 1.6, the canard vortices increase inlet recovery above the wing alone (LEX-off) levels but are not as effective in improving inlet performance as the baseline LEX vortices.

3.3 COMPARISON WITH MORE CONVENTIONAL INLET INSTALLATIONS

In order to set the results from the VATOL inlet/airframe model into the context of practical aircraft systems, VATOL top inlet performance (recovery) data have been compared with typical performance data for fighter aircraft employing more conventional inlet installations. The aircraft utilized in these comparisons are the YF-16 (Reference 8), which has a fuselage-shielded inlet system, Northrop's YF-17 prototype (wing-shielded inlet), and an advanced Northrop fighter configuration with side-mounted, two-dimensional external compression inlets with fixed, vertical ramps.

Figure 24 presents comparative results at Mach numbers of 0.9, 1.6 and 2.0. The results reflect differences in inlet design and mission requirements and do not allow a precise determination of the relative merits of the different integration options. They do, however, show the following: The VATOL inlet provides recoveries at least comparable to those of the other aircraft over the cruise range of angles of attack ($0^\circ < \alpha < 3^\circ$). At the transonic operating condition shown, the top inlet performance levels are competitive out to at least 25° angle of attack. Supersonically, top inlet performance deteriorates with angle of attack, primarily due to increases in local inlet Mach number (high shock system losses). In contrast, the performance of the fuselage- and wing-shielded inlets improves with

angle of attack because of the precompression provided by the forebody and/or wings. Supersonic angle of attack capability for fighter aircraft is typically limited to less than 15° angle of attack at Mach 1.6 and to approximately 10° at Mach 2.0, based on load factor constraints. Figure 24 shows that the top-mounted inlet at these angle of attack conditions gives "adjusted" recoveries which are distinctly, but not drastically, lower than those of the other inlet installations.

It is perhaps apropos to comment that the VATOL inlet system has not undergone the many hours of developmental testing that each of the other inlet systems presented in Figure 24 has, thus, the performance of the VATOL inlet system could most likely be improved through similar development efforts.

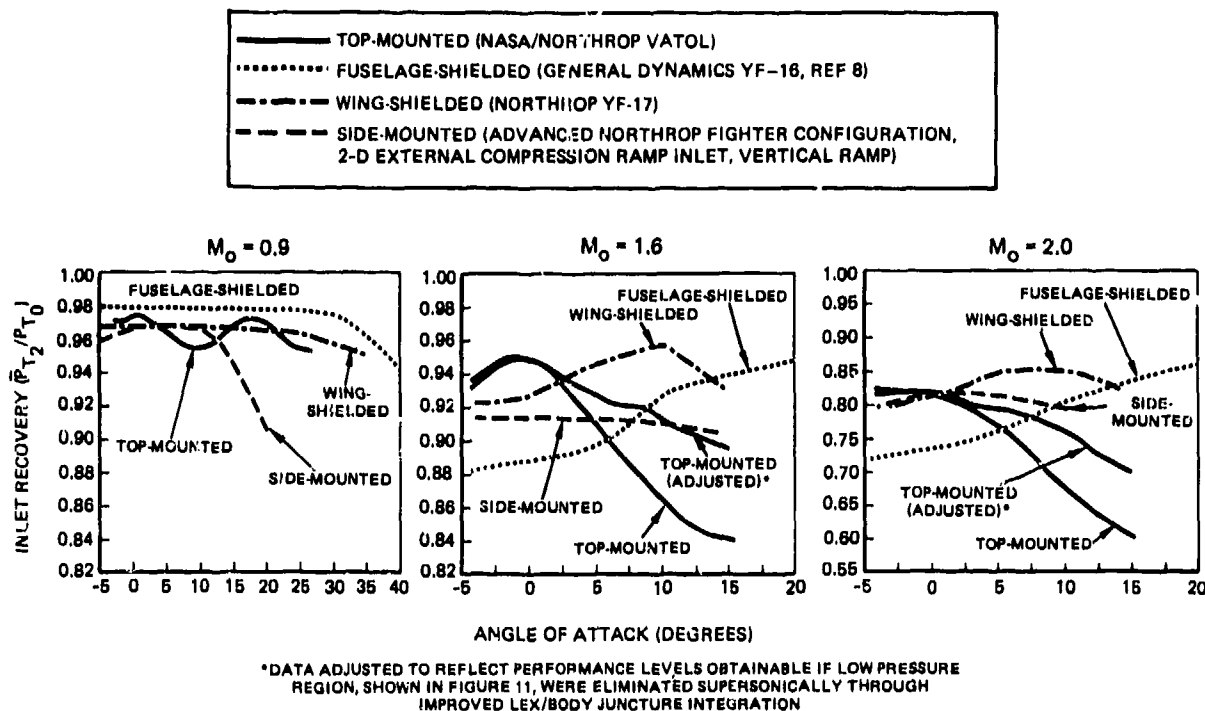


FIGURE 24. COMPARISON OF INLET RECOVERY CHARACTERISTICS FOR TOP AND CONVENTION INLET INSTALLATIONS

4.0 CONCLUSIONS

The study described in this paper has generated extensive data on top-inlet flow field and engine-inlet performance characteristics at subsonic, transonic, and supersonic speeds. From an initial assessment of the data the following conclusions can be drawn.

- The VATOL top-inlet configuration maintains relatively good subsonic and transonic inlet performance characteristics at zero sideslip over the entire -3° to 27° angle of attack range tested. In sideslip top inlet performance in general deteriorates, but a preliminary assessment of engine-inlet compatibility shows no apparent problems over the subsonic and transonic ($0.6 \leq M_o \leq 1.2$) test envelope.
- For the configuration tested, ingestion of low-energy flow from the LEX/body juncture serves as a major contributor to inlet performance losses. This highlights the importance of attention to detail when integrating the LEX into the forebody, especially during the preliminary design process.
- Top inlet performance is sensitive to canopy-dorsal integration and the location and strength of the wing leading-edge extension (LEX) vortices.
- The sweeping action of the wing leading-edge extension (LEX) vortices can significantly enhance top inlet performance characteristics at angle of attack. In addition, available data indicate that the effectiveness of these vortices can be extended to higher angles of attack by employing wing planforms with low adverse pressure gradient, which delay the onset of LEX vortex burst.
- Supersonically, top-mounted inlet systems experience an inherent increase in local inlet Mach number at angle of attack. This undesirable characteristic reduces inlet performance and may prohibit application of this concept to vehicles which require a high-degree of supersonic maneuverability. However, the prospects of creating designs with subsonic and transonic maneuver capabilities appear promising.

The foregoing conclusions demonstrate the highly configurational-dependent nature of top-mounted inlet systems. This indicates that major components of the airframe design must be evolved interactively with the inlet system not only in the preliminary design process, as is conventional, but also during the inlet/airframe development testing phase. The parametric studies reported on in this paper together with previous work (References 1-5) will, however, provide valuable design guidance for fighter aircraft incorporating top-mounted inlet systems.

1. Williams, T. L. and Hunt, B. L., "Top Inlet System Feasibility for Transonic-Supersonic Fighter Aircraft Applications," AIAA Paper 80-1809, August 1980.
2. Prince, S. W., "A Flow Field Study for Top-Mounted Inlets on Fighter Aircraft Configurations," David Taylor Naval Ship Research and Development Center Report ASD-79/03, January 1979.
3. Ridder, S. O., "Wind Tunnel Test at Low-Speed of a Dorsal Air Intake on a Fighter Configuration," AGARD-CP-247, January 1979.
4. Surber, L. E. and Rhoades, W. W., "Top-Mounted Inlet Flow Field Testing for Future Fighter Aircraft," AIAA Paper 79-1147, June 1979.
5. Rhoades, W. W., "Experimental Definition of Top-Mounted Inlet Flow Fields," AFFDL-TR-79-3088, Volume I, August 1979.
6. Gerhardt, H. A. and Chen, W. S., "Study of Aerodynamic Technology for VSTOL Fighter/Attack Aircraft - Vertical Attitude Concept," NASA CR-152131, May 1978.
7. Küchemann, D., "The Aerodynamic Design of Aircraft," First Edition, Pergamon Press, 1978.
8. Hawkins, J. E., "YF-16 Inlet Design and Performance," Journal of Aircraft, Volume 13, Number 6, June 1976.

6.0 ACKNOWLEDGEMENTS

The authors wish to thank Mr. Bob Beaton for his assistance in the preparation of data presented in this paper.

SOME RAE RESEARCH ON SHIELDED AND UNSHIELDED FUSELAGE MOUNTED
AIR INTAKES AT SUBSONIC AND SUPERSONIC SPEEDS

by
J. A. Ross
I. McGregor
A. J. Priest

Aerodynamics Department
Royal Aircraft Establishment, Bedford
Beds MK41 6AE, UK.

SUMMARY

This paper summarises RAE work aimed at improving the incidence performance of fuselage-mounted intakes at subsonic and supersonic speeds. The effects of simple changes in intake geometry, such as increasing contraction ratio and altering lower lip shape, are first considered; it is shown that such modifications can be beneficial at subsonic speeds, but drag penalties tend to limit their use at higher Mach numbers. Two intake locations that potentially offer a good degree of incidence shielding - underfuselage and understrake - are then examined. It is concluded that satisfactory performance can be obtained with an understrake installation, but a detailed study of strake shape, slots, splitter plates and boundary-layer diverters must be made if the combination is to be successful over the whole of the intended flight envelope. However, for the configurations tested, the underfuselage location offers generally better intake performance at lower technical risk. Finally, some results for a side-mounted staggered lip intake are presented, together with some two-dimensional calculations of the mutual interference effects that occur between the upper and lower lips. It is suggested that, with development work currently in hand, an intake of this type can be competitive with an underfuselage installation.

NOTATION

A cross-sectional area of streamtube or duct
 C_D drag coefficient, based on intake entry area
CR intake contraction ratio, A_{en}/A_{th}
DC60 distortion coefficient defined as $(\bar{P}_{60_{min}} - \bar{P}_f)/q_f$, where $\bar{P}_{60_{min}}$ is the lowest value of the mean pressure over any 60° sector of the engine face.
L strake length
M Mach number
MFR mass flow ratio, A_∞/A_{en}
P total pressure
 ΔP $P_\infty - P$
w strake width
q dynamic pressure
 α angle of incidence
 β angle of sideslip
 δ compression surface angle
 ϵ shock wave angle
 η total pressure recovery, \bar{P}_f/P_∞

Suffices

en entry
ext external
f engine face
L local value
th throat
- free stream
rms root mean square
o datum value

1 INTRODUCTION

Over the past few years there has been very considerable interest in improving the combat agility of strike-fighter aircraft, and this has resulted in a need to fly at much greater angles of incidence and sideslip over a wide range of speeds. This expansion of the flight envelope has affected many aspects of aircraft design and layout, including

those of the propulsion system. Indeed, air intake performance may well be crucial under these conditions. Not only is it necessary to maintain a high level of pressure recovery so that engine thrust is preserved, but total pressure distortion and turbulence of the airflow at engine entry must be kept down to specified levels if engine malfunction is to be avoided.

The problem is essentially that of suppressing, or delaying the onset of, the flow separation that tends to occur on the lower lip of an intake as its incidence is increased. There are basically three ways of doing this, although in practice these methods may be combined to some extent.

(a) Modifying the lower lip so that its susceptibility to flow separation is reduced. This can be done by means of shaping, cambering and increasing the contraction ratio, or by using slots or BLC techniques such as suction or blowing. Another possibility is the use of a hinged cowl lip^{1,2}; this is additionally attractive in that it affords a means of varying intake entry area so that matching of intake and engine airflows can be achieved over a wide range of conditions.

(b) Mounting the intake underneath some other component of the aircraft - fuselage, wing or wing strake - so that it is shielded to a greater or lesser degree from the incident flow.

(c) Extending the upper lip of the intake forward so that it provides a measure of shielding to the lower lip. Such a 'staggered' intake may bear a strong resemblance to a rectangular inlet with external compression ramp intended for efficient operation at supersonic speeds, but conceptually the two designs are quite distinct.

This paper summarises RAE work in these three areas. In section 3 the effects of some simple geometrical changes on the performance of a side-mounted pitot intake are considered: in addition to pressure recovery and distortion data, measurements of the changes in intake drag at subsonic and supersonic speeds are shown. Two intake locations that potentially offer a good degree of incidence shielding - underfuselage and understrake - are explored in sections 4 and 5, the latter in some detail. Finally, some results for a side-mounted staggered lip intake are presented, together with some two-dimensional potential flow calculations of the mutual interference effects that occur between the upper and lower lips in an intake of this type.

2 MODELS AND TEST FACILITIES

Three separate models (which will be denoted by Models I, II and III) were used in this investigation, and they are shown in Fig 1. All were of modular construction so that configuration changes could be easily made. Models I and III were intended primarily for measurements of internal flow and were equipped with a single intake and duct: this was normally located on the port side of the fuselage, but on Model I it was possible to simulate an underfuselage installation by changing the fuselage module, whilst retaining the same intake and duct. It was also possible to measure intake performance in isolation on both these models. Model II was designed primarily to measure intake drag and was equipped with an intake and duct on each side of the fuselage: these could be removed to measure the datum drag of the fuselage. This model was only tested over a small range of incidence due to balance strength limitations. Further details may be found in Ref 3.

All three models were provided with means of controlling and measuring the airflow through the intakes. Pressure instrumentation was more extensive on Models I and III and included both steady and unsteady (rms) pressure measurements at a representative engine face location. Pressure recovery (η), mass flow ratio (MFR) and distortion parameter DC60 were obtained from 72-point total-pressure surveys. In addition, pitot rakes could be fitted in the intake throat region on Model III for diagnostic purposes.

The intake and duct could be removed from Model III and replaced by rakes of pitot tubes and yawmeters to measure the flowfield in the region normally occupied by the intake, or at an alternative forward location.

The intake duct on Model I was quite long, 9.3 engine-face diameters between throat and engine face, and had a very low rate of diffusion. That on Model III was shorter, with a length of 5 engine-face diameters and an area ratio A_f/A_{th} of 1.6. The internal shaping of the ducts on Model II was not representative of a full-scale aircraft and was intended merely to produce a reasonably smooth flow distribution at the measuring station.

The Table below shows the facilities and range of test variables used with each model, although not all configurations have been tested over the complete range available. Limited tests have also been made on most configurations to investigate the effects of sideslip. For certain intake configurations tested on Model I, the ARA 9 ft x 8 ft transonic tunnel was used to extend the incidence range to considerably higher values than were feasible in the RAE 3 ft x 3 ft tunnel.

3 SIMPLE MODIFICATIONS TO IMPROVE THE INCIDENCE PERFORMANCE OF SIDE-MOUNTED INTAKES

3.1 The beneficial effect of increasing lip thickness and contraction ratio on intake performance at low speeds is well known, but there is not a great deal of information on the effect of such modifications at transonic and supersonic speeds. A series of intakes was therefore designed and tested on Model I to provide data on internal performance,

	Model I	Model II	Model III
Tunnels used	RAE 3 ft x 3 ft ARA 8 ft x 9 ft	RAE 3 ft x 3 ft	RAE 8 ft x 8 ft RAE 13 ft x 9 ft
Subsonic/transonic M_∞ , α range	$M_\infty = 0.6$ to 1.05 $\alpha = -8^\circ$ to $+19.3^\circ$ (RAE) $M_\infty = 0.6$ to 1.20 $\alpha = +16^\circ$ to $+36^\circ$ (ARA)	$M_\infty = 0.6$ to 0.95 $\alpha = 0^\circ$ only	$M_\infty = 0.25$ to 0.85 (Flow surveys) $M_\infty = 0.85$ $\alpha = -6^\circ$ to $+22^\circ$ (Intake tests)
Supersonic M_∞ , α range	$M_\infty = 1.4$ to 1.8 $\alpha = -8^\circ$ to $+16^\circ$ (RAE)	$M_\infty = 1.5$ to 2.0 $\alpha = 0^\circ$ only	$M_\infty = 1.4$ to 1.8 $\alpha = -6^\circ$ to $+13^\circ$

whilst a closely related, but not identical, series of intakes was used on Model II to assess the effect on cruise drag.

The baseline configuration on each model was a rectangular pitot intake with a contraction ratio of 1.08, and changes to the intake geometry were restricted to the internal lines forward of the intake throat and to the external cowl lines forward of the cowl maximum cross section.

These changes comprised (Fig 2):

- increasing contraction ratio (CR = 1.15, 1.25, 1.35 on Model I and CR = 1.25, 1.40 on Model II), the increase in cowl highlight area being uniformly distributed on the upper, outboard and lower cowl lips;
- increasing CR to 1.25 and concentrating all the highlight area increase on a thickened, symmetrical lower lip (Model I only);
- increasing CR to 1.25 and concentrating all the highlight area increase on a thickened and cambered lower lip;
- introducing slots on the lower cowl lip for the CR 1.25 and 1.35 cowls at subsonic conditions (Model I only).

All intakes were fitted with a wedge-type boundary-layer diverter with a 50° apex angle. Diverter height, h , could be varied, but for the present tests h was constant and about 20% greater than the thickness of the boundary layer on the side of the fuselage at zero incidence. A splitter plate was not used.

3.2 Some results from Model I at free-stream Mach numbers of 0.9 and 1.4 are summarised in Figs 3 and 4. These show the pressure recovery, η , and distortion parameter, $-DC60$, as a function of incidence for a constant throat Mach number, M_{th} , of 0.6. This value of M_{th} may be regarded as somewhat low, but because of the small amount of internal diffusion in the duct actually corresponds to an engine entry Mach number of approximately 0.55.

At $M_\infty = 0.9$, significant gains in pressure recovery at high incidence are obtained by increasing contraction ratio uniformly on the three active lips of the cowl, from CR = 1.08 to CR = 1.35. These gains can be sustained to slightly higher incidences by opening a lower lip slot, although at a cost of a significant increase in $-DC60$ levels. For the CR = 1.25 intakes, performance is further improved by concentrating all the additional highlight area on the lower lip, 'thickening and cambering' proving more effective than symmetrical thickening; again, using a lip slot causes slight increases in both η and $-DC60$.

At $M_\infty = 1.4$, increasing CR from 1.08 to 1.15 has virtually no effect at incidences less than 12° , but improves both recovery and distortion levels at higher incidences. Further increase in CR is generally detrimental to the internal performance when the increase is applied to the three active lips, but can still be beneficial (at positive incidences) if applied in the form of a thickened and cambered lower lip.

Drag results for the similar range of cowl lip variants tested on Model II are illustrated in Fig 5. Results are for zero incidence only and show the intake external drag as a function of M_∞ , for the same value of M_{th} , 0.60, as for the internal performance data.

3.3 Considering the internal performance and external drag results as a whole, it may be concluded that, at subsonic speeds, both contraction ratio increases and lower lip reprofiling can offer worthwhile gains in intake internal performance at high incidence,

but at the cost of some intake drag penalty at cruise. Supersonically, any gains in internal performance from such modifications are at best marginal and the intake drag penalties can be severe, except for quite small increases in contraction ratio. Overall, a contraction ratio in the region of 1.15 to 1.2 appears to represent a reasonable compromise between subsonic and supersonic performance for pitot intakes of this type.

It is, however, important to emphasise the limitations attendant upon the present results. In general, assuming the engine-face area and the cowl maximum cross-sectional area to be fixed, both throat and highlight areas can be selected independently to achieve an optimum balance between internal and external performance. In these tests only the highlight area has been varied and this has tended to bias the results against low external drag at subsonic speeds due to the reduction in cowl projected area and the increase in spillage (for a given engine flow) that occurs as the contraction ratio is increased. On the other hand, reducing throat area increases M_{th} for a given engine flow and this tends to depress pressure recovery. Consequently further work is required before the effects of changing lip geometry can be fully assessed.

4 INTAKE SHIELDING BY MOUNTING THE INTAKE UNDERNEATH THE FUSELAGE

4.1 Although arguments may be raised against an underfuselage intake installation on such grounds as the greater difficulty of store carriage and the greater possibility of foreign object ingestion, previous studies^{1,2} have shown distinct aerodynamic advantages for this location. In particular, it offers a much 'cleaner' environment for the intake than the junction region between the fuselage and wing or wing leading edge strake, where, as will be shown in the following section, complex flowfields can develop at high incidence.

By changing the fuselage module on Model I it was possible to simulate an underfuselage intake installation and thus obtain data directly comparable with that for the same intake mounted on the side of the fuselage, and also provide comparative data for the assessment of the performance of the staggered lip intake described in section 6. Two new forebodies were used and are shown in Fig 6. The long forebody 'A' was geometrically similar to that used previously on Model I, and the intake was located underneath the body at the same longitudinal position as when mounted on the body side. The short forebody 'B' enabled the intake to be mounted considerably nearer to the nose of the model, and was of similar shape to forebody 'A' ahead of the intake entry plane.

Most of the tests were made in the RAE 3 ft x 3 ft tunnel using the baseline 1.08 contraction ratio intake, but some additional tests (using the long forebody 'A' and the 1.15 CR intake) were made at higher incidences at transonic speeds in the ARA tunnel.

4.2 The results are shown in Figs 7 and 9, a constant throat Mach number of 0.6 again being used as a convenient basis for comparison.

At $M_{th} = 0.9$, forebody length has very little effect on either pressure recovery or distortion at positive incidences, although at negative angles performance holds up better with the short forebody. Compared with the same intake mounted on the side of the fuselage, the rate of fall-off of pressure recovery with incidence is greatly reduced by the shielding effect of the fuselage. A contraction ratio effect is still evident and pressure recovery at high incidences is better maintained by the 1.15 CR intake.

At $M_{th} = 1.4$ it is notable that the pressure recovery at zero incidence is greater than the normal-shock recovery. Since frictional losses in the duct are of the order of 0.02, the mean total pressure of the air entering the intake is consequently some 0.03 higher than would be predicted for a normal shock at the free-stream Mach number. Although this could be partly due to the local Mach number being less than the free-stream value, a more likely explanation is the formation of a lambda shock system ahead of the intake, so that part of the air entering the intake passes through an oblique shock and a much weaker normal shock, instead of a single normal shock (Fig 8). Unfortunately, such a system tends to introduce flow distortion and -DC60 levels are increased. In practice, it would probably be necessary to use a splitter plate or similar device to either suppress the formation of the lambda shock (although this would reduce pressure recovery), or prevent the entry of the separated boundary layer into the intake. Again, differences due to forebody length are scarcely significant and fuselage shielding effects are noticeable above 10° incidence.

The situation at $M_{th} = 1.8$ is broadly similar, although here the performance is better with the underfuselage intakes over the whole of the incidence range. It is also apparent that the underside of the fuselage is acting as a kind of pre-entry compression surface, pressure recovery increasing steadily with incidence, but it is much less effective in this respect than a two-dimensional wedge used to generate an oblique shock ahead of an intake, if the wedge angle is regarded as the equivalent of the forebody incidence. Differences in pressure recovery due to forebody length are very small, although there is some effect on distortion levels.

The behaviour in sideslip at zero incidence shows considerable variation with Mach number (Fig 9). Subsonically, pressure recovery varies little over the range $\beta = \pm 8^\circ$ (and this is confirmed at incidences up to 30° by the results for the 1.15 CR intake shown in Fig 21), but -DC60 tends to increase, particularly with the long forebody. At supersonic speeds, disruption of the lambda shock system is believed to be responsible for the comparatively large changes in pressure recovery and -DC60 that occur as the sideslip angle is varied.

4.3 Overall, the results confirm those of previous studies of underfuselage intake installations. Subsonically, a high level of performance is attained over a wide range of incidence and sideslip. At supersonic speeds, interaction between the intake shock system and the fuselage boundary layer may pose some problems unless adequate preventive measures are taken, but these are essentially no different from those that can occur with an unshielded side-mounted intake.

Forebody length ahead of the intake does not appear to be a very significant parameter, provided the width of the intake is less than the width of the forebody at the intake entry plane.

5 INTAKE SHIELDING BY MOUNTING THE INTAKE UNDERNEATH A LEADING EDGE STRAKE

5.1 The concept of sustaining intake performance at high angles of attack by positioning the intake beneath a wing or leading-edge strake has received considerable attention. The principle was demonstrated during the 'Tailor-Mate' program⁴ and used on the YF-17 aeroplane⁵; more recently this type of configuration has been studied at low speed by Lotter and Malefakis¹.

This section describes an experimental study, which was made using Model III (Fig 1), to investigate shielding effects of a strake and to identify problems arising from the complex flows existing near the junction of a strake and fuselage. The main emphasis was on how intake performance is affected by strake geometry, presence of strake bleed, and the form of the boundary-layer diverter.

The four strake geometries used are shown in Fig 10: slots were provided at the strake and fuselage junction so that the effect of strake bleed could be investigated. The tests consisted of both flowfield surveys and measurements of the internal performance of a square pitot intake ($CR = 1.20$) mounted underneath the various strakes. They included an examination of the effectiveness of several forms of boundary-layer diverter between intake and fuselage and between intake and strake undersurface.

5.2 Flow survey results

Mean flow angles over the survey region, with and without a strake, are shown in Fig 11. At both subsonic and supersonic speeds, the presence of the strake decreases the mean local incidence, and increases the mean local sidewash angle. These overall effects are very slightly reduced by the use of strake bleed. The flowfield under a strake is quite complex at moderate to high incidences (Fig 12), and there are considerable variations in local flow angle over the survey plane. A vortex, which appears to originate near the lower fuselage corner, develops beneath the strake, leading to a large region of low total pressure in the intake entry plane. The extent of this region, in which pressure loss coefficients ($\Delta P/q$) as high as 0.5 occur, increases with increasing incidence, with increasing length of strake ahead of the survey plane and with increasing thickness of fuselage boundary layer, but is independent of strake width. It is greatly reduced by strake bleed at low speeds, but bleed effectiveness deteriorates with Mach number and becomes quite small at supersonic speeds.

The influence of strake width and length ahead of the survey plane is summarised in Fig 13, using the smallest strake, (planform 'B'), as reference. In terms of mean flow angles, the shielding effect of a strake appears to increase with strake width, but vary little with strake length.

Sideslip causes considerable changes to the understrake flowfield. On the leeward side (β positive in Fig 14) the size of the understrake vortex increases, the region of low total pressure expands and both $\bar{\alpha}_L$ and $\bar{\beta}_L$ are increased: these effects are reversed on the windward side.

5.3 Intake performance

5.3.1 Subsonic speed

Intake performance for two strake geometries both with and without strake bleed is shown in Fig 15 for $M_\infty = 0.85$ and at a constant throat Mach number of 0.7. Results from isolated intake tests provide a datum with which to compare installed intake performance. Comparison of installed and isolated intake performance at the same conditions of incidence and free-stream Mach number show the effects of strake shielding whilst comparison with isolated intake performance at mean local flow conditions provides a measure of performance deviation from the 'ideal' shielded intake performance.

Pressure recovery can be improved significantly by understrake shielding at incidences beyond that at which the isolated intake develops total-pressure losses due to lower lip separation, but pressure recovery is highly dependent on strake geometry. Strake bleed improves pressure recovery at higher incidences in all cases by reducing the extent of the low total-pressure region under the strake. Also pressure recovery is reduced considerably in the presence of longer strakes such as planform 'O', relative to that for the shorter strake planform 'A', owing to the greater extent of the low total-pressure region from the understrake vortex. Fall-off in pressure recovery for shielded configurations where improvements over the isolated intake are found occurs with the onset of lower lip separation. The local incidence at which this occurs agrees well with the free-stream incidence at which separation is detected for the isolated intake.

With the exception of the long strake configurations at zero and moderate negative incidence (where -DC60 values are increased due to a local boundary-layer effect and vortex ingestion respectively) distortion level is controlled by the same lip separations and low total-pressure ingestion as pressure recovery. Consequently distortion level is generally low where pressure recovery is high and vice versa. However, the overall effects of the lip separations and low total-pressure ingestion are much greater on distortion than on pressure recovery and consequently at higher incidences the distortion level of the installed intake is higher than that of the isolated intake. On the other hand, unsteady pressure level, which for the isolated intake increased rapidly beyond 16° of incidence, remains low up to the highest incidences considered in the tests.

5.3.2 Supersonic speeds

Intake performance at near-critical mass flow conditions is shown in Fig 16 for Mach numbers of 1.4 and 1.8.

Results are more highly dependent on strake geometry than at subsonic speeds and strake bleed has only a small effect. Intake performance for configurations with the long strakes 'O' is inferior at nearly all incidences to that for configurations with the short strakes 'A'.

At positive incidence pressure recovery is increased considerably relative to the isolated intake, mainly due to reduced local Mach number. All configurations show losses in pressure recovery and large increases in distortion level at negative incidence due to vortex ingestion. Large pressure recovery losses and corresponding increases in distortion level are evident near zero incidence for the long-strake configurations, due to the understrake boundary-layer diverter being too thin to cope with the thicker boundary layer on the longer strakes. Similar effects are evident at incidences above 8° , due to ingestion of some of the low total-pressure region. At Mach numbers in excess of 1.4, pressure recovery for short strake configurations is noticeably higher than that which is predicted from isolated intake results at local flow conditions.

Distortion level at $M_\infty = 1.4$ for short strake configurations is comparable with isolated intake values up to about 7° of incidence, above which the shielded configurations show reduced distortion level. At Mach numbers above 1.4 distortion levels at low positive incidence are much greater than the values found for the isolated intake, but fall steadily with increasing incidence to near the isolated intake values at the highest incidences considered. The reason for the observed behaviour of pressure recovery and distortion level is basically the same as was illustrated for the underfuselage intake in Fig 8. However, in this case the normal shock is now interacting with both the fuselage and strake boundary layers leading to the shock configuration shown in Fig 17. Most of the intake capture plane is covered by a two-shock system, except for a small triangular region near the outboard lower corner where the flow is compressed only by the normal shock. The sudden decrease in total pressure over this region gives rise to the large -DC60 values at low incidence. These values reduce at higher incidences as this region disappears as local Mach number decreases and the whole intake becomes immersed within the oblique shock waves.

Unsteady pressure levels are always increased over those of the isolated intake but normally lie within acceptable levels. The only exception is the long strake planform 'O' at the higher Mach number, where considerable dynamic activity occurs at all incidences other than 4° .

5.3.3 Intake performance in sideslip

Excursions to moderate angles of sideslip affects intake performance only on the leeward side. Fig 18 illustrates that losses in pressure recovery and increases in both steady state distortion and unsteady pressure level occur beyond a certain sideslip angle. These effects are greatest at supersonic speeds, where they are significant beyond sideslip angles of 2° for short strakes and at even lower angles for long strakes. Behaviour is similar at subsonic speeds, but a higher sideslip angle can be tolerated before performance deterioration becomes significant. For instance, for a short straked configuration with bleed, significant deterioration does not occur until a sideslip angle of 5° is exceeded.

Pressure measurements at the intake throat show that on the leeward side in sideslip large amounts of air can be ingested from the enlarged understrake low pressure region. Also, flow surveys show that local flow angles increase rapidly on the leeward side with increasing sideslip angle, (Fig 14), so that local incidence values greater than model incidence can be present at moderate sideslip angles. These effects lead to the situation where there are no benefits from strake shielding, but the attendant problem of low-pressure ingestion remains.

5.4 Concluding remarks

At both subsonic and supersonic speeds some benefits can be obtained by using a strake to shield an intake from the effects of incidence. However, the results are highly configuration dependent, with performance depending on the exact nature of strake geometry, boundary-layer diverter geometry, and strake-bleed geometry. Problems likely to arise include increased distortion at higher incidence at subsonic speeds, high distortion at low incidence at supersonic speeds, and a sensitivity of performance of the leeward intake to sideslip.

The present work suggests ways in which some of these problems may be overcome. Careful tailoring of the boundary-layer diverter geometry (notably thickening) in conjunction with the strake bleed system is likely to offer performance improvement at high incidence and in sideslip at subsonic speeds. Good performance is likely to be sustained to higher incidences by shifting the lower cowl lip from the region where local flow angles are greatest and shielding is at a minimum. At supersonic speeds, distortion levels are most likely to be improved by control of the shock-wave boundary-layer interaction by means of appropriate splitter plates, and these may be aspirated if required.

6 THE BENEFICIAL EFFECT OF LIP STAGGER

6.1 Küchemann and Weber⁶ have shown that, at zero incidence, staggering the lips of an otherwise symmetrical two-dimensional inlet causes increased velocity increments on the rear lip and decreased increments on the forward lip. Hence it might be supposed that lip stagger will tend to increase the likelihood of flow separation on the rear lip under certain conditions. However, it was considered that for thin-lipped intakes these conditions would only arise near zero incidence and at mass flow ratios appreciably greater than unity, whereas at more normal mass flow ratios, the incidence shielding effect of the forward lip on the rear lip was likely to be of much greater importance. To check this hypothesis, some calculations were made of the velocity distribution over a simplified two-dimensional model of an intake in incompressible flow. This intake, of 1.25 contraction ratio, was modelled from two flat plates of identical thickness and with the same 2:1 ratio semi-elliptic nose shape. The calculations were made using a modified version of a panel method program originally intended to deal with multiple aerofoils, and covered a range of stagger angles, incidences and mass flow ratios. Fig 19a shows the maximum velocity on the inside of the lower lip, as a function of stagger angle, for incidences of 0° , 10° and 20° and mass flow ratios of 0.6 and 1.0. The powerful effect of stagger in reducing the peak velocity on the lower lip at high incidence is very apparent and, in accordance with the original assumption, of much greater significance than the slight increase in peak velocity that occurs at zero incidence when MFR = 1.0. Even quite modest stagger angles (around 20°) produce a worthwhile reduction in peak velocity and, at the other extreme, 70° of stagger would give almost complete incidence shielding to the lower lip under most flight conditions.

It should be added that this benefit is not gained without a corresponding penalty. Fig 19b shows the maximum velocity on the outside of the upper lip of the intake. With increasing stagger, the upper lip effectively loses the shielding effect of the lower and the peak velocity increases. This increase in peak velocity is much less than the reduction which occurs on the lower lip, but in principle it could lead to some increase in spillage drag.

6.2 The above analysis suggests that the maximum benefit from lip stagger will be obtained by using a larger stagger angle (60° or more) but, for initial testing of the concept, a less extreme value of 45° was selected. Such an intake (with a contraction ratio of 1.25) was constructed and tested on Model I in the RAE 3 ft x 3 ft tunnel and later, at higher incidences, in the ARA 8 ft x 9 ft tunnel. The throat dimensions and duct shape between throat and engine face were the same as for the tests described in section 3.

The results, for a constant throat Mach number of 0.6, are summarised in Figs 20 and 21. At $M_\infty = 0.9$, over most of the incidence range from -4° to $+30^\circ$, the performance is equal to (or very slightly better than) that of the 1.15 CR intake mounted underneath the fuselage. Above 30° incidence, η starts to fall-off fairly rapidly and -DC60 increases. However, the main disadvantage occurs at supersonic speeds, as shown by the results for $M_\infty = 1.4$. At incidences greater than 8° , recovery and distortion levels are slightly better than those of the 1.08 CR intake mounted underneath the fuselage, but, at lower angles, η undergoes a steep decline. The reason for this is almost certainly due to a shock - boundary-layer interaction on the inside of the upper lip of the intake causing a major separation of the flow. If this is the case, it should be curable by using a suitable design of boundary-layer bleed.

The effect of sideslip on pressure recovery at $M_\infty = 0.9$ is shown in Fig 21. The recovery tends to fail at positive sideslip angles (when the intake is on the leeward side of the body), the effect becoming more pronounced with increasing incidence. However, this problem is inherent in all side-mounted intake arrangements and is not specific to the staggered configuration. Some alleviation should be possible by employing a thicker boundary-layer diverter.

6.3 In general, the results obtained at subsonic speeds from these preliminary tests confirm the theoretical predictions that lip stagger is a powerful technique for improving intake performance at high incidence. Provided that the problem of fall-off in pressure recovery at low incidence at supersonic speeds can be overcome by the use of a suitable boundary-layer bleed system, it is concluded that it should be possible to design a side-mounted staggered lip intake that will closely match the performance of an underfuselage pitot intake installation over a wide range of speeds.

7 CONCLUSIONS

All the methods of improving intake performance at high incidence considered in this paper - lip shaping, inlet shielding and lip stagger - are effective to some extent. The usefulness of lip shaping is mainly confined to subsonic speeds, where considerable

benefits can be obtained by increasing contraction ratio, thickening and cambering the lower lip, and incorporating a lip slot. However such modifications can incur a large supersonic drag penalty and a contraction ratio between 1.15 and 1.20 is likely to be near optimum for a pitot intake intended to cover a wide speed range.

The flowfield under a strake is quite complex at high incidence, but a considerable degree of incidence shielding can be achieved by an intake in this location. The best configuration is a fairly short and broad strake with adequate boundary-layer bleed in the strake-fuselage junction, and such an arrangement can give excellent intake performance at subsonic speeds. The main problems occur at higher Mach numbers, due to interaction between the intake shock and the boundary layers on both the fuselage and the underside of the strake. Considerable detail development work on boundary-layer diverters and splitter plates is likely to be necessary before these problems can be satisfactorily overcome in a practical design. As with all side-mounted intakes, some deterioration of performance is to be expected in sideslip when the intake is on the leeward side of the body.

The underfuselage intake installation is attractive aerodynamically, and intake performance can be maintained up to high angles of incidence and over a wide range of sideslip at subsonic speeds. Shock boundary-layer interaction problems can arise at supersonic Mach numbers, but their solution should prove much simpler than for an understrake intake. Length of fuselage ahead of the intake does not appear to be very significant, except at negative incidences.

The concept of using lip stagger to provide shielding of the lower lip has been demonstrated and, for an intake with a moderate degree of stagger, incidence performance at subsonic speeds can approach that of an underfuselage intake installation. The main problem is a deterioration of pressure recovery at low incidence at supersonic speeds, but it is considered that this should be curable with a suitable boundary-layer bleed.

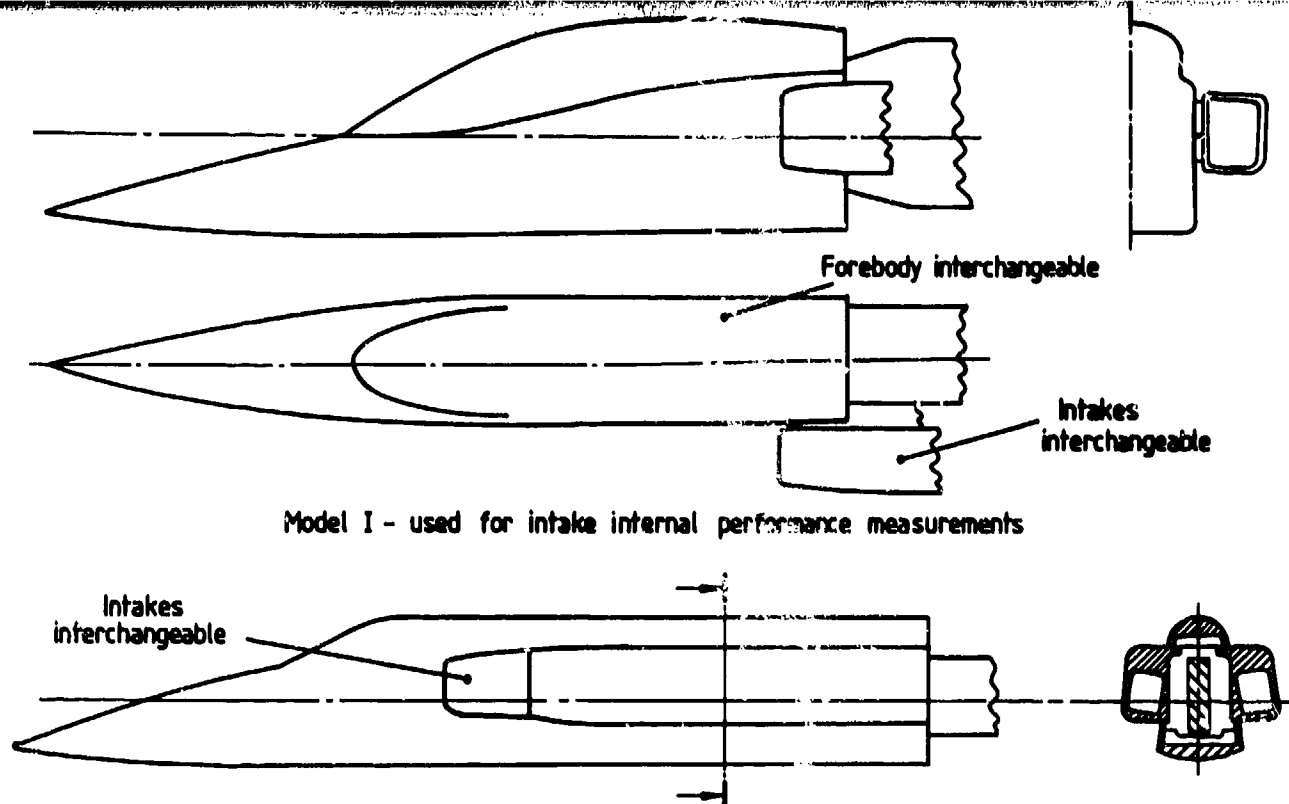
Acknowledgment

The authors would like to acknowledge the assistance of Mr W Hirst of ARA Ltd in carrying out some of the tests described in this paper.

REFERENCES

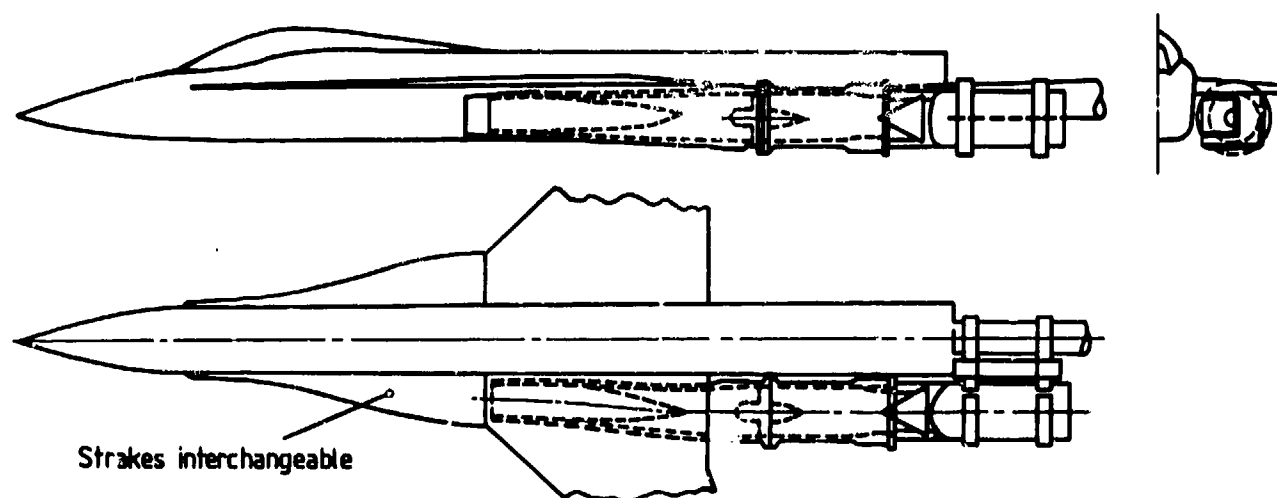
- 1 K W Lotter and J Malefakis, Intake design and intake/airframe integration for a post-stall fighter aircraft concept. AGARD CP247, Paper No.32, October 1978
- 2 J A Cawthon, Design and preliminary evaluation of inlet concepts selected for manoeuver improvement. AIAA Paper 76-701, July 1976
- 3 M D Dobson and E L Goldsmith, The external drag at subsonic and supersonic speeds of fuselage-side air intakes for strike fighter aircraft. ICAS Paper 70-49, 1970
- 4 L E Surber and D J Stava, Supersonic inlet performance and distortion during manoeuvring flight. AGARD CP91, Paper No.25, September 1971
- 5 J Patierno, YF-17 design concepts. AIAA Paper 74-936, August 1974
- 6 D Küchemann and J Weber, Aerodynamics of propulsion, Chapter 4, p 73. McGraw-Hill Book Company Inc, NY, 1953

Copyright
©
Controller HMSO London
1980



Model I - used for intake internal performance measurements

Model II - mounted on force balance and used to measure intake external drag
(flow measuring equipment not shown)



Model III - used for flowfield surveys and intake internal performance measurements

Fig.1 The three intake models used in this investigation
(models are not shown to same scale)

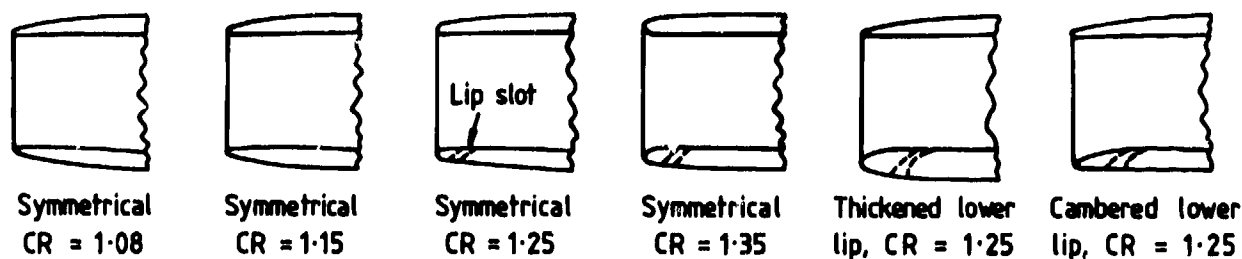


Fig.2 Intake lip variants tested on Model I, A_{th} constant for all intakes

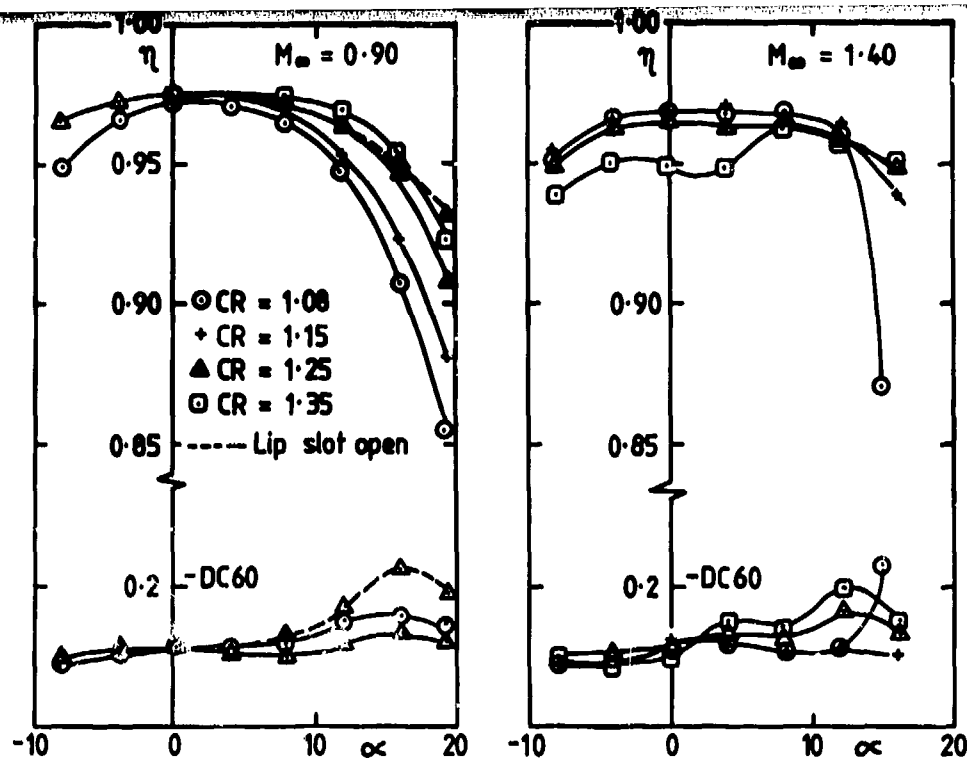


Fig. 3 Effect of varying contraction ratio on intake internal performance. $M_{th} = 0.6$

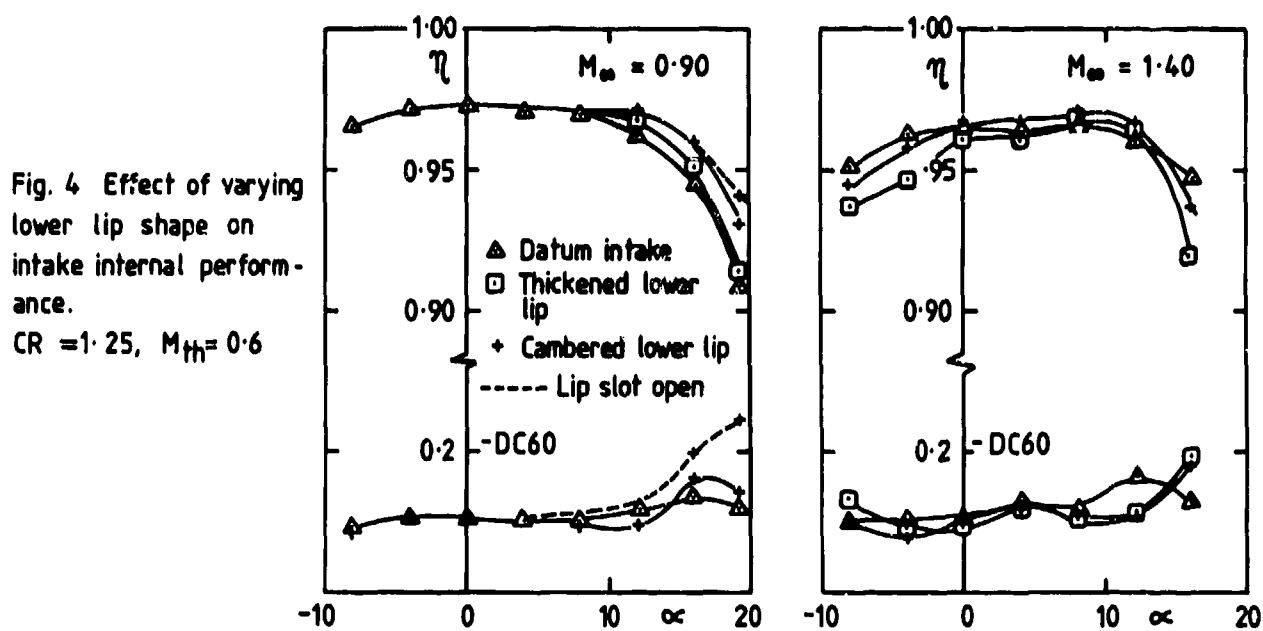


Fig. 4 Effect of varying lower lip shape on intake internal performance. $CR = 1.25$, $M_{th} = 0.6$

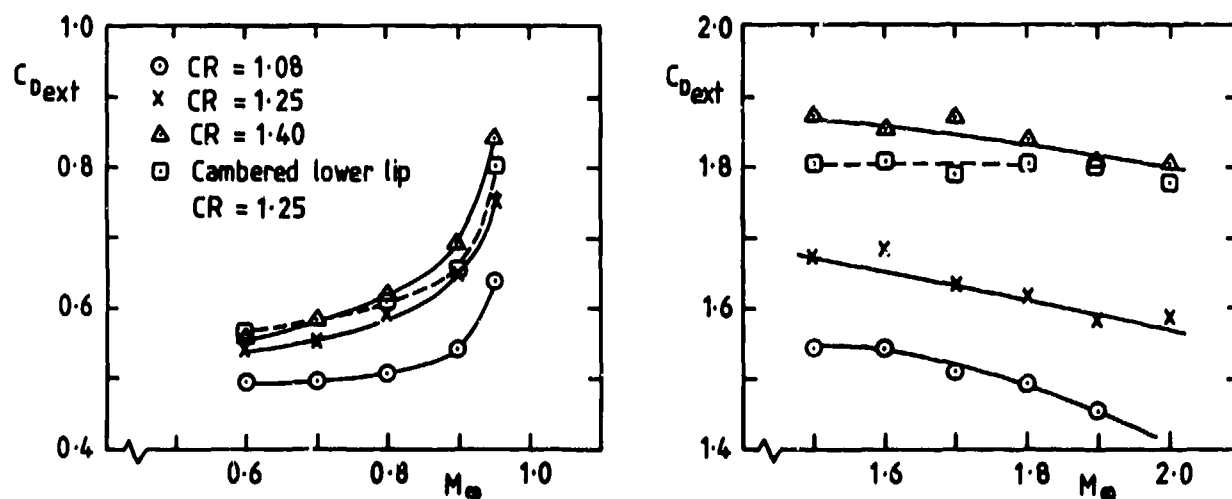


Fig. 5 Effect of contraction ratio and lip shaping on intake drag, $\alpha = 0^\circ$, $M_{th} = 0.6$

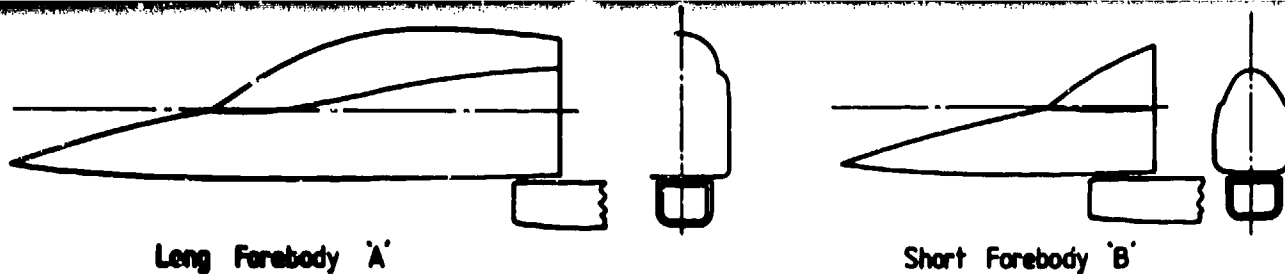


Fig. 6 Alternative underfuselage intake arrangements tested on Model I

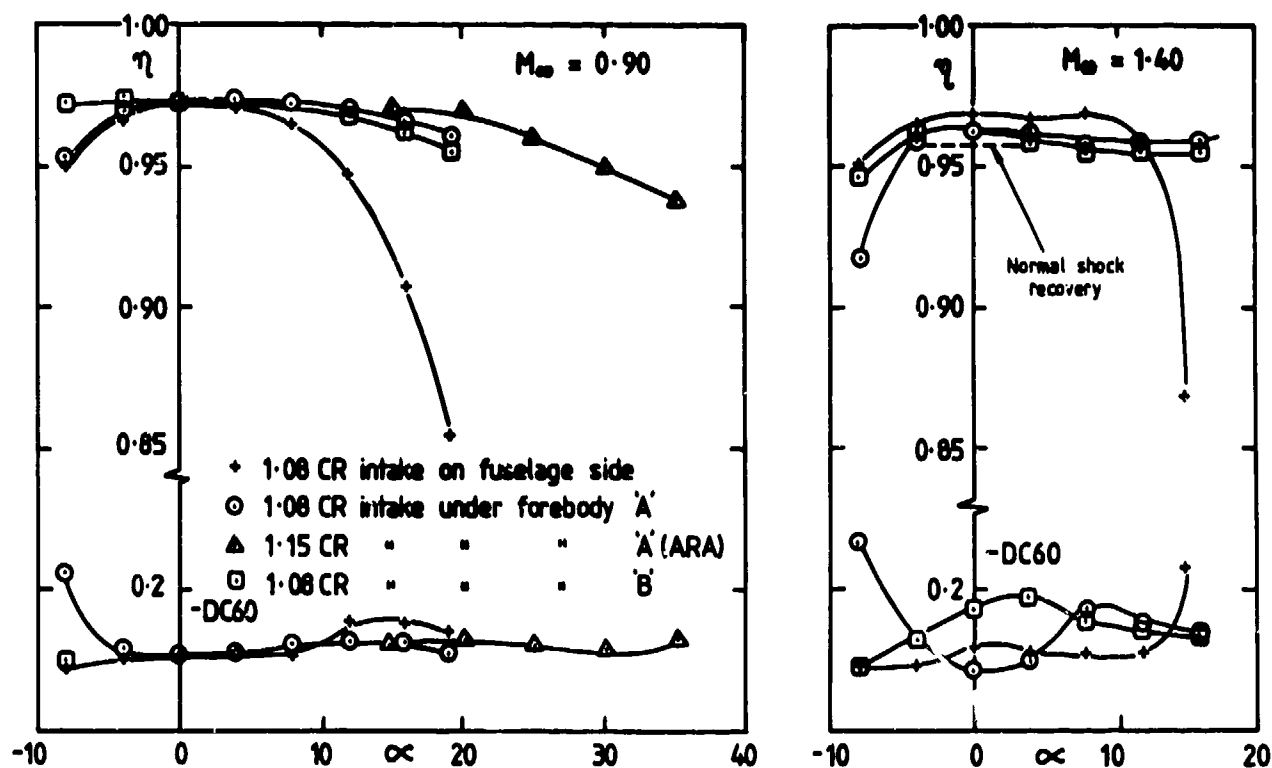


Fig. 7 Internal performance of underfuselage intake configurations tested on Model I. $M_{th} = 0.6$

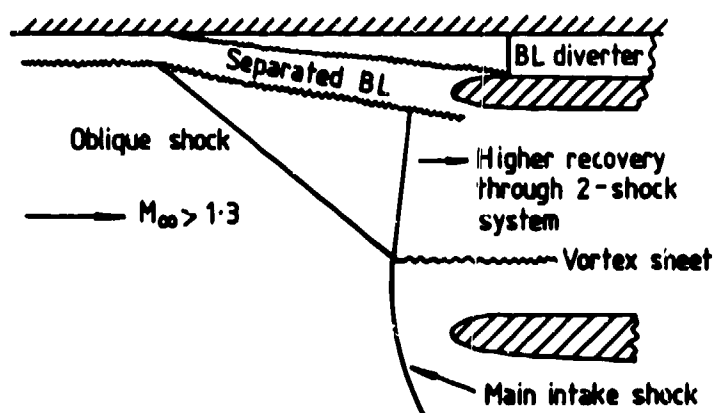
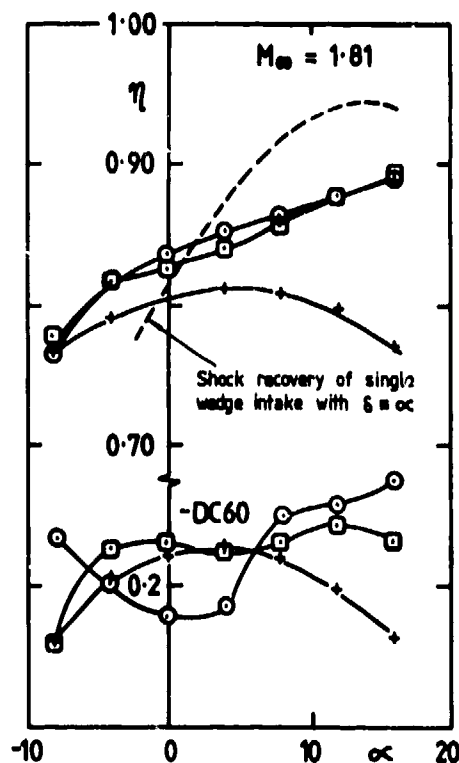


Fig. 8 Formation of lambda shock system ahead of a pitot intake (diagrammatic)

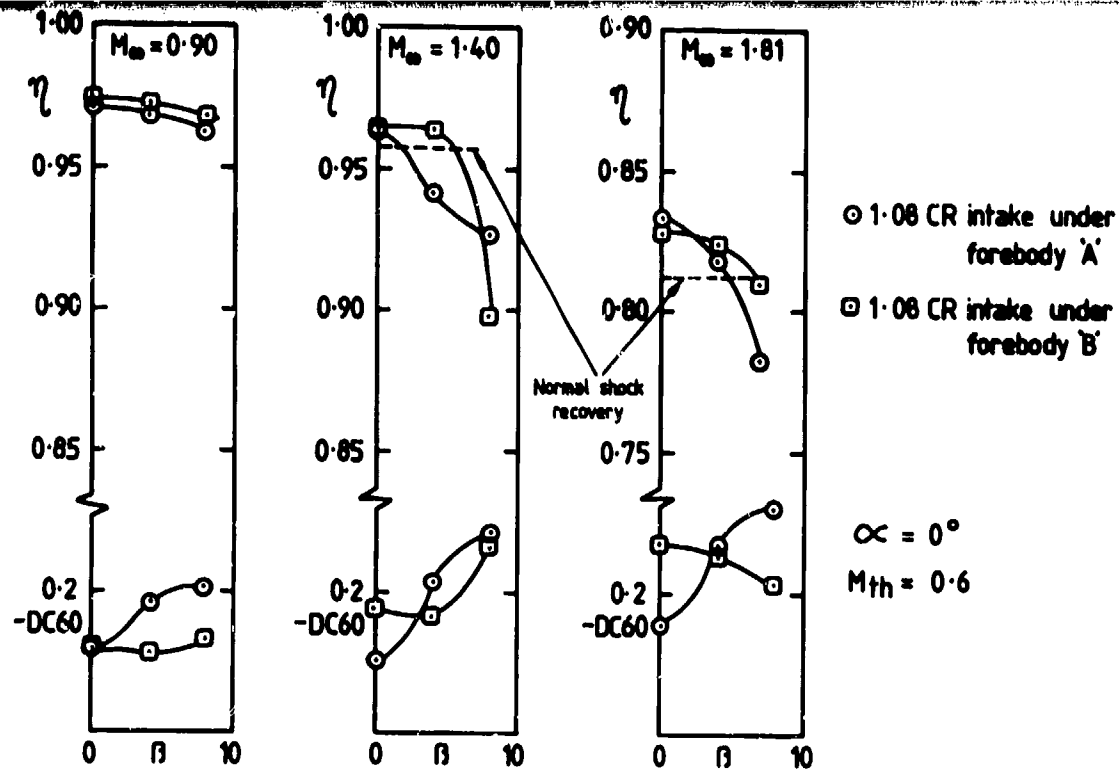


Fig. 9 Effect of sideslip on internal performance of underfuselage intakes

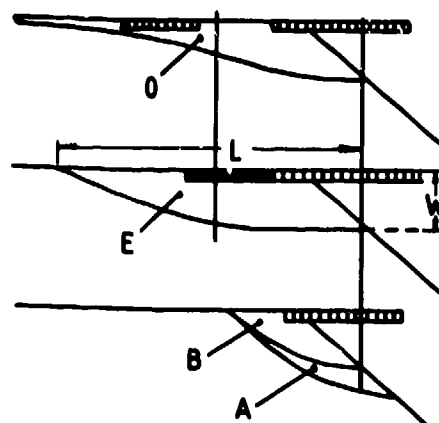


Fig. 10 Strake and bleed geometries tested on Model III

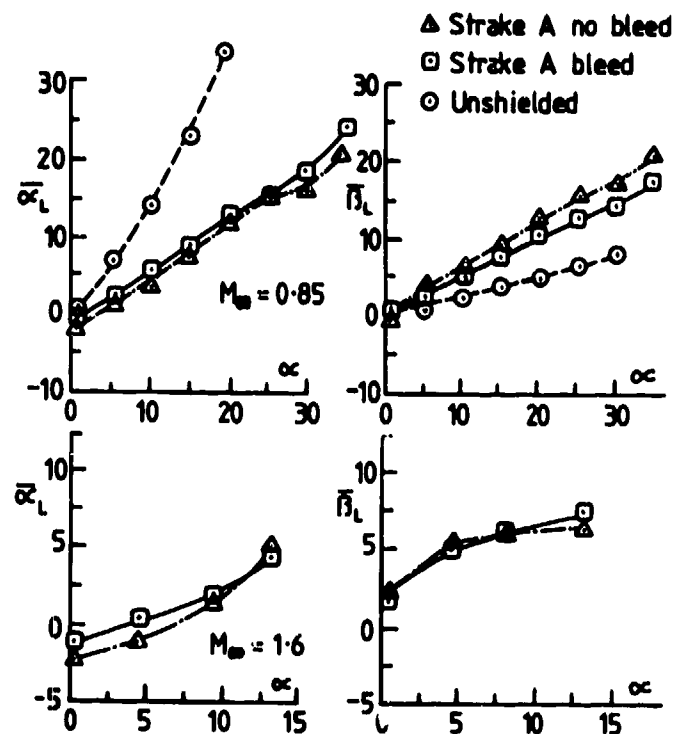


Fig. 11 Variation of mean local flow angles with incidence

————→ increases with increasing α ————→ decreases with bleed

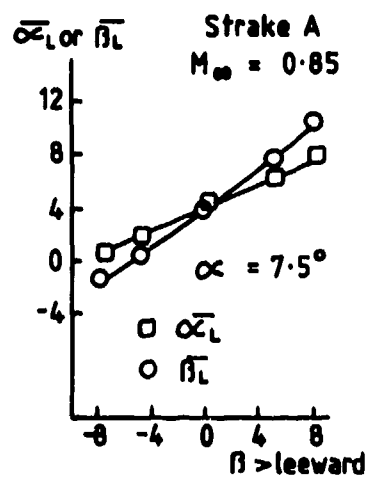


Fig. 14 Variation of local flow angles with sideslip angle

Fig. 13 Variation of mean local flow angles with stroke length and width

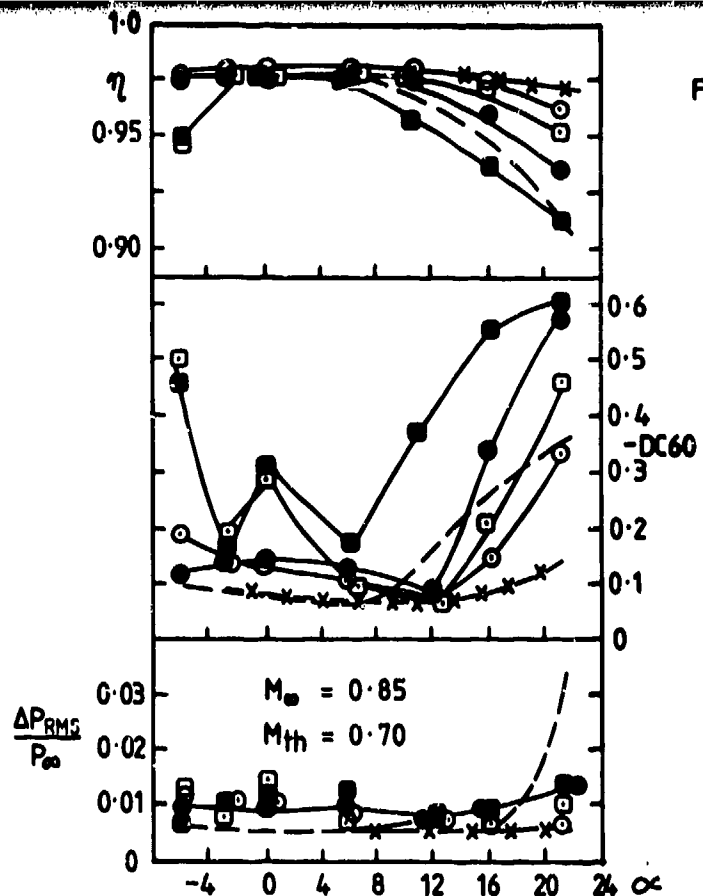


Fig. 15 Influence of strake geometry on intake performance at subsonic speed.

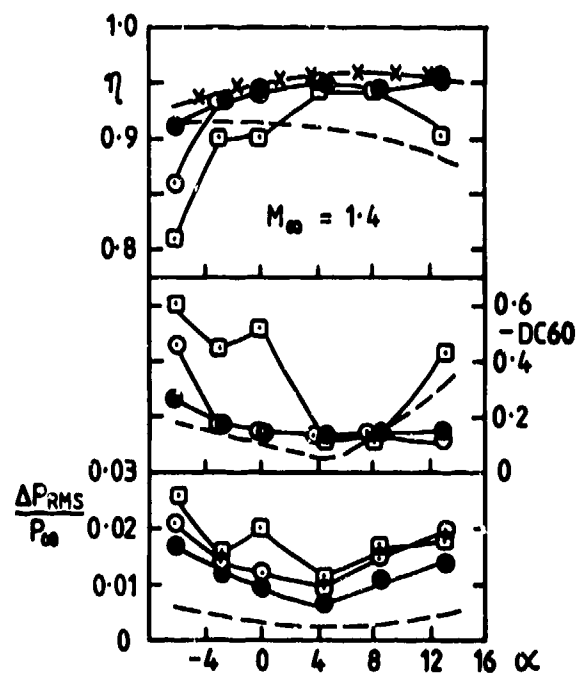
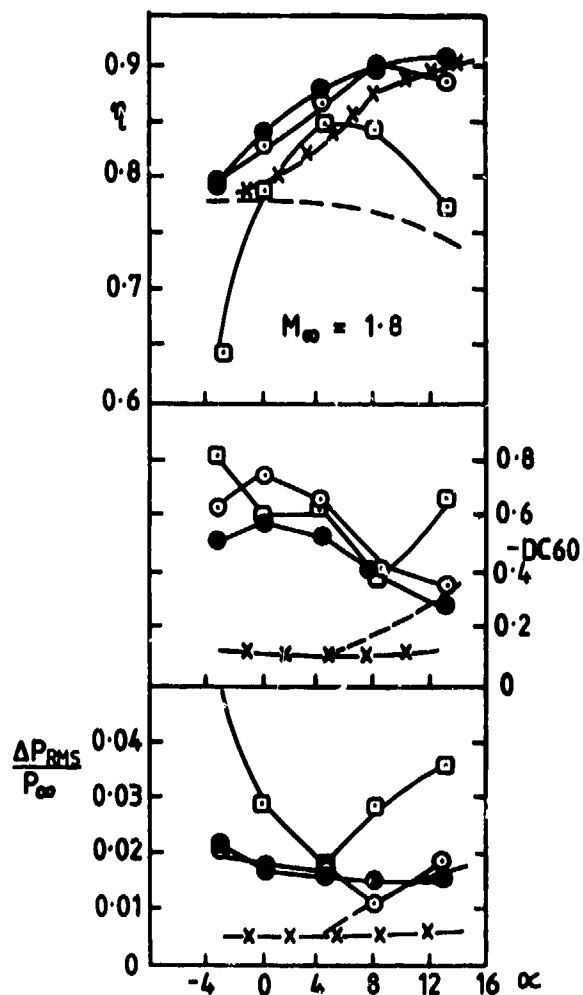


Fig. 16 Influence of strake geometry on intake performance near critical point at supersonic speeds.



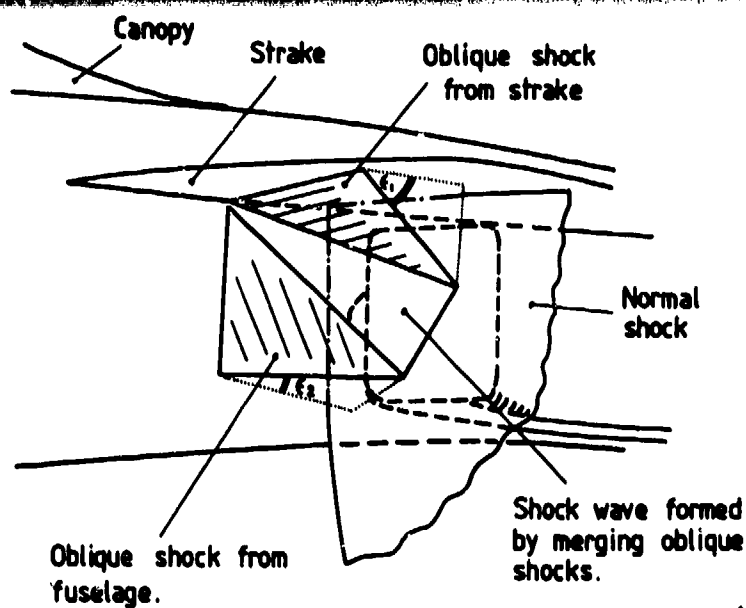


Fig. 17 Shock wave pattern at higher supersonic Mach numbers (Diagrammatic only)

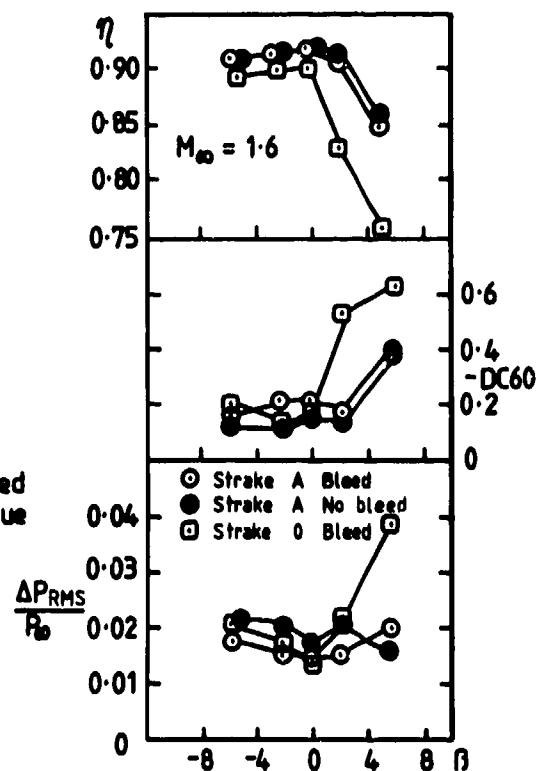


Fig. 18 Variation of intake performance with sideslip

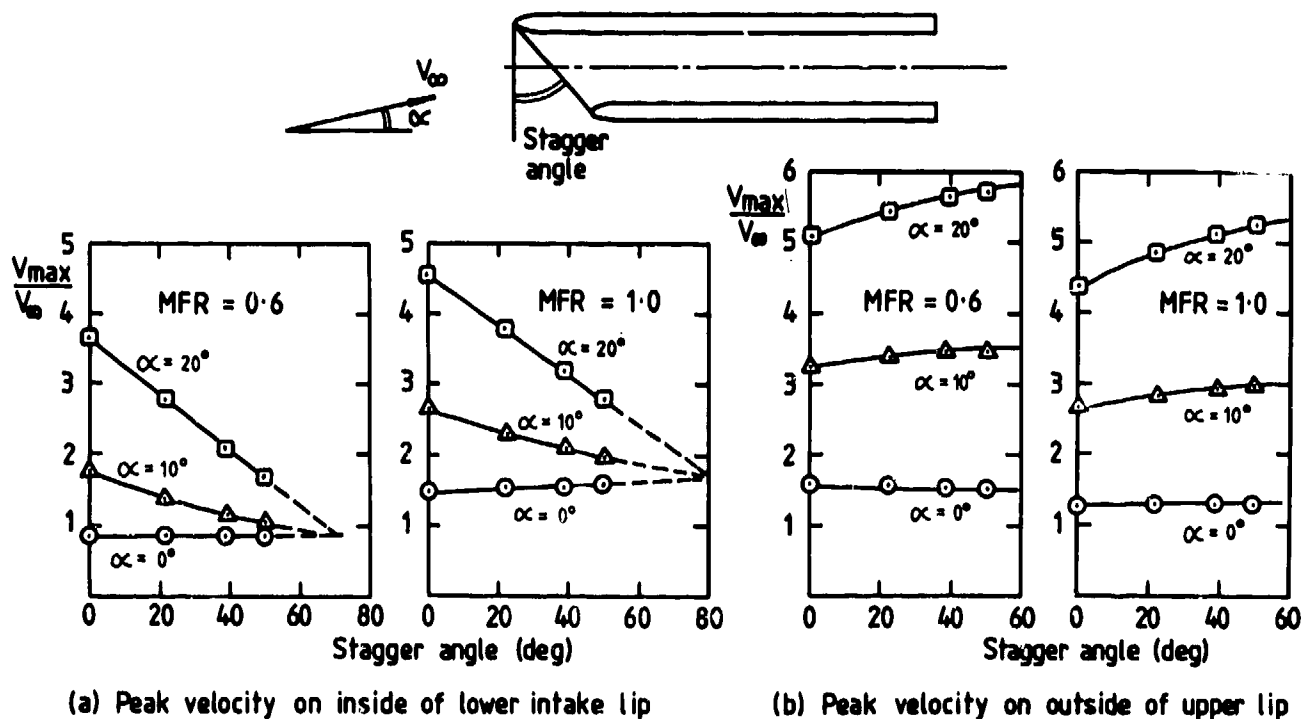


Fig. 19 Theoretical peak velocities on lips of a 2-dimensional staggered intake, CR = 1.25

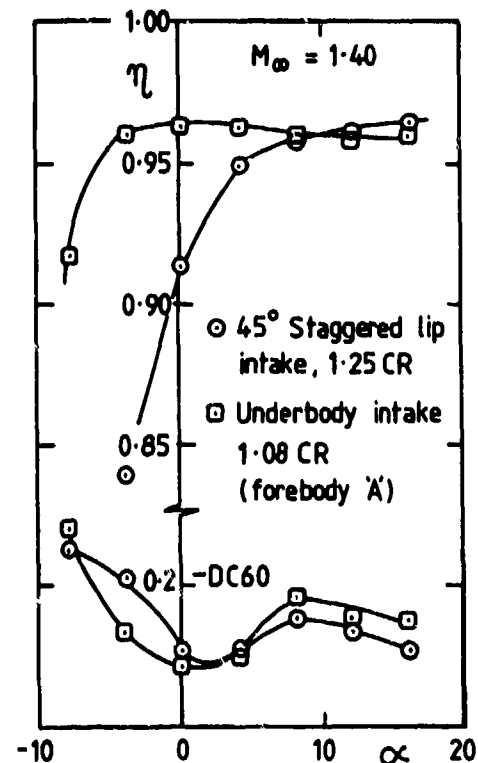
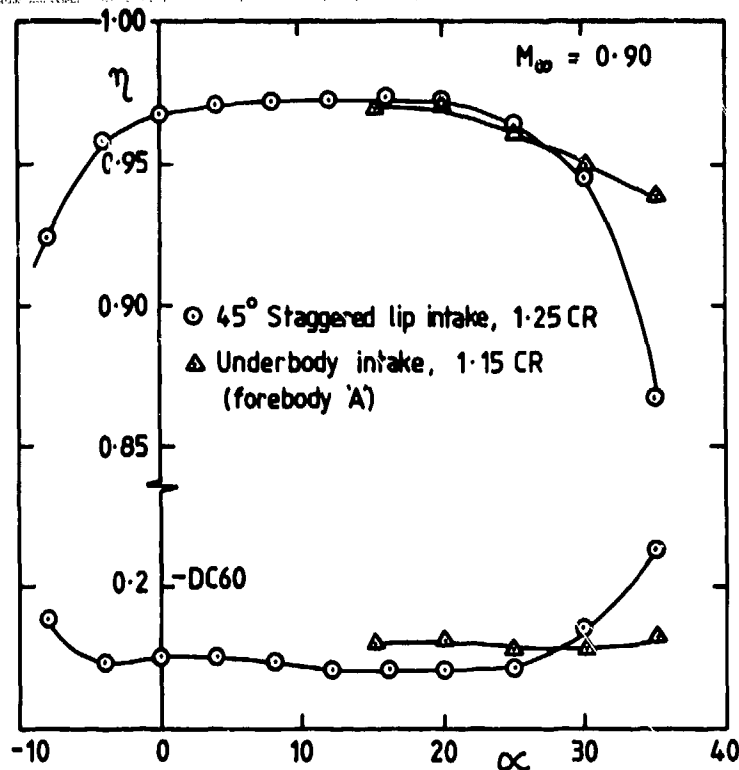


Fig. 20 Comparison of internal performance of 45° staggered and underbody intakes, $M_{th} = 0.6$

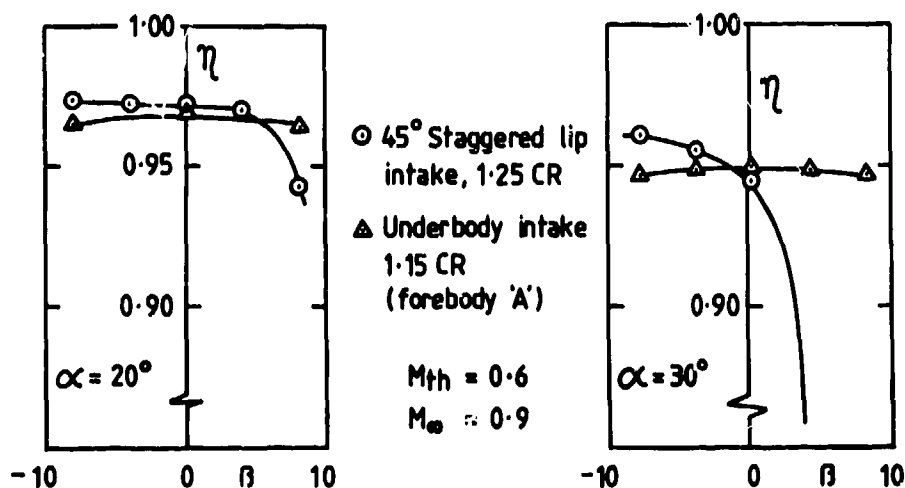


Fig. 21 Effect of sideslip on pressure recovery of staggered and underbody intakes

PREDICTION AND MEASUREMENT OF TIME-VARIANT,
THREE-DIMENSIONAL FLOWS IN MILITARY AIRCRAFT INTAKES

by

D. E. Colbourne and J. E. Flitcroft
National Gas Turbine Establishment
Pyestock, Farnborough, Hants GU14 0LS
England

SUMMARY

Projected enhancements to the operational capabilities of future military aircraft present designers with challenging aerodynamic and structural problems. An early indication of installation effects which may compromise engine performance or stability can reduce both design and subsequent development costs. Theoretical and experimental techniques have been developed at NGTE to quantify these effects and thus contribute to the optimisation of installed powerplant performance.

The development of a computational method suitable for predicting the three-dimensional flows within the diffuser sections of aircraft intakes is described. The Paper discusses a novel, fast, method for automatic grid-generation, applicable to ducts of any smoothly varying cross-sectional shape. The development of a finite-volume, time-marching method for solving the flow equations is also described. The validity of the chosen techniques is discussed in the light of comparisons with analytical and empirical results.

Whilst the theoretical methods are beginning to yield useful results in predicting steady, quasi-inviscid duct flows, empirical techniques have been developed to examine flows in which viscous or time-variant effects are dominant. A rotating yaw meter rake has been developed at NGTE to undertake detailed flow surveys at the exit of model diffusers, and results may be obtained from tests both in isolation and in the presence of a compressor. The development of instrumentation and data processing facilities for measuring instantaneous engine face total pressure distortion in small scale models is also described, together with the validation of this technique by comparison with results from a full-size replica of the intake tested under free-jet conditions.

1. INTRODUCTION

The tactical and strategic specifications for military aircraft, and proposed enhancements for future projects, have progressively increased the performance required of both airframe and powerplant. Extensions to the flight envelope, and increased agility within that envelope, have presented the designer with challenging aerodynamic and structural problems. In particular, extremes of speed and attitude have extended the range of operation over which powerplant intakes are required to perform compatibly with the engine. An early indication of installation effects which may compromise engine performance or stability is thus a necessary part of design, development and improvement phases. Both theoretical and experimental techniques have therefore been developed at NGTE to quantify these effects and thus contribute to the optimisation of installed intake performance.

The designs for most aircraft intake systems include a diffuser section which decelerates the incoming air from high subsonic speeds at the throat to a Mach number of 0.4 to 0.5 at the engine face. Any flow maldistributions present at the throat will, depending on the design of this diffuser, be accentuated, changed or attenuated before reaching the engine. The cross-sectional shape at the throat, the relative positions of inlet and engine and the position of structural features fundamental to the aircraft design will all be constraints on how this diffusion can best be achieved.

With the increasingly high costs of full-scale testing a method for assessing time-averaged diffuser performance during the design phase will reduce both design and subsequent development costs. At NGTE two approaches to this problem have been developed, one theoretical the other experimental, both of which can be applied flexibly and relatively cheaply at an early stage of, and as a contribution towards, the design process.

Whilst these experimental facilities are useful for establishing the time-averaged sensitivity of subsonic diffuser designs to flow non-uniformities, it is recognised that engine stability is also affected by flow distortions persisting for only about one engine revolution. Consequently facilities have been developed to assess the levels of time-variant flow non-uniformity likely to be encountered in candidate intake designs. An area of the aircraft operating envelope where significant non-uniform, time-variant flows are likely to be found is in high speed supersonic flight, where strong shock waves are present at the diffuser entry. To complement the time-averaged diffuser performance measurements, NGTE has therefore developed facilities for the supersonic testing of both full-size and scaled intakes equipped with dynamic pressure measuring instrumentation.

2. COMPUTATIONAL FACILITIES

A theoretical approach to analysing the flow in diffusers requires a scheme for solving the three-dimensional compressible flow equations within ducts of any smoothly varying cross-sectional shape. As enhanced computing facilities and improved solution algorithms become available, increasingly sophisticated flow simulations may be obtained within acceptable time-scales¹. However, whichever calculation method is adopted - whether finite-difference, finite-volume or finite-element - the basic problem of how to model the diffuser boundary accurately, and where to place the calculation grid-points, or element nodes, within this boundary, must first be solved.

Any practical diffuser may be divided up by a series of cross-sectional surfaces, not necessarily parallel, and its geometry specified by the X, Y, Z co-ordinates of several points around the perimeter of each cross-section. For axial boundary fitting, the corresponding boundary points on each cross-section may be joined by parametric cubic splines². The problem of grid-generation then reduces to one of establishing a reasonable distribution of grid-points on each of these arbitrarily shaped surfaces. It is possible to use a large number of regularly shaped grid elements (Figure 1(a)), and this grid enables the flow equations to be solved in their simplest form, but with complicated boundary conditions. Alternatively, a smaller number of curvilinear elements may be used to form a piecewise fit to the boundary (Figure 1(b)). The resulting flow equations are now more complicated, but with very simple boundary conditions, and this approach, with the boundary accurately represented, is to be preferred. Since, for efficient implementation of the flow solution algorithms, there must also be an ordered numbering of the grid-points on and within the boundary³, the best method of fitting the boundary may be considered as a full transformation of each cross-section into a curvilinear boundary coincident co-ordinate system. This process is illustrated in Figure 2. As explained by Gordon and Hall³, this process is equivalent to the solution of Laplace's equation for the grid-point co-ordinates and, although computationally expensive³ an automation of this process has been presented by Chu⁴. This work has been extensively developed by Thompson et al (eg Reference 5) and, widely used for external flow calculation, it appeared to have potential for application to the duct flow problem.

A summary of the Thompson method, and how it was implemented at NGTE is given in Reference 6. However, the quality of the grid-point distribution thus obtained proved to be highly dependent upon the cross-sectional shape of the duct, requiring considerable user interaction with the computer program to achieve a satisfactory distribution. The requirement for an automatic grid-generation process was therefore not satisfied, and, due to the iterative nature of the solution process, computing times (on the ICL 1904S*) of 120 to 360 seconds were required for each plane. These drawbacks, of quality and expense, appear to be similar to those reported by Roberts and Forester⁷ when using the Thompson grid-generation method for their duct flow calculations.

A novel, fully automated, method of grid-generation was therefore developed at NGTE, which is based on an analytical rather than an iterative solution to Laplace's equation. A full description of the method, including all the relevant intermediate calculations, is given in Reference 6, but the basic philosophy may be summarised as follows.

If the distribution of any property U, specified on the circumference of a circle, radius R, is given by a function

$$U = U(R, \phi) \quad \dots(1)$$

and if the distribution of that property within the circle $u = u(r, \theta)$ satisfies Laplace's equation

$$\nabla^2 u = 0 \quad \dots(2)$$

then a solution will be given by Poisson's Integral Formula (see, eg Reference 8).

$$u(r, \theta) = \frac{1}{2\pi} \int_0^{2\pi} U(R, \phi) \frac{R^2 - r^2}{R^2 - 2Rr \cos(\theta - \phi) + r^2} d\phi \quad \dots(3)$$

Further, if the function (1) is a Fourier series, ie

$$U(R, \phi) = a_0 + \sum_{n=1}^{\infty} (a_n \cos n\phi + b_n \sin n\phi) \quad \dots(4)$$

then an analytical solution to Equation (3) may be derived⁶ which is of the form

$$u(r, \theta) = a_0 + \sum_{n=1}^{\infty} \left(\frac{r}{R}\right)^n (a_n \cos n\theta + b_n \sin n\theta) \quad \dots(5)$$

In practice, since U is only specified at a finite number of points, N, the Fourier series must be truncated to terms in $\cos k\phi$ and $\sin k\phi$, where $k = N/2$ if N is even, and $k = (N - 1)/2$ for N odd.

Returning to the grid-generation problem, if U is the X, Y or Z co-ordinates of points around the duct boundary, then the co-ordinates of the grid-points within the boundary will be given by

$$x(r, \theta) = a_{x0} + \sum_{n=1}^k \left(\frac{r}{R}\right)^n [a_{xn} \cos n\theta + b_{xn} \sin n\theta]$$

and similarly for $y(r, \theta)$ and $z(r, \theta)$. The parameters r, θ refer to grid-points within a generating circle, whose distribution will govern the distribution of physical grid-points within the duct boundary. A suggested criterion for a good distribution of grid-points within an arbitrary shape is that the grid elements thus generated should be of equal area, and the r, θ distribution is chosen to meet this criterion with the generating circle. The grid generated within a circular boundary by this method is shown in

Figure 3. It is, by definition, also the distribution of grid-points within the generating circle, and thus illustrates the accuracy of the method. For an asymmetric inlet shape, the method produces the distribution shown in Figure 4. For all shapes, the program requires no user intervention to modify the generated grid, and only 12 to 24 seconds computing time per plane. Thus a fully automated technique has been programmed and an order-of-magnitude saving in computer time has been demonstrated. If, later, boundary layer effects are to be modelled, increased grid definition close to the duct walls may be obtained simply by reducing the r increment for the grid lines close to the boundary of the generating circle.

2.2 FLOW CALCULATIONS

The solution method for the flow equations currently adopted at NGTE is a finite-volume time-marching scheme, originally developed by Denton for blade-to-blade flows in turbomachinery⁹. This method was chosen mainly for its simplicity and corresponding computational speed. The method has been adapted to calculate the flow in two-dimensional and axisymmetric ducts and in these simplified forms the stability and convergence of the time-marching process has been thoroughly investigated. Informative graphical output facilities have also been developed to assist with the analysis of results from the flow calculations. The grid-generation program and the full 3-D finite-volume time-marching algorithms have been linked so that solutions to the three-dimensional Euler equations for compressible, inviscid flow within ducts of any smoothly varying cross-sectional shape (ie any practical diffusers) may now be obtained. A form of presentation similar to that used for experimental results (see Section 3) has been developed to assist in the analysis of the calculated flows. An important feature of this combined geometry/flow calculation package is the facility to examine quickly and easily the effect of changes in geometry on the diffuser exit flow, thus enabling the programs to be employed as a useful part of the design process.

Two examples of some preliminary results from this 3-D flow calculation package are now presented.

A theoretical investigation of the cross-flow generated within a curved, square cross-sectioned, duct, based on the secondary flow theory of Reference 10, has demonstrated that if the duct is subjected to a non-uniform axial flow at inlet, a degree of circumferential flow will be generated at the duct exit. A similar geometry was investigated using the 3-D flow calculation package. When subjected to a non-uniform total pressure distribution at inlet, the flow at exit from a 14° bend was calculated to be as shown in Figure 5. With the current size of computer used for this simulation, a very coarse grid had to be used, but the essential features of the secondary flow are visible.

A general, asymmetric, S-bend diffuser, whose geometry is illustrated in Figure 6 has also been examined. A feature of the flow calculation method is that the development of the flow can be examined at several stations along the duct, as illustrated by Figure 7, showing the non-axial components of the flow about 2/3 of the way along the duct. Further validation of the flow calculation method will be undertaken by comparison with the results obtained for this duct using the experimental facilities described below.

3. INTAKE DIFFUSER TESTING

If the structural or operational requirements of an aircraft do not allow for an optimum diffuser design to be achieved, a degree of flow maldistribution may have to be tolerated. However, an early assessment of the engine performance penalties thereby incurred may be obtained by examining the effect of the diffuser exit flow on a compressor.

Two complementary rigs have therefore been established at NGTE for assessing the performance of aircraft intake diffusers. A diffuser, scaled to 30.5 cm engine face diameter and constructed accurately, cheaply and quickly in glass-fibre-reinforced plastic, may be connected to a well-instrumented 2-stage transonic fan (described in Reference 11) or to a dummy version of that compressor. This dummy compressor consists of a duplicate casing and a representative centre body only, air being induced through the rig by an ejector system well downstream.

The primary feature of both rigs is a rake of 5-hole yaw meter probes, which may be installed just upstream of either compressor, to measure the flow delivered by a diffuser both in isolation and in the presence of rotating turbomachinery. The rake is shown installed in the compressor in Figure 8. The large dome protruding through the centre of the rake covers the Vibrometer slip-ring unit, used to transmit blade strain-gauge signals. It can also be seen that the probes on adjacent arms of the yaw meter rake are at different radii, such that by rotating the rake (while the rig is running) and recording data at equal increments, a complete circumferential picture of the flow at the centre of eight equal-area rings may be obtained.

The normal compressor face time-averaged total pressure distributions may be established but in addition the static pressure distribution, (and hence, if required, Mach number) as well as the circumferential and radial flow angles relative to each probe can be calculated. Results for a 24-position (ie $7\frac{1}{2}^\circ$ increment) test run, involving less than one hour's running, may be presented graphically as shown in Figure 9. The tail of each arrow indicates the position to which the data apply, the direction of the flow at that point is illustrated, and the length of the arrow is proportional to the non-axial flow angle (see scale). The radial outflow near the centre is, of course, due to the bullet.

4. DYNAMIC DISTORTION TESTING

This section of the Paper reviews those facilities equipped with dynamic pressure measuring instrumentation, including discussion of particular problems encountered during their development. It concludes with the results of comparative tests performed to establish that time-variant total pressure distortion measurements made in the model test facility, with models of about 1/10 full-size, can be used to predict the levels likely to be encountered in the full-size inlet operating at the same conditions.

4.1 DATA ACQUISITION

The instrumentation systems used at NGTE to measure and record the engine duct total pressure fluctuations are of conventional design¹². As Figure 10 shows the signals from the miniature pressure transducers are conditioned by instrumentation amplifiers before being transmitted by land-line to a 42 track FM magnetic tape recorder in a central data recording facility. Although normally ac coupled during total pressure measurements, the instrumentation can be dc coupled to permit calibration of the system using steady reference pressures. Data identification is obtained by recording an IRIG B standard time-code signal on one of the magnetic tape tracks. The time-averaged total pressures are measured separately using probes adjacent to, but radially displaced from, the transducers and connected by long lines to a scanning valve measurement system.

Experience has shown that in the test facilities at NGTE fine debris in the air supply require the miniature transducers to be located in protective mountings. Designing such mountings for the small scale models was a particular problem because a flat frequency response was required up to about 2 kHz. After an evaluation of both resonant and non-resonant designs the method adopted as most practicable was the baffle probe arrangement shown in Figure 11 which could be fitted over the 2.3 mm diameter transducer. By keeping the length from entry to transducer less than 7 mm the traditional requirement for a flat response (ie making the maximum frequency of interest less than 1/5 of the fundamental resonant frequency) was satisfied. Calibration on a phonic wheel rig showed that up to the scaled cut-off frequency of 1.8 kHz the probe response was flat to within 0.6 per cent (Figure 12), the maximum deviation occurring at that frequency. In many hours of testing using these mountings no transducer failures attributable to particle damage have occurred and regular checks have not shown any blockage of the mountings.

4.2 DATA ANALYSIS

The time-variant inlet distortion data are analysed using either a computationally slow, but versatile suite of programs on an ICL 1904 digital computer or, at rates approaching real time processing, with an analysis package based on an EAL Pacer 600 hybrid computer. The all-digital method provides the maximum values of Rolls-Royce, Pratt and Whitney and General Electric distortion indices occurring in the data sample and plots the engine face contour patterns associated with the peak values. The hybrid method calculates only the Rolls-Royce index, the sector distortion coefficient DC₉. DC₉ is the difference between the average engine face total pressure and the average total pressure in the lowest pressure sector of angle θ , expressed as a fraction of the local dynamic head. Depending upon the program used by the digital part of the machine, the hybrid method can either determine the peak value of up to four different sector angle parameters at one pass or, by treating the values at each time interval as samples from a population, provide a detailed statistical analysis of one sector distortion coefficient. In both digital and hybrid methods the transducer signals are filtered to attenuate frequencies corresponding to less than one engine revolution.

Although more than two orders of magnitude faster than the all-digital method, analysis using the hybrid computer is inherently less accurate. This is partly a reflection of the lower accuracy of the analogue computation used to weight and average radially the transducer signals, but also due to the less sophisticated, but computationally faster, curve fitting methods used in the digital part of the machine (Figure 13) to determine the extent and location of the low pressure sector. However a series of comparative tests performed by analysing the same taped records with both systems showed that in practice only small differences occurred (Figure 14). In more than 60 per cent of the cases the all-digital and hybrid values of DC₉ agreed within 5 per cent and in all cases were within 10 per cent of each other. The hybrid method was therefore adopted as the principal method for all routine analysis of time-variant inlet distortion data by NGTE. It has since been used to support tests of isolated intakes both at full-size and as scale models in the NGTE facilities and of an installed intake model in two UK wind tunnels.

When analysing full-size inlet data using the hybrid computer the magnetic tape is usually replayed at 1/8 of the speed at which it was recorded. This permits the filtered and radially averaged signals from the analogue computer to be sampled for transfer to the digital machine at a rate at least five times the cut-off frequency of the 'engine speed' filter, whilst simultaneously satisfying the basic machine operating requirement that all digital computation on data sampled at one instant is completed before the next sample is taken. The minimum sampling rate is necessary to prevent significant sampling errors being incurred. As Figure 15, the results of an analysis of two test conditions at various sampling rates shows, it is only when the sampling rate exceeds about twice the filter cut-off frequency that the peak value observed becomes relatively insensitive to further increases, indicating that the true peak value is being approached.

Analysis of model intake data is intrinsically a more difficult computational task than analysing full-size inlet data, although the mathematical operations are similar. The reason is that the effective sampling rate at the analogue/digital computer interface must increase in direct proportion to the size reduction, because the scaling rules for inlet turbulence¹³ require the cut-off frequency of the filter (used to condition the analogue signals prior to digitising) to be increased by the inverse of the model fractional scale to maintain similitude. Whilst the simplest method of increasing the effective sampling rate was to reduce the tape replay speed, using the same digital calculation routines, in practice the limiting step-down ratio of the replay unit was often reached first. To re-record the data and use further time expansion would introduce unacceptable errors. The solution adopted was to refine the digital program, introduce lower level program languages for the time-critical routines, and thereby minimise the number of operations performed. By adopting such methods, using only a 4-fold increase in time expansion, data from a 1/12 scale model of an installation can now be analysed, whilst maintaining the 5/1 ratio of sampling rate to filter cut-off frequency, assuming a maximum LP compressor speed of 12,000 rev/min.

In addition to being able to analyse measurements made in models of different scales the hybrid computer package can also accept data from either 8 arm or 12 arm rake configurations, using existing interchangeable analogue patch panels and digital software. Although the rake geometries are limited to 5 transducers/arm and 3 transducers/arm respectively by the 40 track limit of the tape recorder, less extensive rakes or individual failed transducers can easily be dealt with without the need for repatching or manual potentiometer adjustments. The changes are made through the software routines in the digital

computer which set digitally controlled attenuators on the analogue machine. The routines are such that when a failed transducer signal is eliminated the weightings on remaining signals are automatically readjusted. The hybrid computer is thus both a rapid and a flexible method for analysing inlet distortion data.

4.3 MODEL TO FULL-SCALE COMPARISONS

Supersonic powerplant research programmes at NGTE have shown that an adequate simulation of time-averaged intake flow properties can be achieved with small ($\approx 1/15$) scale models tested in small facilities, provided that the major part of the Reynolds number reduction due to scaling is offset by increased stagnation pressures¹⁴. When powerplant compatibility requirements, particularly for military applications, began to demand instantaneous total pressure distortion levels, the tests reported here were undertaken to determine the feasibility of making such measurements in the same small facilities. The source of full-scale intake data for the comparison was a test programme that had been carried out on a 2-D, variable geometry, external compression intake with a long curved diffuser in Cell 4, the large free-jet test facility at NGTE. The Cell 4 facility is described in more detail in a recent paper by Ashwood and Philpot¹⁵.

Whilst the intake model was a 1/9 scale replica of the Cell 4 duct in all essential aspects, the amount of engine duct instrumentation had to be decreased to reduce the additional blockage that resulted from having to use similar size transducers in both full-size and model intakes. The number of measurement points was reduced from five to three per rake arm, although the symmetrical 8 arm arrangement was retained to preserve the circumferential definition. For structural reasons the model rake needed a centre body, not present in the full-size rake, with the consequence that the rake-plane areas were not equivalent. To enable the measured distortion coefficients to be compared directly the full-scale intake values have been corrected to the scaled rake plane area, using one-dimensional isentropic flow theory to determine the ratio of the dynamic heads. The other main features of the data acquisition and analysis system have already been described in the previous two sections.

The model was tested in the 0.3 m diameter, high pressure, intake test rig at NGTE with jet Mach numbers of 1.8 and 2.2. A schematic arrangement of the facility showing the interchangeable, fixed Mach number, blowing nozzles and the model mounted on its pitching frame is presented in Figure 16. The comparison data were obtained by setting the model ramp angle and incidence to the appropriate Cell 4 value and making measurements at a series of choked exit positions, to obtain data at a range of duct Mach numbers that bracketed the full-scale intake value. In general only one dynamic comparison point was available at any one combination of incidence and ramp angle, because the Cell 4 tests had usually been conducted with the intake under the control of its automatic scheduling system. The model test Reynolds number of 4×10^6 based on intake capture height was at least 2/3 of the value at which the full-scale intake tests were carried out and was also double the value at which Reynolds number effects had been previously observed to produce significant changes¹⁴.

Before the model and full-scale intake time-variant data were compared it was necessary to establish that there was adequate agreement between the time-averaged measurements. To assist in making the comparison some additional full-scale intake results, obtained with only time-averaging instrumentation, have been included. Figure 17 shows a comparison of the average engine duct pressure recoveries at the critical operating point over a range of ramp settings for both test Mach numbers at one incidence. In general the agreement was good with the difference being less than 0.5 per cent of the free-stream total pressure. On average the model intake recovery was slightly higher than that of the full-scale intake, but this was probably due to the fewer measurement points in the model rake, rather than an indication of significant differences in intake performance.

A comparison of the time-averaged total pressure distortion coefficients at similar operating points is presented in Figure 18. The model and full-size intake distortion levels shown are those observed with the intake operating near the critical point at three different incidences, for a range of ramp settings. There is a broad level of agreement between the results, although for some points a sizeable difference can be observed. To determine whether the discrepancy in the time-averaged distortion levels was a real effect, or merely the result of the different rake configuration in the two intakes, a series of engine face total pressure contour plots was prepared, of which Figure 19(a) and (b) are examples. These showed that even where there were differences in distortion levels, the range of recovery levels and the locations of the high and low pressure regions were usually similar. For instance in Figure 19(a) the corresponding full-scale and model intake DC 90 values were 0.339 and 0.406 respectively. Thus it was concluded that the differences in distortion coefficients were essentially due to the different rake configurations. It was therefore reasonable to attempt a comparison of the time-variant data.

The two parameters used in the comparison were the average rms turbulence levels in the engine ducts and the peak values of the instantaneous sector distortion coefficient DC 60 observed in equivalent periods of data analysis, with the intakes operating at nominally similar steady conditions. In all cases the transducer signals were filtered to attenuate frequencies greater than 200 Hz in the full-scale data, or its scaled equivalent in the case of the model signals.

A comparison of both average turbulence and peak distortion levels over an intake characteristic are presented in Figure 20. For reference purposes the average intake recovery is also included, all parameters being plotted against normalised intake mass flow. Both model and full-scale curves showed an increase in turbulence and distortion levels as the intake became super-critical and both exhibited the lowest levels of distortion near the critical operating point. The level of agreement was therefore considered to be satisfactory.

A comparison over a wider range of conditions, including results from tests at extreme attitudes and with the intake operating off the normal control line, showed that although the peak distortion levels were generally within 20 per cent agreement (Figure 21) larger differences were observed in both senses. The discrepancies were however not significantly greater than could have arisen due to a combination of the known differences between the model and the full-scale intakes and the inevitable errors associated

with making nominally identical measurements. For instance differences of about 20 per cent could be expected from a combination of (i) the inherent errors in the respective measurement and the calculation processes, (ii) the effect on the peak value of fewer measurement points in the model rake and, (iii) the inevitable variation between extreme values in different samples, even when taken from identical populations.

The indication was therefore that the influence of additional factors which could produce differences, such as the redistribution of flow imposed by the model rake centre body or the discrepancies between the nominal and the actual intake settings at similar operating conditions was relatively small. Consequently, within the limitations imposed by the physical constraints and the inherent difficulty of comparing extreme values of time-dependent variable, the tests were considered to show that instantaneous inlet distortion measurements were practicable in the small test facilities at NGTE. Agreement was best at the lower distortion levels, suggesting that the models would provide a more reliable indication of the levels at normal operating conditions than at extreme ones. However since high levels were apparently over-estimated the potential problem areas would be highlighted and not hidden.

5. CONCLUSIONS

Two facilities, one theoretical the other experimental, have been developed at NGTE for assessing the time-averaged performance of the diffuser section of aircraft powerplant intakes. The current capabilities of both approaches to analysing the essentially three-dimensional flows arising in such ducts have been presented in this Paper. As part of the finite-volume time-marching flow calculation package of computer programs, a novel, fully-automated, method for grid-generation within ducts of any smoothly varying cross-sectional shape has been developed. An order-of-magnitude saving in computing time over a currently popular method has been demonstrated. The grid-generation program may be easily extended to provide any extra geometry-dependent information required for other flow solution methods. It is suggested that the flexible computational approach can make a valuable contribution to the diffuser design process. The usefulness of the theoretical approach will be extended as new algorithms and larger, faster, computing facilities become available. Confirmatory experimental data can be obtained relatively cheaply and quickly from the experimental rigs, and can also give an early indication of any problems which may subsequently arise due to interaction with the engine.

Data acquisition and analysis facilities for model and full-scale intakes, equipped with dynamic pressure measuring instrumentation, have been described. By comparing the time-averaged and time-variant results from both model and full-scale intake tests it has been shown that instantaneous inlet distortion measurements can usefully be made in small scale facilities similar to those currently available at NGTE. This will permit more reliable preliminary evaluations of new designs, or modifications to existing inlets, to be made whilst maintaining the short time-scales and low running costs associated with small facilities.

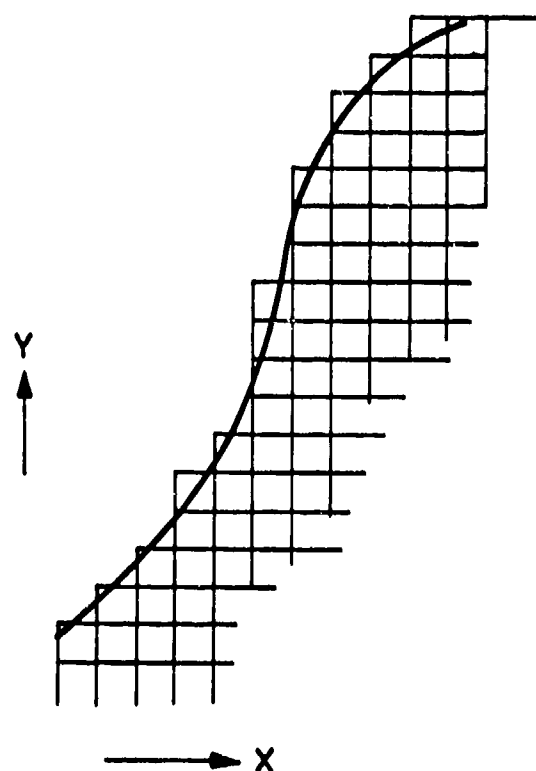
REFERENCES

1. D. R. Chapman, Computational aerodynamics development and outlook, AIAA Paper 79-0129, AIAA Journal, Vol. 17, December 1979
2. J. L. Walsh, J. H. Ahlberg, E. N. Nilson, Best approximation properties of the spline fit, Journal of Mathematics and Mechanics, Vol. 11, No. 2, 1962
3. W. J. Gordon, C. A. Hall, Construction of curvilinear co-ordinate systems and applications to mesh generation, Int. Journal for Numerical Methods in Engineering, Vol. 7, 461-477, 1973
4. W. H. Chu, Development of a general finite difference approximation for a general domain, Part 1, Machine transformation, Journal of Computational Physics, Vol. 11, 348-359, 1973.
5. J. F. Thompson, F. C. Thames, C. W. Mastin, Boundary-fitted curvilinear co-ordinate systems for solution of partial differential equations on fields containing any number of arbitrary two-dimensional bodies, NASA CR-2729, July 1977
6. D. E. Colbourne, C. G. Burton, A fast method for grid-generation, NGTE Report R79001, July 1979
7. D. W. Roberts, C. K. Forester, Parabolic procedure for flows in ducts with arbitrary cross-sections, AIAA Paper 78-143, AIAA Journal, Vol. 17, January 1979
8. E. Kreyszig Advanced engineering mathematics, John Wiley, 2nd Edition, 1967.
9. J. D. Denton, A time-marching method for two- and three-dimensional blade-to-blade flows, ARC R&M 3775, 1975.
10. H. B. Squire, K. G. Winter, The secondary flow in a cascade of aerofoils in a non-uniform stream, Journal Aero Sci., Vol. 18, p. 271, 1951
11. R. K. Oldham, A comparison of two transonic compressors designed for a pressure ratio of 1.88, 3rd International Symposium on Air Breathing Engines, Munich, March 1976
12. W. G. Schweikhard, Test techniques, instrumentation and data processing, AGARD-LS-72.
13. D. A. Sherman, D. L. Motyoka, G. C. Oates, Experimental evaluation of a hypothesis for scaling inlet turbulence data, AIAA Paper 71-669, 7th Joint Propulsion Conference

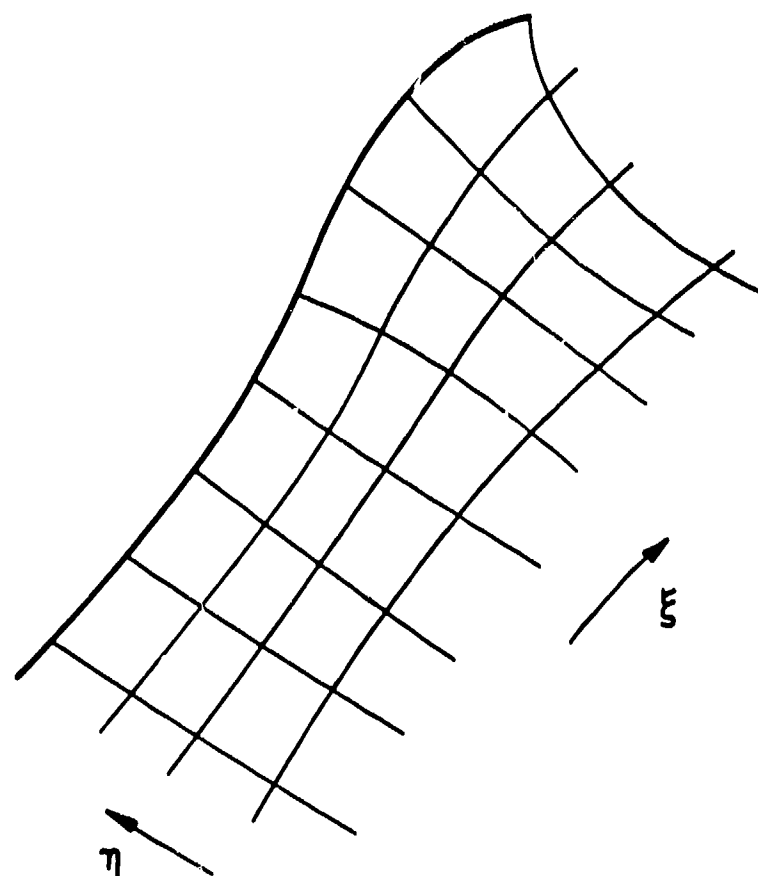
14. J. D. Bryce, B. J. Cocking, Some effects of Reynolds number on the performance of an air intake proposed for Concorde, NGTE Report R304, 1968
15. P. F. Ashwood, P. de B. Philpot, Free-jet testing of powerplants for aircraft and missiles, AGARD PEP Symposium on Engine Testing, Turin, September 1980

Reports quoted are not necessarily available to members of the public or to commercial organisations.

Copyright © Controller HMSO London 1981



(a) REGULAR GRID



(b) GENERAL CURVILINEAR GRID

Fig.1 Fitting a calculation grid to a curved boundary

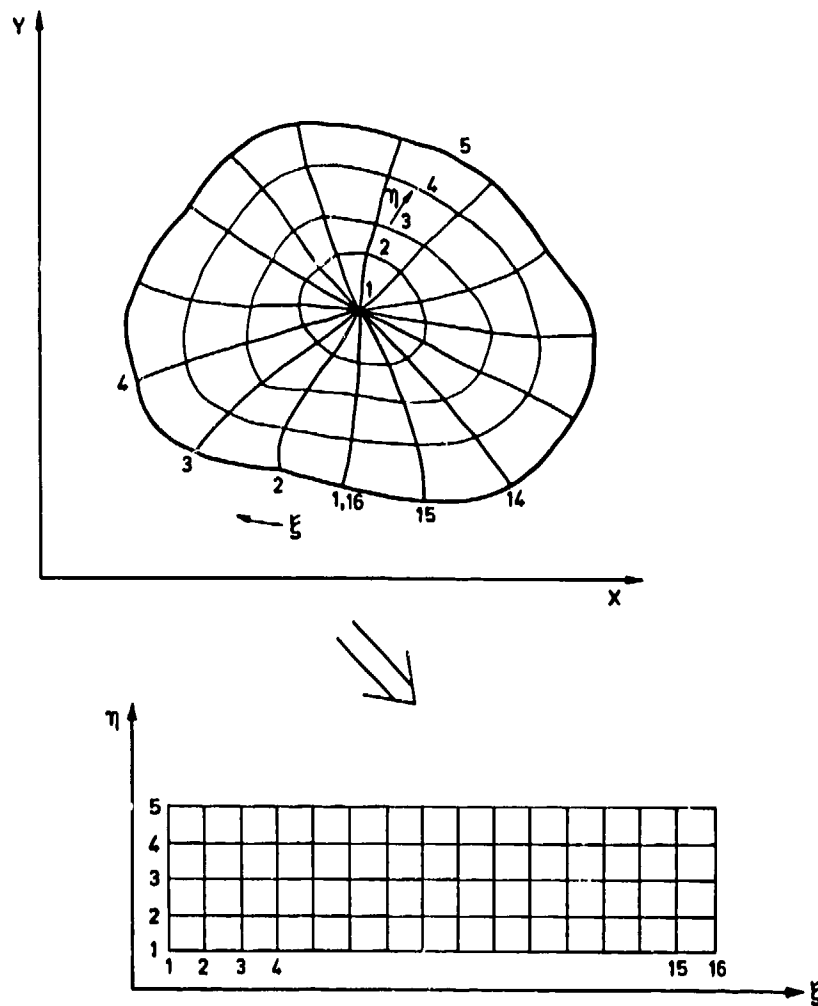


Fig.2 Transformation of general closed region

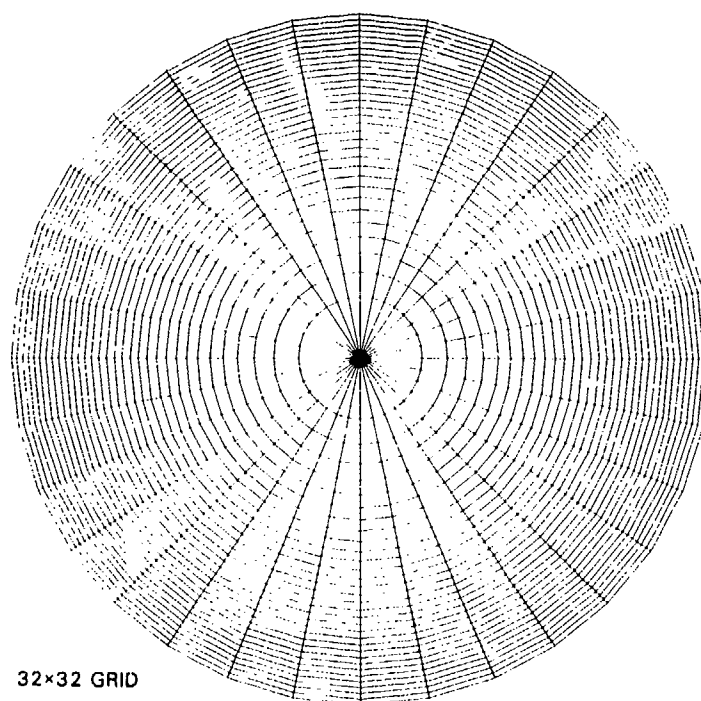


Fig.3 Grid generated within circular boundary

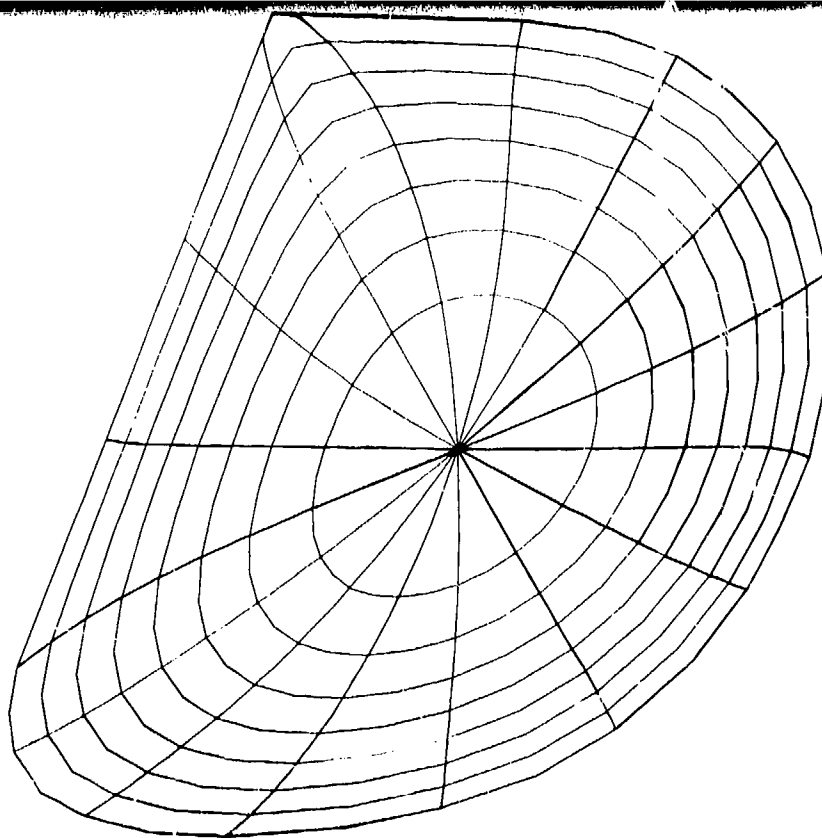


Fig.4 Grid for duct flow calculation

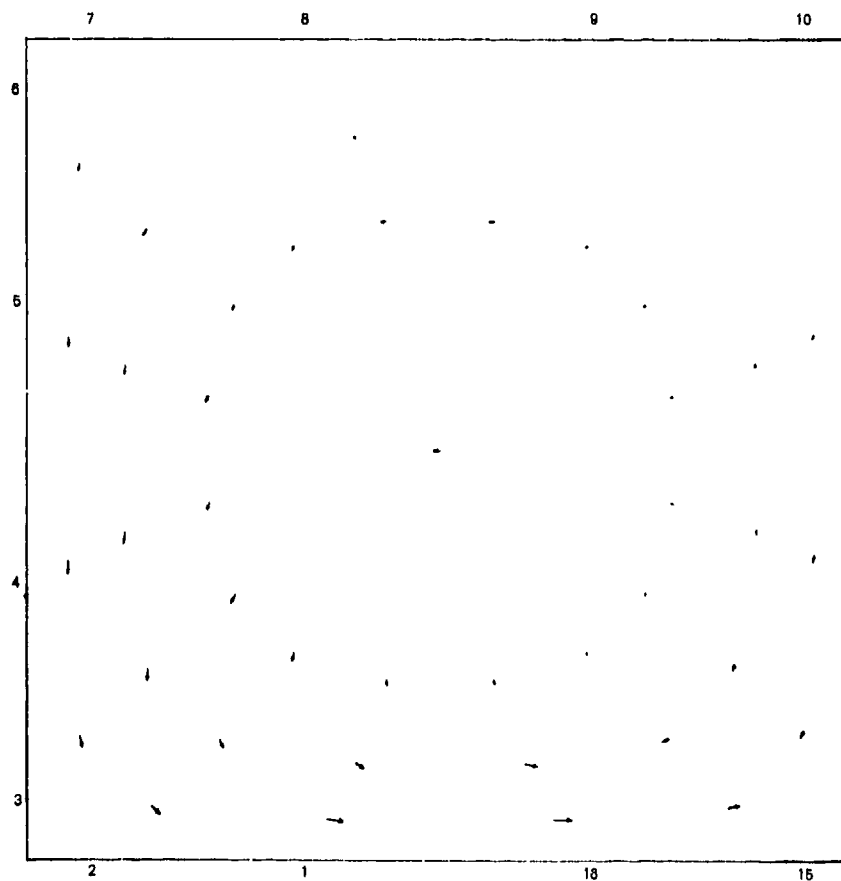


Fig.5 Outlet flow from 14° bend

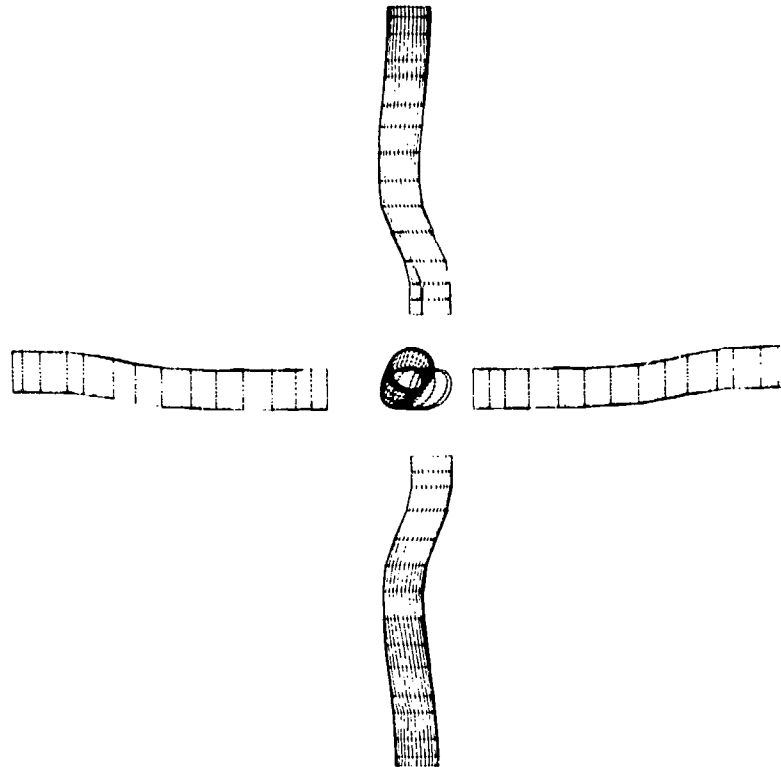


Fig.6 Asymmetric S-bend duct

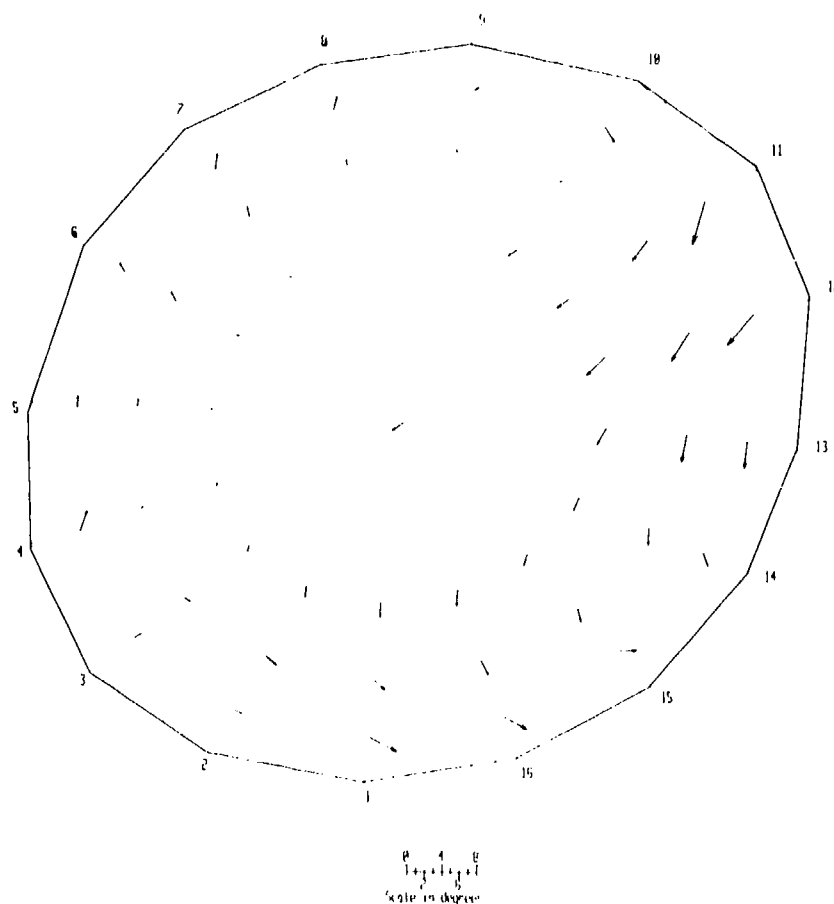


Figure No. 2

Fig.7 Non-axial flow components



Fig.8 Yawmeter rake installed in compressor

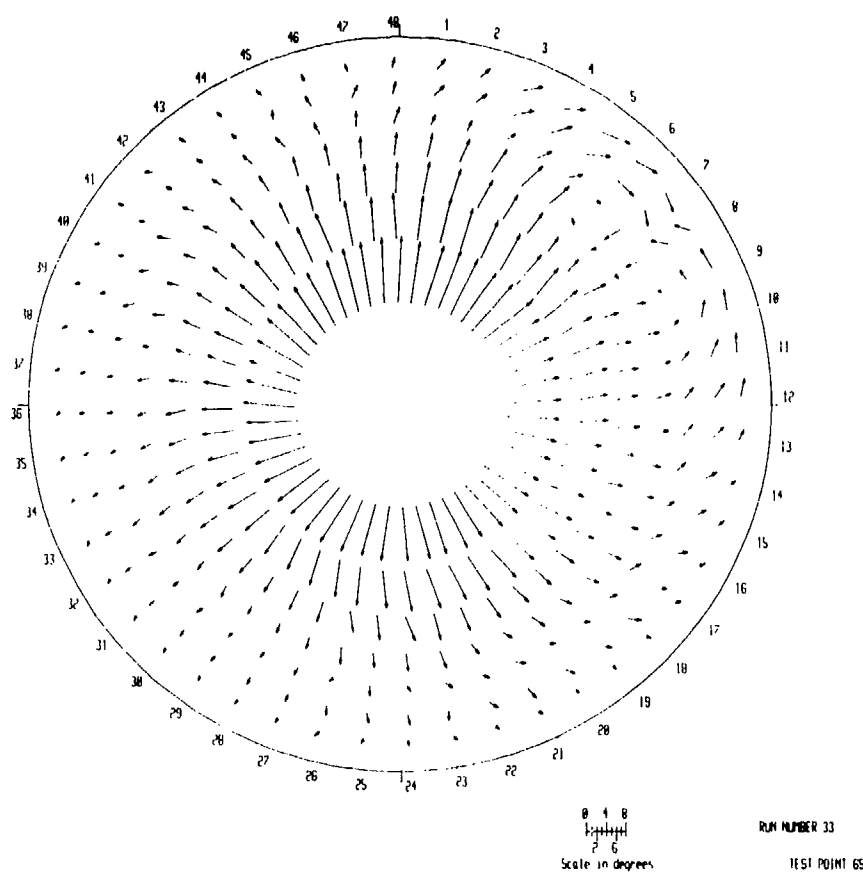


Fig.9 Results from yawmeter rake

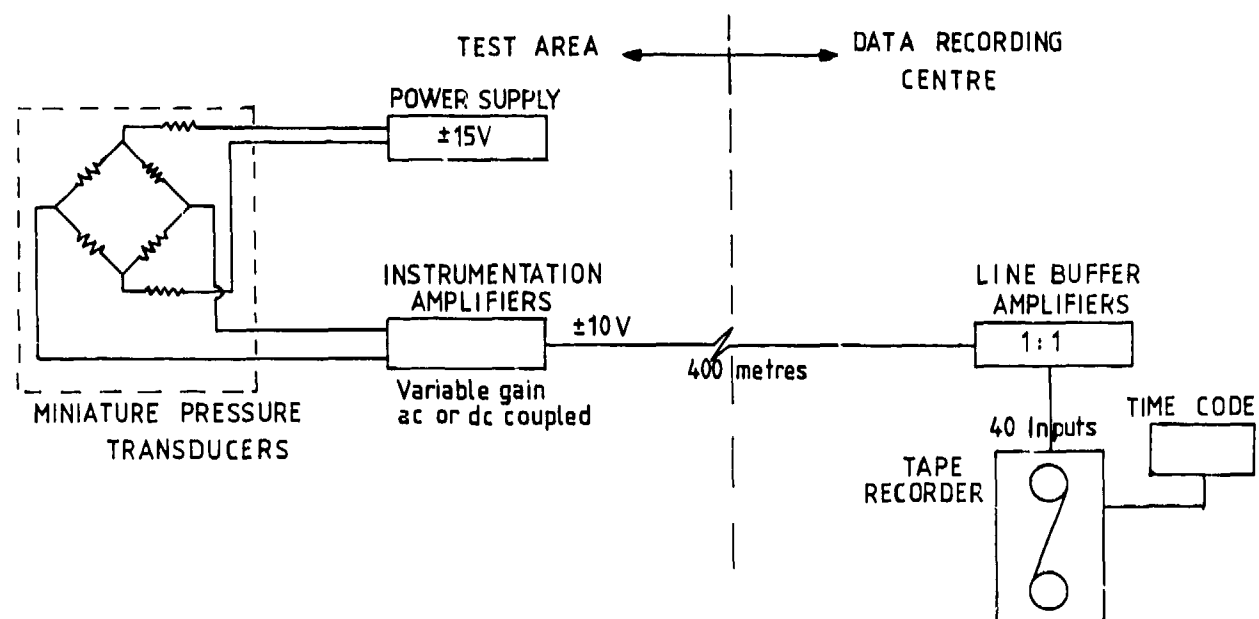


Fig.10 Schematic diagram of the data acquisition system

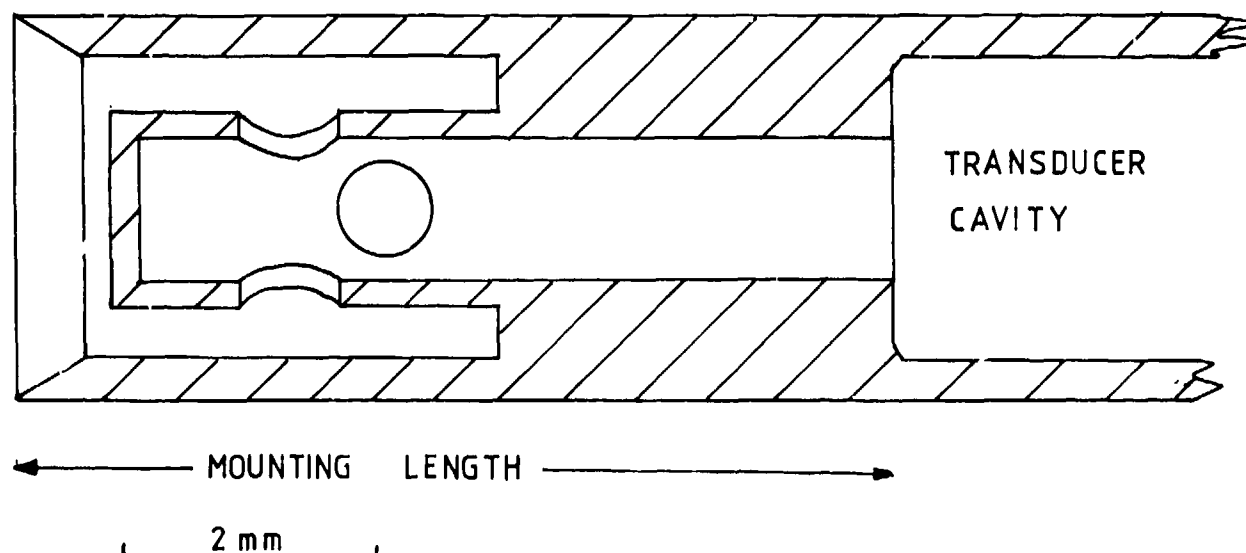


Fig.11 Sectional view of baffled probe mounting

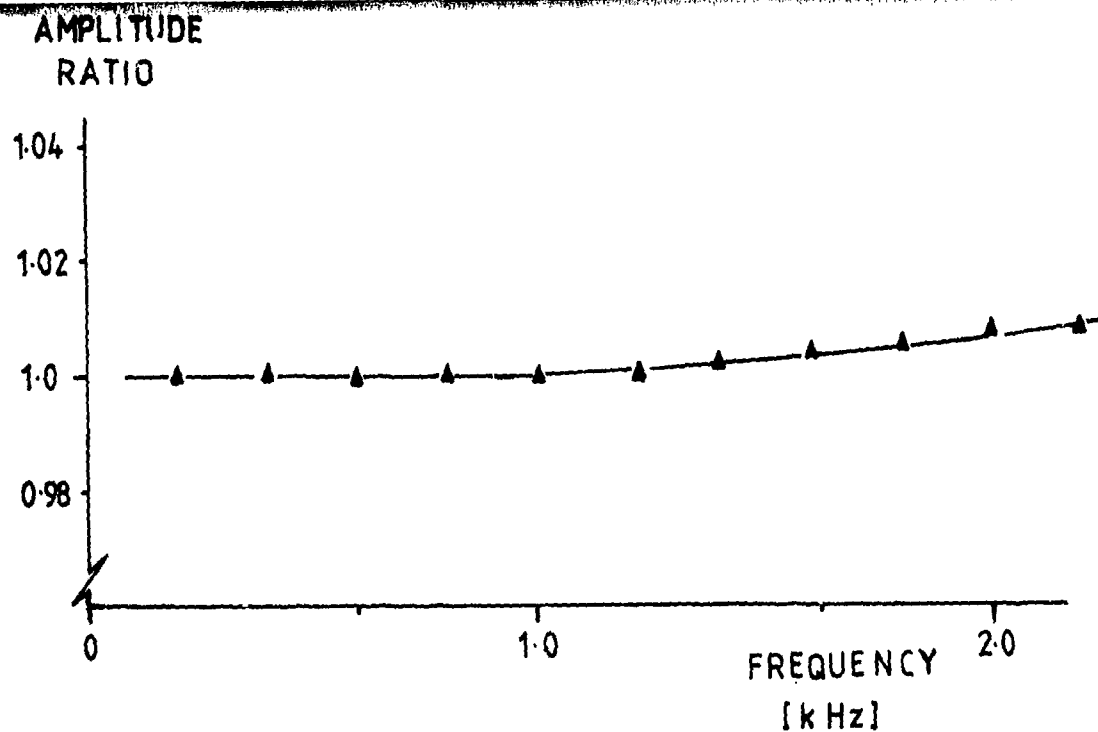


Fig.12 Baffled probe frequency response

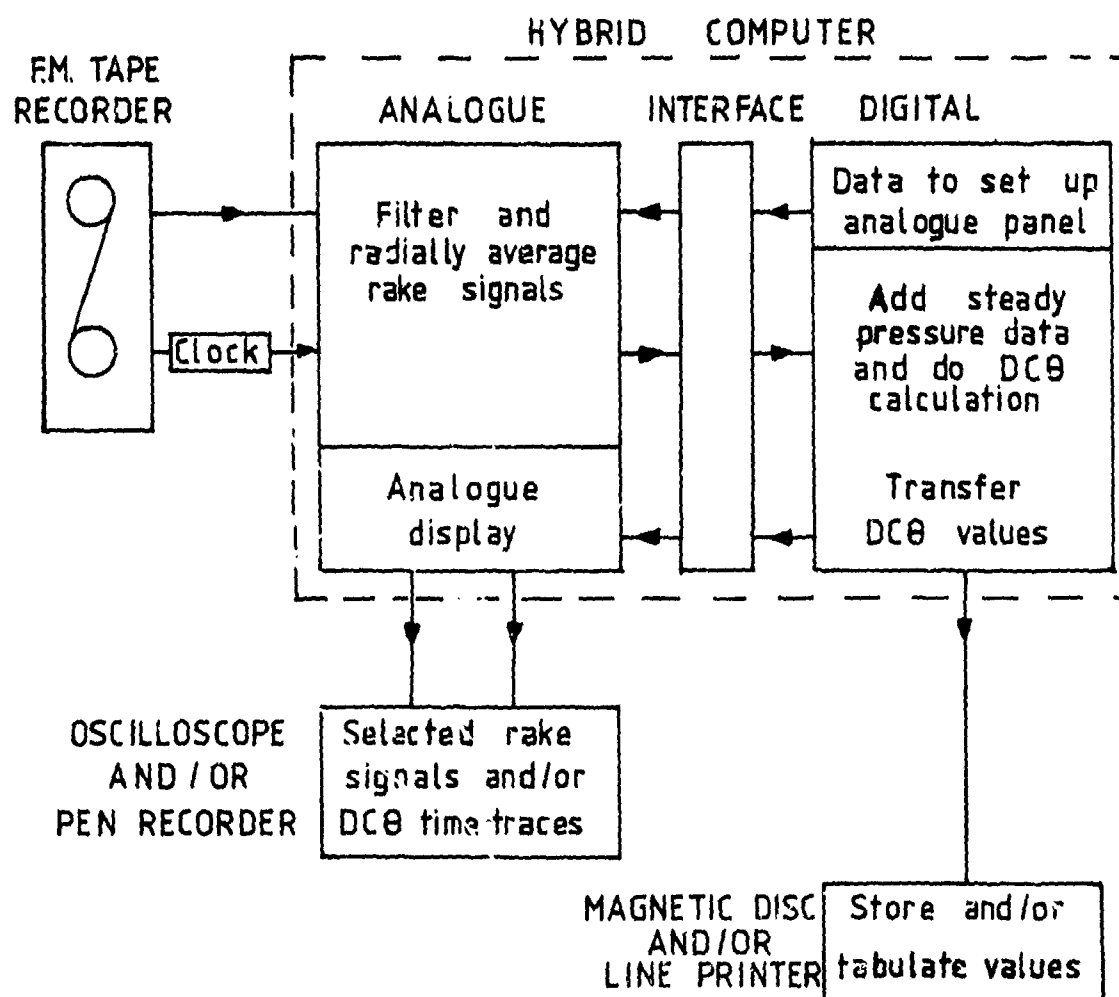


Fig.13 Schematic diagram of the data analysis system

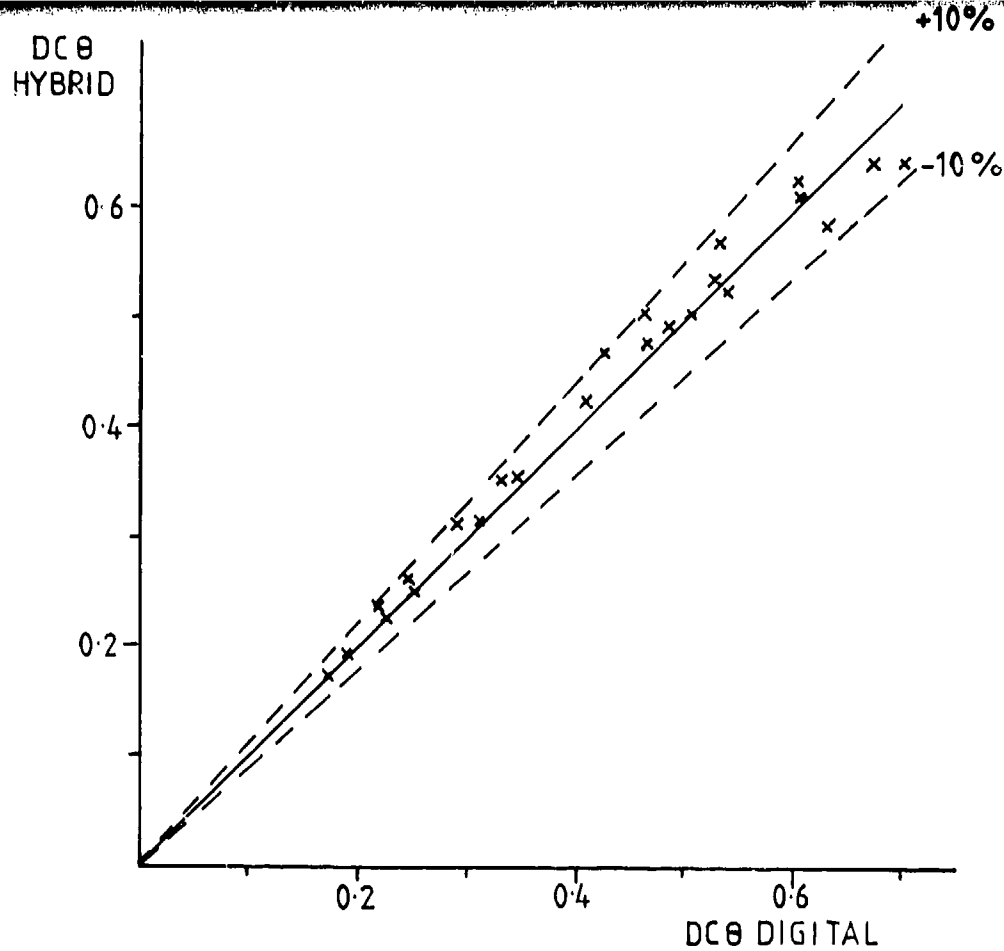


Fig.14 Comparison of distortion analysis methods

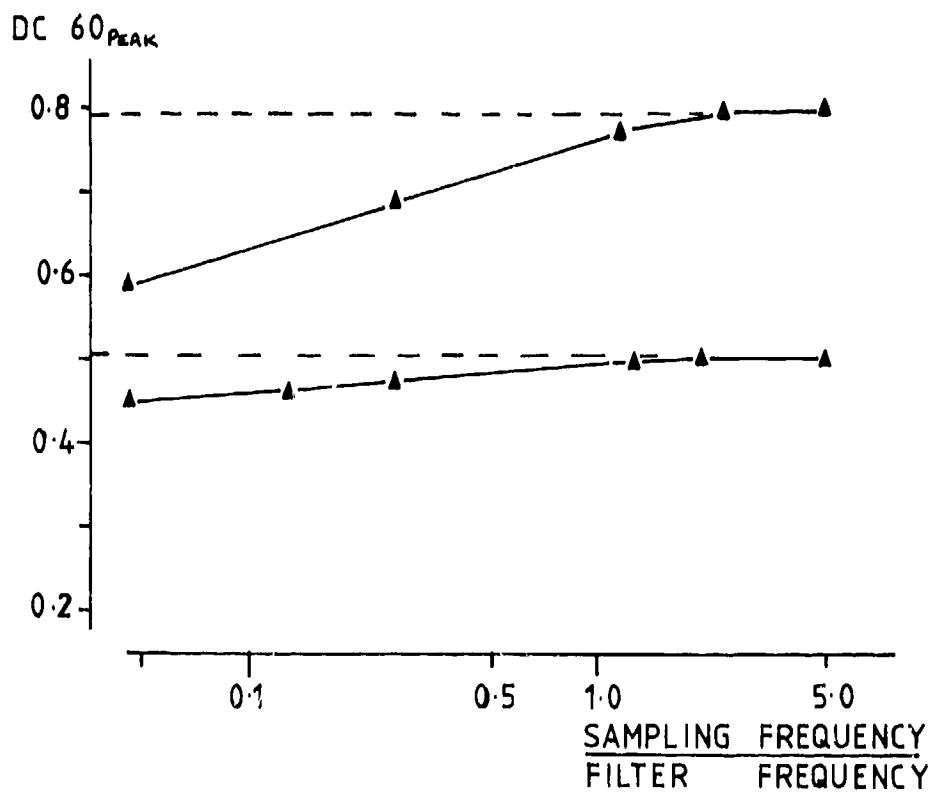


Fig.15 The effect of sampling frequency on DC 60 peak distortion level

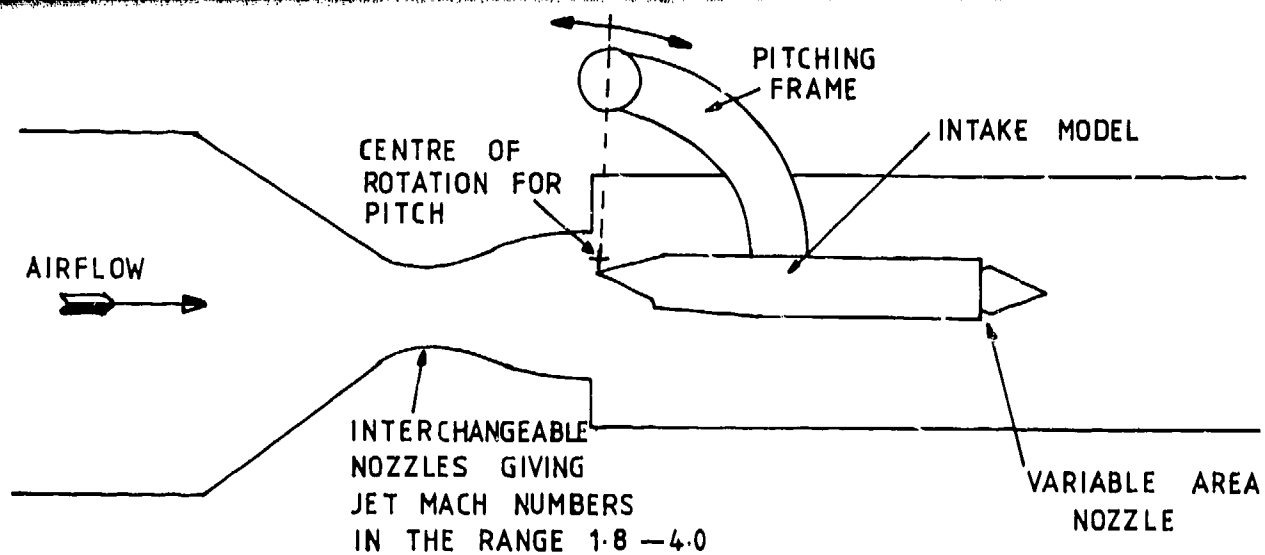


Fig.16 Schematic arrangement of the intake test rig

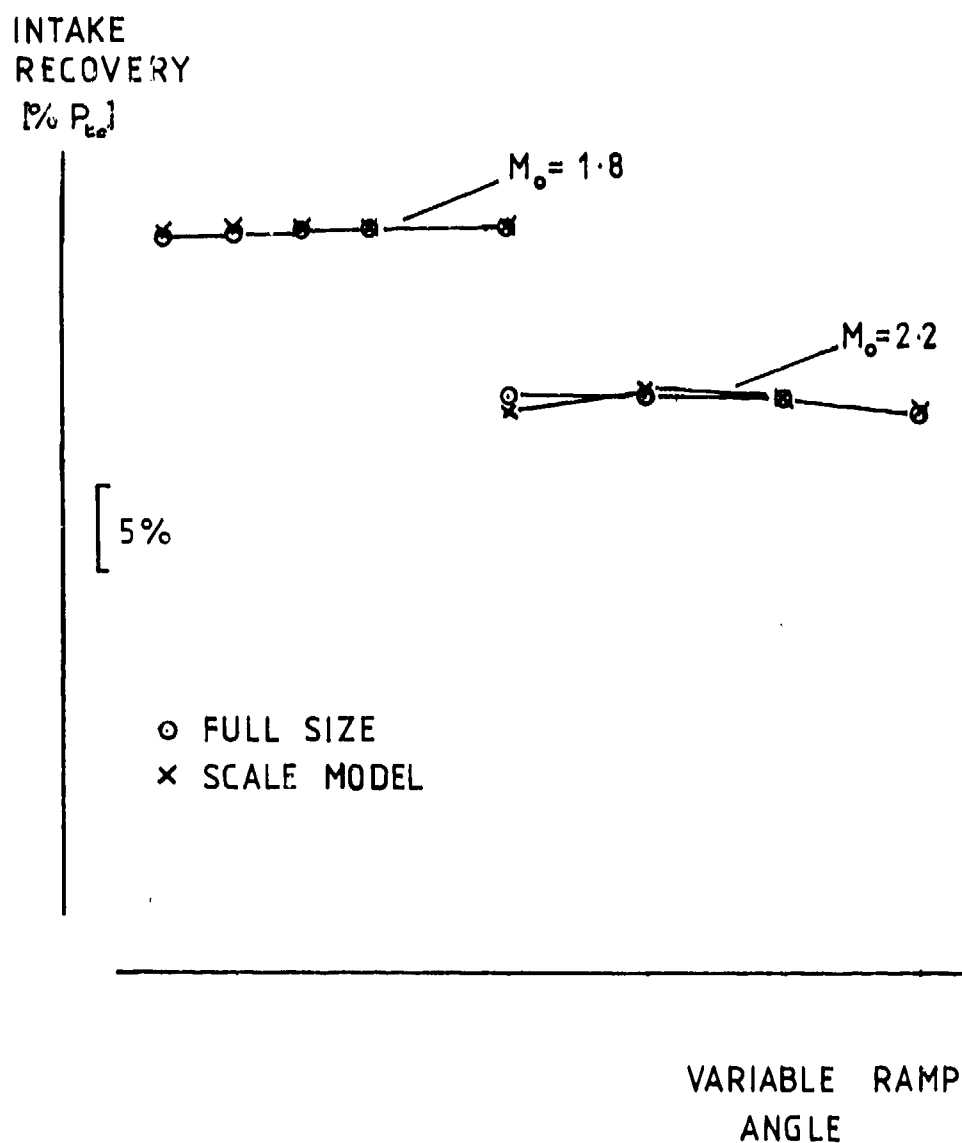


Fig.17 Comparison of full size and model intake total pressure recoveries

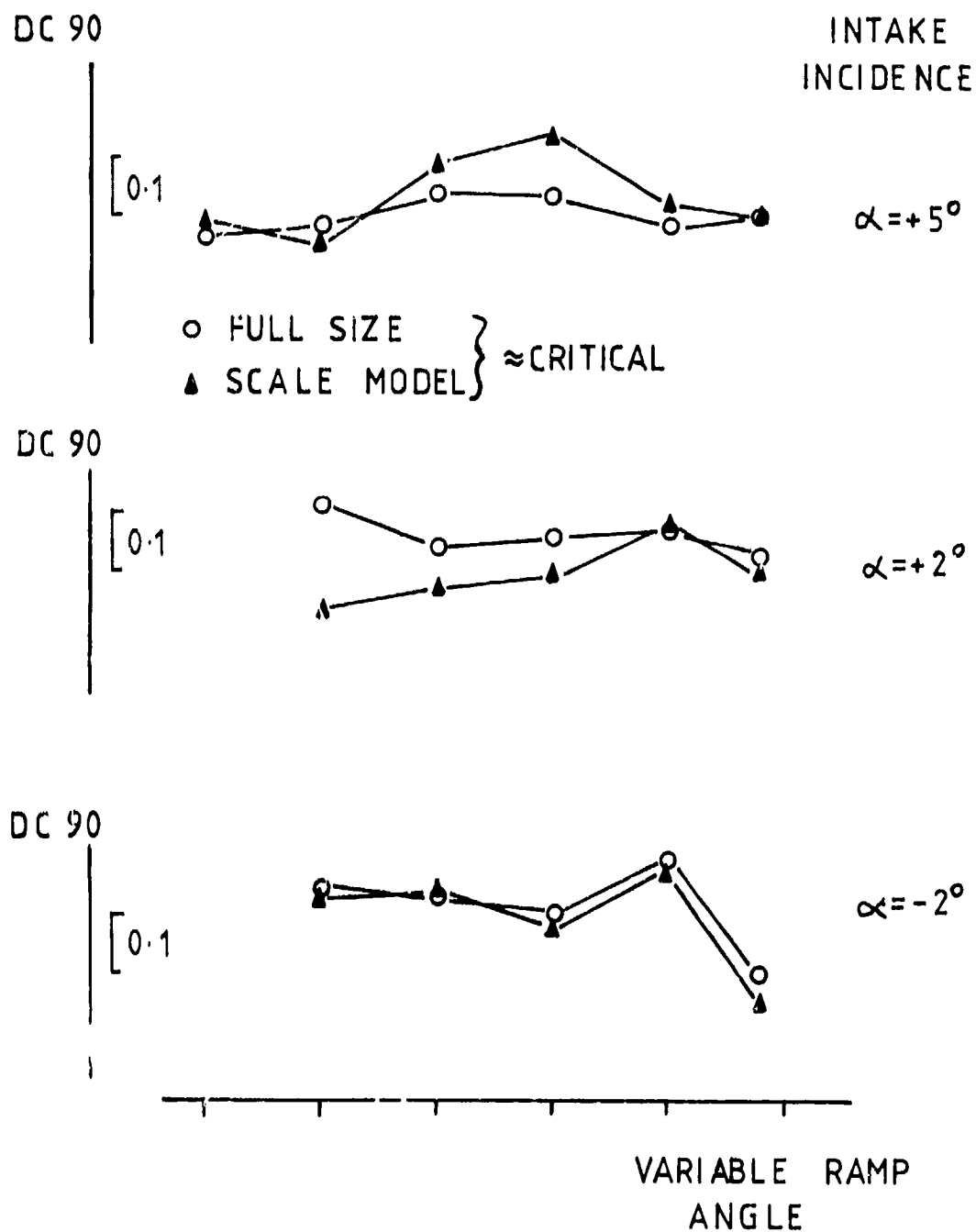
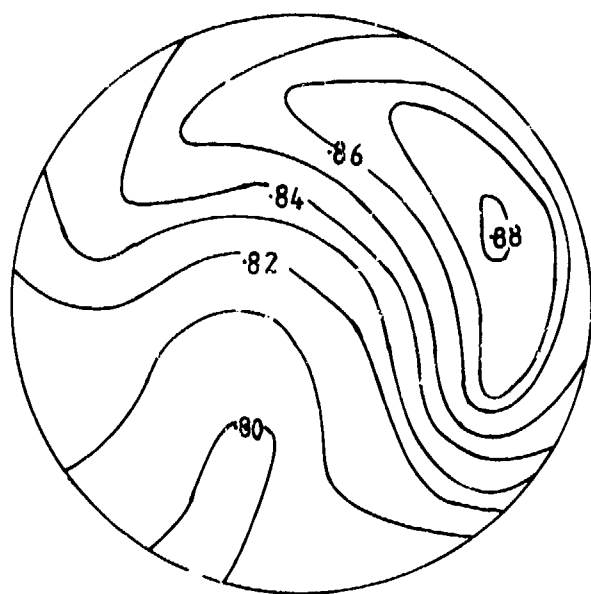
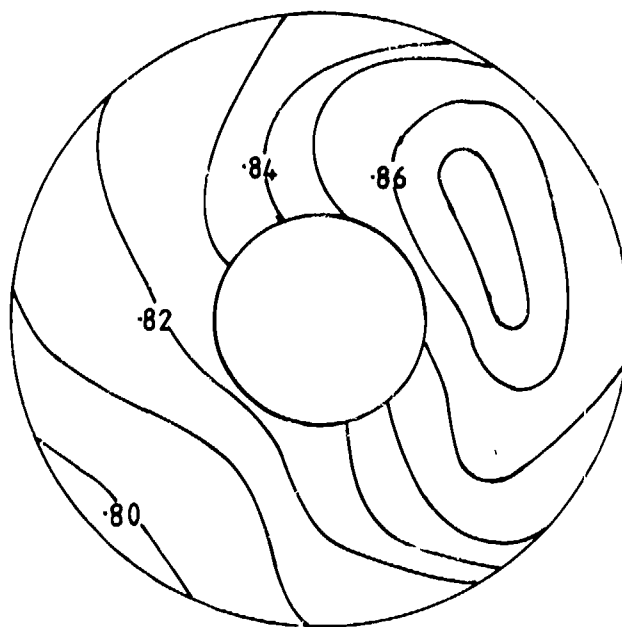


Fig.18 Comparison of time averaged distortion levels at $M_0 = 2.2$

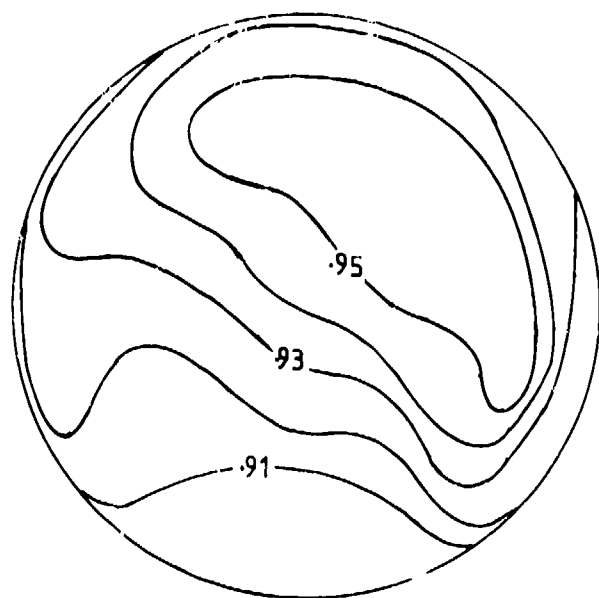


FULL SIZE

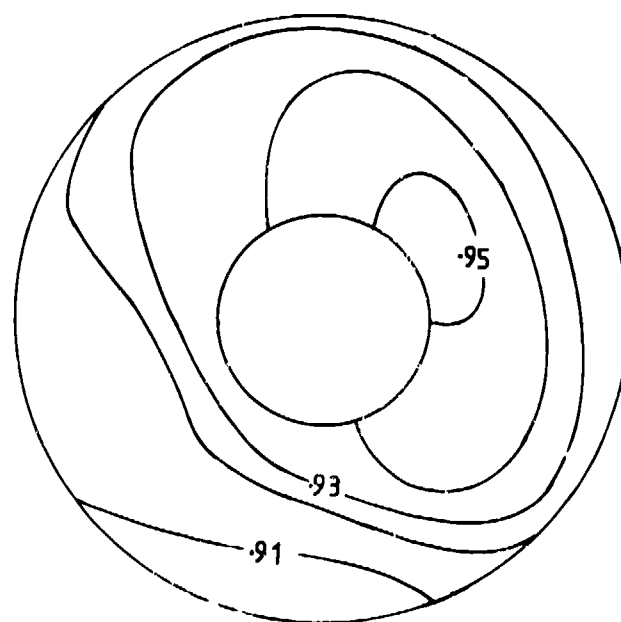


SCALE MODEL

a) SUPERCRITICAL INTAKE OPERATION AT $M_0 = 2.2$



FULL SIZE



SCALE MODEL

b) SUBCRITICAL INTAKE OPERATION AT $M_0 = 1.8$

Fig.19 Comparison of engine duct total pressure distributions

RECOVERY FACTOR

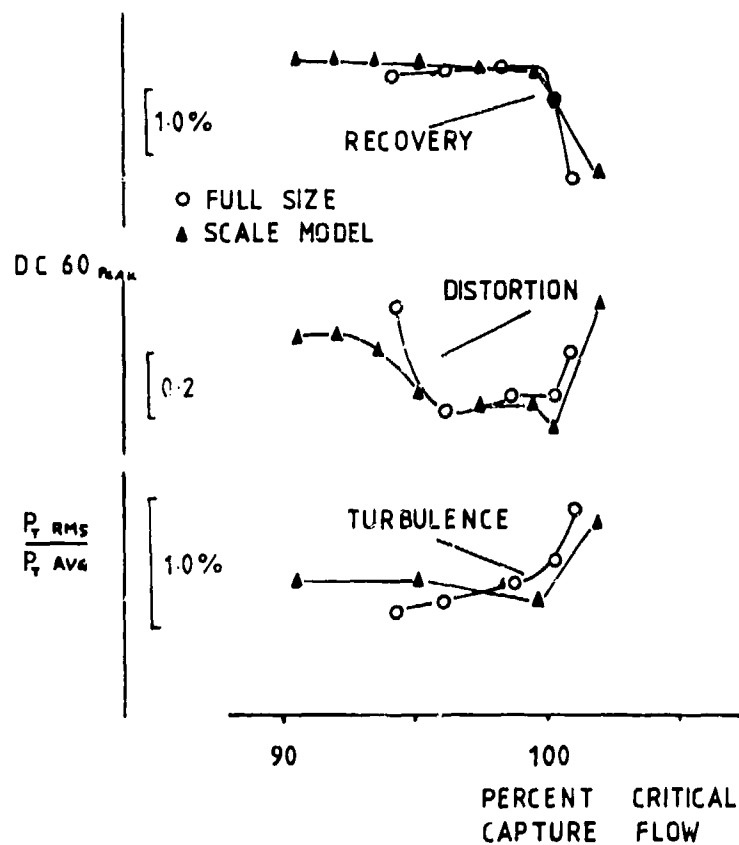


Fig.20 Comparison of model and full size intake operating characteristics

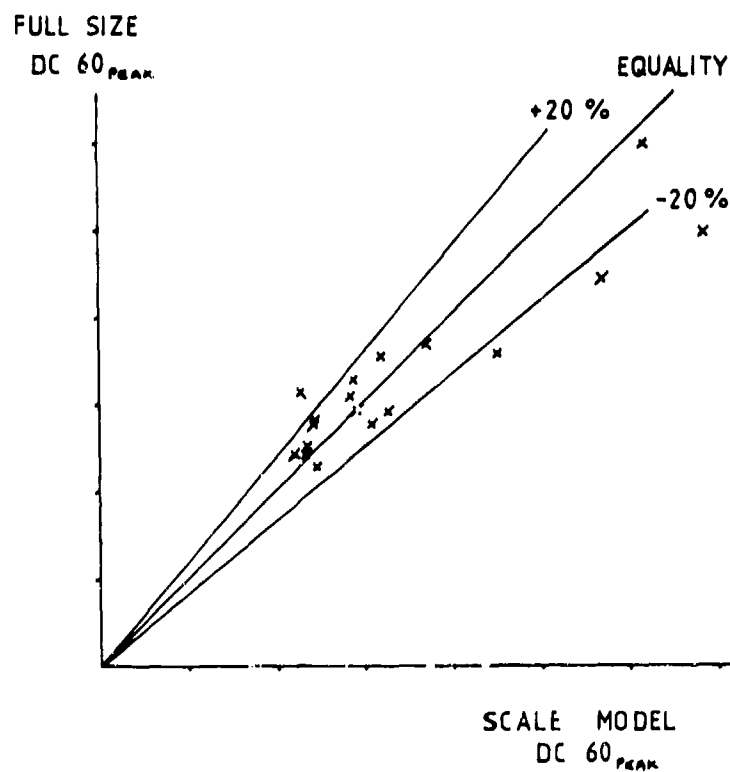


Fig.21 Comparison of full size and model intake peak distortion levels

EFFECTS OF INTAKE GEOMETRY ON CIRCULAR
PITOT INTAKE PERFORMANCE AT ZERO AND
LOW FORWARD SPEEDS

A.C. Willmer }
T.W. Brown } British Aerospace, Aircraft Group, Filton, Bristol
E.L. Goldsmith Royal Aircraft Establishment, Clapham, Bedford

SUMMARY

A series of experiments complementing and extending the work of Blackaby and Watson (NASA 1954 and '55) on circular cross-section pitot intakes at Mach numbers from 0 to 0.21 and angles of incidence and sideslip from 0° to 40° are presented. Measurements were made at the engine face of 72 pitot pressures, 4 unsteady pitot pressures, swirl angle at six positions and boundary layer profiles at four positions. Static pressure distribution around the cowl lips and along the diffusers were also measured. Five cowl lips covering a range of contraction ratios and lip shapes were tested with both a straight and an S bend diffuser. The effect of inserting parallel section spacers between the cowl lip and the front of the subsonic diffuser and between the end of the subsonic diffuser and the engine face instrumentation and the effect of a thin lip slot upstream of the intake throat were evaluated.

NOTATION

A	duct or stream tube cross sectional area	O_r	S duct offset
a	Longitudinal semi axis of cowl lip ellipse	P	total pressure
b	radial semi axis of cowl lip ellipse	q	dynamic head $\frac{1}{2}\rho V^2$
C_d	discharge coefficient	V	speed
CR	contraction ratio A_{0n}/A_t	x	longitudinal ordinate
DC_{60}	flow distortion index defined as the minimum $\frac{P_{min60} - P_{0mean}}{P_{0mean}}$	y	lateral ordinate
d	diameter	α	incidence
ER	cowl lip ellipse ratio a/b	β	sideslip
l	duct length	ΔP	$P_{0n} - P_e$
M	Mach number	ΔP_{lip}	$P_{0n} - P_t$
		η	total pressure recovery P_{0n}/P_e
		<u>Suffixes</u>	
		o	engine face
		en	highlight plane
		t	throat
		-	freestream

1. INTRODUCTION

Interest in pitot intakes for use in highly manoeuvrable fighter aircraft for flight at Mach numbers from zero to 1.8 prompted a programme of both low and high speed tests on circular section pitot intakes at incidence up to 40° . Although practical aircraft designs of intake are seldom of simple shape, choice of circular cross-sections enables systematic model changes to be made in an economical manner and for measurements to be compared with existing theoretical methods of prediction for both the inviscid and viscous flow components. A later series of tests will investigate changes of cross-section shape from the entry to the engine face.

Little systematic low speed pitot intake testing has been done since the 1954-55 work of Blackaby and Watson^{1,2} and the lip geometries chosen have some features that are common to those tested in refs 1 and 2. This work extends Blackaby & Watson to establish the sensitivity of intake performance and compatibility to detailed lip design and diffuser geometry particularly at high throat Mach number and high incidence. It includes an assessment of duct offset, a subject hitherto not studied systematically.

Measurements include a limited assessment of engine face swirl and pitot pressure fluctuation reflecting today's awareness of the importance of these aspects of flow quality to intake-engine compatibility. More comprehensive measurements are planned in future test phases.

2. DESCRIPTION OF THE MODEL

Figure 1 and associated table shows the model components. Six axi-symmetric lips and two diffusers, one with an S shaped centre line, were available. The diffusers have common area distribution and length and are of circular cross section. Constant section parallel spacers of various lengths could be inserted between the diffusers and the cowl lips and between the diffusers and the engine face.

2.1 Cowl Lips

The values of contraction ratio were chosen to provide a range from values typical of civil aircraft ($CR = 1.25$) to those applicable to military aircraft and to coincide with those of Blackaby and Watson ($CR = 1.078$ and 1.177). The internal lip profile from the highlight to the throat is a quarter ellipse. Inviscid compressible flow calculations³ indicated that there was a decrease in lip surface supersonic velocities at high speed conditions by increasing the ellipse ratio (ratio of major to minor axis) from 2 to 5 and that for a given ellipse ratio the lip pressure distribution at low forward speed and high throat Mach number was improved but the high speed distribution was not adversely affected by adopting a blunter profile than an ellipse shape. Thus ellipse ratios of 2 and 5 were designed for the 1.078 contraction ratio (lip 2 and 1) and an inner profile defined by a 'super-ellipse':

$$\left(\frac{x}{a}\right)^{2.4} + \left(\frac{y}{b}\right)^{2.4} = 1$$

was designed for the contraction ratio 1.177 (lip 6).

The junction between the cowl lip and the diffuser or spacer was always at the throat. All the cowl lips had external profiles defined by NACA 1-85-35 proportions for at least one throat radius aft of the highlight position.

One of the lips (lip 3.1) was provided with thin slots. These had a total flow area of 10% of the throat area and because of the requirement for inter-changeability of the lips all the slot area was located ahead of the throat. High speed tests on a rectangular intake with a similar slot indicated a small beneficial effect at high incidence and no adverse effect of the slot at supersonic speeds. A standard circular arc bellmouth entry was also provided and tested with all diffusers and entry and exit parallel section combinations under static conditions. For all lips the throat diameter was 128.8 mm. Pressure tappings were located on the inside and outside surfaces of the lip along four lines (at 90° intervals) to match up with similar tappings in the diffusers.

2.2 Diffusers

Both diffusers are 457.2 mm long ($l/d_e = 3$) and have an area ratio of 1.400 (gross) or 1.3074 (net) reflecting the difference due to the engine face centrebody.

The wall profile of the straight diffuser is defined by

$$\frac{d - d_t}{d_e - d_t} = 3 \left(1 - \frac{x}{l}\right)^4 - 4 \left(1 - \frac{x}{l}\right)^3 + 1$$

For the S bend diffuser, the same expression is used but x is measured along the centre-line and d is measured perpendicular to the centre line.

The centre line is defined by

$$\frac{y}{l} = \frac{O_f/1}{2} \left[1 - \cos\left(\pi \frac{x}{l}\right) \right]$$

where $O_f/1 = 0.3$ for the S bend diffuser reported in this paper.

Pressure tappings are located along four generators spaced around the diffuser at 90° intervals.

2.3 Spacers

Several cylindrical extension pieces were made to fit the front or the rear of the diffusers. These allowed either the throat or the diffuser to be lengthened so that the lip separation region had a constant area section, in which to reattach or the mixing process in the subsonic diffuser more nearly to be completed. This permitted ducts upto a total length of $l/d_e = 6$ to be studied.

2.4 Engine Face Metering Section

The engine face diameter of 152.4 mm was determined by the compressed air supply available to drive the airflow ejectors. A scaled up version of the standard RAE (Bedford) flow cell⁴ which has been calibrated to allow air flow to be measured was used. This calibration was checked against the bellmouth calibration during the initial testing.

2.4 Engine Face Metering Section (Contd)

Instrumentation at the engine-face is shown in figure 2. Twelve radial arms at 30° intervals, each carry six pitot tubes radially spaced so that each pitot surveys $1/72$ of the engine face nett area. On every second arm, one pitot was incorporated into a 3-hole yawmeter head. On every third arm, one pitot was flanked by a Kulite pitot-type sub-miniature pressure transducer (CQ - 080 series with Boeing screen), to measure unsteady pressures.

Twelve wall static tapings were fitted midway between the twelve radial arms and at $6\frac{1}{8}^\circ$ offset from each horizontal and vertical arm, a 6-pitot wall boundary-layer rake was fitted.

3. TEST CONDITIONS

Fig 3 shows the model mounted in the low speed 12ft x 10ft Wind Tunnel at British Aerospace, Filton. Air was drawn through the model by an ejector pump driven by compressed air. This ejector also acts as the model chassis carrying the model gravity and aerodynamic loads to the tunnel supports.

The capacity of the ejector is such that it was possible to choke the flow at the inlet throat. The test technique consisted of taking pressure recovery-mass flow characteristics (typically 12 mass flow conditions) at fixed tunnel speed and angle of incidence or sideslip.

Table I shows the test conditions.

TABLE I

Nominal V m/sec	Nominal M _∞	Reynolds number based on intake throat diameter d _t
0	0	0
18.3	0.054	1.61×10^5
36.6	0.108	3.23×10^5
70.1	0.207	6.18×10^5

At a mean throat Mach number of 0.6 the Reynolds number based on mean throat conditions is 1.48×10^6 .

Incidence and sideslip angles of up to 40° were tested.

4. DISCUSSION OF RESULTS

At low forward speeds except at very low rates of flow the size of the ingested streamtube is almost always larger than the capture streamtube of the intake. Under these conditions at zero angle of incidence flow separation occurs all round the periphery of the lip (Fig 4(a)) and the majority of the loss in total pressure that is measured at the engine face is due to this separation followed by turbulent mixing of the flow in the diffuser. As angle of incidence increases from zero this separation will gradually concentrate on the inside of the lower lip and will occur even when the streamtube size is smaller than the entry size (Fig 4(b)). The losses measured at the engine face will be a function of:

- lip shape
- contraction ratio A_{en}/A_t
- the size of the streamtube relative to the capture area A_{∞}/A_{en}
It is often convenient to use the inverse of this ratio so that losses measured at static conditions ($A_{en}/A_{\infty} = 0$) can be plotted
- the initial Mach number at the beginning of the diffuser. This is non-uniform under conditions of separation but is conveniently characterised by the one dimensional throat Mach number M_t based on the geometric area and derived from measurements at the engine face.
- the geometry of the subsonic diffuser i.e. its area distribution, shape, wall surface area and diffuser area ratio
- angle of incidence

Since both lip geometry and diffuser geometry can be changed on this model it is desirable to separate these losses in total pressure emanating from the diffuser from those caused by the cowl lip. Diffuser losses were obtained from tests at nominally zero forward speed with a bellmouth entry fitted.

4. DISCUSSION OF RESULTS (Contd)

At a given throat Mach number M_t the losses were then subtracted from the losses measured at the engine face at the same value of M_t with a given lip at all conditions of forward speed and incidence. Thus lip loss is defined as:

$$\left(\frac{\Delta P}{P_\infty}\right)_{\text{lip}} = \left(\frac{\Delta P}{P_\infty}\right)_{\text{for lip configuration at zero or at forward speed}} - \left(\frac{\Delta P}{P_\infty}\right)_{\text{for bellmouth configuration at zero forward speed and incidence}}$$

The lip loss defined above is probably better described as a lip loss plus a diffuser interaction loss.

If the basic diffuser were such that its losses were higher than would be expected from skin friction considerations then this approach would be an oversimplification.

Lip loss should be defined with reference to a configuration with a parallel pipe following the lip rather than a diffuser. However this would entail repeating the experiments with a reduced size engine face and it is suspected that the results would not be significantly different from those derived in this experiment.

4.1 Effects of Transition Fixing

A limited number of tests were made to investigate the effects of transition fixing on lip 1 and lip 4.

The transition strip used was lead-based tape with a serrated leading edge, the tape being 0.2 mm thick and 5 mm wide.

In Figure 5 free transition is compared with transition on the highlight, this being the position which was found to have the largest effect on the intake characteristics.

For lip 1, fixing transition has negligible effect on DC_{60} or intake recovery. Lip 4 shows an improvement with fixing for both of these parameters at high incidence, but the critical incidence is not changed.

Changes to swirl angle and to root mean square (rms) pressure level at the engine face were negligible.

It was concluded that transition fixing has a negligible effect for low contraction ratio and only a small effect at high contraction ratios. The fitting of transition strips compromises the geometry of the lip profile confusing comparisons between different lips. For these reasons all subsequent tests were transition free.

4.2 Effect of Contraction Ratio

The prime geometric variable that affects losses and flow distribution is the lip contraction ratio. As will be seen in section 4.3, for low speeds, the variation within a given family of lip shapes for a given contraction ratio is small. Thus comparisons are shown (Fig 6) at zero and 40° incidence between contraction ratios of 1.078, 1.177 and 1.25 that have ellipse ratios of 5, 5 and 2 respectively. As can be seen lip losses decrease continuously with decrease in streamtube size (increase in A_{en}/A_∞) at zero incidence as would be expected. However at 40° incidence after remaining constant or even slightly decreasing from the level of the losses at zero forward speed, the losses then increase rapidly with decrease in streamtube size.

The incidence at which this change in trend with streamtube size is illustrated in Fig 7. For lip shapes 1 and 3 at a throat Mach number of 0.6 the change in sign of losses versus streamtube size (the condition at which losses are independent of streamtube area) occurs at $\alpha = 27^\circ - 28^\circ$. For lip shape 4 losses are much smaller and there is virtually no change in sign of losses versus streamtube size (except at very low values of A_{en}/A_∞); nevertheless there is still an incidence where the losses are independent of streamtube size.

In this experiment, at low values of throat Mach number, this increasing loss appears to be still in evidence when the streamtube size is less than the entry size ($A_{en}/A_\infty > 1$). Tests at higher forward speeds ($M_\infty = 0.3 - 1.0$) at high incidence are needed to indicate the exact variation of this important trend at all throat Mach numbers. Some tentative projections are available at $\alpha = 30^\circ$ by comparing results for the CR 1.177 lip with some from an isolated rectangular intake⁵ with approximately the same contraction ratio, 1.15 at $M_\infty = 0.6$ and 0.9 (Fig 8(a)).

The alignment of low and high speed measurements is better illustrated by plotting the lip loss divided by the throat dynamic pressure versus M_∞/M_t (Fig 8(b)). This form of collapse, which in effect combines the influence of streamtube size and throat Mach number, is useful in presenting the overall performance as contraction ratio is varied. An example is shown at zero angle of incidence in Fig 9.

4.2 Effect of Contraction Ratio (Contd)

Engine face flow distortion coefficients DC_{60} are shown plotted in a similar manner to the losses as a function of streamtube size and throat Mach number at angles of incidence of 0° and 40° in Fig 10. DC_{60} is mainly dependent upon streamtube size and independent of throat Mach number in the range $M_t = 0.2 - 0.5$. Somewhat lower values of DC_{60} occur for throat Mach numbers of 0.6 and 0.7 for lips 1 and 3. At these throat Mach numbers the local values of Mach number adjacent to the cowl lip surface are supersonic resulting in turning without separation or perhaps with a small bubble of separated flow followed by shock recompression. This will not be followed by shock induced separation if the Mach number is less than 1.3. If lip losses are plotted versus M_t then in general it can be seen from Fig 11 that they vary linearly for lip shape 1 but for lips 3 and 4 there is a sudden change of slope. In general the magnitude of the slope of the loss versus M_t appear to correlate roughly with the variation of DC_{60} with throat Mach number and streamtube size. Thus for lip 4 (CR 1.25) the higher values of DC_{60} at $M_t = 0.6$ and 0.7 where the streamtube size is large, are associated with the higher slope of the loss curve (Fig 10 & 11). Similarly for lip 3 (CR 1.177) the lower slope for the loss curve at high throat Mach number occurs with the lower values of DC_{60} (Fig 10 & 11).

4.3 Effect of Change of Lip Profile

The effect of a change of ellipse ratio from 2 to 5 is wholly beneficial to the velocity distribution on the inside of the cowl lip at high flight speeds and zero incidence as illustrated in Fig 12(a). It would be expected that there is some penalty to be paid in reduced performance at low speeds and high incidence for use of a higher fineness ratio ellipse as shown in Fig 12(b) for CR = 1.078. However, as can be seen this appears to be largely confined to the smaller streamtube size and more particularly at higher angles of incidence which suggests that at this contraction ratio the adverse pressure gradients around the lip are nearly always sufficiently high to separate the boundary layer whatever the shape of the profile.

At zero forward speed the effect of making the lip blunter by increasing the index of the ellipse equation from 2 to 2.4 reduces the calculated maximum supersonic velocity and hence the adverse pressure gradient substantially as shown in Fig 13(a). The super ellipse is disadvantageous only at 30° incidence at the highest forward speed.

Obviously the effect of any profile change for a given contraction ratio is going to be a fairly complex function of streamtube size and incidence and probably requires both high speed and low speed tests to define properly the boundaries between separated and unseparated flow.

4.4 Effect of Spacers on a Straight Duct

Full results over a range of forward speeds are available for the addition of an entry spacer, and at $M_\infty = 0.21$ for an exit spacer. As with the lip profile change the beneficial effects of an entry spacer are largely confined to losses at the smaller streamtube size and the higher angles of incidence (Fig 14). In general flow distortions are made slightly worse. The changes with exit spacer at $M_\infty = 0.21$ have, as would be expected, a negligible effect on losses but substantially reduce flow distortion at all incidences.

4.5 Effect of a Lip Slot

At angles of incidence above 30° the presence of a lip slot (lip 3.1) substantially reduces losses increasingly as streamtube size decreases but at lower incidences the reductions are small (Fig 15). In contrast the effect of the lip slot on flow distortion is adverse at high incidence but slightly favourable at low incidence. The limited results at $M_\infty = 0.21$ show that the effect of changing from a straight to an S bend diffuser is in general favourable to flow distortion but results in no change in losses. The unsteady pressure variations tend to follow the variation of losses with streamtube size and incidence rather than the DC_{60} values.

4.6 Effect of Offset Diffuser

Comprehensive results at all forward speeds and angles of incidence are only available for the S bend diffuser fitted with an exit spacer for lip shapes 3 and 4. Thus comparisons have been made between the straight diffuser without exit spacer and the S bend diffuser with exit spacer with the addition of spot points at $M = 0.21$ for the straight diffuser with exit spacer. As can be seen in Fig 16(a) for lip 3 the major effect of the S bend diffuser both on losses and flow distortion is at large streamtube sizes (static and very low forward speeds). The much lower flow distortion for the S bend diffuser at smaller streamtube sizes is obviously due to the favourable effect of the exit spacer as illustrated by the corresponding results for the straight diffuser with exit spacer.

In contrast to lip 3, for lip 4 the major effect on losses is at the smaller streamtube sizes and the higher angles of incidence (Fig 16(b)).

4.6 Effect of Offset Diffuser (Contd)

Flow swirl angle (defined as positive for clockwise rotation looking downstream), which is less than 5° for all the configurations discussed so far, is more significant with the offset duct. Unsteady pressure rms levels also are somewhat higher for the offset duct.

4.7 Offset Diffuser at Incidence and Sideslip

Comparison of the effects of incidence and sideslip (Figure 17) shows that the S bend intake is far less sensitive to a given magnitude of sideslip than to the same value of incidence. The intake represents a port installation on a fuselage side. Positive sideslip (as defined for these tests) means that the relative wind is from the port side, and in effect straightens out the intake aerodynamically. The effect on the total pressure contours at the engine face is illustrated by Figure 18.

4.8 Comparison with Blackaby and Watson Results

The Blackaby and Watson lip shapes had the same contraction ratios of 1.177 and 1.078 but with an ellipse ratio of 3.6 and they had a small forward spacer aft of the lip and before the start of the conical diffuser. As can be seen in Figure 19 at zero incidence, the agreement between the two results is very close for the CR 1.177 lip and also for the CR 1.078 lip at the higher forward speeds. There are some small discrepancies at and near static conditions. Agreement in the variation of lip loss with angle of incidence up to 25° is again very good.

4.9 Maximum Mass Flow and Throat Discharge Coefficient

The measured maximum mass flow is presented as a throat discharge coefficient C_d (defined as the ratio of measured maximum mass flow to ideal calculated mass flow based on geometric area). Figure 20 shows C_d at incidences of 0 and 40° as a function of free stream Mach number. The agreement at zero incidence with the results of reference 1 is very close.

At zero forward speed, the maximum flow is also presented in terms of M_{en} , the mean Mach number at the highlight plane. Figure 21 shows data from the present experiment and from references 6 to 11. This presentation clearly shows two regimes, one for attached flow (high contraction ratio), where the flow is set by choking in the throat, and one for separated flow (low contraction ratio). Here the limit is set by a constant value of M_{en} . This separated flow limit has been found to be mainly a function of M_∞ with minor corrections for incidence. The attached flow limit is largely independent of forward speed.

4.10 Engine Face Unsteady Pressure Measurements

Unsteady pressures presented in the preceding sections refer to the maximum rms value of the four engine face transducers. In fact there is considerable variation of rms level around the engine face as illustrated in Figure 22. Examination of engine face total pressure contours showed that the high rms pressures appeared to be measured in regions of high pressure gradient. This postulated relationship is shown in Figure 23 where the radial pressure gradient is taken as an approximation to the true value.

Data from all four transducers over the full incidence range are plotted for both diffusers with lip 1. Unsteady pressures in the offset diffuser tend to be higher than those in the straight diffuser at a given radial pressure gradient, which indicates that other parameters are also important. Much useful work remains to be done in relating unsteady pressures to steady state pressure fields.

Selected data points have been analysed to produce pressure spectral density plots. This analysis was made with averaged samples and covers a frequency range from 0 to 5 KHz.

Note that the ordinate of a pressure spectral density plot is the square root of that for a power spectral density.

Figure 24 shows a typical result for all four transducers. The spectra are noticeably different for each location. Resonances are present which are harmonics of the natural frequency of the complete model and ejector assembly.

Figure 25 shows the spectra for the top transducer at several incidences. Increasing incidence is seen to produce higher harmonics and to increase the peak spectral density level. This suggests an edge tone mechanism. Data from the thicker lips show less marked resonances and fewer harmonics, as would be expected for an edge tone.

Since the data obtained contains aerodynamic resonances specific to the test equipment and since there is some suspicion that rms pressure levels are related to local total pressure gradients, there are obvious problems in applying model results of this type to a full scale aircraft configuration. Thought needs to be given on how to correctly represent the boundary condition presented by an engine.

5. CONCLUSIONS

Low speed tunnel tests on a family of inlet geometries have been reported. Inlet total pressure loss has been separated into lip and diffuser contributions.

Good agreement exists between measured lip losses and previously published data.

Lip losses may be decreased by increasing contraction ratio, fitting a lip slot or a forward spacer.

Steady state flow distortion at the engine face is decreased by increasing lip contraction ratio or by fitting an aft extension. Forward extensions and a lip slot are less effective.

For the S duct tested, distortion levels are set by the diffuser as much as by incidence. Sideslip, however, lessens the distortions.

Flow swirl angles at the engine face are low for all conditions with the straight diffuser. Higher values are found with the S duct at high incidence.

Engine face unsteady total pressures are related to local pressure gradients. A forward spacer is effective in reducing rms pressures.

Pressure spectra at the engine face show features related to the test configuration which would give difficulties in interpreting the results for an aircraft installation.

REFERENCES

1. An experimental investigation at low speeds of the effects of lip shape on the drag and pressure recovery of a nose inlet in a body of revolution.
J.R. Blackaby and E.C. Watson, NACA TN 3170 April 1954
2. Low speed investigation of the effects of angle of attack on the pressure recovery of a circular nose inlet with several lip shapes.
J.R. Blackaby NACA TN 3394 May 1955
3. The effect of intake lip geometry and diffuser shape on predicted surface and flow field Mach number distributions at subsonic speeds.
E.L. Goldsmith RAE Technical Report to be published
4. The characteristics and calibration of two types of airflow metering device for investigating the performance of model air intakes.
I. McGregor RAE Technical Report 71212 November 1971
5. Unpublished RAE Results.
6. Effect of entry-lip design on aerodynamics and acoustics of high throat-Mach-number inlets for the quiet, clean, short-haul experimental engine.
B.A. Miller, B.J. Dastoli and H.L. Wesoky NAS: TM-X-3222 May 1975
7. The effect of lip-shape on a nose-inlet installation at Mach numbers from 0 to 1.5 and a method for optimising engine-inlet combinations.
E.A. Mossman and W.E. Anderson NACA RM A54B08 1954
8. Axially symmetrical pod air intakes. The effect of lip shape on the ground running performance.
P.A. Simpson Rolls Royce Report DMB/WFW.10/PDS December 1960
9. Some internal-flow characteristics at zero flight speed of an annular supersonic inlet and an open-nose inlet with sharp and rounded lips.
J.R. Milillo NACA TIB/4294 July 1954
10. Some internal-flow characteristics of several axisymmetrical NACA 1-series nose air inlets at zero flight speed.
C.R. Bryan and F.F. Fleming NACA TIB/4295 July 1954
11. Internal performance of subsonic pod intakes.
C.M. Baxter Rolls Royce Report IAR 00014 September 1970
12. Noise Attenuating intakes. Variation of intake performance with lip curvature.
C.M. Baxter Rolls Royce Report IAR 05022 January 1971

Acknowledgement

The work described in this paper was funded by the Procurement Executive, Ministry of Defence. The authors wish to thank British Aerospace for permission to publish this paper. Acknowledgements are also due to our colleagues who conducted the tests, particularly Messrs. A.F. Barker, C.S. Wellman and B.C. Bessant.

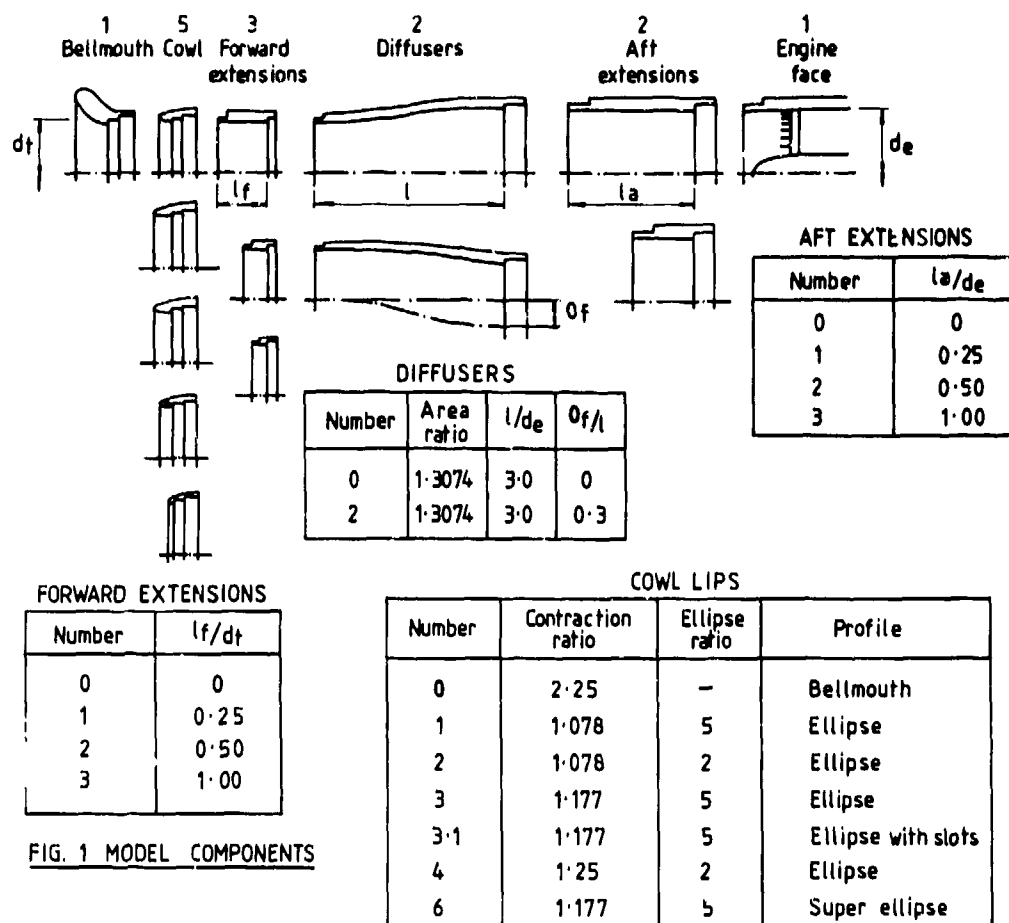


FIG. 1 MODEL COMPONENTS

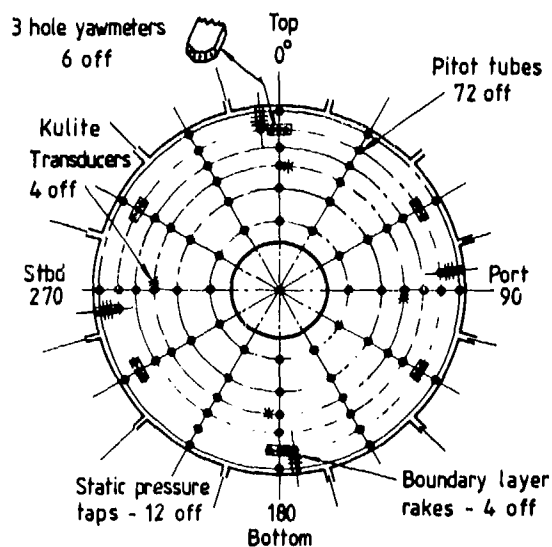


FIG. 2 ENGINE FACE INSTRUMENTATION

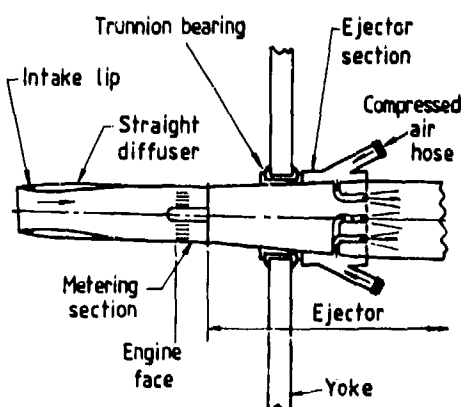


FIG. 3 TEST INSTALLATION

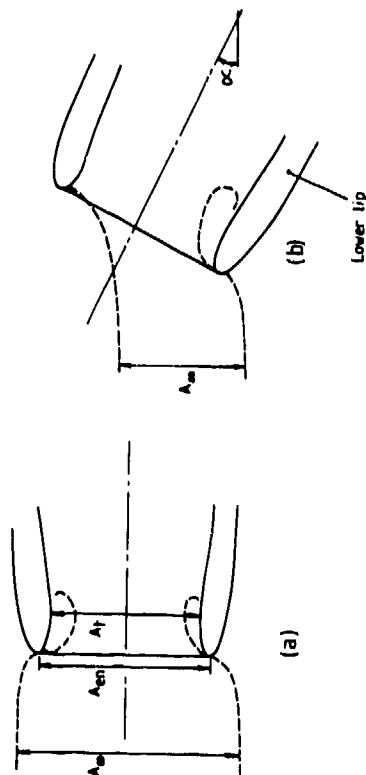


Fig. 4 Lip Separation

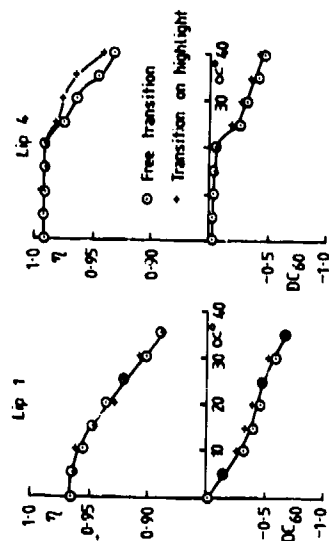


FIG. 5 EFFECT OF TRANSITION FIXING ON INTAKE CHARACTERISTICS

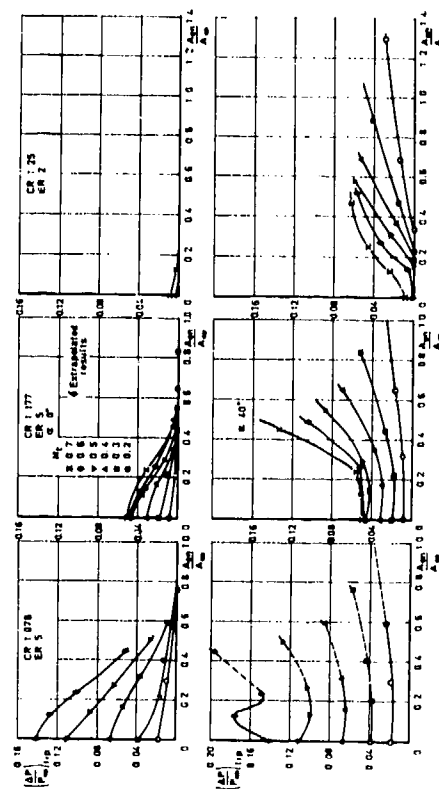


Fig. 6 Variation of lip loss with streamtube size and throat Mach No at incidence angles of 0° and 40° for contraction ratios of 1.078, 1.177 and 1.25

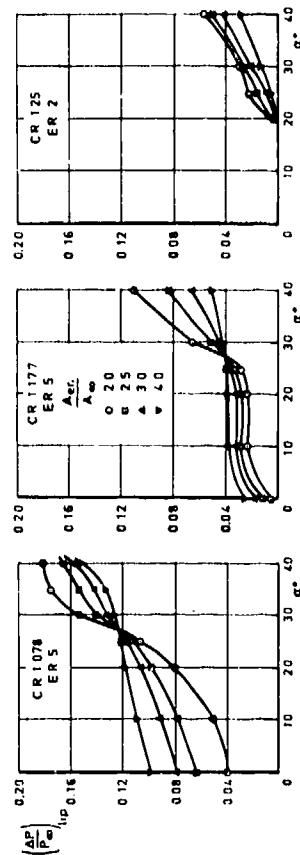


Fig. 7 Variation of lip loss with streamtube size and angle of incidence for a throat Mach No of 0.6

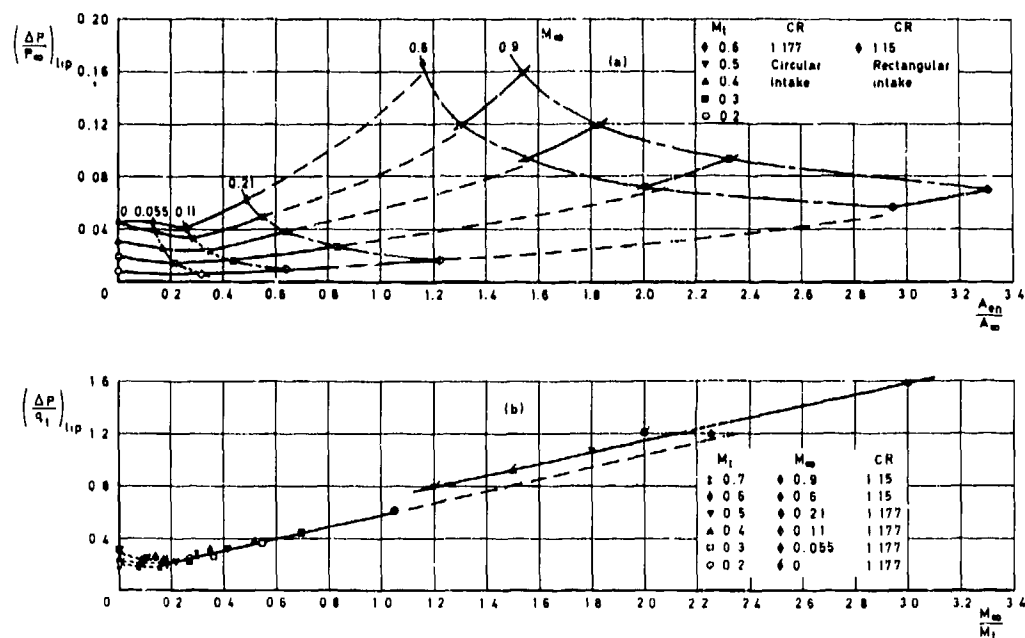


Fig 8 a & b Lip loss variation at low & high speeds at $\alpha = 30^\circ$

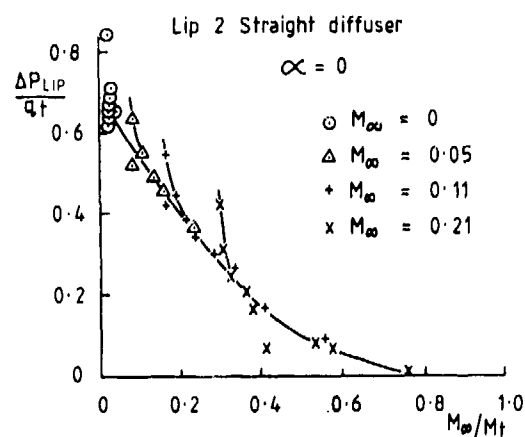


FIG. 9 EXAMPLE OF AN ALTERNATIVE LIP LOSS PRESENTATION

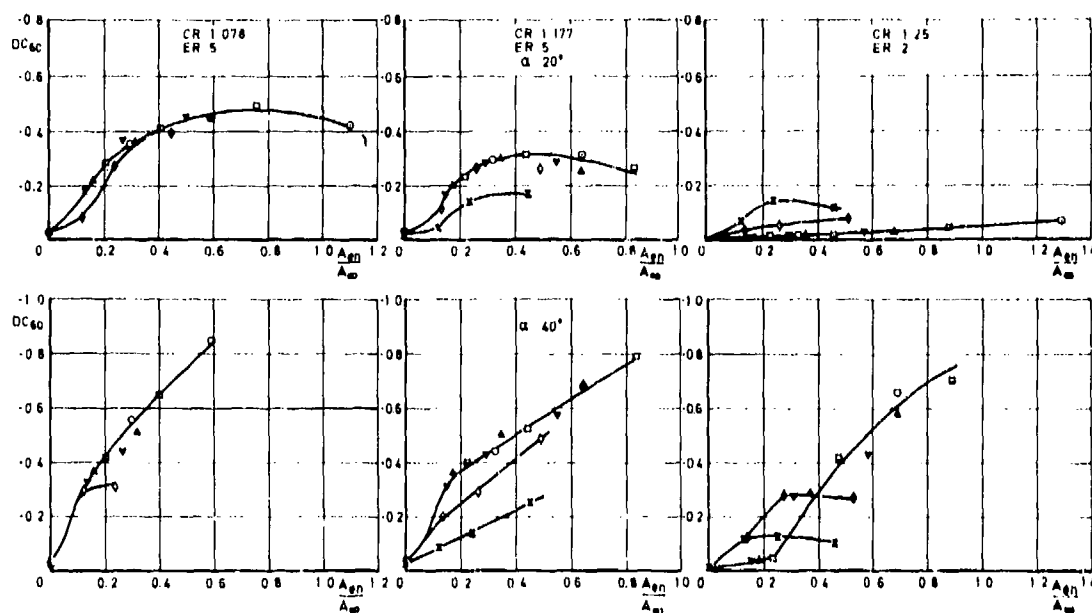


Fig 10 Variation of engine face flow distortion with streamtube size and throat Mach No at incidence angles of 20° and 40° for contraction ratios of 1.078, 1.177 and 1.25

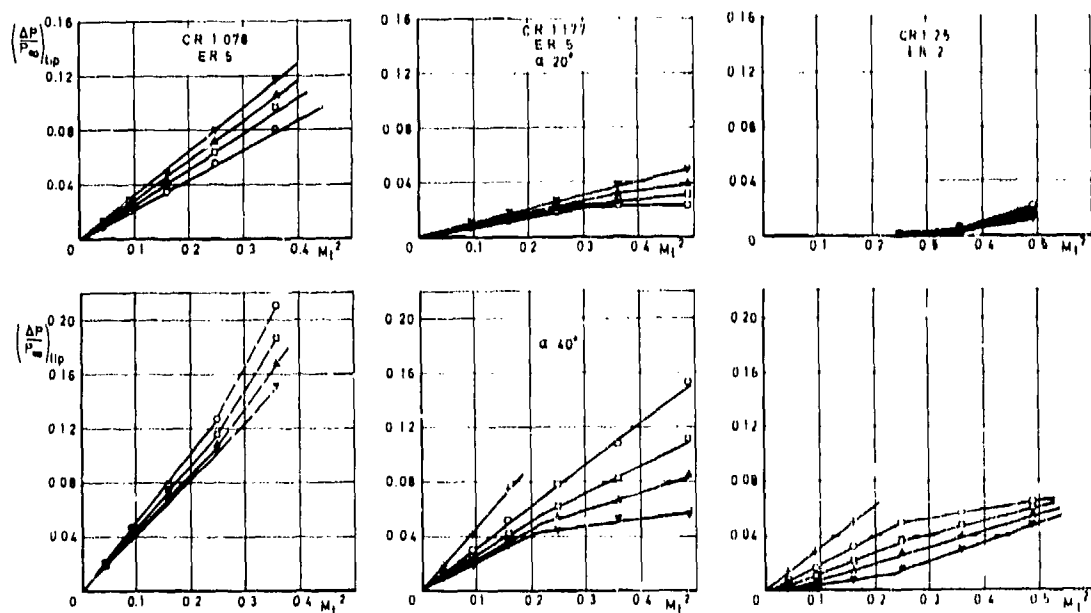


Fig 11 Variation of lip loss with streamtube size and M_1^2 at incidence angles of 20° and 40° for contraction ratios of 1.078, 1.177 and 1.25



Fig 12a Effect of change of ellipse ratio on calculated lip surface Mach No distribution for CR 1.25, CR 0.85 and $M_\infty = 0.9$

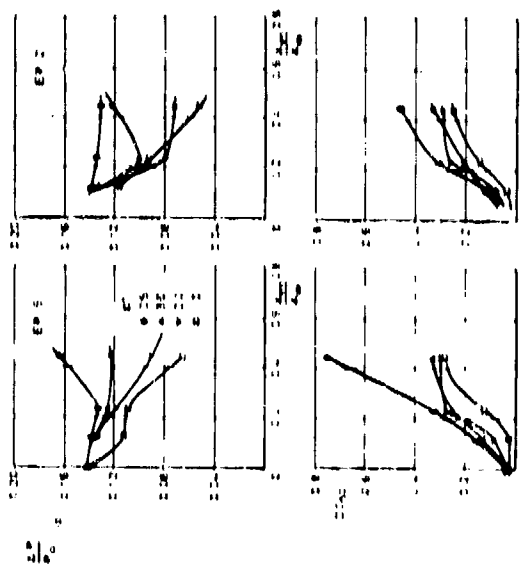


Fig 12b Comparison of performance of ER 2 and S ellipse lip stages for CR 1.078 lip at $M_\infty = 0.6$

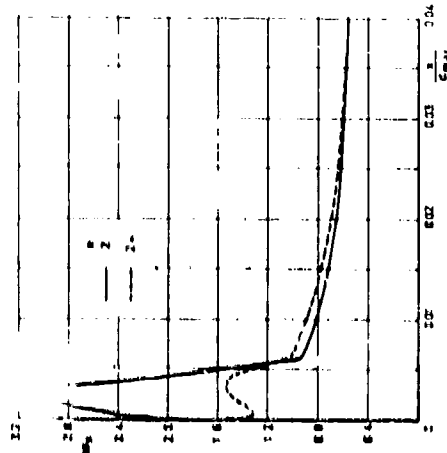


Fig 13a Effect of change of ellipse ratio on calculated lip surface Mach No distribution at zero forward speed ($M_\infty = 0.4$, CR 1.15 and ER 5)

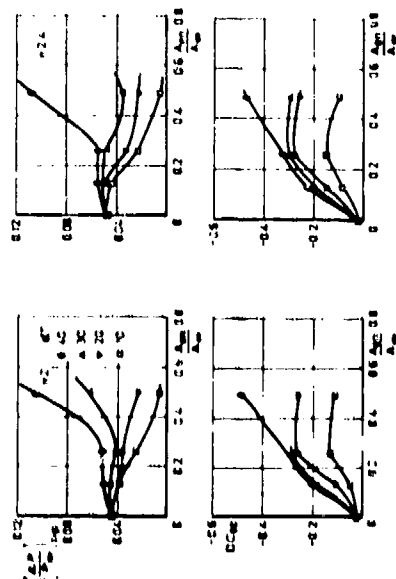


Fig 13b Comparison of performance of ellipse and supere' lip shapes for CR 1.177 lip at $M_\infty = 0.6$

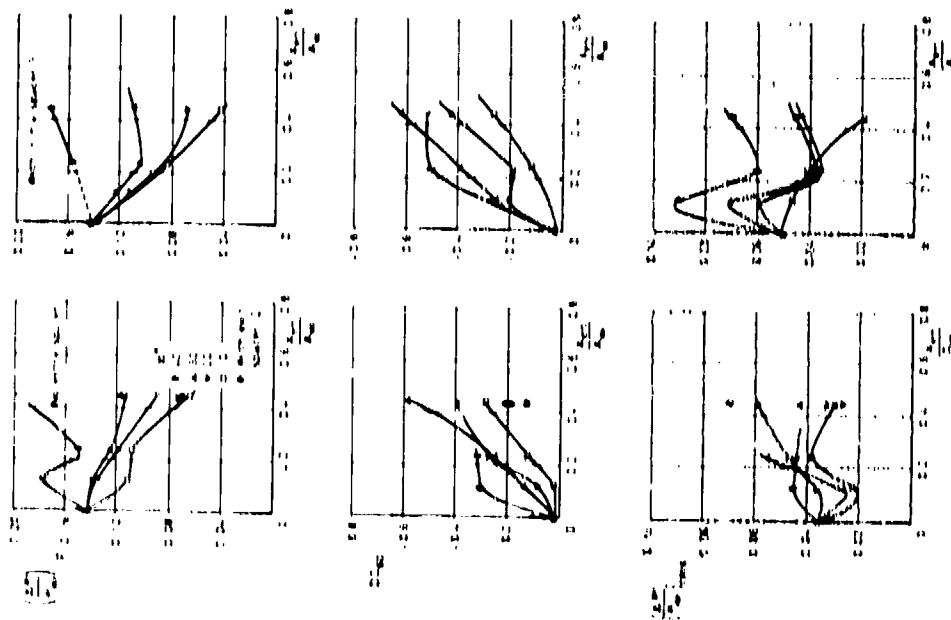


Fig. 14 Comparison of performance with and without entry and exit spacers at a throat Mach No of 0.51 OR 1.078, ER 51

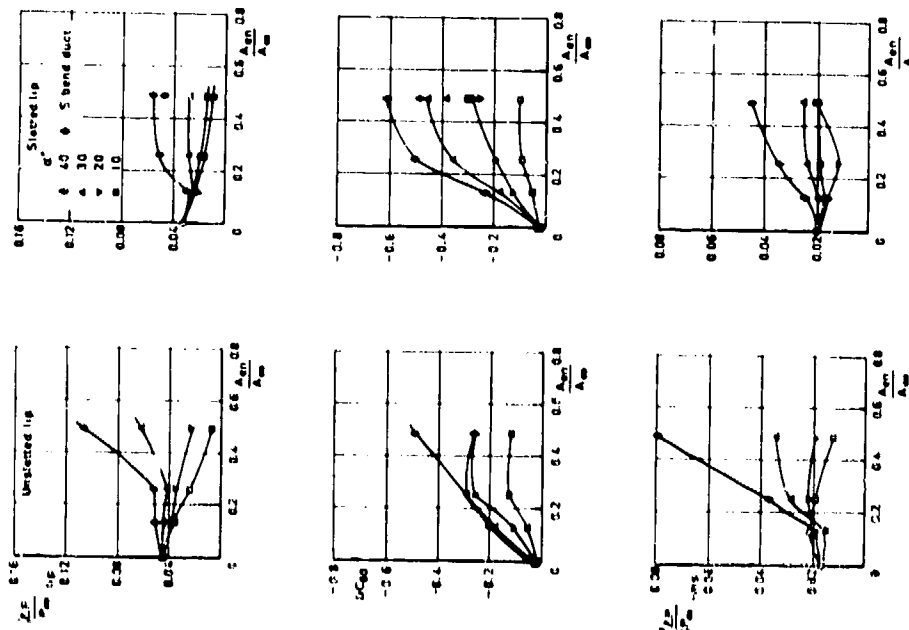


Fig. 15 Comparison of performance of unslotted and slotted lips at a throat Mach No of 0.5 (CR1177 ERS)

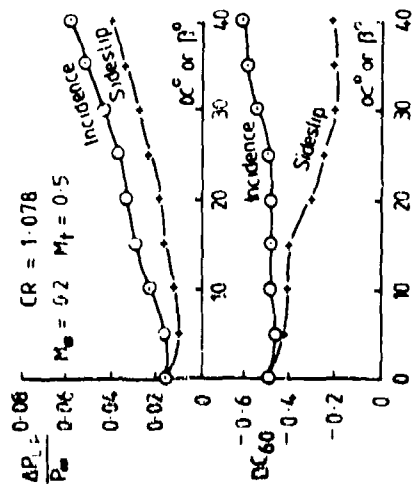


FIG 17 COMPARISON OF INCIDENCE AND SIDESLIP EFFECTS WITH THE S DUCT

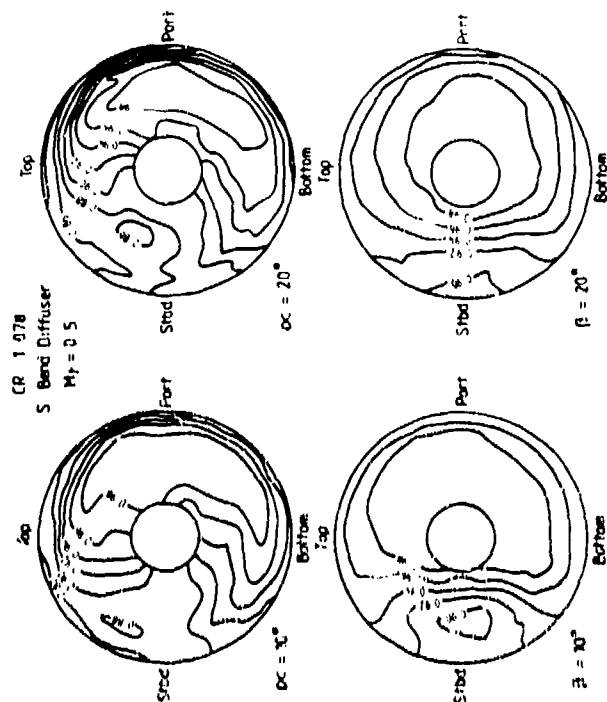


FIG 18 COMPARISON OF INCIDENCE AND SIDESLIP EFFECTS ON ENGINE FACE TOTAL PRESSURE RECOVERY CONTOURS

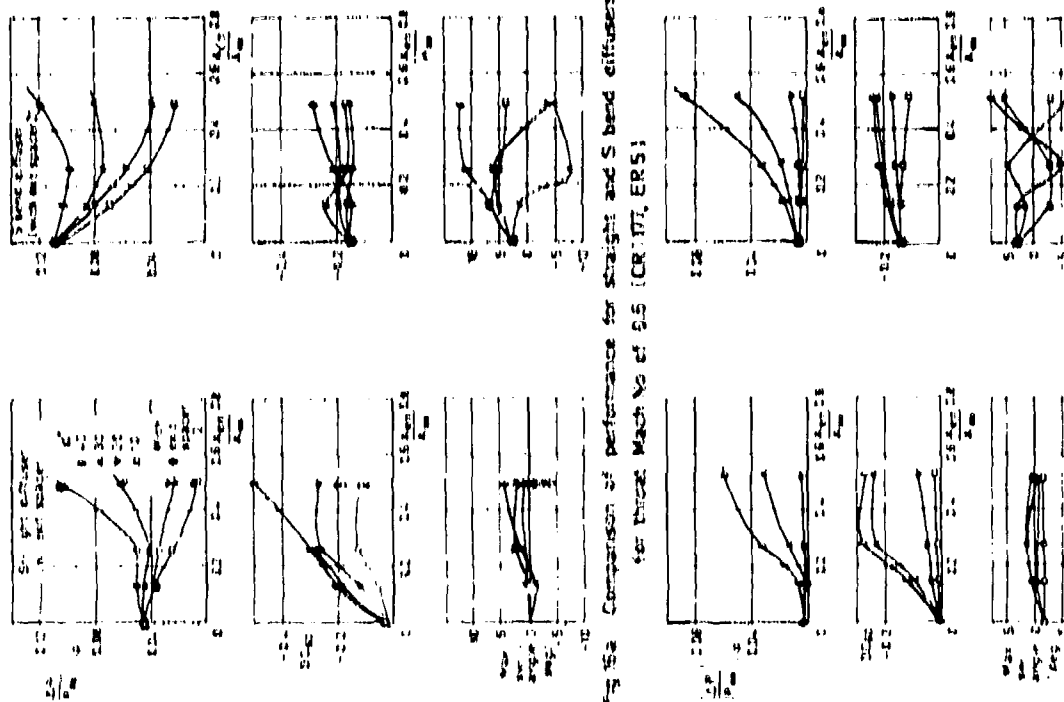


FIG 19a Comparison of performance for straight and S bend diffusers for throat Mach No of 0.5 (CR 1.078, ER 5)

FIG 19b Comparison of performance for straight and S bend diffusers for throat Mach No of 0.6 (CR 1.25, ER 2)

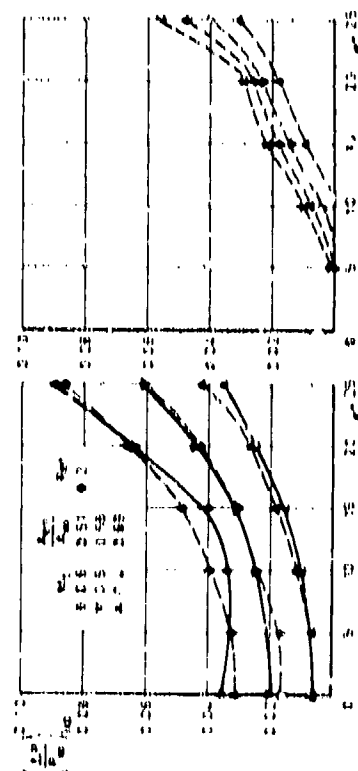
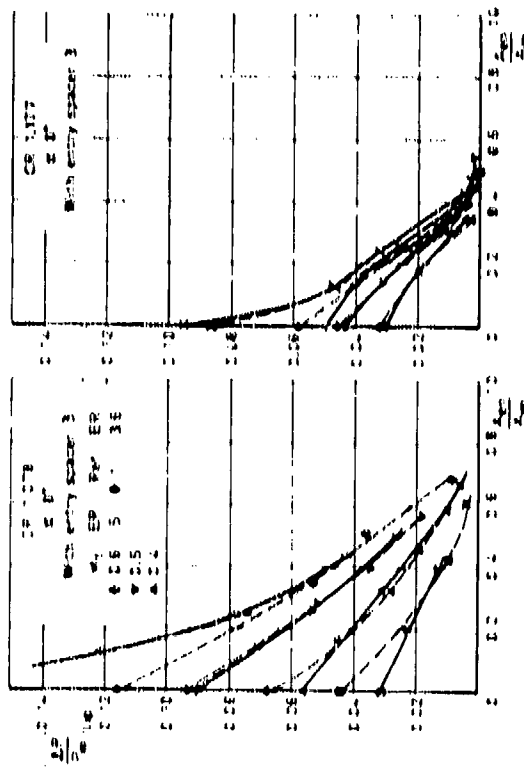


Fig 18 Comparison of results with those from Refs 1 & 2

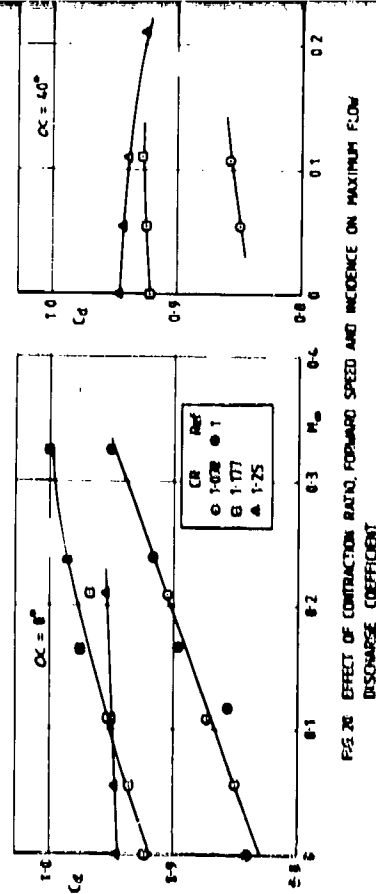


Fig 26 Effect of contraction ratio, forward speed and incidence on maximum flow discharge coefficient

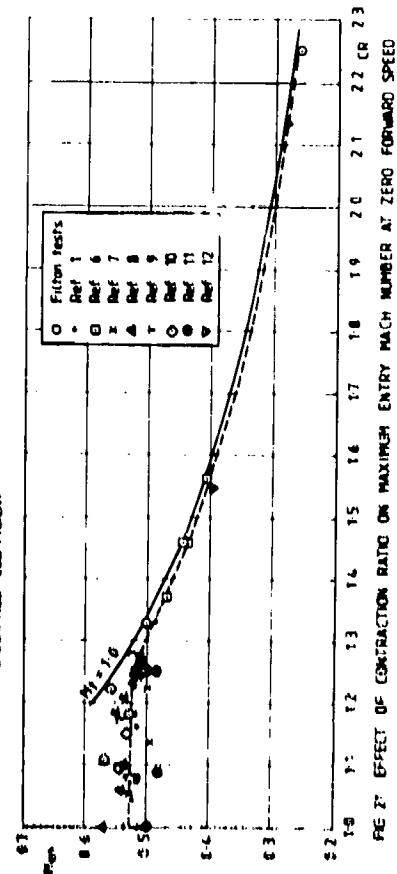


Fig 27 Effect of contraction ratio on maximum entry Mach number at zero forward speed

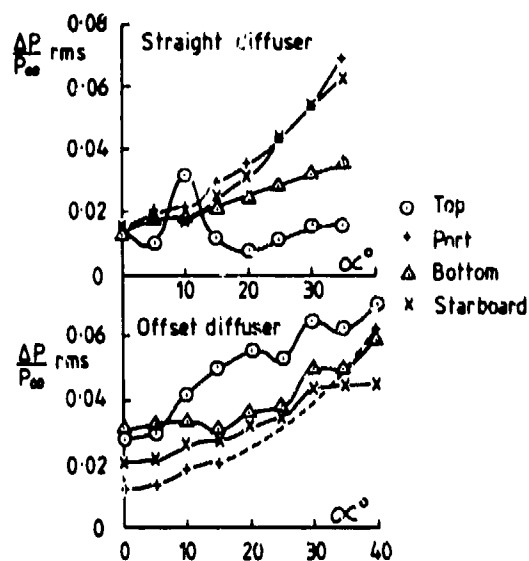


FIG. 22 VARIATION OF UNSTEADY PRESSURE AROUND THE ENGINE FACE

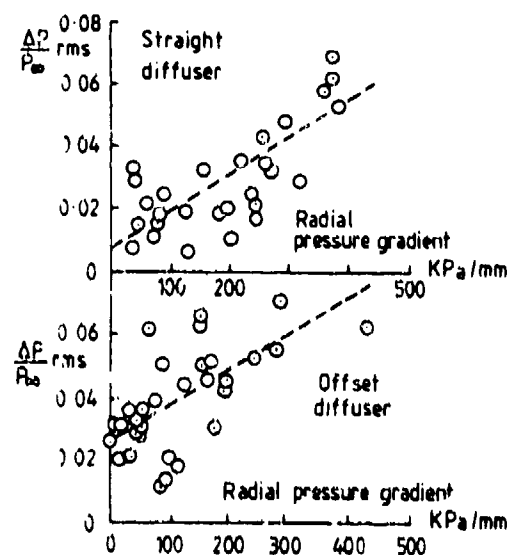


FIG. 23 RELATIONSHIP BETWEEN UNSTEADY PRESSURE LEVEL AND PRESSURE GRADIENT

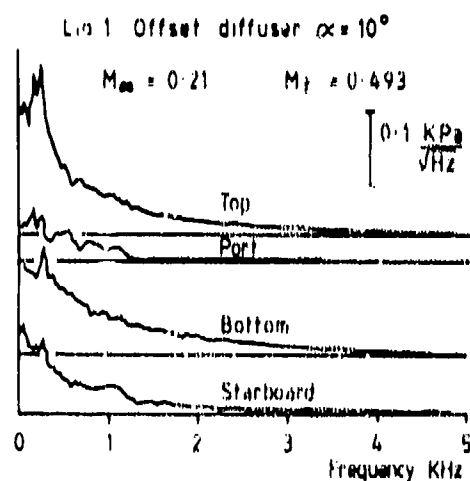


FIG. 24 PRESSURE SPECTRAL DENSITY AT POINTS AROUND THE ENGINE FACE

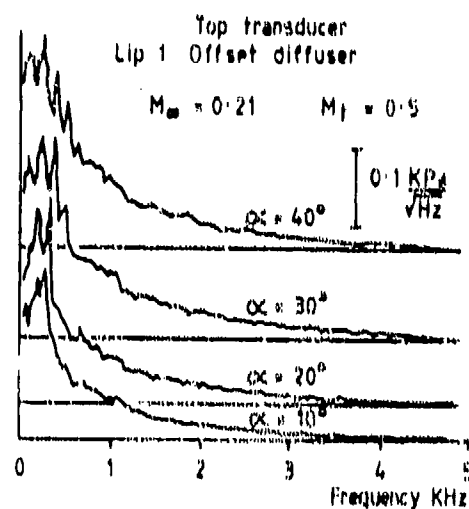


FIG. 25 EFFECT OF INCIDENCE ON PRESSURE SPECTRAL DENSITY

ÉCOULEMENTS TRANSSONIQUES DANS UNE PRISE D'AIR EN GRANDE INCIDENCE ET EFFET DE TRAPPE DE SOUFFLAGE

par A. Dymant - Professeur
P. Grenier - Ingénieur
J.P. Flodrops - Ingénieur
Institut de Mécanique des Fluides
5, bd Paul Painlevé, 59000 - Lille (France)

RÉSUMÉ.-

Cette étude expérimentale est consacrée à l'écoulement dans une prise d'air bidimensionnelle schématisée en grande incidence. L'écoulement amont est subsonique et le débit interne est réglable.

L'objectif de l'étude est essentiellement l'examen des phénomènes consécutifs aux décollements, en particulier la réhomogénéisation de l'écoulement interne.

Une partie de l'étude a consisté à tester un dispositif d'amélioration de l'homogénéisation : il s'agit d'une trappe de soufflage naturel qui peut être complétée par une écoppe destinée à guider l'air capté.

L'aspect global de l'écoulement interne est étudié par sondages dans différentes sections. L'analyse des phénomènes instationnaires est faite à l'aide de visualisations ultra-rapides. Des visualisations classiques permettent de caractériser l'écoulement moyen.

L'implantation d'une trappe de soufflage améliore très sensiblement les performances de la prise d'air. Le coefficient de débit σ et la pression totale moyenne p_{tm} au niveau du compresseur sont considérablement augmentés.

L'adjonction d'une écoppe destinée à guider l'air vers la fente n'a qu'une faible influence sur σ et p_{tm} au niveau du compresseur ; mais elle apporte un gain appréciable en ce qui concerne la rapidité de l'homogénéisation de l'écoulement interne.

LISTE DES NOTATIONS.-

H	hauteur de l'entrée d'air bidimensionnelle
k	rapport de l'aire de la fente à B
M	nombre de Mach
M_{int}	nombre de Mach interne, valeur moyenne de M en $x^* = B$
p	pression
p_{tm}	pression d'arrêt moyenne dans une section
q	débit total capté
Re	nombre de Reynolds $\frac{\rho V_0 H}{\mu}$
s	aire de la section de la prise d'air
x^*	abscisse réduite $\frac{x}{H}$
z^*	cote réduite $z \frac{z}{H}$
α	incidence
γ	rapport des chaleurs spécifiques
Δt	intervalle de temps entre deux clichés
λ	rapport de l'aire du col sonique à l'entrée à 90°
μ	viscosité
ρ	masse volumique
σ	coefficient de débit $\sigma = \frac{q}{q_0}$

Indice :	a	conditions en amont
	l	conditions d'arrêt locales
	i	conditions génératrices de l'écoulement amont.

1 - INTRODUCTION.-

Les avions de combat futurs seront caractérisés à la fois par une meilleure manœuvrabilité et par un domaine de vol plus étendu que pour ceux en service actuellement. Cela va se traduire par la conception d'appareils capables d'évoluer à très grande incidence, dans des conditions où l'écoulement subit un décollement généralisé. Il est certain que pour ce type d'avion, les prises d'air doivent faire l'objet d'une attention toute particulière.

Le rôle de la prise d'air est de fournir au moteur, dans tous les cas de vol, la quantité d'air nécessaire, et ce dans les meilleures conditions. Dans le plan d'entrée du compresseur, la pression d'arrêt doit être la plus forte possible. En outre, l'écoulement doit être suffisamment uniforme et permanent pour éviter le décrochage du compresseur. Il faut également que la prise d'air interfère le moins possible avec l'avion et que la résistance de captation reste à un niveau acceptable. Ceci nécessite de pouvoir atténuer, sinon supprimer, les effets du décollement qui risque de se produire à l'entrée en vol à grande incidence.

Une étude expérimentale de ce problème a été menée à l'I.M.F.L., avec le soutien de la D.R.E.T.¹ sur une maquette de prise d'air bidimensionnelle à grande incidence. Nous présentons dans ce qui suit certains des résultats de ces travaux.

2 - MOYENS D'ESSAIS.-

Les essais se sont déroulés dans la soufflerie transsonique de l'I.M.F.L. C'est une petite soufflerie à retour à fonctionnement continu. Les conditions génératrices sont atmosphériques. Le maintien de la température d'arrêt est assuré par un échange d'air avec l'extérieur, au travers d'un dessiccateur.

La veine d'expérience est rectangulaire, de section $200 \times 40 \text{ mm}^2$. Les parois hautes et basses sont à fentes longitudinales. La perméabilité est voisine de 7 %.

La maquette est constituée par deux plaques parallèles d'écartement $H = 12 \text{ mm}$, d'allongement 8. Le bord d'attaque de la plaque supérieure est un biseau d'angle 15° .

La plaque inférieure de la maquette comporte deux parties : une fixe, à l'arrière, et une amovible à l'avant (fig.1). Cette dernière est constituée soit par un bord d'attaque pointu identique à celui de la plaque supérieure, soit par un bord arrondi, appelé lèvre.

Des essais ont été réalisés avec une trappe de soufflage située à 10 mm du bord d'attaque. La largeur de la fente est d'environ 7 mm et son angle de pénétration est $\theta = 30^\circ$.

Dans un autre montage, la fente est précédée d'une découpe qui prolonge simplement la paroi arrière de la fente vers l'avant, sur une longueur de 8 mm .

Pour ces deux dernières configurations, seul le bord d'attaque arrondi a été utilisé.

La maquette comporte deux orifices de pression statique percés sur chaque paroi intérieure aux abscisses $X^* = 4$ et $X^* = 8$. D'autres orifices ont été percés sur la lèvre. Une prise disposée à l'intérieur de la fente permet de déterminer le débit capté par celle-ci.

Trois peignes de sondes d'arrêt permettant de déterminer le profil de vitesse interne moyenne aux abscisses réduites $X^* = 4, 8$ et $1,5$. Ce dernier n'a été utilisé que pour les essais avec fente.

Les deux peignes situés en $X^* = 4$ et 8 sont constitués par 9 sondes dont 3 sont recouvertes à 180° pour permettre l'évaluation de la vitesse dans un domaine décollé. Le peigne en $X^* = 1,5$ comporte 4 sondes d'arrêt normales, 3 sondes d'arrêt courbées à 180° et 2 sondes de pression statique situées à 1 mm des parois : il permet en particulier de déterminer la part du débit interne capté par la section d'entrée.

Le dispositif d'aspiration est réalisé de manière à obtenir une obstruction aussi faible que possible. Des tuyères de régulation du débit capté sont disposées entre la maquette et la pompe d'aspiration.

Les visualisations ont été faites par sténoscopes et par ombroscopes à l'aide de deux dispositifs.

Le sténoscope interféromètre IMEL qui permet l'observation de l'écoulement moyen, avec des temps de pose de $2,5 \cdot 10^{-3} \text{ s}$ par exemple, est également équipé d'une source-éclair.

Les "chronologues" de conception I.S.T.² composés de 24 sources-éclair et qui permettent d'étudier l'évolution du phénomène en fonction du temps à l'aide d'observations par ombroscopie ou sténoscopie (1).

¹ Direction des Recherches, Études et Techniques du Ministère de la Défense

² Institut Franco-Allemand de Recherche de Saint-Louis

Les expériences ont été réalisées dans les conditions suivantes :

- Le nombre de Mach moyen au niveau du compresseur est nominalemeut compris entre 0,30 et 0,45. Mais certains essais ont été faits pour des valeurs plus faibles.

- A l'incidence 40° nous avons testé les quatre maquettes. Le nombre de Mach M_0 est alors limité à 0,38 à cause de l'obstruction. Les différences observées entre le bord d'attaque pointu et la lèvre sont extrêmement faibles et nous ne présenterons les résultats que pour cette dernière configuration, en les comparant à ceux obtenus pour la fente et la fente avec écope. La relative inefficacité de la lèvre peut s'expliquer par le fait que pour le nombre de Reynolds réalisé, le décollement est laminaire. Il se produit donc très près du point d'arrêt, avant le contournement de la lèvre. A grand nombre de Reynolds on aurait un décollement turbulent plus tardif et la hauteur de la bulle serait moindre.

- A l'incidence 20° seuls 3 modèles ont été utilisés : bord d'attaque pointu, fente et fente avec écope. Le nombre de Mach M_0 était de 0,50.

Il ne faut pas perdre de vue qu'à l'incidence géométrique réalisée en soufflerie, correspond en atmosphère infinie une incidence plus importante, mais qu'il nous est impossible d'évaluer.

3 - INCIDENCE 40°.-

3.1 - Evolution de l'écoulement interne.

Les pressions mesurées dans le conduit, pour $M_{int} = 0,40$ sont présentées dans le tableau ci-dessous rapportées à la pression critique de l'écoulement amont.

Configuration	$X^* = 1,5$	4	8
Lèvre	-	0,617	0,740
Lèvre et Fente	0,996	1,095	1,142
Lèvre, Fente et Ecope	0,934	1,210	1,220

Ces valeurs représentent la moyenne des mesures sur chacune des deux plaques : l'écart par rapport à la moyenne est toujours inférieur à 2 %.

On constate une recompression entre $X^* = 4$ et $X^* = 8$: le conduit joue le rôle d'un diffuseur. Cet effet est nettement moindre en présence de la trappe et il disparaît lorsqu'on implante l'écope.

La figure 2 présente les résultats du sondage sous la forme P/P_c fonction de la hauteur réduite Z^* . On peut constater dans la plan $X^* = 1,5$ une très forte dissymétrie de l'écoulement due à la poche de décollement. Cette dissymétrie existe toujours à $X^* = 4$ pour les cas lèvre seule et lèvre avec fente ; par contre le cas lèvre, fente et écope, présente déjà une homogénéisation presque parfaite. En $X^* = 8$ la bonne homogénéisation est réalisée dans les trois cas. En ce qui concerne le débit, la figure montre qu'il est plus grand quand il existe une fente et que l'écope apporte peu de modifications.

Pour les essais avec trappe, le poigne placé en $X^* = 1$, permet de déterminer le débit capté par la section d'entrée. Par ailleurs, la pression mesurée à la fente fournit une évaluation du débit passant par la trappe. La somme de ces débits devrait être égale à celui déterminé en $X^* = 4$ et $X^* = 8$. Cela n'est pas toujours vérifié du manière satisfaisante à cause probablement des effets tridimensionnels. Ces effets sont également la cause de l'écart observé entre le débit mesuré par les tuyères de régulation et celui obtenu par intégration dans la plan médian du conduit.

On constate que la fente joue un rôle primordial dans le phénomène de captation. D'après les sondages, la plus grande partie du débit interne passe par la fente. Il peut arriver, lorsque le débit est faible, que l'apport de l'entrée d'air soit pratiquement nul.

Sur la figure 3 qui représente l'écoulement moyen dans le cas de la fente, l'importance prime par le décollement à l'entrée (noter bien que la fente joue le rôle principal dans la captation). Il faut noter que le jet pénètre à l'intérieur du conduit avec un angle supérieur à 0 de sorte qu'une importante bulle de décollement existe en aval de la fente.

Un calcul approché simple peut être fait lorsque la fente et le col formé à l'entrée sont tous deux coniques. Dans ce cas, les symboles soulignés désignent des grandeurs réduites sans dimension à l'aide des valeurs critiques de l'écoulement amont (fig. 4). L'angle α est rapporté à l'écoulement à l'abscisse du col conique, et on suppose de ce fait, la présence de la fente, la vitesse moyenne V_0 est nulle. En présence de la fente, il existe un effet d'induction.

En faisant l'hypothèse que la pression \overline{p}_0 est égale à 1, on obtient :

$$\gamma \lambda = \overline{p}_0 \left(1 + \frac{\gamma V_0^2}{\gamma + 1} - \frac{\gamma + 1}{\gamma} V_0^2 \right) - 1 - \gamma R \sin \theta \cos \theta$$

et

$$\frac{2}{\gamma+1} (1-\lambda) \bar{V}_e \approx \frac{\bar{F} \bar{V}}{\frac{\gamma+1}{2} - \frac{\gamma-1}{2} \bar{V}^2} - \lambda - R \sin \theta$$

Par ailleurs on a

$$\bar{p}_0 \bar{V}_0 \sigma = \frac{\bar{F} \bar{V}}{\frac{\gamma+1}{2} - \frac{\gamma-1}{2} \bar{V}^2}$$

Considérons les essais présentés sur la figure 2. Désignons par q_{EA} et q_F respectivement les débits passant par l'entrée d'air et la fente. Dans le cas de la fente seule, les sondages en $X^* = 8$ et $X^* = 1,5$ donnent $\sigma = 0,75$, $q_{EA} = 0,39q$ et $q_F = 0,61q$, tandis que le calcul effectué à partir des valeurs de p et \bar{V} mesurées en $X^* = 8$ conduit à $\sigma = 0,74$, $q_{EA} = 0,37q$, $q_F = 0,63q$ et $\lambda \approx 0,086$, $\bar{V} \approx 0,12$. Pour le cas fente avec écoupe, on obtient par le calcul $\sigma = 0,80$, $q_{EA} = 0,39q$, $q_F = 0,61q$, $\lambda \approx 0,12$ et $\bar{V} \approx 0,10$, tandis que l'expérience donne $\sigma = 0,80$, $q_{EA} = 0,34q$ et $q_F = 0,66q$. Les sondages en $X^* = 1,5$ fournissent pour λ la valeur approchée 0,15.

Ces relations permettent donc, par des mesures dans une seule section, d'avoir une estimation correcte de la façon dont les débits se répartissent entre l'entrée d'air proprement dite et la fente. Elles mettent en évidence le rôle inducteur joué par la fente en ce qui concerne le débit dans le plan d'entrée. En effet, les valeurs trouvées précédemment, $\lambda = 0,086$ et $\bar{V} = 0,12$ conduisent à une valeur du débit entraîné égale à 20 % du débit total. Mais nous avons remarqué qu'en absence de la fente, le calcul précédent est nettement moins satisfaisant.

Lorsque le débit interne est faible, le col n'est pas amorcé et le bord d'attaque supérieur se trouve dans la zone de mélange issue du bord d'attaque inférieur. Alors, l'entrée d'air n'est pas alimentée en permanence à cause d'un battement de la zone de mélange, le bord d'attaque supérieur se trouvant tantôt à l'intérieur de cette zone, tantôt au-dessus. Ce phénomène donne naissance à des ondes acoustiques internes parfaitement visibles sur les clichés (fig. 5 et 6). Dans certains cas, elles se propagent à l'intérieur de la zone décollée et se réfléchissent sur la paroi inférieure. Pour la configuration de la figure 5, leur fréquence N a pu être évaluée. Elle est de l'ordre de 30 kHz ($N M/V \approx 2,7$). D'une manière générale, les phénomènes instationnaires sont très bien mis en évidence à la projection d'un film d'animation réalisé à partir des clichés de visualisation ultra-rapide et qui est montré à l'occasion de la présentation orale.

Avec l'adjonction de l'écoupe, la qualité de l'écoulement est encore améliorée, surtout en ce qui concerne la rapidité avec laquelle se fait l'homogénéisation.

La comparaison des sondages (fig. 2) avec ceux faits sans écoupe montre qu'en $X^* = 4$ l'homogénéisation est presque réalisée tandis que sans écoupe, il semble subsister un faible courant de retour ; c'est pour cette raison que la pression n'augmente plus entre $X^* = 4$ et 8.

Les visualisations de l'écoulement moyen montrent que l'écoupe guide le courant qui passe par la fente (fig. 7). Le jet pénètre avec un angle voisin de θ et le décollement créé en aval de la fente est considérablement amoindri. L'excellente homogénéisation de l'écoulement interne est parfaitement visible sur les clichés de visualisation ultra-rapide.

3.2 - Comparaison des résultats globaux.

L'amélioration du fonctionnement de l'entrée d'air peut être représentée par la donnée des valeurs globales σ , coefficient de débit, et p_{tm} , pression d'arrêt moyenne, mesurées dans le plan compresseur en $X^* = 8$ (fig. 8). On constate que l'adjonction de la trappe conduit à une forte augmentation de σ et p_{tm} , à nombre de Mach interne donné. L'amélioration supplémentaire apportée par l'écoupe reste, sur ces points, relativement modeste, de l'ordre de 5 % de la valeur obtenue pour la fente seule.

On peut évaluer la distorsion de l'écoulement, définie par l'amplitude de variation de la pression d'arrêt moyenne dans une section, rapportée à sa valeur moyenne (fig. 9). On constate alors ce que les photographies de visualisation laissent préjuger : en $X^* = 4$, l'homogénéisation est presque parfaite en présence de l'écoupe, tandis que sans écoupe, la distorsion reste relativement élevée. Il est vraisemblable que cet effet d'homogénéisation rapide de l'écoulement moyen se retrouve aussi sur les fluctuations.

4 - INCIDENCE 20°.

Les premières expériences sur la prise d'air à $\alpha = 20^\circ$, antérieures aux essais présentés ci-dessus, portaient sur une maquette à bord d'attaque pointu. Elles ont été complétées par des essais avec fente puis avec fente et écoupe.

Le comportement global est qualitativement le même à 20° qu'à 40° .

Dans le cas du bord d'attaque pointu, l'ensemble des résultats concernant les grandeurs moyennes montre une bonne homogénéisation de l'écoulement entre $X^* = 4$ et 8. En $X^* = 4$, le recollant est fait mais les vitesses demeurent encore très faibles à proximité de la paroi inférieure (fig. 10). Par contre, en $X^* = 8$ la vitesse est quasiment constante dans toute la section.

En ce qui concerne la pression d'arrêt p_t (fig. 11) les effets de la dégradation sont très sensibles en $X^* = 4$ près de la paroi inférieure tandis qu'à la paroi supérieure, p_t s'écarte peu de p_{t0} . Par contre, en $X^* = 8$ où l'homogénéisation est faite, p_t est pratiquement constant; la perte de pression génératrice est de 20 à 25 % dans toute la section.

Une séquence de visualisation ultra-rapide par striescopie est donnée sur la figure 12. Elle met bien en évidence l'interaction entre les structures tourbillonnaires et les ondes de choc qui a été déjà signalée en (1). On constate que cette interaction favorise l'homogénéisation de l'écoulement, mais au prix d'une perte de pression d'arrêt. Les clichés indiquent qu'en $X^* = 8$ l'écoulement est homogène et qu'il ne l'est pas en $X^* = 4$, ce qui est en accord avec les sondages.

Des mesures de fréquence et de vitesse de propagation des tourbillons ont pu être faites pour les photographies de la figure 12, dans une zone située à environ 1 cm du bord d'attaque : on obtient environ 90 kHz ($N H/V_0 \sim 6$) et 240 m/s respectivement.

Aucun essai n'a été fait avec le bord d'attaque arrondi seul car on sait, d'après ce qui a été constaté à $\alpha = 40^\circ$, que les différences entre bords d'attaque pointu et arrondi sont minimales.

Les sondages effectués avec le bord d'attaque arrondi équipé de la fente avec et sans écope montrent que l'écope n'apporte pas d'amélioration (fig. 10 et 11). En $X^* = 4$, l'écoulement est déjà uniforme dans les deux cas.

Par rapport au bord d'attaque pointu, l'amélioration est notable : en ce qui concerne σ et p_{tm}/p_{t0} , à $M_{int} \sim 0,40$, on passe de 0,64 et 0,74 à 0,78 et 0,93 respectivement (fig. 13).

Les visualisations des figures 14 et 15 confirment les résultats des sondages : peu de différences apparaissent entre l'essai sans écope et celui avec écope.

5 - CONCLUSION.-

Cette étude confirme l'intérêt de l'association de deux outils d'investigation, l'un classique, mesures de pression moyennes, l'autre moins habituel, visualisations ultra-rapides, pour la compréhension de phénomènes complexes. Les visualisations ultra-rapides constituent, d'ailleurs, la seule approche instantanée du phénomène qui soit possible, étant données les dimensions de nos maquettes.

L'implantation d'une trappe de soufflage améliore très sensiblement les performances de la prise d'air : à incidence 40° le coefficient de débit σ et la pression d'arrêt moyenne p_{tm} au niveau du compresseur sont augmentés de plus de 50 % et deviennent comparables aux valeurs obtenues à incidence 20° en absence de trappe. La plus grande partie du débit capté passe par la fente de soufflage.

L'adjonction d'une écope destinée à guider l'air vers la fente n'a qu'une faible répercussion sur les grandeurs globales σ et p_{tm} au niveau du compresseur. Par contre, elle apporte un gain considérable en ce qui concerne la vitesse d'homogénéisation de l'écoulement interne : à mi-chemin entre la section d'entrée et le compresseur, l'écoulement moyen est déjà quasiment uniforme. En outre, les visualisations ultra-rapides ne montrent pas l'existence de grosses structures en $X^* = 8$.

Enfin, à l'incidence 20° la trappe améliore également beaucoup l'écoulement interne. Mais, l'implantation d'une écope ne paraît pas nécessaire.

REFERENCES.-

- (1) DYPENT et GRYSION

AGARD CP 227 "Unsteady Aerodynamics".

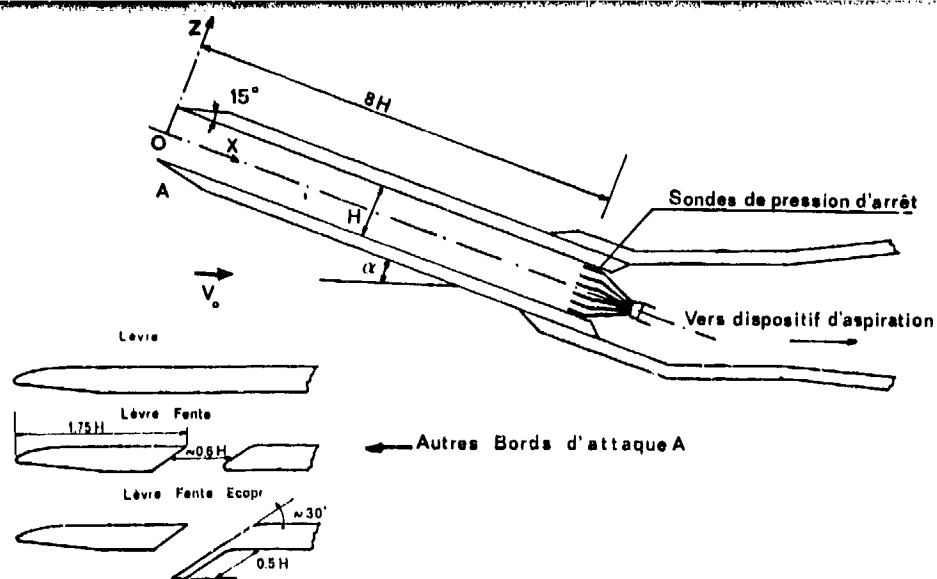


Fig:1 Maquettes

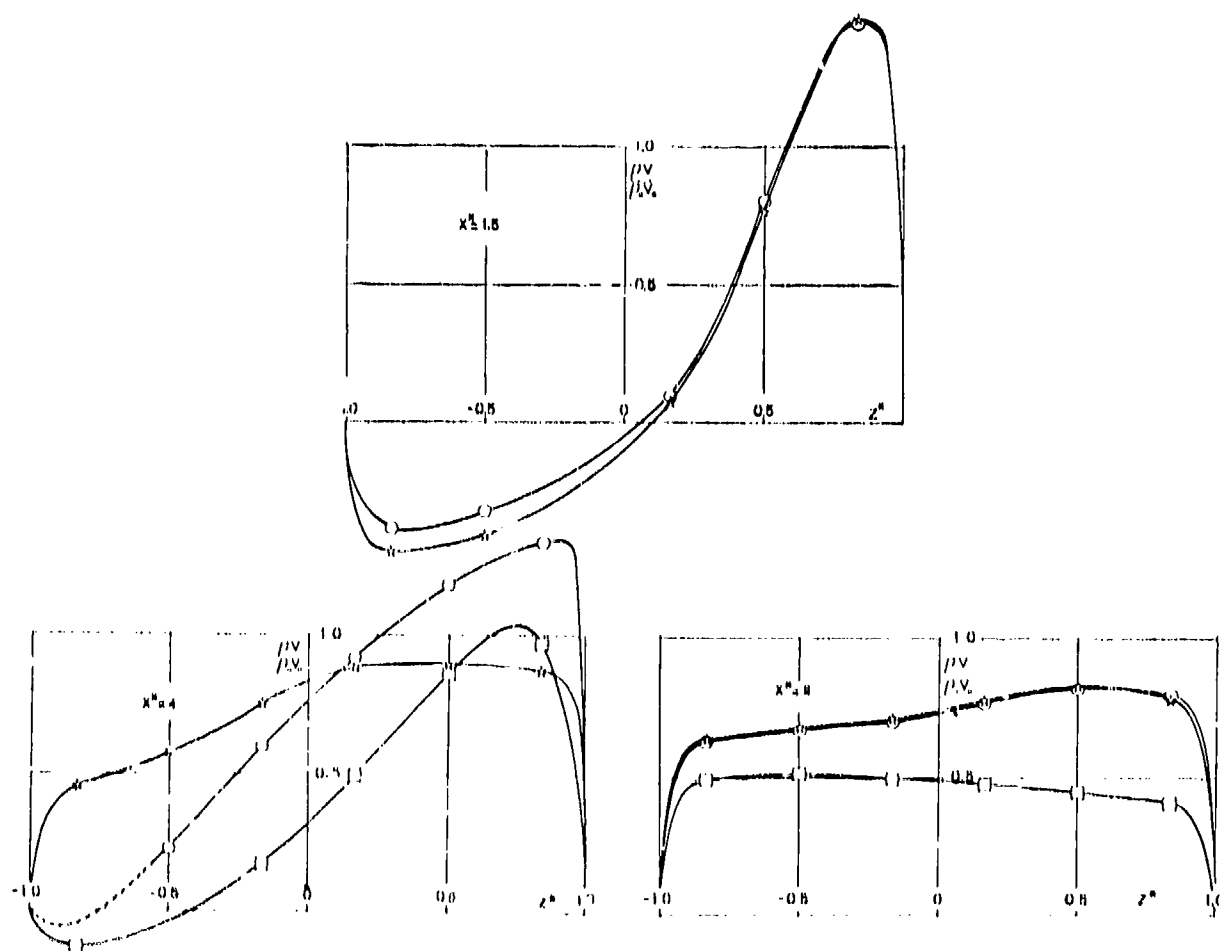


Fig:2 $\alpha = 40^\circ$ $M_\infty = 0,38$ $M_{int} = 0,40$
(\square Lèvre , \circ Fente , \times Écopé)

0,36

0,44

Fig.3 Stroboscopes, pose 2,5ms
Lèvre avec fente $\alpha = 40^\circ$ $M_0 = 0.38$

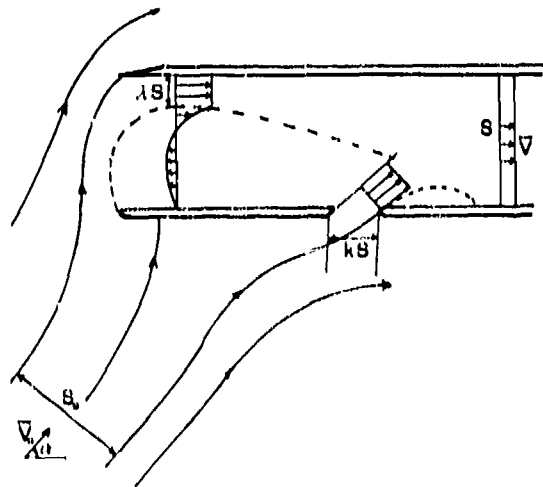
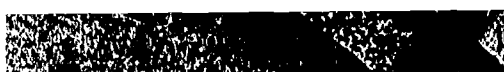


Fig. 1



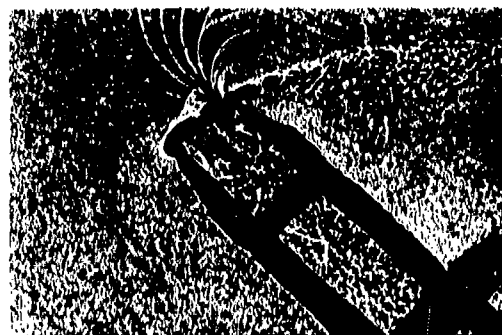
1



2



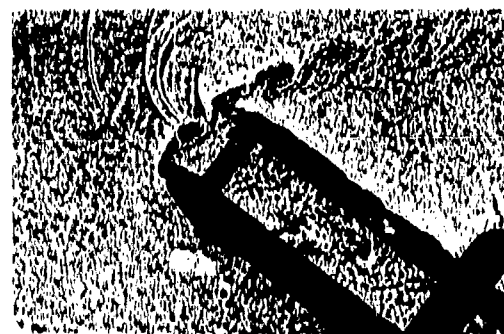
3



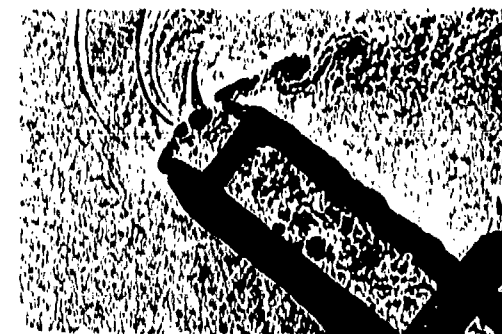
4

Fig. 5 Ombroscopies, pose 0.3 μ s

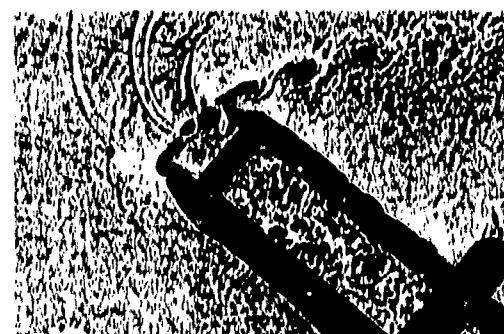
B.A. Pointu $\alpha \approx 40^\circ$, $M_{int} = 0.128$, $\Delta t = 10 \mu$ s



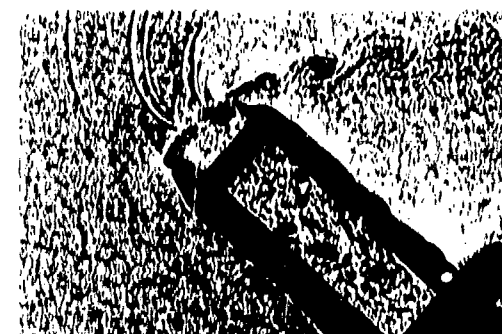
1



2



3



4

Fig. 6 Ombroscopies, pose 0.3 μ s

Fente $\alpha \approx 40^\circ$, $M_{int} = 0.3$, $\Delta t = 10 \mu$ s



Stroboscope . pose 2,5 ms

LÈVRE FENTE ÉCOPE

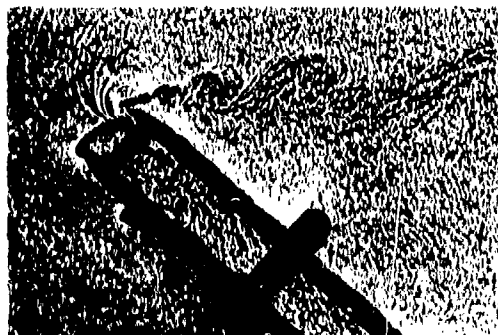
$\alpha = 40^\circ$

$M_\infty = 0,38$ $Re = 9 \cdot 10^4$

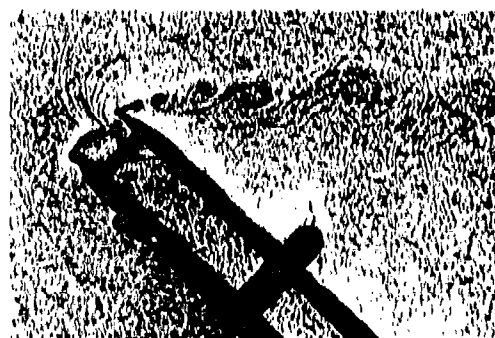
$M_{int} = 0,46$

Ombroscopies . pose 0,3 μ s

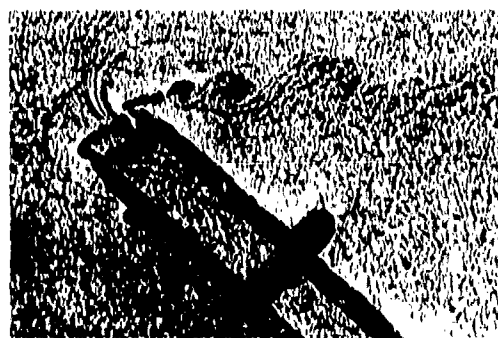
$\Delta t = 20 \mu$ s



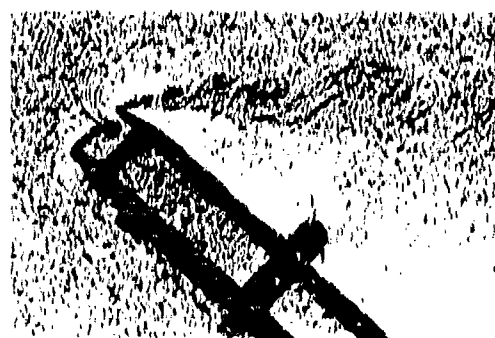
1



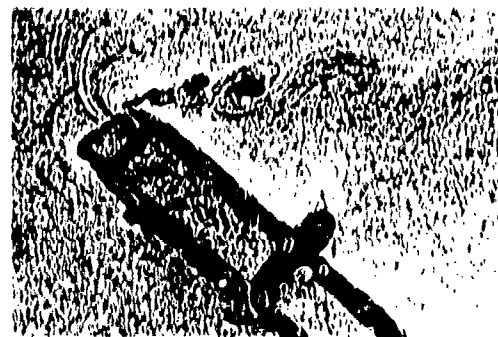
4



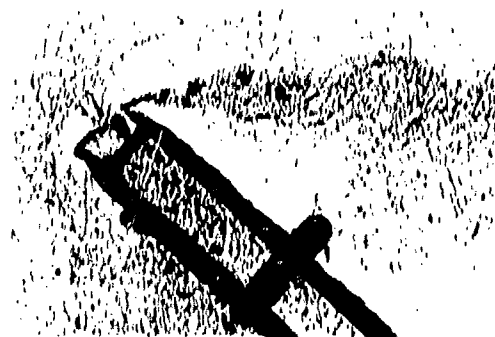
2



5



3



6

Fig. 7

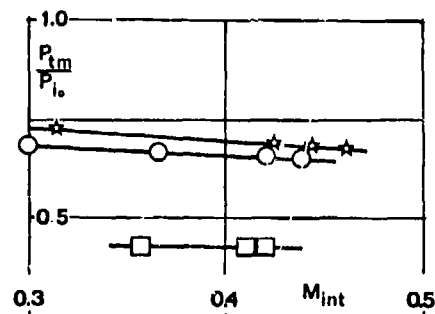
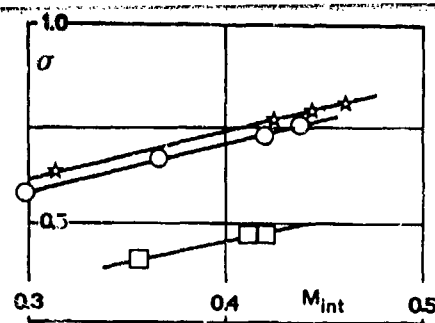


Fig. 8 $\alpha = 40^\circ$ $M_0 = 0.38$, $X^* = 8$
 □ Lèvre ○ Fente ☆ Écope

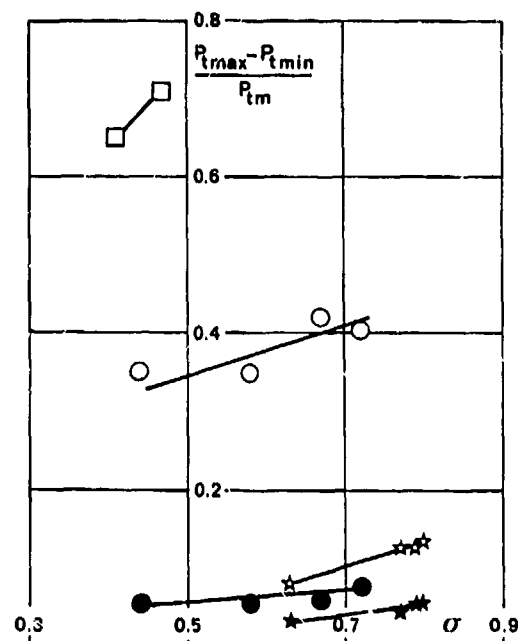


Fig. 9 Distorsion $\alpha = 40^\circ$ $M_0 = 0.38$
 □ Lèvre ○ Fente ☆ Écope $X^* = 4$
 ● Fente ☆ Écope $X^* = 8$

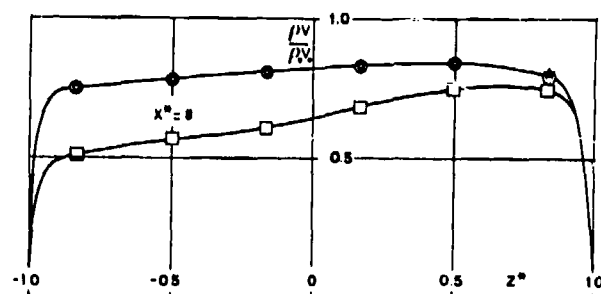
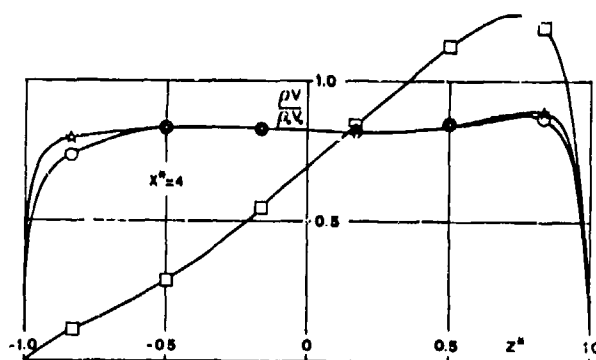
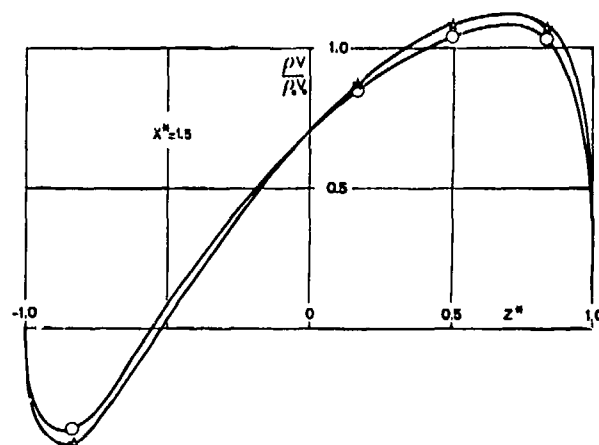


Fig. 10 $\alpha = 20^\circ$ $M_0 = 0.50$ $M_{int} = 0.4$
 □ B. A. Pointu ○ Fente ☆ Écope

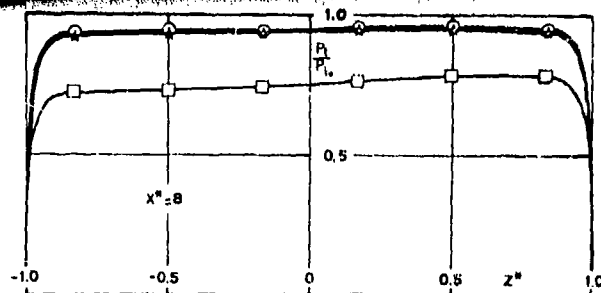
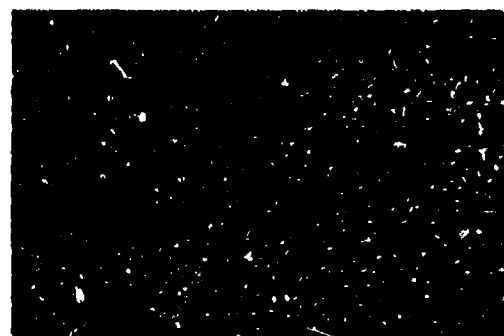


Fig : 11 $\alpha = 20^\circ$ $M_o = 0,50$ $M_{int} = 0,40$
(\square B. A. Pointu , \circ Fente , \star Écope)



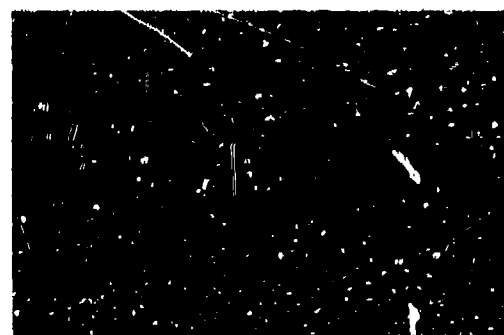
1



2



3



4

Fig : 12 Strioscopes , pose $0,3 \mu s$
 $\alpha = 20^\circ$, $M_o = 0,50$, $M_{int} = 0,40$, $\Delta t = 10 \mu s$

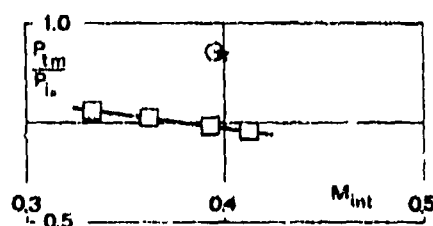
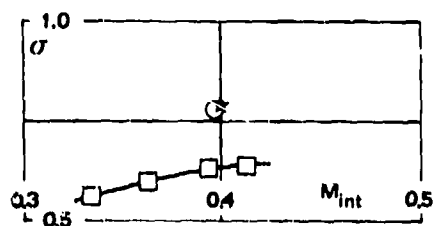
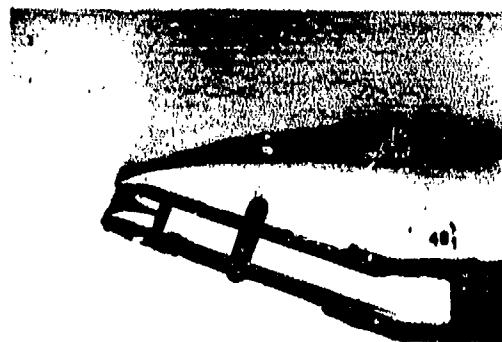


Fig : 13 $\alpha = 20^\circ$ $M_o = 0,50$
(\square B. A. Pointu , \circ Fente , \star Écope)



Strioscopie , pose 2,5ms

LÈVRE FENTE

$$\alpha = 20^\circ$$

$$M_o = 0.5 \quad Re = 1,1 \cdot 10^5$$

$$M_{int} = 0,4$$

Ombroscopie , , or , 10 μ s

$$\Delta t = 20 \mu s$$

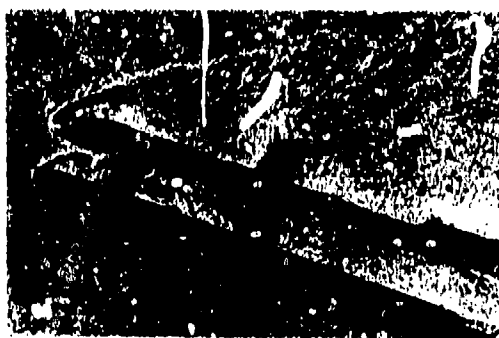
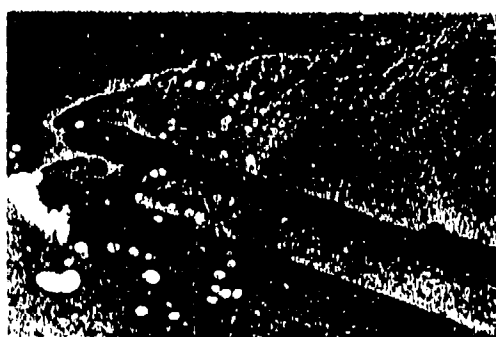
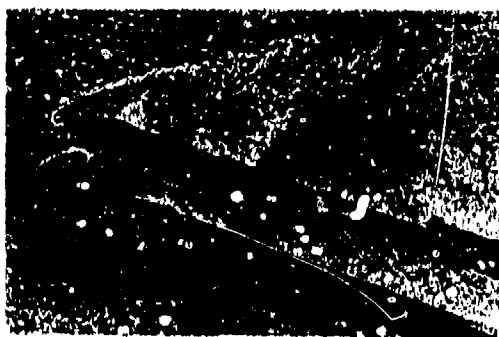
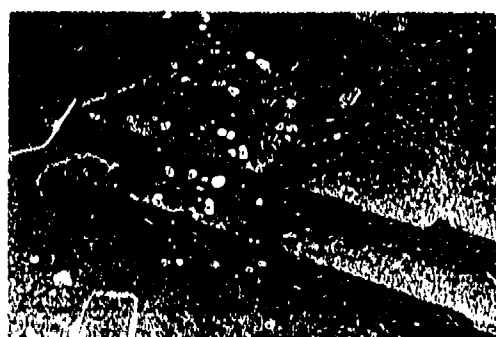
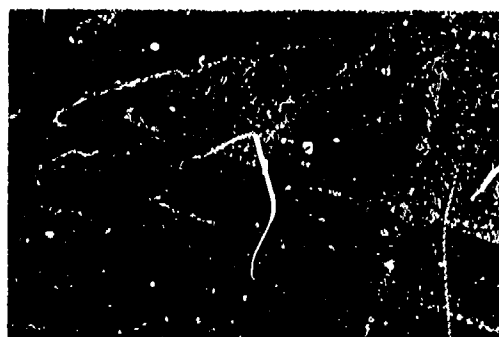
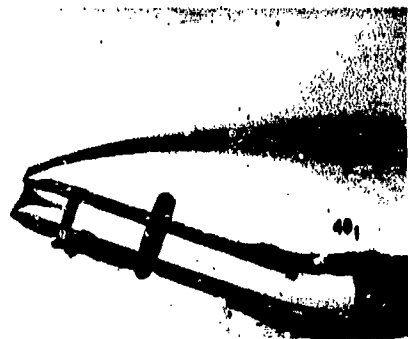


Fig. 14



Strioscopie , pose 2,5 ms

LÈVRE FENTE ÉCOPE

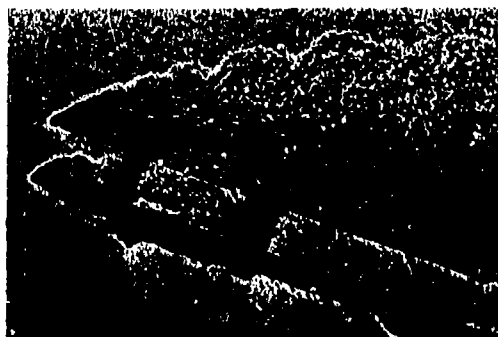
$$\alpha = 20^\circ$$

$$V_0 = 0,5 \quad Re = 1,1 \cdot 10^5$$

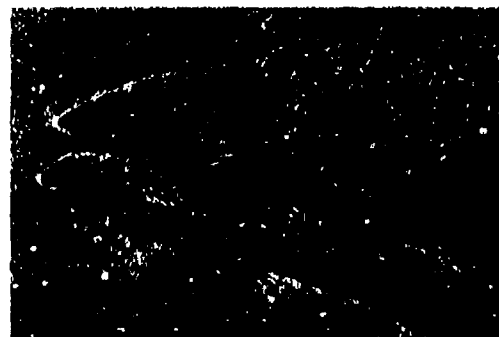
$$M_{int} = 0,4$$

Ombroscopies , pose 0,3 μs

$$\Delta t = 20 \mu s$$



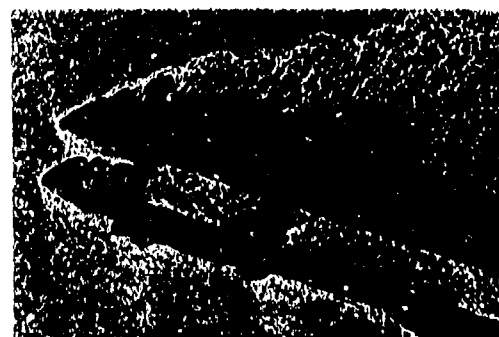
1



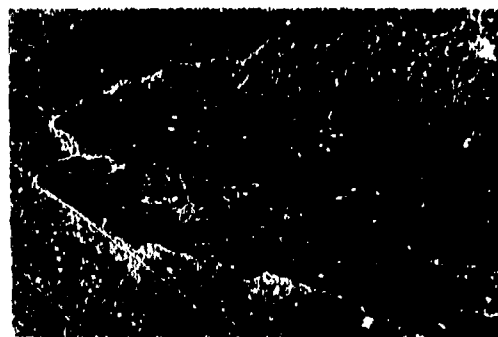
4



2



5



3



6

Fig. 15

CALCULATION OF TRANSONIC AIR-INTAKES USING A COMPUTER PACKAGE
FOR INVISCID AND BOUNDARY LAYER FLOWS

by

Ciro W. Lucchi
Theoretical Aerodynamics - UFE122
Messerschmitt-Bölkow-Blohm GmbH
Postfach 801160
D-8000 München 80
West Germany

SUMMARY

A finite-element method has been developed to solve the full potential equation for transonic flows in a two-dimensional engine intake.

To insure simplicity of formulation and mass conservation, the subdomain finite-element technique has been chosen. The full potential equation being expressed in the ϕ -formulation, a successive line over-relaxation algorithm was developed to solve the system of non-linear algebraic equations. Stability in the supersonic domain was obtained using Hafez' artificial compressibility method.

Herring-Mellor's finite-difference code has been incorporated to compute two-dimensional compressible laminar-turbulent boundary layers. A fixed transition or Dunham's transition criterion may be chosen.

The inviscid method has been tested on single airfoils and cascade profiles. The viscous-inviscid method has been tested on a few single profiles, such cases having been computed exhibiting difficulties expected to occur in the calculation of two-dimensional intakes: high leading-edge suction peaks and strong shocks.

Computations have been carried out on a two-dimensional Tornado-like air-intake at $M = 0.7$ and α between 0° and 12° , the viscous-inviscid coupling having been used at $\alpha = 0^\circ$.

Results compare relatively well with the experiment considering that measurements were taken on a Tornado model. Improvements to the mathematical model are expected to appreciably enhance the method's capabilities as a design tool.

LIST OF SYMBOLS

A_0/A_c	mass flow ratio at the engine face
M	local Mach number
M_∞	freestream Mach number
Re	Reynolds number
\vec{U}	local velocity vector
u	norm of velocity
α	angle of incidence
γ	specific heat ratio
ϕ	potential
ρ	density

1. INTRODUCTION

In the development of modern combat aircrafts, particular attention is being given to combat manoeuvres at transonic speeds requiring high angles of attack. These are amongst others dependent upon the engine-airframe integration, the air-intake design playing an important role. Within the current research program at the Military Aircraft Division of Messerschmitt-Bölkow-Blohm emphasis has been placed upon improving the experimental and theoretical capabilities in designing advanced air-intakes.

Two- and three-dimensional numerical methods have already been developed to compute the transonic flow on axisymmetric [1+3] and three-dimensional [4] inlets. These works have been exclusively confined to geometries with thick leading edges as opposed to sharp leading edges appearing on two-dimensional inlets of supersonic combat aircrafts.

Having as far-reaching goal the numerical modelling of a complete three-dimensional wing-body-engines configuration, the present two-dimensional research program was started using the full potential formulation in the potential function.

Looking for a suitable numerical method, the following criteria have been defined: 1) simplicity, 2) capability for complex geometries, 3) computational speed. A full mass conservative formulation may always in a more or less simple manner be incorporated; this should not however contradict the first criterion.

Satisfying these criteria, a subdomain finite-element method was developed [5]. The full potential equation in the potential function written in conservative form is discretized using the above-mentioned method which also insures mass conservation in the numerical scheme. A mesh generation method using only geometrical considerations has been found to insure simplicity of implementation and such flexibility as needed for complex three-dimensional configurations; the grid allows the use of line solution methods (successive over-relaxation as in this work, ADI) and always displays smooth variation of the ele-

ments sizes and intersection angles far from 0° . Stability in the supersonic domain was achieved by adapting Hafez' artificial compressibility method [6] to the finite element technique. A mesh refinement algorithm is included.

Accuracy and reliability were the main reasons for choosing the Herring-Mellor's boundary-layer code [7].

The inviscid method has been tested on several single airfoils and cascade profiles [5]. Results compare favorably with conservative finite-difference methods both in accuracy and computing time. Strong shocks were accurately predicted, slightly forward of the trailing edge too.

In the computation of air-intakes at transonic speeds two kinds of difficulties were expected to appear that may cause a boundary-layer computation to break down: high suction peaks at the upper lip leading edge and strong shocks. The viscous-inviscid method has first been tested on a few single profiles*. The first difficulty was examined on the 5% thick MBB-A10 airfoil: because of its relative insensitivity in that region, the boundary-layer code did not detect the expected leading-edge separation bubble; the simulation of this physical phenomenon requires additional research. The second difficulty was examined on the 13% thick DFVLR-R2 airfoil; it was solved by smearing the shock over a few elements [8].

In the next paragraphs more information is presented on the inviscid method and the results obtained to-date with the air-intake program are described.

2. METHOD

The steady, inviscid, irrotational flow is governed by the full potential equation

$$\vec{u} = \nabla \phi \quad (1)$$

$$\nabla \cdot (\rho \nabla \phi) = 0 \quad (2)$$

$$\rho = [1 + \frac{\gamma-1}{2} M_\infty^2 (1 - u^2)]^{\frac{1}{\gamma-1}} \quad (3)$$

\vec{u} and ρ being normalized by their freestream values.

Integrating eq. (2) over the surface and applying Gauss' divergence theorem, the integral form of the continuity equation appears

$$\int_C \rho \nabla \phi \cdot \vec{n} \, ds = 0 \quad (4)$$

C being the contour of integration and \vec{n} the outer normal vector. Eq. (4) formally defines the subdomain finite element method; main characteristic is the conservative form. Neumann-type boundary conditions are imposed on the surface. A far-field solution is given on the domain boundaries and an experimentally-obtained mass flux is assigned at the engine face.

Details of the finite element method are presented in Ref. [5].

3. COMPUTATIONS

The center section geometry of the Tornado's air-intake has been modified to apply the method. In particular, all bleed system has been removed, but the sharp upper lip leading edge has been retained (geometry GEO-1, the full mesh on figure 1, a detail on figure 2). With this geometry results could be obtained in a very small angle of attack range (less than 1°). Cause for the numerical break-down is the infinite velocity at the leading edge when the stagnation point does not coincide with the leading edge.

This problem was partially removed by thickening the upper lip in its front part by inserting a NACA 0012 symmetric airfoil (geometry GEO-5, figure 3, a detail). Results were obtained at $M = 0.7$ with angles of attack between 0° and 9° with the inviscid code (figures 4 and 5 for these two angles). At $\alpha = 12^\circ$ the computation broke down after the 21st iteration starting from the case at $\alpha = 9^\circ$ (figure 6, 15 iterations, normal aspect, figure 7, 21 iterations, beginning of break-down). The cause is the same as before: excessive velocity at the leading edge going into vacuum; this problem has its origin in the assumptions of potential flow theory and is independent of the numerical method.

Results at $\alpha = 0^\circ$ (figure 4) show the existence of a strong suction peak; computations with the viscous Herring-Mellor code did not detect any leading-edge separation; because of the relative insensitivity of any boundary-layer code in the starting region of the boundary layer no accurate prediction of flow separation and separation bubble length can be obtained without additional empirical information. The viscous and inviscid solutions do not differ appreciably in this test case.

The theoretical results on the outer surface of the lower lip differ considerably from the experimental ones at $\alpha = 0^\circ$ (figure 4): three-dimensional effects are here predominant. Not so at $\alpha = 9^\circ$ (figure 5).

Theoretical and experimental results on the inner surfaces (upper and lower lips) agree relatively well at both angles of attack considering that the first are two-dimensional

* Work in progress. A report will appear in spring 1982.

computations and the second were measured on a Tornado model. At $\alpha = 9^\circ$ the experimental data show boundary-layer separation on the lower lip inner surface; the suction peak is well predicted by the inviscid method. The presence of side walls justifies the assumption that a two-dimensional theoretical research contributes appreciably to the understanding of air-intake flowfields*.

No other Mach number has been investigated: the mathematical model developed up to now presents some deficiencies (mostly shown by the high suction peak on the upper lip) which require a detailed investigation before the method is tested at higher Mach numbers.

4. CONCLUDING REMARKS

The numerical method that has been presented promises much needed accuracy and reliability as a design tool in the development of two-dimensional air-intakes. The results obtained to-date show a relatively good comparison with measured data where the assumption of two-dimensionality holds.

Improvements to the mathematical model are expected to appreciably enhance the method's accuracy.

REFERENCES

- [1] Arlinger B.G., Axisymmetric inlet flow at low supersonic Mach numbers, in Symposium Transonicum II, Springer-Verlag, 200-207, 1976
- [2] Chen L.-T., Caughey D.A., Calculation of transonic inlet flowfields using generalized coordinates, J. Aircraft, 17, 167-174, 1980
- [3] Chen L.-T., Caughey D.A., Higher-order finite-difference scheme for three-dimensional transonic flowfields about axisymmetric bodies, J. Aircraft, 17, 668-676, 1980
- [4] Reyhner T.A., Transonic potential flow computation about three-dimensional inlets, ducts and bodies, AIAA Paper 80-1364, 1980
- [5] Lucchi C.W., Subdomain finite element method to compute the transonic potential flow around a profile or in a cascade, MBB/FE122/S/R/1508, 1980
- [6] Hafez M.M., Murman E.M., Artificial compressibility methods for numerical solution of transonic full potential equation, AIAA Paper 78-1148, 1978
- [7] Herring H.J., Mellor G.L., Computer program for calculating laminar and turbulent boundary layer development in compressible flow, NASA CR-2068, 1972
- [8] Lock R.C., A review of methods for predicting viscous effects on aerofoils and wings at transonic speeds, AGARD-CP-291, 1981

ACKNOWLEDGEMENT

This work was supported by the Messerschmitt-Bölkow-Blohm GmbH, Independent Research Program.

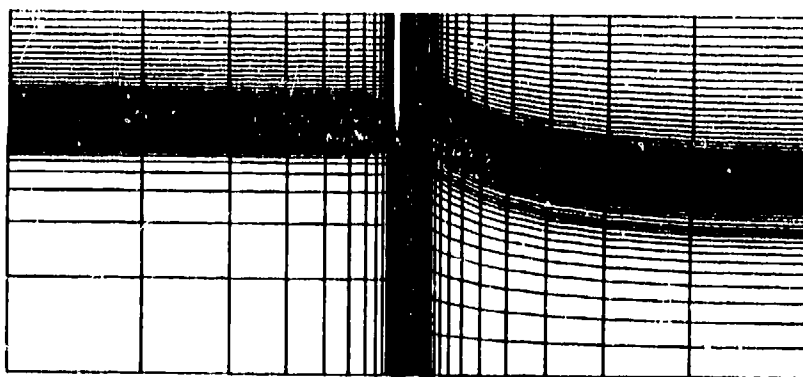


Fig. 1 Mesh for geometry GEO-1 (turned 90°)

* The discontinuity in the experimental pressure distribution appearing at approximately $x = 1.5$ on the upper lip inner surface corresponds to a boundary-layer bleed

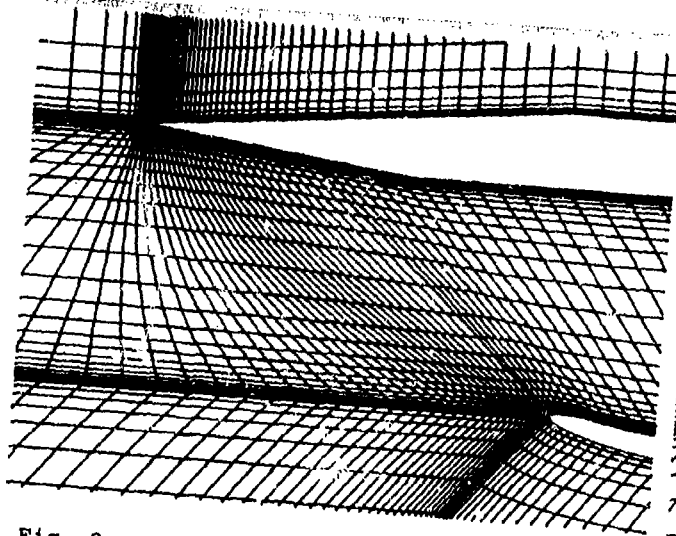


Fig. 2 Mesh for geometry GEO-1 (detail)

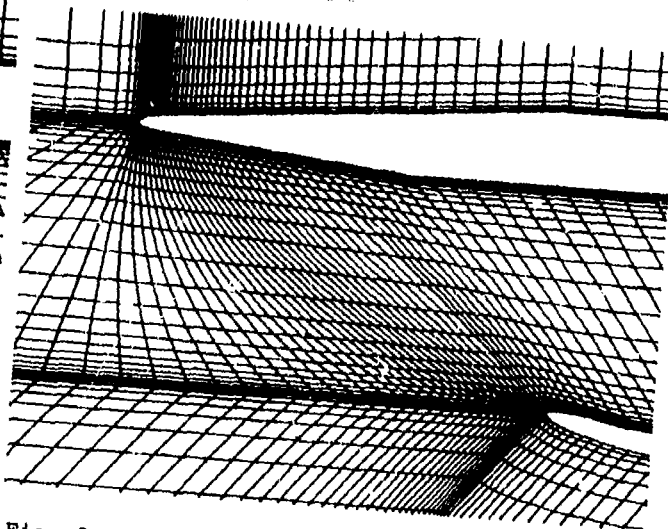


Fig. 3 Mesh for geometry GEO-5 (detail)

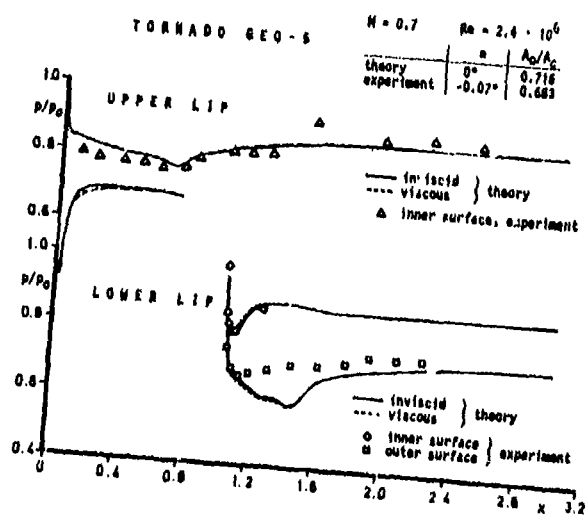


Fig. 4 GEO-5 at $M = 0.7$, $\alpha = 0^\circ$ (inviscid and viscous solutions)

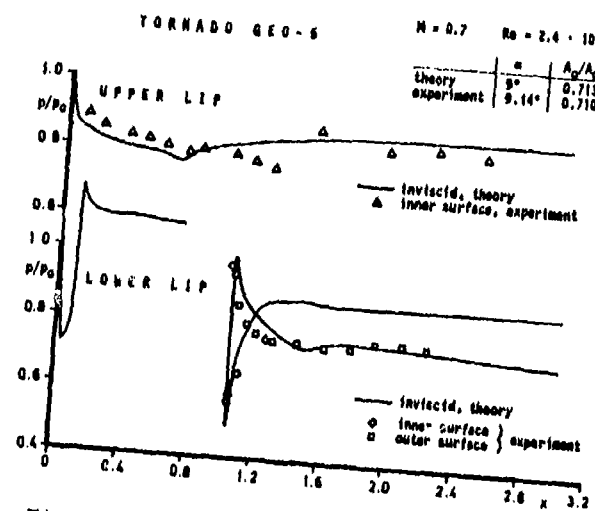


Fig. 5 GEO-5 at $M = 0.7$, $\alpha = 9^\circ$ (inviscid solution)

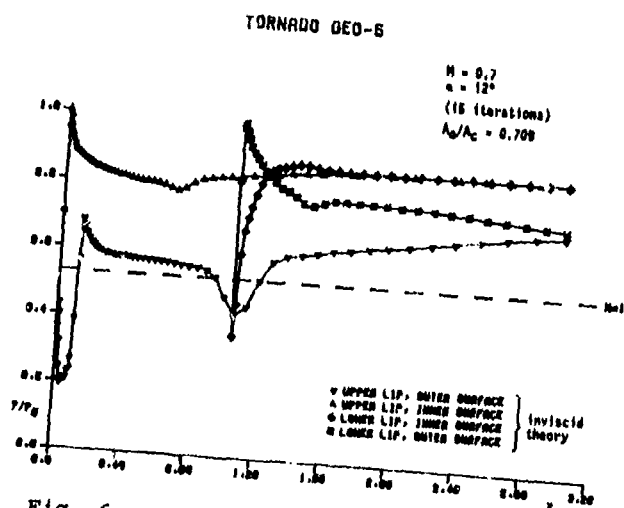


Fig. 6 GEO-5 at $M = 0.7$, $\alpha = 12^\circ$, 15 iterations

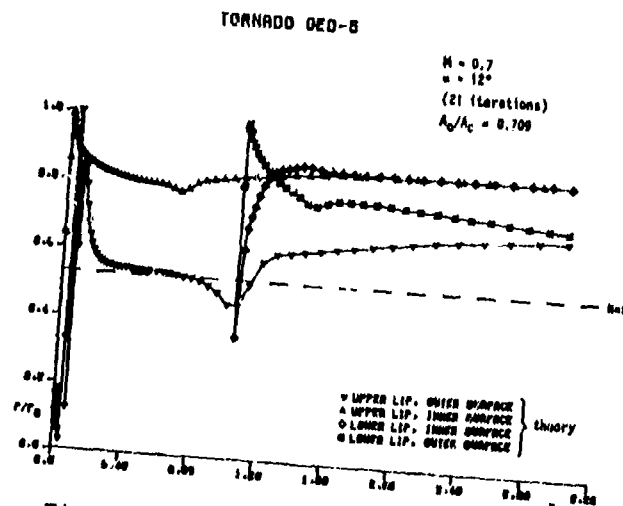


Fig. 7 GEO-5 at $M = 0.7$, $\alpha = 12^\circ$, 21 iterations

SUBSONIC MILITARY AIRCRAFT ENGINE INTAKE:
AN INTEGRATED THEORETICAL-EXPERIMENTAL DESIGN

by

G. Bertolone and L. Fornasier

Combat Aircraft Group
Aeritalia Società Aerospaziale Italiana P.A.
10146 Torino, Corso Marche 41 - Italia

SUMMARY

As initial steps of a long term effort aimed at design and performance evaluation of engine air intakes by computer aided methods, two numerical codes were recently developed for the simulation of the intake-induced flow field in two dimensional transonic and three dimensional subsonic cases.

Both codes were obtained in a very straightforward way by modification of existing codes suitable for the computation of the exterior flow past airfoils (by a finite element method) and about three dimensional arbitrary configurations (by a panel method). Computed results and comparison with experimental data pertinent to the analysis of a single bifurcated intake prove the usefulness of the present numerical schemes for engineering applications.

In addition to the above described theoretical study, the second part of this paper deals with two peculiar experimental problem areas: engine face auxiliary doors design and side intakes diverter shape optimization. Following an extensive testing program performed on a static model, the engine face auxiliary doors with annular air admission into the primary long type duct appears to be a good alternative to the classical solution placed at the main inlet entry.

Diverter geometry influence both on aerodynamics, in terms of drag coefficient, and intake performance, in terms of distortion coefficient, was moreover investigated, testing a low speed model, and the results are presented in this paper.

Nomenclature

h	- Diverter width
a'	- Diverter upper profile length
b'	- Diverter upper profile height
a''	- Diverter lower profile length
b''	- Diverter lower profile height
b_T	- $b' + b''$ Diverter total height
r	- Leading edge radius
A_0	- Freestream area of captured flow
A_{HI}	- Intake hilite area
A_{TH}	- Intake throat area
A_2	- Engine face area
A'_{HI}	- Primary intake hilite area
A'_{TH}	- Primary intake throat area
A''_{HI}	- AID hilite area
A''_{TH}	- AID throat area
C_R	- A_{HI}/A_{TH} Inlet contraction ratio
C'_R	- A'_{HI}/A'_{TH} Primary inlet contraction ratio
C''_R	- A''_{HI}/A''_{TH} AID inlet contraction ratio
M_0	- Freestream Mach number
M_{TH}	- Intake throat Mach number

M_2	- Engine face Mach number
M'_{TH}	- Primary intake throat Mach number
M''_{TH}	- AID throat Mach number
P_0	- Freestream static pressure
P_{T0}	- Freestream total pressure
q_0	- Freestream dynamic head
P_{T2}	- Engine face total pressure
q_2	- Engine face dynamic head
ΔP_T	- $P_{T2} - P_{T0}$ Intake pressure losses
$P_{T\ 60^\circ \min}$	- Engine face 60° sector minimum total pressure
$\Delta P'_T$	- Primary intake pressure losses
$\Delta P''_T$	- AID pressure coefficient
C_P	- $(P - P_0)/q_0$ Pressure coefficient
C_P^*	- Sonic pressure coefficient
C_D	- Frictionless diverter drag coefficient based on frontal diverter reference area
DC_{60°	- $(P_{T\ 60^\circ \min} - P_{T2}) / q_2$ Distortion coefficient

1.1 Engine Air Intake Analysis by Computational Methods

1.1.1 Introduction

Current trends exhibited by modern military aircrafts to increase both the thrust-to-weight ratio and the engine by-pass ratio emphasizes the demand of numerical tools for supporting the design of the air intakes and evaluating the interference effects induced by the engine massflow on the aerodynamic characteristics of the overall configuration.

The first part of this paper is aimed at demonstrating that a fairly acceptable simulation of the flow past two-dimensional and three-dimensional engine air intakes may be obtained by use of numerical methods derived from existing and well-tested codes suitable for the computation of the external flow past airfoils and about arbitrary three-dimensional lifting bodies. For this purpose the following items must be added to the basic codes:

- definition of a control surface suitable for calculating the mass flow entering the intake
- definition of a computational device required to modify the intake mass-flow
- definition of an iterative loop for matching the prescribed mass-flow condition.

The main advantages of such a type of approach are that it allows a considerable reduction in the coding time in comparison to the case of "ad hoc" developed codes without introducing appreciable penalties in the computing time and that the high commonality of the new codes with the basic ones enables to exploit the existing pre-and post-processor packages, such as graphic display of input/output data and boundary layer analysis codes.

Experience gained at Aeritalia from use of two numerical codes developed for the computation of three-dimensional subsonic and two-dimensional transonic intakes gave evidence of the usefulness of the above mentioned approach for many engineering applications.

A brief survey on the mathematical background of the two codes and an application to the analysis of a single engine bifurcated intake are presented.

1.1.2 3-D Subsonic Intake Analysis by a Panel Method Code

a) General Features of the Mathematical Model

The most efficient solution for the simulation of the exterior flow about arbitrary three-dimensional lifting bodies is provided by the Panel Method. Under the basic assumptions of steady, irrotational and incompressible flow it solves the Laplace differential equation of the velocity potential function by transformation into a set of linear equations whose unknowns are the strengths of piecewise distributions of mathematical singularities (panels of source/sinks and doublets) spread

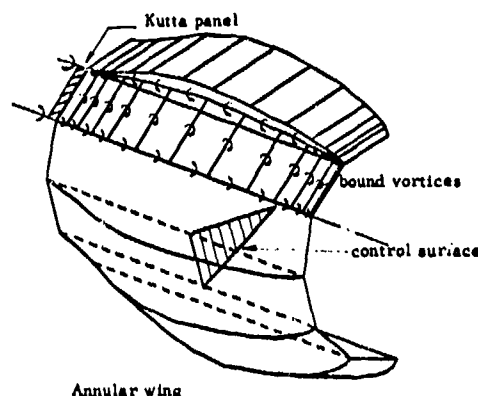
in a proper arrangement within the body volume. Each linear equation specifies the fulfilment of the Neumann boundary condition on the body contour (i.e. vanishing of the normal velocity on the surface panels) and of the Kutta condition at the trailing edge of the lifting surfaces, whilst the zero perturbation condition at infinity is implicit in the singularity methods.

In the present version of this method - which was derived from the MBB Standard Panel Method (1) - the external surface of the body configuration is fitted by flat panels of sources/sinks of constant strength whilst the lifting terms are provided by doublets arrangements whose strength is determined by imposition of zero normal velocity on dummy panels at the trailing edge aligned with the local bisector (the so-called Kutta panels). Use of Goetherth's similarity rules allows to compute compressible, but still subcritical, flows.

To describe the way by which the capability to simulate intake-induced flow was added to the basic code, let us consider for sake of simplicity an isolated axisymmetrical nacelle.

Computing this configuration like an annular wing by the basic Panel code a simulation of a mass flow A_0/A_{H1} very close to unity should be expected, the actual value of A_0/A_{H1} being determined by the circulation induced by the bound vorticity on each slice of the annular wing. This analogy suggests that in order to control the total mass flow entering the intake it is sufficient to change the value of the bound vorticity by relaxing the Kutta condition at the trailing edge of each circumferential slice.

The geometry of real intakes is much more complex than that of an isolated nacelle; however the same device for controlling the inlet mass-flow may be retained provided that a proper arrangement of bound vortices may be defined between the interior wall and the exterior cowl of the intake.



For matching the prescribed mass-flow in a trial-and-error mode two basic options are available in the present code:

- iterate by rotating the Kutta panels
- or
- iterate directly on the strength of each bound vortex arrangement.

At each iteration step the actual value of the mass flow is computed by integration of the velocity field at a control surface, usually at the throat section.

b) Comparison of Theory and Experiment

In order to investigate the influence of some geometrical details on the performance a 1 : 7.2 scale model was tested in the Aeritalia 2 x 2 sq. mt. Low Speed Tunnel (see para 2.2.1). The model was instrumented for measurement of pressure distributions on the cowl lips, the diverter and the plate.

The choice of elliptical profiles for the external and internal cowl lips was led by a trade-off analysis performed by the present method on a simplified axisymmetrical mathematical model of the intake, aiming at reducing the pressure peaks for preventing flow separations at the design conditions.

Computations for an intake-fuselage configuration fully representative of the SEBI low speed model except for the absence of the diverter and the plate (Fig. 1.1) were later carried out for evaluating the capability of the present method to deal with such a complex configuration.

Comparison of theoretical vs. experimental data pertinent to the three cowl sections of Fig. 1.2 for the test conditions of Fig. 1.3 are presented in Figs. 1.4 through 1.9.

Although no simulation of the viscous effects is taken into account by the theory a fairly acceptable agreement between theory and experiments is shown for the near-design conditions of Fig. 1.4 and 1.5, especially on the external cowl where boundary layer interaction has negligible effects. At off design conditions (Figures 1.6 + 1.9) the poor correlation exhibited on the suction side of the cowl lips is essentially due to local flow separations where the theory predicts very large positive pressure gradients. Visualizations of the flow performed with oil at equivalent conditions show a similar pattern of local separations; however a favourable effect of Reynolds Number is expected at full scale.

1.1.3 2-D Transonic Intake Analysis by a Finite Element Method Code

a) General Features of the Mathematical Model

The two-dimensional intake code is essentially a by-product of a recently developed numerical program which performs the computation of transonic flow in presence of recompression shocks about two-element airfoils (2). The general features of this program are the following:

- solution of the full potential equation of gasdynamics by Eberle's formulation of the Finite Element Method (3) which is based on the variational principle stating that the work necessary to deform the fluid is a minimum with respect to the prescribed boundary conditions. For steady flow this formulation is equivalent to state that

where

$$\iiint_V \rho q q_{,i} dV = 0$$

ρ = fluid density
 q = a normalized velocity
 ϕ = velocity potential
 V = fluid volume

This integral equation is solved by numerical integration using quadrilateral bilinear isoparametric elements.

- Use of a computational grid obtained by a conformal transformation which maps the exterior of the two airfoil-element into an annular domain (4);
- iterative solution of the resulting quasi-linear equations by a successive line over-relaxation (SLOR) scheme in the radial direction;
- use of a rotated artificial density scheme (5) - (6) which maintains an upwind bias for any orientation of the computational cell with respect to the local velocity vector in order to stabilize the numerical procedure when the local flow is supersonic.

In the present formulation the Finite Element Method is fully conservative and numerically very stable, so it seemed attractive to attempt to adapt this code for the computation of two-dimensional intakes, following the same procedure outlined in the previous section.

Since the region close to the intake lips only interests, both the upper and the lower cowl may be extended downstream by a dummy fairing ending with a cuspidate trailing edge: this enables to use the same grid generation of the basic code.

The contribution of each computational cell to the integral term pertinent to the pivot point P (sketch a) is equivalent to the mass flow through the diagonal AA': thus the total mass flow entering the intake may be computed in a consistent way by summing up the contribution of the cells adjacent to a grid line cutting vertically the interior nozzle (sketch b). The same feature is used for building up the computational device required for controlling the mass flow entering the intake: since in the basic code the Kutta condition (which defines the circulation around the two elements and hence the mass flow through the two cells adjacent to the trailing edge (sketch c) in order to alter the circulations in an antisymmetric mode it is sufficient to allow a symmetric "transpiration" of the flow through the two trailing edges.

A trial-and-error iterative process to find the proper "transpiration" is again used for matching the required mass flow-condition.

In order to speed up the convergence rate which is very slow for the circulations on the mesh size required for achieving a good resolution of the shocks, successive mesh grid divisions with intermediate interpolation of the potential distribution are used (7): computations carried out with four mesh divisions gave evidence that circulations and mass-flow are frozen since the crudest grid computation whilst pressure distributions are more sensitive to the mesh size (figures 1.10 through 1.13)

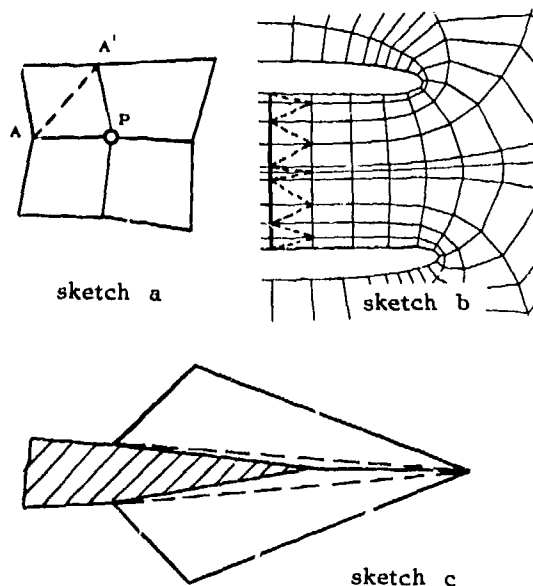
b) Computed results

Although the SEBI configuration do not belong to the two-dimensional type of intakes a rough investigation of the SEBI transonic characteristics was carried out by computing a section cutted vertically through the intake (cowl A and C of figure 1.2). Figures 1.14 through 1.16 present the transonic pressure distributions computed at zero angle of attack.

1.1.3 Conclusions

Two numerical methods for the simulation of the flow about engine air intakes are presented. Both codes were adapted from existing codes suitable for the computation of the external flow about arbitrary lifting bodies (limited to subsonic flows) and past transonic airfoils. Presented results prove the usefulness of this engineering approach to the design of the engine air intakes.

Extensions aiming at the simulation of three-dimensional transonic flow about intakes in presence of the body (by 3-D Finite Elements) and computation of viscous interaction (by the transpiration technique) will be pursued in the next future.



2.1 Engine Face Auxiliary Doors

2.1.1 Introduction

High engine intake lip losses suffered at take-off conditions by many military aircrafts, can be drastically reduced using secondary air supply. Rear auxiliary doors, with secondary airflow annular admission, placed very close to the compressor face, when compared with the typical forward installation near the primary inlet, present remarkable advantages in performance which can easily overcome space and complexity penalizations. Above mentioned auxiliary doors types will be referred in this document as "REAR AID" and "FORWARD AID".

"REAR AID" have been employed on the AERITALIA G91Y ground attack and close support aircraft, powered by two GE J85 turbojets: unacceptable engine instability or surges have never been experienced, in the AID operational range, which can be attributed to the air mass flow supply system.

FIGURES 2.1, 2.2, 2.3 schematically show G91Y AID installation: the secondary air enters through a series of four spring loaded doors, opened by suction effect, and goes into an almost cylindrical chamber with annular air admission to the main duct.

The performances of G91Y "REAR AID" can be written down in the following way:

$$A''_{HI}/A'_{TH} = .32 ; (\Delta P_T/P_{T0})_{w/o AID} = 7.3\% ; (\Delta P_T/P_{T0})_{w/ AID} = 4.9\%$$

2.1.2 Experimental Results

A "single engine bifurcated intake (S.E.B.I.) suction model" of a subsonic single engine military aircraft (Fig. 2.4) was built and extensively tested at static conditions to investigate the effects of "REAR AID" in terms of recovery factor P_{T2}/P_{T0} and distortion level DC_{60° .

The model is characterized by a long bifurcated duct intake type, with low inlet contraction ratio (≈ 1.20) and therefore sensible losses and distortion level ($P_{T2}/P_{T0} = .93$ and $DC_{60^\circ} = .20$) at take-off static condition without AID.

With regard to "REAR AID" configuration, the secondary throat area A'_{TH} can be changed in the full range from 0% to 120% of the primary throat area A'_{TH} , while the secondary hilite area A''_{HI} can vary opening 2, 4 or 6 inlet ports. Thus a large range of contraction ratios up to $A''_{HI}/A'_{TH} = 3.5$ can be reproduced. Five values of A''_{HI}/A'_{TH} (1.20, 1.39, 1.66, 2.21, 3.32) and six values of A'_{TH}/A'_{TH} (.180, .360, .525, .719, .858, 1.08) were tested for a total of 15 configurations.

Fig. 2.5 presents the distortion maps at the engine face at the same corrected air flow for:

- a) bell mouth inlet w/o AID
- b) actual inlet w/o AID
- c) actual inlet with AID

$$(A''_{HI}/A'_{TH} = 1.66, A'_{TH}/A'_{TH} = .36)$$

Fig. 2.5, c clearly explains the advantage of the "REAR AID" use: recovery factor increase and distortion level reduction; in particular we can observe that DC_{60° for case c) is better than case a) because the circumferential boundary layer is eliminated and the "splitter effect" is strongly attenuated.

Fig. 2.6 shows the "REAR AID" pressure losses versus secondary throat Mach number M'' . The influence of A''_{HI}/A'_{TH} is well explained: lip losses increase when contraction ratio decreases. The strong influence of A'_{TH}/A'_{TH} at the same A''_{HI}/A'_{TH} is apparently difficult to justify, but this effect is due to model geometry: only A''_{HI} and A'_{TH} can be changed while the intermediate room geometry is fixed, therefore the impingement and turbulence losses increase with secondary air flow W'' and W'' increases with A'_{TH}/A'_{TH} .

For example

$$\begin{aligned} A'_{TH}/A'_{TH} = .360 &\rightarrow W''/W = .20 \\ A'_{TH}/A'_{TH} = .853 &\rightarrow W''/W = .35 \end{aligned}$$

On a real application the impingement and turbulence losses could be reduced by the optimization of the "REAR AID" internal geometry; in particular the secondary flow duct could be carefully shaped, better than on the "S.E.B.I. suction model", from the hilite up to the annular exit into the primary duct. Moreover the hilite internal lip radius could be increased to improve performances.

What about leads to the conclusion that for an operating installation with fixed geometry the "REAR AID" recovery factor wouldn't be so far from the values of fig. 2.6, a, where the impingement and turbulence losses are low because of reduced A'_{TH}/A'_{TH} .

The fig. 2.7, a represents synthetically, at take-off static condition, the results in terms of recovery factor which is equal to .93 for the model primary duct without "REAR AID". The above mentioned figure can be used to design "REAR AID":

- a) knowing A''_{HI}/A'_{TH} ; i.e. the available space to install the aux. ports, fig. 2.7, a supplies the optimum A'_{TH}/A'_{TH} to get max P_{T2}/P_{T0} .
- b) knowing P_{T2}/P_{T0} that has to be reached, AID dimensions are supplied in terms of min.

A''_{HI}/A'_{TH} and, consequently, of A''_{HI}/A''_{TH} .

Likewise, fig. 2.7.b shows a similar diagram regarding the distortion parameter DC_{60° : a strong influence is exerted by the A''_{TH}/A'_{TH} value (i.e., by the secondary air flow percentage), while a large range of A''_{HI}/A'_{TH} values doesn't affect so much the results. From fig. 2.7.b it's evident that with "REAR AID" most benefit can be expected in terms of distortion improvement: a ratio A''_{TH}/A'_{TH} of .20, which means $W''/W = 10\%$ for the tested model, suffices for DC_{60° .

2.1.3 "REAR AID": an extension to the supersonic inlets

"REAR AID" are more useful if pressure losses and distortion level in the primary duct at static and low subsonic conditions are considerably high, like in supersonic aircraft inlets. If performance of a given primary duct without AID are known, it's possible to draw design diagrams similar to those of fig. 2.7 with the aid of fig. 2.6.a, under assumption of same primary and secondary duct static pressure at the mixing section; thus a preliminary assessment of performance level for an engine air supply system with "REAR AID" can be made. This procedure was followed to compare the effectiveness of the "REAR AID" and the "FORWARD AID" for military aircraft supersonic ($M_0 = 2$) bidimensional intake application. Fig. 2.8 shows the "REAR AID" advantages.

- Same A''_{HI} and A''_{TH} : 50% reduction in pressure losses
70% reduction in distortion
- Same recovery factor: 50% reduction in area
55% reduction in distortion

2.1.4 Conclusions

For engine air supply systems, characterized by high pressure losses and distortion level in the main inlet at static and low subsonic conditions, the "REAR AID" with annular air admission into the primary duct appear to be a good alternative to the classical "FORWARD AIR". The following principal advantages can be listed:

- considerable pressure recovery factor improvement
- very large distortion reduction
- sensible "splitter effect" attenuation in the case of a single engine bifurcated intake.

To design the most profitable operational configuration, "REAR AID" concept substantiation and optimization could suggest further investigation to measure, at the engine face, local deflection from the axial flow, turbulence level and dynamic distortion.

2.2 Diverter Aerodynamics

2.2.1 Introduction

The majority of the military aircrafts air intakes are provided with a "DIVERTER", i.e. with a boundary layer discharge channel which hinders the low energy flow near the fuselage from being ingested by the engine. Diverter geometry influence, both on the aerodynamics and the intake performance, presents some interesting aspects which can be investigated by a wind tunnel testing.

To this purpose a "single engine bifurcated intake (S.E.B.I.) low speed model" of a subsonic military aircraft was designed with a $1/7.2$ scale factor and tested in the AIT 2×2 sq. ft. wind tunnel. The mass flow ratio A_0/A_{HI} at different typical flight conditions was reproduced at $M_0 = .20$ varying, by an ejector, the engine air flow.

Four diverter configurations, with same height b_T and same width h , with or without plate, with symmetrical or asymmetrical profile, with blunt or sharp leading edge, were experimentally investigated (Fig. 2.9).

Each configuration incorporates two static pressure probes distributions along the diverter profile equally spaced at $1/3$ and $2/3$ of the diverter width. Static pressure tappings are provided on the fuselage upstream of the diverter and three boundary layer total pressure rakes (seven probes each) are placed just ahead of the inlet.

The diverter profiles are defined by elliptical types equations with exponent ≤ 2

A data reduction system supplied profile pressure coefficient C_p , the drag coefficient C_D (based on the diverter frontal area), and engine face distortion parameter DC_{60° .

2.2.2 Experimental results

Fig. 2.10 shows fuselage pressure distribution for two diverter types ("B" and "D") at different test conditions.

At fixed incidence the A_0/A_{HI} parameter exerts a great influence on the pressure field round the profile on the upper surface at $\alpha = 0^\circ$ diverter "B" reveals for $A_0/A_{HI} = .46$ (typical mini-

minimum cruise value) a $-0.5 > C_p > -1$ suction zone which disappears for $A_0/A_{HI} = 2.0$ (typical take-off value).

Blunt or sharp leading edges play an important rôle: comparing for example diverters "B" and "D" at $A_0/A_{HI} = .46$, the former presents a larger suction high velocity zone than the latter; what above is emphasized by incidence where the sharp diverter shows poor characteristics: in Fig. 2.10 at $\alpha = 10^\circ$ and $A_0/A_{HI} = .46$ the large zone of overpressure ($C_p > .5$) for diverter "D" is evident.

In general diverter C_p distribution at $A_0/A_{HI} < 1$ is similar to a typical airfoil profile distribution, while at $A_0/A_{HI} > 1$ the intake suction affects (more or less) the pressure coefficient depending by intake hilite distance from the diverter leading edge and configuration with or without the plate. Increasing the A_0/A_{HI} value over the unit, the velocity reduces along the profile, flattening the C_p diagram. This is evident in Fig. 2.11 which presents C_p distribution for all tested configurations: b) and d) C_p diagrams are more interesting because recorded at $A_0/A_{HI} = .46$, meaningful value for the flight cruise conditions. Blunt profiles have more advantageous characteristics in terms of negative C_p level than sharp ones and, therefore, reduce drag coefficient C_D induced by pressure distribution.

Moreover Fig. 2.11 shows boundary layer shape, derived by a total pressure rake placed in the "Z" position on the intake centerline; it's possible to observe a remarkable difference only in the $A_0/A_{HI} = 2.0$ case, where high P_T/P_{T0} losses were registered along the diverter width for the configurations with the plate.

Figs. 2.12 and 2.13 show drag coefficients C_D versus A_0/A_{HI} respectively at $\alpha = 0^\circ$ and $\alpha = 10^\circ$, while the Fig. 2.14 presents the C_D variation with incidence at $A_0/A_{HI} = .60$. The drag coefficients are derived from C_p integration along the profile up to the diverters and where C_p values for different configurations are very close. The results show considerable C_D fluctuations, in the order of some percent of the total clean aircraft zero incidence drag coefficient C_{D0} .

In Fig. 2.14 is evident the advantage of diverter "B" and the convenience to place the profile few degrees nose up relatively to aircraft horizontal axis, to reduce C_D without transonic deteriorations.

The above reported considerations are strictly valid for testing Mach number $M_0 = .20$ and may be extended to the subsonic field up to $M_0 = .6$; at transonic velocities blunt diverters negative pressure peak could be too high and shock waves could be thought to arise markedly reducing blunt shape C_D advantages. Anyway this is only partially true because of two facts which should cause in transonic flight a peak velocity reduction if compared with the same profile moving in an undisturbed flow: the diverter is surrounded by a low speed boundary layer flow and A_0/A_{HI} values < 1 (typical of a high velocity flight) slow down the flow in the intake hilite zone. In any case experimental evidence of above considerations through a transonic test appears essential for a flow field understanding.

Fig. 2.15 shows the distortion parameter DC_{60° versus A_0/A_{HI} at $\alpha = 0^\circ$ and $\alpha = 10^\circ$ for the different configurations: the diverter plate has a peculiar influence on distortion; DC_{60° actually increases when A_0/A_{HI} decreases; configurations without plate (replaced by thin lip) usually show the opposite trend.

2.2.3 Conclusions

- From a drag standpoint the blunt diverters, at subsonic velocity, have a better behaviour in terms of C_D , the difference with the sharp diverters reaching the order of some percent of aircraft C_{D0}
- C_D decreases with incidence, therefore it could be useful to adapt the diverter at positive angle of attack of few degrees, compatibly with adequate transonic performance.
- Optimization of the diverter geometry and of the relative distance between its lead edge and intake hilite station could eliminate the plate with consequent weight saving and de-icing deletion.
- Plate elimination increases intake performances in terms of distortion level in the normal $A_0/A_{HI} < 1$ flight conditions range. The advantage could be in the order of 50%.
- A transonic wind tunnel test is recommended to substantiate low speed results and check their applicability to the complete typical C. A. S. aircraft velocity envelope.

REFERENCES

1. Kraus, W.: "PANEL METHODS IN AERODYNAMICS" VKI Lecture Series 87 on "Computational Fluid Dynamics", 15-19 March 1976, Rhode-Saint Genese, Belgium
2. Fornasier, L.: "CALCOLO DEL FLUSSO TRANSONICO ATTORNO AD UN PROFILO A DUE ELEMENTI CON UN METODO AGLI ELEMENTI FINITI", Cooperazione Politecnico di Torino e Aeritalia GVC, 1981
3. Eberle, A.: "EVALUATION OF A MINIMUM PRINCIPLE FOR TRANSONIC FLOW COMPUTATIONS BY FINITE ELEMENTS", GAMM Conference on Numerical Methods in Fluid Dynamics, 1979, Köln, FRG

4. Zannetti, L. and Colasurdo, G.: "TRASFORMAZIONE CONFORME DEL CAMPO ESTERNO A DUE ELEMENTI DI FOGLIA ARBITRARIA IN UNA CORONA CIRCOLARE" Cooperazione Politecnico di Torino e Aeritalia GVC, 1980
5. Fornasier, L. "A ROTATED ARTIFICIAL DENSITY FOR FEM", Aeritalia - MBB Collaboration in Numerical Fluid Dynamics, MBB-UFE 122 - AEROMT-489, 1980
6. Eberle, A. and Schmitz, D.M.: "ENGINE AIR INTAKE DESIGN SUPPORT BY USE OF COMPUTATIONAL METHODS", ICAS 1980, Munich, FRG
7. Eberle, A.: "TRANSONIC POTENTIAL FLOW COMPUTATIONS BY FINITE ELEMENTS: AIRFOIL AND WING ANALYSIS, AIRFOIL OPTIMIZATION, DGLR/GARTeur 6 Symposium on "Transonic Configurations" Bad Harzburg 1978, FRG

ACKNOWLEDGEMENTS

The authors wish to acknowledge Aeritalia's permission to present this paper. The views expressed in this paper are those of the authors personally and not necessarily those of Aeritalia.

Figure 1.1 - Panelling of the SEBI Low Speed Model

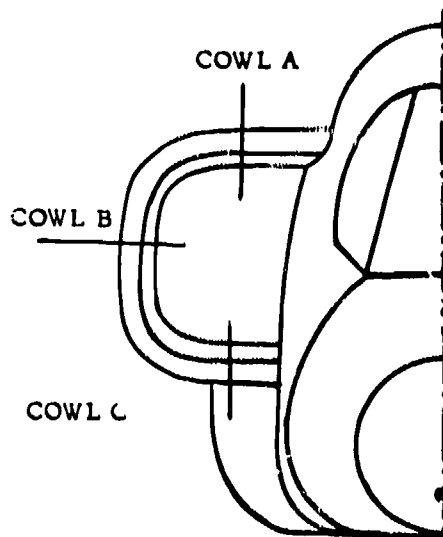
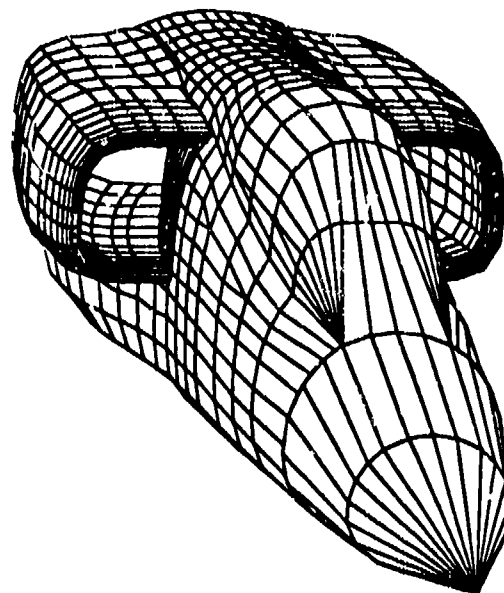


Fig. 1.2 - Position of pressure plots

FIGURE	TEST RUN	MACH NO.	AOA ^(°)	Λ_0/Λ_{TH}
1.4	1	.20	4.0	.66
1.5	2	.20	0.0	.84
1.6	20	.20	0.0	.27
1.7	28	.20	0.0	2.5
1.8	7	.20	16.0	.89
1.9	23	.20	16.0	1.58

(°) Angle of attack

	Ext	Int
Theory	—	---
Experiments	⊙	+

Fig. 1.3 - Conditions for theoretical vs. experimental data comparisons.

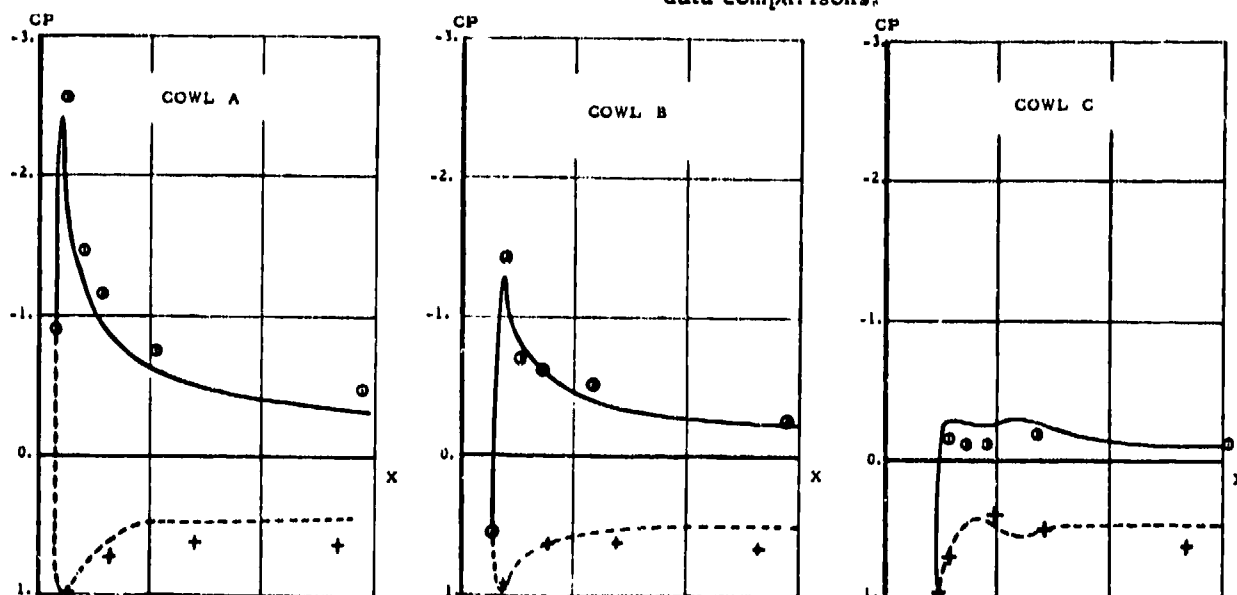


Figure 1.4

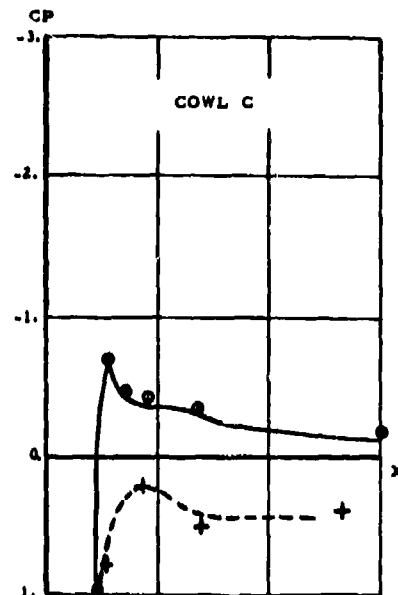
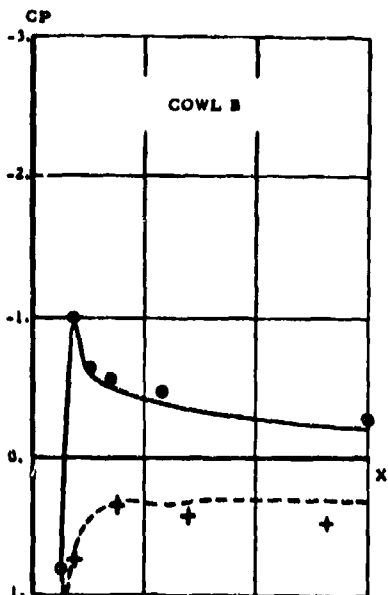
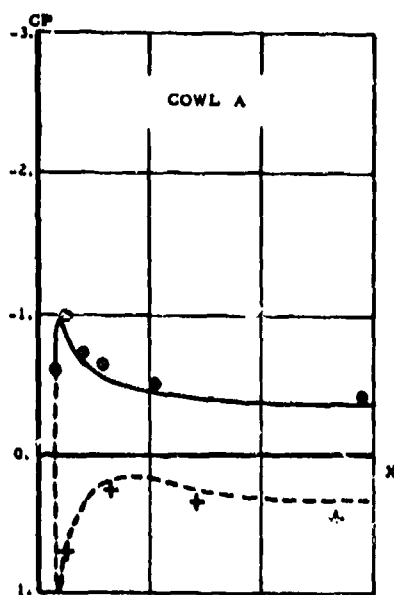


Figure 1.5

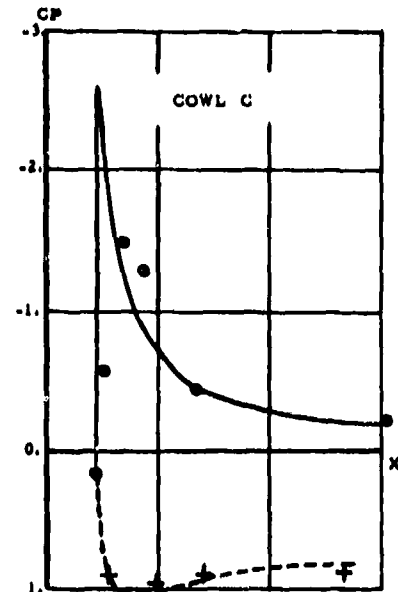
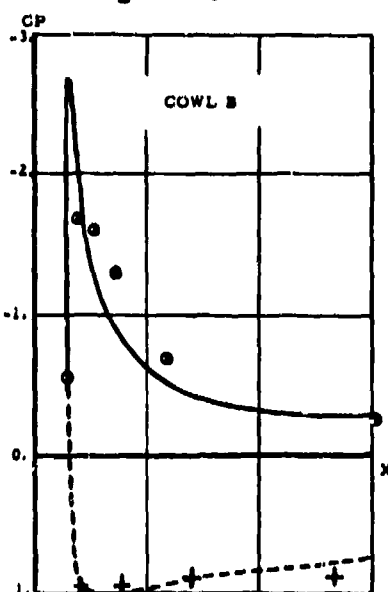
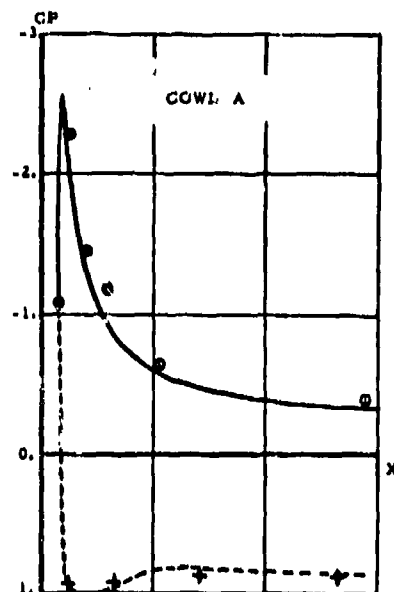


Figure 1.6

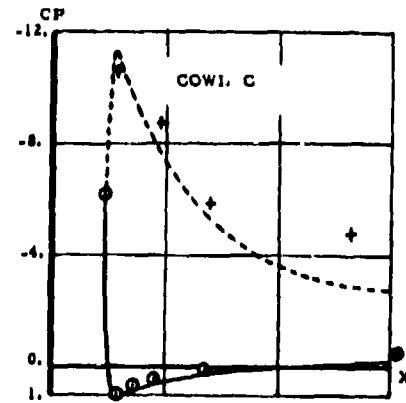
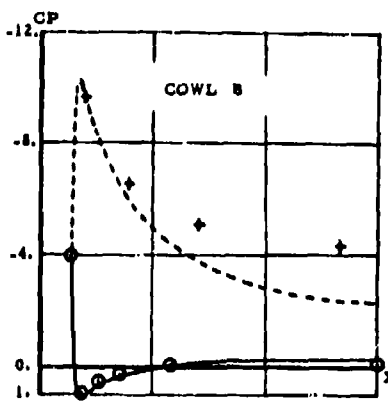
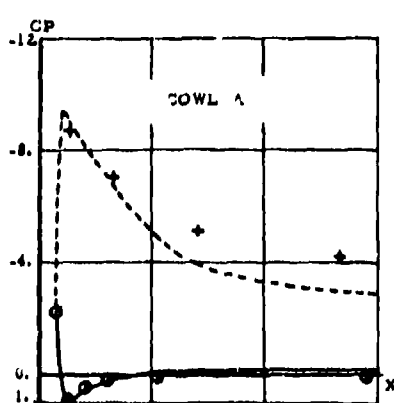


Figure 1.7

Note: See figure 1.3 for test conditions

	Ext	Int
Theory	—	---
Experiments	⊙	+

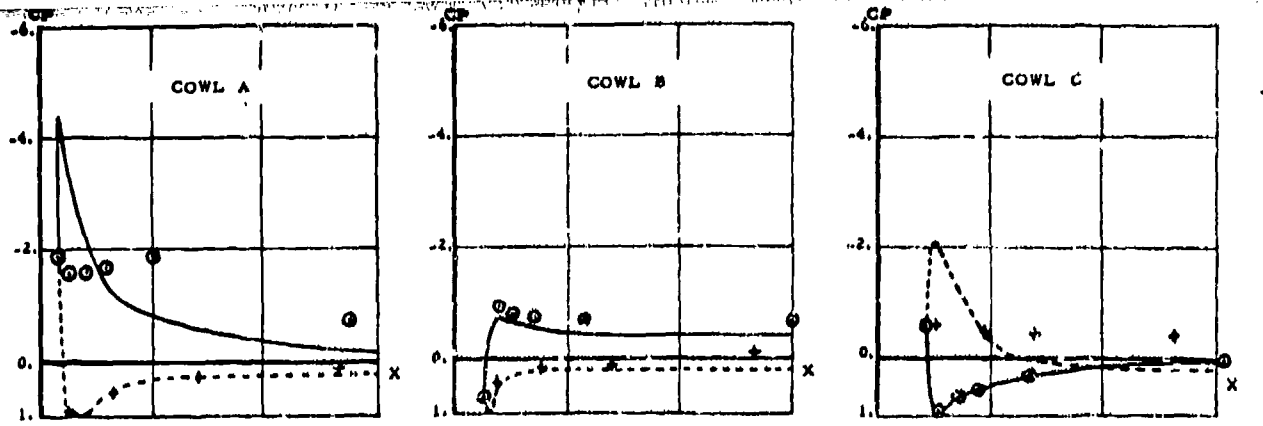


Figure 1.8

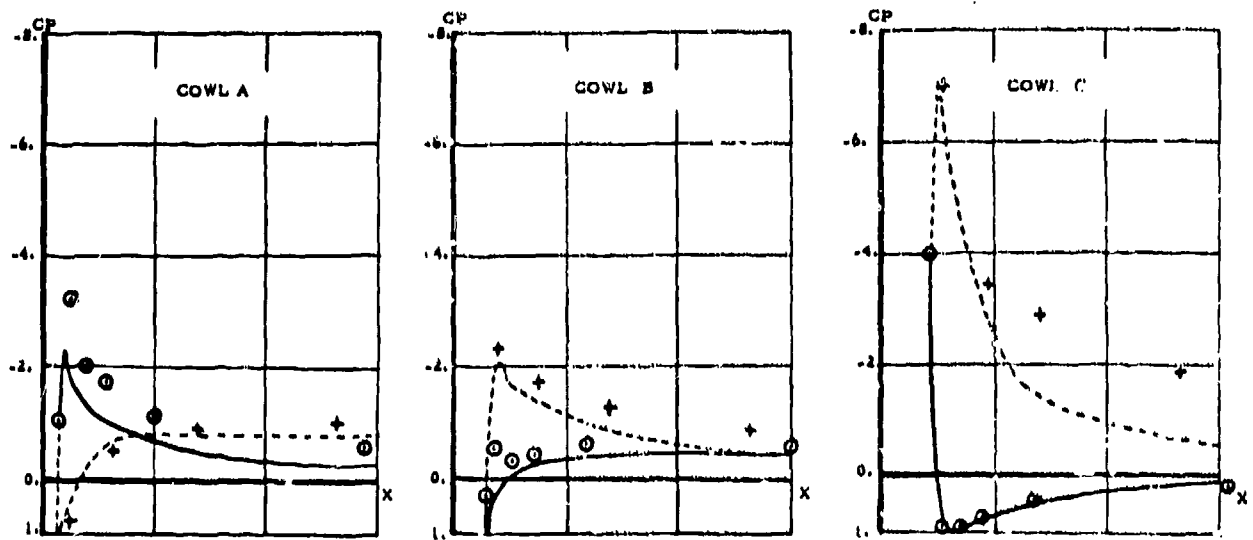


Figure 1.9

Note: See figure 1.3 for test conditions

	Ext	Int
Theory	---	---
Experiments	⊙	+

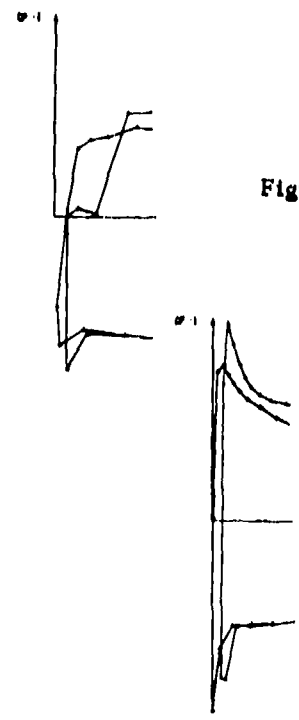


Figure 1.10 - Initial mesh grid

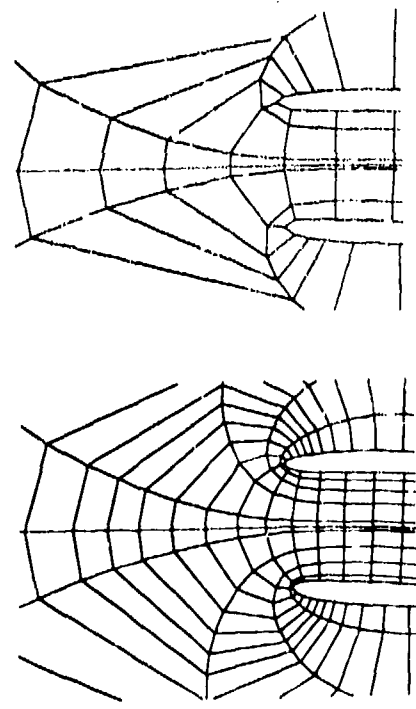


Figure 1.11 - First intermediate mesh grid

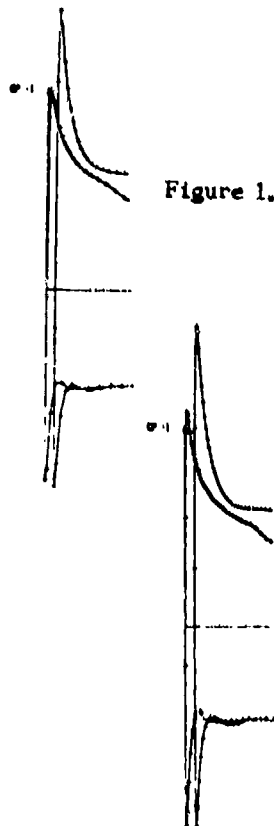


Figure 1.12 - Second intermediate mesh grid

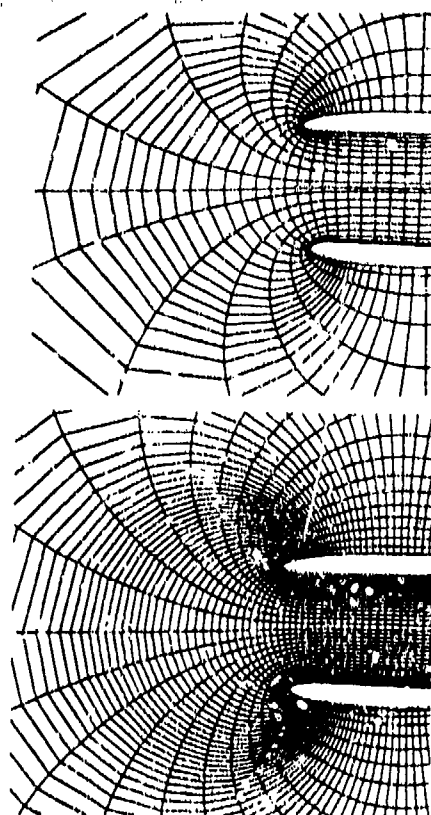


Figure 1.13 - Final mesh grid

ALFA	= 0°
MACH	= .70
Λ_0/Λ_{HI}	= .57

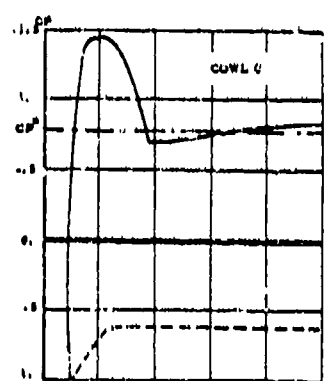
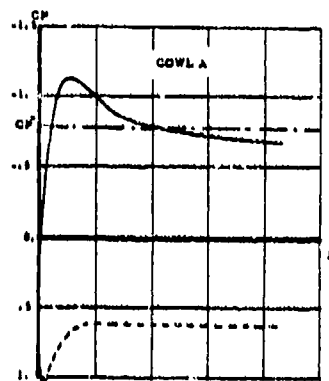
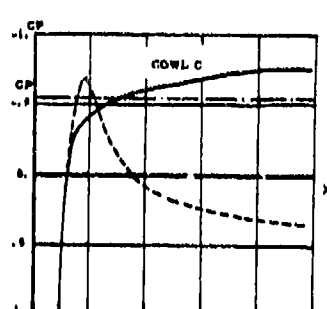
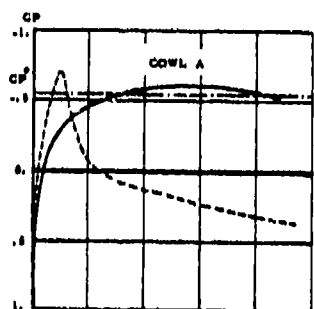


Figure 1.14



ALFA	= 0°
MACH	= .76
Λ_0/Λ_{HI}	= .73

Figure 1.15

ALFA	= 0°
MACH	= .76
Λ_0/Λ_{HI}	= .57

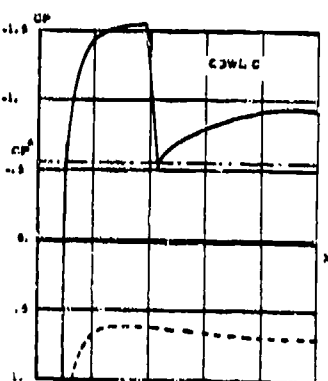
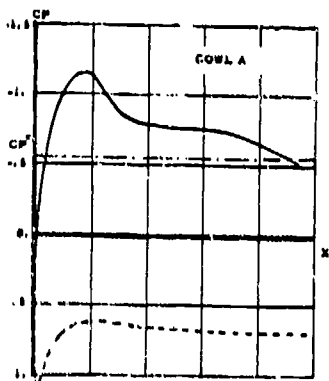


Figure 1.16

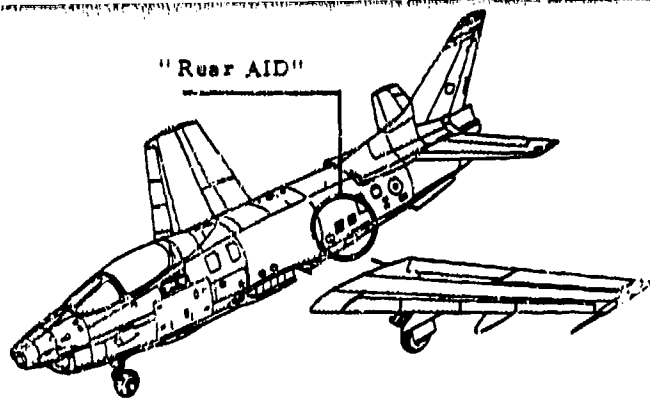


FIG. 2.1 : G 91 Y rear AID location

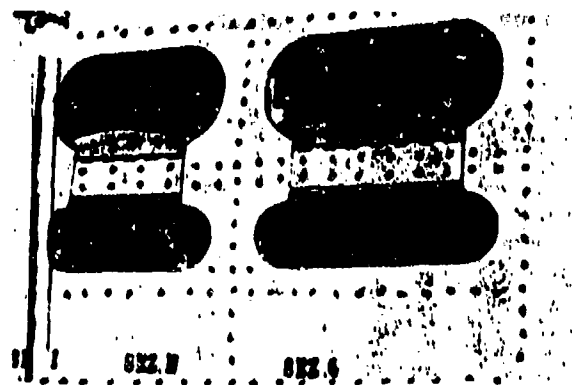


FIG. 2.2: G 91 Y rear AID particular

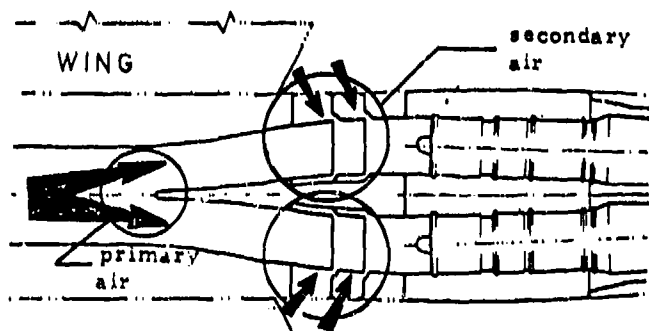


FIG. 2.3 G 91 Y engine air supply system

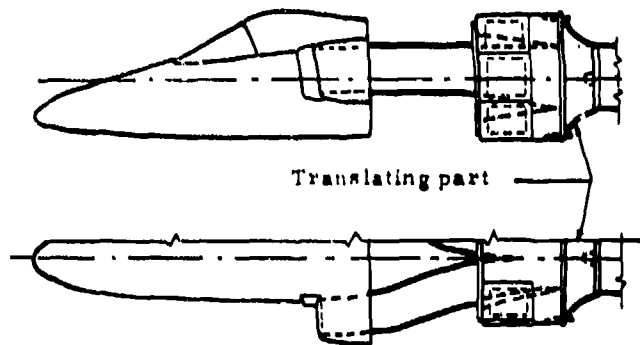
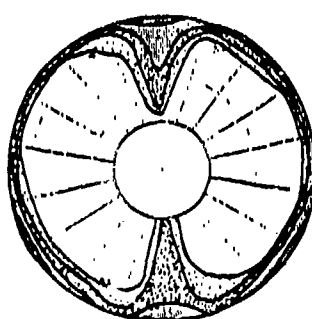
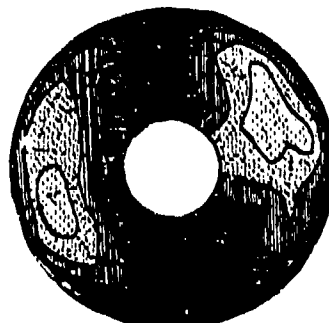


FIG. 2.4: "S. E. B. I. suction model" arrangement.

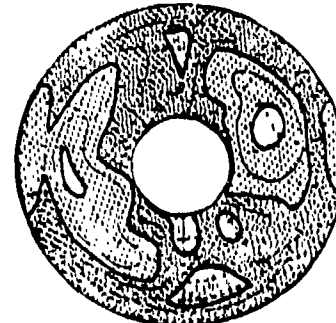


a) Bell mouth w/o AID

P_{T1}/P_{T0} %
88.88
89.94
91.94
93.90
95.88
97.88



b) CR=1.2 primary inlet w/o AID



c) CR=1.2 primary inlet with rear AID

FIG. 2.5 : "S. E. B. I. suction model" distortion maps at $M_2 = .58$

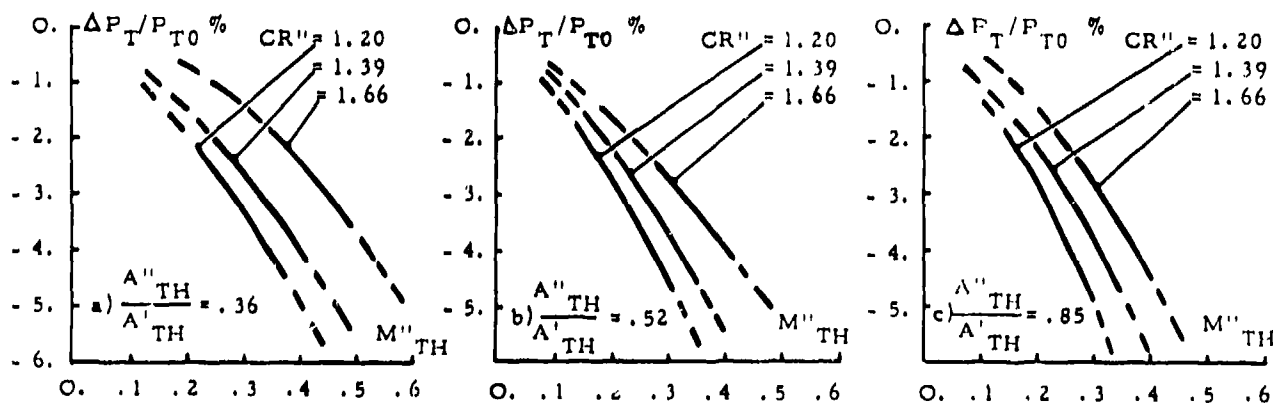


FIG. 2.6 : "S. E. B. I. suction model" rear AID test results

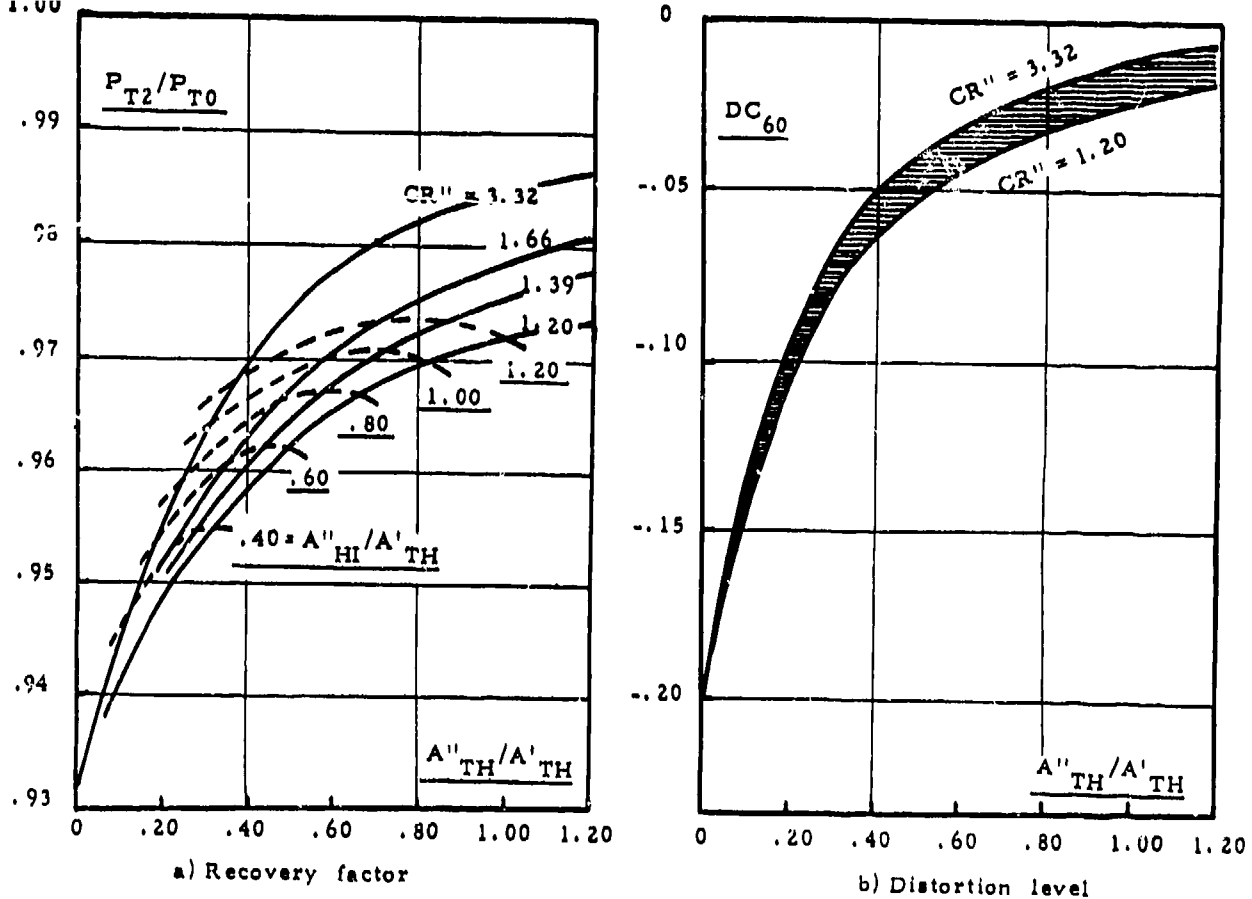


FIG. 2.7 : Suction model with "rear AID": testing results at take-off static condition

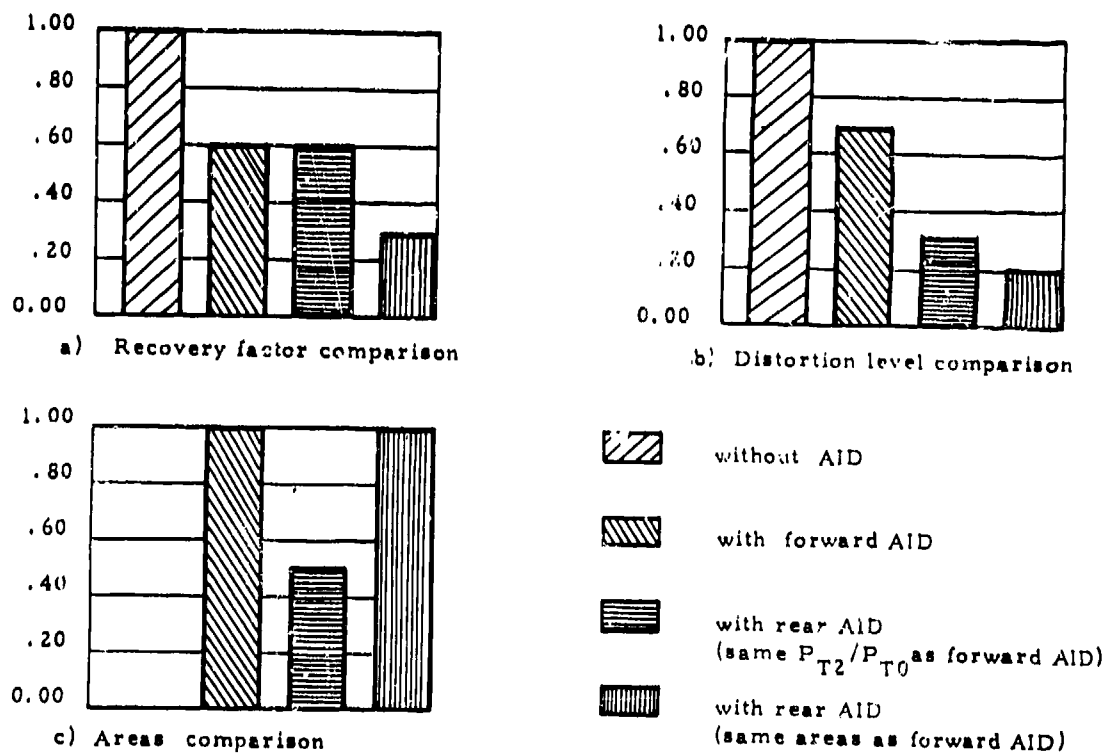


FIG. 2.8 : Supersonic intake: AID effectiveness comparison at take-off static condition

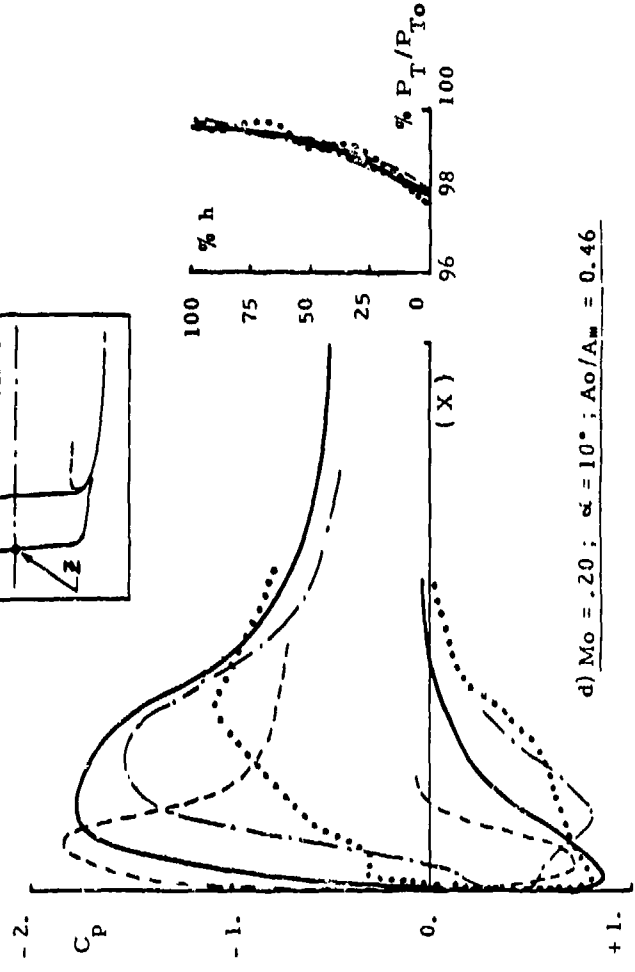
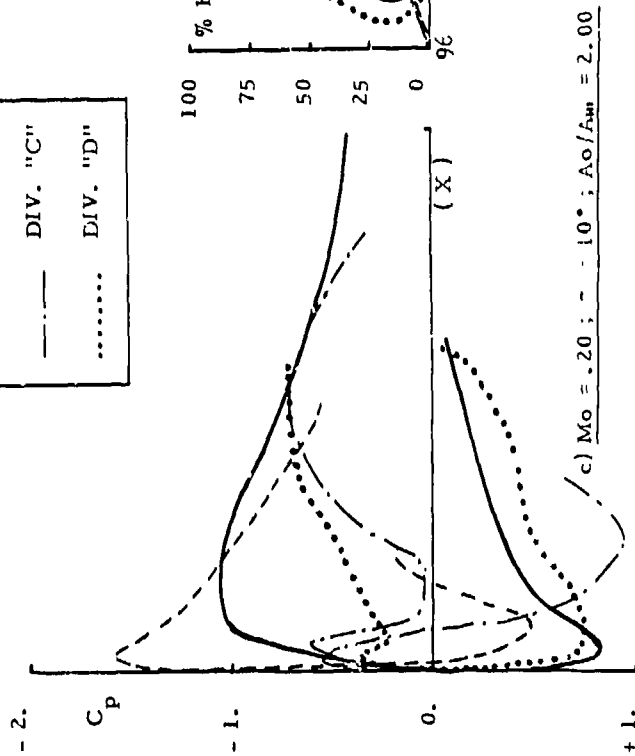
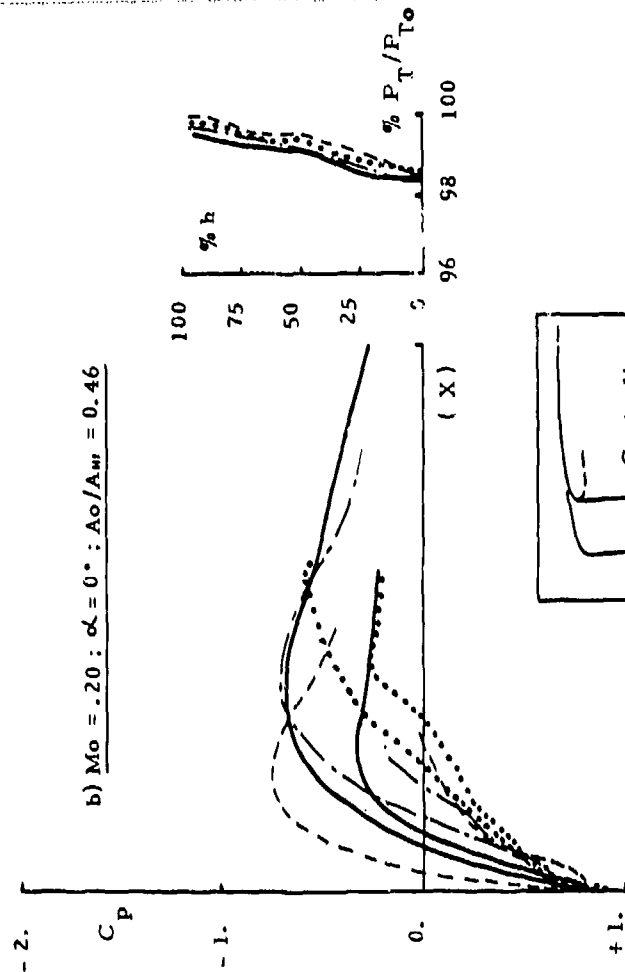
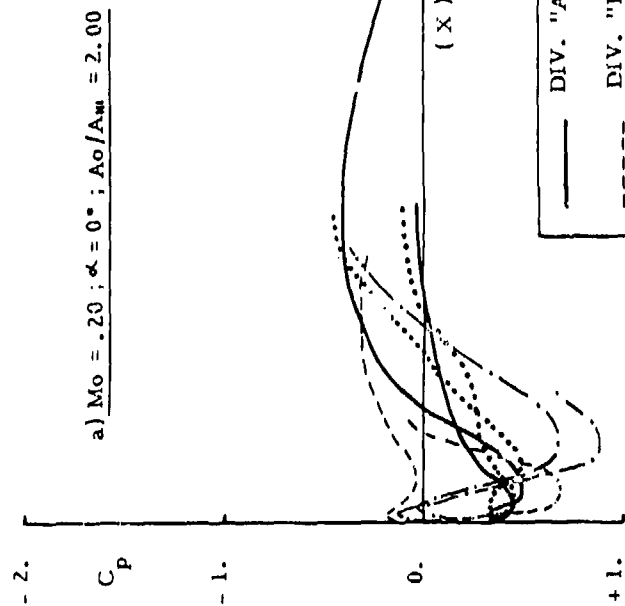


FIG. 2.11: Diverter C_p distribution - Boundary layer shape at the station Z

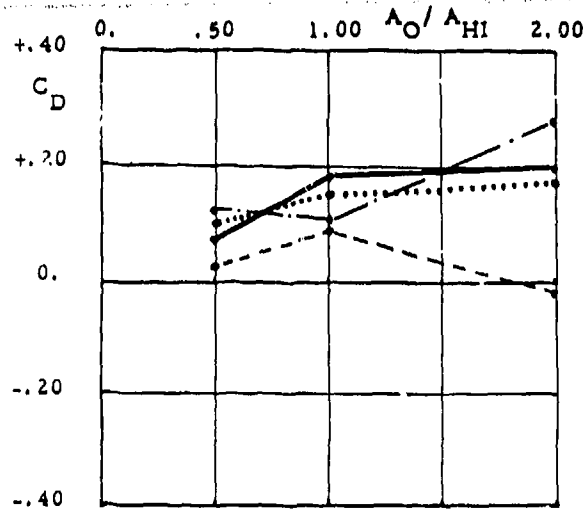


FIG. 2.12: Drag coeff. at $\alpha = 0^\circ$, $M_0 = .2$

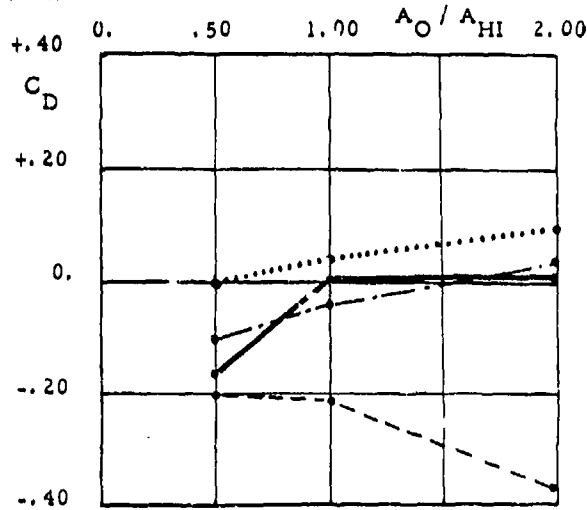


FIG. 2.13: Drag coeff. at $\alpha = 10^\circ$, $M_0 = .2$

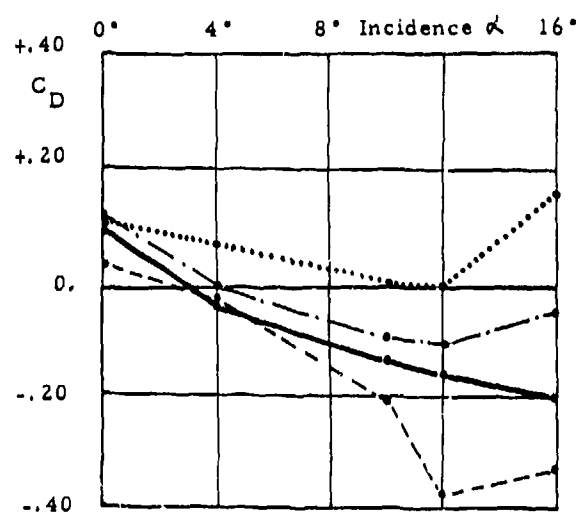


FIG. 2.14: Drag coeff. at $A_0/A_{HI} = .60$, $M_0 = .2$

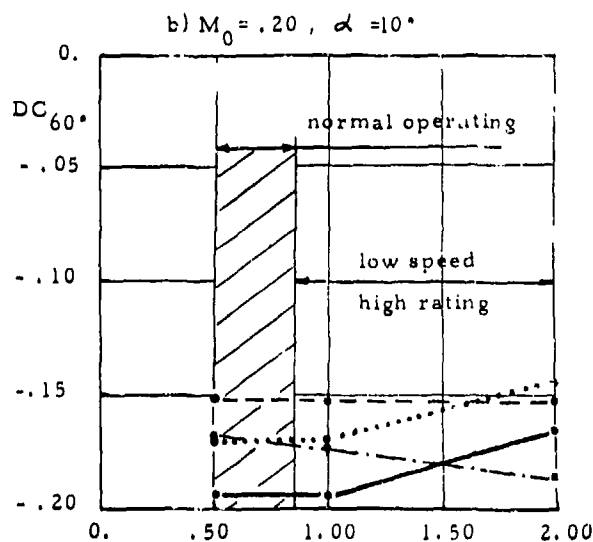
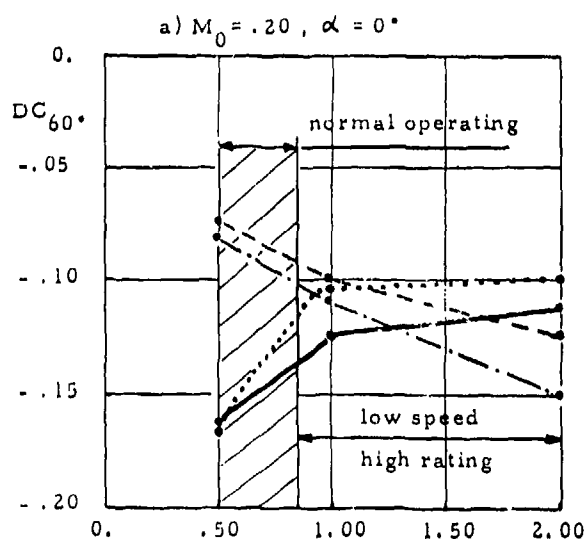
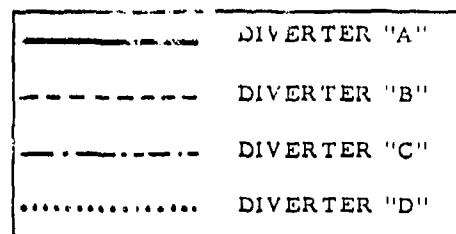


FIG. 2.15: "S. E. B. I. low speed model" distortion levels

THE DESIGN AND DEVELOPMENT OF THE TORNADO ENGINE AIR INTAKE

by

C.P.Stocks
Principal Flight Test Engineer
BAe Warton Division
Warton Aerodrome
GB

N.C.Bissinger, Ph.D.
Messerschmitt-Bölkow-Blohm
Unternehmensbereich Flugzeuge
D 8000 München 80
Postfach 801160
FRG

SUMMARY

The design and development of the Tornado supersonic intake is described outlining the critical aerodynamic design areas with special emphasis on compatibility; the problem of design loads is also reviewed.

The philosophy and operation of the automatic control system is discussed.

Finally, the propulsion system behaviour in flight and some examples of intake-airframe interaction are described.

LIST OF SYMBOLS

A_c	Intake capture area	P_t	Total pressure
A_o	Free-stream area of intake flow streamtube	RAE	Royal Aircraft Establishment Bedford, UK
ARA	Aircraft Research Association Bedford, UK	Re-No	Reynolds number
B.L.	Boundary Layer	TU	Turbo Union
Cell 4	Supersonic high altitude test facility at NGTE, Pyestock	W/T	Windtunnel
			Absolute value
		α	Aircraft incidence
DFVLR	Deutsche Forschungs- und Versuchsanstalt für Luft- und Raumfahrt e.V.	δ_2	Second ramp angle
FTB	Flying test bed	η	Pressure recovery
I/B	Inboard	θ	Polar coordinate in compressor face
M	Mach number	τ_{87}	Swirl, i.e. circumferential flow angle on 87 % radius of measuring plane
ms	Milli seconds		
m/s	Meter per seconds		
NGTE	National Gas Turbine Establishment Pyestock, UK	Subscripts:	
O/B	Outboard	o	Free stream condition
P_1	Steady state static pressure at compressor entry	CL	Center line
P_2	Steady state static pressure at compressor exit	EF	Engine face
P_{SB}	Static bleed void pressure	MAX	Maximum
		MIN	Minimum
		RMS	Root mean square

1. INTRODUCTION

The TORNADO Aircraft (Fig.1) is the product of European collaboration between airframe and engine companies designed to meet the requirements of the German, Italian and British airforces with whom it is now in service.

The two seat aircraft is twin engined with a shoulder mounted variable geometry wing and a low tailplane. The engines, TU RB 199, are located in the rear fuselage and are equipped with thrust reversers which in conjunction with a sophisticated high lift system give a well balanced take off and landing performance.

The engines are fed by variable geometry two dimensional intakes located on the fuselage side forward of the wings. The intakes are designed to satisfy the conflicting requirements of greater than Mach 2 operation and a very wide incidence operating envelope at subsonic speeds.

To achieve these aims compatibility and performance have been accorded equal status in all assessments. Having achieved the desired aerodynamics an intake control system has been designed with the performance and precision to exploit the aerodynamics.

This paper reviews the evolution of the Tornado engine intake design from concept to flight, highlighting the critical design areas and the design actions initiated to secure, in collaboration with TU, an efficient and flexible propulsion system.

2. ENGINE INTAKE LAYOUT

The air intakes are disposed on each side of the forward fuselage (Fig. 2). The compression ramps form the upper surface of the intake. The intake datum is aligned parallel to the fuselage datum (zero cant angle) and the first ramp is fixed, the second ramp is variable relative to the first ramp. The third (subsonic) ramp is mechanically linked to the second ramp and is hinged at its trailing edge.

The variable ramps are positioned by an electro-hydraulic actuator under the control of the Air Intake Control System (AICS).

The compression surface boundary layer is bled through the wide slot, formed between the trailing edge of the second ramp and the leading edge of the third ramp, into the void above the ramps to be exhausted overboard through a rearwards facing scoop on the top surface of the intake.

Each intake is equipped with two blow in auxiliary doors which maintain high pressure recovery under take off and landing conditions.

The intakes are connected to the engines by low diffusion angle ducts which have an elongated S shape planform.

Ploughshare shaped boundary layer diverters separate the intakes from the fuselage side.

3. AIR INDUCTION SYSTEM NOMENCLATURE

Intake aerodynamics is concerned with four main topics:

- Intake pressure recovery
- Intake spillage drag
- Distortion
- Swirl

Intake pressure recovery is the mean total pressure recovered at the engine-intake interface referred to free stream total pressure. Engine thrust is directly related to pressure recovery on a greater than 1:1 basis.

Intake spillage drag is the drag associated with the intake running at less than full mass flow. At subsonic/transonic speeds full mass flow (zero spillage drag) is achieved when the intake throat Mach number is equal to free stream Mach number. Supersonically full mass flow is defined by the shock wave geometry.

Distortion in the airflow at the engine-intake interface is seen as the non-uniformity of the total pressure distribution. Increasing distortion leads to increasing loss of engine surge margin. Distortion is usually described in coefficient form. The coefficient adopted by TU is DC_θ and defines the maximum total pressure deficit in an angular segment θ of the compressor face, as a fraction of the mean dynamic head.

By-pass engines have been found to be sensitive to pressure distortion existing for a very short period of time (less than one compressor revolution). This instantaneous distortion is measured during intake model tests and used for the determination of the engine/intake compatibility boundaries of a propulsion system. Generally speaking high distortion levels accompany low pressure recovery levels and are typical of high intake mass flow conditions, especially at high incidence subsonic Mach number and at high supersonic Mach number flights.

Distortion tolerance of by-pass engines can be reduced drastically when distortion is accompanied by intake flow angularity. Circumferential flow angles are defined as swirl. Swirl is an additional important intake flow parameter in the overall performance of the propulsion system. The description of a swirl coefficient is highly desirable, however, is not yet fully codified into practical and common use. Therefore, this paper refers to swirl on the circumference of a specific intake duct radius.

4. TORNADO INTAKE DEVELOPMENT MODELS; TOOLS

Small scale models were tested during development of the intake (Fig.3), comprising static, low speed, subsonic and supersonic models. Extensive use was made of the Cell 4 facility at NGTE, Pyestock, where full-scale testing of an isolated Tornado intake in front of a reheated RB 199 was carried out, the majority of the testing being with the intake under automatic control.

The main test parameters have been internal performance, drag, steady state and instantaneous distortion and swirl.

Internal performance was measured with Pitot rakes across the intake duct at an agreed interface between intake and engine.

Two techniques were adopted for intake drag measurements, namely the conventional method of determining drag increments where the complete model, i.e. intake plus fuselage, is balance mounted and a novel technique, where the intake only was balance mounted allowing absolute intake drag to be measured.

Dynamic flow fluctuations were recorded by Kulites. Steady state and Kulite pitots were positioned side-by-side (Fig. 4a).

Instantaneous distortion coefficients, turbulence and time-variant pressure recovery were calculated using an analog on-line system (Fig. 4b).

Five-hole probes on a separate rake were used for the measurement of flow angularity, i.e. swirl (Fig. 4c).

Prior to full-scale intake testing the performance of the air intake control system (AICS) in terms of stability and response has been demonstrated on an AICS-rig, comprising actual electronic and hydraulic aircraft hardware with simulated pneumatic and electrical stimuli inputs.

5. INTAKE DESIGN

5.1 Fuselage Flow Field and Intake Orientation

At subsonic speeds there is considerable upwash aggravating the cowl design problem. At supersonic speeds there is a downwash (Fig. 5) reducing first ramp shock strength but increasing the strength of the shocks further downstream with attendant shock boundary layer interactions.

The cowl design problem is essentially of a subsonic nature and is considered in chapter 5.3.

The supersonic downwash problem has been alleviated by increasing the cant angle of the intake from an initial -3 degrees to 0 degrees which increases first ramp flow turning and restores compression balance across the shock system. Fig. 6 shows typically how the turbulence and distortion characteristics across the intake throttling range are reduced by increasing the cant angle from -3 to 0 degrees.

5.2 Diverter

The fuselage boundary layer diverter is sized for a width/full boundary layer thickness ratio of unity (Fig. 7). Side elevation is a ploughshare shape of relatively low aspect ratio. This shape was optimised in combination with inboard sideplate geometry in transonic drag tests.

5.3 Intake Cowl Lip

From combat studies it has become increasingly evident that at subsonic speeds very high incidence operation gives significant tactical advantages, for interception roles good acceleration to high supersonic Mach numbers is required.

For Tornado these requirements have been met successfully using a fixed cowl geometry, the design of which can be regarded as the most critical and difficult in the overall intake design.

At subsonic speeds increasing incidence leads to cowl flow separation as illustrated by the water tunnel flow visualisation photographs in Fig. 8. With separation comes increased distortion level resulting in reduced engine surge pressure ratio. Large tail-plane angles and wing sweeping have to be accommodated by the hydraulic system resulting in large power off-take demand. The power off-take lifts the engine running line with a further significant reduction in surge margin, engine handling on top of all this leads to a very sensitive situation where a classical compatibility problem can well occur.

To combat this situation increased incidence tolerance can be obtained by cowl blunting, but at the expense of rapidly deteriorating supersonic intake performance via increased cowl wave drag and reduced capture and reduced pressure recovery from increased terminal shock standoff. Fig. 9 indicates how the compatibility parameters improve with lip contraction ratio and also the dramatic increase in shock standoff.

A substantial decrease in instantaneous distortion has been achieved in the Tornado intake development by applying cowl blunting and de-cambering for a small and acceptable deterioration in supersonic performance; the original and current cowl shapes are compared in Fig. 10a, the resulting reduction in turbulence (distortion) is shown in Fig. 10b. The supersonic penalties are illustrated by figs. 10c and 10d in terms of mass flow deficit and shock standoff respectively.

The level of blunting is, however still insufficient to ensure that the cowl is free of flow separation over the required incidence range at maximum engine ratings.

It would then seem inevitable that for a modern combat aircraft with unshielded intakes cowl flow separation will occur well within the required incidence envelope. The task of the intake designer is to ensure that under such high incidence conditions the flow at engine entry is conditioned so as not to provoke engine surge. This task is eased by the fact that instantaneous distortion does not increase proportionately with increasing incidence, but reaches a plateau value at very high incidence (Fig. 11a). It is conjectured that this is due to the increasing incidence reducing the effective intake stagger causing flow turning to be more equitably balanced between ramps and cowl (Fig. 11b) hence tending to suppress the cowl side separation.

With the advent of a separated cowl flow a further potentially de-stabilising engine flow property can occur if there is appreciable curvature of the flow in the same plane as the plane of separation (Fig. 12 a). The differences in centrifugal forces (due to velocity differences) between the high and low energy flows in the intake produce static pressure gradients which cause secondary flows, i.e. cross flows. This mechanism is the same as in fully developed pipe flow in curved ducts where the symmetrical boundary layer results in the classic twin swirl pattern which has zero mean swirl. In an intake duct where the boundary layer is separated on one wall, e.g. downstream of the cowl lip, the mechanism produces a bulk swirl with nearly solid body rotation superimposed by 'twin swirl'.

The flow angles with this composite pattern, measured near to the engine face for high angle of attack are shown in Fig. 12b together with the associated isobar distribution (Fig. 12c). The largest flow angles are connected with the lowest total pressures. The position of the low total pressure area indicates a rotation of the cowl separation flow by about 210 degrees.

The strength of both bulk and 'twin' swirl depends, for a given Mach number, intake geometry, and engine mass flow on incidence only. This is demonstrated in Fig. 12d, where the mean, the maximum and the minimum swirl on the circumference of the outermost measuring station is plotted as a function of incidence. As can be seen, there is a strong increase in mean swirl at intermediate incidences and a plateau value is reached at higher incidences. The same dependency on incidence was found for instantaneous distortion (Fig. 11a). As a measure for the strength of the 'twin swirl' the differences between mean and maximum swirl or mean and minimum swirl can be considered. These values nearly double with increasing incidence.

If the sense of rotation of the swirl is contra to that of the engine compressor, assuming no interaction from inlet guide vanes, additional losses in surge margin to those already accruing from distortion ensue. This could be expected in the port intake (Fig. 12a).

In this context it is worth pointing out the dangers of misleading results from tests of a full scale intake-engine combination in the presence of multi-armed Pitot rakes which may have powerful flow straightening properties and mask a problem.

5.4 High Ramp Angle Subsonic Diffuser

The Tornado aircraft was conceived as a compact fighter of the minimum size compatible with its diverse roles.

To secure minimum possible supersonic drag cross sectional area in the centre fuselage section must be particularly closely controlled. Consequently volume for the main undercarriage is at a premium and the intake duct turning into the centre fuselage needs to be accomplished as rapidly as is compatible with achieving good duct lines.

A short third ramp results from this approach reducing ramp hinge moments, allowing a modest actuator, minimising hydraulic demand.

At high ramp angles, however, the short ramp results in high diffusion rates which can lead to deterioration in duct flow quality.

High ramp angles are associated with high Mach number operation where the diffuser entry flow can already be adversely affected by external shock boundary layer interactions.

Under these conditions it was recognised that there was danger of separated flow in the vicinity of the third ramp with associated unsteady flow and the probability of flow swirl.

Using the same (simplified) flow model as in the preceding chapter 5.3 Fig. 13a shows the creation of swirl due to third ramp flow separation. The sense of rotation is contra to that one of the swirl stemming from cowl flow separation. Again, mean swirl is a bulk swirl superimposed by 'twin swirl'. Also, the area of largest flow angles is the one with the lowest total pressures (Fig. 13b and 13c). The dependency of bulk and 'twin' swirl strength on ramp angle is shown in Fig. 13 d.

From these data, surge proneness of the starboard engine during high supersonic Mach numbers, i.e. high ramp angle, operation is a possibility due to the swirl rotating contra to the first engine compressor stage.

5.5 Anti Icing System

Each intake has its own independent ice protection system which is an electrical anti/de-icing type. When the system is operating the leading edges are anti-iced by continuously heated mats and areas behind them de-iced by cyclically heated mats. Power intensities and cycle times are arranged so that the maximum size of ice shed into the engine from heated areas will be $150 \times 25 \times 7$ mm or 18.4 gram mass. The third ramp leading edge is not heated and ice shed from there is acceptable to the engine.

The areas of the intake covered by heater mats are shown in Fig. 14.

The electrical load for the whole ice protection system during a cycle does not exceed 6.85 kW.

The continuously heated anti-iced areas initially de-ice the intake lips if necessary and then prevent ice from forming whilst the de-icing system is operating. The cyclically heated areas allow ice to build up during a predetermined period of time and then shed it progressively. The complete cycle for both intakes takes 128 seconds. The pieces of ice entering the engine are the size quoted earlier or smaller so that no degradation is caused to engine performance.

Operation, either automatic or manual, of the de-icing system is inhibited on the ground to avoid overheating the mats.

The performance of the Propulsion System as a whole has been tested at the NGTE Icing Facility, Pyestock, and the results verified that the intake has sufficient icing protection for 15 minutes of continuous maximum icing conditions.

5.6 Air Intake Control System

The Air Intake Control System (AICS) has been described in depth elsewhere (Ref. 1), but for completeness a brief description of the system will be given here.

The purpose of the AICS is to position the intake to achieve maximum installed thrust and exploit the operating limits of the intake.

Each intake has its own totally independent AICS which comprises a digital computer with its associated air data sensors and an electro-hydraulic actuator, the design philosophy is operate fail safe.

The AICS has two normal modes of operation:

Open loop for operation at less than $M = 1.3$ ---
closed loop operation for greater than $M = 1.3$ flight.

In the open loop mode the intake is held at a constant throat area with the second ramp fully collapsed.

At $M \geq 1.3$ the intake ramps are positioned as a function of Mach number, incidence and engine mass flow demand. Mach number and incidence are obtained from the side pitot-static system and air direction detectors respectively. Engine mass flow demand is determined from a sensor measuring pressure in the ramp void. This pressure when normalised by free stream pitot pressure uniquely defines mass flow for given free stream conditions and intake geometry. A value of this void pressure recovery can be chosen which represents the optimum intake operating point for a given ramp angle and free-stream condition. Schedules of the optimum void pressure recovery are stored in the AICS digital computer, the actual value of η_B measured in the void is compared with the scheduled value, the resulting error signal is fed to the actuator via its associated servo system and ramp angle is changed until actual and scheduled bleed pressure recoveries are identical.

Limiting ramp angles, which are a function of Mach number and incidence only, chosen to give maximum buzz and supercritical intake operating margins over-ride the closed loop operation under low ("Hot Day") and high ("Cold Day") engine flow conditions respectively.

The AICS is provided with Built In Test Equipment (BITE) which has the dual modes of continuous self checking in flight and a more comprehensive system check prior to flight.

For the flight test programme the AICS has been fully instrumented and additionally has the facility of allowing manual control of the intake.

5.7 Intake Structural Loads

As a result of engine surge, pressure waves are set up in the induction system which produce loads which are analogous to hammer shock in pipes. Hammer shock pressures design the Tornado ducts, ramps and linkage systems.

Maximum hammer shock pressures increase essentially linearly with increasing engine compression ratio (Fig. 15a). These data include subsonic and supersonic flight condition results. For the RB 199 in Tornado, duct peak surge pressures of the order of twice free-stream total pressure have been experienced.

Such pressure levels can usually be accommodated in the circular sections of the duct, the associated hoop stresses not being critical. Moving parts, however, are especially vulnerable, ramp loads can be intensified by the hammer shock waves accelerating into the void above the ramps whilst auxiliary doors are liable to structural damage under slamming loads. Reference 2 gives a detailed review.

The pressure rise time associated with the hammer shock is extremely short (Fig. 15b), of the order of 1 millisecond. The sudden surge pressure application can result in stress amplifications. In Fig. 15c the increased stress level expressed as a gain factor is clearly influenced by duct panel size and correct sizing of the panel can give appreciable alleviation.

Hammer shock loading cases are especially important for prototype aircraft where surge occurrence frequency can be high during initial flying. As flying progresses the frequency decreases dramatically due to establishment of clearance envelopes and general development. On this basis there could be a case for more lenient surge loading cases to be specified for production aircraft.

6. FLIGHT TESTING

6.1 Programme Tasks

The objective of the flight test programme was to establish and ensure that the performance and the operational envelope of the intake and its control system is compatible with the overall weapon system requirements.

To meet the objective programme tasks as indicated below were initiated:

- Measurement of intake internal performance in terms of pressure recovery and steady state distortion as a function of mass flow, Mach number and incidence.
- Assessment of the AICS in open and closed loop operation.
- Acquisition of adequate data from "On Control" and "Off Control" intake operation for comparison with the wind tunnel data bank to provide confident successive clearances.
- Confirmation of aircraft recovery procedures specified for AICS failures.
- Measurement of intake loads under engine surge conditions for confirmation of structural integrity.

Comprehensive flight test instrumentation, measuring more than 70 parameters, was installed in the intake and duct of the intake/engine development aircraft. During the testing telemetry was used extensively to monitor critical parameters. Also in flight re-fuelling was standard procedure to expedite the programme.

6.2 Subsonic Tests

In addition to measuring intake performance using a conventional Pitot rake much attention was devoted to ensuring propulsion system compatibility at high incidence including the effect of large power offtakes and simultaneous engine handling. This part of the testing will be dealt with in detail in this section. The programme culminated in a highly successful result, no surges were experienced at target incidence even under severe engine handling and extreme power offtake conditions.

Experience showed initially that surges occurred at less than target incidence with intake flow conditions at which instantaneous distortion levels were not excessive. The surges were confined to the left hand installation.

The fact that the problem was handed re-focussed attention on intake flow swirl. The combination of instantaneous distortion and swirl, rotating contra to the fan in the port installation, was apparently sufficient, in the absence of compressor inlet guide vanes, to cause surge. The right hand engine in a co-rotating swirl environment was surge free as anticipated.

A simple fence was introduced into the intake on the intake centre line just downstream of the cowl lip and extending downstream for the length of the duct inboard bend (Fig. 16a). The fence had been shown in wind tunnel tests to inhibit the development of bulk swirl by preventing the duct secondary flow from interacting with the low energy air emanating from the separated cowl. In Fig. 16b the reduction in swirl on the circumference of the 87 % duct radius and the reduction in mean swirl on that radius as a function of incidence due to the cowl fence can be recognised.

Flight tests showed the fence to be highly effective allowing a propulsion system incidence envelope to be defined compatible with the high incidence requirement of the aircraft (Fig. 16c).

6.3 Supersonic Tests

At supersonic speeds the full flight envelope has been successfully demonstrated. The AICS behaved precisely as predicted and no development problems were experienced.

At $M > 1.35$ the characteristics of the RB 199 Main Engine Control Unit (MECU) are such that there is virtually no engine mass flow variation with throttle position, mass flow varies only as a function of ambient temperature and Mach number. As variations in ambient temperature, on a given day, are likely to be small only a small ramp angle variation and hence a small area of the intake's required operating range can be investigated. In order to rapidly gain assurance that the intake was behaving as expected, intake characteristics at constant mass flow conditions were measured and assessed.

The technique adopted involved, at constant flight conditions, driving the intake off schedule using the manual control facility. Excursions were made to buzz onset, decreasing ramp angle, and also to surge induced by supercritical intake operation, increasing ramp angle. Intake parameters recorded during the ramp traverses were then compared with wind tunnel data.

Excellent agreement was found to exist between the flight measurement and the small scale wind tunnel data as shown by Fig.17 where the ramp angle versus void pressure ratio relationship and also buzz onset are compared.

As supersonic flight testing proceeded towards the maximum design airspeed and hence the intake ramp angle approached its maximum value, surges began to occur in the right hand installation. Again a handed problem indicated swirl to be the engine destabilising agent. The origin of the swirl being the thickened boundary layer on the subsonic ramp caused by the high diffusion rate associated with the high ramp angle (see chapter 5.4).

To reduce the swirl content of the duct flow, two fences (Fig. 18a) were introduced into the duct at about two engine diameters upstream of the engine face, one on the bottom centre line, the other on the inboard centre line. During model tests these fences had been shown to substantially reduce swirl (Fig. 18b).

Subsequent flight tests were highly successful, permitting flight to the maximum Mach number/air speed combination. Fig.18c indicates the improved intake/engine operating range due to the provision of fences.

The cowl fence described in chapter 6.2 also showed a potential for reducing swirl at supersonic Mach numbers (Fig. 18d). Flight tests for final proof are being conducted.

7. INTAKE AIRFRAME INTERACTIONS

In a close coupled configuration similar to that of Tornado, the flow field induced by the intake, in its different modes of operation, has significant modifying influences on the overall aircraft aerodynamics.

By carefully planned and phased wind tunnel tests during the definition phase of Tornado such problems were surfaced and solved whilst the aircraft configuration was relatively fluid.

The lifting vortices shed from the inboard and outboard corners of the leading edge of the intake produce sidewashes at the fin which reduce the effectiveness of the fin in sideslip (Fig. 19).

The vortex from the inboard intake corner tends to be de-stabilising at low incidence. At high incidence the outboard vortex is pronounced and in conjunction with the forebody and canopy vortices can cause a noticeable reduction in weathercock stability. The high aspect ratio fin of Tornado maintains its effectiveness under such conditions.

When the intake is running at less than full mass flow, spillage around the swept outboard sideplate produces a vortex. At high incidence the vortex breaks down and passes over the wing not sensibly interacting with other aircraft components.

At low to moderate incidence the vortex is constrained to pass close to the tailplane root unloading the leading edge of the tailplane and driving the aerodynamic centre aft (Fig. 20).

The shift leads to a reduction in effective tailplane stiffness and it was necessary to change the planform slightly by making minor changes to the tailplane leading edge to recover flexible aircraft longitudinal stability.

8. CONCLUDING REMARKS

In this paper we have attempted to highlight some of the problems encountered by the intake designers in the real world of design and development of a successful Multi Role Combat Aircraft.

The designer must be aware of what the overall weapon system design strategy is and recognise where to concentrate his main effort, considering not only induction system problems but also intake interactions with other aircraft components.

The major component with which the intake interacts is the engine. We do not apologise for making such an obvious statement. The importance of close continuous contact and co-operation with the engine manufacturer cannot be overstressed neither can testing of the engine-intake combination at the earliest juncture such that potential problem areas can be highlighted, discussed and resolved in the most cost effective way for the overall propulsion system.

In this way the 'gods of compatibility and performance' are equally propitiated and the success of the overall project is greatly enhanced.

REFERENCES

- 1 J. Peikert "An Air Intake Control System for a Supersonic Fighter Aircraft"
AGARD Conference Proceedings No. 151, Paper No. 18
- 2 K.W. Lotter "Dynamic Pressure Loads in the Air Induction System of the Tornado
N.C. Bissinger Fighter Aircraft"
AGARD Conference Proceedings No. 248, Paper No. 2

ACKNOWLEDGEMENT

The authors wish to acknowledge their indebtedness to the Directors of BAe, Aircraft Group, Warton Division and MBB, Unternehmensbereich Flugzeuge for permission to publish this paper. The views expressed are their own and not necessarily those of their Company.

Because of the large amount of work involved, the development of a complex intake has to be a team enterprise. However, it is not possible to name everybody here. It must suffice to say that the sum of individual efforts within PANAIA intake design team has led to a successful conclusion.

The authors would also like to thank their colleagues at ARA, DFVLR, NGTE and RAE for their close cooperation during the development of the Tornado intake.

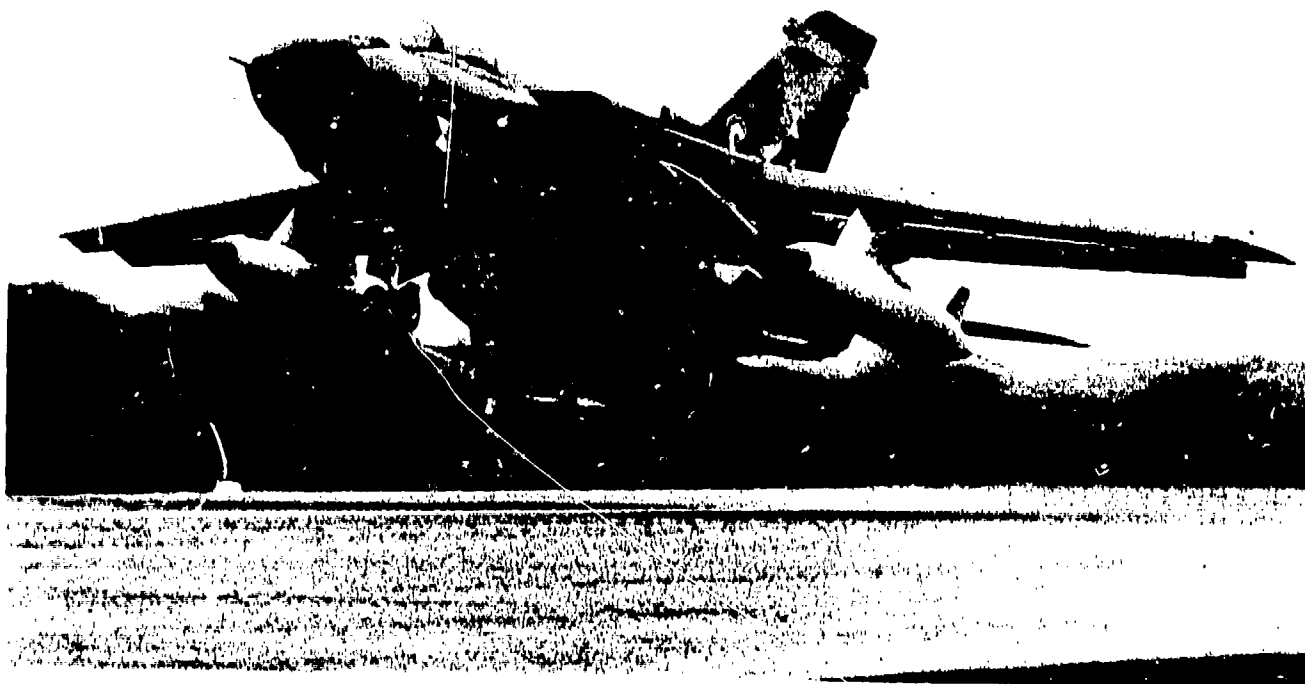
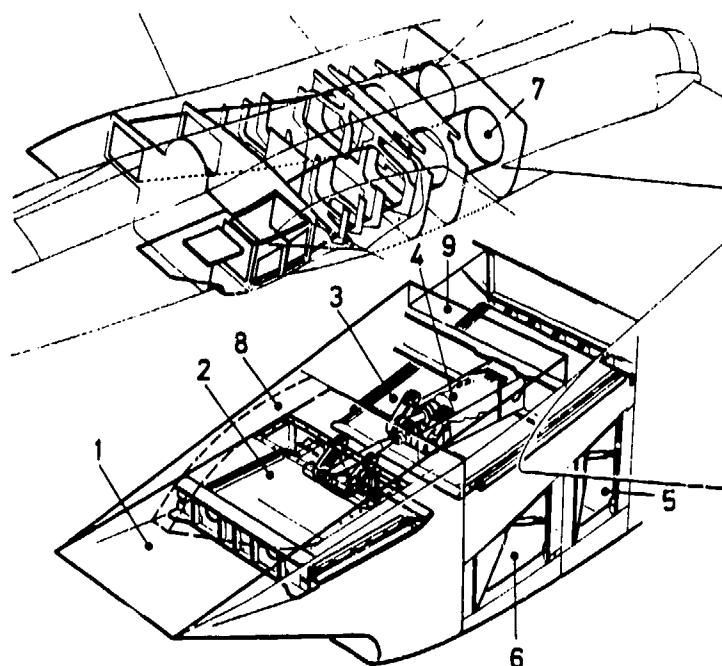


Fig. 1 Multi-Role Combat Aircraft Tornado



- | | |
|------------------|------------------------------------|
| 1 FIRST RAMP | 5 REAR AUXILIARY INTAKE |
| 2 SECOND RAMP | 6 FORWARD AUXILIARY INTAKE |
| 3 THIRD RAMP | 7 INTAKE DUCT |
| 4 RAMPS ACTUATOR | 8 BOUNDARY LAYER DIVERTER |
| | 9 RAMP BOUNDARY LAYER BLEED OUTLET |

Fig. 2 Engine Intake Layout

Responsible Company	Scale	Purpose	Test Site	Test Range	Re-No (based on capture height)	Special Features
AIT	1/4	auxiliary intake development	AIT	M = 0		
MBB	1/4	low speed intake development	DFVLR	#68 m/s		suction available
MBB	1/6.5	internal performance; drag; instantaneous distortion; swirl	DFVLR ARA RAE	static to supersonic	1.2×10^6	suction available; extreme incidence and sideslip combinations
BAA Aircraft Group Warton Div.	1/10	internal performance; drag	BAA Warton	supersonic	1.7 to 2.5×10^6	"isolated" intake tests and "fuselage on" tests; intake cell balance mounted for drag
BAA Aircraft Group Warton Div.	1/7	swirl	BAA Warton	40 m/s		suction available
PANAVIA, TURBO-UNION/ NATIONAL GAS TURBINE ESTABLISHMENT	1/1	compatibility margin evaluation of engine-intake combination; intake control system dynamics evaluation	NGTE Pyestock	supersonic	5.5×10^6	isolated intake; pitch transients; Mach transients; temperature transients; engine power off-take; engine bleed effects; reheat effects; buzz + surge characteristics

Fig. 3 Tornado Intake Development Models

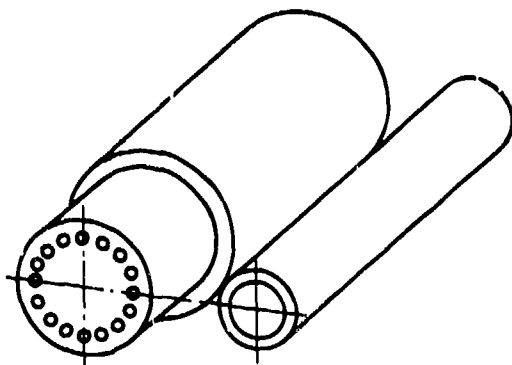


Fig. 4a Kulite and Pitot Probes

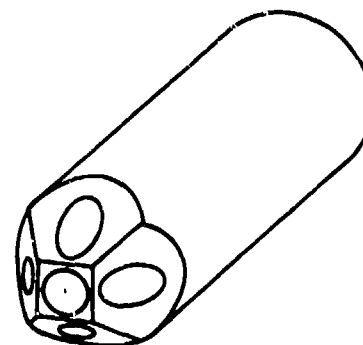


Fig. 4c Five Hole Probe

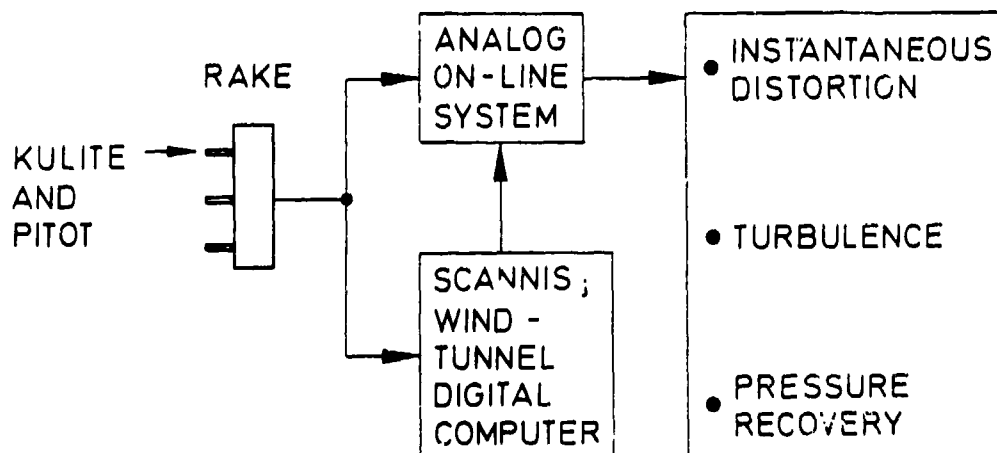


Fig. 4b Data Reduction Flow Diagramme

Fig. 4 Probes and Data Reduction System

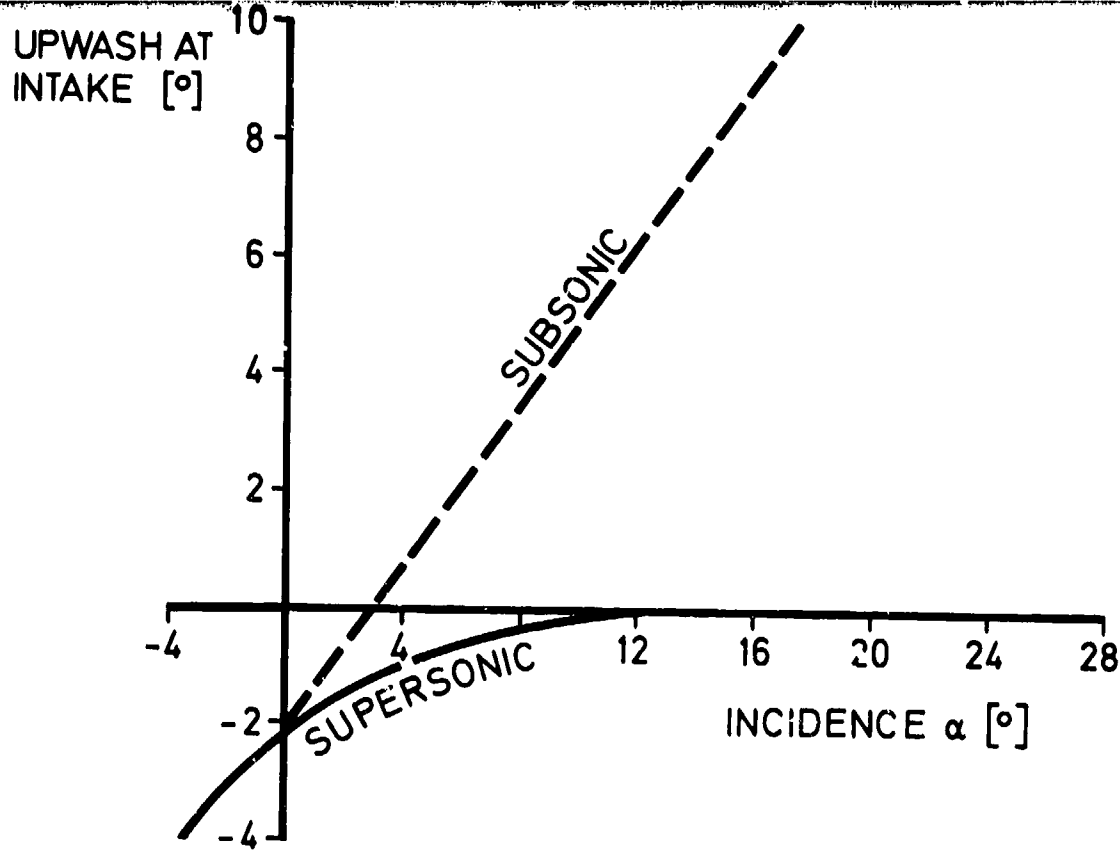


Fig. 5 Upwash at Intake Location

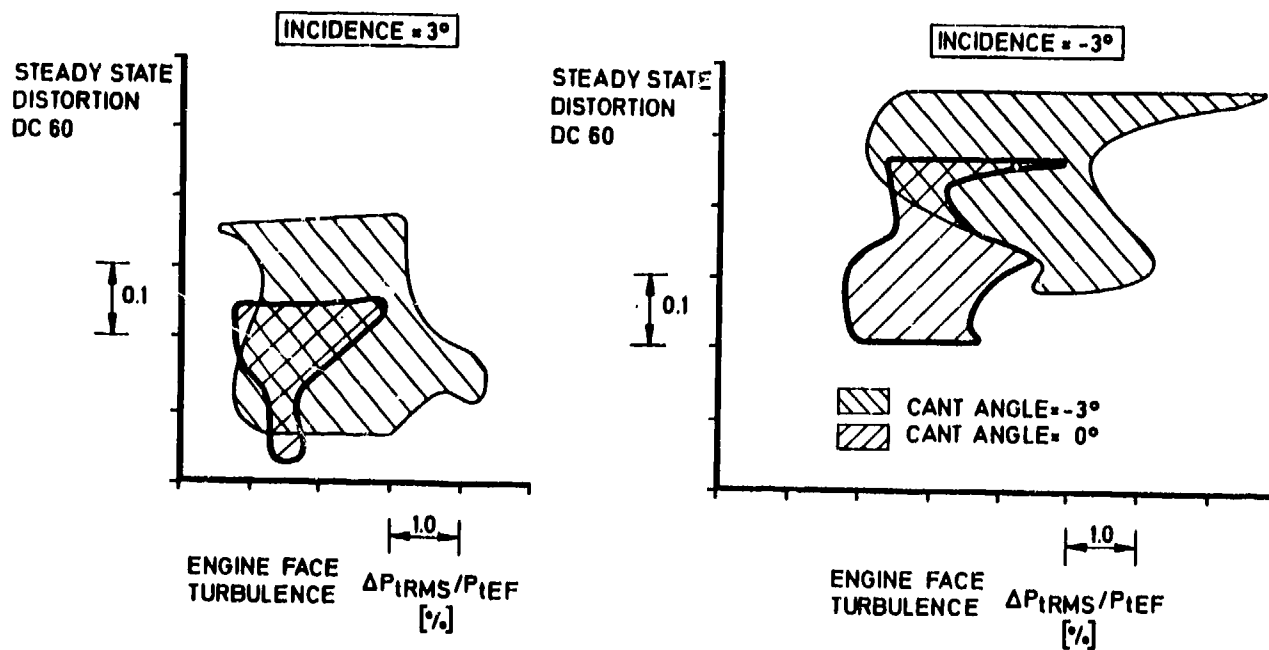


Fig. 6 Comparison of Cant Angle Effects on Intake Distortion over Intake Useful Operating Range at $M = 2.0$

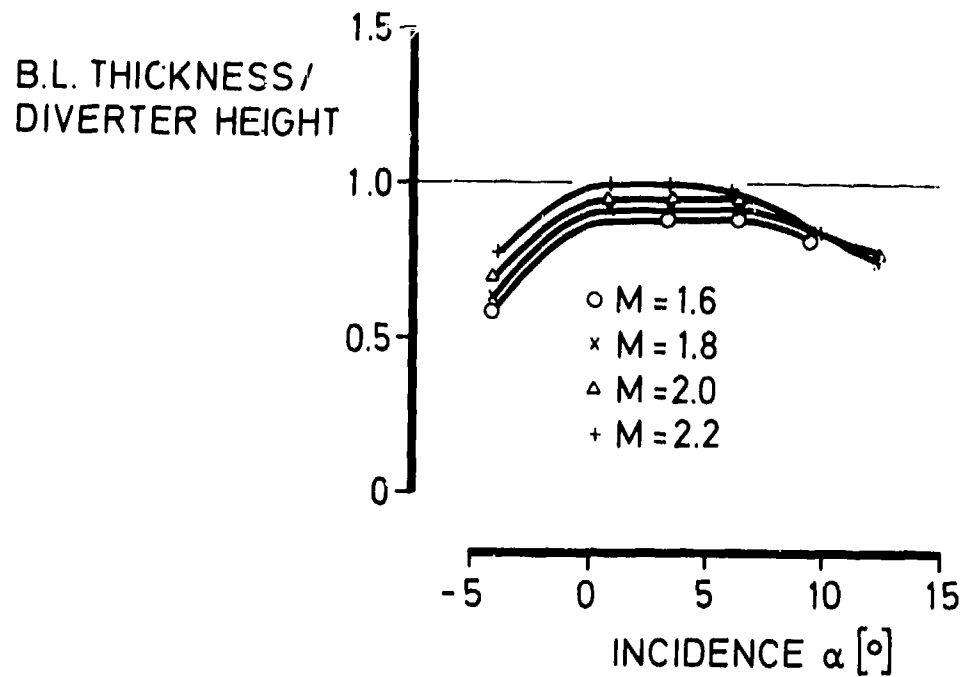
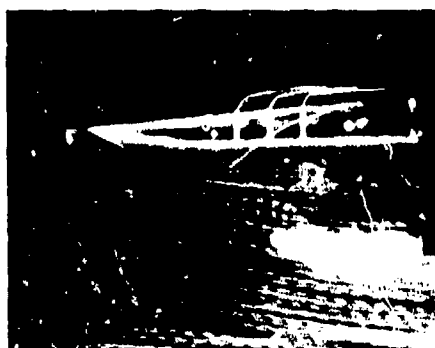
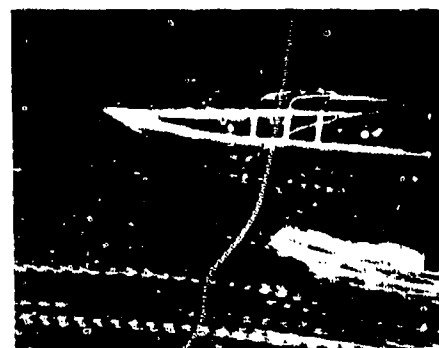


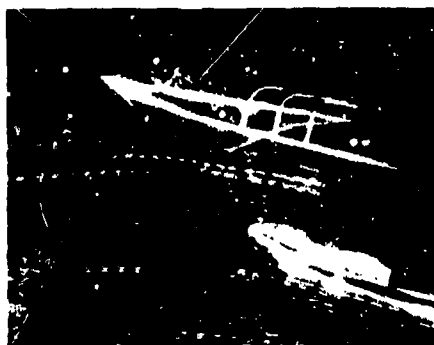
Fig. 7 Variation of Fuselage B.L. Thickness with Incidence at Intake Leading Edge Based on Model Test Data



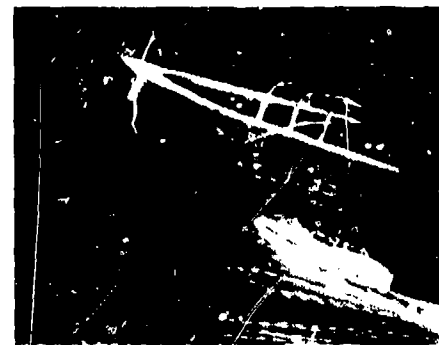
INCIDENCE $\alpha = 0^\circ$



INCIDENCE $\alpha = 5^\circ$



INCIDENCE $\alpha = 15^\circ$



INCIDENCE $\alpha = 20^\circ$

CAPTURE RATIO $A_0/A_C = 0.65$

Fig. 8 Flow Visualization Photographs: Variation of Cowl Flow with Incidence

COMPATIBILITY PARAMETERS ARE
FOR 20° INCIDENCE AND FULL
MASS FLOW THROUGH INTAKE

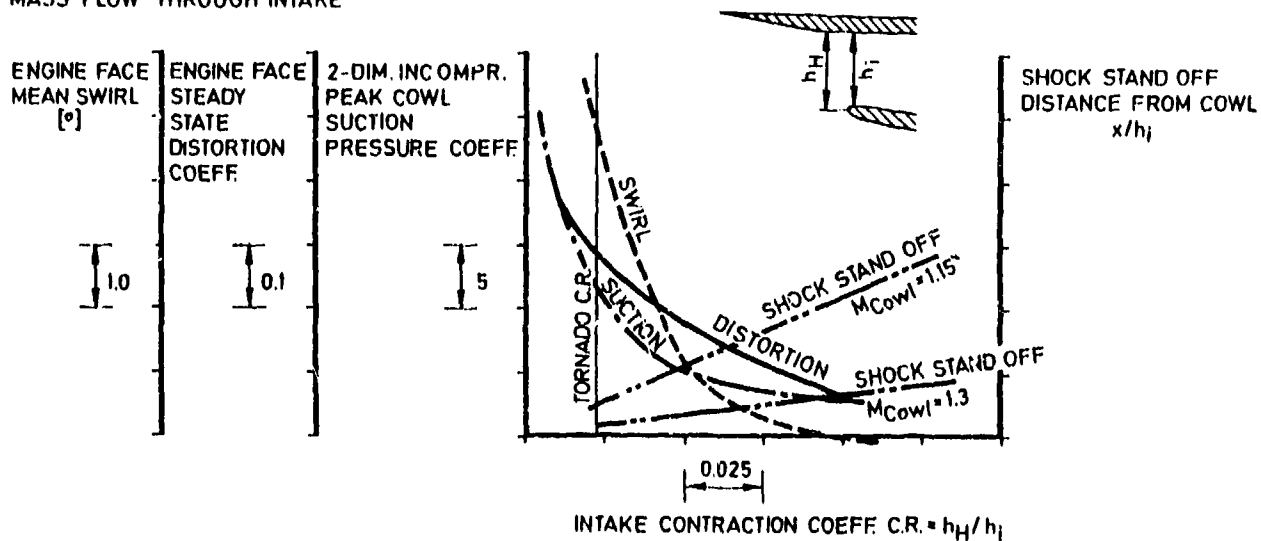


Fig. 9 Intake Cowl Design Problem

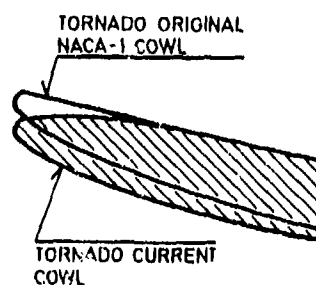


Fig. 10 a Comparison of Cowl Shapes

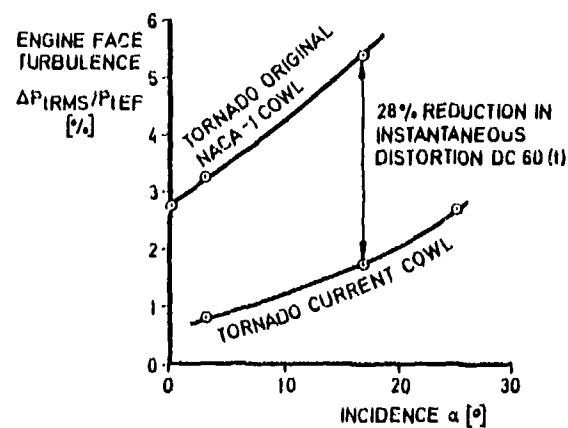


Fig. 10 b Engine Face Turbulence for Different Cowl Shapes

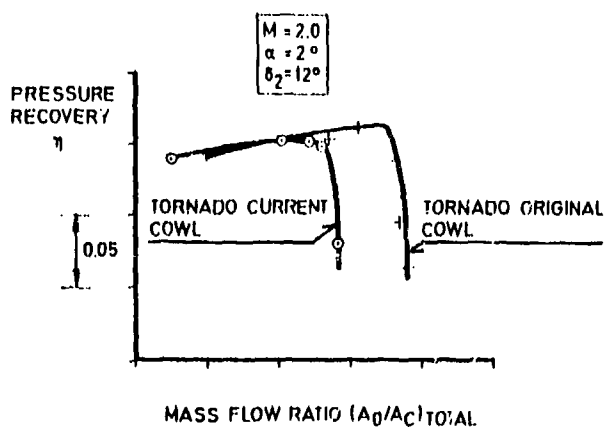


Fig. 10 c Pressure Recovery for Different Cowl Shapes

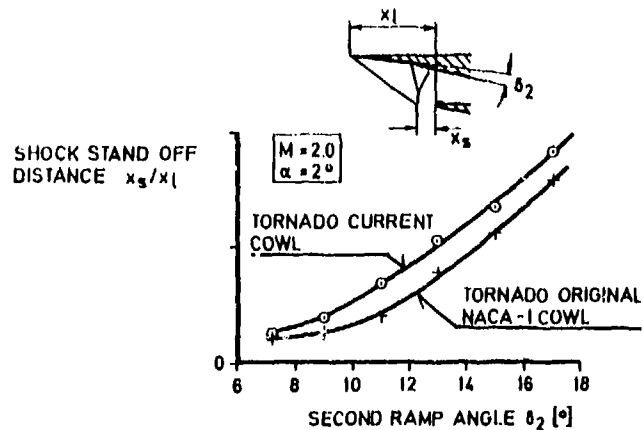


Fig. 10 d Shock Stand Off Distance for Different Cowl Shapes from Model Tests

Fig. 10 Effect of Cowl Bluffness on Internal Performance

INSTANTANEOUS
DISTORTION
DC 60 (t)

0.1

Critical Level
DC 60 (t)

$M = 0.5$

$M = 0.7$

TARGET
INCIDENCE

MAX. DRY POWER SETTING
SEA LEVEL

5
INCIDENCE α [°]

Fig. 11a Instantaneous Distortion Versus Incidence

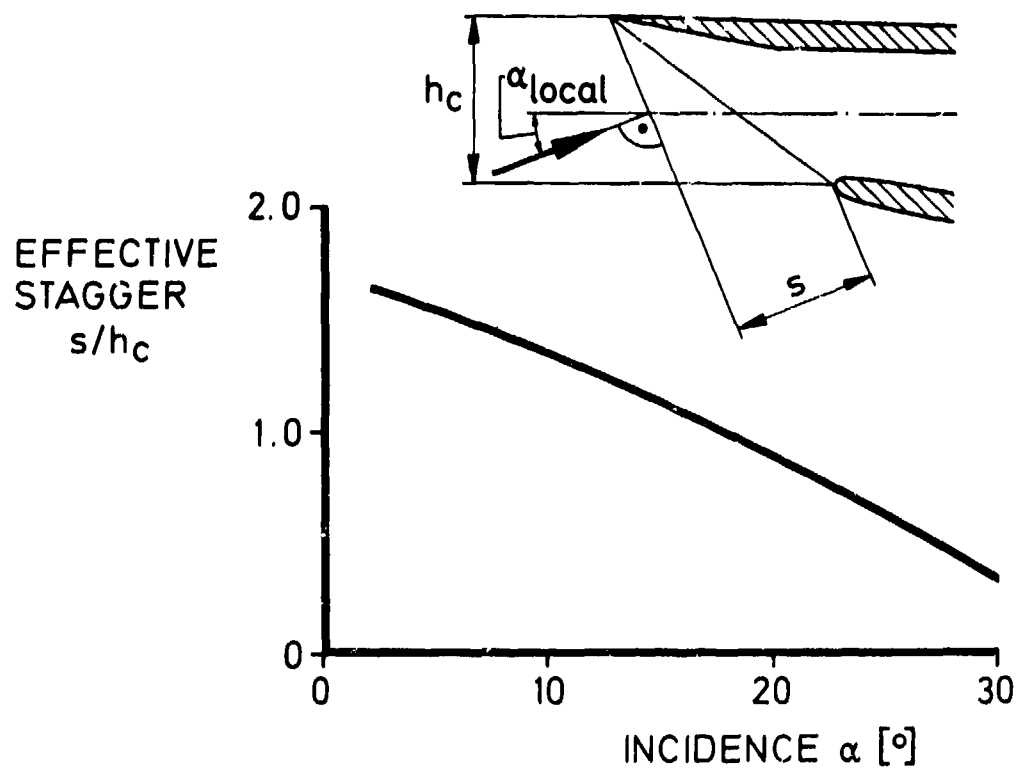


Fig. 11b Reduction of Effective Stagger with Increasing Incidence

Fig. 11 Instantaneous Distortion and Effective Stagger

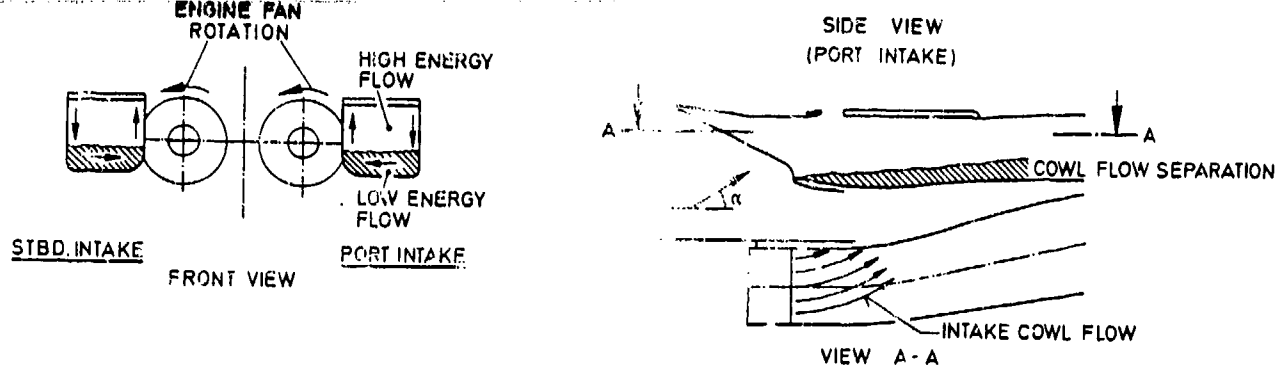


Fig. 12a Secondary Flows in Intake at Subsonic Mach Numbers and High Angles of Attack

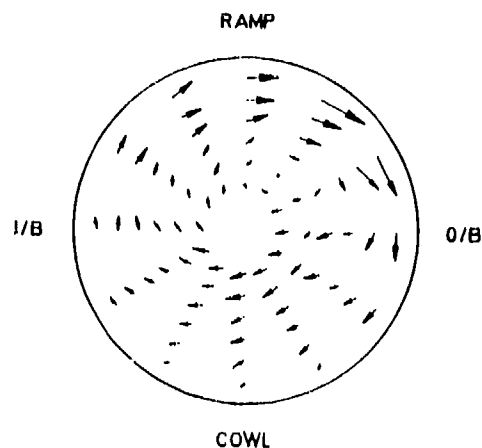


Fig. 12b Flow Angles at Engine/Intake Interface

PORT INTAKE
LOOKING AFT

$M = 0.7$
 $\alpha = 20^\circ$
 $\delta_2 = -6^\circ$
 MAX DRY ENGINE
 MASS FLOW

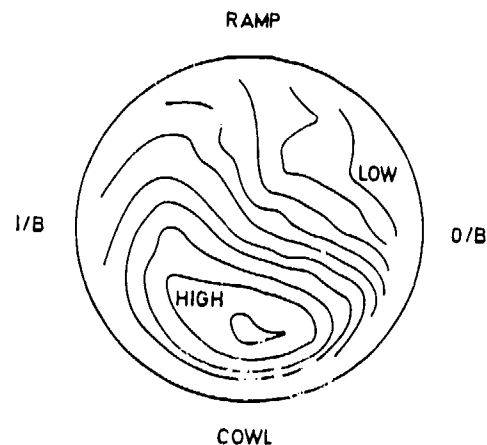


Fig. 12c Isobars at Engine/Intake Interface

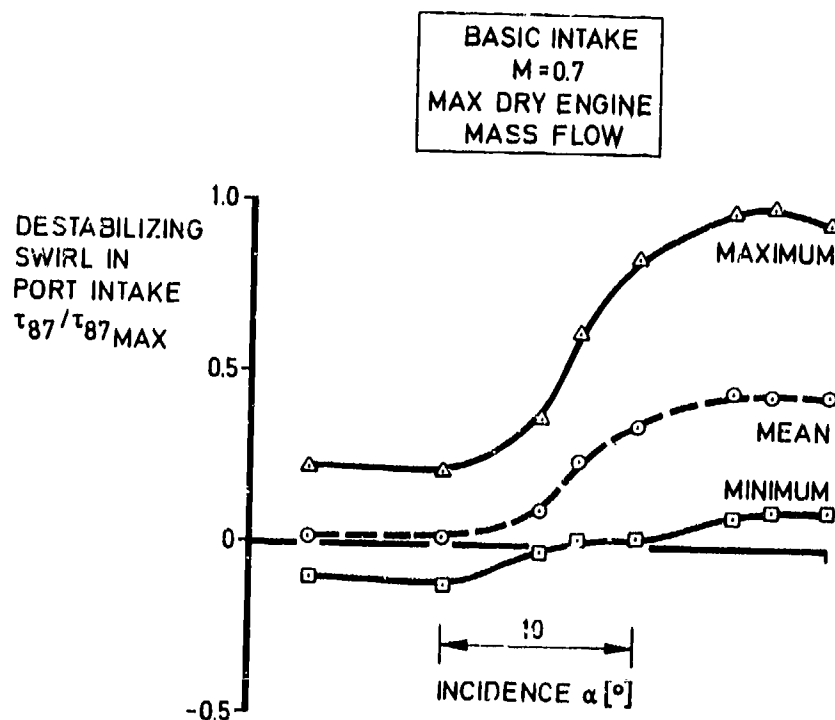


Fig. 12d Maximum, Mean and Minimum Swirl Versus Incidence

Fig. 12 Subsonic, High Angles of Attack Problem

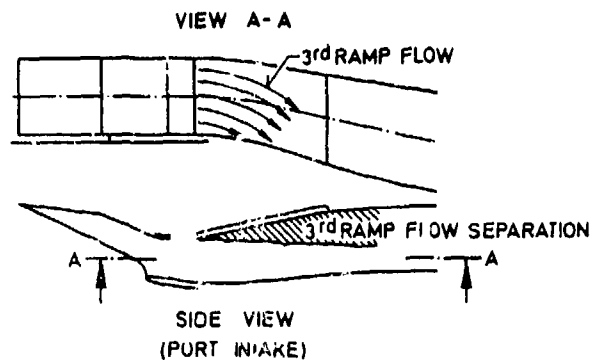
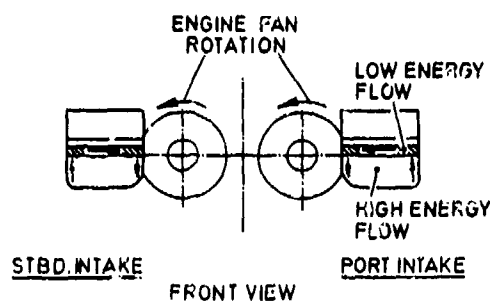


Fig. 13a Secondary Flows in Intake at Supersonic Mach Numbers and High Ramp Angles

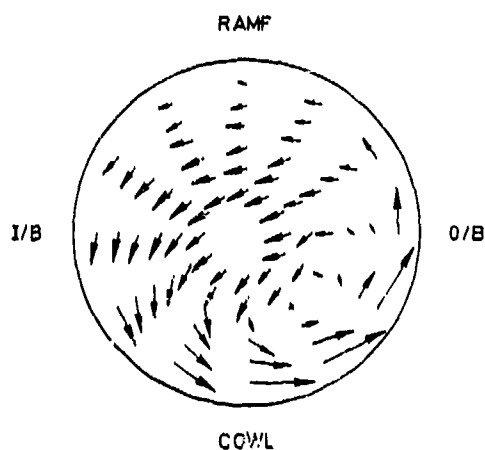


Fig. 13b Flow Angles at Engine/Intake Interface

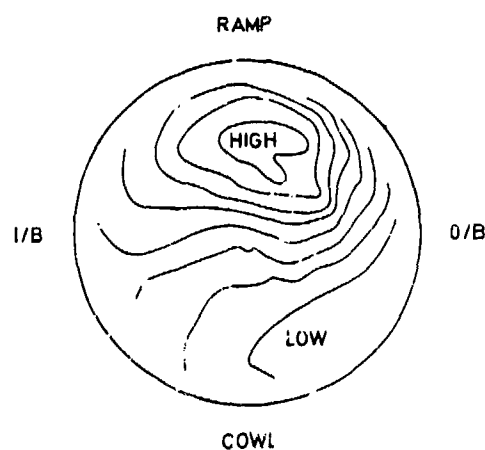


Fig. 13c Isobars at Engine/Intake Interface

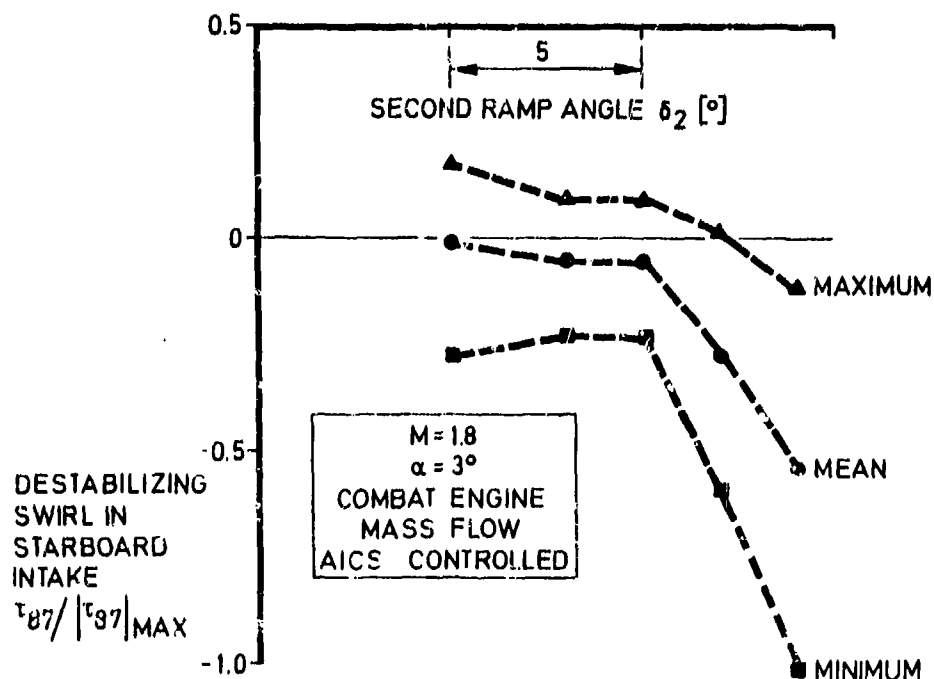


Fig. 13d Maximum, Mean and Minimum Swirl Versus Second Ramp Angle

Fig. 13 Supersonic, High Ramp Angles Problem

ALL LEADING EDGES
CONTINUOUSLY
ANTI-ICED

- 1 TOP LIP SPRAYMAT
- 2 SIDE LIP SPRAYMAT (OUTBOARD)
- 3 SIDE LIP DUMMY MAT (OUTBOARD)
- 4 BOTTOM LIP SPRAYMAT
- 5 SIDE LIP DUMMY MAT (INBOARD)
- 6 SIDE LIP SPRAYMAT (INBOARD)

Fig. 14 Heated Areas of Intake

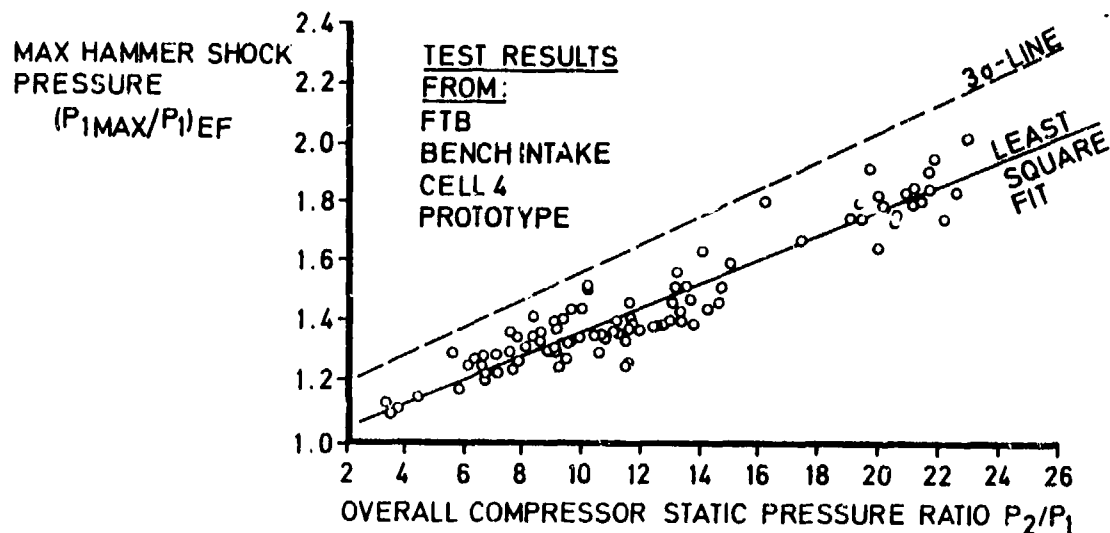


Fig. 15a Maximum Hammer Shock Pressure Versus Compressor Pressure Ratio

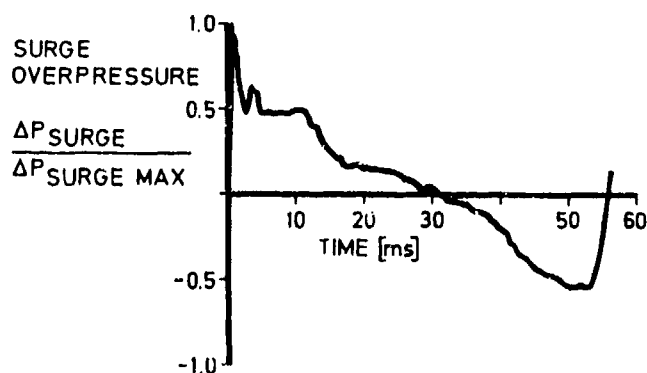


Fig. 15b Typical Surge Signature

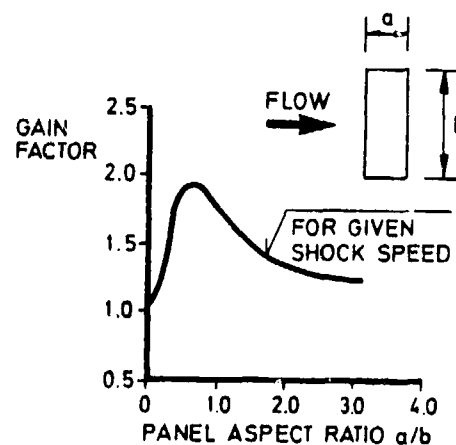


Fig. 15c Possible Surge Load Amplifications for Intake Skin Panels

Fig. 15 Intake Surge Loads

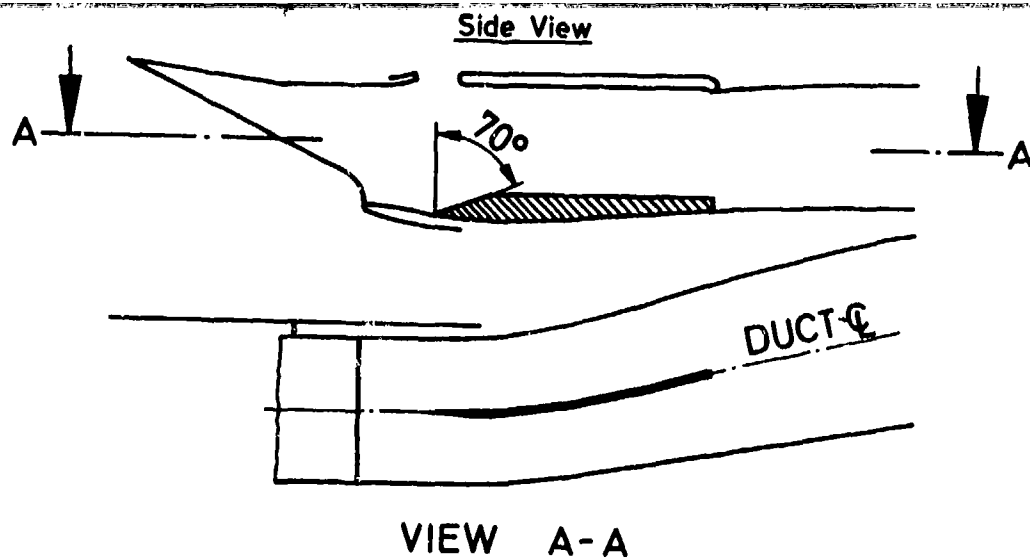


Fig. 16a Cowl Fence in Tornado Intake

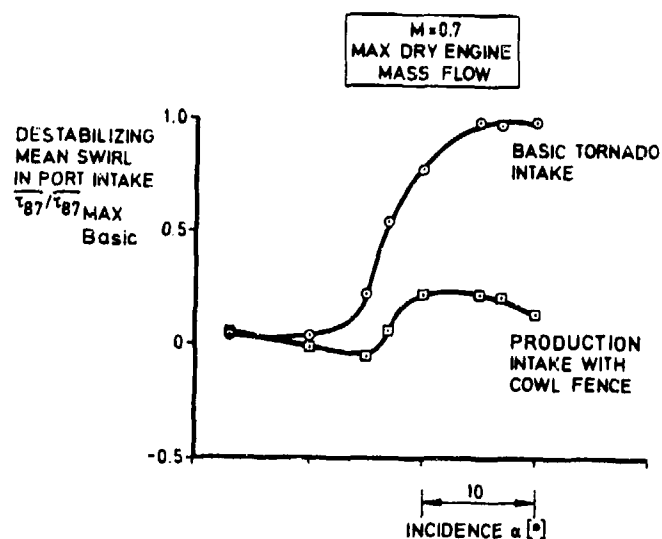
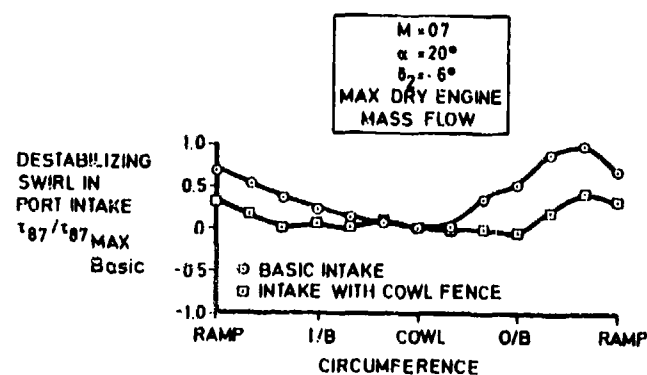


Fig. 16b Reduction in Mean and Local Swirl Due to Cowl Fence

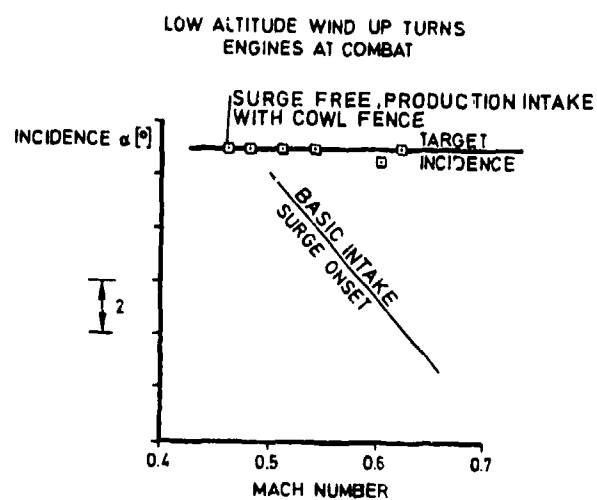


Fig. 16c Extension of Incidence Limit Due to Cowl Fence

Fig. 16 Subsonic High Incidence Problem Solution in Port Intake

SECOND WEDGE
ANGLE δ_2 [°]

$M=1.6$
 $\alpha=2^\circ$

2

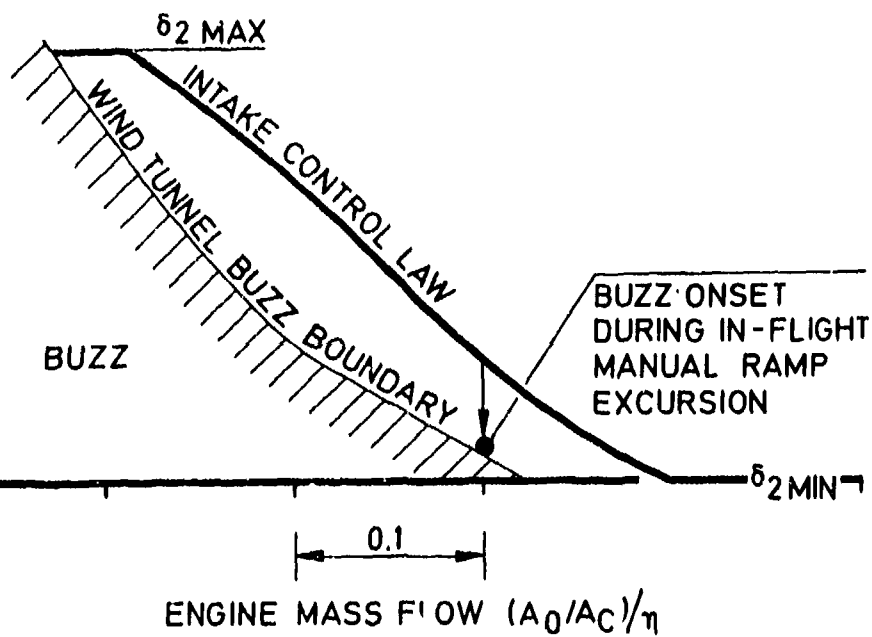


Fig. 17a Buzz Onset

BLEED VOID
PRESSURE
 P_{SB}/P_{t0}

OPEN SYMBOLS: W/T DERIVED
CLOSED SYMBOLS: FLIGHT MEASUREMENTS

$M=1.8$
 $\alpha=3^\circ$

0.1

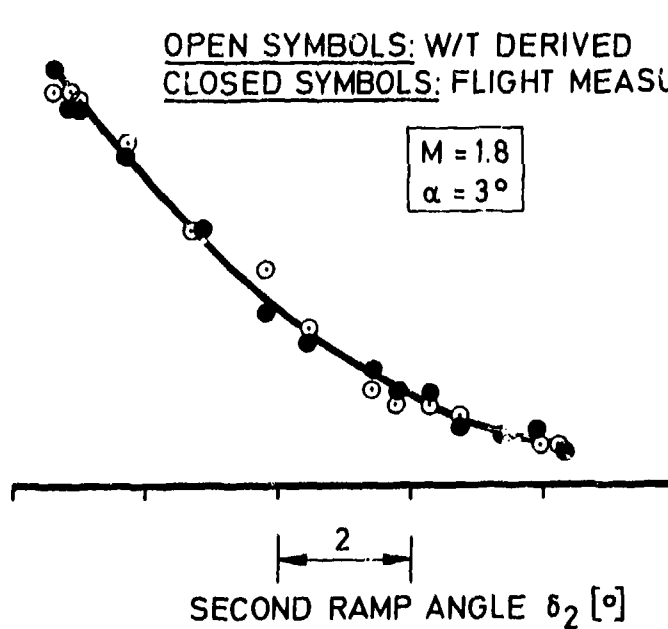


Fig. 17b Change of Intake Control Pressure with Second Ramp Angle

Fig. 17 Comparison of Flight and Windtunnel Data

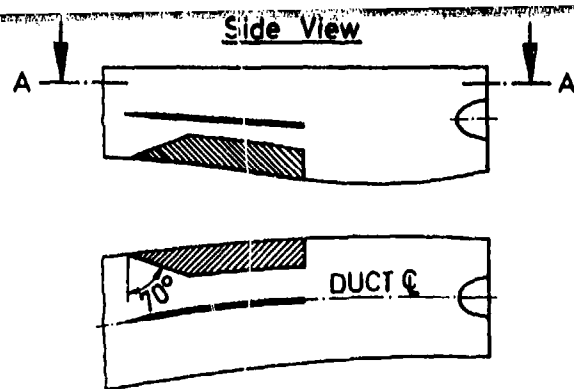


Fig. 18a Duct Fences In Starboard Intake Duct

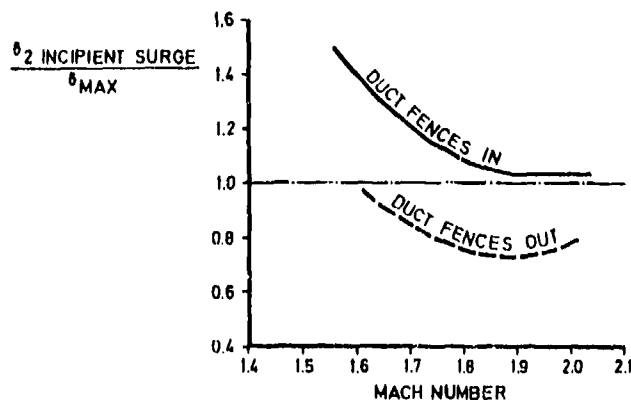


Fig. 18c Extension of Mach Number Limit Due to Duct Fences

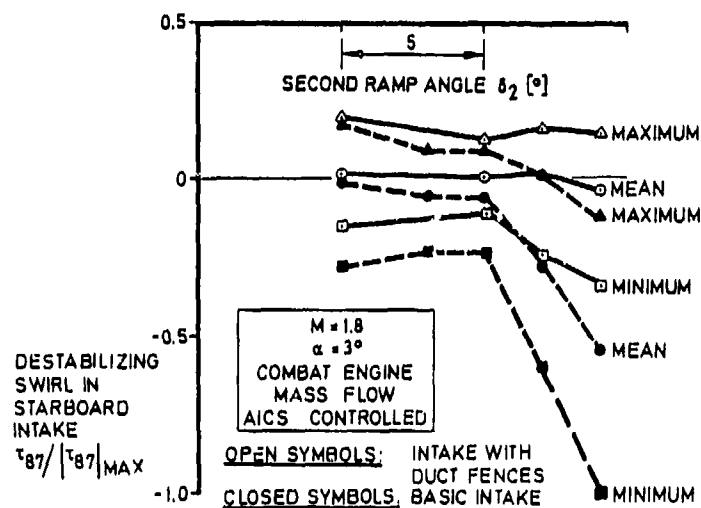


Fig. 18b Reduction in Minimum, Mean and Maximum Swirl Due to Duct Fences

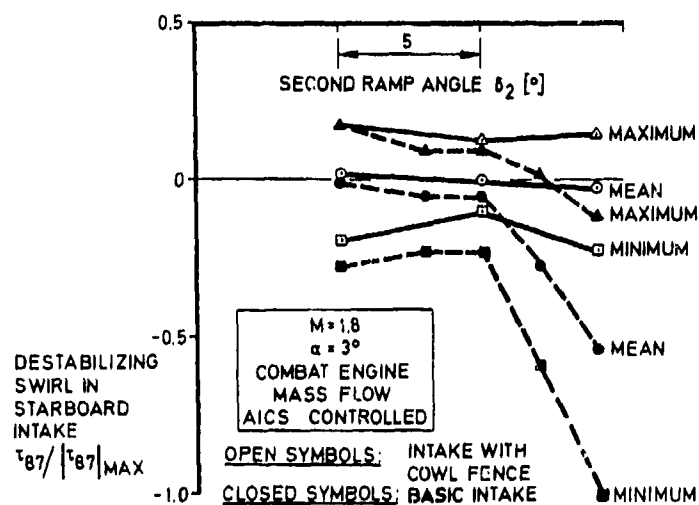


Fig. 18d Reduction in Minimum, Mean and Maximum Swirl Due to Cowl Fence

Fig. 18 Supersonic High Ramp Angle Problem Solution in Starboard Intake

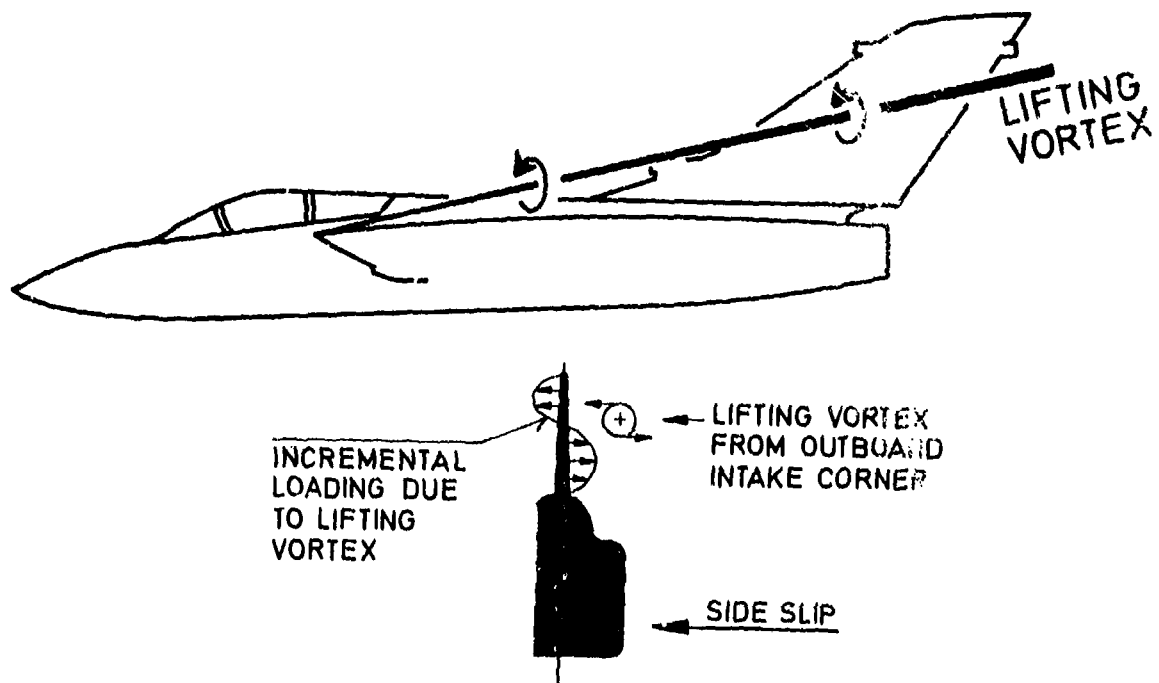


Fig. 19 Intake Lifting Vortex Interaction with Fin at High Incidence

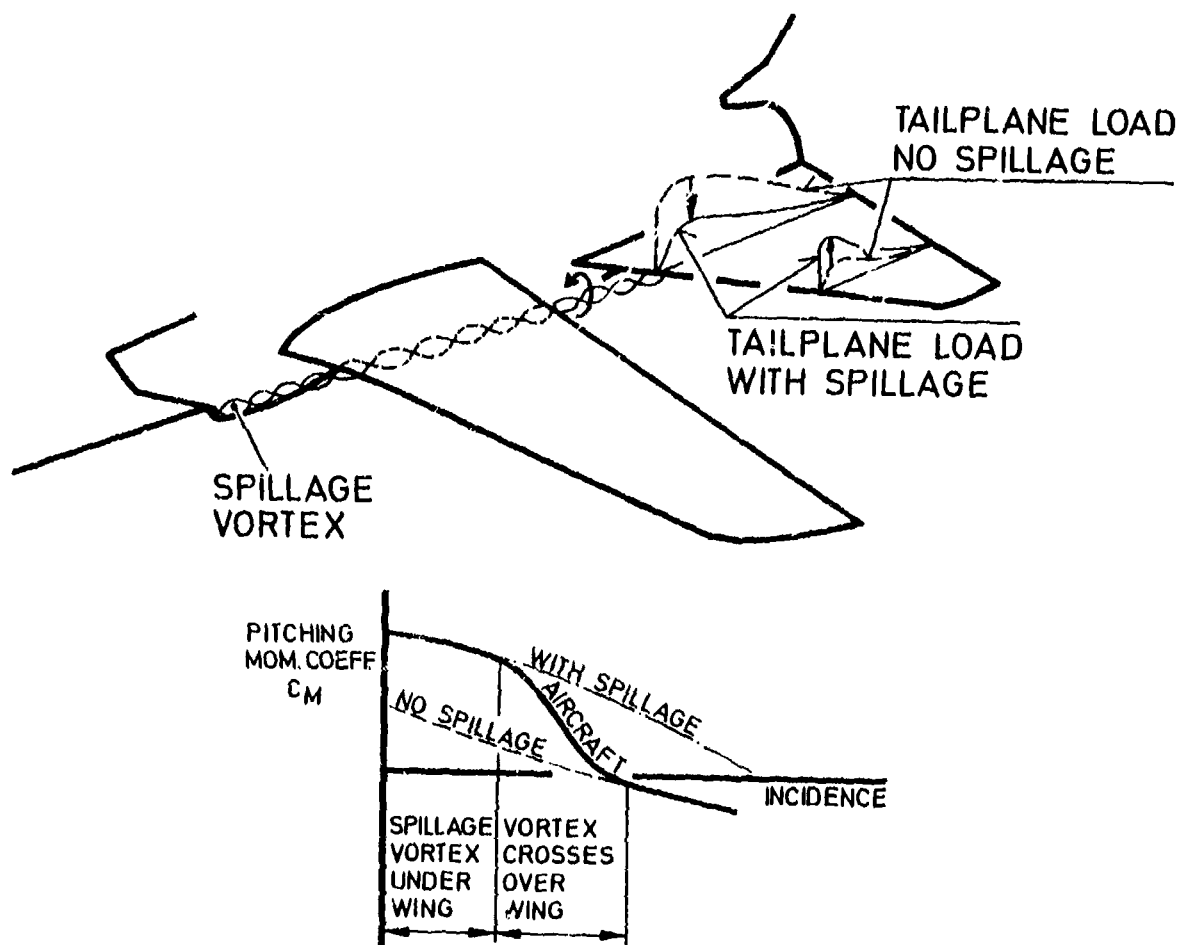


Fig. 20 Intake Spillage Vortex Interaction with Tailplane at Low Incidence

INTEGRATION OF ADVANCED EXHAUST NOZZLES

by

Douglas L. Bowers
James A. Laughrey
Air Force Wright Aeronautical Laboratories
Wright-Patterson Air Force Base, Ohio 45433
USA

SUMMARY

Airframe/propulsion integration plays an ever increasing role in aircraft design as the mission requirements for advanced tactical aircraft become more stringent. Reduced cruise drag, increased maneuverability and improved short takeoff and landing (STOL) performance have been associated with integration of advanced exhaust nozzles. Advanced exhaust nozzles can be either axisymmetric or nonaxisymmetric and may have independent throat and exit area control, thrust vectoring and thrust reversing.

The potential for significant aircraft performance improvements lies in the proper utilization of advanced exhaust nozzle technology in concert with other emerging aircraft technologies. Potential benefits examined for advanced exhaust nozzles include reduced cruise drag, especially in twin jet aircraft and, for propulsion installations where the nozzle exit is near a lifting surface, a possible increase in lift that allows a reduced cruise angle of attack and therefore reduced cruise drag. It is shown that an advanced thrust vectoring nozzle can be used in conjunction with reduced static margin and a canard to provide aircraft trim and reduce total aircraft cruise drag.

Thrust vectoring and thrust reversing are considered for maneuvering and STOL performance. Large improvements in instantaneous maneuver or a smaller aircraft for the same mission requirements can be derived from thrust vectoring. Thrust reversing is identified as a desirable option for STOL performance on high thrust-to-weight military aircraft. While an axisymmetric exhaust nozzle can incorporate some of these capabilities, a non-axisymmetric exhaust nozzle can offer a design flexibility which provides the required reverse thrust and additional installed aerodynamic benefits.

LIST OF SYMBOLS

ADEN	Augmented Deflector Exhaust Nozzle	TV	Thrust vectoring
AR	Aspect Ratio	$W/S_{WT/O}$	Wing loading at takeoff
Axi	Axisymmetric	2-D	Two dimensional
A/B	Afterburning	2-D C-D	Two dimensional convergent divergent
α	Angle of Attack		
δ_c	Canard deflection angle		
δ_N	Nozzle deflection angle		
C_{FGRev}	Reverse gross thrust coefficient		
C_L	Lift coefficient		
C_D	Drag coefficient		
C_M	Moment coefficient		
C_p	Pressure coefficient		
C_T	Thrust coefficient		
C_{T-D}	Thrust-minus-drag coefficient		
kt	Knots		
G	Load factor		
NPR	Nozzle pressure ratio		
Sec	Seconds		
STOL	Short takeoff and landing		
TOGW	Takeoff gross weight		

1. INTRODUCTION

During the past 10 to 15 years, the technology of the jet engine exhaust nozzles and its integration into military aircraft has produced some rather unique concepts. The main concern during the 60's and early 70's was designing configurations where the installed exhaust system did not cause excessive drag or thrust loss. The research and development programs being conducted investigated design variables including nozzle type, tail location, type of interfairing, and nozzle spacing. Configurations such as the F-16 and F-18 are examples of aircraft with axisymmetric nozzle installations that are very efficient with very low drag and thrust penalties. Other configurations, however, did not fare as well because of various design restrictions. Among the more promising design schemes proposed to minimize the drag were concepts incorporating nonaxisymmetric or two-dimensional nozzles into aircraft. Wind tunnel data from exploratory research models indicated that it might be possible to reduce afterbody/nozzle drag of twin engine aircraft with non-axisymmetric nozzles due to a reduction in separated flow regions.

An indication of possible improved performance was presented in Reference 1 where it was concluded "For a twin-engine installation, the thrust-minus-aftbody drag performance of the twin two-dimensional [wedge] nozzle integration is significantly higher, for speeds greater than a Mach number of 0.8, than the performance achieved with twin axisymmetric nozzle installations". The data, shown in Figure 1, indicates a thrust-minus-drag penalty for a twin axisymmetric nozzle installation compared to a single axisymmetric nozzle of equal nozzle flow area. This single versus twin installation penalty does not appear to exist for the nonaxisymmetric nozzle. A reduction of the external wetted area was given as a reason for the better performance of the twin nonaxisymmetric nozzle.

Other experimental data, reported in Reference 2, indicated that vectoring the flow of a nonaxisymmetric nozzle near the trailing edge of a wing generated a lift increment similar to that obtained from experiments with jet flaps. In this 1976 summary of related research, conducted at the NASA Langley Research Center, it was concluded that induced effects from thrust vectoring generally resulted in increases in lift and decreases in drag at constant angle of attack. This lift increment was caused in part by a component of the thrust and in part by the exhaust jet favorably influencing the flow over the lifting surface. The latter component is the result of a reduction in the separated flow, similar to that obtained with boundary layer control, and to a favorable influence on the flow around the wing sometimes referred to as "supercirculation". In general, the higher the aspect ratio or width of the nozzle, the greater the increment of induced lift. With these improvements in lift, discussion in the technical literature began to reflect possible improvements in fighter aircraft maneuverability and agility, particularly in the flight regime away from the design point of the wing.

A related development was the emergence of the vectored-engine-over-wing (VEO) concept, an adaptation of upper surface blowing (USB) to a fighter aircraft. This scheme, reported in Reference 3, uses the jet exhaust to change the wing aerodynamics for improved lift and also produce vectored thrust. Once again, the improved wing aerodynamics is attributable to thrust induced circulation and the reduction of separated flow on the wing flap. The coupling of spanwise blowing with the VEO concept gave promise of further improvement of lift, particularly at low speeds and high angles of attack.

The benefits attributed to nonaxisymmetric nozzles and the VEO concept are overall drag reduction, improved lift-drag polars, and improved aircraft agility. However, the reduction in drag of an integrated nonaxisymmetric nozzle on a closely spaced twin-jet aircraft turned out to be more difficult to accomplish than the original data (References 1, 4) indicated, particularly when trimmed aircraft performance was finally determined. The information being generated indicated that merely recontouring the aft fuselage for non-axisymmetric nozzles, particularly one designed originally for axisymmetric nozzles, was not sufficient to realize an aftbody drag reduction. The inclusion of vectoring with these concepts did hold some promise if integrated into a lifting surface and if it could be trimmed.

Until the last 3 or 4 years most of the interest in advanced nozzles has been how they might be used to improve cruise performance and aircraft agility or maneuverability. More recently, operational considerations have generated an increased interest in short takeoff and landing (STOL) capability where it appears propulsive lift concepts utilizing vectorable and reversible nonaxisymmetric nozzles might be of benefit. Initial assessment of the STOL performance requirements indicates that the vectoring capability will be used both on takeoff and landing. The nozzle thrust deflections required, however, are larger than the 30 degree maximum desired for maneuvering and cruise trim. Preliminary investigations have shown a need of up to 25 degrees of vectoring for takeoff and 60 degrees for landing. The same studies also show a need for almost immediate thrust reversing after touchdown if landing roll distances are to be less than 1000 feet. Current efforts are being directed to determine if vectoring and reversing can be accomplished with an axisymmetric nozzle. With the high vector angles needed and the complexity of a reverser, however, it appears that a nonaxisymmetric nozzle may be best suited for propulsive lift STOL.

This paper discusses some of the more pertinent attributes of advanced nozzles (both axisymmetric and nonaxisymmetric) and their incorporation into an aircraft to improve cruise performance, maneuverability and STOL operation. Most of the discussion will address the installed aerodynamic performance of the nozzles. A more complete discussion needs to include information on structural integrity, cooling requirements and the difference in weights for the various concepts.

2. ADVANCED EXHAUST NOZZLE INTEGRATION FOR CRUISE PERFORMANCE

The F-111 aftbody/nozzle, Figure 2, was designed for optimum thrust and not necessarily minimum drag. As much as 30 to 60 percent of the total aircraft drag has been attributed to the aftbody/nozzle and would therefore appear to be a fruitful area for a drag reduction by utilizing advanced exhaust nozzles. The F-15 aftbody/nozzle, shown in Figure 3, appears to be an aerodynamically tailored area. The predominantly negative pressure coefficient contours shown in Figure 4 indicate that the F-15 nozzle boattail forces in cruise are essentially all drag with only a small amount of thrust on the lower boattail surface.

Based on these examples, airframe/propulsion integration specialists proposed the nonaxisymmetric or 2-dimensional (used synonymously) exhaust nozzle to reduce cruise drag for advanced tactical aircraft. The benefits of this nozzle were purported to be 1) reduced interference drag with aircraft booms and tail surfaces, 2) reduced aftbody/nozzle flow separation, and 3) overall better integration with the "rectangular" fuselage of twin engine aircraft. References 1-16 are representative of efforts seeking to identify and quantify these attendant drag benefits.

To date, the expected payoff in reduced cruise drag for advanced exhaust nozzles has been difficult to realize. Indications are that the airframe/propulsion integration of these propulsion components must be done very carefully. The message is clear concerning the installation of nonaxisymmetric nozzles on future aircraft, that is, the installed drag benefit is not inherent for these exhaust nozzles. The aftbody contour upstream of nozzle boattail is as important as the nozzle boattail contour. The proper contouring for an advanced exhaust nozzle will require analytical tools which go beyond simple empirical methods. Advanced paneling methods and Navier-Stokes analysis may be necessary for the proper integration of advanced exhaust nozzles into an aircraft.

For the high fineness ratio air-to-surface aircraft, Figure 5, which is designed for a cruise Mach number of 2.0, the proper aftbody/nozzle contouring for different nozzle types is critical. The aftbody/nozzle contours and the resulting pressure distributions for an axisymmetric and two nonaxisymmetric exhaust nozzles are shown in Figure 6. The contouring of the advanced axisymmetric nozzle, designed for subsonic cruise, is gradual on the aftbody with a rapid change near the nozzle exit to give a 24 degree final boattail angle. The contours of the two nonaxisymmetric exhaust nozzle installations also change slowly on the aftbody and close down to a 23 and 18 degree final boattail angle, respectively, for the aspect ratio 3.6 and 7 nozzles. These contours, while not radically different from the axisymmetric nozzle contour, result in surface pressure distributions which show more expansion and more or less recompression compared to the axisymmetric exhaust nozzle. Looking at a three-dimensional pressure coefficient contours for the axisymmetric nozzle, Figure 7, the 24 degree boattail and gradual closure in the aftbody gives a large region of thrust on the aftfacing nozzle surface. The difference in drag at 0.9 Mach number, as shown in Figure 8, is 23 drag counts ($C_D = .0023$) for the low aspect nozzle and 11 drag counts ($C_D = .0011$) for the higher aspect ratio nozzle.

The installed drag of nonaxisymmetric nozzle can be comparable to axisymmetric nozzles for this aircraft type but only after utilizing a very careful design procedure. Drag benefits for nonaxisymmetric exhaust nozzles have been shown more consistently on aircraft with pod mounted engines with the nozzle exit at or near a lifting surface (References 3, 5, 10, 12, 15, 16). An aircraft configuration of this type is shown in Figure 9 (Reference 10). Compared to an axisymmetric nozzle, the single expansion ramp nozzle (SERN) installed on this aircraft reduced drag at the cruise condition leading to a large improvement in specific range, Figure 10. The cruise benefits are primarily due to a favorable lift/drag relation for the SERN nozzle. With the integration of this nozzle near the wing trailing edge, the total aircraft lift becomes a function of the engine power setting. The wing pressures (not presented) provide evidence of this favorable interaction of the nozzle and wing flows. Upstream of the nozzle exit, the upper surface pressures decrease and the lower surface pressures increase due to the presence of the nozzle jet. This change in wing pressures, both upper and lower surface, contributing to increased lift, was also verified in References 11 and 14.

Since the influence of the exhaust flow on the wing flow field is not easily understood and is often confused, a short discussion of the phenomenon may be helpful. The preponderance of the experimental data obtained to date indicates there is a positive contribution to lift from vectorable nozzles when they are properly integrated near the trailing edge of a lifting surface. The flow phenomenon responsible for this favorable lift increment has not been well defined for most of the configurations evaluated. For the three aircraft configurations assessed in Reference 15, it was concluded the thrust induced effects were small when compared to the direct jet effects. The thrust induced effects were attributed to boundary layer control (BLC) of the flow in and around the nozzle and the trailing-edge wing flap plus some induced circulation. The amount of induced circulation determined was minimal and configuration dependent. In other evaluations, such as reported in Reference 10, the thrust induced effects have not been separated between that caused by BLC or by induced circulation. In such cases it is sometimes incorrectly assumed by those reviewing the results that all of the thrust induced lift can be attributed to induced circulation of "supercirculation". In Reference 10 the thrust induced lift was approximately 3 times the direct jet lift. A similar relationship between thrust induced lift and direct jet lift was also reported in Reference 9. The conclusions of Reference 15, however, conflict with those of Reference 9 and 10. The different results are probably attributable to the different levels of dynamic pressure at which the data was obtained.

At low values of dynamic pressure, C_T will be high and therefore the lift coefficient due to direct jet lift will also be high. At high values of q , and similar thrust levels, the C_T will be less and the contribution of the direct jet lift to the total aircraft lift will be correspondingly lower.

In general, at the lower speed regimes, such as during approach and landing, the thrust induced lift is a smaller percentage of the total lift required than it is at higher flight speeds. From the information presented in the above references it is estimated that at the lower speeds the thrust induced lift is between 6 to 12 percent of the total required, while at the higher speeds 10 to 15 percent of the total lift can be attributed to the induced lift. Whether this induced lift is created by BLC or induced circulation or both is not clearly defined, particularly in the case of the data obtained at the higher Mach numbers.

For a given mission profile an aircraft cruises at a nearly constant total lift coefficient which corresponds to an angle-of-attack depending on the wing/tail design and aircraft speed and altitude. When the aircraft lift is supplemented by a favorable nozzle flow/wing interaction as described in the previous paragraphs, the required wing lift can be reduced, thereby reducing the required angle-of-attack for cruise, and subsequently reducing the cruise drag. For the aircraft shown in Figure 9, and relative to a 0 degree thrust vector, an exhaust nozzle with a 10 degree down thrust vector supplemented the lift through the favorable wing interaction and direct jet lift, to reduce the cruise angle-of-attack by 1.3 degrees. The reduction of cruise drag, partially offset by the axial thrust loss due to vectoring, results in a 10.5 percent increase in specific range.

Reduced or negative static margin is playing an increasing role in future aircraft development. Canards in place of (or in addition to) the horizontal tail have demonstrated benefits for these aircraft. When the nozzle is used in conjunction with another aircraft trimming device, such as a canard, the two devices can be interplayed to enable the aircraft to fly at a minimum aircraft cruise drag condition. For the aircraft presented in Figure 5, the canard and nozzle thrust vectoring combination reduced the aircraft takeoff gross weight by 3 percent when compared to the no vectoring aircraft which utilized only the canard for aircraft trim. The canard and nozzle deflection schedules for aircraft trim with and without thrust vectoring are shown in Figure 11. Notice that for the no-thrust vectoring case, the canard deflection is still increasing past minus 13 degrees as angle-of-attack exceeds 16 degrees while thrust vectoring keeps the canard deflection to minus 8 degrees or less. The loss of thrust due to thrust deflection is more than offset by reduction in aircraft drag. References 5 and 13 also indicate this favorable trim drag benefit for thrust vectoring. The F-111 configuration in Reference 13 utilized thrust vectoring to reduce the horizontal tail size with a corresponding reduction in drag and weight.

In summary, when considering installed cruise drag of advanced exhaust nozzles in tactical aircraft, the following lessons have been learned to date:

1. The installed drag benefit for advanced exhaust nozzles is not inherent and may require sophisticated analytical procedures and experimental verification to ensure correct aftbody/nozzle contours.
2. For propulsion installations where the nozzle exit is near a lifting surface, the lift required for aircraft cruise can be partially obtained by the direct jet lift and thrust induced lift. The reduced lift required of the wing allows a reduced cruise angle of attack and reduced cruise drag.
3. An aircraft cruise drag benefit can be obtained by using nozzle thrust vectoring in conjunction with the canard for aircraft trim.

3. ADVANCED EXHAUST NOZZLE INTEGRATION FOR AIRCRAFT MANEUVER

Aircraft size often depends on the maneuver requirement levied on the vehicle. Consequently, designers have developed efficient aircraft lift systems to meet the maneuver requirement. Through new airfoils, planforms, and variable sweep wings, the aircraft can have the desired maneuver performance but often at the expense of other mission legs. The best maneuver lift system, for example, may create a penalty in supersonic cruise. The advanced exhaust nozzle can offer an alternative to a wing compromise. An efficient cruise wing with lower maneuver capability may be coupled with a thrust vectoring exhaust nozzle to supplement the maneuver capability and improve overall mission performance. These exhaust nozzles can be used to increase the maneuver capability or can be used to reduce aircraft size and maintain capability. This section will address several different aspects of the contribution of advanced exhaust nozzles to enhance aircraft maneuver.

The influence of the jet exhaust on a lifting surface as discussed in a previous section is the basis for some of the maneuver benefits of installed exhaust nozzles. This phenomenon produces lift and drag (though not as much proportionally as to lift) by changing the overall wing flowfield, and, depending on the location of the jet to the aircraft center-of-gravity, a change to the pitching moment. Advanced exhaust nozzles nominally have the capability for ± 30 degrees thrust vectoring. The vectored jet has been related to a mechanical aerodynamic flap which varies in length with power setting, but does not have separated flow as on a 10-15 degree metal flap. As a result, there are greater lift increments and a reduced drag penalty.

The maneuvering benefit for vectoring advanced exhaust nozzles is primarily evident at higher angles-of-attack corresponding to the aircraft instantaneous maneuvering envelope. Reference 9 indicates that most of the drag polar improvements are above 8 degrees angle-of-attack where the wing flow tends to separate. As angle-of-attack is increased, an increasing amount of thrust vectoring is beneficial. Figure 12 presents the powered polar improvements as the nozzle deflection increased from 0 to 30 degrees. The lift increment resulting from the thrust vectoring also depends on the configuration. For the aircraft configuration shown in Figure 9, a pod mounted engine installation near the wing, there is a .125 increase in the thrust-removed-lift coefficient for 20 degrees thrust vectoring at 8 degrees angle of attack. The same aircraft configuration, at 0.9 Mach number, 20,000 feet altitude, 27,000 pound weight, with 20 degrees of thrust vectoring provides a lift increment which increases the sustained maneuver G's by 6 percent. The change in G's with nozzle deflection for this aircraft is shown in Figure 13.

Another benefit for advanced exhaust nozzles in the instantaneous turn envelope is the ability to utilize the aircraft maximum lift coefficient after the canard control limit has been reached. Using estimated high angle of attack data for the aircraft shown in Figure 5, thrust vectoring of 8 degrees could be utilized to trim the aircraft at its maximum lift coefficient at the instantaneous maneuver condition after the canard control power limit had been reached at a negative 20 degrees deflection. This use of thrust vectoring, Figure 14, translates into a 25 percent improvement in turn rate at 0.9 Mach number, shown in Figure 15.

Rather than increase maneuverability, the increased lift at the maneuver condition due to advanced exhaust nozzles can be utilized to obtain the aircraft instantaneous load performance at lower angle of attack and subsequently lower aircraft drag. The results in Reference 4 indicate that the combination of the direct jet lift and the lift enhancement due to the nozzle with a 6 degree deflection provides a lift coefficient increment of .063. If the total aircraft maneuver lift coefficient required is 0.8, the nozzle lift contribution allows the lift now required from the wing/body to be reduced by the nozzle provided increment. The reduced angle of attack for the reduced lift required results in a drag reduction of 243 drag counts ($C_D = .0243$).

An additional benefit of advanced exhaust nozzles is maneuverability and agility at high lift and/or low dynamic pressure conditions. The pitch and roll control available when aerodynamic surfaces lose control power provide added aircraft flexibility and survivability.

In summary, when considering the impact of advanced exhaust nozzles on aircraft maneuver, the following lessons have been learned to date:

1. Advanced exhaust nozzles show the most benefit for aircraft maneuver when used in conjunction with canards and relaxed static margin.
2. The vectored exhaust jet during maneuver acts like a mechanical flap except that its length varies with power setting and it does not have separated flow.
3. The benefit derived from advanced exhaust nozzles at maneuver angles-of-attack is increased G capability.
4. If increased maneuver is not required, the lift increment due to the nozzle can be used to maintain the total lift required for maneuver, reduce aircraft angle of attack, and therefore reduce aircraft drag and takeoff gross weight.

4. ADVANCED EXHAUST NOZZLE INTEGRATION FOR STOL PERFORMANCE

Recent emphasis on STOL has evolved from an anticipated requirement to operate from bomb damaged runways and/or unprepared areas. STOL as a specific performance goal is undefined and STOL performance for one class of vehicle is not the same as for another class of vehicle, for example, the F-16 versus the B-1 aircraft. The goal of the current STOL related efforts is to develop an efficient STOL capability for high performance tactical aircraft. Nominal STOL takeoff and landing ground roll distances being considered are 1000 feet though the distances range from 0 feet up to 1500 feet or more.

Technology areas being investigated to improve STOL capability include high lift aerodynamics, thrust vectoring and thrust reversing. A combination of these may be needed to obtain the desired low approach speeds and to overcome the resultant trim and control problems. The information shown on Figures 16 and 17 was generated under a current program investigating advanced exhaust nozzles for improved STOL performance and gives an indication of the total lift required as a function of takeoff and landing distance for the air-to-surface aircraft being considered. This data is for an aircraft with pod mounted engines located beneath the wing and with the nozzle exit near the wing trailing edge. It is assumed this arrangement will provide a thrust induced lift contribution to the total required lift. A one thousand foot ground roll takeoff distance is possible due to approximately equal parts aerodynamic and thrust vectoring lift plus an additional increment for thrust induced lift to obtain the required lift coefficient of 2.0. Notice that as the takeoff distance is reduced, the required thrust vectoring increment increases while the lift enhancement and aerodynamic lift increments are essentially constant.

The components of thrust vectoring and induced lift are approximately equal for the 1000 foot landing distance. The aerodynamic component of lift is twice as large as both

nozzle components combined. Also, as the required landing distance is decreased, the nozzle components of the lift increase while the aerodynamic lift remains constant. The results of this preliminary investigation indicate that to attain this level of lift and the resultant short distances, the nozzles may need to be vectored up to 30 degrees on takeoff and 60 degrees on landing. In addition to vectoring, the nozzles may have to have relatively high aspect ratios to allow the exhaust jet to influence a larger section of the wing to produce the thrust induced lift required.

Ongoing STOL studies indicate that nozzle requirements for thrust vectoring and thrust reversing change as the takeoff and landing ground roll distances required are decreased well below a 1000 foot nominal value. For a 750 foot balanced field length, the approach speed for an air-to-surface aircraft decreases to 105 knots from a nominal 145 knots for a conventional approach. Thrust vectoring, less than 45 degrees, and thrust reversing are required. For a 300 foot balanced field length, the approach speed required is now less than 70 knots. Thrust vectoring has taken over the thrust spoiling function and more propulsive moment balancing and reaction controls (like the Harrier control system) are required.

Generally the goal for STOL performance is balanced field length, that is, takeoff distance equal to landing distance. If takeoff distance is acceptable below a reasonable distance, the landing ground roll problem can be approached with thrust vectoring to reduce approach speed and thrust reversing to spoil thrust and to reduce the ground roll. The nominal goal for thrust reverser efficiency is 50 percent of intermediate thrust which has been met in most designs that have been tested to date (References 9, 12). For a 30,000 pound air-to-air aircraft, the landing ground roll, Figure 18, is reduced from 2830 feet to 980 feet with a reverse thrust of 50 percent. The improvement is even more significant for a wet runway. With the reduced braking efficiency on the wet surface, the reduction is 5650 feet. Note that the thrust reverser tends to significantly reduce the wet runway ground roll problem.

The comparable air-to-surface aircraft ground roll reduction is shown in Figure 19. When compared to idle power with and without a speedbrake, the ground roll with a thrust reverser was reduced approximately 2500 feet with a total ground roll of 1500 feet.

Many other factors govern the effectiveness of the nozzle as a contributor to STOL performance. For example, maximum STOL performance can be realized when approach speeds are minimized, the engine is maintained at maximum dry power, and the reverser is deployed at touchdown. The mechanical and control complexity of these advanced nozzles will also impact their utilization in a STOL mission. As thrust reversers are refined, difficult design problems must be solved which will determine the best nozzle type. Both axisymmetric and nonaxisymmetric exhaust nozzles must be investigated for their application to advanced aircraft STOL.

In summary, for the application of advanced exhaust nozzles for STOL in advanced tactical aircraft, the following lessons have been learned to date:

1. Balanced field length including increased lift at takeoff and a reduction of approach speed and ground roll during landing may require utilization of nozzle thrust vectoring and/or thrust reversing.

2. As the STOL distances are reduced, the required exhaust nozzle capability (thrust vectoring and thrust reversing) varies significantly.

3. Further work is necessary to define the role of advanced exhaust nozzles for advanced STOL aircraft.

5. OTHER TECHNICAL FACTORS FOR ADVANCED EXHAUST NOZZLE INTEGRATION

Aerodynamic considerations alone will not be the final determinant in the selection of an advanced exhaust nozzle for an aircraft configuration. Nozzles are also separated by total weight, cooling flow required, and internal performance. The degree of thrust reversing and vectoring will also drive nozzle selection. The use of carbon/carbon composites to reduce nozzle weight is one of the other factors being considered in the development of advanced nozzles. Factors which are unknown quantities at this time but which offer possible payoffs are reduced cost, simplicity, and a reduced structural penalty by mounting the nozzles directly to the airframe. The aircraft configuration and the type of mission can also have a significant impact on the nozzle selections. Consideration of all these factors and the aerodynamic performance determine the best advanced nozzle for a particular tactical aircraft.

6. CONCLUDING REMARKS

Some of the impacts of advanced exhaust nozzles on tactical aircraft have been discussed for cruise, maneuver, and STOL mission requirements. While current and projected US government and industry efforts are continuing in the advanced exhaust nozzle area, the emerging trends are as follows:

1. When used as a trimming device, advanced exhaust nozzles with thrust vectoring can provide significant aircraft cruise drag reduction. The aftbody/nozzle installation for advanced airframes and exhaust nozzles must be approached very carefully to demonstrate an installed drag benefit.

2. For maneuver, advanced thrust vectoring exhaust nozzles show advantages at high angle of attack. Improved turn rate and instantaneous maneuver performance can be provided by utilizing these advanced exhaust nozzles in advanced aircraft.

3. For STOL, advanced exhaust nozzles with both thrust vectoring and thrust reversing may be necessary. Thrust vectoring up to 60 degrees (or higher) and a propulsive lift control system may be required.

The choice of exhaust nozzle for a tactical aircraft is driven by aerodynamic characteristics, mission requirements, and many other factors. The potential for significant aircraft performance improvements lies in the proper utilization of advanced exhaust nozzle technology in concert with other emerging aircraft technologies.

7. REFERENCES

1. Maiden, D. L.
Petit, J. E. "Investigation of Two-Dimensional Wedge Nozzles for Advanced Aircraft", Journal of Aircraft, Vol 13, No. 10, October 1976, pp. 809-816.
2. Capone, F. J. "Summary of Propulsive-Lift Research in the Langley 16-Ft Transonic Tunnel", Journal of Aircraft, Vol 13, No. 10, October 1976, pp. 803-808.
3. Bradley, R. G.
Jeffries, R. R.
Capone, F. J. "A Vectored-Engine-Over-Wing Propulsive-Lift Concept", AIAA Paper No. 76-917, AIAA Aircraft Systems and Technology Meeting, Dallas, Texas, September 1976.
4. Hiley, P. E.
Wallace, H. W.
Booz, D. E. "Study of Non-Axisymmetric Nozzles Installed in Advanced Fighter Aircraft", AIAA Paper No. 75-1316, AIAA/SAE 11th Propulsion Conference, Anaheim, California, October 1975.
5. Lander, J. A.
Nash, D. O.
Palcza, J. L. "Augmented Deflector Exhaust Nozzle (ADEN) Design for Future Fighters", AIAA Paper No. 75-1318, AIAA/SAE 11th Propulsion Conference, Anaheim, California, October 1975.
6. Goetz, G. F.
Young, J. H.
Palcza, J. L. "A Two-Dimensional Airframe Integrated Nozzle Design With Inflight Thrust Vectoring and Reversing Capabilities For Advanced Fighter Aircraft", AIAA Paper No. 76-626, AIAA/SAE 12th Propulsion Conference, Palo Alto, California, July 1976.
7. Willard, C. M.
Capone, F. J.
Konarski, M.
Stevens, H. L. "Static Performance of Vectoring/Reversing Non-Axisymmetric Nozzles", AIAA Paper No. 77-840, AIAA/SAE 13th Propulsion Conference, Orlando, Florida, July 1977.
8. Bergman, D.
Mace, J. L.
Thayer, E. B. "Non-Axisymmetric Nozzle Concepts for An F-111 Test Pod", AIAA Paper No. 77-841, AIAA/SAE 13th Propulsion Conference, Orlando, Florida, July 1977.
9. Hiley, P. E.
Kitzmilller, D. E.
Willard, C. M. "Installed Performance of Vectoring/Reversing Nonaxisymmetric Nozzle", AIAA Paper No. 78-1022, AIAA/SAE 14th Joint Propulsion Conference, Las Vegas, Nevada, July 1978.
10. Schnell, W. C.
Grossman, R. L. "Vectoring Non-Axisymmetric Nozzle Jet Induced Effects on a V/STOL Fighter Model", AIAA Paper No. 78-1080, AIAA/SAE 14th Joint Propulsion Conference, Las Vegas, Nevada, July 1978.
11. Bowers, D. L.
Buchan, F. "An Investigation of the Induced Aerodynamic Effect of a Vectored Non-Axisymmetric Exhaust Nozzle", AIAA Paper No. 78-1082, AIAA/SAE 14th Joint Propulsion Conference, Las Vegas, Nevada, July 1978.
12. Laughrey, J. A.
Drape, D. J.
Hiley, P. E. "Performance Evaluation of an Air Vehicle Utilizing Nonaxisymmetric Nozzles", AIAA Paper No. 79-1811, AIAA Aircraft Systems and Technology Meeting, New York, August 1979.
13. Bergman, D. "Thrust Vectoring Applied to Aircraft Having High Wing Loading", AIAA Paper No. 79-1818, AIAA Aircraft Systems and Technology Meeting, New York, New York, August 1974.
14. Bowers, D. L. "Propulsive Aerodynamics of an Advanced Nozzle/Forward Swept Wing Aircraft Configuration", AIAA Paper No. 80-1158, AIAA/SAE/ASME 16th Joint Propulsion Conference, Hartford, Connecticut, July 1980.
15. Paulson, J. W., Jr. "An Analysis of Thrust-Induced Effects on the Longitudinal Aerodynamics of STOL Fighter Configurations", AIAA Paper No. 80-1879, AIAA Aircraft Systems and Technology Meeting, Anaheim, California, August 1980.

16. Hutchison, R. A.
Sevingy, B. G.
Capone, F. J.

"Investigation of Advanced Thrust Vectoring Exhaust Systems
for High Speed Propulsive Lift", AIAA Paper No. 80-1159,
AIAA/SAE/ASME 16th Joint Propulsion Conference, Hartford,
Connecticut, July 1980.

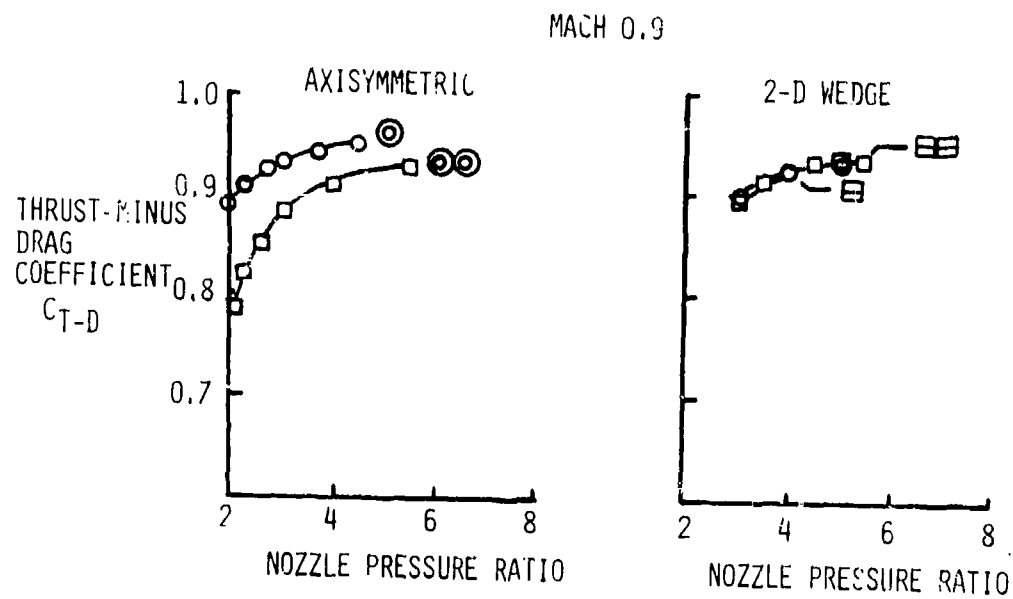


Fig. 1 Single versus twin nozzle installed performance

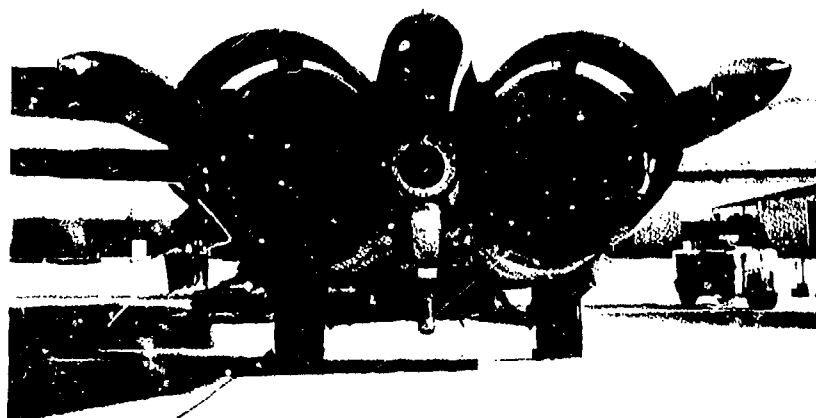


Fig. 2 F-111 aftbody/nozzle

MACH 0.87 $\alpha = 5^\circ$ NPR = 4.5

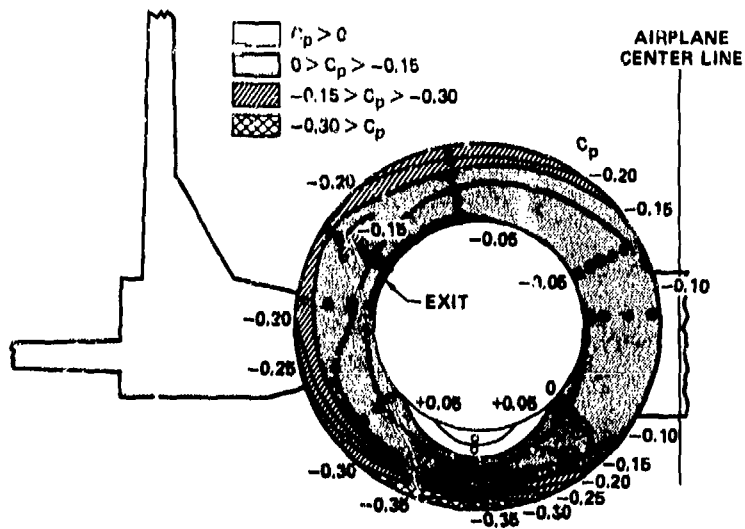
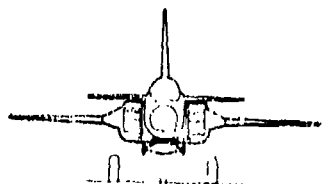
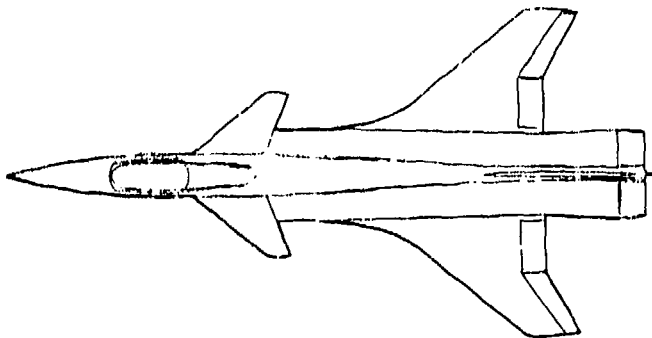


Fig. 4 F-15 nozzle pressure contours at subsonic cruise



TOGW CLASS 43,000 POUNDS
W/SW T/O 110 POUNDS PER
SQUARE FOOT

Fig. 5 Air-to-surface aircraft

DRY POWER MACH 0.9 NPR = 3.5 $\alpha = 0$

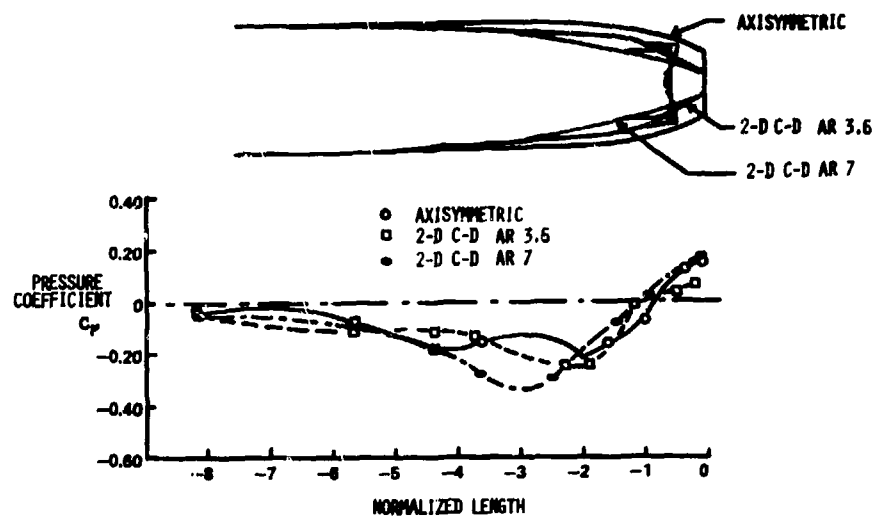


Fig. 6 Aftbody/nozzle contours and pressure distributions

SUBSONIC CRUISE DRY POWER
MACH 0.9 $\alpha = 4^\circ$ NPR = 3.5

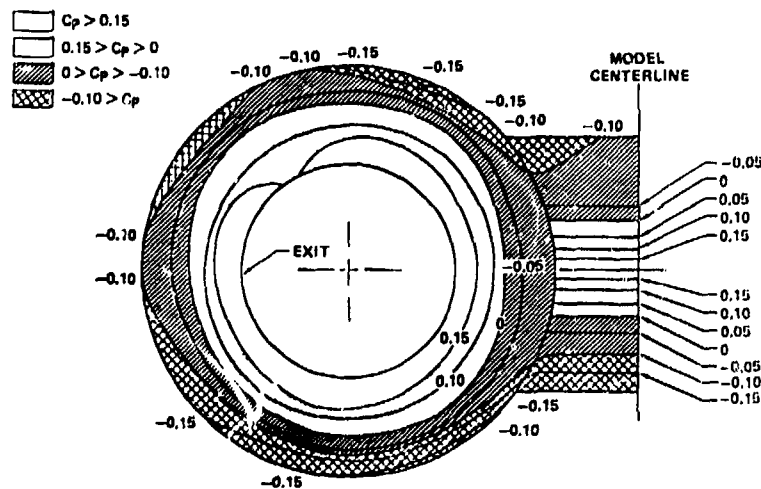


Fig. 7 Aftbody/nozzle pressure contours

MACH 0.9 DRY POWER $\alpha = 0^\circ$

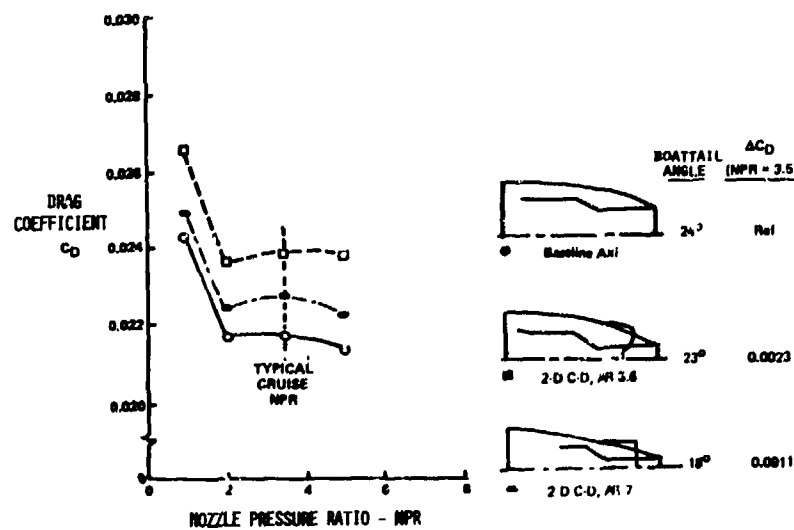


Fig. 8 Subsonic cruise drag comparison

Fig. 9 Advanced aircraft with pod mounted engines, Reference 10

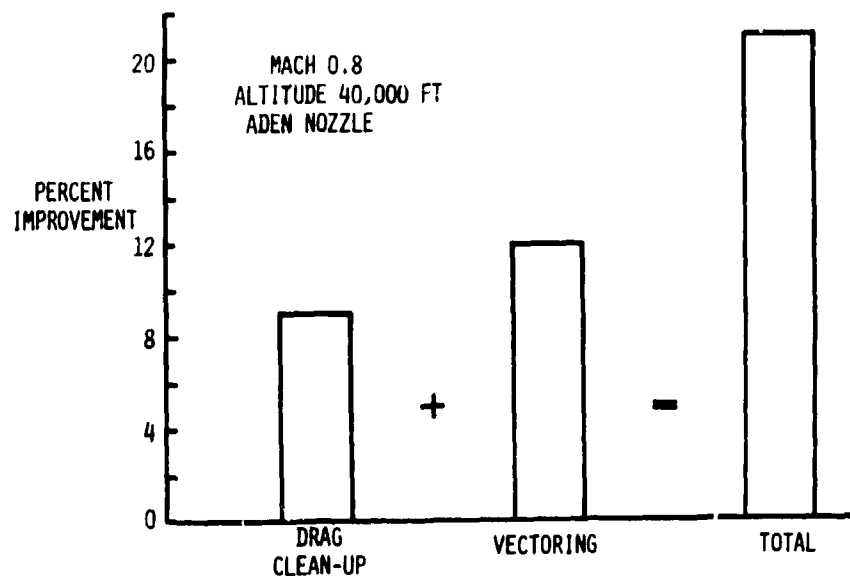


Fig. 10 Range improvement relative to axisymmetric baseline, Reference 10

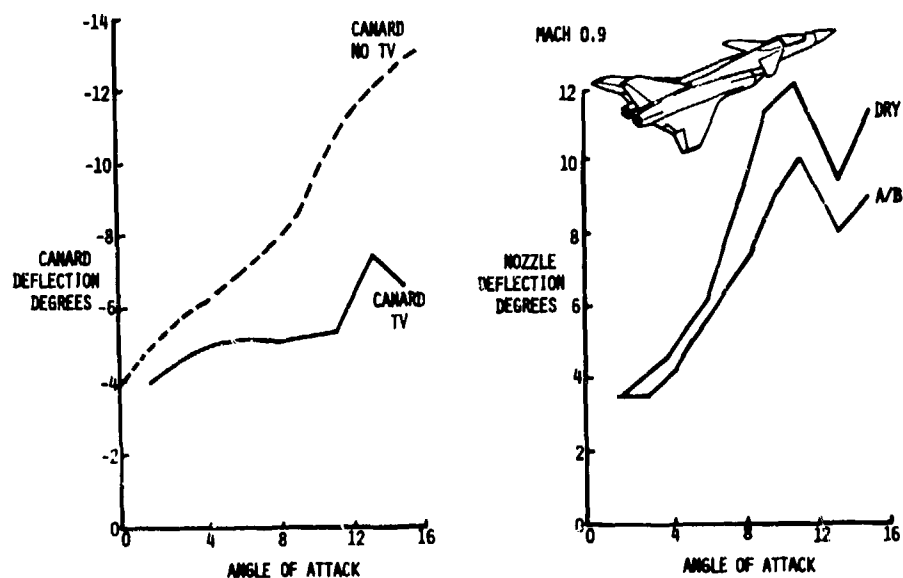


Fig. 11 Reduction of canard deflection for trim using thrust vectoring

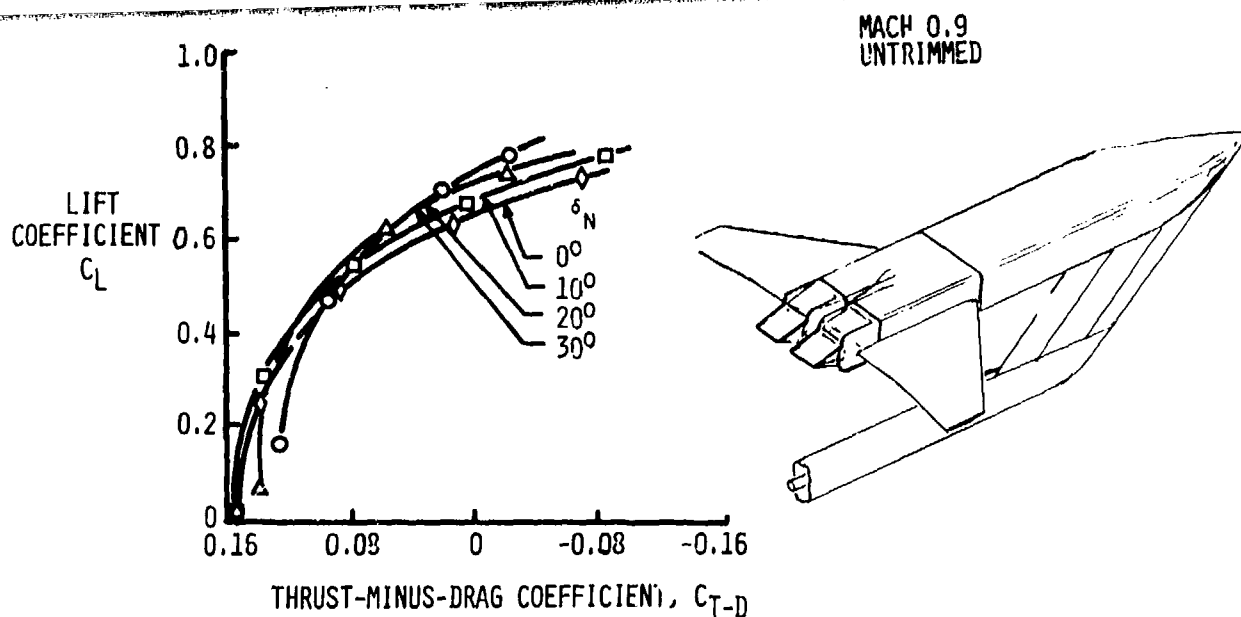


Fig. 12 Powered polar improvement with thrust vectoring, Reference 8

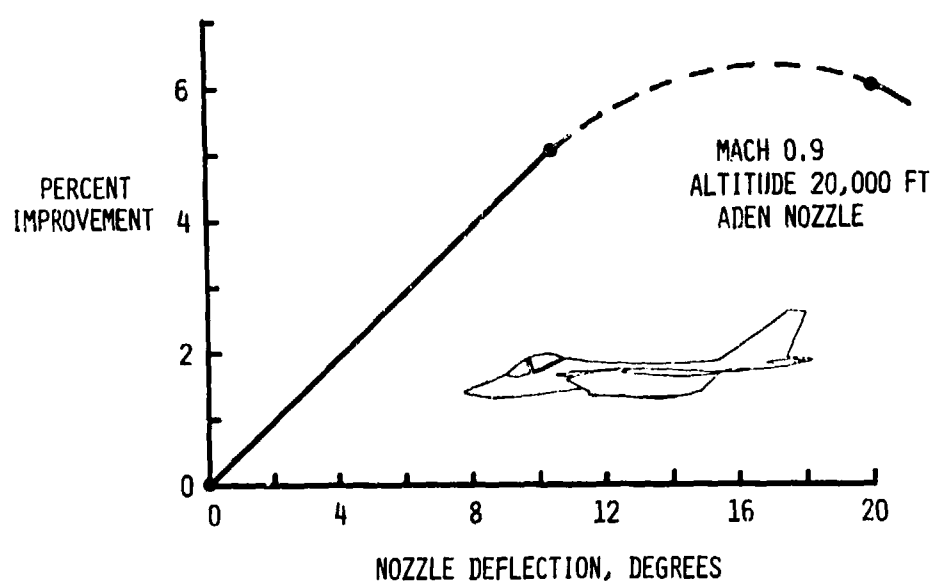


Fig. 13 Improvement of G-capability with thrust-vectoring, Reference 10

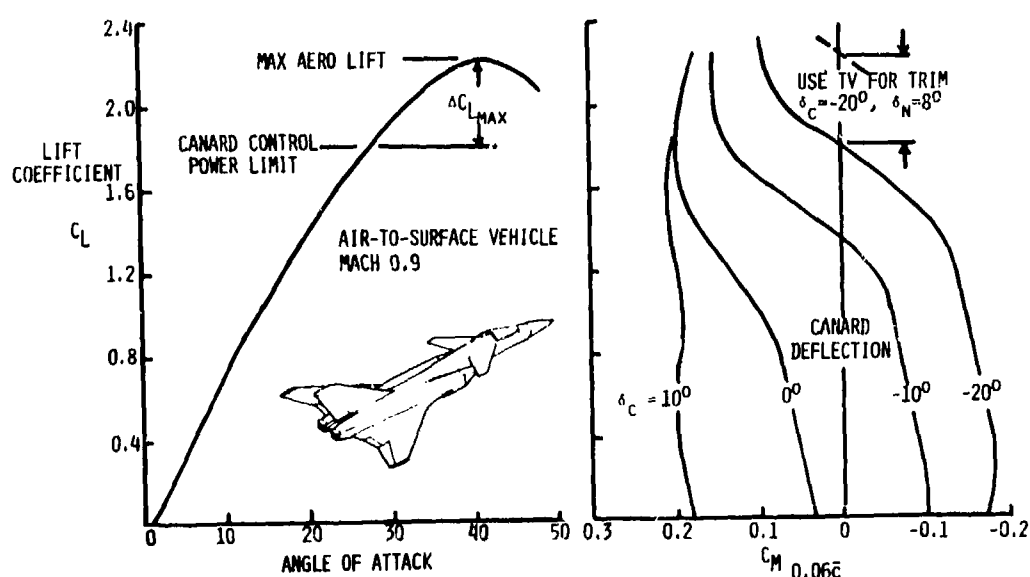


Fig. 14 Thrust vectoring utilization for maneuver enhancement

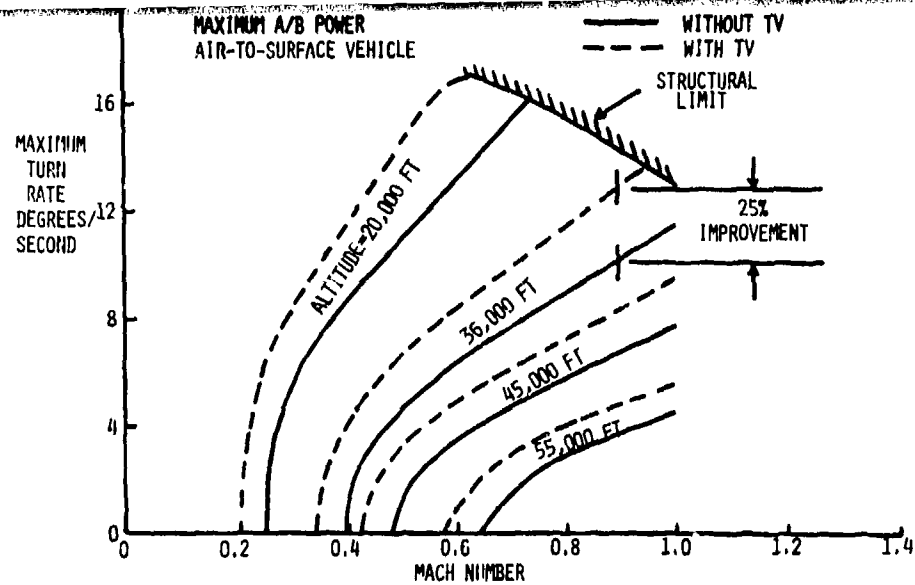


Fig. 15 Improvement in maximum turn performance with thrust vectoring

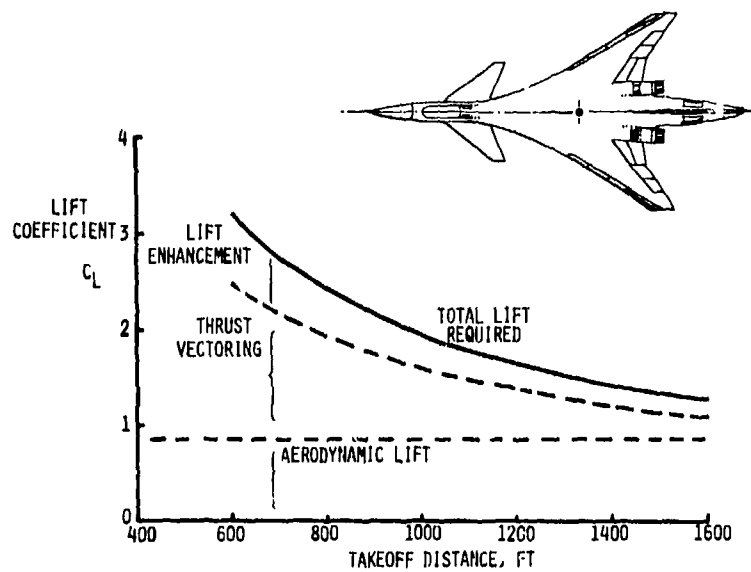


Fig. 16 Lift coefficient required for takeoff

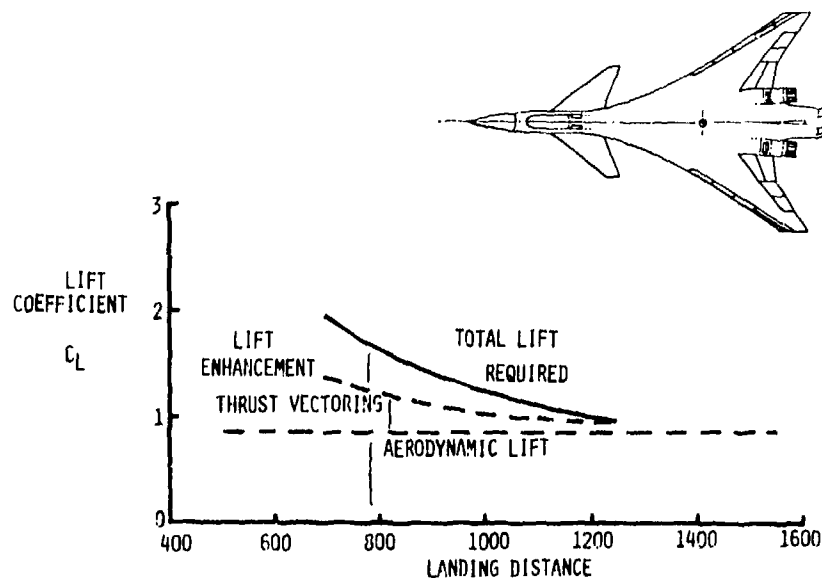


Fig. 17 Lift coefficient required for landing

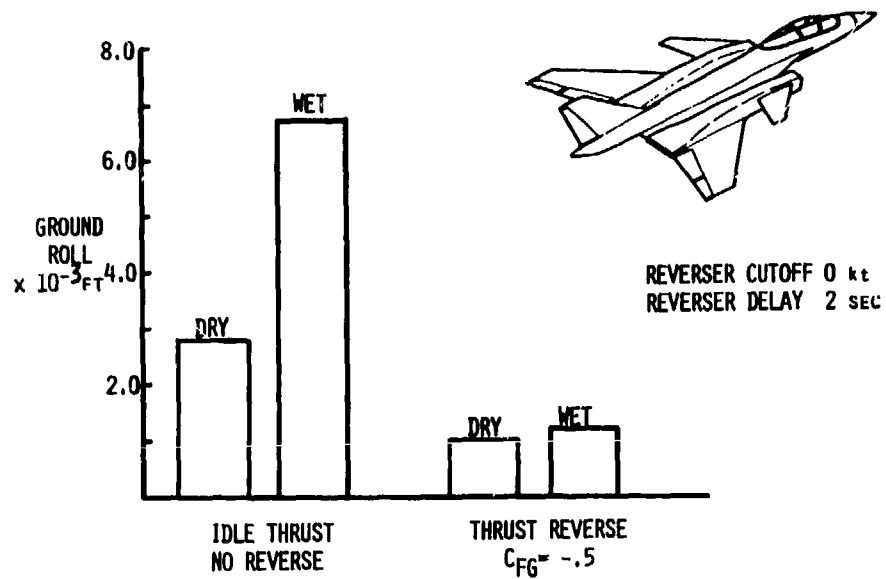


Fig. 18 Reduction of ground roll using thrust reverser, air-to-air aircraft

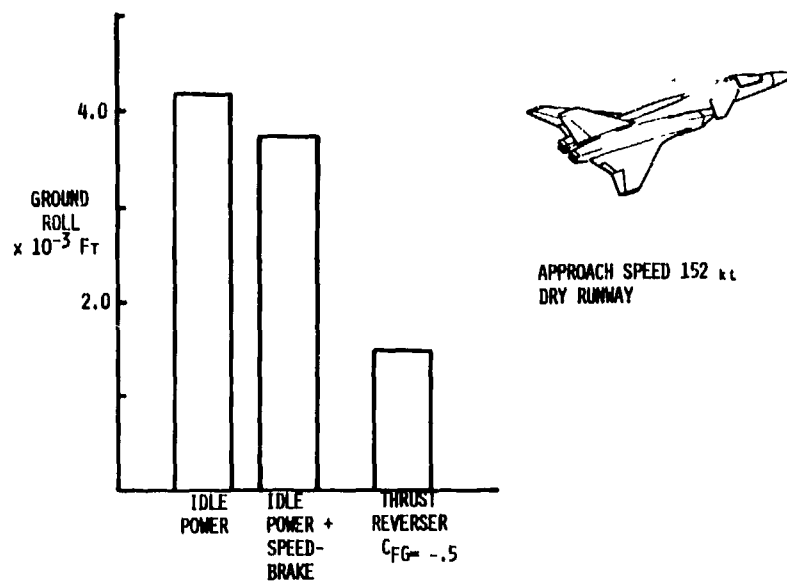


Fig. 19 Reduction of ground roll using thrust reverser, air-to-surface aircraft

The Subsonic Performance of Practical
Military Variable Area Convergent Nozzles

by
L.R. Harper
Installation Aerodynamics Group
Rollis-Royce,
P.O. Box 3, FULTON, Bristol,
England.

Summary

Performance considerations involved in the selection of a variable area nozzle for reheated engines for combat aircraft are discussed. The main emphasis is on dry operation at subsonic speeds since drag, weight, leakage and other penalties in this regime can prevent an aircraft attaining its design radius of action.

Zero-base nozzles are compared with a Moving Shroud nozzle which has a substantial annular base area in dry setting. It is shown that the drag penalty of the latter type of nozzle is small and may be outweighed by benefits in terms of weight, leakage, etc.

The implications of possible future developments in lightweight/high temperature materials is discussed.

It is concluded that until these developments are fulfilled the Moving Shroud nozzle remains the optimum nozzle for combat aircraft.

List of Symbols

A Projected area normal to free stream direction

A_b Annular base area

A_e Nozzle exit area

A_m Afterbody maximum cross sectional area

C_{DA} Afterbody pressure drag coefficient = $D_r / q_\infty A_m$

C_p Pressure coefficient = $(p - p_\infty) / q_\infty$

C_x Thrust coefficient

$= \frac{\text{Measured Gauge Thrust}}{\text{Gauge Thrust of Ideal Convergent Nozzle, same flow and pressure ratio}}$

D_p Pressure Drag

p Local static pressure

p_∞ Free stream static pressure

p_t Nozzle total pressure

q_∞ Free stream dynamic head

β_e Afterbody chord angle

β_f Nozzle final boattail angle

γ Ratio of specific heats

θ Nozzle convergence angle

1. Introduction

Reheated turbofan engines require nozzles whose throat area can be varied by a factor of typically about two.

A variety of alternative mechanical arrangements have been devised to achieve this, notably the Moving Flap, Iris, Balanced Beam, and Moving Shroud nozzles. The selection of the nozzle type for any military aircraft/engine installation depends on the balance of a number of considerations, the relative importance of which depend on the particular mission.

- i) Internal Performance - Thrust Coefficient
- ii) External Performance - Drag
- iii) Cooling
- iv) Leakage
- v) Weight
- vi) Complexity, Maintainability, etc.
- vii) Ability to fit thrust reversers

This paper considers performance aspects of the selection process. The main emphasis is on dry operation at subsonic speeds since it is in this regime that some nozzles have high drag, and performance losses in subsonic cruise, or excessive weight, can prevent the aircraft from attaining its intended radius of action.

Two dimensional and ejector type nozzles are extensive subjects in their own right, and will not be considered in this paper.

2. General Description of Alternative Nozzle Types

Before discussing the various performance aspects in detail it will be useful to take a brief look at the main geometrical features of the alternative nozzle types. With some rather sweeping generalisation we can categorise the nozzles into the three types sketched in Fig. 1; the short flap, sometimes called the moving shroud nozzle, the long flap, and the iris. All can be designed to provide convergent-divergent geometry in the reheat mode and this has implications on the dry, convergent, performance.

The conflicting arguments for the different types are clearly evident. The moving shroud nozzle is mechanically simple, compact and light, and has a low boattail angle, but has a large annular base in the dry setting. The other nozzles have near zero base area but at the expense of either a high boattail angle or long petals. Long petals are heavy and lead to high actuation loads. These can be eased by ingenious mechanical design but if this requires additional volume at the upstream end of the nozzle then a further increase in boattail angle may result.

The short length of the moving shroud nozzle permits use of a simple, relatively low weight, target type thrust reverser, and this has proved a valuable feature on the Tornado MRCA.

3. Internal Performance

The thrust and discharge characteristics of a conical convergent nozzle are functions of the convergence angle and the nozzle pressure ratio as shown in Figs 2 and 3. There are also γ effects but these are small for convergent nozzles particularly at the moderate temperatures of dry operation. In dry mode the convergence angle of a short flap nozzle may be high, about 40° ; however at pressure ratios appropriate to cruise, between 2:1 and 4:1, the thrust coefficient is close to unity. The discharge coefficient at these conditions, on the other hand, is low, about 90%. This is beneficial to the extent that it means that the geometric area to which the nozzle has to be closed-down is significantly larger than the required effective flow area, so that the annular base area is reduced. In addition, the petal travel is reduced.

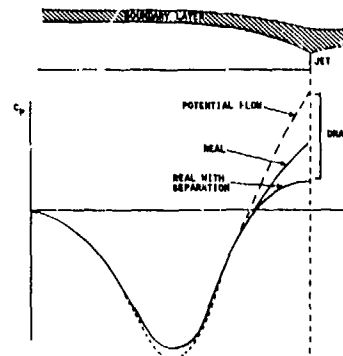
Nozzles which are convergent-divergent in reheat mode may have a double-convergent or convergent-parallel profile in dry mode. Performance losses due to this geometry will be discussed in a later paper.

4. Nozzle Afterbody Drag

If we examine the origins of nozzle afterbody drag it becomes evident why this is often quite a large fraction of total aircraft drag. Pressure drag is, of course, simply the result of the external air flowing over the afterbody failing to provide the pressure distribution which would have existed in potential flow.

$$D_p = \int (p - p_{\text{potential}}) dA$$

The real local static pressure differs from the potential flow value because the free stream is displaced from the body surface by the boundary layer. The boundary layer thickness at the rear of the afterbody increases rapidly for two reasons; firstly the body diameter decreases by typically a factor of three so that even a constant cross sectional area of boundary layer would occupy three times the thickness, and secondly the boundary layer growth rate is accelerated by the adverse pressure gradient.

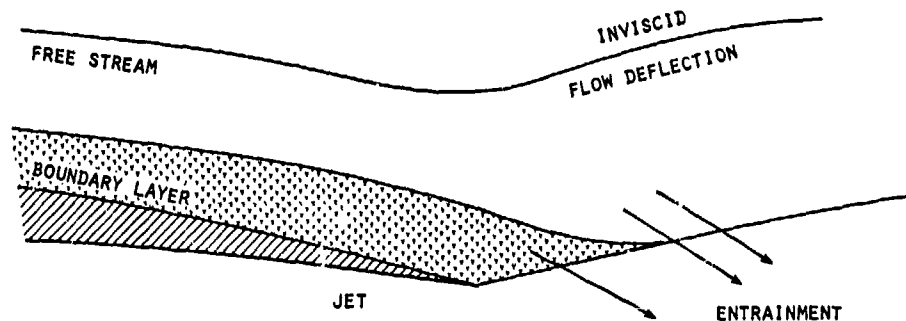


If the boattail angle is increased the recompression eventually becomes sufficiently severe to cause boundary layer separation, with a further increase in drag.

At higher subsonic Mach numbers the flow around the "crest" of the afterbody may become locally supersonic. In this case shocks are formed and a wave drag component is incurred.

The influence of initial boundary layer thickness on afterbody drag has long been a subject of discussion, particularly in the context of application of model data to full scale. The model layer is often unrepresentatively thick because the test Reynolds number is low relative to flight, also afterbody test rigs often have a long forebody or support sting. Fortunately it has been found by a number of workers (refs 8 and 9) that initial boundary layer thickness and Reynolds number have little effect on drag coefficient. A thick boundary layer reduces both the peak suction and the peak recompression (see Fig. 4), the integrated pressure drag remaining near constant. However, the reduction in the suction peak does result in some increase in drag rise Mach number.

Attempts to derive theoretical solutions for afterbody drag have generally run into problems, partly because of the difficulty in representing the jet and its influences on the free stream at the rear of the body through flow deflection and entrainment. However, work on this problem is continuing and some recent approaches look encouraging.



The magnitude of these effects is illustrated by the variation of drag with jet pressure ratio, Fig. 5.

To circumvent the shortcomings of presently available analytical methods we have correlated drag with simple geometrical parameters using the continuing growing volume of model test data. Perhaps the most obvious parameter is final boattail angle, as plotted in Fig. 6. This confirms the expected trend for drag to increase with boattail angle; it can be seen that this is progressive, there is no abrupt change of drag with the appearance of separation, which is generally found to occur at about $\beta_f = 18^\circ$. This is consistent with the proposition that pressure drag is a consequence of boundary layer thickening and separation is a stage in this.

While this plot is a useful guide to trends it is not entirely successful in collapsing drag for different shape afterbodies. A more satisfactory correlation has been obtained using boattail "chord angle", β_c , see Fig. 7; this is an index of the fineness ratio of the overall nozzle/afterbody combination. This approach is consistent with the finding that a body which is boattailed over a long length is less sensitive to the final boattail angle.

The moving shroud type of nozzle differs from those covered in the previous correlations in that it has a substantial annular base area. Data from tests of this type of geometry are plotted as a function of base/max. area ratio, and boattail chord angle, in Fig. 8. This shows that, especially at higher boattail angles, small amounts of annular base cause little increase in drag. This is presumably because the scale of the base is small relative to the boundary layer thickness at the end of the nozzle. However, for low boattail angles and A_b/A_m greater than about 10%, drag increases near linearly with base area; $C_{DA} = 0.13 A_b/A_m$ and since $C_D = D/q_0 A_m$, $D/q_0 = 0.13 A_b$ i.e. the base drag of a given nozzle is independent of A_m . A similar relationship to this has been established for more complex twin nozzle afterbodies using an effective base area which includes unfaired central base area etc.

It is evident from Fig. 8 that if a moving shroud nozzle is to be used its base area should be as small as possible. Fig. 9 shows the extent to which attention to detail design has reduced base area on a recent nozzle relative to earlier geometries.

5. Weight

Nozzle weights cover a wide spectrum because of differences in actuation method, range and versatility of area variation, materials etc. Fig. 10 illustrates this for some alternative designs of nozzle all having the same final boattail angle. Also shown in Fig. 10 is the result of a design study of one particular type of nozzle to assess

the variation of weight with boattail angle. Weight increases rapidly when boattail angle is reduced to a low value to achieve low drag, as nozzle petal length increases and causes progressively larger cantilevered loads and consequently involves more massive structure.

Included on Fig. 10 is the weight of the R8199 moving shroud nozzle, illustrating the substantial saving which this provides relative to the more sophisticated nozzles unless high boattail angles are accepted.

Great attention is paid to methods for minimising nozzle weight. For example the "Balanced Beam" nozzle is arranged to use the internal pressure distribution to minimise the loads so that petal structural weight can be reduced. Some nozzles use ingenious linkages to minimise the number of actuators. However, in some cases these design "improvements" can themselves incur penalties. For example, if the mechanism bulk increases too much, the nozzle fairing lines may be impaired with an increased boattail angle and a consequent drag penalty. Also, increased complexity is likely to adversely affect cost, reliability, maintainability etc.

Weight can also be reduced by use of low weight materials. If sufficient cooling is maintained during reheat operation then titanium petals can be used instead of the more usual high temperature nickel alloys. In this case the weight savings must be balanced against the performance penalty in reheat operation due to increased cooling flow.

6. Cooling

Cooling is not normally required in dry operation but is will be briefly mentioned here because of its effects on nozzle design.

In reheat operation a cooling airflow of several percent of the total nozzle flow is needed to cool the nozzle petals and structure and since this flow is not available for reheat fuel addition there is a proportional loss of reheat thrust boost. The quantity of cooling air required depends on the nozzle length to be cooled, the method of cooling and the safe working temperature of the nozzle materials. This will be discussed in more detail in a later paper, but it is evident that a short nozzle is attractive and that there will be benefits from future developments in high temperature materials and in cooling technology.

7. Leakage

The amount of flow which can leak from a nozzle depends on the quality of the sealing between the petals, the petal length, and the internal/external pressure differential. Generally leakage is less significant in the reheat, con-di, mode since the petal length/nozzle diameter ratio is smaller and the internal/external differential pressure is lower in the divergent section of the nozzle. Also, for iris nozzles in reheat, the petals are retracted so the seal length is short.

Simple overlapping petals provide adequate sealing for nozzles which are relatively short in dry mode but on longer nozzles the leakage penalty can become unacceptable and more sophisticated seals may become justifiable. In this case there will be the penalty of additional weight and complexity.

8. Mission Implications

The significance of weight, drag, and leakage will be illustrated by their effect on aircraft range for a representative strike mission. Cooling is not considered since this only affects combat performance.

8.1 Weight

The penalty of increased nozzle weight can be quantified in various ways. If the aircraft is Take Off Weight (TOW) limited then an equal weight of stores, or fuel, must be removed. If we assume that all the weight surfeit is debited to fuel load, and that only the cruise legs of a mission can be eroded, then substantial loss of range is incurred. In a recent aircraft project strike mission calculation 100 lb. additional nozzle weight, vis. 100 lb. fuel penalty, represented 4% loss of range.

On the other hand, if the aircraft is not TOW limited then, to a fair approximation, we may assume that the fuel consumption during all segments of the mission is increased in proportion to the increase of aircraft weight. But, if the total fuel capacity is limited, then all the extra fuel used must be debited from the cruise segment. In this case, for the same example as used above, 100 lb. extra weight represented 1.3% loss of range.

8.2 Drag

We have, in an earlier section, presented nozzle/afterbody drag as a coefficient based on afterbody maximum cross sectional area. For a typical combat aircraft the total aircraft drag coefficient based on this area varies from about 0.2 at zero lift to about 0.3 at cruise. Therefore, an afterbody drag coefficient of 0.01 is equivalent to about 5% of zero lift drag or 3% of cruise drag, and so, for a given fuel capacity, an increase of 0.01 CDA would represent 3% loss of cruise range.

From Figs 7 and 8 we see that, depending on the afterfuselage geometry, a good practical zero base nozzle might have CD_A between 0.005 and 0.01 lower than an equivalent "moving shroud" nozzle, representing a cruise range gain of 1.5 to 3%.

8.3 Leakage

Leakage of flow from the nozzle represents an equal percentage loss of gross thrust. At cruise conditions the gross to nett thrust ratio is generally about two, so that 0.25% leakage is equivalent to approximately 0.5% loss of nett thrust, or of cruise range.

8.4 Nett Effect of Weight, Drag and Leakage

The contributions made by weight, drag and leakage are compared in Fig. 11. It is evident that even for a very low drag nozzle it will be difficult to obtain an overall range improvement of more than about 1%.

9. The Future

In order to realise the potential benefits of zero base nozzles, and of convergent-divergent geometry, the penalties associated with weight and cooling must be minimised. Some improvements will be achieved by design innovations which will reduce weight, cooling, and leakage losses but the more major steps forward are likely to come in the use of new materials and improved cooling technology. Fig. 12 shows the way in which the potential improvements are interrelated.

Reduced cooling flow, or reduced material temperatures at the same flow - which would permit use of lower weight materials, could be achieved by use of impingement cooling. This has been proposed for Two Dimensional nozzles which otherwise have very large cooling penalties. However, this would involve a considerable increase in mechanical complexity, and if HP compressor bleed air is used the engine performance penalty will be proportionately larger than for a film cooling system using fan air.

The recently developed carbon composites offer the prospect of high working temperatures, up to perhaps 2000°C and therefore reduced cooling flow, combined with large weight savings - up to maybe 50%. These materials require anti-oxidation coatings, and the development of these to withstand service on overlapping petals may have some way to go.

10.0 Conclusions

It has been shown that at the present state of technology the Moving Shroud Nozzle, as used on the RB199 engine in the Tornado MRCA, is very competitive with zero base nozzles in terms of overall performance. It is light, mechanically simple, reliable, and its short length permits a target type thrust reverser to be used. Therefore, it is concluded that this type of nozzle will remain the optimum choice for combat aircraft until further technology advances permit substantial improvements in the overall performance of the more sophisticated nozzles.

References

1. E.Z. Henry and M.S. Cahn.
Part 1 Preliminary results of an investigation at Transonic Speeds to determine the effects of a heated propulsion jet on the drag characteristics of a related series of Afterbodies.
NACA RN L55 A24a & NACA RM L56 G12. March, 1955.
2. D.E. Reubush.
Effects of fineness and closure ratios on boattail drag of circular-arc afterbody models with jet exhaust at Mach Nos. to 1.3.
NASA TN-D-7163. May 1973.

and

Effect of fineness Ratio on Boattail drag of circular-arc afterbodies having closure ratio of 0.50 with Jet Exhausts at Mach Nos. to 1.3.
NASA TN-D-7192. May 1973.
3. O.M. Pozniak.
Afterbody Drag Measurements at Transonic Speeds on Twin Jet Afterbodies Terminating at and Beyond the Nozzle Exit Plane.
ARA Report No. 35. June, 1974.
- 4.)
5.) Rolls-Royce Unpublished D ..
6.)
7. J. Reid, A.G. Kurn and J.F.V. Crane.
Subsonic drag of Iris and Translating Shroud Nozzles.
Unpublished MOD (PE) Data.
8. Improved Nozzle Testing Techniques in Transonic Flow.
AGARD-AG-208. Sept. 1974.

9.

J. Reid and A.G. Kurn.
The Effect of Boundary Layer Thickness on Afterbody Drag.
RAE TR 79083. July, 1979.

VARIABLE AREA NOZZLE TYPES

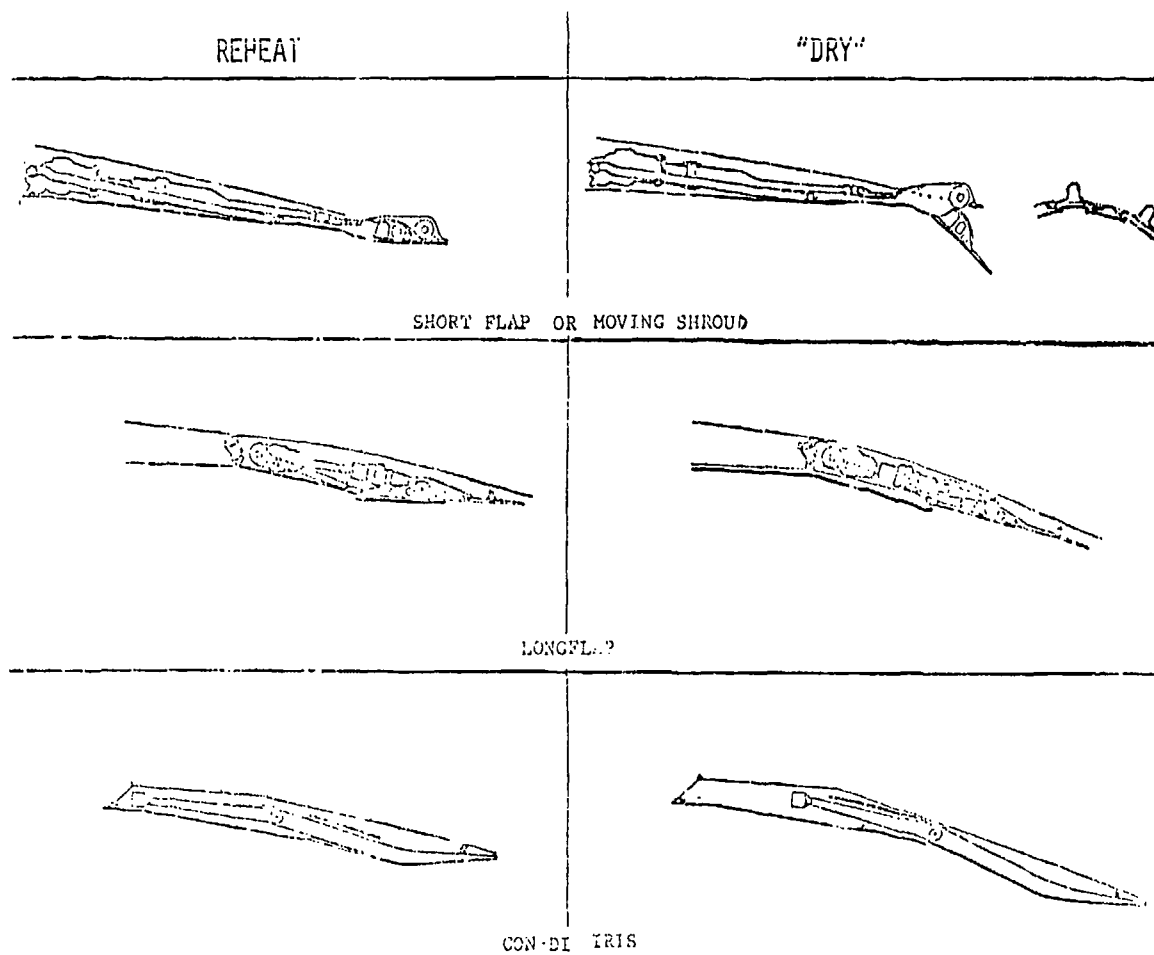


FIG. 1

Convergent nozzle internal performance

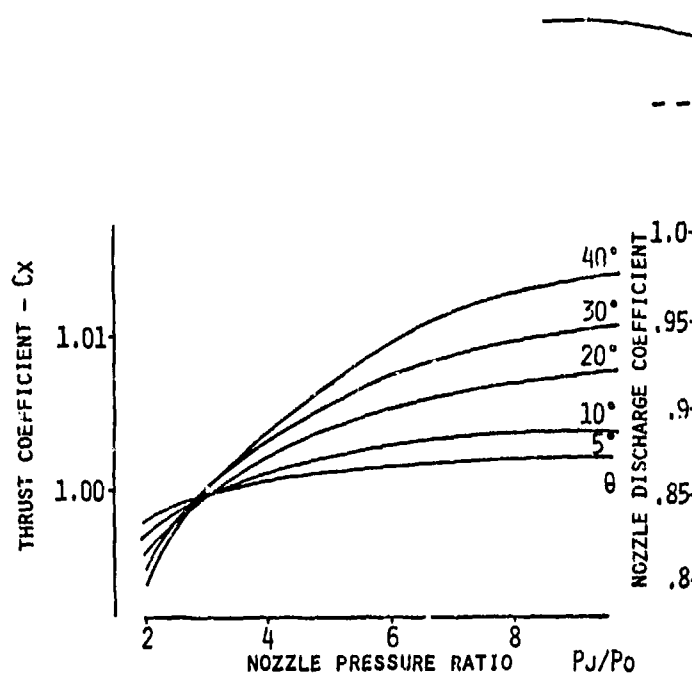


FIG. 2

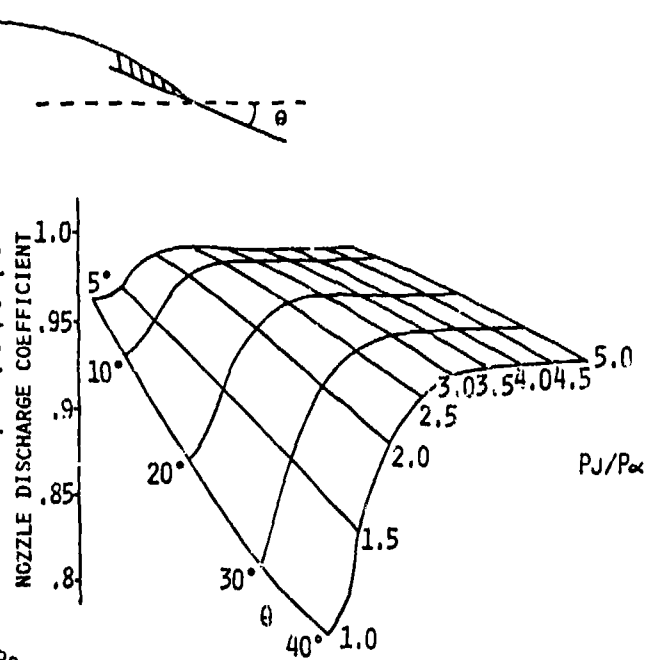


FIG. 3

Effect of boundary layer thickness

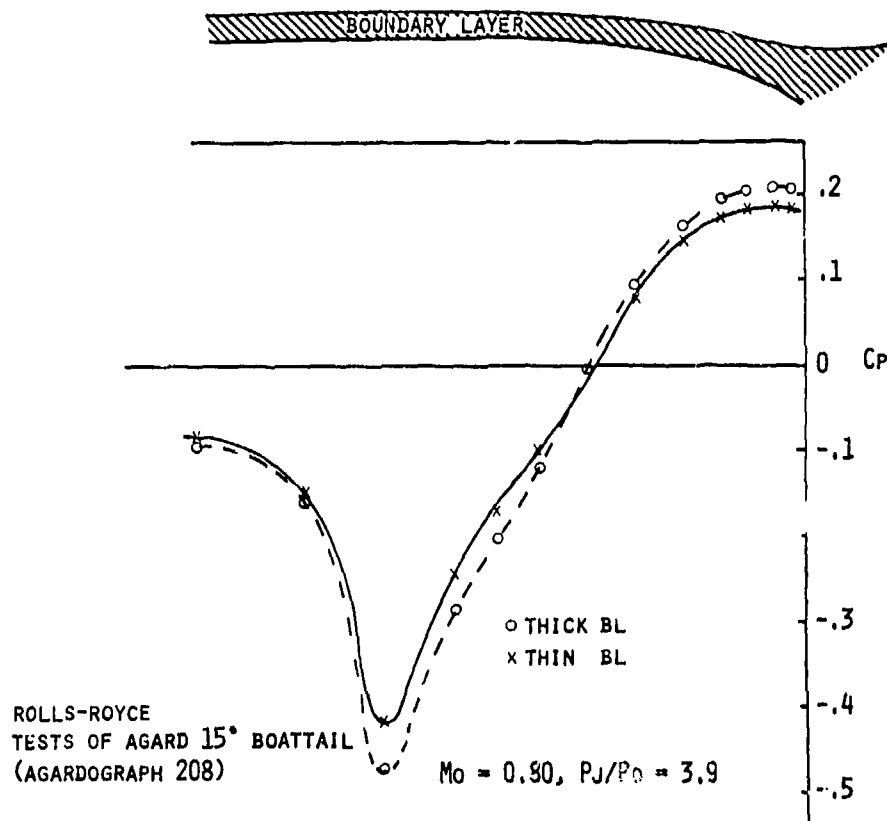
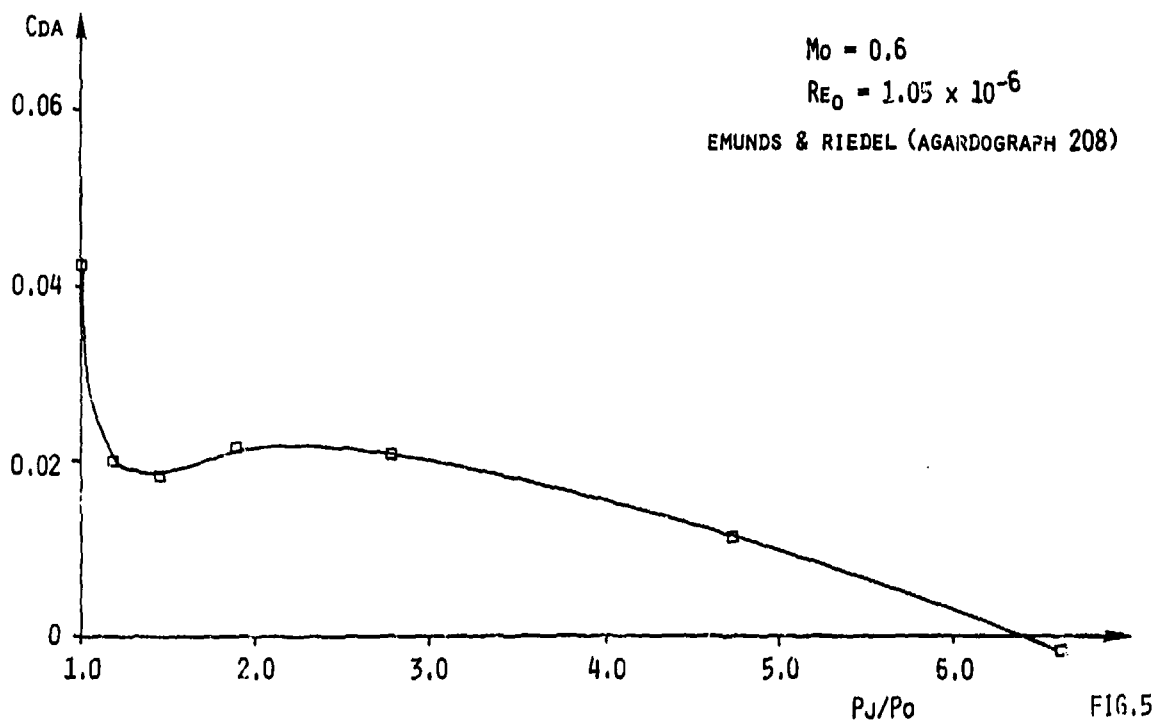


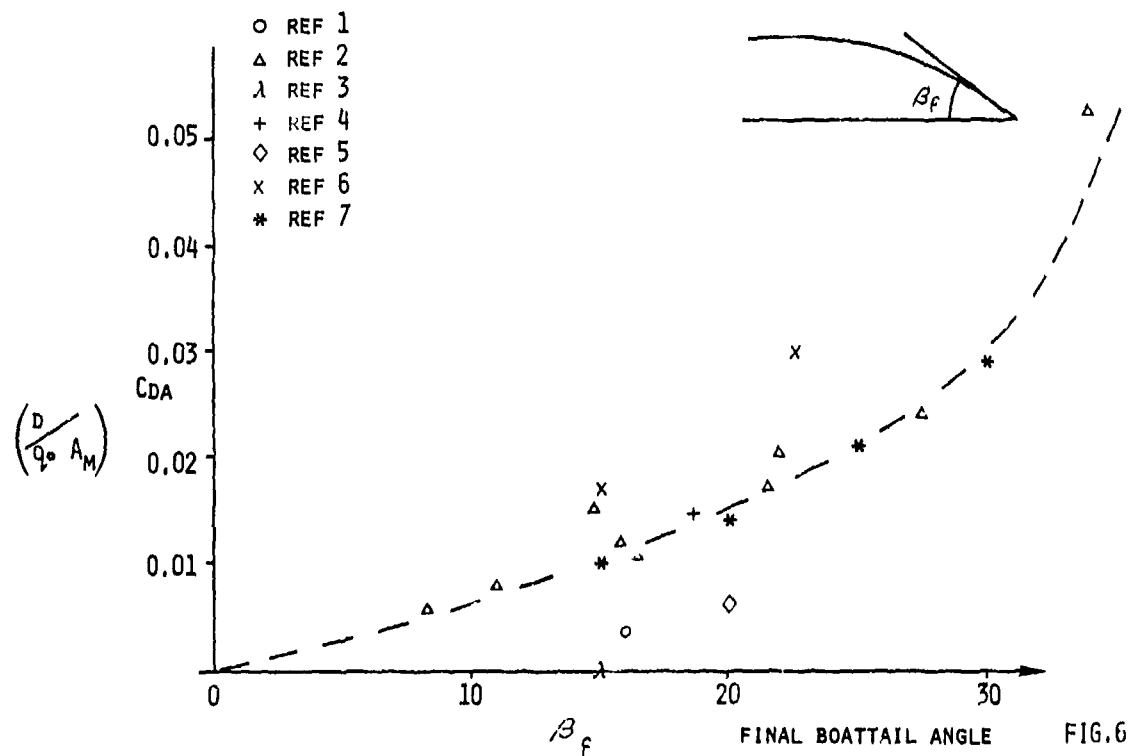
FIG. 4

Effect of nozzle pressure ratio on drag

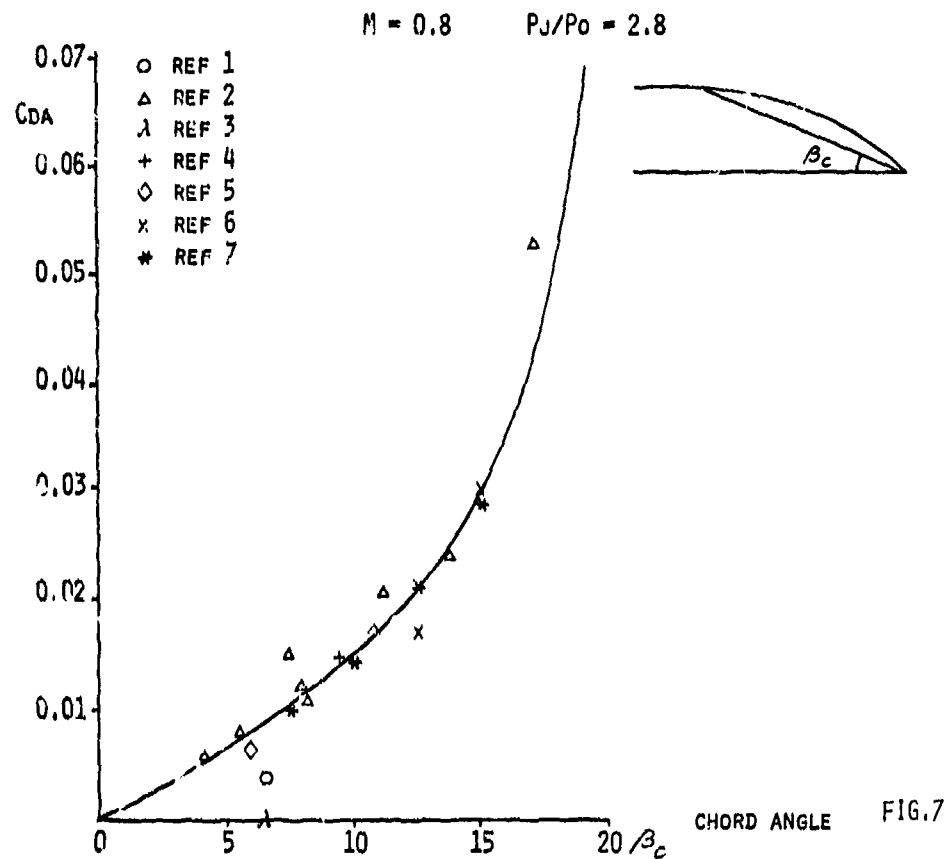


Drag coefficient of zero base nozzle afterbodies

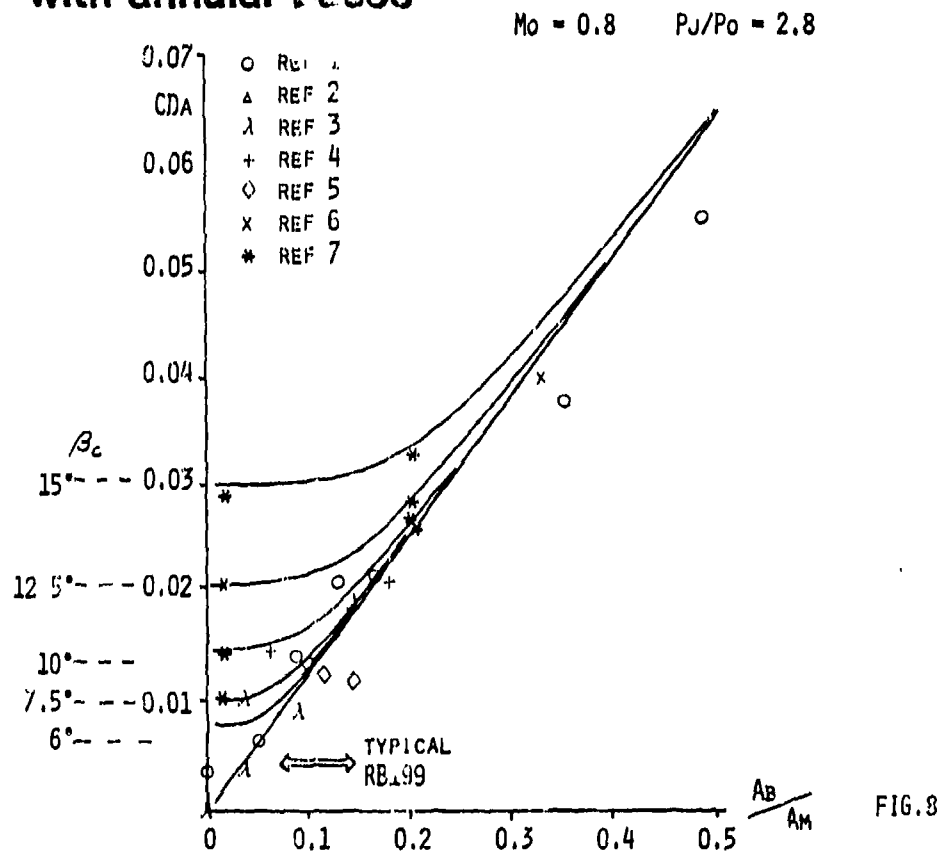
$M = 0.8$ $P_j/P_o = 2.8$



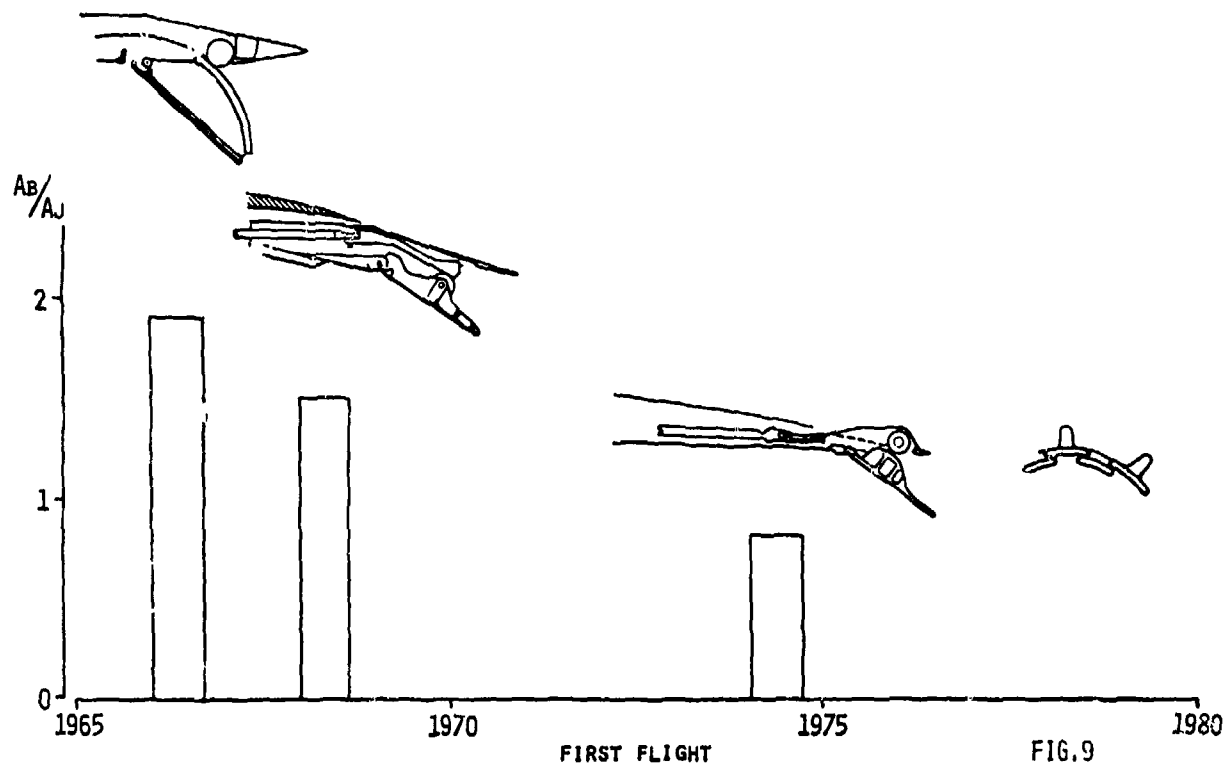
Drag coefficient of zero base ...arboodies



Drag coefficient of nozzle afterbodies with annular bases



Moving shroud nozzle base area in dry setting



Nozzle weight (RB199 scale)

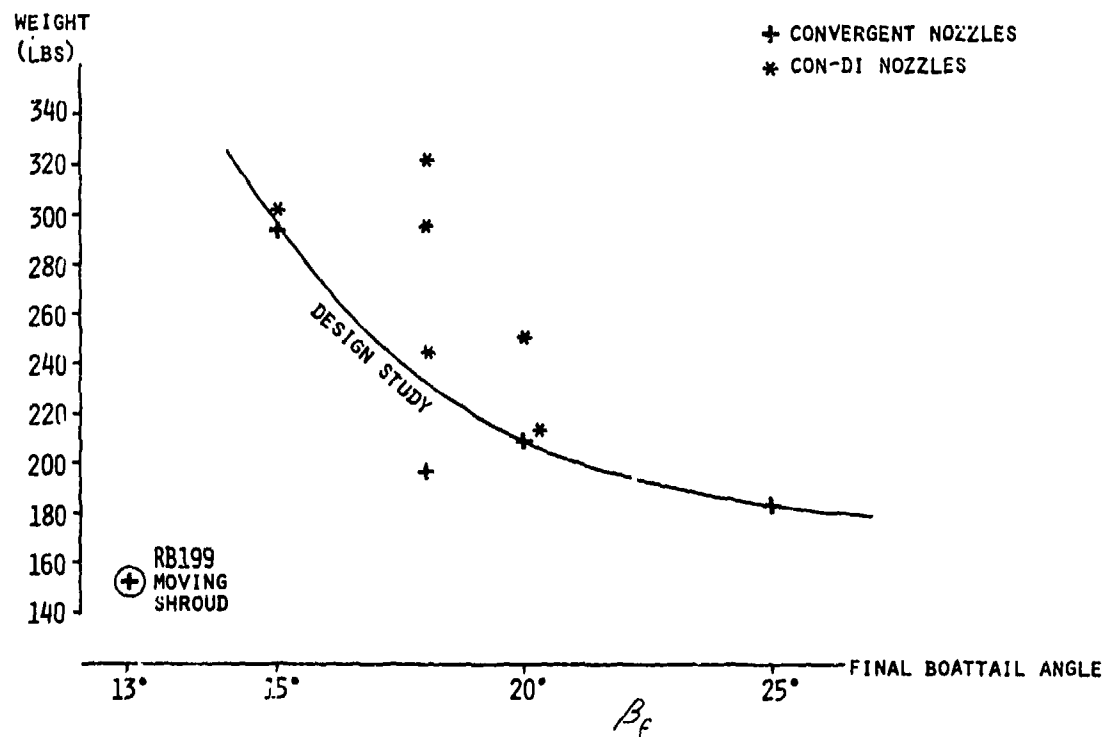


FIG.10

Range improvement provided by practical zero base nozzle relative to 'moving shroud' nozzle

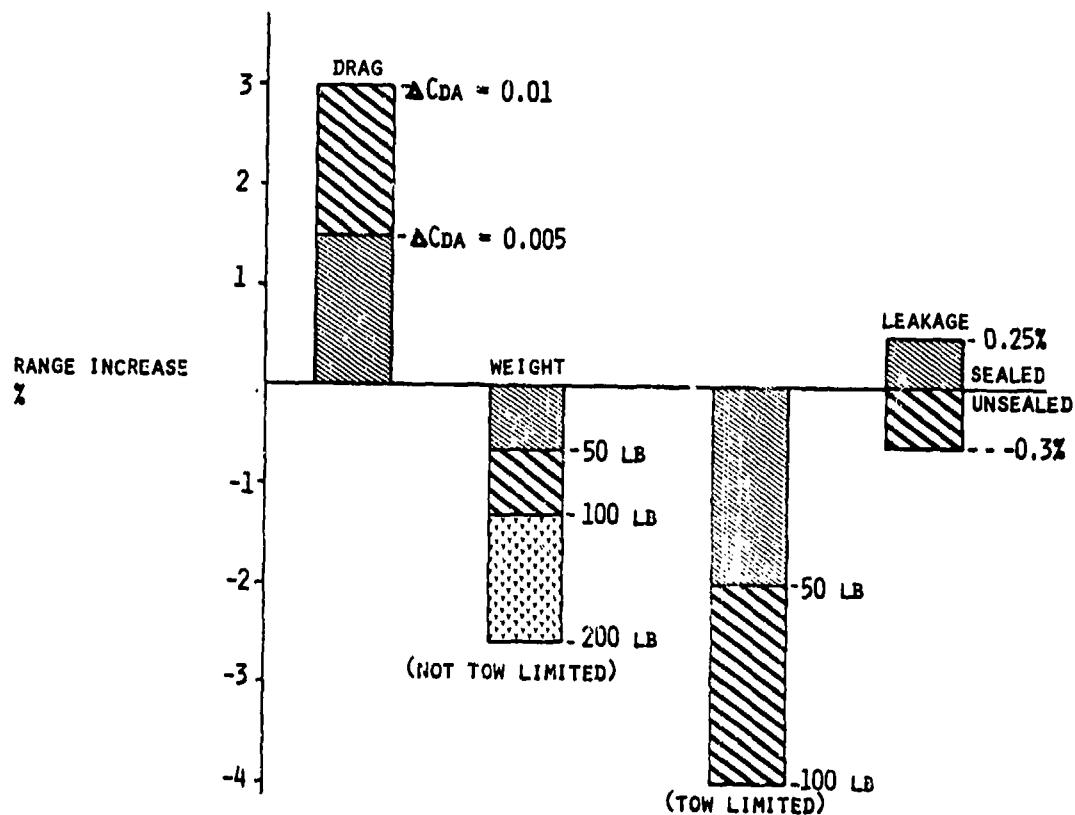


FIG.11

Future developments

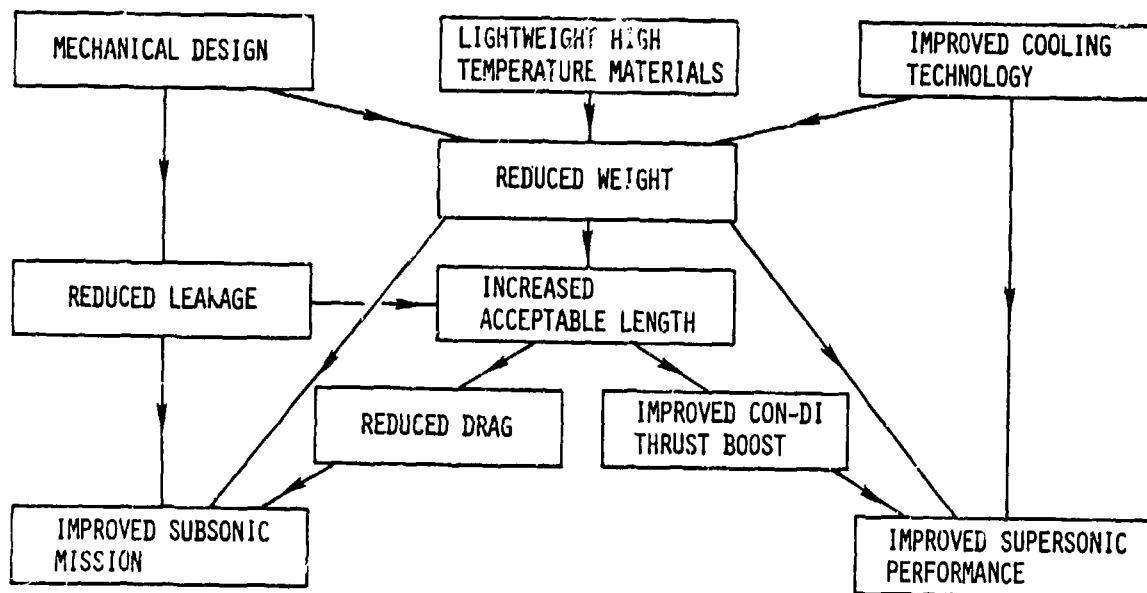


FIG.12

COMPARISON OF DIFFERENT NOZZLE CONCEPTS FOR A REHEATED TURBOFAN*

H. Grieb, R. Vedova, H. Enderle, H. Nagel

MTU MOTOREN- UND TURBINEN-UNION MÜNCHEN GMBH

Postfach 50 06 40, 8000 München 50

Summary:

For a reheated turbofan of the 70 kN thrust class several concepts of convergent and convergent/divergent nozzles are investigated and compared in view of performance, weight, complexity and the influence on afterbody drag of a combat aircraft. For all nozzles the same afterburner configuration and performance was assumed.

The influence of different nozzle cooling concepts with subsequent cooling air requirements on thrust is investigated. For the convergent/divergent nozzles the optimum ratio of exit area/throat area being dependent on nozzle concept and nozzle pressure ratio is identified.

The comparison of performance shows that fully variable convergent/divergent nozzles promise some advantages against the simple convergent nozzle at high nozzle pressure ratios. However, the higher weight and complexity of convergent/divergent nozzles lead to the conclusion that the choice of convergent/divergent nozzles for reheated turbofan engines in combat aircraft is not generally justified from the outset.

Symbols

A	m ²	area (cross section)	L	m	length
b	$\frac{\text{kg/h}}{\text{daN}}$	specific fuel consumption	M	kg/s	mass flow
C _D	-	drag coefficient, related to aircraft cross sectional area	MN	-	Mach number
C _F	-	net thrust coefficient, related to one-dimensional, isentropic convergent nozzle	p	bar	pressure
D	m	diameter	R	m	radius
F	daN	net thrust	T	K	temperature
G	kg	weight	x	m	length of film cooling layer
H	km	flight altitude	η	-	efficiency
			λ	-	divergence (area ratio) A_8/A_7
			ρ	kg/m ³	density

Indices

2	LP compressor exit
6	afterburner exit
7	plane behind primary nozzle section
8	plane behind secondary nozzle section
∞	main flow, ambience
c	cooling
E	engine
N	nozzle
t	total
th	nozzle throat
W	wall

Abbreviations

AC	aircraft cross sectional area
B	nozzle base area
BPR	bypass ratio
OPR	overall pressure ratio
TET	turbine entry temperature

Further symbols and indices are explained in the context.

* The investigation forming the basis of this study was sponsored by the Ministry of Defence of the Federal Republic of Germany, Department RÜ Fo 4.

1. Introduction:

The configuration of the afterbody section of combat aircraft with afterburner engines largely affects the total drag of the aircraft. In addition, the development effort expended in the optimization of the afterbody section is considerable. This effort is characterized by the trend away from the simple convergent nozzle with large base area in dry operation towards the convergent/divergent nozzle with a favourable aerodynamically faired afterbody section with moderate contour angle and minimum base area.

A first rough analysis of various nozzle concepts, assuming isentropic flow and ignoring the effects of nozzle contour and cooling requirement, indicates that at high nozzle pressure ratios, i.e. with engines of high specific thrust or low bypass ratio, the thrust would benefit considerably from convergent/divergent nozzle configurations especially in the supersonic flight regime.

This initial apparently attractive picture, however, requires closer examination, paying attention to the nozzle contour, the aerodynamic losses in the nozzle and, in particular, the nozzle cooling air requirement in reheat operation in order to be able to assess realistically the gain in thrust attainable with convergent/divergent nozzles. Further, detailed design studies are necessary in order to determine the extra weight expected with sophisticated convergent/divergent nozzles in comparison with simpler convergent nozzles. Finally, estimation of the afterbody drag of the aircraft requires proper assessment of the afterbody configuration.

In the study about to be presented, a systematically selected variety of convergent and convergent/divergent nozzles with different variability and complexity is investigated in order to obtain a comparison of the potential thrust gains at certain flight conditions, the attendant weight penalties and the afterbody drag to be expected at a relevant subsonic flight condition. The findings should then contribute to recognizing the advantages and disadvantages with regard to the effectiveness of the aircraft as a whole, expected with the various nozzle concepts in their proper relationship.

2. Nozzle concepts investigated

Comparison is made here between the following 5 nozzle concepts shown schematically in Fig. ①.

Convergent nozzles

1. Short-flap nozzle with large base area in dry operation
2. Long-flap nozzle with small base area and acceptable boattail contour angle

Convergent/divergent nozzles (of small base area and acceptable boattail contour angle)

3. Simultaneously variable single-hinge long-flap nozzle
4. Consecutively variable double-hinge long-flap nozzle
5. Two-parametrically variable double-hinge long-flap nozzle

These nozzles were tailored to suit a modern reheated turbofan engine in the 70 kN thrust class with the following design parameters at ISA, SLS:

Turbine entry temperature	1650 K
Pressure ratio	24
Bypass ratio	1.27
Specific thrust with afterburning	95 $\frac{\text{daN}}{\text{kg/s}}$

While the results presented here naturally apply only to engines of the basic type assumed, the conclusions to be drawn for engines of lower bypass ratio, i.e. of higher specific thrust or higher nozzle pressure ratio, will become fairly apparent.

The various nozzle designs considered here have no provision for secondary flow being ingested from the intake via the engine bay into the nozzle. The modest airflow required for venting the space between the nozzle flaps and the fuselage skin is ignored. Also the small air leakage through the gaps between the nozzle flaps is neglected.

The actuating possibilities with convergent/divergent nozzles will become apparent from Fig. ②. With the simultaneously variable convergent/divergent nozzle a definite relationship exists between throat area and area ratio A_8/A_7 . This relationship, in the design selected here, is approximately linear*, so that in dry operation the nozzle contour is necessarily convergent and in reheated operation necessarily divergent.

The consecutively variable nozzle remains convergent until the maximum throat area is reached, while at maximum throat area, i.e. at maximum reheat, any desired divergence A_8/A_7 short of a given limit can be selected. With the two-parametrically variable nozzle the throat area and the divergence can be combined arbitrarily within the given limits. Finally, it should be kept in mind that with convergent nozzles the nozzle throat will always be at the nozzle exit, while when convergent/divergent nozzles are being opened, the throat area will shift from plane 8 to plane 7.

* Other designs with non-linear relationship are known.

3. Mechanical design

The requirements governing the layout and mechanical design of convergent/divergent nozzles reveal that with given divergence the growth in nozzle length, on the one hand, is associated with an asymptotically diminishing improvement in nozzle efficiency, i.e. in thrust gain, as long as the influence of the cooling air requirement is ignored, and in a reduction of afterbody drag. On the other hand, the penalties associated with the increase in the cooling air requirement and a rather progressive increase in weight have to be reckoned with. Optimization of the nozzle layout and design thus becomes a complicated task.

In order to produce realistic weight data, mechanical designs of all nozzles considered including their actuation mechanisms were carried out on the basis of nozzle contours being optimized in the sense mentioned above. Fig. ③ illustrates the various designs of the 5 nozzles investigated. Apart from the reference nozzle, which has 14 master flaps, they each consist of 12 masterflaps and 12 slave flaps plus the actuating mechanism for moving the flaps radially in order to achieve the nozzle areas selected. The master and slave flaps of the two convergent nozzles and the simultaneously variable C/D-nozzle are of a single piece, while those of the consecutively and two-parametrically variable nozzles consist of two hinged parts.

The actuating mechanisms of all nozzles consist of the same suitably modified components. The pneumatic operating system employs a rotary valve-controlled air motor, flexible shafts routed in rigid guide tubes, and four synchronously driven ballscrew spindles. The latter serve to move a polygonal ring in the axial direction, which indicates the radial movement of the flaps via rollers. The two-parametrically variable nozzle requires two of these systems.

The various axial positions of the nozzles result from the requirement for equal length and roughly the same cross sectional areas of the afterburner up to the nozzle throat as well as for acceptable boattail contour angles and minimum base areas. With the convergent long-flap nozzle the length of the afterburner was extended somewhat over that of the convergent short-flap nozzle in the interest of an acceptable boattail contour angle and a small base area, while the axial position of the flap hinges was retained.

A more detailed description is given for the two-parametrically variable nozzle, the design of which is shown in Fig. ④. Here the two hinged parts of master and slave flaps form the primary (convergent) and the secondary (convergent or divergent) nozzle section. The primary master flaps are hinged to a box-shaped reinforcing ring at the end of the conical section of the reheat jet pipe. Cam-shaped tracks on the outside of the primary master flaps transform the axial movement of the ring via actuating rollers into the radial movement of these flaps. The master flaps of the secondary nozzle section are attached to links which, together with the master flaps of the primary section, form parallelograms. At the pivot points of the links these parallelograms rest on rollers on inclined tracks of a second outer moving ring. With the consecutively variable nozzle this outer moving ring is rigidly connected to the inner moving ring and simultaneously is moved axially, while with the two-parametrically variable nozzle, shown here, use is made of a second actuating mechanism, mentioned above, to effect independent axial displacement of the outer moving ring. The slave flaps, which also consist of two hinged parts, are arranged for overlap between the master flaps and are supported by and operated together with the master flaps. The gas pressure forces the straight edges of the more flexible slave flaps against the flat inner surfaces of the stiffer master flaps for a snug fit without gaps. All circumferential gaps required to maintain the freedom of movement of hinged parts are sealed by thin metal plates under the gas pressure.

4. Cooling concept

The cooling requirements for the nozzle flaps are given by the thermal conditions at the following essential operating points:

Flight altitude	h	0	11	km
Flight Mach number	MN	1.2	2.2	
Temperatures				
- afterburner exit	T_{t6}	2080	2130	K
- LP compressor exit	T_{t2}	450	490	K
- max. wall temperature	$T_{w,max}$	1150	1150	K
required				
cooling efficiency				

$$\eta_c = \frac{T_{t6} - T_{w,max}}{T_{t6} - T_{t2}} \quad 0.57 \quad 0.60$$

The cooling concepts under discussion or applicable here are shown schematically in Fig. ⑤. The simple single blow-in concept, represented on the left, is suited primarily for nozzles with short flaps. The double blow-in concept, illustrated on the right, serves for keeping the amount of cooling air required for nozzles with longer flaps as low as possible.

With the latter cooling configuration a portion of the cooling air is ducted through a heat shield extending into the variable part of the nozzle to a second air-ingestion slot. This moving heat shield consists of metal plates which are rigidly connected to the master flaps. Yet another cooling system employing triple blow-in, where the third blow-in occurs in the divergent section of the nozzle, was not pursued because of the considerably more complicated design with lesser saving in cooling air in comparison with the double blow-in concept.

The cooling efficiencies attainable for convergent/divergent nozzles with single and double blow-in cooling system, calculated according to [1], are represented in Fig. ⑥ in relation to the cooling layer parameter containing the length of the cooling film and the cooling air flow. The greater value of the cooling layer parameter, occurring at the required cooling efficiency for double blow-in against single blow-in indicates the reduction in cooling air requirement expected with the double blow-in concept. For comparison, measured data according to [2] and theoretical data according to [3] have been added for the case of single blow-in. The effect of heat transfer by convection on the thermal loading of the heat shield was computed separately by means of standard procedures.

Computation of the cooling efficiency and, thus, the cooling air requirement did not include the following factors, listed here together with the plus or minus effects they tend to have on the cooling air requirements:

	Tendency
- Degree of turbulence of main and cooling air flows	+
- Surface roughness of flaps and heat shields (including dirt deposits)	+
- Corners and edges at flap-to-flap transitions	+
- Heat transfer by radiation	+
- Temperature of main flow with afterburning, decreasing towards the nozzle contour	-

Except for the convergent short-flap nozzle employing the single blow-in system, the double blow-in cooling configuration was selected for all other nozzles, i.e. for the long-flap nozzles. The resultant cooling air flows are shown in Fig. ⑦ in comparison to measured data [4] taken on an iris nozzle, whose cooling system is comparable to a single blow-in arrangement.

5. Nozzle weights

The nozzle designs illustrated in Fig. ③ resulted in the weights shown in Fig. ⑧. The afterburner parts located behind the flange at the transition to the conical section of the afterburner were included. Apart from the nozzle itself, all actuating elements, including the rotary air motor, but not the outer nozzle fairing i.e. the fuselage skin, have been added. Significantly, the weight rises progressively as the length and variability of the nozzles are increased. Referred to the weight of the entire engine, the nozzle weight increase relates rather unfavourably to the potential gain in thrust, as will be shown later on. The number of parts (excluding fasteners etc.) finally conveys an impression of the complexity of design accompanying extra variability.

6. Nozzle control

With the convergent nozzles, control is limited to the selection of the proper exhaust area with due consideration being paid to the contraction of the jet cross sectional area, see Fig. ①.

With the simultaneously variable convergent/divergent nozzle the area ratio A_8/A_7 is clearly governed by the nozzle throat area A_7 selected. At a moderate nozzle pressure ratio p_{t6}/p_∞ , a significant degree of divergence will cause a drop in thrust, because in that case shock fronts will occur inside the nozzle with subsequent shock losses and flow separation. To keep convergent/divergent nozzles at least as efficient as convergent nozzles, then, the following minimum nozzle pressure ratios should be maintained:

divergence	A_8/A_7	1.1	1.4
minimum nozzle pressure ratio	p_{t6}/p_∞		
- dry operation		3.0	4.4
- reheated operation		3.4	4.6

With the simultaneously variable convergent/divergent nozzle, accordingly, the degree of divergence reached at maximum throat area, i.e. at max. reheat, can be determined only by trade-off between the optimum values at various flight conditions. In the present case of an engine having a bypass ratio of 1.27 the divergence was figured to be an optimum at 1.15. This optimum value will necessarily be the higher, the higher the specific thrust of the engine, i.e. the lower the bypass ratio. At a very low bypass ratio the optimum divergence would be about 1.3.

For the consecutively or two-parametrically variable nozzle the effect of flight Mach number and altitude on optimum divergence in reheated operation is illustrated in Fig. ⑨. The plot makes it apparent, on the one hand, that in low-level subsonic flight the divergence should at least in the present case be smaller than 1, i.e. that the configuration should be convergent, meaning that a simultaneously variable nozzle is expected

to cause disadvantages. On the other hand Fig. ⑨ illustrates that divergences exceeding 1.15 will be favourable only in supersonic high-level flight.

In the case of the two-parametrically variable nozzle the optimum divergence in max. dry operation is about the same as that for max. reheat.

With engines of low bypass ratio, higher optimum divergences would be expected chiefly in subsonic flight, while in the regime of high supersonic flight Mach numbers exceeding 1.5, the influence of bypass ratio on optimum divergence fades. Moreover, at the extremely high nozzle pressure ratios occurring here, the ultimately achievable divergence is reached anyway.

With consecutively or two-parametrically variable nozzles it will be important to prevent a cylindrical nozzle throat from being formed by the secondary flaps, because this may entail substantial thrust losses. These losses result from local supersonic flow regions in the vicinity of the contour kink where the transition is made to the cylindrical section. In the present case, therefore, according to [5], the control provisions were selected to ensure a markedly convergent contour at an area ratio A_8/A_7 smaller than 0.825, or divergence settings greater than 1, at which the flow through the divergent nozzle section remains supersonic or is still accelerating.

7. Performance data (thrust coefficients)

The standard definition of the thrust coefficients referred to the gross or net thrust of the one-dimensional isentropic convergent nozzle implies equal gas temperatures and equal nozzle pressure ratios in the entire cross section of the nozzle. In the case of reheated operation this prerequisite does not hold any longer. The thrust coefficient is significantly influenced by the fact that the nozzle cooling air does not participate in afterburning. Fig. ⑩ illustrates the effect the cooling air requirement has on engine performance at various flight conditions. The cooling air required accordingly causes a reduction in net thrust as well as in specific fuel consumption.

Fig. ⑪ then shows the resultant net thrust coefficients for max. reheat operation leading to conclusions as follows:

- The convergent long-flap nozzle compares approximately with the short-flap, i.e. the reference, nozzle. This will be readily appreciated if it is remembered that the contours of both nozzles are very gently curved in reheated operation, see Fig. ③ and their cooling air requirements are approximately the same.
- The simultaneously variable nozzle affords advantages over the convergent nozzles only in the supersonic regime at medium to high flight altitudes, these advantages being modest enough in all cases compared. At low altitudes, as well as in the entire subsonic regime, its performance is clearly inferior to that of the convergent nozzles.
- The consecutively and the two-parametrically variable nozzles are equal in reheated operation, as they are controlled to have the same divergences. Moreover, both nozzles are inferior to the convergent nozzles in the entire subsonic regime, but are expected to give a maximum of 5% gain in net thrust in the range of high supersonic flight Mach numbers at high altitudes.

In max. dry operation the relationships are essentially different. Firstly, the cooling air flow generally has no detrimental effect on the thrust coefficient. Secondly, with the convergent short-flap nozzle, the high contour angle at the nozzle exit, see Fig. ③, causes overexpansion near the wall, which benefits the thrust coefficient. Compared with the short-flap nozzle, the convergent long-flap nozzle, as well as the simultaneously and the consecutively variable nozzles, both of which are convergent in dry operation, exhibit a relatively gently curved contour preventing overexpansion at the nozzle exit near the wall. These phenomena contribute to the relations of net thrust coefficients for max. dry operation as shown in Fig. ⑫:

- The convergent long-flap nozzle as well as the simultaneously and consecutively variable convergent/divergent nozzles are inferior to the convergent short-flap nozzle, above all, at medium and high altitudes at supersonic flight Mach numbers
- The two-parametrically variable convergent/divergent nozzle is the most favourable in the regime of medium to high altitudes, as its design permits optimum divergence to be attained.

Compared with the results shown here, which hold true only for an engine with a bypass ratio of 1.27, at a lower bypass ratio the nozzle pressure ratios achieved at various flight conditions will be higher, as shown in Fig. ⑬, with the result that the above relationships concerning the net thrust coefficients will shift towards lower flight Mach numbers. On the one hand, noticeable thrust gains cannot be expected with convergent/divergent nozzles at nozzle pressure ratios below 5. On the other hand, in the range of nozzle pressure ratios above 10, no significant further gain in thrust can be expected, as ultimate nozzle divergences are limited to values of 1.4 to 1.5. After all, the generally-held maxim of convergent/divergent nozzles lending themselves for use preferably in engines of low bypass ratio is highlighted in Fig. ⑬.

8. Integration into the afterbody

Assessment of the various afterbody configurations of a combat aircraft, which could be designed for the nozzles compared, or the estimation of the afterbody drag they might cause, is an onerous job and, because of the number of parameters involved, is far beyond the scope of this study. This applies all the more to twin-engined aircraft. Therefore, the clean-cut afterbody of a single-engined aircraft serves as an example for tracing in rough outline the effect of the main parameters

- boattail contour angle at nozzle exit and
- base area,

achieved with the nozzles under study in dry and reheated operation on afterbody drag. For this example, Fig. (14) shows the effect the boattail contour angle and the base area are predicted, [6, 7, 8, 9], to have on the afterbody drag coefficient in subsonic flight at $MN = 0.8$ and at the relevant nozzle pressure ratio $p_{t6}/p_{\infty} = 2.8$. It then follows that at practicable boattail contour angles of $15 - 20^\circ$, moderate base areas up to 7 % of the fuselage cross-sectional area must not necessarily be detrimental. When the nozzles under study are related to Fig. (14), it becomes apparent that in reheated operation the differences in afterbody drag coefficient will be modest enough, while in dry operation the large base area of the convergent short-flap nozzle entails considerable extra drag. In dry operation the two-parametrically variable nozzle will give the best results. The divergent setting according to Fig. (9) will be beneficial, especially in subsonic flight.

9. Summary and Evaluation of Results

Under the assumptions made here the comparison of the long-flap nozzles under study with the convergent short-flap nozzle as the most simple concept shows the following pattern in view of the net thrust coefficient:

- The convergent long-flap nozzle is approximately equal in reheated operation, but is inferior in dry operation at supersonic flight Mach numbers.
- The simultaneously variable convergent/divergent nozzle is inferior in reheated operation, except in supersonic flight at high altitude, where a small gain in thrust is achievable. In max. dry operation it behaves similar to the convergent long-flap nozzle.
- The consecutively variable convergent/divergent nozzle is superior in reheated operation in the regime of supersonic flight Mach numbers at medium and high altitudes, but is inferior in dry operation, similar to the long-flap nozzles mentioned before.
- The two-parametrically variable convergent/divergent nozzle compares in reheated operation with the consecutively variable nozzle, but affords substantial advantages in dry operation, especially in the supersonic range.

At the point of predicted afterbody drag all nozzles are about equal in reheated operation, while in dry operation the convergent short-flap nozzle suffers from a noticeable disadvantage.

From the aspects of weight and complexity of the nozzles, it will be well to note that it is cardinally the convergent/divergent nozzles with wide potential for variation that involve a considerable penalty which, with a view to overall effectiveness of the aircraft, appears to cancel the benefits afforded in terms of thrust coefficient and afterbody drag. This holds true especially in the case of the two-parametrically variable nozzle.

With nozzles for engines of lower bypass ratio, results are expected to bear out the greater merits of the convergent/divergent nozzles. It is certainly worthwhile to state that the choice between the more complex convergent/divergent nozzles and the simple convergent short-flap nozzle must be made individually in every case.

Acknowledgements

The authors are particularly indebted to the MTU München GmbH and to the Federal German Ministry of Defence for permission to publish this study.

References

- | | | |
|-----|----------------|--|
| [1] | MTU | "Realisierbarkeit konvergent/divergenter Düsen zur Erhöhung der Effektivität zukünftiger Kampfflugzeuge"
MTU-Report 79/O35, 1979, unpublished |
| [2] | Rolls-Royce | "Nozzle Cooling Requirements and Temperature Profiles in the RB 199 Engines"
Rolls-Royce BED Report AP 5663 (1969), unpublished |
| [3] | R.J. Goldstein | "Film Cooling - Advances in Heat Transfer"
Academic Press, Vol. 7 (1971) |

- [4] W.C. Schnell "F-14A Installed Nozzle Performance"
AIAA Paper, No. 74-1099
- [5] J.M. Hardy "Blocage Tri-dimensionnel Interne dans une Tuyère
Convergente Bi-conique"
L'Aéronautique et L'Astronautique 28-1978 No. 73
- [6] B.Z. Henry, M.S. Cahn "Part 1 Preliminary Results of an Investigation at
Transonic Speeds to Determine the Effects of a
Heated Propulsion Jet on the Drag Characteristics
of a Related Series of Afterbodies"
NACA RN L55 A24a & NACA RM L56 G12. March, 1955
- [7] D.E. Reubush "Effects of Fineness and Closure Ratios on Boattail
Drag of Circular-Arc Afterbody Models with Jet
Exhaust at Mach Nos. to 1.3"
NASA TN-D-7163. May, 1973
and
"Effect of Fineness Ratio on Boattail Drag of Circular-
Arc Afterbodies Having Closure Ratio of 0.50 with Jet
Exhausts at Mach Nos. to 1.3"
NASA TN-D-7192. May, 1973
- [8] O.M. Pozniak "Afterbody Drag Measurements at Transonic Speeds on
Twin Jet Afterbodies Terminating at and beyond the
Nozzle Exit Plane"
ARA Report No. 35. June, 1974
- [9] J. Reid, A.G. Kurn "Subsonic Drag of Iris and Translating Shroud Nozzles"
and J.F.V. Crane RAE TR 7811. September, 1978

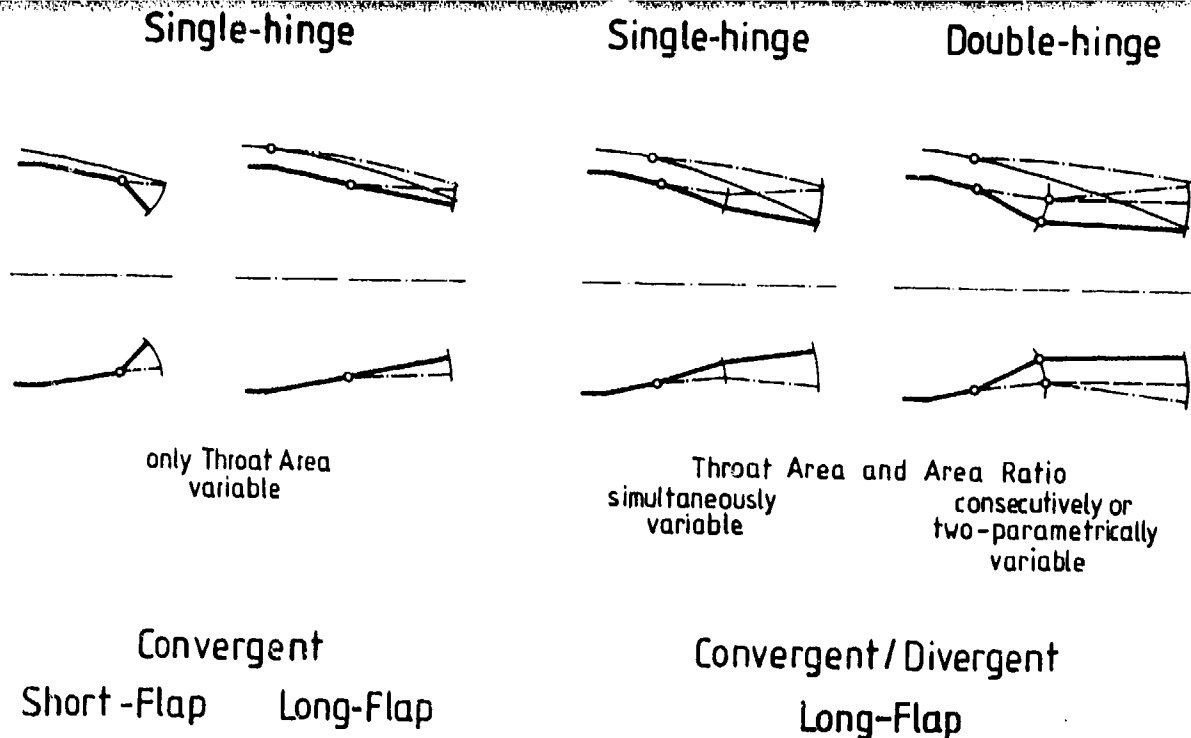


Fig. 1 Nozzle Concepts Compared

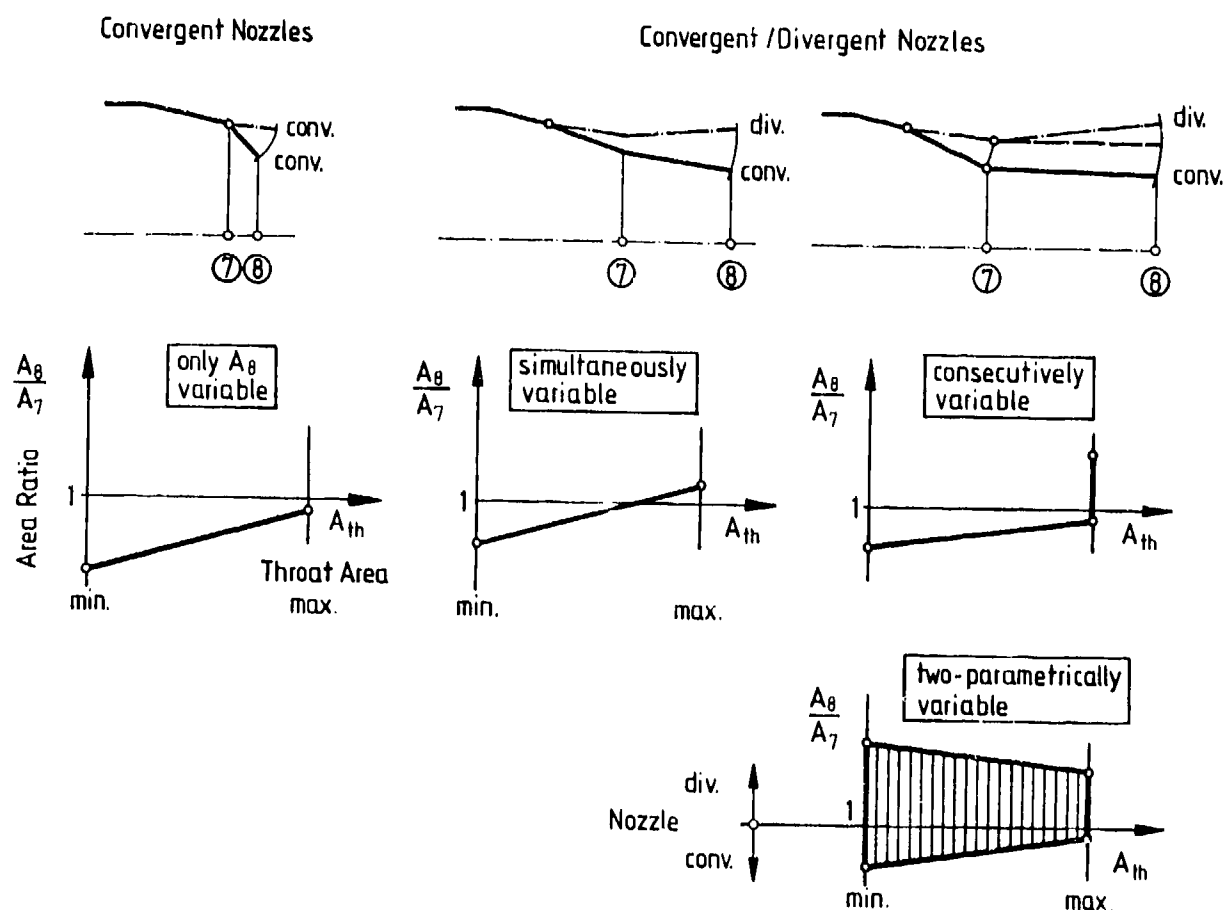
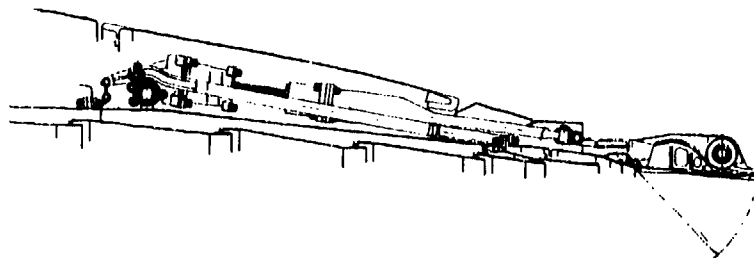
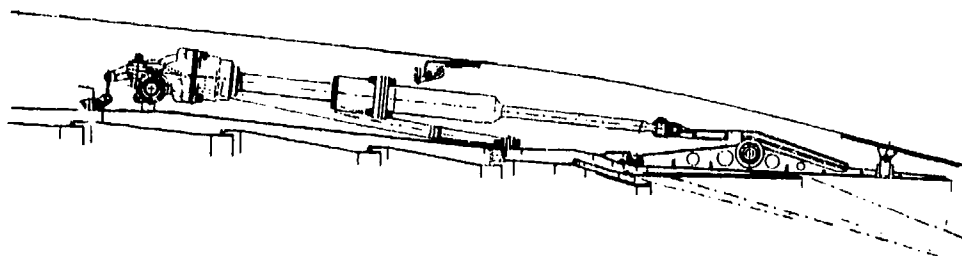


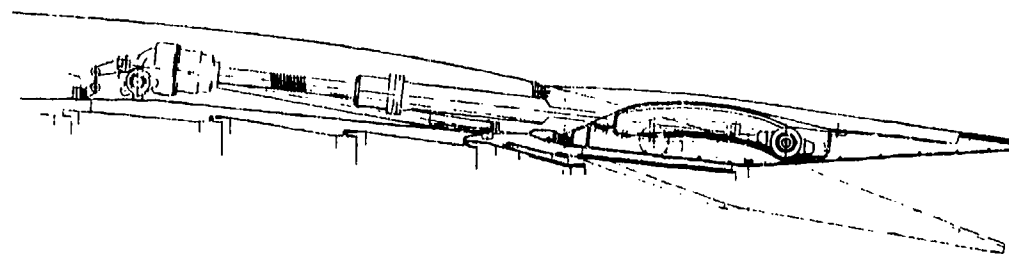
Fig. 2 Control Schemes of Nozzles Compared



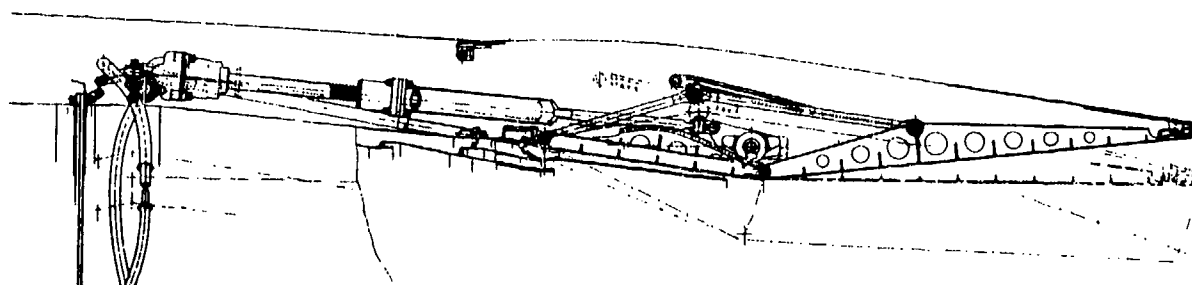
Convergent Short-Flap Nozzle (Reference Nozzle)



Convergent Long-Flap Nozzle

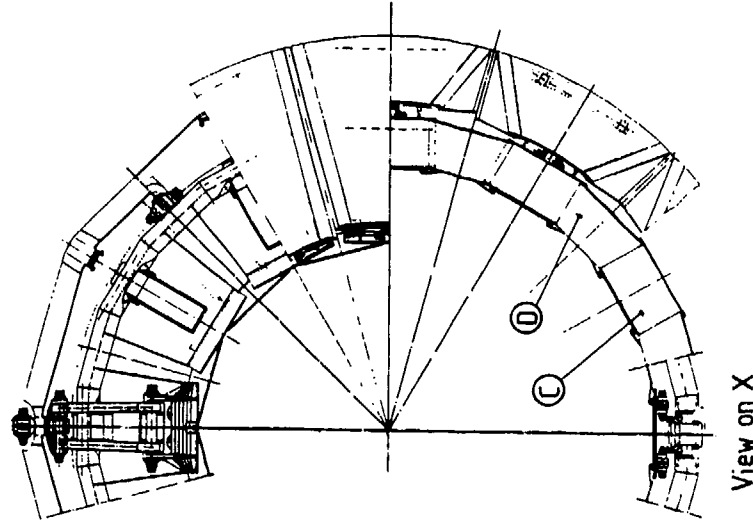
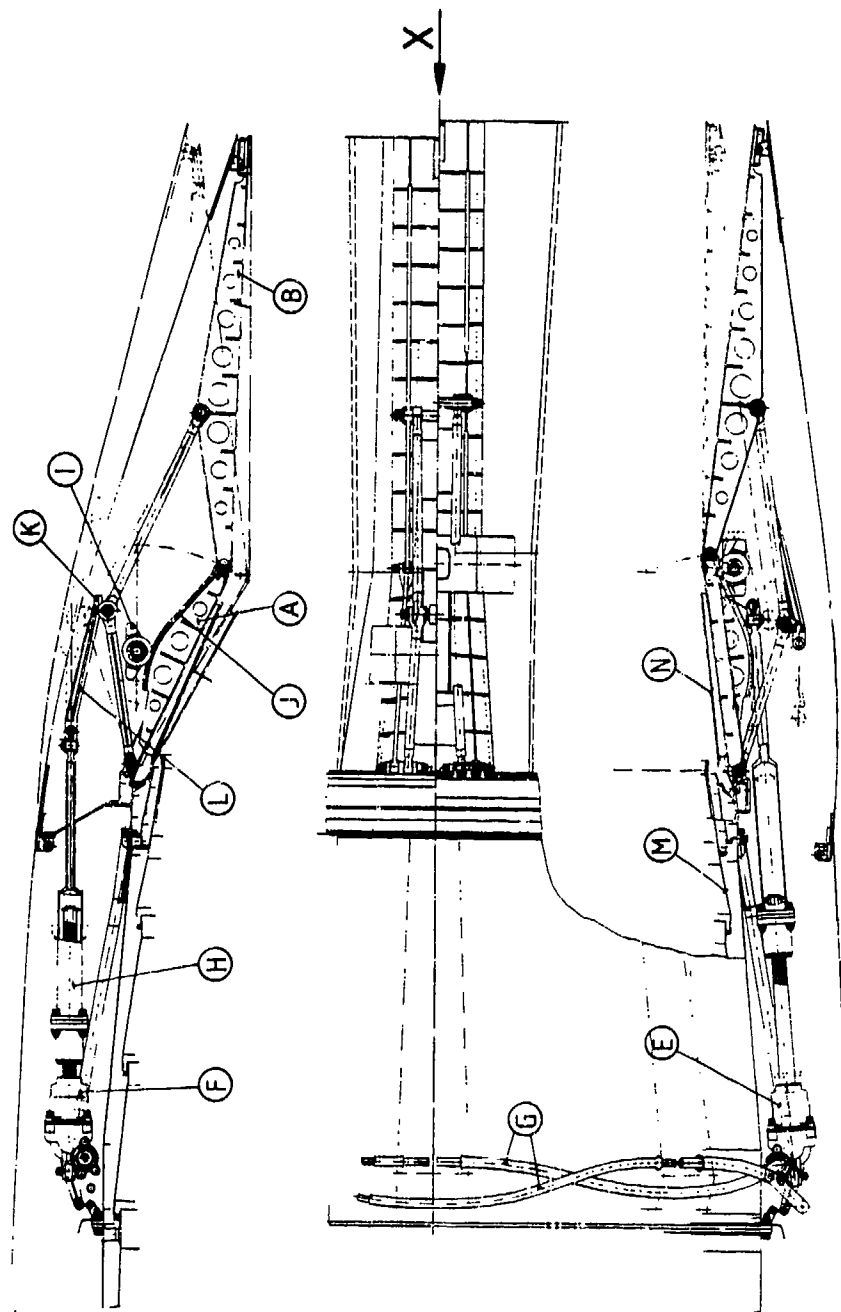


Simultaneously Variable C/D Nozzle



Consecutively or Two-Parametrically Variable C/D Nozzle

Fig. 3 Design and Axial Position of Nozzles Compared



- | | | | |
|-----------------------|------------------------|----------------------|------------------------------|
| (A) Primary Section | (E) Actuating System 1 | (I) Moving Ring 1 | (M) Afterburner Heat Shield |
| (B) Secondary Section | (F) Actuating System 2 | (J) Cam-shaped Track | (N) Flap Mounted Heat Shield |
| (C) Master Flap | (G) Flexible Shafts | (K) Moving Ring 2 | |
| (D) Slave Flap | (H) Ball-screw Spindel | (L) Inclined Track | |

Fig. 4 Design of Two-Parametrically Variable Convergent/Divergent Long-Flap Nozzle

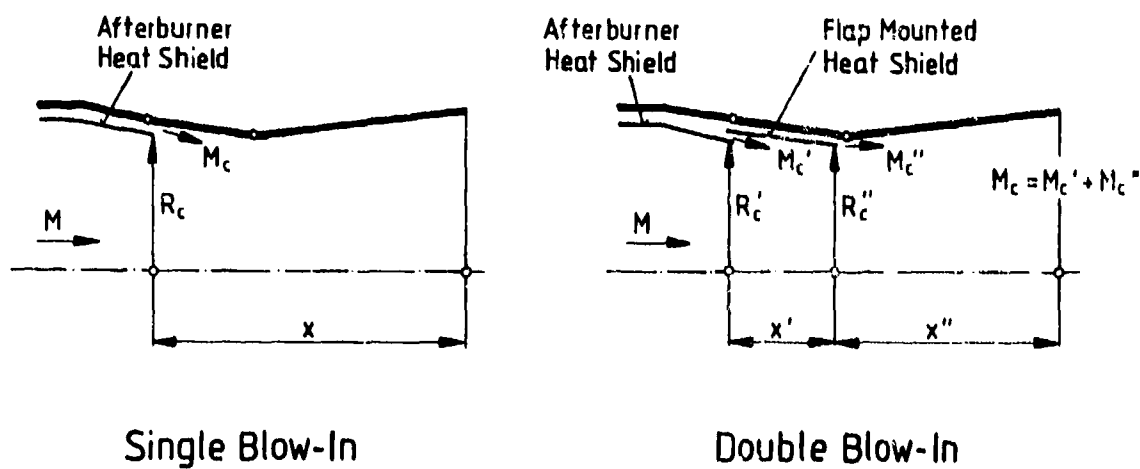


Fig. 5 Cooling Concepts Generally Considered for Convergent and Convergent/Divergent Nozzles (Example Drawn for Two-Param. Var. Nozzle)

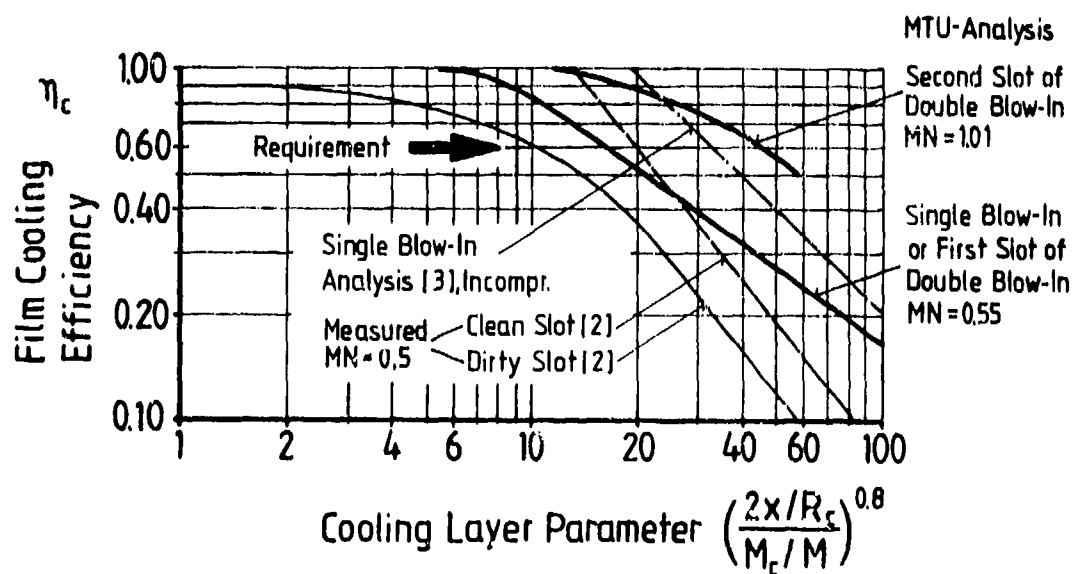


Fig. 6 Influence of Film Cooling Layout Parameter and Configuration on Cooling Efficiency (Example for Convergent/Divergent Nozzles)

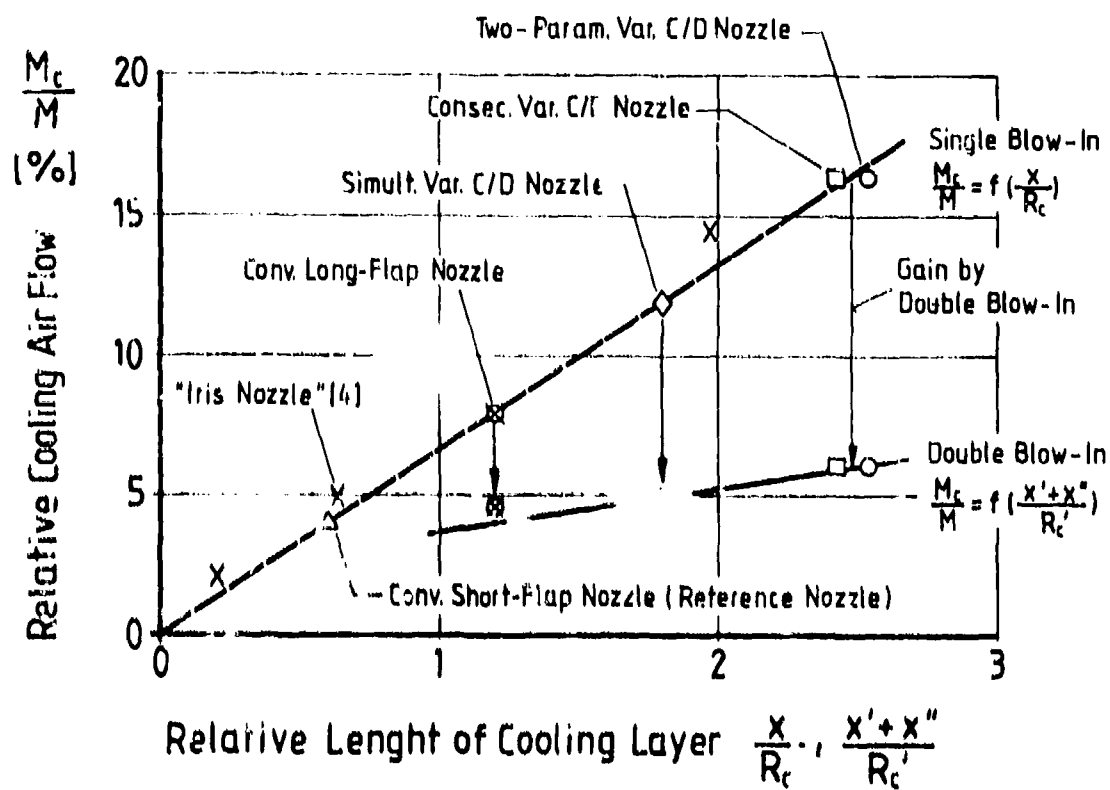


Fig. 7 Required Cooling Air Flow for Convergent and Convergent/Divergent Nozzles

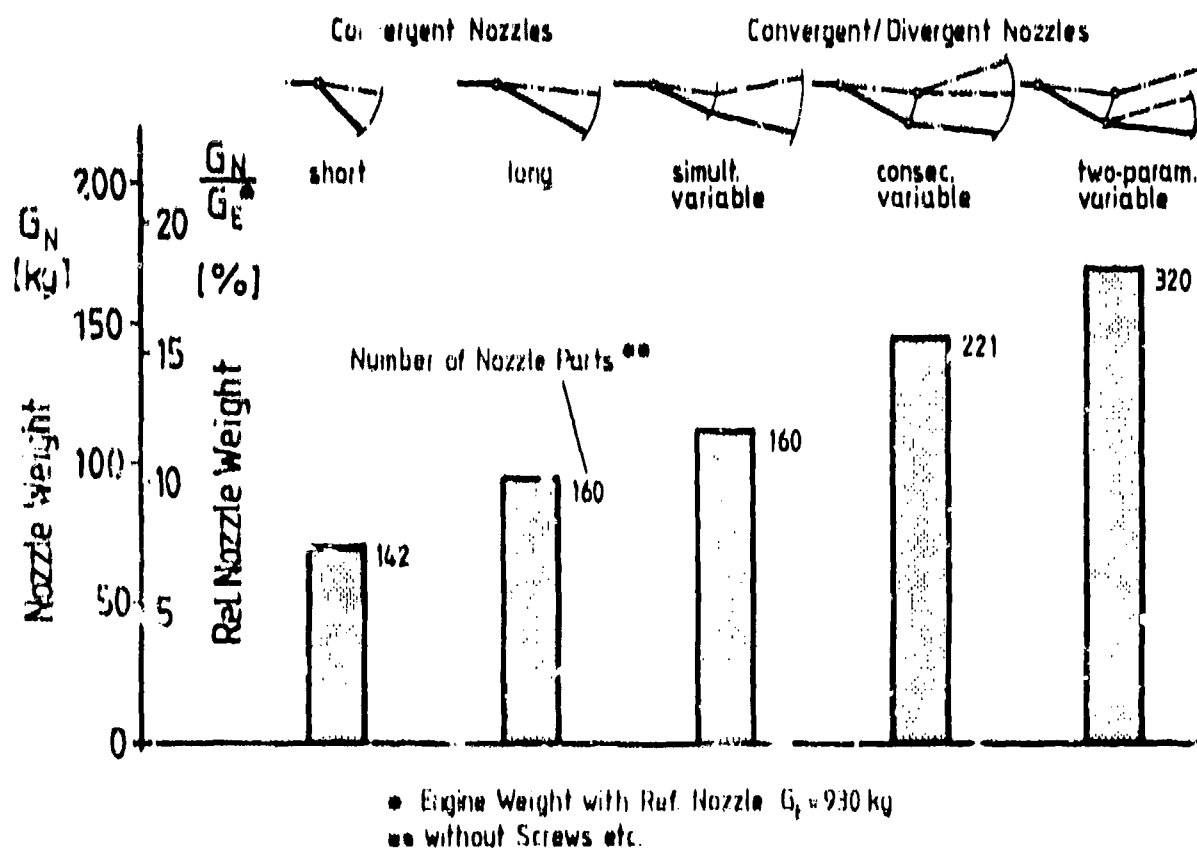


Fig. 8 Comparison of Nozzle Weight and Complexity

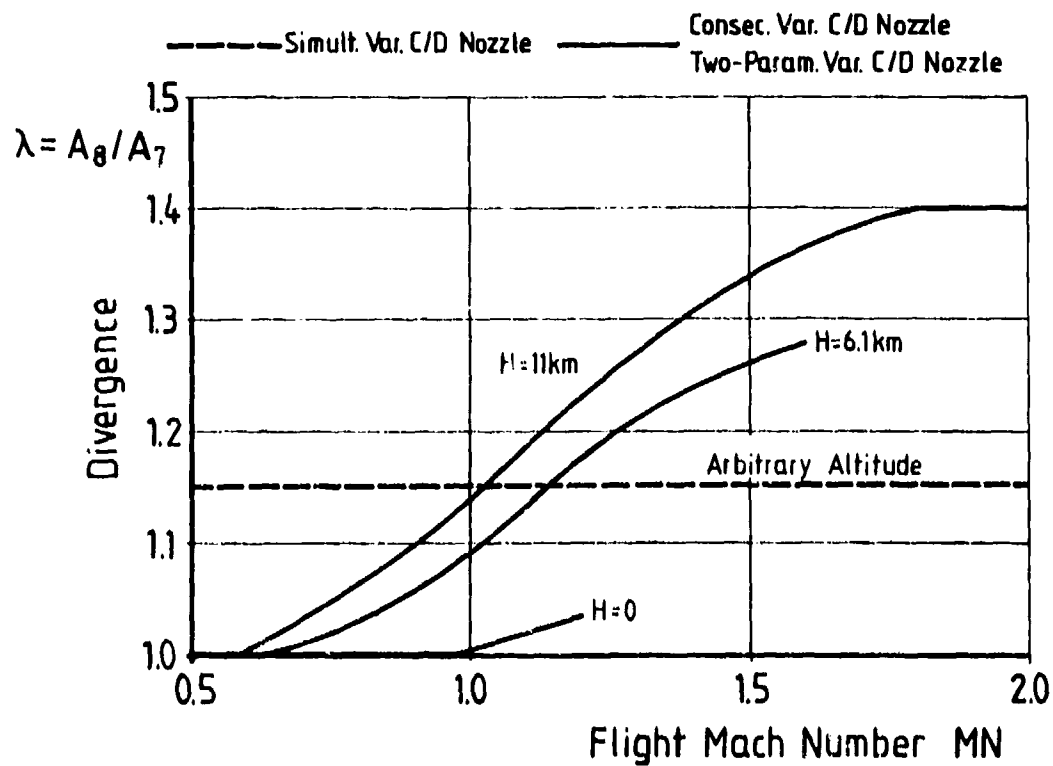


Fig. 9 Optimum Divergence of Convergent/Divergent Nozzles at Max. Reheat

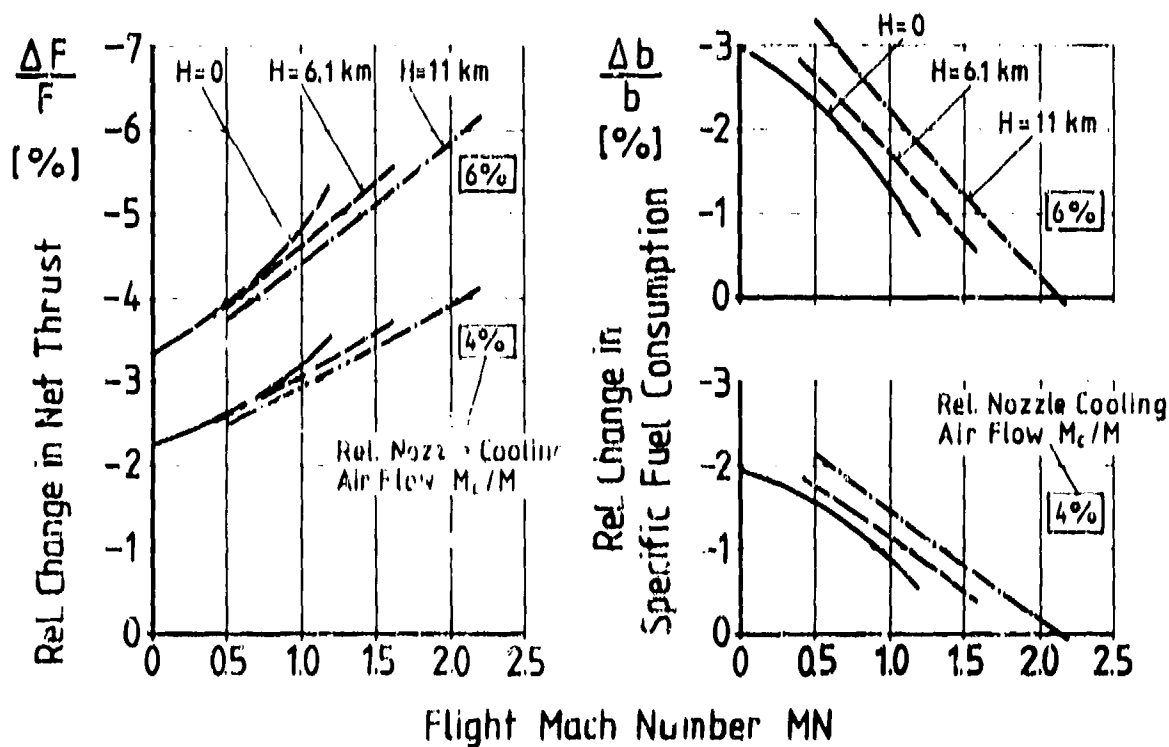


Fig. 10 Influence of Nozzle Cooling Air Flow on Net Thrust and Specific Fuel Consumption at Max. Reheat

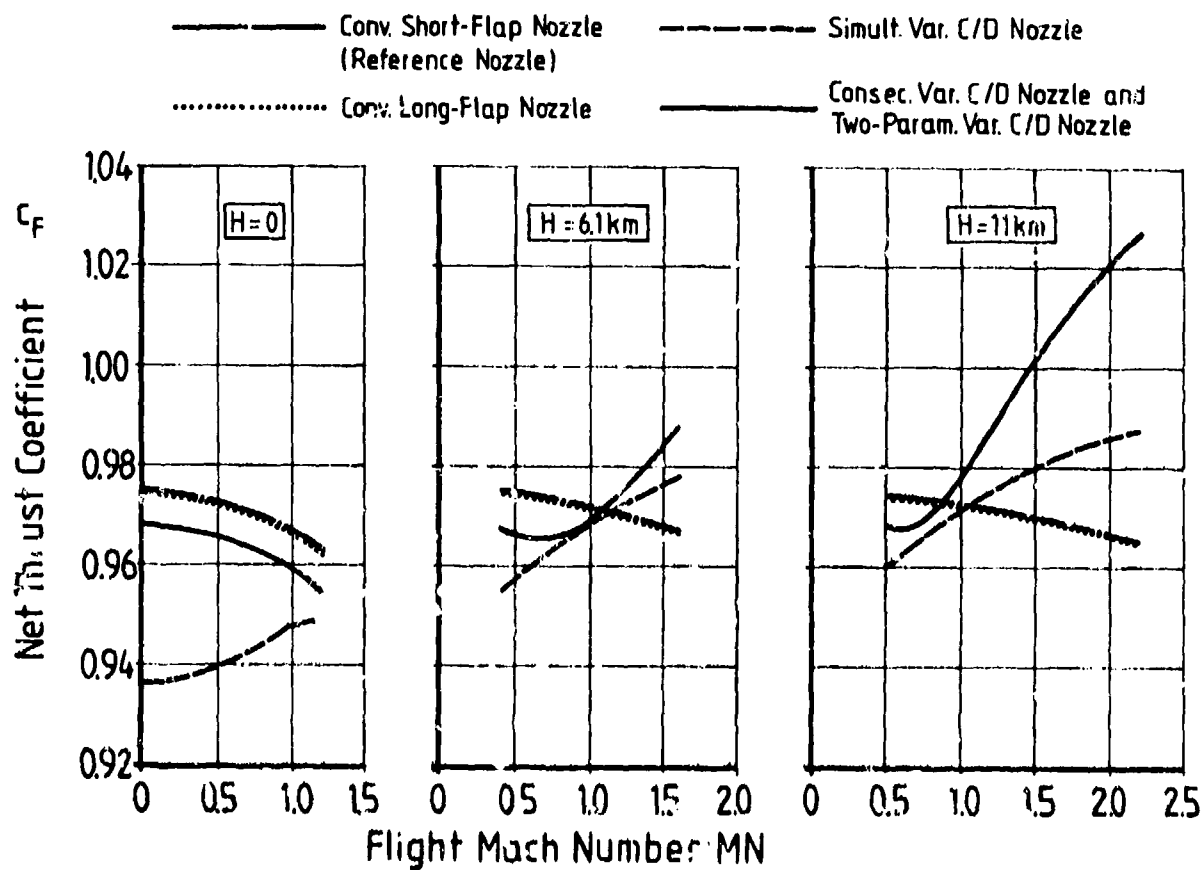


Fig. 11 Net Thrust Coefficient of Nozzles Compared at Max. Reheat

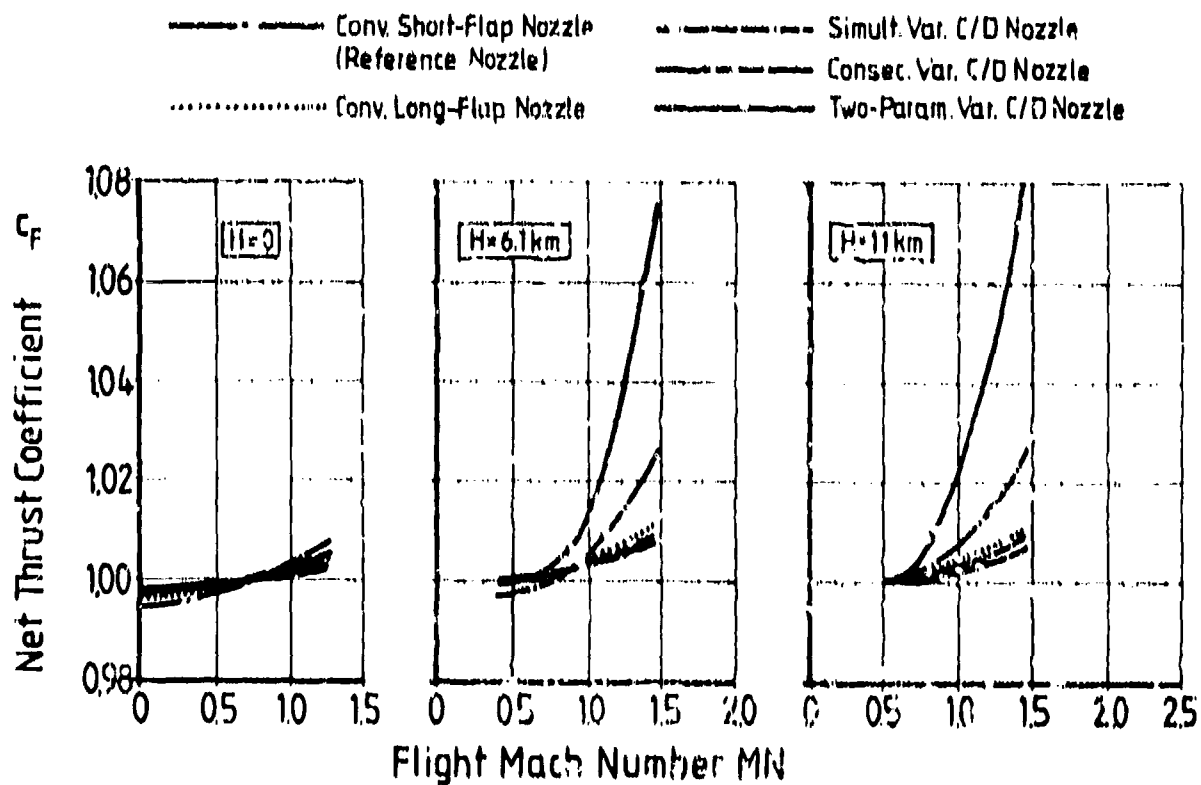


Fig. 12 Net Thrust Coefficient of Nozzles Compared at Max. Dry

TET = 1650 K
 OPR = 24
 BPR = Parameter

ISA, SLS, Max. Reheat

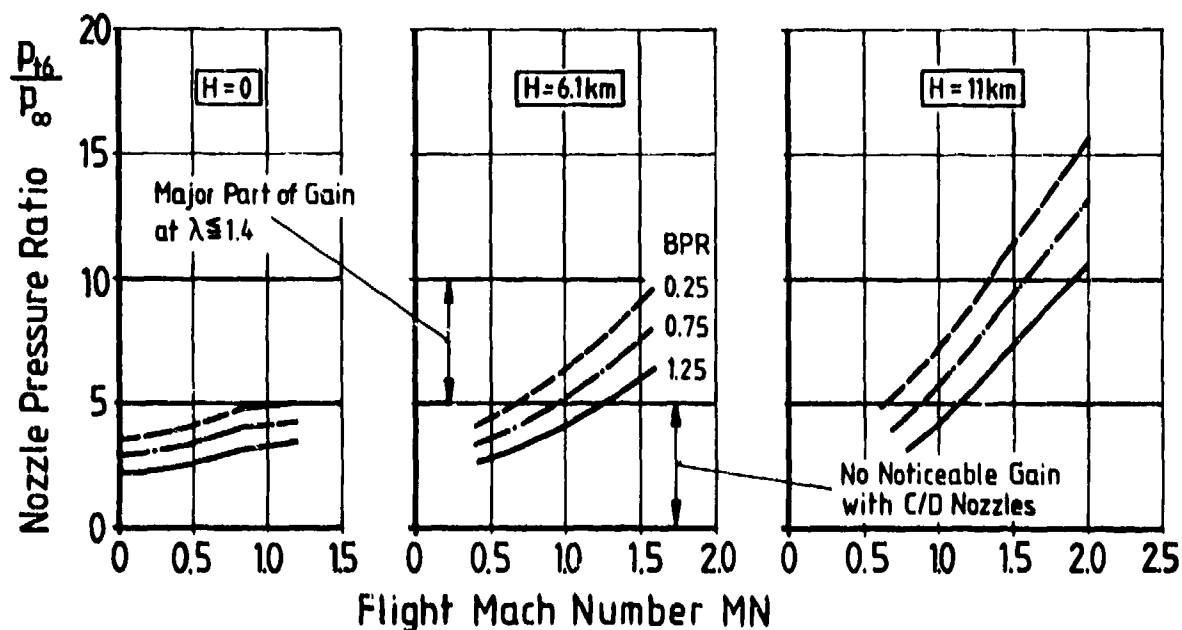


Fig. 13 Influence of Engine Design on Nozzle Pressure Ratio at Max. Reheat

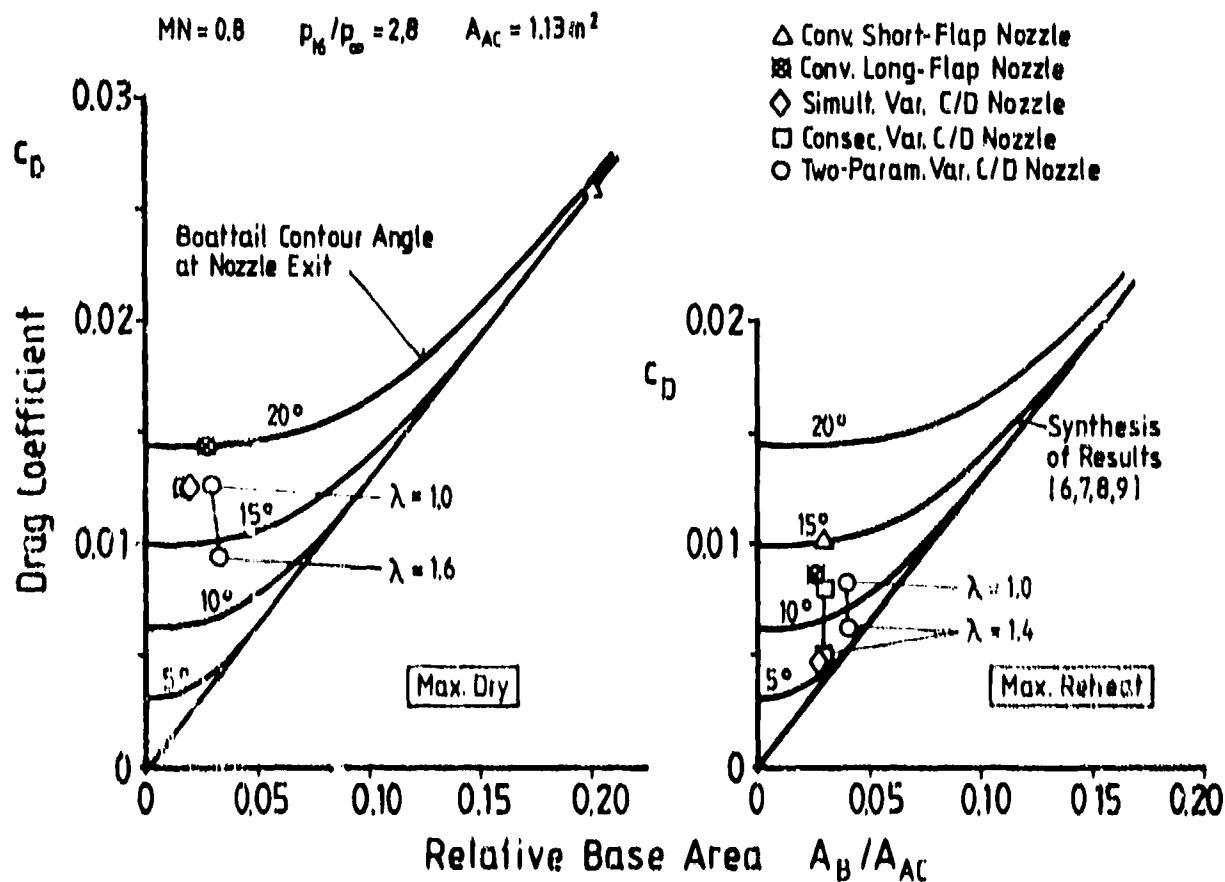


Fig. 14 Influence of Nozzle Concepts on Afterbody Drag Coefficient

ADVANCED EXHAUST NOZZLE TECHNOLOGY

by

Ronald J. Gildewell
Aero Propulsion Laboratory
Air Force Wright Aeronautical Laboratories
Wright-Patterson Air Force Base, Ohio USA

and

Robert E. Warburton
Pratt & Whitney Aircraft Group
Government Products Division
West Palm Beach, Florida USA

SUMMARY

Recent developments in turbine engine exhaust nozzle technology indicate the potential for significant advancements in the state-of-the-art. These technologies include nonaxisymmetric nozzles, thrust reversing, and thrust vectoring. Trade studies have been performed to determine the impact of these developments on the thrust-to-weight ratio and specific fuel consumption of an advanced high performance, augmented turbofan engine. Results are presented in a manner which provides an understanding of the sources and magnitudes of differences in the basic elements of nozzle internal performance and weight as they relate to conventional, axisymmetric nozzle technology. These comparisons are presented for three categories of nozzle functional capability: jet area and exit area control, thrust reversing, and thrust vectoring. This provides an understanding of the engine performance penalties associated with adding functional requirements to each of the nozzles considered in this study. Conclusions are presented and recommendations are made with regard to future directions of advanced development and demonstration.

SYMBOLS

A_e	Nozzle exit area
A_j	Nozzle throat area
AR	Nozzle aspect ratio (throat width/height at cruise power)
C_D	Nozzle/afterbody drag coefficient (wing area reference)
C_V	Velocity coefficient
F_n	Maximum thrust at sea-level static
TSFC	Uninstalled specific fuel consumption
$TSFC_{inst}$	Installed specific fuel consumption
W	Augmentor/nozzle weight
W_c	Total augmentor/nozzle cooling flow (percent of total air flow)
W_t	Engine weight

INTRODUCTION

Several areas of ongoing exploratory and advanced development offer potential for significant advancement in turbine engine exhaust nozzle technology. Substantial time and resources must be invested in each of these technology areas to properly develop their potential for production application.

To properly evolve a new technology into full-scale development in the turbine engine, after its conceptual value has been proven, substantiation must be provided of its ability to survive and function properly in the environment of the turbine engine. The ability to integrate any new technology with the remainder of the turbine engine must be proven. Just as importantly, its predicted performance, durability, reliability, maintainability and cost must be verified. The accomplishment of these tasks ultimately requires a full-scale ground test on a turbine engine. Since the time and resources that must be devoted to such a demonstration are so great, the Air Force, as well as industry, must be highly selective in the technologies they pursue. Often, a new technology which exhibits a great deal of potential for highly specialized applications must be placed on the "back burner" while another, with equal or greater potential for a broader range of applications, is being actively pursued in advanced development. This paper attempts to prioritize potential exhaust nozzle technology advancements, and makes recommendations regarding the path which should be taken in pursuing their development.

DISCUSSION

Emerging areas of development in turbine engine exhaust nozzle technology can be classified in several general categories. These include (1) nonaxisymmetric nozzles, (2) thrust reversing, and (3) thrust vectoring.

Nonaxisymmetric Nozzles

Nonaxisymmetric nozzles offer the potential for reduction in nozzle/afterbody drag. They offer aircraft and propulsion installation designers another degree of flexibility in tailoring the nozzle/afterbody installation to a specific aircraft design. Nonaxisymmetric nozzles may also have an advantage over axisymmetric nozzles when considering the addition of functional capabilities such as thrust reversing and/or thrust vectoring. The exhaust system weight and performance penalties encountered when adding functions to the nonaxisymmetric nozzle may be less than with the axisymmetric nozzle; however, the basic nonaxisymmetric nozzle is generally heavier than its axisymmetric counterpart.

Many government-sponsored programs have investigated the advantages and disadvantages of nonaxisymmetric nozzles in areas such as weights, cooling flow requirements, and internal performance. In addition, efforts are being made to determine the installed performance characteristics of various nonaxisymmetric exhaust systems in advanced aircraft.

Thrust Reversing

Thrust reversing has potential for application to current and advanced high performance aircraft for landing approach control and ground roll reduction. The potential also exists for using thrust reversal in flight for maneuverability enhancement. Thrust reversers can be very effective in reducing landing distances to levels comparable to takeoff distance capabilities, thereby providing balanced field length. They also provide a means of deceleration less sensitive to runway conditions than conventional means of braking. Problems do exist, however, in integrating the reverser both with the aircraft to minimize any adverse impact on the effectiveness of the vertical stabilizer, and with the turbine engine to avoid large performance penalties and stability problems.

Thrust Vectoring

Thrust vectoring has the potential to improve the ability to trade energy for increased instantaneous turn capability with high performance aircraft. However, the penalty in exhaust system, engine case and mount weights with thrust vectoring can be prohibitive. This is particularly true since the value of improving instantaneous turn capability at the expense of further losses in specific excess power is highly questionable.

Thrust vectoring also has potential for reducing field length requirements below that which can be achieved with thrust reversing alone. Properly employed during the takeoff ground roll, thrust vectoring can significantly reduce the distance required prior to rotation. Thrust vectoring also has the potential to reduce aircraft approach speed, and thus reduce landing distances and touch-down dispersion. Requirements for future tactical aircraft appear to be directed toward a combination of STOL and supersonic capabilities. This could be satisfied to a degree with thrust reversing; however, it is not clear how much STOL capability will be required to effectively counter runway denial operations. Thus, the degree of thrust vectoring required, if any, remains to be defined. If thrust vectoring is required to further enhance STOL capability, it may have a significant impact on installed performance and operational capabilities of the aircraft.

STUDY RESULTS

The purpose of this study was to determine the impact of the previously discussed exhaust system technologies on engine thrust-to-weight, and engine specific fuel consumption. An attempt was also made to assess the impact on installed performance based on existing data. An analysis was conducted on several advanced exhaust nozzle concepts, both axisymmetric and nonaxisymmetric, incorporating different combinations of nozzle functions. For each concept, weights, cooling flow requirements, and internal performance were defined. These results then allowed for the determination of engine thrust-to-weight, and specific fuel consumption. Throttle-dependent drag was then estimated for each concept so that a preliminary assessment of installed specific fuel consumption could be made.

Baseline Conditions

The baseline engine used for this study was an advanced, moderate bypass ratio, afterburning turbofan engine with an axisymmetric convergent-divergent nozzle. The functional capabilities of the baseline nozzle were confined to jet area and exit area control.

The cooling systems were sized for sea-level takeoff, maximum afterburning, which was also the condition at which engine thrust-to-weight was evaluated. Internal nozzle performance was calculated for subsonic and supersonic cruise since these are the flight conditions where specific fuel consumption is of critical importance.

Study Configurations

The configurations considered in this study are summarized in Table I. Note that there are three basic functional groups for comparison. Group 1 comprises configurations 1 and 4 which provide a comparison of the axisymmetric and nonaxisymmetric convergent-divergent nozzles with jet area and exit area control only. Group 2 includes configurations 2 and 5 and compares the axisymmetric and nonaxisymmetric nozzles with jet area and exit area control, and the added function of thrust reversing. Group 3 then consists of the remaining configurations 3, 6, 7 and 8, which compare axisymmetric and various nonaxisymmetric nozzles with jet area and exit area control, thrust reversing and thrust vectoring. The nonaxisymmetric nozzles in this group include the nonaxisymmetric convergent-divergent nozzle, the MADIEN, and the plug nozzle. Note that only low aspect ratio (AR = 4.0) nonaxisymmetric nozzles were considered during this study.

Table I. Study Nozzle Configurations

Configuration		
1	Axisymmetric (C-D)	A _j and A _e Control
2	Axisymmetric (C-D)	A _j and A _e Control, Upstream, T/R
3	Axisymmetric (C-D)	A _j and A _e Control, Upstream, T/R and T/V
4	Nonaxisymmetric (C-D)	A _j and A _e Control
5	Nonaxisymmetric (C-D)	A _j and A _e Control, T/R
6	Nonaxisymmetric (C-D)	A _j and A _e Control, T/R and T/V
7	Nonaxisymmetric MADIEN*	A _j and A _e Control, T/R and T/V
8	Nonaxisymmetric Plug	A _j and A _e Control, T/R and T/V

*Multi-Application Deflector Exhaust Nozzle.

● Configuration 1 — Axisymmetric Baseline

The baseline nozzle is an axisymmetric convergent-divergent nozzle with variable jet area and exit area. This configuration is shown in Figure 1, and consists of balance, convergent, and divergent flaps, located axially, adjacent to a similar series of axial seals. Fifteen (each of these flap and seal strings make up the flowpath, giving an approximation of a circular cross section.

● Configuration 2 — Axisymmetric with Upstream Thrust Reverser

Thrust reversing capability is added to the baseline axisymmetric nozzle through the use of a clamshell arrangement located upstream of the afterburner/nozzle module shown in Figure 2. During reversed thrust operation the clamshell uncovers reverser ports located on the top and bottom of the engine case and deflects the exhaust flow into the ports. Exit flow angle is controlled through cascade vanes located in each port. The portion of the exhaust system downstream of the reverser is the same as in configuration 1.

● Configuration 3 — Axisymmetric with Upstream Thrust Reverser and Thrust Vectoring

This configuration, shown in Figure 3, consists of a translating nozzle for conventional jet area control with an additional actuation system for exit area control as in the previous configurations. The clamshell reverser system is located just upstream of the nozzle (downstream from that of configuration 2). Thrust vectoring up to 20 deg is accomplished through a gimbal arrangement which rotates the whole aft section of the nozzle. This nozzle is similar to that of configurations 1 and 2 in terms of kinematics.

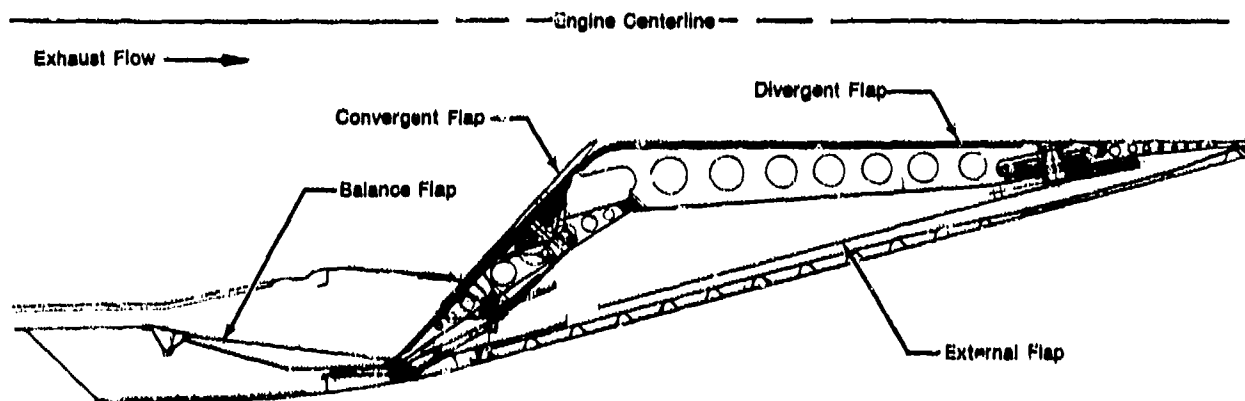


Figure 1. Advanced Axisymmetric Nozzle with Jet Area and Exit Area Control

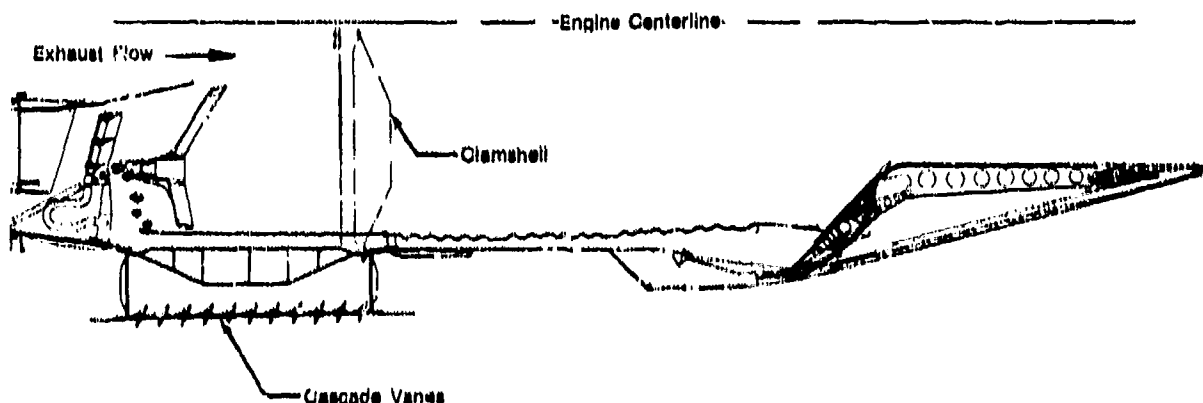


Figure 2. Advanced Axisymmetric Nozzle with Jet Area, Exit Area Control, and Upstream Thrust Reverser

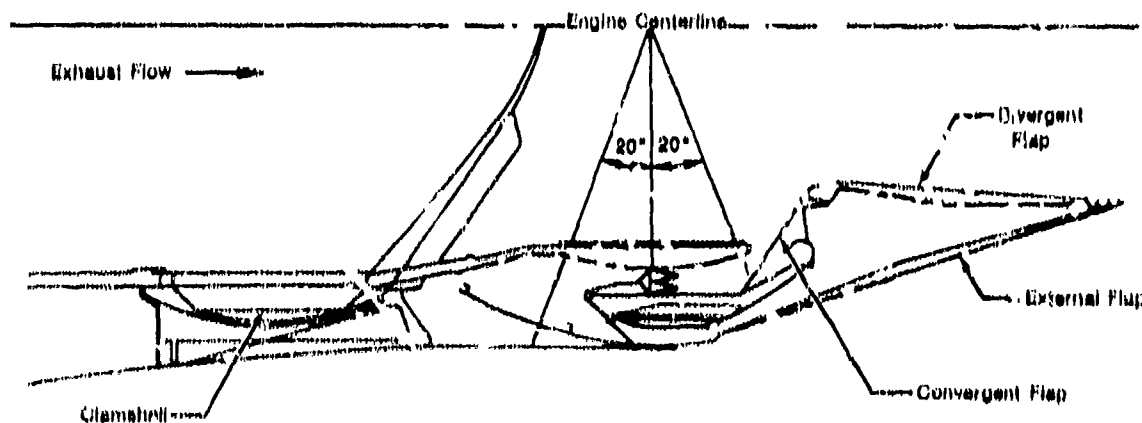


Figure 3. Advanced Axisymmetric Nozzle with Jet Area, Exit Area Control, Upstream Thrust Reversing, and Thrust Vectoring

● **Configuration 4 — Nonaxisymmetric Convergent-Divergent Nozzle**

This nonaxisymmetric (two-dimensional) convergent-divergent nozzle, shown in Figure 4, is typical of two-dimensional nozzles in that the nozzle cross section is square or rectangular with a transition from a circular cross section upstream of the nozzle. This type of nozzle usually results in a fewer number of moving parts since the sidewalls are stationary. The major moving parts are the top and bottom flaps, which are used to control jet area and exit area. This particular configuration consists of two convergent flaps (top and bottom), two divergent flaps, and two external flaps which serve as aerodynamic fairings as well as the means by which exit area is controlled.

● **Configuration 5 — Nonaxisymmetric Convergent-Divergent with Thrust Reversing**

This nozzle configuration, shown in Figure 5, is similar to configuration 4 except that the convergent flaps are allowed to pivot around their mid-axial location to close off the axial flowpath. The forward end of the convergent flap opens the reverser ports top and bottom, which in turn directs the flow out of the ports, resulting in reversed thrust.

● **Configuration 6 — Nonaxisymmetric Convergent-Divergent with Thrust Reversing and Vectoring**

This configuration, shown in Figure 6, is similar to that of configuration 5 with the added capability of deflecting the divergent flaps in unison either up or down. This results in vectored thrust in either the upward or downward direction. This added function requires stronger (usually heavier) divergent flaps and a more complicated actuation system than needed for area control alone.

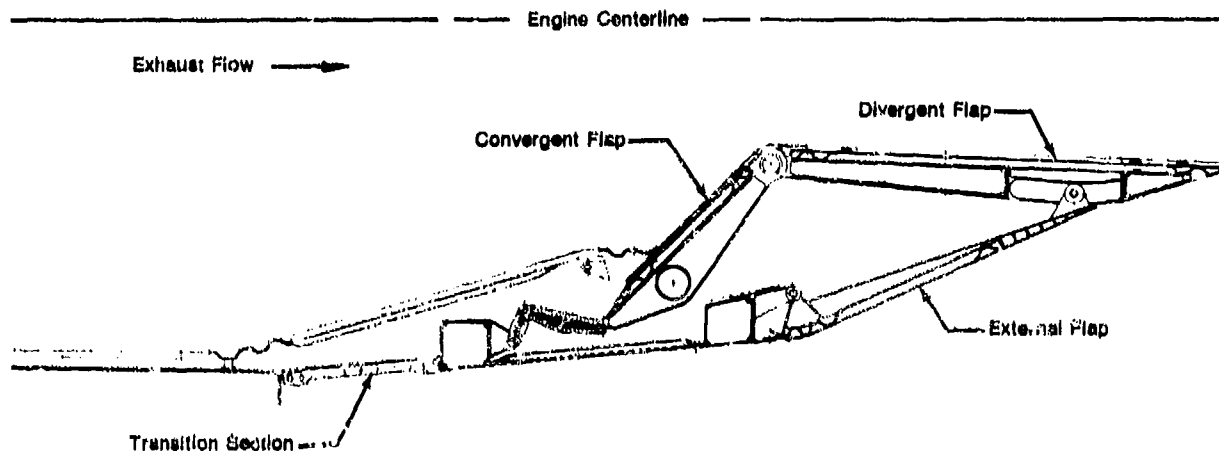


Figure 4. Nonaxisymmetric Convergent/Divergent Nozzle with Jet Area and Exit Area Control

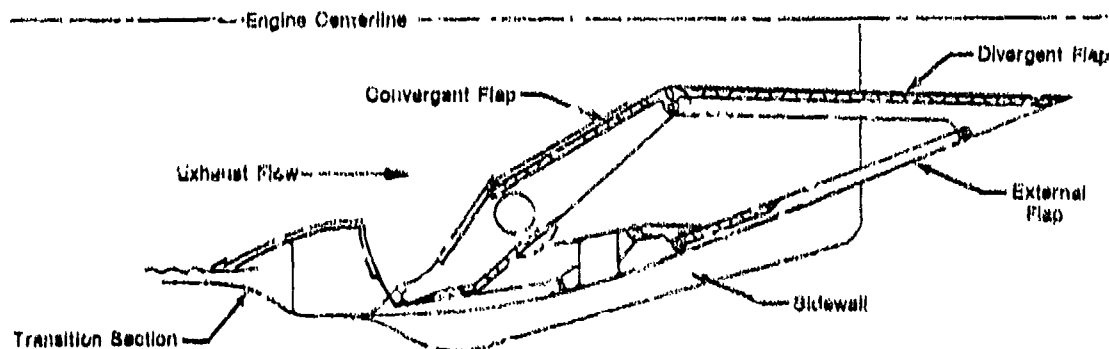


Figure 5. Nonaxisymmetric Convergent/Divergent Nozzle with Jet Area, Exit Area Control, and Thrust Reversing

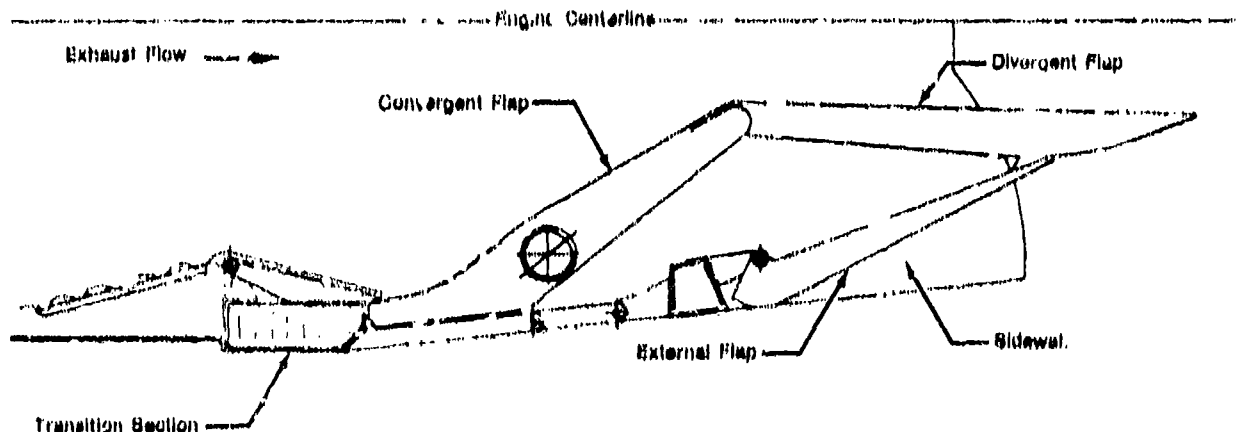


Figure 6. Nonaxisymmetric Convergent/Divergent Nozzle with Jet Area, Exit Area Control, Thrust Reversing and Thrust Vectoring

● **Configuration 7 — Multi-Application Deflector Exhaust Nozzle (MADEN) with Thrust Vectoring and Reversing**

This configuration, shown in Figure 7, is another nonaxisymmetric nozzle also having thrust reversing and thrust vectoring capabilities. Unlike the nonaxisymmetric convergent divergent nozzle, this nozzle is not symmetrical between top and bottom, but rather incorporates an expansion ramp in addition to the convergent and divergent flaps of the previous configuration. Reversing is accomplished in a similar manner to the technique used in configurations 5 and 6 — by rotating the convergent flaps inward to the engine centerline while at the same time opening reverser ports at the forward end of the convergent flap. Vectoring is accomplished by deflecting the divergent flaps, as well as the expansion ramp, either up or down.

● **Configuration 8 — Nonaxisymmetric Plug Nozzle with Thrust Reversing and Vectoring**

The plug concept, shown in Figure 8, uses the pivoting boattail flaps to control both jet area and internal area ratio. Unlike the previous nozzles, a fixed relationship exists between the jet area and the internal expansion area ratio which prevents complete performance optimization with nozzle pressure ratio. The plug body provides thrust vectoring by rotating about the plug pivot. Upward rotation of the forward portion of the plug body causes a redistribution of the exhaust flow by increasing the percentage of flow through the lower throat passage and simultaneously canting the lower throat plane in the desired vectoring direction. Thrust reversing is accomplished by rotating the aft section of both boattail flaps inward until they contact the plug. The forward sections of the boattail flaps rotate outward in the rotation process, opening the reverser ports.

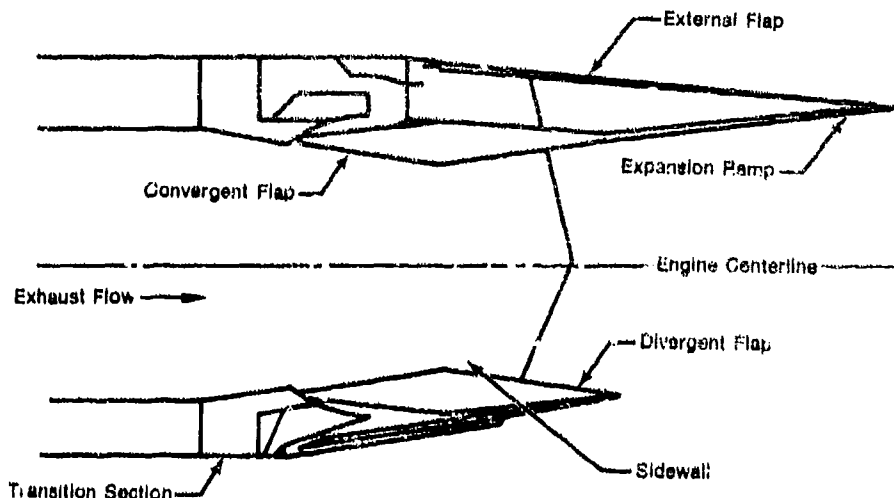


Figure 7. Nonaxisymmetric Multi-Application Deflector Exhaust Nozzle with Jet Area, Exit Area Control, Thrust Reversing, and Thrust Vectoring

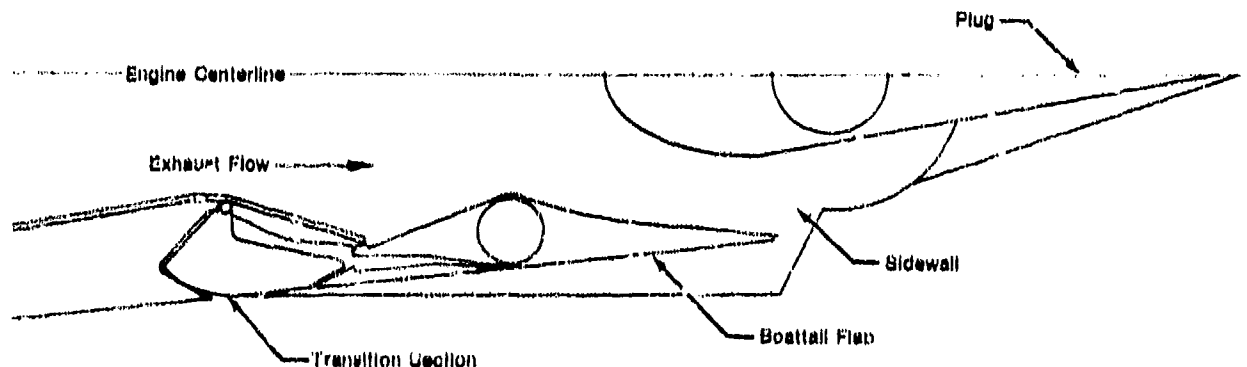


Figure 8. Nonaxisymmetric Plug Nozzle with Jet Area Control, Thrust Reversing, and Thrust Vectoring

Weight Comparison

Figures 9a, 9b, and 9c present a comparison of estimated augmentor/nozzle weight of the various study configurations relative to that of the baseline (configuration 1). Each figure presents a comparison of weight for those configurations having the same functional capability (the three groups previously discussed). These weight estimates were obtained primarily from the "Advanced Exhaust Nozzle System Demonstration" program, Reference 1, or updated information obtained from recent studies.

In comparing the results shown in Figure 9a, axisymmetric versus nonaxisymmetric with jet and exit area control, it can be seen that the axisymmetric has a 10% weight advantage over the nonaxisymmetric configuration. Figure 9b reveals that when thrust reversing is added to each of the nozzle concepts, the nonaxisymmetric is nearly 3% heavier than the baseline configuration, and the upstream reversing axisymmetric is nearly 48% heavier.

Figure 9c gives a relative comparison of the axisymmetric and three different nonaxisymmetric nozzles with area control, thrust reversing, and thrust vectoring. The MADEN was lightest, being 41% heavier than the baseline, followed by the axisymmetric at 51%, the convergent divergent nozzle at 58%, and finally the plug nozzle which was 91% — nearly twice as heavy as the baseline nozzle.

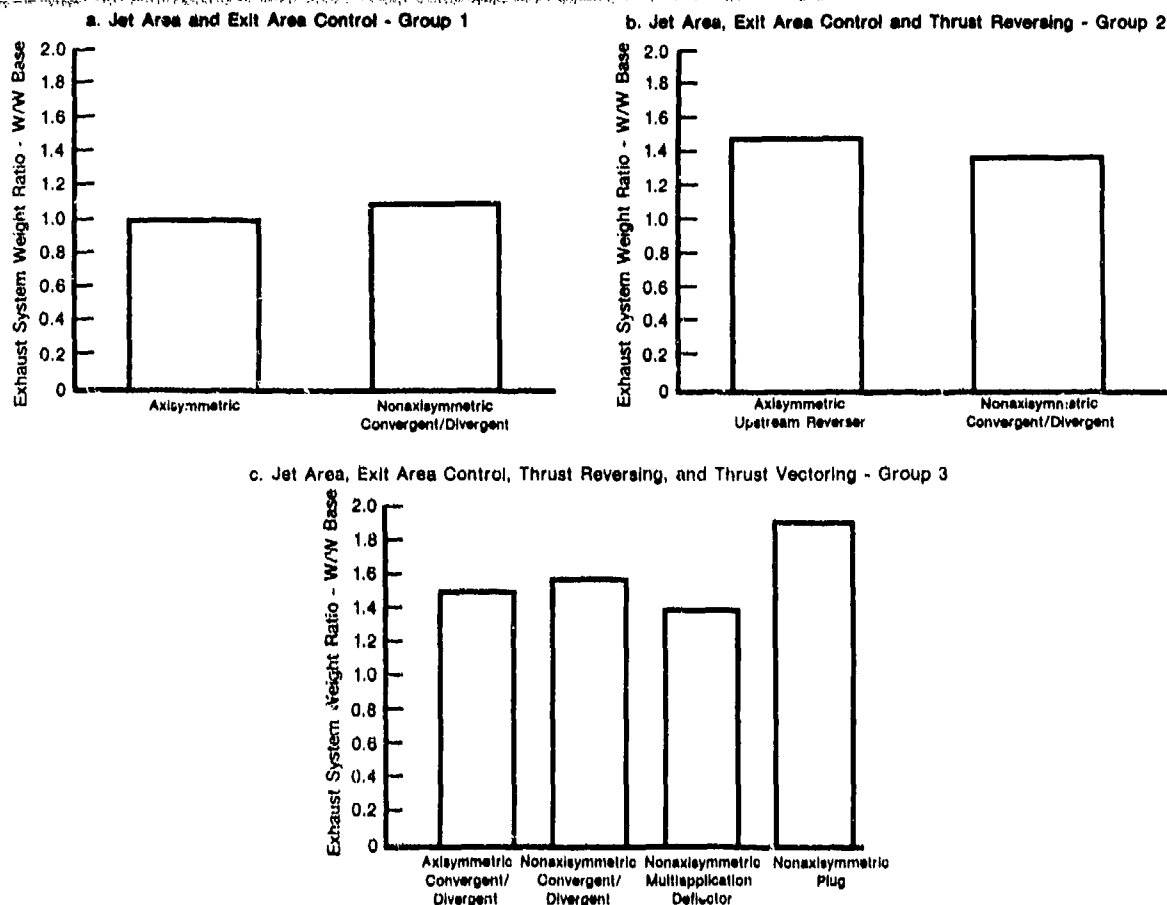


Figure 9. Exhaust System Weight Comparison (Afterburner and Nozzle)

Cooling Flow Requirements

Since the configurations were sized for the same basic afterburning engine, all augmentor/nozzle concepts required cooling to provide thermal integrity. Figures 10a, 10b, and 10c provide a comparison of the augmentor/nozzle cooling requirements relative to the baseline exhaust system for the three previously defined study groups.

In the comparison given in Figure 10a the nonaxisymmetric convergent-divergent nozzle with area control requires approximately 28% less cooling than its axisymmetric counterpart. Figure 10b shows that the same trend is true when thrust reversing is added. The difference is 22% for the upstream reversing axisymmetric relative to the nonaxisymmetric. It is apparent from Figures 10a and 10b that the upstream axisymmetric reverser requires no more cooling flow than the baseline. The nonaxisymmetric cooling requirements also change very little when thrust reversing is added. Less coolant flow is required for the nonaxisymmetric than the axisymmetric configuration since the former lends itself better to more efficient cooling techniques.

The results of the comparison of the three nonaxisymmetric nozzles, shown in Figure 10c, reveal that no additional cooling is required when thrust vectoring is added to the convergent-divergent configuration with area control and thrust reversing. The MADEN requires a considerably larger amount of coolant (48% more than the baseline) because of the extremely long expansion ramp flap, and also because of the less efficient cooling system selected in an effort to minimize weight. The axisymmetric requires 37% more cooling flow than the baseline, whereas the plug cooling system requires 18% more than the baseline. Despite the additional requirement for cooling the plug, more efficient cooling techniques minimize this cooling requirement.

Internal Nozzle Performance

The internal nozzle performance relative to the baseline nozzle is presented in Figures 11a, 11b, and 11c, again for the three study groups. These figures show comparisons for both subsonic and supersonic cruise since these are the conditions at which an advanced fighter aircraft operates a substantial part of the time. The internal nozzle performance shown in these figures is presented in terms of velocity coefficient (C_v). The nozzle C_v 's, shown in Figures 11a, 11b, and 11c, include the effects of nozzle leakage and performance losses due to cooling.

A comparison of the axisymmetric and nonaxisymmetric nozzles with area control in Figure 11a shows the latter with a slight edge in terms of internal performance (0.80%) over the baseline nozzle for subsonic cruise. For supersonic cruise, performance levels are identical for both nozzles. The same conclusions also are true when thrust reversing is added, shown in Figure 11b, since aerodynamically there is no difference with or without the thrust reversing function with either nozzle concept.

In comparing the axisymmetric and nonaxisymmetric nozzles with thrust vectoring, Figure 11c, one finds little difference between the nonaxisymmetric convergent-divergent nozzle (0.80% better than baseline), the MADEN (0.70% better than baseline) and the axisymmetric nozzle (0.50% better) for the subsonic cruise condition. The plug concept, on the other hand, has much lower nozzle performance (-4.8%) than the baseline at the subsonic cruise condition. This is due to the fixed relationship between jet area and internal expansion area ratio with the plug concept, which prevents complete performance optimization at a given operating condition. At supersonic cruise the baseline and the nonaxisymmetric convergent-divergent exhaust nozzle internal performance is the same. The lower cooling losses of the vectoring/reversing axisymmetric result in 0.5% higher performance than the baseline. The MADEN has 1.3% lower supersonic performance than the baseline, and the plug once again is significantly inferior, 8.9% lower than the baseline configuration, at supersonic cruise.

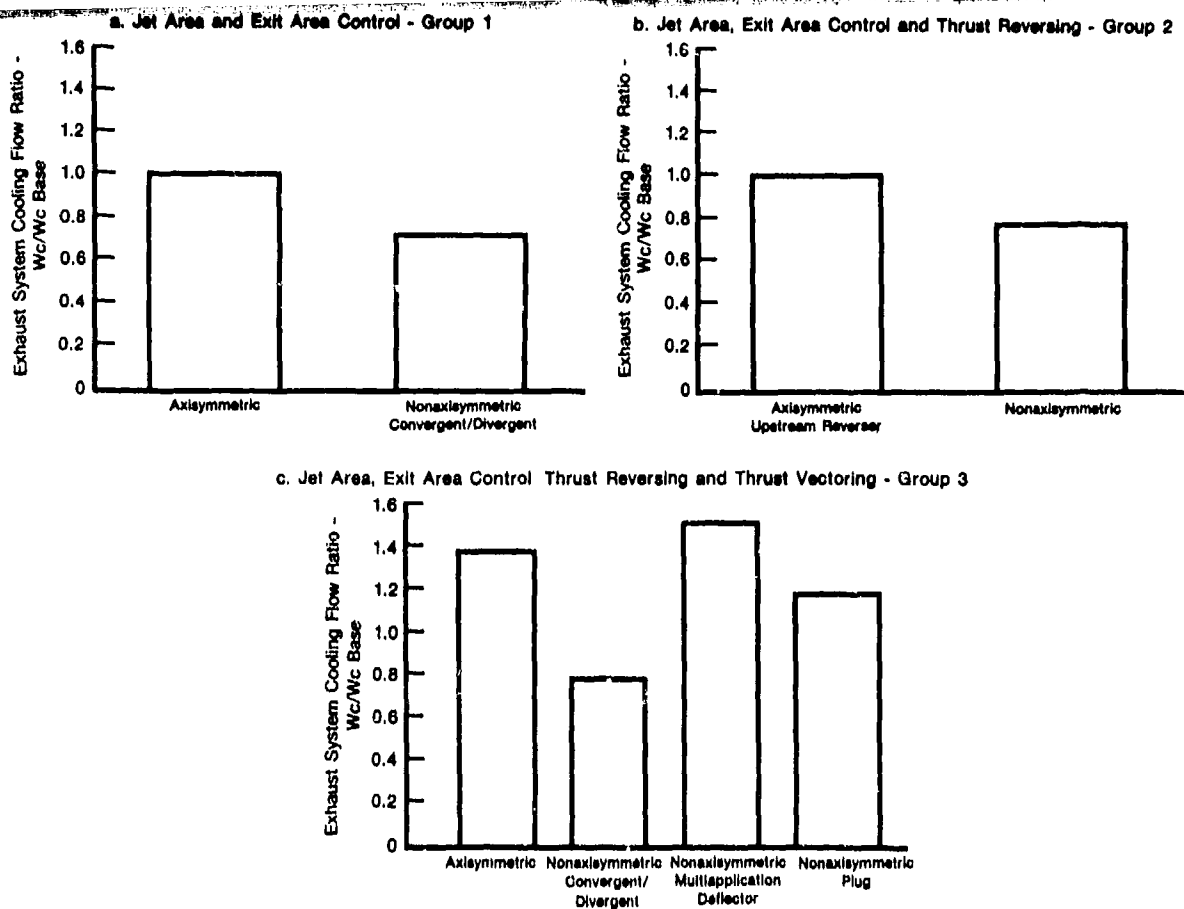


Figure 10. Exhaust System Cooling Flow (Afterburner and Nozzle)

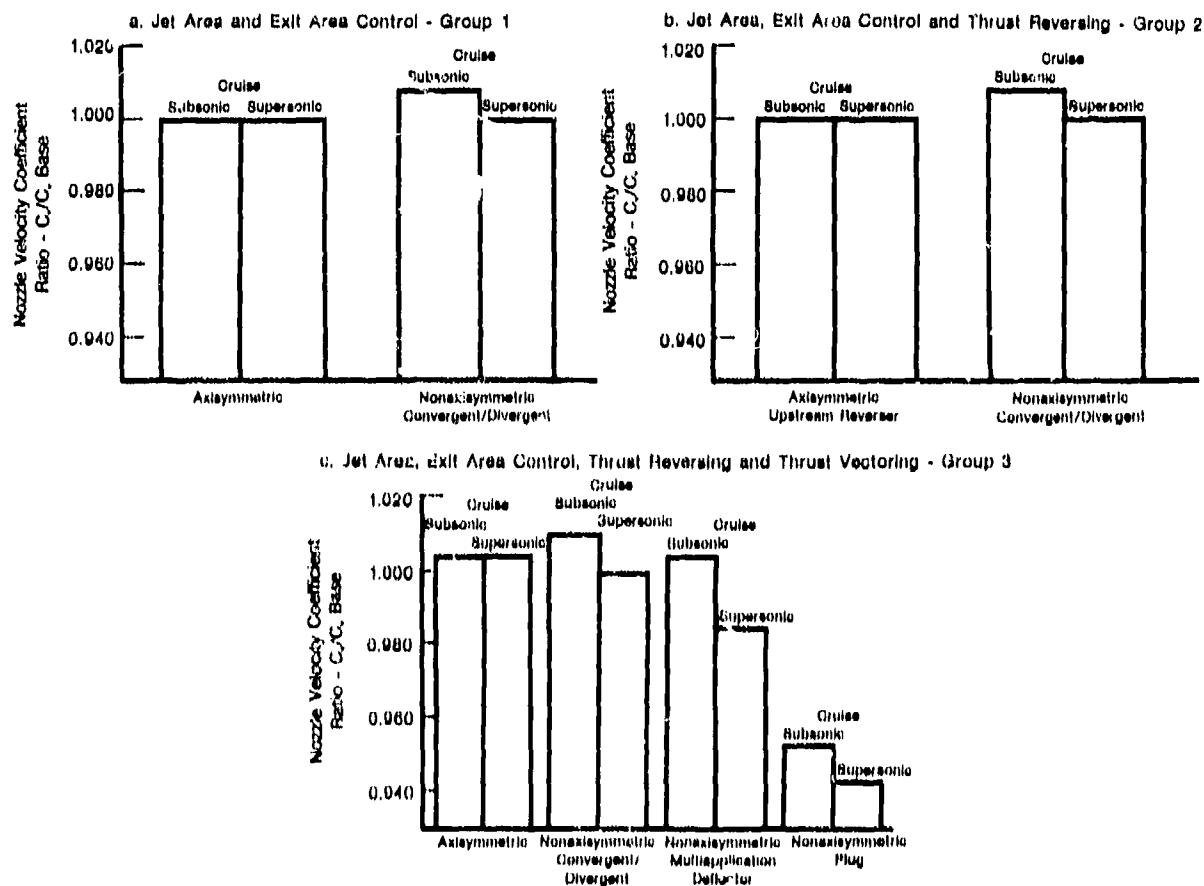


Figure 11. Exhaust Nozzle Velocity Coefficient (Including Cooling and Leakage)

Each of the nozzle configurations considered will have an impact on engine performance either in terms of weight or internal performance. The impact of exhaust system weight (thrust-to-weight) and nozzle aerodynamics (performance) on engine performance is obvious. However, the performance can be affected by nozzle cooling in two ways. First, the amount of cooling and the location at which it is discharged into the main gas stream can affect nozzle C_p , and has been included in the values given in Figures 11a, 11b, and 11c. Cooling flow also has an impact on afterburning thrust; if a smaller amount of flow is required for cooling, then there is more flow available for burning, and thus more thrust will result. To compare the nozzle concepts in terms of their impact on engine performance, engine thrust-to-weight and thrust specific fuel consumption have been calculated for each nozzle configuration.

● Engine Thrust-to-Weight

Engine thrust-to-weight comparisons are given in Figures 12a, 12b, and 12c for each nozzle configuration relative to the baseline nozzle. The operating condition assumed for this analysis was sea-level static, maximum afterburning. From Figure 12a it can be seen that the baseline nozzle resulted in the engine with the highest thrust-to-weight, followed closely (within 1.0%) by the nonaxisymmetric convergent-divergent nozzle with area control. The addition of reversing gave the nonaxisymmetric convergent-divergent nozzle a slight edge (92% of baseline) over the upstream reversing axisymmetric (91% of baseline) as shown in Figure 12b. The addition of thrust vectoring resulted in the MADEN with the advantage, 91% of baseline thrust-to-weight, with the convergent-divergent nonaxisymmetric and axisymmetric nozzles next each at 90% baseline thrust-to-weight as shown in Figure 12c. As might be expected, the nonaxisymmetric plug made a poor showing at 77% of the baseline thrust-to-weight.

Thus, it appears there is very little difference in terms of engine thrust-to-weight between the axisymmetric, and the nonaxisymmetric convergent-divergent or MADEN with similar capabilities. Only the nonaxisymmetric plug nozzle surfaced as a clear loser.

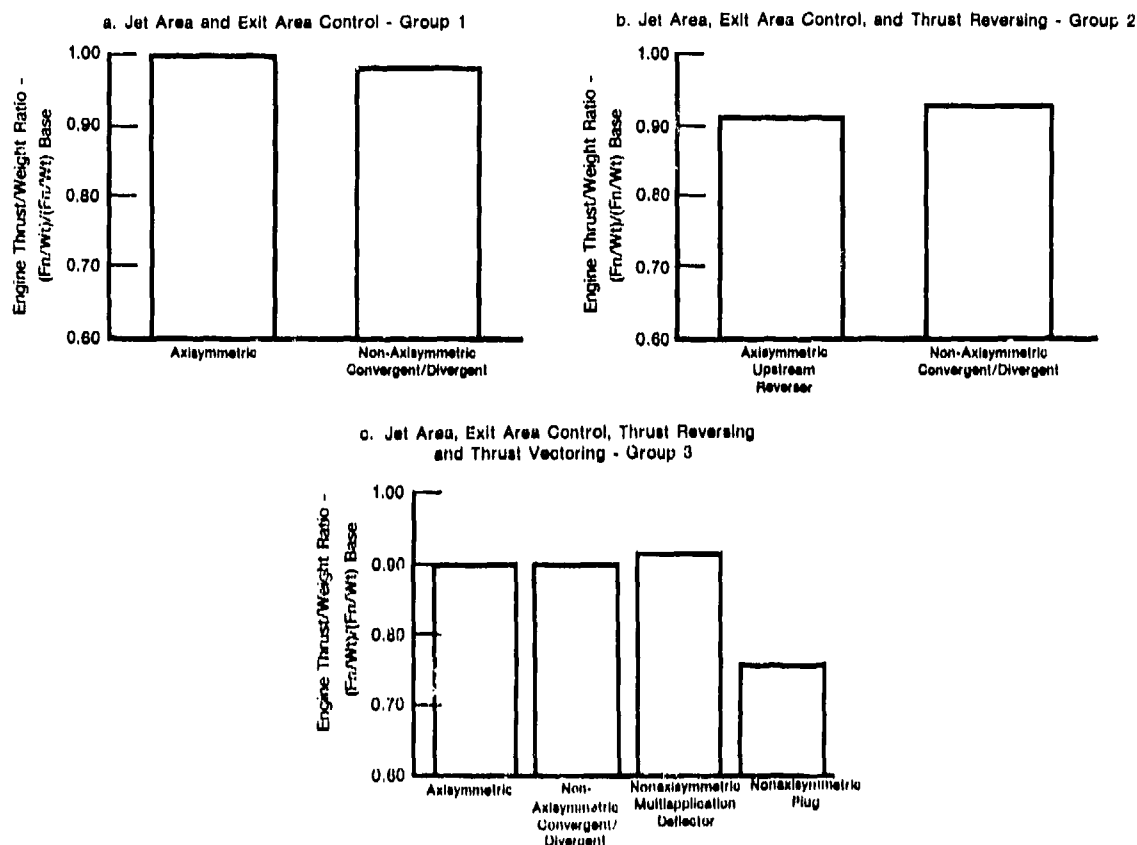


Figure 12. Engine Thrust/Weight Comparison (Sea Level Static - Maximum Afterburner)

● Uninstalled Engine Thrust Specific Fuel Consumption

Subsonic Cruise

Engine TSFC comparisons, at constant power setting, are given for the three study groups in Figures 13a, 13b, and 13c for subsonic cruise. Figure 13a shows a 1.4% improvement in TSFC for the nonaxisymmetric nozzle with area control relative to the baseline axisymmetric configuration. Figure 13b shows similar results for the group 2 nozzles with thrust reversing added. For the fully functional nonaxisymmetric nozzles compared in Figure 13c, the convergent-divergent nozzle retains a slight edge of 1.4% (under the baseline axisymmetric) versus 1.3% for the MADEN. The axisymmetric was next with 0.90% under the baseline with the plug nozzle again fairs poorly with a 10.4% higher TSFC than the baseline axisymmetric.

Supersonic Cruise

Figures 14a, 14b, and 14c show the supersonic TSFC comparisons, at constant power setting, relative to the baseline axisymmetric for the study nozzle configurations. Figures 14a and 14b conclude that there is no difference between the axisymmetric and nonaxisymmetric convergent-divergent configurations with area control, as well as with thrust reversing added. Figure 14c, in comparing the axisymmetric and three nonaxisymmetric fully functional nozzles, shows the vectoring/reversing axisymmetric 1.3% lower than the baseline and the convergent-divergent nozzle equal to the axisymmetric baseline. The multi application deflector exhaust nozzle TSFC is 3.5% higher than the baseline, and the plug 17.5% higher.

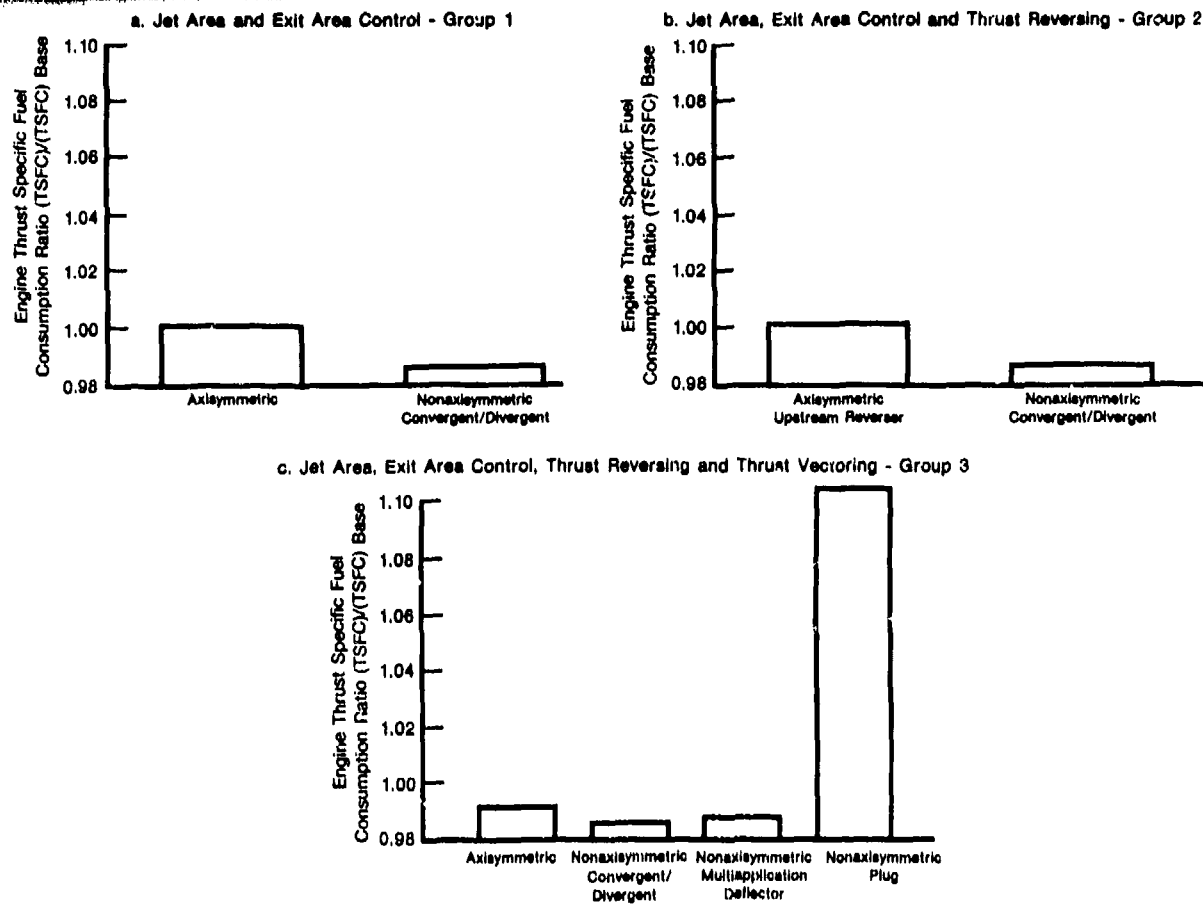


Figure 13. Thrust Specific Fuel Consumption - Uninstalled (Subsonic Cruise)

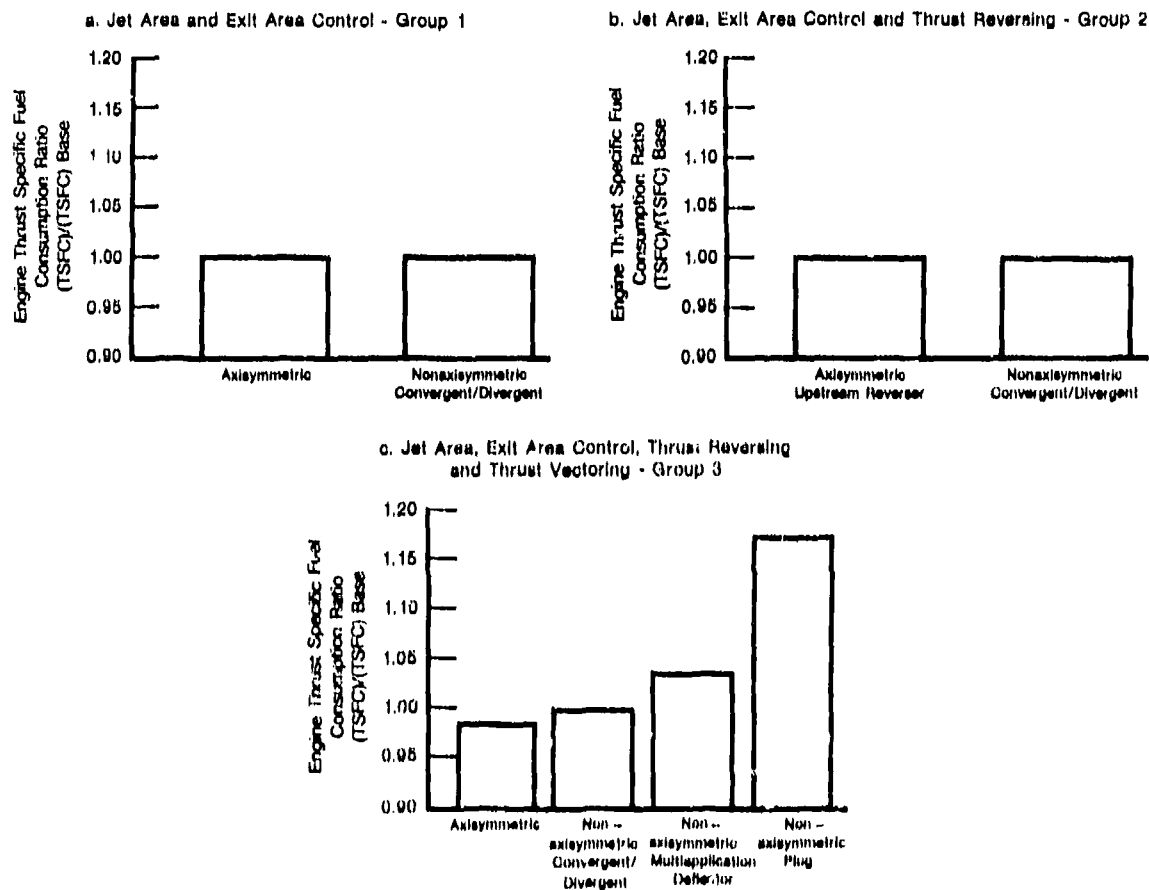


Figure 14. Thrust Specific Fuel Consumption - Uninstalled (Supersonic Cruise)

● Installed Engine Thrust Specific Fuel Consumption

The exhaust nozzle is a unique component of a military turbine engine in that its integration with high performance aircraft can have a large impact on the performance of the overall weapon system.

Because of this impact, an attempt was made to compare the relative installed thrust specific fuel consumptions of some of the study configurations. To do this, throttle-dependent, nozzle/afterbody drag was estimated based on windtunnel data from previous studies. This data was then used to generate installed thrust specific fuel consumption values for selected configurations, for a subsonic cruise flight condition. The results of this study by no means is meant to represent an absolute installed thrust specific fuel consumption comparison for the overall weapon system, since this would require that the drag effects of the specific overall weapon system be included.

In addition, in order to have a direct comparison of the axisymmetric and the nonaxisymmetric configurations, the axisymmetric configuration 1 was again used for the baseline. Thus, installation effects are included in this comparison which may unjustly penalize one or the other nozzle types (axisymmetric or 2-D), depending on the nozzle type for which the basic study aircraft was optimized. The inclusion of the installation effects was deemed necessary in order to obtain a direct comparison between the nozzle types for a given aircraft configuration.

As one might expect, depending on the aircraft configuration, engine location, and installation, different installed performance results will occur. Absolute results would therefore depend on such things as whether the engine is mounted under the wings vs in the tail, or whether the engines are closely spaced vs wide spacing, single engine vs twin engines, and number and location(s) of the vertical stabilizer(s).

Since many of these configurations have been evaluated in other studies, a minimum/maximum band is presented for the nonaxisymmetric nozzles relative to the axisymmetric baseline.

These results are shown in Figure 15a for the group 1 nozzle configurations. This figure indicates that the nonaxisymmetric convergent/divergent nozzles can be from 3% worse than the axisymmetric baseline to 3% better. The same is true when thrust reversing is added, as shown in Figure 15b. The axisymmetric with thrust reversing and vectoring is slightly better than the baseline axisymmetric, as shown in Figure 15c, due to its better uninstalled thrust specific fuel consumption. The nonaxisymmetric convergent/divergent thrust reversing and vectoring configurations are the same as shown in Figures 15a and 15b. The nonaxisymmetric MADEN nozzle results, shown in Figure 15c, indicate that installed thrust specific fuel consumption can vary from as good as the axisymmetric baseline to 1.6% better than the baseline configuration. Due to the lack of windtunnel data on the plug nozzle, no attempt was made to assess installed performance effects. Although limited data was available for specific aircraft configurations, it was insufficient for general conclusions.

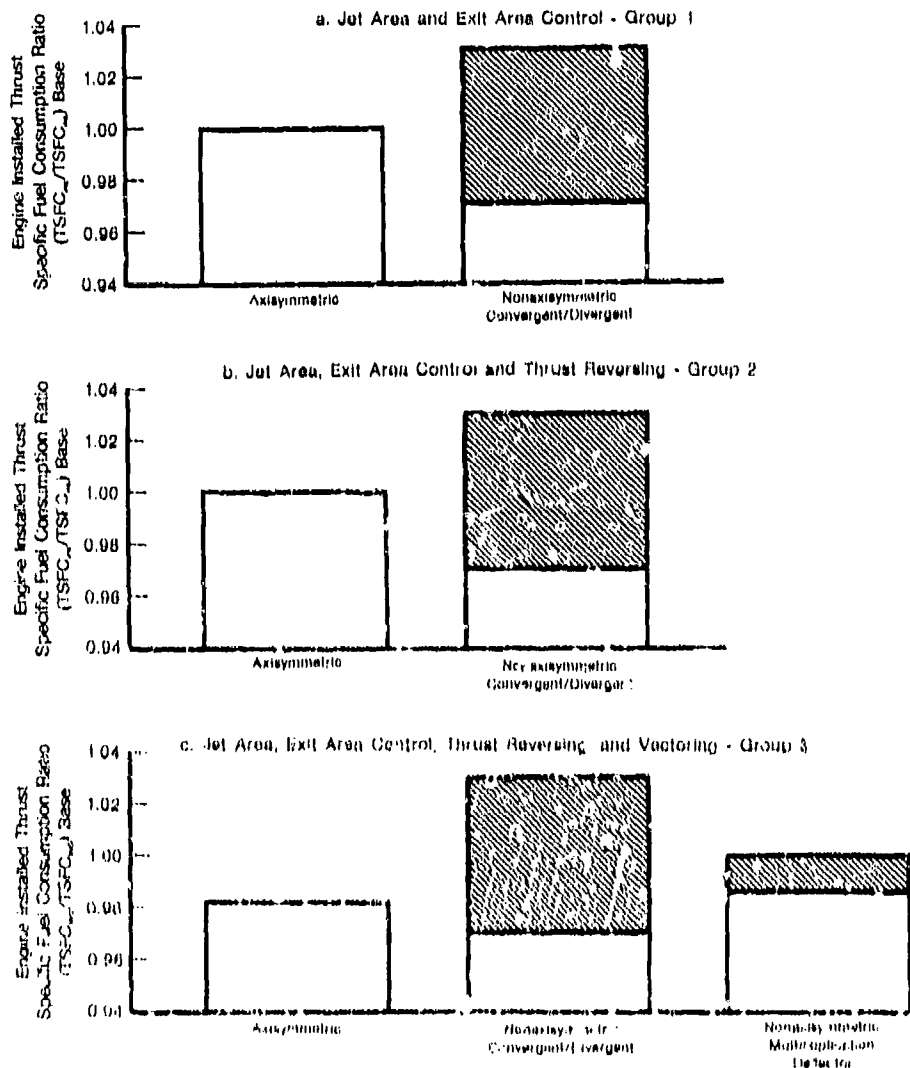


Figure 15. Thrust Specific Fuel Consumption - Installed (Subsonic Cruise Angle of Attack = 0)

The results of this study indicate that it is possible to get reversals in rankings when comparing uninstalled and installed thrust specific fuel consumptions. It also should be noted that these installed comparisons are only for subsonic cruise conditions and in some cases different results may occur for supersonic cruise conditions. The results shown in this paper therefore indicate that installation effects must be taken into account when evaluating engine performance with various nozzle configurations.

CONCLUSIONS

Based on the results of this study, the following conclusions are drawn:

1. Axisymmetric nozzles are competitive with nonaxisymmetric nozzles in terms of their impact on engine performance, regardless of the number of functions the nozzle is required to perform.
2. Installation effects must be accounted for in evaluating the impact of various, generically different nozzle configurations on engine performance.
3. The impact of adding additional functional capabilities (i.e., thrust vectoring, thrust reversing) to the exhaust nozzle is significant only in terms of engine thrust-to-weight.
4. The penalties in all aspects of engine performance associated with using a plug nozzle are very great regardless of the functions which the nozzle is required to perform.

RECOMMENDATIONS

The following recommendations are made regarding the paths of future development in exhaust nozzle technology based on the knowledge gained from this study:

1. Future development of multi-functional exhaust nozzles should give equal consideration to both axisymmetric and nonaxisymmetric nozzles.
2. If additional functions are required to be performed with future exhaust systems, efforts should be concentrated on minimizing their negative impact on engine thrust-to-weight.
3. Any future consideration of the plug nozzle as a design option should be minimized, if not eliminated.

REFERENCES

1. Pratt & Whitney Aircraft Group, Government Products Division, "Advanced Exhaust Nozzle System Demonstration," (Contract No. F33615-78-C-2400), Report FR-10909, Quarterly R&D Status Report No. 2, 27 November 1978.
2. McDonnell Aircraft Company (Prime), Pratt & Whitney Aircraft Group, Government Products Division (Sub), "Advanced Exhaust Nozzle System Concepts Demonstration," Contract F35615-77-C-3094.
3. Wolfe, L.D., and Fanning, A.E., "Advanced Nozzle Technology," AFAPL-TR-78-20, June 1978.
4. Glidewell, R.J., "Advanced Technology Exhaust Nozzle Installed Performance Comparison," AFAPL-TM-79-12, March 1979.
5. Glidewell, R.J., "Installation Trades for Axisymmetric and Nonaxisymmetric Nozzles," AIAA 80-1084, June 1980.

A NUMERICAL INVESTIGATION OF EXHAUST PLUME TEMPERATURE EFFECTS ON NONAXISYMMETRIC NOZZLE/AFTBODY PERFORMANCE

by

K. M. Peery
Specialist Engineer
Boeing Military Airplane Company
Seattle, Washington 98124
U.S.A.

and

Lt. D. L. Russell
U.S. Air Force Wright Aeronautical Labs
Wright-Patterson AFB, Ohio 45433
U.S.A.

SUMMARY

Nonaxisymmetric nozzles are being investigated for future generations of military aircraft to meet diverse mission requirements. One nozzle of this type, a single expansion ramp nozzle (SERN), has undergone extensive wind tunnel testing. For reasons not well understood, the SERN test data revealed that a significant variation in nozzle flow field characteristics occurred as the exhaust total temperature was changed. In the present work a two-dimensional Navier-Stokes flow analysis procedure was used to simulate the SERN flow field in an attempt to understand this effect. Steady state solutions were obtained using an explicit time-dependent method utilizing efficiency-improving techniques such as body-fitted mesh, coupled computational regions, wall functions, automatic alignment of mesh with mixing layers, and vectorized execution on a CRAY 1 computer. Many possible contributing factors to this effect are discussed. The factors investigated in the present study (temperature-dependent specific heat capacities and the effect of exhaust plume temperature on mixing layer spreading rates) were found not to be solely responsible for the effect of exhaust total temperature on the nozzle flow characteristics. A normal shock on the expansion ramp was evident in the SERN experimental data that was not predicted with the 2-D analysis. This shock was present whether the exhaust total temperature was hot or cold and its position was dependent on the total temperature. Based on work to-date, an extension of the present study is suggested to predict this effect. The work demonstrates the capabilities and some of the problems in applying a Navier-Stokes flow analysis procedure for computing complex viscous nozzle flows. The importance of measuring upstream condition in flow experiments is emphasized if the data is to be utilized for explanation of flow variations which occur or for flow analysis validation.

LIST OF SYMBOLS

C	= sonic velocity	x, y, z	= Cartesian coordinates
C_V	= specific heat capacity at constant volume	δ	= boundary-layer thickness ($U/U_e = 0.99$)
\bar{C}_V	= mean specific heat capacity at constant volume	ϕ	= relative fuel-to-air ratio, $(f/a)_{\text{actual}}/(f/a)_{\text{stoich}}$
C_p	= specific heat capacity at constant pressure	ρ	= density
CP	= pressure coefficient = $\frac{p - p_\infty}{\frac{1}{2} \rho_\infty u_\infty^2}$	λ	= second viscosity coefficient
e	= specific internal energy	κ	= von Karman constant (≈ 0.41)
E	= total energy density	η	= distance coordinate, normal to wall
k	= ratio of specific heat capacities (C_p/C_V)	τ_{xy}	= shear stresses
K	= turbulent eddy thermal conductivity	σ_x, σ_y	= normal stresses
M	= Mach number	μ_e	= laminar viscosity coefficient
\bar{n}	= unit normal vector	μ_t	= turbulent eddy viscosity coefficient
NPR	= nozzle pressure ratio		
NTT	= nozzle total temperature		
P	= pressure		
\bar{q}	= total velocity vector		
Q_x, Q_y	= Cartesian heat flux components		
R	= gas constant		
S	= surface area		
t	= time		
T	= absolute temperature		
u, v	= Cartesian velocity components		
V	= volume		

Subscripts

t	= total thermodynamic state
∞	= freestream
o	= reference
e	= value at outer edge of boundary layer
w	= wall value

INTRODUCTION

Nonaxisymmetric nozzle installations are being investigated for future generations of military aircraft to meet diverse mission requirements. One such nozzle is the single expansion ramp nozzle (SERN) shown in Figure 1. The SERN flow field contains mixed subsonic and supersonic regions in which shocks, compression waves, and expansion waves interact with boundary layers and mixing layers. The three-dimensional geometry of the SERN results in the flow field being somewhat three-dimensional as illustrated in Figure 2. The nozzle was designed using the traditional approach in which model scale parametric testing is used to build a data base from which the full scale nozzle performance is predicted.

The traditional test based approach to nozzle design is slow and increasingly expensive. Since model scale results are often difficult to extend to full scale, iteration with full scale testing is usually required to achieve a satisfactory design. The advances in computer technology have created considerable interest in developing analytical procedures for simulating nozzle flows. These computer programs can be used by the designer to supplement and guide his parametric testing program and thus reduce the number of models which must be tested to achieve a satisfactory design. As computers and numerical algorithms become more powerful, the role of analysis in nozzle design will probably increase. Eventually nozzle design will evolve to an analysis based design approach. Parametric testing will be conducted on full scale configurations, replacing model scale parametric testing. The use of testing will shift to validation of the analysis and confirmation of the final design parameters.

Extensive wind tunnel testing of the SERN has been conducted to acquire an understanding of its complex flow field. Because nozzle wind tunnel testing is easier and less costly with unheated exhaust air, much of the experimental data for the SERN has been obtained in this manner. However, at a given nozzle pressure ratio, a significant variation in nozzle flow field characteristics occurs as the total temperature of the exhaust gas is changed. This effect is illustrated in Figure 3, where experimentally measured CP distributions (References 1 and 2) on the SERN external expansion ramp are plotted for various exhaust total temperatures.

A schematic diagram of the SERN flow field is shown in Figure 4. Of particular interest is the location of the shock or (strong compression wave) on the expansion ramp. The shock's position was experimentally found to shift with changes in exhaust total temperature. In Figure 3 for $M_{\infty} = 1.4$ the shock, indicated by the sudden rise in the measured CP distribution, remains in the same position for exhaust total temperatures of 667, 833, and 1056°K, but shifts dramatically at 278°K (the unheated case, no combustion). The CP distribution upstream of the shock is also seen to change significantly from heated to unheated exhaust. However, for $M_{\infty} = 0.85$ there is a more gradual change as the exhaust total temperature is changed.

In Reference 2 an effort was made to experimentally simulate heated exhaust nozzle flows with unheated exhaust nozzle flows. It was assumed that the effects of changing exhaust temperature occurred because the ratio of specific heat capacities was changing. The technique consisted of adjusting the NPR such that the computed initial inclination of the unheated exhaust plume matched that of the heated exhaust plume. The results were satisfactory at $M_{\infty} = 1.2$, but failed to give good results over the entire range of freestream Mach numbers from 0.5 to 1.5. These results suggest that the temperature dependence of the ratio of the specific heat capacities may be a contributing factor to the observed changes of the flow field with exhaust total temperature, but that other mechanisms are probably involved.

The wall boundary layers on the outer surface of the nozzle test apparatus are influenced to some extent by the heat transfer from the nozzle surface which has no external cooling system. The increase in boundary layer displacement thickness resulting from the heat transfer reduces the extent of expansion experienced by the supersonic flow turning over the boattail of the nozzle. This affects the location of the boattail shock, the susceptibility of the boundary layer to separation, and the initial exhaust plume inclination.

The large change in velocity across the mixing layers caused by the difference in temperature of the external flow and the heated exhaust gas, enhances the turbulent mixing, and thus increases the spreading rate of the mixing layers. Interactions of the mixing layers with shocks and expansion waves are affected. The interaction of the supersonic exhaust plume with the external flow downstream of the expansion ramp could result in the formation of an oblique shock wave. The influence of the exhaust temperature upon the spreading rate of turbulent mixing layer could alter the amount of turning required by the exhaust flow at the trailing edge of the expansion ramp. If the amount of turning is great or the exhaust flow Mach number is low, an oblique shock structure may not be possible, giving rise to the formation of a normal shock on the expansion ramp as shown in Figure 4.

Relaminarization may occur in the internal boundary layers which undergo an extremely strong and extensive acceleration through the nozzle throat and expansion ramp. The sudden change in the flow field as the exhaust temperature is decreased, shown in Figure 3, suggests that a change has occurred in the upstream internal flow conditions. Such a behavior could be due to boundary layer relaminarization. Slight perturbations in the expansion ramp boundary layer produced by changes in the exhaust temperature may be substantially amplified by downstream shock/boundary-layer interactions.

Since detailed experimental measurements (particularly total pressure and total temperature profile surveys) have not been taken, changes in flow conditions (other than average nozzle total temperature) upstream of the nozzle throat could be the cause of the changes in the nozzle flow field between heated and unheated exhaust flows. Secondary flows and total pressure and total temperature cross stream nonuniformities probably occur downstream of the flame holder, shown in Figure 1, particularly when combustion is present for the heated exhaust cases. The substantial influence which upstream conditions have on developing jet plumes has been shown in Reference 3.

The effects of changing exhaust total temperature as well as detailed information on the fluid dynamic mechanisms which are involved can be studied by solving the governing mathematical equations of the flow.

Once an analysis procedure has been developed and validated, full scale and model scale flow simulations can be obtained in a relatively short period of time for many different nozzle flow conditions. Such analyses yield detailed information (e.g., temperature, velocity, pressure, density, Mach number) at all locations in the flow field. It is usually not feasible to obtain this information experimentally in wind tunnel tests, yet it is invaluable to the nozzle designer for understanding the nozzle flow field.

A need exists for an analysis procedure capable of accurately simulating the flows (both internal and external) of nozzles for understanding wind tunnel test data and supplementing nozzle design parametric testing. An analysis procedure has been developed and is presented for analyzing two-dimensional/axisymmetric nozzle and afterbody flows (References 3, 4, and 5). Using an explicit time-dependent method approximate steady state solutions to the Navier-Stokes equations (together with conservation equations for mass and energy and zonal turbulence models) are obtained. Several efficiency-improving techniques are contained in the procedure including body-fitted generalized mesh, wall functions, mesh fitting of mixing layers, multiple coupled computational regions, and vectorized execution on the CRAY I computer.

The objective of the present work was to simulate the SERN flow field with the 2-D nozzle analysis to understand at least qualitatively the exhaust temperature effect. Many possible factors have been identified which could contribute to this effect. In the work described herein the first steps toward this objective were taken by considering the effects of temperature-dependent specific heat capacities and the effect of exhaust temperatures on the mixing layer spreading rates (including the interaction of the external flow with the exhaust jet downstream of the expansion ramp).

ANALYSIS

The unsteady ensemble-averaged two-dimensional Navier-Stokes equations, conservation of energy equation, and conservation of mass equation can be written for turbulent flow of an ideal gas with temperature-dependent properties in integral form for a fluid volume V bounded by the surface S as

$$\frac{\partial}{\partial t} \int_V \bar{U} dV + \int_S \bar{H} \cdot \bar{n} dS = 0 \quad (1)$$

The Cartesian vector \bar{U} and the second order Cartesian tensor \bar{H} are defined as

$$\bar{U} = \begin{Bmatrix} \rho \\ \rho u \\ \rho v \\ E \end{Bmatrix}$$

$$\bar{H} = \begin{Bmatrix} \rho u & \rho v \\ \rho u^2 + \sigma_x & \rho uv + \tau_{xy} \\ \rho uv + \tau_{yx} & \rho v^2 + \sigma_y \\ u(E+P) + \tau_{yx}v + \sigma_xu + Q_x & v(E+P) + \tau_{xy}u + \sigma_yv + Q_y \end{Bmatrix}$$

where

$$E = \rho(e + \frac{1}{2}(u^2 + v^2))$$

$$e = C_v(T - T_0)$$

$$\sigma_x = P - \lambda(\frac{\partial u}{\partial x} + \frac{\partial v}{\partial y}) - 2\mu \frac{\partial u}{\partial x}$$

$$\sigma_y = P - \lambda(\frac{\partial u}{\partial x} + \frac{\partial v}{\partial y}) - 2\mu \frac{\partial v}{\partial y}$$

$$Q_x = -K(\frac{\partial T}{\partial x})$$

$$Q_y = -K(\frac{\partial T}{\partial y})$$

$$\tau_{xy} = \tau_{yx} = -\mu(\frac{\partial u}{\partial y} + \frac{\partial v}{\partial x})$$

$$\lambda = -\frac{2}{3}\mu$$

$$\mu = \mu_l + \mu_t$$

$$K = \frac{\mu C_p}{Pr_t}$$

Closure of the equations is obtained by use of an eddy viscosity turbulence model. The Reynolds stress terms are approximated by the product of an eddy viscosity and a mean flow velocity gradient. The Reynolds heat flux is computed by the product of the eddy viscosity, a specific heat capacity, and a mean flow temperature gradient divided by the turbulent Prandtl number. A two-layer mixing length model is used for computing the boundary layers on the nozzle surfaces (Reference 7), where in the inner layer the eddy viscosity is computed as

$$\mu_t = \rho (\kappa \eta)^2 \frac{\partial u}{\partial y} \quad (2)$$

where η is the distance normal to the wall. In the outer layer the eddy viscosity is computed as

$$\mu_t = \rho (0.09 \delta)^2 \frac{\partial u}{\partial y} \quad (3)$$

where the boundary layer thickness must be estimated locally. At points within the boundary layer both inner and outer values of μ_t are computed and the minimum value used.

In the mixing layer, the eddy viscosity is approximated by the mixing length formula (Reference 19, pages 549-550)

$$\mu_t = 0.017 \rho L \Theta |\Delta u| \quad (4)$$

where L is the thickness of the mixing layer, Δu is the difference between the tangential velocities across the layer, and Θ is a coefficient defined as

$$\Theta = \left| \frac{u_1 - u_2}{u_1 + u_2} \right| \quad (5)$$

In the above expression, u_1 is the tangential velocity above the mixing layer and u_2 is the tangential velocity below the layer. The mixing layer thickness is assumed to vary linearly with distance from the trailing edge of the upper cowl at x_0 . Starting with an initial thickness of L_0 equal to the combined inner and outer boundary layer thicknesses, the mixing layer thickness L was computed as

$$L = 0.12(x - x_0) + L_0 \quad (6)$$

The laminar viscosity is computed from Sutherland's viscosity relation

$$\mu_k \text{ (kg/m-sec)} = 17.1 \times 10^{-6} \left(\frac{T}{273} \right)^{3/2} \left(\frac{273 + S}{T + S} \right) \quad (7)$$

where T is in units of degrees Kelvin and $S = 110^\circ \text{K}$.

The equation of state relation for an ideal gas is

$$P = \rho R T \quad (8)$$

R is the gas constant which is nearly constant ($287 \text{ J/Kg-}^\circ\text{K}$) over a range of temperatures from 200°K to 2500°K and fuel-to-air ratios of 0.06 and less.

The extreme range in fluid temperatures present in nozzle flows with heated and unheated exhaust requires that the properties of the gas, namely the specific heat capacity, be computed as a function of temperature. Equilibrium C_p data for air with products of combustion of $(\text{CH}_2)_n$ taken from Reference 8 was fit in a piecewise fashion with linear and quadratic polynomials. The ratio of specific heat capacities, k , is computed as

$$k = \frac{R}{C_v} + 1 \quad (10)$$

The temperature is computed from the specific internal energy using the mean specific heat capacity.

$$T = e/C_v + T_0 \quad (11)$$

where C_v is defined as

$$C_v = \int_{T_0}^T C_v dT / (T - T_0) \quad (12)$$

The analytic expressions for the specific heat capacity were integrated from a reference temperature of $T_0 (= 0^\circ\text{K})$ to obtain curve fits for the mean specific heat capacities. The curve fits reproduce the C_p data to better than 0.2 percent accuracy over the range of temperature from 200°R (111°K) to 2600°R (1444°K).

The governing equations are solved using the explicit predictor-corrector finite difference algorithm of MacCormack (References 3, 11, 12, 13, 14, 15, and 16) in conservation law form for a nonorthogonal body-fitted computation mesh. Steady state solutions are obtained as asymptotic limits to this time-dependent method. The forms of the difference equations and their use in the method are given in Reference 3.

Resolution of turbulent boundary layers requires a very finely spaced computational mesh near the solid boundaries. However, the CFL stability condition for explicit schemes demands an exceedingly small time step size which drives the computation time prohibitively large for practical nozzle design calculations. To partially alleviate this difficulty in the present analysis wall functions as described by Launder and Spalding (Reference 9) are used to obtain the wall shear stresses and convective fluxes in the mesh cells bordering solid boundaries. This allows the boundary layer to be adequately resolved with significantly fewer (and larger) mesh cells, thereby allowing larger stable computational step sizes, and thus lower computational costs.

In the application of the wall functions it is assumed that a constant shear stress region exists in the boundary layer in which the compressible law-of-the-wall (Reference 10) given below is valid.

$$\frac{u_*}{u_s} = \frac{1}{\kappa} \ln \left(\frac{\eta u_s}{\nu/\rho} \right) + 5.1 \quad (13)$$

The shear velocity, u_s , is defined as

$$u_s = \sqrt{\tau_w/\rho_w} \quad (14)$$

and u_* is defined as

$$u_* = (u_e/\psi^{1/2}) \arcsin \psi^{1/2}(u/u_e) \quad (15)$$

where

$$\psi = \left(\frac{k-1}{2} \right) M_e^2 / \left(1 + M_e^2 \frac{k-1}{2} \right)$$

Given the tangential velocity at a point in the boundary layer logarithmic region (the center of the cell bordering the wall), Equation 13 is solved for the wall shear stress. The mass flowing tangentially through the cell is calculated by integrating Equation 13 along the vertical edge of the cell.

In regions of low velocity and particularly regions where there exist large second derivatives in the conservative field variables, the algorithm requires additional smoothing to prevent numerical instability. An explicit smoother is used in the present analysis similar to the fourth-order pressure term introduced by MacCormack (Reference 15). In addition a linear diffusion term was added to each equation to damp large transients created early in the computation by the initial conditions.

Up to three fluid streams can be analyzed simultaneously for which up to three mesh regions are generated—one per fluid stream. In the computational logic space each region is rectangular and has a separate I-J indexing scheme as shown in Figure 5. I-mesh lines are generated as vertical and parallel lines to the y-coordinate axis and J-mesh lines are generated to fit the nozzle surfaces. In the calculations to be described, the exhaust flow and external flows are computed in separate, but fully coupled, computational regions. This technique of subdividing the flow field into several coupled computational regions conserves computer storage, eases mesh generation, and allows alignment of the mesh lines with flow streamlines.

Fitting a computational mesh to flow field discontinuities (e.g., shocks and slip surfaces) has been shown to reduce the generation of computational noise (References 16 and 17). Fitting can also be used to position fine mesh for resolving thin mixing layers between fluid streams. During the calculation the y-coordinates of cell vertices on mesh lines between mesh regions are continually and automatically moved according to the transport equation

$$\frac{\partial Y}{\partial t} = \beta (\bar{v} - \bar{u} \frac{\partial Y}{\partial x}), \quad (16)$$

where Y is the y-coordinate of the mesh cell vertices, \bar{u} and \bar{v} are simple averages of local cell centered velocity components, and β is a damping coefficient. With upwind differencing for $\frac{\partial Y}{\partial x}$, forward differencing for $\frac{\partial Y}{\partial t}$, and $\beta = 0.1$ the scheme is stable. A similar technique was used in Reference 18 to compute the movement of a free surface of an incompressible liquid.

In the present analysis, at steady state, the mesh is aligned with the dividing streamlines between the fluid streams. The other J-mesh lines are periodically adjusted to conform to the fitted mesh lines to avoid large differences in neighboring cell volumes.

RESULTS AND DISCUSSION

The two-dimensional analysis procedure was used to simulate the SERN flow field for the 16 cases listed in Table 1 covering a range of NPR's from 3 to 6, NTT's of 278°K and 1111°K, and freestream Mach numbers of 1.2 and 1.4. The objective of these calculations was to determine if the two-dimensional analysis, which included temperature-dependent specific heat capacities and influence of exhaust temperature on the mixing layer spreading rates, could simulate the experimentally observed "exhaust temperature effect," and if so, identify the dominant mechanisms causing the effect. By inspection of Figure 1, showing the geometry of the

SERN, it is evident that the flow is three-dimensional. Therefore, the results from the present calculations could not indicate more than qualitative trends and the characteristics of the mechanisms responsible for the change in the flow field as the exhaust total temperature is changed.

The 16 flow fields were computed on the inner computational domain shown in Figure 6. This domain contains the exhaust flow stream and one external stream. The downstream boundary of the domain is located a short distance downstream of the expansion ramp trailing edge where it was assumed that the flow was totally supersonic. This assumption was a result of a number of preliminary calculations (at $NPR = 5$, $M_\infty = 1.2$ m, and unheated exhaust) in which the outflow boundary was located far downstream (at $x = 3.2$ m). The flow was always found to be supersonic along the vertical line that is presently the outflow boundary of the inner computational domain (at $x = 0.6$ m). The portion of the lower boundary of the inner domain, which extends downstream of the trailing edge of this expansion ramp, was assumed to be parallel with the nozzle axis and on which a free-slip boundary condition was applied. This last assumption was checked by calculations and is discussed later in the text.

The freestream static pressure, static temperature, and velocity were prescribed on the external inflow boundary at $x = -0.2$ m, which is slightly upstream of the beginning of the boattail curvature. The boundary layer profile at the external inflow boundary was computed using the one-seventh power law solution for a turbulent boundary layer on a flat plate with zero pressure gradient (Reference 19, page 598). For the freestream Mach numbers of 1.2 and 1.4 the boundary layer was estimated to be 41 mm thick. The internal nozzle inflow boundary was located at $x = -0.1$ m where the nozzle total pressure, total temperature and flow angle were specified. Using the one-seventh power law solution as before, the boundary-layer thicknesses at this location were estimated to be 8.9 mm for the cases with unheated exhaust and 12.7 mm for the cases with heated exhaust. The prescribed flow angle along this boundary was obtained by linear interpolation between the slopes of the upper and lower surfaces. In the heated cases ($NTT = 1111^\circ K$) the fuel-to-air mass ratio was 0.022. Since detailed measurements of total pressure and total temperature profiles were not available for specifying upstream flow conditions at the internal nozzle inflow boundary, uniform profiles of these quantities were prescribed.

Placement of the computational mesh is important to the accuracy of the resulting numerical solution. A problem nearly always exists in determining how much mesh is necessary for adequate resolution of all length scales of a particular problem. Because of a lack of practical methods to estimate absolute truncation errors, currently the only available technique to assess the errors is to compute the flow field using a series of computational grids of increasing mesh density.

The nozzle flow field for case No. 1 was computed several times using computational meshes consisting of from 323 to 3316 cells for the inner domain. The resulting CP distributions on the expansion ramp are plotted in Figure 7. As the mesh density increases the CP distribution seems to approach an asymptotic limit. Limited core size on a Cyber 175 computer prevented further mesh refinement even though a definite asymptotic limit was not reached. Little difference was found in the computed solution between the mesh of 3316 cells and that of 3173 cells, yet the former mesh with twice the mesh density near the exit plane of the nozzle required twice the computational time. Therefore, the latter computational mesh was selected for subsequent computations of the nozzle flow fields. Approximately two hours of CPU computation time was required per calculation on a Cyber 175 using the selected mesh. The selected computational mesh is displayed in Figures 8 and 9 at steady state for cases No. 1 ($NPR = 3$) and No. 4 ($NPR = 6$), respectively, from Table 1. Note the differences in mesh alignment reflecting the significant difference in plume expansion between the two cases. The mesh is expanded exponentially upstream, downstream, and away from the nozzle surface. At steady state the mesh aligned with the dividing streamline between the internal and external flows which served to position fine mesh in regions of large gradients to improve resolution and reduce computational noise.

Initial conditions for the first of these calculations were uniform flow through the domain. These crude initial conditions caused large transients in the initial part of the calculation which required a substantial amount of damping to avoid numerical instability. The initially heavy damping using the linear diffusion terms accelerated convergence and were turned off later in the calculation. The initial conditions for subsequent calculations were obtained from results of the first calculation or some other calculation previously completed. It was estimated that this saved approximately ten percent in computational costs.

The results of these calculations are shown in Figures 10 through 13. The computed flow fields for cases No. 9 and No. 13 are representative of all the calculations and are displayed in Figures 10 and 11 by Mach number contour plots. These cases are for the heated and unheated exhaust at $NPR = 3$ and $M_\infty = 1.4$. As in all shock capturing numerical techniques the shocks are smoothed due to the action of numerical and artificial diffusion. Shocks appear in the contour plots as steep gradient regions where contours of Mach numbers are closely spaced. Mixing layers are clearly shown in the Mach number plots by closely spaced contours. Mixing rate in the heated exhaust case of Figure 11 is seen to be greater than in the unheated case of Figure 10, because the velocity difference across the layer is much greater in the former case. In the present mixing layer turbulence model no account was given for the increase in turbulence level contributed by the boundary layer wake, so in the unheated cases where the velocity difference across the layer was small, the mixing rate is slightly underpredicted.

The contour plots indicate that partial cancellation occurs in the Prandtl-Meyer expansion fan originating at the cowl trailing edge due to the compression turning of the supersonic jet on the external expansion ramp. The plots also show little reflection from the mixing layer of the expansion fan or compression waves. The flow field downstream of the expansion fan under the mixing layer is thus relatively uniform up to the compression wave created by the turning on the expansion ramp surface at about $x = 0.35$ m.

No significant changes occurred in the computed flow field when the exhaust total temperature was changed from 277. to 1111. K. This indicates that the experimentally observed exhaust temperature effects are not directly attributable solely to the temperature dependence of either the ratio of specific heat capacities or the spreading rate of the mixing layers. In the computed flow field of case No. 5 with heated exhaust, a normal shock formed in the exhaust jet in the position of the shock on the expansion ramp

illustrated in Figure 3. The subsonic flow downstream of the normal shock extended to the outflow boundary at $x = 0.6$ m. The supersonic boundary conditions were inappropriate for subsonic outflow and thus invalidated the results of this particular calculation. However, it is interesting to note that the CP distribution on the external expansion ramp computed for this case was more similar to the measured CP distribution than any of the other 15 cases computed.

The computed distributions of CP on the expansion ramp surface and upper boattail surface are plotted in Figures 12 and 13 for all of the cases for $M_\infty = 1.4$. Similar results were obtained for $M_\infty = 1.2$. The behavior of the calculated CP distribution on the expansion ramp is similar to the measured CP distribution reported in Reference 20 and shown in Figure 14, in that the CP distribution between the nozzle exit plane ($x = 0.23622$ m) and the shock increases in level as the NPR increases. However, in the computed flow fields (except case No. 5) a weak oblique shock wave was positioned on the expansion ramp where a normal shock appeared to be located in the experimental data. The computed oblique shock wave did not move with changes in NPR, M_∞ , or NTT, as did the normal shock wave in the measured data, but was apparently generated by the curvature of the expansion ramp. The calculated boattail CP distributions display trends with changes in NPR and exhaust temperature similar to those found experimentally in Figure 15 (Reference 20). The boattail shock moves forward as the NPR and the exhaust temperature are increased. Again there are significant differences between computed and measured boattail CP distributions.

The salient feature of the computed flow fields is the absence of the normal shock on the expansion ramp which was evident in the SERN experimental data. Since the exhaust temperature effect is dependent upon the presence of this normal shock, the effect was not predicted. The presence of the normal shock could be caused by the interaction of the external stream with the exhaust jet downstream of the expansion ramp. The computed results for case No. 5 suggested that the formation of the normal shock might result from such interaction. To investigate this interaction, the flow field was recomputed for case No. 5 on the larger computational domain shown in Figure 6. In this calculation the external flow below the nozzle (as shown in Figure 6) was added to the computational domain and the outflow boundary was shifted downstream to $x = 1.4$ m. The computational mesh for this calculation is shown in Figure 16. The portion of this mesh that overlays the inner computational domain coincides with the previous mesh. In this calculation two mixing layers were computed and the mesh automatically adjusted so that at steady state it was aligned with the two dividing streamlines between the three streams. This calculation required 550K (octal) words of incore storage which exceeded the maximum random access memory available on the Cyber 175 computer used for the preceding calculations. A CRAY 1 computer, having ample in-core storage for this calculation, was recently acquired by The Boeing Company and was made operational in time for this calculation to be performed. A substantial speedup in computational time was also realized. After removing IF statements from the Fortran DO-loops, computational time decreased by a factor of 16 compared to the Cyber 175. The computed Mach number contours for this case are shown in Figure 17. This time however a normal shock did not occur in the exhaust flow on the expansion ramp.

The reasons why the normal shock occurred in the SERN experimental data and not in the computed flow are not well understood. As mentioned in the introduction there are a number of factors which could contribute to the "exhaust temperature effect" and also to the absence of this normal shock which were not studied in the present work. At present the two factors believed to be most responsible are the three-dimensional effects and the effects of upstream internal nozzle conditions. It is recommended that a numerical investigation be performed using the present analysis procedure in which the upstream internal flow conditions (boundary conditions) are distorted and the effects on the nozzle flow field studied.

In an investigation of a nonaxisymmetric wedge plug nozzle reported in Reference 6, a two-dimensional flow analysis procedure similar to the present procedure was inadequate in computing wedge surface static pressures for NPR above about 3. Surface oil flows suggested that three-dimensional effects in the flow field became substantial above this NPR. The flow field of the SERN also has a three-dimensional character as indicated in Figure 4. A two-dimensional analysis procedure cannot accurately simulate this flow field effect.

Had more detailed experimental measurements been collected during the testing of the SERN, this "exhaust temperature effect" may have been easier to examine and an understanding about the phenomena easier to reach. The work presented in Reference 3 demonstrated the significant effect that upstream conditions inside the nozzle can have on the external flow field. The important measurements of the upstream total pressure and total temperature profiles entering the converging section of the nozzle and measurements of the external boundary layer are absent from the SERN data. Without sufficient detailed data it is extremely difficult to define and quantify the effects of the exhaust flow total temperature, let alone attempt to understand it. This shortcoming of the SERN experimental data is a typical problem encountered in efforts to validate computer flow analysis procedure by comparisons to experimental data. If test data on the flow characteristics of nozzles/afterbodies (or other aircraft components) is to be used for code validation, the test plan should be coordinated and consistent with the validation needs of the code developer.

CONCLUSIONS

A viable analytical procedure has been developed and used for the computation of compressible viscous two-dimensional nozzle flow fields with temperature-dependent specific heat capacities. Several flow field computations were presented covering a range of NPRs from 3 to 6 for freestream Mach numbers of 1.2 and 1.4 and exhaust total temperatures of 277°K and 1111°K which have demonstrated its capabilities.

Comparisons were made of the computed trends in the SERN surface CP distributions with changes in exhaust total temperature to those measured in experiment. The present two-dimensional analysis, which included temperature dependent specific heat capacities, effect of exhaust temperature on the mixing layers spreading rates, and the interaction of the exhaust jet with the external flow, did not predict the presence of a normal shock on the expansion ramp that was evident in the SERN experimental data. The exhaust temperature effect, being directly dependent upon the presence of the normal shock, was therefore not predicted. Several possible reasons have been discussed why the shock did not appear in the computed flow fields and follow-on work has been suggested.

The importance of having detailed flow field measurements, including the internal and external upstream flow conditions, for understanding the experimental test results and for flow analysis validation was illustrated in the present work.

REFERENCES

1. Robinson, C. E., "Exhaust Plume Thermodynamic Effects on Non-axisymmetric Nozzle Afterbody Performance in Transonic Flow," Arnold Engineering Development Center Technical Report, TR-78-24, August 1978.
2. Robinson, C. E., and High, M. D., "Exhaust Plume Temperature Effects on Nozzle Afterbody Performance Over the Transonic Mach Number Range," Arnold Engineering Development Center, TR-74-9, July 1974.
3. Peery, K. M., and Forester, C. K., "Numerical Simulation of Multistream Nozzle Flows," AIAA J., **18**, No. 9, September 1980, pp. 1088-1093.
4. Forester, C. K., "Numerical Simulation of the Interaction of Jet and Freestream Flows in Engine Exhaust Systems," AIAA paper No. 78-144, January 1978.
5. Barton, J. M., Birch, S. F., Forester, C. K., Paynter, G. C., Peery, K. M., and Roberts, D. W., "The Computation of Complex Jet and Nozzle Flows," presented at the JANNAF 12th Plume Technology Meeting, Colorado Springs, Colorado, November 1980.
6. Carson, G. T., and Mason, M. L., "Experimental and Analytical Investigation of a Nonaxisymmetric Wedge Nozzle at Static Conditions," NASA Technical paper 1188, July 1978.
7. Cebeci, T., and Smith, A. M. O., Analysis of Turbulent Boundary Layers, Academic Press, New York, 1974.
8. Keenan, J. H., and Kaye, J., Gas Tables, John Wiley and Sons, Inc., New York, 3rd Ed., 1950.
9. Launder, B. E., and Spalding, D. B., "The Numerical Computation of Turbulent Flows," Computer Methods in Applied Mechanics and Engineering, Vol. 3, pp. 269-289, 1974.
10. Mathews, D. C., Childs, M. E., and Paynter, G. C., "Use of Cole's Universal Wake Function for Compressible Turbulent Boundary Layers," AIAA J. of Aircraft, March 1970.
11. McCormack, R. W., and Paullay, A. J., "Computational Efficiency Achieved by Time Splitting of Finite Difference Operators," AIAA paper No. 72-154, January 1972.
12. Baldwin, B. S., McCormack, R. W., and Delwert, G. S., "Numerical Techniques for the Solution of the Compressible Navier-Stokes Equations and Implementation of Turbulence Models," AGARD-LS-73, February 1975.
13. Mikhail, A. G., Hankey, W. L., and Shang, J. S., "Computational of a Supersonic Flow Field Past an Axisymmetric Nozzle Boattail with Jet Exhaust," AIAA paper No. 78-993, July 1978.
14. Delwert, G. S., "Computation of Separated Transonic Turbulent Flows," AIAA Journal, Vol. 14, No. 6, June 1976.
15. McCormack, R. W., and Baldwin, B. S., "A Numerical Method for Solving the Navier-Stokes Equations with Application to Shock-Boundary Layer Interactions," AIAA paper 74-603, June 1974.
16. McCormack, R. W., and Paullay, A. J., "The influence of the Computational Mesh on Accuracy for Initial Value Problems with Discontinuous or Non-Unique Solutions," Computers and Fluids, Vol. 2, pp. 339-361, Pergamon Press, 1974.
17. Schiff, L. B., "The Axisymmetric Jet Counterflow Problem," AIAA paper 76-325, July 1976.
18. Hirt, C. Y., Nichols, B. D., and Romero, N. C., "SOLA: A Numerical Solution Algorithm For Transient Fluid Flows," Los Alamos Sci. Lab., Report No. LA-5852, 1975.
19. Schlichting, H., "Boundary-Layer Theory", McGraw-Hill, New York, 1968.
20. Russell, D. L., "Nonaxisymmetric Exhaust Plume Temperature Effects on an Isolated Afterbody", Air Force Flight Dynamics Laboratory, Wright-Patterson AFB, Ohio, Feb. 1981.

ACKNOWLEDGEMENTS

Work presented in this technical paper was funded by the U.S. Air Force Wright Aeronautical Laboratories through contract F33615-79-C-3018.

Case No.	NPR	NTT	M _∞	T _∞	P _∞
1	3	277.°K	1.2	241.°K	23606. N/M ²
2	4	277.°K	1.2	241.°K	23606. N/M ²
3	5	277.°K	1.2	241.°K	23606. N/M ²
4	6	277.°K	1.2	241.°K	23606. N/M ²
5	3	1111.°K	1.2	241.°K	23606. N/M ²
6	4	1111.°K	1.2	241.°K	23606. N/M ²
7	5	1111.°K	1.2	241.°K	23606. N/M ²
8	6	1111.°K	1.2	241.°K	23606. N/M ²
9	3	277.°K	1.4	223.°K	18195. N/M ²
10	4	277.°K	1.4	223.°K	18195. N/M ²
11	5	277.°K	1.4	223.°K	18195. N/M ²
12	6	277.°K	1.4	223.°K	18195. N/M ²
13	3	1111.°K	1.4	223.°K	18195. N/M ²
14	4	1111.°K	1.4	223.°K	18195. N/M ²
15	5	1111.°K	1.4	223.°K	18195. N/M ²
16	6	1111.°K	1.4	223.°K	18195. N/M ²

TABLE 1. Flow Field Calculation Cases

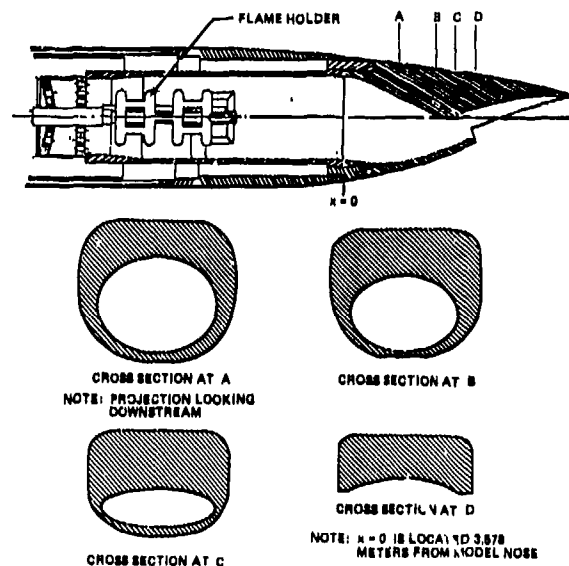


Figure 1. Single Expansion Ramp Nozzle Geometry

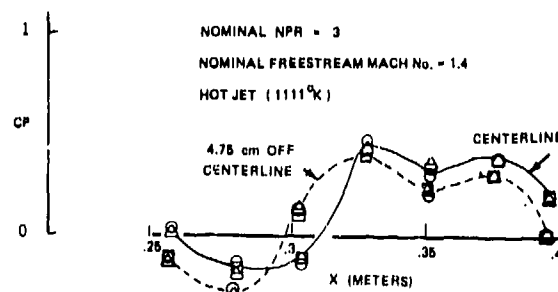


Figure 2. CP Distributions on Expansion Ramp

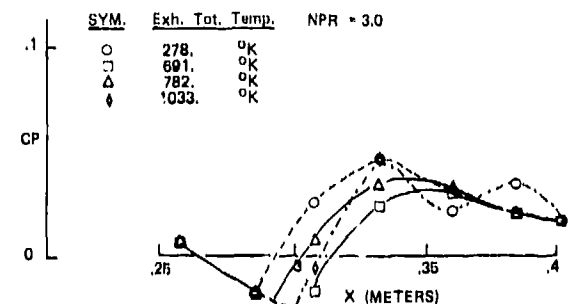
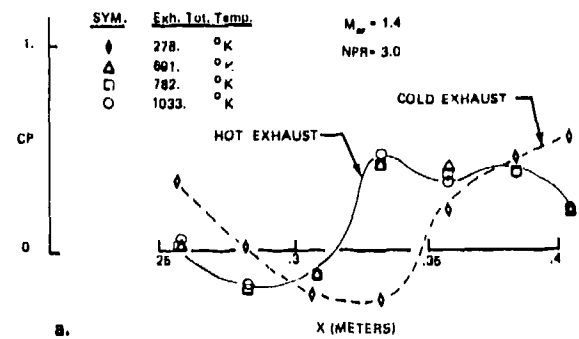


Figure 3. Expansion Ramp CP Distributions for Various Exhaust Total Temperatures (a) M_∞ = 1.4 and (b) M_∞ = 0.85

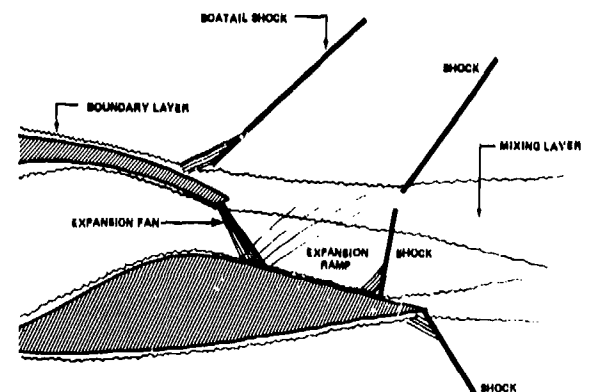


Figure 4. Schematic Diagram of SERN Flow Field

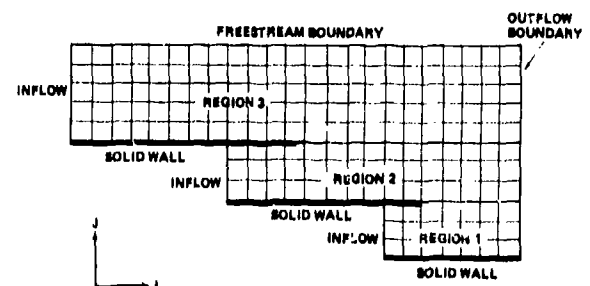


Figure 5. Multiple Region Computational Logic Space

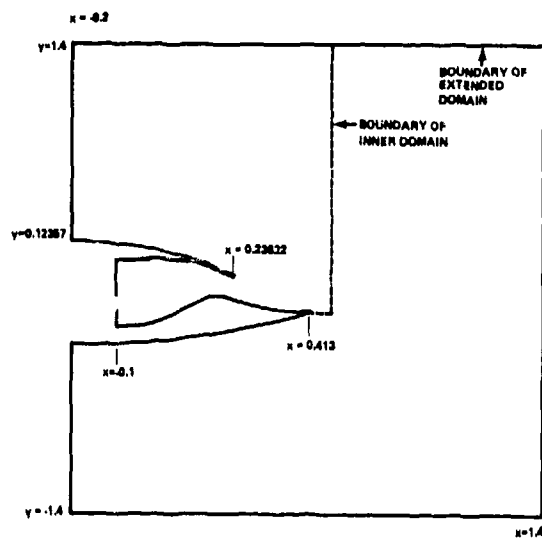


Figure 6. Physical Computational Domains

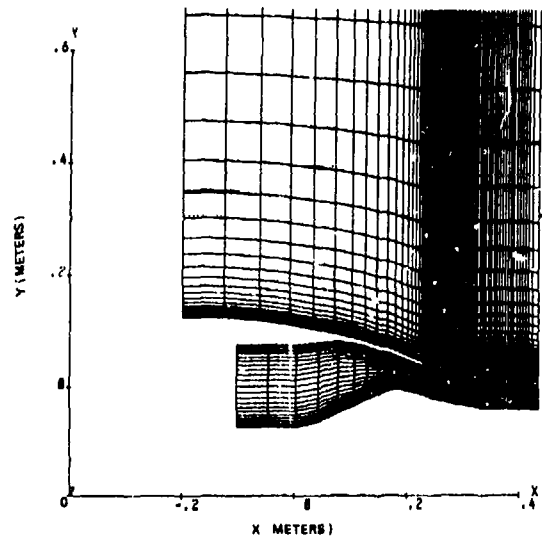


Figure 9. Computational Mesh for Case 4 - NPR = 6, $M_{\infty} = 1.2$, NTT = 277 °K

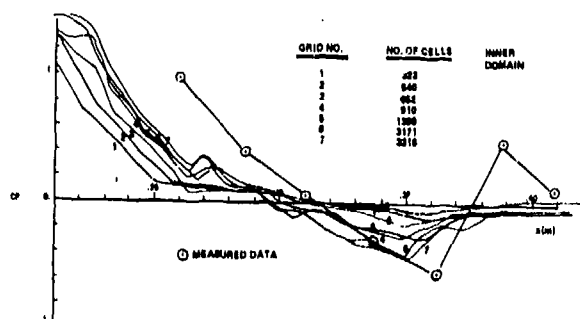


Figure 7. Computed CP Distributions on Nozzle Expansion Ramp Using Various Computational Grids ($M_{\infty} = 1.2$, NPR = 5, Unheated)

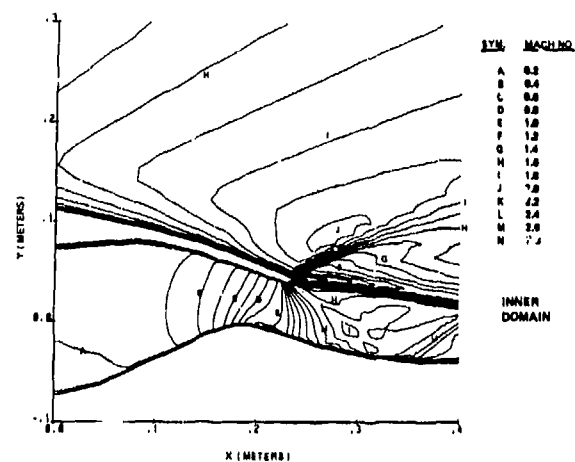


Figure 10. Computed Mach Number Contours for Case Number 9, $M_{\infty} = 1.4$, NPR = 3, NTT 277 °K

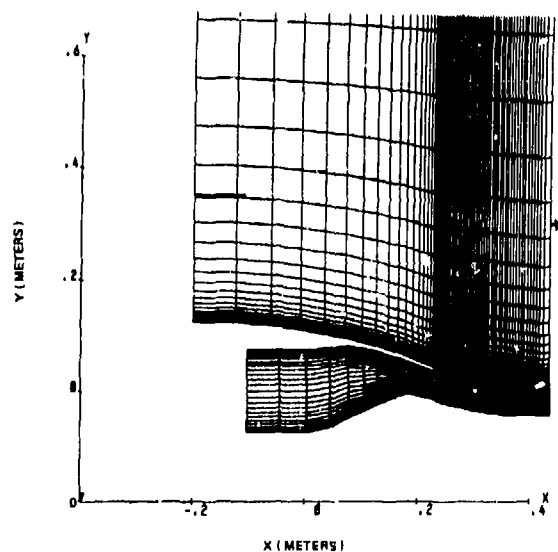


Figure 8. Computational Mesh for Case 1 -NPR = 3, $M_{\infty} = 1.2$, NTT = 277 °K

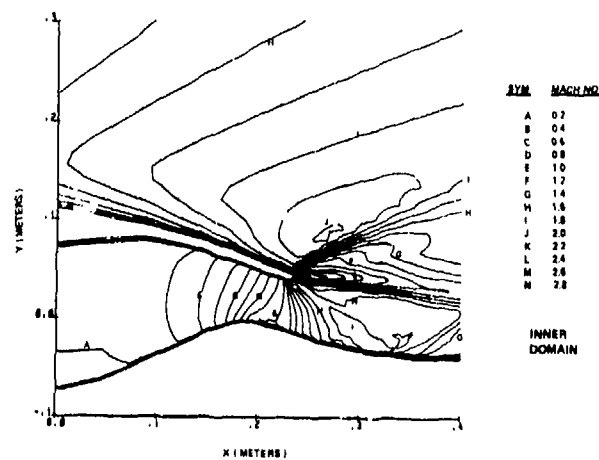


Figure 11. Computed Mach Number Contours for Case Number 13, $M_{\infty} = 1.4$, NPR = 3, NTT 1111 °K

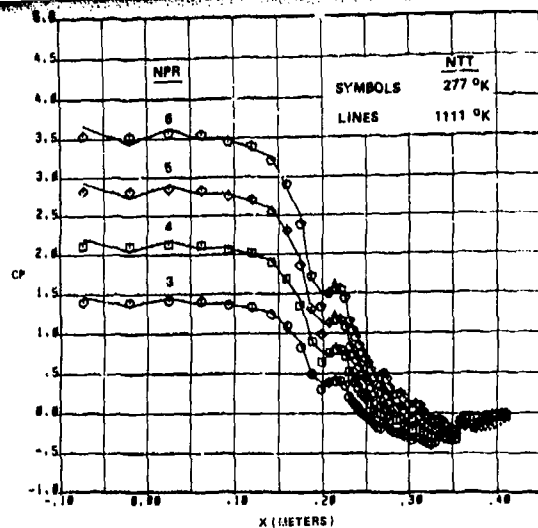


Figure 12. Computed CP Distribution on External Expansion Ramp, $M_\infty = 1.4$

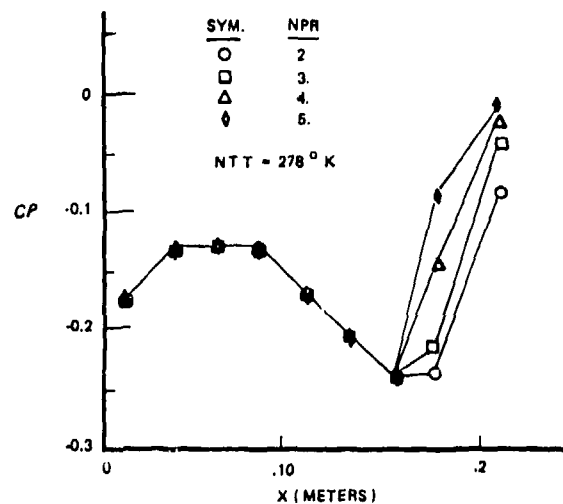


Figure 15. Measured Boattail CP Distribution at $M_\infty = 1.4$

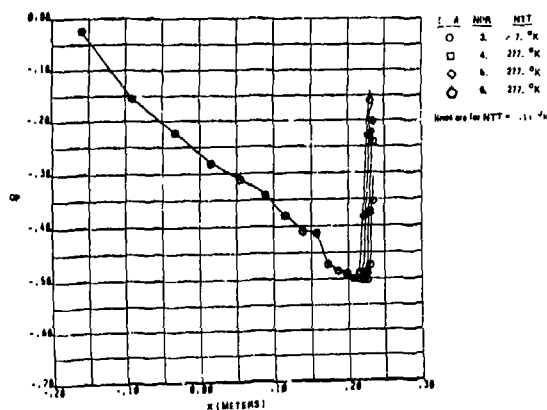


Figure 13. Computed CP Distribution on Nozzle Boattail, $M_\infty = 1.4$

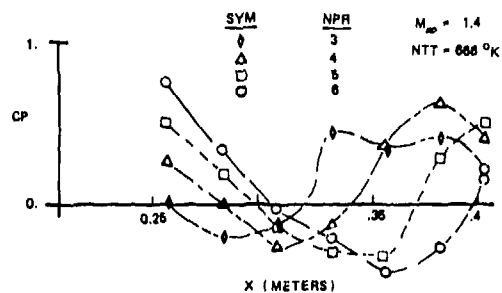


Figure 14. Measured Expansion Ramp CP Distributions at $M_\infty = 1.4$

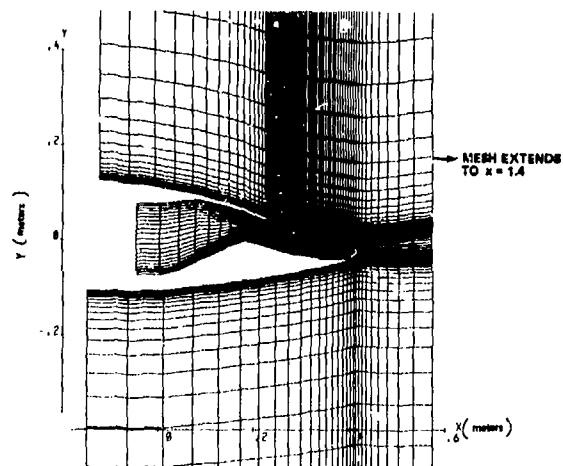


Figure 16. Computational Mesh for Extended Domain

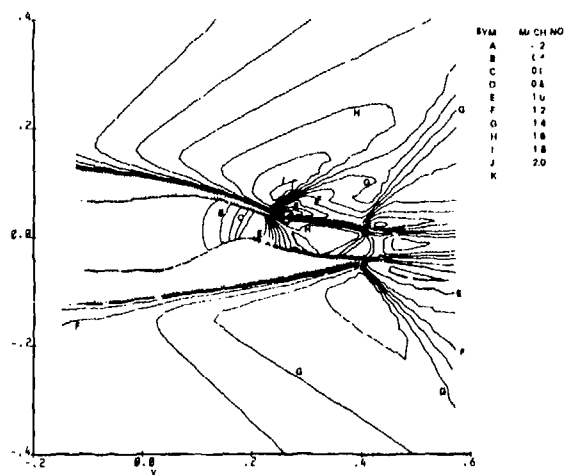


Figure 17. Computed Mach Number Contours for $M_\infty = 1.2$, $NPR = 3$, $NTT = 1111$ °K for the Extended Domain

A REVIEW OF THE EFFECT OF REYNOLDS NUMBER ON AFTERBODY DRAG

O M Pozniak
Aircraft Research Association Ltd
Manton Lane
Bedford
England MK41 7PF

SUMMARY

The reported effects of a change in Reynolds number or boundary layer thickness on the afterbody drag of axisymmetric bodies and military type aircraft are reviewed with the aim of assessing their significance.

Neglecting the effect of Reynolds number on the calibration of some tunnels had resulted in a misleading indication of a significant increase in afterbody pressure drag with Reynolds number.

It is concluded that a better understanding of the reported trends, after allowing for calibration errors and installation effects where appropriate, is obtained if the significance of different Mach number regimes and of boattail steepness combinations is recognised.

At subsonic Mach numbers and in the absence of flow separations, significant but compensating pressure changes are found such that there is little effect on the afterbody pressure drag of complete afterbodies.

In the presence of flow separations, the effects of Reynolds number tend to be small when the location of the flow separation is fixed as a result of a sudden change in the boattail contour, but on afterbodies with more continuous contours, the location of the point of separation can be affected; conflicting factors are then involved and the afterbody drag can increase or decrease by modest amounts, or remain unaffected by Reynolds number changes.

Significant increases in drag for increases in Reynolds number have been consistently reported for high subsonic Mach numbers above the drag rise.

SYMBOLS

A	Area	M	Free stream Mach number
A _g	Nozzle exit area	Mc	Mach number from plenum pressure
A ₁₀ , A _{max}	Maximum body cross-sectional area	NPR	Nozzle pressure ratio = P _J /P
C _{A2}	Afterbody axial force coefficient by pressure integration	P	Free stream static pressure
C _{DA}	Afterbody drag (friction + pressure) coefficient	P _J	Jet total pressure
C _{DAP}	Pressure drag coefficient build up = $\int C_p d(A/A_{max})$	PS ₉	Nozzle exit static pressure
C _{DA2}	Afterbody pressure drag coefficient	P ₀	Stagnation pressure
C _{DF}	Friction drag coefficient	R	Radius
C _{DFP}	Forebody pressure drag coefficient	R _c	Radius of curvature of a circular arc body of same area ratio and boattail angle
C _{DNP}	Nozzle pressure drag coefficient	Re	Reynolds number based on length
C _{D0}	Aircraft zero lift drag coefficient	SL	Sea level
C _{DP}	Complete body pressure drag coefficient	T ₀	Stagnation temperature
*Additional subscript W denotes wing reference area, otherwise body maximum cross-section as reference area.		W/T	Wind tunnel
C _p	Pressure coefficient	x	Axial position
C _p *	Pressure coefficient at sonic conditions	x _s	Axial position of separation
C _{pRen}	Pressure coefficient at a Reynolds number of Ren (n = 1, 2, 3 etc)	α	Incidence
C _p	Mean pressure coefficient on wall or model	β	Terminal boattail angle
d	Body diameter	β _c	Chordal boattail angle
d _j	Jet diameter	δ*	Boundary layer displacement thickness
L	Body length	θ	Boundary layer momentum thickness
l	Afterbody length	θ _w	Wall angle

1. INTRODUCTION

Concern about the ability to predict full scale afterbody drag from wind tunnel tests was aroused by the magnitude and variety of the effects of Reynolds number observed in the past. An example of such conflicting effects (Fig 1) was noted by Schnell (Ref 1). Some test programmes led to the conclusion, which could be supported by a plausible explanation in terms of viscous effects, that afterbody drag initially rises and then falls as Reynolds number increases, Fig 2, thus making full scale drag prediction uncertain.

MACH - 0.9
CIRC. ARC/
CONICAL
NOZZLE

SYM	SPONSOR	NAME	EFFECT ON
A	LEWIS	SCALE	NOZZLE
B	AFFOL	DENSITY	AIRFRAME
C	AFFOL	DENSITY	NOZZLE
D	LANGLEY	DENSITY	NOZZLE
E	LANGLEY	TEMP SCALE	NOZZLE

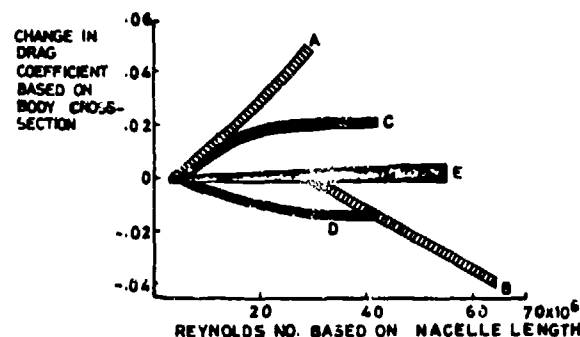


FIGURE 1 REYNOLDS NUMBER PARADOX (REF 1)

The adequacy of conventional drag accounting procedures in which afterbody pressure drag is assumed to be independent of Reynolds number whilst the change in friction drag is calculated from boundary layer theory was being questioned. Even the validity of ascribing some of the drag variations observed during tunnel tests to the change in Reynolds number was challenged.

These problems coincided with the increased significance of afterbody drag due to the trend for selection of engine cycles which require increased airflow and hence the likelihood of magnified installation effects. The problems are particularly acute for military type aircraft with variable area nozzles installed in the fuselage and especially with the steep external profiles which can result from the reduced nozzle area associated with cruise at high subsonic speeds. The situation has led to much recent activity adding to the available data.

A survey (Ref 3) of some of the scattered information was made with the aim of identifying any pattern that emerged with regard to the effect of Reynolds number on afterbody drag. The conclusions that were drawn are presented here and illustrated by examples from the available data. Mainly conventional military type aircraft which are characterised by fuselage engine installations with jets emerging at the rear are considered here; caution should be exercised in drawing conclusions with regard to configurations which are radically different.

2. AFTERBODY DRAG, FLOW FIELD AND TEST RANGE

The skin friction drag can normally be estimated adequately provided there are no separations and the position of transition is known. The variation of skin friction drag with Reynolds number follows well known laws and the reduced friction drag component at full scale conditions can be estimated.

The afterbody pressure drag, however, is the result of lack of balance of the much larger rearward acting forces resulting from the suction on the initial part of the boattailing and the thrust forces generated by the pressure recovery on the rear of the boattail. In the absence of forebody interactions on an afterbody terminating in a cylindrical sting or jet, potential flow theory indicates a balance of pressure forces resulting in zero pressure drag. In real flow on conventional configurations, the boundary layer accumulated on the relatively long front fuselage significantly displaces the effective contour of the afterbody and gives rise to a pressure or form drag. A change in Reynolds number affects the development of the boundary layer; on the forebody a change in Reynolds number has generally a small effect on pressures but on the afterbody whose reducing circumference tends to reinforce the effective growth of the accumulated boundary layer, there can be larger changes in the pressures which may lead to significant effects on the pressure drag.

A sketch of a typical flow field surrounding an afterbody is shown in Fig 3 and illustrates further possibilities for so called viscous/inviscid interactions, i.e. interactions between the boundary layer and external flow: on steep afterbodies, in addition to the displacement effects of the boundary layer, separations may be present which reduce the pressure recovery on the rear of the boattail and thus have a significant effect on drag. At high Mach numbers, further possibilities for strong viscous/inviscid interactions arise because of the presence of shocks whose strength and location can be affected by the displacement effects of the boundary layer and by the possibility of shock induced separations. The complex flow field is further influenced by the exhaust plume and entrainment effects. These interactions are summarised on the diagram below:

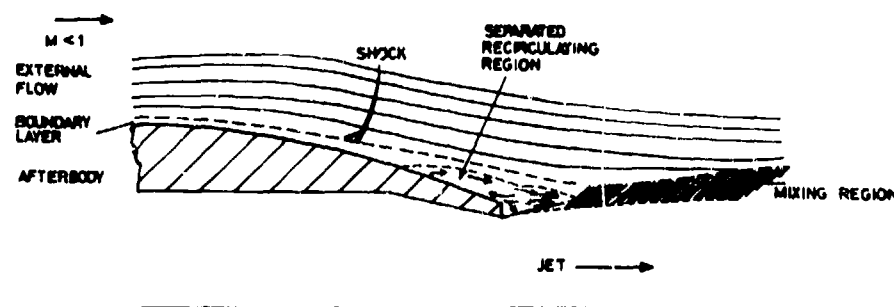
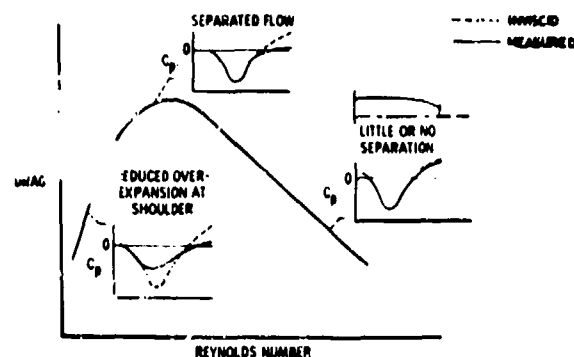


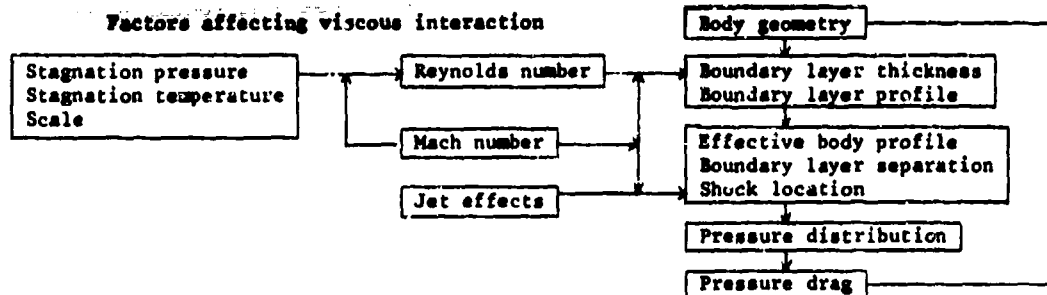
FIGURE 3

AFTERBODY FLOW FIELD

At high Mach numbers, further possibilities for strong viscous/inviscid interactions arise because of the presence of shocks whose strength and location can be affected by the displacement effects of the boundary layer and by the possibility of shock induced separations. The complex flow field is further influenced by the exhaust plume and entrainment effects. These interactions are summarised on the diagram below:

FIGURE 2 REYNOLDS NUMBER EFFECT ON PRESSURE DRAG (REF 2)





In the literature, afterbody drag is variously related to unit Reynolds number or a characteristic Reynolds number based on length or diameter. Unit Reynolds number is not a useful parameter where change in scale is involved either in model tests or comparison with full scale. Reynolds number based on a characteristic length is only applicable to a common geometry, and not where, for instance, a change in forebody length is involved. Neither are unit nor characteristic Reynolds numbers convenient parameters where viscous interactions are investigated through direct changes of the boundary layer. It is arguable that a more universally useful parameter is the ratio of body diameter to boundary layer displacement or momentum thickness at the start of the boattail.

The maximum Reynolds number available presently in transonic wind tunnels is an order smaller than for full scale flight resulting in about 50% proportionately thicker boundary layers for model tests. For 0.05 to 0.1 scale models of typical fighter aircraft, the boundary layer displacement thickness to body diameter ratio is typically 0.012-0.015 full scale and 0.017-0.021 model scale, Fig 4. The body fineness ratio (ie length/diameter) and the ratio of wing area to maximum cross-sectional area of afterbody both range typically from 8-12. Unless otherwise noted, Reynolds number here is based on model length and afterbody drag coefficients are referred to the afterbody cross-sectional area and are thus about 10 times those referred to wing area.

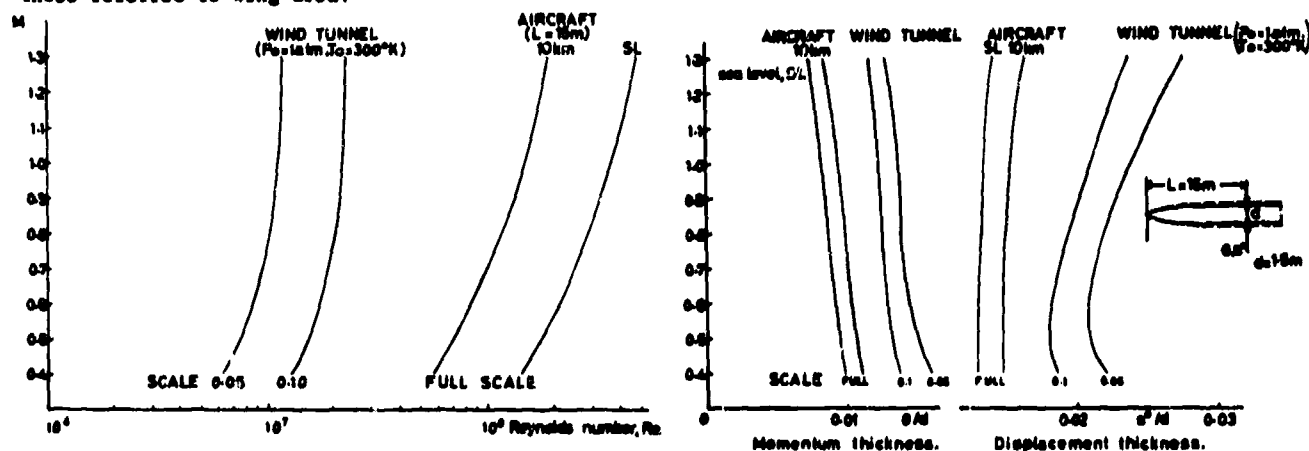
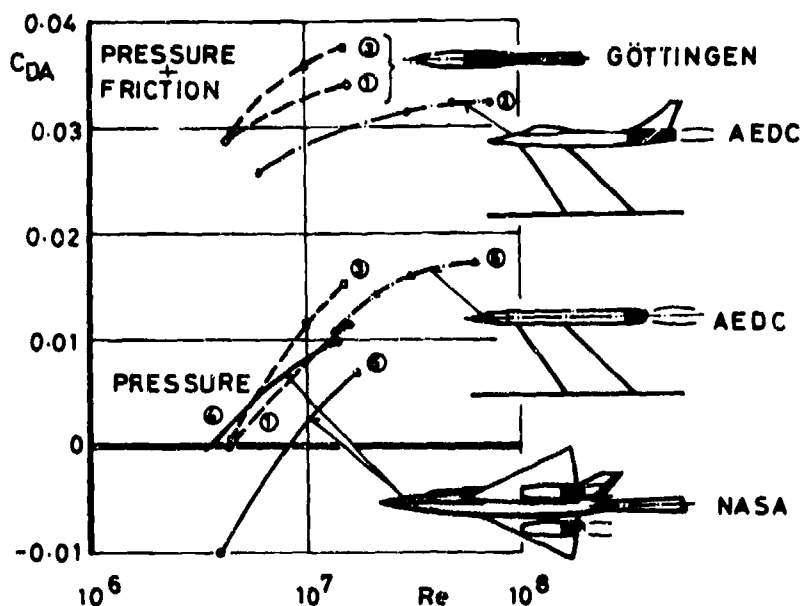


FIGURE 4 TYPICAL WIND TUNNEL TEST AND FULL SCALE RANGE OF REYNOLDS NUMBER AND BOUNDARY LAYER THICKNESS



Curve No.	M	$\frac{d}{\delta^*}$		Ref.
①	0.8	—	AB1	36
②			AB3	44
③	0.9	3	twin jet fighter	45
④	0.6	7	J-85 nacelle on F-106	23
⑤	0.6	3	axisym. body, $\theta_C = 10^\circ$	46

FIGURE 5 REYNOLDS NUMBER EFFECT ON AFTERBODY DRAG (REF 4)

3.1. Effect of Tunnel Calibration

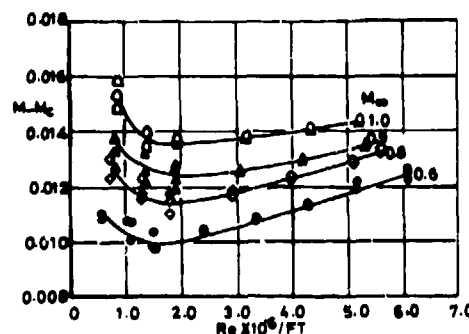
Aulehla and Besigk (Ref 4) in a paper presented in 1974 (Ref 5 contains additional data), drew attention to the sensitivity of afterbody drag derived from part body tests to possible errors associated with tunnel testing.

Some afterbody pressure drag measurements in a variety of tunnels, Fig 5, showed an unexpected increase in afterbody pressure drag with Reynolds number which made extrapolation to full scale uncertain. Combining pressure and friction drag (profile drag) reduced the increase but did not eliminate it.

Aulehla and Besigk analysed in detail pressure measurements on axisymmetric bodies (Fig 6) in the Göttingen tunnel. The pressure changes, Fig 6, can be considered as consisting of compensating increases of expansions and recompressions relative to a datum change in pressure which affects the whole body. The effect on the drag of the complete afterbody was slight, but the magnitude of the change in afterbody pressure drag apparent for the Göttingen tests shown in Fig 5 corresponded mainly to the change in this datum. A comparison of the changes in the mean of the pressure coefficients on the model and on the tunnel wall, Fig 7, showed them to be similar. This was some of the circumstantial evidence which led the authors to suggest that the afterbody drag variation with Reynolds number of the type observed for the Göttingen and AEDC-16T investigations might be due to a systematic error in static pressure, and furthermore, that the variation of the averaged tunnel working section wall pressures was a sensitive indicator of the magnitude of this error. The results shown in Fig 5 were based on tunnel calibrations performed at a fixed Reynolds number which are normally adequate for most types of tests such as drag measurements on complete bodies. The authors concluded that for testing techniques which are very sensitive to small deviations in free stream static pressure such as part-model testing, or for transonic testing with unstable shock locations which are sensitive to Mach number change, calibrations at a nominal Reynolds number may no longer be adequate.

Following the AGARD Nozzle Afterbody (NAB) tests, (Ref 7) additional calibrations over a range of Reynolds number were performed in the AEDC-16T in 1975, (Ref 8). The calibrations were within the normally accepted accuracy but a systematic variation was in fact found, Fig 8, which can be significant in terms of the effects on afterbody drag measurements. The calibration is shown as the difference between the Mach numbers derived from working section centre line static pressure and the plenum pressure. Interpreting Fig 8 results, it can be noted that the plenum pressure is higher than the free stream static pressure and furthermore, at subsonic Mach numbers, except for a 'bucket' at low Reynolds number, this pressure difference increases with Reynolds number. (Jackson, Ref 8, notes that an adequate explanation for the 'bucket' at the low Reynolds number has not yet been found).

M = Average Centre Line Mach Number
 M_c = Equivalent Plenum Chamber Mach Number.



Wall angle, $\theta_w = 0^\circ$

CYLINDER

$M_0 = 0.8$

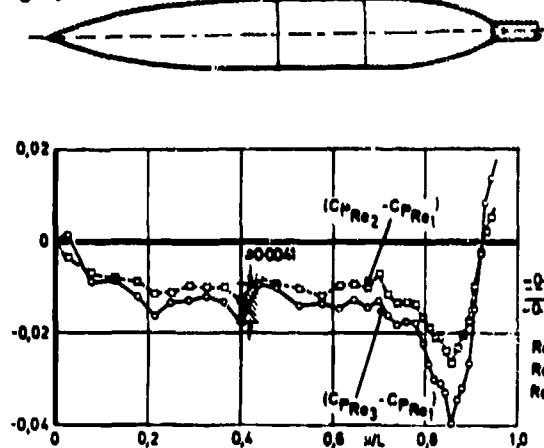


FIGURE 6 CHANGE IN PRESSURE DISTRIBUTION DUE TO REYNOLDS NUMBER
 $M = 0.8$ (REF 5)

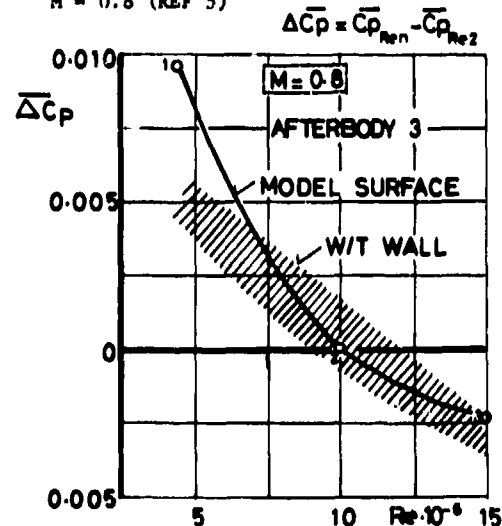
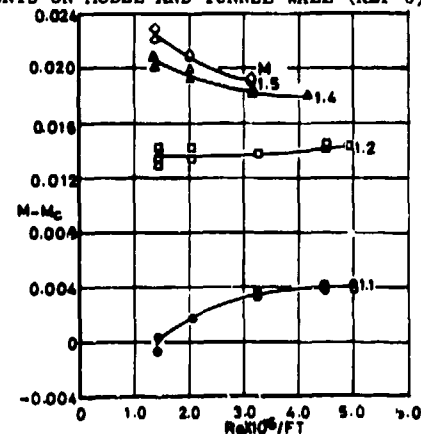


FIGURE 7 COMPARISON OF CHANGES IN MEAN PRESSURE COEFFICIENTS ON MODEL AND TUNNEL WALL (REF 6)



θ_w = Optimum Wall angle Schedule

FIGURE 8 AEDC-16T MACH NUMBER CALIBRATION FOR VARIOUS REYNOLDS NUMBERS
 WALL POROSITY 6% (REF 8)

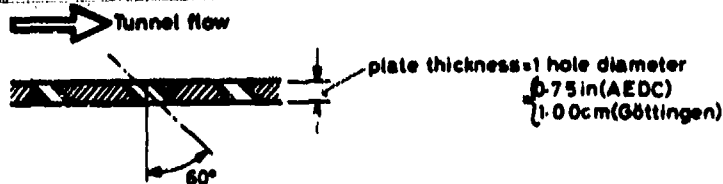


FIGURE 9 TUNNEL WALL PERFORATION DETAILS IN AEDC-16T AND GÖTTINGEN 1 METRE TRANSONIC TUNNELS (REF 6)

○ CALIBRATION AT 1000 lb/ft²
 □ REYNOLDS NUMBER CALIBRATION

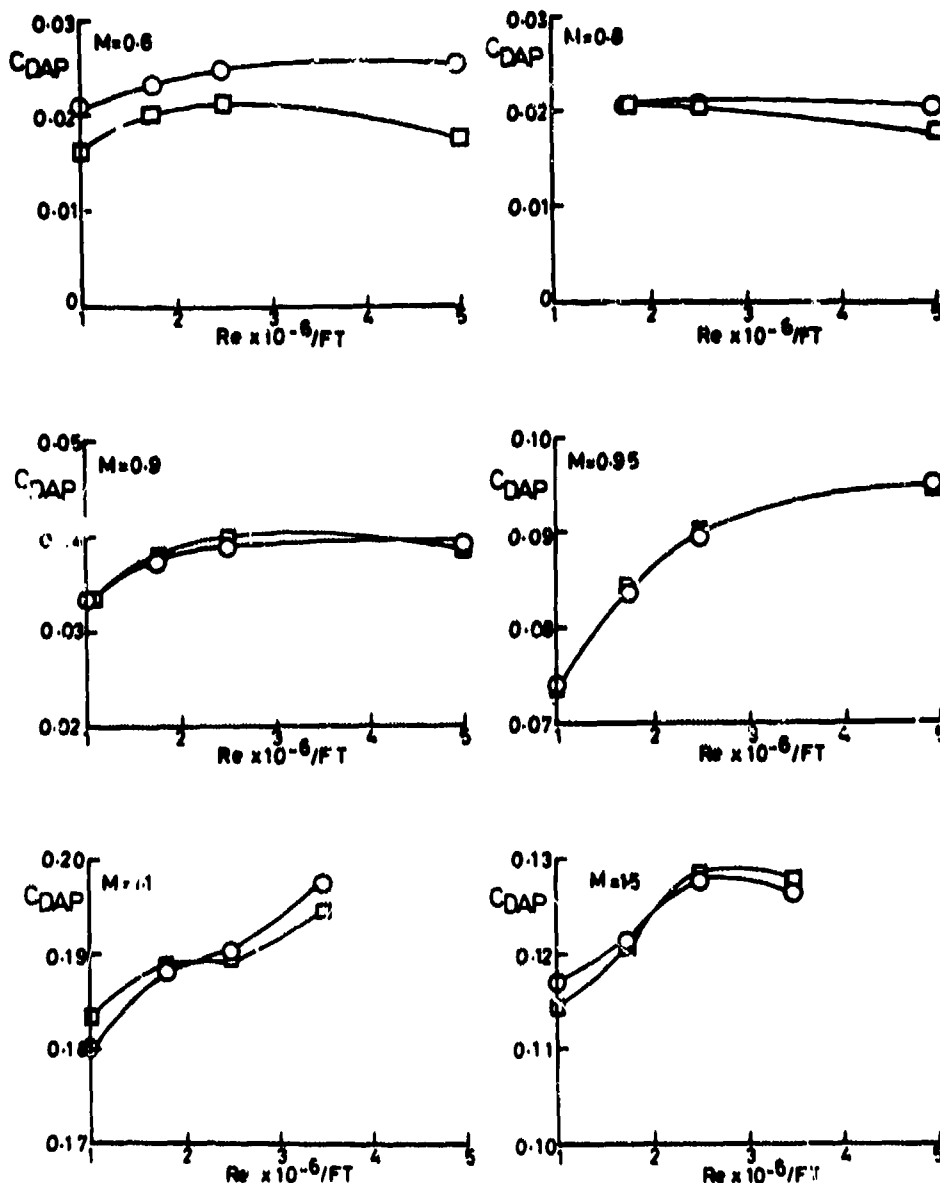


FIGURE 10 EFFECT OF TUNNEL CALIBRATION ON INTEGRATED PRESSURE DRAG FOR AGARD NAB (REF 8)

An explanation for the general trend in changes of tunnel calibration was put forward by Aulehla, (Ref 6). He suggested that it is a result of the forward inclined perforations acting as flush inlets, whose recovery increases as the wall boundary layer becomes thinner as the Reynolds number is raised. Both the AEDC-16T and the 1m x 1m Göttingen transonic tunnels have similar working section walls: the perforations in both cases are circular holes inclined forward by 60° from the perpendicular, Fig 9.

The resulting reduction in the pressure drag of a typical afterbody (nett/maximum projected area ratio = 0.8) due to the change in the tunnel calibration between Reynolds numbers of 2×10^6 and 5×10^6 is listed below.

M	0.6	0.8	0.9	1.0	1.2
ΔC_{DAP}	0.0048	0.0024	0.0016	0.0008	0.0008

The table shows that the consequence of not using a calibration corresponding to the actual test Reynolds number may be significant at $M = 0.6$ but reduces rapidly with increasing Mach number.

Jackson (Ref 8) shows a comparison of afterbody pressure drag, Fig 10, of an AGARD nozzle afterbody based on the originally standard AEDC-16T calibration at 1000 PSF stagnation pressure with that obtained by using the correct Reynolds number calibration. The data show that the correction at $M = 0.6$ reduced the overall afterbody pressure drag variation, but that at the higher Mach numbers the difference is marginal and significant increase of drag with Reynolds number still remained at $M \geq 0.95$.

Similar results were obtained by Spratley et al (Ref 9) from pressure measurements on axisymmetric sting mounted bodies without jet representation. The area distribution of the bodies was typical of high performance military aircraft. The results, Fig 11, indicate that taking account of the variation of the tunnel calibration with Reynolds number at $M = 0.6$ has virtually removed any observable variation of fore-, aft- and complete-body drag; whereas assuming that a calibration at a single Reynolds number applies throughout the range had indicated a reduction in the pressure drag of the forebody of 0.018 and an increase in afterbody pressure drag of 0.014. At $M = 0.9$, the afterbody pressure drag variation based on the tunnel calibration at the correct Reynolds number was negligible for the contoured afterbody and there was an increase of only about 0.004 for a 15° boattail. The amount of Mach number deviation required to eliminate these residual Reynolds number effects at Mach number of 0.9 was still within the range of measurement uncertainty. However, the deviation required at $M = 1.2$ was too large to eliminate the observed drag increase of about 0.01 which the authors suspect to be due to the presence of a significant viscous/inviscid interaction.

The failure to account for the variation of the tunnel calibration with Reynolds number is thus a likely explanation for the increase of pressure drag shown in Fig 5 only for some of the tests at Mach numbers below 0.9. Other investigations mentioned in later sections of this report, eg Ref 10, show that at Mach numbers high enough for shock-induced separations to be present or at Mach numbers close to or above the drag-rise value, genuine increases in pressure drag are likely to occur and this may well be a contribution to the variation shown by curve 2 in Fig 5 for instance.

The NASA data, shown in curves 4 and 5 of Fig 5, were obtained in the 8ft x 6ft supersonic wind tunnel on different scale models. The data for the lower Reynolds number is from a sting mounted, 5% scale model and for the higher Reynolds number from a 21% scale, floor mounted half model. The differences in technique may well be the main cause of the observed differences in drag; a view which is supported by the differences in drag observed on identical boattails tested in different facilities during the AGARD-NAB programme (Refs 11,12) and which is considered further in later sections of this report.

3.2. Recent Axisymmetric Configurations and AGARD-NAB Tests

To investigate further the conflicting effects of Reynolds number reported in earlier investigations, an experimental study by Blaha et al (Ref 10) of the effect of boundary layer thickness and, to a limited degree, of boundary layer profile on the flow over sting-supported axisymmetric boattail afterbodies without jet representation was conducted in the NASA Lewis Research Center's 8ft x 6ft wind tunnel. The boundary layer thickness was varied by changing model length and by using a series of slotted rings. The range of boundary layer displacement thickness explored was from about 0.01 to 0.05 body diameters. This investigation is particularly informative because of the wide range of diagnostic techniques employed; surface statics to obtain pressure distributions, movable probes and fixed rakes to

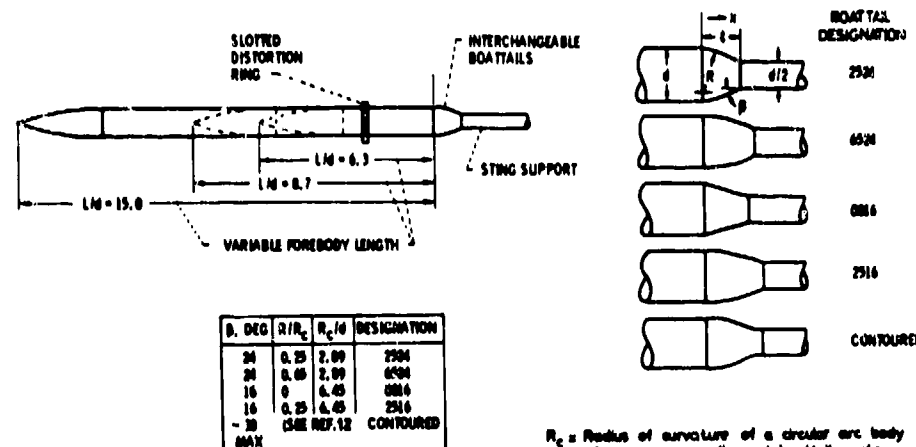


FIGURE 12a

a. model details

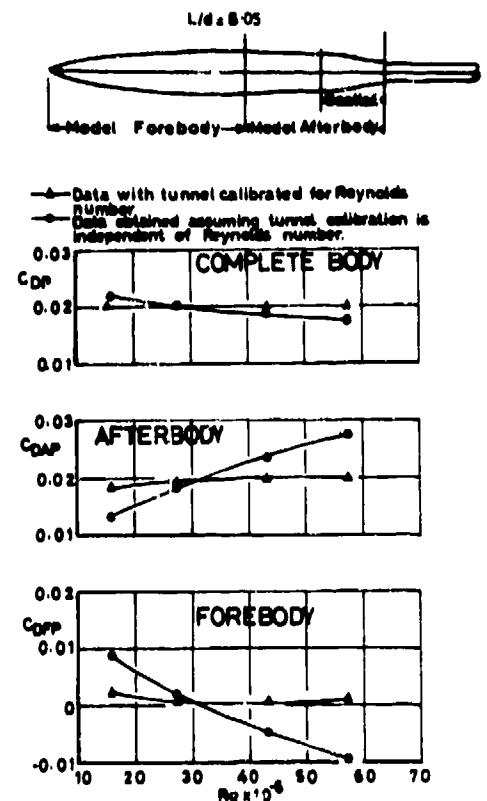


FIGURE 11 EFFECT OF TUNNEL CALIBRATION ON PRESSURE DRAG COEFFICIENTS FOR CONTOURED BOATTAIL CONFIGURATION $M = 0.60$ (REF 9)

R_c = Radius of curvature of a circular arc body of same area ratio and boattail angle

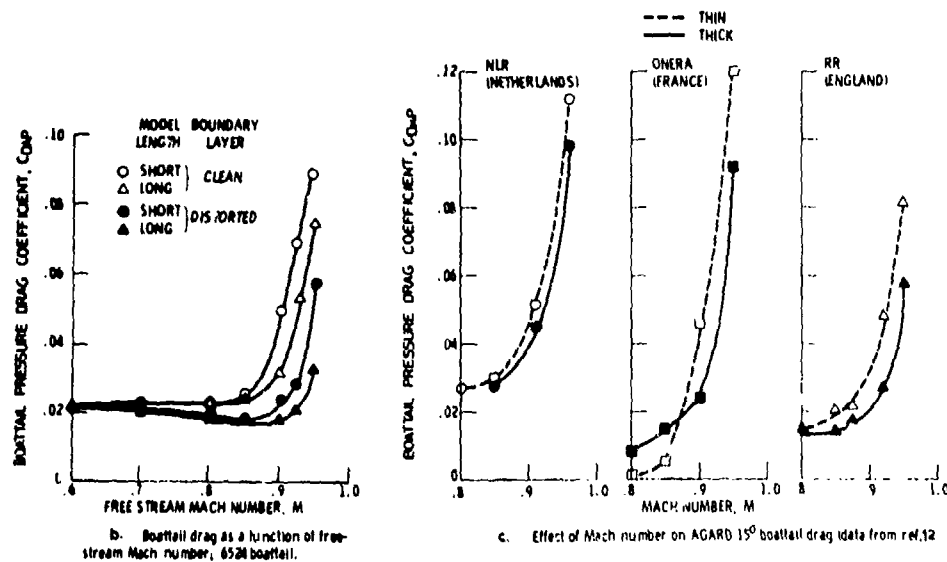


FIGURE 12 AXISYMMETRIC BOATTAIL MODEL DRAG TESTS (REF 10)

obtain boundary layer flow profiles and fluorescent mini-tufts to establish regions of separated flow. The results of this NASA investigation are examined here in some detail as they exemplify many of the trends which appear to be common to much of the data examined during this survey.

Details of the models are shown in Fig 12a. Four round shouldered and one sharp shouldered model were tested. In the designation used, the first two digits represent the ratio of the radius of the shoulder to that of a full circular arc; the last two digits denote the terminal boattail angle.

The effect of boundary layer thickness on the variation of drag with Mach number for one of the round shouldered bodies is shown in Fig 12b. The main effect of increasing boundary layer thickness is to postpone the drag-rise Mach number; similar effects, Fig 12c, were observed in the presence of a jet on the AGARD 15° boattail (Ref 11) which, in the designation used in Ref 10, would be an approximate 7523 boattail.

At $M = 0.6$ for a flow which is mainly attached, reduction of the boundary layer thickness resulted in suction at the shoulder and pressure recovery at the rear increasing ($\Delta C_p = 0.07$) in a compensating manner, Fig 13a, resulting in little effect on drag, Fig 14a. At $M = 0.9$, however, significant areas of flow separation were present on the 6524 boattail, Fig 13b. The dashed lines are used to denote limits of what in Ref 10 were described as 'areas of increased tuft movement and turbulence' and which were

Tuft pictures of flow
SOLID LINE - REVERSED FLOW
DASHED LINE - HIGHLY TURBULENT FLOW



$\delta^*/d = 0.01$



$\delta^*/d = 0.04$

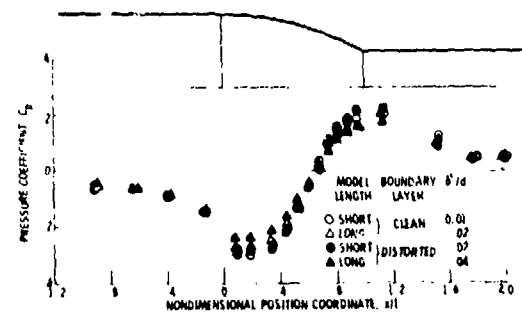


$\delta^*/d = 0.01$

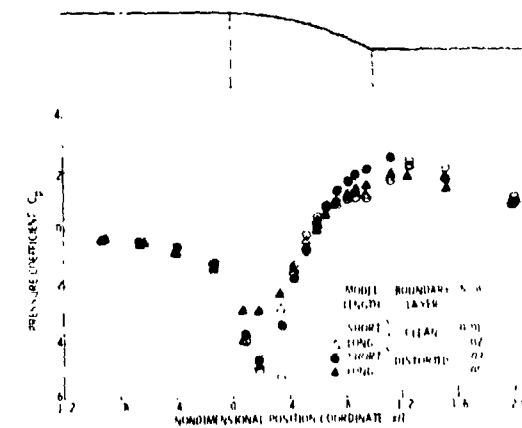


$\delta^*/d = 0.05$

$$\delta^*/d = \frac{\text{Boundary layer displacement thickness}}{\text{Body diameter}}$$

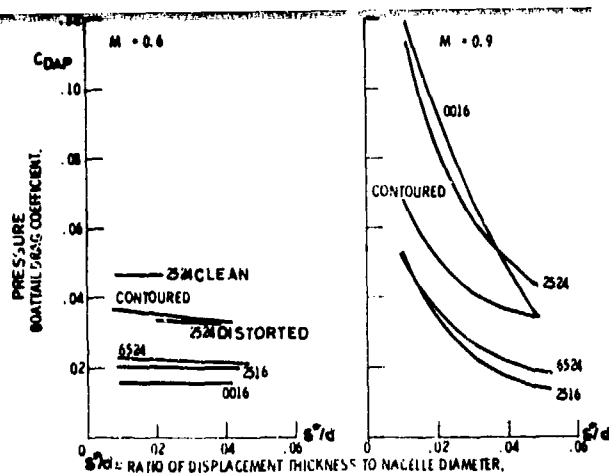


a. $M = 0.6$

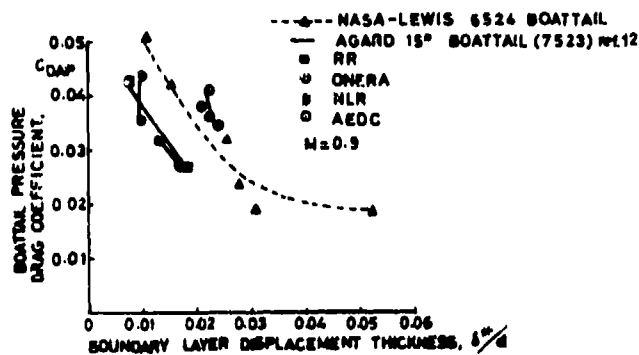


b. $M = 0.9$

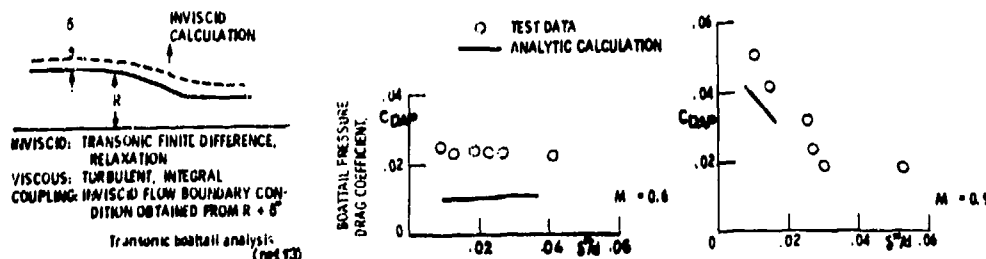
FIGURE 13 FLOW AND PRESSURES ON 6524 BOATTAIL (REF 10)



a. Effect of boundary layer thickness



b. Comparison of results from several different tests



c. Comparison of analytic and experimental pressure drag 6524 boattail geometry.

FIGURE 14 EFFECT OF BOUNDARY LAYER DISPLACEMENT THICKNESS ON BOATTAIL DRAG (REF 10)

probably areas of intermittent separation. In the presence of the thinner boundary layer the limits marked by the dashed lines were somewhat extended, but the areas of 'flow reversal' and continuous separations marked by solid lines were significantly increased and the recompression on the aft boattail reduced. There was also a marked increase in the suctions indicating areas of supersonic flow at the shoulder whereas, for the thickest boundary layer, the suctions were of a similar level to those observed at $M = 0.6$. This, of course, is in accord with the drag variation of Fig 12 which shows that the drag rise has been postponed to just beyond $M = 0.9$ for the thicker boundary layer.

Fig 14 shows the effect of boundary layer thickness at $M = 0.6$ and $M = 0.9$ for all the range of boattails tested. At $M = 0.6$ there is little effect of boundary layer changes on afterbody drag except for the 2524 boattail. Two curves are shown for this boattail, the upper for varying boundary layer displacement thickness without and the lower with distortion rings present. The tuft pictures, Fig 15, show that on this body extensive areas of separation and flow reversal were present at $M = 0.6$ and, in particular, that the areas of permanent flow reversal were reduced by the presence of the distortion rings; the corresponding pressure distribution shows that the drag reduction is mainly due to the improved pressure recovery at the rear of the boattail.

At $M = 0.9$, the drag of each of the boattails tested correlated against boundary layer thickness irrespective of whether this was varied by changes in body length or through the addition of distortion rings, Fig 14. There is a significant increase in pressure drag as boundary layer thickness is reduced, the pressure drag changing more rapidly for thin boundary layers and tending to level out for thicker boundary layers. In such a case, tests in wind tunnels over a limited, low Reynolds number range would significantly underestimate the change in drag between test and full scale Reynolds numbers.

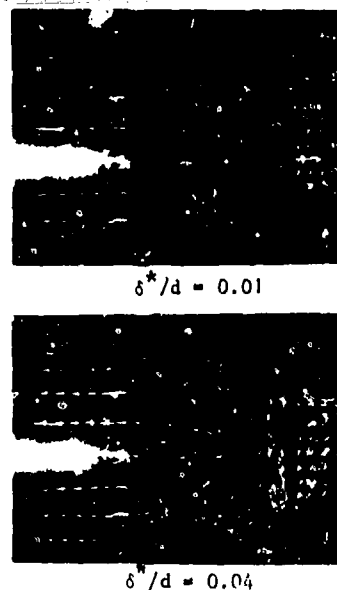


FIGURE 15 FLOW VISUALISATION AND PRESSURES ON 2524 BOATTAIL (REF 10)

All the boattails tested exhibited some flow separation at $M = 0.9$ and the drag changes are the result of changes in the over-expansion at the shoulder and changes in the separated region on the rear of the boattail.

The geometries tested included a case where the change in boundary layer thickness affected not the extent but the nature of the separation. This occurred on the conical 0016 boattail where the sharp corner fixed the separation point, Fig 16. For the thickest boundary layer the boattail flow was very turbulent and as the boundary layer became thinner the turbulence intensity increased and 'permanent flow reversal' eventually occurred over the entire boattail. Downstream of the shoulders, the pressures decreased significantly as the boundary layer became thinner and resulted in the large drag increase observed.

Comparisons of the boundary layer effects on the 6524 boattail with tests in different facilities of the similar AGARD 15° boattail (Ref 12) are shown in Fig 14b. The AGARD data were obtained in the presence of a flowing jet and boundary layer thickness variation both by changing model length and by blowing. Fig 14c shows a comparison of the pressure drag determined experimentally and analytically. The analytic calculations were based on the 'viscid-inviscid' interaction procedure of Chow et al (Ref 13) which does not take into account the presence of flow separation. Although for the experimental and analytic comparisons shown in Figs 14b,c the drag levels are different, the variation of drag with boundary layer thickness is essentially in agreement. At $M = 0.6$ both experiment and analysis indicate that boundary layer thickness has little effect on drag. At $M = 0.9$ the data from Ref 10, the AGARD tests (Ref 12) and analysis (Ref 13) show a similar trend for drag to increase as the boundary layer thickness is reduced.

The range of the change in boundary layer thickness investigated in this study exceeded the 50% change normally expected between full scale condition and model tests in a large tunnel. The largest change in drag at $M = 0.9$ that was indicated for a realistic range is about 0.025 equivalent to 25 drag counts.

An extensive programme to improve nozzle testing techniques at transonic speeds was executed under the auspices of the AGARD Propulsion and Energetics Panel (Refs 11,12,14). The programme involved pressure measurements in different facilities on a standardised range of axisymmetric nozzle-afterbody shapes ('AGARD-NAB'). The range, Fig 17, consisted of a 10° boattail, chosen to be free from flow separations at subcritical Mach numbers, a 15° boattail on which at some Mach numbers shock-induced separations were present and a 25° boattail with rounded shoulders which had separated flow at all Mach numbers. The effects of variations of Reynolds number and boundary layer thickness at Mach numbers from 0.8 to 0.95 formed part of the investigation and were reviewed by Zonars, Loughrey and Bowers (Ref 12). The pressure drag for some of the tests listed in Ref 10 is shown replotted in Fig 17 in terms of either quoted or estimated values of the ratio of boundary layer displacement thickness at the start of the boattail to body diameter ratio. Plotted in Fig 17 are results of tests for a range of Reynolds number obtained by changing tunnel stagnation pressure, eg AEDC-16T and ARL-CFF as well as tests for which the boundary layer displacement thickness was reduced by blowing, eg RR. The AEDC-16T and the RR tests were with a flowing jet represented whereas for the ARL-CFF tests the jet was simulated by a cylindrical sting.

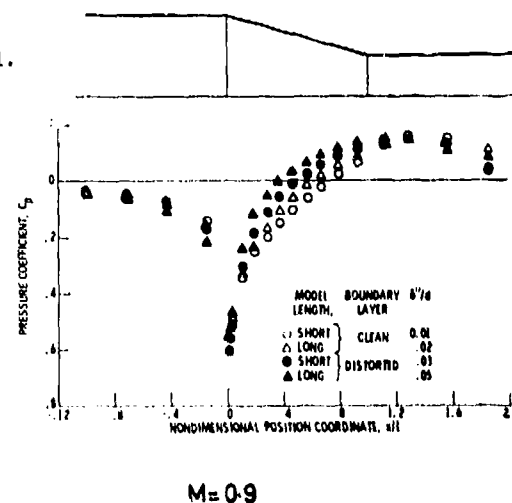
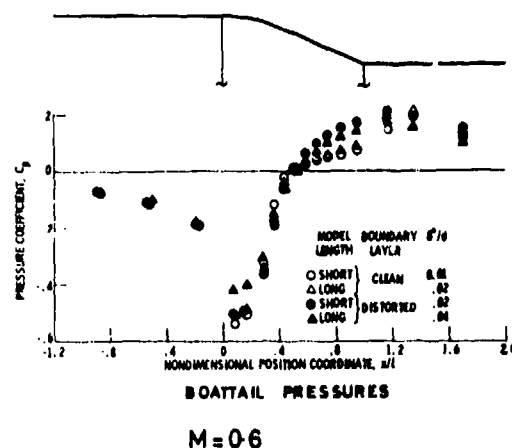


FIGURE 16 PRESSURE DISTRIBUTION ON THE 0016 BOATTAIL (REF 10)

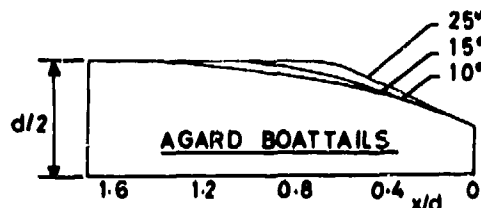
A recent calibration of the AEDC-16T tunnel at various Reynolds numbers (Refs 8,9) referred to earlier, indicated that these data reported in Ref 12 are subject to marginally significant errors at $M = 0.8$, but that at $M = 0.9$ and 0.95 these errors are small.

It is clear from the derived data that differences in the boundary layer thickness are not the only reason for differences in the level of afterbody pressure drag obtained from tests in different facilities, and an examination of these formed the main subject of the AGARD NAB programme. However, tests in a single facility should give a true indication of the effects of Reynolds number or boundary layer properties, provided possible flow velocity and direction changes are carefully allowed for.

The range of the ratio of boundary layer displacement thickness to body diameter, δ^*/d , investigated in each of the facilities was of the order of the change from model to full scale, say $\delta^*_{\text{MODEL}}/\delta^*_{\text{FULL SCALE}} = 1.5$ and the ranges of absolute values of δ^*/d for the ARL-CFF and the RR tests with blown boundary layer extended to likely full scale values.

BOATTAILS

- 10° 15° 25°
• □ ◇ AEDC(16T) STAGNATION PRESSURE VARIATION WITH JET, $NPR = 3$.
- □ ◇ ARLCFF STAGNATION PRESSURE VARIATION, CYLINDRICAL STAGNATING JET.
- □ ◇ RR, NATURAL AND BLOWN BOUNDARY LAYER, WITH JET FLOW REPRESENTED.



3% BOUNDARY LAYER DISPLACEMENT THICKNESS AT $x/d = 1.6$
 C_{DAP} = AFTERBODY PRESSURE DRAG (BASED ON BODY CROSS-SECTIONAL AREA).

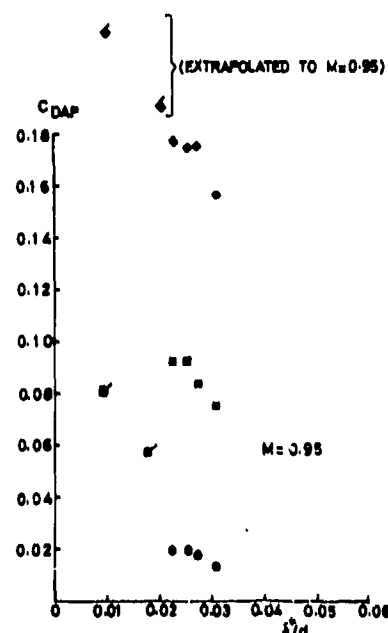
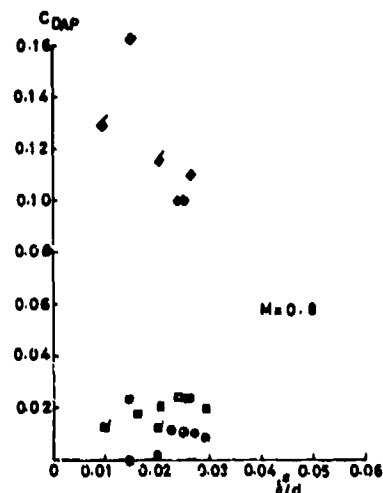
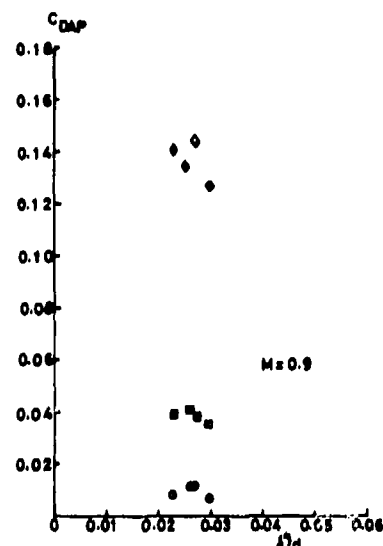


FIGURE 17 SUMMARY OF VARIATION OF PRESSURE DRAG WITH BOUNDARY LAYER THICKNESS AGARD BOATTAILS 10°, 15°, 25° (REF 12)

At $M = 0.8$ for the 10° and 15° boattail, drag changes did not exceed 0.005 which is of the order of the precision of the experimental data. The pressure distributions (not reproduced in Fig 17) in common with those from other investigations showed that quite large increases, $|\Delta C_p| \approx 0.05$, occurred in the suctions at the boattail shoulders and in the pressure recoveries at the rear for reductions in boundary layer thickness or increase in Reynolds number and that these changes in the pressures have a compensating effect on drag.

At $M = 0.95$, increasing the Reynolds number or decreasing boundary layer thickness over a range that encompasses tunnel and full scale values, resulted in an increase in the afterbody pressure drag by about 0.02 equivalent to say, 20 aircraft drag counts for the 15° and 25° boattail configurations. The corresponding pressure distributions (not shown in Fig 17) were characterised by only small changes in the expansion region near the shoulder, the increase in drag being principally due to the reduced recompression in an apparently separated flow aft of the shock. The results for the 10° boattail show a much lower drag variation.

At $M = 0.9$, the effect of Reynolds number on the drag of the steeper boattails is in a similar direction but less severe than at $M = 0.95$. The drag changes were principally due to changes in the expansion at the shoulder with only a small change in recompression region at the rear.

It has been noted elsewhere in this report that the changes with Mach number of the effect of Reynolds number on drag found during the AGARD-NAB tests is in general agreement with those of other investigations.

For the 25° boattail at $M = 0.8$ different drag trends were obtained from the three investigations shown; these tests differ in being either with or without a flowing jet, and for the RR tests involved substantial changes in boundary layer shape factors. Each of these factors may be significant in the

presence of flow separations. For instance, the drag of a similarly steep boattail (Ref 10) was found to be sensitive to boundary layer profile.

Lately, the unique capabilities of a cryogenic tunnel to test an individual model over a wide Reynolds number range in one facility has been utilised to test boattails, similar to those of the earlier tests, in isolation (Ref 15), and installed under a wing-body combination (Refs 16,17). The results of both the isolated and installed tests, in spite of the presence of significant installation effects, showed little change in boattail drag with Reynolds number at Mach numbers ranging from 0.6-0.9. The characteristic Reynolds number range in these tests for a body of a fineness ratio of 8 was about 2 to 50×10^6 and drag coefficient (based on body area) changes were less than 0.005. Tests (Ref 18) on axisymmetric boattails in the 0.3 metre Transonic Cryogenic Tunnel (0.3m TCT) illustrate the typical sensitivity to scale effects of local pressure distributions and hence drag build up and the compensating effect on overall drag at low Mach numbers (Fig 18).

Some indication of the effect of changes in the boundary layer thickness on pressures and drag of axisymmetric boattails with an annular base surrounding the jet can be obtained from tests reported by Crane (Ref 19). The boundary layer was thinned by reducing the length of the front shaft support and by suction. At $M = 0.8$, changing from long to short shaft reduced the boundary layer momentum thickness from 0.015 to 0.010 body diameters and increased the suction at the start of the boattail by $(-\Delta C_p) = 0.04$ but had little effect on the base pressure, Fig 19. The effect was an increase in the boattail and hence also in the complete afterbody (boattail and base) drag coefficient of the order of 0.01. A further reduction in boundary layer momentum thickness to 0.003 body diameters increased the pressure recovery on the rear of the afterbody by about $\Delta C_p = 0.04$ and increased the extent of the suction on the boattail without an increase in the level of the suction peak. These changes made a compensating contribution to boattail drag alone but the overall drag decreased due to the higher base thrust. Flow visualisation confirmed that at $M = 0.8$ the external flow was attached over the entire boattail. In conclusion, it should be noted that although the boundary layer thickness was varied over a range which probably exceeds that typical between model tests and full scale flight, the overall pressure drag coefficient variation did not exceed about 0.01 (based on body area) but an extrapolation of the results with the thicker boundary layer would have been quite misleading.

Some word of caution with regard to drawing firm conclusions from comparisons of the tests with different shaft lengths: the changes involved different axial locations in the tunnel and therefore may have been subject to errors due to pressure gradients, or since pressures were measured along a top generator only, due to changes in flow direction (Ref 6).

The flow over a bluff base is naturally separated, and like other separated flows, may be sensitive to the shape of the boundary layer profile and this may also be a contributory factor in the irregular variation of afterbody drag with boundary layer thickness shown by the results of Ref 19. Reid and Kurn (Ref 20) investigated the effect of boundary layer thickness on the pressure drag of a range of circular arc afterbodies, Fig 20, with and without bases, at a Mach number of 0.8. The steepness of the bodies varied such that both fully attached flow and varying degrees of separation were represented. Although reducing the boundary thickness moved the separation point significantly downstream the drag increase from the steeper effective profile at the start of the boattail was almost completely balanced by the increased pressures on the rear such that there was little or possibly only a marginal increase in drag.

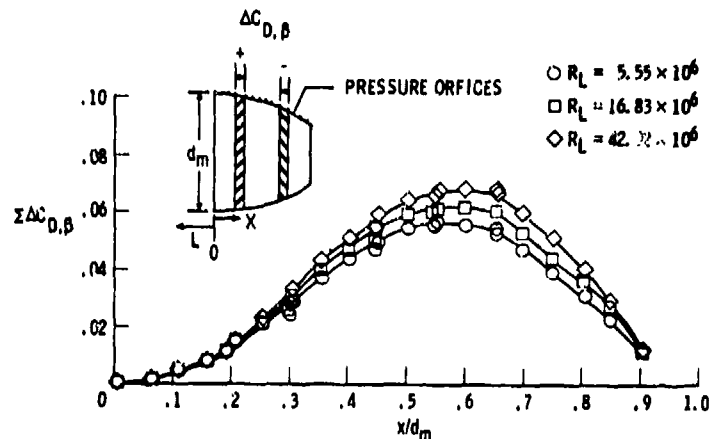
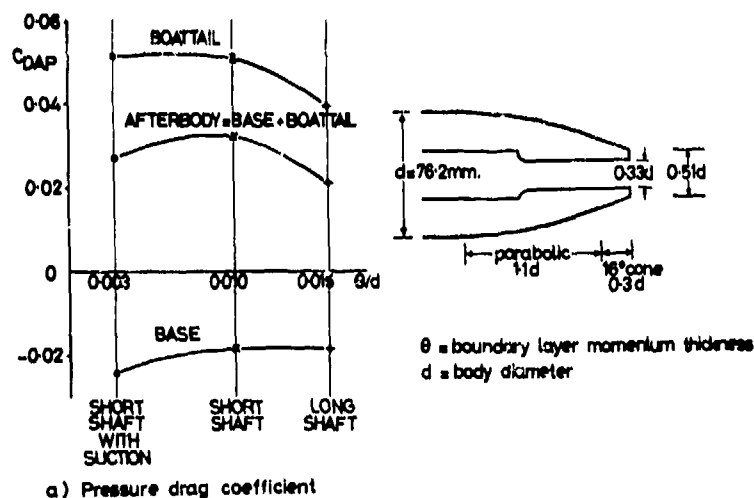
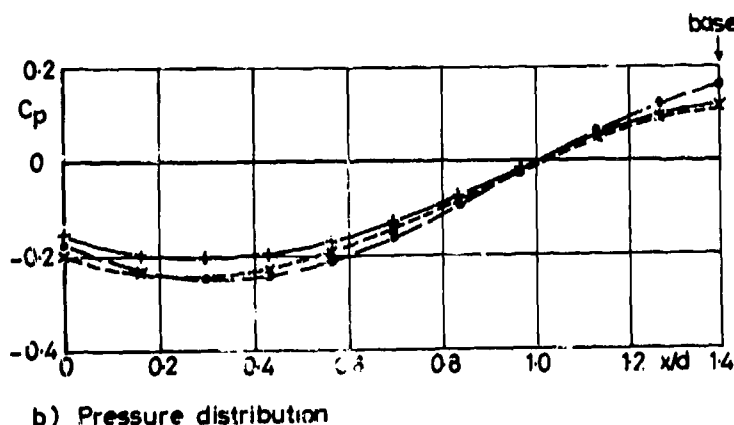


FIGURE 18 TYPICAL EFFECTS OF REYNOLDS NUMBER ON BOATTAIL DRAG BUILD UP
 $M = 0.60$ (REF 18)

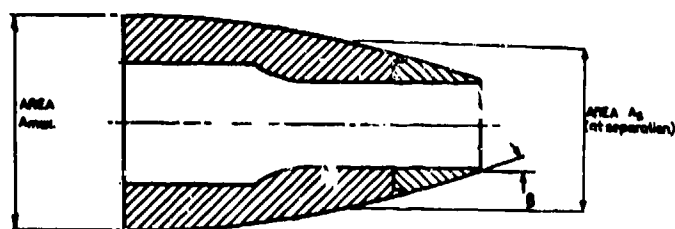


a) Pressure drag coefficient

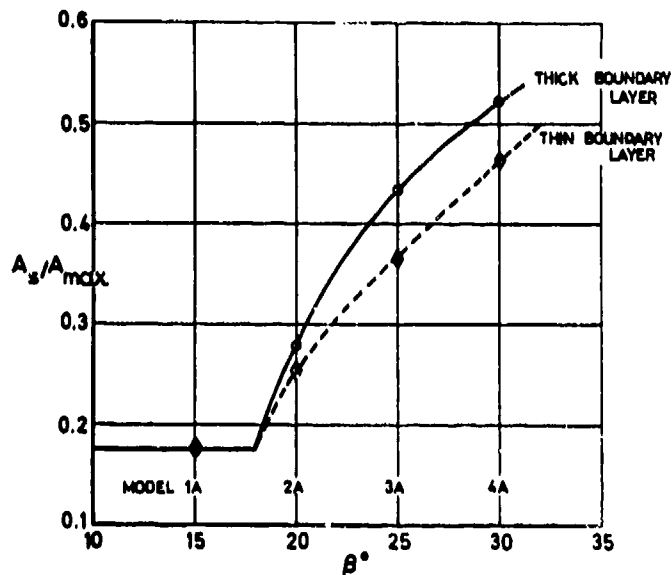


b) Pressure distribution

FIGURE 19 EFFECT OF BOUNDARY LAYER THICKNESS ON A PARABOLIC, AXISYMMETRIC AFTERBODY WITH BASE (REF 19)
 $M = 0.8$ $PJ/P = 3$



a. Model A



b. Boundary layer separation $PJ/P=3.5$

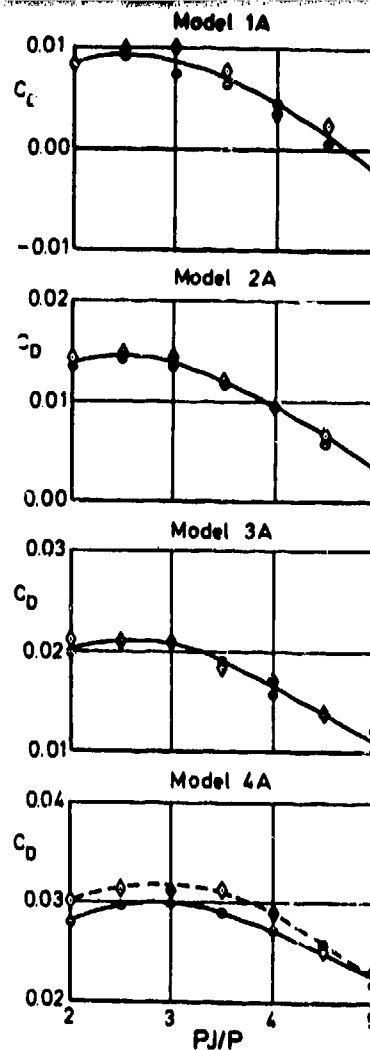


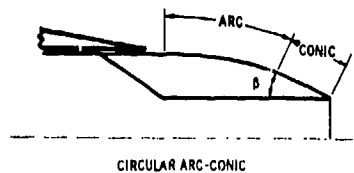
FIGURE 20 EFFECT OF BOUNDARY LAYER THICKNESS ON SEPARATION AND AFTERBODY DRAG (REF 20)

3.3. NASA - F-106 Data

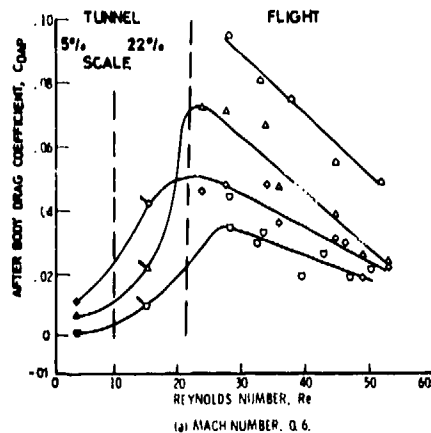
Measurements of the installed boattail pressure drag over a wide range of Reynolds number have been made by NASA on an extensive range of boattails mounted behind underwing nacelles on an F-106 type delta aircraft during tunnel and flight tests.

Examples (Ref 2) of the measured pressure drag at $M = 0.6$ and 0.9 from these tests (Refs 21-25) plotted against the characteristic Reynolds number, Fig 21, showed an unusual and large drag variation, which implied that it would be impossible to extrapolate to flight Reynolds numbers the boattail drag data obtained from wind tunnel tests, and is the source from which the type of drag variation shown in Fig 2 was derived.

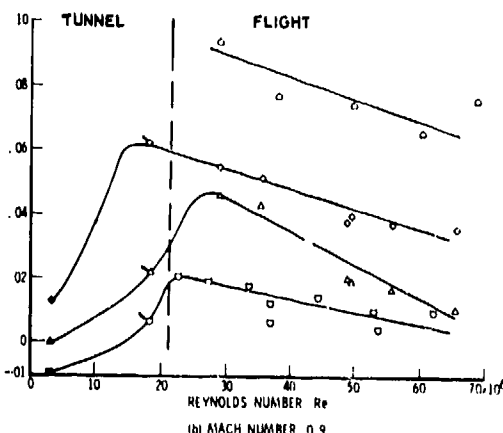
The magnitude of the drag increase shown at the lower range of Reynolds numbers is not in general agreement with the axisymmetric data, particularly from later investigations described in the previous section, which tend to



CIRCULAR ARC-CONIC



(a) MACH NUMBER 0.6



(b) MACH NUMBER 0.9

FIGURE 21 REYNOLDS NUMBER EFFECT ON PRESSURE DRAG OF CIRCULAR ARC BOATTAILS (REF 2)

R = radius of boattail shoulder
 R_c = radius of circular arc of same projected area and terminal boattail angle.

WIND TUNNEL TESTS		FLIGHT TESTS		NOZZLE	
5% scale solid plume simulator	22% scale half model turbulent simulator			100 %	Description
▲	▽	△	▽	28	24 extended
●	▽	△	▽	65	24
○	▽	○	▽	25	24
●	▽	▽	▽	25	16

show little if any change in pressure drag at low subsonic Mach numbers. The data, as shown in Fig 21, are in fact from wind tunnel tests with different scale models and from flight tests over a Reynolds number range which did not overlap. At the lowest Reynolds number the results are from a 5% scale sting mounted full span model with closed inlets and solid jet simulator and next up the scale from a 22% floor mounted half span model tested both with a turbine powered and also with a solid plume simulator. In general, the drag at the lowest Reynolds number of the flight tests shows a further substantial increase in relation to the tunnel tests. It is most likely that the difference in drag between the data from different models and flight test is not entirely due to the difference in Reynolds number but is caused by the differences in test technique. It was noted previously that significant differences in relation to Reynolds number effects were, for instance, also found between measurements in different facilities during the AGARD nozzle afterbody investigations (Refs 11,12).

Flights were made at different altitudes in coordinated turns to obtain data over a significant range of Reynolds number at constant incidence. The flight test results consistently indicate a reduction in boattail drag with increase in Reynolds number, although the exact rate is uncertain due to the scatter of the data. The presence of separations during flight tests and changes in their extent were indicated by wool tufts. That the observed movement of the separation point would affect the drag on a 19° boattail in the observed manner has also been verified analytically (Ref 26).

In some instances, the position of the separation point varied intermittently. The presentation of the paper by Wilcox and Chamberlin (Ref 2) at the previous AGARD propulsion symposium in Rome, was accompanied by a cine film obtained during flight tests which showed the existence of an intermittent separation on the extended boattail with 0.25 shoulder radius ratio, R/R_c , and 24° terminal boattail which exhibited a significant variation of drag over the flight test range of Reynolds number. In this instance, the pressures recorded by the instrumentation system were intermediate between the attached and separated case. Even though the limits of the extent of the separation might not change under these circumstances, a change with Reynolds number in the degree of intermittency may result in change of measured drag. Earlier reports (Refs 27,28) from flight tests with similar (and some probably identical) boattails on the F-106 aircraft noted a similar reduction in drag with increase in Reynolds number, and in this case the circumferential extent of separations was reduced, Fig 22.

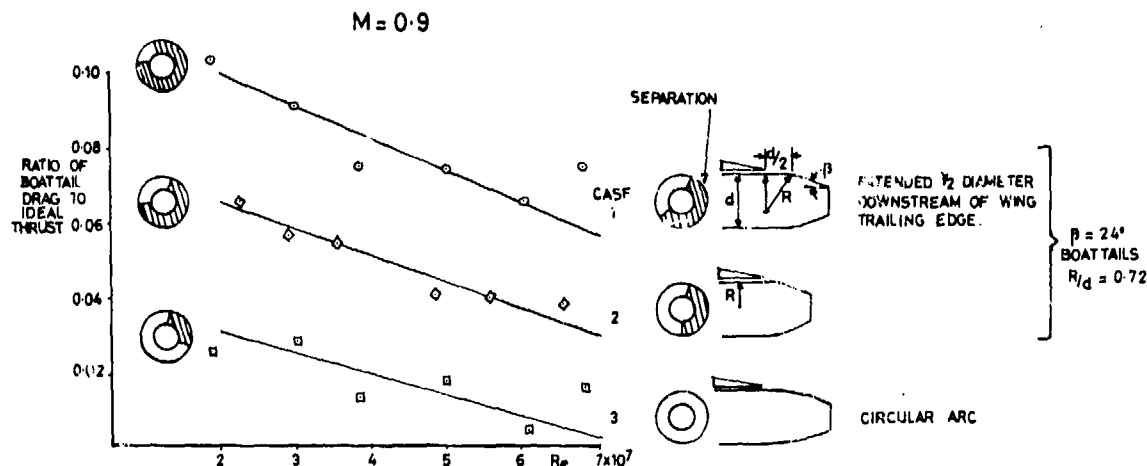


FIGURE 22 REYNOLDS NUMBER EFFECT ON BOATTAIL DRAG FROM FLIGHT TEST (REF 27)

During flight tests, although incidence and Mach number were kept constant, some variation in elevon angle is apparent in the results presented in Refs 21,23,26 and it is not clear whether this may have had an influence on the boattail drag.

Another possible contribution to the observed drag variation arises from the presence of a significant and favourable interference effect on the nozzles close to the wing trailing edge which is apparent from the higher drag of the '2524 extended' configuration where the 2524 boattail was located half a nozzle diameter further downstream of the wing trailing edge, Fig 21. In this sense, the F-106 boattail data may exhibit the 'part body' sensitivity to Reynolds number highlighted by Aulehla and Besigk (Ref 4). However, the results of flight tests for a contoured boattail (Ref 21) which showed little movement of the point of separation showed only a slight decrease in drag at both $M = 0.7$ and 0.9 . Very little change in pressure drag at Mach numbers below 0.9 was also observed during tests (Refs 16,17) on smooth boattails installed under a wing-body combination, which were tested in a cryogenic tunnel over a wide range of Reynolds number which encompassed the F-106 flight and tunnel comparisons.

It seems therefore safe to conclude that the changes in drag observed during the F-106 tests, such as curves 4 and 5, Fig 5 and Fig 22, are due to interference and installation effects and for the flight results were due to changes in flow separation which may not have been entirely due to Reynolds number effects.

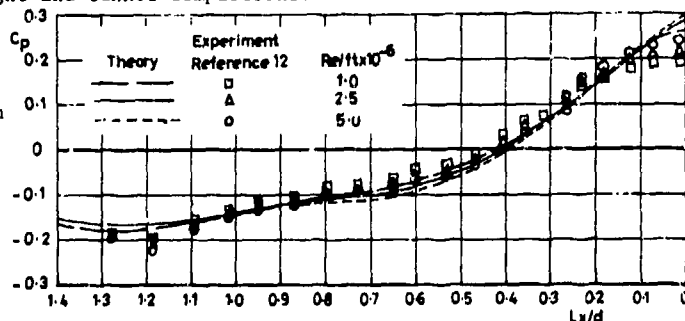
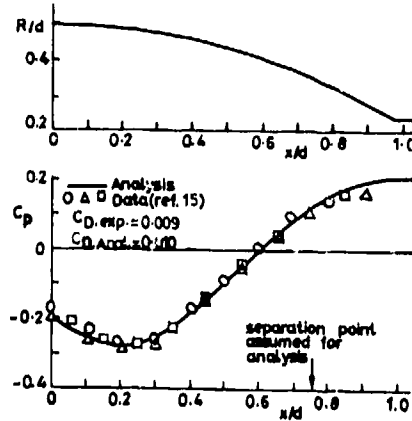


FIGURE 23 EFFECT OF REYNOLDS NUMBER ON AFTERBODY PRESSURE DISTRIBUTION (REF 29) ($\beta = 10^\circ$, $M = 0.9$, $NPR = 3$)

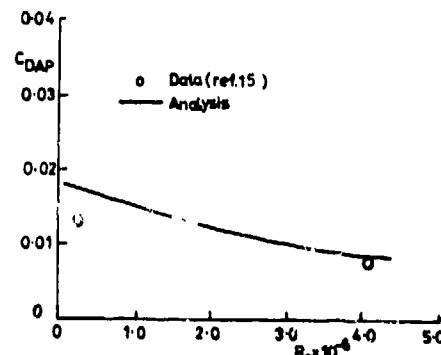
3.4. Analytical Results - Subsonic

The trends for the suction on the front of the boattail and the pressure recoveries on the rear to increase with Reynolds numbers for gentle boattails at subsonic Mach numbers, are also generally predicted by those analytical methods (Ref 29) in which the inviscid free stream flow is calculated about the effective boattail consisting of the geometric boattail with the boundary layer displacement thickness added, Fig 23. This confirms that the observed changes of pressure distribution with Reynolds number are essentially due to the change in boundary layer displacement thickness modifying the effective contour of the afterbody.

Presz et al (Ref 30) have recently formulated a viscous flow calculation that incorporates an improved analytical model which includes the effects of skin friction, axial pressure gradient and nozzle jet entrainment on the separated reverse flow region. The separation point prediction described by Presz (Ref 31) is used. The combined analysis was found to predict both the magnitude of the afterbody pressures and pressure drag and also their variation with Reynolds number. A comparison of the predicted and experimental values of pressure distribution and the variation of afterbody pressure drag with Reynolds number for a circular arc conical afterbody tested in the NASA Langley's 1/3 metre cryogenic tunnel (Ref 15) is shown in Fig 24. The analytic prediction and the experimental data both show a reduction in afterbody pressure drag with increase in Reynolds number at $M = 0.6$ for this sting-mounted boattail on which a flow separation is present. The predicted reduction is almost twice the experimental value, which is no more than 0.005 of C_{DAP} .



a) Pressures

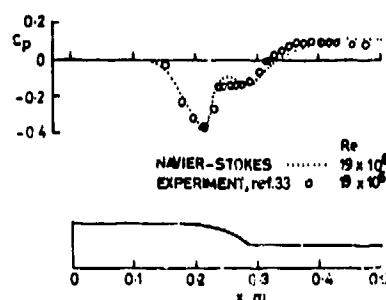


b) Drag variation with Reynolds number.

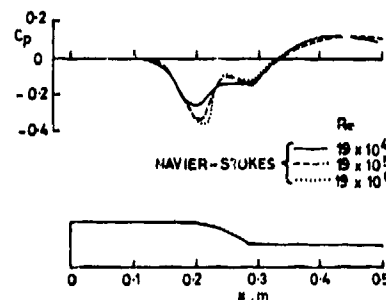
FIGURE 24 COMPARISON OF MEASUREMENTS AND PREDICTION (REF 30)
CIRCULAR ARC - CONICAL BOATTAIL, $M = 0.6$

3.5. Analytical Results - Supersonic

Holst (Ref 32) exploited a numerical technique to produce results over a wide range of Reynolds number at a Mach number of 1.3. A time-dependent, finite difference method was employed to solve the compressible Navier-Stokes equations for turbulent, separating flows on axisymmetric boattails with jet plume simulators and comparisons were made with the experimental data of Reubush (Ref 33). Fig 25 shows the pressure coefficient distributions calculated for a range of Reynolds number for a configuration with a relatively steep boattail on which a flow separation is present. The calculated results show good agreement for high Reynolds number with the experimental data except for slight differences in the pressure plateau region, Fig 25a. An increase in Reynolds number results in a steepening of the pressure rise due to the shock wave and produces two opposing effects on afterbody drag: firstly, the expansion ahead of the separation and secondly, the pressure in the separated region are both increased. The calculated change in the pressure distribution is also much larger for a Reynolds number increase from 19×10^4 to 19×10^5 than for a further increase to 19×10^6 .



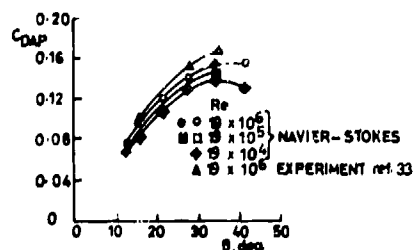
a. Experimental and theoretical pressure distributions.



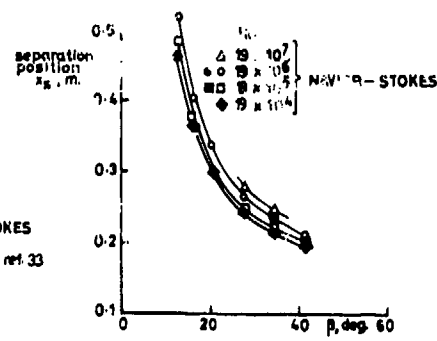
b. Pressure coefficient variation with Reynolds number.

FIGURE 25 REYNOLDS NUMBER EFFECT ON AN AXISYMMETRIC AFTERBODY, $\beta = 34^\circ$,
WITH CYLINDRICAL PLUME SIMULATOR, $M = 1.3$ (REF 32)

OPEN SYMBOLS - COARSE SOLUTION
CLOSED SYMBOLS - REFINED SOLUTION



a. Boattail pressure drag coefficient versus boattail angle.



b. Separation position versus boattail angle.

FIGURE 26 CALCULATED EFFECT OF REYNOLDS NUMBER FROM REF 32, $M = 1.3$

The variation of the calculated boattail pressure drag coefficient C_{DAP} for a range of boattail angles, also from Ref 32, is shown in Fig 26a for Reynolds numbers of 19×10^4 , 19×10^5 and 19×10^6 . The numerical results at Re of 19×10^6 fall below the experimental values by about 6 to 12% even though the trend seems to

be correct; better agreement in drag level was obtained assuming a different value of eddy viscosity relaxation parameter to that employed for the bulk of the calculations. The good agreement of the evaluated variation of drag with boattail angle with the experimental result increases the confidence in the analytically predicted Reynolds number variation. For all the cases considered, the calculations indicate a rearward movement of the separation point accompanied by a small increase in C_{DAP} with increasing Reynolds number; this increase in pressure drag is about 0.015 for all except the extreme cases considered. A small increase in the boattail pressure drag with increasing Reynolds number at low supersonic Mach numbers is in agreement with the experimental data for the AGARD-NAB (Ref 34), eg Fig 10.

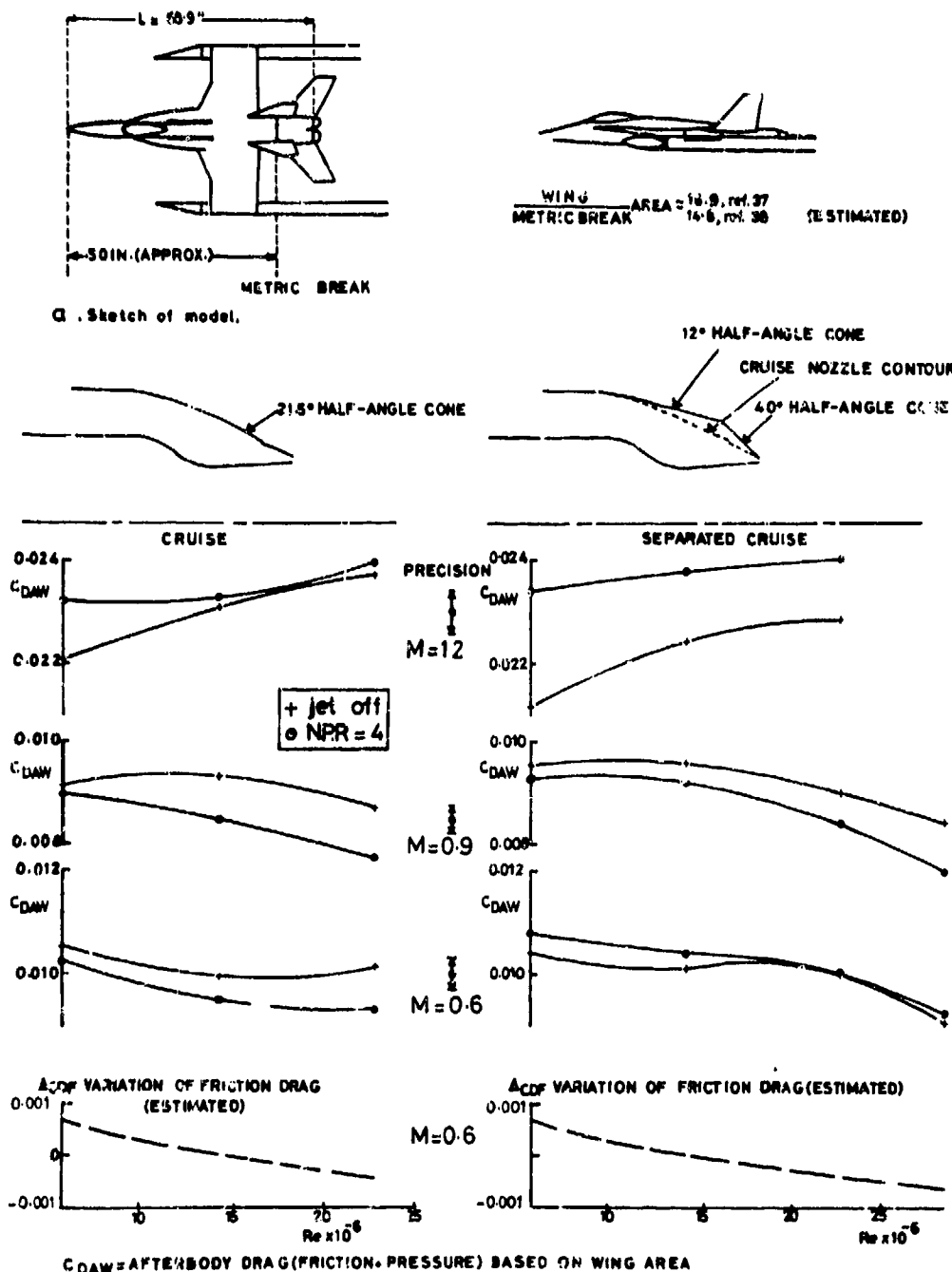
3.6. Fuselage Installations

Data on other than axisymmetric configurations is relatively scarce, and results from some recent additions are presented in this section.

Afterbody pressure drag measurements (Ref 35) on 0.11 scale single-engine aircraft model (F-16) over a range of characteristic Reynolds number of 12×10^6 to 28×10^6 showed a measurable reduction in drag at $M = 0.6$ for the smallest nozzle area setting only, for larger nozzle settings and at Mach numbers of 0.9 and 1.2 neither experimental data nor prediction indicated any significant Reynolds number effects. Further tests on a 0.25 scale model are planned which will permit an overlap of the Reynolds range with full scale.

Data showing the effect of Reynolds number variation on the afterbody drag of a twin-nozzle fighter (YF-17) model have been presented by Price (Refs 37,38) and Fanning and Glidswell (Ref 39). Ref 38 shows

afterbody drag with nozzle pressure ratio variations at $M = 0.6$, 0.9 and 1.2; the afterbody drag from force measurements (friction + pressure), which includes the drag of the tailplane, has been replotted in Fig 27 against Reynolds number. The Reynolds number variation was from 6×10^6 to 35×10^6 . The effect of Reynolds number was explored on two configurations, a cruise nozzle and a 'separated' cruise nozzle. The latter nozzle has a steep terminal contour and was designed as a high drag nozzle specifically to evaluate Reynolds number effects on separated boattail regions. At subsonic speed the drag decreases with increasing Reynolds number; this decrease, however, is similar to the variation of friction drag estimated from the data of Refs 37,38. Any deduced changes in pressure drag with Reynolds number are within about ± 0.0005 and within the precision of the data. Similar results at $M = 0.9$ are indicated by the data in Ref 37 for configurations without tails and in the presence of non-metric tails and for cruise and reheat nozzles, the latter having less steep final boattailing.



C_{DAW} = AFTERBODY DRAG (FRICTION + PRESSURE) BASED ON WING AREA

b. Effect of Reynolds number on afterbody drag.

FIGURE 27 CLOSELY SPACED TWIN JET CONFIGURATION (REFS 37,38)

At $M = 1.2$ the drag increased with increasing Reynolds number indicating the probability of an even larger increase of possibly $\Delta C_{DAP} = 0.03$ in the pressure drag based on body cross-sectional area. (Wing to body area ratio = 16.9). There is also a tendency, although within the precision of the data, for the jet-on drag variations to be less than those jet-off.

The difference in the variation in drag between the cruise and the 'separated' cruise nozzle was also generally within the precision of the data. However, the steepness of the boattailing of the cruise nozzle was such that some separations may have been present even on this configuration. These tests were conducted in the AEDC-16T wind tunnel and although details of the calibration used are not specified, the data are probably subject to the small corrections (Refs 8,9), Fig 10, resulting from not taking the change in tunnel calibration with Reynolds number into account.

Fanning and Glidewell (Ref 39) report the results of later tests with pressure plotted afterbodies on a model which is similar to that shown in Fig 27a. The latest tunnel calibration of the AEDC-16T tunnel which accounts for changes in the working section static pressure with Reynolds number, was used for data reduction. The axial force coefficient based on wing area and obtained from the integration of pressure is shown in Figs 28a,b for a Mach number of 0.9. The data were obtained without boundary layer transition fixing. Fig 28a shows the results grouped together for each of the three nozzle settings employed in the tests and Fig 28b for 4 pressure ratios. The curves show that afterbody axial force component derived from pressure for a given nozzle size and jet pressure tends to increase as Reynolds number increases and that both the effect of nozzle size (or closure ratio) and jet pressure are Reynolds number dependent. The Reynolds number dependence of nozzle closure effects is lowest for under-expanded jets and Reynolds number effects on afterbody drag tend to be greatest jet-off for all three nozzle settings investigated. The authors also note that nozzle closure and jet pressure effects at characteristic Reynolds numbers based on body lengths of 7 to 15 x 10⁶ at which many jet effect tests have been conducted, are not representative of those occurring at higher Reynolds numbers. However, the magnitude of any of the effects over the range of Reynolds numbers investigated was generally less than $\Delta C_D = 0.001$ based on wing area or less than about 0.015 on body cross-sectional area. The pressure distributions in Ref 38 also suggest that at $M = 0.9$ some areas of supersonic flow are likely to be present on this model, and under these conditions some increase in pressure drag with Reynolds number would be expected.

To summarise, the subsonic results for this twin jet installation show little or only small increases in afterbody drag with increasing Reynolds number and they occur mainly in the presence of flow separations and local supersonic regions and possibly are subject to installation interference which may create effective part-body effects.

An interesting comparison of the extent of the flow separations observed full scale with trends indicated during model tests investigating the effects of thinning the boundary layer is available for the convergent-divergent iris nozzle on an F-14 aircraft (Ref 1).

FOR SKETCH OF MODEL SEE FIG. 27a
 A_{10}/A_9 = MAXIMUM CROSS-SECTIONAL AREA
 NOZZLE EXIT AREA

P_{S9}/P = NOZZLE EXIT STATIC PRESSURE
 AMBIENT STATIC PRESSURE

Re = REYNOLDS NUMBER BASED ON FUSELAGE LENGTH

C_{APW} = AFTERBODY AXIAL FORCE COEFFICIENT BY INTEGRATION OF PRESSURES BASED ON WING AREA

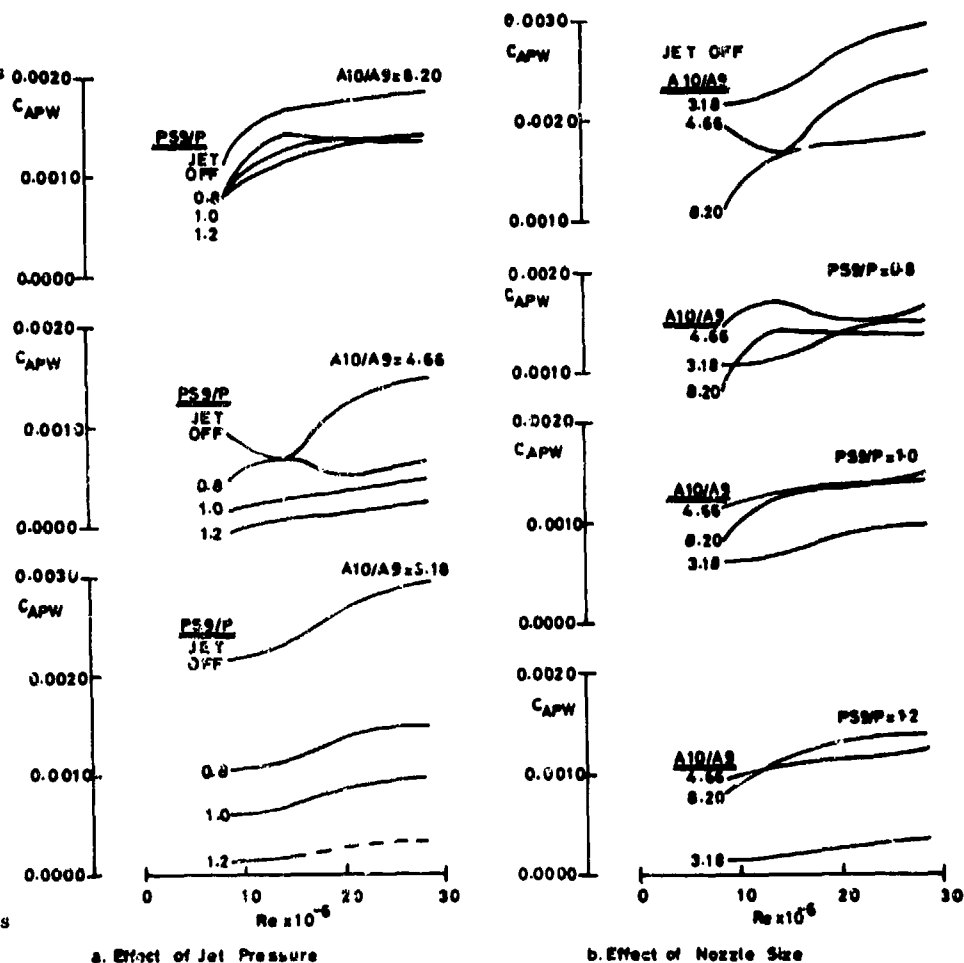
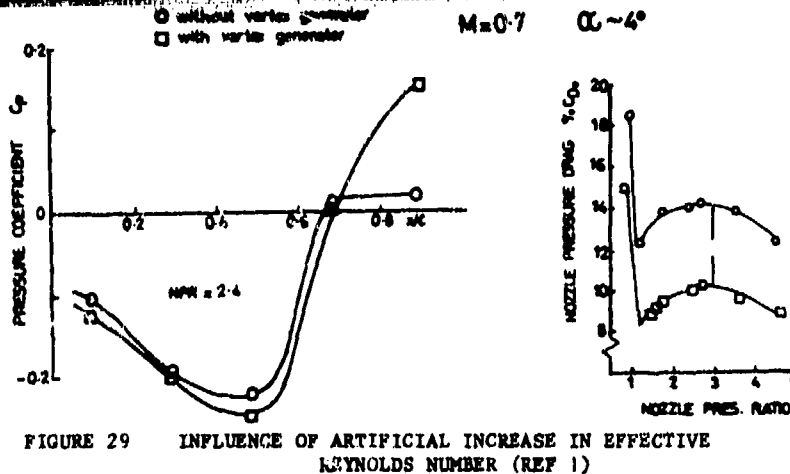


FIGURE 28 EFFECT OF REYNOLDS NUMBER ON AFTERBODY AXIAL FORCE COEFFICIENT FROM PRESSURE INTEGRATION. CLOSELY SPACED TWIN JET CONFIGURATION (REF 39)

To obtain a qualitative indication during model tests of the effect of Reynolds number on the nozzle drag, the boundary layer was energized by means of an array of vortex generators upstream of the 'customer connect' station. The pressure distribution indicated that at a Mach number of 0.7, the separation on the nozzle was largely eliminated with a drag reduction of 4% of aircraft minimum drag, Fig 29. Surface oil flow patterns on a 1/12 scale model at a Reynolds number based on nacelle length of 4×10^6 and in flight at a range of $40-60 \times 10^6$ were also obtained. In spite of the large difference in the Reynolds number range, the flow separation was still present on the full scale aircraft. The flow pattern in flight was essentially similar with the extent of separation possibly slightly aft of the 2/3 cruise nozzle length indicated during the wind tunnel tests.



The effect of thickening the boundary layer artificially on an F-14 type model with similar nozzles has also been reported (Ref 40), Fig 30. The boundary layer was thickened in two stages by means of a fence consisting of 3 and 7 wires respectively, spaced on supports surrounding the model just downstream of the inlets. The forces and pressures on the nozzles alone were measured and in the presence of the thickest boundary layer the nozzle drag coefficient based on wing area was about 0.001 lower at Mach numbers of 0.7 and 0.8 than with the thinner boundary layer without fences. The lower drag with the fences was due to decreased suction on the forward part of the nozzles, whereas the pressures near the trailing edge were little affected. However, flow separations were reported by Schnell (Ref 1) on a similar model and so are likely to have been present in this case as well and are a probable reason for the relatively low pressure recovery at the trailing edge of the nozzles. In the absence of the compensating effect of changes of the pressure recovery on the rear of the body, pressure drag decreased as a result of the lower suction in the presence of the much thickened boundary layer. It is worth noting that energizing and hence effectively, thinning the boundary layer by means of vortex generators (Ref 1) had also resulted in a reduction in drag through quite a different effect: the suppression of flow separations. These F-14 experiments not only show the highly non-axisymmetric nature of the boundary layer on twin jet installations, Fig 30, and therefore that effects may not necessarily be similar to those found on axisymmetric configurations, but also the difficulties in interpreting the results of boundary layer modification tests to arrive at full scale drag levels.

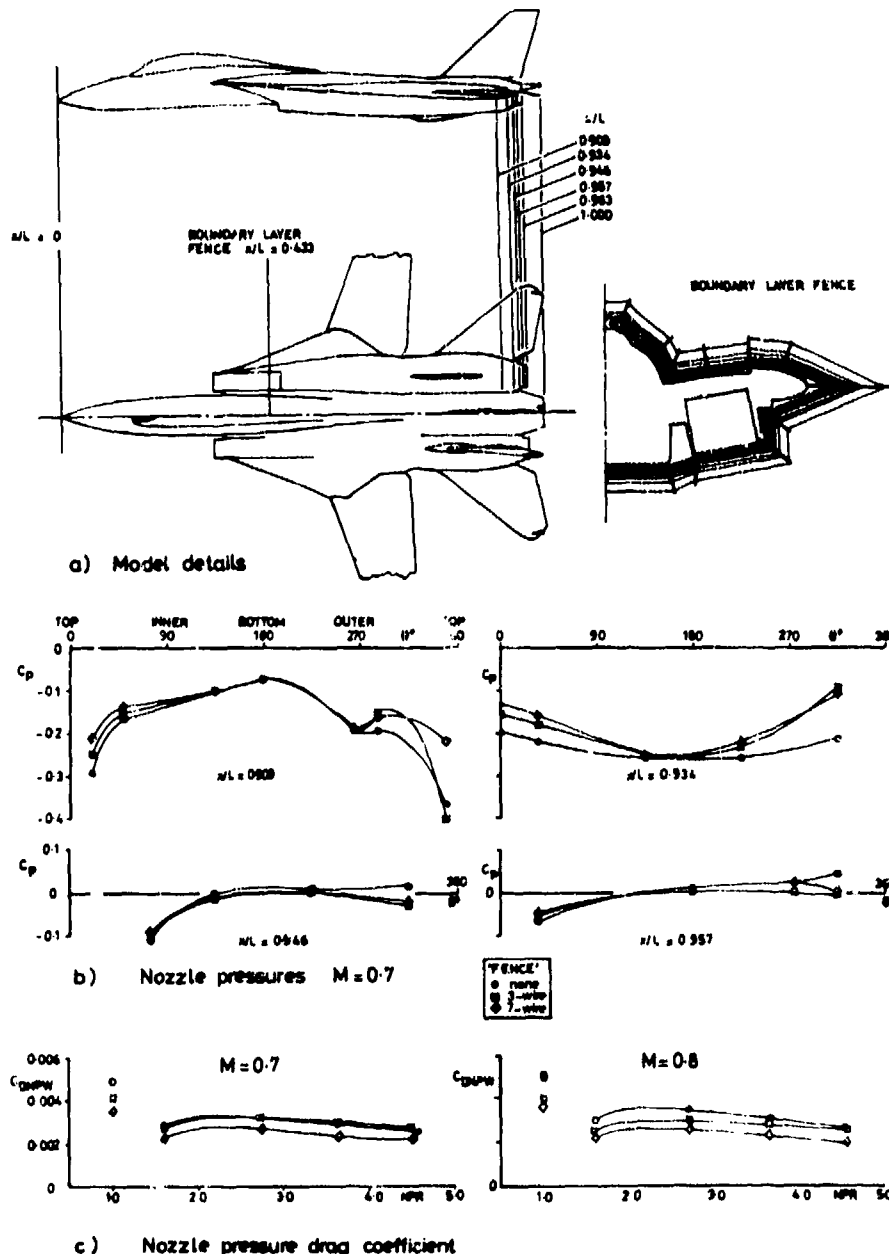


FIGURE 30 EFFECT OF BOUNDARY LAYER MODIFICATION ON NOZZLE PRESSURES AND DRAG (REF 40)

3.7. Nacelle Installation

Nacelle or pod installations in general differ from fuselage installations in several respects:

- the maximum body cross-section in relation to nozzle exit area is smaller
- they are generally shorter with increased likelihood of strong forebody and afterbody interaction
- they may be immersed in the interference flow field from major components of the aircraft such as wing or fuselage.

The data shown in Fig 3 of Ref 34 (not reproduced here) are an example of the increased sensitivity of part-body drag to a change in Reynolds number. In this case the pressure drag of a 15° AGARD axisymmetric nozzle afterbody, excluding that on the rearmost 0.3 diameter, exhibited a noticeable increase with Reynolds number even at moderate subsonic Mach numbers, whereas the pressure drag of the complete body, Fig 5 of Ref 34, which includes changes in the pressure recovery at the rear in full, shows only minor variations in general. Similar part-body effects may be expected on nacelle afterbodies.

Pressure drag trends similar to those observed on complete axisymmetric afterbodies were observed on the aft nacelle of a 0.06 scale model of the B-1 aircraft during variation of Reynolds number in the AEDC-16T wind tunnel (Refs 34,41). A pressure map presented in Ref 41 shows that the suction forward and the pressure recoveries at the rear increased in a substantial but compensating manner. The effect on pressure drag (Ref 34) at $M = 0.8$ was relatively small but larger increases with Reynolds number were observed at higher subsonic Mach numbers and at low supersonic Mach numbers. The variation of aft nacelle drag with Reynolds number at the higher Mach numbers meant that the confidence with which the results could be extrapolated to flight Reynolds numbers was greatly reduced. Some zones of flow separation were identified by flow visualisation during the tunnel tests and it was intended to monitor these during the planned flight tests. The authors note that it is the change in separation regions which may often be a primary contribution to any lack of correlation between tunnel and flight data.

The data presented by Richey et al (Ref 42) for the B-1 aircraft configurations includes one of the few available comparisons of flight and wind tunnel results. Comparisons of the B-1 aircraft aft-nacelle pressure differences and forces derived from pressure measurement at matched conditions from flight and from wind tunnel tests at Mach numbers from 0.75 to 1.2 are presented. At Mach numbers below the nacelle drag divergence Mach number there were small regions where pressure coefficient differences between flight and wind tunnel exceeded 0.05 but in general they were less than 0.01. These differences tended to compensate resulting in drag level differences which, over a wide range of conditions, varied within 6 drag counts or 18% of nacelle drag. At higher Mach numbers, particularly supersonic, a more consistent bias towards higher pressures and hence lower drag on the full scale aircraft became evident. For the example shown in Ref 42, the drag difference was 14 drag counts or 20% of flight nacelle drag. The trend for full scale aircraft pressure drag to be lower is counter to the Reynolds number effects observed during tunnel tests (Ref 34). It suggests that the differences between tunnel and flight results may not be solely due to Reynolds number but may contain other effects such as support interference and intake flow effects, and very possibly part-body effects had also become important in this case.

4. DISCUSSION AND CONCLUSIONS

Some of the widely varying afterbody pressure drag trends with Reynolds number that caused concern some years ago can now be partly resolved.

Some false indications of increasing afterbody drag for increasing Reynolds number at low subsonic Mach numbers were the result of neglecting Reynolds number effects on wind tunnel calibration. Other confusing indications can be obtained by neglecting differences in test techniques, considering incomplete boattails and through not fully appreciating the importance of different Mach number/boattail steepness regimes which emerge as the most significant factors. For this reason, conclusions with regard to the effect of Reynolds number are considered here separately for various Mach number ranges and severity of boattailing.

4.1. Subsonic-Gentle Boattails

At subsonic speeds below the critical Mach number, for gentle boattails on which extensive flow separations are absent, experimental and theoretical results are in agreement in showing that an increase in Reynolds number or the direct reduction of the boundary layer thickness results in significant changes in the pressure distribution; both the suction at the start of the boattail and the recovery at the rear are increased typically by about $|\Delta C_p| = 0.05$. The pressure changes are, however, compensating to a large degree, such that any pressure drag coefficient (C_{Dp}) variation that may occur is generally within the accuracy of the results, i.e. generally within 0.005 based on body cross-sectional area.

Analysis suggests that these pressure changes are the direct result of the change in the effective contour of the boattail due to changes in the displacement thickness of the boundary layer.

The analytic data and most of the experimental data is for isolated boattails, but similar insensitivity of afterbody drag to Reynolds number variation has been reported for some installed smooth boattails.

Although the drag of the complete afterbody may not be sensitive to changes in Reynolds number, the pressure changes are such that significant change in part-body drag can occur. For instance, the drag of a nozzle alone may well show a decrease in pressure drag whereas the rest of the boattail may exhibit a corresponding increase. Fortunately, the practice of considering nozzle drag separately is becoming less prevalent.

Neglecting the effect of Reynolds number on the calibration of some tunnels had resulted in the erroneous indication of an increase in afterbody pressure drag for some experimental results in this regime.

4.2. Subsonic, Steep Boattails with Flow Separation

On boattails of sufficient steepness for flow separation to be present, there are opposing trends at work. On the one hand, the thinner boundary layers, which are present at high Reynolds numbers or are the results of a simulation technique, can negotiate steeper pressure gradients without separating. On the other hand, the effective steepness of the boattail and hence also the pressure gradient, is increased. Which of these trends is dominant probably affects the extent of flow separation. In general, it has been found that afterbody drag at subsonic and transonic speeds changes in proportion to the magnitude of the boattail projected area affected by separation (Ref 43). However, drag changes which may be expected to result from a change in the extent of separation, which affects the final pressure recovery, resulting from a change in the boundary layer thickness, may be compensated by the change in suction on the front of the boattail resulting from the effective change in the contour (Ref 20). These considerations are consistent with the variety of drag trends that have been reported for these conditions, both small increases and decreases as well as no variation have been noted.

On balance, on smooth but steeply contoured boattails with 'free' separations, both experimental data (Refs 15,21) and analytic data (Ref 30) tend to indicate a small reduction in drag for increase in Reynolds number or for thinner boundary layers.

On afterbodies where the separation is triggered by a rapid change or discontinuity in the contour such that the extent of separation does not change with Reynolds number, there is generally also little change in drag. Examples of such results that may be cited are those reported for configurations with annular bases (Refs 19,20); for a separated cruise nozzle in a twin jet (YF-17 type) installation (Ref 38); contoured nozzle installation in the F-106 (Ref 21) and the F-14 (Ref 1) and for conical boattails (Ref 10).

There is also some indication that the boundary layer shape factor may be a significant parameter under these circumstances; for instance, on the 2524 boattail of Ref 10, distortion of the boundary layer changed the level of drag. Such a dependence on the boundary layer profile may well be the reason for the different drag trends obtained from different techniques for the 25° AGARD-NAB by Zonars (Ref 12). Such changes in drag may not necessarily be associated solely with a change in the extent but possibly with the unsteady nature of the separation also.

Direct modification of the boundary layer in tunnel tests to simulate Reynolds number changes can be quite misleading with regard to the drag trends in the presence of separations, particularly if the boundary layer modification is unrepresentative of that occurring naturally; it is possible to induce changes which in all likelihood may not happen between model and full scale situations.

The large drag reductions observed for increases in Reynolds number during flight tests of underwing installations of steep boattails (eg Fig 22), were associated with extensive reductions in the extent of the separations.

Analytic methods, which are currently available for axisymmetric cases only, generally rely on empirical separation criteria which do not as yet account for Reynolds number effects.

4.3. High Subsonic Mach Numbers

Close to or above the drag-rise Mach number of the afterbody, consistent and significant trends are indicated by experimental data and also by theory.

The main effect of increasing Reynolds number or reducing boundary layer thickness is to reduce the drag-rise Mach number. This effect is the result of increased suction at the start of the boattail which occur in the absence of the ameliorating effect due to the presence of the boundary layer on the effective steepness of the boattail contour. Below the drag-rise Mach number, boundary layer thickness has little effect on drag but once the boundary layer thickness is reduced beyond the value at which the drag-rise Mach number is exceeded, further thinning of the boundary layer results in significant increase in afterbody pressure drag due to the increase in wave drag. Thus, the variation of boattail drag with increasing Reynolds number changes from being negligible over the entire Reynolds number range at low Mach numbers, to being negligible at low and significant at high Reynolds number when the Mach number is intermediate, to a continuous increase at higher Mach number. The rate of change of drag tends to be greatest in the presence of thin boundary layers, particularly, of course, at the intermediate Mach numbers, and hence, assessment of drag trends based on a limited Reynolds number range in the wind tunnel does not give an adequate indication of the full scale value under these conditions. The variation of drag is least for gentle contours.

The interaction of the shock with the boundary layer usually results in the eventual separation of the latter which affects the pressure recovery on the rear of the boattail and hence the drag. Again, the appearance and the extent of shock-induced separations is subject to conflicting factors such as shock strength and the ability of the boundary layer to withstand the pressure rise; some experimental results for axisymmetric boattails (Ref 10) show a larger extent of separation with a thin boundary layer. These conflicting factors probably mean that the changes in flow separation are quite minor in some cases. Some analytic data (Ref 13) give reasonable agreement of wave drag change due to boundary layer thickness effects, but the separation criteria are probably less reliable. The drag in this regime is, however, very sensitive to Mach number variation (Ref 6), and as a consequence, neglecting Reynolds number effects on the tunnel calibration may result in significant errors.

4.4. Low Supersonic Mach Numbers

At moderate supersonic Mach numbers viscous effects may affect the location of the shock near the rear of the boattail and this in turn has an effect on drag, but once again the location of any resulting separation is subject to conflicting factors. In general, experimental data show a moderate rise in drag with increases in Reynolds number, for example Ref 37 for axisymmetric boattails and Refs 37 and 38 for closely spaced twins. Analytically computed data (Ref 32) are in agreement in showing that the general

4.5. Effect of Jet

Some results suggest that the variation of afterbody drag with Reynolds number may be less jet-on than jet-off or with solid jet plume simulators, but the evidence is not sufficiently extensive to confirm this as a general trend.

4.6. Concluding Remarks

Other than near the drag-rise and supersonic Mach numbers, real Reynolds number effects were found to be of limited magnitude; the assumption that trends established over a small range of Reynolds number in wind tunnels persist to full scale conditions appears to be generally unjustified. Support interference and the presence of faired inlets or unrealistic transition can make the drag variation observed in the wind tunnel unrepresentative. Boundary layer transition may be affected by wind tunnel turbulence or edge tones from porous walls or fixed in an unrepresentative manner and may lead to uncertainties in the computed skin friction. The impossibility of perfect simulation in wind tunnel tests obscures the comparisons from different facilities and flight, also the accuracy of afterbody drag measurements in the past is insufficient to identify clearly the limits of the Reynolds number effects. Because of uncertainty in the drag breakdown of complete aircraft, afterbody drag comparisons between wind tunnel and flight are probably best obtained from detailed boundary layer and pressure measurements on the afterbody and these are rarely available.

The conclusions drawn in the earlier sections are largely based on axisymmetric data which may have limited applicability for real configurations. On real non-axisymmetric installations, separations are usually present and under these conditions, Reynolds number effects appear to be variable and are difficult to predict to the high accuracy desired for defining performance. An instance where such specific information would be of particular importance is when the effect on performance of nozzle length, with its strong impact on nozzle weight, is being balanced against boattail angle and its effect on drag.

REFERENCES

1. Schnell, W C, F-14A installed nozzle performance. 1974. AIAA paper 74-1099.
2. Wilcox, F A, Chamberlin, R, Reynolds number effects on boattail drag of exhaust nozzles from wind tunnel and flight tests. 1974, NASA TM X-71548. 1975, AGARD CP 150, Paper 21.
3. Pozniak, O M, A review of the effect of Reynolds number on afterbody drag. 1980. ARA Report 56.
4. Aulehla, F, Besigk, G, Fore- and afterbody flow field interaction with consideration of Reynolds number effects. 1974. AGARD CP 150, Paper 12.
5. Aulehla, F, Besigk, G, Fore- and afterbody flow field interaction with consideration of Reynolds number effects. 1975. AGARD-AG-208, Paper II-F.
6. Aulehla, F, Drag measurements in transonic wind tunnels. 1976, MBB UFE 13150. 1977, AGARD Specialists Meeting on Aircraft Performance Prediction Methods, Paris, Paper 7.
7. Galigher, L L, Jackson, F M, Robinson, C E, Description of the AGARD Nozzle Afterbody experiments conducted by the Arnold Engineering Development Center. 1975. AGARD-AG-208, Paper I-G.
8. Jackson, F M, Calibration of the AEDC-PWT 16-foot tunnel with the propulsion test section at various Reynolds numbers. Final report, October 1974 - June 1975. 1978. AEDC-TR-77-121.
9. Spratley, A B, Thompson, E R, Kennedy, T L, Reynolds number and nozzle afterbody configuration effects on model forebody and afterbody drag. 1977. AIAA 77-103.
10. Blaha, B J, Chamberlin, R, Bober, L J, Boundary layer thickness effect on boattail drag. 1976, AIAA 76-676 (oral presentation), NASA TM-X-73443.
11. Ferri, A (ed), Improved nozzle testing techniques in transonic flow. 1975. AGARD-AG-208.
12. Zonars, D, Laughrey, J A, Bowers, D L, Effect of varying Reynolds number and boundary layer displacement thickness on the external flow over nozzle boattails. 1975. AGARD-AG-208, Paper I-F.
13. Chow, W L, Bober, L J, Anderson, B H, Numerical calculation of transonic boattail flow. 1975. NASA TN D-7984.
14. Jaarsma, F, Technical evaluation report on the PEP Working Group No 4 on improved nozzle testing techniques in transonic flow. 1976. AGARD-AR-94.
15. Reubush, D E, Putnam, L E, An experimental and analytical investigation of the effect on isolated boattail drag of varying Reynolds numbers up to 130×10^6 . 1976. NASA TN D-8210.
Also earlier presentation of limited data:
Reubush, D E, The effect of Reynolds number on boattail drag. 1975. AIAA 75-63.
16. Reubush, D E, Effect of Reynolds number on the subsonic boattail drag of several wing-body configurations. 1976. NASA TN D-8238.
Limited data also presented in:
Reubush, D E, The effect of Reynolds number on the boattail drag of two wing-body configurations. 1975. AIAA 75-1294.
17. Reubush, D E, Experimental investigation to validate the use of cryogenic temperatures to achieve high Reynolds numbers on boattail pressure testing. 1976. NASA TM X-3396.
18. Ray, E J et al., Review of design and operational characteristics of the 0.3m transonic cryogenic tunnel. 1979. 1st Symposium on Cryogenic Wind Tunnels, University of Southampton, Paper 28.

19. Crane, J F W, The effect of base cavities on the drag of an axisymmetric afterbody with a sonic nozzle, between $M_\infty = 0.8$ and 1.3 . 1977. RAE TR 77144.
20. Reid, J, Kurn, A G, The effect of boundary layer thickness on afterbody drag. 1979. RAE TR 79083.
21. Chamberlin, R, Flight Reynolds number effects on a contoured boattail nozzle at subsonic speeds. 1974. NASA TM X-3053.
22. Wilcox, F A, Comparison of ground and flight test results using a modified F-106B aircraft. 1973. AIAA 73-1305.
23. Chamberlin, R, Blaha, B J, Flight and wind tunnel investigation of the effect of Reynolds number on installed boattail drag at subsonic speeds. 1973. AIAA 73-139, NASA TM X-68162.
24. Chamberlin, R, Flight investigation of 24° boattail nozzle drag at varying subsonic flight conditions. 1972. NASA TM X-2626.
25. Wilcox, F A, Samanich, N E, Blaha, B J, Flight and wind-tunnel investigation of installation effects on supersonic cruise exhaust nozzles at transonic speeds. 1969. AIAA 69-427.
26. Chamberlin, R, Flight Reynolds number effects on a fighter-type, circular arc 19° conic boattail nozzle at subsonic speeds. 1974. NASA TM X-3121.
27. Beheim, M A, Anderson, B H, Clark, J S, Corson, B W, Stitt, L E, Wilcox, F A, Supersonic exhaust nozzles. 1970. NASA SP-259, pp 233-282.
28. Postlewaite, J E, Saleman, U, Exhaust system interaction programme - final technical report. 1973. AFAPL-TR-73-59, AD-769086.
29. Cosner, R R, Bower, W W, A patched solution of the transonic flowfield about an axisymmetric boattail, 1977, AIAA 77-227.
30. Presz, W M, King, R W, Buteau, J D, Putnam, L E, An improved analytical model of the separated region on nozzle boattails. 1978. AIAA 78-995.
31. Presz, W M, Pitkin, E T, Flow separation over axisymmetric afterbody models. 1974. J Aircraft, Vol 11, pp 677-682.
32. Holst, T L, Numerical solution of axisymmetric boattail flowfields with plume simulators. 1977. AIAA 77-224.
33. Reubush, D E, Experimental study of the effectiveness of cylindrical plume simulators for predicting jet-on boattail drag at Mach numbers up to 1.30 . 1974. NASA TN D-7795.
34. Robinson, C E, Price, E A, Effect of Reynolds number on the nozzle afterbody performance of the AGARD nozzle afterbody and the B-1 0.06 -scale model at transonic Mach numbers. 1975. AIAA 75-1321.
35. Glidewell, R J, Stevens, H L, Presz, W M, Effects of Reynolds number and other parameters on the throttle-dependent nozzle afterbody drag of a 0.11 scale single-engine aircraft model. 1979. AIAA 79-1167.
36. Besigk, G, Halbempirische Theorie zur Bestimmung des Heckwiderstandes. 1971. MBB-Report UFE 628/1-70.
37. Price, E A, Afterbody drag investigation of a twin-nozzle fighter-type model at Mach numbers from 0.6 to 1.5 . 1972. AEDC-TR-72-87.
38. Price, E A, Afterbody aerodynamic characteristics and support system interference on a twin-jet fighter-type aircraft model at Mach numbers from 0.6 to 1.5 . 1974. AEDC-TR-74-13.
39. Fanning, A E, Glidewell, R J, Reynolds number effect on afterbody, throttle-dependent pressure forces. 1973. AIAA 75-1295.
40. Reubush, D E, Mercer, C E, Exhaust-nozzle characteristics for a twin-jet variable-wing-sweep fighter airplane model at Mach numbers to 2.2 . 1974. NASA TM X-2947.
41. Richey, G K, Petersen, M W, Price, E A, Wind tunnel/flight test correlation program on the B-1 nacelle afterbody/nozzle. 1976. AIAA 76-673.
42. Richey, G K, Bowers, D L, Kostin, L C, Price, E A, Wind tunnel/flight test correlation program on the B-1 nacelle afterbody/nozzle at transonic conditions. 1978. AIAA 78-989.
43. Ozniak, G M, Paines, A B, Afterbody drag measurements at transonic speeds on a series of twin- and single-jet afterbodies terminating at the jet exit. 1973. ARC CP 1266.
44. Besigk, G, Influence of Reynolds number on drag evaluation. 1974. MBB-Report UFE 1078.
45. Antonatos, P F, Surber, L E, Laughrey, J A, Stava, D J, Assessment of the influence of inlet and aftbody/nozzle performance on total aircraft drag. 1973. AGARD CP 124, Paper 15.
46. Richey, G K, Preliminary data of the AGARD Ad Hoc Study 'Improved Nozzle Testing Techniques in Transonic Flow'. 1974. AFFDL

DISPOSITIF DE SIMULATION AU BANC COMPRESSEUR
D'UNE PRISE D'AIR A GRANDE INCIDENCE

par

Bertrand DELAHAYE

Société Nationale d'Etudes et de Construction de Moteurs d'Aviation (SNECMA)
77550 MOISSY CRAMAYEL - FRANCE

Gérard LARUELLE

Office National d'Etudes et de Recherches Aéropatiales (ONERA)
92320 CHATILLON - FRANCE

R E S U M E

L'un des objectifs primordiaux des chasseurs modernes est la manœuvrabilité ; celle-ci nécessite une étude approfondie de la compatibilité avion-moteur. Le motoriste doit donc, lors même de la mise au point du compresseur, évaluer pour l'ensemble du domaine de vol la perte de charge au pompage entraînée par la distorsion de manche.

Un dispositif, constitué d'un pavillon dissymétrique ou même simplement d'un tube biseauté, destiné à reproduire au banc compresseur les grosses structures tourbillonnaires rencontrées en vol à grande incidence, a été testé en soufflerie à l'ONERA puis expérimenté au banc compresseur du centre d'essais de la SNECMA à Villaroche.

Les essais en soufflerie (échelle 1/4) ont permis une comparaison des écoulements au niveau de l'entrée du compresseur dans une prise d'air cylindrique en incidence ($0 \leq \alpha \leq 40^\circ$) à $M = 0,6$ avec ceux obtenus au point fixe dans les diverses versions du dispositif envisagé.

A la suite de ces essais, la SNECMA a également effectué au banc compresseur une caractérisation de l'écoulement délivré par la manche taillée en biseau à 30° alimentant un fan (échelle 1) monoétage transsonique.

Les valeurs obtenues au banc sont confrontées aux résultats maquette en vue de valider le dispositif, en tenant compte des corrections d'échelle pour la bande passante et le temps d'acquisition.

S U M M A R Y

Increased manoeuvrability requirements for modern fighter aircraft involve an extensive inlet-engine compatibility analysis.

Therefore, during the early stages of compressor development, the engine designer must estimate the surge margin loss resulting from inlet dynamic distortion over the complete flight envelope.

A bell-mouth with varying lip thickness and a level-edged duct have been designed to simulate the large vortices generated in an inlet at high angle of attack in a compressor test facility ; the simulator has been tested in a wind tunnel at ONERA and validated in a compressor test facility at SNECMA's Villaroche test center.

The flow at the inlet/engine interface plane has been characterized in the wind tunnel both for a 1/4 scale cylindrical duct at a Mach number of 0.6 and angles of attack up to 40 degrees and for different versions of the simulator in static conditions.

Thereafter, a 30 degree level edged duct has been tested at SNECMA with a full scale transonic fan stage. Scaling rules for acquisition time and frequency are used to compare the measurement in front of the fan with the results obtained in the subscale wind tunnel model.

Etude effectuée avec le soutien financier de la DRET pour la partie essais en soufflerie.

Pour accroître leur manoeuvrabilité, les avions militaires des nouvelles générations devront évoluer à des incidences de plus en plus élevées. Ces avions sont conçus avec des prises d'air optimisées pour les vols supersoniques dont les bords d'attaque sont minces. A grande incidence, un décollement important est créé à l'intérieur de la manche, au niveau du bord d'attaque d'intrados, et des tourbillons sont ainsi créés dès l'entrée (fig. 1a). Tout au long du diffuseur une certaine homogénéisation s'effectue, mais celle-ci ne peut être parfaite au niveau du plan d'entrée compresseur situé à quelques diamètres seulement de l'entrée d'air. Il en résulte des conditions d'alimentation qui peuvent perturber le fonctionnement du moteur. Un travail de qualification, dans le plan d'entrée compresseur, de l'écoulement délivré par de telles prises d'air en incidence est donc nécessaire. Il peut être réalisé en soufflerie dans un premier temps, puis poursuivi en vol.

Par ailleurs, l'aérodynamicien doit fournir un moyen, si possible peu coûteux, de simulation de cet écoulement pour la mise au point des moteurs, lors des essais au banc. En effet, les moyens de simulation au point fixe des distorsions dans le plan compresseur, actuellement utilisés dans les bancs des motoristes, ne permettent pas de représenter les effets instationnaires de façon satisfaisante ; ils sont généralement constitués d'un grillage à perméabilité variable qui ne crée qu'une distorsion moyenne, la taille des mailles limite les effets instationnaires à une turbulence assez homogène et de faible intensité. Les autres dispositifs utilisés, bien qu'ils reproduisent plus fidèlement l'alimentation du moteur pour des conditions réelles d'un vol à grande incidence, nécessitent des installations complexes et fort onéreuses.

Un moyen de simulation simple est proposé ; il consiste en une prise d'air non axisymétrique : tube biseauté, ainsi que l'a proposé M. Lazareff, ou ayant un rayon de bord d'attaque évolutif, dénommés respectivement "biseau" ou "bourrelet" par la suite (fig. 1b). Avec de tels dispositifs pour des fonctionnements au point fixe, un décollement plus ou moins important apparaît dans la manche comme c'est le cas pour les prises d'air placées en incidence.

Les premiers résultats obtenus à l'ONERA et à la SNECMA avec ces moyens de simulation font l'objet du présent document. En particulier les cartographies de l'écoulement au niveau du plan d'entrée compresseur obtenues en soufflerie dans une prise d'air schématisée en incidence seront comparées avec celles obtenues dans diverses prises d'air non axisymétriques en fonctionnement au point fixe. Pour terminer, une étude de l'écoulement en divers plans d'un compresseur transsonique monoétage de recherche alimenté par un "biseau" confirme la faisabilité de la simulation recherchée, y compris en ce qui concerne l'instationnaire.

2 - VISUALISATIONS AU TUNNEL HYDRODYNAMIQUE -

La qualification en soufflerie de l'écoulement dans le plan entrée compresseur, pour les prises d'air en incidence, a été réalisée avec une entrée d'air schématisée constituée d'un tube cylindrique de 4 ou 8 diamètres de longueur, dont le bord d'attaque est aiguisé.

Pour effectuer des essais au tunnel hydrodynamique, une prise d'air, d'un diamètre de longueur seulement, a été utilisée compte tenu des dimensions de l'installation. La figure 2 présente cette prise d'air placée à 40° d'incidence. La visualisation [1] par bulles d'air éclairées dans le plan médian est effectuée pour un coefficient de débit (A_{00}/A_1) de 1. Cette photographie met en évidence le point d'arrêt placé à l'intrados de la prise d'air qui induit un contournement du bord d'attaque aigu d'où un décollement important à l'intérieur de la manche ; un second décollement est également mis en évidence à l'extrados de la manche.

L'écoulement interne présenté sur cette photographie peut être comparé à celui obtenu avec une prise d'air biseautée fonctionnant au point fixe. La seconde vue présentée sur la figure 2 montre une telle prise d'air alimentée avec un coefficient de débit très important $A_{00}/A_1 = 15$, car le point fixe $A_{00}/A_1 = \infty$ ne peut être réalisé dans l'espace confiné du tunnel hydrodynamique.

Deux décollements apparaissent dans cette configuration :

- un petit à l'extrémité amont du biseau qui se résorbe rapidement,
- un de grande taille, à l'intérieur de la manche, comparable à celui de la prise d'air en incidence.

3 - ESSAIS EN SOUFFLERIE -

3.1 - Moyens d'essais -

Tous les essais, y compris ceux au point fixe, ont été effectués dans la grande soufflerie transsonique du centre de Modane-Avrieux de l'ONERA [2]. Les conditions génératrices correspondent aux conditions ambiantes ($P_0 \approx 0,9$ bar, $T_0 \approx 290$ K).

La prise d'air cylindrique, à l'échelle 1/4 environ d'une manche d'avion militaire, a été essayée essentiellement pour un nombre de Mach amont de 0,6 et pour diverses incidences comprises entre 0 et 40°.

Le montage d'essais est schématisé sur la figure 3. Il comprend d'amont en aval :

- la prise d'air dont les variantes seront précisées ultérieurement,
- une allonge cylindrique permettant des mesures à 4 ou 8 diamètres du plan d'entrée,
- un peigne rotatif au niveau du plan compresseur,
- un obturateur réglable à distance,
- des joints souples permettant la rotation de la partie amont grâce à une tourelle intégrée au plancher de la veine,
- une trompe à air comprimé assurant l'extraction du débit.

L'axe de la maquette est fixé à 1,4 m du plancher ; la mise en incidence de la prise d'air, obtenue grâce à la tourelle, est en fait une mise en dérapage dans la soufflerie. La figure 4 montre l'installation en veine.

Les différentes formes d'entrée d'air essayées sont regroupées sur la figure 5. Pour les essais en incidence la prise d'air "droite" a été utilisée : c'est un cylindre de 184 mm de diamètre, légèrement biseauté au bord d'attaque de 4 ou 8 diamètres selon l'allonge installée.

Trois tubas biseautés ont été essayés au point fixe : les inclinaisons du plan d'entrée étant respectivement de 30, 45 et 60°. Comme pour la prise d'air droite, le bord d'attaque est mince. La position du plan de mesure (4 ou 8D) est repérée par rapport au milieu du biseau.

La dernière configuration essayée au point fixe, appelée "Bourrelet" est constituée par un pavillon dont le rayon de bord d'attaque évolue régulièrement de $D/4$ à 0 suivant la position angulaire autour de l'axe de la manche.

La qualification de l'écoulement dans le plan entrée compresseur est obtenue grâce à un peigne tournant équipé de 36 prises de pression d'arrêt réparties en équisurface. Ces pressions sont mesurées avec des capteurs "Kulite" intégrés en extrémité de chaque prise. Ce peigne et le système d'acquisition associé sont décrits dans la référence [3].

La majorité de l'exploitation présentée ci-dessous résulte d'acquisitions numériques effectuées à 1 550 Hz pendant environ 1 seconde pour les diverses configurations.

3.2 - Comparaison : prise d'air en incidence - point fixe -

Les résultats obtenus en soufflerie dans la prise d'air en incidence et pour les deux types de simulation vont être présentés en parallèle.

3.2.1 - Efficacité moyenne -

Les prises du peigne étant réparties en "équisurface", l'efficacité est obtenue par une moyenne arithmétique dans l'espace des rapports de pressions d'arrêt locales à la pression génératrice. La figure 6 présente l'évolution de cette efficacité moyennée dans le temps (sur 1 seconde), en fonction de l'incidence pour la prise d'air droite, avec un nombre de Mach amont Mo de 0,6 et un nombre de Mach interne, au niveau du plan de sondage M_2 voisin de 0,6 également. A incidence nulle, l'efficacité est proche de 1, la prise d'air ne perturbe quasiment pas l'écoulement, seules les couches limites internes accroissent l'entropie. Lors de la mise en incidence, le décollement interne apparaît et fait chuter l'efficacité moyenne. Pour le plan

$X/D = 8$, la perte d'efficacité est légèrement plus forte qu'à $X/D = 4$, compte tenu du frottement qui s'exerce sur les parois ; toutefois, l'essentiel de la perte est dû au décollement situé à l'entrée de la manche.

Sur cette même figure, sont présentées les efficacités obtenues avec la prise d'air biseautée à 30° et le bourrelet pour des fonctionnements point fixe ; le nombre de Mach interne M_2 est également voisin de 0,6. Comme précédemment, on retrouve la perte due au frottement entre les plans $X = 4D$ et $8D$.

L'essentiel est de constater que l'efficacité ainsi obtenue avec le bourrelet est égale à celle mesurée dans la prise d'air droite à environ 22° à $Mo = 0,6$. Pour le biseau de 30°, on trouve une incidence équivalente de 35°.

3.2.2 - Cartes stationnaires de pression d'arrêt -

La figure 7 regroupe des cartographies d'isobares moyennes dans le temps, obtenues dans le plan de mesure situé à 4 diamètres de l'entrée. Sur la partie gauche, on peut voir l'évolution de la carte de pression d'arrêt en fonction de l'incidence pour la prise d'air droite. Lors de la mise en incidence, le décollement se forme dans la partie inférieure de la manche et provoque des pertes de pression d'arrêt en aval. On constate qu'à 20° la partie supérieure n'est que partiellement affectée ; ce qui n'est plus le cas lorsque l'incidence atteint 40°.

Sur la partie droite de la figure, les cartographies obtenues au point fixe avec le biseau et le bourrelet sont présentées. On peut vérifier que le réseau d'isobares stationnaires relevé dans la prise d'air en bourrelet est proche de celui établi avec la prise d'air droite à 20° d'incidence à Mach = 0,6. Pour le biseau coupé à 30°, on retrouve des niveaux intermédiaires à ceux obtenus dans la prise d'air droite placée à 30° et à 40°, de plus la forme générale est conservée.

Les mêmes remarques peuvent être exprimées à partir de la figure 8 qui est relative au plan $X/D = 8$.

La comparaison des figures 7 et 8 montre l'influence de la longueur de la manche sur les cartes de pression d'arrêt moyenne ; une homogénéisation importante se développe dans ce tronçon de la manche placé en aval du recollement. Pour obtenir une bonne simulation, il sera nécessaire de conserver la longueur globale de la manche.

Il faut noter que les cartes stationnaires de pression d'arrêt sont, à la précision des mesures près, généralement symétriques, ce qui n'est pas le cas des cartes instantanées qui de plus évoluent de façon aléatoire en fonction du temps à configuration donnée. Ainsi la comparaison directe entre les moyens de simulation au point fixe et une prise d'air en incidence ne peut se faire, du point de vue des cartes de pression d'arrêt, que sur les valeurs moyennes dans le temps.

3.2.3 - Coefficients de distorsion -

Chaque motoriste utilise ses propres coefficients de distorsion ; la présente étude a tenu compte des principaux coefficients . La référence [4], par exemple, rappelle leur définition.

L'exploitation suivante résulte d'acquisitions numériques à 1 650 Hz des pressions d'arrêt instantanées dans le plan compresseur, pendant 1 seconde. Ainsi, à chaque instant il est possible de calculer divers coefficients de distorsion puis d'en extraire la valeur moyenne, les valeurs maximale et minimale et même l'écart type sur la période d'enregistrement.

La figure 9 montre l'évolution de ces valeurs caractéristiques d'un certain coefficient de distorsion (IDC moyen) en fonction de l'incidence de la prise d'air à Mach 0,6.

Pour les faibles incidences ($\alpha < 10^\circ$) la distorsion est très limitée, mais au-delà, elle évolue très rapidement ; la valeur moyenne est multipliée par 10 environ lorsque l'incidence passe de 0 à 40° . Il en est de même de la valeur maximale, alors que les minima évoluent très lentement.

Comme pour l'efficacité moyenne (fig. 6), les niveaux de distorsions obtenus au point fixe ont été placés sur ces courbes. On constate que pour le bourrelet, les points se positionnent dans une fenêtre comprise entre 20° et 25° et pour le biseau de 30° dans la plage $30,40^\circ$.

Il est certain que la simulation d'une incidence précise est délicate, mais elle résulte en grande partie de l'imprécision du calcul des coefficients de distorsion instantanée avec un nombre limité de prises (36) ; la référence [5] indique des erreurs possibles de plus de 20 %.

Si l'on considère d'autres coefficients de distorsion (H , KD_2 , $K\theta$, $DC60$, IDC ...) les fenêtres ainsi obtenues évoluent légèrement ; on peut toutefois, en effectuant une moyenne des incidences, milieu de ces fenêtres, pour les divers coefficients considérés, assez bien préciser les incidences d'une entrée d'air droite qui sont simulées par les deux dispositifs d'essais au point fixe considérés.

X/D	4	8
- le biseau 30°	34°	37°
- le bourrelet	21°	24°

Ces valeurs sont à rapprocher de 35° et 22° obtenues en comparant les efficacités globales.

3.2.4 - Fluctuations de pression -

La figure 10 donne les valeurs des fluctuations de pression (écart type exprimé en % de la pression génératrice P_1) en fonction de la position angulaire dans la prise d'air. Ces résultats ont été obtenus à partir d'enregistrements analogiques à grande bande passante, des pressions mesurées au niveau des capteurs placés sur la 3ème couronne ($r/R = 0,62$) du peigne.

Pour la prise d'air droite, à incidence nulle, les fluctuations de pression dans la bande 25 Hz, 10 kHz sont très faibles ($\sim 0,2$ % de la pression génératrice), elles correspondent au niveau de bruit moyen de la soufflerie.

Lorsque l'incidence croît, une évolution rapide apparaît. A faible incidence ($10-20^\circ$), les fluctuations s'intensifient surtout côté intrados de la manche (en aval du décollement). Pour les incidences plus fortes, le niveau global s'élève et de plus les maxima se déplacent alors de l'autre côté de la manche.

Dans le réseau de courbes de la figure 10 correspondant à diverses incidences de la prise d'air droite à $Mo = 0,6$, il est possible de placer les courbes obtenues au point fixe avec la prise d'air biseautée à 30° et avec le bourrelet. Comme précédemment, on constate que le biseau 30° simule une incidence voisine de 35° et le bourrelet une incidence légèrement supérieure à 20° .

Ce résultat est intéressant car il prouve que la simulation est valable également du point de vue instationnaire ; les fluctuations dans le plan compresseur sont bien situées et avec des niveaux corrects.

3.2.5 - Influence du nombre de Mach interne -

Tout ce qui précède a été obtenu avec un nombre de Mach dans le plan entrée compresseur constant et voisin de 0,6. Si l'on modifie le débit l'écoulement interne est modifié. En particulier si on l'augmente, l'efficacité interne va chuter et la distorsion va croître compte tenu du fait que le contournement de bord d'attaque s'effectue à plus grande vitesse. Il faut comparer cet effet sur la prise d'air en incidence et sur les moyens de simulation au point fixe.

La figure 11 présente en fonction du nombre de Mach interne M_2 , les évolutions d'un coefficient de distorsion (KD_2) en valeurs moyenne, maximale et minimale, pour la prise d'air biseautée à 30° et pour la prise d'air droite à $Mo = 0,6$ pour des incidences de 30° et 40° .

Si l'on considère les valeurs moyennes, on constate que le biseau ($\varphi = 30^\circ$) simule toujours la prise d'air droite vers 35° si le nombre de Mach interne est conservé. Cette conclusion peut également s'appliquer pour les valeurs minimales, mais plus difficilement pour les valeurs maximales.

3.2.6 - Influence de la découpe des biseaux -

Après avoir montré qu'un biseau utilisé au point fixe pouvait servir pour simuler le fonctionnement d'une prise d'air schématisée cylindrique en incidence, il faut connaître l'influence de la découpe de biseau sur l'écoulement interne qui s'établit afin de pouvoir simuler, dans une étape ultérieure, n'importe quelle prise d'air d'avion.

Des visualisations au tunnel hydrodynamique montrent que l'importance du décollement interne est peu affectée par la découpe du biseau dans la plage étudiée ($\varphi = 30$ à 60°).

Les essais en soufflerie confirment cette information qualitative ; la planche 12 présente les évolutions d'un coefficient de distorsion (IDC moyen par exemple) en fonction du nombre de Mach interne : on peut constater la très faible influence de la découpe du biseau. Il faut noter en particulier que les écarts entre les courbes présentées sont peu significatifs compte tenu de l'imprécision des mesures effectuées sur un temps limité.

En considérant l'efficacité moyenne qui est calculée de façon beaucoup plus précise, on constate que l'angle du biseau a une légère influence à nombre de Mach M_2 donné : plus la découpe est inclinée par rapport à l'axe du tube (φ décroissant) plus l'efficacité moyenne chute ; toutefois cette influence est limitée.

En effet, pour un nombre de Mach interne voisin de 0,6 qui a été considéré pour la majorité des essais et en particulier avec la prise d'air droite en incidence à $Mo = 0,6$ une modification de 30 à 60° de la découpe du biseau conduit à une plage d'incidences simulées très réduite (32 à 35° environ).

Au contraire, le fait de remplacer un biseau par un bourrelet modifie considérablement l'incidence simulée ; si l'angle du biseau n'a que peu d'influence, le rayon de bord d'attaque lui par contre est déterminant.

Pour trouver des formes de prise d'air non axisymétrique, fonctionnant au point fixe et permettant de simuler une prise d'air quelconque d'un avion placé à grande incidence, il faudra donc jouer non seulement sur la forme de la découpe mais aussi et surtout sur la valeur des rayons de bord d'attaque.

4 - ESSAI DU BISEAU ($\varphi = 30^\circ$) AU BANC COMPRESSEUR -

4.1 - Moyens d'essais -

Les essais ont été effectués au banc compresseur de la SNECMA à Villaroche. Le montage se compose d'un compresseur monoétage transsonique de recherche dont le pavillon d'admission habituel est remplacé par une manche du type biseau taillé à 30° . L'ensemble de 800 mm de diamètre est placé dans la chambre de tranquillisation (fig. 13). La distance manche d'admission - compresseur est également de 4 diamètres.

L'instrumentation de la machine comprend :

- 8 peignes de type sabre placés à l'amont du compresseur, chaque peigne étant équipé de 5 prises de pression d'arrêt ; la valeur stationnaire est relevée en extrémité du tube d'amortissement grâce à un capteur commuté par scanivalve, la composante dynamique est mesurée par des capteurs de type Kulite placés en extrémité des prises pitot, la membrane sensible affleurant la paroi interne du tube. De plus, une sonde de température équipe chaque peigne.
- 8 peignes de 8 prises combinées "pression d'arrêt - température" en sortie du compresseur.
- 4 sondes directionnelles stationnaires utilisées pour les sondages en pression d'arrêt et en direction (inclinaison par rapport à des plans radiaux) dans les plans notés 1, 3 et 4 sur la figure 13.
- Des prises de pression statique pariétales dans les divers plans de mesure.

Le conditionnement et l'acquisition des mesures dynamiques ont été réalisés grâce à une chaîne numérique capable d'enregistrer en continu sur un disque de calculateur, 32 voies échantillonnées à 2 kHz pendant 25 secondes. Les signaux étant filtrés dans la bande 0,2 Hz - 630 Hz, l'échantillonnage est réalisé de manière simultanée sur toutes les voies grâce à des échantillonneurs-bloqueurs. Après un transfert du disque sur une bande 1 600 BPI, les informations recueillies sont traitées en temps différé sur ordinateur.

De plus, pendant les essais, des jauges collées sur les aubes et les peignes sabre ont permis la surveillance des niveaux de contrainte rencontrés. Un capteur d'accélération était également placé à l'extrémité de la manche afin d'en surveiller les déplacements.

La caractérisation de l'écoulement a été effectuée jusqu'à 90 % du régime nominal pour plusieurs points du champ compresseur ; l'isovitesse nominale n'a pu être explorée à cause des sollicitations aérodynamiques jugées dangereuses pour l'ensemble manche-compresseur. L'essai réalisé comprend une étude de la dynamique de l'écoulement dans le plan entrée compresseur (2) en considérant notamment les coefficients de distorsion usuels, la qualification du plan (1) situé dans la manche en pression d'arrêt et direction et enfin des mesures dans le compresseur proprement dit (plans 3 et 4).

4.2 - Ecoulement au niveau du plan entrée-compresseur -

Bien que les conditions d'alimentation de la manche en biseau du banc compresseur ne soient pas celles de l'atmosphère illimitée, à cause du confinement relatif à la présence de la cuve de tranquillisation, le décollement interne subsiste ; ce confinement est d'ailleurs comparable à celui rencontré lors des essais au tunnel hydrodynamique (fig. 2).

Comme lors des essais en soufflerie, le décollement provoque une perte de pression d'arrêt qui se traduit par une alimentation hétérogène du compresseur. La figure 14 montre la cartographie des pressions d'arrêt obtenue à partir des informations fournies par les capteurs stationnaires pour un nombre de Mach moyen dans

la manche voisin de 0,43. Cette carte est à comparer à celle obtenue avec le même biseau en soufflerie où le débit interne est assuré par un extracteur (fig. 7) ; une zone de faible pression s'est formée en aval du décollement qui dans le banc compresseur se situe en haut de l'installation, contrairement aux essais en soufflerie où le biseau est retourné ; ceci explique l'inversion des cartographies présentées. Les niveaux de pression obtenus sont très voisins ainsi que la forme générale de la carte ; on vérifie également la parfaite symétrie de l'écoulement moyen dans ce plan.

Par contre en instationnaire aucune symétrie instantanée n'est mise en évidence comme on peut le voir sur la figure 15 obtenue pour le même fonctionnement du moteur à partir des pressions instationnaires filtrées à la fréquence de rotation de la machine.

La planche 16 présente les évolutions en fonction du temps de trois coefficients de distorsion (IDC, IDR et $K\theta$) pour une fréquence de coupure correspondant au quadruple de la fréquence de rotation du moteur (en haut) puis à la fréquence de rotation du moteur (en bas). Ces courbes montrent l'aspect instationnaire et de plus aléatoire de l'écoulement interne abordant la machine.

L'intensité du décollement variant avec le nombre de Mach interne, le profil de pression d'arrêt devant le plan compresseur évolue ; la figure 17 traduit ces constatations sous forme de coefficients de distorsion stationnaires et maximaux. L'influence du régime de rotation apparaît mineure par rapport à l'évolution avec le nombre de Mach ; IDCmax et IDR max croissent fortement avec le nombre de Mach alors que le coefficient $K\theta$ diminue car la pression dynamique de l'écoulement intervient au dénominateur de son expression.

Un coefficient de proportionnalité pouvant atteindre 3 entre les valeurs maximales et stationnaires démontre qu'il est indispensable de mesurer les valeurs instationnaires maximales de la pression d'arrêt si l'on veut réellement quantifier l'hétérogénéité de l'écoulement alimentant le moteur.

4.3 - Écoulement dans la manche -

Les sondages réalisés plus en amont dans la manche (plan 1) illustrent la nature du phénomène. Les cartographies de pression d'arrêt et d'angle azimutal (fig. 18) montrent que le contournement du bord "supérieur" du biseau provoque un décollement qui tend à être comblé par des écoulements circonférentiels engendrant un champ d'incidence dont les maxima (-19° et $+28^\circ$) se trouvent précisément à la limite de la zone décollée. La carte de turbulence du plan 2 qui a été établie avec une bande passante équivalente à la vitesse de rotation de la machine souligne également que la zone la plus turbulente est la zone frontière.

Les cartographies de pression d'arrêt indiquent clairement une diminution de la distorsion stationnaire entre les plans 1 et 2 : le coefficient de distorsion H passe, par exemple, de 0,241 à 0,145.

La longueur de la manche apparaît bien comme un paramètre fondamental de la simulation.

4.4 - Écoulement dans le compresseur -

La figure 18 synthétise les résultats obtenus pour un nombre de Mach moyen dans la manche de 0,43 et un régime de rotation égal à 90 % du régime nominal. Le profil de distorsion stationnaire de pression d'arrêt est modifié à la traversée du compresseur (roue mobile et redresseur) ; l'homogénéisation de l'écoulement s'opère d'ailleurs d'autant mieux que le point de fonctionnement est plus éloigné du pompage bien que les effets radiaux prennent de l'importance.

En sortie, les écoulements circonférentiels ont fortement diminué ; il s'est créée une distorsion thermique azimutale qui ne coïncide d'ailleurs pas avec la distorsion de pression. Une certaine symétrie persiste pour chacune de ces cartographies avec une rotation de l'axe de plusieurs degrés dans le sens de rotation de la machine.

L'instrumentation classique utilisée permet donc d'effectuer les études qui sont habituellement faites sur des compresseurs alimentés par un écoulement stationnaire hétérogène. En particulier la figure 19 représente les points de fonctionnement dans l'hypothèse de huit compresseurs en parallèle fonctionnant sur cinq nappes de courant différentes. Le rapport de compression est calculé à partir des points homologues amont et aval situés sur une même ligne de courant dans le cadre de l'hypothèse précédente ; le débit est déterminé à partir des conditions amont du point considéré.

4.5 - Comparaison avec l'essai en soufflerie -

Les mesures au banc compresseur et en soufflerie présentent quelques différences qui peuvent avoir une influence sur les conclusions à tirer de la comparaison des essais.

Hormis l'échelle qui oblige à corriger la bande passante, le plan de mesures à $X/D = 4$ n'est pas placé au même rapport de moyeu, le nombre et le positionnement des prises sont différents. En outre les nombres de Mach internes considérés en soufflerie sont supérieurs aux nombres de Mach obtenus au banc compresseur. Malgré ces restrictions, les valeurs de divers coefficients de distorsions portés planche 20 pour les points échelle 1 et pour le point échelle 1/4 calculé dans des conditions proches de l'essai au banc se comparent favorablement tant en stationnaire qu'en instationnaire. On notera cependant que les coefficients obtenus sur la maquette sont légèrement inférieurs aux coefficients obtenus au banc compresseur.

5 - CONCLUSION -

Le plan compresseur d'une prise d'air schématique de forme cylindrique a été qualifié en pression d'arrêt instationnaire ; les paramètres étudiés ont été l'incidence, le nombre de Mach interne et la position du plan de sondage.

Une qualification équivalente a été réalisée en soufflerie puis au banc compresseur dans des prises d'air non

axisymétriques fonctionnant au point fixe. La comparaison des résultats montre qu'il est possible de simuler au banc ce qui se passe au niveau plan compresseur d'une prise d'air cylindrique en incidence pour ce qui est de :

- l'efficacité moyenne
- la carte moyenne de pression d'arrêt
- l'amplitude des distorsions
- la localisation et le niveau des fluctuations de pression.

Les visualisations au tunnel hydrodynamique confirment l'identité de nature des écoulements internes.

Dans les simulations envisagées, deux paramètres sont à conserver : la longueur de la manche et le nombre de Mach moyen dans le plan compresseur.

Si le pavillon dissymétrique, dénommé Bourrelet, permet la simulation d'une incidence modérée ($\sim 20^\circ$), les biseaux assurent une plage d'incidence plus élevée ($30 - 35^\circ$) mais limitée, même en modifiant l'angle de la découpe.

Afin de pouvoir simuler une prise d'air donnée à incidence quelconque, il sera nécessaire de définir une prise d'air non axisymétrique en jouant sur l'inclinaison du plan d'entrée et surtout sur la valeur des rayons de bord d'attaque dans le plan d'entrée.

Cette définition pourra avoir lieu sur maquette avant de recevoir une application au banc partiel ou au banc complet.

Le motoriste disposera alors d'un moyen souple et économique de simulation de l'écoulement dans une prise d'air réelle en incidence et donc d'évaluation de la sensibilité du compresseur à la distorsion.

REFERENCES

- [1] H. WERLE et M. GALLON
Sur l'écoulement autour d'une prise d'air.
Recherche Aérospatiale n° 1975-2.
- [2] M. PIERRE et G. FASSO
Le centre d'essais aérothermodynamique de Modane-Avrieux.
Note Technique n° 166 - 1970.
- [3] M. GRANDJACQUES
Mesures instationnaires dans une prise d'air.
15ème Colloque de l'AAAF - Marseille 7 à 9 Novembre 1978.
- [4] M. CLYDE MELICK Jr, ANDRES HYBARRA
Estimating maximum instantaneous distortion from inlet total pressure RMS measurements.
AIAA n° 78 970.
- [5] F. STOLL, J.W. TREMBACK et H.M. ARNAIZ
Effect of number of probes and their orientation on the calculation of several compressor face distortion descriptors.
NASA TM 72 859.
- [6] G. LARUELLE
Etude des distorsions instationnaires dans les prises d'air à forte incidence.
"L'Aéronautique et l'Astronautique", (à paraître 1981).

VISUALISATIONS AU TUNNEL HYDRODYNAMIQUE

- Avion en incidence



PRISE D'AIR DROITE $\alpha = 40^\circ$

- Prise d'air schématique

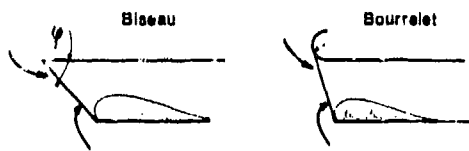


(a)

$$A_2/A_1 = 1$$



- Simulation point fixe



(b)

BISEAU $\psi = 30^\circ$

$$A_2/A_1 = 15$$

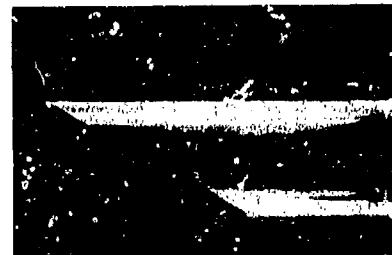


FIG. 1

FIG. 2

MONTAGE D'ESSAIS

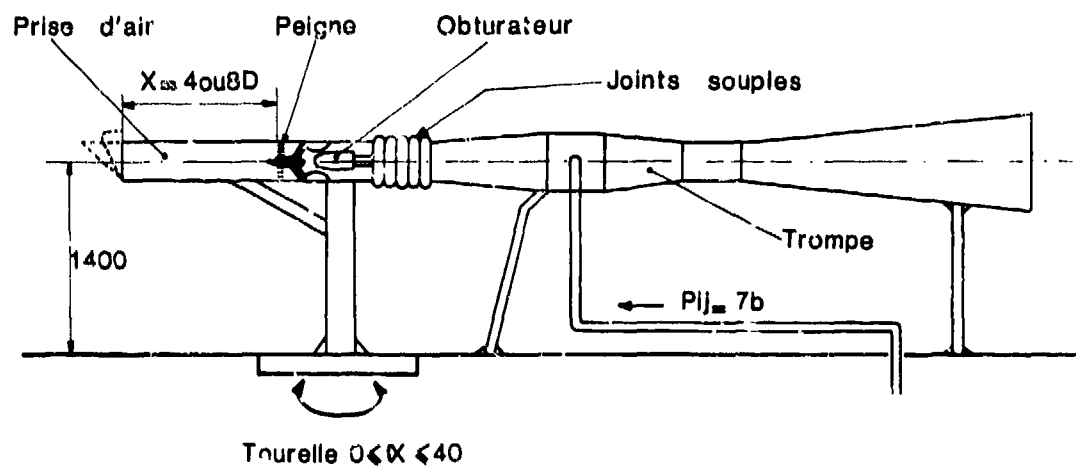


FIG. 3

VUE DU MONTAGE EN VEINE Soufflerie S1 Ma



FIG. 4

• Prise d'air droite

$D = 184$

• Biseaux

$\psi = 30^\circ$

• Bourrelet

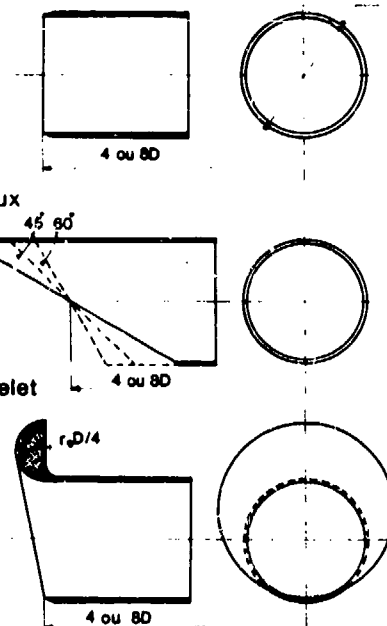


FIG. 5

PRESSIONS D'ARRET MOYENNES

$M_2 \approx 0.6$

$X/D = 4$

PRISE D'AIR DROITE

BISEAU ($\psi = 30^\circ$)

EFFICACITE

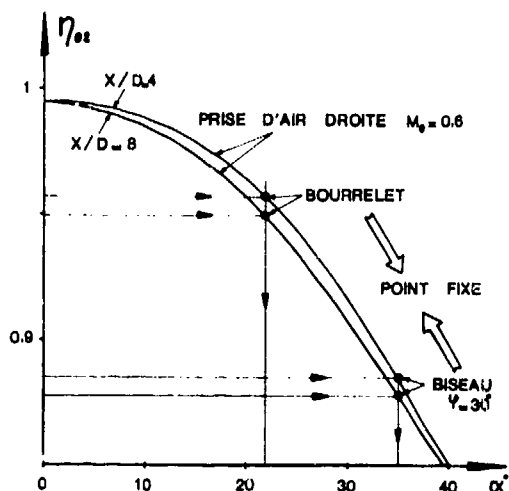


FIG. 6

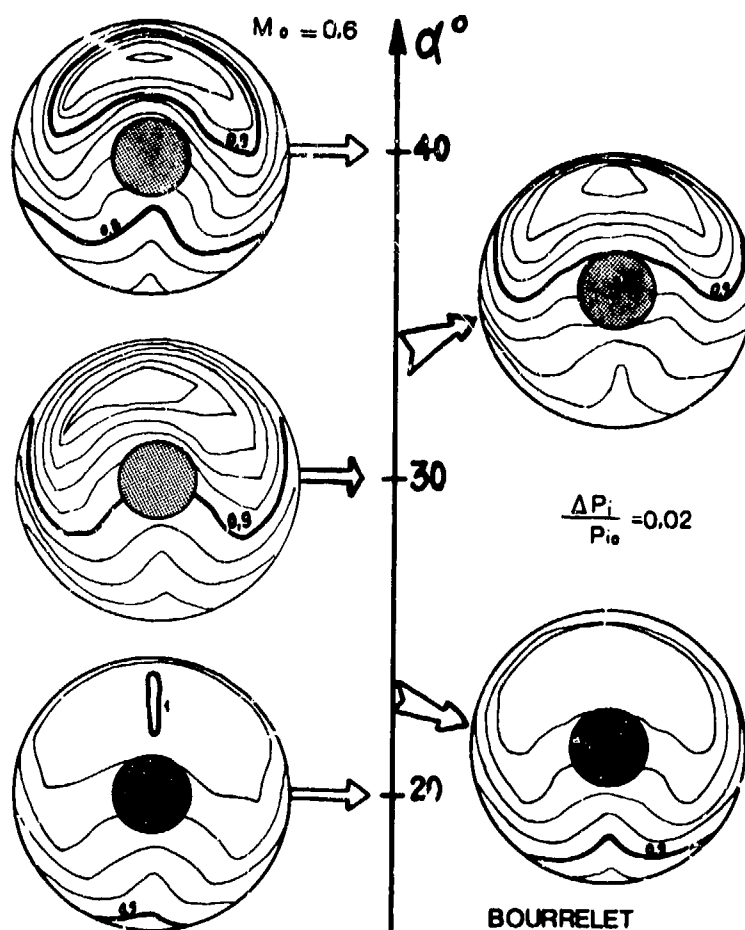


FIG. 7

PRESSIONS D'ARRÊT MOYENNES $M_2 = 0.6$ $X/D = 8$ PRISE D'AIR DROITE BISEAU ($\psi = 30^\circ$)

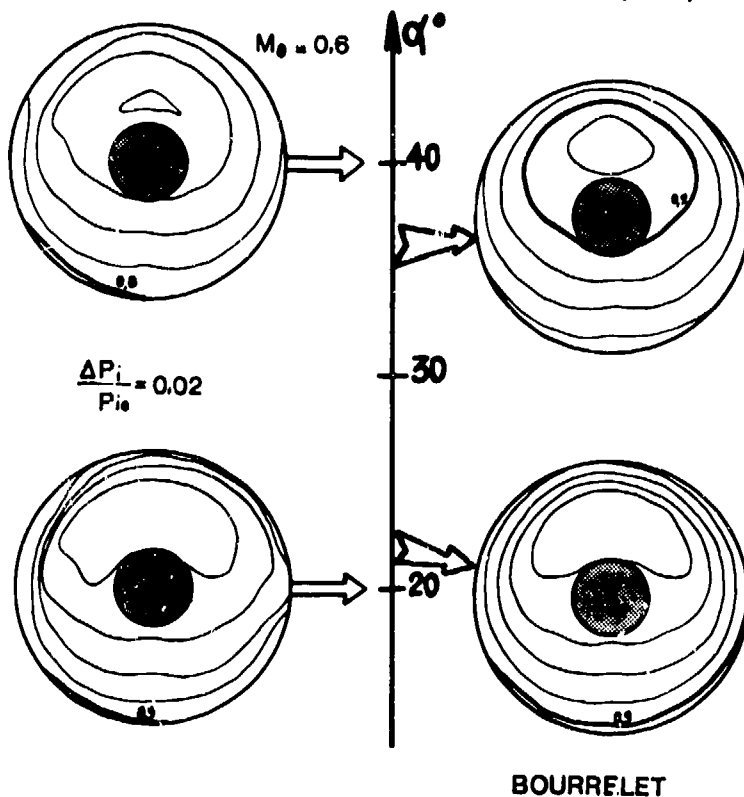


FIG. 8

COEFFICIENT DE DISTORSION

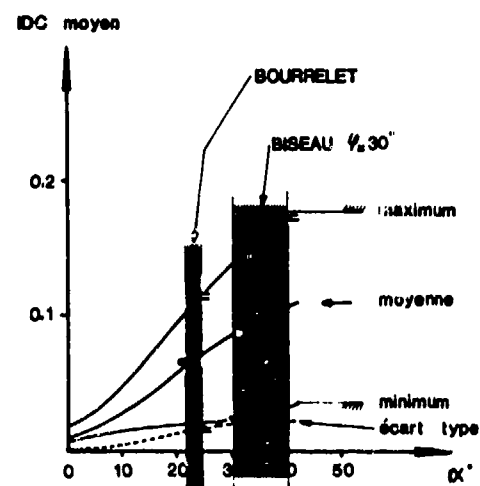


FIG. 9

FLUCTUATIONS DE PRESSION

$X/D = 4$

$r/R = 0.62$

PRISE D'AIR DROITE
 $M_2 = 0.6$

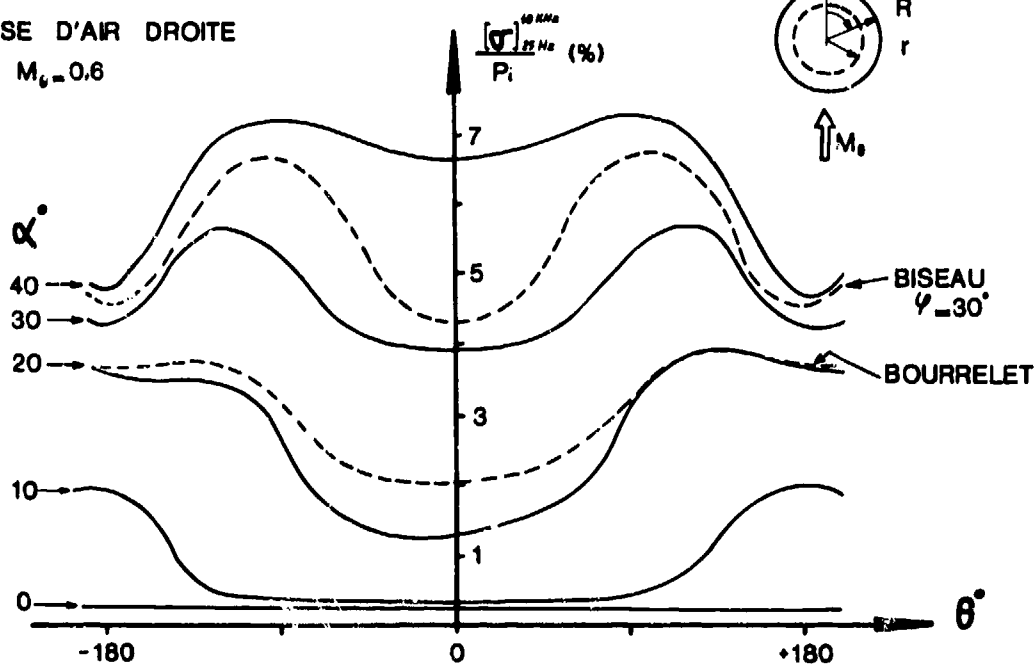


FIG. 10

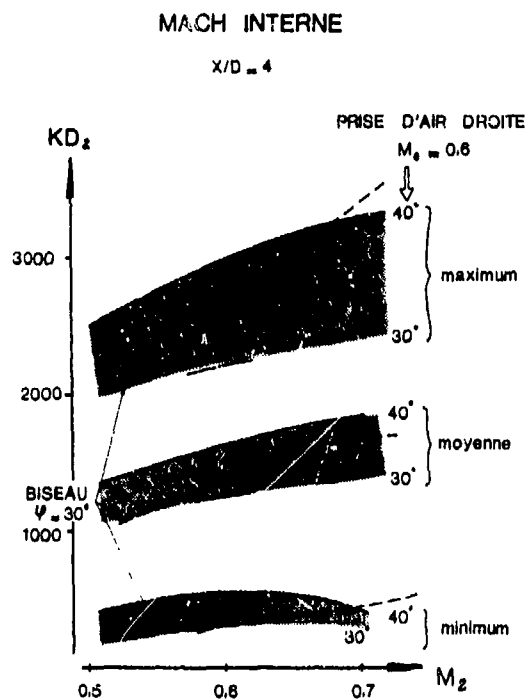


FIG. 11

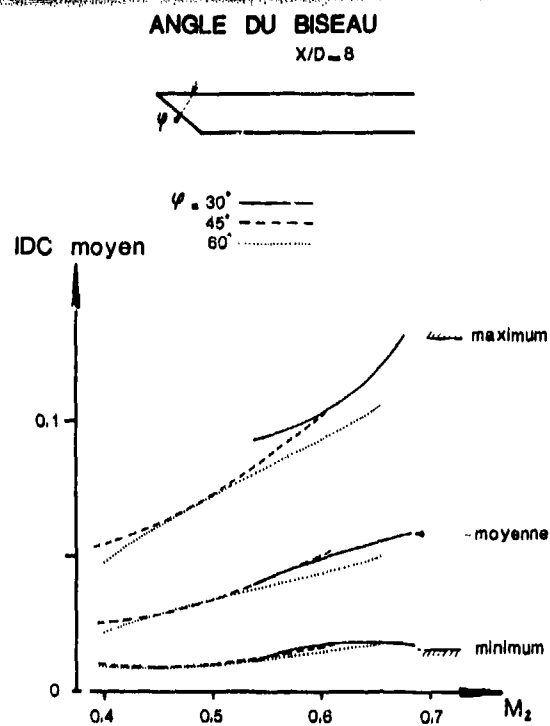


FIG. 12

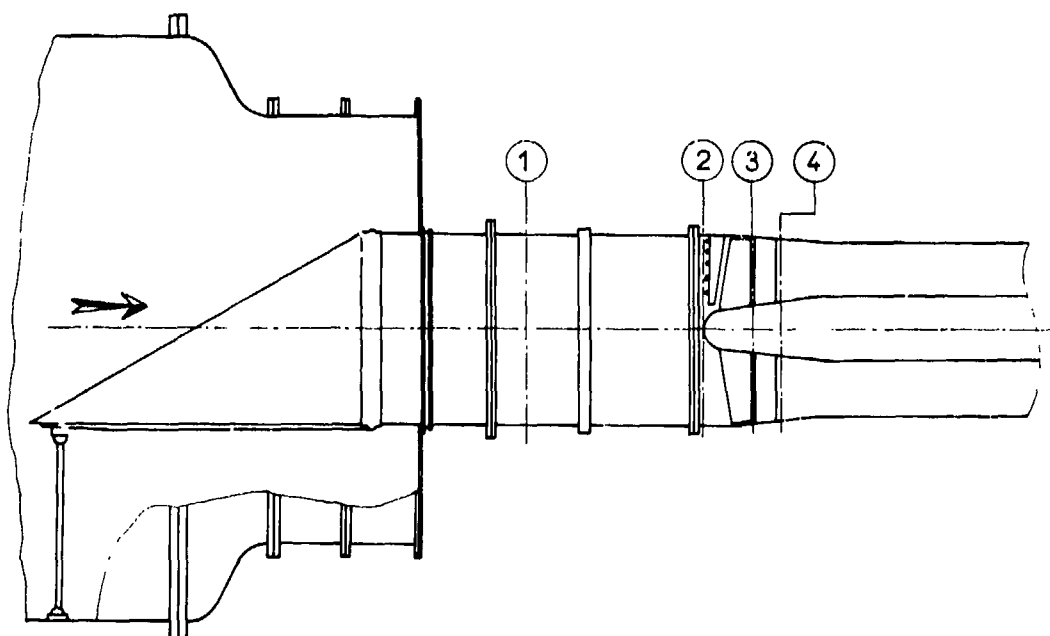


SCHÉMA DU DISPOSITIF AU BANC COMPRESSEUR

FIG. 13

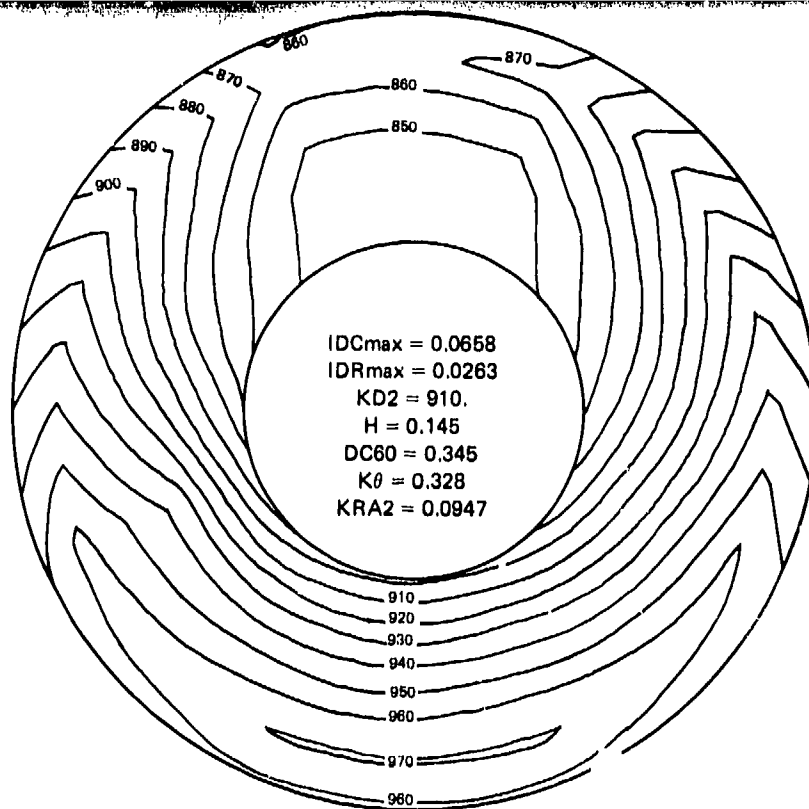


FIG. 14

CARTE STATIONNAIRE DE PRESSION D'ARRET-PLAN 2
($P_i/P_{i0} \times 1000$)

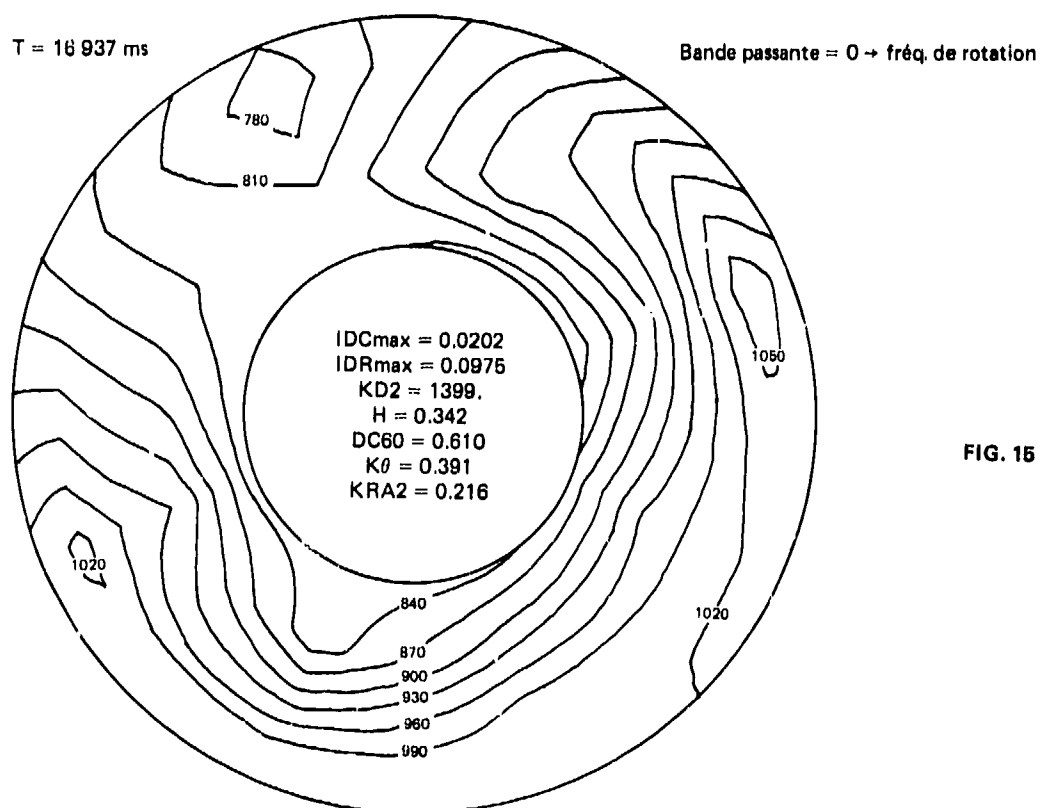
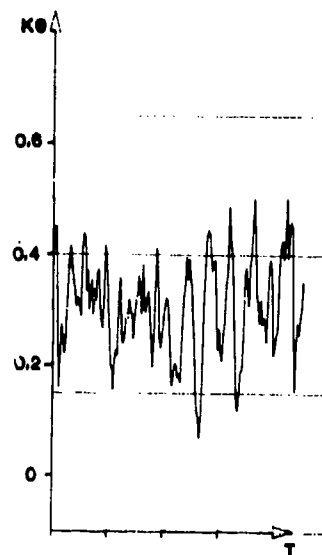
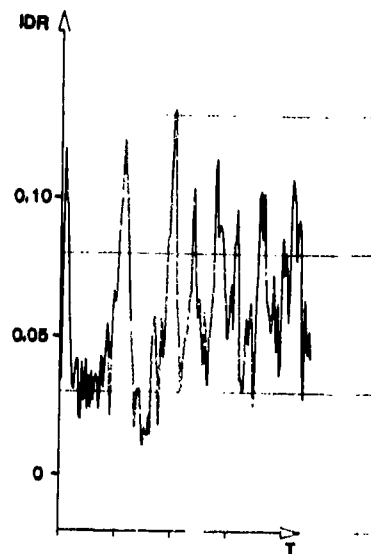
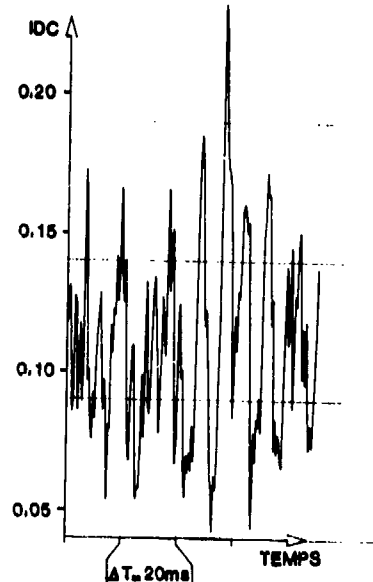


FIG. 15

CARTE INSTANTANÉE DE PRESSION D'ARRET-PLAN 2
($P_i/P_{i0} \times 1000$)

FILTRAGE A 630 Hz

MACH INTERNE = 0.43



FILTRAGE A 150Hz

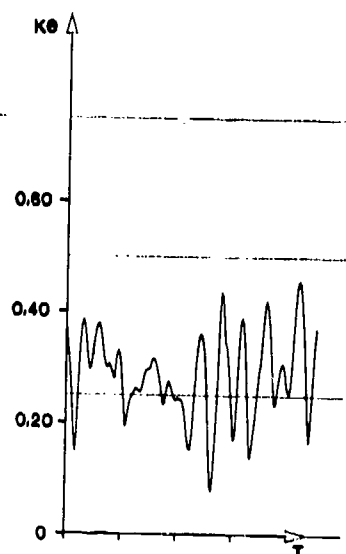
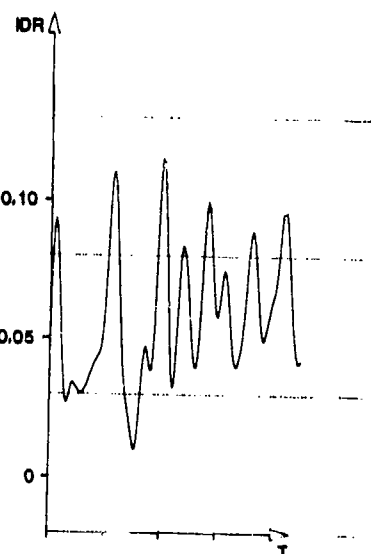
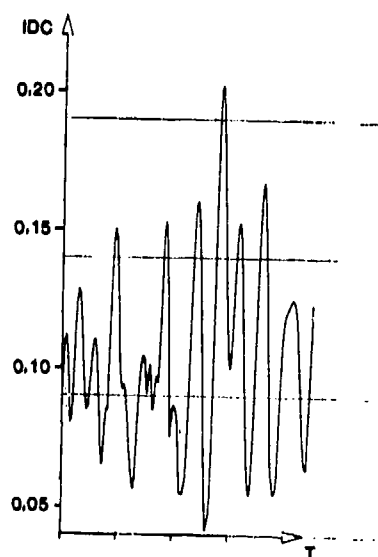


FIG. 16

COEFFICIENTS DE DISTORSION INSTANTANÉS

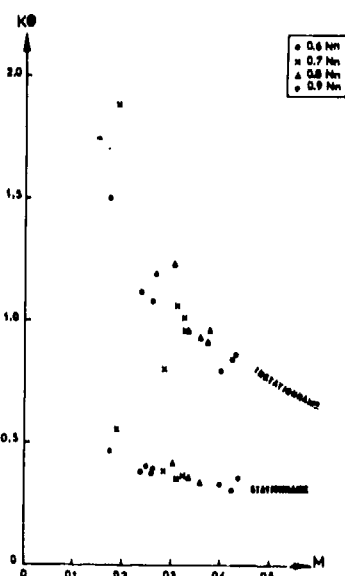
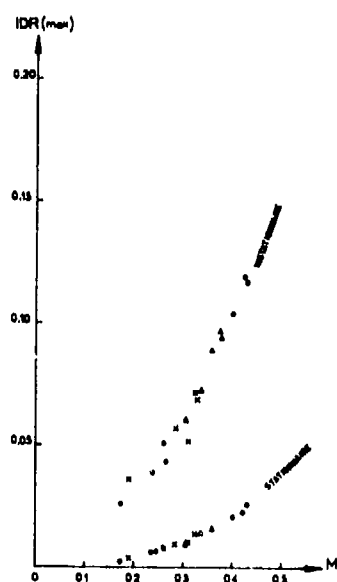
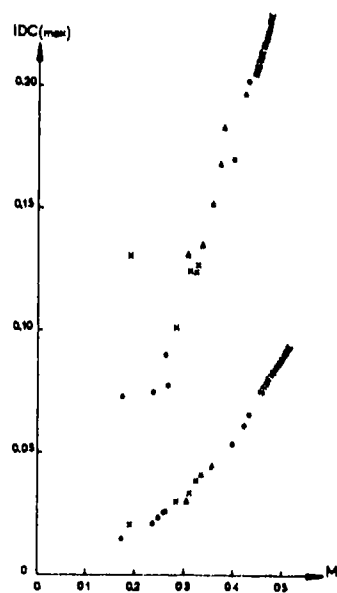


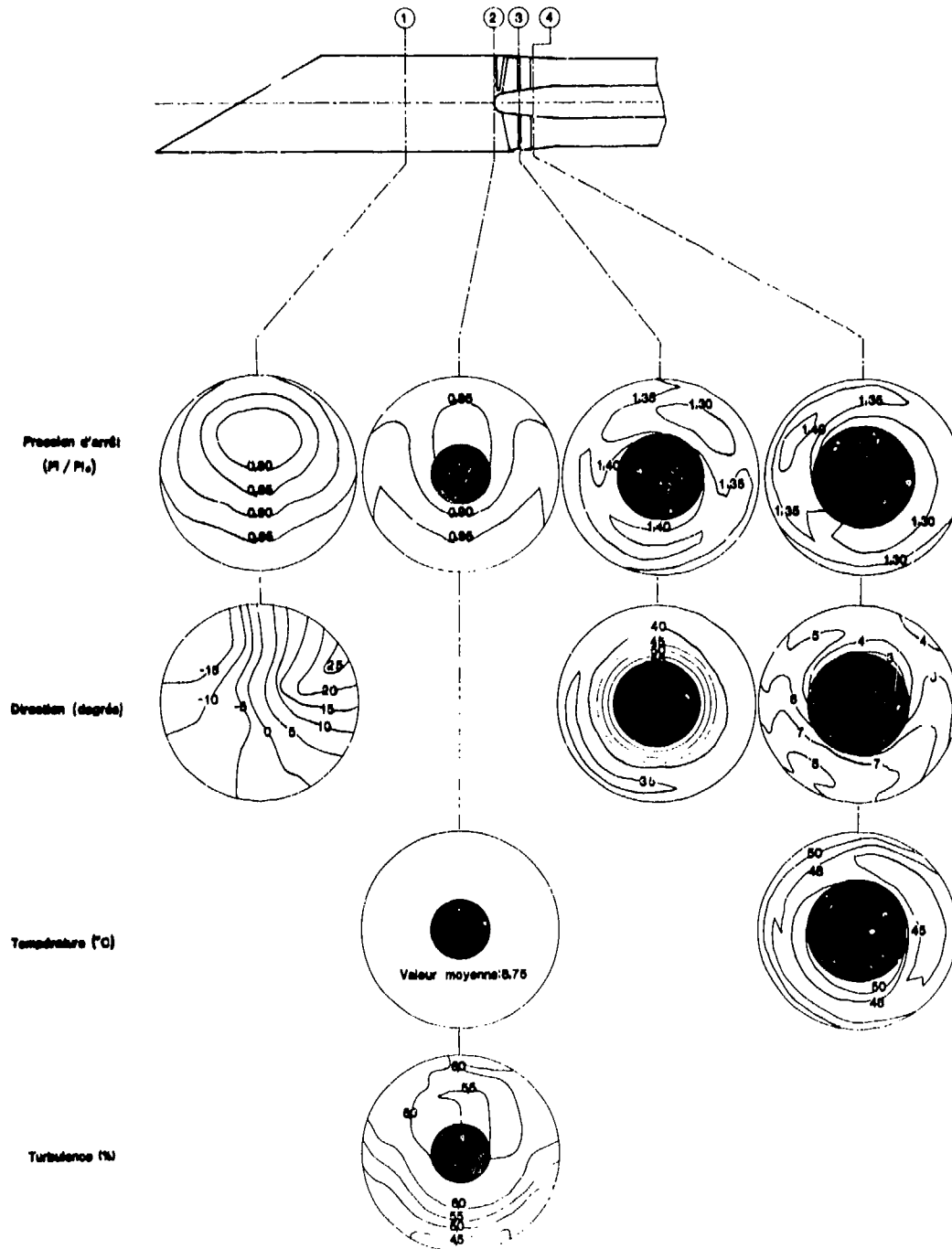
FIG. 17

INFLUENCE DU NOMBRE DE MACH INTERNE

FIG. 12

CARTOGRAPHIES

Mach interne 0.43



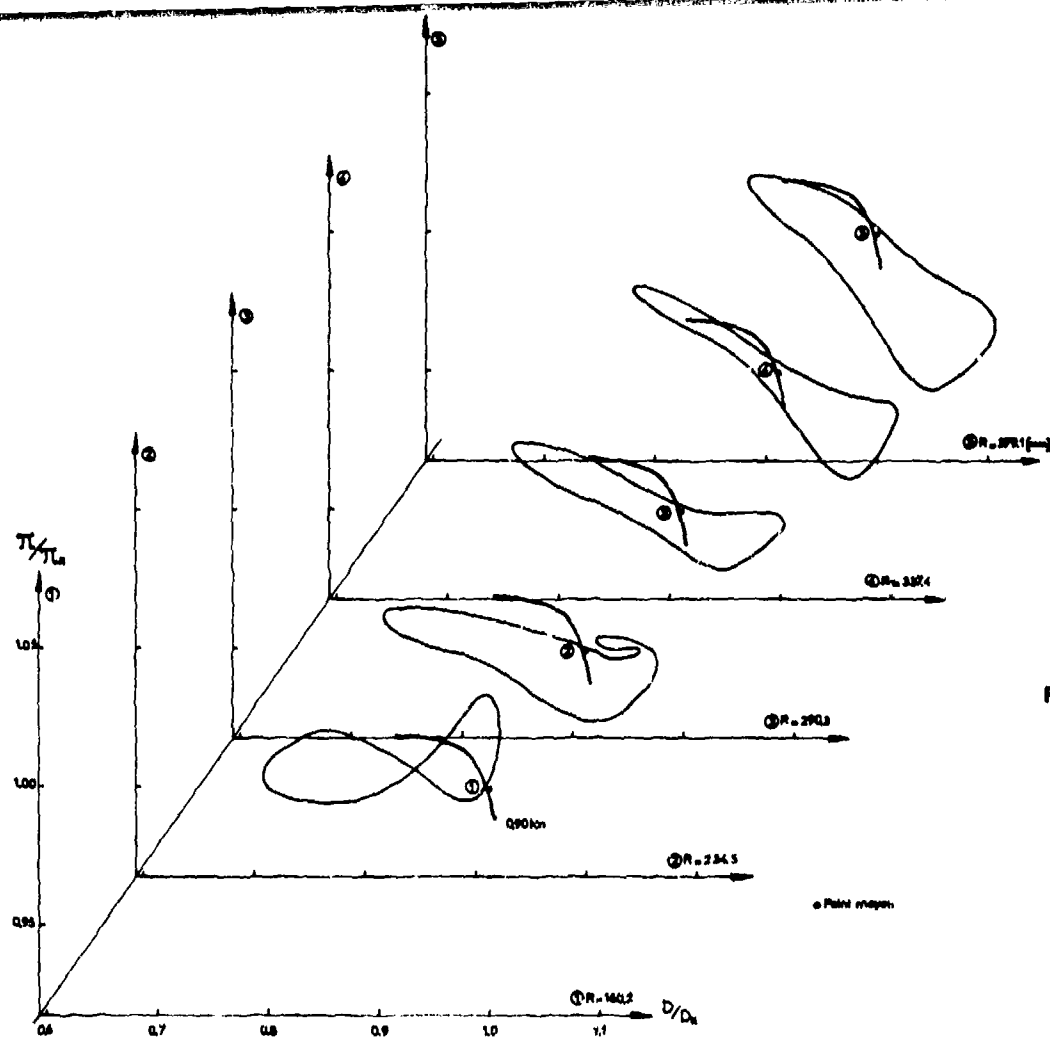


FIG. 19

FONCTIONNEMENT HYPOTHÉTIQUE DU COMPRESSEUR EN ÉCOULEMENT PERTURBÉ

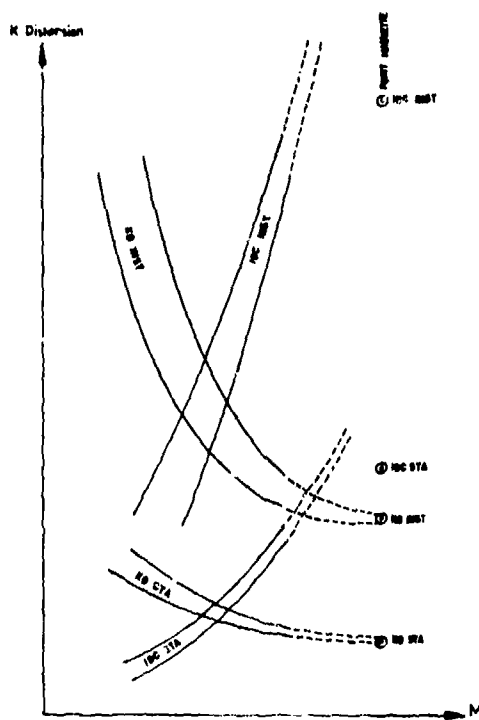


FIG. 20

COMPARAISON ESSAI-BANC ESSAI-MAQUETTE

**SYSTEME D'ACQUISITION ET D'ANALYSE
POUR ESSAIS DYNAMIQUES D'ENTREES D'AIR**

Pierre PERRIER

Avions Marcel Dassault-Bréguet Aviation (AMD-BA)
78, Quai Carnot - 92214 ST CLOUD - France

Bertrand DELAHAYE

Société Nationale d'Etudes et de Construction de Moteurs d'Aviation (SNECMA)
77550 MOISSY CRAMAYEL - France

Gérard LARUELLE

Office National d'Etudes et de Recherches Aérospatiales (ONERA)
92320 CHATILLON - France

0. INTRODUCTION

L'augmentation du domaine de vol des avions de combat conduit à des points de fonctionnement correspondant à une bien plus grande variation des caractéristiques aérodynamiques instationnaires à l'entrée du réacteur, que par le passé. Pour évaluer si cette augmentation du domaine de fonctionnement sera effectivement acceptable pour les compresseurs et réacteurs du futur, il faut d'abord acquérir une connaissance suffisante des écoulements. Une telle connaissance passe par la mesure d'un nombre suffisant de caractéristiques instationnaires de l'écoulement. Mais, d'autre part, on doit limiter les points de mesures à un niveau acceptable tant au point de vue du prix que de la possibilité de traitement instantané ou différé. C'est une chaîne de mesures tenant compte de ce compromis nécessaire que nous décrivons dans cet exposé après en avoir donné les clauses techniques et les capacités de traitement retenues.

Ce travail résulte d'une collaboration triangulaire, entre avionneur, motoriste et organisme de recherche, dont le but est de rendre complémentaires les recherches des uns et des autres, permettant ainsi une économie de moyen et une homogénéité des méthodes choisies pour l'analyse et l'interprétation des résultats. Il a été financé, dans ce but, par le Ministère de la Défense.

1. EVOLUTION DES PROBLEMES DE DEFINITION DE L'ECOULEMENT A L'ENTREE DU REACTEUR

1.1 - Les problèmes de compatibilité entre l'écoulement fourni par les manches à air des avions et l'écoulement acceptable par un turboréacteur ont été longtemps ignorés par suite de trois effets favorables existant simultanément ou partiellement sur les avions militaires anciens :

- utilisation de compresseurs dont les caractéristiques aérodynamiques étaient très éloignées du maximum possible avant décrochage des pales ;
- utilisation de manches d'amenée d'air très longues avec des dimensions élevées des sections de passage conduisant à une très bonne homogénéisation de l'écoulement à des vitesses assez faibles ;
- conditions de vol limitées à des angles d'incidence et de dérapage modérés, le plus souvent pour éviter à l'avion le voisinage de zones de décrochage mal contrôlées ou conduisant à un risque important d'engagement en vrille mal récupérable.

Les Avions Marcel Dassault-Bréguet Aviation ont toujours visé à obtenir un fonctionnement normal des avions militaires aux grandes incidences, de façon à ne pas imposer de limitation d'emploi aux pilotes, y compris en régime de vrille, l'avion étant étudié pour être récupérable (réf. 1) ; aussi la SNECMA a-t-elle, de son côté, maintenu également les moteurs équipant ces avions dans un réglage et une définition de qualité équivalente. Cependant l'augmentation importante des performances des avions récents permise par les gains sur la motorisation, les commandes de vol et l'aérodynamique à grande incidence conduit maintenant à faire voler normalement à des incidences supérieures à 30° et à des vitesses aérodynamiques pouvant être nulles (MIRAGE 2000). L'utilisation de manches à air très longues n'est pas toujours possible ou peut être très coûteuse en poids ; enfin les moteurs eux-mêmes ne peuvent augmenter leur rapport poussée/poids sans une recherche de la performance, en particulier sur les compresseurs ; ceux-ci, plus chargés, donc plus près de leurs limites non seulement localement mais sur l'ensemble des éléments, peuvent avoir des fonctionnements extrêmes avec aubages partiellement ou totalement décollés.

1.2 - Nous allons passer en revue rapidement les éléments devant caractériser l'écoulement aérodynamique.

1.2.1 - Il importe de caractériser l'écoulement d'abord du point de vue de son interaction avec le compresseur. Spatialement, ceci revient à connaître cet écoulement devant le moteur à un temps donné en fonction de ses coordonnées radiales et circonférentielles : c'est la carte d'entrée d'air. Mais il faut aussi connaître l'interaction entre étages caractérisée par la succession en fonction du temps de la carte et l'espacement résultant relatif à la distance inter-étages pour théoriquement ne rien laisser échapper de l'interaction entre étages. En fait, les essais montrent que les fluctuations à haute fréquence, relativement au temps de passage inter-aube, ne sont pas caractéristiques des décollements globaux, de même que les fluctuations spatiales, trop petites par rapport à une fraction de circonférence, sont amorties par le fonctionnement en grille d'aube de l'étage (réf. 2).

1.2.2 - L'augmentation des nombres de Mach à l'entrée du compresseur a conduit à une diminution du taux de diffusion dans l'entrée d'air entre la section de col et l'entrée compresseur, mais il n'a pas été toujours possible de maintenir des architectures d'avion avec manches très longues par suite de leur coût élevé dans le bilan de masse de l'avion. De toute façon l'interaction de l'aspiration des aubes et de leur champ local sur l'écoulement reste toujours faible dans la pratique au contraire des manches ultra-courtes de nacelles d'avion civil. Aussi peut-on caractériser valablement l'écoulement dans la manche en l'absence de réacteur, ce qui simplifie les essais. Les manches sont le siège de phénomènes instationnaires qui sont caractérisables à deux niveaux différents :

- soit par des fluctuations d'une frontière nette entre zones de haute pression et zones de basse pression et dont la fréquence peut être accrochée sur des temps de propagation de perturbations basés sur la longueur du tuyau ;
- soit par des fluctuations turbulentes de la vitesse en grandeur et direction dont les fréquences les plus basses dépendent directement des tailles des grosses structures de la turbulence, elles-mêmes directement limitées par le diamètre moyen local de la manche à air. Ces deux types de fluctuations sont créés et entretenus essentiellement à l'extérieur ou sur les lèvres de l'entrée d'air, mais il n'est pas exclu que des rétreints ou des courbures excessives de la manche les créent ; les décollements correspondants sont alors d'autant plus inacceptables qu'ils sont au voisinage de l'entrée du réacteur, car ils ne peuvent être amortis par une longueur de manche suffisante.

1.2.3 - Les causes de perturbations créées à l'entrée d'air et dans son voisinage dépendent essentiellement des conditions de vol de l'avion et de ses performances exprimées en nombre de Mach, et incidence et dérapage pratiqués :

- a) Pour les faibles nombres de Mach, l'écoulement devient identique à l'écoulement au point fixe et peut être caractérisé par celui-ci, sous réserve des aspirations des couches limites induites par l'aspiration sur les parois voisines (ces aspirations peuvent conduire à des écoulements tourbillonnaires en trombe importants).
- b) Pour les grands nombres de Mach supersoniques, les problèmes majeurs de distorsion à l'entrée moteur sont créés par les irrégularités du champ aérodynamique et les intensités inégales des chocs amont. On peut caractériser la carte à l'entrée moteur par trois types de zones :
 - les zones où le rendement est proche du niveau moyen souhaité et ne dépend que des distorsions du champ amont créé par les dispositifs de recompression isentropique ou par chocs obliques retenus ;
 - les zones où le rendement est proche du rendement du choc droit, au pire associées à des zones en survitesse par rapport à l'écoulement amont ;
 - les zones où le rendement dépend non seulement du rendement de chocs mais aussi des pertes de charges turbulentes créées, soit par des interactions chocs - couches limites de paroi, soit par des décollements locaux.

Les distorsions sont ainsi maximales pour des écoulements amont à Mach élevé et à fonctionnement non uniforme, la non uniformité résultant de chocs droits ou obliques n'ayant, bien entendu, pas de raison d'être stationnaire en général. Excepté pour les zones fortement turbulentes créées par des décollements proches des parois du conduit, l'écoulement est très bien caractérisé par les pertes de pressions d'arrêt qui sont un reflet des pertes d'entropie amont par suite de la très faible diffusion de celles-ci en l'absence de limites turbulentes caractéristiques. Comme ces variations de rendement peuvent être très élevées à Mach 2 et ont provoqué les premiers problèmes importants de distorsion inacceptables par les compresseurs, comme elles sont mesurées simplement par des prises de pressions d'arrêt instationnaires, les cartes correspondantes sont bien connues et exploitées actuellement. Elles peuvent cependant ne pas rendre compte de rotations d'ensemble ou des turbulences locales créées dans les rétreints ou les angles.

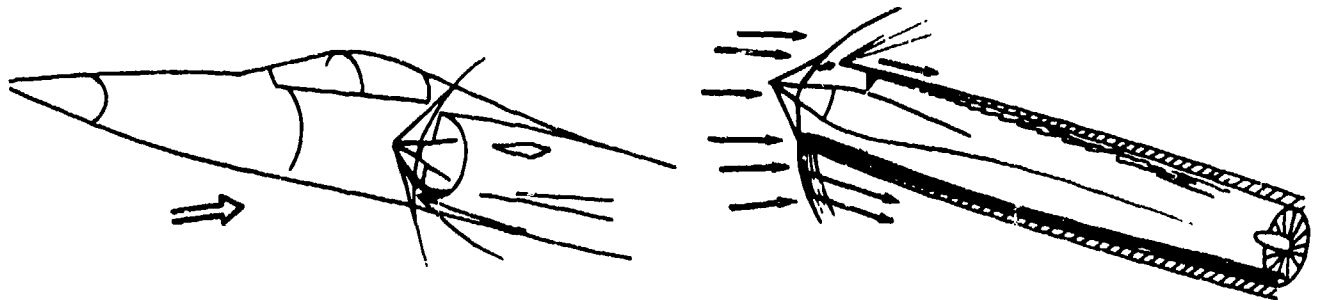
- c) Pour les nombres de Mach intermédiaires où les pertes de charge par augmentation d'entropie dans les chocs sont faibles, le phénomène prépondérant est, au contraire des cas précédents, la fluctuation du vecteur vitesse ; elle est créée par les gros tourbillons des structures turbulentes qui ont pris naissance en général aux lèvres des entrées d'air ou dans leur voisinage après un décollement. La fluctuation maximale de perte de pression d'arrêt relevée par un pitot atteint alors la variation entre la pression d'arrêt de l'écoulement externe, c'est-à-dire la pression d'arrêt avion et une pression un peu inférieure à la pression statique à l'entrée moteur dans le cas d'écoulements de retour à l'entrée compresseur, elle dépend donc fortement du nombre de Mach avion. Il y a une combinaison d'incidence et de dérapage maximum, de débit maximum du moteur et de nombre de Mach de l'avion vers les plus hautes altitudes en transsonique qui donnera les décollements les plus importants associés aux fluctuations maximales de vitesse et de pression et, souvent, à des débuts de pertes entropiques notables. C'est la zone du domaine de vol qui risque d'être la plus critique et qui se caractérise davantage par une fluctuation de la direction de la vitesse que par une fluctuation de son intensité. Elle est assez mal mesurée par une prise de pitot et demanderait plutôt une prise d'incidence locale ; en particulier tous les tourbillons d'axes colinéaires à l'axe de la manche sont seulement mesurables en incidence locale.

Dans ces écoulements turbulents, il est important cependant de distinguer deux gammes de dimensions ou de fréquences d'intérêt très différents : les fréquences correspondant aux plus grosses structures turbulentes de la taille de la manche à air (et malheureusement avec les vitesses actuelles d'entrée des compresseurs de fréquence proche de la rotation moteur) et les fréquences beaucoup plus élevées de la turbulence interne dont l'intensité influera assez directement l'extinction des grosses structures. Les premières sont les seules intéressantes pour le fonctionnement du réacteur, les secondes peuvent être mesurées surtout pour aider à la compréhension des dissipations internes à la manche, elles donnent aussi le niveau global de turbulence à l'entrée du réacteur (figure 2).

a) Fonctionnement très basse vitesse



b) Fonctionnement à grand nombre de Mach



c) Fonctionnement à grande incidence transsonique

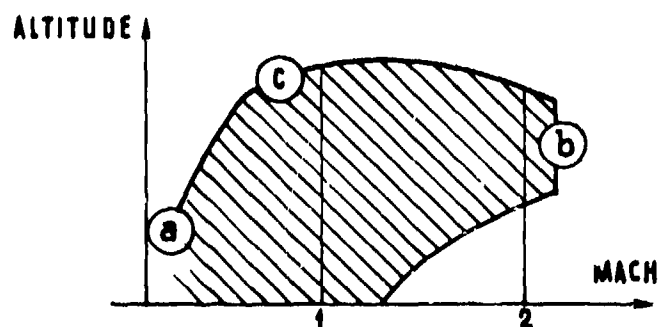
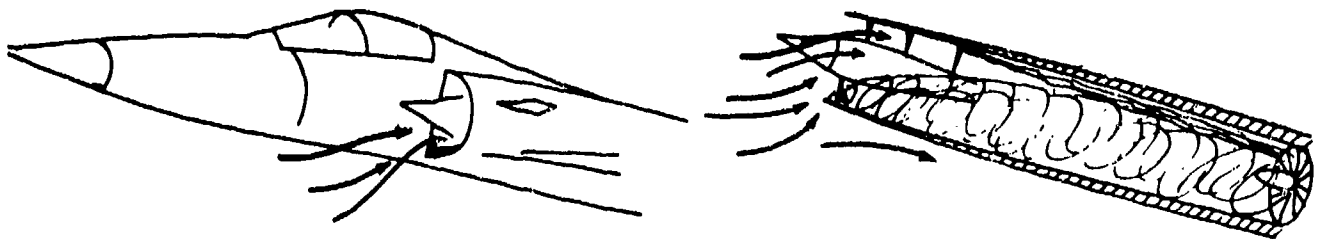


FIGURE 1

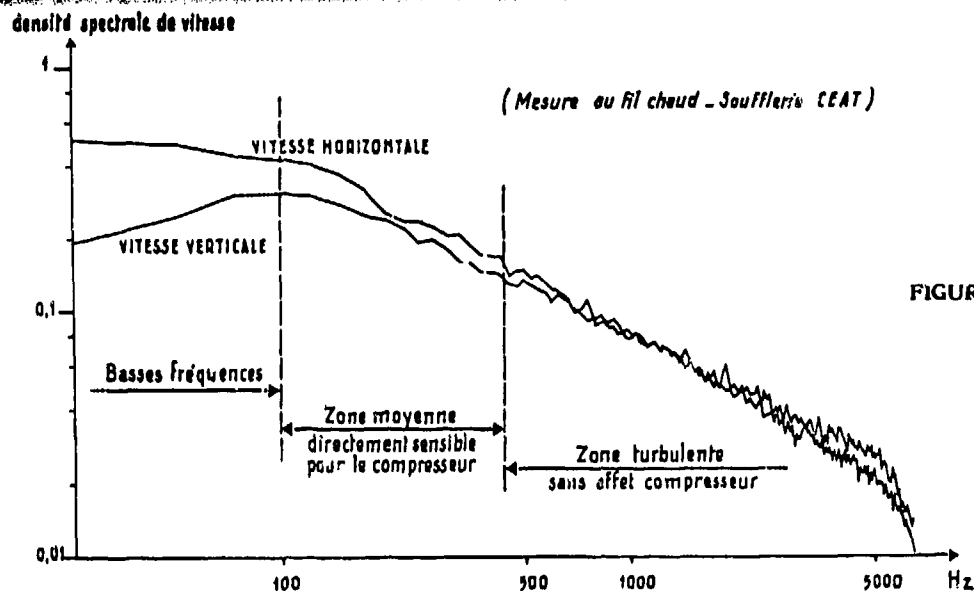


FIGURE 2

- 1.3 - Historiquement, les mesures de compatibilité manche-réacteur ont conduit à caractériser les cartes de pressions d'arrêt stationnaires en supersonique et à noter ainsi leurs distorsions maximales, étant entendu que les fonctionnements anormaux très instationnaires de manche (avec buzz, pompages divers, etc...) devaient d'abord être éliminés. Ensuite, on a caractérisé ces cartes dans tout le domaine de vol de l'avion et on les a reliées aux ennuis rencontrés ailleurs qu'en supersonique. La très mauvaise corrélation obtenue a conduit à la mesure des cartes instationnaires de pression d'arrêt qui ont permis de diminuer cette incohérence générale. Cependant l'augmentation du prix de l'installation et du coût du dépouillement associé limite la généralisation de cette technique qui est, de toute façon, assez incomplète. Nous présenterons, dans la suite, trois voies pour économiser sur ces coûts élevés en les rendant plus homogènes et plus efficaces, tant au niveau des essais préliminaires en soufflerie que des essais au banc et essais en vol. C'est sans perdre de vue une telle recherche d'économie que doit être trouvée la place de mesures plus correctes de l'écoulement instationnaire turbulent décrit en (1.2.2) ci-dessus à l'aide de mesures locales d'incidence et de pression d'arrêt couplées.

En résumé, il nous faut acquérir plus économiquement une information plus complète sur l'écoulement.

2. METHODES D'ACQUISITION ET D'ANALYSE

- 2.1 - Partant d'une définition suffisamment serrée des cartes instationnaires, on peut d'abord essayer de réduire la quantité d'informations à traiter en utilisant des paramètres de corrélations statistiques portant sur un prétraitement des données. Deux voies d'économie sont possibles : on peut, soit admettre une corrélation d'ensemble spatiale ou temporelle de l'écoulement en plusieurs points déduit d'un modèle a priori, soit admettre une telle corrélation en la déduisant de mesures d'ensemble dans l'écoulement. La première voie a été explorée par Melick et conduit à des résultats intéressants pour leur économie de moyen, elle est décrite en détail dans les références (réf. 3 et réf. 4). Elle présente l'avantage d'une possibilité de contrôle statistique de sa validité, donc d'une évaluation de son erreur statistique probable mais elle conduit à masquer les cartes instantanées sous le moule probabiliste choisi. On doit pouvoir l'inclure systématiquement comme complément instationnaire à partir d'une évaluation en quelques points des composantes instationnaires et d'une carte détaillée globale stationnaire. Comme le résultat ne dépend pas de façon exagérée de la loi de probabilité inconnue des fluctuations de l'écoulement, et en se limitant à une précision moyenne (20 %) sur les composantes instationnaires, notre expérience nous conduit à la recommander de toute façon. Admettre une corrélation déduite des essais, nécessite un traitement en deux temps. On peut encore se contenter d'ajuster les coefficients des fonctions de Melick, qui ont une certaine valeur théorique à des mesures expérimentales voisines.
- 2.2 - On peut également admettre que les mesures doivent permettre de caractériser les points critiques de fonctionnement pour le compresseur, mais il faut alors faire une saisie pendant un court intervalle de temps de l'ensemble de l'écoulement. S'il était possible de connaître a priori le critère instationnaire le plus réaliste pour le moteur, alors la mesure de celui-ci devrait permettre de ne retenir, pour exploitation détaillée que les extrema de ce critère. Une évaluation approximative de l'extrémum peut être faite à partir d'une détection en amont du plan d'entrée d'air de coefficients extrêmes, soit type Melick, soit plus complets portant sur l'incidence locale et la pression d'arrêt. Alors cette indication devrait permettre un enregistrement limité de la carte globale avec des informations portant sur les corrélations spatiales et temporelles et sur les turbulences moyennes locales.
- 2.3 - On donne, dans la 4ème partie, ci-dessous le Cahier des Charges qui a été retenu pour la définition du système d'acquisition et d'analyse général indépendamment de tout processus d'allègement du traitement (méthode statistique de loi fixée a priori) ou du nombre des données stockées (choix à partir d'indicateurs en amont des zones de temps où l'on gardera et traitera les données expérimentales recueillies). Mais la quantité des données à acquérir et à traiter est très élevée.

On va donc décrire ci-dessous en détail un processus d'allègement du traitement et du stockage dont le but sera de permettre, pour le cas de l'essai en soufflerie où les contraintes sont les plus difficiles à satisfaire (à cause de la proportionnalité à l'échelle des fréquences maximales à prendre en compte), d'assurer un suivi des essais en direct et un dépouillement allégé des mesures. Son but est double :

- guider l'ingénieur d'essais pour rechercher les configurations intéressantes,
- préciser les zones à dépouiller sur la bande magnétique numérique ou analogique enregistrant la totalité des points de mesure.

3. MOYEN ALLEGÉ DE TRAITEMENT ET D'ACQUISITION POUR ESSAIS EN SOUFFLERIE

3.1 - Si on retient la taille maximale acceptable de maquettes dans les grandes souffleries de Modane de l'ONERA, on est conduit à des échelles de maquette proche du 1/5ème, soit des fréquences maximales d'échantillonnage nécessaires 5 fois plus élevées qu'en vol ou au banc. Comme un nombre de points de mesure élevé est requis (réf. 5) pour caractériser une manche en fonction des quatre paramètres : nombre de Mach amont, nombre de Mach à l'entrée du compresseur, incidence et dérapage, et ceci pour plusieurs configurations, il est très important de disposer de moyens allégés d'évaluation instantanée de la qualité de l'écoulement pour que l'ingénieur d'essai puisse guider le programme d'essai au mieux. On désigne habituellement une telle installation sous le terme de surveillance en temps réel de l'essai ou "quick-look".

3.2 - Les critères pour la définition d'un bon "quick-look" sont :

- réduction maximale du temps d'essai (donc du coût),
- limitation maximale de l'intervention humaine,
- possibilité d'utiliser la solution de secours existante au niveau des chaînes d'acquisition de Modane pour un dépouillement local,
- possibilité de simplification de la méthode compte tenu de l'expérience qui sera progressivement acquise.

On ne dépouillera en temps réel (ou quasi-réel) que les zones intéressantes où la distorsion est la plus élevée. Il est donc nécessaire d'avoir un détecteur de ces instants. Sachant que les fortes distorsions dans le plan compresseur sont obtenues lorsque de grosses perturbations passent, on cherchera à détecter ces grosses bouffées en amont de ce plan. Pour ceci, des sondes seront placées à environ un diamètre en amont du plan compresseur. Un critère simple, basé sur les indications fournies par ces sondes, déclenchera l'acquisition puis le traitement de l'ensemble des pressions du peigne pendant le passage de la perturbation à leur niveau.

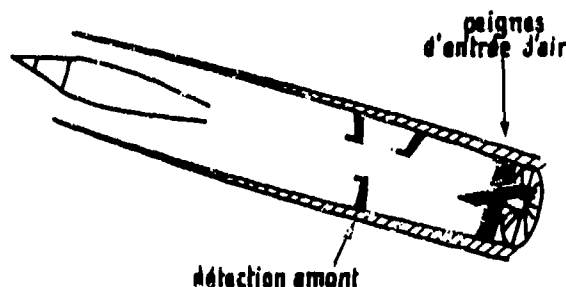
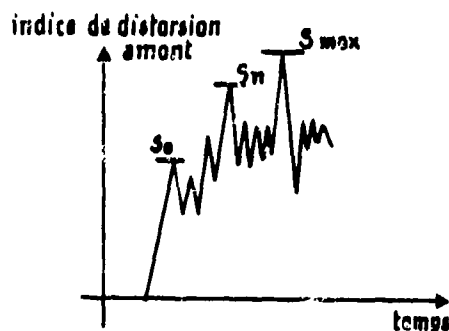


FIGURE 3

3.3 - Indice de détection :

Il doit être simple, car son calcul doit être nettement inférieur au temps de propagation de l'écoulement entre les détecteurs et le plan compresseur ($\approx 2 \text{ ms}$ si $X = 2 D$).

Une exploitation effectuée à l'ONERA montre qu'une pression d'arrêt (avec ses maxis ou ses minis) est un mauvais indice ; par contre, le maximum de différence entre deux pressions d'arrêt obtenues en des points diamétralement opposés, dans le plan de symétrie, prévoit environ les 2/3 des pics des divers coefficients de distorsion. Il faut noter cependant que tous les coefficients de distorsion envisagés (K, KD, IDC, IDR) ne donnent pas des extremums aux mêmes instants.

Ainsi, pour détecter le maximum de pics de distorsions, on envisage l'utilisation de 4 à 6 détecteurs ; 6 étant un maximum pour deux raisons :

- nombre d'informations à traiter en temps réel,
- création de sillages perturbant l'écoulement dans le plan de mesure.

L'indice de détection actuellement proposé est $I_d = P_{\max} - P_{\min}$ sur les "n" détecteurs installés.

3.4 - Critère de détection

L'indice de détection est calculé en temps réel, avec un programme en assembleur, avec une fréquence d'acquisition voisine de 16 KHz.

On se fixe un intervalle de temps " t_0 " pendant lequel on recherche le maximum de l'indice de détection qui servira de 1er seuil de détection.

$$S_0 = \max_{t=0 \text{ à } t=t_0} (I_d)$$

Un délai d'attente " t_0 " d'environ 0,1 s est envisagé actuellement.

Pour ne tenir compte que des perturbations d'une certaine importance par leur durée, on utilisera un indice moyenné sur plusieurs acquisitions (trois par exemple).

Il faut noter que cette moyenne n'est pas équivalente à la division par trois de la fréquence d'acquisition des détecteurs.

Un tel calcul (6 détecteurs et $n = 3$) s'effectue actuellement au mieux en utilisant une programmation en assembleur en environ 200 μ s ; valeur à comparer avec les 2 ms nécessaires à l'écoulement pour parcourir la distance "détecteurs-plan de mesure".

Ainsi, à partir de l'instant $t = t_1$, où un premier seuil S_0 est défini, l'acquisition sera déclenchée lorsque :

I_d sera supérieur à S_0 .

A cet instant, quatre actions débiteront :

- topage de la bande magnétique, pour retrouver ultérieurement les zones à traiter.
- après un éventuel "temps de retard" t_r , destiné à limiter le volume des informations à traiter, on stockera sur la mémoire tampon les informations recueillies sur le peigne :
 - 55 voies (extension possible à 64)
 - acquisition : 16 KHz
 - durée d'acquisition ~ 3 ms, soit environ : 50 prélèvements par voie correspondant à un historique portant sur 50 valeurs des 55 voies (durée maximale possible 16 ms).
- calcul d'un nouveau seuil de détection S_1 : il sera obtenu en recherchant le maximum de I_d qui suit le déclenchement du point de traitement.
- interdiction de lancer un nouveau point d'acquisition avant un "feu vert" qui sera précisé ultérieurement, fonction du traitement effectué en temps réel.

3.5 - Tests de choix du point de mesure

Lorsque le "feu vert" sera donné au système de détection, le déclenchement suivant sera effectif lorsque

I_d deviendra supérieur ou égal à S_1 , et ainsi de suite.

L'essai sera considéré comme terminé lorsqu'il n'y aura pas eu de détection pendant un temps prédéfini (t_m voisin de 10 s) ; cela signifiera que pendant ce temps t_m , aucune perturbation plus forte que la dernière détectée n'est apparue (problème posé au paragraphe 1).

Il faut noter que si aucune perturbation supérieure au seuil n'est apparue pendant le temps t_0 , il n'y a pas de déclenchement. Il faut cependant conserver la valeur, par exemple à $t = 0$, pour vérifier qu'il n'y a pas d'erreur sur le niveau du seuil en précisant la configuration étudiée (n° de point).

Si ceci se produit régulièrement, cela signifie que le t_0 est trop grand.

Par ailleurs, pour avoir le traitement de plusieurs points (et d'au moins un dans le dernier cas), on relancera d'office un nouveau cycle avec remise à $t = 0$ ($S = 0$).

3.6 - Traitement du point de mesure

Les informations acquises sur la mémoire tampon sont transférées sur le disque du HP 21C0 de la chaîne d'acquisition. Le traitement demandé consiste à calculer pour les 50 points enregistrés les principaux coefficients de distorsion (K_d , K_D , IDC, et IRD) et de fournir sur une imprimante les valeurs maximales de ces indices pour l'acquisition effectuée.

Un tel calcul a été effectué par l'ONERA sur un HP 21 MXF avec 36 pressions pour les 4 indices définis ci-dessus en 220 ms.

4. CAHIER DES CHARGES DU MOYEN GENERAL DE TRAITEMENT

4.1 - Compatibilité

Les organismes de recherches, les avionneurs et les motoristes utilisant des méthodes similaires d'analyse de l'écoulement, les échanges d'informations entre les différents partenaires doivent être organisés de façon à ce que chacun d'eux puisse directement obtenir les renseignements indispensables à la réalisation de ses objectifs propres.

Cette demande implique une compatibilité aussi poussée que possible entre les matériels et logiciels, de façon à garantir que l'exploitation d'une mesure d'intérêt général sera immédiate et identique chez l'un ou l'autre des participants.

Cette compatibilité ne doit évidemment pas freiner les programmes propres de recherche des Sociétés.

4.2 - Acquisition des données

L'acquisition des données dans le cadre de l'étude des hétérogénéités de l'écoulement devra respecter les diverses recommandations contenues dans les nombreux documents existants qui couvrent l'acquis des mesures précédemment effectuées (réf. 6 et 7).

Le plan de mesure des pressions d'arrêt résulte d'une définition commune unique ; il sera situé le plus près possible de l'entrée du compresseur sans toutefois affecter significativement les performances et la stabilité de la turbomachine, ce qui aurait pour effet de fausser les conclusions des études de compatibilité entrée d'air-moteur.

On rappelle que les études réalisées ont montré qu'il était important pour décrire avec suffisamment de précision les hétérogénéités circonférentielles d'utiliser au minimum huit peignes circonférentiellement équirépartis. La comparaison maquette-banc-vol se fera alors dans une position identique du peigne par rapport à la manche.

Les distorsions radiales seront enregistrées par cinq prises de pression d'arrêt par peigne disposées sur des équisurfaces. Des mesures complémentaires de l'angle d'incidence seront réparties sur chacun des peignes, ainsi que des mesures de température totale.

Des gains sur le temps de traitement sont possibles avec un dépouillement partiel sur ordinateur local, car on peut admettre l'une des réductions suivantes :

- limitation du nombre de points traités (~ 50),
- réduction du nombre de coefficients de distorsion calculés dans le plan de mesure pendant 2 ms,
- intégration de l'histoire de l'écoulement interne sur moins de 3 diamètres de la prise d'air.

4.3 - Mesures complémentaires

Outre les voies stationnaires destinées aux mesures dans le plan amont compresseur, plusieurs voies stationnaires ou instationnaires sont nécessaires pour enregistrer des paramètres supplémentaires qui sont spécifiques à chaque type d'essai (banc, vol, soufflerie) :

- le niveau de turbulence des diverses pressions statiques, des incidences, des références soufflerie, vol,
- les pressions statiques entre étages, la température totale à l'entrée du moteur, certains paramètres de régulation, l'instationnarité résiduelle en sortie du compresseur,, dans le cas de mesure au banc partiel ou au banc moteur.
- quelques-uns des paramètres moteurs cités précédemment, ainsi que des informations sur les paramètres aérodynamiques de l'avion (incidence, dérapage, nombre de Mach) et de la manche dans le cas de mesures sur avion.

Une base de temps doit également être systématiquement enregistrée lors de chaque essai.

Par rapport aux voies de mesure des pressions d'arrêt seules, on peut évaluer, dans chaque cas, à une vingtaine le nombre de voies affectées à ces divers usages : la spécification sera qu'au total 64 voies stationnaires puissent être enregistrées sans déphasage inacceptable entre voies.

4.4 - Bande passante

La bande passante utile des phénomènes dynamiques se détermine par l'influence relative qu'elle a sur le fonctionnement du moteur : ainsi, les distorsions de l'écoulement amont à très haute fréquence (supérieure à 4 fois la vitesse de rotation de la machine) affectent peu la stabilité du compresseur.

La corrélation coefficient de distorsion-perte de marge de pompage la meilleure s'obtient pour une bande passante variable suivant les compresseurs (nombre d'aubes, corde de la roue mobile ...) qui reste cependant proche de la vitesse de rotation de la machine. La figure (4) montre la variation du coefficient IDC max avec la bande passante. On constate que l'évolution autour de la fréquence correspondant à la vitesse de rotation de la machine est importante ; les résultats dépendront du choix de la bande passante utile.

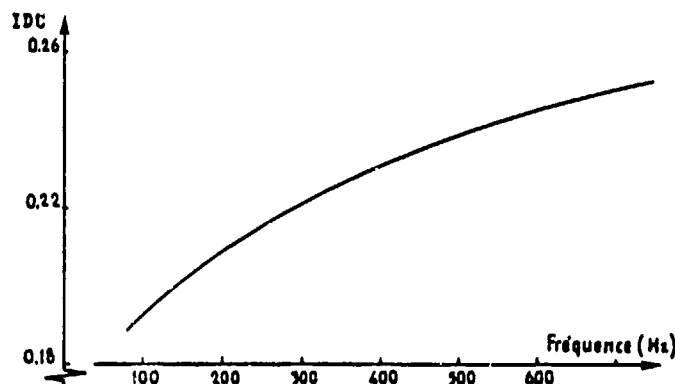


FIGURE 4

Rappelons qu'il faut également tenir compte du facteur d'échelle pour corriger les bandes passantes entre les essais sur maquette et les essais à l'échelle 1.

C'est ainsi que, si on considère que la vitesse de rotation maximum d'un fan est de 250 Hz (soit 15 000 t/mn), la bande passante utile ne dépassera pas 1 000 Hz à l'échelle moteur ; dans le cas d'une maquette à l'échelle 1/4, la bande passante utile sera alors de 4 000 Hz. Si l'acquisition est numérique, un taux d'échantillonnage égal à quatre fois la bande passante est suffisant pour éviter le repliement spectral et les autres erreurs dues à la mémorisation.

Cette bande passante peut évidemment être différente suivant le type de mesure effectué, notamment lors de l'étude des régimes transitoires ou instables.

4.5 - Temps et volume total d'acquisition

Le temps d'acquisition doit être suffisamment long pour que le calcul des coefficients de distorsion instantanés donne un maximum représentatif et assez court pour éviter d'accumuler des informations superflues. A titre indicatif, on donne sur la fig. 5 un exemple caractéristique de coefficients de distorsion calculés sur une manche à air. On voit que les dates des maxima sont extrêmement variables suivant le coefficient de distorsion ou même suivant la bande passante considérée. On admet, avec la plupart des auteurs, que 30 secondes à l'échelle moteur sont suffisantes dans la plupart des cas pour caractériser un point de fonctionnement. Une telle longueur d'acquisition ne pourra être obtenue en configuration de vol stabilisé que pour nombre limité de points du domaine de vol ; pour les autres, on l'obtiendra par répétition des essais (figure 5).

Enfin, le nombre d'essais peut être très variable selon les difficultés rencontrées au cours du développement de l'appareil, et requiert un suivi en temps réel minimum pour orienter les mesures dans les zones importantes à étudier.

Nous donnons (fig. 5) un exemple de sensibilité à ces paramètres, du résultat du calcul du coefficient DC60 qui montre que le résultat est fonction directe de la bande passante et du temps de calcul. La fig. 6 donne un exemple de dépouillement et de calcul continu des paramètres instantanés.

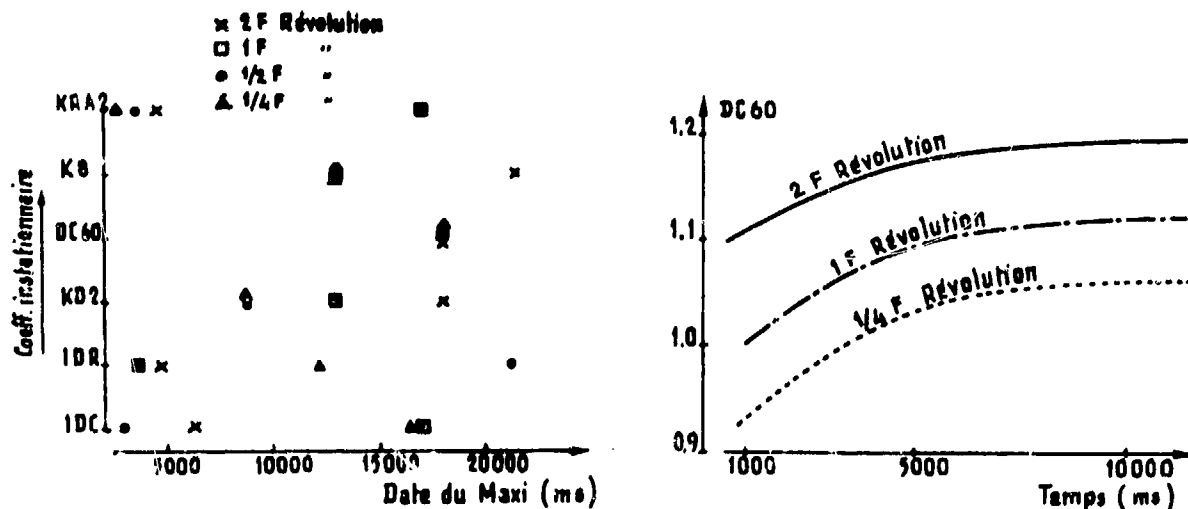


FIGURE 5

Les considérations précédentes nécessitent que le système soit capable d'acquérir au minimum $64 \times 1\,000 \times 4 = 256\,000$ informations numériques datées par seconde à l'échelle moteur ; en soufflerie, le nombre d'informations par seconde est multiplié par l'échelle de la maquette, le nombre global d'informations restant identique et proche de 7 millions pour une configuration (pour 30 secondes d'essais échelle grandeur).

Il est enfin souhaitable que plusieurs dizaines de cas puissent être enregistrés avant changement de support matériel.

COEFFICIENTS DE DISTORSION ET PRESSIONS D'ARRET INSTATIONNAIRES

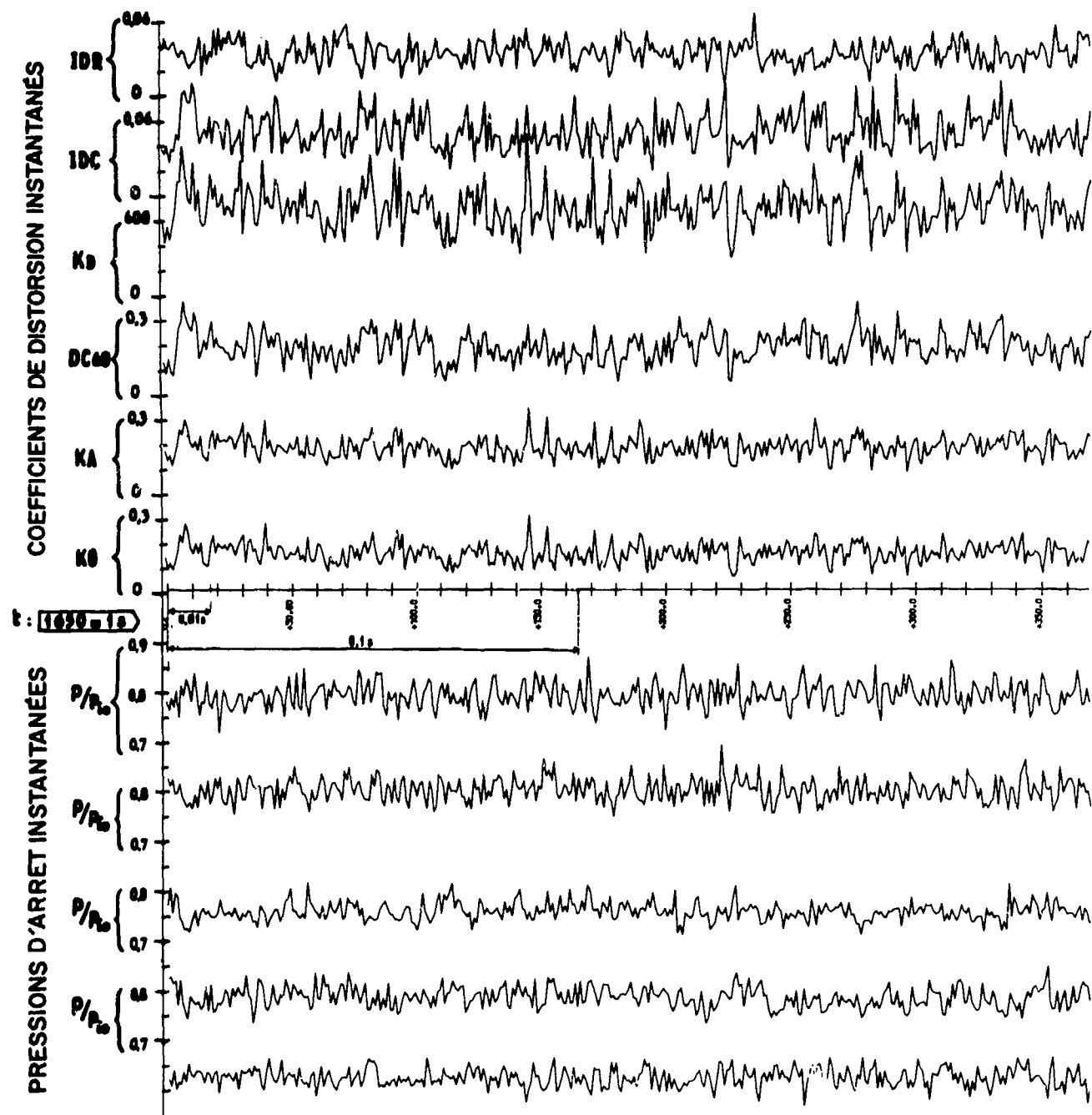


FIGURE 6

Ces informations devraient permettre de reconstituer un champ complet expérimental de vitesses extrêmes, analogue au champ théorique qui est tracé sur la figure ci-dessous et qui est le résultat à temps donné d'un calcul instationnaire des équations de Navier Stokes.

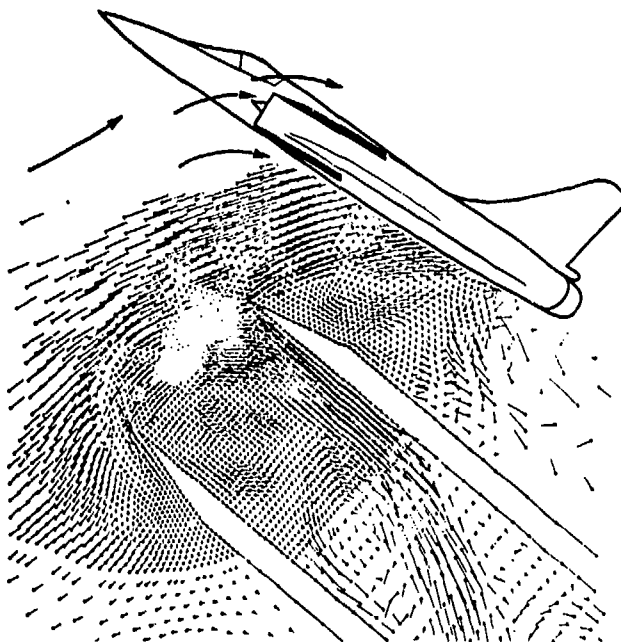


FIGURE 7

4.6 - Précision des mesures

- 4.6.1 - La détermination de la perte de marge induite par une hétérogénéité amont si elle dépend de la précision de la méthodologie (coefficient utilisé, bande passante, ...) requiert une bonne précision sur la mesure de la grandeur physique.

L'objectif fixé est d'effectuer une mesure avec une précision théorique d'environ 5 % pour la partie instationnaire, la précision absolue globale résultante étant, bien entendu, moins bonne ; cette précision caractérisera la fidélité des essais.

Seront distinguées, deux grandes sources possibles d'imprécision :

- 1) la précision des capteurs et la dérive de sensibilité des capteurs et de gain des amplificateurs,
- 2) le non synchronisme entre voies, la distorsion d'amplitude et le filtrage.

- 4.6.2 - On dispose actuellement de capteurs instationnaires ayant le niveau de précision requis mais il faut leur assurer un environnement adéquat. Les capteurs seront protégés afin d'éviter un endommagement rapide en atmosphère polluée, sans toutefois limiter la bande passante utile, un traitement spécial des problèmes thermiques est nécessaire pour éviter une dérive thermique excessive spécialement en vol et en soufflerie (Réf. 8).

Par suite de l'impossibilité d'assurer un fonctionnement sans défaut de l'ensemble des capteurs on assurera le remplacement des capteurs défectueux par une moyenne évaluée sur les capteurs voisins :

- la partie stationnaire sera, si nécessaire, calculée grâce aux n ($n = 3$ ou 4) prises stationnaires P_{TSS} adjacentes :

$$P_{TSS} = \frac{\sum_{i=1}^n \frac{1}{R_i} P_{TSS_i}}{\sum_{i=1}^n \frac{1}{R_i}} \quad R_i : \text{distance entre la prise considérée et la prise détériorée}$$

- la partie instationnaire sera de même calculée grâce aux n prises instationnaires adjacentes :

$$P_{TINS} = \frac{\sum_{i=1}^n \frac{1}{R_i} P_{TINS_i}}{\sum_{i=1}^n \frac{1}{R_i}} \quad R_i : \text{distance entre la prise considérée et la prise détériorée}$$

De plus, un contrôle par une valeur test devra être systématiquement effectuée avant et après essais.

- 4.6.3 - Le non synchronisme entre voies est une source d'erreur qui provient, soit d'un décalage statique ou dynamique entre pistes dans le cas d'un système d'enregistrement analogique, soit de la non synchronisation de l'échantillonnage en cas de numérisation. Un échantillonneur bloqueur par voie peut être indispensable pour assurer la synchronisation de l'échantillonnage, compte tenu de la large bande passante demandée.

La distorsion d'amplitude est fixée par les normes IRIG d'enregistrement magnétique et augmente lorsqu'on s'écarte de la plage linéaire de fonctionnement. L'erreur due au bruit de fond résulte d'un compromis avec l'erreur de distorsion d'amplitude. En effet, pour éviter d'écrêter le signal, il convient d'enregistrer plusieurs décibels en dessous de la pleine échelle, ce qui a pour conséquence de diminuer la dynamique utile. L'erreur peut alors atteindre plusieurs pour cent. Dans un système du type PCM, la dynamique est définie par le nombre de bits de la conversion analogique-numérique (soit 60 dB pour 10 bits) ce qui, avec une marge de 6 dB, conduit à une erreur de 0,2 % pour ce type d'enregistrement.

Le type de filtrage - qu'il soit analogique ou numérique - est également une source d'imprécision.

Rappelons que l'erreur imputable à la distorsion de phase est due au fait que la fonction de transfert d'un quadripôle est complexe et modifie, à la fois, l'amplitude et la phase du signal qui le traverse ; elle se produit en trois points de la chaîne :

- l'enregistreur analogique si ce type d'enregistreur est utilisé,
- le filtre anti-repliement avant conversion analogique digital s'il s'agit d'un filtre classique,
- le filtrage numérique lors du traitement si on utilise un filtre récursif.

Les filtres passe-bas simulés lors du traitement numérique peuvent également être source d'imprécision provenant du type de filtre utilisé ou de la précision souhaitée qui se fait au détriment du temps de calcul. Le tableau 1 présente un exemple de la réponse de divers types de filtres du point de vue du temps de calcul, du déphasage et de la valeur maximum d'un coefficient de distorsion K inst.

TABLEAU 1

TYPE DE FILTRE	DATE DU MAXI.	TEMPS RELATIF DE CALCUL.	VALEUR RELATIVE DE KINST
FILTRAGE ANALOGIQUE F = 630 HZ 48 dB/oct.	T		100
MULTIPLICATION SPECTRALE HANN TUKEY Définition Spectrale $\begin{cases} A(f) = 1 & f < f_1 \\ A(f) = \frac{1}{2} (1 + \cos(\pi(f-f_1))) & f_1 \leq f \leq f_2 \\ A(f) = 0 & f \geq f_2 \end{cases}$			
f1 = 156 HZ 48 dB/oct. Demi-longueur = 30 échantillons	T	162	89.9
f1 = 156 HZ 60 dB/oct. Demi-longueur = 30 échantillons	T	162	89.7
f1 = 156 HZ 60 dB/oct. Demi-longueur = 60 échantillons	T	278	89.8
f1 = 156 HZ 60 dB/oct. Demi-longueur = 20 échantillons	T	123	89.8
MULTIPLICATION SPECTRALE BARTLETT Définition Spectrale $A(f) = \frac{1}{9} (3 + 4 \cos(\pi \frac{f-f_1}{f_2-f_1}) + 2 \cos(2\pi \frac{(f-f_1)}{f_2-f_1}))$ $A(f) = 0 \quad f \geq f_2$			
f1 = 156 HZ 48 dB/oct. Demi-longueur = 30 échantillons	T	161	87.1
LISSAGE SPECTRAL CLASSIQUE. Sur 3 points poids (1/5, 1/5, 1/5, 1/5). f1 = 156 HZ 48 dB/oct. Demi-longueur = 30 échantillons.	T	158	85.1
LISSAGE SPECTRAL HANN TUKEY Poids (1/4, 1/2, 1/4). f1 = 156 HZ 48 dB/oct. Demi-longueur = 30 échantillons.	T	158	85.8
FILTRE RECURSIF BUTTER WORTH f = 156 HZ 8 pôles	T + 4	100	86.0

Le type de filtrage choisi - multiplication spectrale ou lissage spectral - peut avoir une grande importance sur le résultat, alors que la longueur du filtre, ou même sa pente, ont moins d'influence sur les résultats. Le filtre récursif Butterworth 8 pôles est particulièrement performant au niveau du temps de calcul ; cependant, il nécessite une programmation en quadruple précision pour assurer la stabilité numérique et introduit un déphasage important. Il est cependant impossible de fixer des normes, compte tenu des chaînes existantes en soufflerie ou en vol.

Enfin, pour faciliter la recherche, le stockage, l'exploitation et l'interprétation de ces informations, une structure de données commune pour tous les utilisateurs sera définie.

5. SOLUTIONS PROPOSEES

5.1 - Pour la réalisation générale de la chaîne de mesure, on se référera aux planches jointes décrivant le dispositif d'acquisition et d'analyse mis en place. Il peut se développer en :

- dispositif de détection rapide
- dispositif de saisie au banc et en soufflerie
- dispositif de saisie en vol

5.2 - Essais en soufflerie

Le dispositif de détection rapide retenu travaille en liaison avec l'ordinateur CII IRIS 80 du Centre de Modane.

La succession des séquences et tests est la suivante :

- une perturbation est détectée ;
- après un éventuel temps de retard, les valeurs numériques caractérisant 50 cartes instantanées sont stockées en mémoire tampon ;
- l'ensemble est transmis sur le disque du 2100 de la soufflerie ;
- le disque est aussitôt vidé sur l'IRIS 80 qui peut commencer le traitement ;
- le disque étant vidé, il donne le "feu vert" pour une détection suivante.

Ainsi toute l'acquisition, jusqu'à convergence du système peut se faire très rapidement, il n'y a pas d'attente pour le traitement entre deux acquisitions d'une même configuration.

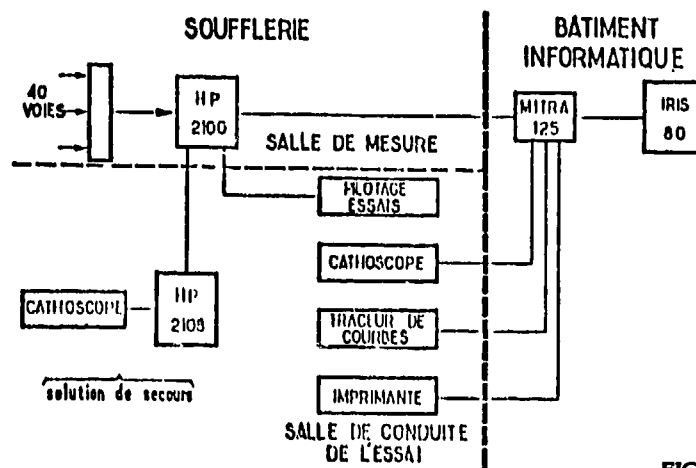
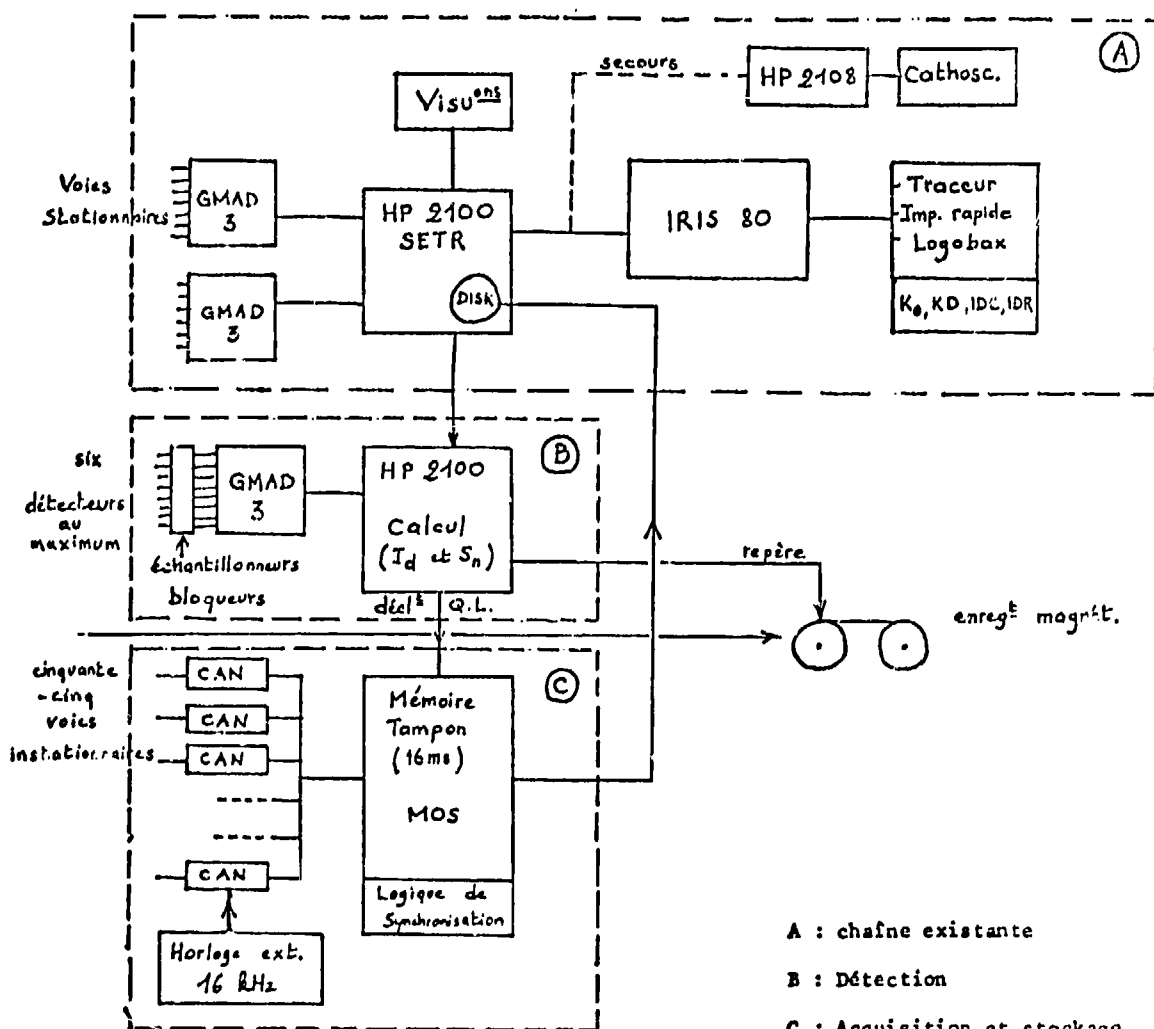


FIGURE 8

- ORGANISATION DE LA CHAÎNE -



A : chaîne existante

B : Détection

C : Acquisition et stockage
Ensemble "Quick Look"

En parallèle, MIRIS 80 travaille et sort successivement, sur une imprimante Logabax, les coefficients de distorsion maximaux calculés pour chaque détection.

Cette méthode permet de réduire les temps d'essai mais, bien sûr, en travaillant en temps quasi-réel.

L'adjonction dans le système de surveillance de l'essai, de l'ordinateur central, pose le problème de sa disponibilité. Dans le cas contraire, l'essai pourrait s'effectuer avec le système de secours habituellement mis en place à Modane qui consiste à réduire le traitement (10 plans au lieu de 50 par exemple à traiter de suite) et à l'effectuer sur le HP 2108 (les autres plans seront toutefois sur le disque du 2100 et donc transférables en temps différé sur l'IRIS 80).

Toute acquisition d'une série de plans de mesure sera suivie d'une sortie précisant les coefficients de distorsion maximaux sans se limiter à la seule sortie de la dernière acquisition qui correspond au maximum de l'indice de détection rencontré pendant l'essai. En effet, les divers coefficients de distorsion n'étant pas maximum au même instant, ils ne seront donc pas nécessairement tous au maximum, lors de la dernière acquisition.

5.3 - Essais au banc

A partir des spécifications générales exposées précédemment, un système complet d'acquisition et de traitement a été défini, ce système est capable de mesures en soufflerie, au banc et en vol.

L'option choisie est celle d'un enregistrement et d'un traitement entièrement numériques, grâce aux matériels performants actuellement disponibles sur le marché.

Les grands principes du fonctionnement général de la chaîne, dans le cadre du banc moteur (figure 9), sont exposés ci-après :

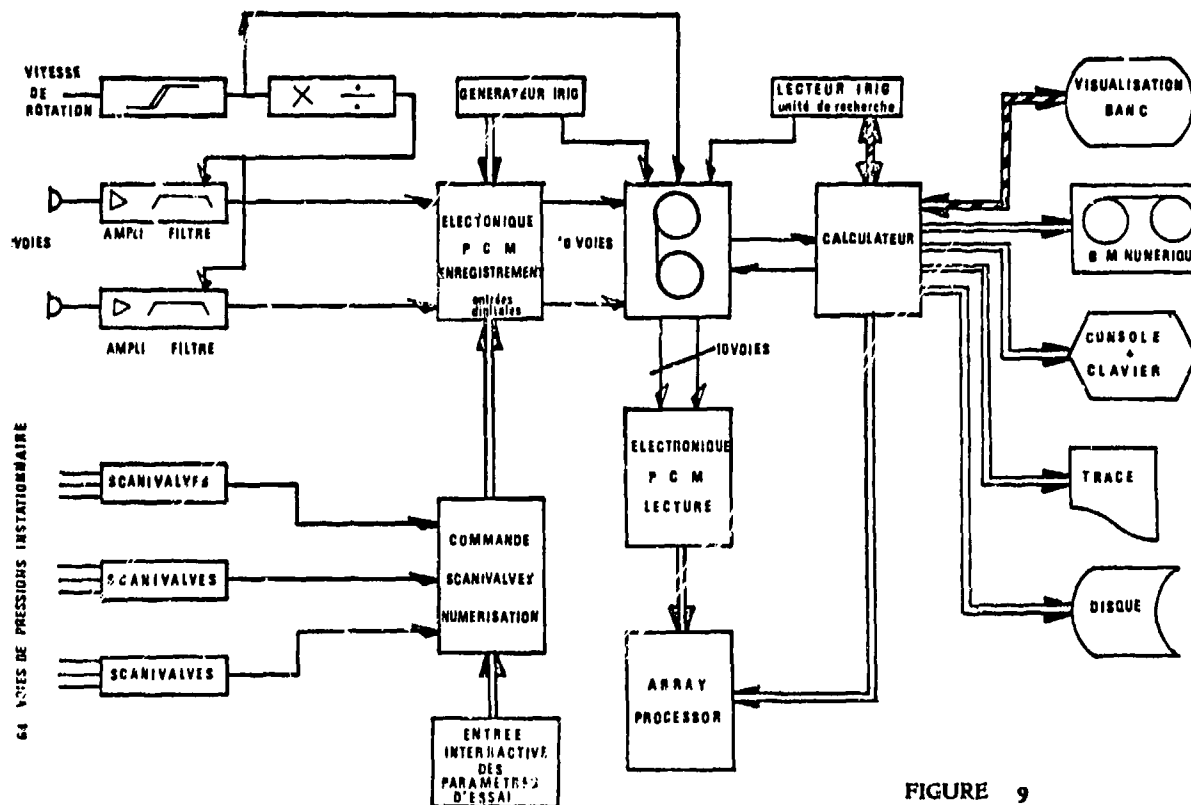


FIGURE 9

- Conditionnement

Les 64 signaux instationnaires sont amplifiés par des amplificateurs à gain variable, de façon à pouvoir tenir compte des dérives de sensibilité des capteurs, puis filtrés par un filtre passe-haut à 0,5 Hz et un filtre passe-bas transverse piloté par la fréquence de rotation de la machine.

Les grandeurs stationnaires sont acquises par un capteur unique commuté par scanivalve.

- Enregistrement

Le système d'enregistrement PCM assure la numérisation sans déphasage et à cadence variable et l'enregistrement des signaux instationnaires acquis séparément par scanivalve. Une base de temps IRIG est également enregistrée sur la même bande que les signaux instationnaires et des voies stationnaires acquises séparément peuvent être mixées.

Dans le cas d'enregistrement avec calcul en temps réel, le calculateur peut positionner des marqueurs sur une des pistes pour sélectionner les moments intéressants en vue d'un dépouillement ultérieur.

- Système de calcul temps réel et de dépouillement

C'est le même système qui est utilisé pour le calcul temps réel et le dépouillement.

Il comprend un array-processor qui assure la réévaluation des capteurs défectueux, le filtrage numérique des signaux, si nécessaire, et le calcul de coefficients simples en temps réel. La recherche et le marquage des instants où ces coefficients dépassent un seuil spécifié est effectué par le calculateur.

En temps différé, le système est capable d'effectuer tous les calculs numériques sur l'enregistrement complet.

Un certain nombre de périphériques - traceurs rapides, console et clavier, disque, - sont interfacés au calculateur. Une liaison avec le banc d'essais et une structure de données centrale est également prévue.

5.4 - Essais en vol

Le dispositif retenu utilisant le même type d'acquisition qu'au banc est trop volumineux et lourd pour être installé dans un avion de combat de la taille du MIRAGE 2000. Aussi pour les mesures de distorsion sur cet avion, on fait appel dans un premier temps à un enregistrement analogique FM multiplexé où la synchronisation parfaite requise entre les différentes pistes est obtenue par une base de temps IRIG sur chaque tête. Cette méthode a fait ses preuves par le passé et elle ne soulève aucune difficulté fondamentale sur le plan technologique.

CONCLUSION

A partir des besoins d'évaluation du champ aérodynamique à l'entrée du compresseur des réacteurs et de ce qui est réalisable avec les moyens d'acquisition et de traitement actuel, on a présenté les spécifications et les détails de réalisation d'un ensemble de mesures. Les caractéristiques aérodynamiques instationnaires à l'entrée du compresseur pourront ainsi être mesurées avec une fiabilité suffisante, tant dans les essais au banc que dans les essais en soufflerie et en vol. L'interprétation des résultats devrait permettre des progrès dans l'évaluation de la compatibilité entrée d'air - réacteur par le choix de critères de sensibilité instationnaires et, par conséquent, permettre une meilleure adaptation du moteur et des cellules aux conditions plus sévères de fonctionnement propres aux nouveaux avions militaires.

REMERCIEMENTS

Les auteurs tiennent à remercier les différents personnels de l'ONERA et M. CZINCZENHEIM (AMD-BA) pour leurs recommandations et leur aide dans la mise au point du système d'acquisition analogique actuellement en usage pour tous les essais d'entrée d'air industriels à l'ONERA à Modane et leurs conseils et recommandations pour la nouvelle chaîne en cours de réalisation qui est décrite dans ce papier.

- Pour la définition de la chaîne des essais en vol AMD-BA : MM. COSTARD et PATUREAU
- Pour le dépouillement des essais : le Département d'Aérodynamique Expérimentale des AMD-BA et le personnel spécialisé des Grands Moyens d'Essais de l'ONERA.
- Pour la définition des clauses techniques : M. EYRAUD et AUZOLLE de la SNECMA.

REFERENCES

1. P. BOHN Aérodynamique de la Nouvelle Génération d'Avions de Combat à Aile Delta - Fighter Aircraft Design - AGARD CP241.
2. G. KARADIMAS Mesures Instationnaires dans les Entrées d'Air - Etudes Préliminaires -
M. GOUTINES Compte rendu interne SNECMA.
B. DELAHAYE
3. MELICK Estimating maximum instantaneous distortion from inlet total pressure
YBARRA RMS measurements AIAA 78 - 970.
BENCZE
4. STEVENS Evaluation of a Statistical Method for Determining Peak Flow Distortion using
SPONG F.15 and F.18 Data AIAA 80 - 1109.
OLIPHANT
5. G. LARUELLE Etude des Distorsions Instationnaires dans les prises d'air à forte incidence -
L'Aéronautique et l'Astronautique 1981 (à paraître).
6. SCHWEIKHARD Test Technics, instrumentation and data processing, AGARD LS-72.
7. ARP 1420 - March 1980 - Gas Turbine Engine Inlet Flow Distortion Guidelines
8. M. GRANDJACQUES Mesures Instationnaires dans une prise d'air - L'Aéronautique et l'Astronautique
n° 74-1979.

A SYNTHESIS METHOD FOR ESTIMATING MAXIMUM INSTANTANEOUS INLET DISTORTION
BASED ON MEASURED INLET STEADY STATE AND RMS PRESSURES

By Ronald Borg
Aerodynamics Department
Volvo Flygmotor AB
S-461 81, Trollhättan, Sweden

SUMMARY

The requirement for maximum instantaneous inlet distortion measurement has increased the cost and work involved in test and data reduction immensely. Therefore, for screening purposes, there is a need for a method to estimate maximum instantaneous distortion based on time averaged values such as steady state and RMS inlet rake pressure using small scale models and relatively sparse instrumentation. A synthesis method based on steady state and RMS pressure measurements has been developed using a simple mathematical computer model which estimates the maximum value of an engine distortion index. The estimated values obtained with the computer model have been correlated with actual measured maximum instantaneous distortion values from several different tests and the results indicate that the method is useful in an inlet-airframe-engine configuration development program.

The method is not proposed to eliminate time correlated multi channel instantaneous distortion measurements, it is primarily intended as a tool for screening configurations before final selection and commitment to more expensive testing. The synthesis method has also been complemented with extreme value analysis of the computer generated distortion data in order to evaluate the likely increase in maximum distortion index with increased time of observation.

LIST OF SYMBOLS

b	weighting term applied to K_{RA2}
D_{C0}	$\theta^\circ = 60; 90; 120; 120$ GG (Rolls Royce)
f_c	cut-off frequency
GG	gas generator
IDC, IDR	circumferential and radial index (G.E.)
K_θ	circumferential distortion index (P & W)
K_{A2}	weighted sum of K_θ and K_{RA2} (P & W)
K_{C2}	core flow circumferential index (P & W)
K_R	radial distortion index (P & W)
K_{RA2}	radial distortion index (P & W)
ΔP_{RMS}	root mean square total pressure fluctuation at a probe around a steady state value
$\overline{\Delta P}_{RMS}$	average of several probe root mean square values
\overline{P}_{T2}	compressor face steady state average pressure
q	average steady state dynamic pressure at compressor face
W_c	corrected engine weight flow
σ	standard deviation
α	angle of attack

INTRODUCTION

In the late 1960:s it became apparent that all inlet testing would have to be carried out with dynamic probe instrumentation in the future in order to properly account for the effects of inlet distortion on the engine stability margin. This is shown for instance in ref 1. The result of this was an immense increase in cost and work involved in screening the data with analogue computers and then followed by digital data reduction of massive amounts of data. Dynamic testing is here understood to mean measurement of maximum instantaneous inlet distortion using multichannel time correlated time variant pressure data. This has been described in ref 2 for example. The measurement of maximum instantaneous inlet distortion also increased the required minimum size of the wind tunnel inlet models to $\approx 1/6$ th scale from $1/20$ to $1/10$ th scale generally used in the early development phase of a project. This was due to the sheer physical size of the multichannel dynamic probe rake required for the time correlated data. This in turn eliminated several smaller types of wind tunnels for inlet work and several facilities also did not have the dynamic data reduction equipment and computer power required for analogue and/or digital data reduction of the inlet data.

SMALL SCALE DYNAMIC INLET TEST

In 1972 a dynamic inlet distortion test was carried out on a 1/10 th scale inlet model of a combat aircraft, ref 3. Due to cost restraints the model used was an existing inlet steady state test model which had been used in a multitude of tests previously. The small scale limited the dynamic probe array to 12 in addition to 16 steady state probes arranged as shown in a half face compressor inlet configuration in figure 1.

The test conditions were the following:

Angle of attack 0 to 25 deg.

Mach number 0 to 0.8.

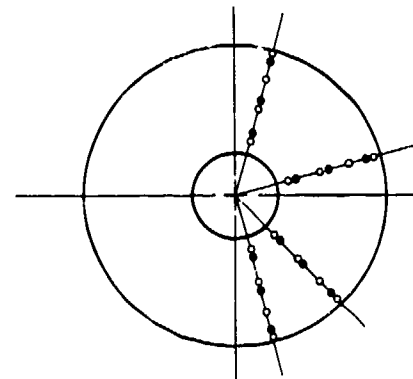
Inlet-engine mass flow varied from 30 % to 110 % of design flow.

Due to cost restraints only 40 % of the inlet test conditions were digitally reduced and screened for maximum instantaneous distortion values with a properly scaled engine response cut-off filter, (1600 Hz), while $\Delta PRMS$ and steady state probe data were measured at all the test conditions. The maximum instantaneous distortion data points were picked from a distortion sample of 500 values of the screened index used. This number was again related to the cost of data reduction. Data at a few test conditions were evaluated with up to 2000 samples but these did not show significant increases in maximum distortion values.

Dynamic distortion data were urgently needed for the RM8B engine computer simulator, but it was clear that the wind tunnel data could not be used directly without some special treatment due to the sparse probe instrumentation used in the test.

Large amounts of steady state distortion data were available from a multitude of previous tests with closely spaced instrumentation (up to 72 probes). There was therefore a great need for a synthesis method that could put together all the data available and estimate the maximum instantaneous distortion at all the flight conditions required for the installed engine simulator.

1/10TH SCALE INLET MODEL HALF FACE INSTRUMENTATION



16 ○ STEADY STATE PROBES
12 ● HIGH RESPONSE PROBES

Fig. 1

COMPUTER MODEL FOR DISTORTION SYNTHESIS

The computer model uses a steady state distortion pattern together with local RMS-pressure fluctuations and a fixed APD-distribution at a number of probe locations or rake geometry. The information is combined to an artificial instantaneous distortion pattern using a computer with a random number generator and a chosen distortion index is evaluated. The process is repeated a large number of times and the generated pattern producing the maximum distortion index is retained. The method is a close analogy to the evaluation of maximum instantaneous distortion in a test. The method was applied to the 1/10 th scale model data.

Analysis of the inlet model test data showed that only 0.1 % of the probe ΔP 's exceeded $\pm 3 \sigma$ in amplitude. Also APD's (Amplitude Power Density) in the form of histograms showed that the pressure data were relatively close in form to a normal Gaussian probability pressure distribution as shown in figure 2.

PSD (Power Spectral Density) analysis of probe pressures showed that the energy was distributed relatively evenly over all frequencies with no concentration to any specific frequencies, ref 3. A check on average vortex size according to a method outlined in ref 4 showed that the average vortex size in the inlet duct was 5 % of the duct diameter based on the measured PSD's. It could therefore be assumed that with the spacing used in the model rake the pressure correlation between probes would generally be weak.

After trying several different approaches to the computer pressure generation as described in detail in ref 5, the method shown in figure 3 yielded the best results when correlated with measured maximum instantaneous distortion.

The normally distributed random numbers are actually generated by adding 12 independent random numbers which are uniformly distributed over the interval (0;1). Such a random number generator is often available in a computer system yielding fast results. By adding 12 such numbers we get a random number which is approximately normally distributed according to the central limit theorem of mathematical statistics. A linear transformation can then be applied to yield a number with the desired mean value and standard deviation.

The input to the computer consists of the measured probe steady state and $\Delta PRMS$ pressure values with the $\Delta PRMS$ values measured with a suitable cut-off filter. The computer then generates a random pressure at each probe and calculates a chosen distortion index value for the rake geometry used. This is repeated until a sufficient number of distortion samples have been generated and the maximum value is retained with its corresponding pressure distribution.

HISTOGRAMS OF MEASURED PRESSURE
AMPLITUDES COMPARED TO NORMAL GAUSSIAN
PROBABILITY DISTRIBUTION
MACH = 0.74 $\alpha = 25^\circ$ $W_c = 281$ lbs/sec

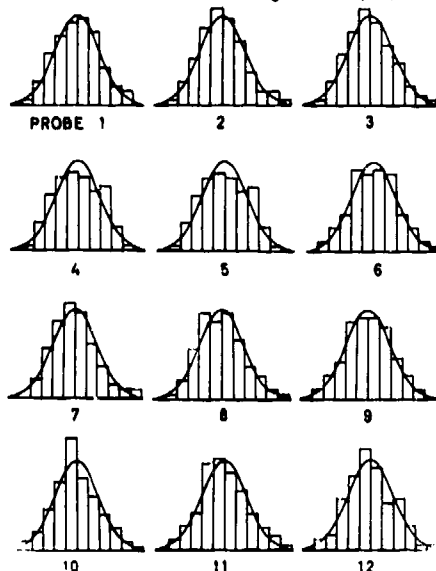


Fig. 2

COMPUTER MODEL FOR RANDOM DYNAMIC PROBE PRESSURE GENERATION

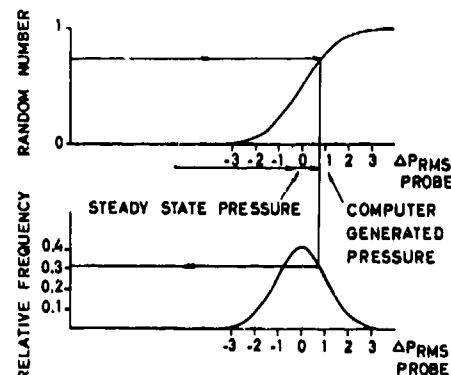


Fig. 3

COMPARISON OF COMPUTER GENERATED MAXIMUM DISTORTION WITH 1/10 TH SCALE MEASURED INSTANTANEOUS VALUES

The values of maximum K_θ circumferential index and K_R radial index obtained from the computer (500 samples) were compared with the maximum instantaneous measured values (500 samples) obtained from the 1/10 th scale model inlet test. Results are shown in figures 4, 5 and 6 with K_θ in figures 4 and 5 for two different inlet configurations and K_R in figure 6. These results are typical for the 49 inlet test conditions that were digitally reduced to obtain instantaneous distortion data, see ref 5. As can be seen the circumferential index is on the average somewhat underestimated while the radial index is overestimated.

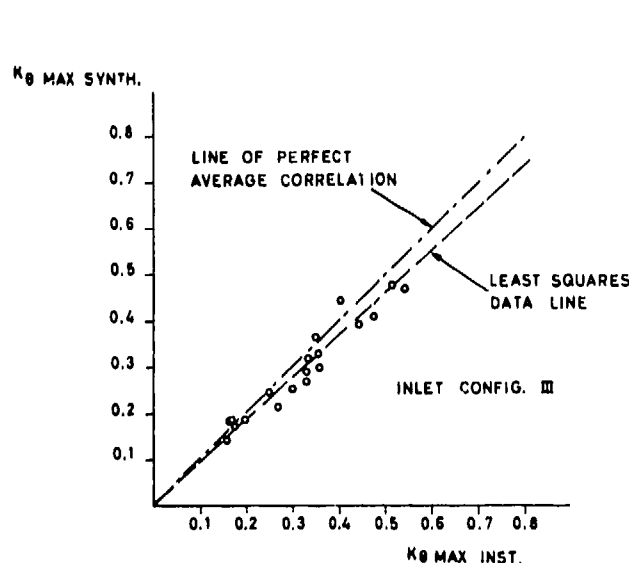


Fig. 4 Comparison of max. inst. and max. synth. distortion

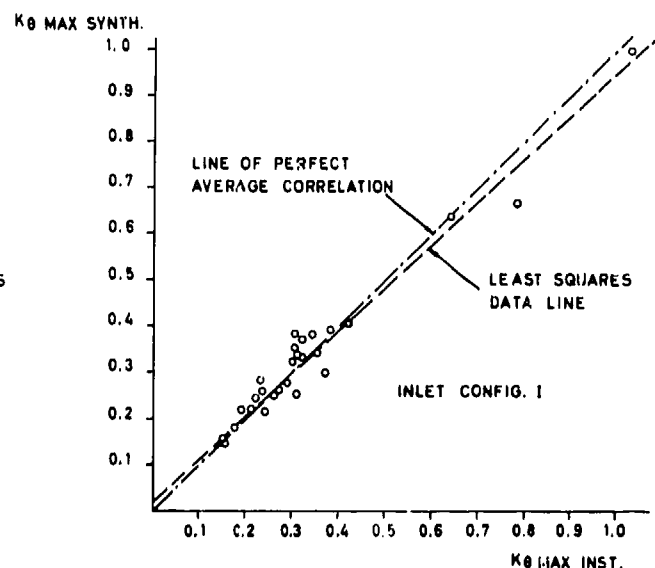


Fig. 5 Comparison of max. inst. and max. synth. distortion

Figure 7 shows the effect of using an average of $\Delta PRMS$ at all probe stations in the computer and then comparing these values with max instantaneous values. This was a check on how sensitive the distortion values are to local turbulence values rather than the average intensity of the turbulence. As can be seen in figure 7 there was no drastic change in correlation when compared to figure 4. Therefore there seemed to be a possibility of using a reduced amount of dynamic probes if these reflect an average of the turbulence intensity and then applying these values to a more closely spaced steady state rake configuration in the computer model.

These results were considered sufficiently encouraging to go ahead and use the method to generate distortion values for the RM8B computer simulator using steady state information from inlet models with dense compressor face rakes and ΔP_{RMS} values from the 1/10 th scale dynamic inlet test.

At this stage it could be argued that the correlation achieved was due to the sparse rake configuration and that the method would not be successful with more closely spaced instrumentation due to increased correlation between probes. It therefore remained to verify the method with maximum instantaneous distortion data obtained in tests with closely spaced rakes (≈ 48 probes) and these data would have to be obtained from sources outside VFA.

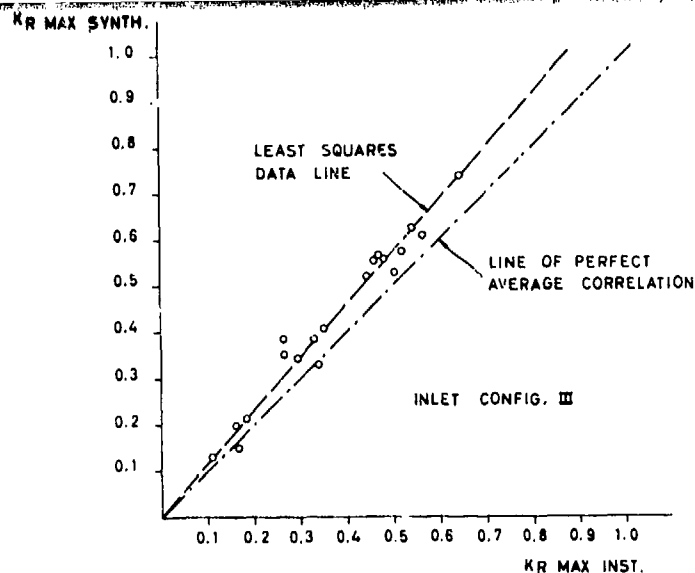


Fig. 6 Comparison of max. inst. and max. synth. distortion

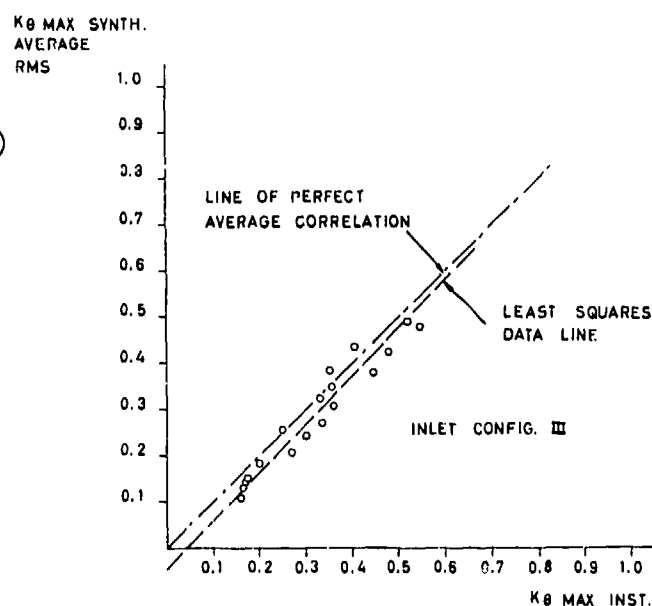


Fig. 7 Comparison of max. inst. and max. synth. distortion

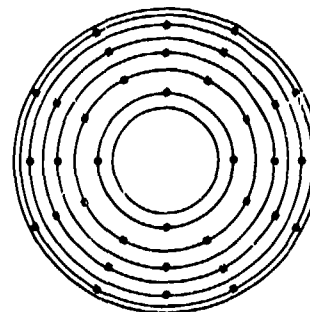
TEST OF THE DISTORTION SYNTHESIZING METHOD ON DATA MEASURED WITH CLOSELY SPACED INSTRUMENTATION

With the kind cooperation of P & W and Rolls Royce it has been possible at different occasions to obtain data for further verification with closely spaced rake configurations.

- I. Four test cases were obtained through P & W Hartford. The results of the application of the synthesis method to these data is reported in detail in ref 6. The data of the four test cases were taken from a test described in ref 7.

Figure 8 shows the rake configuration used in the test and the table summarizes relevant details and data about the test cases used.

RAKE CONFIGURATION FOR P & W HARTFORD TEST CASES WITH CLOSELY SPACED INSTRUMENTATION



36 STEADY STATE AND
36 HIGH RESPONSE PROBES

Fig. 8

CASE	1	2	3	4
$\frac{\Delta P_{RMS}}{P_{T2}}$	0.016	0.022	0.012	0.016
P_{T2}/q	18.87	13.91	16.29	16.29

STEADY STATE (FULL FACE)

K_θ	0.183	0.601	0.544	0.582
------------	-------	-------	-------	-------

MAX INST.

K_θ	0.664	0.859	0.987	1.040
------------	-------	-------	-------	-------

MAX SYNTH.

K_θ	0.591	0.881	0.843	1.009
------------	-------	-------	-------	-------

STEADY STATE (SPLITTER)

K_θ	0.235	0.755	0.242	0.246
------------	-------	-------	-------	-------

MAX INST. (SPLITTER)

K_θ	0.621	1.021	0.889	0.854
------------	-------	-------	-------	-------

MAX SYNTH. (SPLITTER)

K_θ	0.738	0.881	0.843	1.039
------------	-------	-------	-------	-------

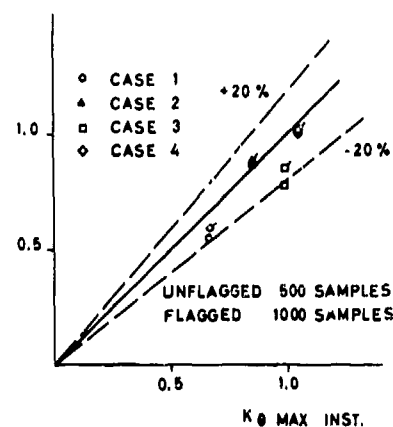
K θ MAX SYNTH.

Fig. 9 Comparison of max. inst. and max. synth. distortion

The input data to the synthesis computer program were given in the form of steady state pressures and ΔP_{RMS} pressures at each probe.

A comparison of K_θ is shown in figure 9. The synthesized data were evaluated with 500 and 1000 samples. It has not been possible to trace the sample size of the instantaneous data. Figure 9 shows that there is a significant improvement when going to 1000 samples and that the correlation is well within $\pm 20\%$ with a trend towards underestimate of maximum instantaneous values for the few cases shown. These results are very similar to the results obtained from the 1/10 th scale model inlet test and gave an indication that the synthesis method did not deteriorate when data with closely spaced instrumentation were used.

Figure 10 shows the result of using full face average ΔP_{RMS} at all probe stations and this apparently increases the underestimate when compared to figure 9 where local ΔP_{RMS} values were used. Figure 11 shows K_θ splitter coreflow calculations and in this case the correlation is more centered.

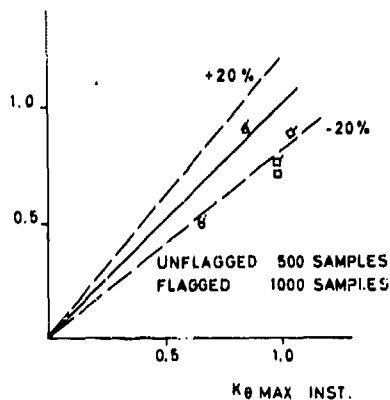
K θ MAX SYNTH
AVG. RMS

Fig. 10 Comparison of max. inst. and max. synth. distortion

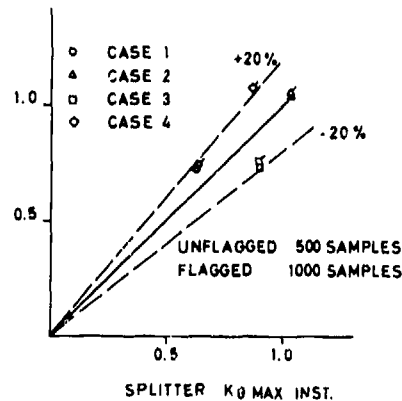
SPLITTER K θ MAX SYNTH.

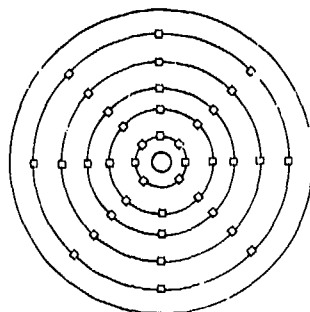
Fig. 11 Comparison of max. inst. and max. synth. distortion

- II. Data of nine test cases were obtained from Rolls Royce representing maximum instantaneous test data from 1000 samples (1 second of digitized data) ref 8. Figure 12 indicates the rake geometry used. The nine test cases are summarized in the table below.

ROLLS ROYCE DISTORTION DATA CASES

CASE	1	2	3	4	5	6	7	8	9
$\frac{\Delta P_{RMS}}{P_{T2}}$	0.012	0.010	0.014	0.010	0.011	0.012	0.015	0.021	0.020
$\frac{P_{T2}}{q}$	7.395	7.863	7.800	8.187	7.985	7.895	7.722	9.219	10.726

RAKE CONFIGURATION FOR ROLLS ROYCE
TEST CASES WITH CLOSELY
SPACED INSTRUMENTATION



40 STEADY STATE AND
40 HIGH RESPONSE PROBES

Fig. 12

STEADY STATE DISTORTION

D_{C60}	0.331	0.174	0.349	0.119	0.188	0.310	0.403	0.421	0.412
D_{C90}	0.297	0.089	0.317	0.103	0.165	0.282	0.371	0.381	0.376
D_{C120}	0.253	0.080	0.278	0.070	0.143	0.242	0.328	0.339	0.336
$D_{C120\text{ GG}}$	0.250	0.042	0.268	0.057	0.109	0.228	0.340	0.291	0.255

MAX INST. DISTORTION

D_{C60}	0.464	0.272	0.484	0.250	0.301	0.329	0.549	0.629	0.658
D_{C90}	0.404	0.234	0.484	0.219	0.266	0.382	0.502	0.569	0.586
D_{C120}	0.332	0.190	0.417	0.182	0.221	0.319	0.441	0.514	0.540
$D_{C120\text{ GG}}$	0.367	0.206	0.390	0.172	0.231	0.321	0.463	0.583	0.496

MAX SYNTH. DISTORTION

D_{C60}	0.450	0.204	0.487	0.234	0.288	0.442	0.524	0.603	0.574
D_{C90}	0.392	0.177	0.436	0.188	0.239	0.370	0.478	0.535	0.516
D_{C120}	0.325	0.163	0.375	0.167	0.205	0.321	0.412	0.468	0.468
$D_{C120\text{ GG}}$	0.393	0.125	0.379	0.131	0.191	0.352	0.461	0.468	0.458

Figures 12 through 16 show the correlation obtained with 500 and 1000 samples with a worthwhile improvement when using 1000 samples. The evaluated index values are $D_{C\theta}$ with $\theta = 60; 90; 120$ and 120 gas generator (3 inner rings). The results are extremely encouraging and the general trend is again towards some underestimate. In reference 8 some additional inlet data are treated by Rolls Royce where also the results of the effect of reduced ΔP_{RMS} probe information shows very encouraging results.

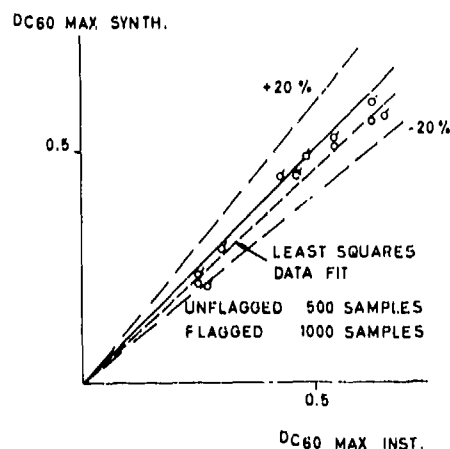


Fig. 13 Comparison of max. inst. and max. synth. distortion

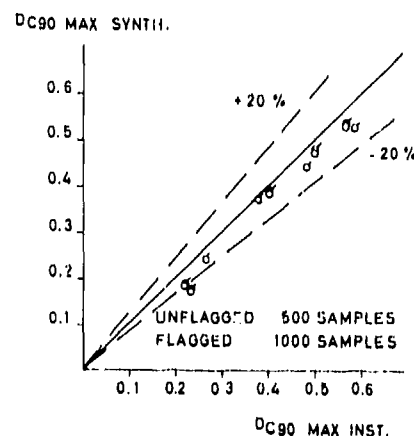


Fig. 14 Comparison of max. inst. and max. synth. distortion

DC120 MAX SYNTH.

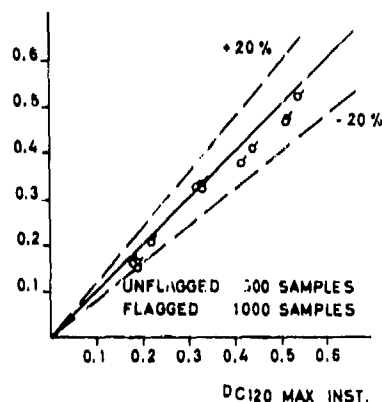


Fig. 15 Comparison of max. inst. and max. synth. distortion

DC120 GG MAX SYNTH.

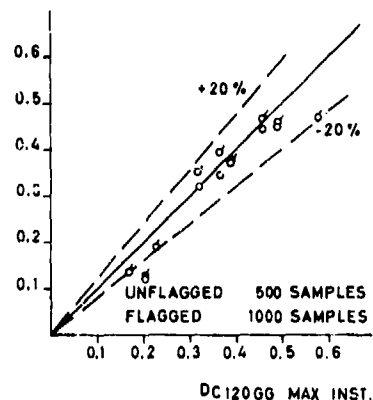
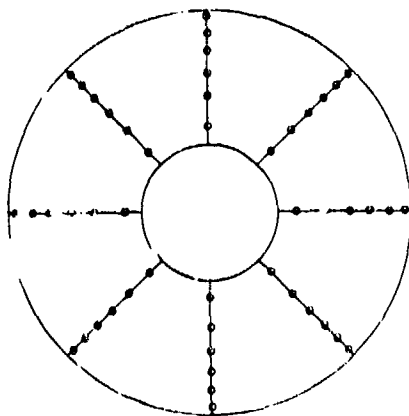


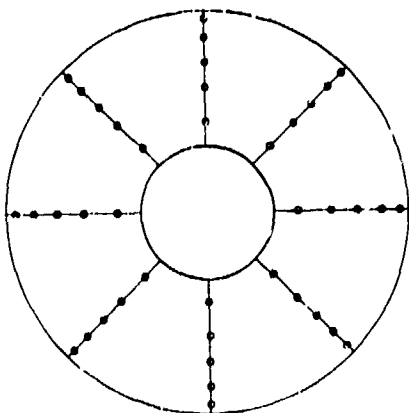
Fig. 16 Comparison of max. inst. and max. synth. distortion

III. Four test cases were obtained from P & W Florida. The application of the synthesis method to these data has been treated in detail in ref 9. The table below summarizes relevant details and data of these test cases. These data have their origin in tests later reported in ref 10 and 11. The sample size used to pick the maximum instantaneous values is presently not known to the author but it is probably greater than 1000. As can be seen from the table cases 1 and 2 are very high ΔP_{RMS} cases while cases 2 and 3 are more normal inlet operating conditions. The rake configurations used are shown in figure 17.

RAKE CONFIGURATION FOR P & W FLORIDA
TEST CASES WITH CLOSELY
SPACED INSTRUMENTATION
TEST CASES 1 AND 2



48 STEADY STATE AND
48 HIGH RESPONSE PROBES
TEST CASES 3 AND 4



40 STEADY STATE AND
40 HIGH RESPONSE PROBES

Fig. 17 A, 17 B

P & W DISTORTION DATA CASES

KA₂ SCREEN

CASE	1	2	3	4
$\frac{\Delta P_{RMS}}{P_{T2}}$	0.107	0.081	0.012	0.022
$\frac{P_{T2}}{q}$	7.06	6.27	6.31	6.08

STEADY STATE DISTORTION

K_θ	0.735	0.695	0.076	0.178
K_{RA2}	0.138	0.110	0.474	0.484
K_{A2}	0.905	0.846	1.072	0.908
K_{C2}	0.463	0.563	0.042	0.168

MAX INST. DISTORTION

K_θ	1.224	1.272	0.069	0.216
K_{RA2}	0.293	0.465	0.520	0.565
K_{A2}	1.585	1.929	1.216	1.068
K_{C2}	1.167	1.150	0.066	0.314

MAX SYNTH. DISTORTION

K_θ	1.179	1.136	0.076	0.262
K_{RA2}	0.378	0.278	0.506	0.529
K_{A2}	1.644	1.528	1.191	1.057
K_{C2}	1.117	1.020	0.096	0.265

KC₂ SCREEN KC₂ MAX SYNTH. DISTORTION

K_{C2}	1.301	1.366	0.162	0.397
----------	-------	-------	-------	-------

Figure 18 shows the results of KA_2 correlation and also includes a comparison of the distortion components that constitute the value of KA_2 namely the circumferential index K_0 and the radial index KRA_2 . The data were screened for max value of KA_2 and the synthesized data is based on 1000 samples. Figure 18 shows that cases 1; 3 and 4 are well predicted in KA_2 while case 2 is 20 % underestimated. Looking at the component values one can expect that getting a good estimate of the individual terms is rather remote when screening on the sum and the plot shows that case 1 and 2 radial terms KRA_2 are off in either direction. Extreme value analysis of a 1000 sample synthesized values shows that the case 2 point has a likely increase to values indicated by the flagged triangle in figure 18, if the sample size is increased to very large values.

Figure 19 shows the results of correlation of KC_2 screened on KA_2 and these results are extremely satisfying. If the synthesized data are screened for maximum KC_2 instead much higher values of KC_2 are obtained as indicated in the table of the test cases. The test cases were also compared using the DC_{60} index and the results are shown in figure 20. Although the P & W data were screened on KA_2 the results are not very different with the synthesized points screened on DC_{60} . Case 2 was also run with 2000 samples and showed a definite improvement. Figure 21 shows the effect of using the rake ring 3 $\Delta PRMS$ values (8 probes) radially constant and it shows virtually no effect on calculated values in figure 20. A midspan ring $\Delta PRMS$ information only, apparently yields very good results as shown also in ref 8 on inlet data not included in this paper.

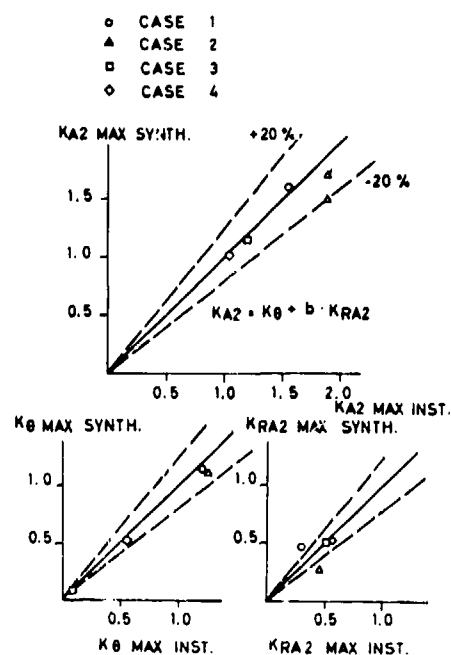


Fig. 18 Comparison of max. inst. and max. synth. distortion

HIGH COMPRESSOR DISTORTION FACTOR.
VALUES SCREENED ON FAN FACTOR KA_2

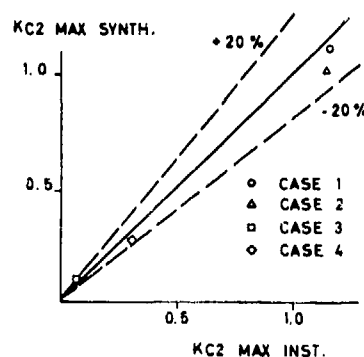


Fig. 19 Comparison of max. inst. and max. synth. distortion

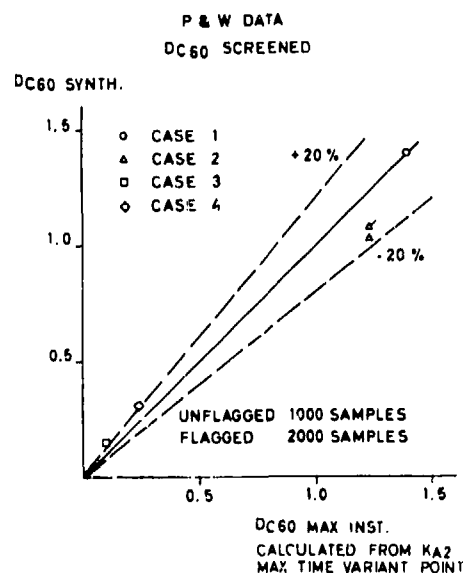


Fig. 20 Comparison of max. inst. and max. synth. distortion

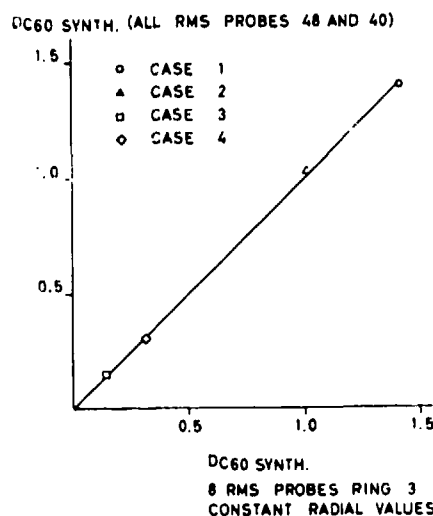


Fig. 21 Comparison of max. synth. distortion with complete and reduced instrumentation

EXTREME VALUE ANALYSIS

Ref 12 describes a method of extreme value analysis of inlet data whereby it is possible to predict the likely increase in an inlet distortion index with time (or sample size) by using a relatively limited sample size or time period of data. Actually 1000 samples is the minimum recommended with 20 extremes and 50 independent samples for each extreme. Extreme value analysis has been incorporated in the synthesis program and is applied to the generated distortion values. Test of the prediction when comparing synthesized and measured values is limited due to lack of instantaneous measured complete data samples. A comparison has been made between measured and synthesized data for data point 29/3 from the 1/10 th scale test, and the results are shown in figure 22. The index K_0 is plotted versus a log time scale and includes synthesized values and measured data values for sample sizes of 500; 1000 and 1500. With sample size 500 the faired curves (3-rd asymptote) show different trends.

This is also the case with 1000 samples where the test data include 3 higher distortion values at the end of the sample while the synthesized values still include only one high value and this results in different extrapolated trends with time.

With 1500 samples the synthesized data have picked up an additional high value point while the test data have not picked up any higher value from the increased sample size.

This now results in quite similar trends of expected distortion values with time or increased sample size. One can then conclude that for this particular data point extrapolation to larger sample sizes requires at least 1500 samples of test data. The 1/10 th scale data which was run with 500 samples for each data point therefore probably does not lend it itself to extreme value analysis with the purpose of extracting a probable increase in distortion value with increased sample size. Work is needed here to define the minimum sample size needed with test data and synthesized data in order to be able to extrapolate a distortion index to larger sample sizes or time periods with reasonable accuracy and still keep the cost down.

If extreme value analysis had been employed in ref 3 (not available at that time) to analyze the minimum sample size required for extrapolation rather than checking the increase in singular maximum values with sample size which led to the value 500 samples it would probably have been found that this value was too small. This does not affect the synthesis work as we were then comparing equal sample sizes of test data and synthesized data.

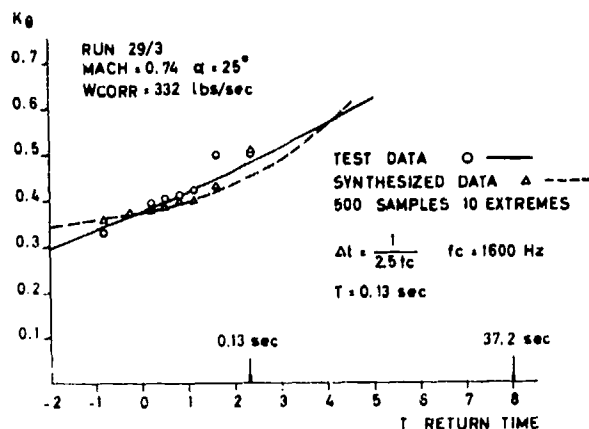


Fig. 22 A Extreme value analysis, 500 samples

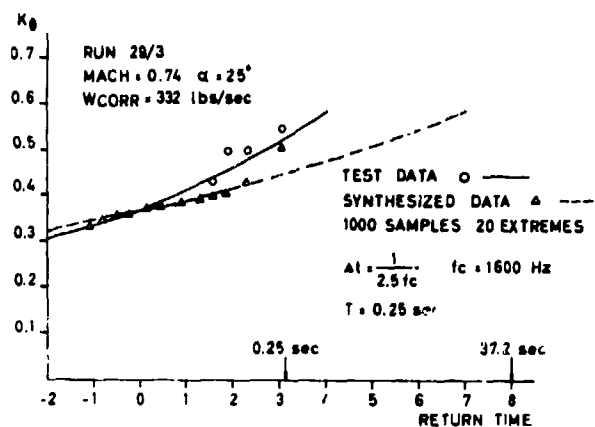


Fig. 22 B Extreme value analysis, 1000 samples

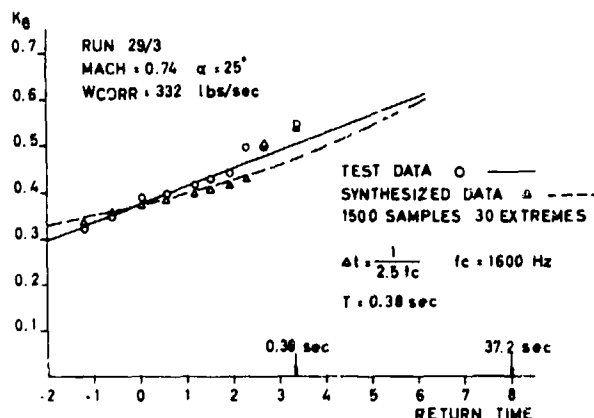


Fig. 22 C Extreme value analysis, 1500 samples

Figure 23 shows a comparison of 3-rd asymptote value at the end of 500 samples (no extrapolation) for 13 data points from the 1/10 th scale inlet test using synthesized distortion and actual measured distortion values. The correlation improves somewhat and there is less underestimate of the synthesized values when comparing the 3-rd asymptote plot with the plot of singular maximum values. The maximum dynamic distortion value from an inlet should probably be defined as a 3-rd asymptote value with ± 3 band based on a certain minimum sample size that yields reasonable extrapolation possibilities.

In this way one obtains a weighted value rather than a value based on a singular maximum instantaneous value.

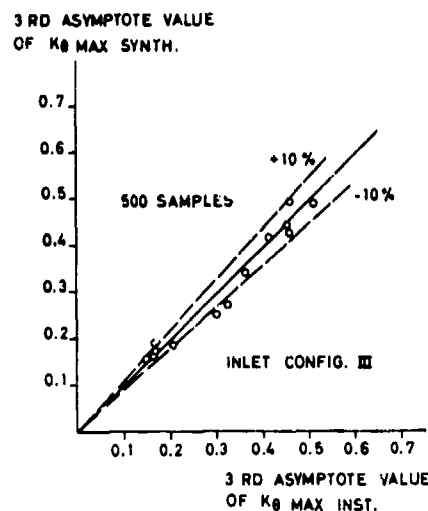


Fig. 23 A Comparison of 3-rd asymptote max. inst. and max. synth. distortion

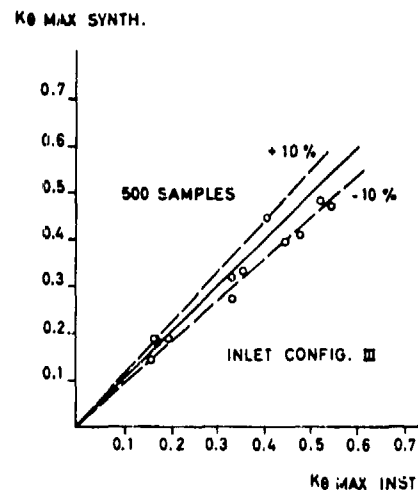


Fig. 23 B Comparison of max. inst. and max. synth. distortion

AVERAGE ΔP_{RMS} FROM REDUCED NO OF PROBES

Midspan ring average ΔP_{RMS} values have been compared to the average of all instrumentation for the tests evaluated in this paper. This is based on the good correlation of results obtained when using only midspan data. Figure 24 summarizes these comparisons and it indicates that a rather good estimate of average turbulence is achieved when using only 20 to 30 % of full instrumentation.

If a rotating rake is used in a small scale model test the required number of installed dynamic probes is further reduced.

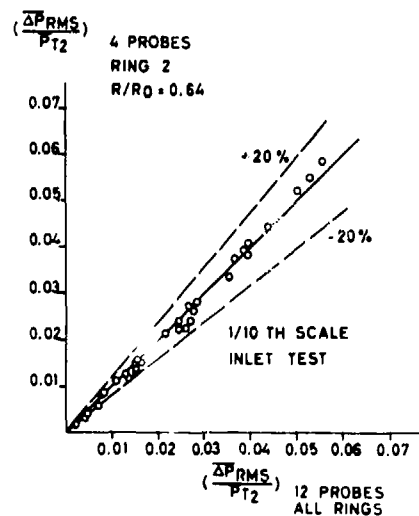


Fig. 24 A Comparison of average ΔP_{RMS} with complete and reduced instrumentation

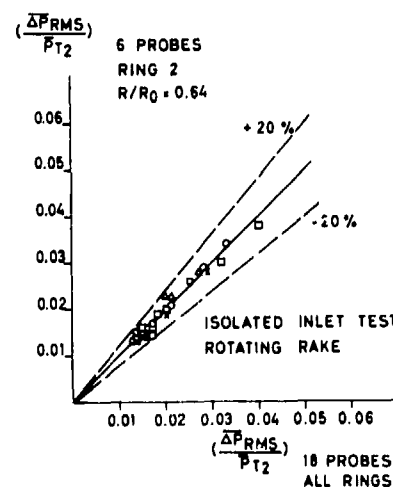


Fig. 24 B Comparison of average ΔP_{RMS} with complete and reduced instrumentation

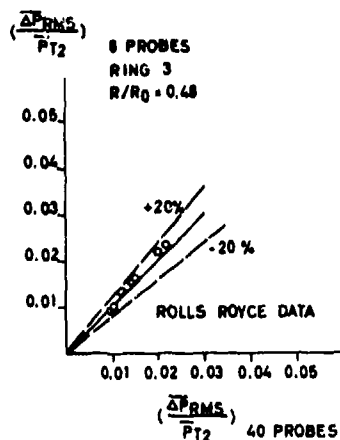


Fig. 24 C Comparison of average ΔP_{RMS} with complete and reduced instrumentation

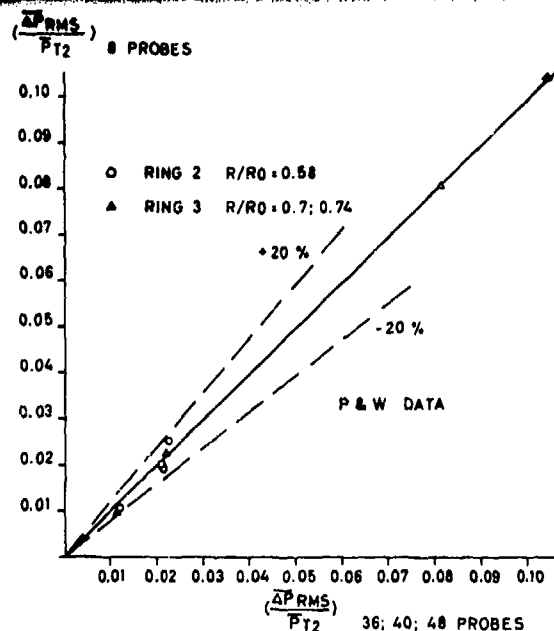


Fig. 24 D Comparison of average ΔP_{RMS} with complete and reduced instrumentation

TEST AND DATA REDUCTION PROCEDURE

Wind tunnel inlet test model.

Small scale $\approx 5\%$ to 10% .

WIND TUNNEL INLET TEST AND COMPUTER PROGRAM DATA REDUCTION PROCEDURE

Figure 25 shows schematically how a small scale inlet test procedure is presently carried out and it also indicates the capabilities of the computer program. The program is presently capable of handling the distortion indices used by P & W; Rolls Royce and G.E. The computer program also has the capability to transform pressure data from inlet rake configurations to engine rig rake configurations before calculating a particular index value. This has been incorporated because the model rakes are not always similar to the rake used in the engine distortion sensitivity tests and distortion indices are sensitive to the rake configuration used in the engine distortion tests.

Compressor face plots can be made of the steady state and maximum synthesized values. Some comparisons of maximum instantaneous pressure patterns with synthesized patterns are included in ref 9.

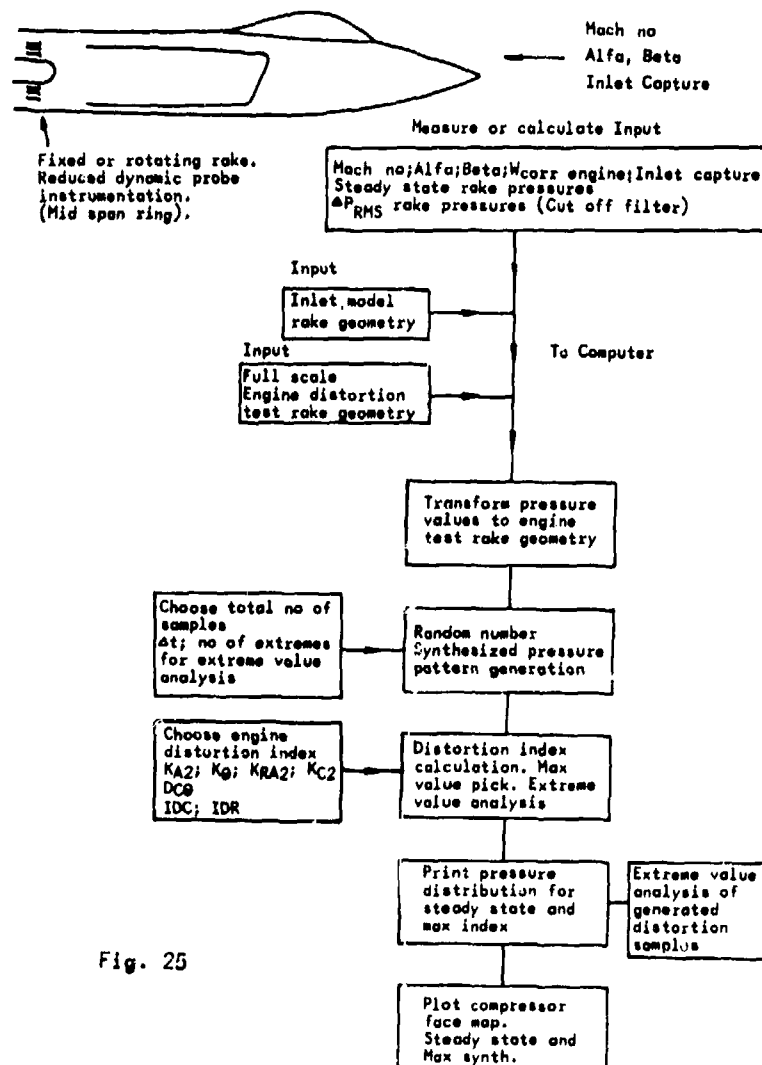


Fig. 25

CONCLUDING REMARKS

A method has been presented that estimates maximum instantaneous distortion and it has been applied to small scale inlet model testing, (10 % to 5 % models).

The main reason for this work has been the high cost of measuring time correlated instantaneous distortion and the work load and cost involved in analyzing such data. Also the large size inlet models required due to the sheer physical size of the dynamic rake instrumentation are not compatible with the transonic/supersonic wind tunnels presently available in Sweden.

The method does not require very costly data reduction equipment or instrumentation and is only slightly more costly than a regular steady state inlet test. The method is not proposed as a substitute for maximum instantaneous inlet distortion testing but rather as a complement in the early development phase of an inlet-engine-aircraft program when screening a multitude of configurations.

The method has shown that it is possible to estimate values of maximum instantaneous distortion using a sample size of a 1000 to well within ± 20 %. Extreme value analysis can be used to further define the likely increase in index value with greater sample sizes.

The method should be used with caution when studying very low inlet mass flow points where it has been shown to underestimate in the subsonic Mach range, ref 8 and also not be used on buzz conditions in the supersonic range. This is due to the assumption of no correlation between probes in the computer model.

REFERENCES

1. G.A. Plourde
B. Brimelow
Pressure fluctuations cause compressor instability.
P & W Aircraft paper presented at the AFAPL
Airframe/Propulsion Capability Symposium 1969.
2. F.R. Lynch
C.J. Slade
Data acquisition and automated editing techniques for
engine inlet tests.
AIAA Paper No 70-596.
3. Motycka D.L
Cavanagh R.B
King R.W
Test results from the 1/10 th scale SAAB model 87 inlet
distortion test at the UARL Main Wind Tunnel.
April 1973.
4. Melich Jr
Clyde H
A feasibility study to define inlet flow quality and
development criteria.
AFAPL-TR-72-14, AD 739858.
5. Borg. R
Tamvel. H
Rosander. G
A method to synthesize dynamic distortion indices based
on data obtained in the 1/10 th scale m87 inlet distortion
test at UARL Main Wind Tunnel.
Volvo Flygmotor AB, report No 361-167, May 1973.
6. Borg. R
Tamvel. H
Rosander. G
Test of the distortion synthesizing method used for
calculation of dynamic distortion indices for the RM8B
engine computer simulator using data with closely
spaced instrumentation.
Volvo Flygmotor AB, report No 361-414, November 1975.
7. R.W. King
J.A. Schuerman
R.G. Muller
Analysis of distortion data from TF-30-P-3 mixed compression
inlet test.
NASA CR-2686, June 1976.
8. J.G. Williams
Synthesis of instantaneous distortion levels.
Rolls Royce Limited Aero-Division-Bristol.
Installation Aerodynamics Dept.
PP/INST/77/22 and PP/INST/78/6.
9. Borg. R
Rosander. G
Test of Volvo Flygmotor AB distortion synthesis method
using inlet data obtained from Pratt & Whitney Florida.
Volvo Flygmotor, report No 361-335, Februari 1980.
10. C.H. Stevens
E.D. Spong
M.S. Hammock
F-15 Inlet/Engine Test Techniques and distortion
methodologies Study.
NASA CR -144 866 through 144 879, June 1978.
11. W.A. Walter
J.T. Delaney
Stability Analysis of YF 401 Engine in a XFV-124 Aircraft.
AIAA-80-1246.
12. J.L. Jacocks, et al
Statistical prediction of maximum time variant inlet
distortion levels
AEDC-TR-74-121 AD/A-004104, Januari 1975.

MODEL TESTING TECHNIQUES FOR MEASURING INLET DRAG

By

James S. Holdhusen
and
James L. Grunnet

Fluidyne Engineering Corporation
5900 Olson Memorial Highway
Minneapolis, Minnesota 55422 USA

Summary

Two methods of measuring inlet drag in transonic flow are described. In the first method, a flow-through nacelle is tested in a transonic wind tunnel. Capture ratio is varied by installing individual annular blockers in the nacelle. Corrections for the drag force exerted by the captured streamtube are determined from blow-through tests in a static test stand. In the second method, drag is determined directly in a single test using a special rig which has a variable-loss throttle. The thrust exiting the control surface is determined by a choked ASME nozzle. A comparison is made of the advantages and disadvantages of the two methods.

Resumé

Deux méthodes pour mesurer la traînée des prises d'air en régime transonique sont présentées. Pour la première, nous employons une nacelle à flux direct (flow-through), installée dans une soufflerie transonique. Le taux de capture est changé par l'installation de bloqueurs annulaires individuels à la prise d'air. Une installation statique à flux soufflé (blow-through) permet le calcul des corrections pour tenir compte de la force de traînée produite par la capture des filets de courant. Pour la seconde méthode, nous mesurons directement la traînée par un essai singulier dans une installation spéciale employant un volet à perte variable. La poussée à la surface de contrôle aval est obtenue par une tuyère ASME sonique. Une comparaison des avantages et désavantages des deux méthodes est présentée.

I. Introduction

Practical considerations, such as the desire to work with larger size models and reduction of complexity and cost, often lead to the conclusion that an isolated inlet test is a logical first step in an inlet development program. For instance, the transonic spillage drag of nearly sharp-edged swept inlets is probably more sensitive to inlet lip radius than it is to flow interference between the inlet and the aircraft. Inlets for wing-mounted turbofan engines are usually far enough ahead of the wing that the only important aircraft flowfield effect is an upwash of a few degrees. This is generally compensated by drooping the front portion of the inlet so that the highlight is perpendicular to the local flow direction. Development testing for cruise performance can either be conducted at an angle of attack equal to the upwash angle or by testing a similar inlet without droop at 0° angle of attack.

Aerodynamic bookkeeping systems for aircraft performance define inlet drag as the axial force component on that portion of the inlet which is in contact with external flow. It is not practical to try and measure this force directly by using a model which is split at the stagnation line since this dividing line between internal and external flow surfaces changes with inlet capture ratio. It thus becomes necessary to devise a means of determining the forces on the structure in contact with the internal flow to apply corrections to the measured axial force on the model. In the first method to be described, this force is determined by blowing air through the inlet model (Ref. 1).

II. Determining Spillage Drag from Flow-Through and Blow-Through Tests of a Nacelle Model

Tests were first conducted using an isolated flow-through nacelle. The nacelle consisted of an inlet forebody which was an undrooped model of a high bypass turbofan inlet, the fan exhaust cowl and a pylon. The model was connected to a three component (drag, lift and pitching moment) balance by a strut which was covered by a grounded windscreen. Grit strips were placed aft of the highlight on both the inner and outer surfaces. Wedges were placed between the pylon and the balance strut to provide variations in angle of attack. The model is shown installed in the Fluidyne 5.5 ft. (1.68 m) transonic wind tunnel in Figures 1 and 2. Four angular blockers were available to provide variation in capture ratio. The outboard surface of the blockers was designed to simulate the shape of inboard surface of the fan nozzle and the core cowl. The

inboard surface of the blockers was a circular cylinder. Total and wall static pressure were measured at an internal reference station which contained three total pressure rakes at 0°, 90°, and 180°.

Separate model assemblies were made with each of the four blockers and tested over a range of Mach numbers up to 0.85. The axial balance force was equal to the sum of the external drag of the nacelle and pylon and the internal drag caused by the forces exerted on the model by the captured airflow.

The magnitude of the internal drag was determined in a separate test in which air was blown through the model (blow-through tests). The inlet forebody was removed and replaced by an axisymmetric duct which had the internal shape of the inlet forebody almost to the highlight and a smooth contraction forward of this point (Figs. 3 and 4). In such an arrangement, the inlet geometry in the region of the stagnation line is purposely not simulated. In the flow-through nacelle, an internal boundary layer is initiated in this region in a highly favorable pressure gradient so that it grows relatively slowly. If this shape and the shape of the captured streamtube were simulated in the blow-through model, the boundary layer on the duct ahead of the stagnation line would separate because of the adverse pressure gradient caused by the abrupt change in wall slope. This would result in a boundary layer thickness further aft which is greater than desired. Since it is desired to have a boundary layer thickness at the beginning of the adverse pressure gradient which is as similar as possible to that occurring in the flow-through nacelle, a contraction was used.

This blow-through nacelle was mounted on a nozzle static test stand with a perforated plate (which was operated choked) and screens to create uniform flow upstream of the contraction. A rake ahead of the contraction verified that flow nonuniformity was so small (+ 0.4%) that the resulting Mach number variations inside the nacelle would generally be less than 0.5%.

Flow was introduced to the model through a choked long radius ASME nozzle which was isolated from the measured structure by a sealed gap of a few thousandths of an inch. The effective area of the seal was calibrated by applying static pressure in the anticipated operating range and dividing by the axial balance force. Before the model was installed, a 4.5 inch choked ASME nozzle was installed in place of the model to check for system bias in thrust and mass flow (Figure 5). Biases of + 0.10% of gross thrust and mass flow are typically achieved for systems of this size. The model and contraction were then installed on the test stand and the mass flow, which was being metered by the upstream 2.5 inch ASME nozzle, was varied over a range which covered the range of reference station Mach number (or corrected weight flow $\frac{w\sqrt{\theta}}{\theta}$) observed in the wind tunnel test.

The internal drag was calculated as the difference between the measured exhaust thrust and the ideal exhaust thrust. Ideal exhaust thrust was calculated by multiplying the known mass flow by the velocity resulting from isentropic expansion from the pressure at the rake ahead of the contraction to ambient pressure. A small correction to internal drag was made which was equal to the drag on this rake plus the drag on the contraction. This correction was less than 10% of the internal drag. The blow-through tests were conducted at an ambient static pressure equal to the wind tunnel total pressure (one atmosphere). The Reynolds number was thus higher in the blow-through tests. This was corrected for by using the Prandtl skin friction coefficient equation:

$$C_f = 0.455 (\log_{10} Re)^{-2.58}$$

It was noted that the ratio P_t/p_{amb} at which the corrected weight flow at the reference station rake was equal to that in the wind tunnel tests was lower than the corresponding total pressure to static pressure ratio in the wind tunnel. (This is attributed to a reduction in discharge coefficient caused by the external flow of the wind tunnel, as will be discussed later.) When the corrected mass flow in the blow-through model correctly corresponds to that in the flow-through tests, it is to be expected that the skin friction and diffusion loss are being properly modeled in the blow-through tests. This was confirmed when the wind tunnel data were corrected by the internal drag coefficients obtained from the blow-through tests. At design capture ratio and Mach number, the nacelle external drag was quite close to a calculated skin friction drag. As the capture ratio was reduced, acceleration of the spilled flow around the inlet outer lip resulted in locally supersonic flow, shock waves, and separation. This spillage drag was calculated as the difference between nacelle external drag at reduced internal flow and the nacelle drag at design flow rate and Mach number. It was found, as expected, that the spillage drag coefficient for a given capture ratio increased as the Mach number increased. The spillage drag coefficients could, for instance, be used to correct the drag coefficient of a force and moment aircraft model operated at design capture ratio.

The flow-through model was then tested over a range of angle of attacks of + 2° to - 4° to determine lift forces. Since the blow-through model tests were not conducted at angle of attack, it is not certain how valid the internal drag coefficients

obtained from those tests are when applied as corrections to the flow-through data at angle of attack. However, the total and static pressure data at the internal reference station indicated that the internal mass flow rate was not significantly altered over this range of angle of attack. From this it can be hypothesized that the internal drag coefficients would not be changed very much over this range of angle of attack.

It is speculated that the exhaust suppression by the external flow could be reduced (and perhaps eliminated) in future tests by designing the annular blocker to have a cylindrical trailing edge (Fig. 6). Other blown nacelle model tests of high bypass turbofan exhaust system conducted in the same wind tunnel show that, at low pressure ratios, conical core nozzles are much more strongly suppressed by the effects of free stream flow than are fan nozzles. The use of such a blocker shape would not compromise the test technique and would result in improved simulation of the internal flow in the blow-through tests. It is further speculated that if such a concept were adopted for test programs using turbine powered simulators (TPS), static calibrations of the TPS would be more accurately applicable to tests conducted with the TPS mounted on a wing or fuselage model. The primary purpose of such a test is to determine the aerodynamic interactions between the TPS and the wing or fuselage. This aerodynamic interaction should not be materially affected by adding a short cylindrical extension to the core cowl of the TPS.

III. Direct Measurement of Inlet Drag Using a Variable Loss Throttle

Another method which we have used to measure inlet drag is conceptually described in Reference 2. This technique, shown schematically in Figure 7, requires only one type of test to determine the external drag of the inlet.

The forces on the structure shown crosshatched in Figure 7 are grounded through a one-component (axial) force balance. A model of the inlet is mounted on a diffusing duct at the end of which is a variable-loss throttle. The throttle consists of two perforated plates having identical hole patterns. The variable porosity resulting from translating one plate with respect to the other results in precisely controllable variation of inlet captured flow.

The perforated plates are operated above choking pressure ratio. There are more than 500 holes in each plate so that the flow leaving the throttle rapidly becomes uniform, and this process is assisted by three screens (Fig. 8). This uniform flow is then accelerated through a choked long-radius ASME nozzle before discharging from the structure which was supported by the force balance.

The control surface for calculating inlet drag passes through the exit plane of the ASME nozzle. The momentum flux passing through this part of the control surface can be calculated with an accuracy close to 0.1% since the thrust coefficient of an ASME nozzle is known to a very high accuracy. This procedure, involving the use of nearly one-dimensional flow properties, may be contrasted to the accuracy problems encountered in more conventional approaches where the momentum flux leaving the control boundaries must be integrated from measured total and static pressure distributions in the distorted flow at the end of the inlet diffuser.

As shown in the appendix of Reference 2, the grounding force, H , accounts directly for all of the forces exerted by the captured flow. The inlet drag can be calculated directly as:

$$D_I = m_\infty (V_n - V_\infty) + A_n (p_n - p_s) + A_4 (p_c - p_\infty) + A_s (p_s - p_c) - H$$

In this equation, A_s is the effective seal area determined from the same type of calibration tests described in the preceding section. Captured mass flow, m_∞ , is calculated using the choked ASME nozzle, of which the discharge coefficient is known to a high accuracy.

The level of bias for this test rig were determined by testing a circular sharp edge inlet in the FluidDyne 5.5 ft. (1.68 m) transonic wind tunnel (Fig. 9). The inlet had a diameter of 5 inches and the external split line was five inches aft of the leading edge. The results are shown in Figure 10, where the inlet drag coefficient (drag divided by freestream dynamic pressure and external inlet area) is compared to the analytical prediction of Crosthwait (Ref. 3). (An external skin friction correction of 0.012 was applied.) The agreement is very good, and these data, taken as a whole, indicate a rig bias of 0.0014. As expected, the measured drag was essentially zero at unity capture ratio.

This procedure is somewhat analogous to checking out the static test stand (used in the blow-through tests described in the preceding section) with a choked ASME nozzle. In each case we can predict the force balance reading in advance of the test. If sufficiently close agreement is not obtained, the instrumentation may be recalibrated. Often the data taken in the checkout tests reveals another problem to be corrected. It may be misalignments or grounding between metric and non-metric components near a split line, or errors in the seal calibration.

This rig has been used to test a swept inlet with a slightly rounded leading edge (Ref. 4). Tests were conducted both in the Fluidyne transonic wind tunnel (Fig. 11) and in the NASA Ames Research Center 6 ft. supersonic wind tunnel. Four different compression ramp settings were tested at capture ratios between 0.4 and the maximum achievable when the inlet throat was choked. Drag coefficients for one of the throat settings are shown in Figure 12 and follow trends that are to be expected. There were 121 static pressure taps on the internal and external surfaces of the inlet. Engine face flow distortion was measured with a rake containing 100 total pressure probes. Configuration details and data at three other ramp settings can be found in Reference 4.

Fig. 13 shows how a model of an inlet for a high bypass turbofan would be installed on this rig. The split line is located at the fan cowl trailing edge. The windscreen can be designed to simulate the exhaust plume shape.

IV. Comparison of the Two Methods

The second method has the advantage, in terms of cost, of requiring only a single test to measure inlet drag. It is also more accurate because there is an addition of errors accompanying the first method since two tests are required. A further advantage of the second method is that bias can be independently assessed directly. Finally, the capture ratio can be accurately set at any desired value in the second method by the variable loss throttle. In the first method, only discrete values of capture ratio are available.

One disadvantage of the second method is that the model size must be smaller than was used in the first method because of rig flow limitations. The maximum captured streamtube is limited to 23 in.² (148 cm²) at Mach 0.8. Another disadvantage is that this rig cannot measure vertical forces. Also, there is a splitline between the aft aft end of the inlet and the windscreen in the second method which is more difficult to keep aligned than the splitline of the windscreen in the wind tunnel test of the first method.

V. Effects of Rig Bias and Scatter on Cruise Performance Prediction

Rig bias (systematic error) and scatter (nonrepeatability) in inlet drag or nozzle thrust coefficient both contribute to errors in performance prediction. A bias error propagates unchanged. The effects of scatter error can be reduced by repeating the tests, and the reduction will be proportional to $1/\sqrt{n}$ where n is the number of tests. An examination of these effects can be performed by statistical analysis using large sample theory and adjusting the required number of repeat tests upward by two to roughly account for the fact that in reality we normally can collect only a small sample of data. (An accurate analysis would use Student's t distribution.)

Inlet drag coefficient is the ratio of inlet drag, D_I , to the multiple of free stream dynamic pressure, q_∞ , and the maximum cross sectional area of the inlet, A_{\max}

$$C_{D_I} = \frac{D_I}{q_\infty A_{\max}}$$

After making the assumption that, at cruise, $F_G = 3 F_N$ and $A_{\max} = 2A_C$ where F_G and F_N are cruise gross thrust and cruise net thrust, it is easy to show that $D_I = 2C_{D_I} F_N$. We can next calculate what error in C_{D_I} (ΔC_{D_I}) corresponds to an error of $0.005 F_N$. This is equal to 0.005 of total aircraft drag so that $0.005 F_N$ is equal to 1 1/2 drag counts.

$$0.005 F_N = 2\Delta C_{D_I} F_N, \text{ therefore, } \Delta C_{D_I} = 0.0025.$$

ΔC_{D_I} will be a function of bias error, B , standard error of estimate, s , and the number of tests, n . At the 90% confidence level, we can write

$$\Delta C_{D_I} = 0.0025 = B + \frac{1.65 s}{\sqrt{n}}$$

The data from the pitot inlet (Fig. 10) had $B = 0.0014$ and $s = 0.0012$. Solving this equation gives $n = 3.24$ and we can conclude that we need 5 or 6 tests to reduce the scatter error to the point that the error in measured C_{D_I} will cause less than 1 1/2 counts error in predicting total aircraft drag. The standard error of estimate for the inlet drag coefficient in the first test method over the test range $0.70 < M < 0.85$ was slightly lower, $s = 0.0011$, but we have no way to know bias and thus cannot conduct such an analysis.

Another commonly used method of measuring inlet drag is to make a momentum defect survey at the trailing edge of a model of the inlet (Ref. 5). It would be useful to have available some data on the repeatability of such tests. One author (Ref. 6) has

commented that this method does not satisfactorily provide an absolute datum drag level. This method would be less attractive when nonaxisymmetric flows, such as would be caused by a pylon, are to be measured. A discussion of the nonrepeatability encountered in a different test technique, the 'earthed' throttle technique, is included in Ref. 7.

It is an interesting fact that this accuracy of drag prediction is almost identical to the accuracy with which we can predict engine thrust from model tests of high bypass engine exhaust nozzle models. Bias is determined by testing an ASME nozzle. For static tests (no external flow) at cruise conditions and with models large enough to have flow rates of about 30 lbs (14 kg) per second, we typically achieve a bias of 0.0010 and a standard error of estimate of 0.0007 for the gross thrust coefficient, although these levels are sometimes exceeded. Thus,

$$0.005 F_N = 0.001667 F_G = \Delta C_{T^*} F_G \quad \text{and}$$

$$0.001667 = \Delta C_T = B + \frac{1.65 s}{\sqrt{n}}$$

results in $n = 3$ and we would estimate five tests as being required to achieve this accuracy.

For transonic isolated blown nacelle tests and static calibration of turbine powered simulators, the necessity to measure a slightly variable ambient pressure adds some nonrepeatability and we typically find $B = 0.0010$ and $s = 0.0010$. This results in $n = 6$ and we would recommend 8 tests to achieve this accuracy. It seems pertinent to point out that if a reasonable number of repeat tests are made, bias errors will contribute more inaccuracy to performance prediction than nonrepeatability. For this reason, we have always attempted to use some means of measuring rig bias for both inlet and exhaust nozzle model tests. Reduction of nonrepeatability errors is also important in order to economize on the number of repeat tests required to achieve a given accuracy. We have a goal of reducing these bias and nonrepeatability errors by 1/3.

References

1. David L. Paul, General Electric Co., "Subscale Inlet Test Techniques," AIAA Turbine Engine Testing Working Group, June 12, 1980.
2. James S. Holdhusen, "Analysis and Demonstration Techniques for Installation Aerodynamic Effects on High-Bypass Turbofans," AGARD Conference Proceedings No. 34, Sept. 1968.
3. E.L. Crosthwait, "Pitot Inlet Additive Drag," AIAA Journal of Aircraft, Vol. 7, No. 6, p. 569, Nov.-Dec. 1970.
4. J.E. Hawkins, F.P. Kirkland and R.L. Turner, "Inlet Spillage Drag Tests and Numerical Flow-Field Analysis at Subsonic and Transonic Speeds of a 1/8 Scale Two Dimensional, External Compression, Variable-Geometry, Supersonic Inlet Configuration," General Dynamics Convair Aerospace Division, NASA Contractor Report CR-2680, April 1976.
5. F. Jaarsma, "Engine-Airplane Interference in Transonic Tests," AGARD Advisory Report AR-36-71, page II-23, August 1971.
6. E. C. Carter, "Experimental Determination of Inlet Characteristics and Inlet and Airframe Interference," AGARD Lecture Series No. 53, page 3-9, May 1972.
7. M. D. Dobson, "The External Drag of Fuselage Side Intakes: Rectangular Intakes with Compression Surfaces Vertical," Aeronautical Research Council, C. P. No. 1269, 1974.

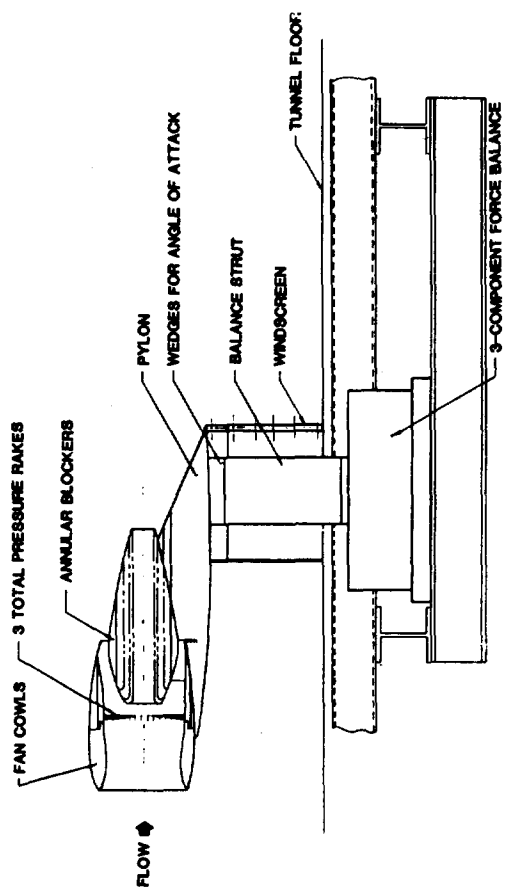


FIG. 1 HIGH BYPASS TURBOFAN FLOW-THROUGH NACELLE AND PYLON

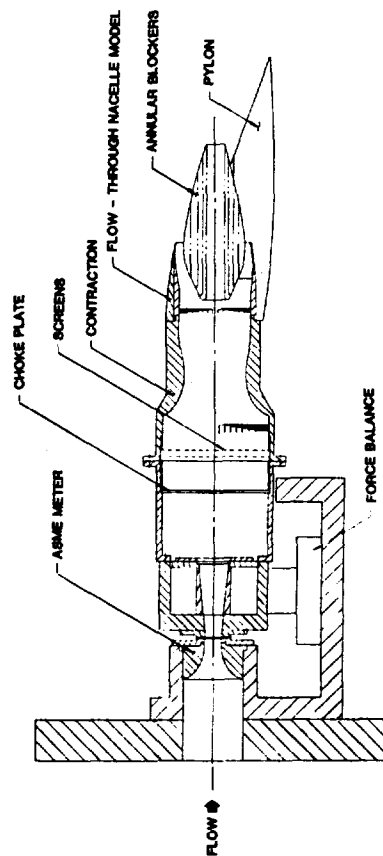


FIG. 3 BLOW - THROUGH TEST OF NACELLE AND PYLON

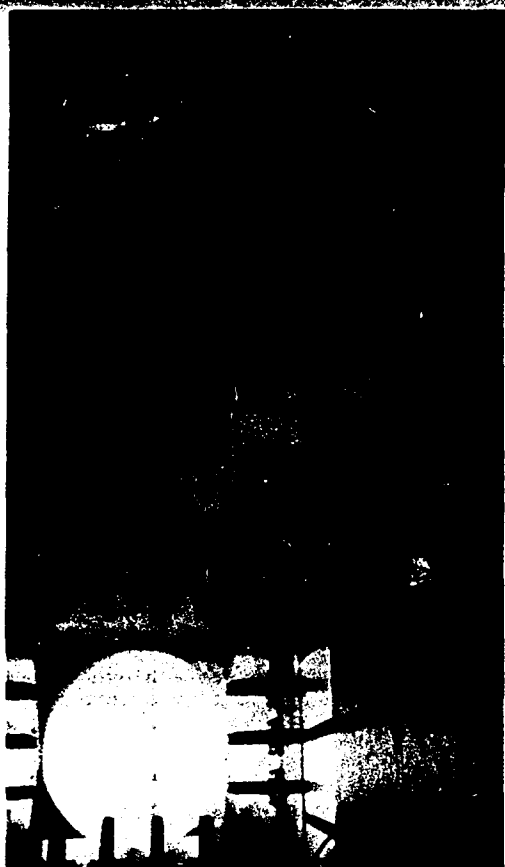


FIG. 2 ISOLATED NACELLE MODEL MOUNTED IN WIND TUNNEL FOR FLOW-THROUGH TESTS



FIG. 4 ISOLATED NACELLE MODEL ON NOZZLE STATIC TEST STAND FOR BLOW-THROUGH TESTS

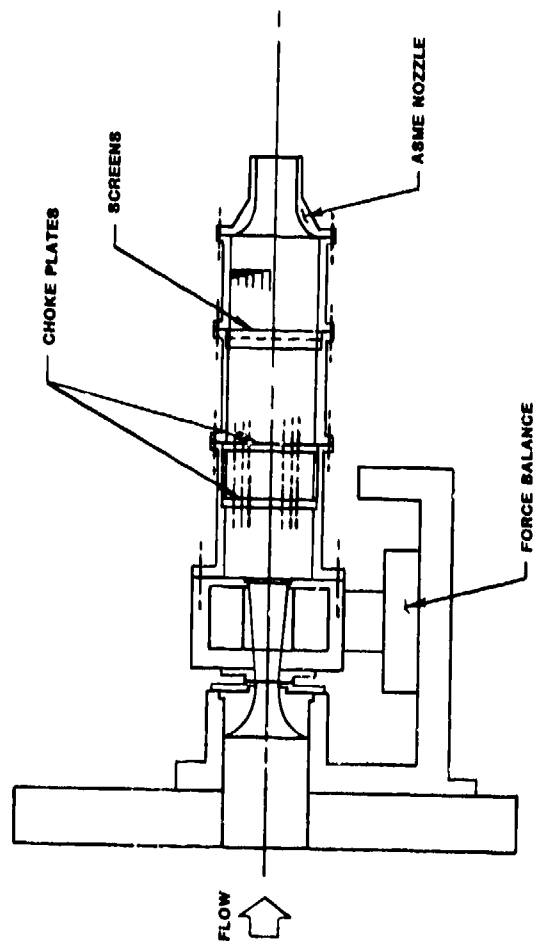


FIG. 5 ASME CHECKOUT MODEL MOUNTED ON STATIC THRUST STAND

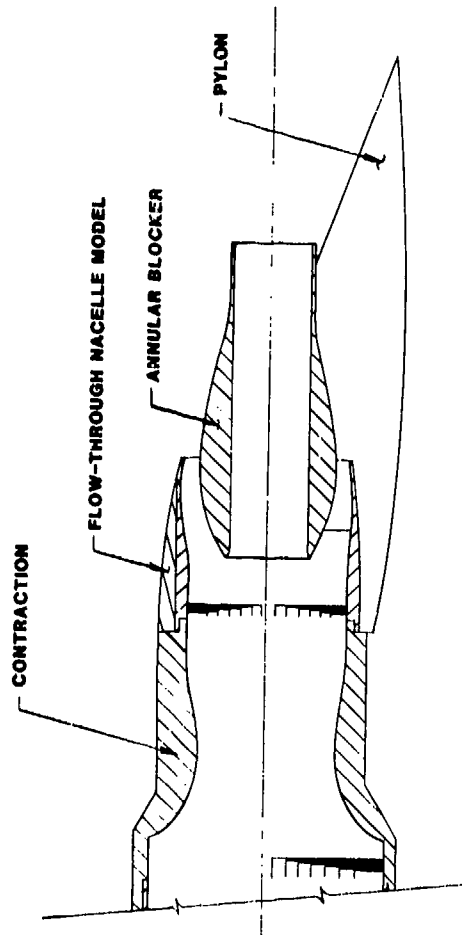


FIG. 6 PROPOSED CHANGE IN DESIGN OF ANNULAR BLOCKER BY ADDING A CYLINDRICAL TRAILING EDGE

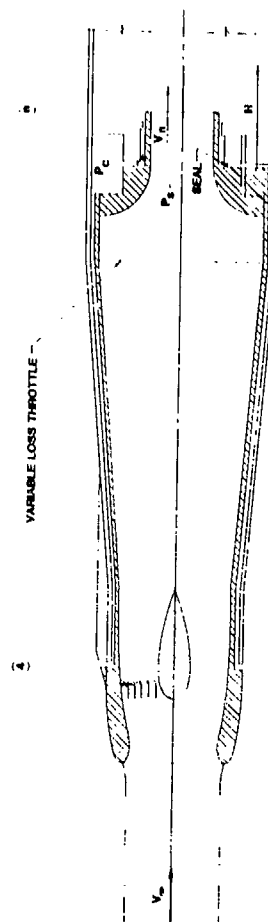


FIG. 7 WIND TUNNEL TEST OF INLET MODEL (SCHEMATIC)

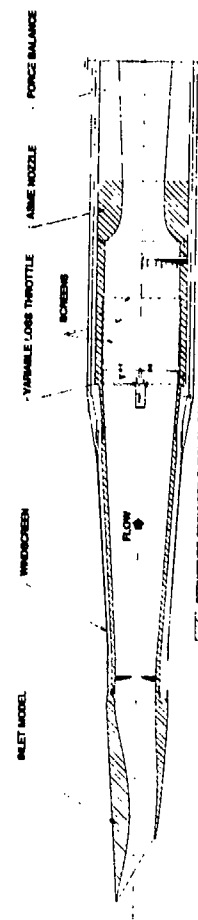


FIG. 8 SWEPT INLET MODEL AND VARIABLE LOSS THROTTLE



FIG. 9 PITOT INLET ON VARIABLE-LOSS THROTTLE DRAG RIG FOR DETERMINATION OF RIG BIAS



FIG. 11 SWEEP INLET MODEL MOUNTED ON VARIABLE-LOSS THROTTLE DRAG RIG

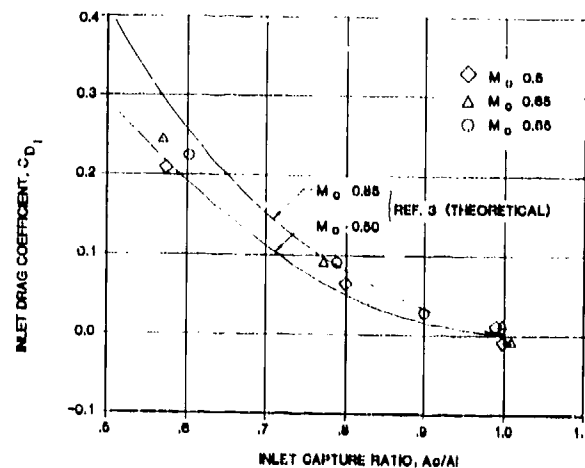


FIG. 10 PITOT INLET DRAG COEFFICIENT

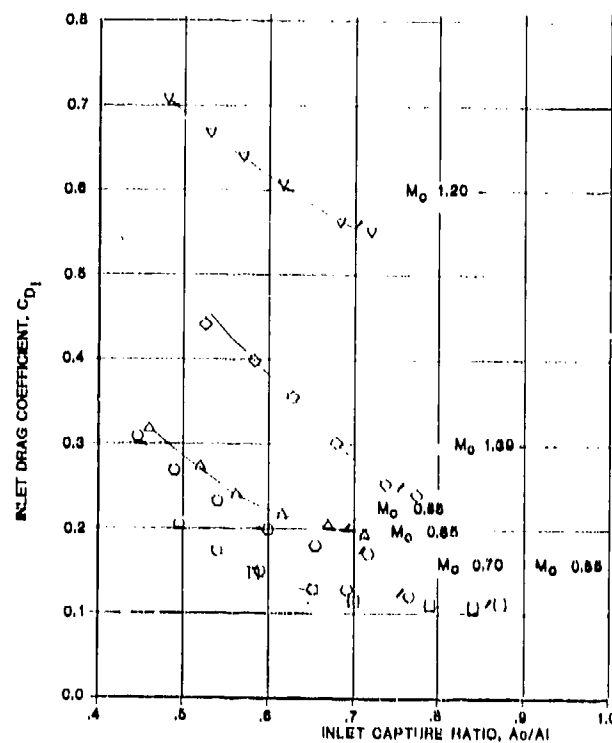


FIG. 12 MEASURED DRAG COEFFICIENT (REF.4)

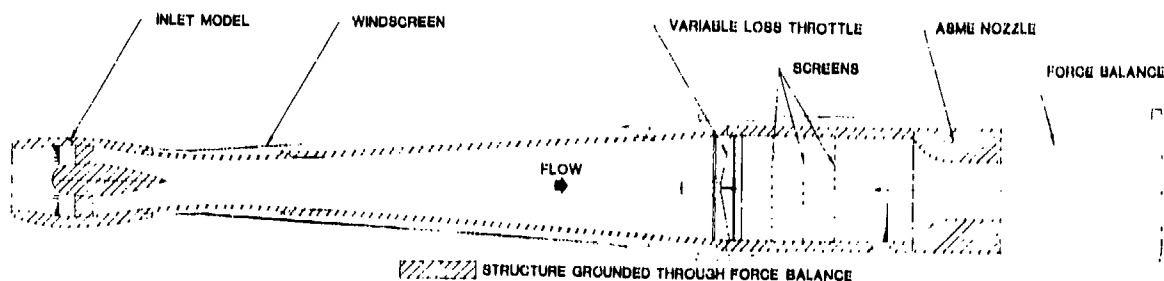


FIG. 13
INSTALLATION OF HIGH BYPASS TURBOFAN INLET MODEL ON INLET DRAG RIG

**COMPRESSOR STALL INDUCING INSTALLATION EFFECTS OF AN
ENGINE CONTROL PARAMETER FOR THE CF-5 AIRCRAFT**

AUTHORS: W.L. Macmillan *
Directorate of Science and Technology
(Ordnance & Vehicles)
Chief, Research and Development Branch
National Defence Headquarters
Ottawa, Canada
K1A 0K2

D.M. Rudnitski &
W. Grabe
Engine Laboratory
Division of Mechanical Engineering
National Research Council of Canada
Ottawa, Canada
K1A 0R6

ABSTRACT

An operative program was established between the Canadian Forces and the National Research Council of Canada to investigate compressor stall problems with CF-5 aircraft, powered by two J85-CAN-15 engines.

Analytic and test cell investigations identified one major cause for compressor stalls as improper operation of the engines' control system under low temperature conditions. Subsequent flight testing demonstrated this control system malfunction to be the result of engine installation effects, which produced an erroneous compressor inlet temperature signal to the main fuel control unit. The flight testing determined the degree of signal error for several flight conditions, such as level flight, high angles of attack, aircraft stalls, and weapons delivery profiles.

Temperature errors were greater at high angles of attack where severe compressor inlet distortion would act cumulatively in reducing the stall margin under this flight condition. Some corrective measures for reducing the errors are described.

NOMENCLATURE

ABFCU	■ Afterburner Fuel Control Unit
ACM	■ Air Combat Manoeuvre
AETE	■ (Canadian Forces) Aerospace Engineering Test Establishment
CIT	■ Compressor Inlet Total Temperature
EGT	■ Exhaust Gas Temperature
IDV	■ Inlet Guide Vane
MFCU	■ Main Fuel Control Unit
N	■ Engine Rotational Speed
N ₂ /N	■ Compressor Corrected (= aerodynamic) Speed
NRC	■ National Research Council of Canada
PLA	■ Power Lever Angle
T ₂	■ Compressor Inlet Total Temperature
W ₂ /W	■ Compressor Corrected Mass Flow
θ	■ Compressor Inlet Total Temperature/Static Temperature, Sea Level, Standard Day
δ	■ Compressor Inlet Total Pressure/Static Pressure, Sea Level, Standard Day

1. INTRODUCTION

One of the prime reasons for the considerable development and engineering effort directed towards designing and testing the CF-5 aircraft engine inlet and installation is to ensure stable engine performance over the aircraft flight and manoeuvre envelope. This stable engine performance is usually understood to be freedom from compressor stalls and compressor blade instability.

* Formerly, Major (Canadian Forces),
Directorate of Aircraft Engineering and Maintenance,
National Defence Headquarters.

In service, the Canadian version of the F-5 aircraft, the CF-5, shown in Figure 1, had proven to be very susceptible to compressor stalls during low inlet total temperature conditions and air combat manoeuvring. The Canadian Forces, in an effort to define and rectify the problem, initiated a co-operative program with the National Research Council of Canada (NRCC). The program consisted of analytic and ground level test cell investigations, culminating in instrumented flight tests at the Canadian Forces Aerospace Engineering Test Establishment (AETE), CFB Cold Lake, Alberta.

This paper outlines an engineering investigative program to correct a situation in which all the classical or standard installation effects in terms of pressure recovery, inlet distortion, spillage, etc., had been determined during the aircraft development, yet upon entering service, a major stall inducing factor attributable to the engine installation was still present. This factor was the improper input to the engine control system of compressor inlet temperature (CIT or T2), a critical engine control parameter. This paper illustrates an example of a subtle installation error which can go undetected, or unappreciated, but yet can have serious consequences on operational capability.

2. AIRCRAFT AND ENGINE, WITH CONTROL SYSTEM

2.1 CF-5 Aircraft

The CF-5 is a twin-engined fighter aircraft with the engines located in side by side bays buried in the aft fuselage. The aircraft is a modified version of the Northrop F-5 A/B aircraft, produced under licence by Canadair. The air induction system consists of two side mounted intakes plus pilot selectable auxiliary inlet doors to improve pressure recovery and engine inlet conditions at high power settings during take off and low speed flights (see Figure 2).

2.2 J85-CAN-15 Engine

The CF-5 is powered by two J85-CAN-15 General Electric afterburning turbojets. The J85-CAN-15 (Figure 3) is a single spool afterburning turbojet engine consisting of an eight stage compressor, annular combustor, a two stage turbine and a fully modulated exhaust nozzle. Besides the variable exhaust nozzle, the engine contains two other elements of variable geometry; namely variable inlet guide vanes (IGV's) and inter-stage bleed valves. These last two items are mechanically linked and vary as a function of compressor rotor speed and compressor inlet total temperature.

2.3 Engine Control System

The engine is controlled by a hybrid system, consisting of a main fuel control unit (MFCU) and an afterburner fuel control unit (ABFCU), both of which are hydromechanical, and an electronic nozzle control. The MFCU determines bleed valve and IGV position and schedules main fuel flow which ultimately controls engine speed. The ABFCU schedules afterburner fuel flow and the exhaust nozzle control varies nozzle area according to a mechanical schedule below a threshold exhaust gas temperature (EGT), above which the nozzle is positioned to keep EGT constant. Reiterating the discussion to the hydromechanical MFCU, its input parameters are the following:

- compressor delivery pressure, from a pressure tap on the compressor case,
- engine rotational speed (N), an engine mechanical input,
- throttle or power lever angle (PLA), a pilot input, and
- compressor inlet total temperature.

2.4 Engine Installation

The engine installation in the CF-5, showing the relative location of the MFCU for both port and starboard engines, is illustrated in Figure 4. The MFCU is located on the lower starboard side of each engine, which places it near the center line of the aircraft for the port engine and near the outer skin for the starboard engine. The physical layout of the engines results in the MFCU of the port engine being exposed to the combined heat flux from both engines near the outer skin wall. In addition, the outboard bleed valve of each engine has its air ducted overboard, whereas the inboard bleed valves merely dump the warm air into the engine bay. As a result, the inboard (port engine) MFCU is exposed to a warmer environment than the outer (starboard engine) MFCU.

2.5 Temperature Sensing System

Rather than getting an air temperature sensed at the compressor inlet, the MFCU's are supplied by air obtained from the undersurface of the aircraft. The air is collected by two scoops, one for each engine, and ducted to the MFCU's through 15-inch lengths of flexible pipe. Airflow is induced through this duct by an ejector at the MFCU which is supplied with compressor discharge air. Once at the MFCU, the air passes over a liquid filled bellows which provides the temperature input to the MFCU fuel flow schedules. It also passes over an electrical temperature sensor which feeds into the nozzle area control in order to cutback EGT when CIT is less than -20°C.

3. COMPRESSOR STALLS

3.1 General Compressor Map

The prime factors leading to compressor stalls in axial compressors have been identified for some time and are illustrated in Figure 5, which represents a compressor map for a simple, single shaft gas turbine with a fixed area exhaust nozzle. A compressor map is a plot of compressor pressure ratio as a function of corrected compressor mass flow, $W/\sqrt{\theta}$, for lines of constant corrected rotor speed, $N/\sqrt{\theta}$. Compressor operating or working lines, steady state and transient, lie somewhere below the surge line. A hypothetical acceleration line from a low power setting (A) to a higher setting (B) has been sketched in.

In simple terms, a compressor will stall if the stall margin, represented as the relative distance between a point on an operating line and the surge line, is reduced such that the compressor operating line intersects the surge line. This can be the result of a lowered surge line, a raised operating line, or a combination of the two. Some of the factors affecting the positions of these lines are included in Figure 5 and are summarized below:

Factors Lowering Compressor Surge Line	Factors Raising Single Spool Compressor Operating Line
Reduced Reynolds numbers	Engine accelerations
Inlet flow distortion	Reduced exhaust nozzle area
Compressor deterioration by wear, deposits, corrosion, or foreign object damage	Increased exhaust gas temperature
Increased tip clearances	Engine tolerances
Manufacturing tolerances	Fuel control tolerances

In addition to the above factors, at high or low corrected speeds, two areas exist where stalls can occur. They are usually avoided by proper functioning of the engine's control system. At low corrected speeds, a stall problem essentially results from different flow requirements at the front and back of the compressor. The front compressor stages require a higher mass flow than the rear stages are capable of handling and the front stages consequently stall. This type of stall has been overcome by engine designs incorporating multiple spools and/or variable IGV's, stators, or bleed valves. At the other extreme, a high corrected speed stall in effect represents a rotational Mach number limitation for the compressor. At this point, the compressor front stages have become choked and the rear stages are either stalled or near stall. Under this condition, the compressor is generally less tolerant to other stall inducing effects such as inlet distortion, engine transients, and compressor deterioration. Most engines incorporate a corrected speed limit (by reducing mechanical speed), beyond which the engine either cannot operate, or else does so with much reduced efficiency and stability margin.

Because the above two stall phenomena are related to corrected rotor speed, $N/\sqrt{\theta}$, they are functions of both engine speed and CIT. It is thus very important that the temperature input to the fuel control be a true representation of the actual compressor inlet total temperature. Since CIT is a total temperature, for a function of ambient static temperature and flight Mach number, the flight conditions can have an important impact on compressor stalls. The relationship between certain compressor stall factors as shown in Figure 5 and an aircraft flight envelope can be seen in Figure 6. Reynolds number effects are generally more pronounced at higher altitudes. Inlet distortion becomes more pronounced as aircraft angle of attack is increased or as flight becomes more uncoordinated with respect to bank and yaw. Inlet distortion is also frequently associated with rocket or gun gas ingestion resulting from weapons firing. Also note that superimposed on Figure 6 are lines of constant CIT = -26°C for standard and for cool day conditions. As will be seen, this represents a critical value of CIT for J85-CAN-15 operation.

3.2 J85-CAN-15 Compressor Stall Counter Measures

The J85-CAN-15 control system provides counter measures against both low and high corrected rotor speed stalls. As mentioned, the engine contains both variable IGV's and bleed valves to avoid low speed stalls. To avoid high speed stalls and preserve stall margin under low CIT conditions, the MPCU is designed to reduce maximum engine rotational speed when CIT is less than -26°C to keep the corrected compressor speed at or below 108% (Figure 7). In addition, the nozzle control system also varies the nozzle area to reduce EGT as a function of CIT at temperatures below -26°C (Figure 8). These two control measures are referred to as "T2 Outback" in J85 engine operation. Engine stall margin will be reduced, especially during throttle transients, if these outbacks do not occur.

3.3 In-Service Stall Experience

In analyzing an in-service stall problem, the important point to note is that while all the factors mentioned previously are cumulative in reducing the stall margin, not all will necessarily be present simultaneously in producing a stall. Thus, in order to properly investigate a stall problem, the individual factors responsible for a particular type of stall must be isolated. At first glance, it appeared that there was no pattern to the in-service compressor stalls. However, as a result of pilot feedback providing such information as airspeed, altitude, attitude, throttle position, etc., just prior to stall, a base of three years of data was built up and a pattern began to emerge with some common denominators appearing. Figure 9 illustrates that compressor stalls generally fell into four regions of the aircraft level flight envelope. Each region has identifiable potential compressor stall cause factors:

Region A. Low speed flight at medium altitudes; stalls typically followed throttle transients. These flight conditions are experienced in certain training profiles and air combat manoeuvring (ACM). This region accounted for 52% of all reported compressor stalls and of these, 71% occurred with a CIT below -26°C . The stall inducing factors were a suspected lack of T2 outback, coupled with inlet distortion associated with the higher angles of attack and aircraft yaw frequently encountered during ACM.

Region B. Stalls at higher altitudes, often occurring during throttle transients, accounted for 17% of all stalls. Of these, 41% occurred with CIT below -26°C . The suspected stall cause factors were lack of T2 outback, decreased stall margin due to Reynolds number effects, and possible degraded compressor condition.

Region C. High speed, low altitude stalls accounted for 15% of all stalls. Under these conditions, CIT is high, hence corrected engine speed is low. If the corrected speed falls sufficiently, actuation of engine variable geometry will help to preserve stall margin. Stalls experienced in this region were attributed to improper variable geometry operation or rigging, and inlet temperature and pressure distortion associated with weapons delivery profiles and gun or rocket gas ingestion.

Region D. Seven percent of all stalls occurred under ground level static conditions during afterburner initiation at very low temperatures. The cause was suspected to be a lack of T2 outback, since further investigation rarely found any engine or control malfunction.

From the above, it can be summarized that the major stall inducing factors were:

- Reynolds number effects,
- inlet distortion,
- low CIT operation (present in over 50% of all stalls), and
- engine transients.

The degree of stall margin reduction resulting from Reynolds number effects and inlet distortion are related to the hardware (compressor and engine intake geometry or design). Since for all practical purposes these were considered fixed and hence a solution involving modifications or alterations to their design would be potentially very expensive, effort was concentrated on the factor of low CIT operation. Another reason for concentrating on this aspect was that pilot comments indicated that the ECM and engine speed outbacks during low CIT operation were not occurring. Since CIT is an input into transient fuel schedules, there was also a potential impact on the last factor noted - engine transients. A critical assessment of the T2 sensor system and its environment led to the suspicion that T2 outback may not have occurred as scheduled.

It was suspected that T2 outback was not taking place properly, and hence stall margin was degraded, for the following possible reasons:

- the total temperature of sample air picked up by the scoop on the aircraft underside was not representative of CIT,
- air was heated in the duct on the way to the MPCU, and/or
- the MPCU became heat soaked, thus affecting temperature sensor operation.

To examine these hypotheses, flight tests with a fully instrumented aircraft were carried out at the Canadian Forces Aerospace Engineering and Test Establishment (CAETP).

4. FLIGHT TEST PROGRAM

The objectives of the flight test program were:

- a. to determine the actual T2 outback for all areas of the CF-5 level flight envelope where CIT below -26°C would be encountered, and
- b. to evaluate the CIT or T2 sensing system and to establish whether any errors existed between the temperature sensed at the MPCU and the true CIT.

4.1 Instrumentation and Data Acquisition

The parameters measured, and location of temperature probes, are given in Figure 10. Basically, the instrumentation provided information on aircraft flight parameters, port and starboard engine parameters, and several temperatures such as external total air temperatures, compressor inlet temperatures and those internal to the T2 sensing systems. The signals from the transducers were filtered, amplified, and recorded on a digital tape unit installed in the rear seat compartment of the CF-5D (dual) test aircraft. The raw data were converted into engineering units on a ground based computer system at AETE and forwarded to NRCC for analysis.

4.2 Test Flight Profiles

The flight test program was devised to concentrate data collection on those flight envelope areas with a high stall frequency. The test program initiated with flights to examine T2 sensing system performance under steady state conditions, then progressed to dynamic system testing during aircraft transients where CIT would be changing, and terminated in complete transient testing, such as in weapons delivery profiles where both CIT and engine parameters vary.

Steady State Testing. To obtain stable (i.e. steady state) data, flights of constant altitude with varying airspeed were made. After arriving at a suitable altitude, the test engine was set at MILITARY power. The airspeed was progressively lowered in steps, thus decreasing CIT, by varying the power setting of the other, non test, engine. The aircraft remained at each test point until CIT was considered stable (typically 2-3 minutes), and then data were recorded for approximately 5 seconds. The airspeed was progressively reduced until the aircraft reached its lower level flight speed limit. At that time, the sequence was repeated with the other engine as the test engine. This series of tests was done at altitudes varying between 25,000 and 35,000 ft and airspeeds between 150 KIAS and M1.05, resulting in CIT's between 0°C and -47°C.

Dynamic Testing. Dynamic T2 system response was obtained by continuously recording data under the following conditions:

- a. throttle transients at essentially stable flight points;
- b. high aircraft attitude stalls, during which the aircraft with fixed power settings was allowed to climb at a 60° nose high attitude, eventually resulting in an aircraft stall;
- c. level flight aircraft stalls, in which the aircraft was maintained at a relatively constant altitude. The aircraft stall was induced by decreasing power settings of the non-test engine thus reducing airspeed and CIT; and,
- d. typical low level weapons delivery profiles where there are considerable throttle movements plus continually changing temperatures, speeds, altitudes, and engine conditions. As the test aircraft was a dual seat CF-5D which does not have guns fitted, no live gun fire tests were performed.

4.3 Test Results and Discussion

- a. Steady State Tests. Representative data from these tests are given in Figures 11 and 12. As shown in Figures 11 a and b, under low values of CIT the outback of engine speed and EGT did not occur to the extent required. Also, a difference was noted between the relative accuracy of engine speed and EGT control, with the control of EGT being more precise. The reason may lie in the fact that engine speed is controlled by the hydromechanical MFCU in an indirect manner through fuel flow whereas EGT is directly controlled by the electronic nozzle control. Additionally, there was a difference in these parameters between the port and starboard engines, with the starboard engine being less adversely affected than the port. These results were repeatable between test flights and can be explained by reference to Figure 12, which shows the T2 sensing system performance during these flights. As may be seen, under these test conditions, the air temperature at the scoop/duct entrance (T21 and T22) was reasonably close to the CIT. However, over the length of the flexible duct, by the time the air reached the fuel control, the temperature had risen as much as 11°C (T23, left engine, CIT = -45°C). The temperature rise was more pronounced for the port engine system and is considered to be due to higher port engine bay temperatures in the area of the MFCU. This was verified by measuring the MFCU case temperatures.

The temperature rise inside the duct creates an error in the T2 sensing system such that the temperature input to the MFCU is no longer representative of the actual CIT. The error increases with decreasing CIT. At CIT's below -26°C, the required T2 outback is delayed, resulting in a N/V/O overspeed condition, with a consequently degraded stall margin. The delayed EGT outback not only results in an engine operating at an unnecessarily high temperature, which is undesirable for engine durability purposes, but in addition, further degrades stall margin.

- b. High Attitude Stalls. Figures 13 a, b, and c illustrate the T2 system response to a high altitude aircraft stall under a reducing CIT environment. T2 system errors (T23 minus CIT) approach 18°C and 11°C for the port and starboard engines respectively at a CIT of -27°C. These errors are significantly greater than those observed under the steady state conditions, and are primarily due to an increased discrepancy between CIT and the temperature of the air at the scoop inlet (T21). This is thought to be a result of boundary layer effects in proximity to the scoops as the aircraft approaches stall.
- c. Level Flight Stalls. Figure 14 demonstrates the T2 system response during a level flight aircraft stall. In this series of tests, because the aircraft was not stalled as rapidly as in the previous high altitude stall, the CIT environment did not change as rapidly in this manoeuvre. Also, the scoop inlet temperature (T21) followed CIT more closely than in the previous stall tests. However, the temperature rise in the T2 duct reached 13°C, exceeding the steady state increase of 10°C at the CIT value of -35°C.

These aircraft stall tests have demonstrated that external temperature discrepancies exist between the compressor face and the scoop in addition to internal system temperature rises found in normal steady state flight. These external discrepancies are probably due to distorted flow and boundary layer effects in proximity to the system scoop. The significance of the increased errors is that under the conditions of high aircraft angles of attack, aircraft stalls, and during stall recoveries, the compressor face would encounter increased inlet flow distortion. The flow distortion and the coincident effects of T2 system errors would be additive to significantly reduce compressor stall margin under these flight conditions.

- d. Weapons Delivery Profiles. The dynamic conditions experienced during a typical weapons delivery are illustrated in Figures 15 a, b, and c (only one engine's parameters are shown since they are essentially the same for both engines). This manoeuvre represents a different situation from the previous ones, in that CIT is relatively warm due to the higher speeds and lower altitudes, and is increasing due both to the altitude decrease and speed build up. As shown in Figure 15c, the initial temperature difference in the T2 duct decreased with time and the remaining error would actually reduce the possibility of compressor stall. Since the engine operating point is now in a low N/V regime, engine variable geometry would be actuated slightly earlier than required due to the error.

5. CORRECTIVE MEASURES

The test program has thus far identified that the existing CIT sensing system provides an incorrect CIT signal to the engine control system. This error is a major contributing factor to a loss of stall margin under low CIT conditions for the CF-5 aircraft.

Developments are now underway by the Canadian Forces and the engine manufacturer to eliminate or reduce the errors. Work thus far has progressed in two areas:

- a. Relocation of the electrical temperature sensor for the nozzle control. From the MFCU to an area of the engine bay where a representative value of CIT may be obtained. This modification has been prototyped, and is presently being test flown, by AETFE. It should effectively remove the T2 error affecting EGT outback. Proper EGT outback would recover some of the lost stall margin under low CIT conditions.
- b. Biasing of the T2 bellows and MFCU. A modification to the MFCU is currently under development by General Electric which will bias the MFCU to take into account an average error in sensed temperature. This would produce an engine speed outback at warmer values of sensed CIT. Such a modification is not as straightforward as it may appear, since the actuation of variable geometry under high temperature (low N/V) conditions must not be adversely affected by a bias developed to correct a low temperature error.

The Royal Norwegian Air Force has further investigated the T2 temperature sensing system on the F-5A/B aircraft. They found that prolonged engine operation at low power setting on the ground leads to high sensing error. Under these conditions engine bay cooling airflow is reduced, thus bay temperatures are high and, in addition, airflow through the T2 sensing duct is lowered due to reduced aspirator effectiveness. In service, these conditions are encountered frequently, such as during a taxi or hold prior to take off. On a cold day, below -26°C, the errors would lead to delayed T2 outback and reduced stall margin as discussed earlier in the paper. As mentioned previously, compressor stalls have often been encountered in cold weather on afterburner initial on for take off. Subsequent investigation determined that a change in pilot technique could reduce this sensing error. The revised procedure requires the pilot to pause at a higher power setting (MILITARY) for thirty seconds (thus increasing airflow through the engine bay and sensing duct) prior to selection of afterburner for take off.

6. SUMMARY

- a. Since its introduction into Canadian Forces service, the CF-5 aircraft has been plagued by compressor stalls and consequent combustor flameouts. A co-operative program between the Canadian Forces and the National Research Council of Canada was launched to investigate the problem.
- b. It was found that, during a three year period, over half the reported stalls occurred at compressor inlet total temperatures (CIT or T2) below -26°C , an operating regime in which compressor speed and exhaust gas temperature (EGT) outbacks (termed T2 outback) are to take place.
- c. An extensive flight program with an instrumented CF-5D aircraft was executed, which showed that significantly higher CIT input signals were given to the main fuel control unit (MFCU) and the exhaust nozzle controller. These erroneous temperature signals would delay the scheduled T2 outbacks, increasing the chances for stalls at high corrected compressor speeds.
- d. Heat transfer from the engine bay environment to the T2 sensing system air duct was identified as a major cause for the higher temperature indication. Asymmetric MFCU locations in the respective engine bays caused greater rates of heat transfer, and hence indicated T2 errors, to the port than to the starboard engine.
- e. Left hand indicated T2 errors ranged from 11°C (CIT = -45°C) at steady state level flight to 13°C (CIT = -34°C) during a level attitude aircraft stall and to 18°C (CIT = -27°C) at a 60° nose high aircraft stall. Right hand engine errors were approximately two-thirds of the left hand ones.
- f. In the case of errors during aircraft stalls, the T2 error arising from the engine bay heat transfer was compounded by an erroneously high total temperature measurement at the T2 system inlet scoop, located on the underside of the aircraft. Increased compressor inlet distortion under this flight condition would add to the delayed T2 outback in pushing the engine towards stall.
- g. Various steps have been considered to alleviate the faults of the T2 sensing system. The most notable to date has been the planned relocation of the sensor providing the temperature input to the nozzle control and which governs the EGT outback.

ACKNOWLEDGEMENTS

The authors wish to acknowledge the contributions of the following individuals in the course of this program:

Mr. M.S. Chappell, National Research Council of Canada, responsible for early program direction, and
Capt. Kent D. Nelson (USAF Exchange Officer), test flight project officer,
Aerospace Engineering Test Establishment, CFB Cold Lake, Alberta, Canada.



FIGURE 1: CF-5 AIRCRAFT FIRING ROCKETS

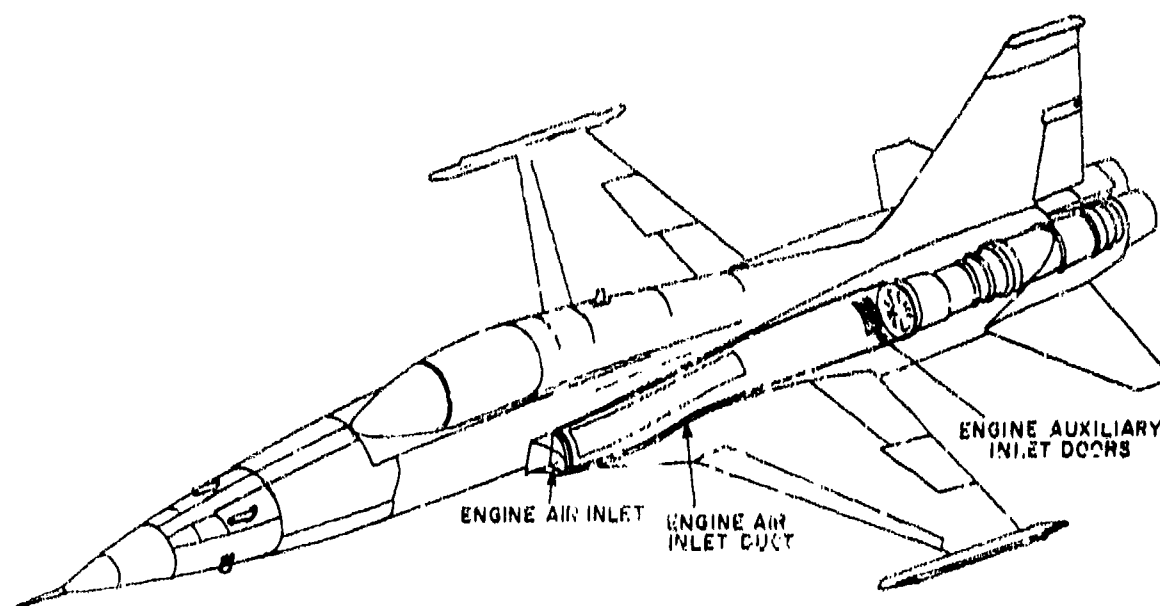


FIGURE 2: CF-5 AIRCRAFT SHOWING AIR INDUCTION SYSTEM

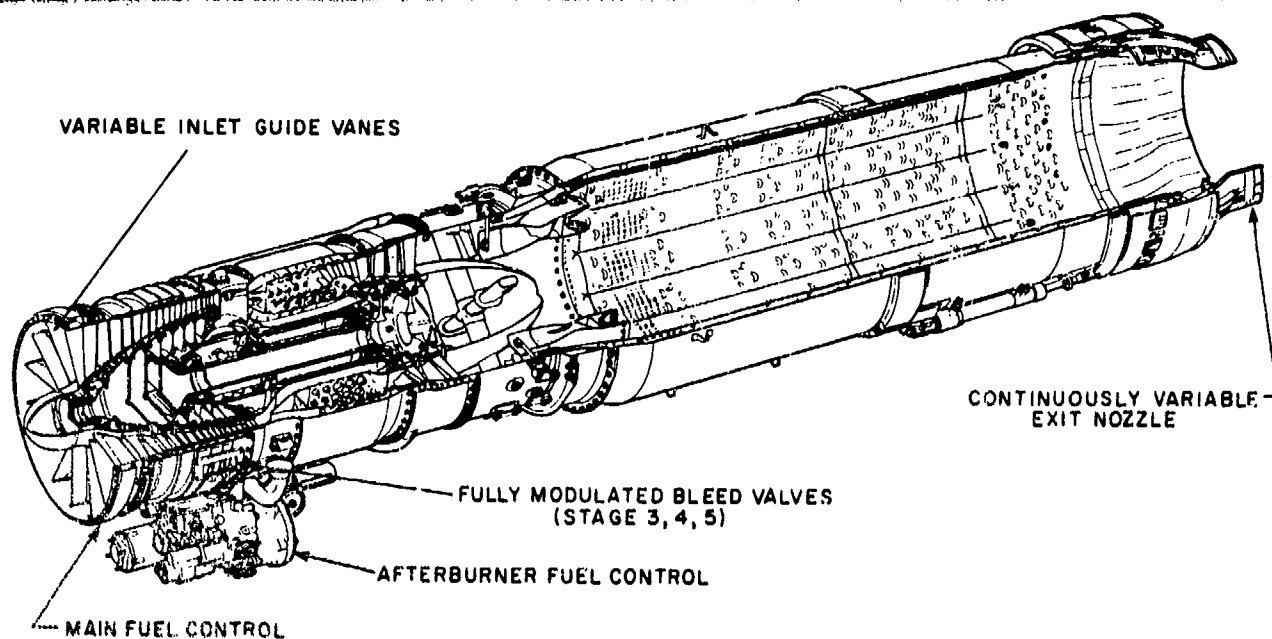


FIGURE 3: J85-CAN-15 CUTAWAY VIEW

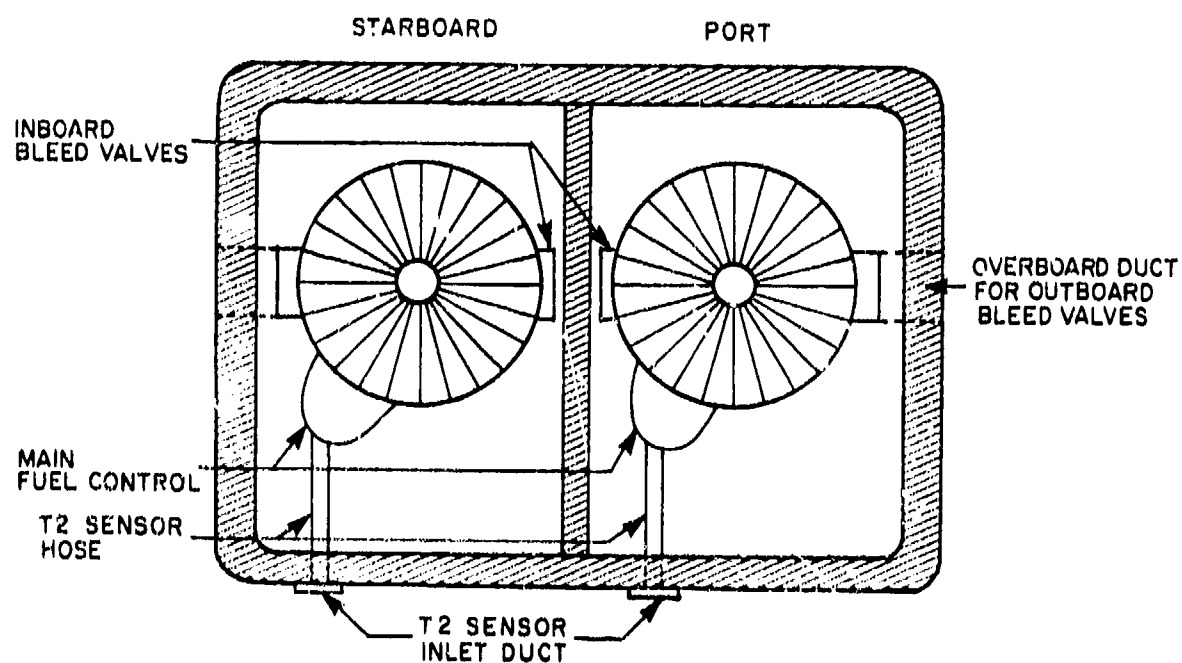


FIGURE 4: CF-5 ENGINE INSTALLATION, VIEW LOOKING AFT FROM COMPRESSOR FACE

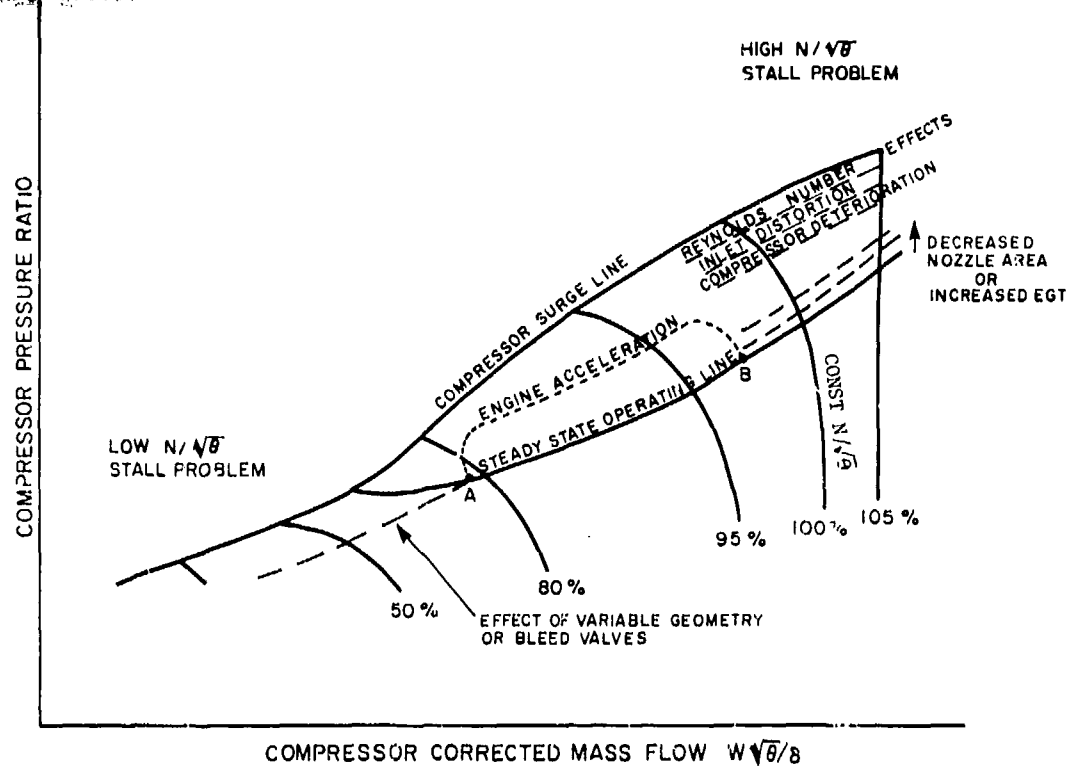


FIGURE 5: GENERALIZED COMPRESSOR MAP FOR A SINGLE SPOOL, FIXED EXHAUST NOZZLE TURBOJET

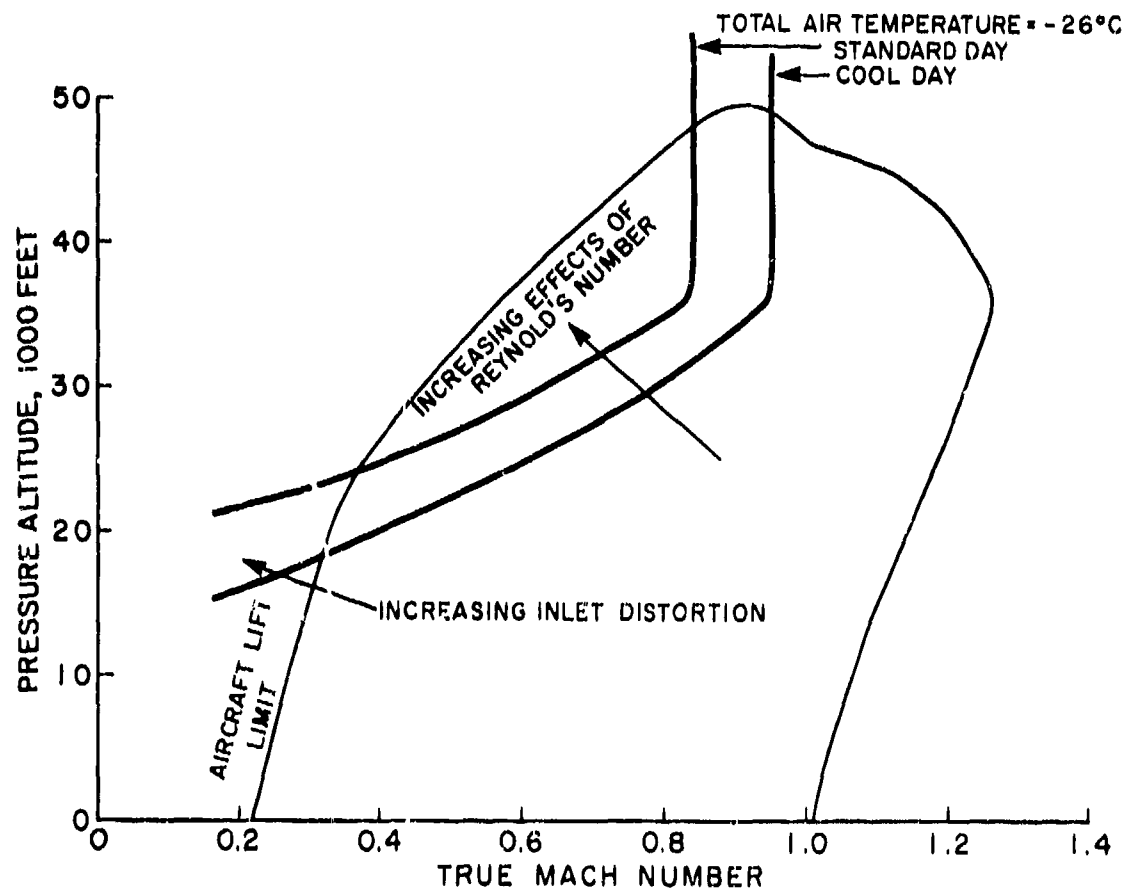


FIGURE 6: CF-5 LEVEL FLIGHT ENVELOPE SHOWING FLIGHT REGIONS AFFECTING COMPRESSOR STALL MARGIN

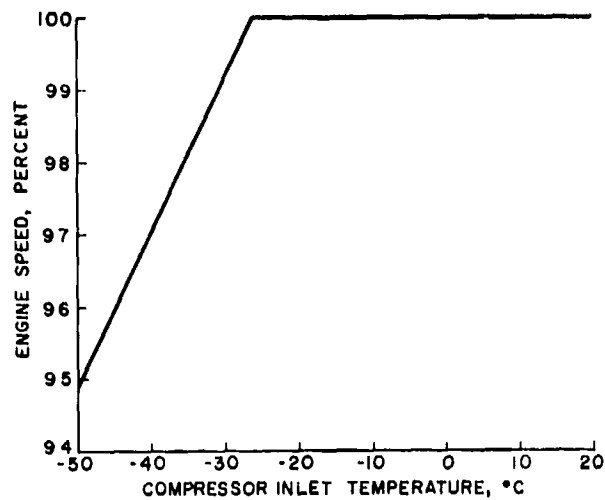


FIGURE 7 : ENGINE SPEED AS A FUNCTION OF COMPRESSOR INLET TEMPERATURE

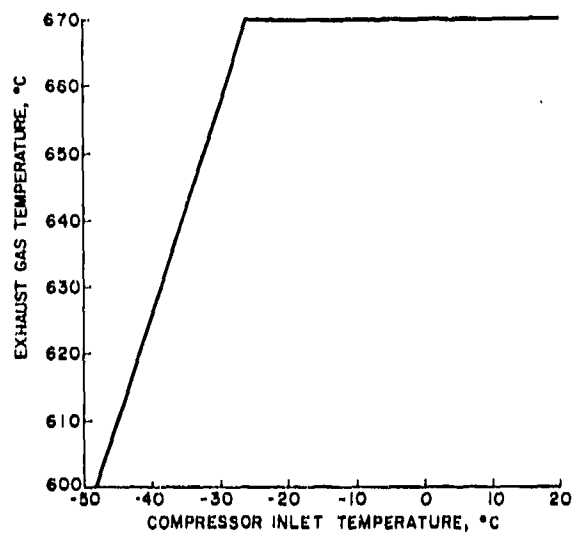


FIGURE 8 : EXHAUST GAS TEMPERATURE AS A FUNCTION OF COMPRESSOR INLET TEMPERATURE

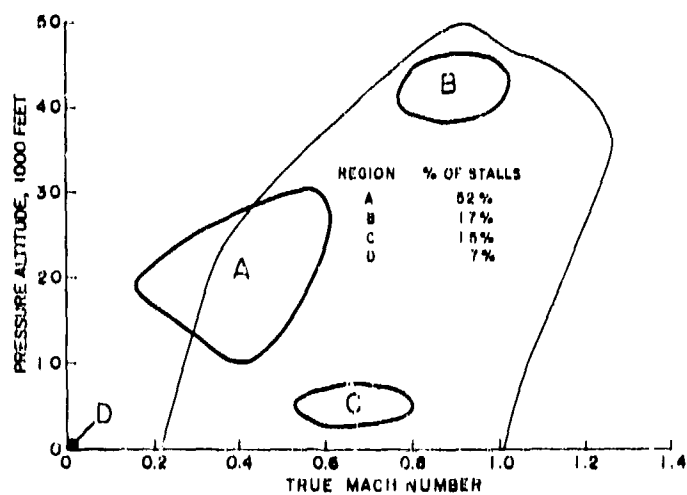
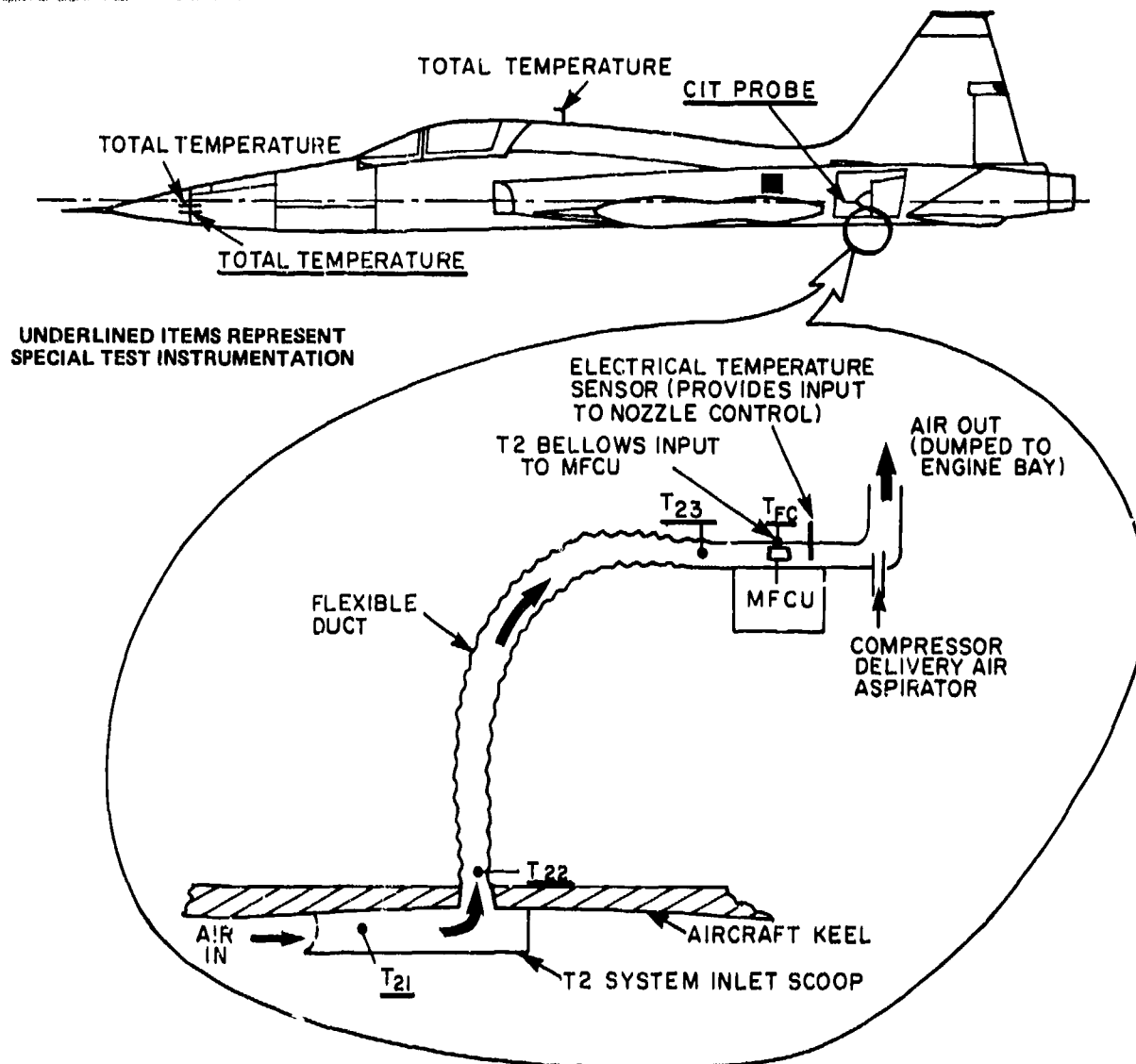


FIGURE 9 : CF-5 LEVEL FLIGHT ENVELOPE SHOWING FLIGHT REGIONS WHERE COMPRESSOR STALLS OCCURRED



PARAMETERS RECORDED DURING FLIGHT TESTS		
AIRFRAME	ENGINES (LEFT AND RIGHT)	T2 SENSING SYSTEM TEMPERATURES (LEFT AND RIGHT)
ALTITUDE	N	CIT - PROBE ON ENGINE BULLET NOSE
AIR SPEED	IGV/BV POSITION	T21 - AIR AT SCOOP INLET
PLA	CDP	T22 - AIR AT DUCT ENTRY
	EGT	T23 - AIR AT DUCT EXIT
TOTAL TEMPERATURE (3 PROBES)	EXHAUST NOZZLE AREA	T _{FC} - MFCU SURFACE

FIGURE 10: CF - 5 SENSING SYSTEM AND TEST INSTRUMENTATION

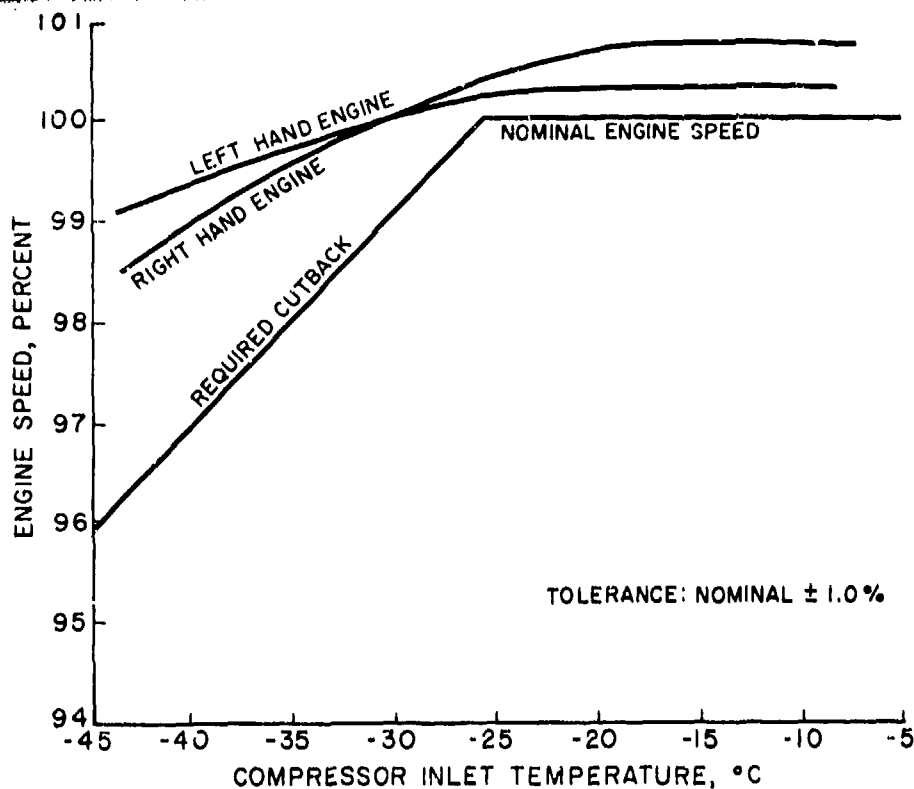


FIGURE 11a: STEADY STATE OBSERVED ENGINE SPEED CUTBACK

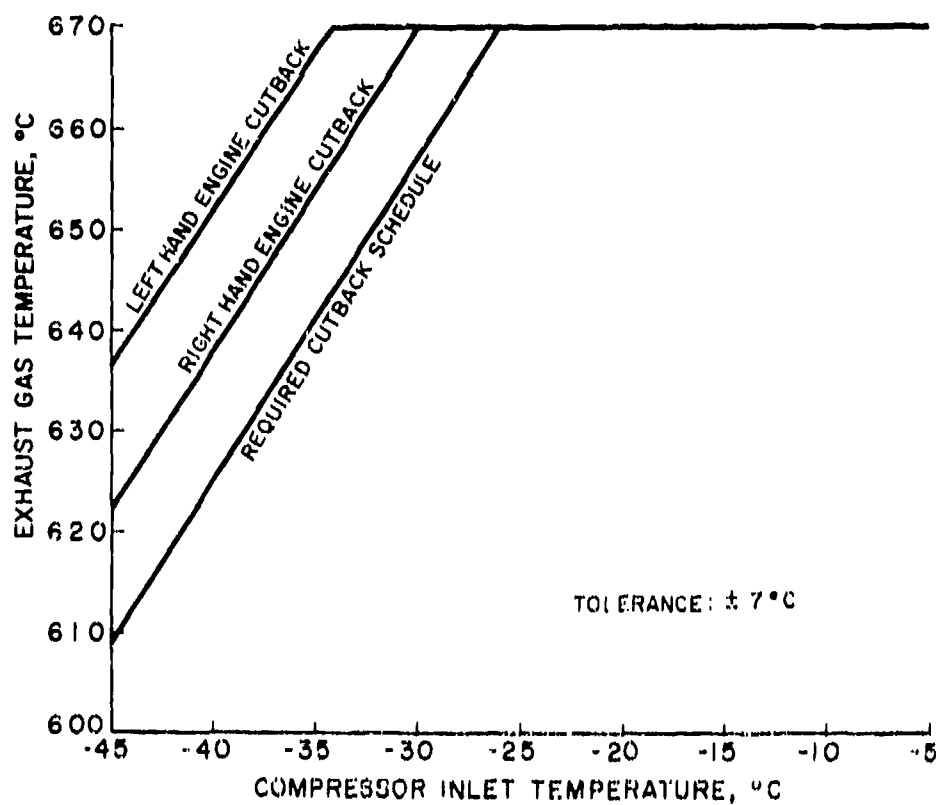


FIGURE 11b: STEADY STATE OBSERVED EXHAUST GAS TEMPERATURE CUTBACK

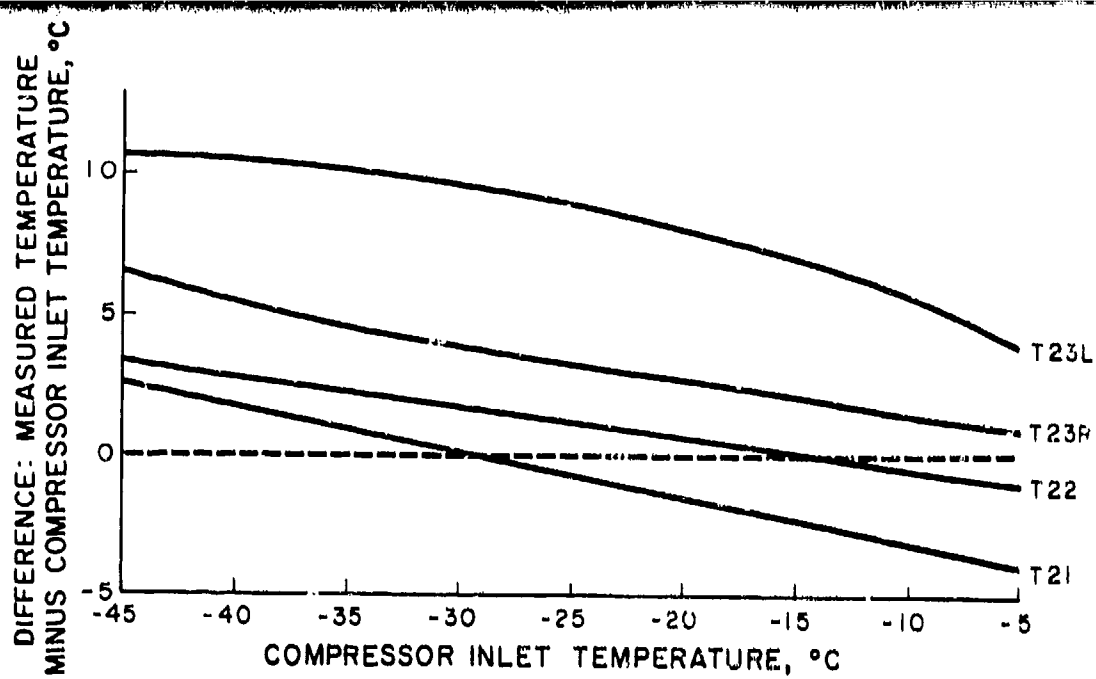


FIGURE 12: STEADY STATE T2 SYSTEM TEMPERATURES

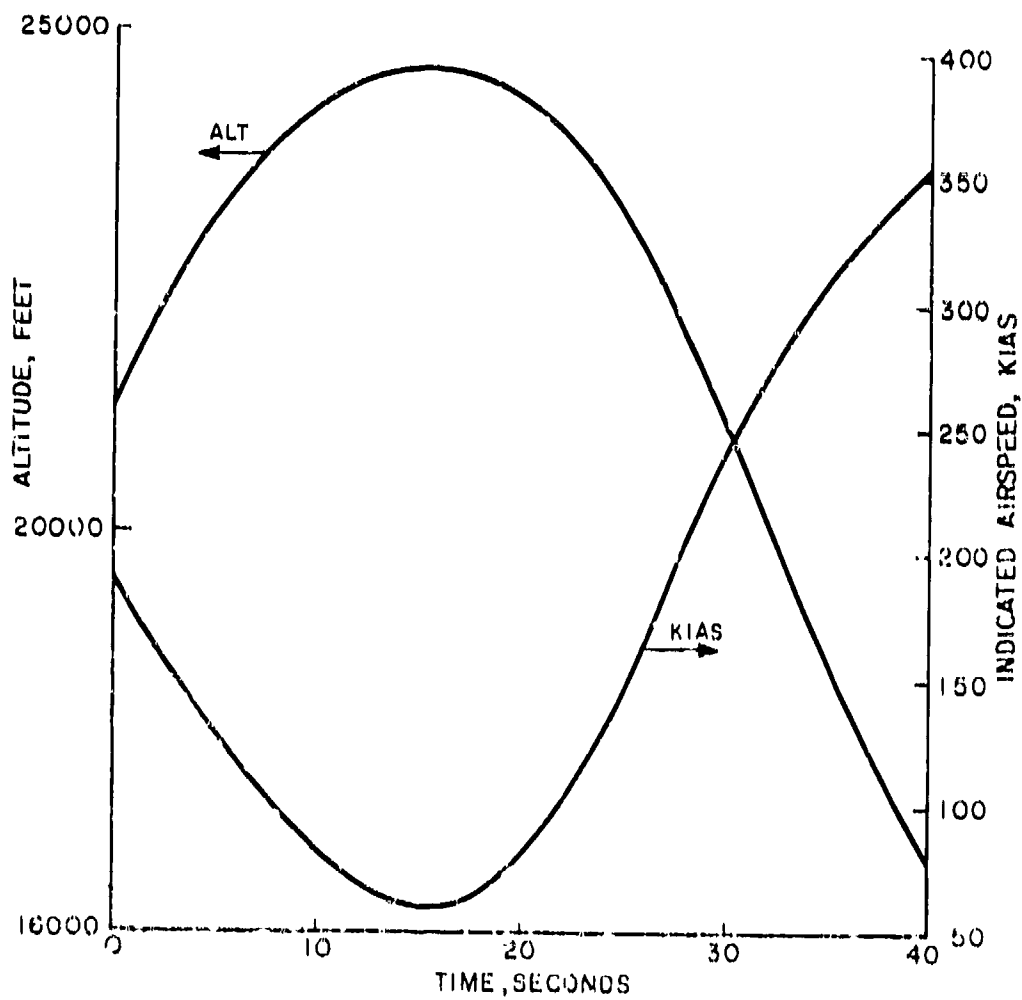


FIGURE 13a: FLIGHT PARAMETERS, 60° ATTITUDE
AIRCRAFT STALL

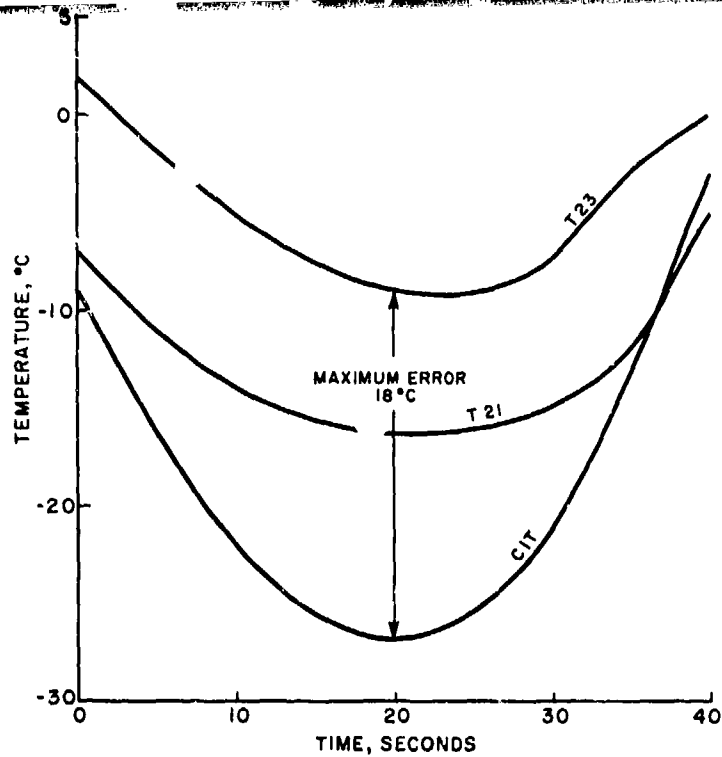


FIGURE 13b: LEFT HAND T2 SYSTEM TEMPERATURES
60° ATTITUDE AIRCRAFT STALL

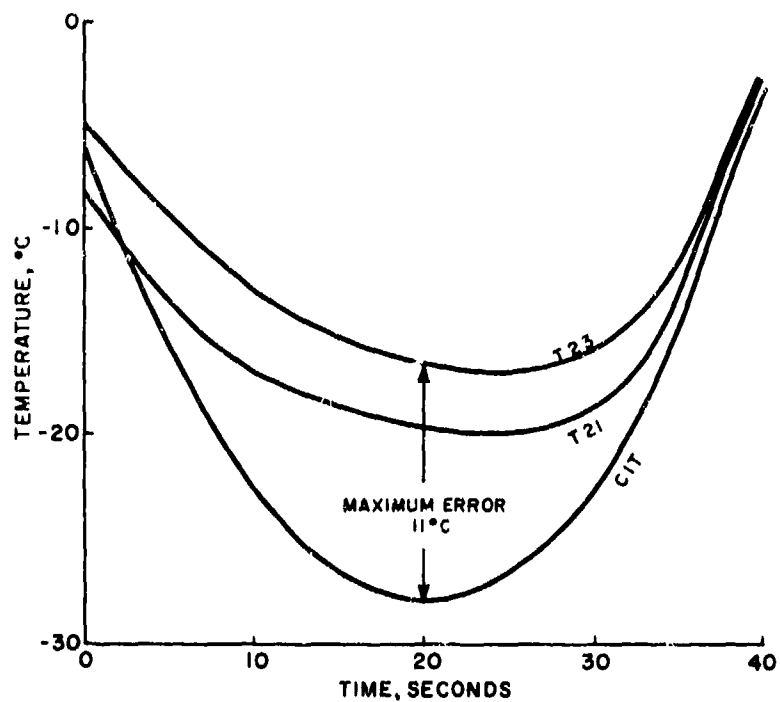


FIGURE 13c: RIGHT HAND T2 SYSTEM TEMPERATURES,
60° ATTITUDE AIRCRAFT STALL

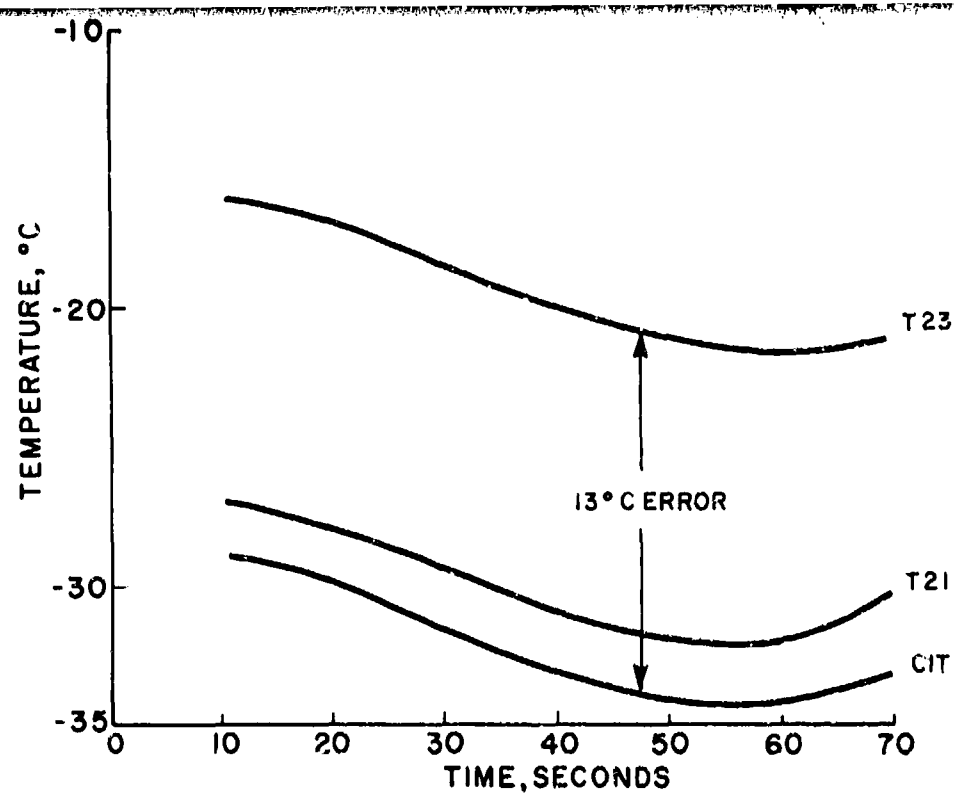


FIGURE 14: LEFT HAND T2 SYSTEM TEMPERATURES, LEVEL FLIGHT AIRCRAFT STALL

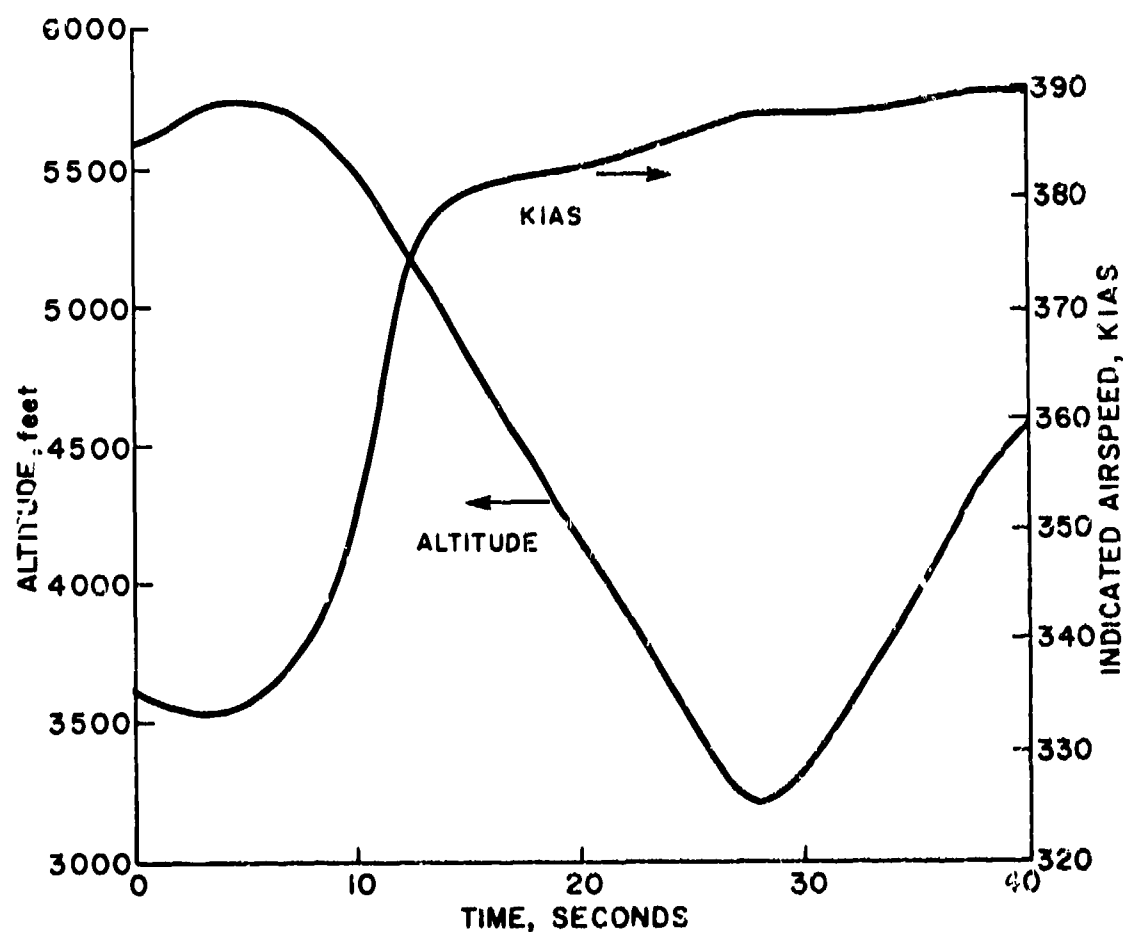


FIGURE 15a: FLIGHT PARAMETERS, WEAPONS DELIVERY PROFILE

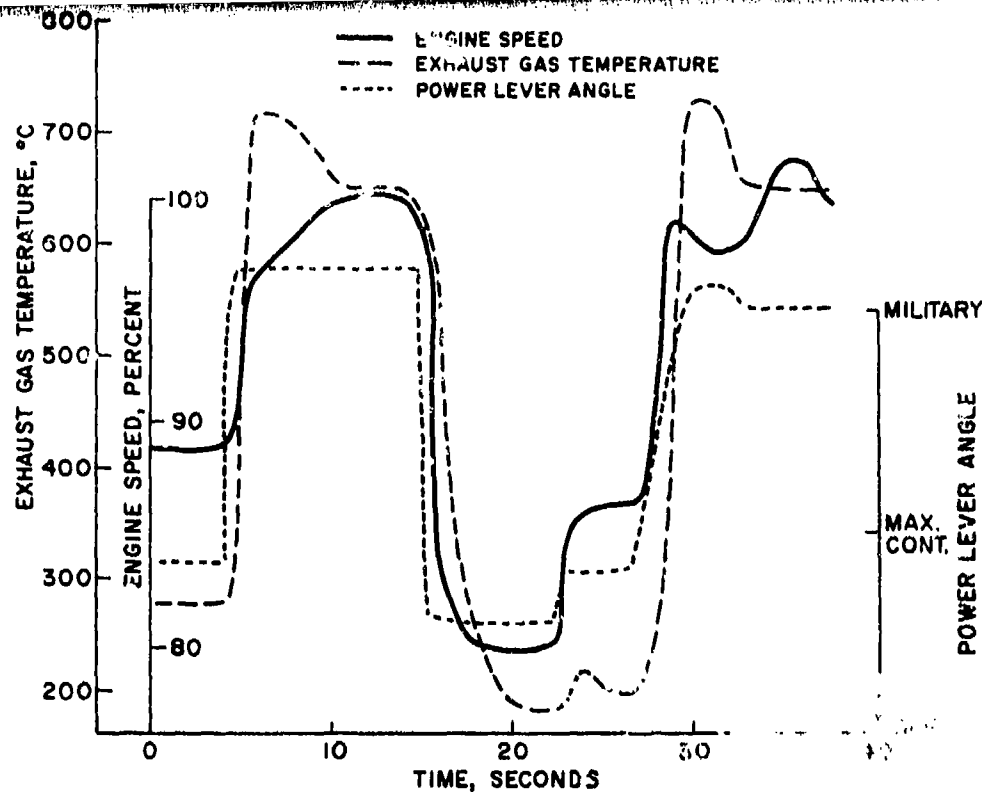


FIGURE 15b : FLIGHT PARAMETERS, WEAPONS DELIVERY PROFILE

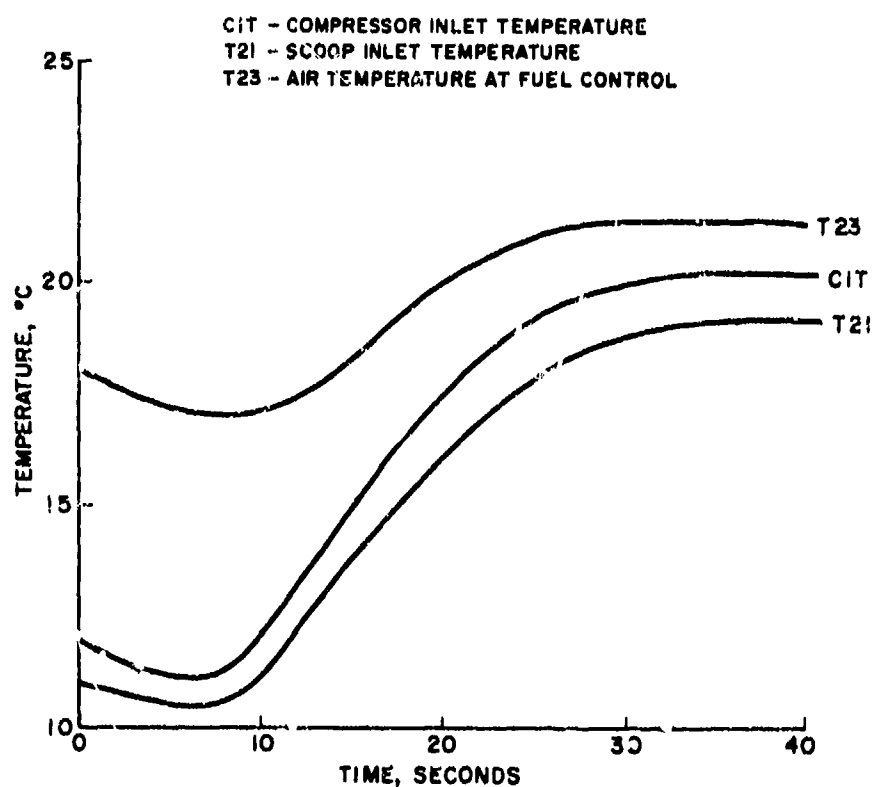


FIGURE 15c : T2 SYSTEM TEMPERATURES, WEAPONS DELIVERY PROFILE

THE ROLE AND IMPLEMENTATION OF DIFFERENT NACELLE/ENGINE SIMULATION CONCEPTS FOR WIND-TUNNEL TESTING IN RESEARCH AND DEVELOPMENT WORK ON TRANSPORT AIRCRAFT

by
B. Ewald and R. Smyth
Vereinigte Flugtechnische Werke GmbH
D 2800 Bremen
Germany

SUMMARY

Research and development work on future transport aircraft demand a reliable assessment of engine interference in order to fully exploit the performance potential of the aircraft. The use of high bypass-ratio turbofans result in nacelles of substantial dimensions causing complex flow phenomena in both low- and high-speed flight conditions. At low speed the problem is further complicated by angle of attack, sideslip, engine-out conditions and slat/flap interference. The determination of propulsion-system interference drag is one of the major tasks in all analytical and experimental work. It is also one area with the largest uncertainties in drag prediction. This paper concentrates mainly on the different experimental methods and their specific roles in various stages of research and development. The main problem here is the simulation and calibration of the propulsion system. Different methods of simulation can be applied. The main types are: flow-through nacelles, powered nacelles (blowing, turbine powered simulators "TPS", ejector powered), inlet models. Turbine powered simulators (TPS) represent the most advanced simulation of the high bypass-ratio engine in model scale. However, complicated model design, accuracy requirements for calibration and operation and costly windtunnel test procedures limit the routine usage of this technique. A large part of the wind-tunnel tests still have to rely upon flow-through nacelles. In addition, a novel flow-through nacelle with a variable plug, already developed and tested by VFW, will be presented. It will be shown that the combination of flow-through nacelles and TPS can be efficiently used in the windtunnel investigation of propulsion-system effects for transport aircraft. Test set-up, calibration methods and evaluation procedures are presented for each method.

LIST OF SYMBOLS

A_E	flow through nacelle exit area	P_1	wall static pressure in inlet
A_{∞}/A_C	Inlet mass flow ratio based on capture area A_C	P_{∞}, P_0	ambient pressure
C, C_{local}	wing chord	P_{T2}	total pressure at fan entry
C_d	nacelle drag	PTF, P_{115}	total pressure in fan nozzle
C_{DF}	fan nozzle discharge coefficient = actual flow/ideal flow	$PT7, P_{14}$	total pressure in primary nozzle
C_{DP}	primary nozzle discharge coefficient	q	dynamic head
C_{GF}	fan nozzle gross thrust coefficient = actual thrust/ideal thrust	SFC	specific fuel consumption = fuel flow/thrust
C_{GP}	primary nozzle gross thrust coefficient	TPS	Turbine Powered Simulator
C_p	pressure coefficient $(p - p_{\infty})/q$	T_{10}	total temperature in inlet
ΔC_D	Interference drag coefficient due to the engine installation Defined in Fig. 2.1	T_{115}	total temperature fan nozzle
$\Delta C_{Dp jet}$	pressure drag coefficient due to jet effect	X	axial distance
F_{GP}	gross thrust primary nozzle	V_A	nozzle exit velocity
F_{GF}	gross thrust fan nozzle including core cowl drag	V_B	primary nozzle exit velocity
F_N	engine net thrust	V_{18}	fan nozzle exit velocity
F_{RD}	ram drag	V_{∞}, V_0	freestream velocity
\dot{m}_1	fan mass flow	W	aircraft weight
\dot{m}_4	TPS turbine mass flow	α	angle of attack
M, M_{∞}	Mach number	β	sideslip angle
M_1	Mach number in inlet throat	δ	absolute pressure relative to standard sea level
p	static pressure	Π_{∞}	total/static pressure of freestream
P_t	total pressure		

1. INTRODUCTION

Modern transport aircraft must offer improved performance characteristics with respect to energy efficiency and operating costs. The dramatic development of fuel prices make fuel consumption the main factor contributing to the build up of operating costs.

Projected fuel prices for 1987 and the impact on operating costs for a typical wide-body transport aircraft is shown in Fig. 1.1 taken from Ref. 8. The high and low projections of fuel price result in fuel costs being 46 % to 70 % of the overall operating costs.

Thus the reduction in mission fuel burned has to be one of the main objectives for future transport aircraft. This requires the application of advanced technology. With respect to aerodynamics and propulsion the objectives must be to minimise the overall drag of the aircraft and reduce fuel consumption of the engines.

Maximum benefits can be achieved by paying careful attention to the nacelle/airframe integration process for a given engine/airframe combination in order to exploit the full performance potential.

The basic elements of advanced aerodynamics and propulsion technology shown in Fig. 1.2 are:

- o Advanced wing design using transonic aerofoils and efficient high lift devices. Improved supercritical wings are characterised by higher aspect ratios and increased thickness.
- o High bypass-ratio turbofan engines with lower specific fuel consumptions.

Modern high bypass-ratio turbofans present today's state-of-the-art in propulsion technology. Compared to the first generation of turbojets they have a 40 % lower specific fuel consumption, see Fig. 1.3. Further improvements are expected to bring an additional reduction of 12 % - 15 %.

One of the main problems which tend to offset these benefits are the relatively large dimensions of these engines, which result in large nacelles close to modern wing profiles of greater thickness. Future energy efficient engines will tend towards even higher bypass ratios as can be seen from Fig. 1.4. Larger engine dimensions also mean higher mass flows in and out of the nacelle.

Installation of these nacelles must therefore take account of interference effects due to closer nacelle/wing spacing and larger flow rates of the nacelle in both low and high speed conditions. This problem is of special importance in the case of the twin-engine transport with a single large powerplant under each wing. A typical twin-engine wide-body transport is shown in Fig. 1.5. Research and development of modern transport aircraft must pay particular attention this problem area in order to obtain the most favourable combination of engine/nacelle and airframe on the basis of reliable theoretical and experimental predictions.

Nacelle/wing integration requires the handling of a highly complicated three-dimensional flow field comprising

- o flow around a swept wing with fuselage
- o inlet and nozzle flows
- o pylon between wing and nacelle

The complex nature of this flow field makes the determination of propulsion system interference drag one of the main uncertainties in the prediction of overall aircraft drag.

A clear definition of installed thrust and aircraft drag taking account of jet-interference and inlet spillage effects is also necessary of the correct breakdown of overall aircraft drag and in order to facilitate the correlation of flight test and model data. A practical thrust/drag bookkeeping procedure also facilitates the efficient integration of development work between engine and airframe manufacturer. It further provides the possibility of identifying specific areas of drag uncertainty, where further research and development efforts should be concentrated.

Although theoretical methods are advancing in this area, windtunnel investigations using different methods of engine simulation play a very important role in the integration of engine and airframe.

This paper will be mainly concerned with the different experimental methods and their specific application at various stages of the research and development work to be done. This will be preceded by a discussion of the main aspects of nacelle/airframe interference at typical high and low-speed flight conditions.

2. ENGINE/AIRFRAME INTERFERENCE EFFECTS

2.1 Description of the General Problem

Interaction of the flow fields from nacelle and pylon influence the lift and drag characteristics of the complete configuration as compared to the characteristics of the wing and fuselage alone. With respect to drag this can be expressed as an Interference Drag Coefficient ΔC_D for a given flight and nacelle flow condition and cribed in Fig. 2.1.

$$\Delta C_D = (C_D)_{\text{total}} - (C_D)_{\text{W+F}} - (C_D)_{\text{Nacelle}} - (C_D, f)_{\text{Pylon}}$$

$(C_D)_{\text{total}}$ total drag of wing + fuselage + nacelle + pylon $(C_D)_{\text{Nacelle}}$ drag of nacelle alone less pylon drag coefficient

$(C_D)_{\text{W+F}}$ drag of wing + fuselage $(C_D, f)_{\text{Pylon}}$ pylon skin-friction drag coefficient

In the case of drag measurements using powered simulators appropriate corrections for simulator net thrust must be applied to the above equation.

The goal for the design of an efficient transport aircraft is to minimise the interference drag ΔC_D by design and arrangement of nacelle and pylon within the structural and functional limitations of the engine installation. It is possible to even achieve a favourable interference drag,

Experience with the present generation of wide-body transport aircraft and windtunnel investigations show that the interference drag problem is not entirely a high-speed problem connected with premature drag-rise effects with increasing flight Machnumbers. Attention must also be paid to low-speed interference in order to achieve the best take-off and climb performance.

Correct understanding of the flow conditions at the inlet and exhaust of the nacelle, pylon and swept wing is necessary for the best possible representation of the full-scale aircraft in the windtunnel. This is also important in the analysis of flight test results, where interference due to different inlet and nozzle conditions is sometimes erroneously looked upon as data scatter. Flow in and out of the nacelle is defined by the thermodynamic cycle of the engine. Flow around the nacelle depends upon nacelle shape and the presence of other airframe components near the nacelle. A simplified description of the interference flow field is shown in Fig. 2.2.

The main parameters influencing the engine/airframe interference for a given nacelle and pylon geometry are the flow conditions at the inlet and nozzles, which vary as a function of flight condition (Machnumber, temperature, angle of attack) and engine speed. Fig. 2.3 indicates the range of flow condition depending upon flight condition. It must be realised that due to the relatively large dimensions of the engines these changes in flow can have considerable effects on the overall lift and drag characteristics of the aircraft.

Nacelle shape plays an important role in the interference problem. One of the main factors here is the nozzle type. This has traditionally been the responsibility of the engine manufacturer, who in most cases is mainly interested in:

- o Thrust and SFC of isolated (non-installed) powerplant at specific points of the mission profile
- o Thrust reverser design
- o Maintainability and commonality of same engine in different aircraft
- o Weight

The present generation of high bypass-ratio engines belongs to the non-mixing type and thus has separate nozzles for the fan and primary exhaust systems. Fig. 2.4 shows the different types of nozzle design. It has been usual practice up to now to select the nozzle combination on the basis of isolated nozzle tests, i.e. without influence of the wing. This may be quite sufficient for preliminary design studies and initial trade-offs for different nozzle types. In final configuration work however the effect of wing and pylon must be considered.

Optimisation of the nozzle system using this traditional method leads to different proposals by the engine manufacturers. Fig. 2.5 shows nacelles for the Airbus A 300 from General Electric and Pratt & Whitney.

Longduct mixing nacelles are also being proposed for future commercial transports. Fig. 2.6 shows proposals of General Electric and Pratt & Whitney.

Closely coupled with the nacelle/airframe interference is the pylon. Careful consideration of this component is necessary due to the following aspects:

- o Fence effect of pylon
- o Division of fan nozzle flow with boundary layers
- o Cross-flow over pylon leading edge under certain flight conditions
- o Interference of pylon and core cowl

Windtunnel tests must include the pylon to simulate a realistic flow field of the nacelle installation. Fig. 2.7 shows the effect of the pylon taken from model tests presented in Ref. 12.

With respect to the inlet, the boundaries of external flow separation must be determined. Inlet external separation can occur at

- o Engine Windmill during take off
- o High Mach number and lower engine power settings.

In summary, the problem of engine/airframe interference must take account of the following factors:

- o Problems typical to high-speed and low-speed
- o Angle of attack/Sideslip
- o Nozzle shape
- o Nozzle flow conditions
- o Inlet flow conditions
- o Mutual interference between nacelle and wing

In order to achieve the maximum benefits from the combination of nacelle and airframe, the process of nozzle selection for future aircraft must be done in an "integrated development approach" between engine and airframe manufacturer. This method must consider mutual interference effects, i.e.

- o nacelle interference on wing and pylon (change in wing pressure distribution)
- o wing interference on nacelle (effect on nozzle performance including modification of cowl pressures)

in early stages of aircraft development work.

2.2 High Speed Interference

Engine/airframe interference at high-speed flight conditions is characterised by modifications in the transonic flow fields of the isolated components with respect to

- o Wing upper surface
- o Wing lower surface and pylon
- o Nacelle, especially core cowl

Fig. 2.8, 2.9 and 2.10 showing measured data from flight test and windtunnel models explain this basic flow phenomenon which is fundamental for all work on nacelle/airframe interference at high and low speed flight conditions. The examples shown are for the case of a conventional wing profile. Stronger interference effects must be expected with the thicker supercritical wing profiles of advanced transport aircraft.

With respect to thrust/drag bookkeeping the following conclusions can be drawn:

- o Nacelle interference on the wing increases wing leading edge "suction", which manifests itself in an apparent drag reduction, if the nacelle forces are not measured in the model test.
- o Wing interference on the nacelle is mainly on the core cowl. Integration of pressures over this surface, leads to an incremental drag. The magnitude of this incremental drag depends upon the core cowl shape.
- o Viscous effects must be taken into account when evaluating model pressures and forces to predict full-scale performance. Differences in the boundary layer characteristics especially with respect to the displacement thickness due to scaling effects can lead to inaccurate predictions for full scale.

It has already been shown that the pylon plays a very important role in the interference problem. Pylon shape can interfere with the core cowl and lead to unfavourable pressure distributions resulting in flow separation on the core cowl. Appropriate shaping of the pylon with respect to thickness distribution and camber can provide drag reduction at cruise. All considerations with respect to the use of a "Universal Pylon" for left and right wing and for different engines must be based on trade-off investigations to assess the overall "drag penalty" for commonality. This requires model tests with correct inlet and nozzle flow simulation.

Besides the understanding of the interference flow phenomenon described above it is also essential to know the characteristics of nozzle flow at cruise conditions in order to make the correct decisions for engine simulation techniques in the windtunnel. For the high bypass-ratio engine this is mainly the fan efflux. As can be seen from Fig. 2.3 this is mainly supersonic flow with nozzle exit Mach numbers ranging from 1.2 to 1.4. The flow over the core cowl consists of a sequence of shock and expansion waves with strong viscous interactions (Ref. 14).

Turning of the supersonic flow at the end of the core cowl, where it meets with the primary stream usually takes place with a shock wave. Experience shows that the strength and position of the shock wave under the wing plays an important role in the nacelle/airframe interference drag problem. Closely connected with this supersonic flow field is the peak Mach number on the pylon which can be related to interference drag increments as can be seen from Fig. 2.11.

Windtunnel tests show that interference drag changes with increasing fan nozzle pressure ratio up to pressure ratios of about 2.2 for a typical transporter configuration. At fan nozzle pressure ratios higher than 2.2 there is hardly any change in interference drag. Thus, it is only necessary to simulate nozzle pressure ratios up to about 2.2 in model tests. For tests with the objective of determining aerodynamic loads on nacelle, pylon and wing it may still be necessary to go up to the highest possible nozzle pressure ratios. The present generation of turbine powered simulators can cover the full range of engine nozzle pressures.

In addition to the influence of fan nozzle pressure ratio on interference drag the effect of inlet mass flow must also be considered. It is not sufficient to use only an isolated fan cowl with true representation of the inlet to determine the change in spillage drag due to changes of mass flow ratio and free-stream Machnumber. A check must be done with the complete configuration of nacelle, pylon and wing in order to take account of three-dimensional effects, especially the upflow at the inlet plane. A crossflow component of this flow field can in certain cases make the outboard sides of the inlet critical. Since spillage drag depends upon boundary layer development and flow separation the effect of Reynolds-Number must be taken into consideration when using model data.

2.3 Low-Speed Interference

The interference problem between nacelle, pylon and wing at low-speed flight is characterised by

- o High angles of attack corresponding to take off and landing
- o Different slat and flap settings
- o Sideslip
- o Engine power settings from Windmill to Go-Around

Fig. 2.12 identifies the parameters involved and typical problems areas.

The main objective here is the determination of the low-speed drag polar for symmetrical and asymmetrical flight conditions. In the case of a twin-engined transport this means:

- o Symmetrical
Both engines at Go-Around Power
- o Asymmetrical
One engine out (windmilling), one engine at Go-Around

The basic flow phenomenon with respect to the complexity of the flow field between wing, pylon and nacelle as already discussed under high-speed interference also applies here. The problem is additionally complicated by the large range of angle of attack and changes in wing geometry due to slat and flap.

Flow observations from flight and model tests show that the highly complex flow field around nacelle, pylon and wing contains substantial cross-flow components and engine power effects.

The low-speed nacelle interference problem is an important task in the nacelle integration process. Especially the high bypass-ratio engine with the trend to larger dimensions and more massflow in and out of the engine has a strong effect on the lift and drag characteristics of the wing at high-lift conditions.

Recent windtunnel investigations on typical wide-body transport aircraft configurations show that jet-effects must be included. This is a very important fact for the decision concerning the use of engine simulating techniques in windtunnel tests. Viscous interaction must also be taken into account in order to correct for scaling effects. This is similar to the high-speed case.

Due to the fact that the nozzles are subcritical in the low-speed flight regime back-pressure effects can influence the thrust and discharge coefficients of the nozzles. The clarification of this problem is very important in the thrust/drag bookkeeping procedures and for cooperation with the engine manufacturer.

3. THE ROLE OF EXPERIMENTS IN NACELLE/AIRFRAME INTEGRATION DEVELOPMENT

3.1 The Need for Experiments

The complex nature of the flow in the nacelle, pylon, wing interference drag problem of modern transport aircraft makes this one of the difficult areas in the drag synthesis of the complete aircraft. Computational methods for the three-dimensional potential-flow including jet-effects are presently in the stages of development. Methods already available are three-dimensional subsonic potential-flow programmes and empirical area ruling methods described in Ref. 16 and 17. Apart from this, investigations of nacelle/airframe interference must still strongly rely on experimental methods in the windtunnel and in flight test. Windtunnel testing with appropriate simulation of the propulsion system constitutes the main source of data on engine/airframe interference effects both in development work for aircraft and

Typical nacelle and engine tests for aircraft development work are shown in Fig. 3.1. Included in these methods is also the engine calibration procedure normally used by the engine manufacturer. Correct understanding of engine calibration techniques is necessary for the evaluation of wind-tunnel and flight-test results and for the final thrust/drag bookkeeping of the complete aircraft. This is not only important due to the equivalence of thrust and drag, but also to compare calibration techniques of simulators used in the windtunnel with those used by the engine manufacturer for the real engine.

The current state-of-the-art of sea level and altitude engine test facilities represents the best the engine manufacturer can do for engine development work. They however do not fully represent the underwing engine installation due to the lack of freestream flow around the nacelle and the wing effect. Fig. 3.2 compares a typical altitude test facility with the actual engine installation under the wing.

Data from all sources of experimental testing should be compatible in order to "close the loop" as shown in Fig. 3.3 in a combined and well coordinated effort by both engine and airframe manufacturer. Ref. 18. describes an integrated systems approach for propulsion system testing with respect to performance.

Among the experimental methods shown in Fig. 3.3 the windtunnel offers the highest degree of flexibility. Modifications can be incorporated quickly and at lower cost. In order to achieve reliable test results, adequate simulation of the propulsion system inlet and nozzle flows is necessary. Simulation techniques, calibration and evaluation are discussed in 4. and 5.

3.2 Engine Calibration

Calibration methods used by the engine manufacturer are shown in Fig. 3.3. The main source of aerodynamic data for nacelle integration is the isolated blown nacelle for the measurement thrust and discharge coefficients. These tests are of high importance because the results are used not only for real engine nozzle calibration but also in the process of thrust determination of model simulators. Testing of the blown nacelle should take account of the following:

- o Freestream suppression effect
- o Effects of real installation, e.g. wing and pylon

During the development of the real engine corrections for full-scale effects can be obtained in order to adjust blown-nacelle data to the real aircraft. The full-scale nozzle data is needed for the calibration of flight test engines for inflight thrust calculation.

One of the most important tasks for validation of full-scale performance in flight test is the determination of inflight thrust. This is a key item in flight test programmes for new aircraft and more often in cases where aerodynamic or engine modifications have been applied to improve overall performance. In flight testing the problem of accurate drag measurement is mainly a problem of thrust determination.

The most accurate method of thrust determination makes use of well calibrated engines using total pressure rakes in the nozzles as shown in Fig. 3.4 to control the flow through the engine. Thrust and mass flow are based on carefully determined nozzle coefficients derived from blown nacelle tests (see Fig. 3.1) and corrections for full-scale. Best accuracy is obtained from direct engine calibration in an altitude test facility.

Flight testing on production aircraft has to make use of the instrumentation available. Different thrust parameters are used by the engine manufacturers:

- o General Electric
Corrected low pressure rotor speed $N_{1\text{corr}}$

$$N_{1\text{corr}} = N_1 \sqrt{\frac{288}{T_{t0}}}$$

$$T_{t0} = \text{total temperature fan entry } ^\circ\text{K}$$

- o Pratt & Whitney
Engine pressure ratio EPR
 $\text{EPR} = P_{T7}/P_{T2}$
 P_{T7} = total pressure in primary nozzle
 P_{T2} = total pressure at fan entry

Engine calibration techniques based on nozzle pressure and temperature measurements and the simple GE method using $N_{1\text{corr}}$ are also applicable to Turbine Powered Simulators (TPS) for windtunnel work. Due to the similarity between real engine and TPS use of this new technique in model testing can improve the cooperation between engine and airframe manufacturer in the area of performance with benefit for the overall accuracy of thrust/drag determination and performance development.

4. ENGINE SIMULATION TECHNIQUES IN WIND TUNNELS

4.1 Flow Through Nacelles

This is the cheapest engine simulation for wind tunnel models of transport configurations and because of their cheapness they are widely used.

Since no energy is added to the internal flow of such a nacelle, the simulation of the jet and its influence on the airframe is wrong except in the windmill case.

On the other hand the intake flow can be matched correctly to the full-scale condition for the high speed flight region. In the low speed flight region the intake flow can be simulated only for the windmill and flight idle cases.

Different flow through nacelle schemes, which are used presently in transport wind tunnel testing, are shown in Fig. 4.1.

o Triple Body Nacelle

This scheme gives a perfect optical simulation of the full-scale engine. Fan cowl, fan nozzle, gas generator cowl and primary nozzle plug are simulated correctly to scale. With this scheme the intake mass flow at a given free stream mach number is fixed by the nozzles exit areas. The mass flow can be reduced by installation of screens or similar drag devices.

o Double Body Nacelle

This scheme allows a higher mass flow due to the larger primary nozzle exit area. Plugs of different sizes may be used in the primary nozzle to adjust the inlet mass flow.

Usefulness of the double and triple body nacelle design is controversial. Since the nozzle exit flow energy is wrong, it seems not to be useful to correctly scale the gas generator cowl and primary nozzle. Due to the wrong jet energy the simulation of aerodynamic interference of the engines rear part is wrong anyway.

On the other hand these nacelle designs have a high internal drag, which is difficult to evaluate with sufficient accuracy. This is even more difficult if drag screens are used to reduce inlet massflow. So the evaluation of airframe drag by subtraction of internal drag is burdened with relatively large errors.

o Skirted Nacelle

In this design the intake lip and fan cowl is correctly scaled downstream to the fan nozzle exit. From this point the solid surface is extended further downstream as to simulate the boundary of the fan jet. The exit area of this single body nacelle is matched to give the desired intake mass flow.

This design scheme gives a low total drag of the nacelle which simplifies internal and external drag separation.

A serious disadvantage of the skirted nacelle is the external flow separation behaviour at high incidence. Separation onset on the fan cowl and its interference with pylon, slat and wing is heavily influenced by the extended fan cowl surface. So the high lift results of a wing in presence of such a nacelle may be misleading.

4.2 Powered Nacelles

4.2.1 Blown Nacelles

The designation "blown nacelle" is used for nacelles with a faired intake and a jet simulation by pressurized air which is fed into the nacelle from external sources. Fig. 4.2 shows three different possibilities to feed pressurized air into the nacelle.

If the air is fed to the nacelle by an external sting, the nacelle is nonmetric. A measurement of the forces acting on the nacelle is possible only by a separate nacelle balance with a force free air bridge. The necessary gap between pylon and nacelle generates additional errors.

Feeding the air through wing and pylon is limited by the available space.

A sophisticated modification of the blown nacelle uses hydrogen peroxide to simulate the hot primary nozzle jet, see Fig. 4.3. This technique gives true simulation of the primary nozzle mass flow and temperature but the test set-up is very expensive and thrust calibration is complicated. With regard to the small interference effects of the primary jet in the case of most transport configurations this large expenditure seems not to be worthwhile.

The general disadvantage of blown nacelles is the nonexistent intake flow. So the use of blown nacelles is based on the assumption that direct and interference effects of the intake flow are independent from the nozzle exit flow effects.

If this assumption is true, effects of intake and nozzle exit flow may be determined by different test arrangements.

In the case of military airplanes with long ducts this assumption is valid and corresponding test procedures are successful. In the case of wing mounted high bypass short duct engines however intake effects and jet effects are coupled to a certain extent by wing and pylon interference effects; main effect in this respect is the wing circulation. Since an extremely high accuracy is essential in today's transport development, the use of blown nacelles is a questionable concept.

Especially questionable are test set-ups with external air supply and nonmetric nacelle. Experience at VFW shows that important parts of the interference effects act on the nacelle and thus tests with metric airframe only may be misleading.

4.2.2 Ejector Nacelle

A typical bypass engine ejector simulator is shown in Fig. 4.4. The ejector nacelle advantage, compared to the blown nacelle is the partial simulation of the intake flow and the reduced feed air mass flow which simplifies the air supply through wing and pylon.

Nevertheless for correct nozzle exit pressure ratios the intake mass flow of an ejector nozzle reaches only 50 to 60 % of the real engine mass flow, which requires complicated correction tests. An additional disadvantage is the extreme mixing turbulence of the nozzle exit flow, which is most different to the real engine jet flow characteristic. This may result in different interference behaviour of the jet; the knowledge in this field is still insufficient.

Despite these shortcomings ejector nacelles are still in use due to their cheapness and simplicity. However their utilization in high accuracy transport tests is certainly not recommended.

4.2.3 Turbine Powered Simulators (TPS)

Historically the TPS is the most recent concept for engine simulation and the most sophisticated too. A typical TPS is shown in Fig. 4.5 and 4.6.

A correctly scaled and calibrated TPS gives geometric similarity of the complete engine pod, correct pressure ratio, temperature and mass flow of the fan jet and correct thrust of the gas generator nozzle. The intake mass flow in relation to the real engine is reduced by the gas generators part of the total mass flow. In the case of a modern 6:1 bypass ratio this results in a 14 % intake mass flow deficit. The standard concept to correct for this is to use a modified intake lip contour which is calculated to give the same streamwise pressure distribution on the external fan cowl surface with the reduced mass flow as in the real engine case. Additional corrections are possible; see chapter 6.

The drive air mass flow is small compared with the blown nacelle or ejector nacelle concepts and the drive air pressure is high. So the air fed through wing and pylon presents no problems.

Since the TPS is normally mounted on the model, the thrust is measured by the balance together with the aerodynamic forces acting on the model. A successful evaluation of drag and interference drag depends on the exact knowledge of the thrust. This thrust calibration over the total speed regime used in the wind tunnel is the real problem of the TPS use. Calibration and wind tunnel test accuracy must be pushed to the utmost limit of the state of the art, otherwise the interference drag effects are hidden by scatter of the results.

4.3 Inlet Models

These models are used to study inlet flow details, inlet flow losses (steady and unsteady) and the inlet flow-compressor compatibility.

Normally, only the fan cowl external and internal contours and adjacent parts of the airframe (wing, pylon) are realized with inlet models and the air is sucked into the inlet by an external compressor.

Recent publications, e.g. [6], show a marked influence of the real compressor on the flow measurement just ahead of the compressor face. This means a measurement without compressor, simply by sucking air through the inlet gives no reliable inlet/engine compatibility judgement.

4.4 Comparison of Simulation Techniques

Fig. 4.7 shows a comparison of different wind tunnel engine simulation techniques and full-scale flight test. Obviously the TPS concept is the optimum engine simulation available for transport configurations in today's wind tunnels. The blown nacelle and ejector nacelle concepts are seriously limited and should not be applied in modern transport development.

Nevertheless the high expenses and the time consuming complexity of TPS tests forbid the general use of this design with all aerodynamic development wind tunnel tests. For this reason the additional use of flow through nacelles is unavoidable. A detailed comparison of the simulation ranges of flow through nacelles and TPS is shown in Fig. 4.8. The flow through nacelle gives a correct simulation for idle and windmill cases. For cruise condition the flow through nacelle only gives correct simulation of the inlet stream tube and the fan cowl external flow. For low speed / high power conditions, i.e. initial climb and approach, the flow through nacelle is wrong.

This comparison leads to a concept for combined utilization of flow through and TPS nacelles in the development process, which is outlined in chapter 6.

5. CALIBRATION AND EVALUATION METHODS

5.1 General Considerations

Calibration and evaluation methods proved to be the key to success in wind tunnel engine simulation. Only sophisticated methods, applied with great carefulness, are able to show the small interference effects we are hunting for.

From a purely scientific point of view a lot of different methods may be derived, which are suited for correct and accurate data evaluation. In the case of practical transport aircraft development however one has to accommodate the wind tunnel evaluation methods to the full-scale engine calibration and specification methods to allow a correct application of the wind tunnel data to the full-scale aircraft performance prediction.

Most full-scale engines are tested in altitude simulation facilities where the thrust is measured for the full range of Mach numbers and altitude. This calibrated and guaranteed thrust includes the scrubbing drag on the gas generator cowl and the scrubbing drag of the fan jet on the pylon as well as the internal loss of the inlet duct flow.

All other losses or influences are depending on the engine installation on an airframe.

In consequence all such effects are considered to be part of the airplane drag:

- Drag of external flow on fan cowl including spillage drag
- External flow influence on nozzle discharge coefficients
- Wing and pylon interference on nozzle discharge coefficients
- Wing and pylon influence on scrubbing drag
- Jet and fan cowl flow influence on wing and pylon flow.

The calibration of engine simulators has to follow closely the full scale engine calibration and specification methods; so the widely used Boeing TPS calibration tank is nothing else than a model scale engine altitude test facility.

This method of tank calibration has been discussed in many papers, so no further discussion is necessary here.

5.2 Calibration of Flow Through Nacelle

The tank calibration facility was invented for the very critical calibration of the turbine powered simulators, but this test set-up may be used for the calibration of flow through nacelles as well.

The necessary flow through nacelle calibrations cover the mass flow calibration over the Mach number range and the internal drag (total drag minus external fan cowl drag). Normally, the mass flow is measured by a Pitot-static rake at the fan position. The internal drag is measured by wake measurements or in crude experiments is estimated by very simple calculations. Obviously the most accurate calibration is achieved in a tank calibration facility; this type of calibration should be used for precise performance tests.

Calibration of a flow through nacelle is much simplified, if the internal drag has a low level even for windmill mass flow conditions, because errors in the evaluation of a low internal drag result in smaller total errors.

This was the main idea of the novel VFW plug nacelle, see chapter 6.

5.3 Calibration of Blown Nacelles and Ejector Simulators

If such nacelles are mounted on the wing, the thrust force is measured by the balance together with all drag forces and an accurate calibration is necessary. In this case only the tank calibration method gives satisfactory results.

If the nacelle is mounted by an external strut, the thrust is not mixed with the drag in the balance and so a rough thrust or nozzle exit pressure calibration is sufficient. In this case however, the corrections necessary for the external mounting rises problems.

Fig. 5.1 shows a half model test arrangement using the ejector simulator shown in Fig. 4.4. In this case the simulator is nonmetric.

A reference to similar clean airframe tests and tests with flow through nozzles had to be established and a correction was necessary for the considerable bulky air feed and nacelle mounting tube.

The figures 5.2 and 5.3 show the enormous amount of different tare tests, that were necessary, with this test arrangement to remove all tares by cross-checking of the influences and to establish the required references to clean airframe and flow through nacelle tests.

Obviously this is not the optimum test technique; despite the large amount of tare tests the final accuracy is not the best.

5.4 TPS Calibration

As outlined already in chapter 5.1, the calibration of turbine powered simulators is normally done in a calibration tank facility. This scheme, originally invented by Boeing, is well known from several publications, so no further description is necessary here.

The experience gathered at VFW showed, that it is relatively simple to achieve a very accurate fan mass flow and fan thrust calibration by fan flow total pressure and total temperature measurement and by fan RPM measurement.

On the other hand extreme care is necessary in the measurement of primary nozzle exit total pressure and total temperature, since the primary nozzle thrust reacts sensitively on variations of these parameters. Extreme accuracy in this field proved to be the key for successful TPS calibration and operation.

A simplified calibration method for TPS was used at VFW successfully for low speed climb performance wind tunnel tests. It was found, that in the low speed regime the external flow Mach number influence on the nozzle discharge coefficients is small and can be neglected. So a very accurate TPS calibration could be achieved with static tests in the wind tunnel. The TPS was mounted on a strut in the test section. The external wind tunnel balance with a force free air bridge was used to measure the static thrust of the TPS. This test set-up is shown in Fig. 5.4.

The evaluation of this static thrust calibration is outlined in Fig. 5.5. The flow discharge coefficient of the primary nozzle was taken from a tank calibration of a similar nozzle configuration and was assumed to be constant over the low speed Mach number range. Repeatability of this calibration proved to be satisfactory also with varying parameters such as drive air temperature.

6. VFW ENGINE INTERFERENCE EVALUATION METHOD

6.1 A Novel Flow Through Nacelle Concept

As was outlined already in chapter 4.1, the flow through nacelle only gives a correct simulation of the intake flow and the external fan cowl flow for part of the flight conditions. The flow over the rear part of the engine and the jet flow is wrong except for the windmill case.

For the other flight conditions the best, i.e. the least wrong, one can achieve from the through flow nacelle, is the correct inlet massflow and correct external fan cowl flow and a fan nozzle exit flow, which is free of disturbance and free of losses.

A nearly loss free flow from the nozzle exit can only be achieved, if there is no screen in the nacelle and if the exit area is the smallest area of the internal flow tube. In this case the desired inlet mass flow must be fixed by the correctly matched nozzle exit area. To combine the matched exit area with the correct geometry of the fan nozzle outer diameter, a correspondingly sized central plug in the nozzle exit plane is necessary.

If this central plug has a variable diameter, different inlet mass flow settings are possible according to different flight and thrust conditions. These considerations led to the VFW Plug Nacelle Concept.

The design principle of this nacelle is shown in Fig. 6.1. Externally the fan cowl is shaped to the scaled geometry of the real engine from the intake lip to the fan nozzle exit. Internally the intake is correctly scaled at least downstream to the fan plane. The internal contour then is streamlined to the fan nozzle exit.

The variable diameter of the central plug, which gives the smallest cross section area of the internal flow always at the fan nozzle exit plane, is achieved by a design of radial lamellas, which are expanded synchronously by a lever and sliding block mechanism. The lamellas are covered by a thin rubber tube which gives a smooth surface at any diameter.

Fig. 6.2 and Fig. 6.3 show the nacelle with maximum and minimum exit area. The rubber cover on the lamellas is removed for these photos. Fig. 6.4 shows the plug nacelle with rubber cover.

The nacelle was tested in a small open test section wind tunnel. Fig. 6.5 shows the fan flow Mach number plotted against free stream Mach number for various exit areas. This diagram clearly shows the possible range of inlet mass flow variations.

The drag of the isolated nacelle, including the drag of the thin mounting strut, is plotted in Fig. 6.6 against free stream Mach number for different nozzle exit areas. The drag coefficient is based on the total frontal area of the nacelle.

The diagramme shows the following drag characteristics:

- o General drag level is low compared with double or triple body nacelles or nacelles with throttling screens.
- o At low Mach numbers drag is decreased with decreasing exit area due to reduced internal flow friction drag.
- o At higher Mach numbers drag is increased with decreasing exit area due to transonic spillage drag (local supersonic flow with shocks on the intake lip).

This behaviour is confirmed by wake flow total pressure measurements. Fig. 6.7 and 6.8 demonstrate the total pressure distribution in the fan nozzle exit plane. Note the loss free nozzle exit area due to the momentum loss of the external flow at high Mach number and small exit area.

The wake flow measurement in a plane behind the plugs rear end (Fig. 6.9) demonstrates also this momentum loss of the external flow with small exit area. This measurement also confirms that there is no or only small separation on the plugs rear end.

These very simple measurements with the VFW plug nacelle confirm the following characteristics:

- o The variable plug diameter allows a range of internal flow Mach numbers from close to the free stream Mach number down to about half that value. Thus the total high speed engine operational range and part of the low speed engine conditions is covered by this nacelle without use of internal drag devices like screens.
- o At all conditions the nozzle exit flow total pressure is very close to free stream total pressure and there is no or only little separation on the plugs rear end. Thus in any case the drag of the internal flow is small which results in small errors associated with evaluation of this drag and its subtraction from the total measured drag.
- o For the range of massflows, the nacelle can achieve, the external flow on the fan cowl and thus also the external nacelle drag is correctly simulated by this nacelle.

6.2 Low Speed TPS Test Set-Up and Results

In the past the use of TPS was limited to the high speed respectively cruise flight regime. Low speed engine interference was not thought to be an important problem and wind tunnel tests in this region were done with much simpler methods like blown nacelles or ejector simulators.

Quite recently the use of different engines on comparable airplanes demonstrated, that also in the low speed flight region the engine interference is sensitively dependent on small configuration changes and that a large portion of climb performance prediction uncertainty is hidden in the engine/pylon/wing interference region. So the most sophisticated engine simulation technique is just good enough to improve this situation.

For this low speed region we decided to introduce the TPS technique in the VFW low speed tunnel. This tunnel has a $2.1 \times 2.1 \text{ m}^2$ test section, a maximum speed of 70 m/s and the circuit is the open Eiffel type. Forces are measured by a weight beam type overhead balance.

Normally half models are used in this tunnel in Airbus development work; a typical scale is 1:16. A turbine powered simulator representing the full scale engine in this scale was available from Tech Development the type TDI 441.

Since in the low speed flight the thrust compared with drag is much larger than in cruise condition, the accuracy problem of TPS testing is even worse in low speed. The first problem was therefore the installation of a very precise force free air bridge in the balance system. A symmetrical system with frictionless flexible steel bellows gave excellent results. The basic accuracy of the balance, which is about ± 0.1 Newton for an axial force balance range of ± 800 Newton, was only slightly reduced by the air bridging to about ± 0.2 Newtons.

The total test set-up in the VFW wind tunnel is shown in Fig. 6.10; Fig. 6.11 gives a close view on the TPS nacelle. Tests with this model were done using the following techniques:

- o Total force measurements.
- o Pressure distribution measurements on nacelle, pylon and wing.
- o Wake flow total pressure distribution behind the engine area.
- o Flow visualization with tufts and oil flow.

The force measurement evaluation method is shown in Fig. 6.12. A lot of repeatability runs with the same configuration and varying conditions like tunnel temperature and drive air temperature were done; the overall repeatability with full TPS power is about ± 4 drag counts.

A typical force measurement result is given in Fig. 6.13. This figure shows the engine installation drag increment plotted against engine power.

6.3 Evaluation and Performance Prediction Method

To give a better understanding of the following ideas, the test configurations used in the experimental field of engine interference evaluation are outlined in Fig. 6.14 and 6.15.

In VFW practice up to now most of the engine effects have been measured using half models. The half model test set-up gives a simpler model, simpler engine simulation, higher Reynolds number and a better accuracy and repeatability of small drag increments. So this wind tunnel philosophy is based on basic performance tests with complete models and engine incremental effect measurements with half models.

The actual evaluation procedure depends on the aim of the wind tunnel test. Fig. 6.16 shows the simple case where the interference effect between engine/pylon and wing/body is evaluated. The encircled numbers on Fig. 6.16 refer to the Fig. 6.14 and 6.15.

The complete evaluation procedure necessary to predict the full-scale aircraft performance is shown in Fig. 6.17.

With respect to the evaluation of the engine thrust this procedure follows exactly the usual method of the full scale engine performance calibration. The TPS tank calibration is a true duplicate of the full scale engine calibration in an altitude test facility. So, if the engine manufacturers specified thrust is added to the performance prediction evaluated as shown in Fig. 6.17, the result should be the true air plane performance.

Normally, in a TPS nacelle the intake lip diameter is reduced compared with the real engine intake to correct for the missing massflow of the gas generator. The effect of this difference in the intake geometry is measured by a comparison of flow through nacelles on the half model with correctly scaled intake and TPS-intake. Exit areas of these flow through nacelles must be adjusted for the correct massflows of both intakes.

Normally, this effect of the TPS-intake modification is small, so this part of the tests and the evaluation may be omitted in most cases.

As shown in Fig. 6.17, the full-scale performance prediction can be derived from the completely evaluated wind tunnel result by two different methods. The reference method derives the wind tunnel test / flight test correlation from a reference airplane, which must be closely related to the airplane being in development. In the case e.g. of the A 300 and the A 310 the difference is slightly too large for absolute reliable results. Therefore at VFW the direct performance prediction method was used with good success. This method uses a direct wind tunnel / flight Re-number extrapolation which is based partly on theoretical methods and partly on generalized wind tunnel / flight test correlation data. A detailed discussion of these methods is beyond the scope of this paper.

It must be well understood, that in the method shown in Fig. 6.16 as well as in the normal full scale engine specification and calibration method one important effect is not separated and evaluated, that is the "External Flow Engine Effect". In the altitude test facility for the full scale engine as well as in the TPS calibration tank the correct nozzle pressure ratios for all Mach numbers and altitudes are simulated. The external flow however, quite apart from real installation interference due to pylon and wing effects, is not simulated. Without doubt the external flow has an influence on the fan nozzle discharge coefficient, the fan jet spreading and the gas generator cowl pressure distribution. These influences change the thrust compared with the altitude facility specified thrust. This influence should not be called an installation effect, as it is evaluated in Fig. 6.17, but an engine external flow effect.

A test and evaluation method, which separates this effect, is shown in Fig. 6.18. Again the encircled numbers refer to the figures 6.14 and 6.15. For simplicity the TPS intake correction, shown in Fig. 6.17, is omitted in this figure.

The comparison of the TPS tank calibration and the isolated TPS wind tunnel result gives the external flow effects. Conventionally the spillage drag and the fan cowl external friction drag is considered to be a part of the airplane drag, so these parts are taken from the flow through nacelle calibration test and subtracted from the total external flow effects. The remaining external flow effect is the influence of the undisturbed external flow on the nozzle discharge coefficients and on the gas generator cowl pressure distribution.

A summary of the engine interference evaluation methods used at VFW, is given in Fig. 6.19. Since TPS testing is an expensive wind tunnel technique, it cannot be used in the early project phase, where the general shape of the airframe is not yet fixed. In this phase engine influence is simulated by flow through nacelles, preferably by the plug type.

Since performance prediction is already very important in this phase, jet influence is considered in the performance prediction by reference air plane data, general experience and theoretical methods.

In the development phase, TPS testing with half models is added to this as outlined in this paper. The performance prediction follows the methods outlined in Fig. 6.17 and 6.18.

During the final development and check out phase accurate performance guarantees have to be established. In this case the inability of the half model to simulate asymmetric cases, may not be acceptable.

In the low speed field, especially the second segment climb is an asymmetric case. In the near future the new DNW low speed wind tunnel will offer the ultimate TPS testing capability.

Turbine powered simulators at a scale of 1 : 9,5 (related to GE CF 6) are built for this tunnel, which is the correct scale for an existing DNW Airbus complete model. This test set-up will give complete simulation of asymmetric one engine out climb cases at high Reynolds numbers and will thus establish reliable performance data. The large scale allows detailed interference flow analysis. This flow analysis is even more improved and realistic with a large scale (1 : 5,4) TPS, which is built for VFW and will be used in high and low speed with an existing half model of the same scale.

7. CONCLUSIONS

With the present state of the art of airplane development, engine interference is one of the important reasons of performance prediction uncertainty, and engine interference optimization is one of the most difficult tasks. This is valid for the cruise speed region as well as for the low speed flight.

At VFW the TPS wind tunnel technique, already well known and widely used in the cruise flight condition, has proven as a valuable and reliable tool also for low speed flap down cases. The combination of this technique with the use of plug controlled flow through nacelles gives reliable performance prediction during all phases of transport development.

Experience with windtunnel programmes using the TPS techniques for the investigation of propulsion system effects on the airframe shows that cooperation with the engine manufacturer is much more efficient. This is not only due to the direct comparison of real engine and TPS calibration methods but also because the test results can be directly related to the real engine/airframe installation. It is recommended that future testing based on the VFW concept outlined here be integrated with the experimental work of the engine manufacturer to an overall experimental approach to the problem of engine/model calibration for performance prediction. This integrated approach will reduce errors in thrust/drag bookkeeping to a minimum and provide the engine manufacturer with a better understanding of airframe effects on the nacelle in order to optimize the engine cycle for actual installed performance.

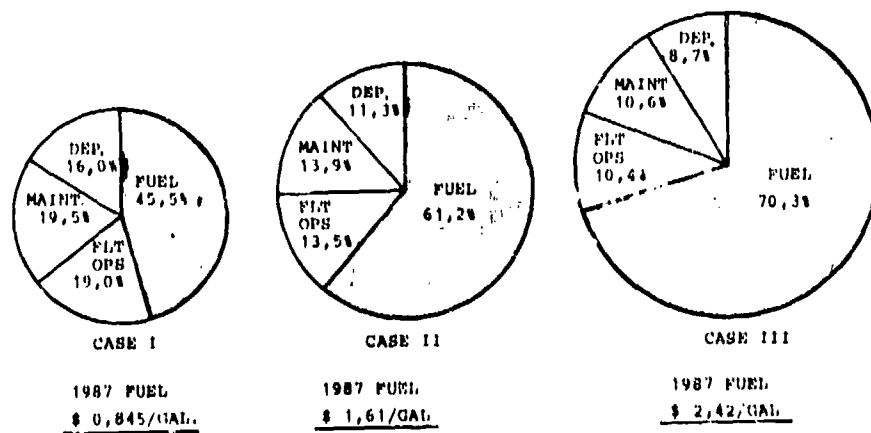
The next generation of transport aircraft may use long-duct mixing turbofans as already demonstrated in the NASA Energy Efficient Engine Programme. The VFW model concept can still be applied here. In the case of the variable-exit-area flow-through nacelle no problems are expected. Modification of the existing generation of non-mixing TPS is not necessary. It is proposed that both primary and fan nozzles remain separated to facilitate calibration for TPS thrust, and the exits coplanar or even allow a very small extension of the primary nozzle as shown in Fig. 7.1. The main objective of simulation should be the pressure ratio and best approximation of the corrected mass flow of the real engine mixing nozzle. In spite of higher fan total pressure ratios lower nozzle pressure ratios are expected due to losses in the mixing process.

This paper has highlighted the problem of interference associated with the installation of high bypass ratio engines in modern transport aircraft and typical procedures for performance prediction by engine and airframe manufacturers. Based on the understanding of interference as being a mutual propulsion system/airframe problem a concept for windtunnel testing has been proposed to separate thrust and drag effects as far as necessary and which is compatible with the thrust/drag bookkeeping for the full-scale aircraft. Further development of this concept will provide the framework for more efficient cooperation between engine and airframe manufacturer in order to exploit the full performance potential of engine and airframe.

REFERENCES

- 1 B. Heilmann Engine effects, proposal for model test technique and transmission to full scale at low speed.
VFW-Kurzbericht Ef-892, Unpublished VFW-Report
- 2 W. Burgmüller Grundlagen zur Triebwerksimulation mittels TPS im Windkanal.
VFW-Kurzbericht Ef-915, ZKP-IFAS-Bericht Nr. 5
- 3 J. Rohde Voruntersuchungen am Prinzipmodell der Triebwerks-Durchfluß-Simulation für das ZKP-Großmodell.
VFW-Kurzbericht Ef-826, ZKP-Flügelsektion-Bericht Nr. 38
- 4 W. Stäger Entwicklung und Eichung eines Ejektortriebwerkes für Windkanalversuche.
DFVLR-Bericht IB 157-78 A 07
- 5 E.H. Frumm The Boeing Simulation Chamber for Static Calibrations of Engine Simulators.
12. Meeting of the Subsonic Aerodynamic Testing Association, May 7, 1976
- 6 W.M. Shain Model Inlet Test with/without an installed Engine.
Boeing Commercial Airplane Co.
- 7 W. Burgmüller Halbmodellmessungen mit Triebwerksimulation durch TPS im VFW-Niedergeschwindigkeitskanal (Grundsatzuntersuchung).
VFW-Kurzbericht Ef-980, ZKP-IFAS-Bericht Nr. 10
- 8 J.W. Swihart A Fresh Look at Aviation Fuel Prices
J.L. Minnick Aeronautics and Astronautics, March 1980
- 9 G. Krenz Transonic Wing Design for Transport Aircraft
Presentation for the AIAA, "Advancing Technology"
Williamsburg, Virginia, USA, March 26-28, 1979
- 10 W.C. Swan The Problem of Installation a Modern High Bypass Engine on a Twin Jet Transport Aircraft
A. Sigalla AGARD CP-124, Flight Dynamics Panel Specialists Meeting
Izmir, Turkey, 10.-13. April, 1973
- 11 W.L. Stewart Preparing Aircraft Propulsion for a New Era in Energy and the Environment
D.L. Nored Astronautics and Aeronautics, Jan. 1980
J.S. Grabmann
C.E. Feiler
D.A. Petrash
- 12 G. Krenz Transonic Wing Technology for Transport Aircraft
B. Ewald Subsonic/Transonic Configuration Aerodynamics, AGARD, Neubiberg, 5.-7. May, 1980
- 13 W.J. Rohling The Influence of Nacelle Afterbody Shape on Airplane Drag
AGARD-CP-150 Airframe/Propulsion Interference. Fluid Dynamics Panel Symposium
Rome, Italy, 3.-6. September, 1974
- 14 B. Munnikma Jet Interference of a Padded Engine Installation at Cruise Conditions
F. Jaansma AGARD-CP-150, Fluid Dynamics Panel Symposium
Rome, Italy, 3.-6. September, 1974
- 15 E.M. Bowes Aircraft Lift and Drag Prediction and Measurement
AGARD-LS-67, Brüssel, 13.-17. May, 1974
- 16 K.D. Klevenhusen Calculation of Wing-Body-Nacelle Interference in Subsonic and Transonic Potential Flow
H. Jakob AGARD, Fluid Dynamics Panel Meeting
H. Struck Toulouse, France, 11.-14. May, 1981
- 17 J.T. Kutney Reduction of Drag Rise on the Convair 990 Airplane, Journal of Aircraft, Jan./Feb. 1964
S.P. Piszkin
- 18 J.F. Stroud Propulsion System Testing Requirements for a Commercial Transport
AGARD PEP-Meeting on Propulsion System Testing, Turin, Italy, Sept. 1980
- 19 M.I.K. Mackinnon Factors Influencing Nacelle Design on 747. AIAA/SAE/ASME 15th. Joint Propulsion
B.K. Mekta Conference, Paper 79-1236, Las Vegas, Nevada, June 18-20, 1979.
- 20 B. Neal Aerodynamic Development of the Engine Nacelle Combination for the Boeing 767 Airplane.
SAE Technical Paper 800731, International Air Transportation Meeting,
Cincinnati, Ohio, May 22-23, 1980

ABSOLUTE VALUES FOR FLIGHT OPERATIONS, MAINTENANCE
AND DEPRECIATION KEPT CONSTANT FOR EACH CASE



Ref. 8

FIG. 1.1 : High - Low Projections of the
Impact of Fuel Price on 1987 DOC's

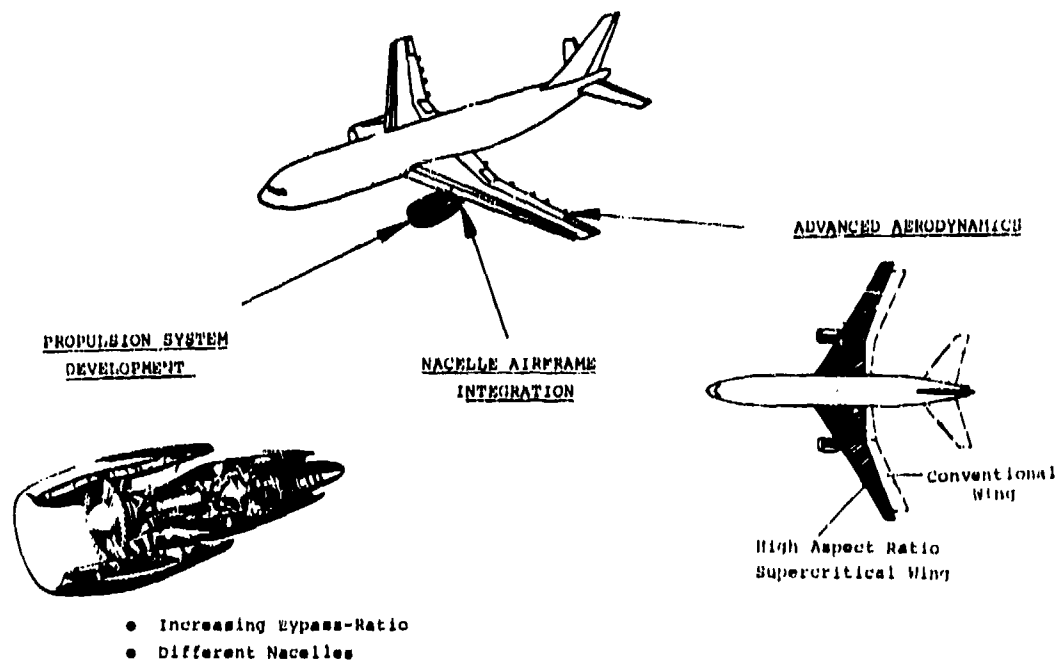


FIG. 1.2 : Aerodynamics and Propulsion for
Future Transport Aircraft

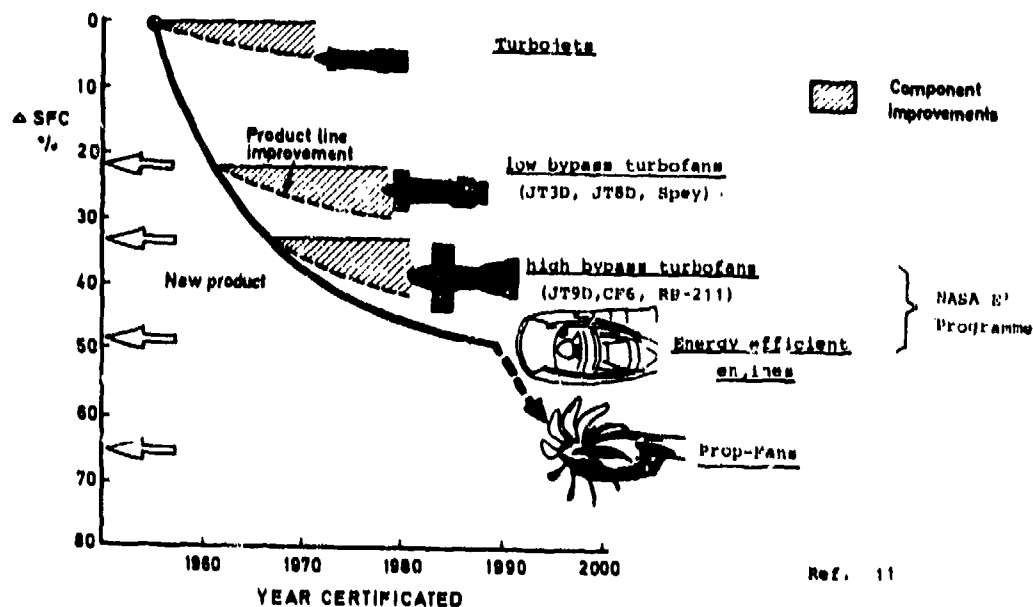
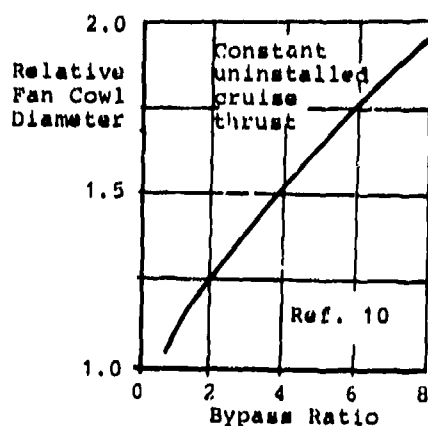


FIG. 1.3 : Development of Specific Fuel Consumption in Cruise (31.000 ft, $M_n = 0,8$)



Larger Fan Cowl

	Second generation turbofan (1970 - 1985)	Advanced turbofan NASA EEE Programme (1985 - 2000)
Bypass ratio	5 - 6	7 - 8
Fan pressure ratio	1,6	1,7 - 1,8
Cycle pressure ratio	25 : 1	35 - 45 : 1
Turbine inlet temperature	1530 °K	1675 °K

FIG. 1.4 : Engines for Transport Aircraft



A300 B	CF6-50C2	52,500 lb. Take-Off Thrust
	JT9D-59A	53,000 lb. Take-Off Thrust

Bypass Ratio 5

FIG. 1.5 : Typical Twin - Engine Commercial Transport Aircraft

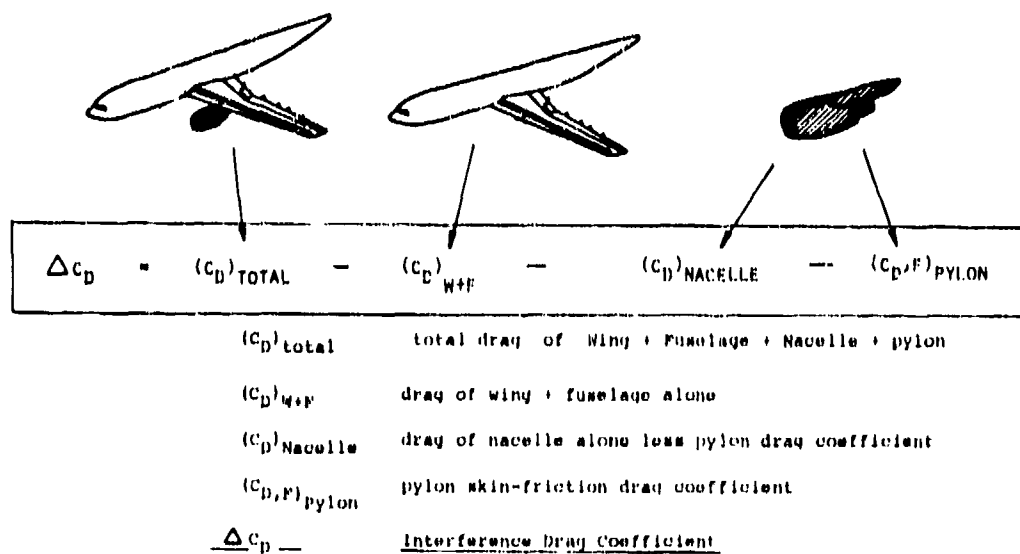


FIG. 2.1 : Definition of Nacelle Interference Drag

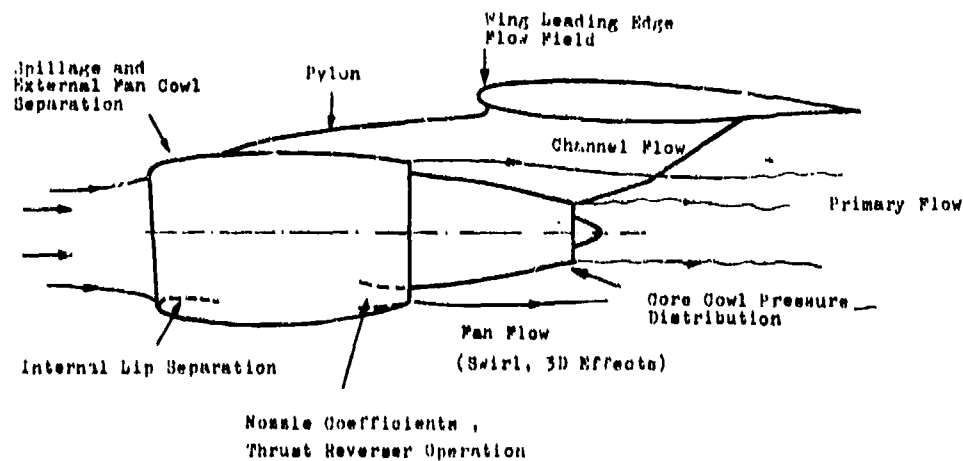
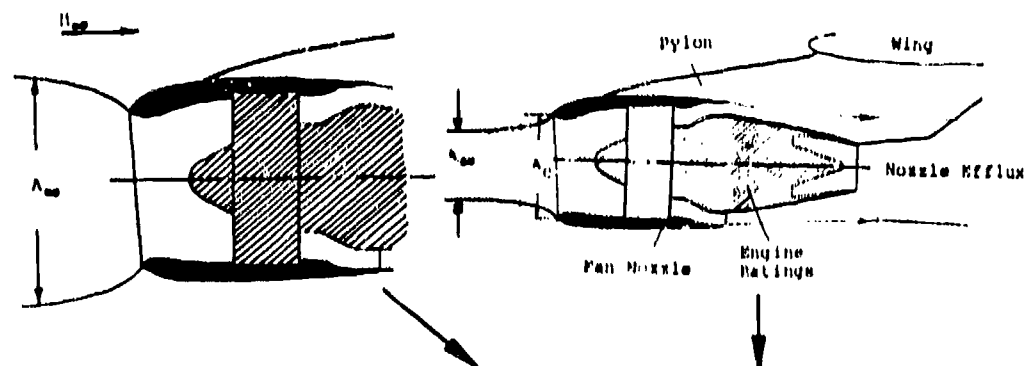
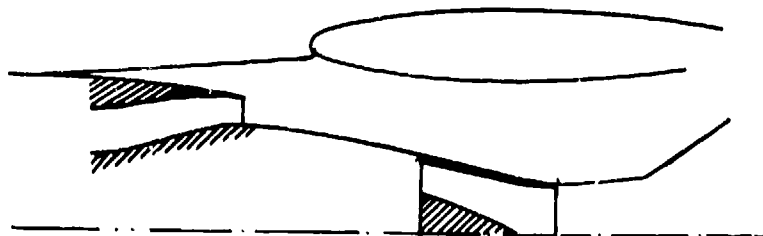


FIG. 2.2 : Interference Flow Field
Nacelle/Pylon/Wing



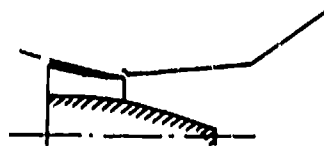
	LOW SPEED		HIGH SPEED	
	Rotation at Take Off	Approach	31,000 ft Climb	31,000 ft Cruise
Inlet Mass Flow Ratio Λ_{∞} / A_C	1,0	1,0	0,75	0,7
Machnumber	0,2	0,3	0,8	0,8
Fan Nozzle Press. Ratio	1,6		2,8	2,6
Primary Nozzle Press. Ratio	1,4		2,2	2,1

FIG. 2.3 : Inlet and Nozzle Flow Conditions



Fan Nozzle
Convergent
Con-D1

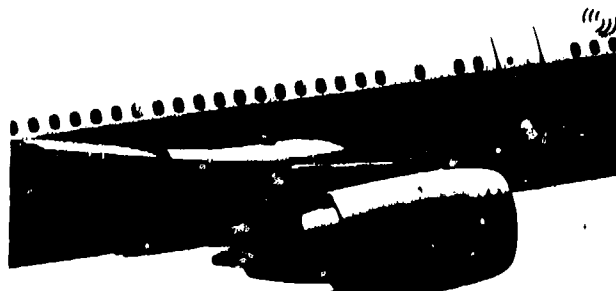
Primary Nozzle Conical
Convergent
Con-D1



Primary Nozzle with Plug
Convergent
Con-D1



FIG. 2.4 : Fan and Primary Nozzle Configurations



GENERAL ELECTRIC CF6-50 C2

SHORT PRIMARY NOZZLE WITH
EXTERNAL PLUG

PRATT & WHITNEY JT9D-59A
CONICAL SHORT PRIMARY
NOZZLE



FIG. 2.5 :

Nacelles for Airbus A300 B



General Electric

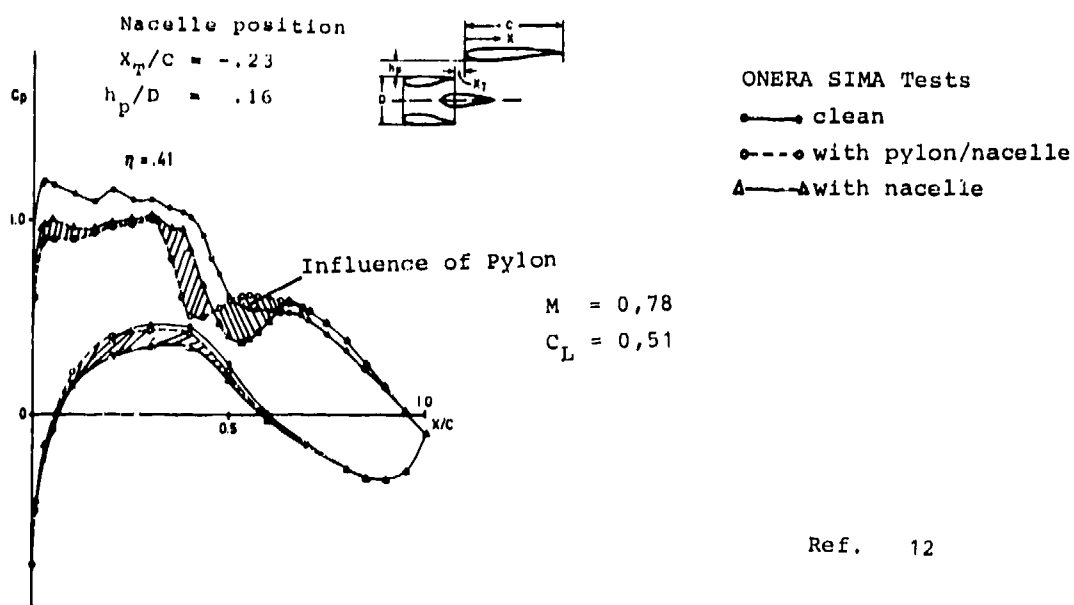
E³ configuration



Pratt & Whitney's E³
configuration

Ref. 11

FIG. 2.6 : Long Duct for Future Energy
Efficient Engines



Ref. 12

FIG. 2.7 : Effect of Pylon on Nacelle/Airframe
Interference

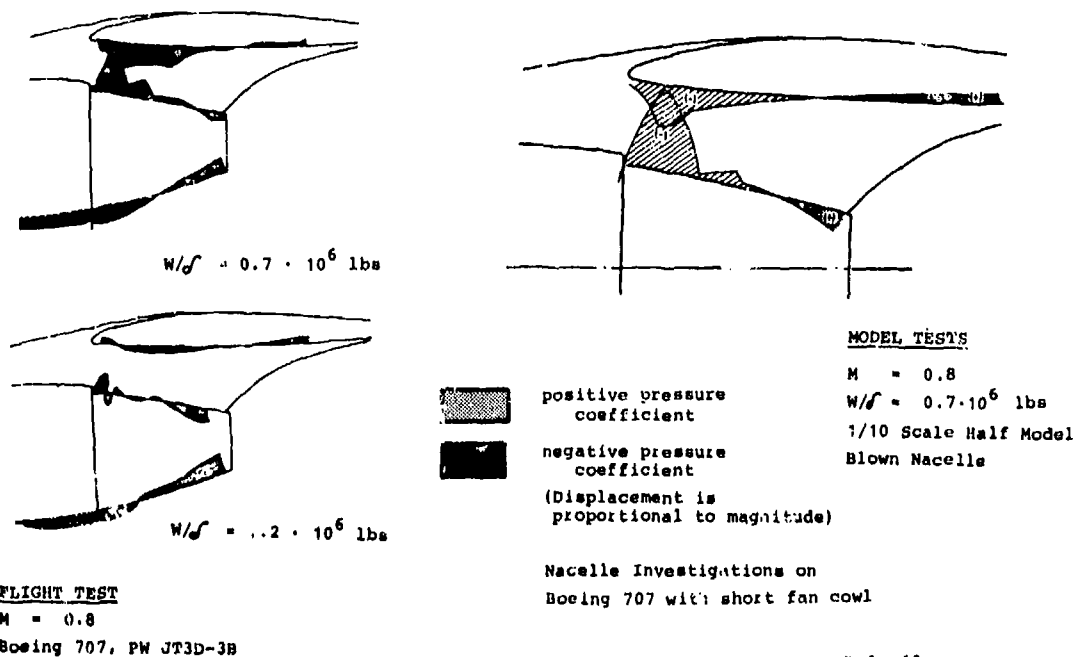


FIG. 2.8 : Interference between Nacelle and Wing

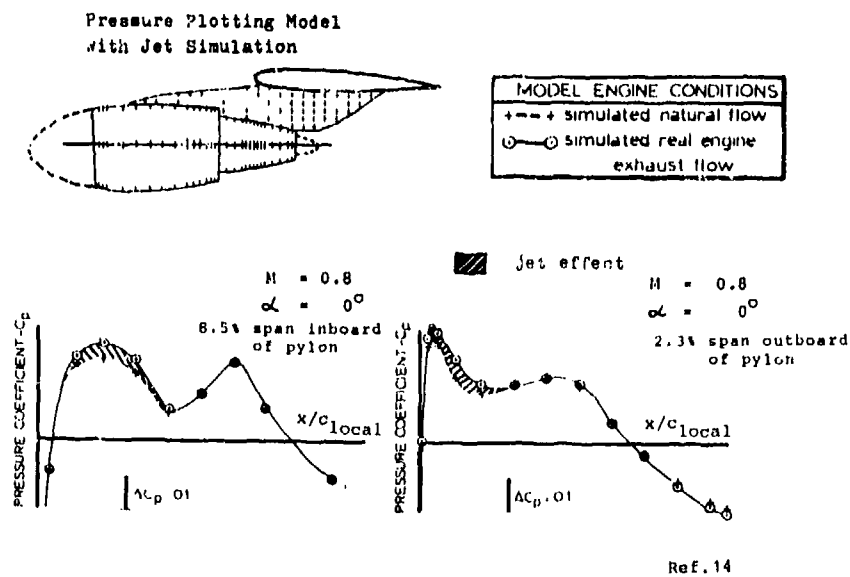


FIG. 2.9 : Jet Effect on Wing Lower Surface

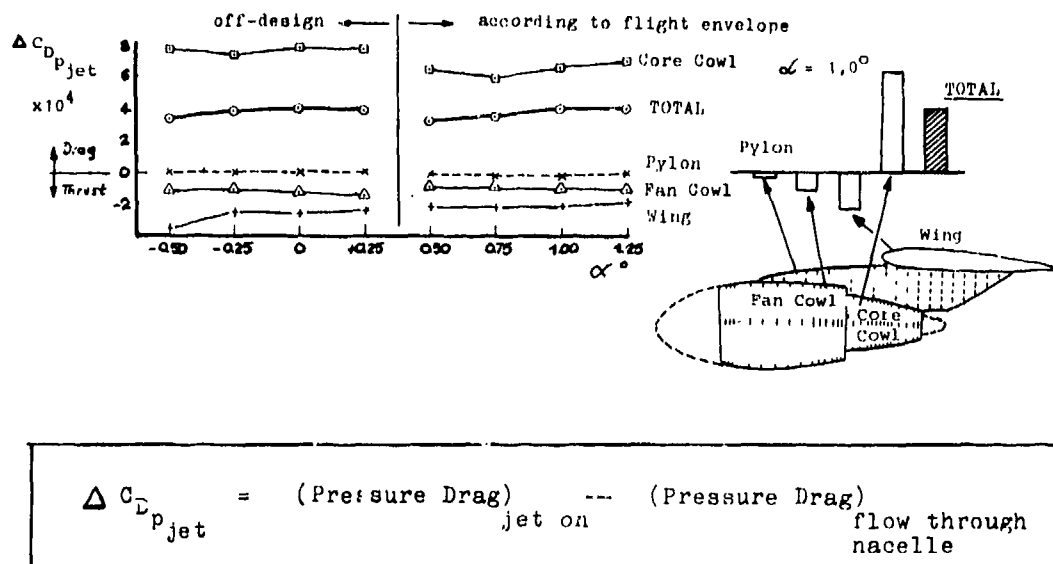


FIG. 2.10 : Pressure Drag due to Jet Effect at Cruise

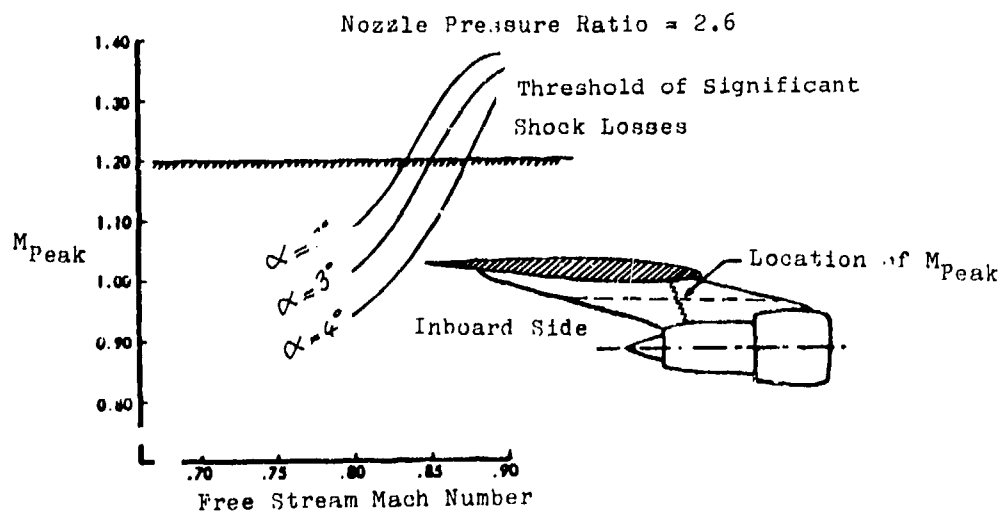
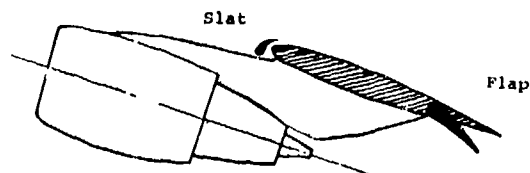


FIG. 2.11 : Peak Mach Number on Pylon

Machnumber
0,2 - 0,4



α^0 corresponding
to $1.15V_s - 1.4 V_s$

Effect of side slip

<u>Problem Areas</u>	<p>① Inlet</p> <ul style="list-style-type: none"> • External Cowl Separation • Internal Lip Separation 	<p>② Flow quality on Core Cowl</p> <p>③ Power effects on Drag</p>
<u>Parameters</u>	<p>Engine RPM</p> <ul style="list-style-type: none"> • Windmill • Go Around • Nozzle Pressure Ratio 1.6 - 1.8 	<p>Nacelle</p> <ul style="list-style-type: none"> • Shape • Position <p>Slat/Flap</p> <ul style="list-style-type: none"> • Take Off • Clean • Landing

FIG. 2.12 : Engine/Airframe Interference
at Low-Speed Conditions

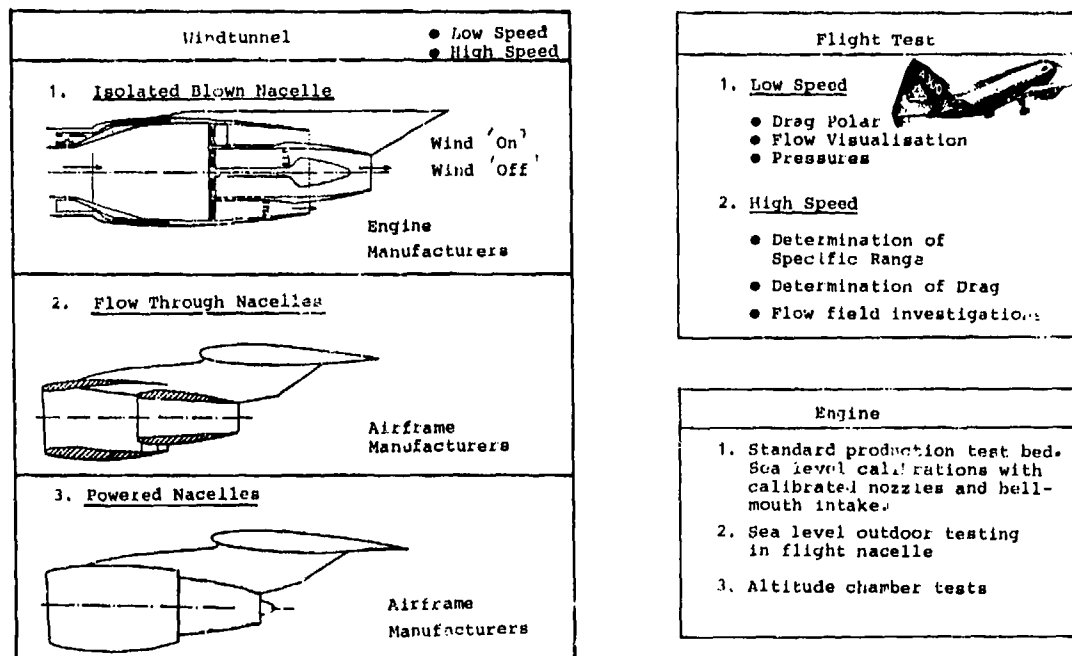
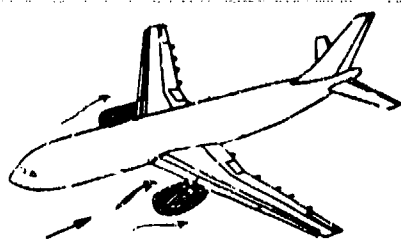


FIG. 3.1 : Experimental Methods for
Nacelle/Airframe Interference



M, α, β

FULLSCALE AIRCRAFT

- Flow around nacelle
- Wing/pylon effects
- Inlet flow distortion

ENGINE MANUFACTURER

- No freestream Altitude test facility
- Ideal inlet flow around nacelle

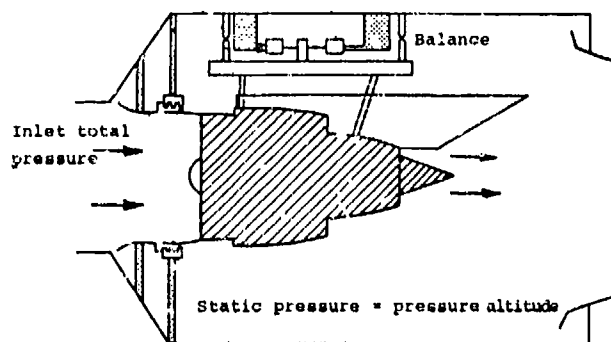


FIG. 3.2 : Representation of Flight Conditions in the Altitude Test Facility for Jet Engines

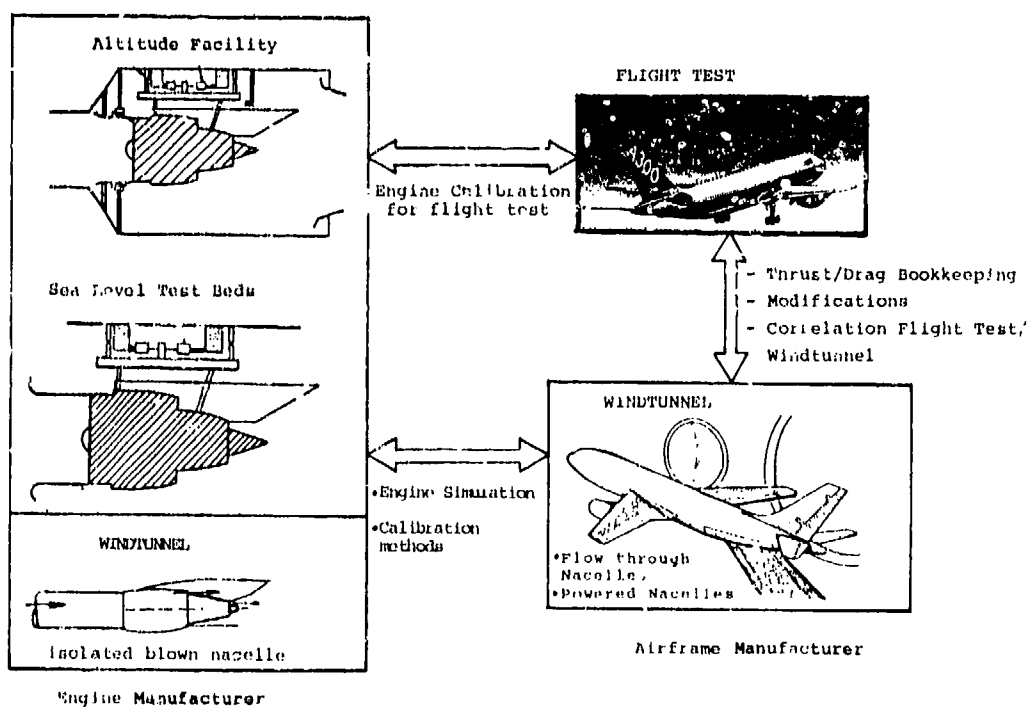
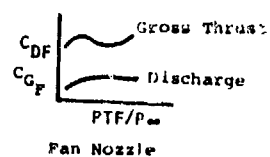
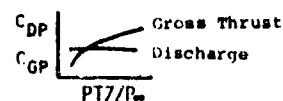


FIG. 3.3 : Integration of Experimental Methods



NOZZLE COEFFICIENTS

From model tests
adjusted to full
scale



Primary Nozzle

Discharge Coefficient

$$C_D = \frac{\text{actual flow}}{\text{ideal flow}}$$

Thrust Coefficient

$$C_G = \frac{\text{actual thrust}}{\text{ideal thrust}}$$

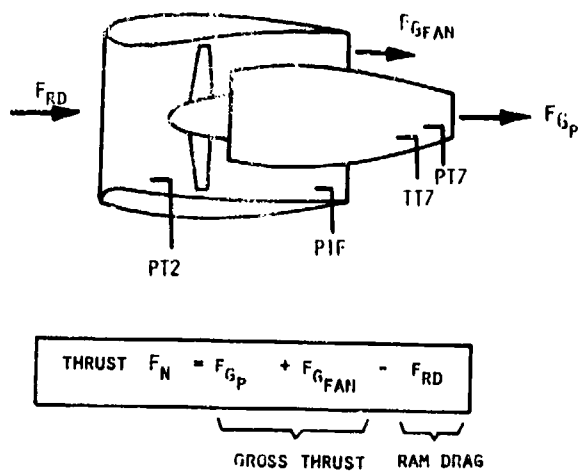
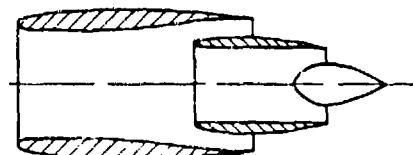
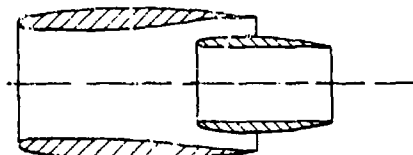


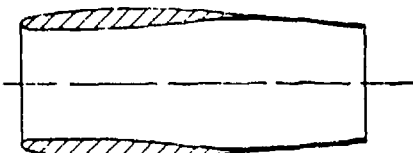
FIG. 3.4 : Inflight Thrust Measurement



1. Triple Body Nacelle



2. Double Body Nacelle



3. Skirted Nacelle

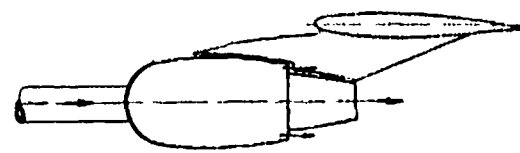
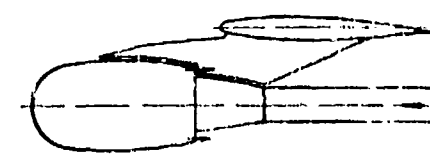
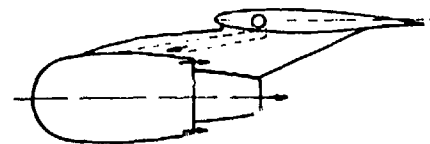


FIG. 4.1: Flow Through Nacelle Design Concepts

FIG. 4.2: Airfeed to Blown Nacelles

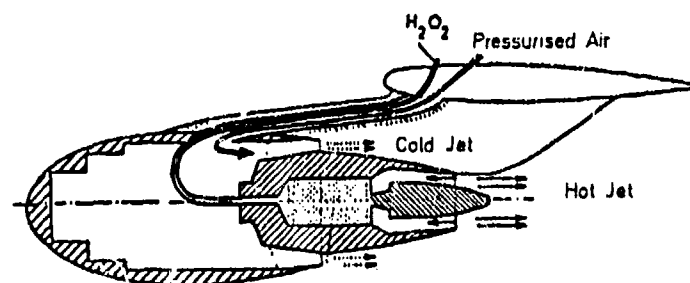


FIG. 4.3: Powered Nacelle with Hydrogen Peroxide Primary Jet Simulation

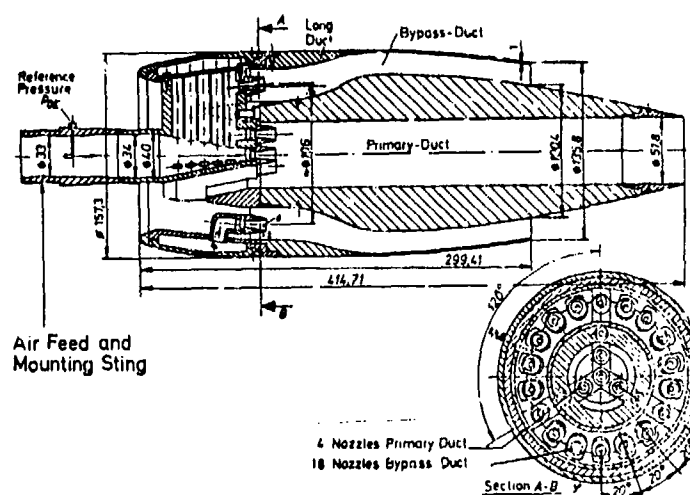


FIG. 4.4: Ejector Engine Simulator Cutaway [4]

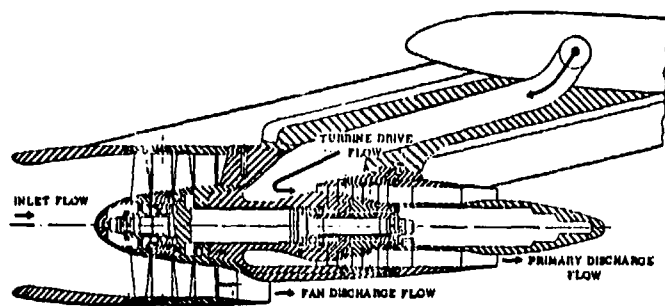


FIG. 4.5: Typical TPS Design, Type TDI 441 [5]

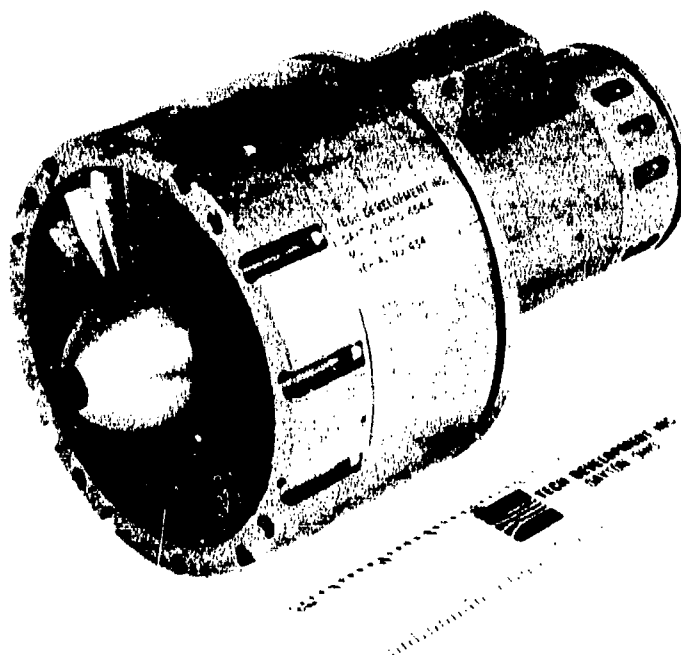


FIG. 4.6: Turbine Powered Simulator

Correct Simulation and Measurement of	Simulation Concept				Flight Test
	Flow Through	Blown	Ejector	TPS	
Free Stream Condition ⁽¹⁾	X	X	X	X	X
Balance Force	X	X	X	X	
Internal Nacelle Drag	X				
Thrust		X	X	X	X
Inlet Flow	(X)	(X)	(X)	X	X
Nozzle Pressure Ratio	Fan	X	X	X	X
	G-Gener.	X	X	X	X
Nozzle Temperature	Fan			X	X
	G-Gener.				X
Jet Flow Condition (Turbulence etc.)				X	X
Inlet/Jet Flow - Interference				X	X
X: Correct Simulation (X) Restricted Simulation (1) Limited WT Re N					

FIG. 4.7: Comparison of Different Engine Simulation Technique Results [2]

Correct Measurement of	Simulated by							
	Climb		Cruise		Idle		Windmill	
	TPS	Fl. Thr.	TPS	Fl. Thr.	TPS	Fl. Thr.	TPS	Fl. Thr.
Inlet Stream Tube	X		X	X	X	X	X	X
Fan Jet	X		X		X		X	X
Primary Nozzle Jet (X) Wrong Temperature	(X)		(X)		(X)		X	X
Fan Cowl Pressure Distribution	X		X	X	X	X	X	X
Gas Generator Cowl Pressure Distr.	X		X		X		X	X
Pylon Pressure Distr.	X		X		X	X	X	X

FIG. 4.8: Comparison of Flow Through Nacelle and TPS Simulation Range [2]



FIG. 5.1: Half Model Test Arrangement with Ejector Engine Simulator

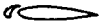




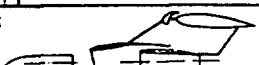

I		Clean configuration
II		Air duct interference
III		Ducted nacelle and pylon
IV		Ducted nacelle with "eyebrow" and pylon
V		Ducted nacelle, mounted on wing
VI		Ducted nacelle with "eyebrow", mounted on wing
VII		Ducted nacelle with hub, mounted on wing

FIG. 5.2: Ejector Test Arrangement Tare and Reference Tests

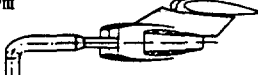
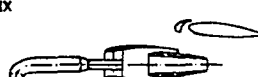
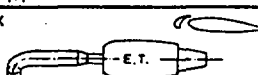
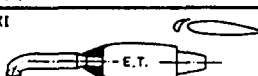


VIII		Nonmetric ducted nacelle with hub and pylon, mounted on supply pipe
IX		Removed pylon $V_A / V_\infty = 1$
X		Ejector engine $V_A / V_\infty = 1$
XI		Ejector engine with covered inlet $V_A = 0 \text{ m/s}$
XII		Metric pylon gap between pylon and ducted nacelle
XIII		Ducted nacelle with covered hub and pylon, mounted on wing

FIG. 5.3: Ejector Test Arrangement Tare and Reference Tests



FIG. 5.4: Static Thrust Calibration of TPS

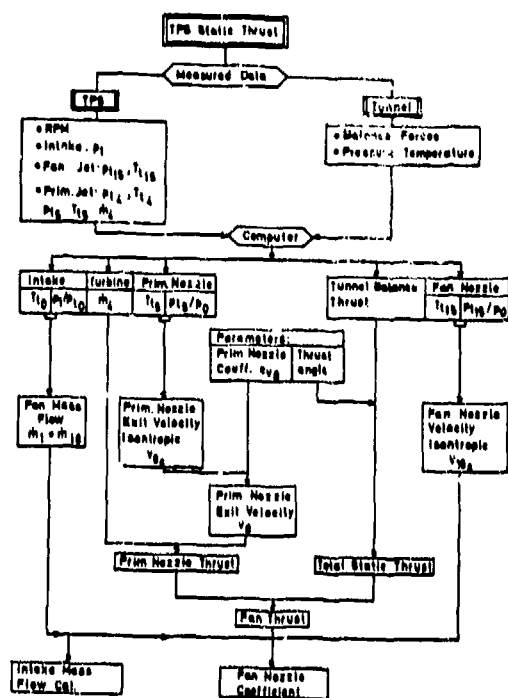


FIG. 5.5: Evaluation of Static Thrust Tests [7]

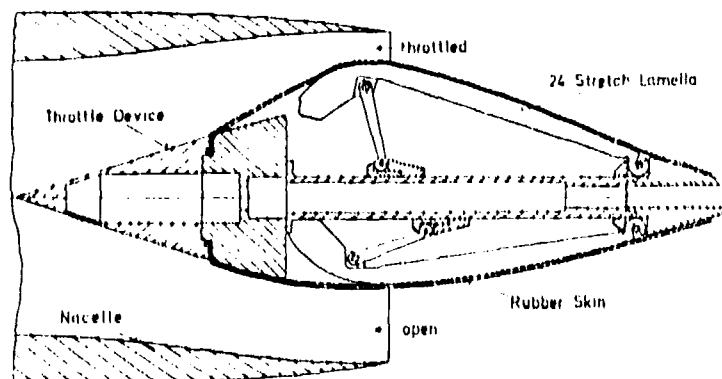


FIG. 6.1: VFW Plug Nacelle Concept



FIG. 6.2: Plug Nacelle with Maximum Exit Area

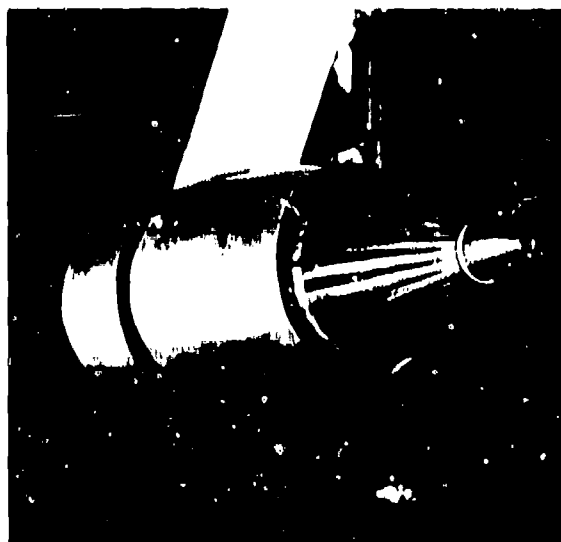


FIG. 6.3: Plug Nacelle with Minimum Exit Area



FIG. 6.4: Plug Nacelle on Free Jet Test Facility

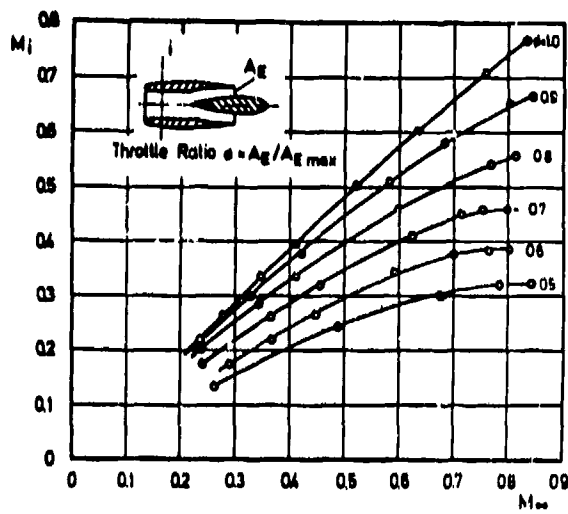


FIG. 6.5 Plug Nacelle Throttling Range [3]

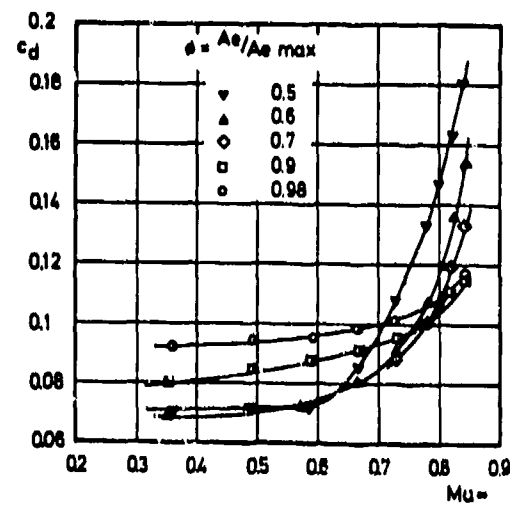


FIG. 6.6: Plug Nacelle Drag Characteristic [3]

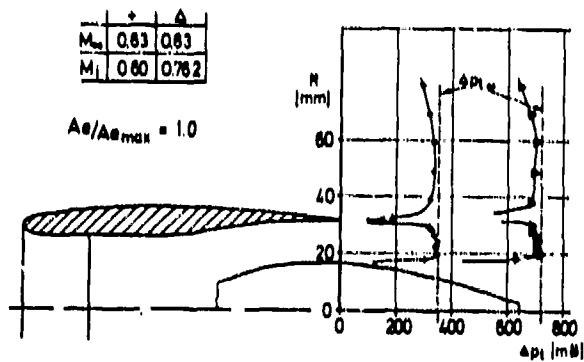


FIG. 6.7: Total Pressure of Internal and External Flow in the Nozzle Exit Plane [3]

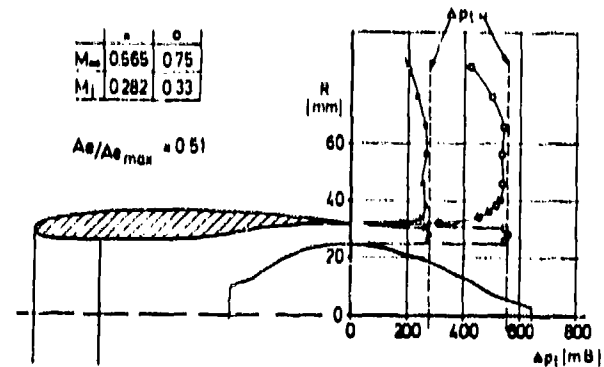


FIG. 6.8: Total Pressure of Internal and External Flow in the Nozzle Exit Plane [3]

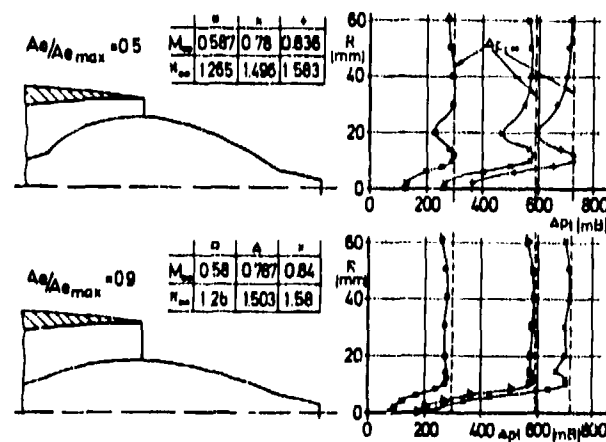


FIG. 6.9: Total Pressure Measurement in Plug Nacelle Wake Flow [3]



**FIG. 6.10: Low Speed Half Model with TPS
(A 300 B4, Scale 1 : 16)**



FIG. 6.11: TPS Nocelle

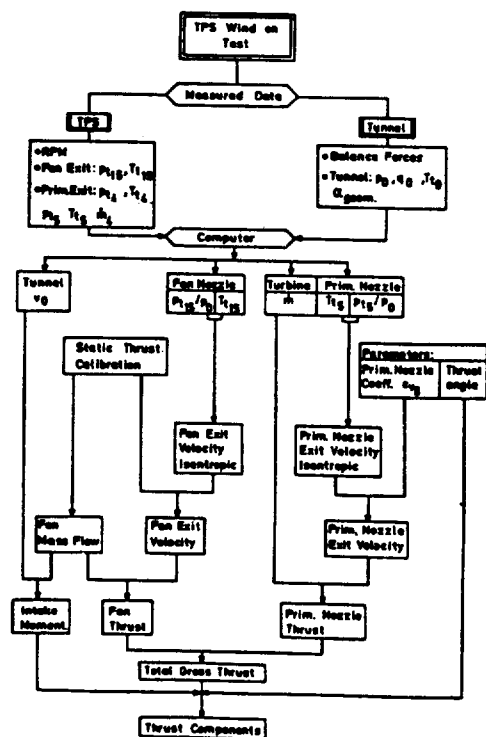


FIG. 6.12: Evaluation Wind on Tests [7]

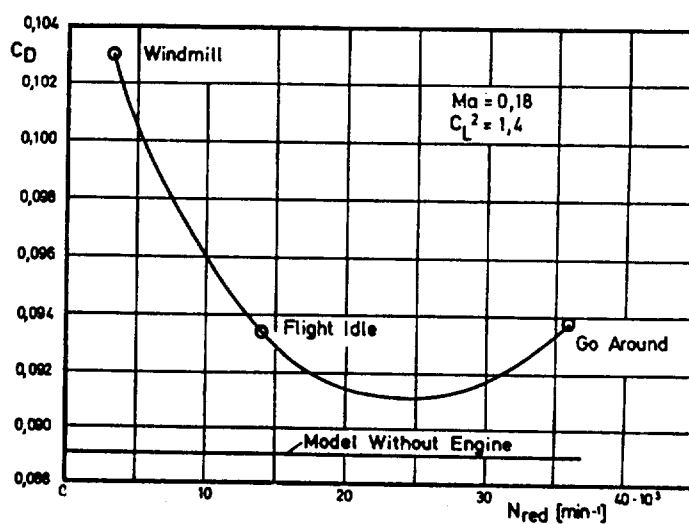


FIG. 6.13: TPS Low Speed Force Measurement

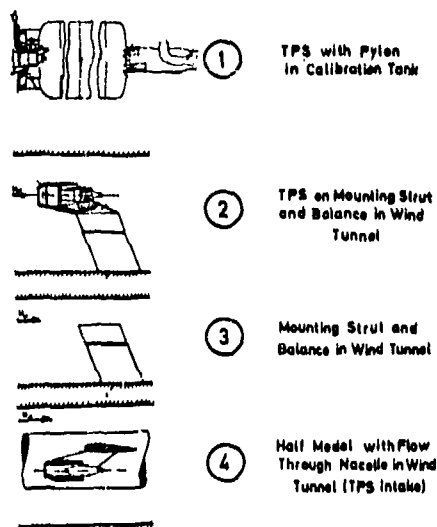


FIG. 6.14: Different Test Configurations [2]

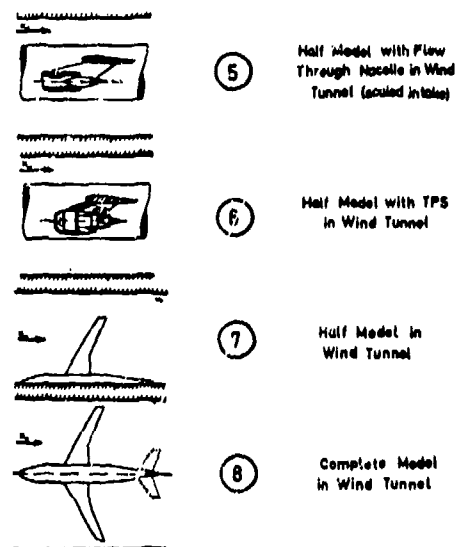


FIG. 6.15: Different Test Configurations [2]

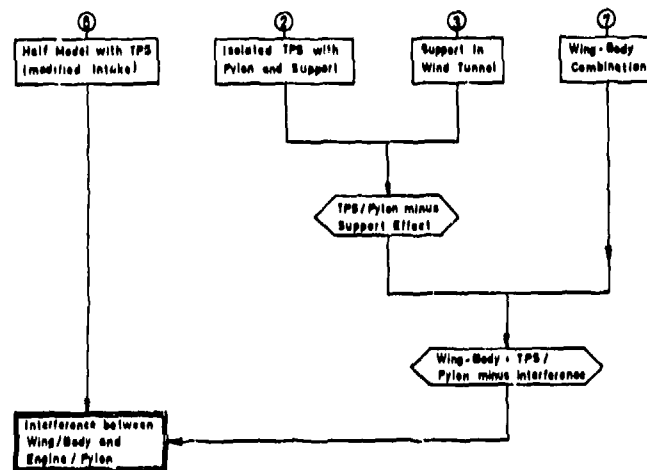


FIG. 6.16: Interference Evaluation Wing/Pylon/Engine [2]

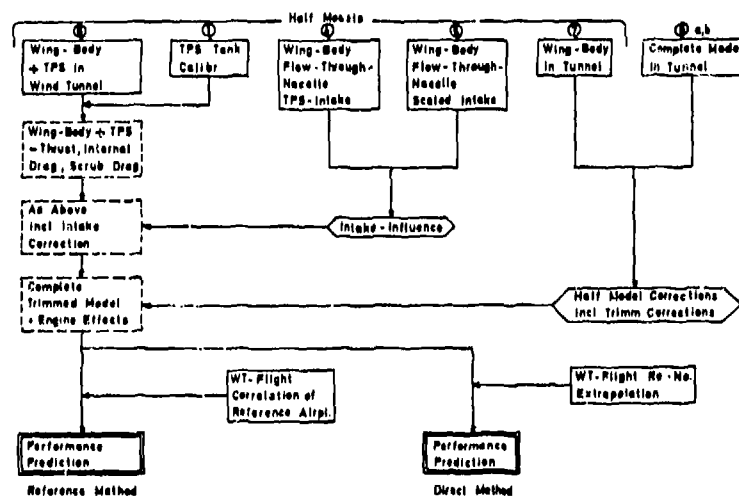


FIG. 6.17: Performance Prediction Full Scale Aircraft [2]

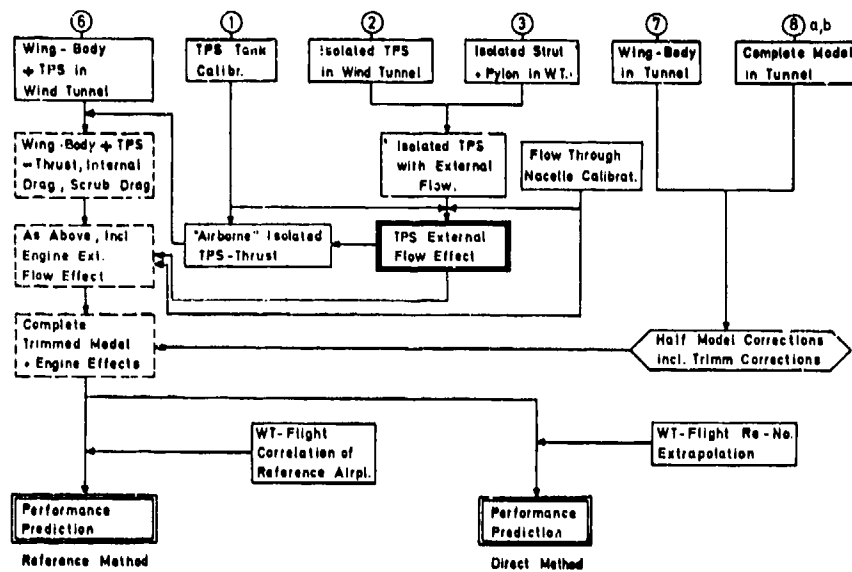


FIG. 6.18: Performance Prediction Method incl. Engine External Flow Effect

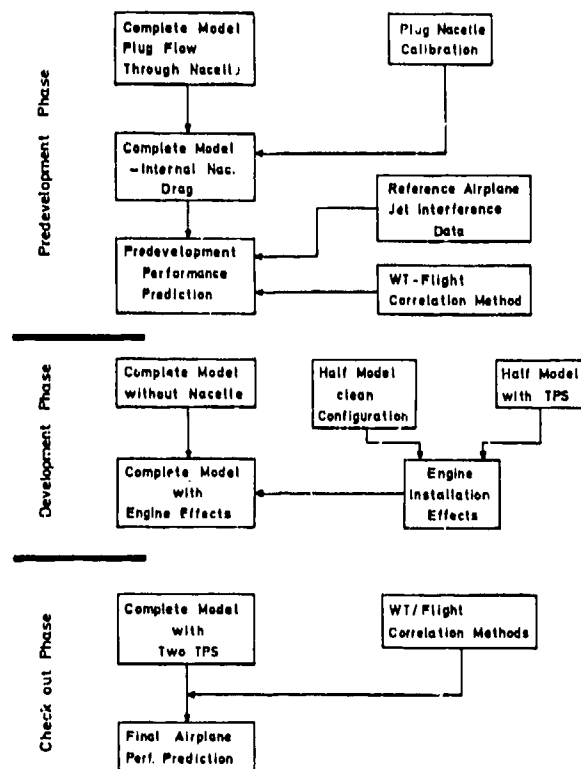
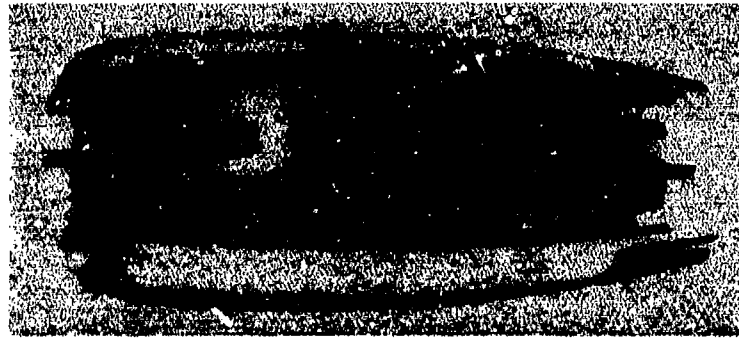
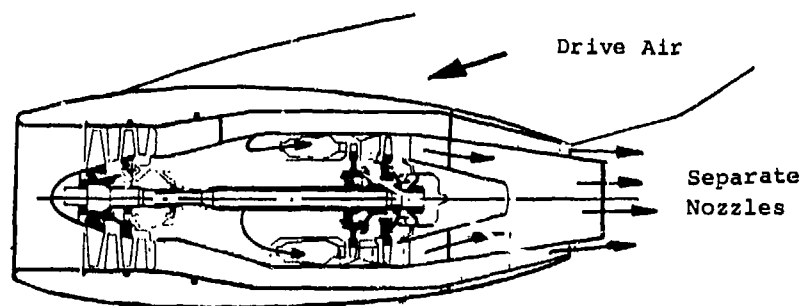


FIG. 6.19: Engine Installation Effects WT Evaluation Philosophy



General Electric's efficient engine
E³ configuration



Example of TPS
for Bypass-Ratio 1.0
mixed flow turbofan

FIG. 7.1 : TPS for Long Duct Mixing Turbofan

ESSAIS EN SOUFFLERIE DE MAQUETTES MOTORISEES

COMPARAISON DE DEUX METHODES DE SIMULATION DES JETS DES REACTEURS

par BECLE JP. (ONERA)

OFFICE NATIONAL D'ETUDES ET DE RECHERCHES AEROSPATIALES,
29 Avenue de la Division Leclerc, 92320 CHATILLON (France)

et PERIN R. (AEROSPATIALE) Toulouse
Société Nationale Industrielle Aérospatiale 31060 Toulouse (SNIAS)

La prévision plus précise et l'optimisation des performances dès le stade de la définition des avions civils a conduit l'AEROSPATIALE à effectuer des essais de maquette motorisée dans les souffleries de l'ONERA au Centre de MODANE-AVRIEUX.

En coopération avec l'ONERA deux méthodes de simulation froide des jets des réacteurs ont été développées.

La première dite "jets soufflés" a bénéficié du montage mis au point antérieurement pour les études de l'avion CONCORDE.

La seconde qui utilise des petites turbines à air a été récemment mise en oeuvre pour les avions de la famille AIRBUS.

Les essais sont effectués sur des demi-maquettes montées sur une balance à 6 composantes traversée par les flux du réacteur.

Un montage original permet quel que soit le principe de motorisation ou le type d'essais (point fixe ou essais en soufflerie) d'utiliser les mêmes moyens de mesure (balance, débitmètres, etc).

Les étalonnages des flux de sortie s'effectuent aux conditions ambiantes de la soufflerie dans le caisson à vide S4B du Centre de l'ONERA à MODANE.

Cet exposé décrit les installations, les moyens de mesure et les méthodes d'exploitation des résultats. L'intérêt respectif de chacune des méthodes de motorisation est analysé : complexité des moyens, durée, précision des mesures et comparaison des résultats.

I - INTRODUCTION

L'importance prise par les problèmes dus à la propulsion sur les avions civils ne permet plus de se satisfaire uniquement d'une analyse de l'interférence des jets par la mesure des répartitions de pression (réf. 1). L'expérience acquise et les progrès réalisés sur les moyens de mesure ont conduit l'Aérospatiale et l'ONERA à se doter de moyens d'essais capables d'accéder aux effets d'installation des nacelles par une pesée globale. A cet effet deux méthodes ont été développées. La première (Turbine Powered Simulator) utilise une turbine à air entraînant une soufflante dont les caractéristiques sont proches de celles du moteur réel. La seconde dite "jets soufflés" analyse séparément les effets de l'entrée d'air de ceux de l'arrière corps.

Cette note décrit les méthodes et les moyens d'essais, les procédures d'analyse. La précision des mesures et la comparaison des résultats obtenus suivant les deux méthodes sont analysées.

II - METHODE D'ESSAIS

L'évaluation des efforts d'installation implique une similitude aussi complète que possible avec l'avion. Les deux méthodes de motorisation des maquettes (nacelle "jets soufflés" ou équipée d'une turbine à air TPS) décrites ci-dessous demandent une procédure d'essais complexe pour satisfaire les exigences du problème posé, et en particulier la précision des mesures.

II.1. - Conditions de similitude.

Les conditions de similitude choisies sont les données géométriques du moteur et le nombre de Mach d'éjection, représenté par le taux de détente du jet (rapport de la pression d'arrêt du jet à la pression statique en sortie).

TPS

Par cette méthode le débit d'air amont ne représente que 80 à 85 % du débit d'air avion et la similitude correcte du champ de vitesse autour de l'entrée d'air nécessite de contracter celle-ci, d'où la nécessité de vérifier l'influence de cette modification sur la traînée de carène. Par ailleurs, si les caractéristiques du jet secondaire sont correctement représentées celles du jet primaire ne le sont pas (voir §IV.3). Enfin le rapport des pressions d'éjection des deux flux, lié au fonctionnement de la turbine, rend cette méthode difficilement adaptable à une simulation de nacelle de type "jets confluent".

Jets soufflés.

Avec la technique jets soufflés, les conditions de similitude choisies sont respectées, sous réserve d'une indépendance effective des effets de l'entrée d'air et des effets de l'arrière corps.

II.2. - Définition des efforts d'installation.

Les essais en soufflerie de maquettes motorisées permettent de déterminer le bilan poussée-traînée de la maquette, mais sans la possibilité de séparer les deux composantes.

Des essais au point fixe ($M = 0$), sont donc nécessaires pour évaluer les performances du moteur (X_N à $M = 0$) dans des conditions de fonctionnement identiques à celles de la soufflerie.

D'une façon générale, la comparaison de la traînée et de la poussée de l'avion peut s'exprimer, selon une décomposition des efforts proposée référence [1], par la différence :

$$(X_1 + \Delta X_{\text{installation motrice}} + \Delta X_{\text{vol}}) - (X_N (M=0) + \Delta X_N (M \neq 0))$$

différence considérée à une portance donnée de l'avion.

Dans cette expression,

X_1 est la traînée du planeur en soufflerie,
traînée obtenue par l'essai en soufflerie d'une maquette de l'avion non équipée de nacelles.

$\Delta X_{\text{installation motrice}}$ est le complément de traînée due à l'installation des nacelles motorisées sur la maquette

ΔX_{vol} est un terme complémentaire, notamment de frottement, qui permet d'obtenir la traînée en vol à partir de la traînée en soufflerie

$X_N (M = 0)$ est la composante suivant X de la poussée des jets mesurée au point fixe pour des mêmes conditions de fonctionnement (pressions génératrices, taux de détente) qu'en vol

$\Delta X_N (M \neq 0)$ est l'influence de l'écoulement extérieur sur la poussée du moteur (suivant X).

Pour obtenir le bilan recherché, la différence traînée-poussée et la portance sont calculées à partir des résultats d'essais à chaque incidence de la maquette, ce qui permet ensuite de se situer à un niveau de portance donné.

La présentation qui suit se limitera essentiellement à la détermination du terme de traînée de la motorisation, ΔX installation motrice, la détermination des termes de portance, en particulier, s'effectuant suivant la même démarche.

La planche 1 présente les différents essais (configurations 1 à 10) effectués soit avec TPS, soit avec jets soufflés, pour accéder à cette détermination.

Plus précisément, à partir des efforts X_1, X_2, \dots mesurés dans les différentes configurations, tels qu'indiqués planche 1 et précisés dans l'énumération qui suit, les termes de traînée d'installation sont obtenus respectivement par les relations suivantes :

TPS

$$\Delta X \text{ Installation motrice} = (X_4 - X_1) - X_N - \Delta X_E$$

Jets soufflés

$$\Delta X \text{ Installation motrice} = (X_2 - X_1) + (X_4 - X_8) - X_3$$

TPS

X_1 Efforts sur le planneur. Configuration 1.

X_4 Efforts en présence des nacelles avion. Simulation des jets avion. Configuration 7.

X_N Poussée nette ($X_8 - W_F \times V_0$)

X_8 Poussée brute définie à $M = 0$ et W_F débit soufflante obtenus par étalonnage au point fixe. Configuration 8.

ΔX_E Influence de la déformation de l'entrée d'air. Configurations 9 et 10.

Jets soufflés

X_1 Effort sur le planneur. Configuration 1.

X_2 Effort en présence des nacelles de référence. Cette nacelle représente l'entrée d'air avion, l'arrière corps étant modifié pour simuler le coefficient du débit au point de vol considéré.

Ce terme est corrigé des efforts internes X_i calculés le long du tube de courant depuis l'infini amont. Configurations 1 et 2.

X_4 Effort en présence des nacelles avion. Simulation des jets avions. Configuration 4.

X_8 Poussée brute définie soit à $M = 0$, soit en présence de l'écoulement extérieur, suivant la brochure moteur considérée. Configuration 5.

X_3 Effort en présence des nacelles de référence avec entrée d'air carénée. Simulation des flux du débit naturel (voir configuration 2).

Ce terme est corrigé de la dynamique de sortie. Configuration 3.

Tous ces résultats sont lissés en fonction de l'incidence ou de la portance et du débit réduit soufflante ($W \sqrt{T} / P_0$).

III - DISPOSITIFS EXPERIMENTAUX

Des dispositifs expérimentaux ont été mis en oeuvre par l'ONERA, au Centre de Modane-Avrioux, pour effectuer ces essais de simulation de moteurs par TPS ou par jets soufflés, au point fixe et en soufflerie transsonique.

III.1. - Simulation des moteurs par TPS.

Un schéma représentatif d'une nacelle utilisée pour les essais est donné planche 2. La nacelle est composée d'un élément moteur (TPS) sur lequel vient se fixer un habillage représentant les formes de la nacelle.

III.1.1. - Fonctionnement de la turbine.

Un débit d'air comprimé, éjecté par la tuyère primaire du moteur entraîne une petite turbine à un seul étage sur l'arbre de laquelle est montée une soufflante. L'air aspiré et refoulé par cette soufflante représente le débit secondaire du moteur. Le taux de compression de la soufflante atteint au régime maximum de la turbine est de 1,65 pour un taux de détente primaire de 3,5.

L'instrumentation nécessaire à la connaissance des différents paramètres du moteur et à la surveillance de la turbine chemine à travers des espaces aménagés dans le bord d'attaque et le bord de fuite du mât et le support de la nacelle.

III.1.2. - Banc d'étalonnage (pl. 3)

III.1.2.1. - Principe du banc.

Le banc d'étalonnage sert à déterminer les caractéristiques du moteur dans les conditions où il sera utilisé dans la soufflerie.

La nacelle est reliée à la balance par un support traversé par une canalisation. Le débit primaire, nécessaire à la mise en rotation de la turbine est fourni par un circuit haute pression (60 bars), et est mesuré par un venturi.

La soufflante du moteur aspire son débit dans une chambre de tranquillisation, fixée elle aussi sur la balance. Le débit secondaire est alimenté par un circuit basse pression (9 bars) et est mesuré par un ou deux cols soniques selon les cas.

Le raccordement chambre de tranquillisation - nacelle s'effectue à l'aide d'un pavillon qui peut, soit être cylindrique, soit représenter l'entrée d'air réelle de la nacelle (pl. 4).

L'ensemble balance - chambre de tranquillisation - nacelle est installé dans un caisson étanche relié au vide. Un col sonique réglable assure le maintien d'une pression statique constante, quel que soit le débit entrant.

Les principales grandeurs mesurées sont :

- les deux débits primaire et secondaire (WF et WG)
- les pressions et températures en amont et en aval de la soufflante (Fi, Ti, PTF, TF)
- les pressions et températures en amont et en aval de la turbine (PCH, TCH, PTG, TG)
- le régime turbine RPM
- la pression statique p
- la poussée globale X

III.1.2.2.- Circuits d'alimentation.

III.1.2.2.1.- Circuit haute pression.

Le circuit haute pression nécessaire à la mise en rotation de la turbine est identique au banc d'étalonnage et dans la soufflerie.

L'installation actuelle comprend :

- une réserve d'air sec de 28 m³ à 270 bars,
- une sphère B2 de 1 m³, réglée à la pression de 60 bars
- une sphère tampon B10
- un réchauffeur assurant la régulation en température de l'air alimentant la turbine
- un filtre arrêtant les poussières de dimension supérieure à 12 μ m, qui pourraient endommager les aubages de la turbine
- une platine de régulation et de mesure comprenant :
 - . une vanne d'entrée
 - . une vanne de mise à l'atmosphère
 - . une vanne de régulation
 - . un venturi
 - . une soupape de sécurité.

L'installation permet un débit de 1 kg/s pendant 1h30 mn environ. Une nouvelle installation en cours de réalisation, permettra un fonctionnement permanent (regonflage à 3 kg/s).

III.1.2.2.2.- Circuit basse pression.

Le circuit basse pression alimentant la soufflante du moteur lors des essais de calibration comprend :

- une réserve d'air sec de 4 500 m³ à 9 bars de pression
- un réchauffeur assurant la régulation de la température de l'air d'alimentation de la soufflante
- un filtre identique à celui du circuit haute pression
- une vanne de régulation
- un dispositif de mesure des débits par cols soniques.

Le niveau maximum de pression disponible à l'amont des cols soniques est de 8 bars.

La régulation des conditions amont des circuits d'alimentation assure une très bonne stabilité de l'ensemble des paramètres de la turbine.

III.1.2.3.- Balance (pl. 6)

L'ensemble chambre de tranquillisation - nacelle est monté sur une balance dont la structure permet le passage de quatre conduits d'air comprimé. Cette balance de paroi à six composantes, est utilisée indifféremment au caisson d'étalonnage, ou dans la soufflerie.

Le découplage entre partie pesée et partie non pesée s'effectue au moyen d'un système de soufflets de faible raideur qui ne modifie pas la sensibilité de la balance. La séparation des flux en deux parties et leur jonction en opposition sur un bloc distributeur annule les effets de fond. Par ailleurs, ce montage assure la mesure directe de la dynamique sortante.

Par suite d'imperfections de montage et d'alignement, un effet résiduel de pression dans les soufflets sur les ponts de la balance est observé. Un étalonnage préalable permet de mesurer cet effet de pression et d'en tenir compte dans les calculs d'efforts. La validité est vérifiée fréquemment (avant chaque essai si nécessaire).

La régulation de la balance à la température de l'air d'alimentation des jets permet de s'affranchir des problèmes que créeraient des gradients thermiques sur la balance.

III.1.2.4.- Pilotage et surveillance.

Le pilotage et la surveillance de l'installation sont assurés par un ensemble de trois consoles (pl. 7) sur lesquelles sont ramenés les commandes des différentes vannes des circuits d'alimentation et le réglage des réchauffeurs de l'installation.

L'indépendance des trois circuits (alimentations primaire et secondaire et évacuation) permet un réglage séparé de chacun des paramètres.

Les surveillances provoquent un arrêt de l'installation en cas de survitesse de la turbine ou d'échauffement anormal des paliers.

Le traitement en temps réel par un ordinateur local des signaux provenant des capteurs mesurant les principaux paramètres (p_1 , T_1 , p , RPM) et la visualisation de leurs valeurs physiques permettent un pilotage aisé de l'installation.

III.1.2.5.- Validation du banc d'étalonnage.

Une tuyère étalon ASME, montée à la place de la nacelle en sortie de la chambre de tranquillisation (pl. 8 et pl. 9) sert de référence en matière de fidélité des essais et de contrôle des quantités caractérisant un jet.

Le débit primaire à haute pression est ramené sur l'alimentation de la chambre de tranquillisation.

Les mesures de débit et de force enregistrées par les capteurs pour différents taux de détente sont comparées aux valeurs théoriques de la tuyère.

L'utilisation soit du débit primaire, soit du débit secondaire, soit des deux débits mélangés, permet de comparer entre elles les différentes mesures des débits.

III. 2. - Simulation des moteurs par jets soufflés.

III.2.1.- Principe de simulation (pl. 10)

Les deux jets, primaire et secondaire sont simulés par deux flux d'air comprimé à haute pression (30 bars) dans la maquette. Les deux flux sont détendus par une succession de plaques perforées jusqu'à la pression d'éjection.

Chaque canal est équipé en une section de référence de prises de pression et de thermocouples permettant, avec la connaissance des débits, de calculer la pression d'arrêt des jets.

Les prises de pression sur la nacelle sont branchées sur un petit commutateur de pression modulaire à deux têtes, placé dans l'ogive de la nacelle.

III.2.2.- Point fixe.

Les essais au point fixe s'effectuent dans le même caisson étanche décrit au § III.1.2.1. Dans ce cas d'essai, la voilure sert directement de support à la nacelle.

Les deux flux d'air comprimé sont issus de la même source haute pression décrite au § III.1.2.2.1., pl. 11.

Un jeu de cols soniques à sections échelonnées et de vannes commandées automatiquement donne une grande souplesse au choix du domaine de fonctionnement du moteur. Le fonctionnement séparé des circuits primaire et secondaire est possible.

III.3. - Essais en soufflerie.

Les essais ont été effectués dans la veine transsonique de la soufflerie S2 du Centre de Modane-Avrieux.

Il s'agit d'une veine de largeur 1,75 m et de hauteur 1,77 m. Les parois verticales sont pleines et les parois horizontales perforées ; la porosité de la veine est de 6 %.

La pressurisation de la soufflerie et sa régulation en température permettent, quel que soit le nombre de Mach de maintenir la pression statique et la température génératrice constantes.

L'acquisition des mesures s'effectue en paliers d'incidence. Un programme d'automatisation commande le positionnement en incidence de la maquette ($\Delta \alpha \leq 0,01$ degré) et règle le nombre de Mach ($\Delta M \leq 0,002$) ; il commande l'acquisition des points de mesure et contrôle leur validité.

Les signaux sont transmis en temps réel à l'ordinateur central qui restitue aux utilisateurs les résultats définitifs sous forme appropriée (console de visualisation, édition, tracés).

Les demi-maquettes utilisées pour les deux séries d'essais (pl. 12-13-14) représentent un avion de transport biréacteur subsonique.

Des essais de nacelles isolées (pl. 15) peuvent être également effectués.

Le circuit d'arrivée d'air, l'instrumentation et la balance sont ceux utilisés au banc d'étalonnage.

IV - METHODE D'EXPLOITATION

IV.1. - Etalonnage de la poussée.

TPS.

La mesure de la poussée est globale et le débit secondaire doit faire l'objet d'un étalonnage. Le paramètre de contrôle pour l'étalonnage du débit secondaire peut être soit une pression statique moyenne, soit une pression totale moyenne mesurées respectivement en amont et en aval de la soufflante. Vu la complexité de l'installation, cet étalonnage ne peut être répété en soufflerie, et une éventuelle dégradation des performances de l'ensemble nacelle-turbine au cours des essais est plus difficile à déceler.

Jets soufflés.

L'affichage et la mesure séparée des débits primaire et secondaire confèrent à cette technique plusieurs points d'intérêt. Elle permet :

- de mesurer les coefficients de tuyère de chacun des flux
- d'évaluer l'influence de l'écoulement extérieur sur ces coefficients de tuyère, c'est-à-dire d'estimer en partie la perte de poussée moteur installé.

Par ailleurs, l'étalonnage peut s'effectuer directement dans la veine de la soufflerie, ou tout au moins être contrôlé après chaque changement de configuration, ce qui assure une vérification permanente de toute l'installation.

IV.2. - Lois d'étalonnage.

La planche 16 présente les lois d'étalonnage utilisées dans notre analyse. La relation directe poussée-débit a pour avantage de faire appel à un nombre limité de mesures, donc d'assurer une précision meilleure. Appliquée à la technique "jets soufflés", elle conduit à une évaluation de la poussée affectée de l'effet de l'écoulement extérieur sur les débits. Son utilisation dans le cas de la méthode TPS nécessite un contrôle rigoureux du rendement de la turbine ; en effet, les variations éventuelles des pertes de charge du circuit primaire ne sont pas prises en compte.

Si l'on se réfère à une brochure moteur établie à $M = 0$ on utilise les lois classiques faisant appel aux coefficients de poussée globale C_T et de débit C_D en fonction du taux de détente fan.

IV.3. - Contrôle de la validité des méthodes d'essais.

TPS.

Cette technique n'assure pas la continuité des débits entre l'amont et l'aval. Pour éviter une pénalité de traînée sur l'entrée d'air, la géométrie de cette dernière est modifiée de telle sorte que le coefficient de débit $C = A_0/A_E$ soit identique à celui de l'entrée d'air réelle. La fonction de transformation dépend de chaque entrée d'air. Un essai spécial sur un montage de nacelle isolée (pl. 1) vérifie si cet objectif est bien atteint et éventuellement permet d'appliquer une correction.

Sur l'arrière-corps, les conditions de similitude avec l'avion du jet primaire ne sont pas remplies. Le taux de détente P_{ij}/P_0 dépend de la conception de la turbine (soufflante à 1 ou 2 étages) et il est en général trop élevé. Il en découle que les répartitions de pression sur le capot moteur et le forme du jet peuvent être modifiées (réf. 1). Cet effet est mis en évidence planche 17 par comparaison aux essais "jets soufflés". Seule une étude spéciale pourrait en évaluer les conséquences.

Enfin, il est impératif de vérifier, lors des essais en soufflerie, que les caractéristiques des jets (distorsion de pression et de température) sont identiques à celles mesurées lors des essais au point fixe, faute de quoi les étalonnages de la poussée deviennent douteux.

Jets soufflés.

Pour valider cette technique l'on doit s'assurer :

- 1°) - que le champ de pression autour de la nacelle n'est pas perturbé par l'obstruction de l'entrée d'air ;
- 2°) - que les caractéristiques des jets ne modifient pas le champ de pression sur l'ogive de l'entrée d'air.

Le contrôle du point 1 s'effectue en comparant les répartitions de pression (voilure-nacelle) mesurées lors des essais des configurations 2 et 3 (voir pl. 1) nacelle avec entrée d'air réelle et nacelle entrée d'air carénée à même débit.

Pour les positions relatives nacelle-voilure étudiées, cette condition est réalisée (pl. 18 et 19).

Une prise de pression judicieusement placée sur le carénage d'entrée d'air a également permis de vérifier l'indépendance de l'ogive d'entrée d'air par rapport au jet.

V - RESULTATS - COMPARAISON DES DEUX METHODES

V.1. - Précision des mesures.

Les mesures sont doublées pour chacune des configurations étudiées, quelle que soit la méthode. Les configurations motorisées sont mesurées à différents taux de détente du flux secondaire (et primaire dans le cas de la technique "jets soufflés"), ce qui représente environ 100 points de mesure par configuration et par Mach.

La précision déduite de l'écart entre deux rotations à mêmes paramètres de fonctionnement du moteur est présentée planche 20. La précision globale sur l'estimation des efforts d'installation peut ainsi être estimée à environ $\pm 0,7$ % de la traînée totale avion.

Notons dans le cas de la technique "jets soufflés" le très bon accord entre les résultats du banc de point fixe et ceux effectués en soufflerie (pl. 21).

V.2. - Comparaison des deux méthodes.

Les planches 22 et 23 présentent, en comparaison, les résultats obtenus suivant les deux méthodes pour un avion moderne de transport commercial équipé de moteurs biflux.

Les écarts observés sur les efforts d'installation sont de l'ordre de 0,5 % de la traînée de l'avion. Ceci démontre la cohérence des deux méthodes compte tenu de leur précision respective ($\pm 0,7$ %). Qualitativement, l'influence de l'installation des nacelles sur le champ de pression voilure est identique. En particulier on note un très bon accord sur la position et l'amplitude de la pointe de survitesse due à l'effet de l'entraînement des jets (pl. 23).

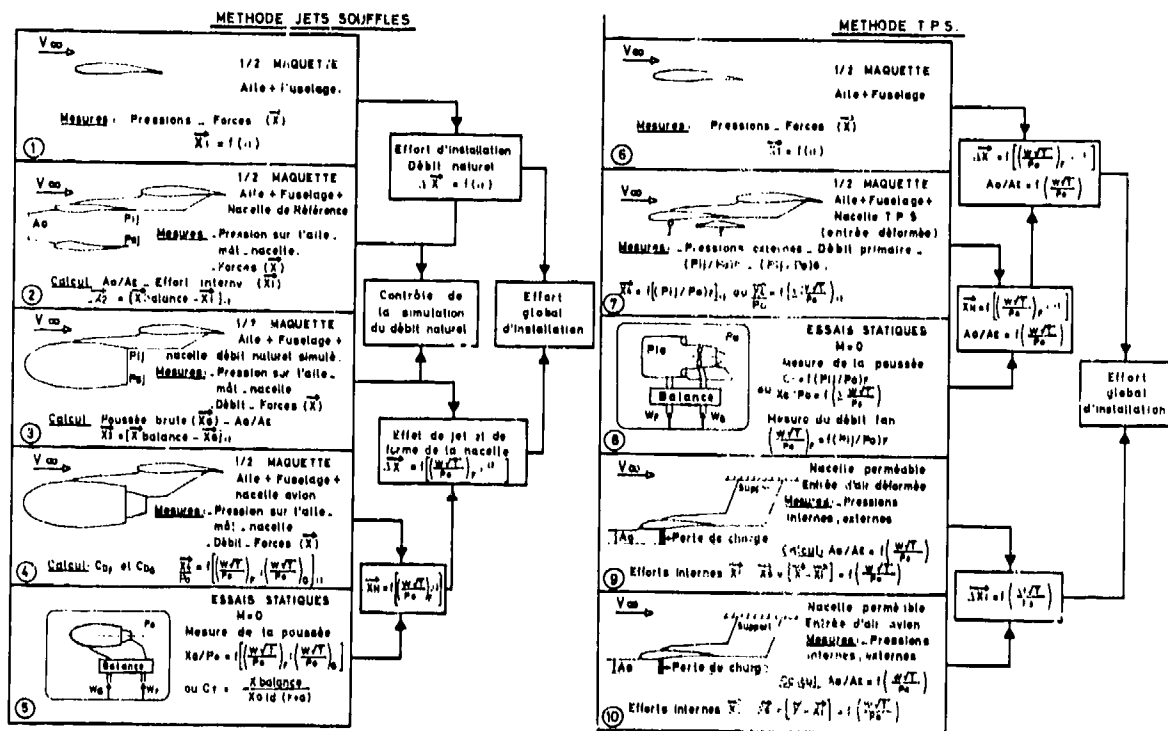
VI - CONCLUSIONS

Cette étude montre que les deux méthodes de motorisation développées par l'AEROSPATIALE et l'ONERA pour évaluer les efforts d'installation du groupe propulsif d'un avion de transport commercial subsonique ont permis d'obtenir une précision satisfaisante et des résultats cohérents. L'expérience acquise nous conduit à penser que ces deux méthodes sont complémentaires. En effet, la méthode TPS nous paraît plus facile d'emploi ; sur une maquette équipée d'un nombre important de prises de pression pour le contrôle des effets locaux, elle est bien adaptée à l'étude d'améliorations de l'interaction nacelle-voilure (positions de nacelle, formes de mât, profils voilure, etc.) pour une installation motrice donnée, mais moins fiable lorsqu'il s'agit de comparer des nacelles de types différents (problème de l'étalonnage). La méthode "jets soufflés" dans ses limites de validité permet un meilleur contrôle du niveau absolu des mesures et de ce fait est mieux adaptée à la comparaison de différents moteurs. En outre, elle seule permet, pour le moment, des études sur des nacelles de type à jets confluents.

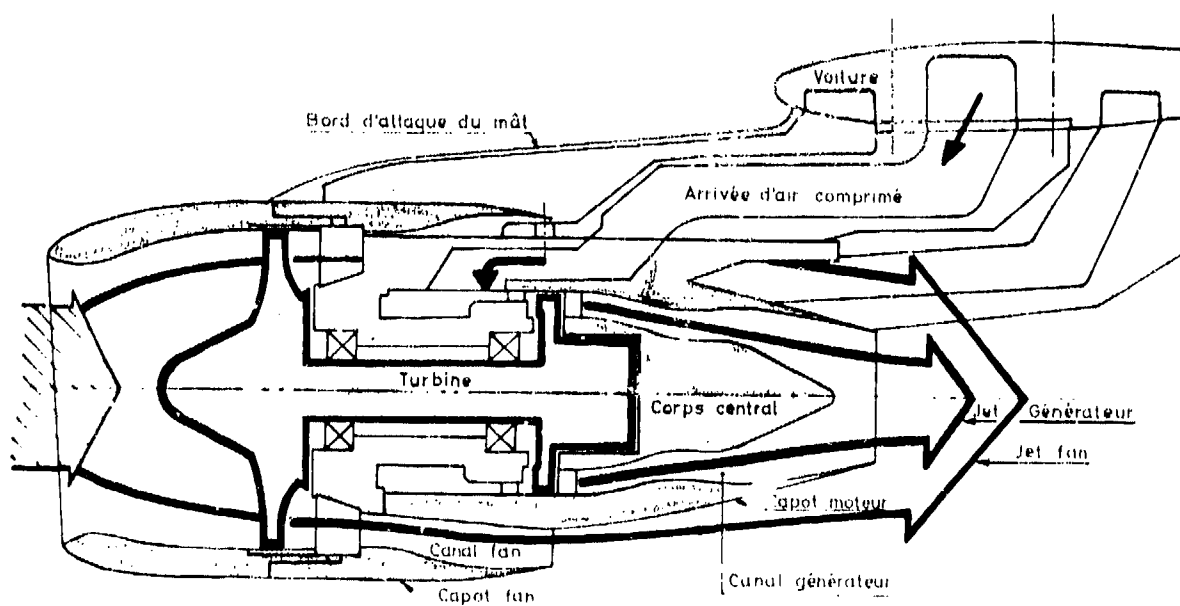
REFERENCE

Réf. 1 : M. SAÏZ - Interaction des jets des réacteurs GE CF650 sur la cellule de l'Airbus en croisière. Simulation en soufflerie.

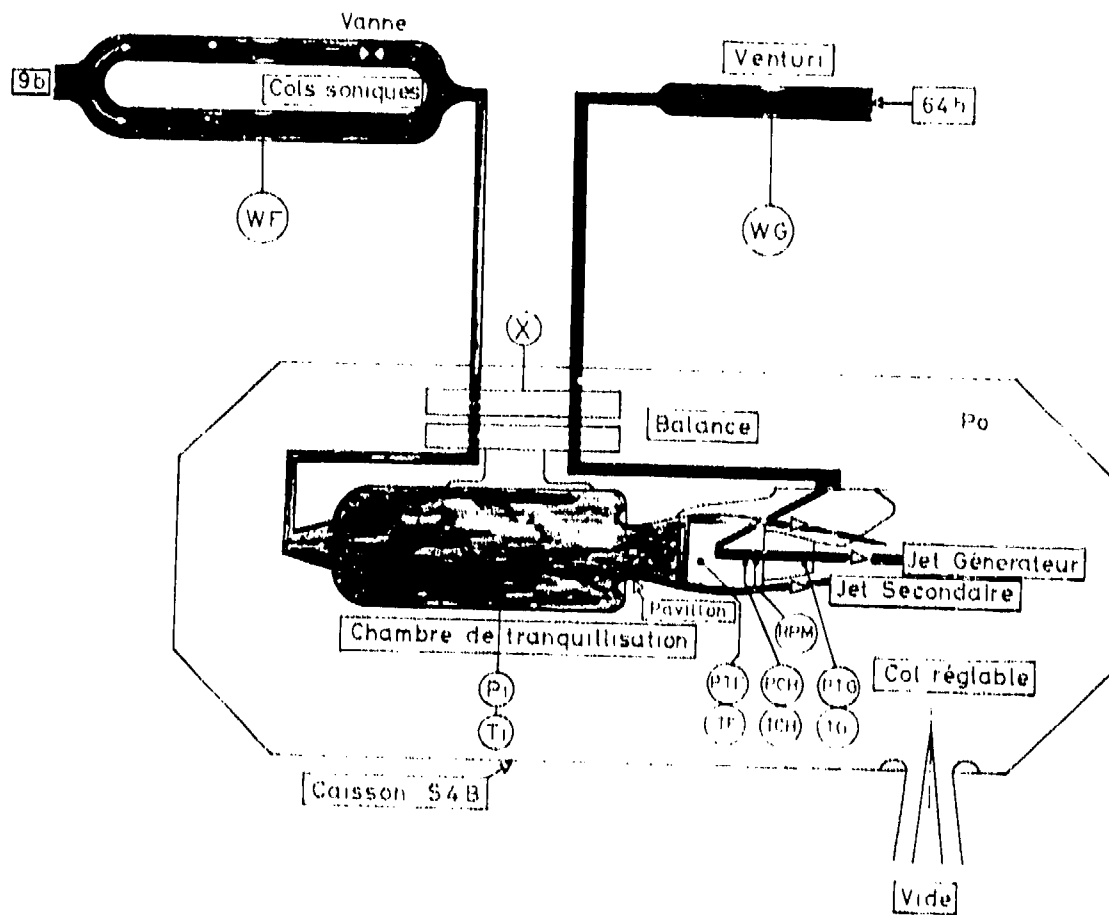
11^e Colloque d'Aérodynamique appliquée - AAAF Bordeaux - Novembre 1974.



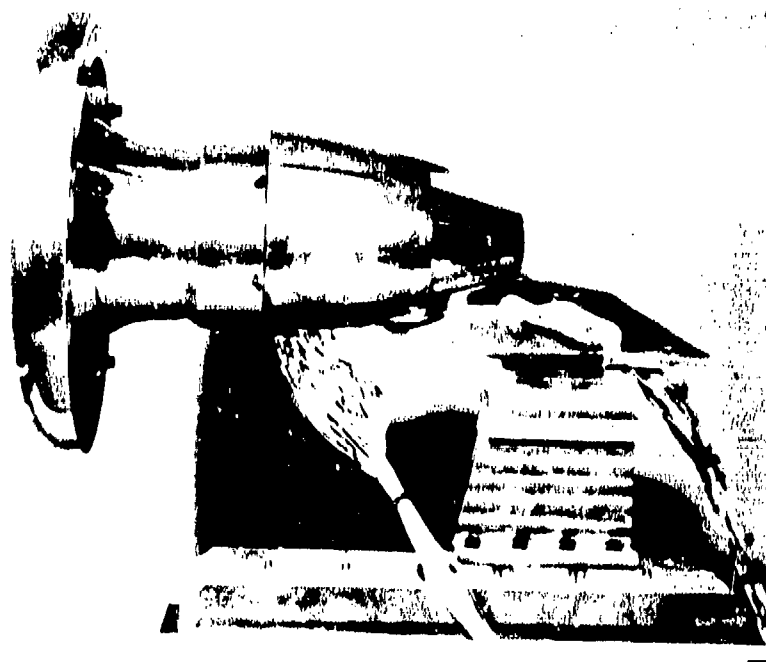
Pl. 1 — Evaluation des efforts globaux d'installation des nacelles.



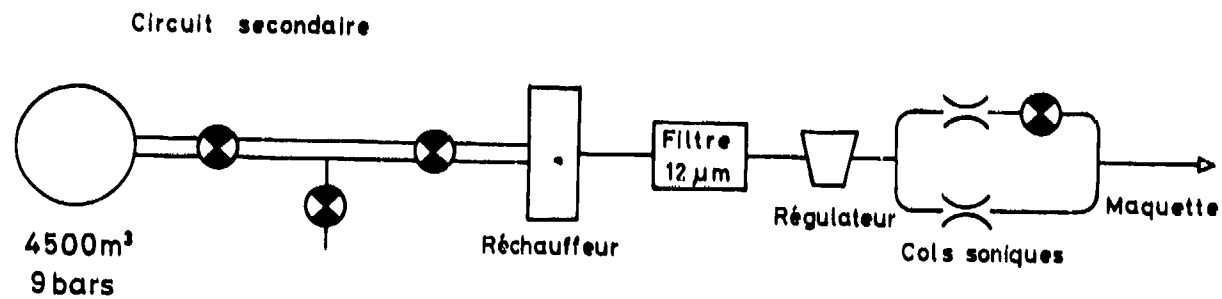
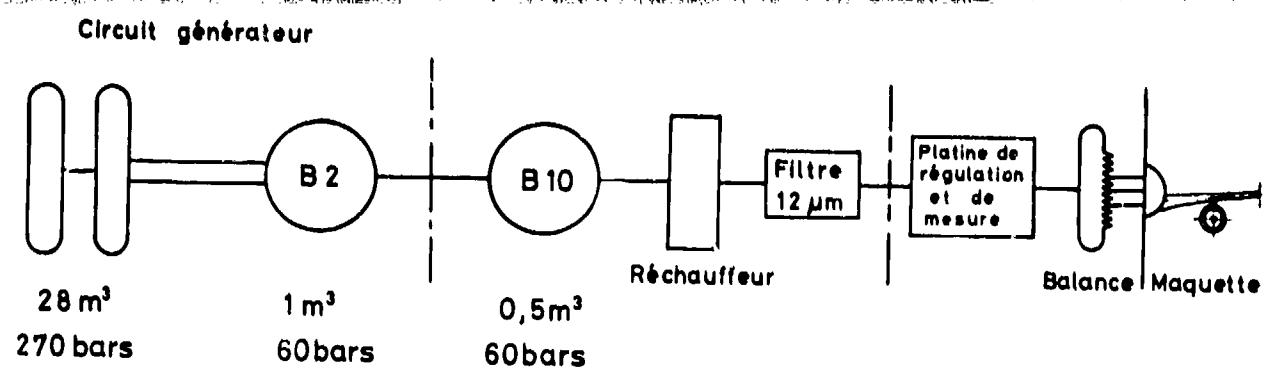
Pl. 2 — Simulation de moteurs par turbine à air.



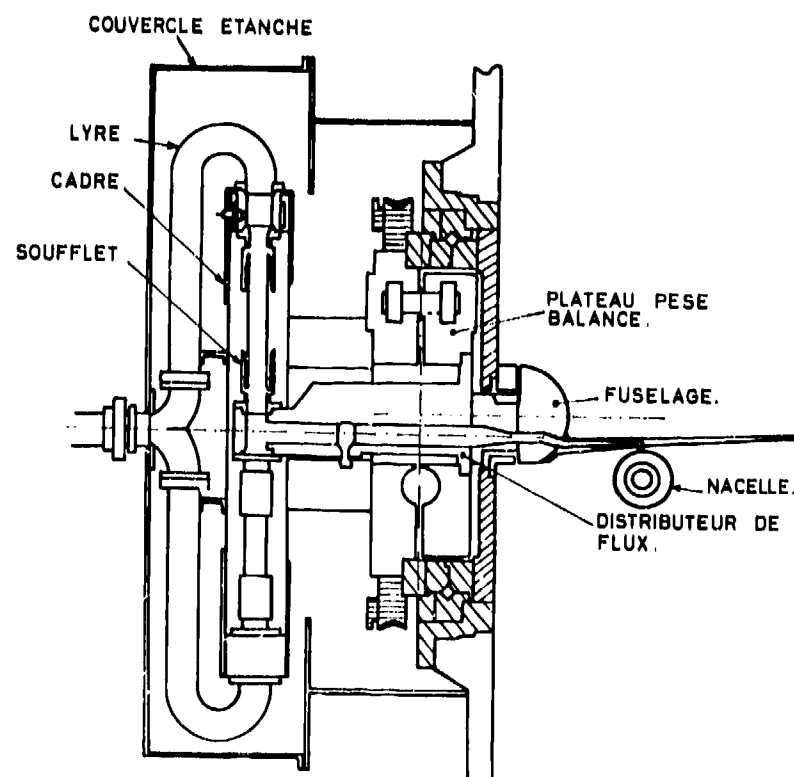
Pl. 3 - Schéma de principe du banc



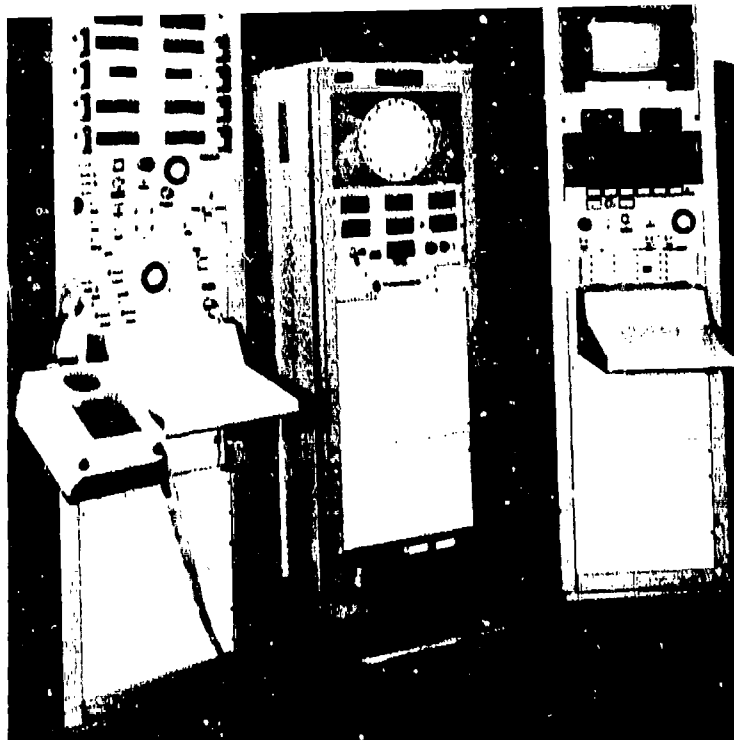
Pl. 4 Nacelle TPS, montée sur un mât support, et équipée de son pavillon d'entrée d'air.



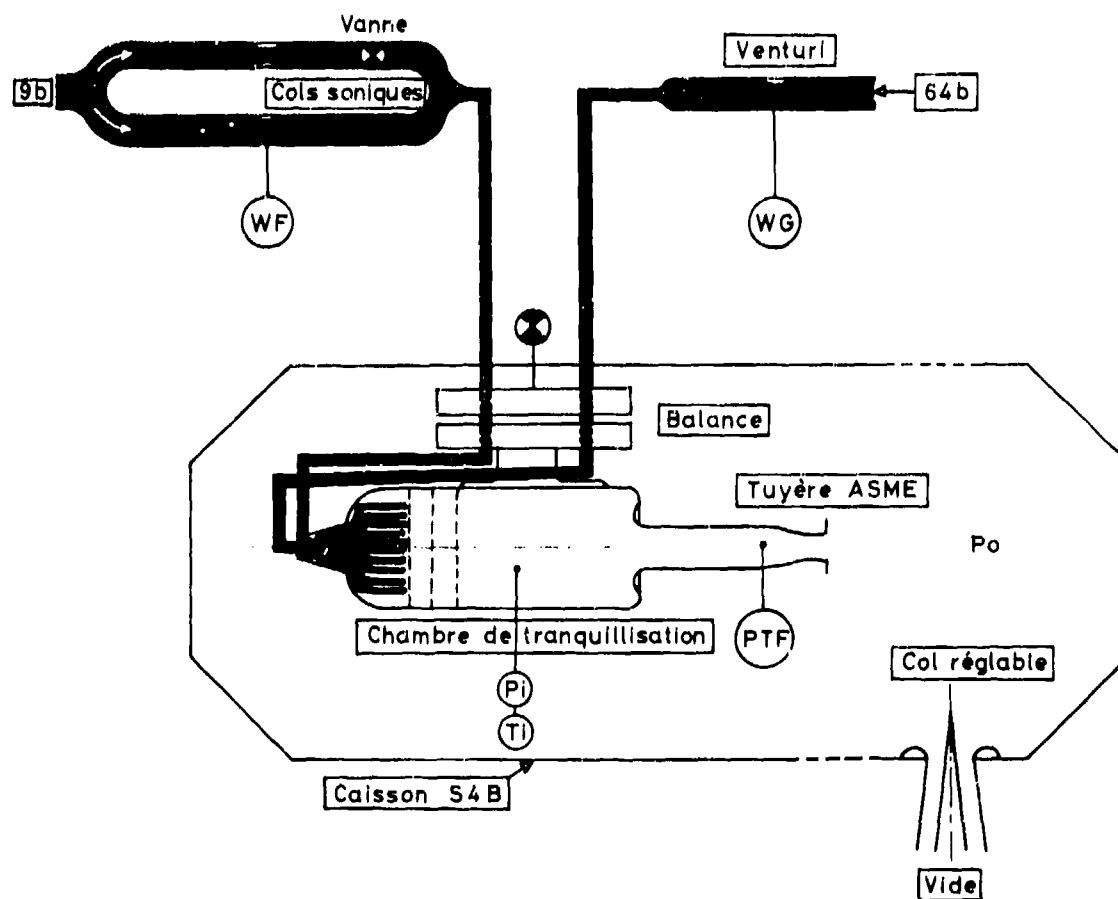
Pl. 5 - Circuits d'alimentation.



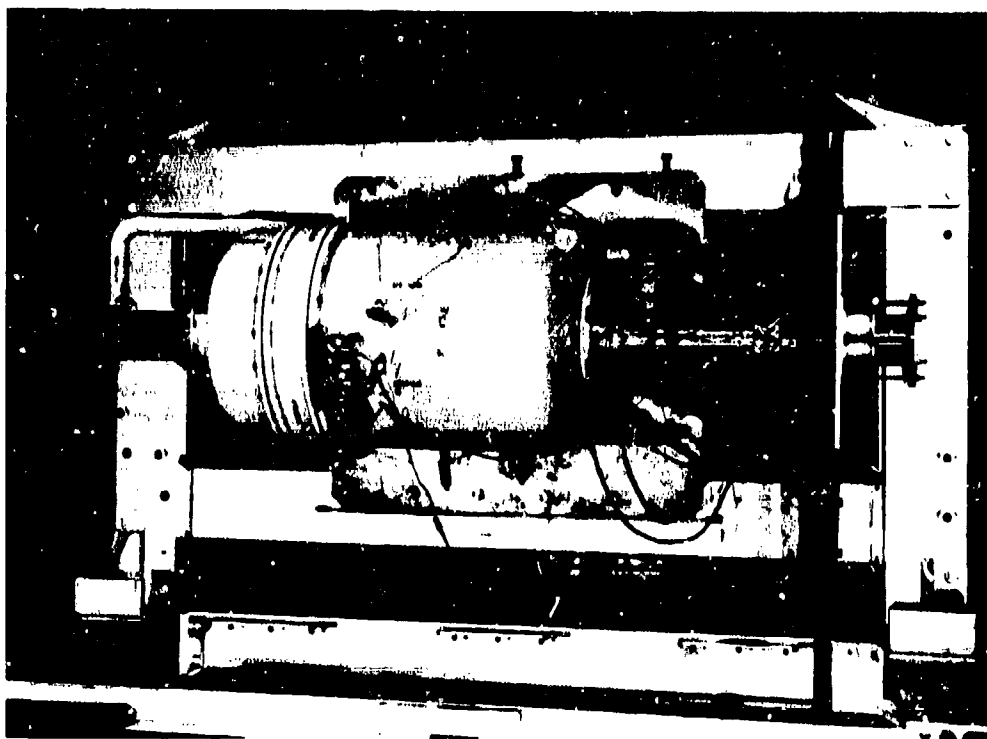
Pl. 5 - Montage de la maquette sur la balance.



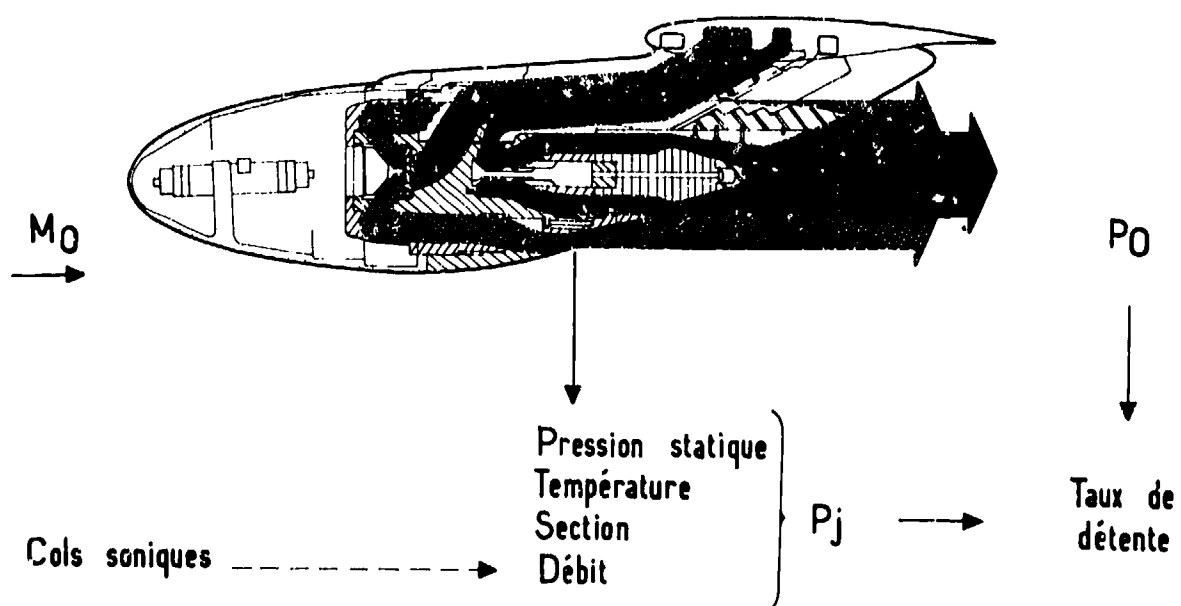
Pl. 7 - Consoles de commande et de surveillance du banc d'étalonnage.



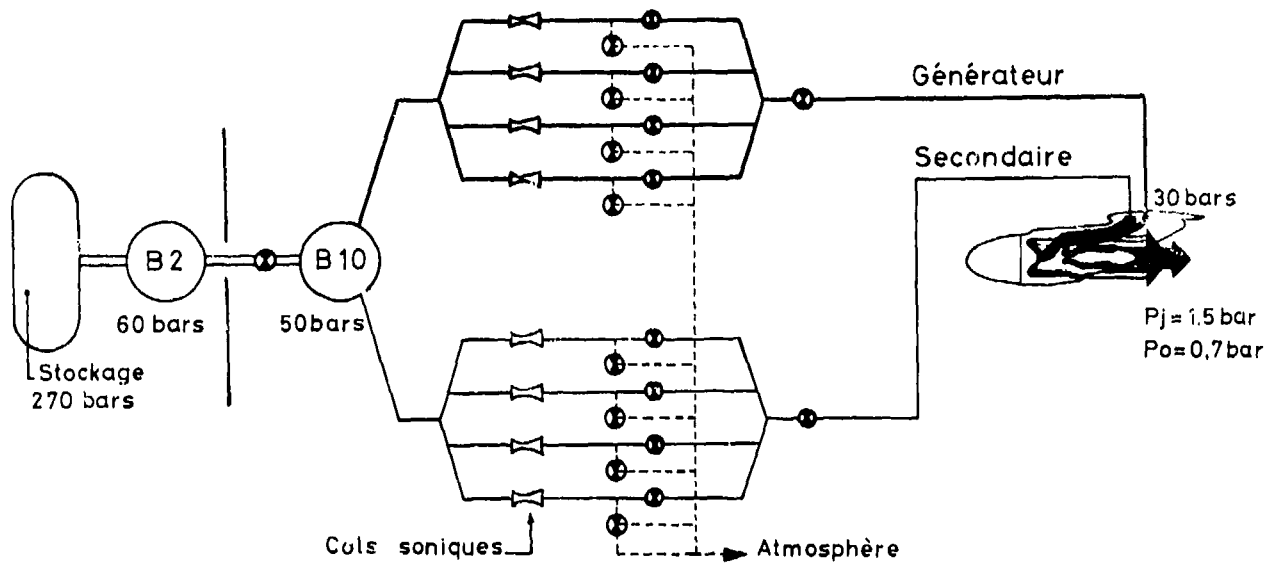
Pl. 8 - Schéma de principe du banc avec tuyère étalon ASME.



Pl. 9 - Chambre de tranquillisation, montée sur la balance, et équipée d'une tuyère ASME.



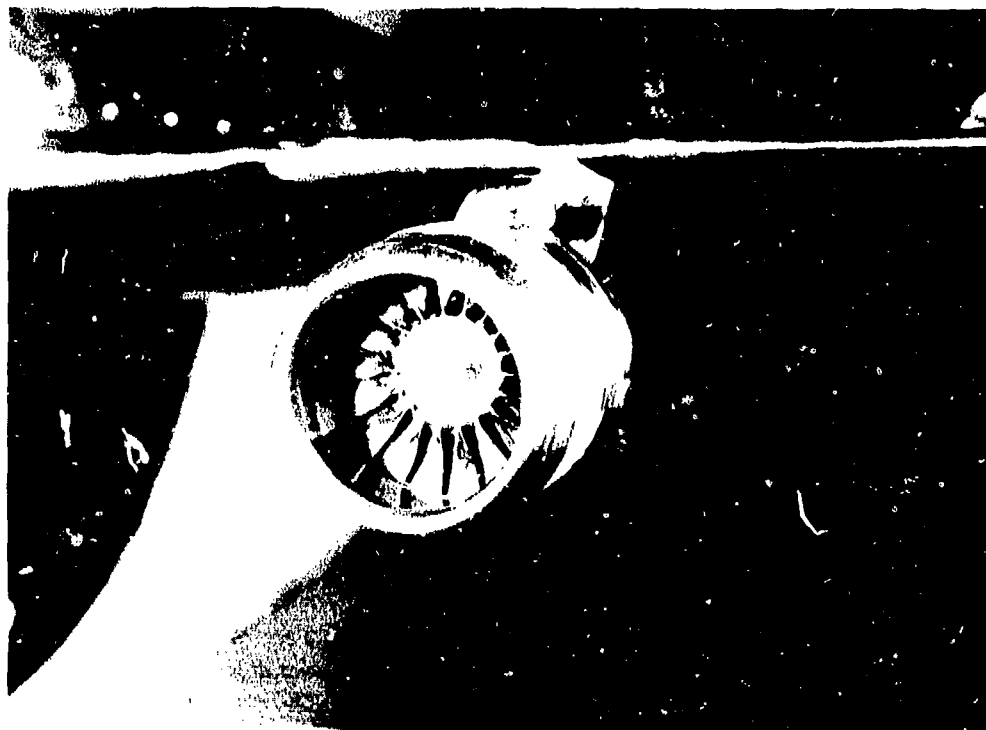
Pl. 10 - Simulation de moteurs par soufflage.



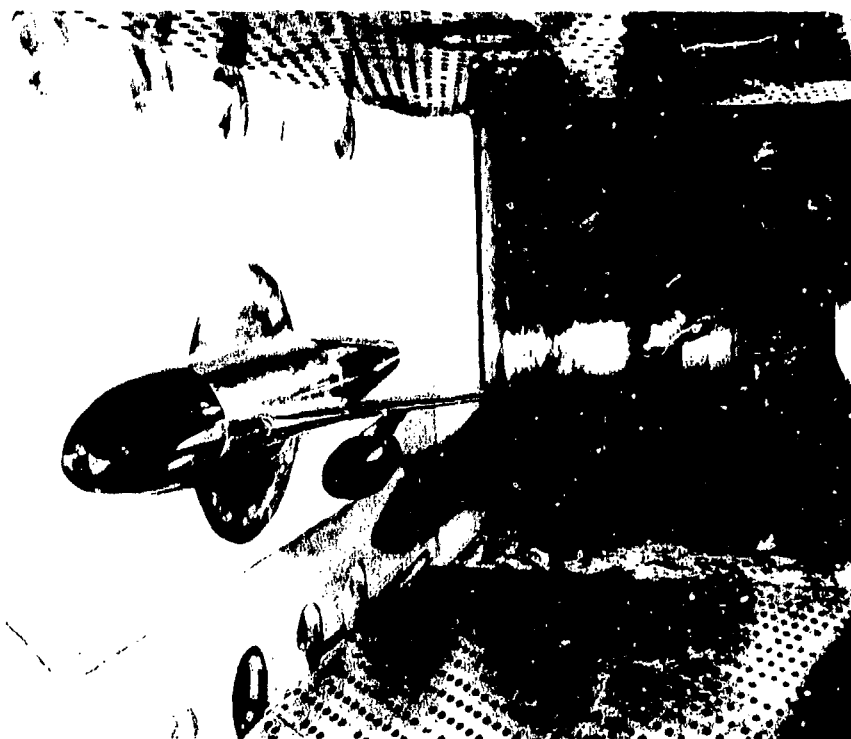
Pl. 11 - Simulation de moteurs par soufflage. Alimentation en air comprimé.



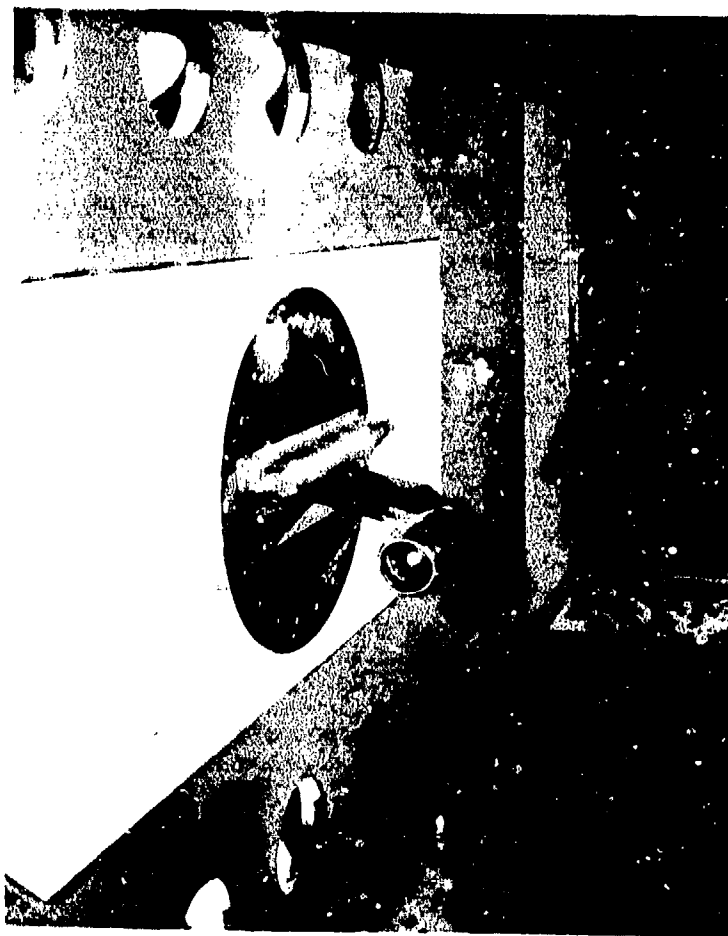
Pl. 12 - Demi-maquette d'avion de transport avec nacelle TPS dans la veine transsonique de la soufflerie S2 MA.



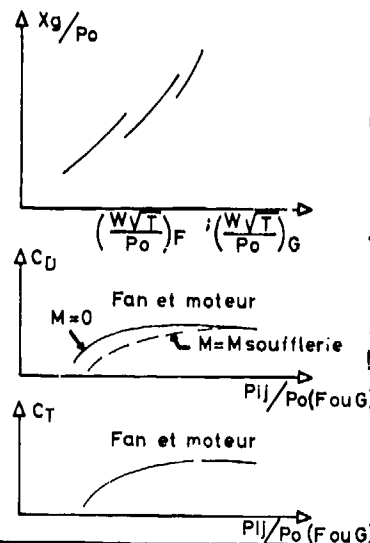
Pl. 13 — Nacelle TPS en veine entrée d'air et soufflante.



Pl. 14 — Demi-maquette d'avion de transport avec nacelle soufflée dans la veine transsonique de la soufflerie S2 MA.



Pl. 15 - Nacelle TPS montée sur mât isolé dans la veine transsonique de la soufflerie S2 MA.



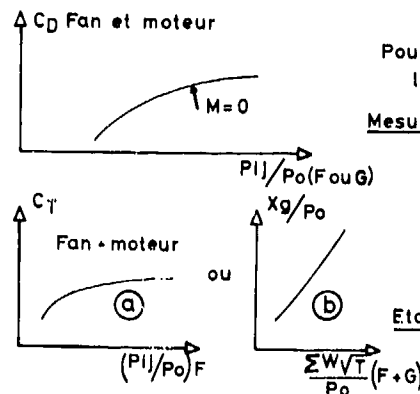
Pl. 16 - Lois d'étalonnage.

METHODE JETS SOUFFLES

Poussée définie avec effet de l'écoulement extérieur.
Mesures: Débits - Températures du fan et du moteur.

METHODE JETS SOUFFLES

Poussée définie avec et sans effet de l'écoulement extérieur.
Mesures: Débits - Températures Taux de détente du fan et du moteur.

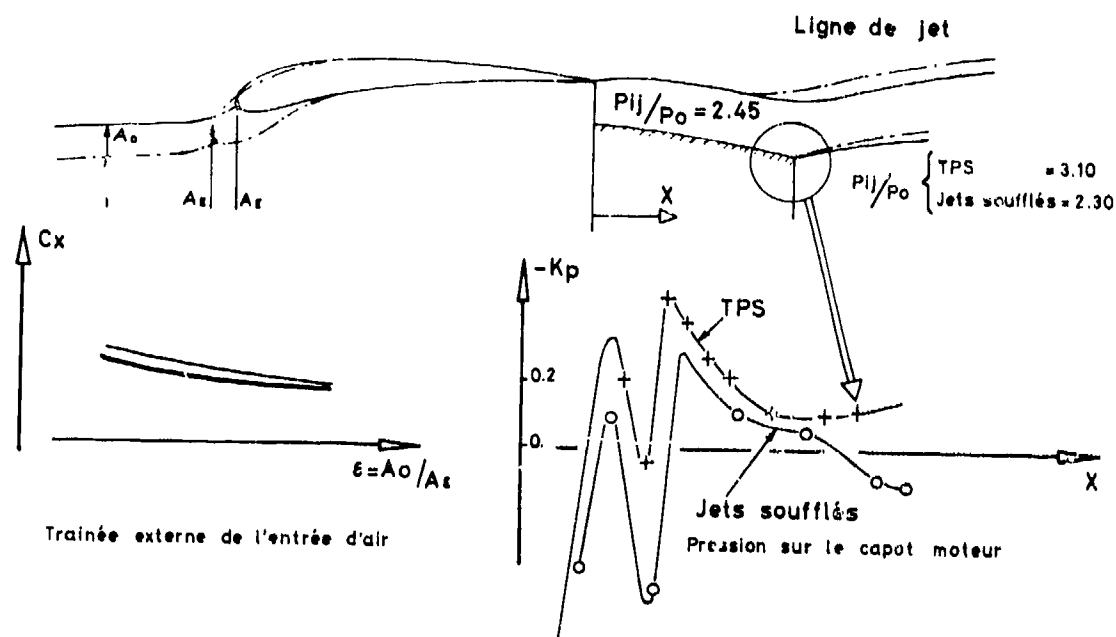


METHODE TPS

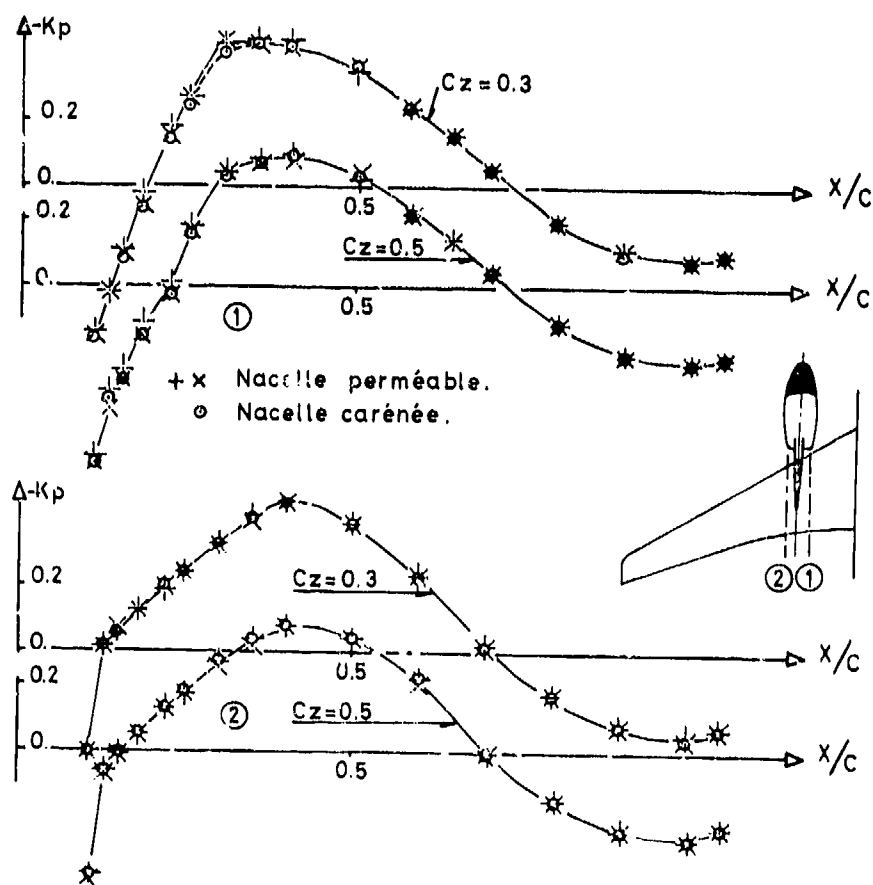
Poussée définie sans effet de l'écoulement extérieur.

Mesures:

- (a) Débits moteur - Taux de détente - Températures du fan et du moteur.
 - (b) Débit moteur - Taux de détente du fan - Températures Fan et moteur
- Etalonnage du débit secondaire.

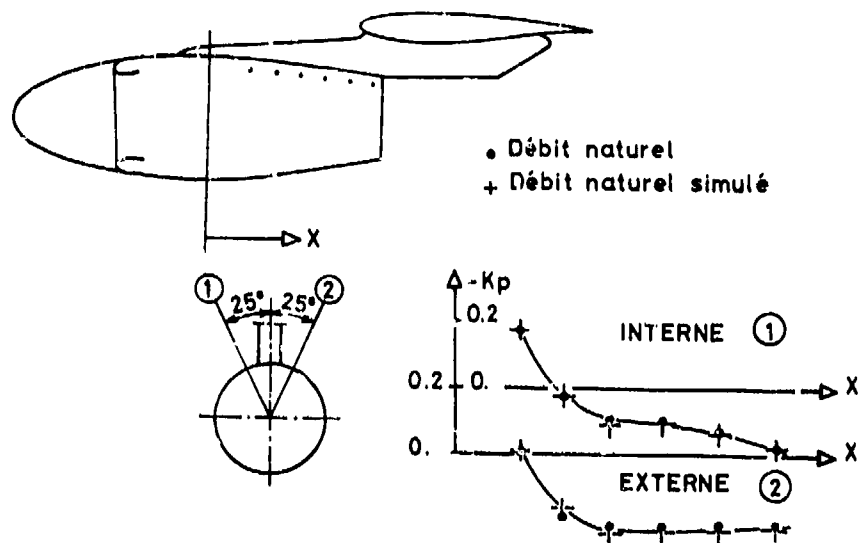


Pl. 17 - Méthode TPS Contrôle de la simulation, comparaison avec les essais en jets soufflés.



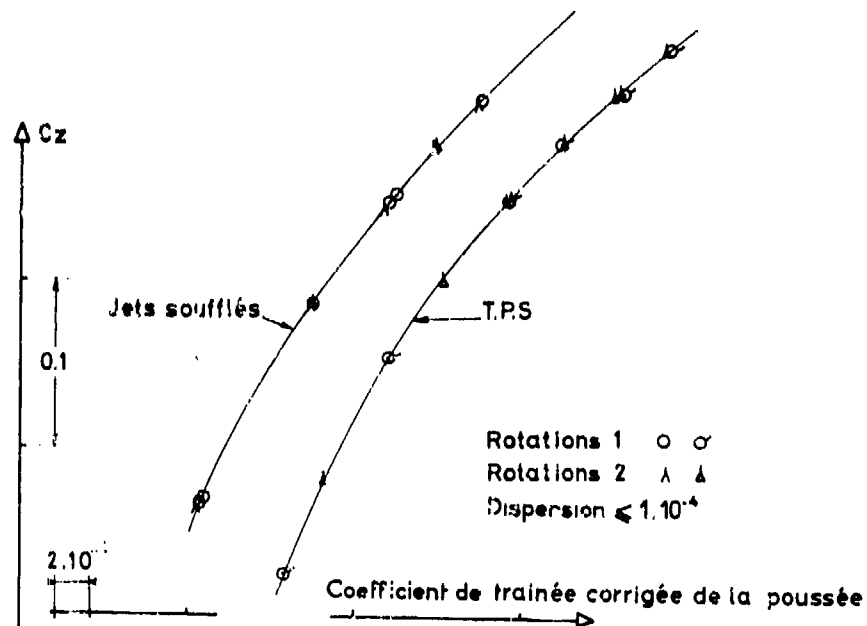
Pl. 18 - Méthode jets soufflés.

Pressions sur l'intrados de la voilure
 Contrôle de la simulation du débit naturel
 Influence du carénage d'entrée d'air.

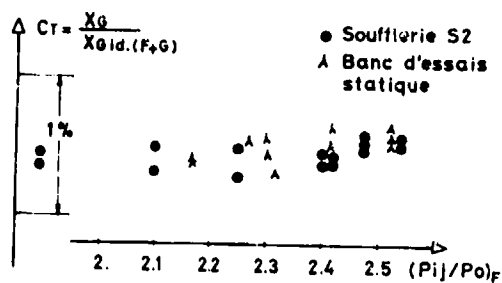


Pl. 19 - Méthode jets soufflés.

Pressions sur la nacelle
Contrôle de la simulation du débit naturel
Influence du carénage d'entrée d'air.

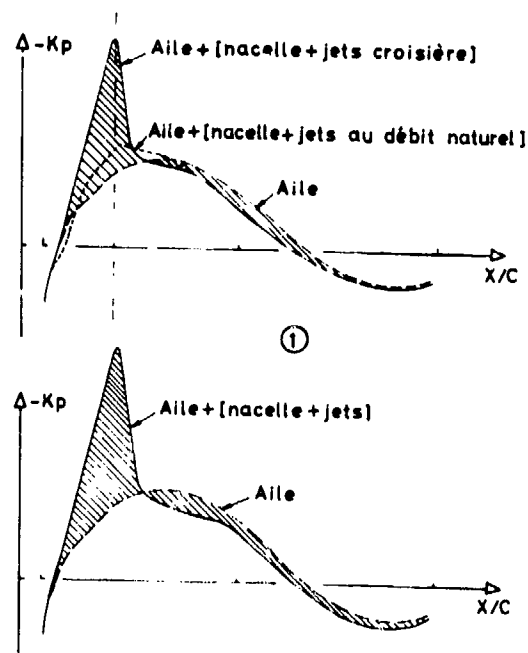
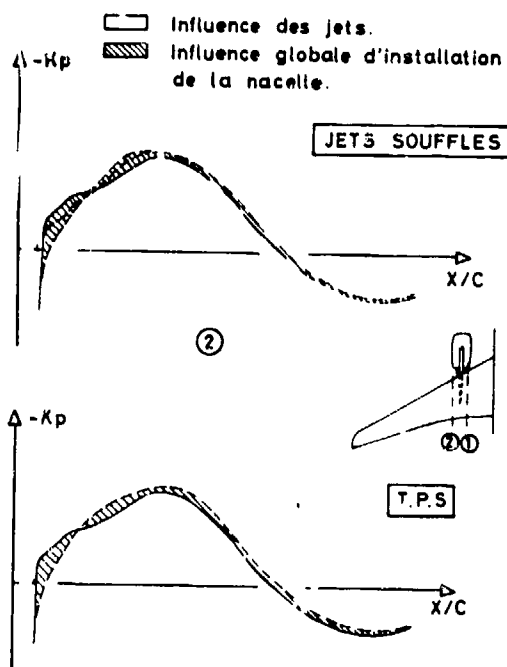
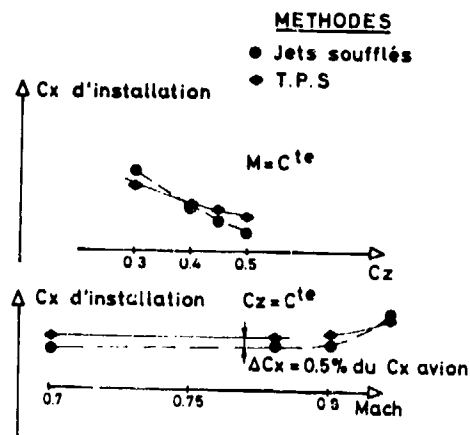


Pl. 20 - Fidélité des mesures.



Pl. 21 - Coefficient de poussée. Fidélité des mesures.

Pl. 22 - Trainée globale d'installation des nacelles. Comparaison des méthodes d'essais.



Pl. 23 - Pression sur l'intérieur de la voilure. Comparaison des méthodes jets soufflés et T.P.S.

WIND TUNNEL TEST AND ANALYSIS TECHNIQUE USING
POWERED SIMULATORS FOR CIVIL NACELLE
INSTALLATION DRAG ASSESSMENT

by

A.E. Harris and E.C. Carter
AIRCRAFT RESEARCH ASSOCIATION LTD.
MANTON LANE, BEDFORD, ENGLAND MK41 7PF

SUMMARY

Full span and semi-span wind tunnel model tests and powered nacelle calibration techniques are discussed in the context of civil nacelle installation drag assessment and optimisation.

In order to achieve the accuracy required for drag analysis it is necessary to determine the installed net thrust of the powered nacelle simulator to the equivalent of at least one aircraft drag count. This implies stringent control of mass flow and thrust accounting and imposes the need for consistency of approach in the wind-on and calibration tests where thrust and mass flow coefficients must be known to 0.1% to 0.2% accuracy. This need for high confidence in the data at all stages of analysis has led to a methodology in which the measured data is combined in various ways to enhance confidence in its final use.

Experiences obtained in the use of a Mach Simulation Tank (MST) for the calibration of turbine powered simulator (TPS) units are discussed. The MST is used to obtain simultaneous mass flow and thrust calibrations with representative internal nacelle conditions in the presence of a quiescent exhaust environment.

Practical problems associated with the design of balance and airfeed arrangements are discussed along with the use of blown and turbine powered simulators.

NOTATION

This refers primarily to FIG.8 which contains some of its own notation.

<u>Principle</u>	P,H	Pressure
	T	Temperature
	A	Area
	W	Mass flow rate
	M	Mach number
	X	Thrust
<u>Secondary</u>	V	Venturi
	I,i	Intake
	P,T	Primary, Turbine
	F	Fan
	G	Gross (referring to thrust)
	T	Total
	S	Static
	α	Incidence
	θ	Normalised Temperature $T^{\circ}K/288$
<u>Abbreviations</u>	δ	Normalised Pressure psia/14.7

Abbreviations

AMCV	Total Multiple Critical Venturi Throat Area
ATF	Altitude Test Facility
CRPMI, CRPMT	Corrected rotational speed $RPM/\sqrt{\theta_i}$, $RPM/\sqrt{\theta_T}$
FNPR	Fan nozzle pressure ratio PTF/PS
MCV	Multiple Critical Venturi
MFR	Mass Flow Ratio A_{∞}/A_i
MSIM	Simulated Mach Number
MST	Mach simulation tank
PNPR	Primary nozzle pressure ratio PTP/PS
TFN	Through Flow Nacelle
TPS	Turbine Powered Simulator
CWI, CWT	Corrected mass flow rate $WI\sqrt{\theta_i}/\delta_i$, $WP\sqrt{\theta_T}/\theta_T$

1. INTRODUCTION

There is more than adequate evidence to show that the performance benefit or penalties of a power plant installation can significantly influence the success of current high economy civil transports. Future trends towards higher by-pass ratios and lower specific thrusts will make the accurate assessment of engine installations even more important, and probably much more difficult.

It is fortunate that the present range of engines and cruise speeds put the critical cruise performance points in a region where external flow coupling of inlet and exhaust is small but accepted and where internal cycle awareness of the external exhaust environment is limited or non-existent. This may not of course be true of other critical flight regimes such as second segment climb.

If it is accepted that the presence of the real flows associated with the engine unit must be simulated in wind tunnel performance tests then we are well on the way to saying that the ideal simulator should be a model engine. The degree of simplification which is accepted leads the choice of simulations from the simplest free-flow nacelle to the blown nacelle, to the ejector, and finally to the turbine powered simulator.

Having chosen an acceptable simulator on the grounds of cost, flow similarity, complexity, accuracy and past experience, etc. then the question of what measurements will give the best assessment of performance and understanding of results must be considered. This in turn will define the nature of the measuring system and the complexity of the model and its instrumentation. Complexity of model in this instance probably meaning the use of a complete model or a half model.

The choice having been made of a particular simulator on a given range of model configurations, consideration must next be given to the best way of defining the performance of the simulator whilst operating in the wind tunnel test environment mounted on the model. The natural approach to this must be the use of a parallel thrust and drag accounting system to that of the full scale engine and airframe accounting system. This requires a model "altitude test facility" capable of simulating the correct wind tunnel environmental pressures and temperatures, and of measuring thrust and mass flow to at least the same degree of accuracy as achieved in the wind tunnel.

The instrumentation of the simulator must be sufficient to define the required mass flow and thrust parameters to the necessary accuracy whilst at the same time being compatible with the simulator size, the tunnel instrumentation, and the data recording facilities. For these purposes it is essential that the simulator is a stable, repeatable unit, which can be calibrated in terms of measured model temperatures and pressures.

To meet these requirements an auxiliary compressed air supply with accurate monitoring of mass flow and temperature and precision servo control of pressure at the simulator is essential. The pressure must be high enough to be compatible with the duct sizes and the balance air transport system, and the air must be sufficiently dry to avoid condensation or icing problems. For blown models a twin servo-controlled high pressure air supply must be provided.

Air transport across model force balances requires close attention to detail in model and balance design and manufacture. For some configurations, rear fuselage mounted units for example, it is essential to use a complete model. This in turn requires complex internal ducting and non-interfering air transport systems within the fuselage and across the balance. For this reason half model balance systems are favoured wherever possible because of the extra space normally available for the balance, air transport, and instrumentation. The half model however brings with it the usual associated doubts in absolute accuracy and possible half fuselage buoyancy forces.

The above problems are considered in detail in this paper which reviews the nature and magnitude of the difficulties and current state of the art in UK testing.

2. THE APPROACH TO DIFFERENT AIRFRAME LAYOUTS

The solution and methods of approach to the representation of power plants must essentially differ from one layout to another. Three different nacelle installation layouts have been considered; these include the underwing installation both close to and remote from the fuselage and the rear fuselage mounted installation, Fig.1.

The rear fuselage installation requires the representation of the full fuselage with the tests being made on a complete model. Complete model testing with simulators is particularly difficult because of the need to transport high pressure air across the balance. As a validation exercise, tests have been made on a 1/25th scale research model with two TPS wing mounted units. This representation, whilst not being a rear fuselage application, has posed all the problems that would arise with such an application. Considerable development was necessary to design a non interfering high pressure air system to cross a standard complete-model balance. The system is based on flexible metal bellows coupling the live and earth balance ends. The air transport across the bellows is normal to the balance axes and equally opposed to avoid pressure interference. The system is designed to minimise thermal interactions between the airflow and balance elements as well as to eliminate mechanical hysteresis. The balance and air transport system was calibrated as a combination with the balance blowing pressure as a small term in the interaction matrix. Use of this technique is the subject of a separate paper in this symposium and so will not be enlarged upon here. The application of these techniques can well be adapted to a rear fuselage configuration when the need arises but the primary method of support would have to be changed as a rear sting mount would be unacceptable. A possible arrangement is shown in the lower Fig. 1; this includes a fully metric fuselage and power units, all mounted from an earthed strut which enters the lower surface of the forward fuselage. The presence of the interfering strut is not an uncommon problem in most afterbody experimental work and has to be accepted as a factor which does not influence the incremental terms that arise from small optimising changes in the rear fuselage/nacelle region. Whatever the final support system that is chosen it is imperative that the wing be included in

the measured drag.

Considering now the wing mounted nacelle, more test configuration options are open to us. If a fully representative installation drag is required then a complete model must be provided and the technical involvement discussed above is necessary. If however the incremental effects of installation changes are considered to be localised to the wing then the half model technique offers considerable advantages. The questions to be asked about the validity of half model testing are not new, neither is there a simple reassuring answer. Nevertheless the simplification introduced into powered simulator testing by the use of half models makes us address the question of whether the technique is acceptable in this instance. In general the lift curve slope obtained from a half model test is the same as that of the complete model if the fuselage centreline stand off distance on the wall is at least a displacement thickness and probably up to two displacement thicknesses. Whilst providing the correct basic lift the longitudinal stability may be slightly modified due to the unrepresentative distribution of fuselage lift. This term would not be expected to be greater than 2% and would also not be expected to change with nacelle/pylon configuration change. However drag is our prime concern here and there can be no justification for believing absolute drag levels of half models although there is evidence to indicate reasonable representation of drag due to lift and good representation of drag increments due to wing build changes (i.e. controls, stores, nacelles etc). In general of course, powered half models are associated with a corresponding unpowered full span model and the above objections probably become academic.

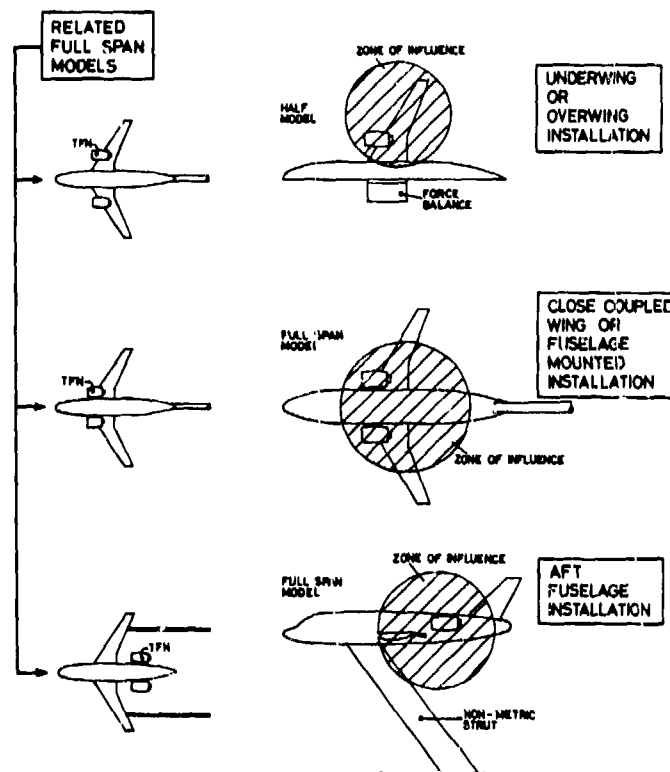


FIG.1 INSTALLATION TYPES AND POSSIBLE MODELS

The final question that remains relates to the fuselage. If it is accepted from the above arguments that accurate installation drag increments can be obtained from a half model then we have to consider whether the half fuselage should be metric. This may appear to be an unnecessary question and "of course the fuselage should be metric" - however the main basis for considering the half model technique at all is the assumption that a true representation of incremental interference which is free from tunnel flow boundary effects, is obtained. For a half model it must be accepted that the fuselage flow is not correctly represented and neither in particular is the fuselage cross-flow. Hence the use of a complete metric half fuselage will require the assumption of consistent floor boundary layer effects which are independent of the wing/nacelle configuration changes. It is our view that if wing/nacelle changes genuinely modify the aft fuselage drag then a complete model must be used; if however such changes do not or may not influence the aft fuselage drag then a non-metric fuselage should be used on the half model. The reason for this view (which is not for the purpose of easing the model design or testing) is that a metric fuselage is an excellent integrator of tunnel buoyancy. Modifications of wing flow and turbine and fan efflux can have small and unpredictable effects on tunnel buoyancy which will be most faithfully integrated as drag changes by the rear fuselage; these would then be incorrectly assumed to be changes in drag associated with the wing/nacelle modifications.

To summarise - it is our belief at ARA that for configurations where nacelle installations are likely to mutually interfere with the fuselage flow then a complete model must be used; for configurations where the effects of nacelle installation and modification are confined to the wing then a half model should be used with a non-metric fuselage. An accepted criticism of this belief is the need for an advance decision of what builds are considered to be independent of the fuselage, but we feel that this is greatly outweighed by the strong likelihood of erroneous answers due to the incorrect representation of aft fuselage flows in the tunnel (typically at $M = 0.8$ an error of one aircraft drag count is caused by a ΔM gradient in the flow over a metric rear fuselage of 0.00075, this is clearly approaching the calibration accuracy and repeatability of most tunnels).

3. THE OPTIMUM SIMULATOR

At the expense of repeating what may have been discussed before, probably with appropriate bias associated with the experience of the particular operator or facility, we would like to briefly address the question of the best or most appropriate power plant simulator, with reference to Fig. 2.

Through flow nacelle (FIG. 2 upper)

This is the simplest and most economic simulator. This provides correct inlet geometry and M.F.R. if the exhaust geometry is enlarged or alternatively reduced inlet M.F.R. with the correct exhaust geometry. Experience at ARA (Ref.1) indicates the latter method to be most desirable in relation

to local wing surface pressures. The modification to inlet geometry to allow for reduced inlet flow, or the increase of spillage around a correctly sized inlet, are both shown to give wing pressure results equivalent to the correct sized inlet and mass flow ratio.

The exhaust flow is unrepresentative in both total pressure and temperature and consequently in exhaust plume shape and stream shears. The optimum methods of nacelle and plume representation by a hard free flow surface may well develop in time as more experience is accumulated with jet flow representative models.

Evidence (Ref.1) suggests that the best through flow nacelle simulation is obtained by the use of full representation of the real cowl shapes in preference to short cuts which do not include the gas generator cowl, or which use a hard body representation of the fan jet boundary i.e. extended cowl. An example of local wing surface pressures is shown in Fig. 3. In this particular case the extended cowl through flow nacelle (TFN) gives a closer result to the powered case but experience indicates that for different installations the particular form of TFN giving the best simulation of the powered case differs - hence the use of TFN nacelles can give unpredictable local interference results and so a powered nacelle must be used in the general case.

Blown Nacelles (Fig.2 mid upper)

The blown nacelle has advantages and disadvantages. All the air that exhausts from the nozzle has been fed into the model so no nacelle measurements of mass flow are needed in the model which simplifies instrumentation (although of course T is needed to give w/T from a feed

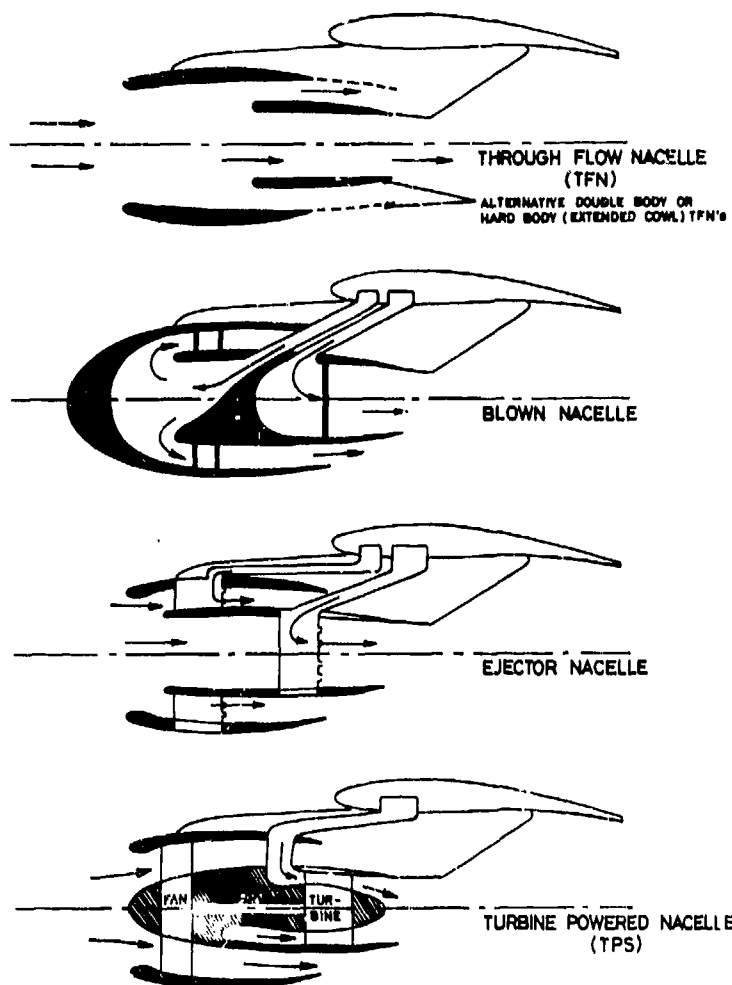


FIG. 2 TYPES OF NACELLE SIMULATORS

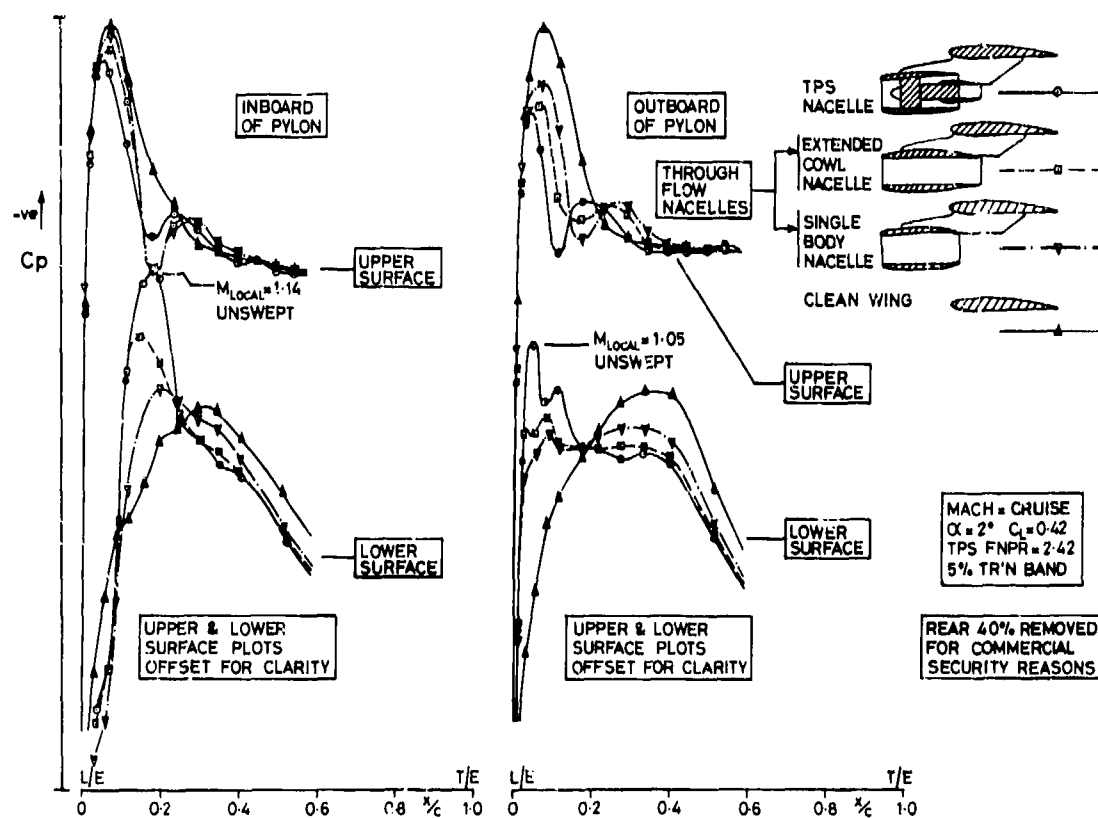


FIG. 3 WING PRESSURES AND FREE FLOW NACELLES

line value of w/T_{100}). The exhaust total pressure of both primary and fan are very low (about 2 atmospheres) in comparison with the supply pressure into the nacelle (about 30 atmospheres); this leads to complex pressure dropping systems giving the problems of non-uniform nozzle pressure distributions and temperature distributions (due to the Joule-Thompson drop). The accuracy of the whole experiment depends upon the repeatability of the instrumentation as it "sees" the pressure and temperature distribution and small changes in performance of the pressure dropping system (say perforated plates) can give different distribution of nozzle pressure and temperature profile from that for which it was calibrated. One significant advantage often quoted for the direct blown nozzle system is its potential for over-blowing for calibration purposes to provide the correct nozzle flight pressure ratios in static calibration. This however requires the dangerous assumption of similarity of flow distribution in the nozzle whilst operating at the elevated (over-blown) absolute pressures and pressure drops; and also requires that any dependence of nozzle thrust and discharge coefficients on internal Reynolds number can be quantified and accounted.

The front of the nacelle for the fully blown nozzle does of course require to be faired. This can be designed to give the same pressure distribution over the inlet cowl region back to the fan nozzle plane for a range of C_p and M conditions whilst allowing for the extra boundary layer displacement surface. So in principle the approach conditions to the flow mixing at the nozzle plane can be correctly represented. However the effects of the displaced "non-captured" inlet stream tube into the gully flow between the nacelle and wing and pylon must have significant effects, albeit unquantified at present.

Ejector Nacelles (FIG.2 mid lower)

The ejector nacelle has the great advantage of high pressure air economy compared with the direct blown nacelle. It would be reasonable to expect to achieve an ejector mass ratio of about 1.5 permitting an inlet flow of about 60 to 65% of the design operating value. This inlet flow deficiency can be reasonably accommodated by inlet cowl redesign.

Multi tube ejectors are essential to achieve the required performance and although it would be a refinement to provide independent fan and core duct ejector pressure controls to give precise engine twin stream schedule matching it should not be forgotten that this facility is readily available to the ejector nacelle if required.

As with the direct blow nacelle, the accuracy provided by the ejector nacelle depends upon the consistency of the flow at the nozzle instrumentation reference plane. This reference plane, by the nature of the internal geometry of the nacelle, is always likely to be closer to the ejector plane than the rules of complete mixing would dictate, possibly an acceptable distance but nevertheless too close for comfort, and too close for guaranteed repeatability. Consequently the accuracy of an ejector simulator is dependent upon the repeatability of the flow from a multitude of minute cond ejector nozzles and their mixing with a distorted flow field.

The Turbine Powered Simulator (FIG.2 lower)

Probably the most significant advantage of the TPS is the large wealth of relevant experience that has been and is being built up in the use of these simulators. The domination of the design and manufacture of these TPS simulators by Tech. Development Inc. of Ohio USA has undoubtedly made a telling impact on the quality and survivability of the units. Insofar as initial cost is a significant consideration, the TPS unit has this factor against it but the cost of TPS, ejector or blown nacelle core power-packages does not represent a major element in the typical total program cost. In any event the initial capital costs of all powered simulators represent quite small proportions of the cost of all programs for which the simulators are likely to be used. In general, a simulator is likely to be associated with a particular major full scale engine and is likely to be used in many cladding variants before it is discarded.

Setting aside the cost aspects it is clear that the TPS offers many technical advantages, not least of which is the representation of the inlet flow. For certain types of nacelle installation the facility to represent 80% of the inlet flow is fundamental; for many other installations where no published evidence is available to predict the importance or otherwise of the presence of the inlet flow it appears that the decision between blown or TPS comes down to past experience or practice. In any event certain facets of nacelle installation aerodynamics dictate that to select a blown simulator requires that high confidence must be placed in the independent influences of intake capture and exhaust stream effects rather than the concept of interrelated inlet and nozzle effects. Certainly in this largely subsonic sphere it appears advisable to assume, unless faced with insurmountable technical obstacles, that the nacelle front end and rear end aerodynamics may well be linked in the complex flow field generated when the nacelle is close coupled to the forward lower surface of a modern advanced wing.

Civil testing at ARA has included development and installed tests using blown nacelle simulators as well as TPS simulators and from this experience it is clear that the control of air supply stability and precision of the data for both simulator types are similarly exacting. To some extent the TPS has an advantage due to the use of linked mass flow accounting methods in the ram drag and gross thrust estimation procedures. Nonetheless both simulators require high precision internal pressure and temperature measurements and accurate calibration facilities. One of the most important points in the blown versus TPS comparison is that in general the blown nacelle requires about three times as much air to be passed through the pylon (or strut) together with all the necessary instrumentation; this considerably enhances the difficulties of pylon (or strut) design.

A disadvantage of the TPS is the tendency for icing which is associated with large temperature drops across the turbine. This aspect is discussed further in section 9 below, but it suffices to note here that this problem has been adequately eliminated using current practices at ARA, whilst avoiding the additional problems that would occur with the use of heated turbine drive air.

4. THE PARALLEL MODEL AND FULL SCALE ACCOUNTING SYSTEM

In simple terms the full scale engine is run on a ground based altitude test facility (ATF) capable of supplying the engine face with air at representative ram total pressure and permitting the nozzles to exhaust into representative ambient pressure. For the real engine, non-dimensional gross thrust and mass flow coefficients are uniquely obtained in static operation in relation to corrected revs. and internal

pressures and temperatures. In application to the installed flight conditions, the ATF static gross thrust is reduced by the ram drag to give the net thrust of the isolated pod in flight. The effects of a uniform external flow field may be introduced as a refinement at this stage, if test data is available, to modify the fan and primary discharge coefficient with corresponding modifications of the in-flight gross thrust. This estimated "free flight" net thrust is then used in conjunction with airframe and cowl drag estimates and installation drag factors to estimate the aircraft performance.

This paper describes current ARA methods in the determination of these installation drag factors. Hence the natural methodology is to run a parallel accounting system for the full scale and model tests - Fig. 4 - where the unknown in the full state equation is the installation drag, which is determined from wind tunnel measurements of the various model builds of wing/body and wing/body/nacelle and installed thrust estimates.

Hence for the model we measure the gross thrust and discharge coefficients in a calibration frame which reproduces the inlet bellmouth flow conditions at the total pressure of the tunnel and exit ambient static pressures at the nozzle exhaust. By use of the relationship of internal instrumentation in the model engine unit, the "free flight" net thrust may be calculated from the calibration static gross thrust and the ram drag. The difference between the "free flight" net thrust and the tunnel measurement of T - D for the engine/airframe model installation provides a measure of the drag of the engine/airframe full scale installation.

The engine nacelle interference drag may be obtained from the above measurement of the drag of the wing/body/nacelle compared with the drag of the wing/body together with the estimated or measured external drag of the nacelle/pylon.

5. BOOKKEEPING AND ACCURACY

In general the thrust and mass flow accounting systems adopted for the model are, wherever possible, parallel to the full scale nacelle performance accounting procedures as noted above. This includes quantity and placement of instrumentation as well as the definitions of coefficients, as far as is practically possible.

The procedures therefore form a composite structure.

For the model test data it is possible to form three distinct groups of functional relationships; these are:

- A Diagnostic and distortion parameters
- B TPS nacelle performance data
- C TPS nacelle coefficients

In Group A the parameters are devised to provide the characteristics of the basic measurements using such basic variables as local total pressure distortion levels.

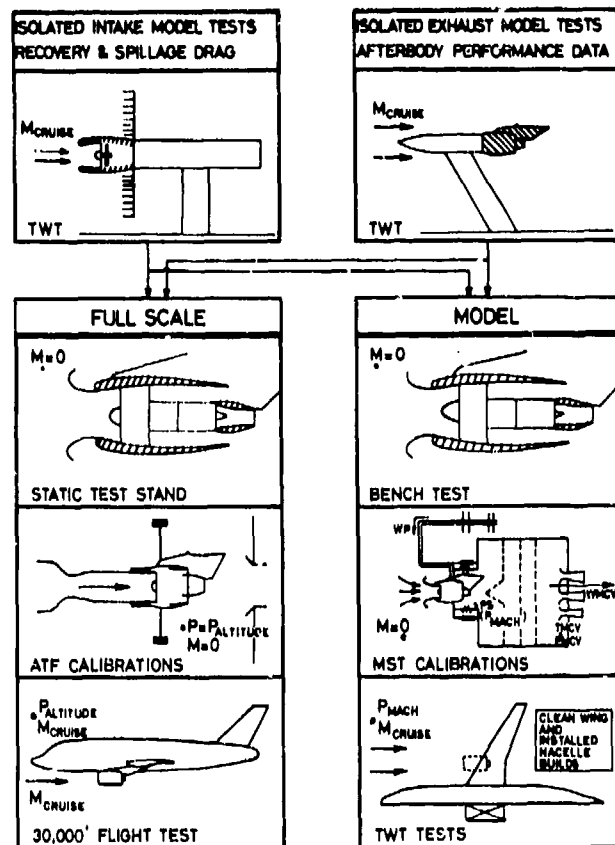


FIG. 4 AIRCRAFT AND MODEL NACELLE INSTALLATION TECHNOLOGY PLAN

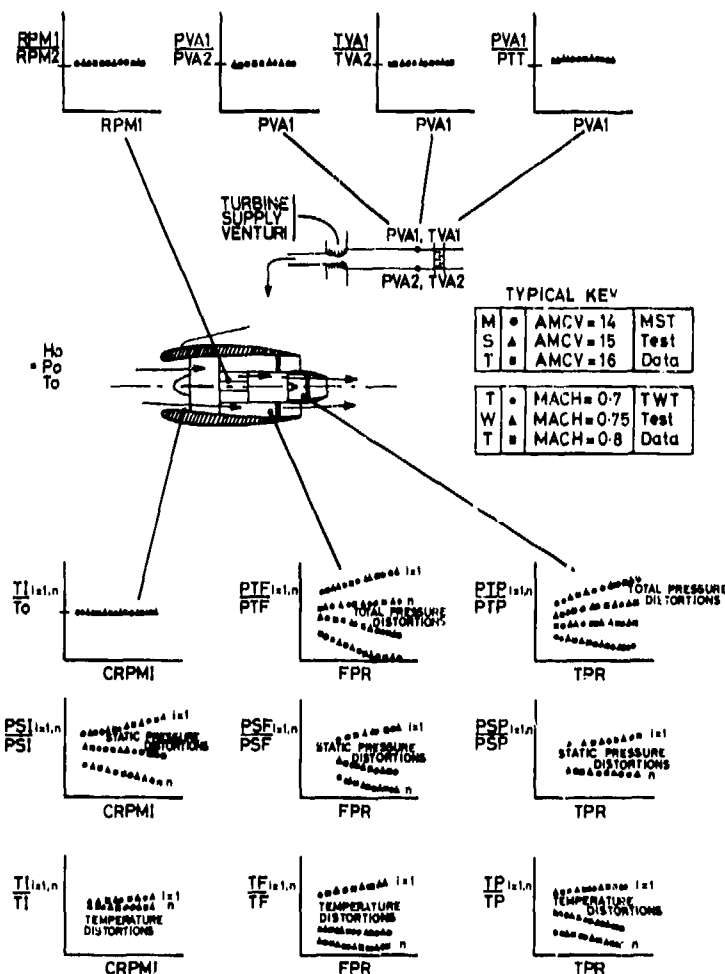


FIG. 5 DIAGNOSTIC AND DISTORTION PARAMETERS

Fig. 5 shows, schematically, the set of plots commonly formed.

In Group B the parameters are for example corrected fan mass flow and fan corrected rotational speed; Fig. 6 shows the sets of relationships commonly formed.

In Group C mass flow and thrust coefficients are developed, for the inlet duct, fan nozzle and primary (turbine) nozzle using in-duct pressure and temperature measurements and derived mass flow and thrust data; Fig. 7 illustrates these parameters and flow zones.

Before addressing the question of what accuracy and repeatability levels are necessary to achieve a given installation drag discrimination level, it is necessary to outline the typical mass flow, thrust and drag accounting procedure. Consider for simplicity, a single TPS nacelle in combination with a half span model.

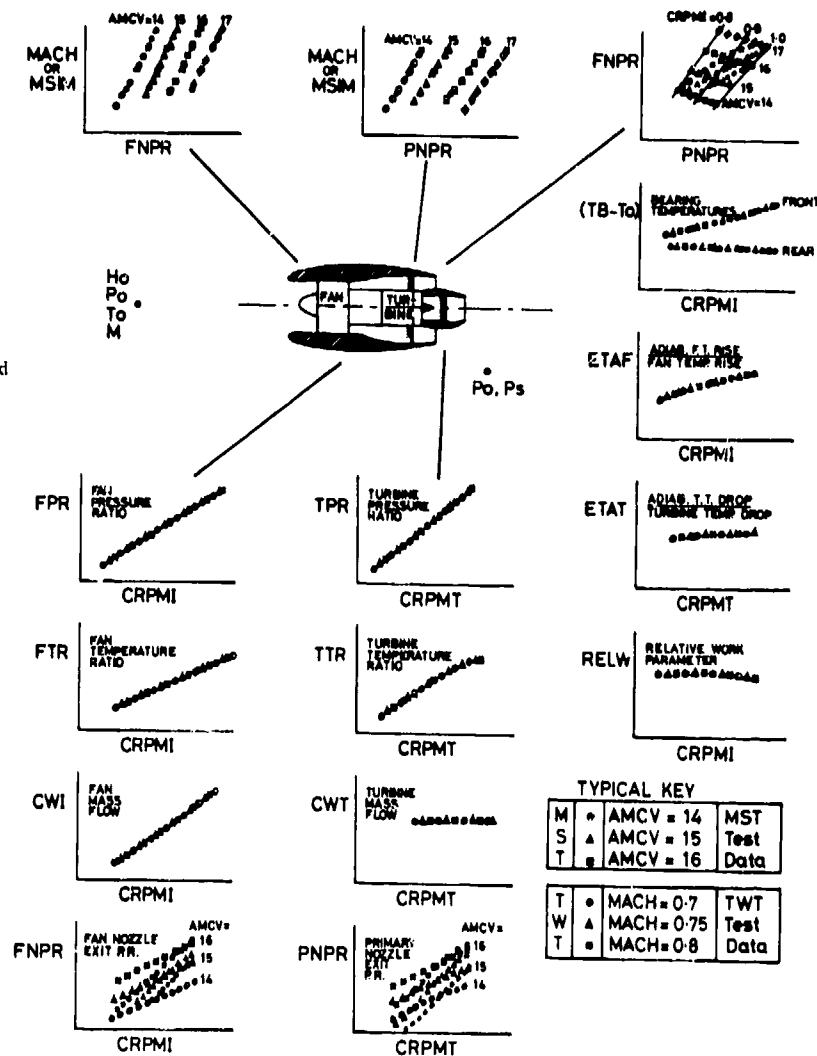


FIG. 6 TPS NACELLE PERFORMANCE DATA

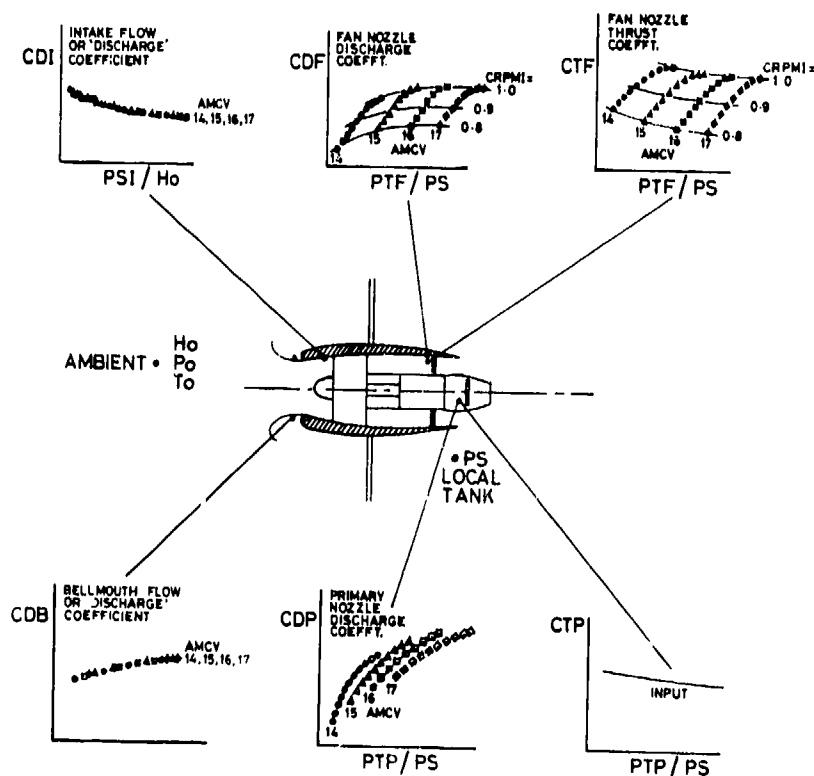
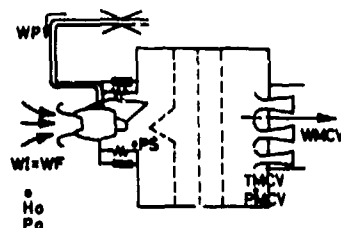


FIG. 7 TPS NACELLE THRUST AND DISCHARGE COEFFICIENTS



M

S

T

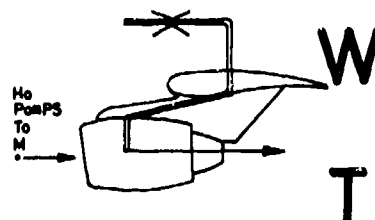
MEASURE OR DEFINE

COMPUTE

PVA, TVA, AVA		WV	HP VENTURI MASS FLOW
PMCV, TMCV, AMCV		WMCV	TOTAL TANK MASS FLOW
WFAN = WMCV - WV		WFAN	FAN NOZZLE MASS FLOW
TI, Ho, PSI, AI	WI = WFAN	CDI	INTAKE 'DISCHARGE' COEFFICIENT
WI, TI, H	$CWI = \frac{WI}{\sqrt{\theta_1}}$	CWI	CORRECTED FAN MASS FLOW
RPM, TI	$CRPMI = \frac{RPM}{\sqrt{\theta_1}}$	CRPMI	CORRECTED FAN SPEED
PTP, TP, AP, PS	WP = WV	CDP	PRIMARY NOZZLE DISCHARGE COEFFT.
$XGP = f(PTP, PS) * WP \sqrt{TP} * \boxed{CTP}$		XGP	PRIMARY NOZZLE GROSS THRUST
$XGF = XBAL - XGP$		XGF	FAN NOZZLE GROSS THRUST
PTF, TF, AF, PS, WFAN		CDF	FAN NOZZLE DISCHARGE COEFFT.
$CTF = XGF / (f(PTF/PS) * WF \sqrt{TF})$		CTF	FAN NOZZLE THRUST COEFFT.

Calibration Coefficients
From MST Boxed Thus
CTF

T



W

T

PVA, TVA, AVA		WV	HP VENTURI MASS FLOW
PTP, TP, PS, AP		CDP	PRIMARY NOZZLE DISCHARGE COEFFT.
$XGP = f(PTP, PS) * WP \sqrt{TP} * \boxed{CTP}$		XGP	PRIMARY NOZZLE GROSS THRUST
RPM, TI	$CRPMI = \frac{RPM}{\sqrt{\theta_1}}$	CRPMI	CORRECTED FAN SPEED
$\boxed{CWI} = f(CRPMI)$		CWI	CORRECTED FAN MASS FLOW
$WI1 = CWI * \frac{\delta_1}{\sqrt{\theta_1}}$		WI1	FAN MASS FLOW
TI, Ho, PSI, AI, CDI		WI2	INTAKE MASS FLOW
PTF, TF, AF, PS, CDF		WFAN	FAN NOZZLE MASS FLOW
$XGF = f(PTF/PS) * \boxed{CTF} * WF \sqrt{TF}$		XGF	FAN NOZZLE GROSS THRUST
$DRAM = WF * M * \sqrt{\gamma RT}$		DRAM	RAM DRAG
AF, NF			FORCE BALANCE AF, NF AXIAL AND NORMAL FORCES
$DRAG = \sum_{VECTOR} [DRAM, AF, NF, XGF, XGP]$			MODEL DRAG
$LIFT = \sum_{VECTOR} [AF, NF, XGF, XGP]$			MODEL LIFT
$C_D = \frac{DRAG}{0.7 \rho S M^2}, C_L = \frac{LIFT}{0.7 \rho S M^2}$		C_D, C_L	MODEL DRAG AND LIFT COEFFICIENT

FIG. 8 MST AND TWT MASS FLOW, THRUST AND DRAG ACCOUNTING PROCESS

Fig. 8 shows schematically the essentials of the MST calibration and TWT (in-tunnel) bookkeeping process. In the case of the isolated nacelle tests in the TWT the process is similar except for the computation of normal force and lift.

In the MST calibration phase of testing as in the TWT phases the above-noted groups A and B of parameters are systematically plotted, examined, and compared. The calibration phase essentially yields a set of nozzle coefficients which represent the characteristics of the nozzle and instrumentation combination. For example, the coefficients will vary as the instrumentation set is varied and for this reason it is essential that the MST and TWT instrumentation standards are identical. Particular emphasis is placed on linked methodology in the TWT phase where ram drag and fan gross thrust terms are computed using an identical mass flow term. It is accepted that leakage of turbine air along the TPS shaft can influence this accounting but currently, in the absence of more specific information, compatibility of test conditions in the MST and TWT is accepted as a solution to the problem. It will be noted also that multiple methods are used to estimate the value of the fan nozzle mass flow rate:

this emphasis is well placed since gross fan thrust levels are typically twice the magnitude of the aircraft model drag and one hundred times the magnitude of the installation drag increments for which we are looking. In practice, drag data is estimated by up to six composite methods in which the principal alternative variable is the fan nozzle mass flow rate; comparisons of the resulting drag data and of increments between builds generated using these alternative methods prove to be most valuable.

The fundamental question is - what size of increment in nacelle installation or interference drag do we wish to discriminate. For civil work the answer must be something of the order of 1 to 2 drag counts where this increment is one half to one percent of aircraft drag. In general, a simple, apparently quite rigorous pre-test error analysis will show that we will be unable to discriminate differences of the order of 1 to 2 counts due to predicted data scatter. However, a fully rigorous statistical/engineering error analysis will show that when all relevant bias (fixed) and repeatability (random) errors are accounted, together with the enhancement of precision due to multiple measurements (samples) it is likely that statistically-significant measurements of this order (1 to 2 counts difference) will be achieved on increments. The full statistical analysis has not been done because this has been rendered academic by the wind tunnel experimental evidence. This evidence shows that from point to point the final drag data exhibits repeatability to well within one half of a drag count and that from drag polar to polar the repeatability is better than ± 0.6 drag counts. A reliable value for build to build repeatability is not available due to the considerable expense of deliberately rebuilding and testing a datum model build a statistically significant number of times. In all of the above, the confidence level has been quite deliberately left out; this is because the precise form of the true drag curves cannot be adequately defined.

The above remarks have also dwelt on the incremental drag type of exercise wherein a given set of MST nozzle coefficients are used for all TWT model builds. The related question of absolute drag accuracies and drag differences between installed nacelle models fitted with varying nozzle systems are more complex and equally prone to the pessimistic answer from a statistical error analysis. In a recent example the MST calibration data was examined using statistical means; four builds of model were considered and in all cases the fan parameters CDF, CTF and their product exhibited a spread (random) of less than $\pm 0.2\%$ at a 2σ or 95% confidence level. Perpetuation of these levels of calibration accuracy into the TWT test indicates that, without regard to the random TWT elements of accuracy, differences between builds of less than 0.8 drag counts would be insignificant; a typical practical level of random TWT error leads to the deduction that for varying nozzle systems, differences of less than about 1 drag counts are not likely to be significant at the 95% confidence level. However, such are the economic consequences that lower levels of confidence are frequently accepted when under all other considerations the designs have equal merit. Also, in practice, MST repeatability levels of $\pm 0.1\%$ are frequently (but not always) achieved.

6. CALIBRATION METHODS AND TEST DATA

The tests in the Mach Simulation Tank (MST) are conducted to determine nozzle coefficients in the presence of a quiescent exhaust environment but under conditions which match model internal pressures to those of the transonic wind tunnel (TWT).

Test conditions are created to simulate TWT Mach number, so far as the nacelle internal duct flows are concerned, by setting up an appropriate pressure difference between the model inlet and exhaust environments. Use of ambient atmospheric pressure upstream of the TPS nacelle creates engine face conditions corresponding to ARA TWT ram total pressure levels whilst pressures in the vicinity of the nozzles are selected to correspond with ARA TWT free stream static pressures at the required simulated Mach number, see Fig. 9.

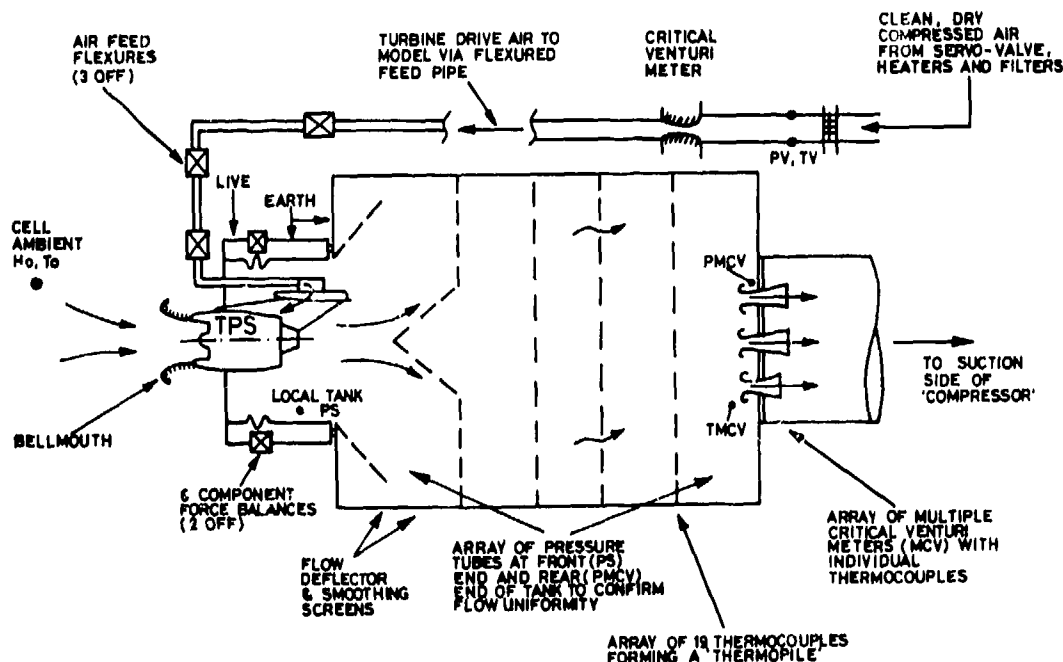


FIG. 9 BASIC ELEMENTS OF MACH SIMULATION TANK

Tank internal pressure conditions are controlled by selection of appropriate tank exit areas AMCV which are related to the total model nozzle area, for a given TPS unit. In order to optimise the precision of the MST exit mass flow measurements, the critical venturi meter concept has been adopted (Ref. 2). The required simulated Mach numbers of the exhaust environment are achieved by the selection of the appropriate critical venturis from a binary range of venturi areas. The relationships between simulated Mach number, model nozzle area and TPS unit rpm are readily obtained from the following equations which are approximately valid for fully choked nozzle conditions.

$$\left| \frac{PT_{NOZZLE}}{PS_{TANK}} \right| = \left| \frac{A_{MCV}}{A_{NOZZLE}} \right| \quad \text{since } (W\sqrt{T})_{TANK} = (W\sqrt{T})_{NOZZLE}$$

$$\left| \frac{PT_{NOZZLE}}{HO_{AMBIENT}} \right| = f \left| \frac{RPM}{CORRECTED} \right| \quad M_{SIMULATED} = f \left| \frac{HO_{AMBIENT}}{PS_{TANK}} \right|$$

In the above relationships the terms PT_{NOZZLE} and A_{NOZZLE} refer roughly to a combined fan and turbine exhaust and with real fan and turbine nozzles the relationships give only an approximate guide to the conditions; in practice more precise relationships and past experience are used to predict the required AMCV values.

Thrust measurements are made by means of a symmetrically placed pair of force balances as shown in Fig. 9; considerable care is given to the calibration of these balances and the various pressure tares which arise due to the high pressure air feed and tank depression. Calibration of the forces and pressure tares are systematically carried out for each model test series.

Fig. 10 shows typical MST operating conditions for a representative TPS nacelle model; the range and numbers of test points are typical of many such tests.

In practice, as evident from Fig. 10 and the above relationships, having selected the value of AMCV for a given test run the levels of simulated Mach number are achieved directly by variation of TPS unit RPM. Conditions in the duct downstream of the tank exit MCV array are maintained at a suitably low level of static pressure, typically 3 psia, to ensure fully choked flow through the venturis.

A venturi meter is used in the high pressure feed line for the measurement of turbine drive air mass flow rate.

In order that the MST facility should have demonstrable accuracy, a periodic practice of testing a set of reference nozzles has been adopted. The results have shown that mass flows from the high pressure venturi meter and tank exit venturis generally match to better than +0.2% whilst the thrust measuring system has been shown to match predicted reference nozzle thrust data also to within +0.2%, (Ref.3).

Characteristic sets of nozzle coefficients from a recent MST test series are shown in Fig. 11; the numbers of points and range of conditions shown are quite typical; in particular, it is policy, whenever practical, to run calibrations both before and after TWT tests. This procedure provides both improved confidence levels and essential continuity of the TPS/nacelle performance evaluations. No serious problems of TPS performance variation have hitherto been encountered.

The coefficients show a clear trend with TPS unit RPM: this arises due to the variations in the sampling of nozzle upstream total pressures and temperatures and is consequent upon the finite set of measuring stations allied to the development of the duct distortion map as a function of unit RPM. The current ARA view is that at a fixed value of FNPR the apparent nozzle coefficients will vary with fan corrected speed and that the magnitude of this variation will depend upon the size of the data sample (numbers of pitots and thermocouples).

The relationships between the means of the measured duct total pressures and temperatures and the apparent 'true' mean values can be identified and evaluated. The procedure involves selection of reference values of fan corrected speed and associated reference sets of nozzle discharge and thrust coefficients (CDF, CTF). It has been shown that the ratios of indicated-to-true total pressures and temperatures can be derived directly from the indicated nozzle coefficients CDF and CTF (Ref. 4).

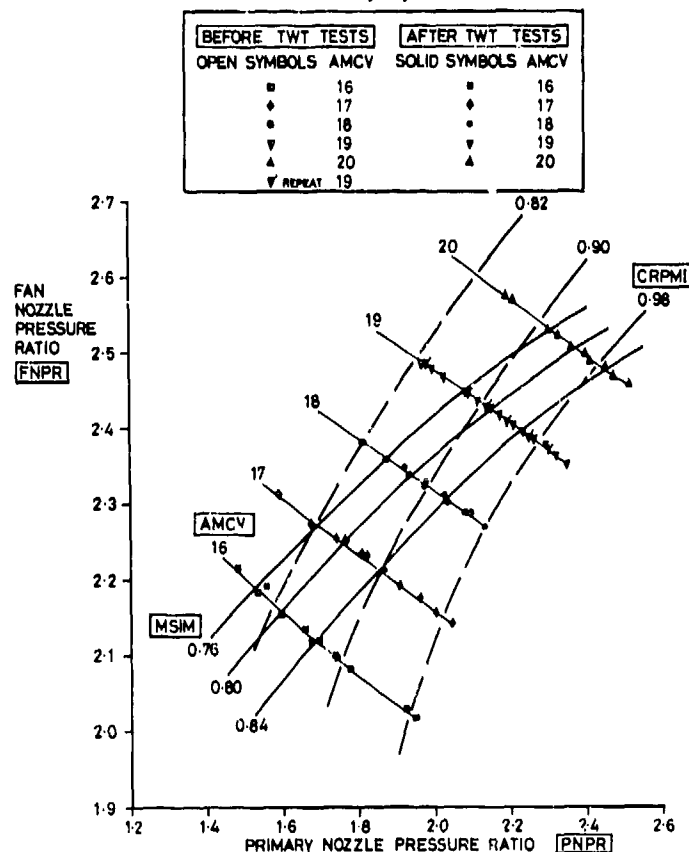


FIG. 10 TPS CHARACTERISTICS FROM MST CALIBRATIONS

It should also be noted that this concept is not new, as evidenced by the work of Kimzey (Ref.5) and Decher (Ref.6).

7. ISOLATED NACELLE TESTS

A number of technical advantages can be claimed for a test plan which includes TWT testing of an isolated nacelle mounted on a strut as shown together with typical drag data in Fig.12.

There are two independent reasons for utilising isolated nacelle tests:

A. For pylon/nacelle calibration purposes as an alternative to MST devised nozzle coefficients. This technique uses nacelle/pylon thrust minus drag measurements on the strut to determine $T - D$ of the nacelle and pylon operating at the correct nozzle pressure ratio in the presence of the correct external stream M_∞ . These measurements in conjunction with theoretical estimates of external pylon and nacelle drag and fan mass flow from calibrated inlet statics (a weak link of this method) and turbine mass flow from a feed line venturi provide thrust and discharge coefficients for the fan and primary nozzles. These coefficients are in principle different from those obtained in a MST calibration due to the effects, if any, of external stream suppression. The primary thrust and mass flow are consistently accounted throughout.

The coefficients, when used for the TWT wing/body nacelle tests, provide the "true" installed net thrust of the nacelle, which when combined with the estimated external drag of pylon and nacelle (via the same method as used in deriving nozzle coefficients) and measured wing drag, yields the aerodynamic drag interference of the installation.

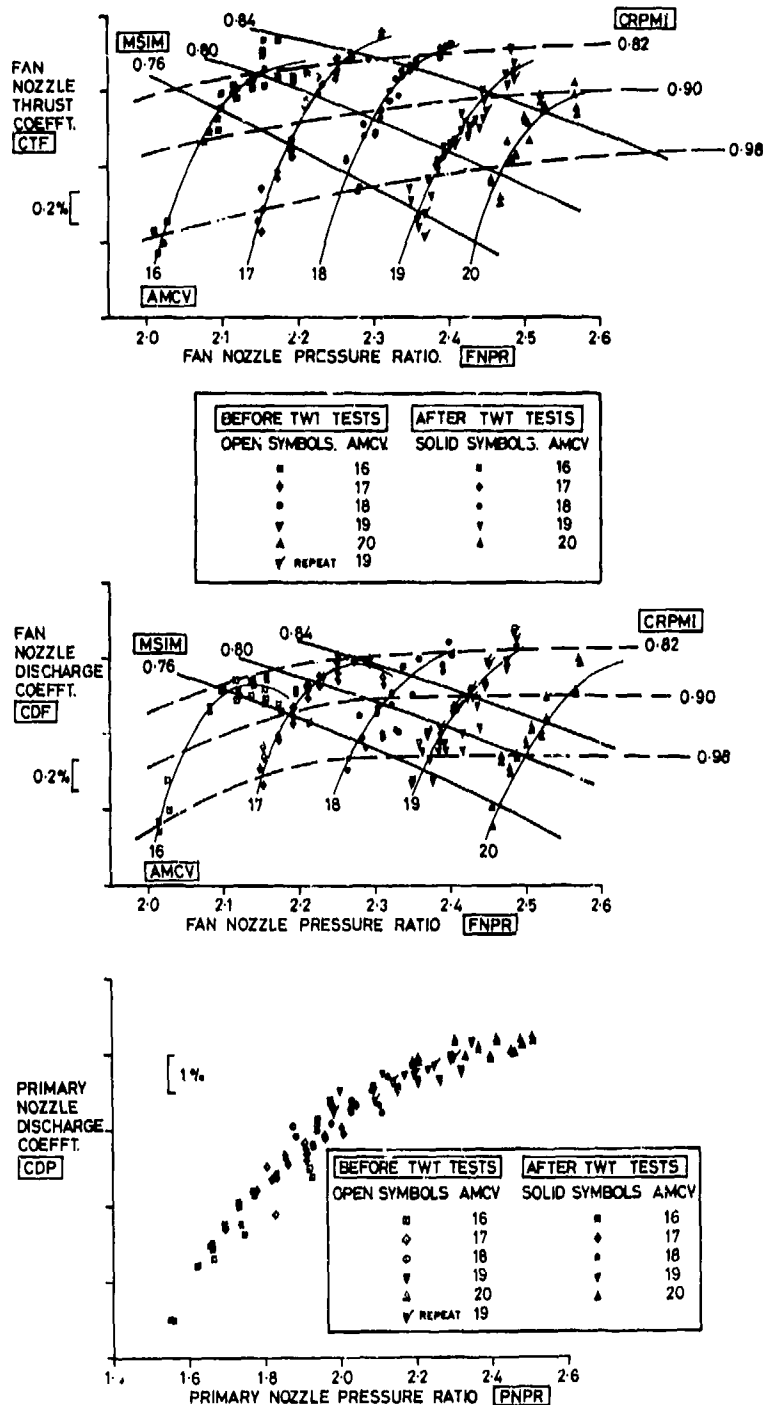


FIG. 11 TPS COEFFICIENTS FROM MST CALIBRATIONS

$$(T - D)_{\text{Nacelle/pylon/strut}} - D_{\text{Strut}} \rightarrow (T - D)_{\text{Nacelle/pylon}} \text{ measured}$$

$$\text{then } (T - D)_{\text{Nacelle/pylon}} - D_{\text{Nacelle/pylon}} \text{ estimated } D_{\text{Ram}}$$

$$+ T_{\text{Nacelle}} \rightarrow C_{\text{Thrust fan}} \cdot C_{\text{Disch fan}}$$

Then using these $C_{\text{Thrust fan}}$ and $C_{\text{Disch fan}}$ coefficients in TWT wing/body/nacelle tests at M_∞

$$C_{\text{Thrust}} \cdot C_{\text{Disch}} \rightarrow T_{\text{Gross}} \cdot D_{\text{Ram}} \rightarrow T_{\text{Net}}$$

$$\text{and } (T - D)_{\text{Wing/nacelle/pylon}} - D_{\text{Wing}} \rightarrow \Delta D_{\text{Nacelle/pylon installation}}$$

$$\text{and } T_{\text{Net}} - D_{\text{Nacelle/pylon}} \text{ estimated } \rightarrow (T - D)_{\text{Nacelle/pylon}}$$

$$(T - D)_{\text{Wing/nacelle/pylon}} - D_{\text{Wing}} - (T - D)_{\text{Nacelle/pylon}} \rightarrow \Delta D_{\text{Nacelle/pylon interference}}$$

B. For installation drag increments utilising the MST static calibration coefficients. This method uses thrust minus drag measurements on the strut in conjunction with static calibration values of C_{Thrust} and C_{Dis} to obtain the external drag of the nacelle and pylon. This makes the assumption of no external flow suppression effects on the nozzle coefficients, or alternatively that such effects are accounted in the derived external drag of the nacelle and pylon. Hence this method also provides the aerodynamic interference increment or an installation drag increment as above, but with any external flow suppression effects included in the interference term viz.

$$(T - D)_{Nacelle/pylon/strut} - D_{Strut} = (T - D)_{Nacelle/pylon}$$

Then using $C_{Thrust\ fan}$ and $C_{Disch\ fan}$ coefficients from MST and consistent primary accounting

$$C_{Thrust}, C_{Disch} \rightarrow T_{Gross}, D_{Kam} \rightarrow T_{Net}$$

$$\text{then } (T - D)_{Nacelle/pylon} = T_{Net} - D_{Nacelle/pylon}$$

and from TWT wing/body/nacelle tests

$$(T - D)_{Wing/nacelle/pylon} - D_{wing} = D_{Nacelle/pylon} - T_{Net}(\text{from MST coefficients})$$

$\rightarrow \Delta D_{Nacelle/pylon}$, interference including external stream suppression on nozzle thrust.

An example of the isolated nacelle drag data is shown in Fig. 12; it is clear that good repeatability of the measurements can be obtained. It is also clear that testing of the isolated nacelle permits evaluation of the mass flow, thrust and drag accounting process under more favourable and predictable circumstances than the installed tests permit. As a result of this important facet of these tests, together with considerations relating to the presence or otherwise of free stream suppression of a nozzle flow, it is currently recommended that this isolated TWT test phase be included whenever a comprehensive technology package is believed to be necessary.

8. INSTALLED NACELLE TESTS

In the installed nacelle/pylon TWT test phase largely conventional test conditions and procedures are adopted. In the planning stages it will have been decided whether the wing/fuselage would be represented by a full span or half span model. In either case the objective of the powered installed test phase will have been clearly identified. In many cases where the aircraft is new it will have been decided that an associated unpowered full span test series is used as a link into the aircraft drag accounting scheme and that the powered tests are to provide a drag increment due to the presence of power and of representative nacelle/pylon exhaust systems; that is, that the powered installed tests provide ΔC_D data due to the difference between through-flow nacelles (TFN) and TPS nacelles. Many alternative approaches are possible, however, and the installed TWT tests may be aimed at determination of either interference drag or installed drag, or both, as described in 7.

An alternative and technically sound approach may on occasion be adopted. This is when a 'flying baseline' build is included in the installed TWT test plan; this approach sets out only to define the differences between candidate configurations of wing/pylon/nacelle and a 'flying baseline' representing a design having known full scale flight performance standards.

Whatever the precise objectives of the installed TWT test phase, and frequently many of the above approaches are combined in the same test entry, there are many common facets to the test techniques.

In a number of recent typical test programmes, the actual build-to-build test sequence has become quite routine; it will enhance the value of this note to describe this routine.

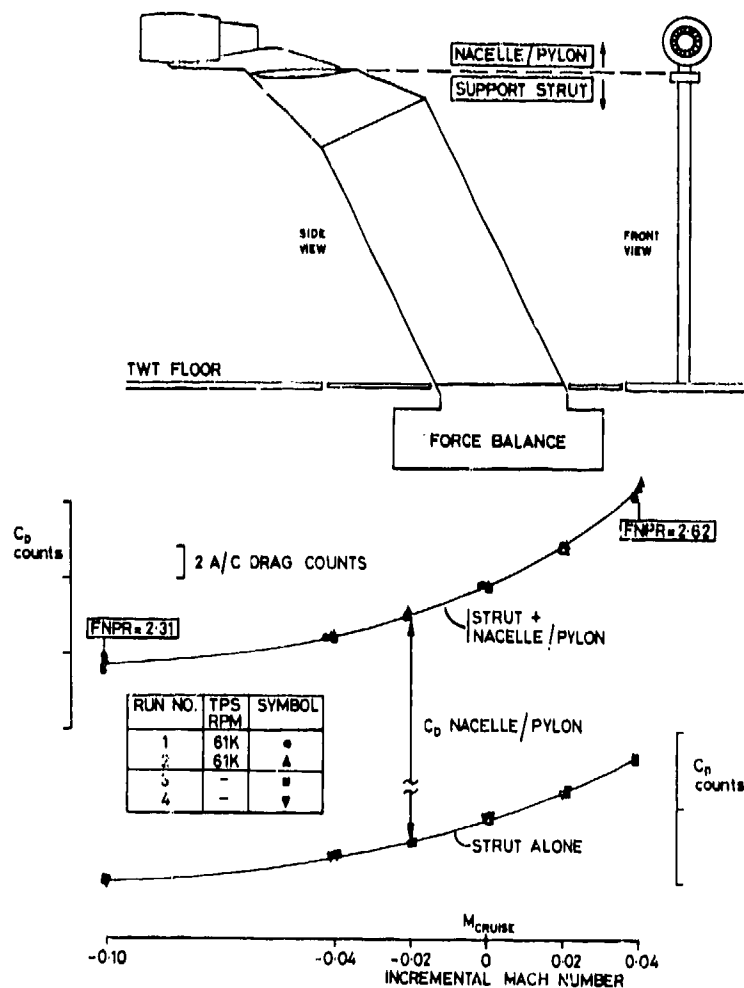


FIG. 12 ISOLATED NACELLE DRAG DATA

- (a) Following on from the usual model and instrumentation checks, a limited set of tests are performed to confirm the effectiveness of the wing transition fixing; the conditions of these tests are selected to encompass the C_L , M conditions within the cruise test envelope. In general, a forward fix at 5% is adopted on both wing surfaces to provide a consistent wing boundary layer flow throughout the nacelle test series. An aft fix for the upper surface might well be more appropriate for the high M cruise C_L design point, but it is possible that measured changes may be incorrectly attributed to nacelle/pylon installation modifications, whereas the changes are more likely to be due to alterations in the upper surface boundary layer transition position with consequent upper surface shock movement. If in fact nacelle/pylon modifications do affect the upper surface shock position at full scale conditions, then the whole test technique becomes much more complex - but probably soluble. Nacelle and pylon transition fixing bands are less easily summarised here.
- (b) Cruise drag tests are conducted in up to three distinct types of traverse; available traverses are
- (i) fixed Mach and TPS rpm and vary model incidence to produce a set of drag polars covering the required cruise lift, M and fan nozzle pressure ratio conditions;
 - (ii) fixed TPS rpm and model incidence and vary Mach number to produce Mach sweep drag data at discrete lift conditions;
 - (iii) fixed Mach and model incidence and vary TPS unit rpm to produce Power Sweep drag data at discrete lift conditions.

Whilst the resulting body of data can provide a valuable network, the most powerful and economic test approach is that of obtaining drag polars; in the ARA TWT incidence variations can be effected rapidly making high rates of data collection possible such that in a recent powered half span model test series, greater than 20 model builds were tested in a 9 day period and over 300 drag polars were obtained. Incidence increments are usually kept down to 0.3° within the cruise envelope and a typical polar contains about 10 to 12 test points. All test points or scans include force and pressure data and in the above tests, 13 scanivalves were used yielding 100 nacelle and pylon pressures and over 300 wing pressures in addition to the force and thermocouple data; in all, over 2 million items of pressure and force data were systematically obtained as well as a total of about 20 surface oil flow studies.

In practical terms, it is found to be most advisable to limit any given tunnel run to about 10 drag polars since the economics dictate that quite regular model inspections are performed to avoid unnecessary repetition of test data in the event of a faulty model build occurring during any given run. A systematic practice of repeating 2 of the key drag polars is also adopted for each build; when test series span more than a day or two it is customary to repeat the datum case such that datum build tests are conducted near to the start and end of the test entry. A typical half span model in the transonic wind tunnel is shown in Fig. 13.

A small selection of typical drag polars and installation drag data are shown in Fig. 14. It should be noted here that the drag levels for a given model build and test condition are usually evaluated at given specific values of lift coefficient. In the case of the half span model it is important that the drag levels are related at equivalent full span lift coefficients. As a rule, a C_L correspondence plot via α is established giving full span or aircraft C_L versus indicated half span C_L ; this is especially necessary when testing with non-metric fuselages but must also be done for metric fuselage comparisons since fuselage-carrying lift is invariably inappropriate due to the floor boundary layer effects. Correspondence conditions are usually established by reference not only to the incidence angle but also to the local

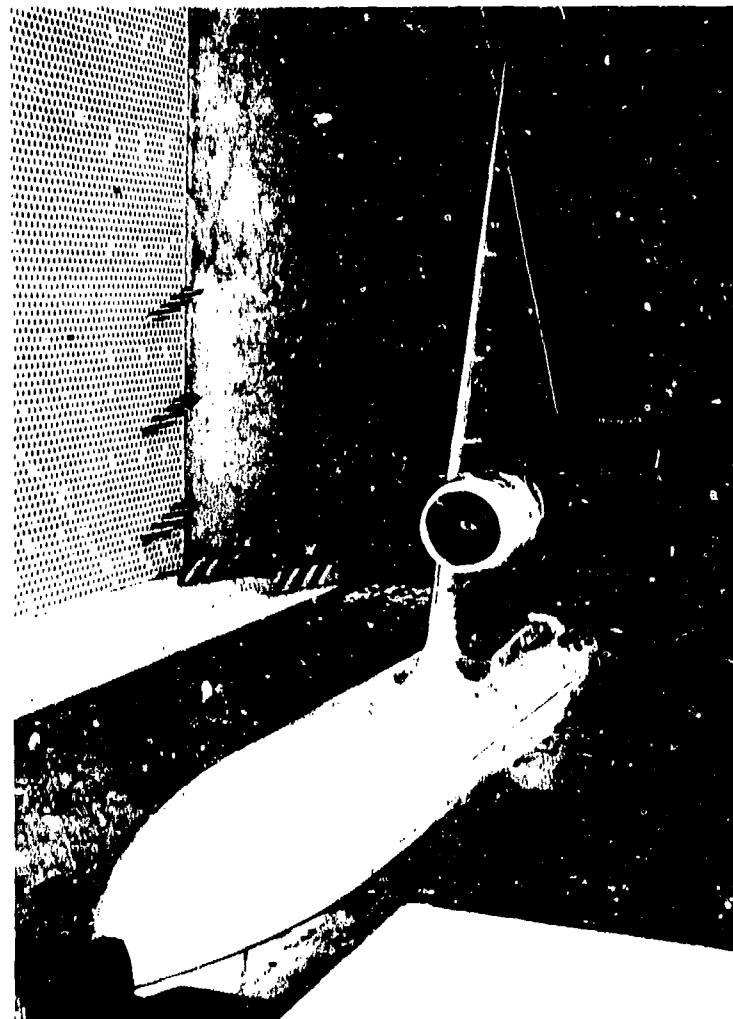


FIG. 13 TYPICAL HALF MODEL HARDWARE

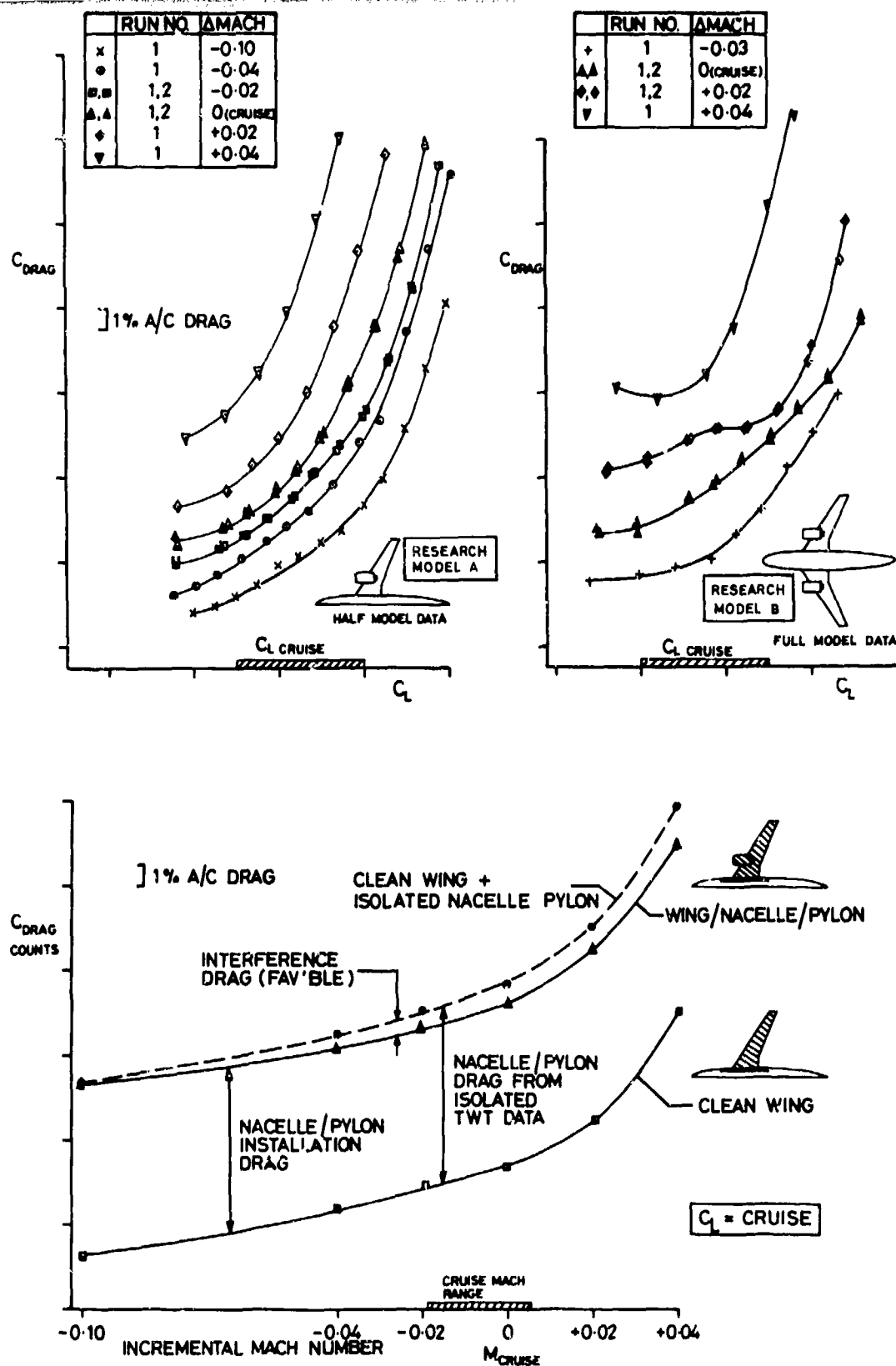


FIG. 14 TYPICAL MODEL DRAG DATA AND REPEATABILITY

aerodynamic conditions in the flow over the lifting surfaces, i.e. surface pressure distributions.

The data shown in Fig. 14 illustrates one or two important aspects of test technique; these are that when looking for small drag differences it is very important to systematically establish and confirm repeatability levels on all builds and that test conditions should be both tightly packed within the cruise flight envelope but also should cover significantly more than the confines of the cruise

envelope as significant aerodynamic interference features frequently materialise near to the edges of the cruise envelope and may be much more readily identified in the extended regions of the test envelope.

The data repeatability in evidence in Fig. 14 is quite typical and it is clear that repeat runs show a spread within +1 drag count. It is relevant to note that the drag data plotted has been computed using force balance measurements of about -300 drag counts, ram drag values of about 250 drag counts and total (fan + primary) gross thrust levels of about 600 drag counts. In the presence of these substantial vectors it is both remarkable and gratifying to achieve the illustrated levels of repeatability of the final drag data.

It is also important that the repeatability levels both from test run to test run as well as from build to build are established.

9. INSTRUMENTATION METHODS, MODEL DESIGN AND POWER CONTROL.

The related problems of numbers and disposition of the nacelle instrumentation is an aspect which appears to lead to nearly as many differing solutions as there are engineers involved; on the one hand it is clear that an extremely large number of measurements is necessary in any given duct in order that the mean value of the measurements will closely approximate the true mean; on the other hand it is equally true that, provided we are dealing with absolutely stable and repeatable duct flows, calibrated for a given fan pressure ratio, it should only be necessary to use a single, well-placed pitot and thermocouple in each duct. However, the real test situation requires that a compromise be struck between these two extremes. Firstly, it is not necessary that the mean of the measurements should be close to the true mean; it is necessary only that the ratio of the mean of the measurements to the true mean shall remain invariant, through all test phases at a given test condition, say corrected rpm. Secondly, to rely on a single measurement in each duct would be extremely hazardous, with the liability of oil contamination or partial leakage or blockage; equally if the nozzle were not fully choked then mass flow variations could go undetected by a single pitot. So in general a reasonably large number of instruments is used in each duct of the simulator to provide an economical sample which will give a reasonable representation of the true mean flow and minimise the technical risk of the loss of some instruments.

The ultimate selection of the internal instrumentation set installed, is primarily defined by the model design office having due regard to the space available; the selected set generally includes intake duct statics and thermocouples, fan duct pitots, statics and thermocouples and primary (turbine) duct pitots and thermocouples - the numbers vary from programme to programme but the key numbers do not differ widely, for example - current practice seems to suggest somewhere between 12 and 30 fan duct pitots, between 7 and 12 primary duct pitots, usually fewer thermocouples and between 4 and 6 intake duct statics. Using this instrumentation and the various weighting and averaging methods previously described, it is practical to assess the mass flow and thrust levels in the various test phases.

It is worth noting that the practice of using pneumatically ganged sets of pitots is not recommended in our view, in this context of TPS cruise drag tests. It is suggested that by reducing the number of readout measurements higher rates of data taking can be achieved but in the present context it would appear to be unwise since the slightest ingress of oil into a ganged set of pitot tubes (which it must be accepted can occur with TPS) could unbalance the pneumatics of the ganged arrangement and could cause an error source in the duct pressures which would be very difficult to trace at the time of the tests. It is therefore considered to be unwise and unjustified to reduce the number of critical internal pressures whilst less important external pressures are recorded. A multi scanivalve system is more than adequate to cope with the total number of pressures, and the only penalty of scanivalve recording is a scan time of 5 seconds as compared to about 2 to 3 seconds, with the corresponding extra blowing time.

The design of the model wing, pylon and nacelle hardware poses many special problems, not least of which are the provision of adequate space for instrumentation and air feed ducts to the TPS as noted above. Further important design aspects include the need for the cowl set and wing/pylon/nacelle assemblies to be free from flow leak paths. As a rule the final sealed nacelle assemblies are subjected to rigorous leak check tests at their maximum operating pressure, whilst all high pressure components and assemblies are subjected to appropriate safety checks at twice the expected pressure levels.

Experience shows that cowl and pylon designs in which the number of components and associated leak paths have been minimised are most successful.

A particular feature of note on the cowl design is that of the tendency for ice formation due to the very low turbine exhaust temperatures; these can be as low as 160°K. The use of an epoxy based fibre or glass cloth laminate material (TUPNOL) for the core cowl components has been shown to give adequate resistance to the heat flows and has thus reduced icing of the core cowl to acceptably minimal levels.

The pressurised oil systems for the TPS bearing feed requires special consideration; system design must be conducive to the maintenance of high standards of cleanliness to totally eliminate contamination and debris; here again the rule is to minimise numbers of components and maximise skill and awareness in the assembly area.

In order that high precision drag data be obtained, it is necessary that a servo-controlled compressed air supply system be used. The dual systems currently in use at ARA provide precision control of TPS unit rpm to better than +0.1%. Finally, of course the success of the whole experimental system depends upon the balance accuracy, repeatability and discrimination; particularly in the presence of a HP dual air feed system. Again, the possibility of achieving this is much greater with a half-model balance in a controlled environment than with a complete model in the tunnel environment.

REFERENCES

1. A.E. Harris and G.I. Pauley
Simulation techniques for pylon mounted turbo-fan engines
A.R.A. Report 36. Oct. 1975.
2. B.T. Arnberg, C.L. Britton and
W.F. Seide
Discharge coefficient correlations for circular arc venturi
flowmeters at critical (sonic) flow. Journal of Fluids
Engineering. pp.111-123. Trans ASME. June 1974
3. M. Pavitt
Results of reference nozzle thrust tests in the ARA Mach
simulation tank. ARA Memo to be published.
4. A.E. Harris
Bookkeeping procedures for mass flows, thrust and drags on
TPS full span model tests. ARA Internal Memo (unpublished) 1978
5. W.F. Kimzey
Some insights into high by-pass ratio turbo-fan engine nozzle
performance from full scale tests in an altitude test cell.
AIAA 6th Propulsion Specialist Conference. June 1970.
6. R. Decher and D. Tegeler
High accuracy force accounting procedures for turbo powered
simulator testing. AIAA 75-1324. Oct. 1975.

ESTABLISHMENT OF AN EXPERIMENTAL TECHNIQUE TO PROVIDE ACCURATE MEASUREMENT OF
THE INSTALLED DRAG OF CLOSE COUPLED CIVIL NACELLE/AIRFRAME CONFIGURATIONS,
USING A FULL SPAN MODEL WITH TURBINE POWERED ENGINE SIMULATORS

by

G. Pugh
Installation Specialist
Rolls-Royce Limited
Derby DE2 8BJ

A.E. Harris
Senior Aerodynamicist
Aircraft Research Association Limited
Bedford MK41 7PF

SUMMARY

Definition and optimisation of installed thrust/drag is a particularly demanding aspect of civil nacelle installation design and development.

A recent programme has been concerned with model to flight comparisons as a means of validating the calibration and thrust/drag analysis techniques employed in wind tunnel tests. The work was related to a modern wide bodied transport, Lockheed L1011, having high bypass ratio RB 211 turbofan engines with two alternative exhaust system designs. Wind tunnel model representation comprised a full span simulation with underwing mounted turbine powered engine simulators.

Calibration techniques included the use of a Mach Simulation Tank in which concurrent mass flow and thrust calibrations were conducted in a quiescent exhaust environment. Data presented includes nacelle thrust and discharge coefficients, installed drag comparisons and finally model to flight correlations.

NOMENCLATURE AND ABBREVIATIONS

AF	Fan nozzle geometric area
AI	Intake duct reference area
AMCV	Individual throat area of critical venturi in MCV array
AP	Primary nozzle geometric area
AVA	High pressure critical venturi meter throat area
C	Local wing chord
CTP	Estimated primary nozzle thrust coefficient
Ho	Freestream (ambient) total pressure
Mo	Freestream Mach number
m	Mass flow
PMCV	MCV upstream total pressure
Po	Freestream (ambient) static pressure
PS	Static pressure in MST adjacent to exhaust nozzles
PSF	Fan duct static pressure
PSI	Intake duct wall static pressure
PSP	Primary duct static pressure
PTF	Fan duct total pressure
PTP	Primary duct total pressure
PVA	High pressure critical venturi meter upstream total pressure
q	Freestream dynamic pressure
R	Universal gas constant
S	Wing planform area
TI	Intake duct total temperature
TF	Fan duct total temperature
To	Freestream (ambient) total temperature
TMCV	MCV upstream total temperature
TP	Primary duct total temperature
TVA	High pressure critical venturi meter upstream total temperature
Vo	Aircraft velocity
W	Aircraft weight
X	Linear dimension from wing leading edge
XAF	TWT axial balance force
XB	MST force balance reading
XNF	TWT normal balance force
α	Fuselage angle of attack
θ	Nacelle angle relative to fuselage datum
β	Nacelle 'toe-in' angle
γ	Ratio of specific heats
Δ	Increment

DERIVED SYMBOLS

CDF	Fan nozzle discharge coefficient	$= \frac{(m \sqrt{TF})_{\text{measured}}}{(m \sqrt{TF})_{\text{ideal}}}$
CDP	Primary nozzle discharge coefficient	$= \frac{(m \sqrt{TP})_{\text{measured}}}{(m \sqrt{TP})_{\text{ideal}}}$
CDOC	Model drag coefficient corrected for thrust, ram drag and lift induced drag	
CLC	Model lift coefficient corrected for thrust	
Cp	Static pressure coefficient	
CRPMI	Corrected TPS fan speed	$= \frac{(RPM/\sqrt{\theta_I})}{(\text{MAXIMUM RPM})}$
CTF	Fan nozzle thrust coefficient	$= \frac{(XGF/m \sqrt{TF})_{\text{measured}}}{(XGF/m \sqrt{TF})_{\text{ideal}}}$
DRAM	Nacelle ram drag	
W/ δ	Normalised aircraft weight	
XGF	Fan nozzle gross thrust	
XGP	Primary nozzle gross thrust	
θ_I	Temperature ratio, local to sea level standard	$= T_I/288$
δ	Pressure ratio, local to sea level standard	$= P_o/14.7$

ABBREVIATIONS

FNPR	Fan nozzle pressure ratio
MGV	Multiple critical venturi meter
MSIM	Simulated Mach number
MST	Mach simulation tank
RPM	Revolutions per minute
SAR	Specific air range
sfc	Engine specific fuel consumption
TPS	Turbine powered simulator
TWT	Transonic wind tunnel

1. INTRODUCTION

This paper describes work carried out to establish an experimental technique aimed at advancing the state of the art in civil, full span, powered model testing. The test work is related to a wide bodied aircraft with underwing mounted turbofan engines featuring alternative standards of exhaust system design. Validation of the technique employed is by model-to-full scale performance correlation. The wind tunnel model was a 1/25th scale full span sting-mounted simulation fitted with turbine powered nacelle simulators (TPS).

The study was initiated after consideration of the state of the art in the mid-seventies. In particular, it was recognised that whilst half-span model tests using powered simulators were commonplace (Refs.1 and 2), little published evidence was available to demonstrate valid model to flight performance correlations, noting especially the importance of spanwise distributions of lift and wave drag. Furthermore, the then likely advent of noise shielded installation designs featuring close coupled arrangements of wings, nacelles, fuselage and empennage were unlikely to prove suitable vehicles for study using half-span models - hence the emphasis on development of the full span method.

The use of TPS units arises from the requirement to reproduce, as closely as possible, the intake and exhaust effects of the installed turbofan engine, together with interactions between the two. To this end, two Tech Development Model 1079 TPS units were acquired for use in the test programme.

An important early consideration was the availability of comparative full scale data including visibility of engine nacelle and aircraft performance procedures. On the practical side, early consideration was given to the key balance airfeed design problem.

The aim of the study was to develop test and analysis techniques of sufficient accuracy to discriminate drag differences between builds of 1 to 2 drag counts (or $\delta C_D \geq 0.0002$); the one drag count level of accuracy was known to be an ambitious target but provided a clear basis for error estimates as well as setting an exacting design objective.

The precise basis of the technique validation procedure involved comparison of model and aircraft drag values for a Lockheed L1011 TriStar with Rolls-Royce RB 211 powerplants configured with 15° and 11° afterbody systems; these are illustrated in Figure 1.

2. FORCE BALANCE/AIRFEED SYSTEM AND MODEL DESIGN

The full span model was designed to simulate a Lockheed L1011 and to include only the two wing-mounted nacelles, the centre engine, fin and tailplane being area ruled; model scale was set at 1/25 based upon an estimated practical maximum tunnel blockage limit of 1% for tests up to Mach 0.87. The airfeed system was designed to minimise pressure effects and stiffness effects of the air transfer arrangements, especially in the normal and axial force directions; stiffness contributions were kept to less than 2% when compared with the basic balance and pressure tares were, by design, very small. At an early stage it was decided to adopt a conventional six-component balance and literally add on an airfeed system. The eight electro-deposited nickel bellows eventually selected from an optimisation study were arranged in vertical equilateral opposed pairs. The arrangement was designed to be capable of supplying sufficient high pressure air for blown, ejector or turbine powered nacelle simulators. Figure 2 shows a schematic of the full span model including the balance/airfeed system, details of the high pressure air supply metering arrangements and the nacelle instrumentation definition.

An important feature of the air-feed design was that thermal effects arising from temperature differences between the HP air supplies and model hardware should not cause extraneous balance forces to arise. To prove this and to generally develop the bellows/balance system, a mock-up and proving rig were built and certain special in-tunnel preliminary check tests were conducted with fully representative airflow pressure and temperature conditions.

Conventional numerical controlled machinery processes were employed in the manufacture of the various wing, fuselage, pylon and nacelle components; in the case of the wing, a computer enhanced 'flight' wing geometry was derived.

The design and fabrication of the nacelle and pylon for this model proved to be quite difficult. In the presence of the very tight geometric constraints imposed by the need to match full scale external geometry at 1/25 scale the provision of space for instrumentation ways and an airfeed duct through the pylon necessitated special vacuum brazing operations on the pylon hardware; Figure 3 shows the model components. The packaging of scanivalve, air ducts, balance and bellows system inside the model fuselage was a comparatively simple matter. The provision of air ducts, instrumentation ways and pylon fixations at the wing/pylon junction proved to be more difficult from the point of view of stress levels since the lift loads on the outer wing panel had, nonetheless, to be adequately (and permanently) supported.

A particular feature of special interest on the model is the provision of glass based laminate (Tufo1) nacelle

Exhaust systems evaluated on full scale aircraft and wind tunnel model

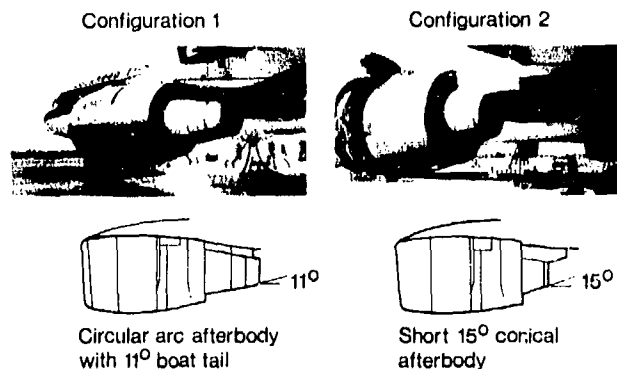
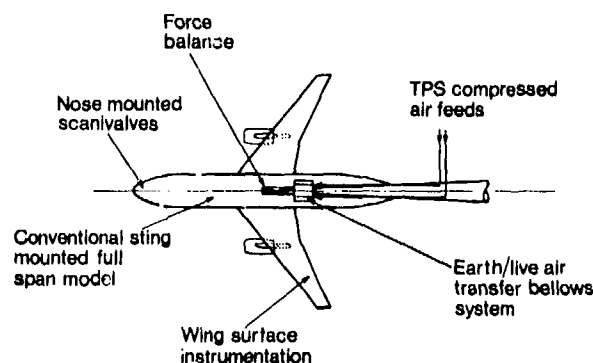
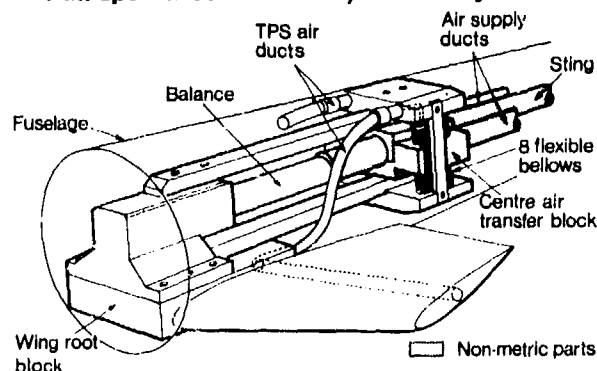


Figure 1

Schematic of full span model



Full span model balance/airfeed system



Nacelle instrumentation

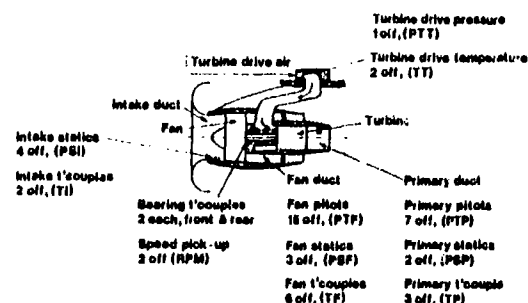


Figure 2

afterbody components. These were designed and developed in order to eliminate the likely formation of ice on the afterbody arising from the very low temperatures developed in the turbine duct exhaust flow. Air temperatures of around 190° Kelvin have been recorded in the primary (turbine exhaust) ducts when using turbine drive air at around ambient temperature. The glass based Tufnol material has proved to be wholly successful in eliminating icing on the afterbody and nozzle trailing edge thicknesses of 0.025 inches have been produced by conventional machining processes.

It should be noted that because of the externally supplied primary (turbine drive) air, the TPS inlet operates at reduced mass flow ratios. Consequently the design of the intake included suitable modification of the forebody cowl and inlet area in order to maintain representative nacelle drag levels whilst the TPS was operating at these lower mass flows.

The complete model assembled in the ARA transonic wind tunnel is shown in Figure 4.

3. MACH SIMULATION TANK THRUST AND MASS FLOW CALIBRATIONS

Details of the ARA Mach Simulation Tank (MST) calibration procedures have been included in the companion paper Reference 3. In this study it was important that a definite and comparable data system was employed on the full scale and model for nacelle thrust and mass flow accounting. For the full scale calibrations an Altitude Test Facility (ATF) is used and the use of the MST provided a strong parallel. In both cases the nacelle internal flow pressures and temperatures were comparable to the 'cruise' test levels, the exhaust pressure ratios were comparable, and both tests were conducted in quiescent exhaust environments. Figure 5 presented here for completeness, shows the 1/25 scale nacelle mounted in the calibration facility; the tank is, in practice, 9 feet in diameter.

Simultaneous measurements of nacelle internal pressures and temperatures, MST total mass flow and high pressure airfeed mass flows, force balances, and tank external and internal conditions lead, by design, to development of a set of nacelle nozzle mass flow and thrust coefficients. In addition, TPS unit performance and nacelle internal flow quality were identified using a composite set of computed variables.

Figure 6 shows typical sets of fan nozzle coefficients for the 15° afterbody system. The discharge and thrust coefficients are clearly shown to depend upon simulated Mach number, or TPS fan rotational speed (rpm), as well as nozzle pressure ratio. This is due to the now well understood 'power effect' which reflects sampling deviations from the true values of duct mean pressure and temperature. These sampling deviations arise due to the use of a finite set of pitots located downstream of the rotating fan which produces variations in the duct

Typical nacelle coating and pylon model components

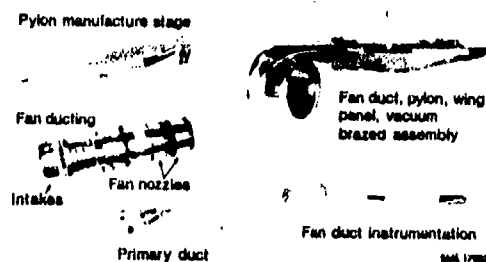


Figure 3

Full span model in transonic wind tunnel

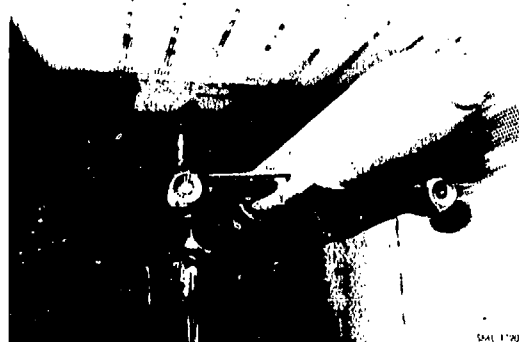


Figure 4

Turbine powered simulator with calibration bellmouth mounted in Mach simulation tank



Figure 5

distortion levels. The sampling errors can be shown to be a function of fan pressure rise at a fixed nozzle pressure ratio, provided the nozzle is 'hard choked'. A more comprehensive discussion of this feature of the data is not necessary here but it is sufficient to note that not only will the observed 'power effects' depend upon the precise definitions of the coefficient involved but will also vary from one TPS unit to another and with the number of instruments used in the fan and primary ducts.

Statistical methods as well as engineering judgement have been used to analyse the calibration data; in general, it can be stated that fan nozzle discharge and thrust coefficients exhibit scatter band widths of less than $\pm 0.2\%$. In addition, mean gross thrust increments measured for the model between the 15° and 11° exhaust configurations compare favourably with full scale engine data.

Typical nozzle coefficient data obtained from Mach simulation tank

Port 15° nacelle

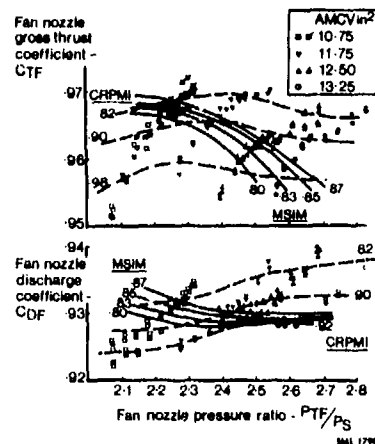


Figure 6

Internal data quality and TPS performance levels are compared with tunnel data in Section 5 below.

4. TRANSONIC WIND TUNNEL THRUST, DRAG, AND MASS FLOW ACCOUNTING

In this particular study a number of alternative methods of thrust drag accounting procedures have been used as recommended in references 4 and 5. Figure 7 gives, in summary form, one typical method which, it will be noted, is based on the use of calculated primary nozzle thrust levels using measured duct total pressures; this particular method closely parallels the procedure used in the full scale analysis. The various methods differ, principally, in the manner in which fan duct mass flow is calculated in the transonic wind tunnel (TWT) test phase; three alternative calculation methods have been used, these are:

- (a) using fan nozzle discharge coefficient, $C_{DF} = f(\text{FNPR}, \text{MSIM})$
- (b) using inlet duct (discharge) flow coefficient, $C_{DI} = f(\text{PSI}/H_0)$
- (c) using fan corrected airflow, $\text{CWI} = f(\text{CRPMI})$

where FNPR = Fan nozzle pressure ratio

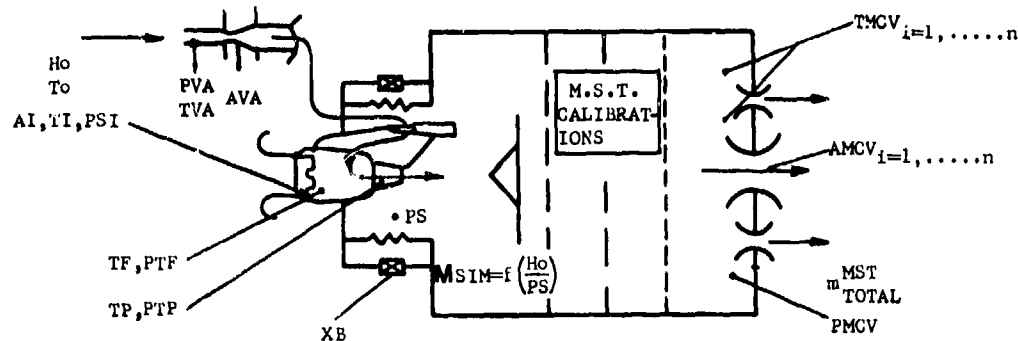
MSIM = Simulated Mach number

PSI = Mean static pressure at intake reference plane

H_0 = Freestream total pressure (TWT) or ambient static pressure (MST)

CRPMI = TPS fan speed corrected to fan upstream conditions

This paper concentrates on the first of the above mentioned methods. In all cases a 'linked method' is employed in which inlet and fan duct mass flows are matched before calculation of the inlet ram drag and nozzle gross thrust terms.



$PVA, TVA, AVA \longrightarrow m_{VENTURI} = m_{PRIMARY} \text{ lb/sec} \longrightarrow$ PRIMARY MASS FLOW RATE
 $PMCV, TMCV, AMCV \longrightarrow m_{MST_TOTAL} \text{ lb/sec} \longrightarrow$ TOTAL TANK MASS FLOW RATE
 $m_{INTAKE} = m_{FAN} = m_{MST_TOTAL} - m_{PRIMARY} \longrightarrow$ FAN AND INTAKE MASS FLOW
 $TO, TI, Ho, PSI, AI, m_{FAN} \longrightarrow GDI = f(Ho/PSI) \longrightarrow$ INTAKE DISCHARGE COEFFICIENT
 $PS, PTF, TF, m_{FAN}, AF \longrightarrow CDF = f(PTF/PS), (\text{and } MSIMULATED) \longrightarrow$ FAN NOZZLE DISCHARGE COEFFICIENT
 $PS, PTP, TP, m_{PRI}, AP \longrightarrow GDP = f(PTP/PS), (\text{and } MSIMULATED) \longrightarrow$ PRIMARY NOZZLE DISCHARGE COEFFICIENT
 $XGP = f(PTP/PS) * CTP * m_{PRI} \sqrt{TP} \longrightarrow$ ESTIMATED PRIMARY SYSTEM GROSS THRUST
 $XGF = XB - XGP - \sum \text{PRESSURE TARES} \longrightarrow$ FAN NOZZLE GROSS THRUST
 $CTF = \frac{(XGF/m \sqrt{T})_{FAN \text{ ACTUAL}}}{(XGF/m \sqrt{T})_{FAN \text{ IDEAL}}} = \frac{(XGF/m_{FAN} \sqrt{TF})}{f(PTF/PS)} \longrightarrow$ FAN NOZZLE THRUST COEFFICIENTS - TO BE USED FOR TWT THRUST CALCULATION

Similar Parameters and Calculations performed for Port and Starboard Nacelle

☐ INDICATES COEFFICIENT FROM OR USED IN MST CALIBRATIONS

☐ $CDF = f(P_{TF}/P_o) (\text{AND } MSIM)$

☐ $CTP = f(PTP/P_o)$

☐ $CTF = f(PTF/P_o), (\text{and } MSIM)$

$PVA, TVA, AVA \longrightarrow m_{PRIMARY}$

PTF, TF, P_o ☐ $CDF \longrightarrow m_{FAN}$

$DRAM = m_{FAN} * Mo \sqrt{SR \cdot To}$

$PTP, TP, m_{PRI}, P_o \longrightarrow GDP (f(PTP/P_o), Mo)$

$XGP =$ ☐ $CTP * m_{PRI} \sqrt{TP} * f(PTP/P_o)$

$XGF =$ ☐ $CTF * m_{FAN} \sqrt{TF} * f(PTF/P_o)$

$DRAG = \sum [DRAM, XAF \cos \alpha, XNF \sin \alpha, (XGF + XGP) \cos(\alpha + \theta) \cos \beta]$

$LIFT = \sum [XNF \cos \alpha, (XGF + XGP) \sin(\alpha + \theta) \cos \beta, XAF \sin \alpha]$

$C_{DRAG} = \frac{DRAG}{qS}$

$C_{LIFT} = \frac{LIFT}{qS}$

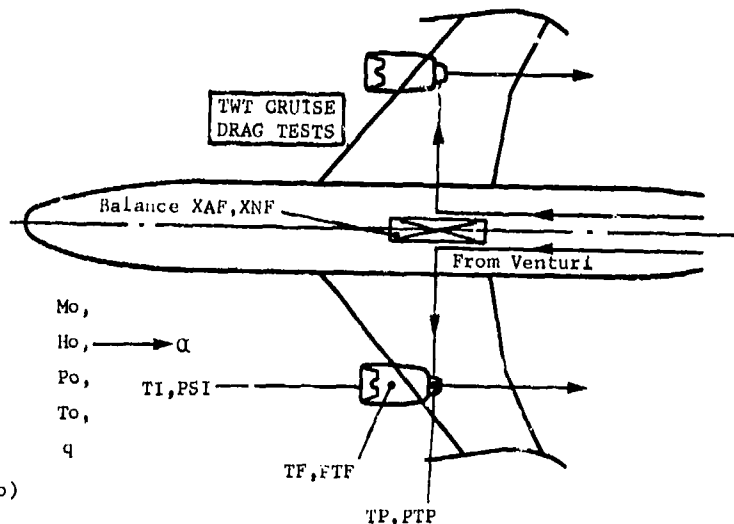


FIG.7 - SUMMARY OF TYPICAL MASS FLOW, THRUST AND DRAG ACCOUNTING METHOD

5. MST AND TWT NACELLE INTERNAL DATA

Figure 8 shows comparisons of the various internal data for both the MST calibration and TWT cruise test conditions.

The fan performance characteristics appear to be virtually unchanged from tank to tunnel. In addition, the distributions of fan duct total pressure are very similar in the two test phases, as evidenced by Figure 9.

Comparisons of performance and local flow conditions of the type presented here have supported the validity of the thrust and mass flow accounting approach, at least, in so far as the local measurements can be held to represent the total internal duct flow conditions.

6. MODEL LIFT AND DRAG DATA

The model was tested over a range of typical cruise conditions at a wind tunnel Reynolds number of approximately 4.0×10^6 per foot.

Mach number 0.80 \rightarrow 0.87

Aircraft fuselage incidence $1^\circ \rightarrow 4^\circ$

Fan nozzle pressure ratio 2.10 \rightarrow 2.60

Drag polars for the model with 15° and 11° afterbody systems are shown in Figure 10 for the maximum TPS power setting only; drag differences between the two builds however, exhibited in Figure 11, clearly illustrate the dependence on fan nozzle pressure ratio and hence the great importance of correctly simulating engine power effects.

The drag data presented here is based on the use of fan nozzle discharge coefficient to estimate fan mass flow; similar drag levels and similar comparative drag increments are obtained using all of the alternative thrust/drag accounting procedures. The spread of the drag data for all methods is generally less than 2 drag counts (overall) and the variation of the drag increments between 15° and 11° is generally less than 0.5 drag counts.

The repeatability of the thrust corrected drag data is generally better than ± 1 drag count; a statistical analysis based on the curves drawn through the data has indicated the 95% confidence band to be ± 0.8 drag counts. At this confidence level it is clear that the observed differences between the results for the 15° and 11° builds is statistically significant.

Typical M.S.T - T.W.T turbine powered simulator nacelle performance comparison

M.S.T	T.W.T
<ul style="list-style-type: none"> ○ AMCV - 11.25 in² △ AMCV - 12.00 in² □ AMCV - 12.50 in² ◇ AMCV - 13.00 in² 	<ul style="list-style-type: none"> × Mach - 0.85

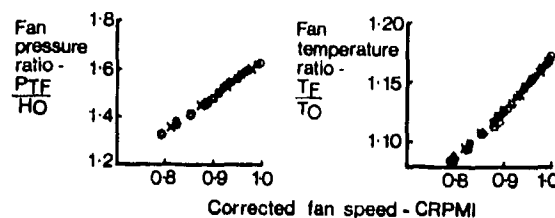


Figure 8

Typical MST/TWT internal flow distribution comparisons

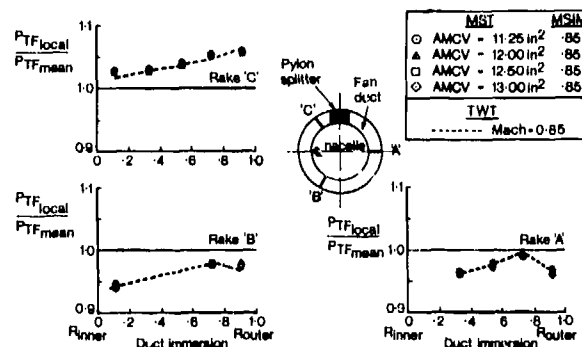


Figure 9

Typical maximum power drag polars for 11° and 15° configurations

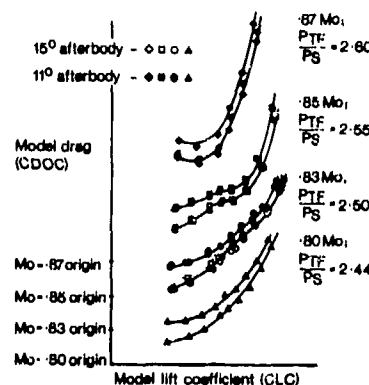


Figure 10

Procedures adopted to convert model drag results into incremental aircraft drag data, for comparison with flight test, are outlined in Figure 12. Second order effects due to changes in engine specific fuel consumption as aircraft drag (and hence net thrust) changes, have not been considered significant.

The effect of the 11° afterbody compared with the 15° configuration is shown in Figure 13, for both the wind tunnel and flight data, in terms of measured percentage drag increment against freestream Mach number. Comparisons between model and full scale are made at typical cruise values of normalised aircraft weight, (W/δ).

Improvements in aircraft drag of up to 2% are exhibited for the 15° afterbody configuration, however it should be noted that the increments presented here are due entirely to differences in installed drag levels, account having been taken of the effect of quiescent thrust differences for both the model and full scale cases. The TOTAL increment in Specific Air Range, which includes both installed drag and quiescent thrust effects, as measured in the flight tests is approximately 3% at representative cruise conditions.

Apart from the 0.83 Mach number condition at high aircraft weight, the model to flight correlation is quite satisfactory, particularly on consideration of the estimated accuracies of the two sets of data, also indicated in Figure 13.

Examples of the local flow conditions in the inboard gully region bounded by the wing lower, pylon and nacelle surfaces are illustrated in Figure 14. A region of high local Mach number and adverse pressure gradient for the 11° afterbody appears to reflect the incremental drag data presented. The peak local Mach number is seen to increase as aircraft incidence is reduced, consistent with increased airflow into the gully area.

Pressure surveys, not presented here, also appear to indicate that the variation in afterbody configuration does not significantly influence the wing upper surface flow field.

Increments in model drag - counts 15° afterbody relative to 11° afterbody datum

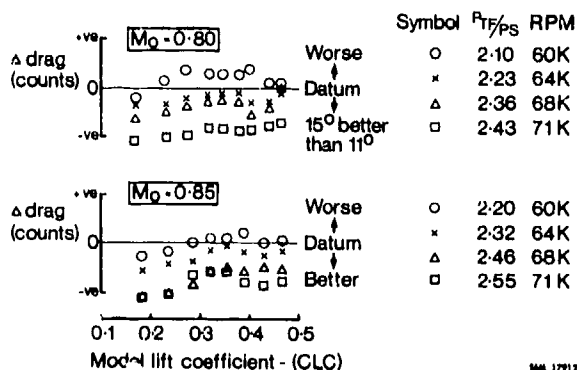


Figure 11

Procedure for comparing model wind tunnel data with full scale flight results

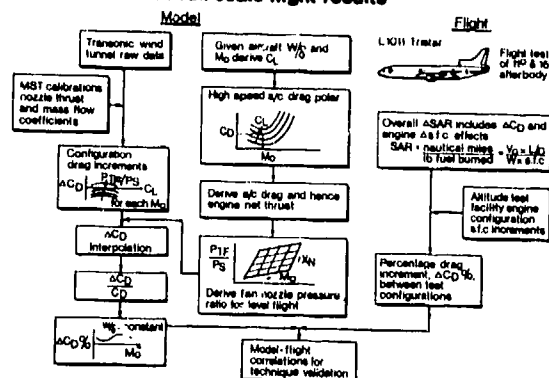


Figure 12

Comparison of model wind tunnel data with full scale flight result

Drag increment of 11° afterbody configuration relative to 15°

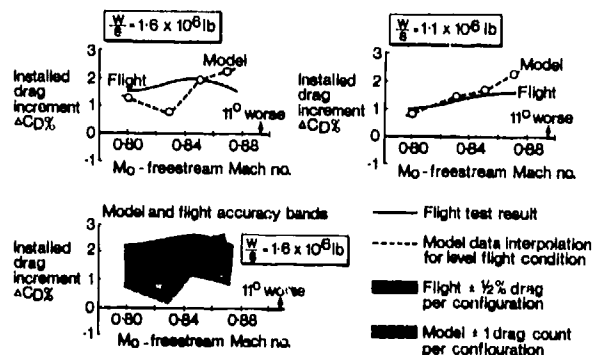


Figure 13

Wing lower surface pressure distributions

$M_o = 0.85$, $\frac{PTF}{PS} = 2.54$

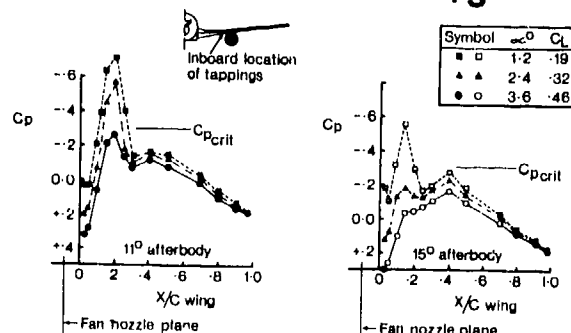


Figure 14

8. CONCLUSIONS

- (a) A full span model test technique for high accuracy subsonic civil installed drag studies has been developed.
- (b) Mach simulation tank thrust and mass flow calibrations have been conducted for 1/25th scale TPS nacelle to repeatability levels of generally better than $\pm 0.2\%$.
- (c) Transonic wind tunnel drag data for the TPS full span model with alternative powerplant after-body systems have exhibited repeatability levels of the order of ± 1 drag count.
- (d) Comparisons of flight and transonic wind tunnel data have shown that the full span model and aircraft increments generally result in up to 2% advantage for the 15° relative to the 11° configuration, thereby establishing confidence in the test technique. This, it should be noted, is only the drag increment. The total increment in SAR, as measured in flight test, is approximately 3% at representative cruise conditions.

9. REFERENCES

- 1. James C. Patterson Jr. 'A Wind-Tunnel Investigation of Jet-Wake Effect of a High-Bypass Engine on Wing-Nacelle Interference of a Subsonic Transport', NASA TN-4693 August 1968.
- 2. R. Decher, W.B. Gillette, and D.C. Tegeler, 'Nacelle Airframe Integration; Model Testing for Nacelle Simulation and Measurement Accuracy': AGARD Specialists' Meeting on Wind Tunnel Design and Testing Techniques, London, UK, October 1975.
- 3. A.E. Harris and E.C. Carter, 'Wind Tunnel Test and Analysis Techniques Using Powered Simulators for Civil Nacelle Installation Drag Assessment', Paper 24, AGARD Proceedings, Toulouse, May 1981.
- 4. MIDAP Study Group, Guide to In-flight Thrust Measurement of Turbojets and Fan Engines. NGTE Report 78004, May 1978.
- 5. Book Keeping Procedures for Mass Flow, Thrust and Drag on T.P.S. Full Span Model Tests, ARA Internal Memorandum, 1978.

10. ACKNOWLEDGEMENTS

The authors wish to acknowledge the valuable assistance of colleagues at Rolls-Royce and the Aircraft Research Association and also to the Lockheed Aircraft Company, without whom this project would not have been possible. The support of MOD(PE) is also gratefully acknowledged.

EVALUATION OF AN EXPERIMENTAL TECHNIQUE TO INVESTIGATE THE
EFFECTS OF THE ENGINE POSITION ON ENGINE/PYLON/WING INTERFERENCE

by

J.A.J. van Engelen, B. Munniksmma and A. Elsenaar
National Aerospace Laboratory NLR
Anthony Fokkerweg 2
1059 CM Amsterdam
The Netherlands

SUMMARY

A flexible experimental technique to study the effect of a variation of engine position for a range of test conditions was evaluated. In this test an underwing mounted $\frac{1}{2}$ fan-cowl engine was investigated at six different positions as a free flow nacelle and as a strut mounted blown nacelle. Pressure and balance force measurements were made. Some typical aspects of the aerodynamic interference are discussed, notably the value of free flow nacelle measurements. Also a comparison of balance weighed and integrated pressure forces is presented.

1. INTRODUCTION

In an early stage of a civil airplane development programme the choice of the engine location has far reaching consequences for the airplane design. The most favourable engine location will be a compromise between the objectives of the involved technological disciplines. For configurations with wing mounted engines it is required from the aerodynamic point of view that penalties due to engine/airframe integration are kept to a minimum as referred to an optimized clean wing and an isolated engine cowlings. Some prominent questions to be answered are:

- how large are the interference lift, drag and thrust terms as affected by the engine position relative to the wing
- how large are the jet effects on flap and tailplane characteristics at take-off and climb-out as dependent on engine location.

To study these aspects in a wind tunnel environment the engine must be represented as accurately as possible. The by far most simple representation of the engine is the free flow nacelle, which simulates the cruise inlet flow and fan cowl geometry. The free flow nacelle can be weighed integrally with the airplane model without any difficulty. More adequate engine simulation is established by using a blown nacelle or a so-called turbo-powered nacelle. Application of these types of model engines mounted on the airframe, introduces problems such as thrust-on-the-balance. Air ducting along the balance and through the limited space in the model is another complication to be expected. Furthermore the latter test set-up is less attractive for a "pathfinder" test where an easy change of engine position is required. Therefore a different test set-up was adopted in the experiment described in this paper. This experiment was meant to explore the aerodynamic consequences of a variation of engine location.

A semi-span model was used, typical for a transport type aircraft with a supercritical wing. A $\frac{1}{2}$ fan-cowl high by-pass engine was located at six different positions underneath the wing. Tests were performed on a free flow nacelle and a blown nacelle. The required flexibility was obtained by mounting the blown nacelle on an additional strut. The test programme included the determination of interference effects on lift and drag, changes in nozzle characteristics, measurements of dynamic loads on the extended flap, rake surveys of the jet location and jet effects on tail characteristics.

The discussion in this paper will be confined to the adopted test technique in relation to the measurement of lift and drag interference at and near cruise conditions. More specifically the following topics will be considered:

- the value of the free flow nacelle as compared to the blown nacelle in an engine/airframe integration test
- the magnitude of the parasitic interference of the additional strut and engine inlet fairing
- the correlation of the interference effects as obtained from pressure and overall force measurements, in terms of relative changes in lift and drag.

When appropriate, results of theoretical calculations (with the NLR panel method) are given to support the experiment.

2. TEST SCHEME AND MODEL CONFIGURATIONS

The test scheme for determination of engine/wing interference effects using free flow and blown nacelles involves test steps as illustrated in Figure 1. The principal steps are:

- the clean wing configuration
- the model equipped with the free flow nacelle without core in order to accommodate the required inlet mass flow
- the model and blown nacelle, simulating the free flow nacelle exhaust conditions
- the model and blown nacelle with core simulating the actual engine nozzle pressure ratios.

Tests on the blown nacelle were performed with and without a splitline and at different power settings.

The semi-span model was mounted in the transonic wind tunnel HST of NLR (fig. 2). The test programme was split up in two parts. First the free flow nacelle was attached to the wing at six different positions, by means of interchangeable pylons. The measurements on this model include overall balance force measurements and local pressure readings at locations of interest on wing, pylon and nacelle (fig. 3).

In the second part of the test programme a blown nacelle with an appropriate faired inlet was used to determine the jet effects. The nozzle was shaped according to the actual engine geometry (fig. 4). The blown nacelle, mounted on an additional strut, was located near the wing/pylon combination at the same positions as investigated using the free flow nacelle. The strut was fixed outside the test section to the semi-span model rig, allowing simultaneous changes in angle of incidence. The engine location was varied simply by the adjustment of the strut location and the exchange of pylons. High pressure air was ducted through the strut into the blown nacelle where it passed a choke plate and a 25 mm slab of metal foam, which provided a smooth total pressure profile. For adjustment of fan and core pressure ratios, the flow distribution was regulated by a remote control valve located in the blown nacelle.

Originally it was intended to perform the larger part of the test programme on the blown nacelle with a splitline to enable balance measurements of the semi-span model and part of the pylon. The splitline with a labyrinth seal, was located in the part of the pylon (fig. 2). The sideways movement of the blown nacelle was restricted by means of adjustable span-wires that ran from the strut to both sides of the tunnel. Although it was possible to make contact-free measurements, the adjustment of the span-wires turned out to be very time consuming. Therefore it was decided to do most of the measurements with the blown nacelle attached to the wing/pylon combination. In that case only pressures were measured. At a later stage in the test program the splitline was slightly widened which proved to be successful. However, only a limited number of measurements was made in this partly metric configuration.

3. A QUALITATIVE DESCRIPTION OF THE PRESSURE INTERFERENCE

When the free flow nacelle is mounted underneath the wing the pressure distribution is affected. A typical example is shown in Figure 5 as increase in pressure coefficient relative to the clean wing. Apparent is a lift loss near the leading edge, a result of a locally reduced effective incidence. Also the velocities further downstream on the wing lower surface are reduced. These effects, well known from literature (e.g., ref. 1, 2) are a straightforward consequence of the displacement flow around the nacelle and jet. Figure 6 shows the change in pressure distribution relative to the clean wing induced by the blown nacelle without the core nozzle (conf. C, fig. 1). The interference effects are very similar. Differences are due to configuration deficiencies such as inlet fairing and strut mounting and will be discussed in paragraph 4.

The pressure distribution with the blown nacelle corresponding to the actual engine exhaust conditions (conf. F) is presented in Figure 6 relative to the free flow nacelle configuration. The shown effect is a combined result of the strut mounting and inlet fairing on the one side and jet interference on the other. With respect to the jet interference the following distinction can be made:

- interference as a result of powersetting (conf. F-D) and
- interference as a result of differences in nozzle geometry between the blown and the free flow nacelle (conf. D-G, see also figure 4)

The influence of powersetting on the pressure distribution is rather small (fig. 7). Minor velocity increments are found on the wing lower surface at high powersetting, due to jet pluming. The pressure interference as a result of the altered nozzle representation, notably the addition of the core nozzle, (fig. 8) is considerably larger. It is comparable in shape and magnitude with the effect of the free flow nacelle installation on the clean wing as presented in Figure 5. With respect to the faired inlet pressure and large changes can be noted resulting in an important increment of the fan pressure drag force (see par. 5).

As was the case with the free flow nacelle, the effects presented in Figure 8 are a straightforward consequence of the displacement flow around the nacelle and jet. This is also illustrated in the same figure by the results of theoretical calculations using two different jet models. In these calculations the jet was represented by a solid body, the dimensions of which were derived from simple continuity considerations for the two nozzle geometries. The calculated pressure differences in Figure 8 are a result of a reduction in jet diameter of 1.5% and an increase in initial jet convergence angle of 3.1°, corresponding to the core cowl addition and the fan nozzle internal contouring (fig. 4). Except for the wing upper surface (where the result of the basically simple panel method is not reliable) the agreement between theory and experiment is quite good. Both from the experiment and from the (although very approximate) theoretical calculations it can be concluded that the aerodynamic interference effects are very sensitive to the representation of the nozzle geometry. The additional effects introduced by a change in engine powersetting are rather small.

It should be remarked that these observations depend on the tested engine configuration. For the fan-cowl engine configuration as tested on the Airbus (ref. 3) the influence of powersetting was more pronounced. Also the correct inlet mass-flow for the free flow nacelle was obtained by removal of the core engine plug only. Consequently the nozzle geometries for the free flow nacelle and the blown nacelle were almost identical in that case.

4. PARASITIC INTERFERENCE EFFECTS

The interference effects due to deficiencies in the blown nacelle configurations were not investigated very thoroughly, based on the presupposition that they are small and cancel each other when one is looking at differences in engine location. However in this paragraph attention will be paid to the parasitic interference as a consequence of:

- inlet fairing
- strut mounting
- splitline

The combined pressure interference as a result of the inlet fairing and strut mounting was determined experimentally by comparison of the configurations C and B (fig. 1). The results (both uncorrected and corrected for splitline interference) are presented in figure 9. Although the effects are generally small some features are discernible. On the fan cowl velocity increments are observed that may be attributed to the inlet fairing (see eg. ref. 3) which causes an increased flow around the nacelle and wing. The slightly S-shaped pressure distribution on the wing lower surface resembles that of figure 5 although less pronounced, suggesting a change in jet contour. The sensitivity of the pressure distribution to the jet contour has already been indicated in paragraph 3. On the wing upper surface a large scatter is observed. This can probably be contributed to the sensitivity of transonic flow to small changes.

Figure 9 also includes theoretical lines presenting the combined effect of inlet fairing and strut. Although not shown in this figure, these effects have been calculated separately. The calculations revealed that the inlet fairing resulted in a small shift of the pressure distribution, in particular on the fan cowl. The strut exerted an unexpected influence on the inboard wing that is not reflected in the experiment and for which no explanation was found.

For a limited number of tests in which only the wing and a part of the pylon are balance weighed a splitline was used. The pressure interference as a result of this splitline is indicated in figure 10. The splitline interference is not negligible but it appears that there is hardly any influence of power setting.

5. BALANCE AND PRESSURE FORCE EVALUATION

In paragraph 3 qualitative results in terms of changes in pressure distributions have been discussed for engine/airframe interference. However, for an evaluation of the optimum engine position one is interested in a quantitative assessment of variations in lift and drag. The question can be raised whether integration of differences in pressure distribution yields valuable information in this respect.

To answer this question the free flow nacelle results will be discussed first. Figure 11 shows the effect of a vertical engine displacement on the integrated normal (C_N) and tangential (C_T) forces for wing, pylon and fan cowl respectively. In this figure force differences are presented relative to a central engine position. The variations are small but systematic. When the contributions of the different components are summed, the total effect especially with respect to the tangential force, is even smaller due to opposite effects on wing and fan cowl. The differences in total pressure forces and overall balance forces are compared in the figures 12 and 13. Although the data show some scatter, trends with Mach and Alpha are roughly the same. Also the opposite effects due to a variation of engine location are clearly visible.

A similar comparison between pressure and balance forces cannot be made for the configurations with the blown nacelle. Only pressure information is available as shown in figure 14 and 15. In this case pressure force differences were determined relative to the free flow nacelle for one particular engine location (the core contribution in conf. D and E in an absolute value). Again the cancelling effects on wing and fan cowl are very pronounced. This is also illustrated by the force increments due to a variation in engine position as indicated by the shaded regions. The changes in total force are much smaller than the observed variations for the different components.

A comparison of the interference pressure forces for the free flow nacelle (conf. B) and the blown nacelle (conf. E) with respect to variation in engine position is shown in figure 16. In the left part of this figure also the corresponding results of the balance force measurements for the free flow nacelle are presented. Although the variations in normal and tangential forces are very small, the trends with engine position are very similar. One is tempted to conclude that for this particular test the free flow nacelle results are reasonably indicative for the selection of the most favourable engine location, notwithstanding the large interference effects introduced by the addition of the core as shown before.

An overview of the correlation between pressure and balance force differences for various cases is given in figure 18. In this figure also some results of the partly metric configurations (conf. C, E and G) are presented. Two comments should be made here. Firstly, the data show some scatter, partly due to measurement inaccuracy as indicated in this figure. Secondly, the pressure forces seem to underestimate systematically the corresponding balance force differences. This will be due mainly to the neglect of skin friction forces and systematic errors in the pressure integration from a limited number of pressure holes. Nevertheless, a correlation is present and this supports the conclusion that trends in interference effects are reasonably good predicted although the magnitudes will be underestimated.

In a few cases additional measurements were conducted with a splitline to enable balance measurements of the wing and a pylon part. In this set-up part of the uncertainty in forces as derived from pressure integration only can be eliminated in principle. Two examples are shown in figure 17: the effect of the actual nozzle geometry as compared to the free flow nacelle (conf. E-C) and the effect of power setting (conf. G-E). The left part of this figure shows a comparison of the pressure and balance force differences on the metric part (mainly the wing). Since one is interested finally in the total interference force, the contribution of the pressure forces on the non-metric part is added to the balance forces on the metric part as shown in the right side of this figure. This result is compared with the total interference force as derived from pressure forces only. The agreement is good as far as the effect of power setting is concerned, but poor for the effect of the addition of the core. In the latter case even opposite conclusions might be drawn with respect to the tangential force. In this particular case however the accuracy was limited by the repeatability of the balance forces (runs made in different test periods have been combined, whereas the effect of power setting was established within one run). Furthermore the comparison is hampered by splitline interference effects as shown by the shaded regions. Due to the opposite forces on the metric

and non-metric parts, the final accuracy will depend on the accuracy of the individual components. Therefore, a definite answer with respect to the value of partly metric tests cannot be given on the basis of the present results. In principle, data obtained from integral balance force measurements with a blown nacelle or a turbine powered simulator will increase the accuracy since the total effect will be measured directly. However, part of this improved accuracy is off-set again by thrust-on-balance problems and the accuracy of the engine thrust calibration.

6. CONCLUSIONS

An experimental technique to investigate the effects of the engine/pylon/wing interference has been discussed. In this investigation an underwing mounted $\frac{1}{2}$ fan-cowl engine was tested as a free flow nacelle and a strut mounted blown nacelle. The measurements included pressure and balance force measurements. Although it must be noted that the investigation was related to one particular engine configuration, it is concluded that :

- accurate simulation of the engine nozzle geometry is of prime importance for an investigation concerning engine/airframe integration. Nevertheless, tests on a free flow nacelle may still be useful for the selection of the most favourable engine position
- a reasonable correlation was established between interference forces as obtained from pressure integration and balance measurements. However, the pressure forces tend to underestimate the balance forces
- for a flexible "pathfinder" test as described in this paper, interference forces derived from pressure integration only appear to be very useful for the determination of trends in interference effects.

7. REFERENCES

1. Bagley, J.A. Windtunnel experiments on the interference between a jet and a wing at subsonic speeds
AGARD CP 35, September 1968
2. Bagley, J.A. and Kurn, A.G. Jet interference on supercritical wings
R & M 3485, RAE, Farnborough, 1977
3. Muunikkuma, B. and Jaarasma, P. Jet interference of a podded engine installation at cruise conditions
AGARD CI 150, March 1975

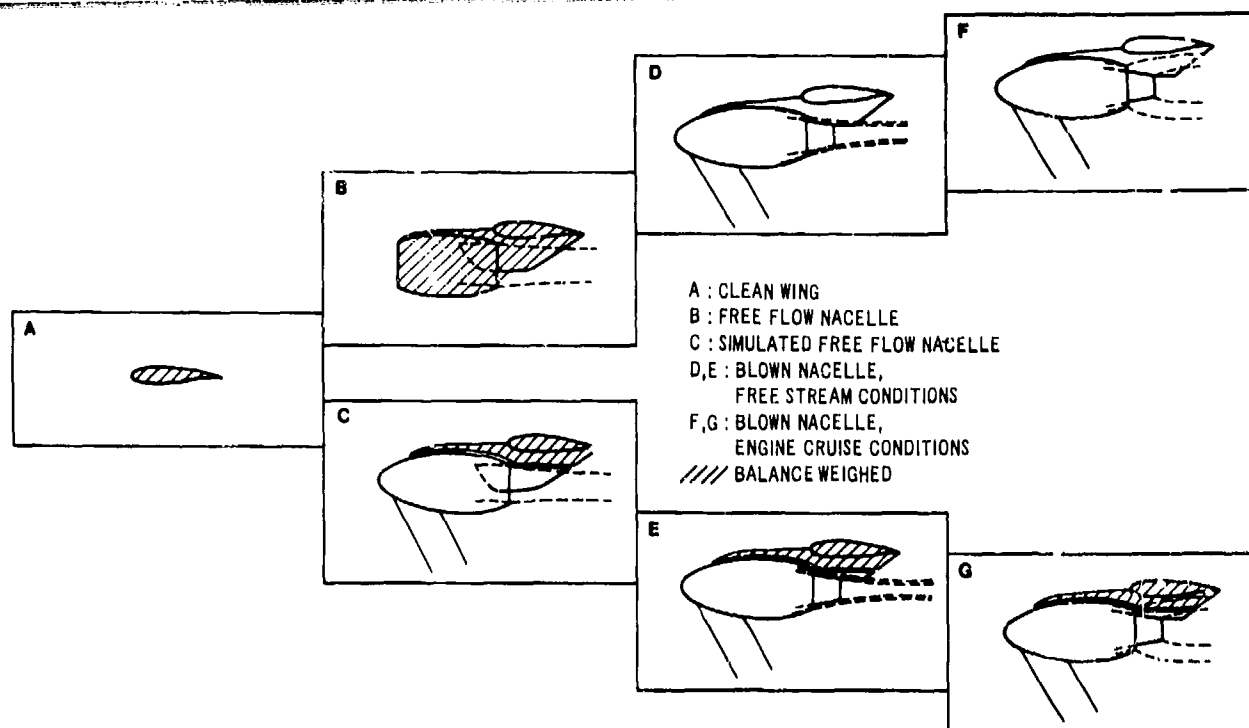


Figure 1 Tested configurations

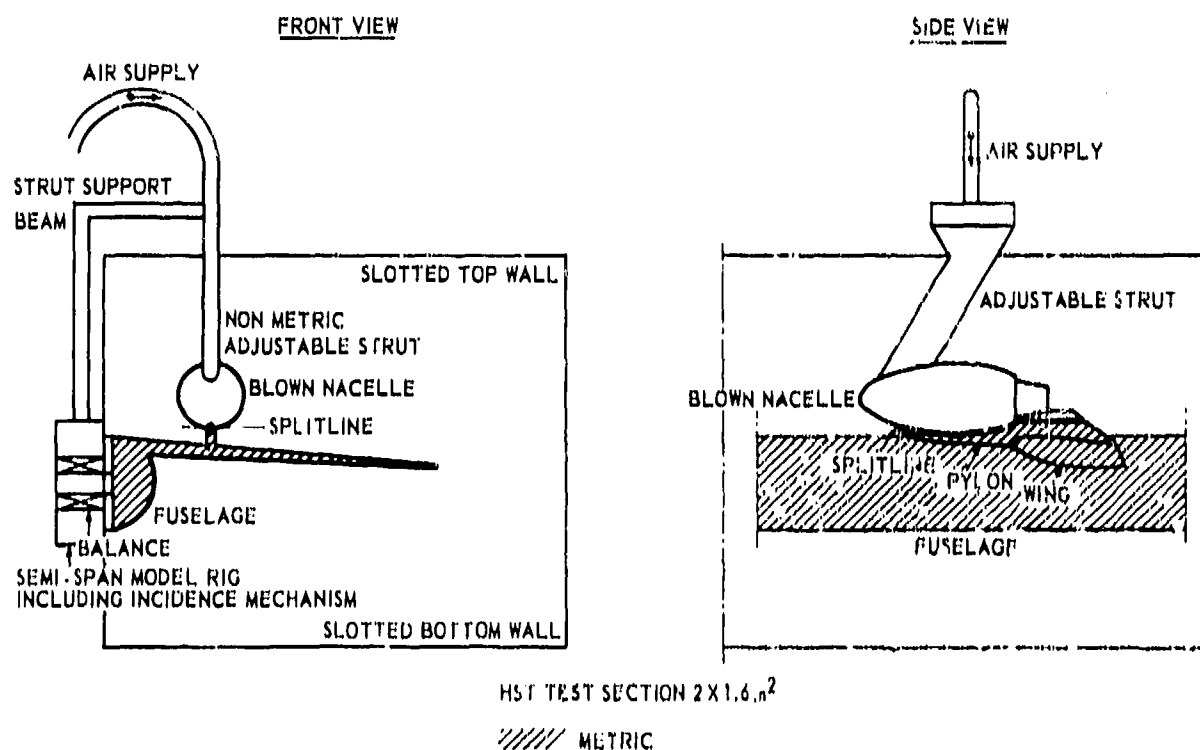
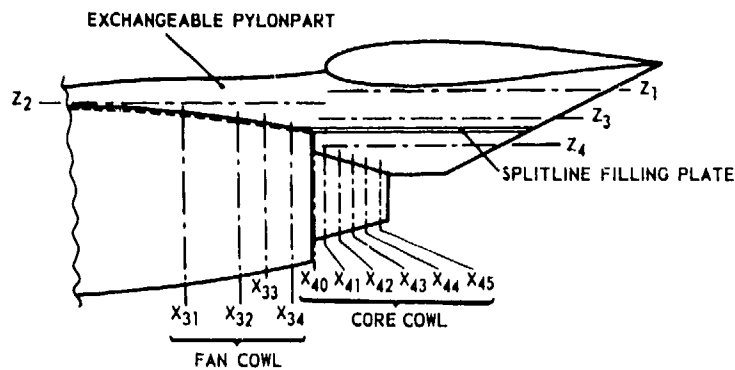


Figure 2 Test arrangement with blown nacelle

SIDE VIEW ENGINE INSTALLATION



REAR VIEW OF NACELLE :

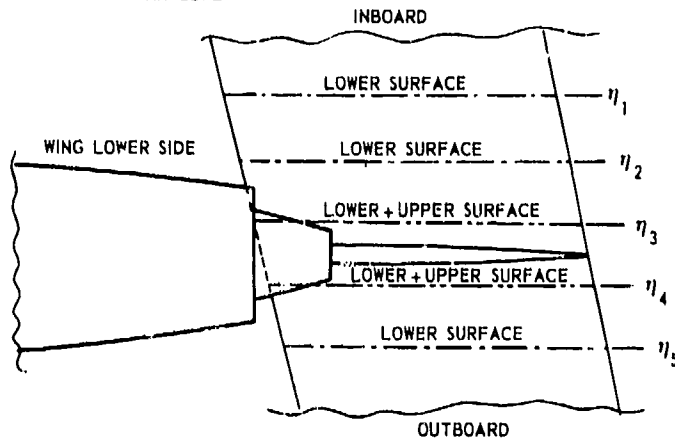
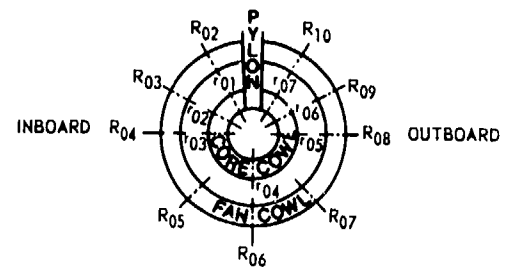


Figure 3 Pressure tap locations

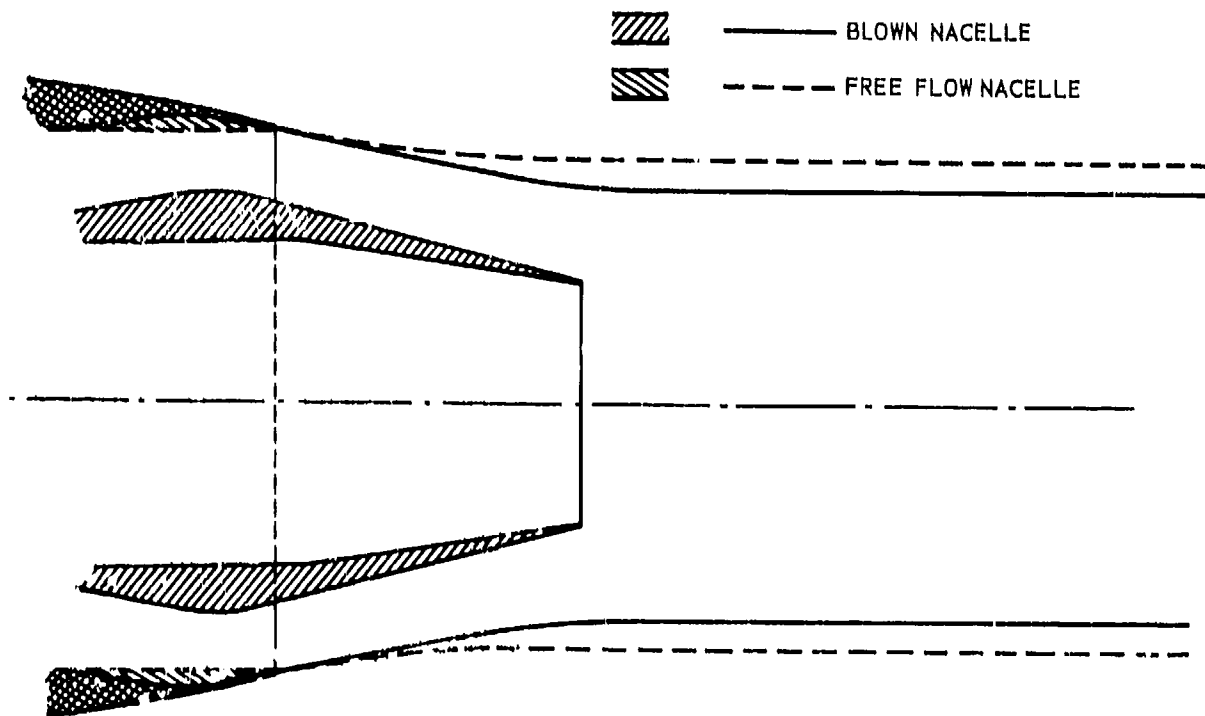


Figure 4 Nozzle geometries with corresponding jet-models

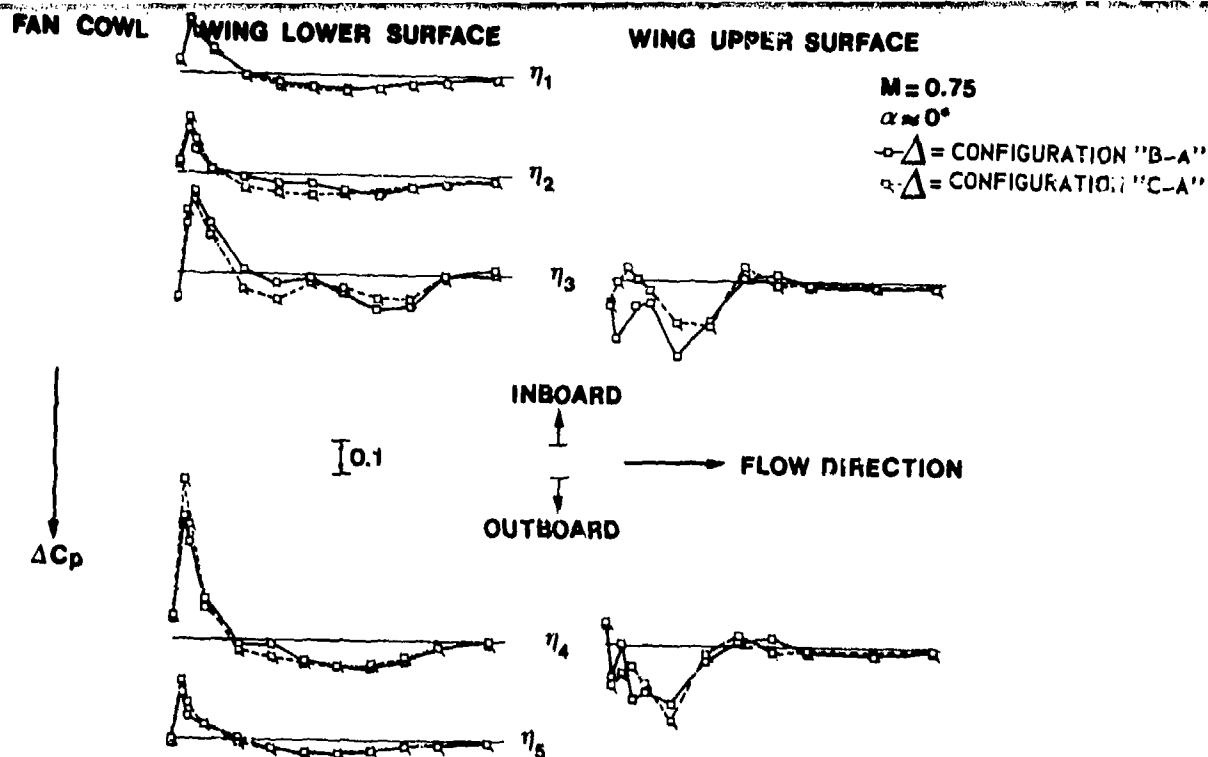


Figure 5 Effect of free flow nacelle on clean wing pressure distribution

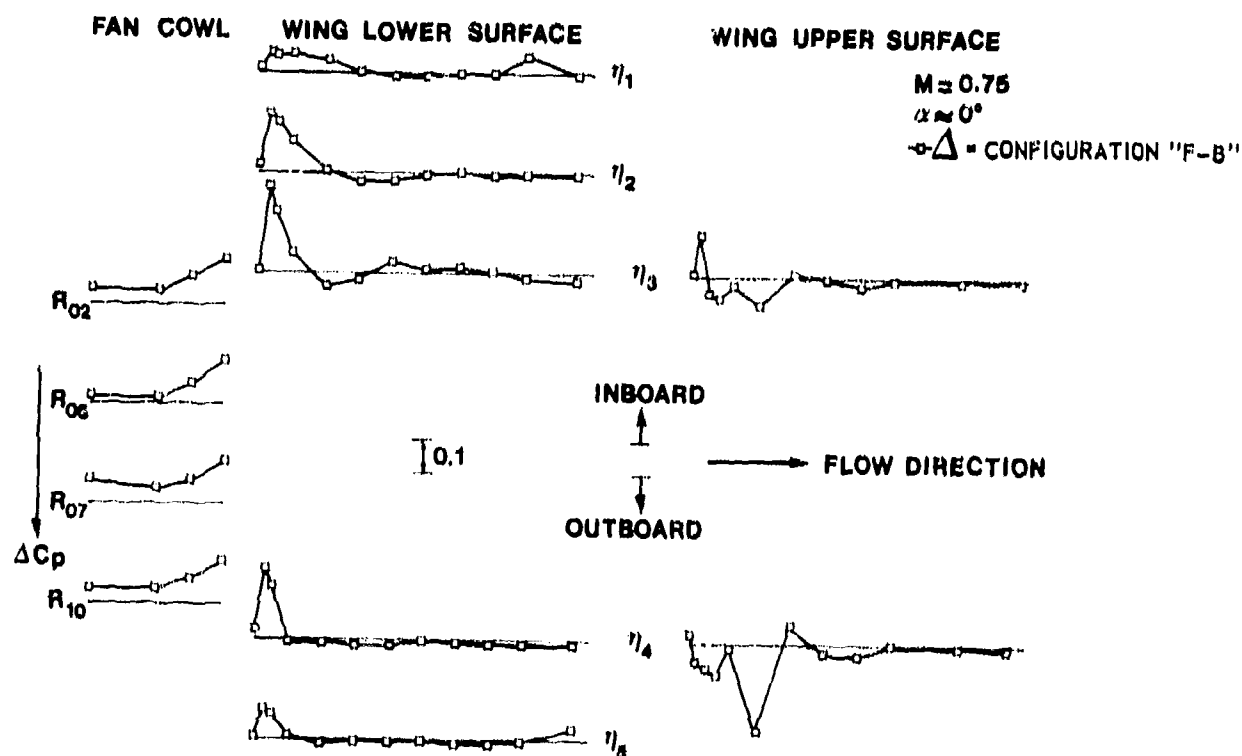


Figure 6 Total effect of blown nacelle on pressure distribution (relative to free flow nacelle configuration)

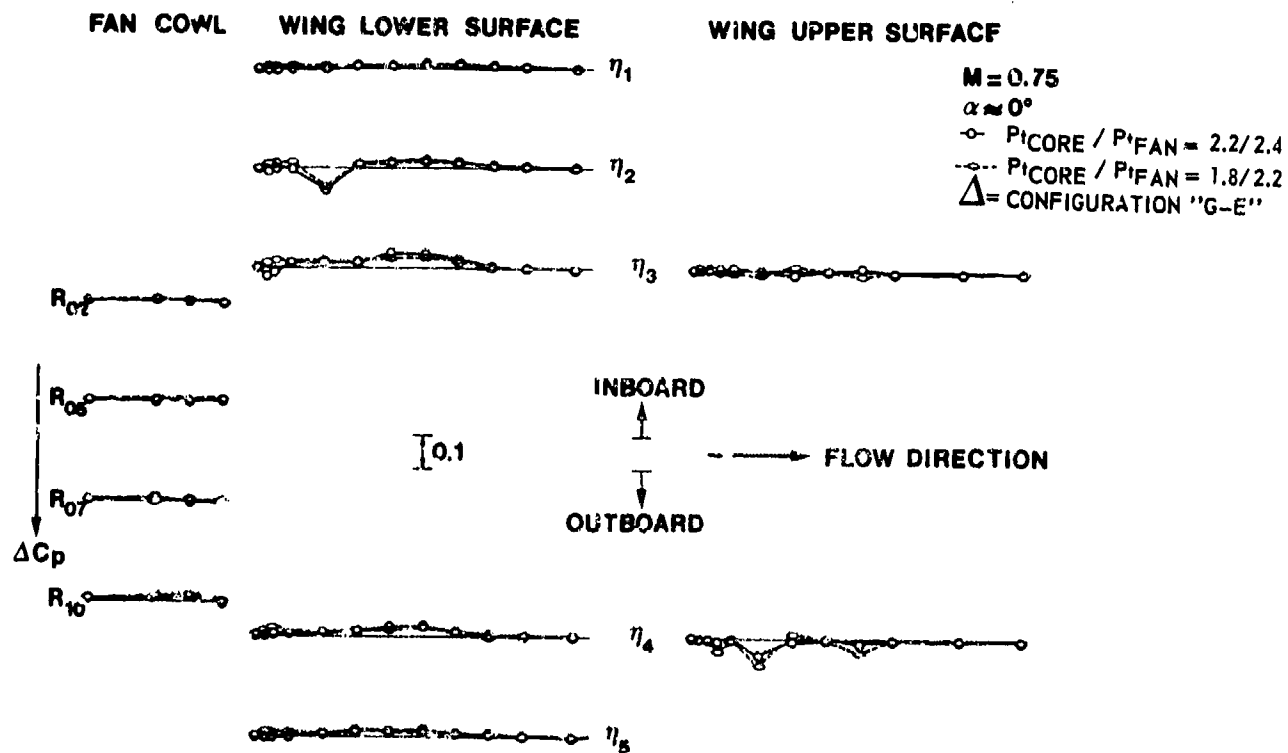


Figure 7 Effect of powernetting on pressure distribution

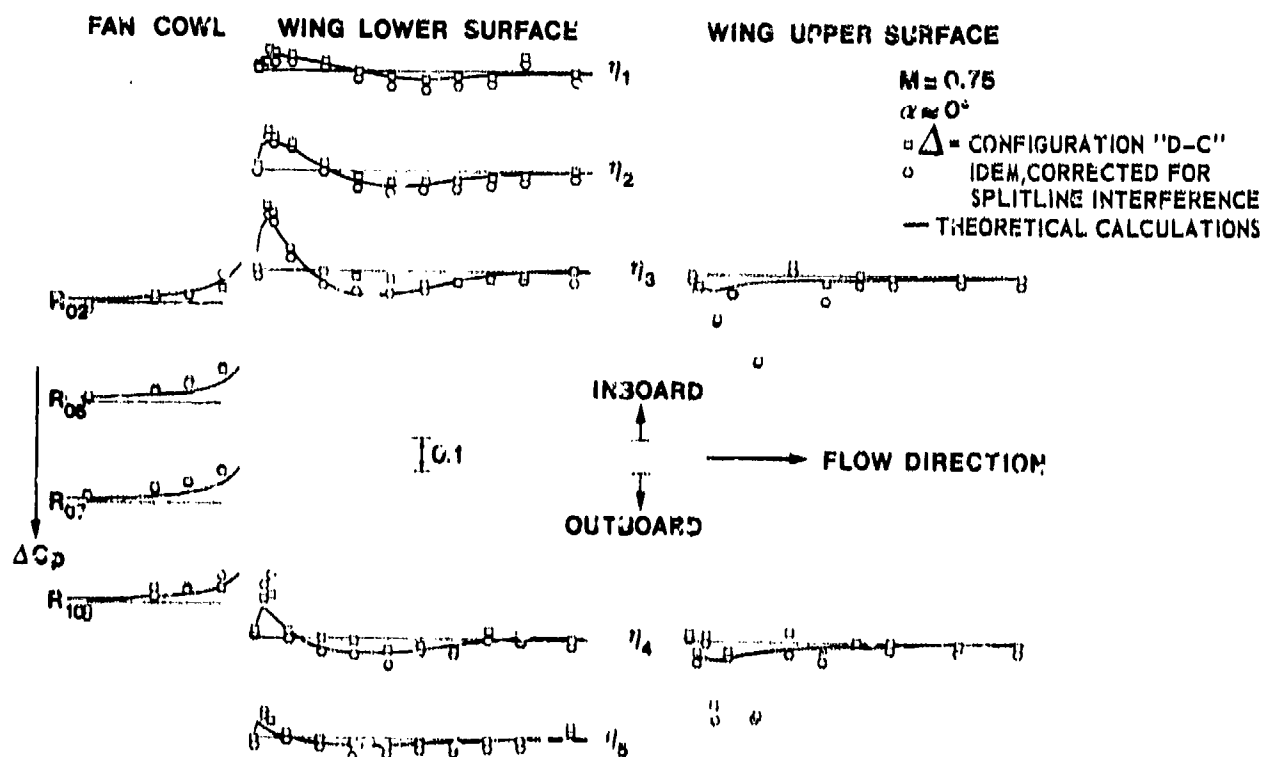


Figure 8 Effect of nozzle geometry on pressure distribution

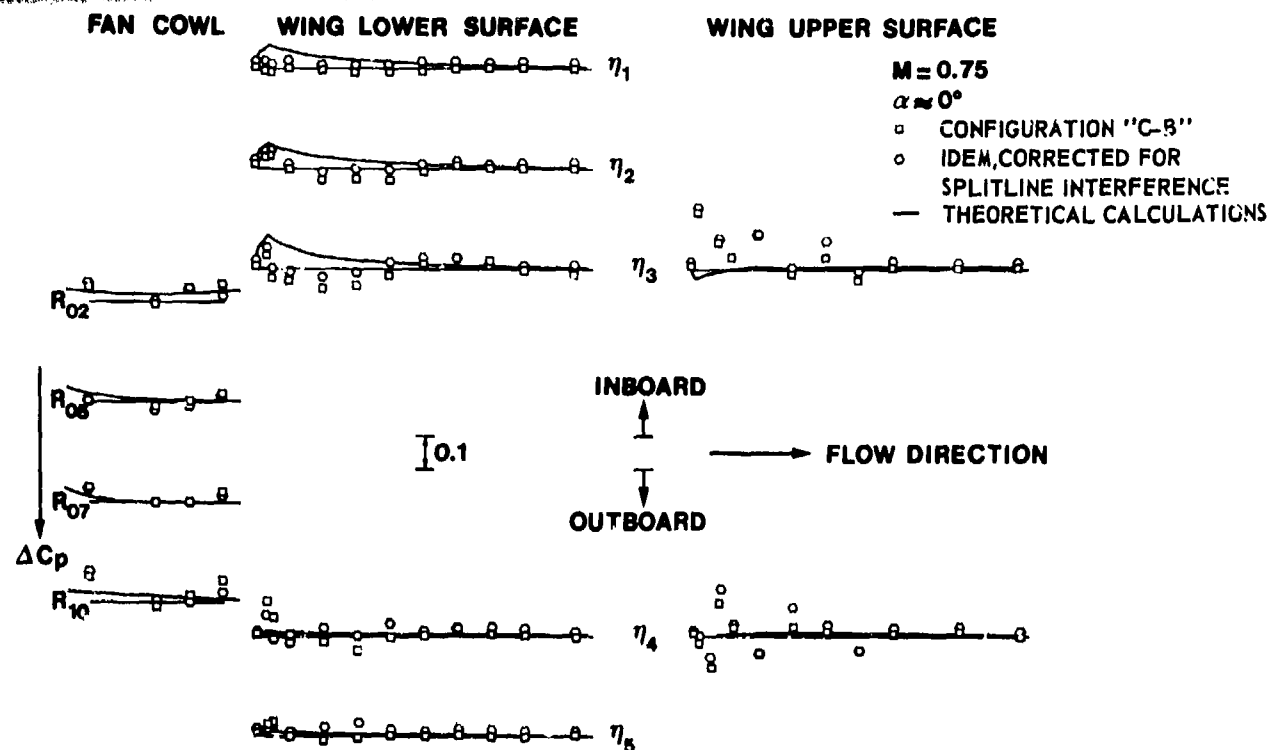


Figure 9 Effect of fairing and strutmounting on pressure distribution

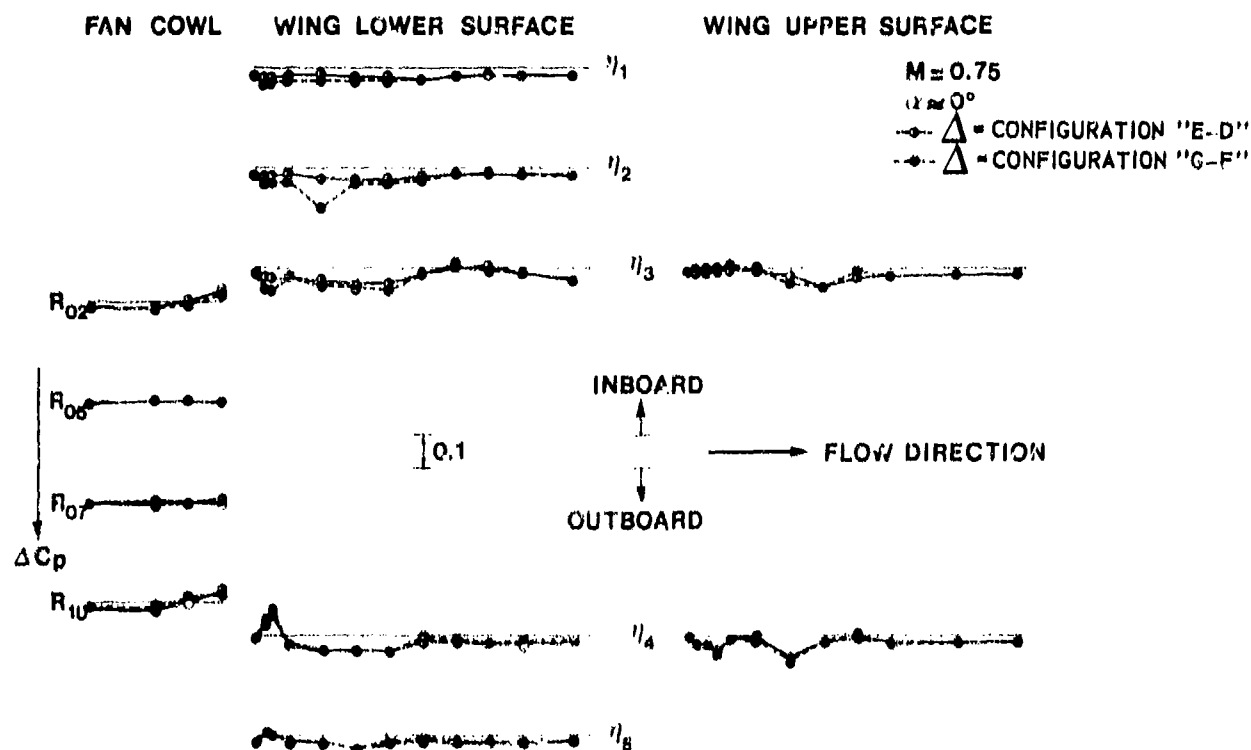


Figure 10 Effect of splitline on pressure distribution

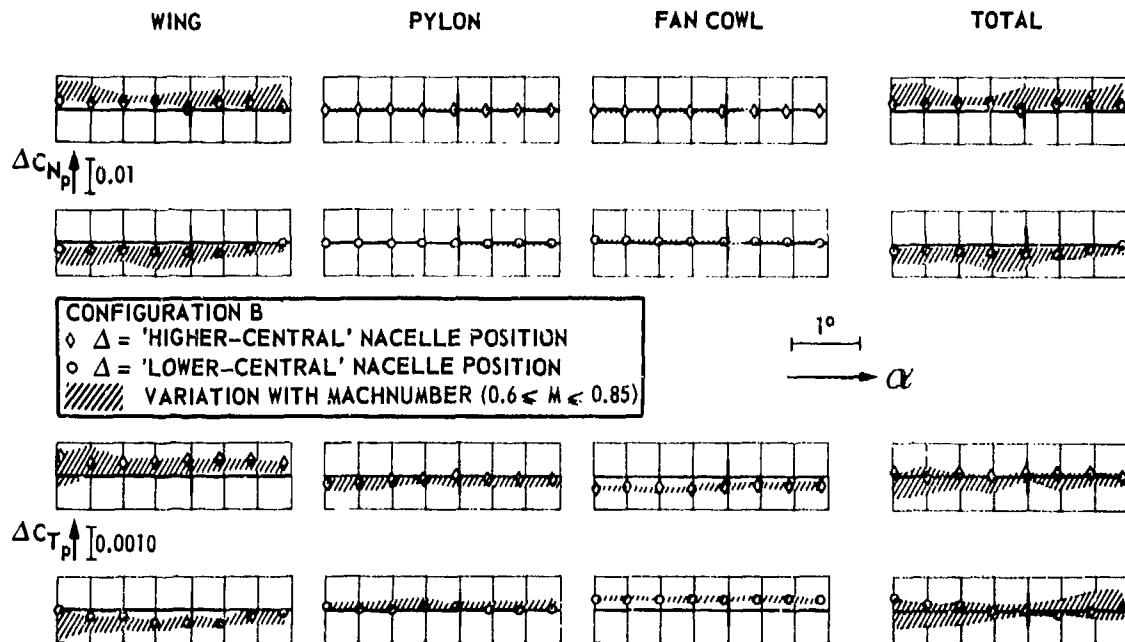


Figure 11 Effect of vertical nacelle position variation on pressure forces (component-split)

CONFIGURATION B
 ◇ Δ = 'HIGHER-CENTRAL' POSITION
 ○ Δ = 'LOWER-CENTRAL' POSITION
 ▨ VARIATION WITH MACHNUMBER ($0.6 \leq M \leq 0.85$)

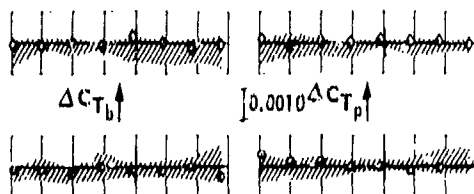
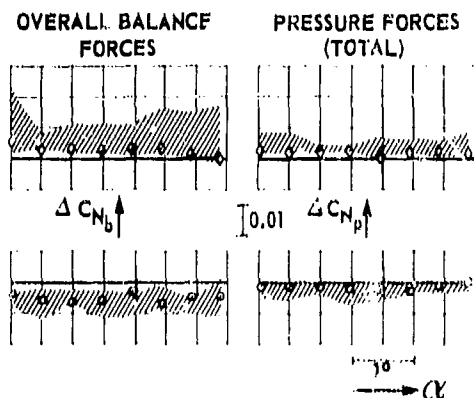


Figure 12 Comparison of balance force and pressure force increments vs Alpha (vertical nacelle displacement)

CONFIGURATION B
 ◇ Δ = 'HIGHER-CENTRAL' POSITION
 ○ Δ = 'LOWER-CENTRAL' POSITION
 ▨ VARIATION WITH α 's ($-2^\circ \leq \alpha \leq 1.5^\circ$)

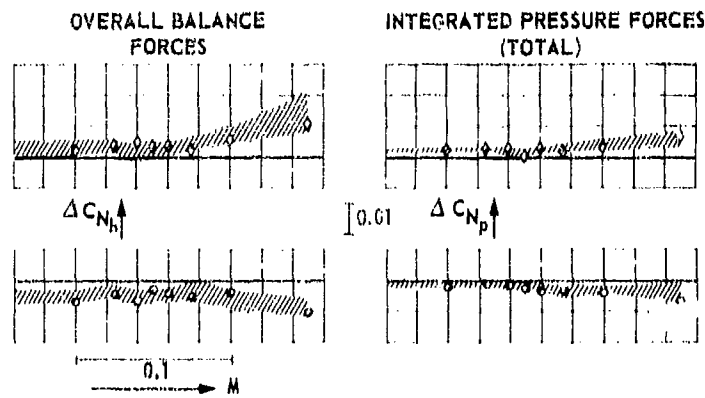


Figure 13 Comparison of balance force and pressure force increments vs Mach (vertical nacelle displacement)

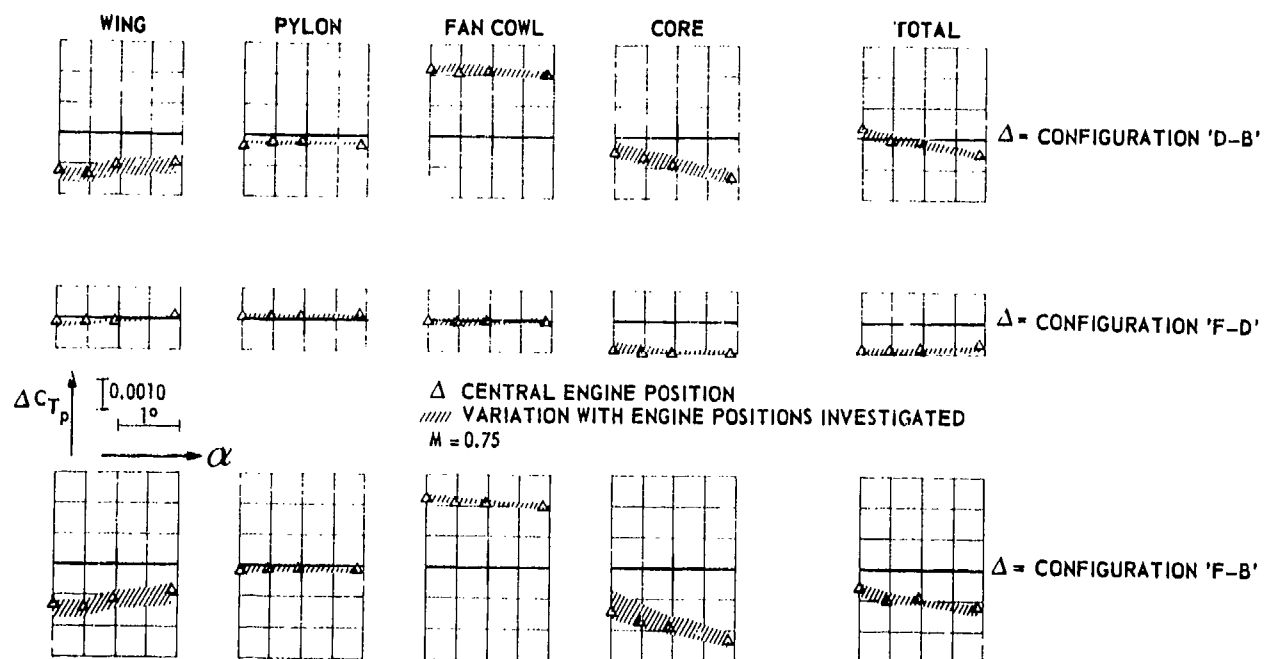


Figure 14 Jet interference on tangential pressure forces (component-split)

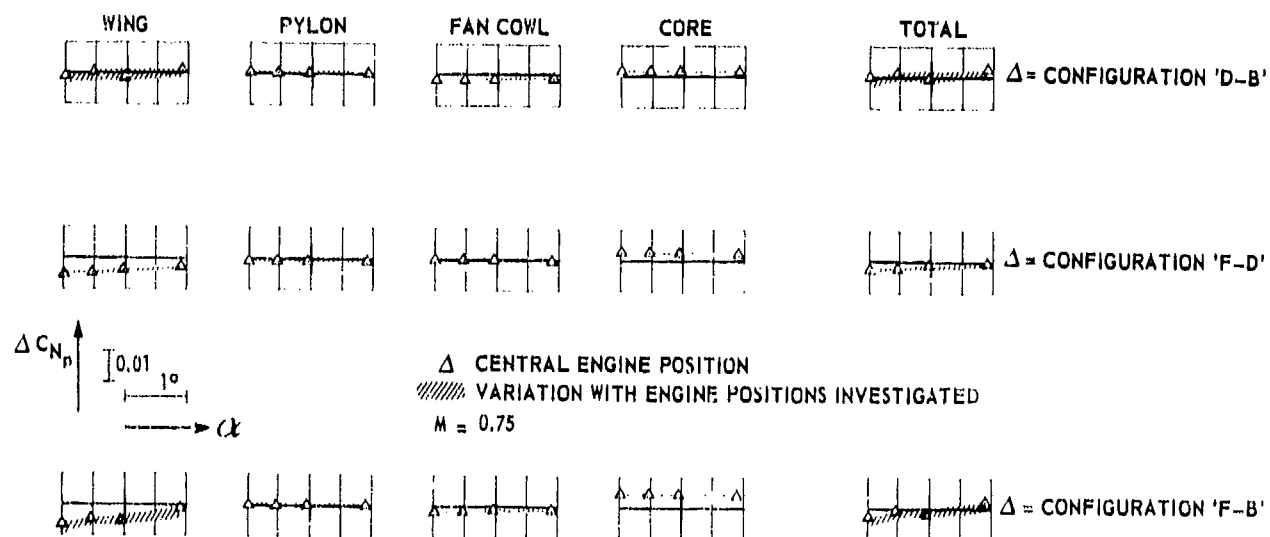


Figure 15 Jet interference on normal pressure forces (component-split)

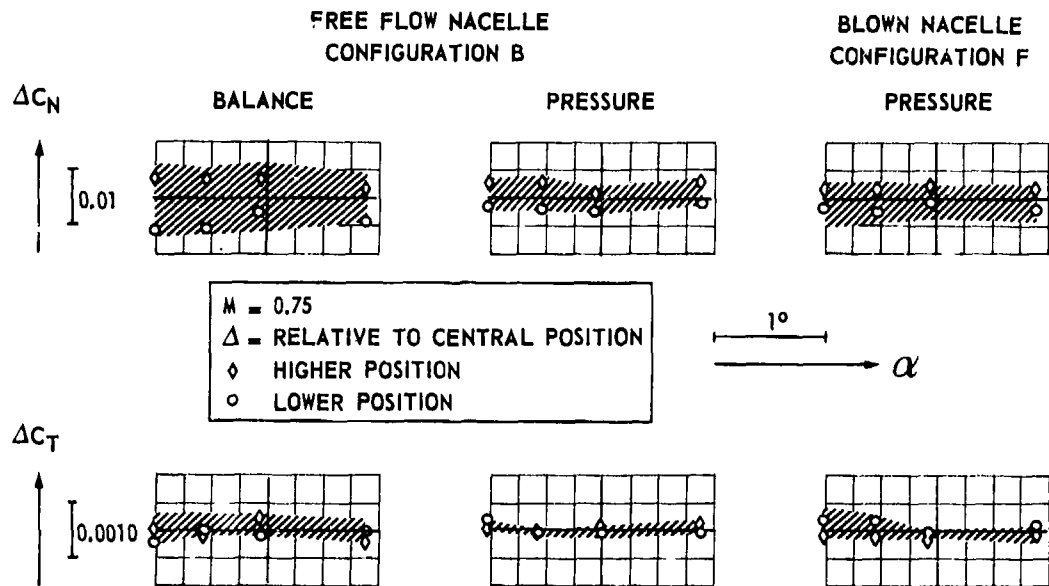


Figure 16 Force increments for nacelle position variation

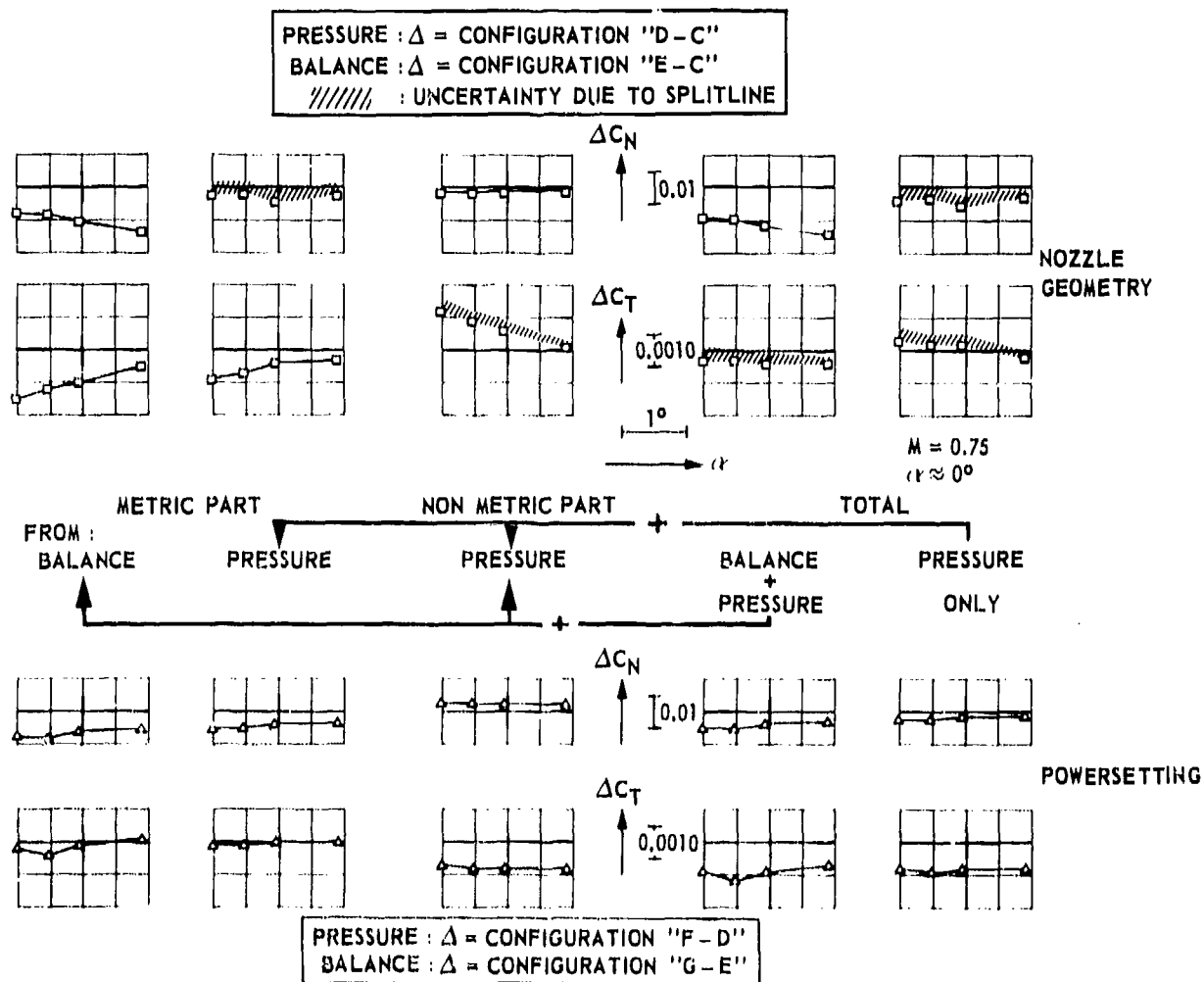
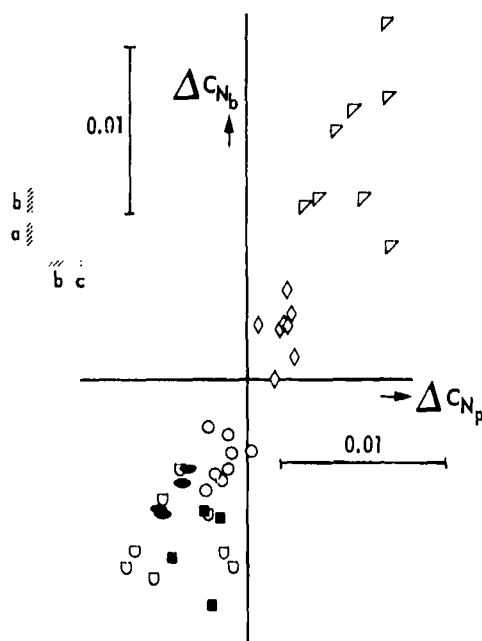


Figure 17 Evaluation of jet interference from a combination of balance and pressure forces, compared with that from pressure forces only



EFFECT OF :

a : 0.1% BALANCE ACCURACY

b : $|\Delta\alpha| = 0.01^\circ$

c : $|\Delta C_p| = 0.005$

OPEN SYMBOLS: INTEGRAL WEIGHED
FREE FLOW NACELLE CONFIGURATIONS

○ M = 0.75 } Δ = 'LOWER-CENTRAL'
○ M = 0.85 } POSITION
◇ M = 0.75 } Δ = 'HIGHER-CENTRAL'
▽ M = 0.85 } POSITION

SOLID SYMBOLS: PARTLY WEIGHED

BLOWN NACELLE CONFIGURATIONS

● { BALANCE : CONFIGURATION 'G-E' }
● { PRESSURE : CONFIGURATION 'F-D' } M = 0.75
■ { BALANCE : CONFIGURATION 'E-C' }
■ { PRESSURE : CONFIGURATION 'D-C' } $-1^\circ \leq \alpha \leq 1^\circ$

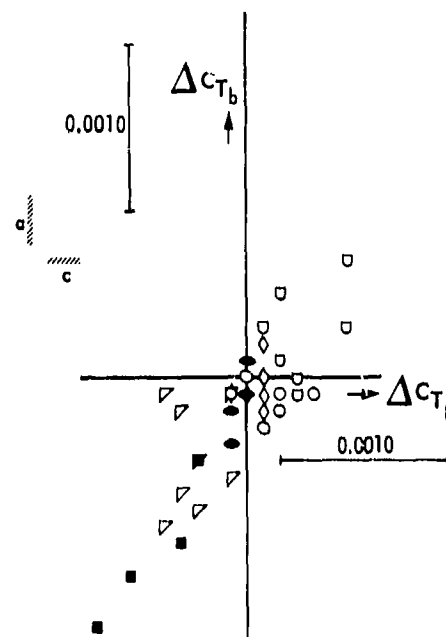


Figure 18 Correlation of balance force and pressure force increments

ESSAIS DE PRISES D'AIR A DES NOMBRES DE REYNOLDS COMPARABLES AU VOL DANS LES SOUFFLERIES F1 ET S1MA DE L'ONERA

par

J. Leynaert

Office National d'Etudes et de Recherches Aérospatiales (ONERA)
92320 Chatillon, France

R E S U M E

La pressurisation de la soufflerie subsonique F1 du Centre du Fauga-Mauzac de l'ONERA a été mise à profit pour réaliser des essais de maquettes de prises d'air d'avion de type "Airbus" à grande échelle afin de bénéficier d'un nombre de Reynolds s'approchant de celui du vol.

Les mêmes maquettes peuvent ensuite être essayées jusqu'à un nombre de Mach voisin de 1 dans la soufflerie S1MA du Centre de Modane-Avrieux.

Les prises d'air d'avion militaire peuvent également être étudiées dans les deux souffleries à des nombres de Reynolds élevés.

Les dispositifs utilisés, les méthodes de mesure et les moyens de tarage et de contrôle mis en oeuvre pour assurer la validité des résultats sont présentés.

1 - INTRODUCTION

Les essais en soufflerie à basse vitesse de prises d'air d'avion civil ont en particulier pour objet de préciser les limites de décollement des couches limites, soit externes, pour le problème critique de la traînée de nacelle en cas de panne de moteur au décollage, soit internes, pour le problème de la distorsion admissible par le moteur par vent de travers au point fixe et à très faible vitesse.

Ces limites de décollement sont directement tributaires du nombre de Reynolds des essais, et ne pouvaient être jusqu'à présent correctement déterminées, faute de moyens appropriés, au moins en Europe.

Le montage d'essai réalisé dans la nouvelle soufflerie F1 pressurisée à 4 bars du centre du Fauga-Mauzac de l'ONERA permet maintenant, sur des maquettes à échelle de l'ordre de 1/4, d'atteindre, à basse vitesse, des nombres de Reynolds comparables à ceux du vol.

Les mêmes maquettes peuvent aussi être essayées jusqu'à un nombre de Mach proche de 1 sur un nouveau montage réalisé pour la soufflerie S1MA du Centre de Modane-Avrieux de l'ONERA.

Les prises d'air d'avion militaire peuvent également être étudiées dans les deux souffleries à des nombres de Reynolds élevés.

Les montages et techniques d'essai dans les deux souffleries font l'objet de la présentation qui suit.

2 - ESSAIS DANS LA SOUFFLERIE F1

2.1 - Fonctionnement général de la soufflerie

La soufflerie F1 fait l'objet d'une présentation détaillée référencée [1].

Seules ses caractéristiques principales sont rappelées ci-après.

La soufflerie mise en service en 1977 fait partie du centre d'essais du Fauga-Mauzac de l'ONERA, près de Toulouse.

La figure 1 en donne une vue d'ensemble.

La veine d'essai présente une section rectangulaire, de 4,50 m de largeur et de 3,50 m de hauteur. La longueur de veine de section constante est de 11 m.

Le diagramme Nombre de Mach - Pression génératrice maximale de la soufflerie est donné figure 2.

Un élément de la veine d'essai, d'une longueur de 8 m, est mobile, et peut être translaté sur un chemin de roulement perpendiculaire au circuit. Cet élément ou chariot, comporte lui-même une partie interchangeable, ou palette, qui constitue le plancher de la veine, selon le schéma de la figure 3.

Plusieurs palettes, supports de différents montages, peuvent ainsi être introduites alternativement dans le circuit.

Hors circuit, ces palettes viennent se ranger dans des alvéoles séparées, dites alvéoles.

Cette disposition permet de préparer les essais sur les différentes palettes dans des conditions assurant le secret des maquettes.

L'installation, représentée dans son ensemble figure 4, comporte 5 alvéoles et 4 palettes, l'un des alvéoles étant utilisé comme banc de tarage des mesures d'efforts pour les différents montages.

Sur les 4 palettes, trois sont actuellement équipées. Ces équipements, secteur porta-dard, tables et supports divers pour montages au plancher, murs verticaux d'écartement réduit avec aspiration de couche limite, pour essais de profils en courant plan, etc... sont décrits réf. [1].

Chaque palette est munie d'un ensemble indépendant de 64 voies de mesure, et d'un ordinateur HP 2100 pour le pilotage des mesures, le contrôle des voies, l'acquisition des données, et la liaison à l'ordinateur central.

Le système de mesure est directement connecté à l'ordinateur central quand la palette est soit placée dans l'alvéole de préparation de l'essai, soit dans sa position d'essai en veine, ce qui permet d'assurer une préparation complète de l'essai hors veine, et un temps de transfert de l'ordre de la 1/2 heure entre la fin de la préparation de l'essai en alvéole, et les premières mesures en veine.

La palette étant en veine, les mesures sont relayées dans la salle de conduite des essais, où les résultats traités par l'ordinateur central sont mis à la disposition des utilisateurs par des écrans cathodiques, des tabulateurs et des tables traçantes.

L'ensemble des résultats est par ailleurs enregistré sur disques, ce qui permet d'appeler le tracé du résultat d'un essai antérieur, pour comparaison avec le résultat de l'essai en cours.

Une bande magnétique des résultats est habituellement également remise à l'utilisateur.

Cet ensemble de moyens informatiques, et ses caractéristiques, sont décrites références [2] et [3].

La maquette étant en veine, et la soufflerie étant pressurisée, des cloisons mobiles, ou portes représentées sur la figure 3, permettent d'isoler la partie du circuit constituée par le chariot, et de dépressuriser seulement cet élément pour accéder à la maquette, ou éventuellement changer de palette. Cette disposition minimise le temps d'occupation de la veine, pour un programme d'essai donné.

2.2 - Montage d'essai de prise d'air d'avion civil

2.2.1 - Description du montage

Plusieurs demandes d'essais à grand nombre de Reynolds de prises d'air d'avion de type Airbus ont conduit à étudier et réaliser en un temps limité (délai inférieur à six mois) un montage utilisant au mieux certains éléments existants ; en particulier le principe a été retenu d'une maquette dont le débit est assuré par simple décharge à l'extérieur de la soufflerie, grâce à la pressurisation de celle-ci. Les dimensions du montage ont été déterminées pour obtenir un nombre de Reynolds d'essai proche de celui du vol, avec une limitation due à l'encombrement du circuit d'extraction. Celui-ci utilise comme élément principal le conduit de dépressurisation de la soufflerie, muni de son silencieux d'échappement. Il est complété par une déviation munie de son propre silencieux. L'ensemble du montage est représenté figure 5.

Le diamètre intérieur des maquettes étudiées est de 0,35 m au plan d'entrée compresseur. Ce diamètre est à l'échelle 1/5 de celui d'un moteur GPM.56, ou proche de 1/6 pour un moteur d'avion type Airbus A.310.

Avec une telle dimension de maquette, les débits réduits permis par le dispositif d'extraction sont un peu supérieurs à ceux des moteurs étudiés à leur régime maximum.

Un ordre de grandeur du débit maximum atteint en essais est de 75 kg/s à une pression géométrique de 3,85 bars.

Le nombre de Reynolds de l'essai sous 4 bars est donc de 4/5 de celui de l'avion à altitude nulle dans le cas du moteur GPM.56, ou de 4/6 dans le cas du moteur Airbus A.310.

Les nombres de Reynolds maximum d'essai, rapportés au diamètre intérieur de la prise d'air au plan compresseur, (soit 0,35 m) sont représentés figure 6, en fonction du nombre de Mach.

Les débits sont mesurés par deux débitmètres "Venturi" disposés respectivement sur les deux branches du circuit d'extraction. Ce partage du débit, imposé en fait par d'autres considérations, permet de faire des mesures plus précises dans le cas d'un faible débit, en faisant alors passer la totalité de celui-ci par un seul débitmètre, de dimensions réduites.

Le contrôle du débit est assuré par deux vannes pré-réglables disposées en parallèle sur le circuit d'extraction principal, et par deux vanes d'arrêt à l'extrémité de chacune des branches du circuit.

Une vanne d'entrée permet d'isoler l'entrée du circuit.

L'élément du montage supportant le moteur de l'entrée d'air est installé sur une des palettes de la soufflerie, ce qui permet la préparation de l'écoulement en alvéole.

La maquette est fixée à l'extrémité d'un support à rotule donnant un débatement de 35° d'incidence et de 10° de dérapage ; des vérins hydrauliques permettent de faire varier l'incidence et le dérapage en cours d'essai.

Ce support à rotule est placé soit face au vent, sur un support tubulaire de plancher coudé à 90°, pour les essais relatifs au vol en phases de décollage ou d'atterrissage, soit verticalement dans la veine, pour les essais relatifs à l'influence du vent transversal au point fixe ou à très faible vitesse. Des vues en sont données figures 7 et 8.

Par rotation à l'arrêt autour de l'axe vertical du support, le domaine d'essai peut être élargi comme indiqué figure 9.

Un équipement de maquette comprenait, à titre d'exemple, un ensemble de 108 prises de pression d'arrêt disposées sur des peignes dans le plan d'entrée compresseur, et donnant notamment les profils des couches limites internes, des capteurs de pression d'arrêt stationnaires installés de la même façon (40 capteurs montés sur 8 peignes), un ensemble de 200 prises de pression statique réparties sur différentes coupes radiales de la prise d'air, et 4 peignes de 12 prises de pression d'arrêt donnant un relevé des profils de l'écoulement externe au droit du maître-couple de la carène.

2.2.2 - Méthode d'essai

a) Mesures de répartitions de pression

Le débit de la prise d'air entraîne une chute continue de la pression génératrice de la soufflerie. Pour disposer néanmoins de points d'essais sans écarts sensibles de nombre de Reynolds, un fonctionnement par courtes rafales a été retenu, entre lesquelles la pression génératrice de la soufflerie est rétablie par le système général de pressurisation du circuit.

Les mesures de pression stationnaires sont obtenues par l'intermédiaire de commutateurs tournants. A chaque plot du commutateur, la pression mesurée est rapportée à la pression génératrice mesurée au même instant dans la soufflerie. Dans ces conditions, aucun décalage n'a pu être mis en évidence entre la mesure de la référence soufflerie, et la mesure des pressions données par les prises d'arrêt des peignes entrée compresseurs situées hors de la couche limite de la prise d'air. Les rapports de ces pressions, à la pression génératrice mesurée de la soufflerie, restent compris entre 0,999 et 1,001 et sont simplement représentatifs de la précision des mesures.

La mesure du débit s'effectue à partir des mesures classiques de pressions et températures au niveau des deux venturis du montage, en appliquant aux débits obtenus par les formules usuelles des mesures normalisées [4] un coefficient de correction établi par le tarage décrit au § 2.2.3.

Afin de réduire au maximum le temps de rafale, un ou deux essais préliminaires sont effectués en mesurant le débit, pour déterminer le réglage des vannes intermédiaires permettant d'obtenir le débit cherché. Ces vannes étant ainsi pré-réglées aux ouvertures voulues, l'essai proprement dit s'effectue par seule ouverture rapide des vannes d'arrêt à la sortie des conduits. Les mesures de pression par les commutateurs, d'une durée d'environ 10 secondes, commencent dès la fin du régime transitoire d'établissement du débit.

Un exemple de résultat de mesure est donné figure 10.

Pendant la durée de la mesure, la pression génératrice de la soufflerie décroît d'un peu plus de 1 %. La température génératrice de la soufflerie décroît également, par suite de l'effet de détente de l'air du circuit.

Le débit mesuré Q décroît simultanément. Le débit réduit mesuré de la prise d'air, $\frac{Q\sqrt{T_1}}{P_1}$, reste par contre bien constant, sans qu'il soit nécessaire de modifier le réglage des vannes pendant la durée des mesures.

La dispersion des mesures, de l'ordre de $\pm 0,2$ % du débit, résulte de faibles instabilités de l'écoulement observées au niveau des venturis.

L'écart de temps minimum entre deux points d'essai successifs, en incluant un point d'ajustement du débit, est d'à peu près 5 minutes.

b) Recherche de l'incidence limite de décollement à faible débit

La recherche de la limite de décollement externe en incidence à faible débit s'effectue par accroissement continu de l'incidence de la maquette, à débit réduit donné, et par mesures simultanées et continues d'un certain nombre de pressions stationnaires et stationnaires choisies sur la carène et sur les peignes externes.

L'expérience montre que l'apparition du décollement se traduit par un saut brusque et simultané des diverses pressions mesurées, celles situées dans la zone de décollement prenant toutes un même niveau, proche de la pression statique de l'écoulement général de la soufflerie.

Ce résultat signifie l'établissement brusque d'une large zone décollée, ce qui est caractéristique d'un décollement engendré par le bord d'attaque. La non représentation, sur la maquette, de la forme externe du fuselage au-delà du maître couple risque peu, de ce fait, d'être une cause d'erreur dans

la détermination de la limite de décollement externe du fuseau.

La forte discontinuité de l'écoulement à la formation du décollement externe implique en corollaire un hystérésis de celui-ci. A débit donné, le décollement persiste en effet sur une large plage d'incidence quand on réduit celle-ci en deçà de l'incidence où le décollement s'est établi.

Ce résultat montre que la technique d'essai qui consisterait à fixer la maquette à une certaine incidence (dans la plage d'hystérésis), et à établir ensuite de débit, ne permettrait pas d'obtenir la limite de décollement définie précédemment, et qui est celle, recherchée, de la prise d'air de l'avion, en cas de réduction du débit moteur à incidence donnée (atteinte sans décollement). On se heurterait en effet au phénomène d'hystérésis précédent, ou sous une autre forme : à l'incidence considérée, la configuration initiale, de débit nul, provoque le décollement externe, qui reste établi lorsque le débit nominal est progressivement établi, contrairement à ce qui se produit si le débit est d'abord établi à incidence nulle (ou réduite en deçà de la plage d'hystérésis).

Ceci est illustré figure 11 ou, selon l'incidence initiale de l'essai (10° ou 16°), la carène est soit sans décollement jusqu'à $27,5^\circ$ d'incidence, soit constamment décollée.

2.2.3 - Tarage des mesures de débit

L'utilisation de venturis, d'une part, dont la précision absolue indiquée par la norme [4] est au maximum de $\pm 0,5\%$ (abstraction faite des erreurs dues à la précision des mesures de température et de pression), et dont l'installation n'est pas conforme aux indications de la norme en ce qui concerne les conduites amont et aval, et d'autre part, le fait que l'écoulement n'est pas strictement en équilibre par suite de l'évolution des pression et température génératrices au cours des mesures, ont conduit à réaliser des essais de tarage des mesures de débit, en remplaçant simplement les prises d'air essayées par des pavillons à col sonique.

Ces pavillons, caractérisés par un rapport de 4 entre le rayon de courbure de la génératrice au col et le diamètre du col, ont fait l'objet de calculs décrits référence [5], et prenant en compte l'effet de gaz réel (effet "viriel"), l'effet de courbure de la ligne sonique, et l'effet des couches-limites. La précision du débit ainsi déterminé est de l'ordre de $\pm 0,2\%$.

Les pavillons sont prolongés par des diffuseurs de façon à obtenir des profils d'écoulement interne assez peu différents de ceux de l'essai, au moins au voisinage de leur amorage (figure 12). Leurs diamètres de col sont de 0,32 ; 0,26 et 0,12 m.

Le tarage a été effectué en faisant passer le débit par le conduit principal seulement, puis par l'ensemble des deux conduits, le conduit secondaire n'étant utilisé dans les essais qu'en complément du conduit primaire.

Le coefficient de tarage obtenu pour le premier venturi a été exprimé sous la forme d'un rapport
$$\frac{\text{débit réel}}{\text{débit mesuré selon la norme}} = f(M_v),$$
 M_v étant le nombre de Mach au col du venturi. La valeur de ce rapport varie de 1 pour $M_v \leq 0,15$ à 0,96, pour $M_v = 0,6$.

Le tarage du venturi n° 2, utilisé à un nombre de Mach au col constant (débit limité par l'ouverture unique de la vanne de sortie), a conduit à un coefficient de tarage
$$\frac{\text{débit réel}}{\text{débit mesuré selon la norme}} = 1,02.$$

L'incertitude du débit ainsi mesuré, compte tenu d'une certaine dispersion des résultats, est estimée de l'ordre de $\pm 0,5\%$. Des points de mesure plus nombreux et plus complets, avec certaines précautions supplémentaires pour les mesures de pression et de température, sont prévus pour préciser cette évaluation.

2.2.4 - Exemple de résultats

Différentes formes de prises d'air ont déjà été essayées, sous contrainte d'avionneurs et de motoristes. Les résultats étant propriété industrielle, seules quelques indications d'ordre général sont présentées.

Les essais concernant la qualification de l'écoulement interne n'ont été effectués qu'au nombre de Reynolds maximum. Ils permettent de connaître l'efficacité de la prise d'air (pression d'arrêt moyenne dans le plan compresseur rapportée à la pression génératrice amont) à différents débits, nombre de Mach, et incidences, et les coefficients de distorsion stationnaires et instationnaires.

L'influence du vent transversal (essais avec le montage "vertical" à 90° de dérapage) confirme les indications générales de fonctionnement présentées référence [6], et conduit au diagramme de la figure 13 : pour une vitesse donnée de vent transversal, V_N , un décollement s'exerce à faible débit; il se résorbe pour un débit plus important, puis réapparaît à grand débit, par suite du développement d'une zone supersonique avec recompression par choc autour du bord d'attaque de la carène face au vent.

Les essais concernant la recherche de la limite d'incidence sans décollement externe, à faible débit, (problème de traînée de l'avion en cas de panne de moteur au décollage) ont été réalisés à plusieurs nombres de Mach et nombres de Reynolds.

Les résultats montrent une influence très importante de ces deux paramètres. Un exemple (déjà présenté référence [1]) est reproduit figure 14. Il s'agit de résultats à un même coefficient de débit de la prise d'air, d'une valeur de l'ordre de grandeur de ceux d'un moteur en régime de moulinet.

A un nombre de Mach donné, l'incidence de décollement croît constamment avec le nombre de Reynolds, jusqu'au nombre de Reynolds maximum de l'essai. Un tracé logarithmique est proposé sur la figure pour extrapoler le diagramme jusqu'aux nombres de Reynolds de vol, ce qui est le plus usuel pour l'effet de ce paramètre. On peut toutefois hésiter sur cette façon d'extrapoler les résultats, une extrapolation linéaire étant également concevable. Une telle extrapolation donnerait une différence de l'ordre de 1 ou 2° sur l'incidence limite au Reynolds de vol à altitude nulle. Cette incertitude est à comparer à l'erreur que l'on commettrait en ne considérant que les résultats aux Reynolds les plus faibles de l'essai, à 1,5 bars de pression génératrice (nombre de Reynolds déjà très élevé, vis à vis de ceux pratiqués jusqu'à présent, compte tenu de la dimension de la maquette) : les écarts sont alors de l'ordre de 8°. Il faut aussi souligner que l'artifice consistant, à faible vitesse, à étudier l'effet du nombre de Reynolds en jouant sur la vitesse de l'écoulement, c'est-à-dire en faisant abstraction de l'effet du nombre de Mach, est ici totalement en défaut, le nombre de Mach ayant un effet très important, et contraire à celui du nombre de Reynolds, dès les plus faibles nombres de Mach.

Il est intéressant de présenter l'influence du coefficient de débit de la prise d'air sur l'incidence de décollement. Celle-ci est de la forme indiquée figure 15 (résultats présentés à iso-Reynolds).

On remarque d'une part que l'incidence de décollement croît linéairement avec le coefficient de débit, et, d'autre part, que la pente est relativement élevée : une incertitude de 0,1 sur le coefficient de débit se traduit par un écart de 2,5° sur l'incidence de décollement. Ceci pose le problème de la valeur du coefficient de débit imposé par un moteur en panne sur l'avion en vol à grande incidence, qui est en général mal connu.

2.3 - Prises d'air d'avion militaire

Les prises d'air d'avion militaire sont de dimensions nettement plus petites que celles des avions civils, mais elles ne peuvent être dissociées de l'ensemble de l'avion. Pour un avion de type Mirage 2000, il est toutefois possible d'étudier dans la soufflerie le comportement de l'avion complet à l'échelle 1/4, et, dans ce cas, le nombre de Reynolds de fonctionnement de la prise d'air est strictement respecté dans la soufflerie pressurisée à 4 bars.

La figure 16 présente un montage possible pour ce type d'essai.

3 - ESSAIS DANS LA SOUFFLERIE SIMA DE MODANE-AVRICUX

De part ses dimensions, la nouvelle soufflerie F1 de Fauga est complémentaire de la grande soufflerie SIMA de Modane, dont la veine fait 8 m de diamètre, et dont la pression génératrice est la pression atmosphérique : les mêmes maquettes peuvent être étudiées en subsonique élevé à SIMA, et à basse vitesse et pression génératrice de 4 bars à F1.

3.1 - Caractéristiques générales de la soufflerie

Cette soufflerie située au Centre d'essais de Modane-Avriceux de l'ONERA, dans les Alpes, est décrite référence [7].

La figure 17 en donne une vue générale.

La veine d'essai représente un tronçon de circuit de 8 m de diamètre, et 14 m de long. Ce tronçon est monté sur rails. Trois veines interchangeables existent, disposées comme indiqué figure 18, et permettant, comme au Fauga, d'assurer la préparation d'un essai pendant le fonctionnement de la soufflerie sur un autre essai.

Un nombre de Mach maximum proche de 1 peut être atteint.

3.2 - Montage d'essai de prise d'air d'avion civil

La figure 19 représente le montage d'essai de prise d'air d'avion civil, dans la veine d'essai n° 2. Un mât, fixé au plancher de la veine, supporte un conduit qui, à l'amont, reçoit le dispositif sur rotule de tenue et orientations en incidence et dérapage de la maquette de la prise d'air, et qui, à l'aval, se prolonge par un venturi, puis par un col de sortie de section réglable.

La partie amont du montage est décrite précédemment, du montage d'essai dans la soufflerie F1.

La figure 20 est une photo du montage dans la veine.

Le débit est assuré par l'écoulement naturel. Les essais ont montré que le débit représentatif du débit maximum du moteur pouvait être atteint à partir d'un nombre de Mach de 0,5.

Le venturi, qui précède un élément de section constante et un nid d'abeille destinés à régulariser l'écoulement, a fait également l'objet d'un tarage, de la même façon qu'au Fauga, c'est-à-dire en remplaçant la prise d'air par les cols soniques suivis de diffuseurs mentionnés au § 2.2.3. Les résultats de ce tarage ont conduit à considérer un rapport $\frac{\text{débit réel}}{\text{débit mesuré selon la norme}} = f(Mv)$, rapport variant de

1,025 à $Mv \leq 0,3$ à 1,01 pour $Mv = 0,6$.

La maquette étudiée peut comporter le même équipement qu'au Fauga.

Les mesures portent, pour une première part, sur la qualification de l'écoulement interne à différents nombres de Mach, incidences, dérapages, et débits réduits. Tous les points de mesure pouvant s'effectuer sans discontinuité, les résultats sont obtenus en peu de temps.

L'équipement standard de la soufflerie comporte 40 voies de mesure, qui peuvent être complétées par une deuxième chaîne de mesure, si nécessaire. Cet équipement est relié à l'ordinateur central qui, comme au Fauga, travaille en dialogue avec la soufflerie, et avec les mêmes terminaux.

La quantité d'information acquise nécessite toutefois de faire un choix sur les éléments à suivre en temps réel.

Les essais ont également pour but de préciser, si possible, la traînée de la prise d'air.

Celle-ci peut être obtenue à partir des bilans de quantité de mouvement entre le plan d'entrée compresseur et l'infini amont (pour le tube de courant passant par la prise d'air), de l'intégration des pressions sur tout le contour interne et externe de la prise d'air, et de l'évaluation des frottements sur la carène.

L'équipement de la maquette permet ces différentes évaluations, le frottement étant évalué par un calcul.

Le fait que la maquette ne reproduise la forme externe de la nacelle réelle que jusqu'au maître-couple, où le montage devient cylindrique, peut toutefois être critiquable pour évaluer cette traînée, si la courbure du fuselage réel dans cette région est assez prononcée pour que l'écoulement y devienne supercritique. Différents aspects de cette question sont discutés référence [8] et [9]. Dans le cas actuel des avions de type Airbus, cette limite n'est généralement pas atteinte, et l'étude de la traînée effectuée peut être considérée comme représentative, notamment en ce qui concerne l'influence d'une réduction du débit sur le développement de la traînée.

La présence de peignes externes permet également de détecter la formation d'une traînée à partir du relevé des profils de pression d'arrêt. Lorsque cette traînée devient importante, c'est-à-dire à Mach élevé et débit réduit, les ondes de choc qui terminant la zone de surdétente de bord d'attaque prennent toutefois une grande extension, et dépassent largement la hauteur des peignes utilisés. Une étude quantitative de la traînée par sondage externe nécessiterait alors un sondage sur une surface importante de la veine, selon la technique décrite référence [10], ce qui est peu praticable dans le cas notamment de prises d'air non de révolution.

3.3 - Essais de prises d'air d'avion militaire

En subsonique élevé, comme à basse vitesse, la caractérisation du fonctionnement des prises d'air d'avion militaire nécessite l'utilisation d'une maquette complète de l'avion.

La figure 21 montre une maquette de l'avion Mirage 2000 à l'échelle 1/4 installée sur le support tripode axial amovible de la soufflerie S1, dans la veine d'essai n° 1 munie de fentes longitudinales pour rendre la veine perméable, et permettre les essais en subsonique élevé de maquettes de taux d'obstruction relativement importants. Le support tripode est équipé, à l'amont, d'un mécanisme de mise en incidence et dérapage de la maquette qu'il supporte (débattement de 45° en incidence et 110° en dérapage).

La maquette est équipée pour l'étude de la prise d'air.

Dans le cas des essais en subsonique élevé, le débit naturel est suffisant pour représenter le fonctionnement réel de l'entrée. Un système d'extraction du débit par trompe existe également, pour forcer le débit dans le cas d'essais à grande incidence et nombre de Mach réduit.

La même maquette est utilisable au Fauga, les dards supports de maquette étant compatibles entre les deux souffleries.

Il faut par ailleurs signaler que la partie avant de la maquette comportant la prise d'air peut être placée dans la soufflerie S2 de Modane, pour étude de la prise d'air en supersonique. Ce montage est représenté figure 22 par la vue de la maquette dans cette soufflerie (veine rectangulaire, hauteur 1,935 m, largeur 1,75 m, nombre de Mach variable jusqu'à $M = 3$, pression génératrice variable jusqu'à 2,5 bars).

4 - CONCLUSION

Les montages d'essais de prises d'air d'avion civil, sur des maquettes de grandes dimensions, dans la soufflerie F1 pressurisée à 4 bars, et dans la soufflerie sonique S1MA, ont été présentés.

Les mêmes maquettes peuvent être essayées dans les deux souffleries dont les moyens d'essais sont complémentaires.

La même complémentarité existe pour les essais de prises d'air d'avion militaire à des nombres de Reynolds comparables au vol, sur des maquettes d'avion complet à l'échelle de l'ordre du 1/4.

REFERENCES

- 1 J.M. CARRARA et M. MASSON - Three years of operation of the ONERA pressurized subsonic wind tunnel - ONERA TP 1980 - 129
- 2 G. DELATTRE - Data acquisition and processing in a large aerodynamic test center - AIAA paper n° 78.774 (1978)
- 3 Ph. POISSON-QUINTON - Some new approaches for wind tunnel testing through the use of computers - First intersociety atlantic aeronautical conference - Williamsburg USA - 26-29 march 1979 - ONERA TP 1979 - 24
- 4 Association Française de Normalisation - Norme NF x 10102 (1971) - Mesure de débit des fluides au moyen de diaphragmes, tuyères et tubes de venturi
- 5 B. MASURE, J.L. SOLIGNAC et P. LAVAL - Mass flow rate measurement by means of a sonic throat - ONERA TP 956 (1971) - Symposium sur les écoulements - Pittsburg May 1971 - Prétirage 1.3.115
- 6 J. LEYNAERT - Engine installation aerodynamics - AGARD Lecture serie n° 67 on prediction methods for aircraft aerodynamic characteristics 1974 -(with corrections in AGARD CP 150, 1974)
- 7 M. PIERRE - Caractéristiques et possibilités de la grande soufflerie sonique de Modane-Avrieux - NT ONERA n° 134 (1968)
- 8 J. LEYNAERT - Entrée d'air arrière-corps de fuselage moteur en transsonique - ONERA TP 943 (1971) - AGARD CP 83 (1971)
- 9 F. AULEHLA and G. BESIGT - Reynolds number effects on fore and aftbody pressure drag - AGARD CP 150 (1974)
- 10 E. CARTER - Experimental determination of inlet characteristics and inlet and airframe interference - AGARD LS 53 (1972).

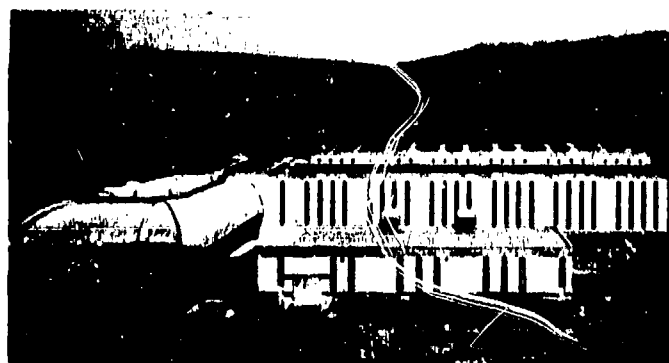


Fig. 1 - Soufflerie F1 de l'ONERA - Centre du Fauga-Mauzac

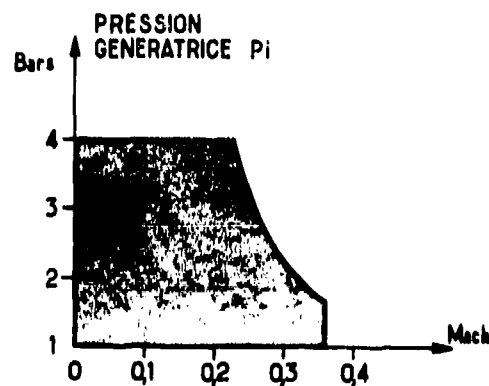


Fig. 2 - Domaine pression génératrice - Nombre de Mach de la soufflerie F1

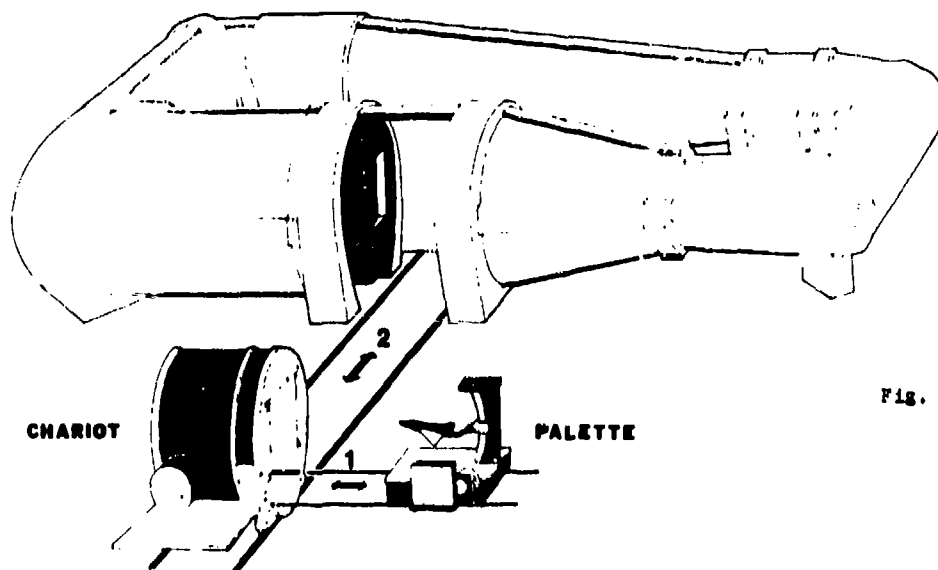


Fig. 3 - Schéma d'aménagement de la soufflerie F1

SOUFFLERIE F1

Fig. 4 - Plan général de la soufflerie F1

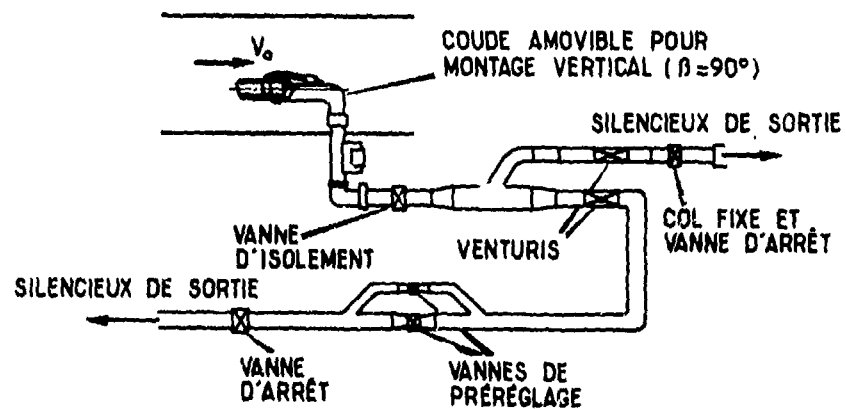
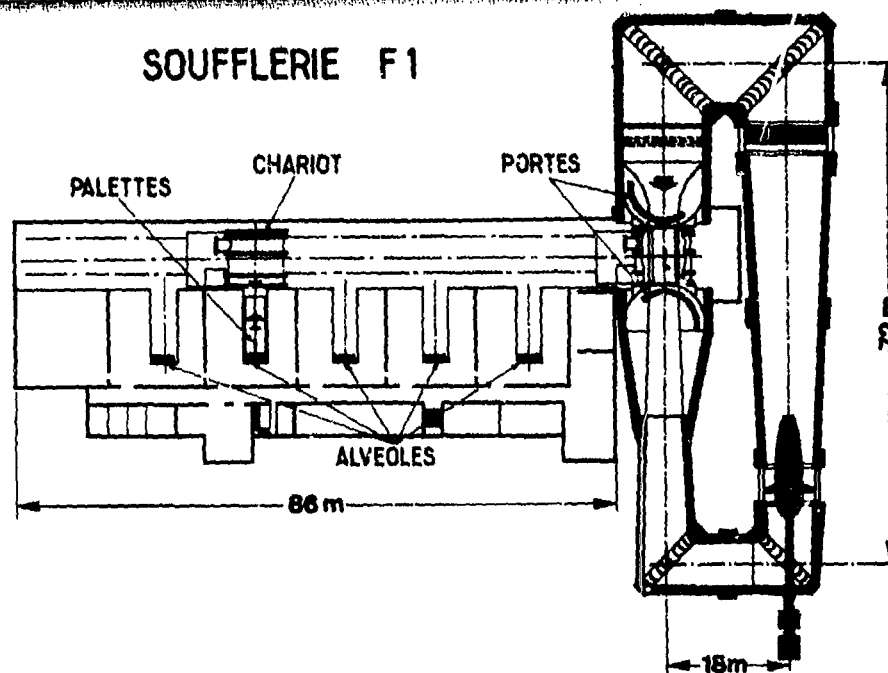


Fig. 5 - Montage d'essai de prise d'air à grande échelle

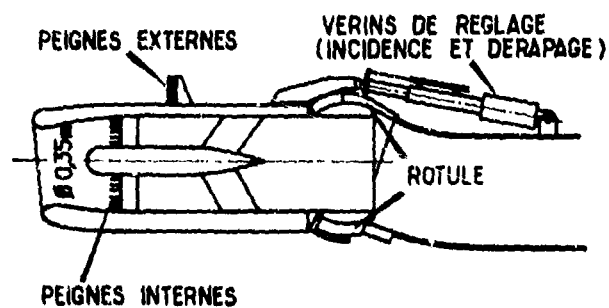


Fig. 6 - Domaine Nombre de Reynolds - Nombre de Mach pour les essais de prise d'air

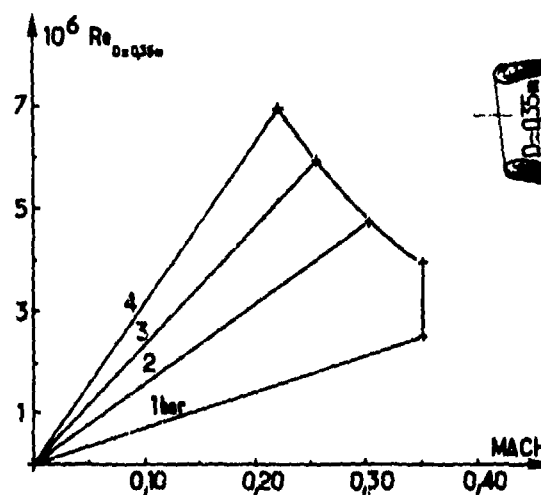




Fig. 7 - Montage d'essai de prise d'air face au vent - Vue en veine (porte fermée)

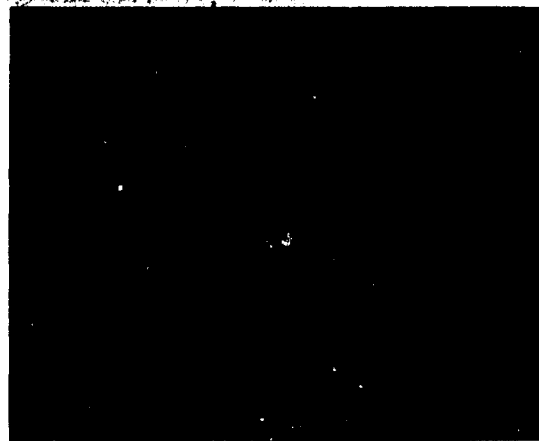


Fig. 8 - Montage vertical pour essai de de prise d'air avec vent transversal

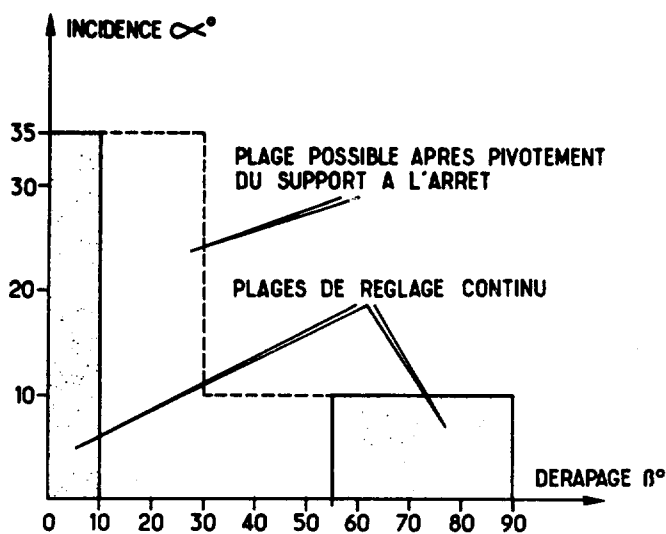
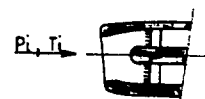
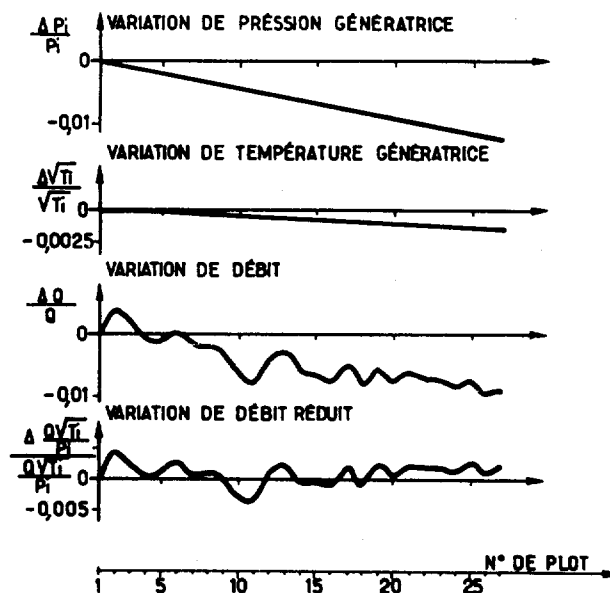


Fig. 9 - Domaine incidence-dérapage du montage d'essai de prise d'air

Fig. 10 - Evolution de l'écoulement pendant la durée d'un point de mesure (commutation de 27 plots à 3 plots par seconde)



$P_1 = 3,8 \text{ bars}$
 $T_1 = 290^\circ\text{K}$
 $Q = 62 \text{ Kg/s}$

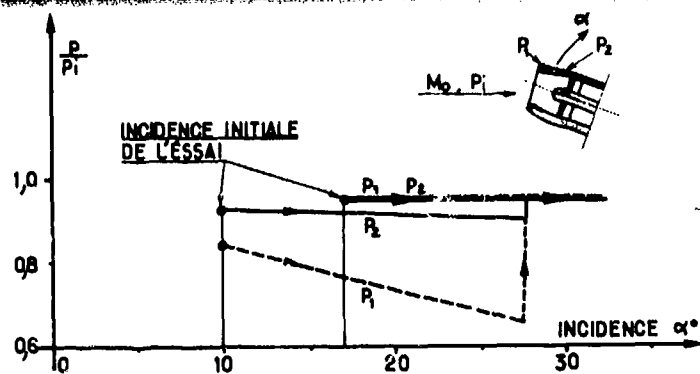


Fig. 11 - Hystérésis du décollement externe, à débit donné : influence de l'incidence initiale de l'essai

Fig. 12 - Pavillons à col sonique pour tarage du débit

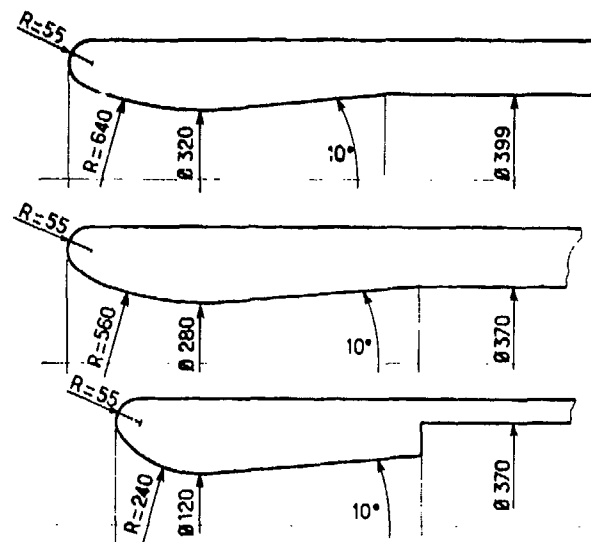


Fig. 13 - Schéma du fonctionnement de la prise d'air par vent transversal

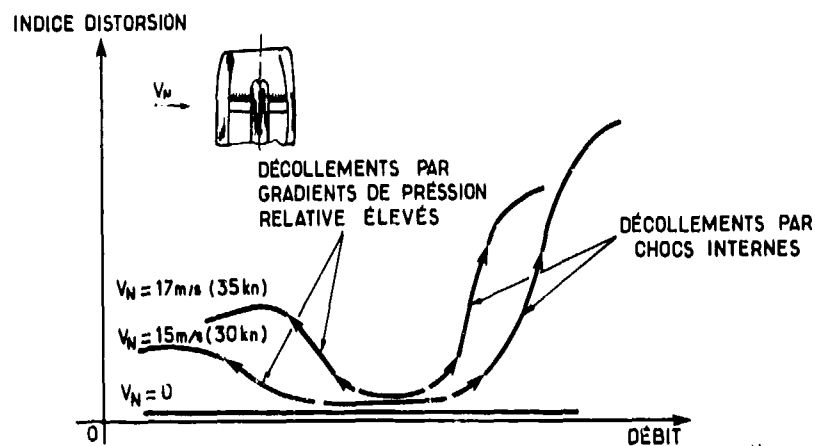
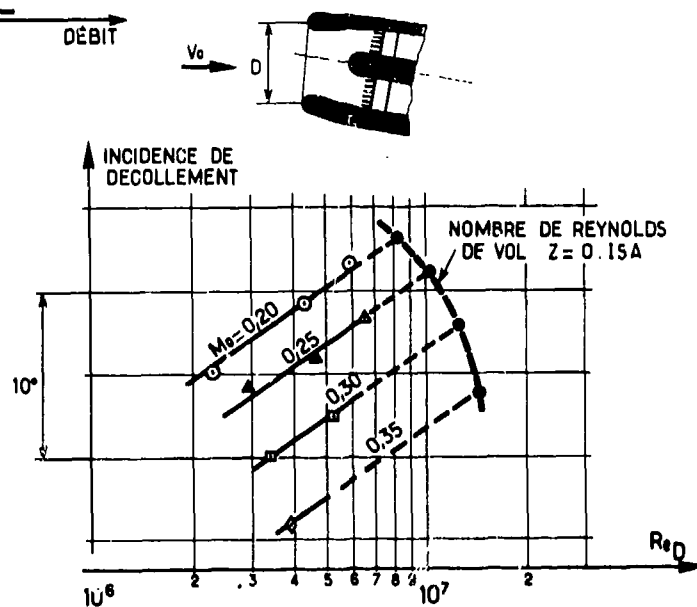


Fig. 14 - Influence du nombre de Mach et du nombre de Reynolds sur la limite de décollement externe, à coefficient de débit donné



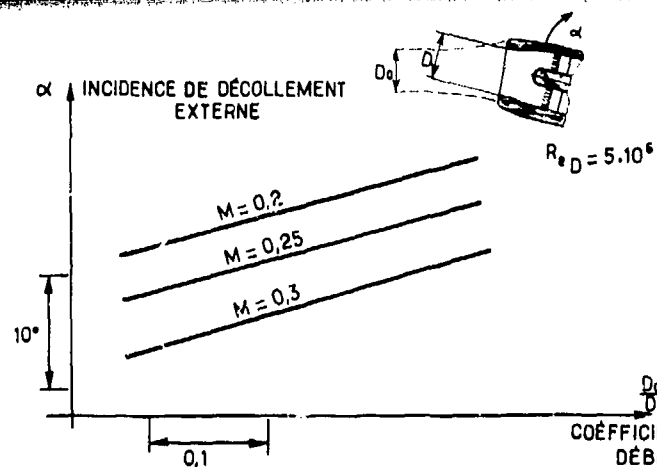


Fig. 15 - Effet du coefficient de débit sur l'incidence de décollement externe

Fig. 16 - Montage pour essai de prise d'air d'avion militaire (échelle $\approx 1/4$)

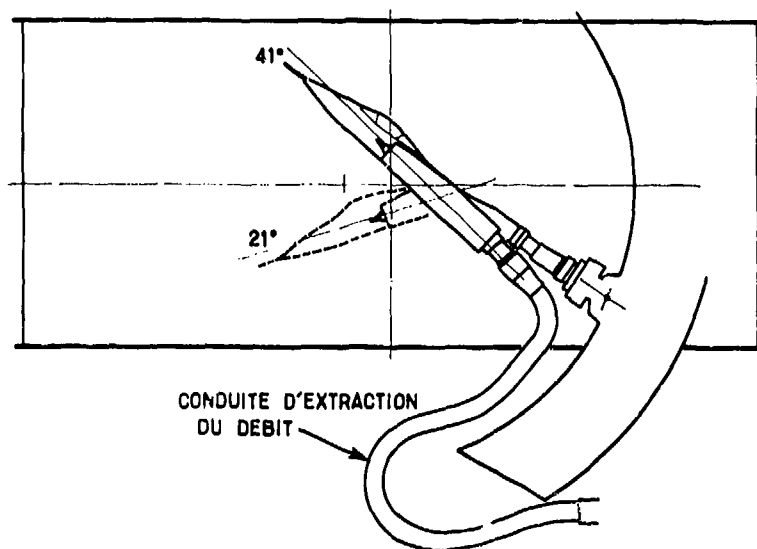
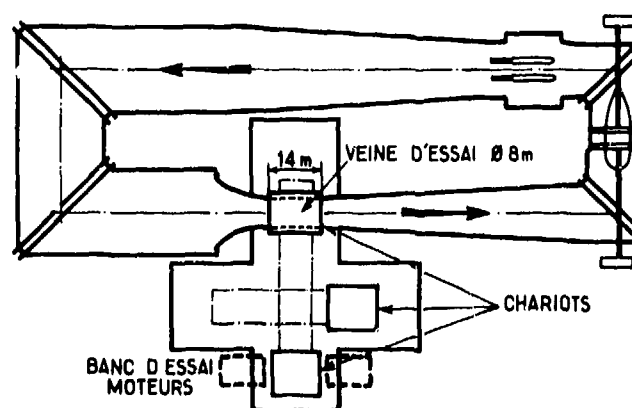


Fig. 17 - Soufflerie S1MA de l'ONERA - Centre de Modane-Avrieux

SOUFFLERIE S1MA

Fig. 18 - Schéma d'aménagement de la soufflerie S1MA



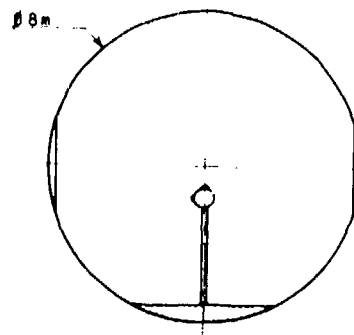
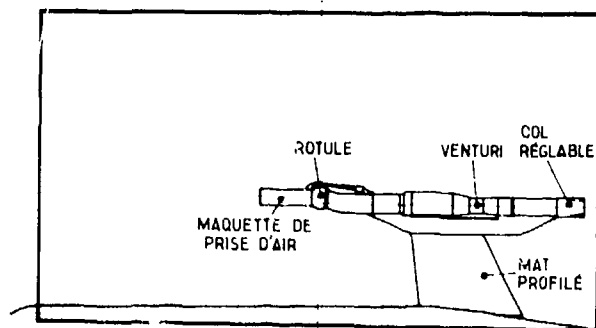


Fig. 19 - Montage d'essai de prise d'air à grande échelle



Fig. 20 - Vue du montage en veine



Fig. 21 - Essai de prise d'air d'avion militaire à l'échelle $\approx 1/4$ dans la soufflerie SIMA

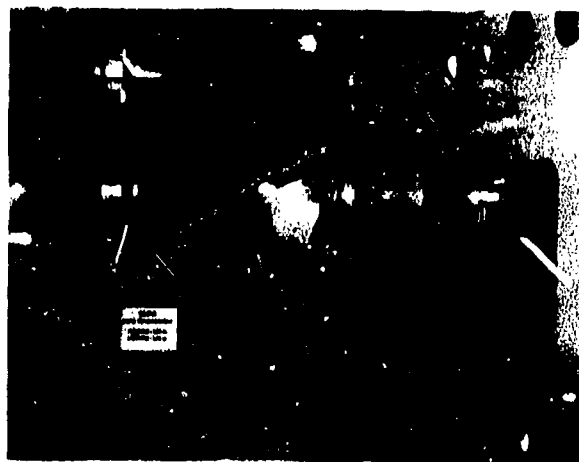


Fig. 22 - Essai de prise d'air d'avion militaire à l'échelle $\approx 1/4$ en supersonique (soufflerie S2MA),

THE INFLUENCE OF CLOSE-COUPLED, REAR FUSELAGE MOUNTED NACELLES
ON THE DESIGN OF AN ADVANCED HIGH SPEED WING

by

R.D. LAUGHER
Research Department
BRITISH AEROSPACE P.L.C.
AIRCRAFT GROUP
Hatfield-Chester Division
Hatfield, Hertfordshire

SUMMARY

An analysis of high speed wind tunnel data shows that the influence of close-coupled, rear nacelles on a wing with modern flow characteristics can lead to substantial cruise performance losses. This result is explained and contrasted with the favourable effects of rear nacelles observed on a wing designed in the early 1960's.

The design approach used on the first of a series of wings aimed at integrating the effect of the nacelle into the basic wing design is described. Particular attention is drawn to the design risk associated with the modified inner wing super-critical flow development when nacelles are not represented in the transonic design calculations. Experimental results from tests on this wing are then described which demonstrate how generally successful the design technique has been.

Finally, some results are presented from more recent theoretical investigations in which an attempt has been made to simulate the interference effect of the nacelle on the wing super-critical flowfield. In this work, a technique has been developed whereby the nacelle and intake streamtube are replaced by an "equivalent interfering body", which is derived from sub-critical flow interference pressures. The results presented show that this technique provides a simple, cost effective tool for the super-critical design of a wing operating in the influence of a rear nacelle.

1. INTRODUCTION

The type of rear engined configurations favoured for many small jet aircraft, where the nacelles are mounted from the fuselage in close proximity to the wing, usually present a number of important aerodynamic design problems associated with the powerplant installation. Of these, the principal areas for consideration are:

- (i) interference effects from the nacelle and intake streamtube on wing flow development
- (ii) minimisation of nacelle installed drag, which requires the avoidance of shocks and/or separated flow in the channels between the nacelle, pylon and fuselage
- (iii) exhaust plume interference on the empennage and aft fuselage
- (iv) avoidance of intake performance losses, or even engine stalls, that can arise from the ingestion of separated flow wing wakes, particularly at high lift conditions and around the buffet boundary.

The subject of the present paper covers only the first of these topics and, in particular, will be concerned with the high speed wing design implications of such nacelle/wing interference effects.

A brief description will first be given of the nacelle/wing interference as observed from wind tunnel tests and, it will be shown that, for a wing with modern aerodynamic characteristics, the nacelle influence is likely to be unfavourable. The magnitude and importance of this effect will be indicated where, for close-coupled configurations, it can be expected that the interference losses on wing performance are likely to be greater than the corresponding effects generally encountered with underwing engine installations on transport aircraft.

On the basis of these observations, a research wing, designated HH5, was designed in 1978 in which an attempt was made to overcome these performance losses by incorporating an allowance for the nacelle/wing interference in the basic design. A broad outline of the design approach adopted on this wing is given in the second section of the paper, together with some experimental data from wind tunnel tests which show the generally encouraging results obtained.

Whilst these results confirm the validity of the concept of the integrated nacelle effect wing, a shortcoming in the design approach adopted for the initial wing HH5, was the absence of any nacelle representation in the transonic flow design calculations done at the time. In the final section of this paper some results are presented from more recent theoretical work in which the nacelle interference effect on the wing super-critical flow is simulated, using an approach where the nacelle and intake streamtube are replaced by an "equivalent interfering body". The geometry of this body is derived from measured sub-critical interference effects but, in principle, could alternatively be obtained from sub-critical panel method calculations.

Figure 1 shows measured chordwise pressure distributions at a number of stations across the span of a wing, and compares the clean wing (i.e. nacelles-off) flow to that in the presence of a through-flow nacelle, at the same overall lift coefficient. The data is taken from high-speed wind tunnel measurements on a model designated N13, made at ARA Bedford under the joint sponsorship of British Aerospace and Rolls-Royce. An analysis of these tests is given by Hutton in ref.1. The nacelle, as shown in the figure, is located in the most forward position tested, with the intake plane coincident with the wing local trailing edge. The conditions shown are for a typical cruise mass flow ratio and a Mach number of 0.82. It is clear that the presence of the nacelle has a major influence on the wing characteristics. The primary effect of the nacelle and decelerating intake stream has been to impose a pressure field over the rear upper surface region of the wing ahead of it. The resulting reduction in suction levels on the rearward wing upper surface are obviously greatest over the inboard wing region, and require an increase in incidence of 1.4 to restore the associated loss in overall lift. The most significant feature of the comparison, however, is the substantial increase in shock strength that is apparent across the entire span for the nacelles-on case, and it is clear that this could be expected to lead to a marked deterioration in performance. It should be said, however, that no attempt was made in these tests to optimise the nacelle/pylon pitch setting angles and, for the case shown, a small download on the nacelle/pylon has been estimated. It could be expected, therefore, that a small reduction in wing performance interference loss could be made through an optimisation of the nacelle settings.

Figure 2 shows a similar comparison of nacelle effect on the N13 model, in this case with the nacelle located one intake diameter downstream of the wing local trailing edge. Since this position was the intermediate of three nacelle locations covered in the tests, it will be referred to here as the "mid" position. It can be seen that, as would be expected, the effects are rather less severe than for the forward nacelle position. As before, an incidence increase (0.67) is necessary to restore the loss in overall load due to the nacelle interference on the inner wing. In contrast to the forward nacelle, there is now little change in shock strength on the inner wing and the small increase in local Mach number at the shock is tending to be offset by comparable improvement in shock sweep. The nett increase in shock strength is essentially confined to the wing outboard of the planform crank.

The effect on overall wing performance of the above changes in flow characteristics are shown in Figure 3 for the "mid" nacelle location. The nacelles-on data has been corrected for the estimated nacelle download to avoid exaggerating performance changes associated with non-optimum nacelle/pylon settings. It is apparent from Figure 3 that there is a significant penalty due to nacelle interference for this wing in terms of both buffet and drag rise performance. For a buffet limited project, the effect amounts to a 5½% increase in wing area and the reduction in drag rise Mach number is around 0.02 in typical cruise Mach number. Unfortunately, insufficient data existed for a similar comparison to be made with the forward nacelle, but from Figures 1 and 2 it might reasonably be inferred that the losses would be substantially greater than for the "mid" nacelle configuration.

At this point then, it might be concluded that nacelle interference for close-coupled rear nacelle-wing configurations will generally have a large unfavourable effect on wing performance. This is not always the case, however, and it can be shown that the performance effect depends crucially on basic wing flow characteristics as well as the relative size and location of the nacelle. As an example of this, drag data from wind tunnel tests are presented in Figure 4, which show the influence of rear nacelles on an early 1960's wing design. The effect of the nacelle can be seen on the drag development with Mach number for a typical cruise value of lift coefficient. It is evident that the nacelle interference effects (which incidentally are more closely coupled than Model N13 "mid" nacelle) are beneficial and increase the drag rise Mach number by approximately 0.015.

Why the sign difference in the performance change due to nacelles for the two models? The answer is in the difference in clean wing flow characteristics between the two wings. This is depicted schematically in Figure 5. For both wings, the presence of the nacelle leads to a reduction of aft suction level over the upper surface of the inboard wing, with an associated improvement in local shock sweep and a reduction in aft loading which requires an incidence increase to restore the overall lift. However, a major difference between the two wings is the balance of shock strengths developing across the span and the nature of the pressure distribution ahead of the shock.

Model N13 has features typical of what would generally be considered good practice in modern wing design. The inner wing develops large regions of isentropically recompressive supercritical flow terminated by relatively weak shock waves, with the overall performance of the wing tending to be dominated by the somewhat stronger shocks developing on the outer wing. For this wing, with the nacelle in "mid" position, the inner wing contributes very little extra drag, as the shock here remains weak with the increase in shock local Mach number tending to be offset by the improved shock sweep; the outer wing, however, has an appreciably strengthened shock due to the incidence increase, and this leads to a significant overall increase in drag. This point is shown in Figure 6 on the basis of a comparison of the spanwise

wave drag distributions estimated from measured surface pressure for the clean wing and mid-nacelle position.

Returning now to Figure 5 and the early 1960's wing; the inner wing, whilst still being less critical than the outer wing, is characterised by relatively further aft and stronger shocks than N13. In this instance, the flow ahead of the shock is expanding and so the local Mach number at the shock is reduced as the shock moves forward due to the presence of the nacelle. The combined effect of the improved inboard wing shock sweep and reduced shock local Mach number yields a reduction in inboard shock strength, such that the increase in overall shock drag due to incidence is more than offset by the reduction of drag from the weaker inboard shock.

Clearly then, a modern wing which is designed to avoid the unfavourable nacelle interference as observed for Model N13, will require features which will lead to significant performance losses when the nacelles are not present. In embarking on the design of a new, integrated nacelle effect wing, it was hoped that, some twenty years on, this could be done in a more controlled and deliberate way than had been the case with the earlier designs.

3. THE HH5 WING DESIGN WITH INTEGRATED NACELLE EFFECTS

3.1. The Design Procedure

The discussion in the previous section highlighted the desirability for maximum cruise efficiency of allowing for the presence of a rear nacelle in the design of the basic wing characteristics. In this section of the paper, a brief description will be given of the design approach adopted on a recent research wing HH5, in which such an attempt to incorporate an allowance for the nacelle interference was made. The wing, which was developed for a moderately close-coupled rear engine configuration, was designed at British Aerospace Hatfield during 1978 and was subsequently tested in the 9' x 8' transonic tunnel at A.R.A. Bedford.

At the time of the HH5 design, no suitable method was available for computing the transonic flow development on a wing in the presence of a rear nacelle. In the absence of such a method, a hybrid design approach was used which involved the development of two wings in parallel.

The first of these wings was designed in isolation from the nacelle effects and was used to establish the "ideal" or target super-critical flow development and its associated wing geometry. A second wing, the nacelle-effect wing, was then derived on the basis of the following assumption:-

Two wings, one of which is in the presence of a rear nacelle, having identical planform and sub-critical pressure distributions, will develop approximately the same super-critical flow development as Mach number and/or incidence are increased.

Following this assumption, the design of the "nacelle-effect" wing was undertaken at essentially sub-critical flow conditions. Having first established a suitable sub-critical pressure distribution (close to "sonic rooftop" conditions) for the "ideal" wing, this pressure distribution was modified by subtracting from it the pressure field due to the nacelle, and the resulting wing pressures were then used in the design of the "nacelle effect" wing. In this process, the nacelle interference pressures were inferred from an analysis of the A.R.A. Model N13 wind tunnel data, using an approach similar to that described in Reference 1. Theoretical flow calculations done at this time using the method of Hardy, Reference 2, to estimate the nacelle interference effects, were found to be useful in giving the variation of spanwise loading changes due to nacelle location but, in detail, gave the wrong form and level of the chordwise distribution of pressure increments. Through this overall procedure then, the second wing was developed with modified camber, twist and thickness with the aim of producing sub-critical pressure distribution changes which hopefully would be exactly cancelled by the presence of the nacelle. In passing, it is perhaps worth noting that the resulting modifications to the thickness distribution of the wing yielded a very worthwhile bonus of a 2½% increase in fuel volume.

Figure 7(a) shows the sub-critical theoretical design pressure distributions for the two wings at a station just outboard of the nacelle. The flow computations were done using the contemporary version of the R.A.E. Inviscid Transonic Wing/Body program, Reference 3. A simple "strip" displacement surface correction was made to the wing ordinates in these calculations to allow for the gross viscous effects. It can be seen from the figure that the differences in the theoretical flows for the two wings are confined essentially to the upper surface aft of 30% chord. These differences are broadly in line with the N13 tests but the suction increments have not been maintained over the rear 20% chord as would otherwise be anticipated from that data. This was a deliberate act of caution in the light of the already severe trailing edge boundary layer conditions associated with the advanced section design standard of the basic wing.

The changes to the pressure distribution shown in Figure 7(a) appear relatively innocuous. Figures 7(b) and 7(c) show the corresponding flow development for typical long range and high speed cruise conditions respectively. For both cruise conditions,

the target flow is characterised by a large region of isentropic supercritical flow terminated by a relatively weak shock. On the integrated nacelle effect wing, with no nacelle representation in the calculation, there is an appreciable re-expansion in the upper surface flow terminated by a substantial shock wave which, although not shown here, increases in strength somewhat alarmingly further outboard. This stage in the design called for a strong act of faith!

3.2. Wind Tunnel Results

The first HH5 test series in the ARA High Speed Tunnel took place in September 1979. The wing was extensively pressure plotted and the tests covered a range of nacelle locations, giving the wing flow sensitivity to both nacelle height and longitudinal location. The data presented in this note is confined to the datum nacelle position on which the design was predicated (intake datum $0.25 \times D_i$ [nacelle intake highlight diameter /aft and $1.18D_i$ up from the local wing trailing edge.]

Figures 8(a), (b) and (c) show the effect of the nacelle on measured pressures at the station just outboard of the nacelle and are directly comparable with the theoretical conditions shown in Figure 7. The general agreement with the anticipated incremental effect of the nacelle is very good, although the reduction in suction level over the rear of the chord is rather greater than designed for. It can be seen that the aft shock for the nacelles-off case is remarkably well predicted and that the nacelle is having the desired alleviating effect in suppressing this shock.

Figure 9 compares the measured nacelles-on pressure distribution with the cruise cases with the theoretical target flows developed on the "ideal" wing. For the high speed cruise case, the level of agreement is very reasonable where the main features of the large region of supercritical flow terminated by a weak shock wave have been achieved, although the leading edge suction levels are appreciably higher than predicted. The same level of agreement cannot be claimed for the long range cruise case. Here, the greater than predicted leading edge suction levels result in a forward shock development where an isentropically recompressing flow was designed for. It can be seen in Figure 8(b) that this forward shock is a feature of both nacelles-on and off cases and is therefore not a failing in the procedure to design for nacelle effects. For all of the measured pressure distributions presented, it is also apparent that there is a shortfall in rear loading from the lower surface, although this again may well be associated with the very low wing nature of the model and the inadequate representation of the fillet in the flow analysis computations done at the time. The general loss of inboard load is summarised in Figure 10 which compares the target spanwise load distribution with the measured loadings.

3.3. Performance Effects on the Nacelle Effect Wing

Whilst the forward shock development and the loss of rear loading clearly leave some scope for further improvement on HH5, the general performance standard achieved by this wing in the ARA tests compares favourably with the best standards of contemporary advanced wings in the U.K.

Figure 11 shows compressibility drag and buffet comparisons for the new wing with nacelles both on and off. Also included in the figure are equivalent data from the N13 model with "mid" nacelles (suitably corrected for nacelle/pylon download). The nacelle interference effects are, as would be expected, favourable on drag for the new wing although the effect is rather more than anticipated at low values of lift coefficient and rather less at high values. It seems likely that this is associated with the double shock development on the inner wing. It is noticeable that the effects on the buffet boundary are much less than those shown earlier in Figure 3 for N13. Again, this may be explained by the extensive load associated with the aft shock on the inner wing for the nacelles off case, which will tend to offset the penalty of the strengthened outboard shock (particularly at the lower Mach numbers).

In considering the drag improvements achieved by HH5 relative to the N13 "mid" nacelle data, it should be borne in mind that roughly half of the apparent gain at low C_L could be attributable to the increased sweep of the new wing, although at higher C_L the sweep advantage will be largely offset by the much thicker inboard wing of HH5.

The improvement in buffet boundary is particularly rewarding since here the sweep differences clearly contribute much less to the gain for the new wing, as can be seen from the similarity in slope between the N13 boundary and a constant $M^2 C_L$ locus.

4. THEORETICAL SIMULATION OF REAR NACELLE/WING INTERFERENCE EFFECTS

Despite the generally encouraging results obtained for the HH5 wing design, there is little doubt that the inability to compute the transonic wing flow development in the presence of the nacelle introduced considerable risk into the design process. At present, the emphasis within the U.K. in the development of numerical solutions for the transonic flow about wing/powerplant combinations is being placed on providing solutions for underwing nacelle/pylon configurations. An alternative approach to the direct modelling of a wing-fuselage and rear nacelle has been developed, however,

and has been found to give very good results. This approach is based on the observed similarity in the measured nacelle interference effect and that which would be expected from a finite body located co-axially with the nacelle, and with its nose longitudinally in the vicinity of the wing trailing edge. The concept of simulating the interference effect by replacing the nacelle and intake stream with an "equivalent interfering body" has been developed at British Aerospace, Hatfield, using a program developed by Albane at the R.A.E., Reference 4. This program, which is an extension of the RAE TSP method and includes interactively calculated viscous effects, was originally intended to be used for the computation of the transonic flow about wing fuselages from which finite interfering bodies, such as weapon stores or external fuel tanks, could be mounted. As will be seen, it nevertheless appears to cope quite adequately with the present class of problem.

Figure 12 shows chordwise pressure distributions on the N13 wing at a station just ahead of the nacelle. The comparison is made at a freestream Mach number of 0.78 and a constant value of incidence giving subcritical flow conditions for each of the clean wing, forward and mid nacelle configurations. Figure 12(a) shows the computed pressures based on the "equivalent interfering bodies" as indicated in the diagram at the top of the figures. These bodies have been designed to simulate the measured effect of the nacelle on the sub-critical wing pressures, as shown in Figure 12(b). In each of the cases shown, the nose of the body is located at 85% of local wing chord and the maximum diameter of the body is approximately equal to the nozzle exit diameter (= intake streamtube diameter far upstream for the isolated through-flow nacelle). The principal difference between the bodies for the two nacelle locations is in the geometry of the forebody shape, where the fineness ratio's (L/D) are 1.09 and 1.67 for the forward and mid nacelles respectively.

The main test of the usefulness of this approach is how adequately the sub-critically derived interfering bodies can be used to simulate the effect of the nacelles for super-critical flow conditions. Figure 13 compares computed and measured wing pressures at $M = 0.78$ and 0.82 respectively, for conditions at which there exists substantial regions of super-critical flow on the wing. It can be seen that the computed flow reproduces remarkably well the main features of the nacelle interaction in terms of changes in shock strength and position and also the upper surface pressures over the rear of the chord. In Figure 14 a direct comparison of computed and measured wing pressures is given for the forward nacelle location at $M = 0.78$. A particularly encouraging feature of this figure is the way in which the measured spanwise variation of the nacelle effect is simulated by the numerical model. It is worth noting that some of the less favourable features of the comparison, such as the over-estimate of the super-critical flow at the root, have also been found for a similar comparison on the clean wing. It is felt that on the basis of experience with clean wing flow computations, see Reference 5, still better agreement will be obtained when the effect of the wing wake is included in the calculations.

On the basis of these very encouraging results it appears that, in the absence of a fully representative modelling of the rear nacelle, the equivalent body approach can provide a simple, cost effective alternative for the computation of both sub-critical and super-critical flows. The fact that the body is based on sub-critical flow interference effects means that, if no suitable experimental data is available, it could in principle be designed from sub-critical panel method calculations. With the range of experimental data now available, it is hoped that in the future it will be possible to establish an empirically based parametric definition of the body which relates it to nacelle size, location and mass flow ratio.

5. CONCLUDING REMARKS

The main points made in this paper can be summarised as follows:-

- (i) Rear nacelles located in close proximity to a wing exert a major influence on the wing flow development across a considerable extent of the wing span.
- (ii) For a wing with modern design characteristics, this influence is likely to be unfavourable and there is therefore a strong case to modify the wing geometry to allow for this effect.
- (iii) An integrated nacelle effect wing (HH5) has been designed with modified camber, thickness and twist. The results from high speed wind tunnel tests on this wing generally validate the design concepts used and demonstrate that the principal aim of designing out the unfavourable influence of the nacelle has been achieved.
- (iv) A technique has been developed, using the concept of an "equivalent interfering body", whereby it has been possible to obtain a very reasonable numerical simulation of the nacelle effect on the wing super-critical flow development. Although lacking the rigour of a fully representative modelling of the nacelle, the standard of the results produced and the simplicity of the computational procedures involved make this technique a very cost effective tool for the super-critical design of wings in the influence of rear nacelles.

REFERENCES

1. P.G.Hutton: "Some Observations On The Effects of Rear-Fuselage Mounted Nacelles On Wing Aerodynamics"
ARC 38.328 App. Aero 139
ARA Report No.55, (November 1979)
2. B.C.Hardy: "A Computer Program To Estimate The Interference On A Wing Due To An Engine Nacelle At Subsonic Speeds"
R.A.E. TR 75074, (July 1975)
3. C.M.Albone
M.G.Hall
Gaynor Joyce "Numerical solutions for transonic flows past wing-body combinations".
IUTAM Symposium Transonicum II,
Gottingen, (September 1975).
4. C.M.Albone: "Some examples of the use of the RAE TSP method for calculating flow past configurations consisting of a wing-fuselage upon which a variety of interfering bodies may be mounted."
RAE T.M. Aero 1845, (June 1980)
(Contribution to AGARD report on computational methods - to be published)
5. M.C.P.Firmin: "Calculations Of Transonic Flow Over Wing/Body Combination With An Allowance for Viscous Effects."
AGARD CP 291
Paper 8, (September 1980)

ACKNOWLEDGEMENTS

The author wishes to thank British Aerospace Public Limited Company for permission to publish this paper. Thanks are also due to Rolls-Royce Ltd. (Aero Division, Bristol) for permission to publish the wind tunnel data from the Model N13 tests. Finally, I should like to acknowledge the assistance given to me by my colleagues in the Research Department at B.Ae. Hatfield, particularly Mr.D.J.Littlewood who contributed much to the work described in the paper.

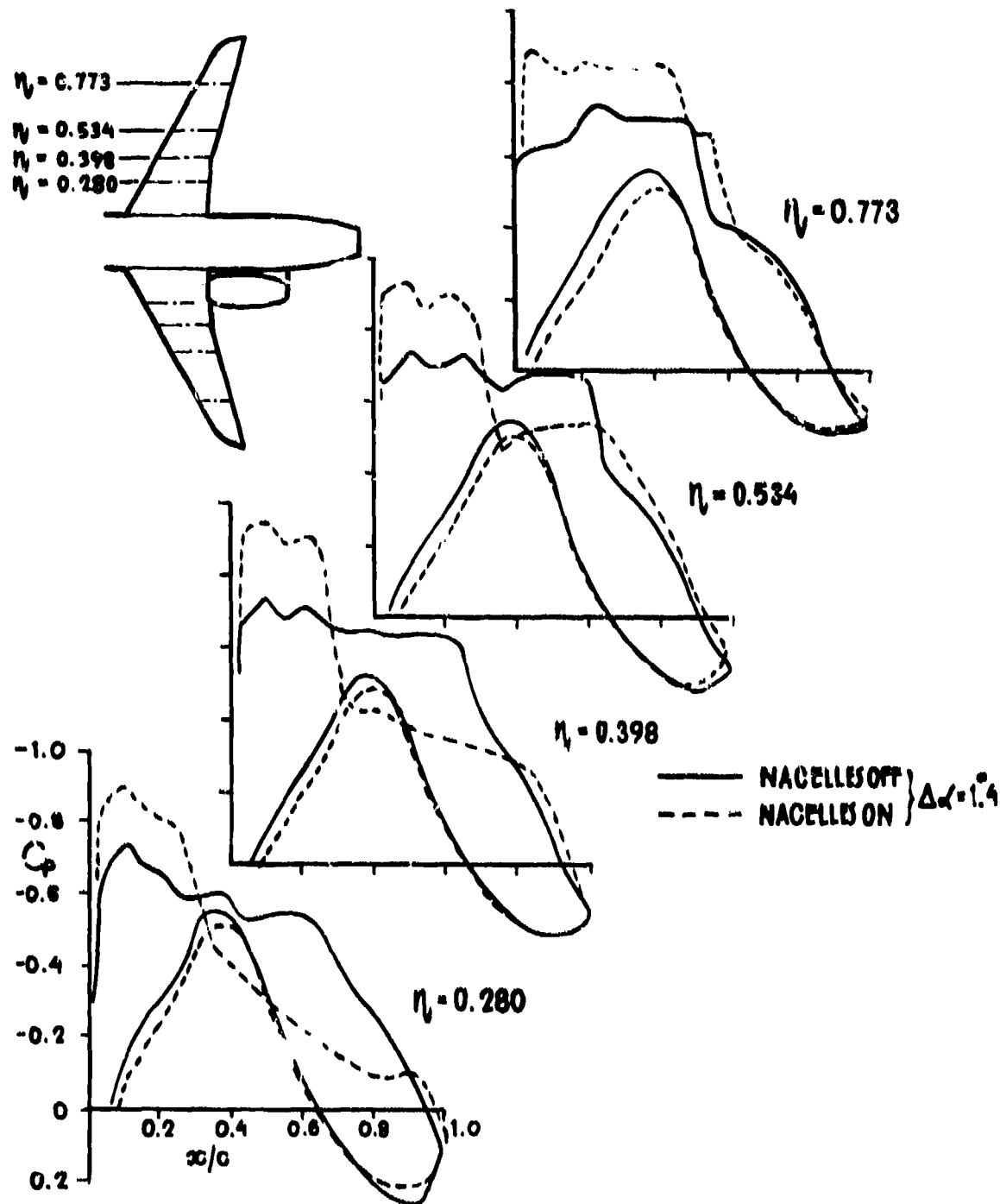


FIGURE 1. MODEL N13 "FORWARD" NACELLE EFFECTS ON WING PRESSURES
(Constant Overall Lift Coefficient)

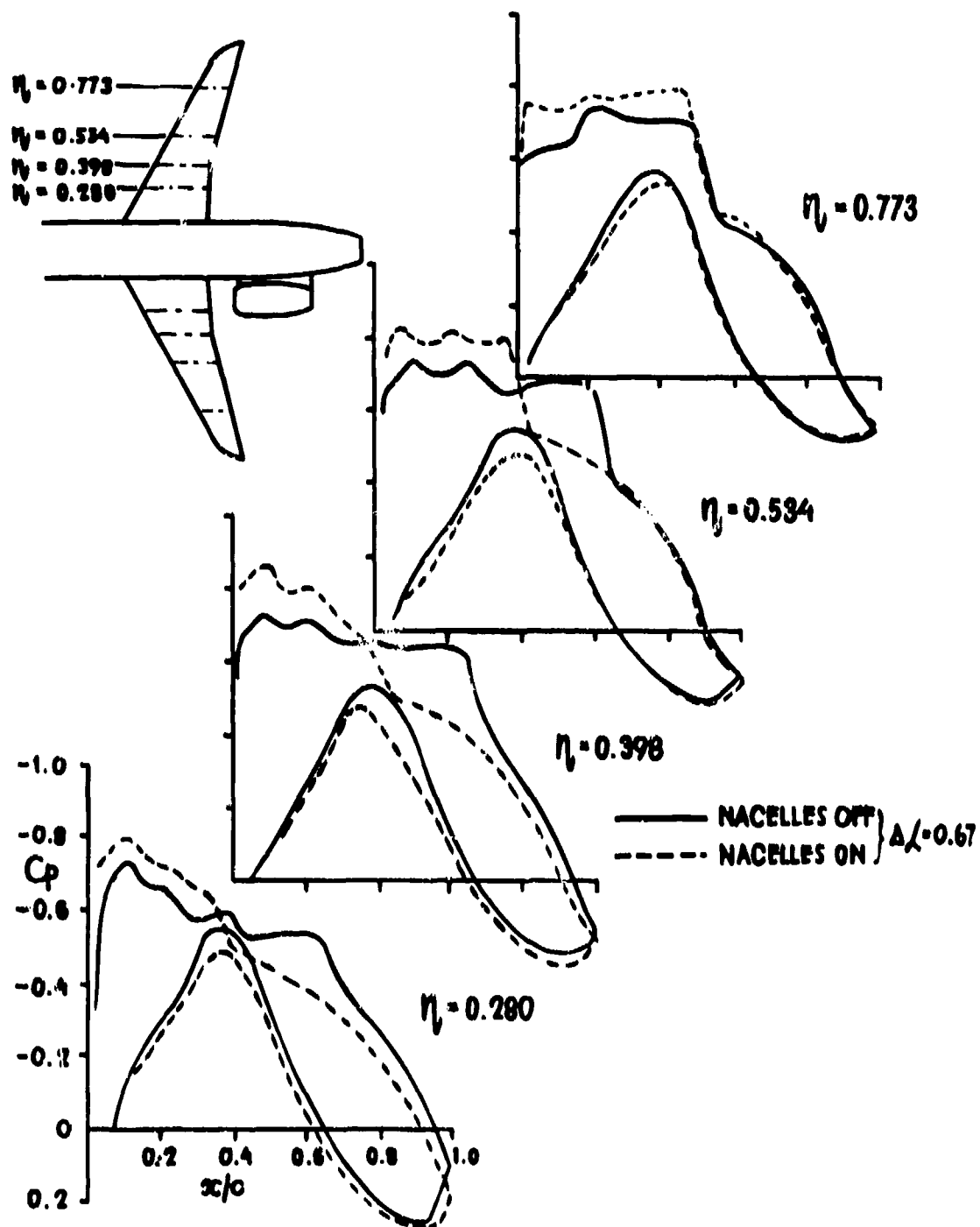


FIGURE 2. MODEL N12 "MID" NACELLE EFFECTS ON WING PRESSURES
(Constant overall lift coefficient)

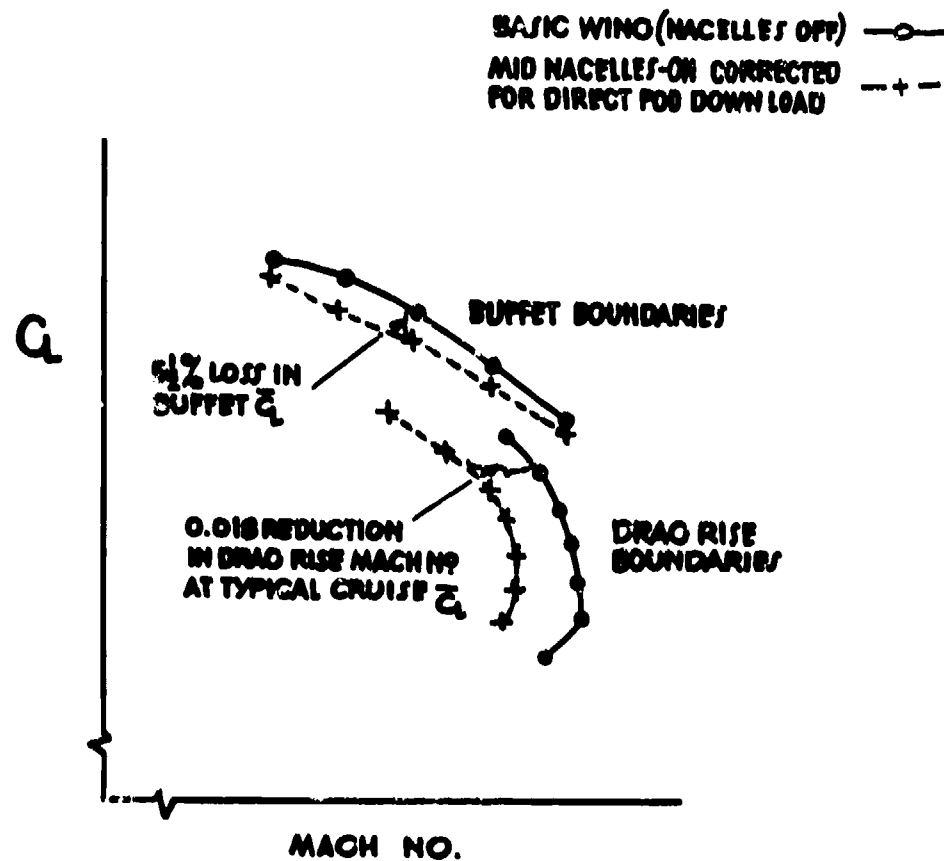


FIGURE 3. MODEL N13 "MID" NACELLE EFFECTS ON WING PERFORMANCE

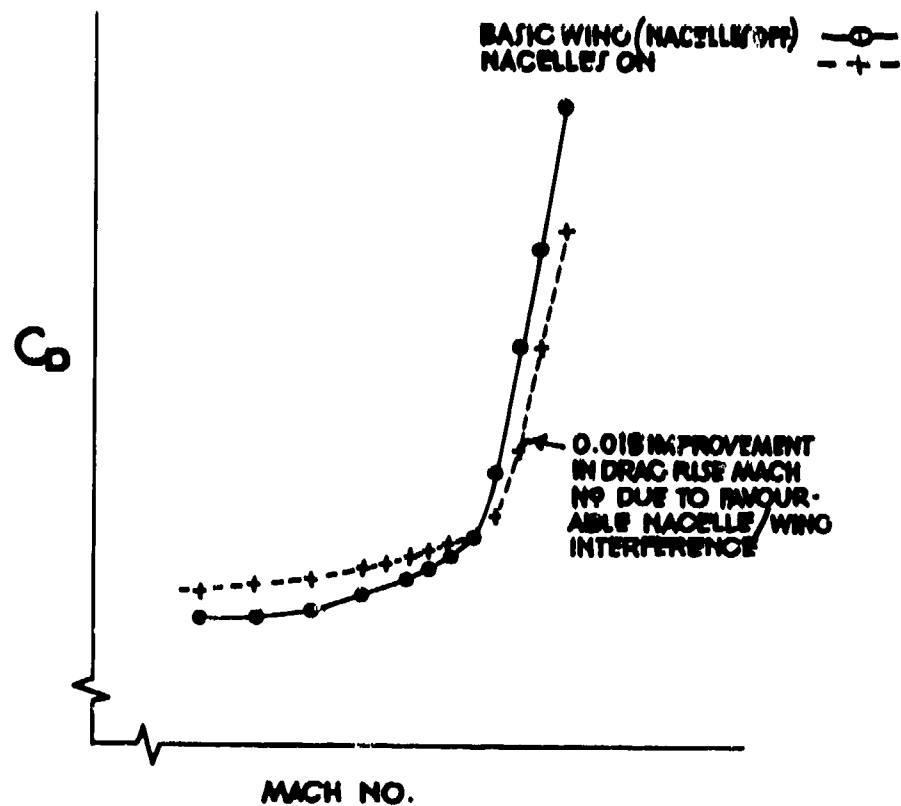
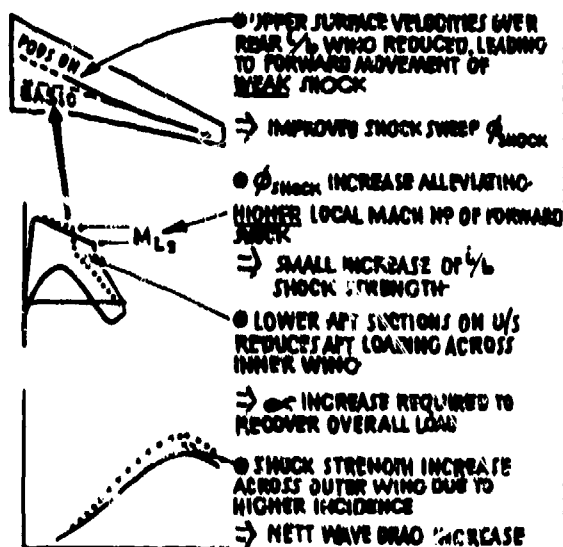


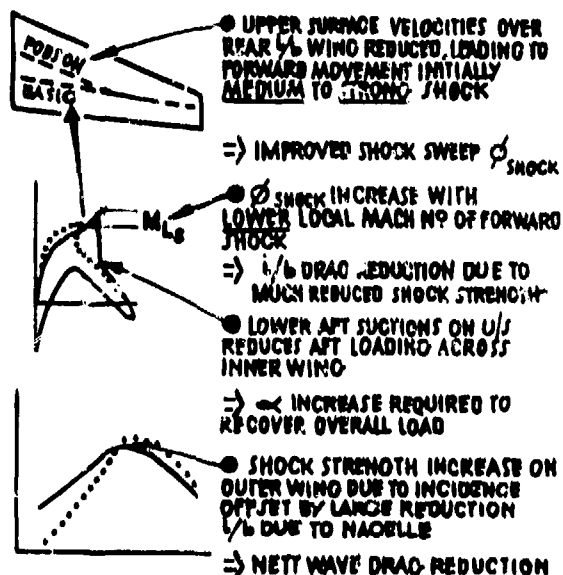
FIGURE 4. REAR NACELLE EFFECT ON DRAG FOR AN EARLY 1960'S WING
(Typical cruise C_L)

'MID' NACELLE EFFECTS :-



MODERN WING CHARACTERISTICS

NACELLE EFFECTS :-



EARLY 1960s WING CHARACTERISTICS

FIGURE 5. CONTRASTING NACELLE EFFECTS FOR DIFFERENT WING CHARACTERISTICS

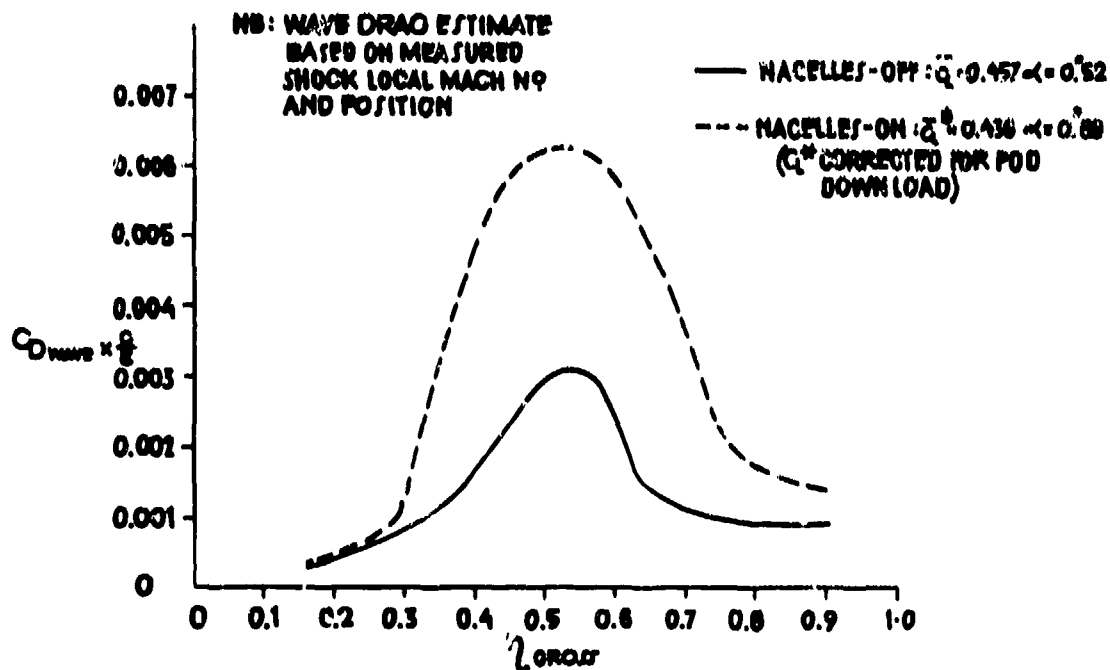
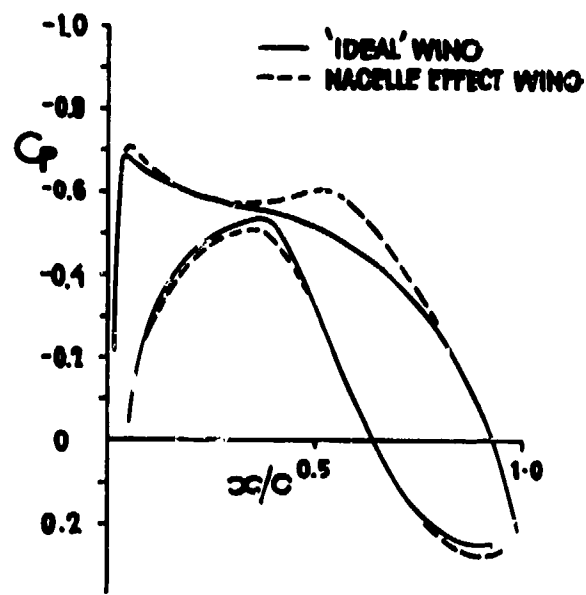
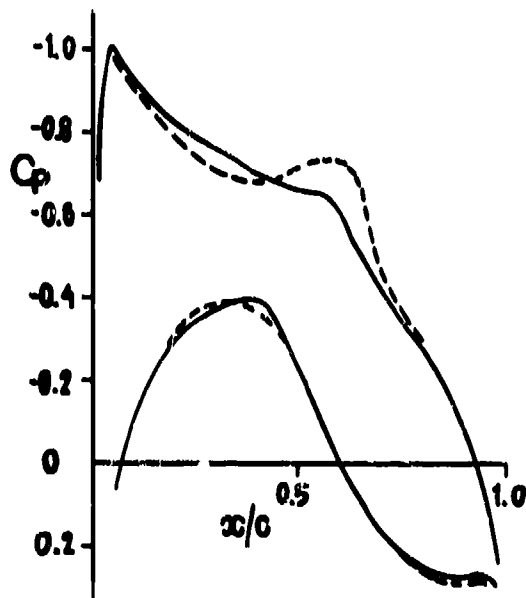


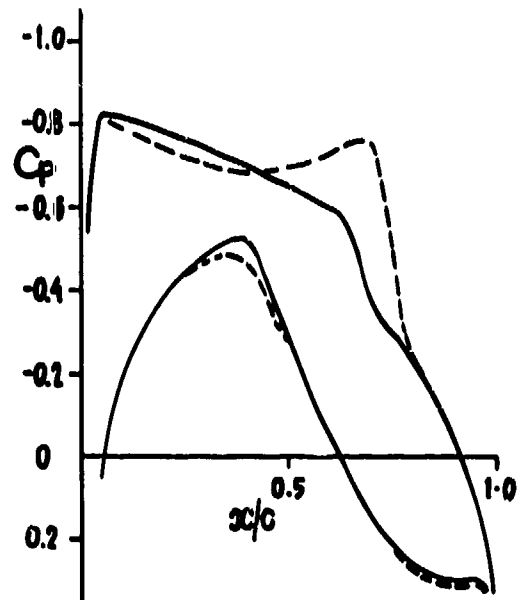
FIGURE 6. MODEL N13 "MID" NACELLE EFFECT ON SPANWISE WAVE DRAG DISTⁿ



(a) SUBCRITICAL



(b) LONG RANGE CRUISE



(c) HIGH SPEED CRUISE

FIGURE 7. COMPUTED HH5 WING PRESSURES JUST OUTBOARD OF THE NACELLE

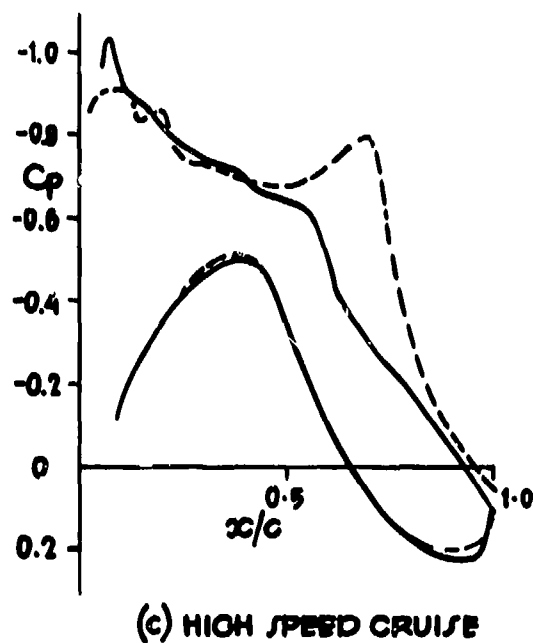
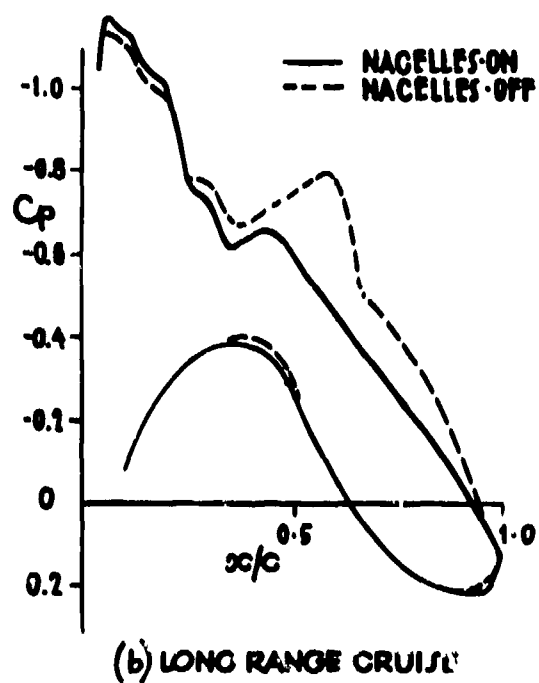
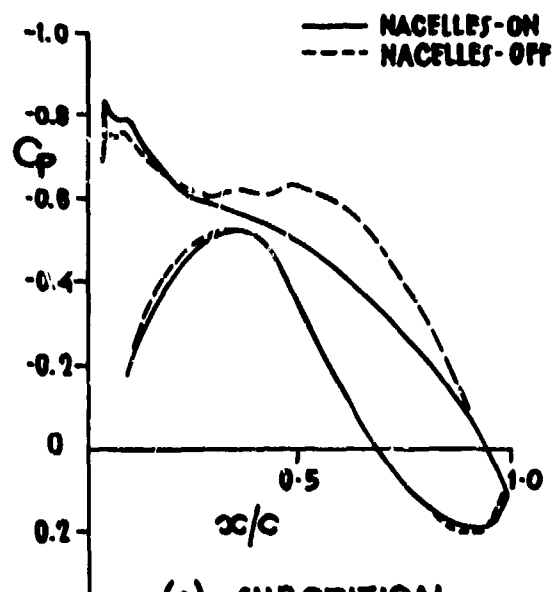


FIGURE 8. MEASURED HH5 WING PRESSURES JUST OUTBOARD OF THE NACELLE

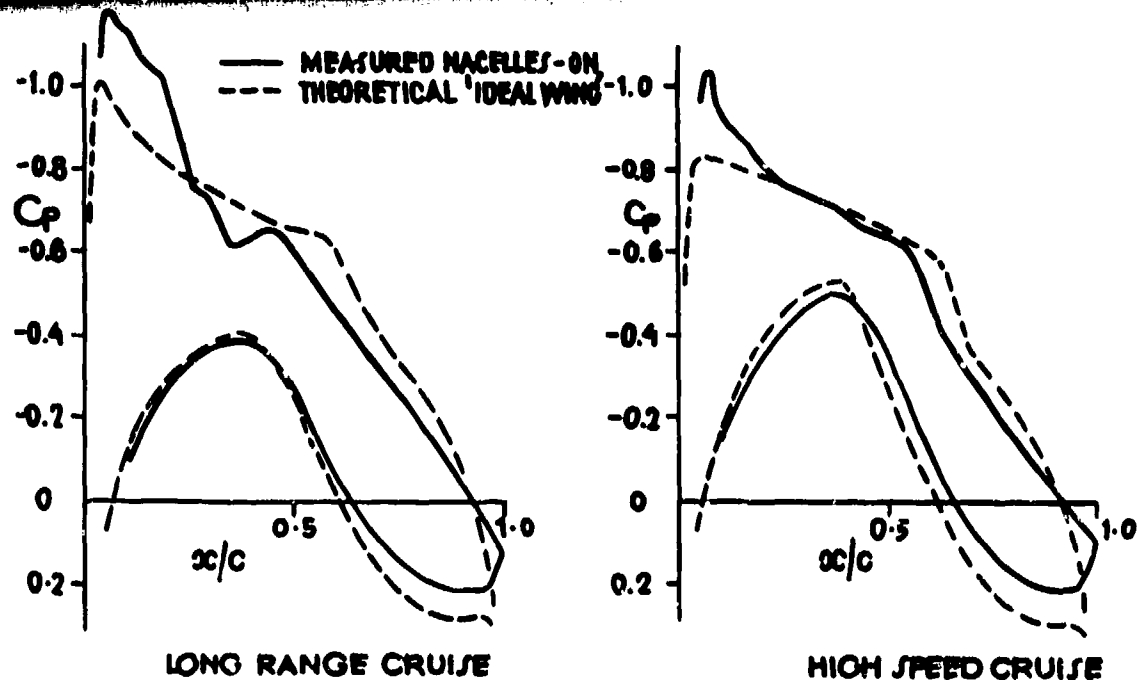


FIGURE 9. TARGET AND MEASURED HH5 "NACELLES-ON" WING PRESSURES
(JUST OUTBOARD OF THE NACELLE)

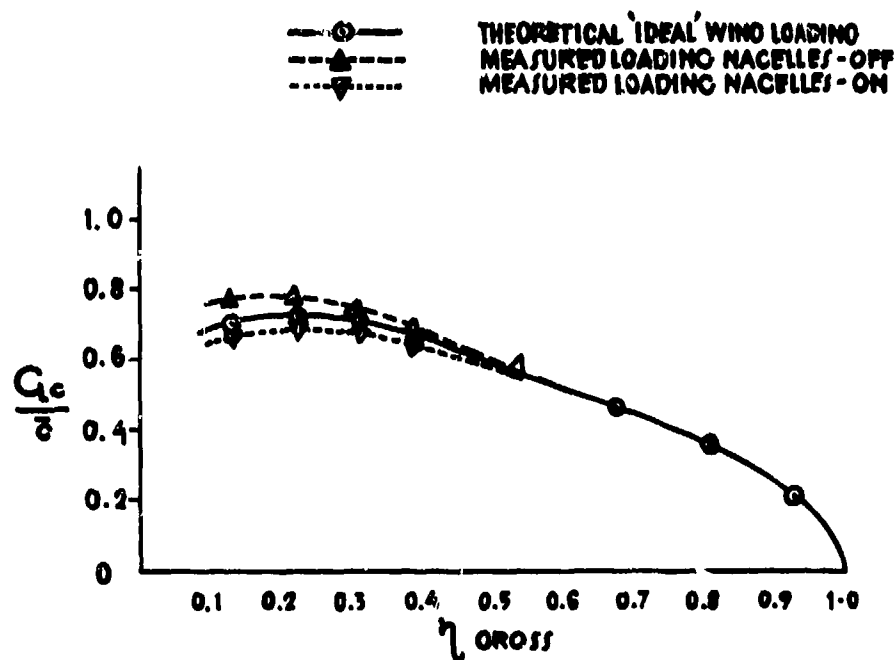


FIGURE 10. TARGET AND MEASURED HH5 SPAN LOADINGS

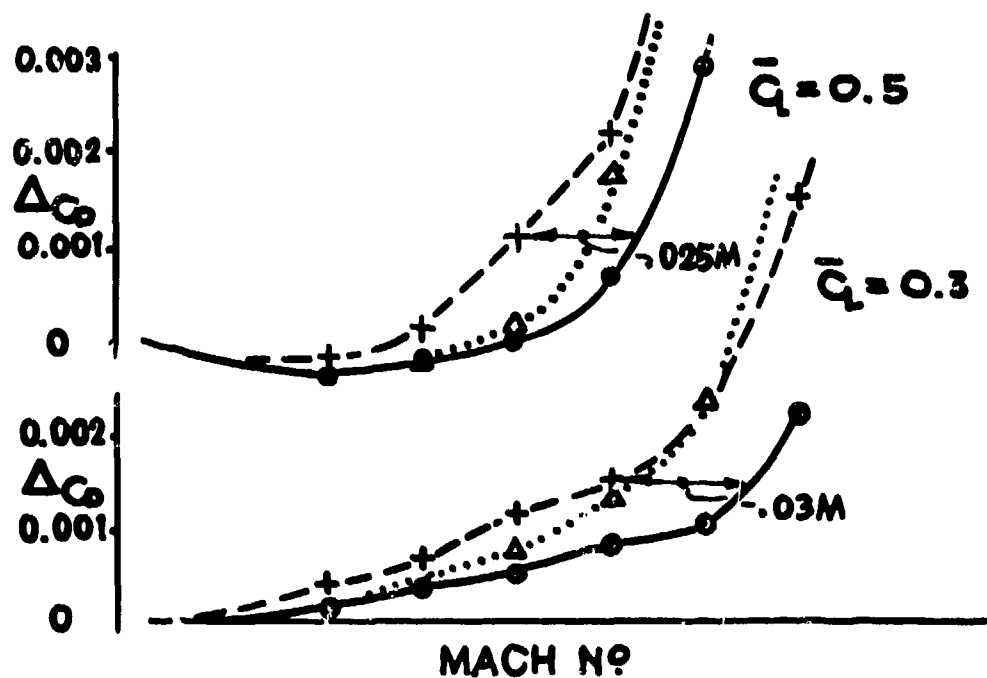
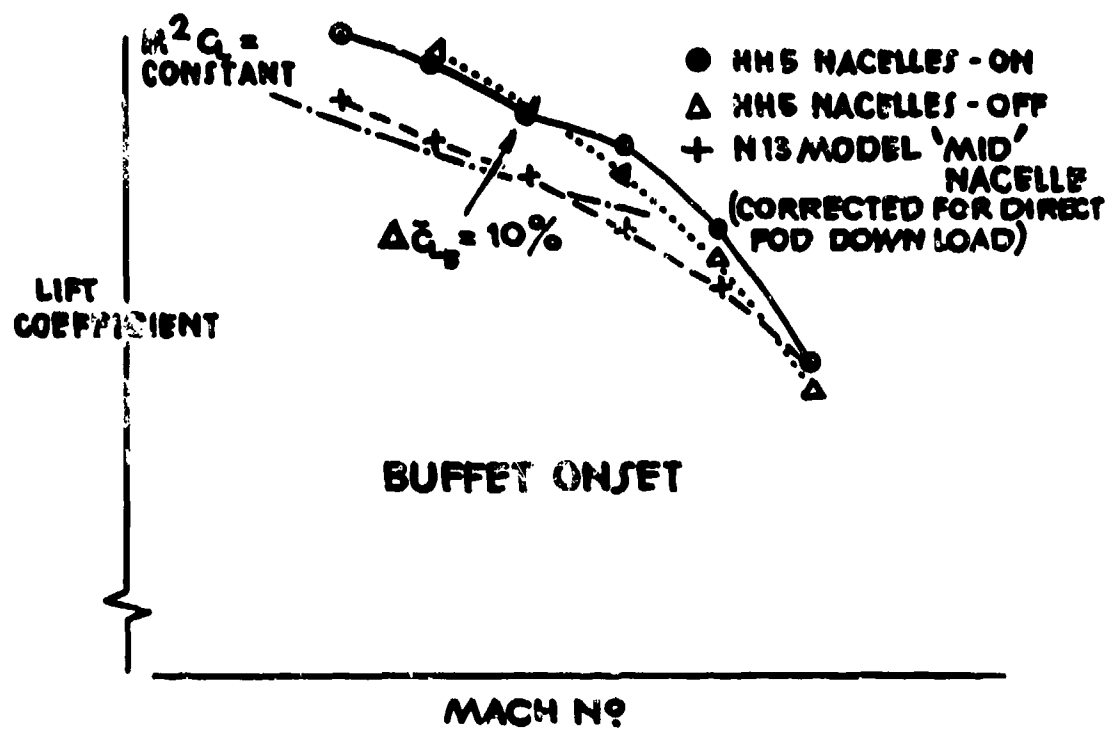


FIGURE 11. NACELLE EFFECTS ON HH5 WING PERFORMANCE

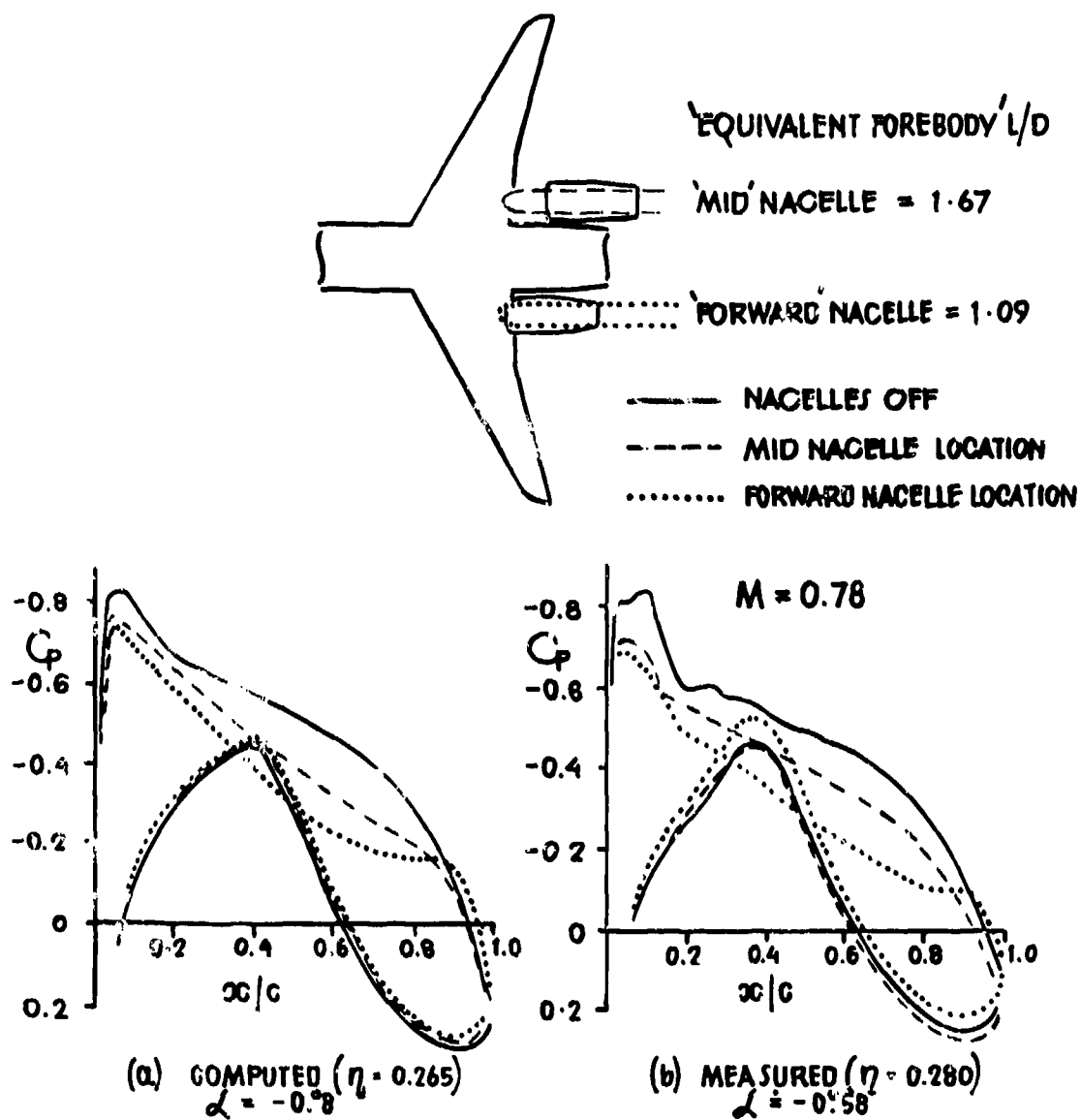


FIGURE 12. NACELLE EFFECT ON N13 SUB-CRITICAL WING PRESSURES AT CONSTANT INCIDENCE

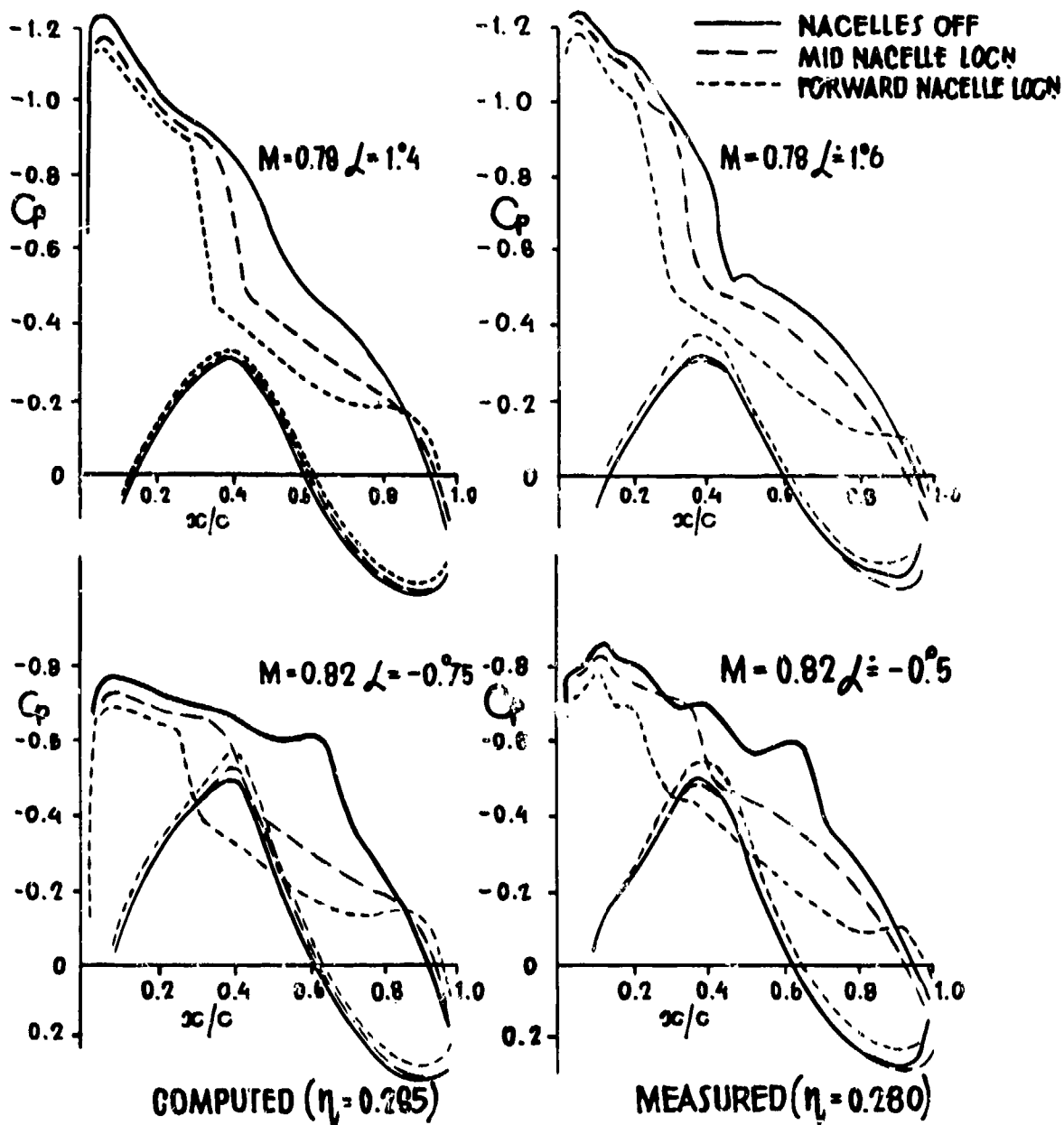


FIGURE 13. NACELLE EFFECT ON N13 SUPER-CRITICAL WING PRESSURES AT CONSTANT INCIDENCE

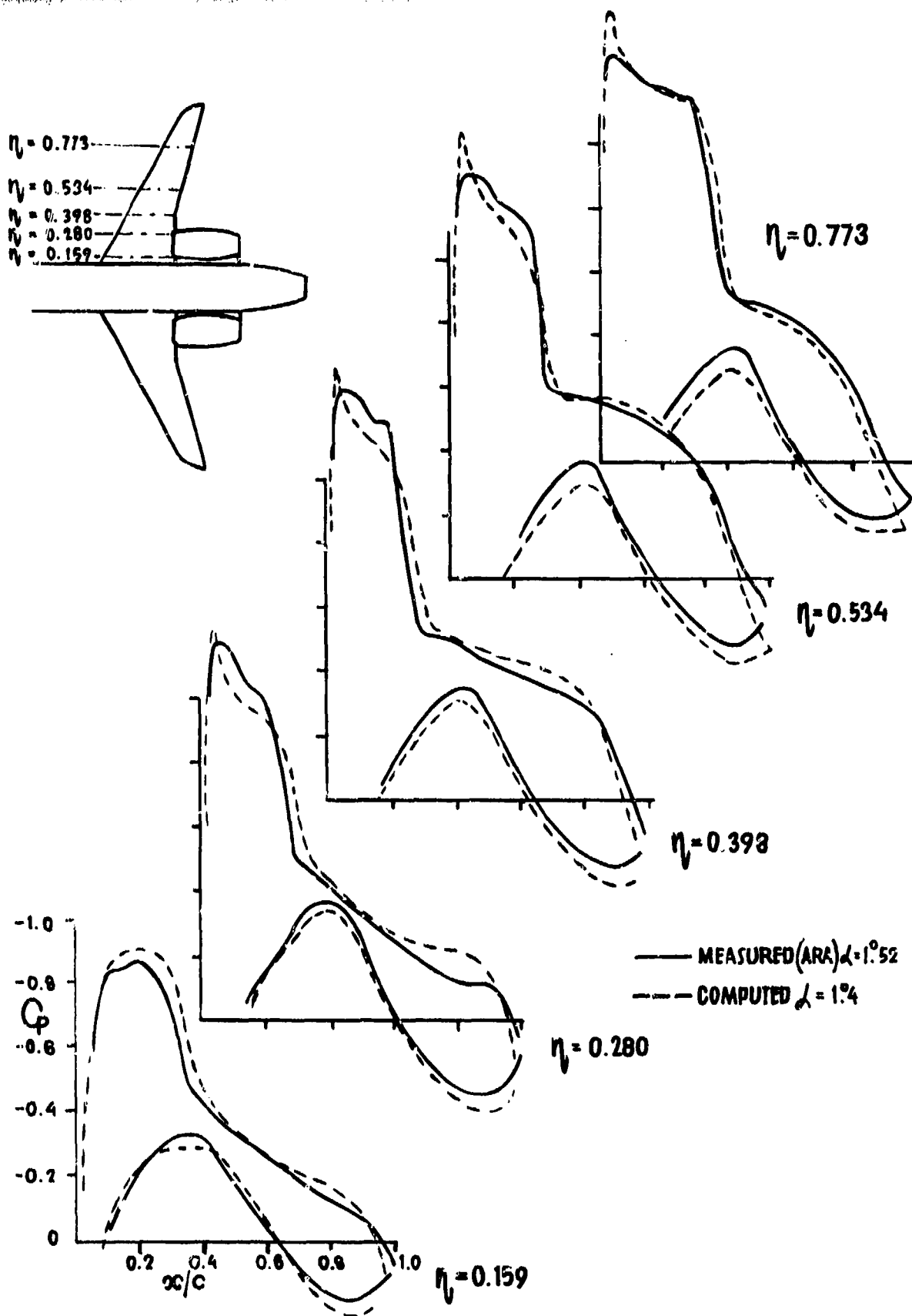


FIGURE 14. COMPUTE AND MEASURED WING PRESSURES FOR MODEL N13 "FORWARD" NACELLE
($M = 0.78$)

AERODYNAMIC ASPECTS OF A HIGH BYPASS RATIO ENGINE INSTALLATION
ON A FUSELAGE AFTERBODY

N. Voogt
J. van Hengst
J.Th. v.d. Kolk *)

Fokker B.V.
Aerodynamics Department
Schiphol Oost
Postbox 7600
The Netherlands

SUMMARY

The paper describes the design process used in shaping rear fuselage mounted large diameter engine nacelles, pylons and fuselage for a transport type aircraft. The objective was to suppress the local velocity levels and pressure gradients in the interest to avoid aerodynamic interference drag of the nacelle-pylon-fuselage combination in high speed cruise flight.

In the design process the shapes of fuselage afterbody, nacelle and stubwing were successively modified in a design-by-analysis process involving a number of iterations with a three-dimensional singularity method for inviscid subsonic flow. Windtunnel tests confirmed the adequacy of the singularity method to analyse complex interference problems.

1. INTRODUCTION

During the last decade requirements for improved fuel efficiency and better noise characteristics have drastically changed the appearance of turbofan engines. The high bypass ratio engines currently being developed have a much increased diameter to length ratio and consequently integration of these engines with the airframe will be more demanding than for engines of the previous generation (Ref.1). In the past integration was established by applying empirical design rules and the configuration was optimized through windtunnel assisted iterations.

Thanks to the achievements in computational aerodynamics the optimization process can now be considerably accelerated. The most important tools in the design process are singularity methods such as the NLR panel method which allows the complex three-dimensional flow problem to be accurately modeled into a numerical scheme. The method can be applied for subcritical inviscid flow.

The paper describes a theoretical investigation and experimental verification of aerodynamic interference at high subsonic Mach number for high bypass engines mounted on a tapering rear fuselage. Figure 1 shows the complete configuration - a narrow body twin jet transport - and compares it to the F28 configuration. Because for both cases the distance between nacelle and fuselage side-wall is kept equal, the interference due to high superelevations in between these bodies potentially will be much stronger for the new configuration.

The computational model - outlined in the next section - is first used to quantify the influence of the various elements contributing to interference.

2. THE COMPUTATIONAL MODEL

Panel methods form the most versatile basis for making detailed predictions of the flow field about a geometrically complex configuration in high subsonic flow. The methods are based upon a potential flow solution to the equations of inviscid and incompressible flow. The basic incompressible solution is modified to account for subsonic compressibility effects. In the case of the NLR panel method which is applied for the present computations, the surface of the configuration is represented by flat panels, each carrying a constant strength source distribution while for lifting cases an additional vortex system is placed on the camber surface and in the wake. The strengths of the singularities are calculated after applying a set of appropriate boundary conditions. Special features of the NLR panel method (Ref.2) include:

- . semi-empirical compressibility terms allowing an accurate prediction of suction levels in highly curved regions such as near the leading edge
- . an iterative method of solution which reduces computing time significantly.

Simulation of powered nacelles requires representation of mass flow through the nacelles. In this respect inlet flow and jet flow can be treated separately. For the present configuration early computations indicated that the influence of the jet behind the nacelle is only of minor importance for the interference problem investigated here. Therefore the jet boundary was simply represented by a cylinder with zero normal velocities.

*) presently employed by NLR

On the front part of the nacelle however, representation of the inflow is essential for an accurate prediction of the supersonic velocities on the nacelle inlet lip. In the present computations inlet flow is modeled by specifying a desired normal velocity distribution in a control plane inside the duct. Like the external nacelle surface, the inlet control plane is represented by source panels. It is well-known that a source distribution is inadequate to represent internal flows (Ref.3). For this reason and also because the internal flow has no influence on interference the control plane was placed at the inlet throat.

3. EXPLORING THE INTERFERENCE PROBLEM

For the configuration shown in figure 1 interference between nacelle and rear fuselage was calculated in the flow field of a high-lift advanced wing. Computations were performed at the adopted cruise design condition of the wing-body combination, for $M = .745$ and $\alpha = -1^\circ$. At the nacelle location the local downwash from the wing calculated for the wing-body combination alone, showed to be 3° . The nacelle-stubwing combination was therefore positioned with 3° incidence relative to the fuselage centreline. The stubwing had in this explorative phase a RAE-104 section scaled to 12% relative thickness and the nacelle a NACA-1-81-72 contour which was modified on the bottom surface to represent the required internal volume of the nacelle. A velocity ratio of 0.9 at the throat corresponding to a mass flow ratio of 0.721 based on the high lift area, was selected as representative for the cruise condition. The complete configuration consisted of 1420 panels among which 648 to represent nacelle and mass flow. The computations were made for the wing-body-nacelle configuration with and without the stubwing.

The calculated pressure distribution for several stations around the nacelle is depicted in figure 2 and compared to a reference pressure distribution computed for the isolated nacelle at $M = .745$ and $\alpha = 0^\circ$. Interference appears to be very severe especially on the bottom part of the nacelle. The pressure distribution on the stubwing (figure 3) and the suction peaks on top and bottom parts of the nacelle show that due to interference effects the pylon is aerodynamically loaded in a downward direction resulting in unwanted supersonic velocities on the lower surface. This flow would be supercritical and consequently would cause high interference drag due to the affected thick fuselage boundary layer. Under these conditions the subsonic panel method can no longer be expected to yield a meaningful prediction of the pressure distribution. The same applies to the pressure distribution on the nacelle quarter below the stubwing.

Although the contribution of the stubwing to the supersonic velocities can not be neglected, the results of figure 2 indicate that interference must primarily be reduced by modifying the channel between nacelle and fuselage.

4. DESIGN COMPUTATIONS

In searching for a configuration with reduced aerodynamic interference and thereby aiming for subcritical flow in order to avoid shock-boundary layer interactions a number of computations was made for the wing-body-nacelle combination wherein the channel between fuselage and nacelle was successively modified. In this process the curvature in the channel is the most important factor. Simply increasing the distance between body and nacelle reduces the supersonic velocities insufficiently. In one of the first computations the distance was increased with one tenth of the inlet diameter, but the resulting drop in suction level was only of the order of $\Delta C_p = .1$.

In the design process the curvature at the inboard side of the nacelle was reduced by rotating the rear part of the nacelle towards the fuselage. On the body side contouring was introduced to create a large concave region. As a guide to the modifications a few criteria can be specified. In the first place the curvature in the concave part of the channel must be strongest in the region of maximum interference. Because the concave part must be preceded by a convex one, the location of maximum curvature in that area must be properly selected. It should not be too close to the nacelle forebody; this would create very high suction on the intake lip at the inboard side of the nacelle. Therefore the fuselage body contouring must be initiated at some distance upstream of the nacelle, although this distance is obviously limited by practical considerations for a transport type aircraft.

Figure 4 shows the considerable effect of body- and nacelle contouring for configuration B defined after a few iterative steps as compared with configuration A with the initial channel shape. On the outboard pressure station the interference has practically disappeared and on the inboard stations the maximum suction level is reduced by as much as $\Delta C_p = .4$. The pressure peaks however are much higher as a consequence of the above mentioned curvature of the flow entering the contoured channel. These peaks can be strongly reduced by the stagnation effect of the stubwing, which should therefore be carefully located.

5. STUBWING DESIGN

Configuration B was adopted as the new basic configuration. The stubwing was also designed through several successive panel method computations. The complicated intersection contours of the stubwing with the fuselage on one side and the nacelle on the other are determined by means of a computer program calculating the intersection point of each stubwing generator with the relevant panels on nacelle and fuselage.

The stubwing has a constant spanwise cross-section which was kept at a 10% thickness to chord ratio. The main objective was to eliminate the high velocity level on the front part of the lower surface. After a few iterations this front part was flattened and given more incidence. The final profile shape as well as the pressure distribution for stubwing and nacelle inboard side are shown in figure 5. Comparison with the previous figure demonstrates the strong influence of the stubwing on the front part of the nacelle adjacent to the stubwing. It should be noted that apart from the local suction peaks near the leading edge the flow around this final configuration is now subcritical.

6. WINDTUNNEL TESTS

In order to verify the calculated interference effects a windtunnel model was defined on the basis of the final rear fuselage configuration and existing wing and body components. Although the surface of the configuration is sufficiently represented to obtain accurate panel method results, the numerically controlled manufacturing process requires a more detailed surface description especially for the rear fuselage. Therefore the GEOLAN geometry definition system which is implemented at the Fokker design office was applied to describe and where necessary to smooth the rear fuselage. From this system any convenient number of points can be generated on the surface. This is illustrated in figure 6 which also shows a top view of the complete configuration represented by panels.

Of the engine installation only the fan cowl part was represented by means of a flow through nacelle. The mass flow of this model represented the cruise flight condition, as used in the calculations and was obtained on the model by trimming the exhaust nozzle area.

The stubwing was fixed to the nacelle and provisions were made to change the angle of incidence of the complete nacelle-stubwing combination over a small range, whereas in the computational model the incidence is fixed at 3 degrees. The reason behind this was the uncertainty about the downwash from the wing which is implicitly used in the computations and was assumed to be about 3 degrees. Because the downwash is directly coupled to wing lift which is overestimated in the computations due to the neglect of viscous effects, the downwash and consequently the required incidence of the nacelle/stubwing combination must be expected to be smaller in the experimental design condition for the same wing incidence angle.

The tests were carried out in the High Speed Tunnel (HST) of NLR in Amsterdam where the model was installed on a Z-sting support as shown in figures 7 and 8. The model was tested with and without the nacelle/stubwing combination for a wide range of Mach number and angles of attack at Reynolds numbers up to 2.2×10^6 , based on the mean aerodynamic wing chord. The discussion of test results will be limited to comparing computation and experiment at the design condition which for the computation was at $M = .745$ and $\alpha = -1^\circ$. Due to viscous effects the experimental design condition is usually found at a different M , α combination (Ref.4) in this case at $M = .75$ and $\alpha = .1^\circ$. The best possible correspondence between measured and calculated pressures on nacelle and stubwing is found when the angle of incidence is set at 2 degrees.

A first comparison of the measured pressure distribution with the calculated result of figure 5 revealed a discrepancy on the lower surface of nacelle and stubwing. Flow visualization tests showed the strong influence of the Z-sting support fairing on the flow field over the lower surface of the fuselage afterbody (figure 9). Therefore that part of the model support (the shaded area in figure 7) was included in the computational model and it was found that the stagnation effect of the model support reduced the suction level on the lower surface of the nacelle-stubwing configuration with $\Delta C_p = .1$, but the influence on the surface above the stubwing was negligible. The measured and calculated pressures on nacelle and stubwing for the configuration with the model support included are compared in figure 10. The flow is subcritical and pressure gradients are moderate.

The nacelle + pylon drag - being the difference between the drag measured for the complete configuration and the drag for the wing-body combination alone - at the design lift coefficient is shown in figure 11 as a function of the free-stream Mach number. It can be observed that the drag contribution of the nacelles and pylons is virtually independent of Mach number up to a Mach number beyond the design value. Consequently it can be concluded that transonic effects - wave drag and shock-induced drag - are avoided. Moreover, a separate drag analysis yields a favourable conclusion with respect to the level of the drag contribution over the full Mach number range.

7. CONCLUDING REMARKS

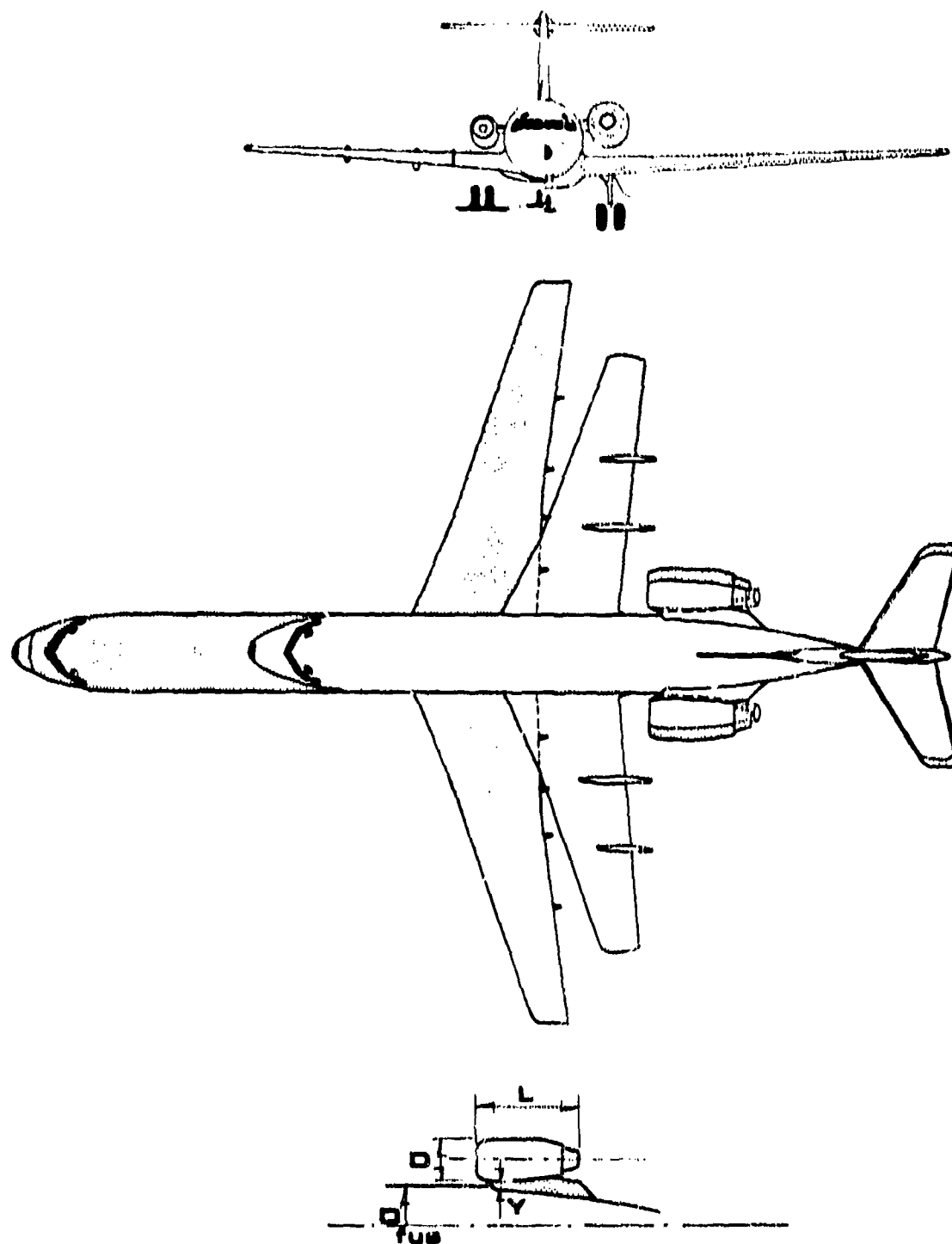
The problem of aerodynamic interference encountered with rear fuselage mounted large diameter nacelles was analyzed by means of the NLR panel method for a free-stream Mach number of 0.75. In the investigation a computational design process was applied, subsequently verified by windtunnel tests. It can be concluded that:

- the NLR panel method is an excellent tool for analyzing complex interference problems in high subsonic flow
- a design was obtained in which unfavourable interference effects were avoided
- for a design Mach number of 0.75 an integrated approach to the shaping of large size nacelles, rear fuselages and pylons showed the need for moderate fuselage body contouring in the nacelle area

- windtunnel results must be corrected for interference effects caused by support struts placed in the vicinity of the nacelle-pylon-body combination.

8. REFERENCES

1. Swan, W.C., Sigalla, A.
'The problem of installing a modern high bypass engine on a twin jet transport aircraft'
AGARD CP 124, paper 17, 1973.
2. Labrujere, Th.E., Loeve, W., Slooff, J.W.
'An approximate method for the calculation of the pressure distribution on wing-body combinations at subcritical speeds'
AGARD CP 71, paper 11, 1970.
3. Rubbert, P.E.
'Subsonic and Supersonic Panel Methods'
AIAA Lecture Series: Applied Computational Aerodynamics, 1977.
4. Slooff, J.W., Voogt, N.
'Aerodynamic design of thick, supercritical wings through the concept of equivalent subsonic pressure distribution'
NLR MP 78011 U, 1978.



$D/L = .44$ Present Configuration
 $D/L = .25$ F28

D_{fus} and Y are similar

FIGURE 1. COMPARISON BETWEEN PRESENT CONFIGURATION AND F28.

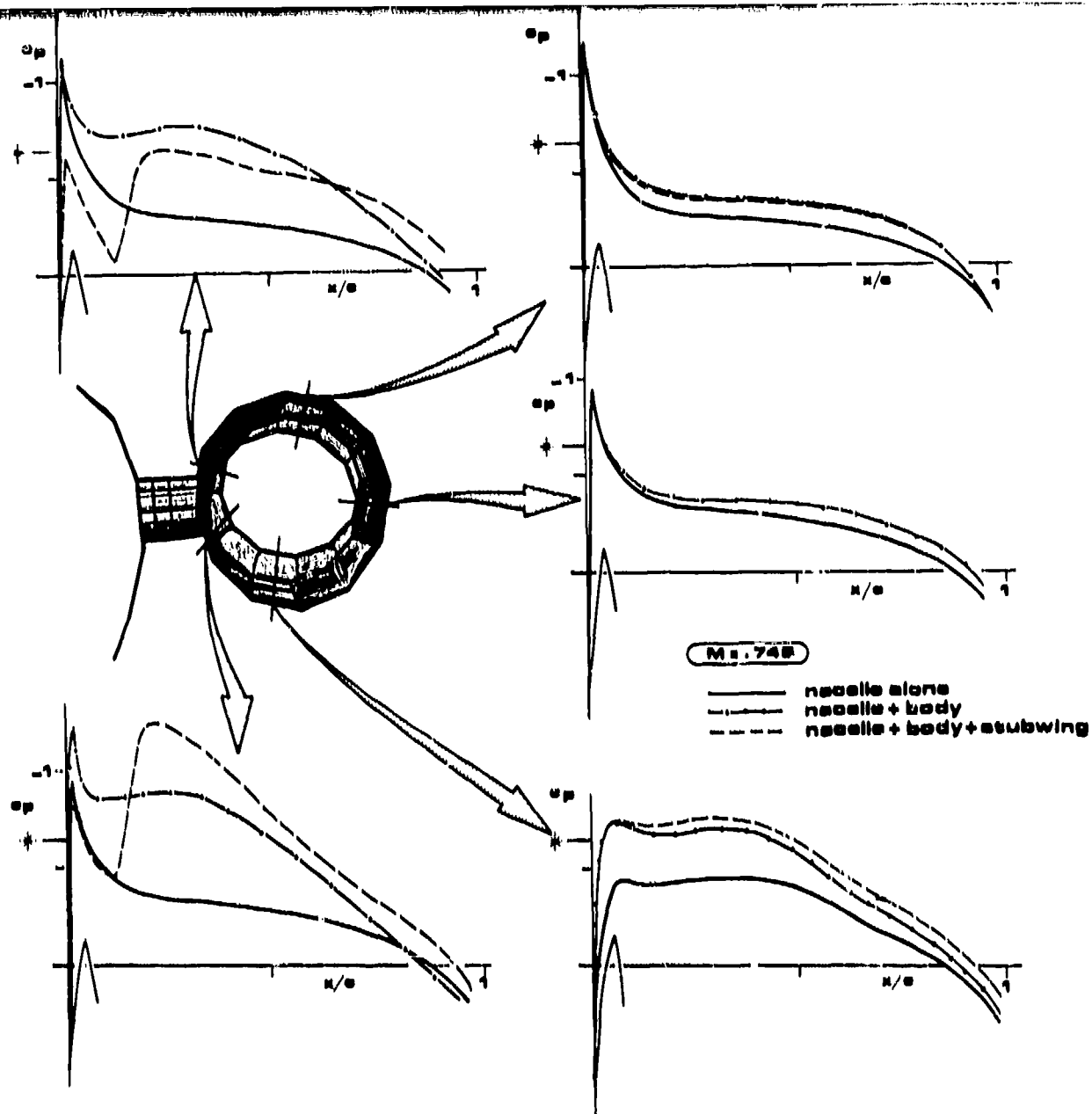


FIGURE 2. CALCULATED PRESSURE DISTRIBUTION AROUND THE NACELLE FOR INITIAL CONFIGURATION.

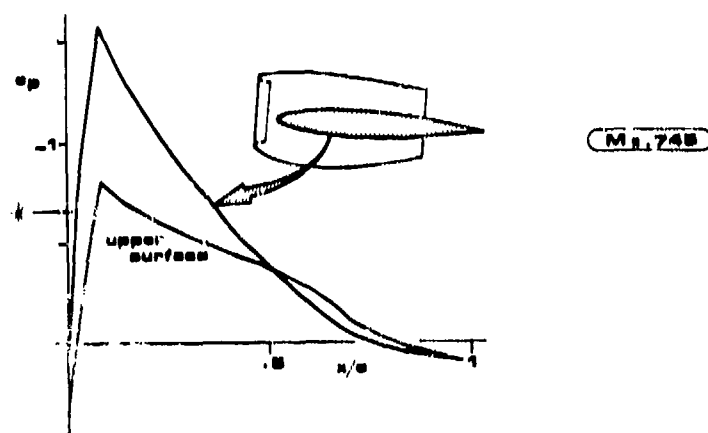


FIGURE 3. CALCULATED PRESSURE DISTRIBUTION ON THE STUBWING FOR INITIAL CONFIGURATION.

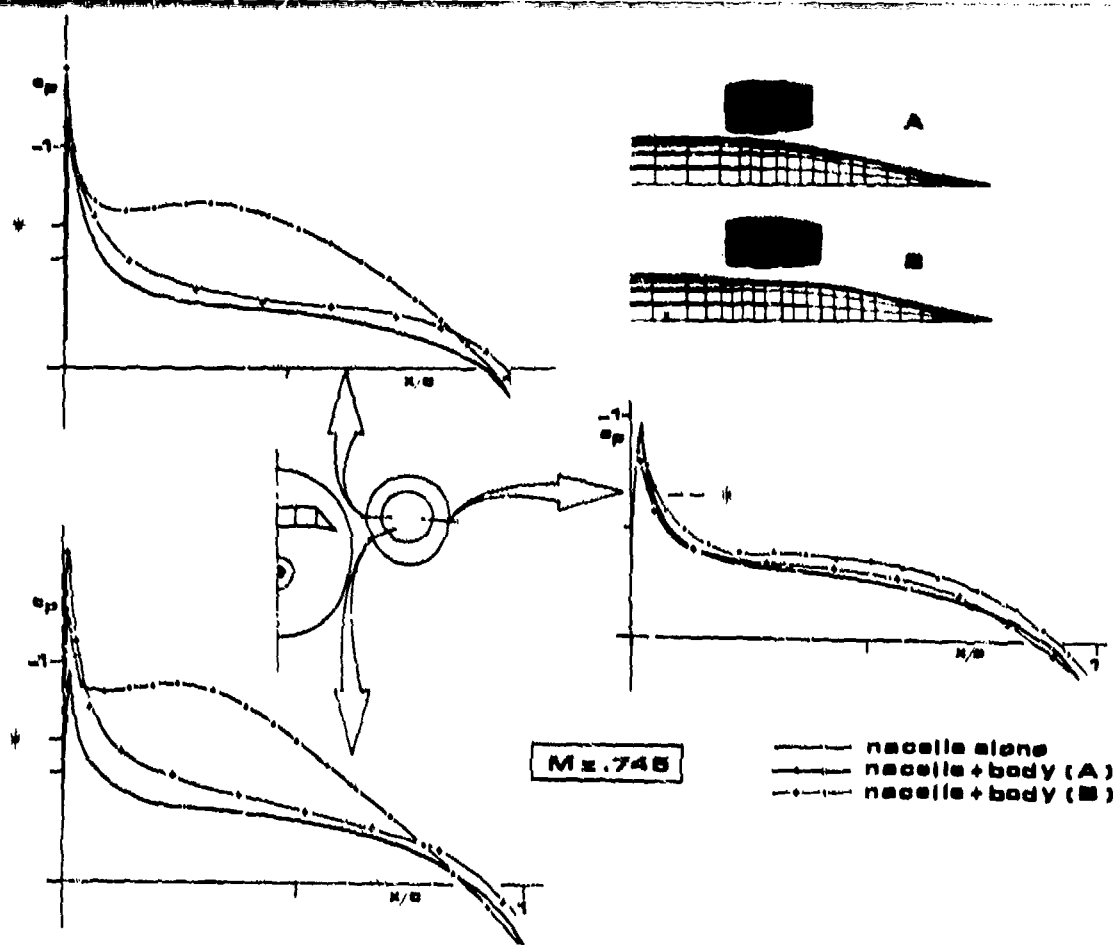


FIGURE 4. EFFECT OF BODY CONTOURING.

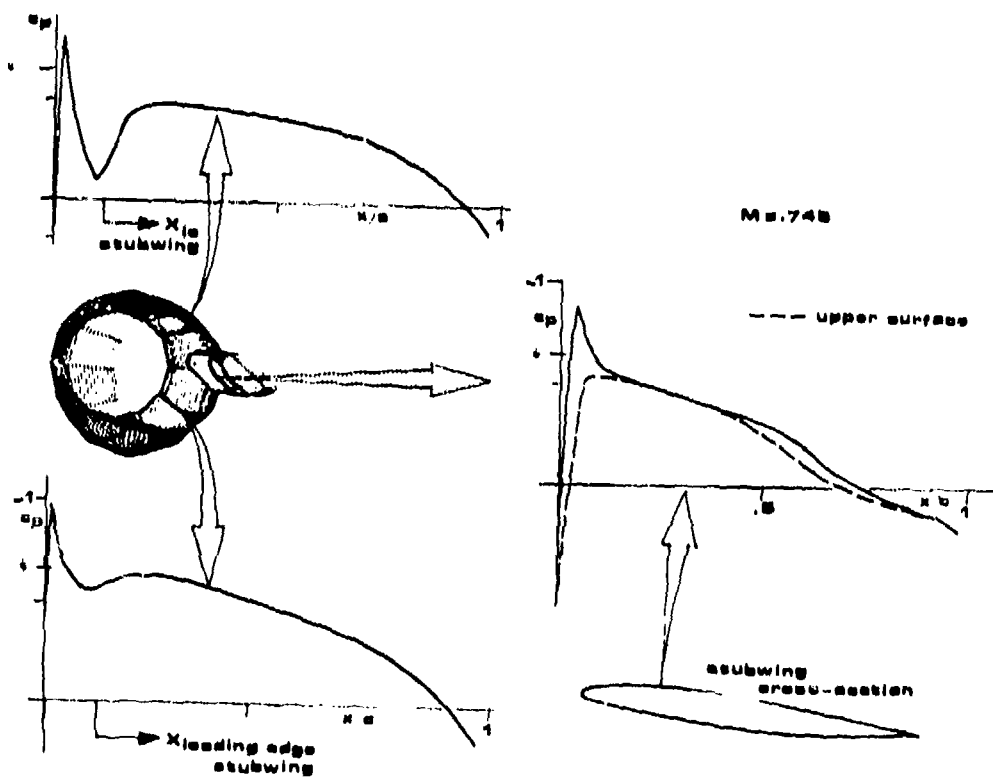


FIGURE 5. CALCULATED PRESSURE DISTRIBUTION FOR FINAL CONFIGURATION.

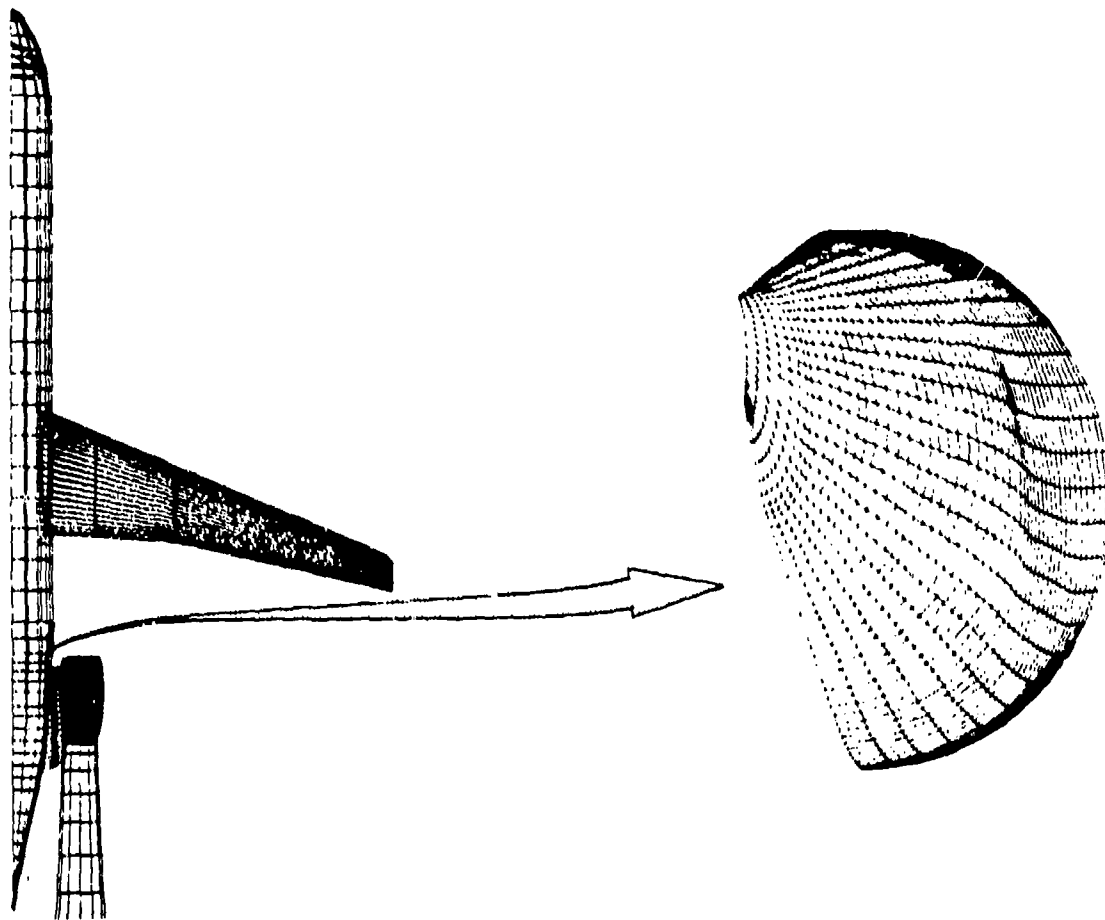


FIGURE 6. GEOMETRIC DETAILS OF FINAL CONFIGURATION.

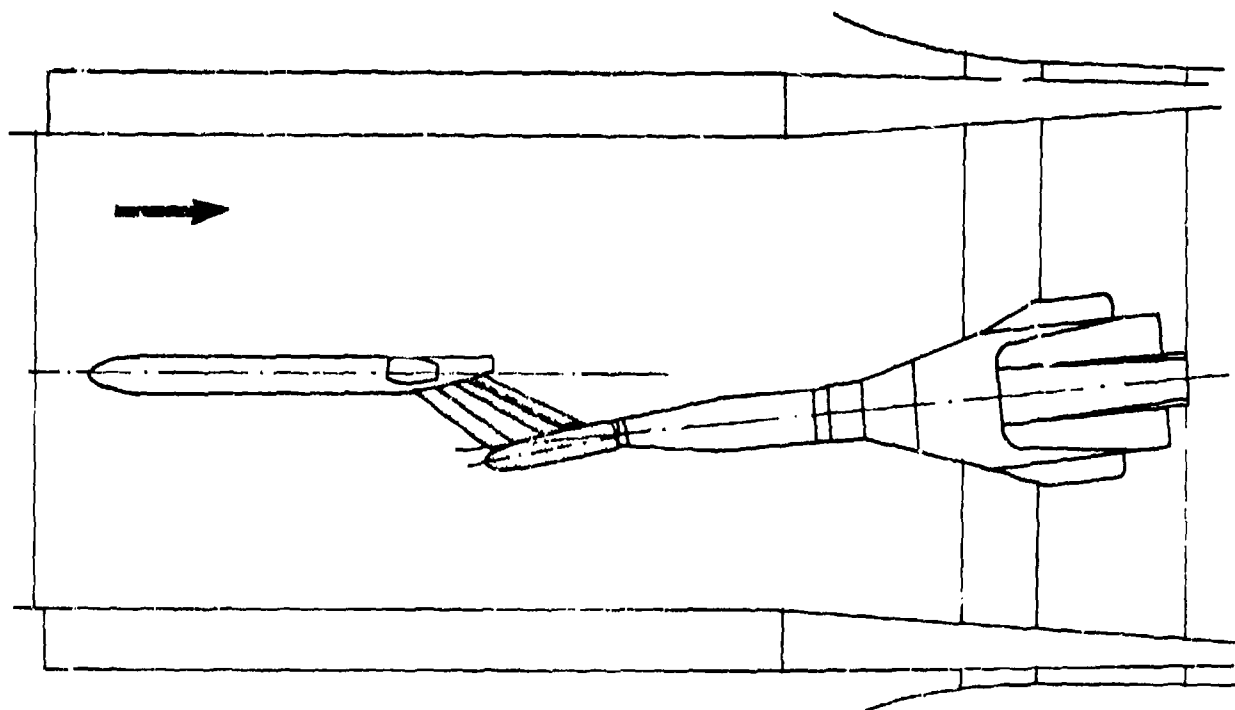


FIGURE 7. MODEL SUPPORT INSTALLATION IN WINDTUNNEL.



FIGURE 8. MODEL INSTALLED IN THE TEST SECTION OF THE NLR HIGH SPEED TUNNEL.



FIGURE 9. OIL FLOW VISUALIZATION ON BOTTOM SURFACE OF REAR FUSELAGE.

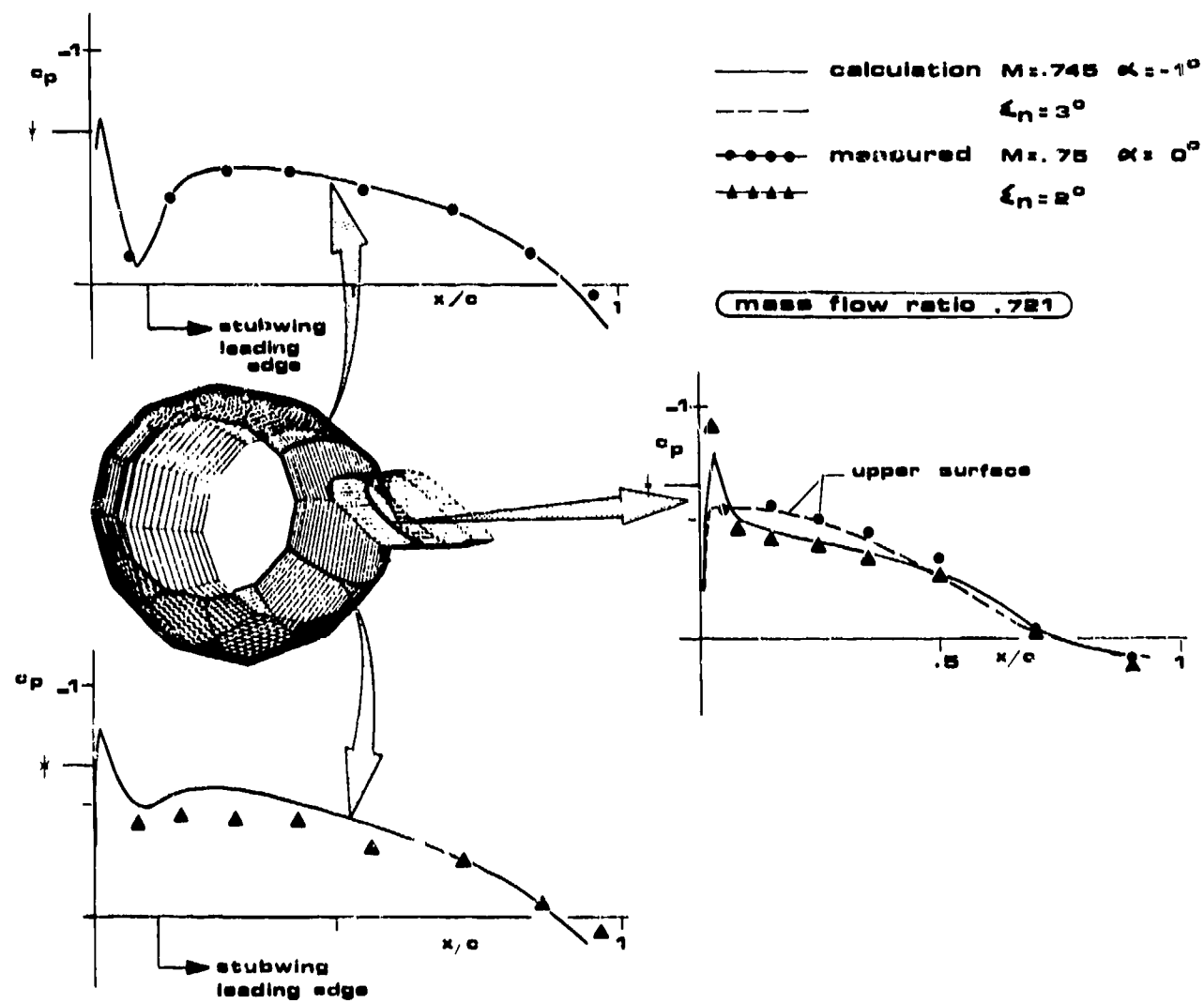


FIGURE 10. COMPARISON OF MEASURED AND CALCULATED PRESSURES.

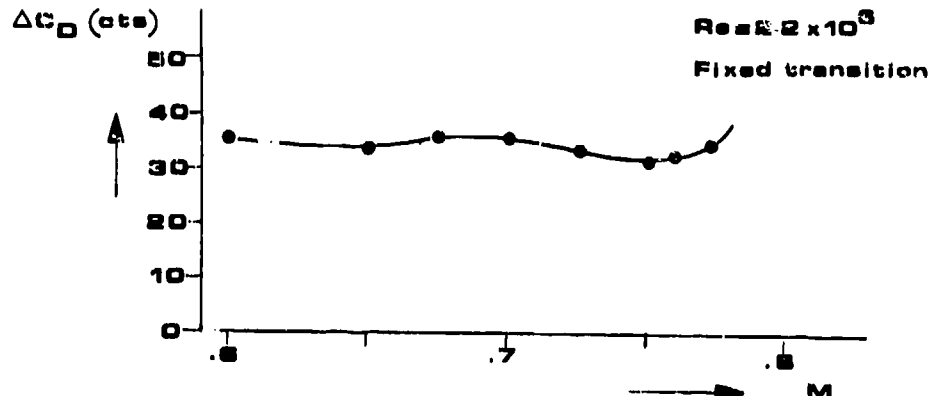


FIGURE 11. MEASURED DRAG OF NACELLE-PYLON COMBINATION.

UNE METHODE NUMERIQUE POUR L'ETUDE DE L'INTERACTION NACELLE-JET-VOILURE

EN ECOULEMENT TRIDIMENSIONNEL NON VISQUEUX

par : G. LE GALL - J. BOUSSAÏET - M. YERMIA

--§--

Service Aérodynamique Théorique
Société Nationale Industrielle Aérospatiale
316, Route de Bayonne - B.P. 3160
31060 Toulouse - FRANCE

RESUME

L'interaction nacelle-jet-voilure est un phénomène tridimensionnel complexe que nous avons abordé, en faisant deux hypothèses simplificatrices : le fluide est incompressible et non visqueux. Avec ces hypothèses, l'ensemble propulsif est modélisé par une entrée d'air dont on contrôle le débit et un jet propulsif dont on contrôle la pression génératrice. La méthode mise au point est une méthode de singularités qui utilise des sources et des doublets de densité constante et des doublets de densité linéaire répartis sur des panneaux plans. Les équations qui régissent le problème constituent un système non linéaire que l'on décompose en une partie linéaire et une partie quadratique. Ces deux parties sont résolues de manière itérative par la méthode de Gauss-Seidel et la méthode de Newton. Les frontières libres de l'écoulement (jet et sillage) sont aussi calculées par un processus itératif qui est intégré aux deux méthodes itératives précédentes. Quelques résultats pratiques sont proposés en écoulement bidimensionnel et tridimensionnel. La comparaison avec des essais permet de juger l'intérêt des hypothèses simplificatrices.

1.- INTRODUCTION -

L'apparition de la nouvelle génération de moteurs à haut taux de dilution pose le problème de l'intégration de l'avion et du système propulsif. SWAN et SIGALLA¹ étudient les diverses positions envisagées pour les réacteurs (au-dessous et au-dessus de l'aile, sur le fuselage), tandis que AHMED² calcule l'influence de la position des nacelles sur la traînée induite. De nombreuses études ont été réalisées pour prédire l'influence d'un jet sur une voilure proche, avec ou sans interaction entre le jet et la voilure.

PUTNAM³ utilise une méthode linéaire où l'aile est représentée par un système tourbillonnaire. La nacelle n'est pas prise en compte, et l'effet d'entraînement du jet est modélisé par une ligne de sources dont les intensités sont obtenues grâce à la méthode de SQUIRE et TROUNCER⁴. Il suppose de plus qu'il n'y a pas d'interaction entre le jet et la voilure.

SPANGLER, MENDENHALL et DILLENUS⁵ ont mis au point une méthode utilisant aussi des systèmes tourbillonnaires et qui peut traiter la voilure, les nacelles et les mâts réacteurs. Le jet est représenté par un cylindre sur lequel sont répartis des tourbillons concentriques jusqu'à l'infini. La géométrie du jet est figée, mais les intensités de singularité sont obtenues par un schéma itératif.

LAN et al (réf. 6 à 11) utilisent aussi une méthode linéarisée pour étudier l'interaction jet-voilure. Le jet est représenté par une double couche tourbillonnaire qui permet de modéliser la différence de pression génératrice et la différence de Mach entre le jet et l'écoulement extérieur. L'interaction entre le jet et l'aile est calculée pour la géométrie et pour les singularités. Le programme permet aussi de traiter des cas où le jet touche la voilure (soufflage extradou). Mais cette méthode ne prend pas en compte l'influence de la nacelle.

SHOLLENBERGER¹² discrétise l'aile et le jet par un système tourbillonnaire. Le jet est modélisé par une nappe de doublets constants (équivalents à des tourbillons linéiques), qui permettent de représenter la différence de pression génératrice. La géométrie du jet est obtenue par un processus itératif.

GILETTE¹³ étudie l'interaction entre la nacelle, le mât et la voilure à l'aide d'une méthode des singularités du premier ordre utilisant des sources et des doublets; Le débit de la nacelle est contrôlé par une plaque de doublets, tandis que la surface du jet est représentée par un système tourbillonnaire. La géométrie du jet est fixe et calculée a priori pour une nacelle de révolution par une méthode de relaxation transsonique.

SNEL¹⁴ étudie l'influence d'un jet propulsif sur une voilure par une méthode des singularités du premier ordre associée à un programme de calcul d'un jet visqueux incompressible. La méthode est basée sur un processus itératif entre les deux programmes. La surface du jet est alors représentée par des panneaux de sources constantes sur lesquels on spécifie un certain débit. Les nacelles traitées par le programme doivent être fermées à l'avant.

L'interaction nacelle-jet-voilure est un phénomène très complexe. Il s'agit d'une configuration tridimensionnelle (nacelle-mât-voilure) qui comprend à la fois des zones à forte compressibilité (ondes de choc dans le jet) et des zones à forte interaction visqueuse (zone de cisaillement entre le jet et l'écoulement externe). Par ailleurs, ces différentes zones sont formées d'écoulements à énergies différentes, ce qui contribue à augmenter les difficultés de modélisation. Au lieu d'aborder le problème dans toute sa complexité, ce qui demanderait un investissement considérable, nous avons essayé de séparer les difficultés pour mieux les résoudre. Nous avons donc fait les deux hypothèses simplificatrices suivantes :

1° - l'écoulement est incompressible

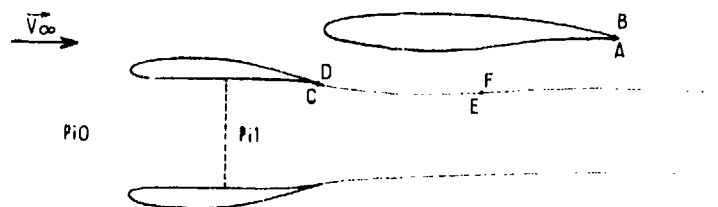
2° - le fluide est parfait (aucun phénomène d'interaction visqueuse).

La première phase de l'étude a été faite en écoulement bidimensionnel. Cette première partie nous a permis de mettre au point et de valider un certain nombre de principes de calcul, qui constituent la base de la méthode tridimensionnelle. Dans le cadre des hypothèses précédentes, nous nous proposons donc de calculer la géométrie du jet en présence de la voilure, et son influence sur celle-ci, pour différentes énergies du jet, et différentes valeurs du débit de la nacelle. La configuration type est illustrée sur la figure 1.

2.- MODELISATION DE L'ENSEMBLE PROPULSIF -

2.1 - Paramètres du système -

Puisque le fluide est incompressible et non visqueux, les seuls paramètres sont ceux qui découlent de la modélisation de l'ensemble propulsif. Les phénomènes complexes qui ont lieu à l'intérieur du réacteur ne peuvent évidemment être pris en compte de façon précise. Du point de vue de l'écoulement extérieur, on peut considérer le moteur comme la combinaison d'une entrée d'air et d'un jet propulsif. Le paramètre caractéristique d'une entrée d'air est son coefficient de débit ϵ : rapport du débit réel au débit que donnerait un écoulement uniforme de vitesse \vec{V}_∞ . Un jet propulsif se caractérise par une énergie supérieure à celle de l'écoulement extérieur, c'est à dire dans le cas de notre hypothèse de fluide incompressible, par une vitesse supérieure. Or, la pression dans le jet à l'infini aval est uniforme et égale à la pression extérieure. Donc, en fonction de la loi de BERNOULLI ($\frac{V^2}{2} + \frac{p}{\rho} = \frac{p_1}{\rho}$), le fluide dans le jet possède une pression génératrice supérieure à celle du fluide externe. On impose donc quelque part à l'intérieur de la nacelle un saut de pression génératrice avec continuité de la vitesse de façon à assurer la conservation du débit. Nous allons montrer que, dans ce cas, le champ des vitesses ne dépend que d'un paramètre adimensionnel δ .



D'après l'hypothèse d'incompressibilité, le calcul de l'écoulement se ramène à la résolution de l'équation de LAPLACE avec les conditions aux limites suivantes :

- vitesses normales nulles sur les corps et la surface du jet,

conditions de JOUKOWSKI sur les corps, soit, en fonction de la loi de BERNOULLI :

$$\begin{aligned} \text{sur l'aile} \quad p_A &= p_B \implies \|\vec{V}_A\|^2 = \|\vec{V}_B\|^2 \\ \text{sur la nacelle} \quad p_C &= p_D \implies \|\vec{V}_C\|^2 - \|\vec{V}_D\|^2 = \frac{p_1 - p_0}{1/2 \rho} \end{aligned}$$

- conditions de glissement sur la surface du jet

$$p_E = p_F \implies \|\vec{V}_E\|^2 - \|\vec{V}_F\|^2 = \frac{p_1 - p_0}{1/2 \rho}$$

On s'intéresse à des écoulements où la vitesse d'entraînement \vec{V}_∞ est non nulle. On peut donc normaliser les vitesses ($V_\infty = 1$). Les deux dernières relations deviennent :

$$\|\vec{V}_C\|^2 - \|\vec{V}_D\|^2 = \delta \quad \|\vec{V}_E\|^2 - \|\vec{V}_F\|^2 = \delta$$

où δ la forme d'un coefficient de pression :

$$\delta = \frac{p_1 - p_0}{1/2 \rho V_\infty^2}$$

Pour une géométrie donnée, et un coefficient de débit donné, le champ des vitesses est donc fonction du paramètre δ . Le système possède ainsi, outre les caractéristiques géométriques des corps, deux degrés de liberté, correspondant aux deux variables indépendantes ϵ et δ .

2.2 - Modélisation du débit variable -

Pour faire varier le débit à l'intérieur de la nacelle, le programme bidimensionnel utilise un corps central dont on modifie la section par affinité à partir d'un corps de référence. Le rapport d'affinité est calculé par un schéma itératif. Il est possible d'étendre ce principe en tridimensionnel, mais nous avons imaginé un modèle plus simple. On sait que la superposition d'un écoulement uniforme de vitesse \vec{V}_0 et d'un doublet de direction parallèle et opposée à \vec{V}_0 est équivalent à l'écoulement autour d'un cercle en bidimensionnel, et autour d'une sphère en tridimensionnel. L'écoulement au centre de la nacelle peut être considéré comme quasi-uniforme et un doublet placé sur l'axe aura un effet de blocage sur l'écoulement interne. En faisant varier l'intensité de ce doublet, on pourra donc contrôler le débit. L'intérêt numérique d'une telle modélisation est le suivant : le calcul du débit se fait par intégration numérique et on obtient ainsi une équation linéaire pour déterminer l'intensité du doublet. Cette équation peut être intégrée dans le système global et on calcule l'intensité du doublet en même temps que celle des autres singularités.

2.3 - Modélisation du jet propulsif -

Dans le cas d'un fluide non visqueux, le jet issu de la nacelle délimite dans l'espace deux zones à énergies différentes. La surface du jet est une surface de glissement, et il n'y a pas de mélange entre les deux écoulements. Le jet se continue donc jusqu'à l'infini dans le sens de l'écoulement. Sa surface est régie par les deux équations suivantes :

- une condition sur la vitesse normale $\vec{V}_n = 0$ (1)

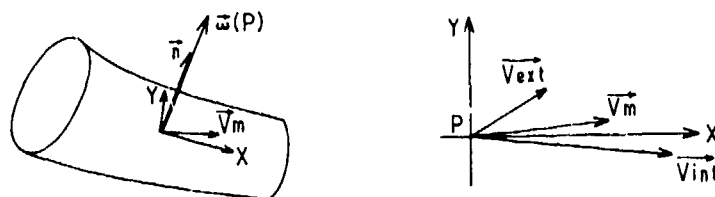
- une condition sur la continuité des pressions : $P_{ext} = P_{int}$

Or le fluide est incompressible, et on peut utiliser le théorème de BERNOULLI. Après normalisation des vitesses on obtient l'expression du § 2.1 :

$$\|\vec{V}_{int}\|^2 - \|\vec{V}_{ext}\|^2 = \delta \quad (2)$$

Pour satisfaire cette équation, on répartit sur la surface du jet des doublets normaux :

$$\vec{\omega}(P) = \omega(P) \cdot \vec{n}$$



A la traversée d'une surface porteuse de doublets normaux, la discontinuité de vitesse tangentielle ne dépend que de $\omega(P)$. Puisque $V_n = 0$, les vitesses tangentielles à l'intérieur et à l'extérieur du jet sont \vec{V}_{int} et \vec{V}_{ext} . On a donc :

$$\vec{V}_{int} - \vec{V}_{ext} = \text{Grad}_{x,y} \omega(P)$$

où $\text{Grad}_{x,y} \omega(P)$ est le gradient de la fonction $\omega(P)$ dans le plan tangent à la surface. Soit

$\vec{V}_m = \frac{1}{2}(\vec{V}_{ext} + \vec{V}_{int})$ la vitesse moyenne en P. Les vitesses \vec{V}_{ext} et \vec{V}_{int} ont alors les composantes suivantes dans le repère local :

$$\vec{V}_{ext} \begin{vmatrix} V_{mx} - 1/2 \partial \omega / \partial x \\ V_{my} - 1/2 \partial \omega / \partial y \\ 0 \end{vmatrix} \quad \vec{V}_{int} \begin{vmatrix} V_{mx} + 1/2 \partial \omega / \partial x \\ V_{my} + 1/2 \partial \omega / \partial y \\ 0 \end{vmatrix}$$

L'équation (2) devient alors :

$$2 \left(V_{mx} \frac{\partial \omega}{\partial x} + V_{my} \frac{\partial \omega}{\partial y} \right) = \delta \quad (3)$$

L'intensité des doublets est donc définie par un système différentiel du premier ordre. Pour obtenir la fonction $\omega(P)$, il faut fixer la valeur de la constante d'intégration. Cette initialisation est obtenue par la condition de JOUKOWSKI sur la nacelle.

L'autre problème de modélisation est dû au fait que le jet se prolonge jusqu'à l'infini. Mais on peut déterminer la fonction $\omega(P)$ lorsque P tend vers l'infini. En effet, à l'infini aval, l'écoulement dans le jet est uniforme de vitesse \vec{V}_j parallèle à \vec{V}_∞ ($V_\infty=1$). La condition de glissement s'écrit donc :

$$\|\vec{V}_j\|^2 - \|\vec{V}_\infty\|^2 = \delta$$

soit :

$$(V_j - V_\infty) 2 V_m = \delta$$

où V_m est la vitesse moyenne à l'infini. L'équation (3) se simplifie :

$$2 V_m \left(\frac{\partial \omega}{\partial x} \right)_\infty = \delta$$

Donc :

$$\left(\frac{\partial \omega}{\partial x} \right)_\infty = V_j - V_\infty = \text{constante}$$

Donc lorsque P tend vers l'infini, la fonction $\omega(P)$ tend vers une fonction linéaire en x.

La surface du jet est donc déterminée par deux équations : $\vec{V}_n = 0$ (1)

$$2 \left(V_{mx} \frac{\partial \omega}{\partial x} + V_{my} \frac{\partial \omega}{\partial y} \right) = \delta \quad (3)$$

Les deux équations ne pouvant être résolues simultanément, on fait appel à un schéma itératif : la fonction $\omega(P)$ est calculée à partir de (3) pour une géométrie donnée du jet, puis on modifie cette géométrie pour satisfaire l'équation (1). On obtient ainsi de proche en proche une géométrie de jet et une fonction $\omega(P)$ qui satisfont le système d'équations (1, 3).

3.- METHODE DES SINGULARITES UTILISEE -

3.1 - Calcul d'écoulement autour de corps portants -

L'AEROSPATIALE a mis au point depuis plusieurs années un programme de singularités du premier ordre permettant de traiter des configurations complexes telles que voilure-fuselage-empannage. Ce programme est assez voisin des méthodes développées au NLR¹⁶ et chez MBB¹⁷⁻¹⁸ et dérivées des travaux de J.L. HESS¹⁹⁻²¹. Le programme repose sur un certain nombre de principes :

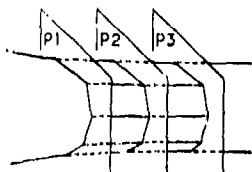
- La géométrie est discrétisée par des panneaux plans qui approximent localement la surface des corps. Ces panneaux ne sont en général pas jointifs.
- Les conditions aux limites sont appliquées sur ces panneaux au centre de chaque panneau.
- Les singularités correspondant à ces conditions aux limites sont réparties sur ces mêmes panneaux : ce sont des sources d'intensité constante par panneau.

On obtient ainsi un programme capable de calculer l'écoulement autour de corps non portants.

Les effets portants sont représentés par un sillage d'épaisseur nulle sur lequel sont répartis des doublets normaux d'intensité constante. Cette nappe de doublets est prolongée à l'intérieur des corps ; on obtient ainsi sur le squelette un certain nombre de panneaux de doublets constants. L'intensité des doublets varie du bord d'attaque au bord de fuite, suivant une loi qui dépend de l'épaisseur locale du corps. Cette loi, fixée a priori, part d'une valeur nulle au bord d'attaque et se raccorde aux doublets de la nappe. La condition de JOUKOWSKI est obtenue en écrivant l'égalité des pressions à l'extrados et à l'intrados du bord de fuite. Comme cette nappe de doublets représente un sillage, on l'équilibre par une méthode itérative, pour aligner les tourbillons issus du bord de fuite avec la vitesse locale²².

3.2 - Discrétisation du jet propulsif issu de la nacelle -

Une nacelle peut être considérée comme une voilure qui se referme sur elle-même. Le jet correspond donc à un sillage issu du bord de fuite de la nacelle. La surface de ce jet peut être discrétisée comme la nacelle par des panneaux plans. Plus précisément, on considère un certain



nombre de plans P_i fixes et perpendiculaires à l'axe des x . Les panneaux du jet sont définis entre deux plans consécutifs. On obtient ainsi des panneaux trapézoïdaux. On répartit sur ces panneaux des doublets normaux ω dont l'intensité est donnée par l'équation (3) :

$$2(Vm_x \frac{\partial \omega}{\partial x} + Vm_y \frac{\partial \omega}{\partial y}) = \delta$$

La solution la plus simple consiste à répartir sur chaque panneau un doublet d'intensité constante. Les dérivées $\partial \omega / \partial x$ et $\partial \omega / \partial y$ sont alors obtenues par différence finie.

Mais la vitesse Vm est une vitesse tangentielle, et on sait que l'erreur numérique sur le calcul d'une telle vitesse augmente quand on se rapproche du panneau²³⁻²⁴. On utilise donc une distribution de doublets normaux linéaires. Comme la variation en y est assez faible, l'intensité des doublets peut être choisie constante en y sur chaque panneau. La dérivée $\partial \omega / \partial y$ est calculée par différence finie. On obtient finalement des panneaux trapézoïdaux sur lesquels sont répartis des doublets normaux dont l'intensité varie linéairement suivant l'axe perpendiculaire aux bases. Un résultat important est la possibilité de calculer exactement la vitesse tangentielle en un point du panneau.

Nous avons vu que le jet se prolonge jusqu'à l'infini aval. Pour discrétiser cette partie du jet on utilise le fait que la fonction $\omega(P)$ possède une asymptote quand P tend vers l'infini. On assimile la surface du jet à un cylindre parallèle à la vitesse d'entraînement et s'appuyant sur la dernière section discrétisée, et on répartit sur ce cylindre des doublets normaux constants en y et variant linéairement en x , avec une dérivée égale à la pente de l'asymptote. Une telle répartition de doublets est équivalente à des tourbillons constants γ distribués sur chaque section droite du jet. Cette singularité est illustrée sur la figure 2 ainsi que le champ de vitesses qu'elle fournit : on obtient, à l'infini, une vitesse nulle à l'extérieur et une vitesse constante à l'intérieur du cylindre, égale à la dérivée $(\frac{\partial \omega}{\partial x})_\infty = \gamma$. Cette dérivée se calcule facilement à partir de la condition sur le jet :

$$\|\vec{V}_j\|^2 - \|\vec{V}_\infty\|^2 = \delta$$

Soit

$$\|\vec{V}_j\|^2 - 1 = \delta$$

En superposant la singularité précédente à la vitesse d'entraînement on obtient :

$$(1 + (\frac{\partial \omega}{\partial x})_\infty)^2 - 1 = \delta$$

V_j étant positif, cette équation admet une seule solution : $(\frac{\partial \omega}{\partial x})_\infty = -1 + \sqrt{1 + \delta}$

3.3 - Discrétisation de l'ensemble nacelle-voilure-jet -

La méthode que nous développons ici s'appuie sur le programme existant déjà à l'AEROSPATIALE en y intégrant la modélisation du jet propulsif. Le choix des singularités utilisées est donc le suivant :

- Sur la surface de la voilure et de la nacelle on utilise des sources constantes réparties sur des pavés plans.

- Pour satisfaire la condition de JOUKOWSKI sur la voilure on utilise la même méthode que précédemment : un sillage modélisé par une nappe de doublets constants (équivalents à des tourbillons) et des panneaux plans de doublets constants sur le squelette, la loi donnant la valeur de ces doublets étant fonction de l'épaisseur relative des profils.
- sur la surface du jet on utilise des panneaux plans trapézoïdaux de doublets normaux linéaires, que l'on prolonge à l'infini par une singularité particulière.
- Pour satisfaire la condition de JOUKOWSKI sur la nacelle on prolonge la discrétisation du jet sur le squelette de la nacelle. On utilise donc des panneaux trapézoïdaux sur lesquels sont répartis des doublets normaux linéaires.
- Pour contrôler le débit à l'intérieur de la nacelle, on place au milieu de celle-ci un doublet ponctuel de direction parallèle à l'axe de la nacelle.

4.- METHODE DE RESOLUTION -

4.1 - Conditions aux limites -

Les conditions aux limites sont les suivantes :

- vitesse normale nulle sur les corps : $\vec{v}_n = 0$
- condition de JOUKOWSKI sur les corps portants :
 - . sur l'aile $\|\vec{v}_{int}\|^2 = \|\vec{v}_{ext}\|^2$
 - . sur la nacelle $\|\vec{v}_{int}\|^2 - \|\vec{v}_{ext}\|^2 = 6$
- condition de glissement sur le sillage de la voilure : $\vec{v}_n = 0$
- condition de glissement sur le jet : $\vec{v}_n = 0$
- condition sur le débit $2 \left(v_{mx} \frac{\partial \omega}{\partial x} + v_{my} \frac{\partial \omega}{\partial y} \right) = 6$

Les conditions de vitesse normale nulle sur le jet et le sillage de la voilure seront résolues de manière itérative ; nous nous intéresserons donc pour le moment au système formé par les autres équations. Ce système peut se décomposer en deux parties : les équations correspondant à l'écoulement non portant, et les équations résultant des conditions de JOUKOWSKI et de la modélisation de l'ensemble propulsif. Les premières équations forment un système linéaire, tandis que la seconde partie est quadratique.

Pour résoudre le système linéaire, on isole les inconnues "sources" correspondant aux équations, et on résout un système avec autant de seconds membres qu'il y a d'équations dans la partie quadratique. Cette résolution est faite par la méthode de GAUSS-SEIDEL par bloc. La partie non linéaire du système d'équations est résolue par la méthode de NEWTON. On initialise la méthode de NEWTON de la façon suivante :

- Au lieu d'écrire la condition de JOUKOWSKI en égalant les pressions extrados et intrados, on écrit que la vitesse normale est nulle en un point situé à 0,5 % de la corde, sur le plan bissecteur du dièdre de bord de fuite. On obtient ainsi une équation linéaire.
- Pour initialiser les doublets du jet, on approxime la dérivée sur les panneaux à la dérivée sur la partie infinie du jet :

$$\forall i \quad \left(\frac{\partial \omega}{\partial x} \right)_i = \left(\frac{\partial \omega}{\partial x} \right)_\infty$$

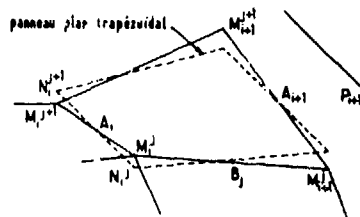
La loi de doublet sur le jet devient ainsi linéaire à partir du bord de fuite de la nacelle, et on obtient toutes les valeurs des ω_i à partir de la condition de JOUKOWSKI sur la nacelle.

4.2 - Calcul de la géométrie des frontières libres -

Pour une géométrie donnée du jet et de la nappe de la voilure, on a vu que l'on peut obtenir l'intensité de toutes les singularités. On est donc capable de calculer la vitesse normale en un point quelconque de ces surfaces. Il s'agit alors de mettre au point un processus itératif pour calculer les géométries de la nappe et du jet, qui sont initialisées par des parallèles à l'axe des x .

4.2.1 - Calcul de la géométrie du jet -

La discrétisation du jet est effectuée à partir de plans P_i perpendiculaires à l'axe des x . Ces plans restent fixes au cours des itérations, et le maillage est donc défini dès que l'on connaît les segments $M_i M_{i+1}$ et $M_{i+1} M_{i+1}^{(k+1)}$ (voir figure ci-dessous) :

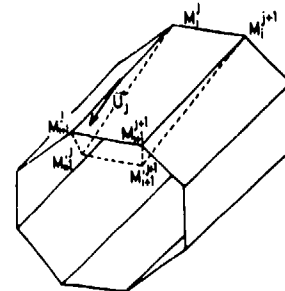


Les panneaux plans sur lesquels sont répartis les doublets linéaires sont obtenus à partir des surfaces gauches $M_i^j, M_{i+1}^j, M_{i+1}^{j+1}, M_i^{j+1}$ par moyenne

$$\frac{\overrightarrow{N_i^j N_i^{j+1}}}{\| \overrightarrow{N_i^j N_i^{j+1}} \|} = \frac{\overrightarrow{M_i^j M_i^{j+1}} + \overrightarrow{M_{i+1}^j M_{i+1}^{j+1}}}{\| \overrightarrow{M_i^j M_i^{j+1}} + \overrightarrow{M_{i+1}^j M_{i+1}^{j+1}} \|}$$

en conservant les milieux A_i et A_{i+1} des segments.

Le calcul itératif de la géométrie du jet se ramène donc à l'équilibre des lignes ($M_0^j, M_1^j, \dots, M_n^j$) qui s'échappent du bord de fuite de la nacelle. On utilise pour cela une méthode analogue à celle de BUTTER & HANCOCK²⁵. On calcule la vitesse au point B_j et on aligne le segment $M_i^j M_{i+1}^j$ sur cette vitesse. Dans certains cas le point B_j est sur le bord d'un panneau de doublets linéaires, et on ne peut y calculer la vitesse. On fait donc une interpolation entre les vitesses calculées au milieu des deux panneaux voisins. Le calcul de la surface du jet se fait alors tranche par tranche : on calcule sur tous les segments d'une tranche les vitesses U_j . On applique alors la méthode précédente pour calculer les points M_{i+1}^{j+1} et on obtient une nouvelle section de jet. La nouvelle géométrie en aval est un cylindre s'appuyant sur cette section et parallèle à l'axe des x .



4.2.2 - Calcul de la géométrie de la nappe de la voilure -

La nappe de la voilure est définie par des panneaux plans sur lesquels sont répartis des doublets constants. Cette discrétisation est équivalente à des tourbillons qui s'échappent du bord de fuite et qui vont jusqu'à l'infini. Ces tourbillons sont représentés par des segments jusqu'à une certaine distance puis par des demi-droites parallèles à la vitesse d'entraînement. Le calcul de la géométrie se fait avec la même méthode que précédemment, tranche par tranche à partir du bord de fuite. Comme d'autre part il y a interaction entre la nappe et le jet, il faut traiter simultanément les tranches de jet et de nappe qui sont face à face.

4.3 - Intégration des différents processus itératifs -

Le schéma du programme de calcul est représenté sur la figure 3. Le calcul des singularités est effectué à chaque itération par deux processus itératifs qui utilisent comme initialisation les résultats de l'itération précédente. Quand on a obtenu la solution du système, on fait converger le jet et la nappe-voilure. Le test de convergence porte sur la différence entre les solutions de deux itérations successives.

5.- RESULTATS PRELIMINAIRES -

La méthode qui vient d'être présentée permet d'analyser l'écoulement autour d'une voilure et d'une nacelle lorsque l'on prend en compte les effets du réacteur, par une entrée d'air de débit variable et par un jet propulsif d'énergie variable. Cette méthode repose sur deux hypothèses simplificatrices : l'écoulement est incompressible et le fluide est non visqueux. Dans ce paragraphe nous présenterons quelques comparaisons avec des résultats d'essais en soufflerie; pour l'interprétation de ces comparaisons, il faudra donc tenir compte des hypothèses précédentes. Voici tout d'abord quelques résultats obtenus lors de l'étude en écoulement bidimensionnel.

5.1 - Résultats en écoulement bidimensionnel -

Les principes de la méthode ont été mis au point sur un programme bidimensionnel. Ce programme permet de traiter des configurations comme celle de la figure 4. Cette planche montre l'influence du paramètre δ sur la géométrie du jet : plus δ est élevé, plus le jet a d'énergie, et moins il est perturbé par la présence de l'aile et de l'aileron. La figure 5 illustre l'influence du jet sur les coefficients de pression et les coefficients aérodynamiques de l'aile. Le jet augmente les C_p de l'extrados et diminue globalement la portance de l'aile. Pour faire varier le débit à l'intérieur de la nacelle, le programme bidimensionnel utilise un corps central dont la géométrie est calculée par affinité à partir d'un profil de référence. La figure 6 illustre l'influence du paramètre δ et du coefficient de débit sur l'écoulement autour de l'aile et de la nacelle. Quand on fait passer δ de la valeur 0 à la valeur 3, la géométrie du jet varie et le débit augmente (resserrement des lignes de courant dans le jet). Pour satisfaire un certain coefficient de débit ($E = 1,19$), on place un corps central qui modifie à la fois l'écoulement à l'entrée d'air et la géométrie du jet.

5.2 - Résultats en écoulement tridimensionnel -

Le cas de calcul le plus simple est la configuration nacelle de résolution isolée. On peut étudier les résultats du programme sur une telle configuration en faisant varier la pression génératrice et l'incidence. Les figures 7 et 8 permettent de comparer la géométrie du jet pour deux valeurs du paramètre δ , quand la nacelle a une incidence de 10° . En débit naturel on retrouve l'enroulement classique d'un sillage, et la formation d'un "jet" dont la section prend une forme de haricot. Lorsque $\delta = 5$, le jet a beaucoup plus d'énergie, il est moins dévié que le jet naturel, et l'enroulement est retardé. Ce comportement caractéristique d'un jet en incidence a déjà été mentionné dans la littérature 12 & 26.

La figure 9 montre l'influence du paramètre δ sur les coefficients de pression de la nacelle. Le saut de pression génératrice se traduit par une augmentation brutale de C_p d'une valeur égale au paramètre δ ; en effet le champ des vitesses est continu, et les coefficients de pression sont calculés à partir de la pression statique à l'infini amont. Sur cette planche on remarque d'autre part une accélération des vitesses sur la lèvre intérieure de l'entrée d'air, et un déplacement du point d'arrêt vers l'extérieur, ce qui correspond à une augmentation du débit.

5.3 - Comparaison avec des résultats d'essais -

L'intérêt essentiel de cette méthode est l'analyse de l'influence du jet sur une voilure, et en particulier sur le champ de pression autour de la voilure. Nous disposons pour cette étude de quelques résultats d'essais, qui n'ont malheureusement pas été réalisés dans des conditions identiques, puisque les nacelles utilisées étaient fermées à l'avant. Ces résultats sont donc à utiliser avec réserve, les comparaisons portant sur l'ordre de grandeur de l'influence du jet plutôt que sur sa valeur réelle.

La première configuration test est celle de la référence 27, présentée sur la figure 10. Il s'agit d'une nacelle simplifiée, l'objet principal de l'étude étant l'interaction entre le jet et la voilure. Cette voilure est une voilure droite d'allongement 3.4, générée par un profil symétrique NACA 0010. Les essais menés avec cette maquette consistaient en une étude paramétrique, à Mach faible, de l'influence du jet sur la voilure, les paramètres étant la position de la nacelle, et la variation de vitesse du jet. Nous nous sommes contentés d'étudier une seule configuration géométrique, en faisant varier l'énergie du jet. La figure 10 fournit les caractéristiques géométriques correspondant à cette configuration. Les seules mesures faites lors des essais concernaient la portance de la voilure. La figure 11 permet de faire la comparaison entre les résultats des essais et ceux de la méthode de calcul. Le programme mis au point indique une variation de portance qualitativement dans le même sens, mais cette augmentation de C_z est inférieure à celle obtenue lors des essais. Cette différence est peut-être due au phénomène d'entraînement du jet non pris en compte dans notre modèle théorique.

La seconde configuration test est celle de la référence 28, présentée sur la figure 12. La voilure est une aile sans flèche non vrillée, avec une section CLARK Y de 11,7 % d'épaisseur relative et 300 mm de corde. Le montage est du type à la paroi. La nacelle est une nacelle de révolution; elle est fermée à l'avant et possède de grandes dimensions par rapport à la voilure (longueur 770 mm, diamètre de sortie 200 mm). Les essais ont été réalisés à faible vitesse et on peut négliger les effets de la compressibilité. Dans son état actuel, ce programme ne permet de traiter que des maillages grossiers. Le maillage utilisé pour étudier cette configuration est illustré sur les figures 14 et 15; la nacelle est découpée en 8 bandes de 40 panneaux, la voilure en 8 bandes de 60 panneaux, et le jet comprend 8 bandes de 25 panneaux. Le découpage sur la voilure est fait de manière à ce que les bandes voisines de la nacelle correspondent aux sections où ont été faites les mesures de pression. La nacelle prise en compte par le programme est ouverte à l'avant. Les conditions ne sont donc pas tout à fait les mêmes que lors des essais; mais étant donné les grandes dimensions de la nacelle, on peut considérer l'influence de l'entrée d'air comme négligeable au niveau de la voilure. Puisque les essais ne prennent pas en compte l'entrée d'air, on n'impose pas de condition sur le débit dans la nacelle. Pour chaque configuration géométrique, deux essais ont été faits pour deux valeurs de la vitesse d'éjection:

- . $V_e = V_0$, ce qui permet de calculer l'influence de la nacelle sans jet propulsif.
- . $V_e = 4V_0$

Les valeurs correspondantes du paramètre δ sont 0 et 15.

Avant de faire les comparaisons avec les essais, il est bon d'avoir une référence qui fournisse les caractéristiques du programme. Un calcul a donc été fait avec la voilure seule. La figure 13 compare les répartitions de portance obtenues par les essais et par le calcul. On retrouve la surestimation classique de la portance obtenue par les méthodes numériques en fluide parfait. Il faut donc s'attendre à la même différence pour les configurations avec nacelle et avec jet.

Les essais réalisés au NLR portaient sur 4 configurations géométriques différentes; à titre de comparaison nous n'avons étudié que deux combinaisons nacelle-voilure, correspondant aux cas I et III des essais: dans le cas I, la nacelle est sous la voilure, tandis que dans le cas III, la nacelle est au-dessus de l'aile; dans les deux cas, l'incidence est nulle. La figure 14 permet d'étudier l'influence du jet sur les C_z de la voilure dans le cas III, quand la nacelle est au-dessus de l'aile. La variation de C_z se fait dans le même sens que les essais mais elle est plus faible. Ce cas est en fait très comparable aux essais du paragraphe précédent, car le jet est très proche de l'extrados de la voilure. La différence viendrait donc de l'effet d'entraînement du jet.

La figure 15 fournit la comparaison entre les répartitions de C_z , dans le cas I. On observe la même surestimation que pour l'aile seule et la présence du jet induit une diminution de portance. Mais cette variation est légèrement plus faible que l'écart mesuré en soufflerie.

La comparaison entre ces deux dernières planches appelle une remarque : la méthode prédit mieux les variations de portance dans le cas I que dans le cas III. Or, dans le premier cas, le jet est plus loin de la voilure que dans le second cas ; l'effet de blocage est donc relativement important. La méthode développée jusqu'ici permet donc de prédire une partie de l'interaction jet-voilure. L'estimation fournie sur les variations de portance locale est meilleure quand le jet n'est pas trop près de la voilure.

6.- CONCLUSION -

La méthode qui vient d'être présentée permet d'analyser l'écoulement autour d'une voilure et d'une nacelle lorsque l'on prend en compte les effets du réacteur décomposés en deux parties : entrée d'air et jet propulsif. L'intérêt d'une telle méthode tient au fait qu'elle permet de traiter l'ensemble comme un tout, sans nécessiter le découpage entrée d'air-jet-voilure. La suite de l'étude portera sur les points suivants :

- . prise en compte de l'effet d'entraînement du jet,
- . corrections de compressibilité,
- . intégration du mât réacteur.

REFERENCES -

- 1) - SWAN W.C. and SIGALLA A.
The problem of installing a modern high bypass engine on a twin jet transport aircraft
AGARD CP-124 (Dec. 1973)
- 2) - AHMED S.R.
Prediction of the optimum location of a nacelle shaped body on the wing of a wing-body configuration by inviscid flow analysis - AGARD CP-150 Paper 25 (1975).
- 3) - PUTNAM L.E.
An analytical study of the effects of jets located more than one jet diameter above a wing at subsonic speeds - NASA TN D-7754 (1974).
- 4) - SQUIRE H.B. and TROUNCER J.
Round jets in a general stream - R & M n° 1974, Brit A.R.C (1944)
- 5) - SPANGLER S.B., MENDENHALL M.R. and DILLENIUS M.F.E
Theoretical investigation of ducted fan interference for transport-type aircraft.
NASA SP-228 pages 703 à 716 (1970)
- 6) - LAN C.E.
Some characteristics of airfoil-jet interaction with Mach number nonuniformity.
AIAA Jnl Vol.11 (Août 1974)
- 7) - LAN C.E. and CAMPBELL J.F.
Theoretical aerodynamics of upper-surface-blowing jet-wing interaction - NASA TN D-7936 (Nov. 1975)
- 8) - LAN C.E. and CAMPBELL J.F.
Theoretical predictions of jet interaction effects for USB and OWB configurations.
NASA SP-406, Paper 13 (1976)
- 9) - LAN C.E.
A theoretical investigation of over-wing-blowing aerodynamics - NASA CR-144,969 (Mars 1976)
- 10) - LAN C.E. and CAMPBELL J.F.
A wing-jet interaction theory for USB configuration - AIAA Jnl - Vol 13 n° 9 (Septembre 1976)
- 11) - LAN C.E. - CAMPBELL J.F. and FILLMAN G.
Theoretical prediction of over-wing-blowing aerodynamics - AIAA Paper 77-575 (Juin 1977)
- 12) - SHOLLENBERGER C.A.
Three dimensional wing/jet interaction analysis including jet distortion influences
AIAA Jnl - Vol 11 n° 9 (Septembre 1975)
- 13) - GILETTE W.B.
Nacelle installation analysis for subsonic transport aircraft - AIAA Paper 77-102 (Janvier 1977)
- 14) - SNEL H.
Evaluation of a method for the prediction of jet-airframe interference - NLR TR-76.132 U (Nov.1976)
- 15) - BOUSQUET J.
Méthode des singularités : théorie et applications - COURS ENSAE
- 16) - LOEVE W. and SLOOFF J.W.
On the use of "panel methods" for predicting subsonic flow about aerofoils and aircraft configurations - NLR MP 71.018 U (Octobre 1971)
- 17) - KRAUS W.
Berechnung der Beiwerte der Längsbervegung aus der Druckverteilung des MBB-Unterschallpanelverfahrens - MBB - UFE 741 (1971).

- 18) - KRAUS W.
Computational fluid dynamics - Panel method in aerodynamics - VKI Lectures Series 87 (1976)
- 19) - HESS J.L. and SMITH A.M.O.
Calculation of nonlifting potential flow about arbitrary three-dimensional bodies
ES 40622 - DOUGLAS AIRCRAFT Co. 1962
- 20) - HESS J.L.
Calculation of potential flow about arbitrary lifting bodies
MDC 15679-01, (Octobre 1972), DOUGLAS AIRCRAFT Co.
- 21) - HESS J.L.
The problem of three-dimensional lifting potential flow and its solution by means of surface singularity distribution - COMPUTER METHODS IN APPLIED MECHANICS AND ENGINEERING (1974)
- 22) - YERMIA M.
Calcul des caractéristiques d'empannages dans le champ tourbillonnaire d'une voilure
98me COLLOQUE D'AERODYNAMIQUE APPLIQUEE de l'AAAF (Octobre 1972).
- 23) - HUNT B. and SEMPLE W.G.
Economic improvements to the mathematical model in a plane/constant - strength panel method
PAPER PRESENTED AT EUROMECH COLLOQUIUM 75 AT RHODE (BRAUNSCHEWIG, WEST-GERMANY) May 1976.
- 24) - HUNT B.
The panel method for subsonic aerodynamic flows : A survey of mathematical formulations and numerical models and an outline of the new British aerospace scheme.
VKI Lectures Series (Avril 1978)
- 25) - BUTTER D.J. and HANCOCK G.I.
A numerical method for calculating the trailing vortex system behind a swept wing at low speed.
AERONAUTICAL Jnl - Vol 75 (Août 1971).
- 26) - MARGARSON R.J.
Analytical description of jet-wake cross sections for a jet normal to a subsonic free stream
NASA SP-218 (Sept. 1969)
- 27) - FALK H.
The influence of the jet of a propulsion unit on nearby wings - NACA TM-1104 (1946)
- 28) - SNEL H.
Evaluation of a method for the prediction of jet-airframe interference - NLR TR-76.132 U (1976).

REMERCIEMENTS

Ce travail a été partiellement financé par le marché DRET n° 77-44-463-00 pour l'étude en écoulement bidimensionnel et par le marché STPA n° 78-98-008-00 pour l'étude en écoulement tridimensionnel.

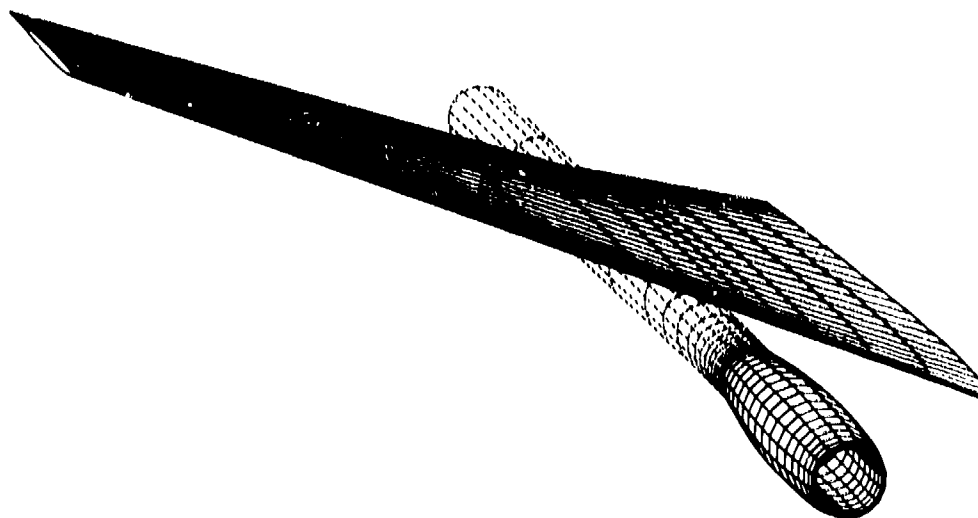


Fig 1. CONFIGURATION NACELLE - JET - VOILURE

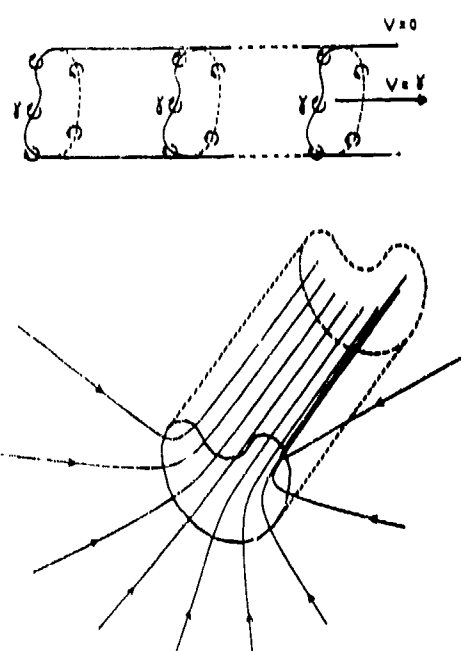


FIG.2-JET NON VISQUEUX INFINI :

Répartition de tourbillons et champ de vitesse

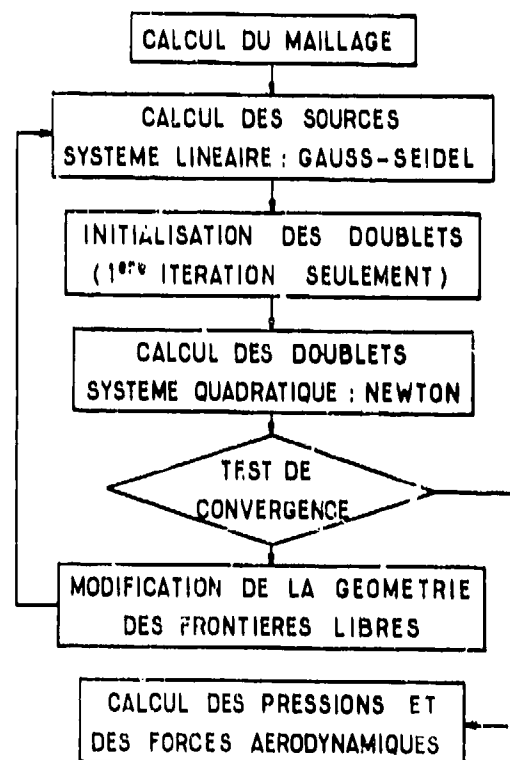


FIG : 3

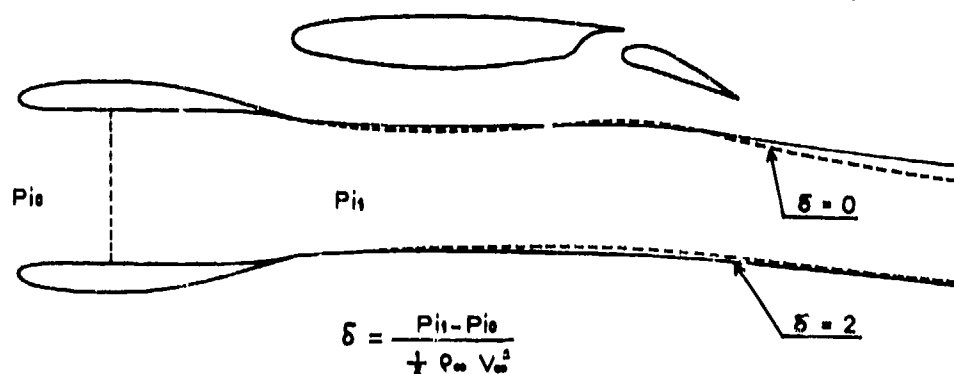


FIG:4-GEOMETRIE DU JET DANS LE CAS OU $\delta=0$ ET $\delta=2$

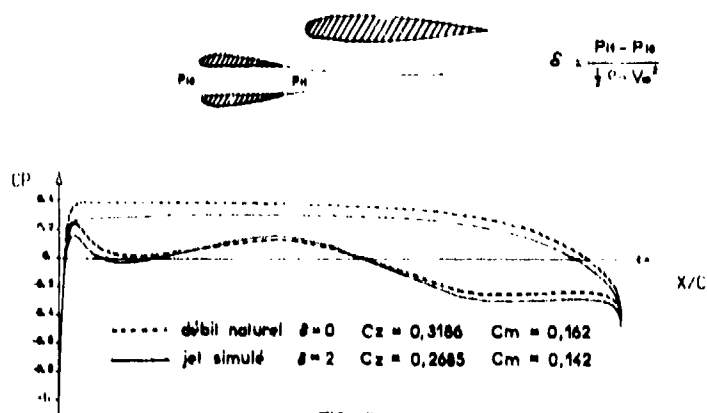


FIG. 5
VALEURS DES CP SUR LE PROFIL DE L'AXE - INFLUENCE DU PARAMETRE δ

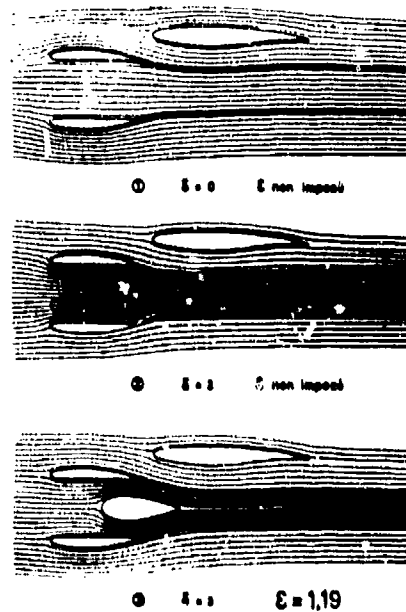


FIG. 6 - ECOULEMENT ENVOISIONNEL
INFLUENCE DE LA PRESSION GENERATRICE ET DU COEFFICIENT
DE DEBIT

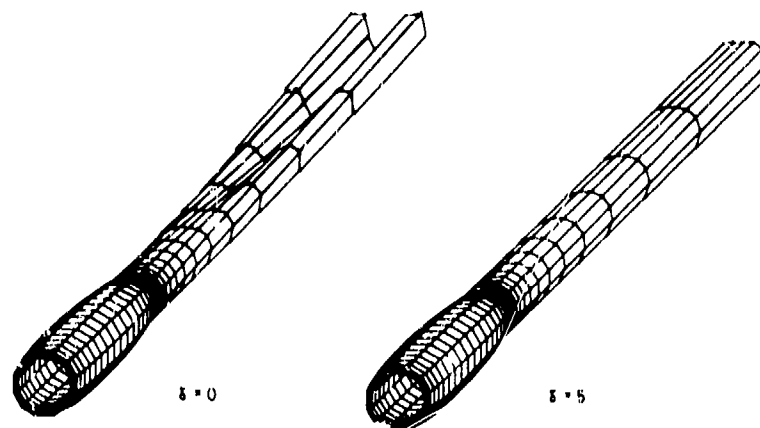


FIG. 7 NACELLE EN INCIDENCE $\alpha = 10^\circ$
INFLUENCE DE LA PRESSION GENERATRICE SUR LA GEOMETRIE DU JET

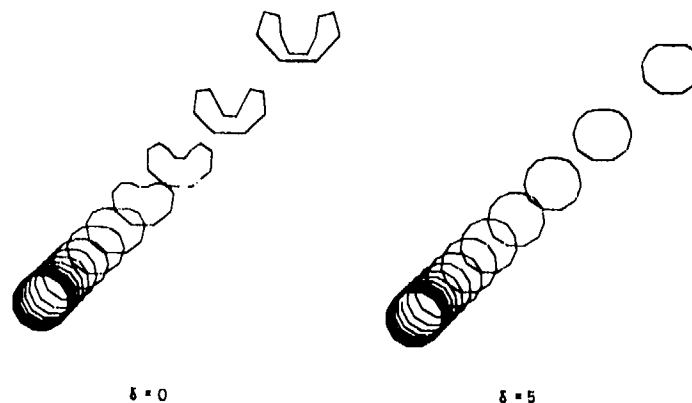


FIG. 8 NACELLE EN INCIDENCE $\alpha = 10^\circ$
INFLUENCE DE LA PRESSION GENERATRICE SUR LES SECTIONS DU JET

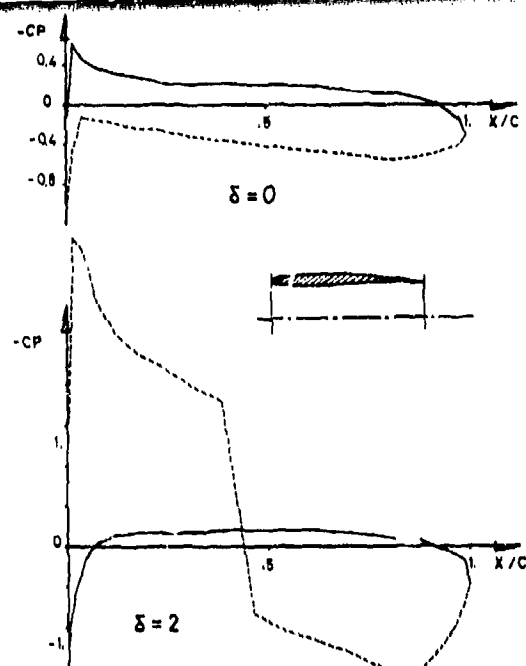


FIG. 9 NACELLE DE REVOLUTION SANS INCIDENCE
INFLUENCE DE LA PRESSION GENERATRICE

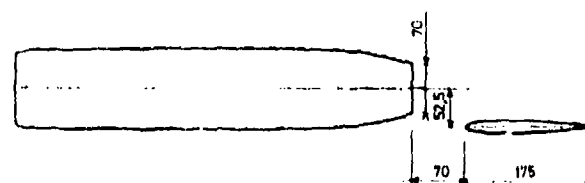


FIG. 10 CONFIGURATION GEOMETRIQUE CORRESPONDANT AUX ESSAIS

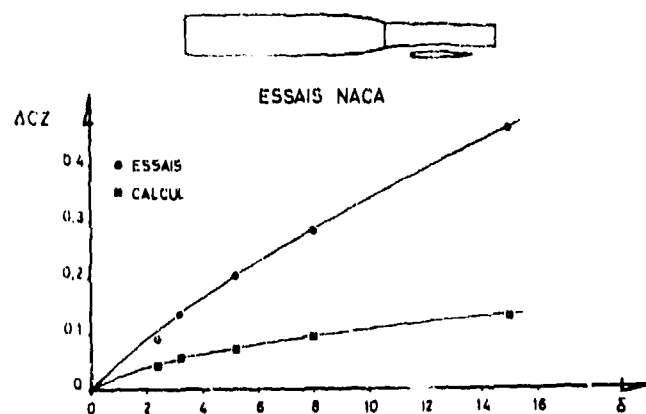


FIG. 11 INFLUENCE DE LA PRESSION GENERATRICE SUR LA PORTANCE DE LA VOILURE

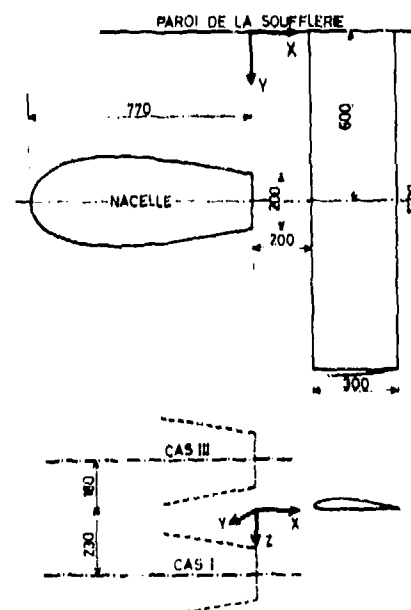


FIG. 12 CONFIGURATION GEOMETRIQUE CORRESPONDANT

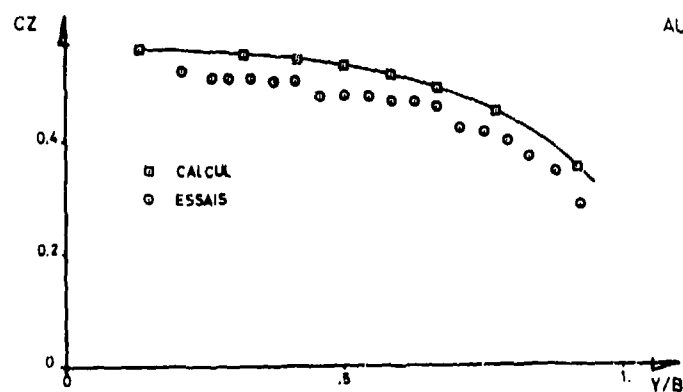


FIG. 13-ESSAIS NLR AILE SEULE REPARTITION DES CZ EN ENVERGURE

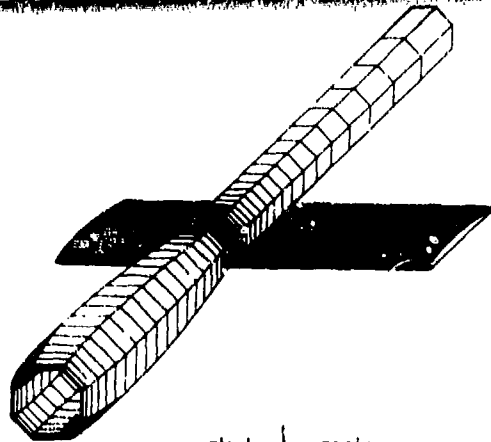


FIG.14 ESSAIS NLR CAS II
INFLUENCE DU JET SUR LA
REPARTITION DE CZ DE L'AILE

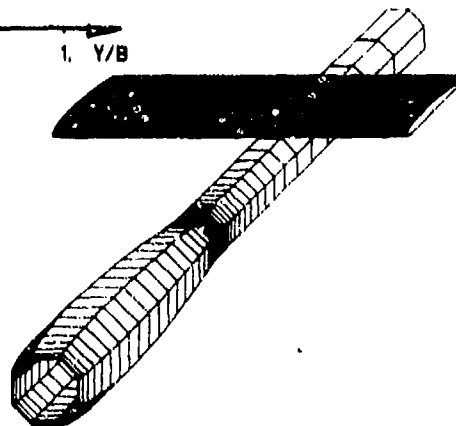
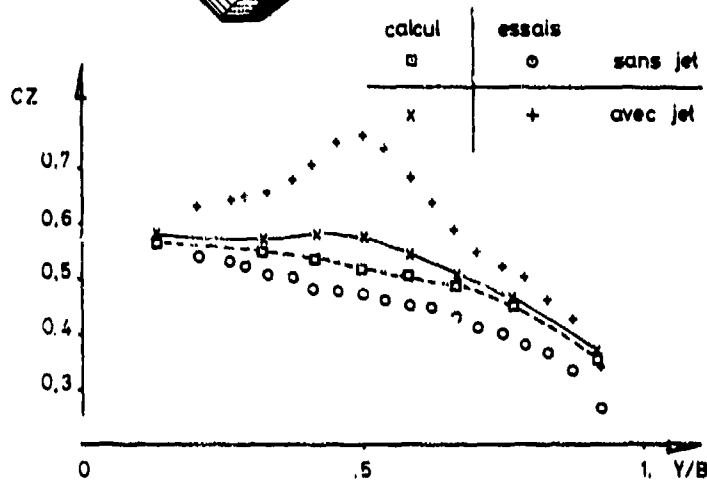
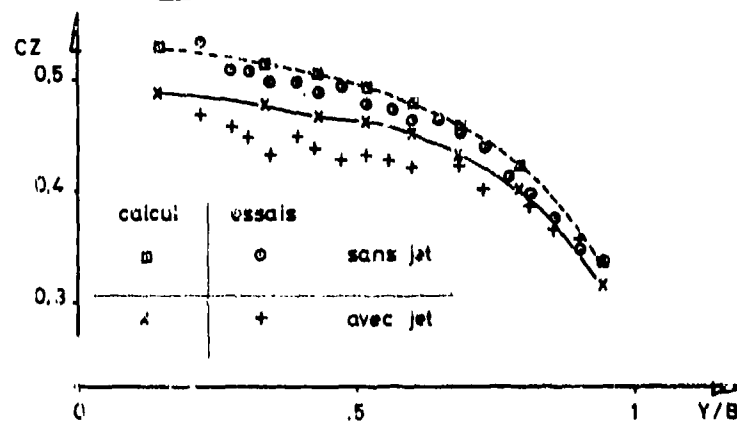


FIG.15 ESSAIS NLR CAS I
INFLUENCE DU JET SUR LA
REPARTITION DE CZ DE L'AILE



CALCULATION OF WING-BODY-NACELLE INTERFERENCE
IN SUBSONIC AND TRANSONIC POTENTIAL FLOW

by
K.D. Klevenhusen
H. Jakob
H. Struck
VFW GmbH
D 2800 Bremen
Germany

SUMMARY

An economic and practical calculation method is presented. The method has been developed especially for transport aircraft wing design with consideration of interferences such as wing-body or engine-airframe interference. A so called "Hybrid Method", consisting of a combination of panel method and finite difference-method, is described as an improvement of a well proved Analogy Method. The panel method is of higher order using linear source and doublet distributions. The transonic flow region is removed from the entire flow field and the panel method is used for calculating boundary values for the subsequent finite difference method. The finite difference method solves the full potential equation in streamline coordinates.

LIST OF SYMBOLS

b	- half span	V_n	- normal velocity
C_l	- lift coefficient	x	} - coordinates
C_p	- pressure coefficient	y	
C_p^*	- critical pressure coefficient	α	- angle of attack
l	- chord length	η	- spanwise station
M_∞	- free stream Mach number	ϕ	- velocity potential

1. INTRODUCTION

The significance of propulsion system/airframe interference flows was diversely assessed in the past. The evaluation was dependant on the aircraft mission which was consequently utilized for the design concept. In the case of V/STOL technology, interference was a main item for research work, whereas in the transport aircraft technology this topic was relegated to lesser importance with the exception of few cases of singular configurations with unorthodox engine positioning as the VFW 614 aircraft. However, it was only after the economic crises called by fuel prices escalation that the interference problem gained befitting importance in transport aircraft technology. The aerodynamic treatment is further complicated with the introduction of shockfree transonic wing technology and engine size problems due to bypass ratio increase.

The principle of interference effects on the wing flow and efficiency at high speeds is outlined in FIG 1. The nearly shockfree flow of the design case, which is advantageous for lift to drag performance, is destroyed and the spanwise lift distribution is affected.

The aim of applied aerodynamics is to reinstate a favourable pressure distribution design concept after considering the interference effects. Furthermore the limiting effects of wing lofting on manufacture, etc., must be considered. It is very important to develop and use suitable theoretical and experimental methods to solve these problems. For the theory it is very essential that the expenditure and accuracy of the method used is matched to the development stage of the programme. Experimental research could also make a contribution using the simulation of the through flow nacelle instead of complicated TPS techniques (see [1]). This applies also for the theoretical treatment of similar problems which are detailed in this paper.

As the object of theoretical research is to render consistent assistance to design work, it is necessary for theoretical methods to satisfy the following conditions:

1. Applicability to the actual design
This necessary condition stipulates that the method should be adapted to the design philosophy.
2. Economic handling
The method should be cost effective requiring a minimum of computer and manpower costs. Further, a rapid repetition of the design iterations should be possible.
3. Practical handling
Simplicity in input and output and handling of the method should be aimed at. It should be unnecessary for the designer to understand the whole theory.

4. Modern state

Reliable modern methods should be applied but care should be taken as not all of these methods warrant superior design. It is the designers task to consider a range of design parameters. After selecting a design philosophy and thereafter, with the correct application of the right method corresponding to the problem, he should be capable of interpreting the computed results in a practical manner as a part of the engineering art.

A further important range of application of theoretical methods is the understanding and interpretation of experimental results. In FIG 2 experimental data at a wing section very close to the pylon/nacelle station shows plausible differences between the pressure distributions of the wing/body alone and the wing/body/nacelle/pylon configuration. The nacelle and pylon have a distinct effect at the lower surface of the wing and give a higher peak and stronger shock at the upper surface.

Considering FIG 3 where the same configuration has the same angle of attack and Mach number, the measured pressure distribution is farther from the pylon than in FIG 2. Here the pylon and nacelle have a smaller effect on the lower surface of the wing as expected due to the greater distance, however, the upper surface of the wing is more greatly affected in the supercritical flow range. The influence of the pylon/nacelle results in a much smaller peak and a much weaker shock. As this result does not seem plausible, theoretical simulation of a similar wing/pylon/nacelle configuration in the subsonic and transonic flow regime was done to clarify this phenomenon.

Theoretical and experimental wing/pylon/nacelle investigations represent the first step in treating jet interferences, which shall be shown at the end of this report.

2. VFW ANALOGY METHOD

A well tested reliable method for designing supercritical wings for transport aircraft is the VFW Analogy method shown in FIG 4. This method is used to calculate the transonic pressure distribution over a wing including wing/body or wing/body/engine interferences. The calculation steps begin with subsonic pressure distributions taken from experiment or 3D panel calculations. This procedure takes advantage of the cheaper, more exact and easier handling of theoretical and test methods of the subsonic flow regime, together with the greater existing experience at hand compared to the transonic flow regime.

In the second step -which requires some experience- analogous profiles, Mach numbers and angles of attack are determined for the desired wing sections.

In the final step the transonic pressure distribution is calculated by a 2D Finite Difference Method after Bauer/Garabedian/Korn/Jameson [2] or the VFW 2D Finite Difference Method which includes the treatment of 2D transonic interferences [3,4,5]. The practical advantage of this quasi 2D procedure for handling wing sections lies in the short computing time which enables many design loops to be repeated. The importance for checking the off-design characteristics and modifying the required section shape must be emphasized. Some results with this method for a wing/nacelle configuration are shown in FIG 5. The comparison of two measured pressure distributions showing the influence of flow through a nacelle on the left compared with the results calculated by the Analogy Method on the right. The comparison of calculations with tests show that the Analogy Method can calculate the significant effects of wing/nacelle interference even with small interference effects.

The comparison in FIG 6 between tests and calculations do not show the same good agreement achieved in FIG 5. It is uncertain whether this represents a limiting case for the Analogy Method or this coincides with the unexplained phenomena in FIGS 2 and 3, which occurred with a greater nacelle wing station distance in FIG 3. For the purpose of solving such limiting cases and simultaneously having two comparative theoretical methods at hand the following Hybrid Method has been developed.

3. VFW-HYBRID METHOD

This Hybrid Method is similar to the Analogy Method but without using analogous profiles, analogous Mach numbers and angles of attack. FIG 7 shows the similarity with the Analogy Method. The calculations begin with a Panel Method but in contrast to the Analogy Method not at subsonic but at the actual transonic Mach number using Goethert's rule. The Panel Method is of a higher order using linear source and doublet distributions. A special algorithm for solving the system of linear equations for determining the singularity strengths allows very short computing times. The calculation of a supercritical wing with 500 panels for example takes only 150 seconds on IBM 3033.

In a second step, boundary conditions are calculated with the Panel Method and in a final step, a Finite Difference Method determines the supercritical flow. The procedure can be explained on basis of FIG 8. Only a small region of the supersonic flow field bounded by Γ_0 , Γ_1 , Γ_2 and Γ_3 is considered for which streamline coordinates are calculated with the 3D Panel Method. This system used is a quasi orthogonal. In this small region, the full transonic potential equation is solved by means of Finite Differences. The boundary conditions prescribed on Γ_1 , Γ_2 and Γ_3 are either the velocity potential (Dirichlet conditions)

or the normal velocity (Neumann condition). The condition of vanishing normal velocity is required for the wing contour Γ_0 . All the above boundary conditions are calculated by the VFW Panel Method.

The 3D streamline coordinate system of a rectangular wing is shown in FIG 9. The coordinates were not determined sectionwise by 2D-methods but calculated together in one step by means of the 3D Panel Method. In the following lifting rectangular wing (see FIG 10) good agreement is achieved between the VFW calculations and Bailey's TSP-Method. In FIGS 11 and 12 calculations are presented for a supercritical wing with rear loading. There is a very good agreement with experimental results.[6]

For the further reduction of the Hybrid Method computer time and achieve ease in handling, a 2 D computing grid was used sectionwise. The grid, similar to the 3D net, is calculated using a 2D Panel Method after [3]. A consequent simplification is then made, wherein, the 3D Finite Difference Method is replaced by a 2D method, applied sectionwise to the 3D transonic full potential equation in which all derivatives in the spanwise direction are prescribed from panel calculations. This means that mathematically, a 2D boundary value problem is solved.

The manner of treating the transonic wing flow sectionwise is similar to the VFW Analogy Method, however, in contrast to the latter, no analogous profiles, Mach numbers and angles of attack are necessary, consequently the application of this special version of the VFW Hybrid Method requires lesser experience than the Analogy Method.

The second version of the VFW Hybrid Method is applied to a wing/nacelle/pylon configuration, see FIG 13. The nacelle wake is simulated with a cone having non-vanishing normal velocities found experimentally. For this case correct knowledge of the wakes contour is less important than that of the normal velocity distribution. The calculated pressure distributions of the clean wing and the wing/pylon/nacelle configuration are shown in FIG 14. Good agreement with the test results of FIG 2 are achieved after matching the lift coefficient. The calculations show stronger shocks compared to the tests which could result among others from either the neglected boundary layer effects or the incorrect shock jump conditions. The normal shock included in the present theory does not quite represent the swept wing condition. The further development of the Hybrid Method thus promises a great range of applications.

4. JET INTERFERENCE

Greater interference effects occur in wing/nacelle/jet configurations. Many experimental and theoretical investigations have been done at VFW to clarify the complicated physical effects and to evolve a mathematical model for prescribing jet effects in the subsonic flow regime. FIG 15 shows a Panel Model of the VFW 614 aircraft. The jet is simulated by a cylinder about 15 diameters length. At the cylinder boundary, normal velocities derived from a semi-empirical theory [7] are prescribed. In the next FIG 16 test and calculated data are compared, showing very good agreement. Furthermore it can be seen, that the jet induces a higher lift for the over-wing nacelle installation.

Much more complicated interference effects have been treated for VTOL aircraft in ground effect [7], see FIG 17. Here, in addition to free jets, a wall jet has also to be simulated. The following FIG 18 shows that the suck-down effects induced by the free jets and the wall jet can also be determined.

These few examples of jet/airframe interference show the utility of the described mathematical jet model for subsonic flow. Further research is necessary and improvements of this model will commence after completing the VFW TPS experiments in the transonic flow regime.

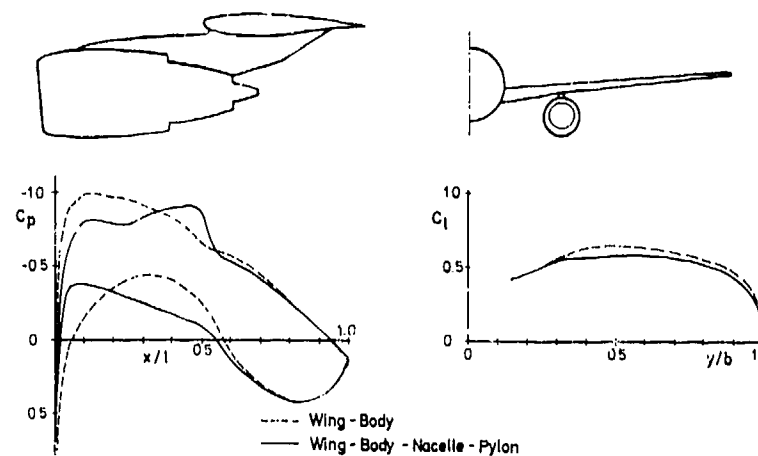
5. CONCLUSION

The methods presented in this report are to be seen as efficient design tools. Short computing time, a minimum of man power and a rapid repetition of the design iterations are the economic features. Practical handling facilitates the design work. The presented VFW Analogy Method requires much experience and engineering art. On the other hand the described VFW Hybrid Method is very similar to the Analogy Method, but requires much lesser experience. With both methods complicated interferences as wing/body/nacelle/pylon interferences can be treated in the transonic flow regime.

7. REFERENCES

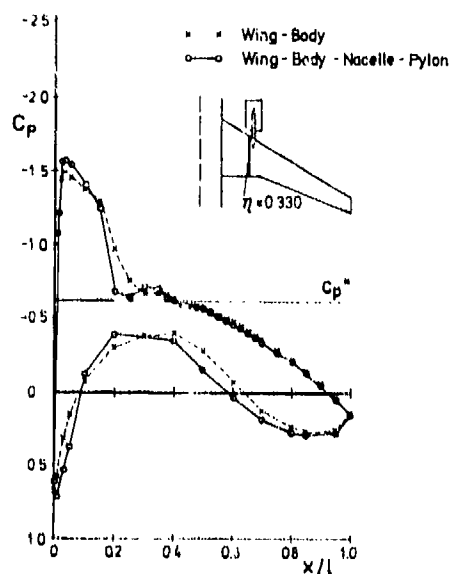
- [1] B. Ewald, R. Smyth
The Role and Implementation of Different Nacelle/Engine Simulation Concepts for Wind-Tunnel Testing in Research and Development Work on Transport Aircraft.
AGARD Symposium on Aerodynamics of Power Plant Installation, 11-14 May 1981.
Toulouse, France

- [2] F. Bauer, P. Garabedian, D. Korn, A. Jameson:
Supercritical Wing Section II.
Lecture Notes in Economics and Mathematical Systems, Vol. 108,
Springer-Verlag, Berlin, Heidelberg, New York, 1975
- [3] K. D. Klevenhusen:
A Calculation Method for Multielement Airfoils in Subsonic and Transonic
Potential Flow.
AIAA-paper 80-0340, 18th Aerospace Sciences Meeting,
Jan. 14-16, 1980/Pasadena, California, USA
- [4] H. Rosch, K. D. Klevenhusen
Flow Computation Around Multi-element Airfoils in Viscous Transonic Flow.
AGARD, Conference Proceedings No. 291, Computation of Viscous-Inviscid Interactions.
29 Sept.-1 Oct. 1980, Colorado Springs. Colorado, USA
- [5] H. Rosch, K. D. Klevenhusen
Flow Computation Around Multi-element Airfoils in Viscous Transonic Flow
12th Congress of the International Council of the Aeronautical Sciences (ICAS).
12-17 October 1980, Munich, FRG, (ICAS-80-11.3)
- [6] K. D. Klevenhusen, H. Jakob, H. Stuck
Neue Rechenverfahren zur sub- und transsonischen Interferenzströmung im ebenen
und räumlichen Fall.
ZKP-Ergebnisbericht Nr. 44, Nov. 1979,
LFK 7511-Flügelsektion.
- [7] H. Struck, K. D. Klevenhusen
The Prediction of Jet Interference Effects by Means of Panel Methods.
Euromech Colloquium 75
Braunschweig/Rhode, 10-13 May, 1976.



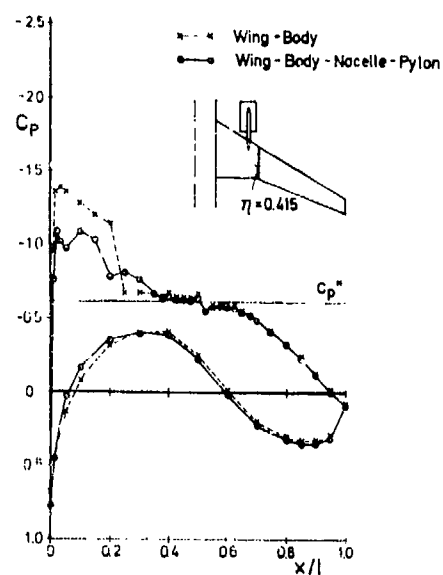
WING - NACELLE - INTERFERENCE

FIG. 1



COMPARISON OF PRESSURE DISTRIBUTIONS
EXPERIMENT ($\alpha = 2^\circ$, $M_\infty = 0.75$)

FIG. 2



COMPARISON OF PRESSURE DISTRIBUTIONS
EXPERIMENT ($\alpha = 2^\circ$, $M_\infty = 0.75$)

FIG. 3

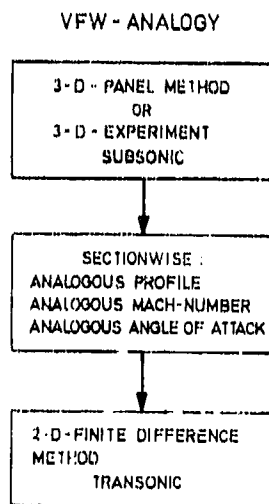
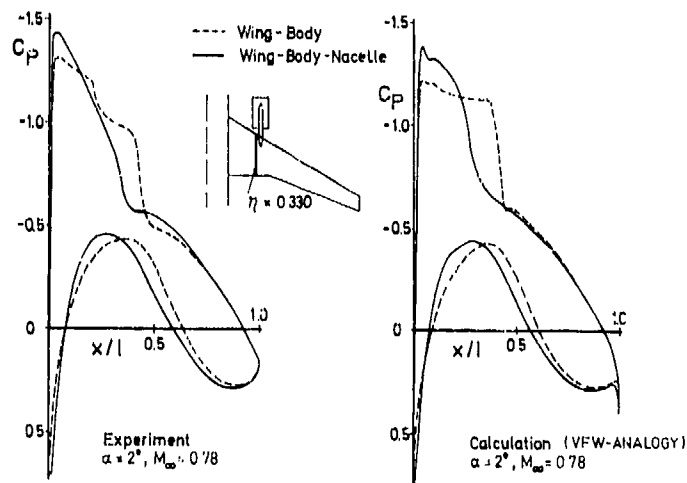
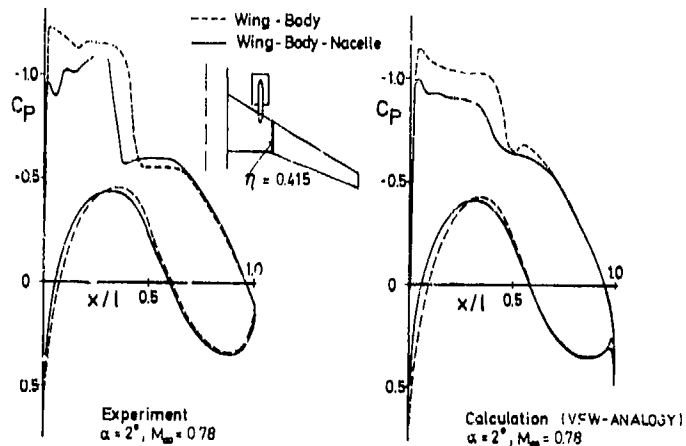


FIG. 4



WING-NACELLE-INTERFERENCE

FIG. 5



WING-NACELLE-INTERFERENCE

FIG. 6

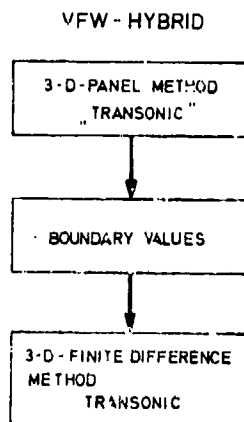
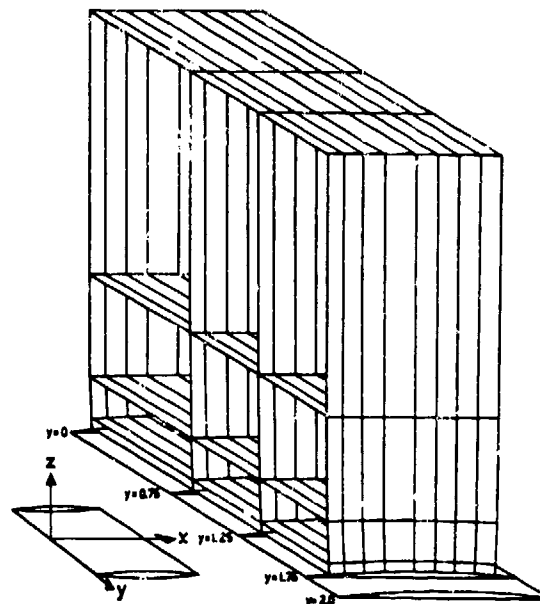
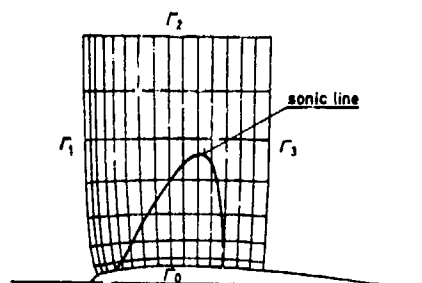


FIG. 7



3D-STREAMLINE
COORDINATES

FIG. 9



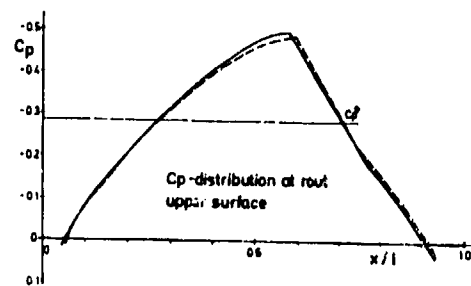
Boundary conditions

$$\text{at } r_0 : \frac{\partial \phi}{\partial n} = 0$$

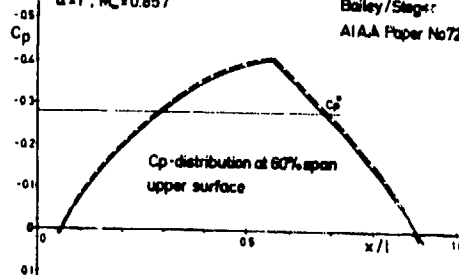
at r_1, r_2, r_3 : Prescription of ϕ or V

SMALL COMPUTING DOMAIN FOR
CALCULATING SUPERSONIC FIELD

FIG. 8

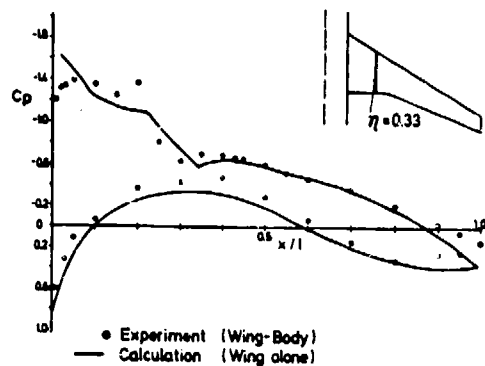


Rectangular Wing $R=4$
Biconvex section 8%
 $\alpha=1^\circ$, $M_\infty=0.857$
Bailey/Stager
AIAA Paper No 72-189



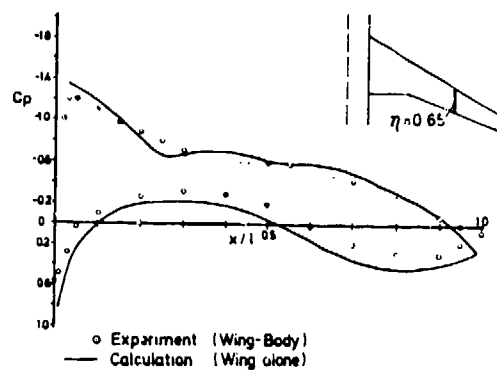
CALCULATED PRESSURE ON
TRANSONIC, LIFTING RECTANGULAR WING

FIG. 10



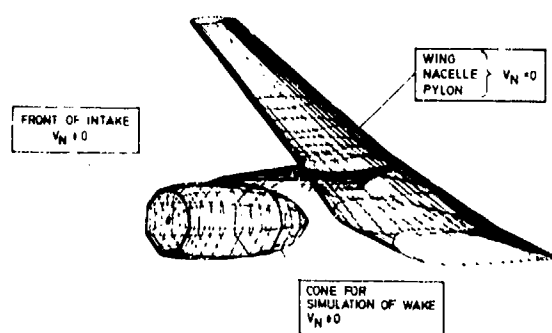
COMPARISON OF PRESSURE DISTRIBUTIONS
 $\alpha = 15^\circ$, $M_\infty = 0.75$, ZKP WING

FIG 11



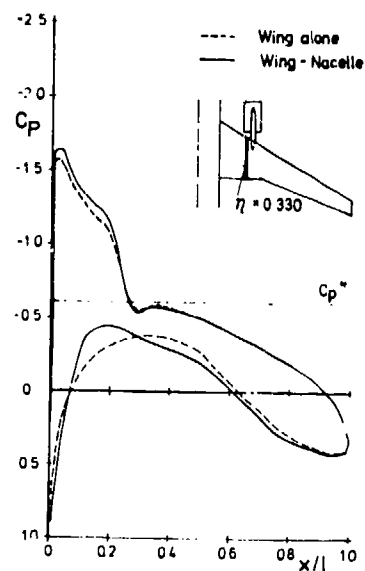
COMPARISON OF PRESSURE DISTRIBUTIONS
 $\alpha = 15^\circ$, $M_\infty = 0.75$, ZKP WING

FIG 12



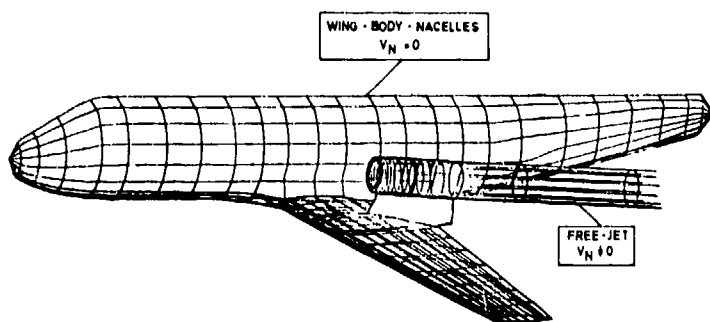
WING-NACELLE-PYLON CONFIGURATION
 PANEL HALF SPAN MODEL

FIG. 13



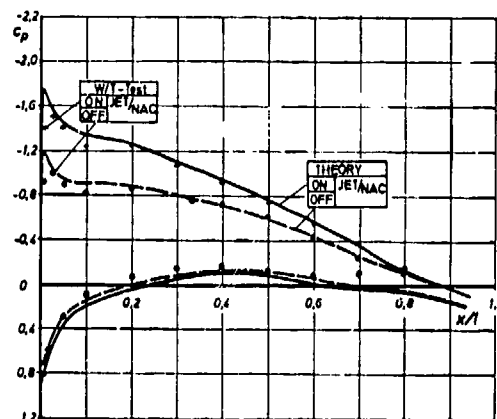
WING-NACELLE-INTERFERENCE
 CALCULATION HYBRID METHOD
 $\alpha = 2^\circ$, $M_\infty = 0.75$

FIG. 14



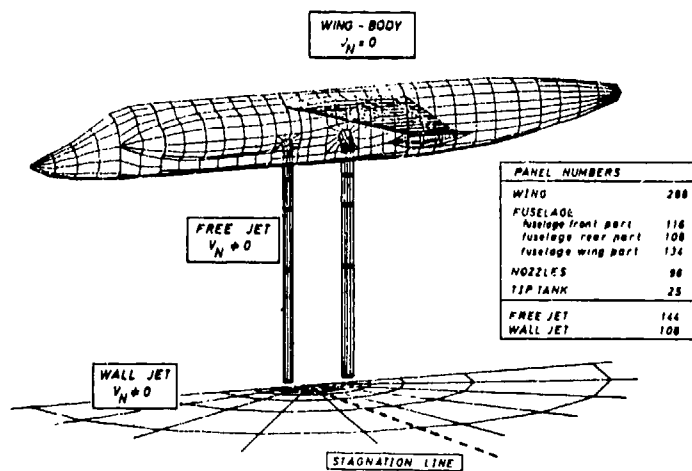
STOL AIRCRAFT
PANEL MODEL

FIG. 15



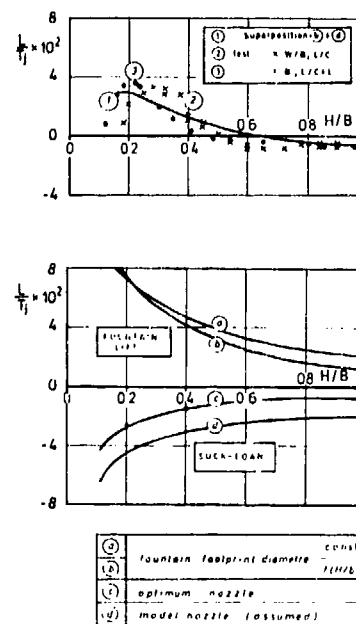
STOL AIRCRAFT
WING / BODY - JET - INTERFERENCE
Over - Wing Nacelles

FIG. 16



VTOL AIRCRAFT (IGE)
PANEL MODEL

FIG. 17



VTOL AIRCRAFT (IGE)
THEORY / EXPERIMENT

FIG. 18

PREDICTION OF SUBSONIC AIRCRAFT FLOWS WITH JET EXHAUST INTERACTIONS

by
D. W. Roberts
Specialist Engineer
Boeing Military Airplane Company
Mail Stop 41-52
P.O. Box 3707
Seattle, Washington 98124
U.S.A.

SUMMARY

A numerical procedure has been developed to calculate the flow fields resulting from the viscous-inviscid interactions that occur when a strong jet exhaust and aircraft flow field coupling exists. The approach used in the current procedure is to divide the interaction region into zones which are either predominantly viscous or inviscid. The flow in the inviscid zone, which surrounds most of the aircraft, is calculated using an existing potential flow code. The viscous flow zone, which encompasses the jet plume, is modeled using a parabolized Navier-Stokes code. The key feature of the present procedure is the coupling of the zonal solutions such that sufficient information is transferred between the zones to preserve the effects of the interactions. The zonal boundaries overlap with the boundary conditions being the information link between zones. An iteration scheme iterates the coupled analysis until convergence has been obtained. The procedure has been successfully used for several test cases for which the computed results are presented.

1.0 INTRODUCTION

New varieties of military and commercial aircraft of interest use a strong coupling between the jet exhaust flow and the overall airplane flow field to enhance performance. These aircraft range from STOL transports such as the Boeing YC-14 and the NASA QSR to combat aircraft with highly integrated nozzles that can be used for life enhancement and thrust vectoring. Development of these aircraft requires the ability to achieve a high performance for a low development cost. The complex flow interactions characteristic of nozzle installations with strong flow field couplings make the development of such installations expensive, high risk undertakings when using conventional parametric test based design approaches. The 3-D flow fields associated with these installations can include mixing layers, wakes, separation, and strong curvature effects as illustrated in Fig. 1. With little applicable experimental data available and without appropriate analytical tools, the designer of such installations is faced with a formidable task.

In the traditional design approach, the designer relies heavily on parametric model scale wind tunnel test simulations of the proposed installation over the range of nozzle and flight conditions to be encountered by the aircraft. The available aerodynamic and propulsion performance data base is used to aid in the selection of a configuration. Analytical procedures that are used are generally 2-D and, therefore, have limited value. High quality model scale wind tunnel tests of complex nozzle installations have proven to be expensive and extremely difficult to implement. Often the details of the boundary layers and the jet plume are not measured. This leads to uncertain results which cannot be meaningfully scaled when designing a larger device. Hence, the test based design approach is usually expensive while providing results of unknown quality.

Developments in computational fluid mechanics and computer technology offer the potential for a significant improvement in the design process. Numerical codes have been developed to model complex 3-D flows. When the appropriate analyses are available, parametric analysis can replace parametric wind tunnel testing in the design process. This offers distinct advantages since the analytical approach allows the designer to maintain precise control over the flow and boundary conditions. Full scale installations can be examined since physical size is not a constraint for a computer program. Furthermore, all of the flow variables can be examined in detail to obtain a better understanding of the flow. Wind tunnel testing is still necessary to validate the analysis and for "fine tuning" the design, but the configuration test matrix can be substantially reduced in size with an equivalent reduction in development cost. As computers increase in size and speed and codes become more efficient, the analytical approach offers an increasingly practical and less expensive alternative for the design process.

Analysis of the complex flow phenomena associated with the strongly coupled nozzle installations with a single flow analysis would require a solution of the complete Navier-Stokes equations. Even with today's flow modeling codes and state-of-the-art computers, this is not practical. Accurate numerical solutions would require vast amounts of storage and days of computer processing time. When the number of parameters to be varied in the design process is considered, one can imagine that the computational costs would be prohibitive aside from the necessary technology developments.

The problem of numerically modeling these complex flow fields can be examined from another perspective. Not all of the flow phenomena of interest occur in all

regions of the flow domain. One can divide the flow domain into separate zones in which only certain phenomena are known to exist. The complete Navier-Stokes equations can then be simplified to model the flow in each zone. Hence, instead of one solution of the Navier-Stokes equations for the full domain, one has a set of simplified zonal solutions that must be carefully coupled together to preserve the interzonal interactions. This reduction in the overall complexity of the problem significantly decreases the computational costs and brings the solution of the problem back into the realm of what is practical to achieve. The zonal modeling approach to the solution of fluid mechanics problems has existed for years. Numerous examples of procedures for successfully coupling potential flow codes to boundary-layer codes have been presented in the open literature. These procedures have typically used a boundary-layer displacement thickness to couple the effect of the developing boundary layer to the potential flow solution. Lemmerman and Sonnad (Ref. 1) have recently demonstrated that a surface transpiration approach is equivalent while offering a reduction in computational costs. Brune, Rubbert, and Forester (Ref. 2) demonstrated a more sophisticated zonal modeling approach by coupling a potential flow code to a 2-D Navier-Stokes code to model the flow separation behind an ellipsoid. The demonstrated success of zonal modeling for these simpler flows suggests that it is a practical and feasible approach for simulating complex 3-D flow fields.

The zonal modeling approach discussed in the following sections was used to develop an analytical procedure for predicting strongly coupled jet exhaust interactions with the overall airplane flow field. In this analysis the flow domain is divided into inviscid and viscous zones. The inviscid zone encompasses the entire aircraft. The viscous zone is carved out of the inviscid zone and surrounds the jet exhaust plume which is dominated by viscous interactions. One can envision more zones such as the 3-D boundary layers on the aircraft surfaces or a separation zone on the nacelle as depicted in Fig. 1, but these are beyond the scope of the present study. In the inviscid zone, a 3-D potential flow solution is computed by the PANAIR pilot code (Ref. 3). A numerical method for the parabolized 3-D Navier-Stokes equations (Ref. 4) is used to calculate the flow in the viscous zone. A key feature of the present work is the development of a solution coupling procedure and an associated iteration scheme that result in converged solutions while preserving the necessary flow of information between the zones.

The present paper discusses the overall solution strategy, the component analyses, the coupling procedure and computed results. Several conclusions are drawn from the work to-date and recommendations are made for further development of the procedure.

2.0 DISCUSSION OF THE COMPONENT ANALYSES

PANAIR Pilot Code

The PANAIR pilot code (henceforth called PANAIR) is a preliminary version of an advanced panel code intended to solve a variety of boundary value problems in steady subsonic or supersonic inviscid flow. This code is discussed in Reference 3. Just the subsonic capability will be considered here, since the coupled analysis procedure is at present limited to subsonic flow.

The PANAIR analysis is based on the assumption that for a wide range of flow conditions, a potential flow solution will substantially describe the flow past a prescribed configuration. This implies that the flow is assumed to be inviscid and irrotational.

The flow past the configuration is considered to be a small perturbation of a uniform flow that exists far upstream. PANAIR generates the potential flow solution in terms of the perturbation velocity potential, ϕ , which is used to calculate the local perturbations in the flow properties. The basic boundary condition employed in PANAIR is that the total mass flux vector be parallel to solid surfaces. Non-solid surfaces can have mass fluxes normal to the surface.

The method used in PANAIR to compute the potential flow is to superimpose fundamental solutions of the partial differential equation for ϕ . These fundamental solutions are sources and doublets whose locations are prescribed but whose strength must be determined to meet the prescribed boundary conditions. The sources and doublets are distributed on continuous networks of quadrilateral "panels" that approximate the surface of the configuration, as well as the vortex sheets shed from trailing edges and other surfaces such as inlet faces and jet plumes. Each panel is divided into subpanels on which the source and doublet strengths are approximated by linear and quadratic functions respectively. These functions contain the unknown source and doublet strengths which are then determined by the simultaneous solution of the algebraic system of equations. The resulting potential and velocity fields are then determined. The pressure field can then be calculated, and the forces and moments on the configuration can be computed.

Paneling

In general a configuration is divided into a system of networks which are composed of panels. The number of networks depends on the complexity of the configuration. The number of panels in a given network will depend upon the detail and accuracy desired from the analysis. To use PANAIR as part of the coupled

analysis, networks for the surface of the configuration and its wakes are supplied. Networks defining the jet plume and its wake are also required. Additional networks are necessary for obtaining the flow properties at points off the body. These panels which do not disturb the flow, are specified with zero jumps in the potential and the normal component of mass flux.

Boundary Conditions

The panels are covered with a continuous distribution of sources and doublets. Boundary conditions are imposed at selected "control points" on the networks to generate the necessary set of equations which are solved for the unknown singularity strengths. Networks can have just sources or just doublets in which case the boundary conditions for the other singularity type are not required. Special options exist for the treatment of wakes.

The user determines the flow behavior by specifying the types of boundary conditions on each of the networks. The most commonly used types of boundary conditions are those for impermeable surfaces, which are used on the wetted surfaces of an aircraft. For the coupled analysis the jet plume network has boundary conditions that allow the specification of the perturbation mass fluxes normal to the panel surfaces. Thus, the plume network is a permeable surface that entrains fluid from the surrounding potential flow.

Parabolized Navier-Stokes Code

The parabolized Navier-Stokes code (PNS) was developed to calculate a particular class of three-dimensional compressible viscous flows. The flows of interest are characterized by a predominant flow direction and by negligible influence of downstream disturbances on the upstream flow. Thus, the assumption is made that the propagation of perturbations in the upstream direction by convection, diffusion, or pressure can be neglected for this particular class of flows. Cross stream propagation is allowed and in fact can be significant. Flows of this type are generally classified as being "parabolic". Numerous internal and external flows ranging from complex 3-D duct flows to 3-D jets mixing with a freestream are known to be parabolic.

The time averaged Navier-Stokes equations with suitable closure for turbulent flows are acknowledged as being sufficient for analyzing complex viscous flow fields. When the parabolic approximations are implemented, the resulting equations are simplified for practical solution in a design oriented computer program. The Navier-Stokes equations are parabolized by neglecting the streamwise diffusion terms and decoupling the streamwise and cross stream pressure gradients. The streamwise pressure gradient is assumed to be uniform at each cross-sectional station. In the PNS code a simple marching solution procedure was implemented which eliminates communication with the downstream flow while solving the parabolized Navier-Stokes equations. Other features of the PNS code, which are discussed in the following sections, are the use of a general coordinate system, the transformation of the flow equations, the pressure-continuity relations, the turbulence model, and the solution procedure.

General Coordinate System

Flows in geometrically complex domains are difficult to compute on standard orthogonal computational meshes such as Cartesian or cylindrical coordinate systems. The difficulties arise because the mesh points do not naturally fall on the boundaries of the flow domain of interest. This results in cumbersome differentiation and interpolation schemes at the boundaries that can achieve only low levels of accuracy. For many flows it is desirable to maintain high accuracy at the boundaries. For this reason significant effort in recent years (Refs. 5-8) has been aimed at generating general coordinate systems that are fitted to the boundaries of the flow domain. In the PNS code a curvilinear mesh is formed in which the boundary mesh points always fall on the natural boundaries of the flow domain and the interior mesh points conform to the boundary shape. This allows the use of standard differencing expressions and maintains high levels of accuracy at the boundaries. The boundary-fitted mesh is particularly suited for coupling with a panel method which also can handle arbitrary geometries. Numerous methods exist for automatically generating the boundary-fitted meshes. These methods offer varying degrees of complexity and capability. Orthogonal meshes can be generated, but absolute orthogonality has not been demonstrated to be necessary or worth the effort, though highly skewed meshes are undesirable.

Transformed Flow Equations

To use the general boundary-fitted computational mesh, the flow equations are formulated with ξ , η , and σ as the independent variables. Using standard transformation relations the Cartesian primitive variable form of the Navier-Stokes equations is transformed to the ξ , η , and σ coordinate system. These equations are parabolized with the σ coordinate specified to be the streamwise or predominant flow direction. The transformed equations are further simplified by requiring that the cross-sectional planes be parallel and perpendicular to the σ coordinate. This limits the amount that the mean centerline of the flow domain can deflect from a straight line, but any significant curvature would typically indicate a non-parabolic flow. In ξ , η , and σ coordinates the parabolized steady, three-dimensional

continuity, momentum and energy equations are as follows:

$$(y_{\eta} \rho u)_{\xi} - (y_{\xi} \rho u)_{\eta} + (x_{\xi} \rho v)_{\eta} - (x_{\eta} \rho v)_{\xi} + (D \rho w)_{\xi} + (E \rho w)_{\eta} + [(J/z_{\sigma}) \rho w]_{\sigma} = 0 \quad (1a)$$

$$F u_{\xi} + G u_{\eta} + (J \rho w / z_{\sigma}) u_{\sigma} + y_{\eta} P_{\xi} - y_{\xi} P_{\eta} = S \quad (1b)$$

$$F v_{\xi} + G v_{\eta} + (J \rho w / z_{\sigma}) v_{\sigma} + x_{\xi} P_{\eta} - x_{\eta} P_{\xi} = S \quad (1c)$$

$$F w_{\xi} + G w_{\eta} + (J \rho w / z_{\sigma}) w_{\sigma} + \frac{1}{z_{\sigma}} \bar{P}_{\sigma} = S \quad (1d)$$

$$F H_{\xi} + G H_{\eta} + (J \rho w / z_{\sigma}) H_{\sigma} = S \quad (1e)$$

where

$$D = \frac{x_{\eta} y_{\sigma} - x_{\sigma} y_{\eta}}{z_{\sigma}},$$

$$E = \frac{y_{\xi} x_{\sigma} - x_{\xi} y_{\sigma}}{z_{\sigma}}$$

$$F = y_{\eta} \rho u - x_{\eta} \rho v + D \rho w,$$

$$G = -y_{\xi} \rho u + x_{\xi} \rho v + E \rho w$$

$$J = x_{\xi} y_{\eta} - x_{\eta} y_{\xi}$$

The appropriate diffusion terms, which are too cumbersome to present, are represented by the S on the righthand side of each equation. The Cartesian velocity components have been retained. The \bar{P}_{σ} which appears in Eq. (1d) represents the constant streamwise pressure gradient for a given cross-section. In addition to the field equations, an equation of state is included, and a calorically perfect fluid is assumed. Sutherland's formula is used to relate the viscosity, μ , to temperature.

Pressure-Continuity Relations

Although the streamwise and lateral pressure gradients have been decoupled to parabolize the flow equations, they are implicitly coupled through the continuity equation. The functional purpose of the pressure gradients is to insure the conservation of mass both globally and locally. Equations have been developed to guarantee this effect, since mass conservation is an essential requirement for an accurate numerical simulation. A relation for \bar{P}_{σ} , which must be calculated for each cross section, is derived from the w-momentum equation and an integral definition for the mass flow rate. Mass is globally conserved by adjusting \bar{P}_{σ} and iterating the w-momentum equation until the predicted mass flow rate reaches a specified level of accuracy. Global mass conservation is required before local conservation can be considered.

Local continuity is satisfied indirectly by means of the lateral pressure gradients P_{ξ} and P_{η} . These pressure gradients are calculated such that the u and v velocity components generated by Eqs. (1b) and (1c) will simultaneously satisfy the continuity equation (1a) everywhere in the computational domain to a specified tolerance. The method used in the PNS code is similar to methods developed for time-dependent flows (Refs. 9,10). A detailed discussion of the present scheme is provided in Reference 4.

Turbulence Model

Closure of the set of flow equations for turbulent flows is achieved by modeling the Reynolds stresses that appear in the time-averaged Navier-Stokes equations. In the PNS code these stresses are modeled by replacing the laminar viscosity μ with a turbulent eddy viscosity μ_{τ} . The eddy viscosity is calculated from the turbulence kinetic energy k and the turbulence kinetic energy dissipation rate ϵ .

$$\mu_{\tau} = C_{\mu} \rho k^2 / \epsilon$$

The values for k and ϵ are calculated using two additional transport equations (Ref. 11), which have the same form as Eq. (1e) with additional terms that model production and dissipation.

Boundary Conditions

The three velocity components u, v, and w are set to zero on impermeable surfaces. An adiabatic wall boundary condition is used with the energy equation. To minimize the mesh requirements in the lower regions of boundary layers, law-of-the-wall functions are used to represent the velocity distribution near the wall. These functions are used to calculate the wall shear stress and the production and dissipation source terms in the turbulence model equations for the wall region. The use of wall functions allows k and ϵ to be accurately predicted in the vicinity of a wall.

All of the differential equations presented above have been transformed to finite-difference form by standard second order centered difference approximations for ϕ and n derivatives and by one-sided upstream differences for ϕ derivatives. An iterative marching solution procedure was developed for the PNS code to allow converged numerical solutions after just one pass through the flow domain. An initial set of data is required at the starting plane. A solution is obtained at each successive cross section before a step is taken downstream to the next lateral plane. A converged implicit solution of the nonlinear flow equations at each plane is achieved by an iterative ADI procedure. Iteration is required at each plane to reduce the accumulation of truncation errors that can result from linearization. Typically, just a few iterations are required to achieve reasonable accuracy unless the flow is changing rapidly in the streamwise direction.

3.0 COUPLING PROCEDURE

The interactions between the jet plume and the surrounding flow field are simulated by the coupling of the component analyses. It is not sufficient to run each code once in its separate zone. The codes must interact in such a manner that the solution for the entire flow field is convergent and unique within the limits allowed by the algebra incorporated in the codes. Each code must provide information to the other code that adequately describes the physical processes being modeled in that zone. The PNS code, which calculates the jet plume development, must provide PANAIR with the effects of entrainment at the plume boundary. PANAIR must use this information and the other aerodynamic effects of the aircraft to calculate the potential flow field and in turn provide boundary conditions for the PNS code. The procedure developed for coupling PANAIR and the PNS code is discussed in the following sections.

Overlapping Computational Zones

The domain in which the flow field is to be calculated is divided into computational zones for the individual codes. The inviscid zone is oriented to include all regions which can be adequately modeled by the PANAIR potential flow solution. The viscous zone is positioned to surround the jet plume where the viscous interactions are predicted by the PNS code. The location of the boundaries for these zones is a significant aspect of the coupling procedure.

Abutting the zones such that the boundaries are coincident does not provide the necessary flow of information for a convergent coupled analysis. Since both codes in effect solve boundary value problems, a specification of boundary conditions on coincident boundaries would lead to unique solutions in each zone that are functions of those boundary conditions. Unless a prior knowledge of the flow properties on the boundaries was available, the flows predicted in each zone would not necessarily bear any resemblance to the physical flow. New information that could be used to update boundary conditions would not be available since the solutions are boundary condition dependent and their boundary conditions are identical. Iteration is useless without new information. Hence, coincident boundaries lead to a coupled analysis that does not allow the codes to interact and exchange information and yields an iteration procedure that will not be reliably convergent.

The proper coupling of these two codes requires that the boundaries of the computational zones not be coincident. Furthermore, the boundaries of each zone should be arranged such that the boundary conditions are dependent upon the solution in the neighboring zone. This allows the necessary transfer of information from one zone to another. In the present coupling procedure, this is accomplished by overlapping the zonal boundaries. This is illustrated in Fig. 2 for the simple case of an axisymmetric nozzle exhausting into a co-flowing freestream. Note that the boundaries of the viscous zone extend well past the edge of the jet plume and into the region that is inviscid flow. The inviscid zone boundaries extend into the viscous zone to a close proximity of the plume edge where the flow is still dominated by inviscid effects. The overlapping region is shared mutually by both zones. Therefore, the boundary conditions applied in the PANAIR code on the plume boundary can be derived from the flow properties calculated by the PNS code. Similarly, the boundary conditions for the viscous zone can be obtained from the PANAIR solution. The overlapping boundaries therefore provide the necessary communication link between the two zones that allows a simultaneous coupled solution for the flow domain.

The solutions computed by PANAIR and the PNS code are consistent within their numerical accuracies for the overlapping region. If the flows under consideration are restricted to those that are parabolic, the P_0 term in the Equation (1d) will be negligible for external flows. By realizing that the flow in the overlapping region is effectively inviscid, the flow equations reduce to the Euler equations. This region is also irrotational since no mechanism is present to generate vorticity. In the overlapping region the PNS code is in effect solving the potential flow equation which is the fundamental equation of the PANAIR analysis. Therefore, the two solutions should be consistent in this region. Due to the numerical approximations incorporated into these two codes, exact consistency cannot be achieved, but the accuracy will be comparable to that obtained for the complete coupled solution. The effect of the size of the overlapping region was not studied, but it should be kept reasonably small, since it would be inefficient to have a large region in which the

flow is actually calculated twice.

Boundary Conditions

The specification of the boundary conditions on the overlapping boundaries is straightforward. The solution from the PNS code is used to calculate the perturbation mass flux through each of the panels that form the jet plume boundary network. This is accomplished by averaging the predicted velocity components and density on the corners of each panel and using the result to calculate the component of the mass flux vector that is normal to the panel. The array of perturbation mass fluxes is stored for access by the PANAIR code.

The boundary conditions for the PNS code are determined from the PANAIR solution in a similar manner. Special panel networks that do not disturb the flow are positioned in the inviscid zone to form the boundaries for the viscous zone. The predicted velocities on the panels are used to generate the boundary conditions for the PNS code. In the PNS code, these velocities are also used to compute the mass flux entering the viscous zone. The upstream boundary of the viscous zone, Fig. 2, forms the initial data plane for the PNS code. On that boundary, the panel velocities are used to calculate initial conditions, therefore, that region is initially irrotational.

Mesh and Panel Generation

The generation of the panels on the overlapping boundaries is directly related to the generation of the computational mesh for the PNS code. All other panels are directly input into PANAIR through the normal input procedure. Various options can be used to define the boundaries for the overlap region. Each of these options affects the method used for generating the mesh and panels. To facilitate the discussion of these options, consider the diagram in Fig. 2.

The outer boundary of the overlap region (and of the viscous zone) is designated to have a computational mesh index of $J=N$. The inner boundary of the overlap region (the plume boundary for the inviscid zone) has the index $J=JNP$. In the PNS analysis, the JNP mesh points are computationally like all other interior mesh points in the viscous zone. The correct usage of the coupled analysis requires that the JNP boundary lies beyond the edge of the viscous plume while not crossing the $J=N$ boundary.

The simplest option for generating the N and JNP mesh points is to specify the N boundary points at the initial plane and allow the N boundary to expand with a prescribed slope for downstream planes. The JNP points are specified at the initial plane on the edge of the plume and projected downstream with a given slope such that the JNP boundary expands. The panels on the N and JNP boundaries are constructed by using the mesh points on these boundaries as the corner points for the panels. The initial plane panels are similarly generated from the initial plane mesh points. Only simple plumes can be considered since the plume trajectory is limited to a narrow path.

The complexity of the shapes of the plumes to be calculated is enhanced by another option in which the N boundary mesh points are specified for the initial plane and for all succeeding downstream planes. The JNP points are specified in a like manner. The associated panels are generated as discussed above. Clearly, this option requires that the user have some knowledge of the expected trajectory of the plume. This information is often available when the analysis is being used to parametrically examine a case for which some experimental data exists for similar flows. Care must be used in specifying the JNP boundary to guarantee it surrounds the jet plume.

Another option was developed for the coupled analysis to automatically track the jet plume. At the initial plane the JNP boundary points are specified. The N boundary points are computed based on the JNP points and the number of mesh points one desires to have between JNP and N . At each of the downstream planes the JNP points are positioned using the vorticity in the most recent plane to locate the plume edge. This procedure involves calculating the vorticity at all points and determining where the vorticity approaches zero, which indicates the edge of the plume. This data is used to project the JNP points downstream to positions that will be outside of the plume. The maximum change in position can be controlled by specifying a maximum slope from upstream to downstream. The N boundary points are then calculated as before, and the panels are generated. This approach to generating the mesh allows the boundaries of the viscous zone to move and distort with the plume. The viscous zone can then be compact and computationally efficient.

Iteration Procedure

One iteration of the solutions in the inviscid and viscous zones will generally not be sufficient to yield a converged solution for the total flow domain. The essential information transfer between the two zones is accomplished by repetitively updating the boundary conditions and generating new solutions for each zone. An iteration procedure was developed for the coupled analyses to automatically perform the necessary data manipulations and transfers without requiring interruptions by the user.

To start the iteration process, an initialization of the boundary conditions on the overlapping boundary of one of the zones is required. This is done by making an

"educated" guess as to what the boundary values should be. The better the guess the fewer the number of iterations to reach convergence. The zone in which one chooses to initiate the iteration is not important, unless auxiliary information is available to yield a better estimate of the boundary conditions in one of the zones. If the viscous zone is the starting point, the velocity components on the initial plane and the outer boundaries must be provided. The freestream velocity components are often adequate for this initialization purpose. By starting with the inviscid zone, one is faced with the task of estimating the perturbation mass fluxes on the plume panel network. First the overlapping boundary networks must be constructed by executing the panel generation portion of the PNS code. Unless knowledge of the jet entrainment is available, the initial plume boundary fluxes can only be guessed. Using a constant flux is sufficient to start the iteration procedure.

As a demonstration of the iteration procedure, assume that the solution is started in the inviscid zone and refer to Fig. 3. The overlapping boundary panels are generated in the PNS code and the perturbation mass fluxes on the plume panel network are initialized. PANAIR is then executed in the inviscid zone. This potential flow solution is used to calculate the boundary conditions for the viscous zone. The next step is the execution of the PNS code in the viscous zone. This will include the generation of new overlapping boundaries if the plume tracking capability is utilized. New values for the boundary conditions on the plume panel network are computed from the viscous zone solution. At this point these new boundary values can be compared with the old values. If a prescribed level of convergence is achieved, the iteration procedure can be terminated. Otherwise, the iteration loop will continue for a given number of iterations. The alternative of starting the solution in the viscous zone has the same iteration loop with the exception that the starting point would be the fourth step in Fig. 3 in which an initialization of the viscous zone boundary conditions is made.

4.0 VALIDATION CASES

To demonstrate and validate the usefulness of the coupled PNS and PANAIR codes, several test cases were set up and run. The main purpose of these tests was to demonstrate the coupling procedure and show that converged solutions can be achieved. In addition information about the behavior of the coupling procedure as the solutions iterate in the different zones could be obtained and used to understand and improve the existing procedure. While the accuracy of the overall solution depends on the accuracy obtainable by each code, the accuracy of the coupled codes can be validated to some level of satisfaction by comparing the computed solutions with existing experimental data when possible. The following cases provide a variety of the applications of the coupled analysis.

Axisymmetric Jet in a Freestream

The first test case, a subsonic axisymmetric jet in a freestream, was used primarily as an aid in the development of the coupling procedure. The simplicity of this case, see Fig. 2, was desirable since the effects of the coupling procedure and the overlapping boundary condition could be readily isolated. In addition, some experimental data and previous computational work were available for comparison. To minimize the computational costs, the symmetry of the case was used to limit the solution domain to half of the jet. In addition just five mesh points were used on the circumference of the jet, while 21 points were used radially. In the overlapping region seven mesh cells were used to separate the inner inviscid zone boundary from the outer viscous zone boundary. The plume tracking option was used to locate the plume edge by monitoring the vorticity. This guarantees that the number of mesh cells in the jet plume will be the same at all stations since the mesh expands at the same rate as the plume. It also ensures that the panels generated for the plume network will be outside of the plume where the strong viscous effects dominate.

The freestream for this case had a Mach number of 0.2. The ratio of the freestream velocity to the jet core velocity was 0.46. In the jet, the initial velocity was given a constant value which gave the initial velocity profile in the viscous zone a top hat distribution. The turbulence quantities were initialized with values that were empirically determined for developing free shear layers. A constant total temperature was used in the jet and freestream. The initial marching step size, ΔZ , for the PNS code was equal to 0.25 of the initial jet radius. The step size was then gradually increased to a maximum of 1.25 initial jet diameters for one run and 2.5 diameters for another to examine the effect of step size. The coupled analysis iteration was started in the inviscid zone.

Experimental data for the axisymmetric jet is available for the decay of the jet centerline velocity and the spreading rate of the jet. Rodi (Ref. 13) has also computed axisymmetric jets using a turbulence model like that incorporated in the PNS code.

The results computed for this case using the coupled PANAIR/PNS analysis are presented in Figs. 4 and 5. The centerline velocity decay is underpredicted, Fig. 4, when compared with the experimental data. However, the present calculations are similar to Rodi's. Rodi concluded that the two-equation turbulence model was adequate for calculating the axisymmetric jet when the velocity ratio was large. However, he also found that the accuracy of the calculations is sensitive to initial conditions, mesh density, and step size. The sensitivity to ΔZ is confirmed by the present

results. Since the initial conditions were not available, this effect could not be confirmed.

Of greater importance was the information about the coupling procedure that was obtained from this test case. The plume tracking option is very effective in minimizing the required amount of computational mesh in placing the mesh and panels in the proper locations. However, since the final plume boundary is not known until the coupled solution converges, the plume tracker, which calculates the new boundary as the solution is marched through the viscous zone, moves the boundary with each iteration of the PNS code. In effect the overlapping boundary locations converge as the flow solution converges. This has a detrimental effect which tends to reduce the overall convergence rate. The boundary conditions for the viscous zone are calculated at the previous boundary positions, whereas, they are used in the PNS code with the new boundaries. The movement of the boundaries has an associated area change and normal velocity error which lead to an error in the mass flux into the viscous zone. It is this small error in entrainment that tends to slow down convergence. This effect is demonstrated in Fig. 6 which shows the convergence histories for the boundary conditions at several locations along the developing jet. At the upstream locations the convergence rate is substantially greater than at the downstream locations. When the plume tracking option was activated, a maximum allowable slope change was specified. In the initial region this maximum slope was achieved for several steps during each iteration through the viscous zone. Hence, the boundary did not move with iteration or affect the local convergence rate. Farther downstream the maximum slope was not achieved, the boundary moved during each iteration, and the convergence rate was reduced. Convergence of the position of the viscous zone outer boundary is not necessary for convergence of the flow solution. To reduce this detrimental effect, the standard plume tracking option could be modified to move this boundary for only a couple of iterations until a rough position for the plume is found. Then the outer boundary should be frozen to allow a more rapid convergence of the flow solution.

A related point of interest is the effect of convergence on the streamwise pressure gradient term \bar{P}_g . As discussed in the section on Pressure-Continuity Relations, \bar{P}_g is adjusted to satisfy overall continuity. For the axisymmetric jet, \bar{P}_g should be zero at all stations. However, initial errors in the boundary conditions lead to an inconsistent mass flow rate which results in a nonzero \bar{P}_g . As the solution converges these errors diminish and \bar{P}_g approaches zero at all streamwise stations.

Axisymmetric Jet Over an Airfoil

The main purpose for developing the present coupled analysis was to provide an analytical method for predicting the effect of the jet plume on the aerodynamics of a given aircraft configuration. To test the coupled analysis for the interaction problem, a test case was set up for an axisymmetric jet positioned over an airfoil of constant cross section. This case provides a degree of flexibility since the jet position can be varied to determine whether the analysis predicts the expected trends.

A schematic diagram for this test case is depicted in Fig. 7. The axisymmetric nozzle of diameter, D_n , is positioned a height, h , above the airfoil. The leading edge of the airfoil and the nozzle exit plane coincide. The half span of the airfoil was $2.5D_n$. The initial conditions for the jet and the freestream conditions were identical to those discussed above for the isolated axisymmetric jet. The natural symmetry plane was used to simplify this problem. The plume tracking option was also used for this case. A fairly coarse computational mesh and panel network representation was used to conserve computer costs since only trends were to be predicted and no experimental data was available.

The coupled procedure was started in the inviscid zone with a PANAIR solution and then iterated. This case was run with the nozzle at three different heights above the airfoil.

The basic result obtained from this study was the net lift on the airfoil. The airfoil drag was not considered since the boundary layers were not part of this investigation and the jet was not allowed to scrub the wing. Fig. 8 presents a plot of the airfoil lift versus the height of the nozzle. The lift has been normalized by the lift of the airfoil without a jet present, and the nozzle height is normalized by the nozzle diameter. One can observe that the increase in lift is greatest when the nozzle is closest to the airfoil and the interaction is the strongest. The entrainment of the jet increases the circulation about the airfoil which enhances lift. Fig. 8 can only be used to observe trends since the actual increment in lift will be a function of the length of the airfoil among other things. However, the trends predicted by the coupled analysis agree with what is found experimentally. This offers encouragement for the use of this analysis in design.

The effect of the interaction of the jet with the airfoil aerodynamics on the convergence of the overall flow solution was substantial. The convergence history for the boundary conditions on the plume network panels closest to the airfoil surface is presented in Fig. 9. With $h/D = 0.9$ the perturbation mass fluxes approach their final values smoothly and quickly in just three iterations. The convergence behavior was substantially different with $h/D = 0.775$. The rate of convergence was still reasonable, but four iterations were necessary, and it appears that one more iteration

may have been warranted. Part of this slowdown might be attributed to the movement of the jet plume boundaries since the plume actually was deflected upwards and then downwards as it progressed over the airfoil. The stronger interaction at the lower height also affects convergence since the plume has a greater influence on the PANAIR solution for the airfoil which in turn has a large influence on the PNS solution for the plume. In general large perturbations reduce the rate of convergence.

USB Nozzle/Wing

A case of practical interest is that of a rectangular nozzle blowing over the upper surface of a wing, see Fig. 10. This upper surface blowing (USB) type of nozzle has been successfully used in recent years on such aircraft as the Boeing YC-14 and the NASA QSR. In the present case the computed results are compared with the experimental investigation discussed in Reference 14.

The PNS code was modified to predict this case by making use of the natural symmetry of the problem. As shown in Fig. 10 the nozzle exit plane is positioned approximately 0.32 of the wing chord, C , from the leading edge. The nozzle half width, R_n , is .21C. The half span of the wing is 6.4 R_n . Since the coordinates for the wing cross section were not available, they were estimated from a diagram in Reference 14. The angle of attack of the wing was set to zero; however, for the experimental data the wing had an angle of attack which is not known. Therefore, direct quantitative comparisons with the data will not be attempted.

The flow properties were set up to simulate one of the experimental test conditions as closely as possible. The freestream Mach number was $M_\infty = 0.6$. The freestream total pressure and total temperature were 67000 N/m^2 and 289°K . The velocity profile at the nozzle exit plane was estimated from the experimental total pressure surveys. The average total pressure in the nozzle was greater than the freestream. Part of the nozzle flow was supersonic which is beyond the capability of the present PNS code, however, most of the viscous zone was subsonic which allowed the PNS code to successfully generate a solution. The boundaries of the inviscid and viscous zones were fixed since the plume tracking option was not designed to work on a solid surface. The computational mesh in the viscous zone was rather coarse, to minimize computer costs in the development phase of this procedure, and provides only qualitative results.

The principle result from this test case is the effect of the nozzle on the pressure distribution on the upper surface of the wing. Since the wing was analyzed at zero angle of attack and the wing cross section was just an estimate, the calculated pressure distribution did not agree well with the experimental data, and a comparison would be of no value. The predicted trends on the other hand were identical to those found experimentally. Figure 11 provides the calculated chordwise pressure distribution at a position $Y=1.8 R_n$ from the nozzle centerline (PANAIR coordinates are used). The distribution for the wing alone and the wing/nozzle with jet thrust are shown. It is observed that with jet thrust the pressure drops below the wing alone curve at approximately $X/C=0.2$ and rises above it at $X/C=0.6$. Hence, the effect of the jet plume is to reduce the lift of the wing at this spanwise position between X/C of 0.2 and 0.6 and increase the lift beyond X/C of 0.6. This trend is exhibited in the experimental data even to the points at which the curves cross (Fig. 16 in Reference 14). This favorable comparison offers encouragement for the potential of the coupled analysis. Since part of the nozzle flow is supersonic, the pressure distribution along the nozzle centerline at $Y/R_n=0$ cannot be accurately calculated. By modifying the method for calculating pressure in the PNS code, these supersonic regions could be predicted. In addition this case should be run again with denser computational meshes and panel networks to assess the effects of truncation errors. The computations for this case were run on a Cyber 7600 computer. With 450 panels for the PANAIR solutions and approximately 400 total mesh points for the PNS solutions, the cost was 155 seconds per iteration of the coupled analysis. Over ninety percent of the time was spent on the PANAIR computations.

5.0 CONCLUSIONS

The most significant conclusion of the work discussed in this paper is that a successful procedure has been developed for coupling PANAIR and parabolized Navier-Stokes solutions to allow numerical simulations of the strong interactions between jet plumes and the overall aerodynamics of aircraft configurations. Overlapping inviscid and viscous computational zones provide the means for information transfer between the solutions. The iterative coupling procedure is automated and yields convergent solutions. The results of the predicted test cases indicate that the coupled analysis is providing the correct trends.

Both of the component analyses are limited as to the types of flows that can be simulated. The present coupling procedure can be extended by modifying the existing analyses and adding new analyses. The complexity of the flows to be predicted will determine the zonal solution strategy and thus which extensions are necessary to the present procedure. The technology developed for the present procedure will be directly applicable to future work.

Detailed experimental data for 3D flows with a strong coupling between the jet and the flow over an aerodynamic geometry is non-existent. This data is necessary if a detailed evaluation of the procedure reported here is to be made.

6.0 REFERENCES

1. Lemmerman, L. A. and Sonnad, V. R., "Three-Dimensional Viscous-Inviscid Coupling Using Surface Transpiration," Journal of Aircraft, Vol. 16, No. 6, June 1979, pp. 353.
2. Brune, G. N., Rubbert, P. E., and Forester, C. K., "The Analysis of Flow Fields with Separation by Numerical Matching," Symposium on Flow Separation, AGARD Fluid Dynamics Panel, 27-30 May 1975, Gottingen, Federal Republic of Germany.
3. Moran, J., Tinoco, E. N., and Johnson, F. T., "User's Manual Subsonic/Supersonic Advanced Panel Pilot Code," February 1978, NASA CR-152047.
4. Roberts, D. W., and Forester, C. K., "Numerical Prediction of Three-Dimensional Subsonic Diffuser Flows," Flow in Primary, Non-Rotating Passages in Turbomachines, American Society of Mechanical Engineers, New York, N.Y., 1979, 133-139.
5. Thompson, J. F., Thames, F. C., and Mastin, C. W., "Automatic Numerical Generation of Body-Fitted Curvilinear Coordinate System for Field Containing Any Number of Arbitrary Two-Dimensional Bodies," Journal of Computational Physics, 15, 1974, pp. 299-319.
6. Smith, R. E. and Weigel, B. C., "Analytic and Approximate Boundary-Fitted Coordinate Systems for Fluid Flow Simulations," AIAA Paper No. 80-0192, January 1980.
7. Chen, L. T. and Caughey, D. A., "Transonic Inlet Flow Calculations using a General Grid-Generation Scheme," Flow in Primary, Non-Rotating Passages in Turbomachines, American Society of Mechanical Engineers, New York, N.Y. 1979, 125-132.
8. Sorenson, R. L. and Steger, J. L., "Simplified Clustering of Nonorthogonal Grids Generated by Elliptic Partial Differential Equations," August 1977, NASA TM-73252.
9. Amsden, A. A., and Hirt, C. W., "YAQUI: An Arbitrary Lagrangian- Eulerian Computer Program for Fluid Flow at All Speeds," March 1973, LA-5100, Los Alamos Scientific Laboratory.
10. Pracht, W. E., "Calculating Three-Dimensional Fluid Flows at all Speeds with an Eulerian-Lagrangian Computing Mesh," Journal of Computation Physics, 17, 1975, 132-159.
11. Launder, B. and Spalding, D. B., "The Numerical Computation of Turbulent Flows," Computer Methods in Applied Mechanics and Engineering, 3, 1974, 269-289.
12. Forester, C. K., "Higher Order Monotonic Convective Difference Schemes," Journal of Computational Physics, 23, No. 1, 1977.
13. Rodi, W., "The Prediction of Free Turbulent Boundary Layers by use of a Two-Equation model of Turbulence," Ph.D. Thesis, Imperial College, London, 1972.
14. Kettle, D. J., Kurn, A. G., Bagley, J. A., "Exploratory Tests on a Forward-Mounted Overwing Engine Installation," Aeronautical Research Council C.P. No. 1207, London, 1972.
15. Landis, F. and Shapiro, A. H., "The Turbulent Mixing of Coaxial Jets," Proceedings of the Heat Transfer and Fluid Mechanics Institute, 1951, pp. 133-146.

7.0 ACKNOWLEDGEMENT

The author wishes to express his indebtedness to his co-worker, Mr. C. K. Forester for his numerous helpful comments and suggestions. This work was supported by the NASA Ames Research Center under Contract NAS2-10100.

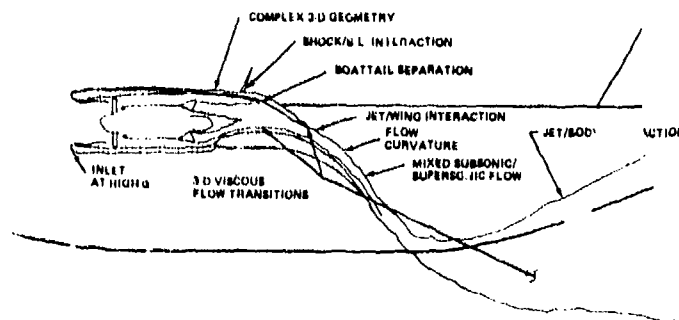


Figure 1. Fluid Flow Problems of Propulsion Powered Lift Installations

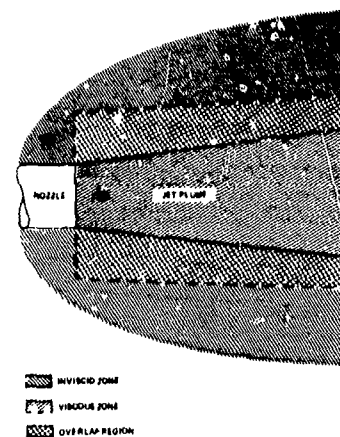


Figure 2. Overlapping Zonal Boundaries

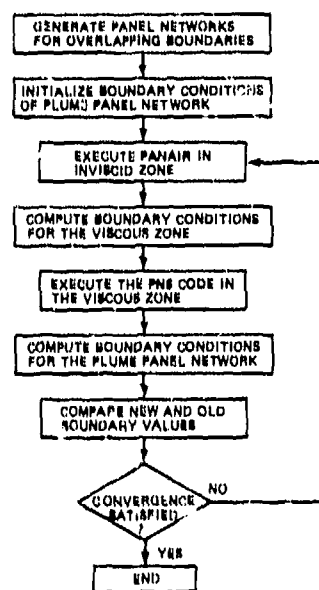


Figure 3. Flow Chart of the Iteration Procedure Used in the Coupled Analysis

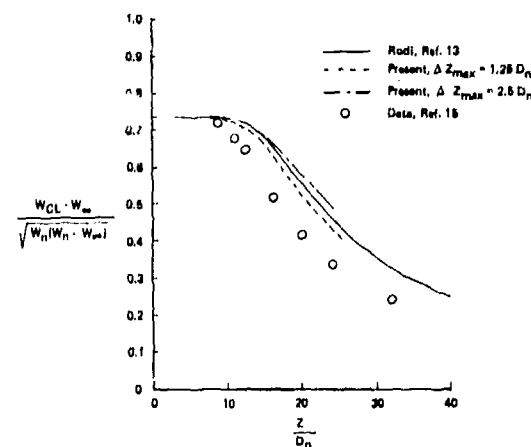


Figure 4. Centerline Velocity Decay for Axisymmetric Jet

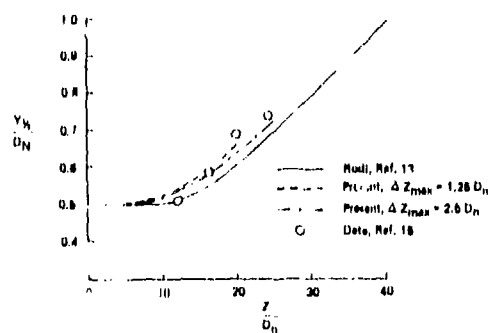


Figure 5. Axisymmetric Jet Spreading Rate

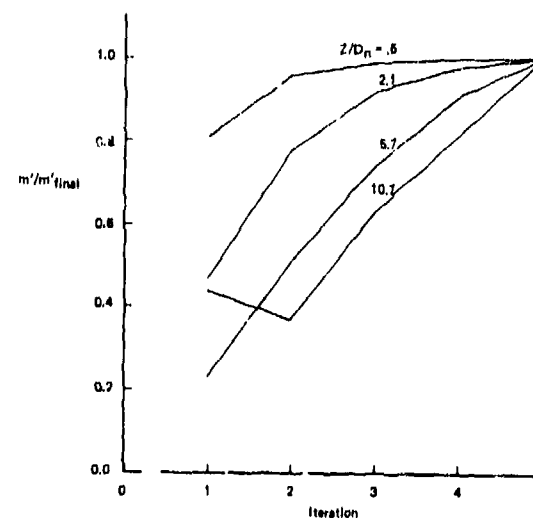


Figure 6. Convergence Rate for Axisymmetric Jet

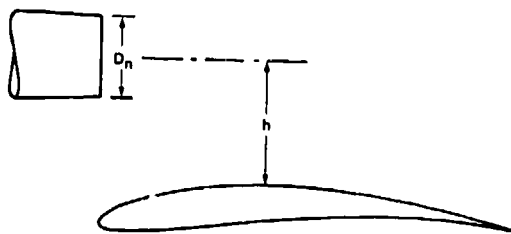


Figure 7. Axisymmetric Nozzle Over an Airfoil

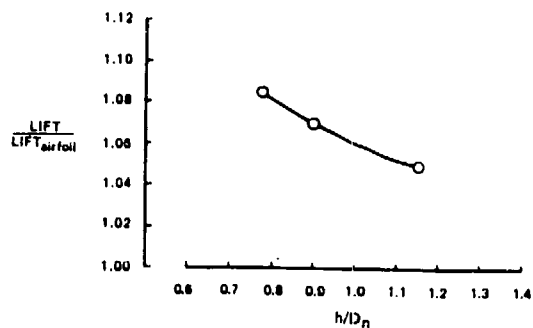


Figure 8. Effect of Nozzle Height on Airfoil Lift

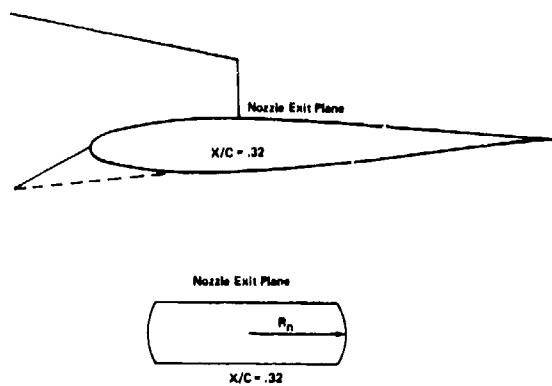
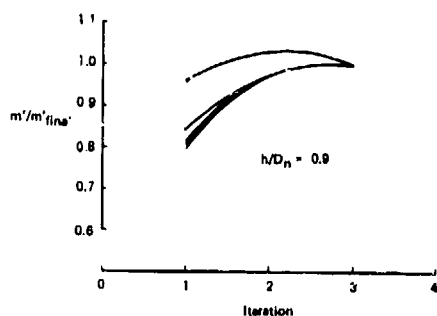


Figure 10. USB Nozzle and Wing

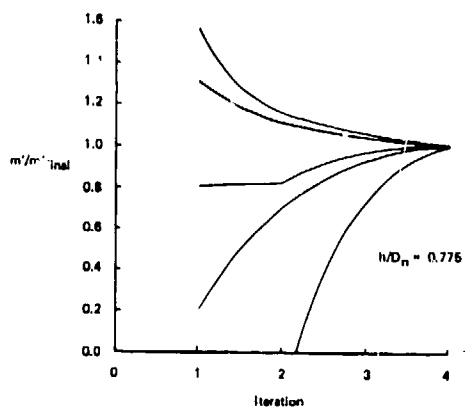


Figure 9. Convergence History for Axisymmetric Nozzle Over an Airfoil

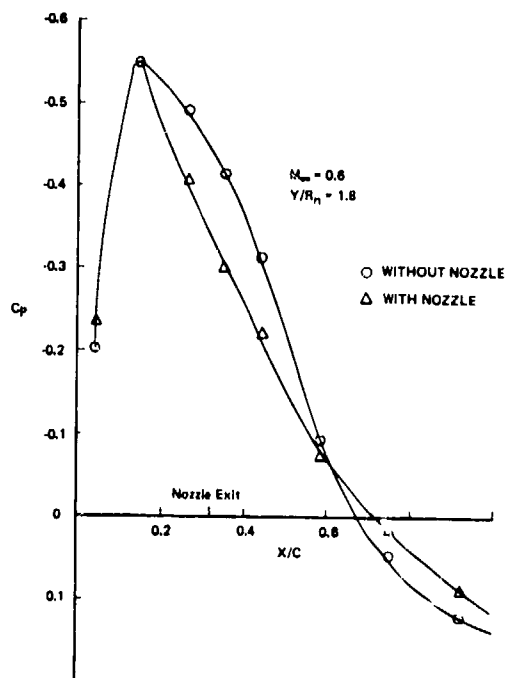


Figure 11. Effect of Blowing Nozzle on Wing Pressures

PROP-FAN INTEGRATION AT CRUISE SPEEDS

H. ROBERT WELGE
DOUGLAS AIRCRAFT COMPANY
MCDONNELL DOUGLAS CORPORATION
LONG BEACH, CALIFORNIA U.S.A.

ABSTRACT

The aerodynamic installation features of a highly loaded turboprop (prop-fan) on an aircraft for flight at Mach 0.8 are discussed. The aerodynamic flow environment in which the prop-fan must operate is shown for both wing and aft-fuselage installations based on analytical studies using advanced surface panel methods. The effects of various prop-fan slipstream parameters on the drag of a supercritical wing are presented; they indicate that only small drag penalties occur. Drag reductions are possible by tailoring the local wing section to account for the rotor-induced flow. Using these inputs, an integrated wing/nacelle is shown. Mission analysis study results using a modified DC-9 Super 80 with wing and aft-fuselage prop-fan installations reveal that fuel savings of 20 to 40 percent can be assessed for the prop-fan relative to the Pratt & Whitney Aircraft JT8D-209 engine. Concluding remarks cover future NASA wind tunnel tests with a subscale (2 foot) powered prop-fan to develop low-drag installations and planned flight tests using a 10-foot-diameter prop-fan to demonstrate structural, acoustic, and drag characteristics on a large scale.

SYMBOLS

A	wing aspect ratio
$b/2$	wing semispan
c	local chord
c_l	local section lift coefficient
C_L	configuration lift coefficient
C_p	pressure coefficient, $p-p_o/q_o$
C_p^*	sonic flow normal to wing quarter-chord
c_{mac}	wing mean aerodynamic chord
ΔC_D	incremental drag coefficient
D	diameter
Δf	incremental profile drag, $drag/q_o$
lb	pounds
M	Mach number
OWE	operating weight empty
p	static pressure
P_T	total pressure
q	dynamic pressure
r or R	radius
S_{REF}	reference wing area
SHP	shaft horsepower
$TOGW$	takeoff gross weight
t/c	thickness-to-chord ratio
V_x, V_y, V_z	velocities in the x, y, z direction divided by free-stream velocity
x/c	fraction of local chord
X, Y, Z	coordinate system, X streamwise, Y spanwise, and Z vertical
η	percent wing semispan
α	angle of attack or prop-fan swirl angle
Λ $c/4$	wing quarter-chord sweep

SUBSCRIPTS

FRP	fuselage reference plane
i	induced
J	jet or slipstream
o	free stream
S	swirl

INTRODUCTION

Increasing fuel prices in the early 1970s prompted the consideration of turboprop propulsion systems for aircraft to reduce fuel consumption and counteract the costs associated with the increasing fuel prices. Turboprop engines have the potential to considerably reduce fuel consumption for a given mission relative to advanced turbofans used today by increasing propulsive efficiency. The increased efficiency is a direct result of simple thrust-momentum equations which state that efficiency decreases as the axial velocity increment through the propulsion unit increases. Turboprops induce smaller velocity increments to a larger air mass flow than do turbofans, thereby increasing efficiency by several percentage points.

For turboprops to be competitive in today's turbofan airline fleet, it is necessary for the aircraft to fly at speeds and altitudes of $M = 0.8$ and 30,000 to 35,000 feet. This is a considerably higher speed than previous turboprops have flown and requires engineering development to ensure low drag and efficient installations. The last large turboprop-powered aircraft used for passenger service in the United States was the Lockheed Electra (Reference 1). It flew efficiently at $M_0 = 0.6$ to 0.65 and used propeller designs that absorbed about 12 shaft horse power per diameter squared (power loading = SHP/D^2 , where D is in feet). Since the horsepower per unit density required of the propulsion system varies as the cube of the velocity for a given drag coefficient, the size of a rotor using this earlier power loading technology would have to increase dramatically for flight at $M_0 = 0.8$. For example, the diameter shown by the dashed line in Figure 1 would be required to power a typical two-engine aircraft at competitive flight conditions. A rotor of this size could not be physically integrated on the aircraft because of insufficient ground, wing, and fuselage clearance, and would present significant vibration and structural problems and weight penalties. So the diameter must be reduced. With a power loading of 37.5 SHP/D^2 at 0.8 Mach and 35,000 feet altitude, the more reasonable installation shown by the solid line in Figure 1 is the result. Rotor designs for this high-power loading must have an increased number of blades and large chords (increased solidity) to maintain high levels of efficiency (Figure 2).

Practical turboprop installations are therefore possible if highly loaded rotors (prop-fans) with high solidity are used to reduce diameter and maintain high efficiency. Additional improvements in efficiency at high free-stream Mach numbers are possible by area-ruling the spinner/nacelle to reduce compressibility effects near the blade root, by using blades that are thin, and by sweeping the blade tips to reduce the local Mach number normal to the quarter-chord line to reduce blade compressibility losses. These prop-fans, initially developed by Hamilton Standard, have been tested by Hamilton Standard and NASA. Detailed descriptions and test data are presented in References 2 through 5. It has been demonstrated that significantly better efficiency is achieved by the prop-fan at $M_0 = 0.8$ than other competitive propulsion systems, as illustrated in Figure 3.

This paper will discuss the aerodynamic installation of the prop-fan on an aircraft for flight near $M_0 = 0.8$. The aerodynamic flow field entering the prop-fan disk area which is produced by adjacent aircraft components will be shown because it is pertinent to the design and efficiency of the prop-fan. The required increases in power loadings are accompanied by increases in propeller slipstream axial velocity and rotational velocity or swirl. Advanced aircraft with prop-fans will also most likely use some form of an aft-loaded or supercritical wing. These wings have large regions of supersonic flow and the perturbations to this flow produced by the axial and swirl velocities could produce significant shock-induced losses. The aerodynamic interactions between the prop-fan and the wing will be discussed. Mission studies using a DC-9 Super 80 aircraft and an efficient prop-fan propulsion installation are presented to indicate net fuel savings.

PROP-FAN INFLOW

When the prop-fan is installed on the aircraft, it is required to operate in a nonuniform flow field produced by the aircraft components. Axial, vertical, and horizontal velocity increments are produced upstream and downstream of the wing and for aft-mounted engine installations, an added local deficit in velocity is present due to the wing boundary layer and shock waves. Velocity perturbations are also produced by the fuselage and engine nacelle. An understanding of the magnitude of these flow nonuniformities must be obtained by the prop-fan designer for both aerodynamic and structural design.

To illustrate these effects, the wing/body shown in Figure 4 has been analyzed using a subsonic surface panel method (Douglas Neumann, Reference 6). Wing-alone and body-alone solutions were obtained to determine the individual influences and the combined results obtained by linear superposition. Computed results upstream of the wing are shown in Figures 5 and 6 for $M_0 = 0.8$ and a lift coefficient (C_L) of 0.5.

Because the fuselage is at a small angle of attack for this C_L and the wing is well aft of the fuselage nose, the fuselage effects were found to be negligible and the results shown are for the wing alone. All the velocities are given relative to the free-stream flow. Over the region considered, the vertical velocity, V_z , (or upwash) is virtually independent of vertical and spanwise position and, as expected, V_z decreases as the distance from the leading edge is increased, being nearly zero at 40 percent semispan ahead of the leading edge. Unlike V_z , the axial (V_x) and horizontal (V_y) velocities are strongly influenced by the vertical position relative to the wing plane, being much smaller at 13 percent semispan above the wing plane than in the wing plane.

A typical prop-fan disk installation has been indicated in the figures. The effect of the upwash and sidewash velocities can be minimized by properly orienting the rotor in the vertical and horizontal planes. However, because the wing is swept, the rotor is much closer to the wing leading edge on the inboard side, thereby producing an unavoidable axial velocity (V_x) increment as the prop-fan rotates. For this example, V_x varies from 0.96 to 1.01 per revolution. This 5 percent spread in velocity is equivalent to a 10 percent variation in dynamic pressure and approximately a 1.5 degree blade angle-of-attack change at the tip.

Decreasing the free-stream Mach number increases the local upwash, as illustrated in Figure 7. Also shown are two points calculated using a 1952 NACA report (Reference 7) and an assumed elliptic wing loading. These results are shown to be in excellent agreement with the more accurate surface panel solution at the lower Mach number. At $M_0 = 0.8$, the disagreement amounts to about 0.5 degree.

Downstream of the wing, the inviscid axial velocity increments, V_x , are negligible. Values of V_y and V_z are shown in Figure 8 for the location relative to the wing and body illustrated in Figure 4. The wing trailing vorticity produces the typical inflow above the wing and outflow below the wing, which increases in magnitude near the tip. The downwash velocities away from the wing plane are nearly equivalent to the value obtained at downstream infinity using classical theory for an elliptically loaded wing ($2C_L/\pi R$). These values are slightly exceeded in the plane of the wing.

When considering an aft-mounted engine installation, the effects of the fuselage afterbody must also be considered since these effects can be significant, as illustrated by the results given in Figure 9. In addition to the inviscid flow, a localized wake is present downstream of the wing, produced by the wing boundary layer flow and shock waves. This wake can have a 10- to 15-percent reduction in free-stream total pressure, as illustrated in Figure 10. These results were obtained experimentally for a different wing than considered above, and were obtained near the wing trailing edge. Mixing will occur downstream, and the wake will get wider and the total pressure deficit will decrease.

The flow field about a typical isolated nacelle is shown in Figure 11 in a horizontal plane passing through the nacelle centerline. These results were obtained using the same surface panel method described earlier. Radial and vertical velocities were found to be independent of Mach number. The radial velocity was also independent of angle of attack (α) whereas for reasonable accuracy, it was found that the vertical, or upwash, velocity varied linearly with α . The induced upwash velocities are relatively small, but significant axial and radial velocity increments occur, much larger than those due to the wing flow.

PROP-FAN EFFECTS ON WING

To produce axial thrust, the prop-fan must increase the velocity of the air flowing through the rotor disk area. In addition to the increased velocity, the prop-fan torque will also produce an angular momentum or swirl velocity in the prop-fan slipstream region. A certain amount of turboshaft engine energy is used to produce this swirl flow which does not produce useful axial thrust to overcome drag and appears as a loss in efficiency of the isolated prop-fan. If this rotational flow can be removed from the flow by some means, then there should be an overall increase in propulsive efficiency.

The increased velocity and swirl downstream of the prop-fan will interact with other aircraft components such as the wing, or engine pylon support for an aft fuselage installation, with subsequent changes in the aerodynamic characteristics of these components. Considering a two-dimensional airfoil section, the increased velocity without swirl will not change the local section lift coefficient (c_l) based on the local dynamic pressure but there will be an increase in the lift. The local velocity increase affects only the profile drag and the compressibility (shock) drag.

The swirl, however, does change the local c_l because the local angle of attack is changed. Changes in both the local section lift and profile drag will occur at subcritical speeds and compressibility drag will change at supercritical speeds. However, the swirl component of onset flow can produce a potential drag reduction because the Kutta-Joukowski law requires that the local lift vector at each spanwise

station be perpendicular to the local onset flow direction. If upwash is present, this will effectively increase the section angle of attack and rotate the lift vector forward relative to the free-stream flow direction, thereby producing an apparent thrust term (Figure 12). The thrust term is not cancelled by the flow on the downwash side of the prop-fan because the section angle of attack is reduced, which results in a smaller normal force vector. The thrust recovery or drag reduction cannot exceed the swirl energy lost in the isolated prop-fan efficiency.

For a three-dimensional wing, in addition to a spanwise integration of the effects described above, there will be distortions in the span-loading which change the downwash across the span and lead to increases in induced drag (Figure 12). To investigate the magnitude of the prop-fan effects on the drag of a three-dimensional wing, an incompressible lifting-line computer program has been used to study prop-fan onset flow effects of different input variables. For this study, the wing shown in Figure 13 was used and the reference prop-fan slipstream and location are also shown. The assumed nominal prop-fan onset flow is shown in Figure 14. The results of different rotor diameters and spanwise locations are shown in Figure 15. As indicated in the figure, the rotor diameter is much more important than the spanwise location and the drag is always reduced from that of the clean wing. The downwash across the span is unfavorably modified due to the large unfavorable distortion of span-load shown in Figure 16, which causes a drag increase. But, by considering the nonuniform upwash onset flow to the wing produced by the prop-fan, the unfavorable downwash effect due to the distorted span-load is more than offset by the favorable forward rotation of the local lift vectors over the prop-fan region.

A variation in the axial velocity increment due to the prop-fan, expressed as total pressure ratio P_{TJ}/P_{T0} , has a negligible effect on induced drag, as shown in Figure 17. The effects of swirl, however, are large and depend on the direction of prop-fan rotation as shown in Figure 18. The drag reduction is much larger if the prop-fans on each side of the wing rotate in such a manner as to produce up-inboard swirl, or increased angle of attack over the inboard half of the prop-fan wake. The drag reduction is larger by a factor of 2 relative to co-rotating rotors where one is up-inboard and one is up-outboard.

The above analytical study considered only the effects of inviscid induced drag. An experimental program was conducted* using a supercritical wing to verify these conclusions and to determine viscous and compressibility effects. The test setup installed in the NASA Ames 14-foot tunnel is shown in Figure 19. The prop-fan onset flow was simulated by using an ejector-powered flow-through nacelle that contained pressurized internal nozzles to increase the total pressure in the outer part of the flow to simulate propeller axial velocity and internal turning vanes (swirl vanes) to produce swirl flow. This simulator approach has inherent experimental approximations to the real prop-fan flow because of the simulator-nacelle effect on the wing flow, but was used with the objective of obtaining an early order-of-magnitude assessment of the drag at low cost. The pressurized air to power the simulator internal nozzles was supplied through the tunnel floor and up the support strut. Nominal measured exit conditions closely approximated the target conditions shown in Figure 14. Different nozzle pressure ratios and swirl vanes were used to simulate various combinations of power and swirl. The wake-rake downstream of the wing traversed spanwise and contained total pressure probes to measure the wake about one-third-chord downstream of the wing trailing edge. A description of the wing-body and the location of the simulator exit are shown in Figure 20. The drag rise Mach number for the isolated wing body was 0.82, 0.81, and 0.79 at C_{Ls} of 0.4, 0.5, and 0.6, respectively.

Results of the test program are shown in Figure 21. The drag increments are taken relative to the zero power/zero swirl condition. The test data show a 10 count ($\Delta C_D = 0.0010$) drag increase up to 7 degrees of swirl and a drag reduction at 11 degrees of swirl. The lifting line analysis using the test simulator onset flow indicates that the anticipated level of induced drag reduction is not achieved. These lifting line results may be too large, however, because the increments in span-load are highly overpredicted compared to the test data, as shown in Figure 22. The experimental results are not sensitive to Mach number or lift coefficient, as shown in Figure 23.

The axial thrust loss levels due to swirl shown in Figure 21 indicate the theoretical potential benefit recoverable from the swirl energy of the prop-fan if recovered totally by wing drag reductions. Douglas studies using the lifting line program have shown that drag levels closer to the theoretical potential benefit are achievable by tailoring the span-load to be closer to an elliptic loading. Planform modifications have also been used to lower the section lift coefficient and reduce profile drag losses.

The effects of power were found to be small as shown in Figure 24, and at $M = 0.8$, up-outboard swirl does increase the drag (Figure 21), confirming the analytical results. The last conclusion is not confirmed at $M_0 = 0.7$, however.

* NASA-sponsored test using Douglas wing/body model and wake rake (References 8 and 9).

Results from the wake-rake survey are shown in Figure 25 for the zero swirl case. Pressure ratios less than one occur because of the simulator/nacelle and wing boundary layer. The spanwise movement of the simulator flow can be seen consistent with previous analysis (Figure 8). Maximum total pressure levels are slightly reduced below those at the simulator exit, indicating small losses in the flow of the simulated prop-fan flow over the wing.

The distortion of the high-energy region due to swirl is shown in Figure 26. The smaller area of the high-pressure region indicates higher losses for this case consistent with the force data. The residual swirl at the trailing edge of the wing appears to be small because there is little distortion in the wing wake.

Wing surface pressure distributions are shown in Figures 27 through 30. The effects of axial velocity are small, but significant effects are shown for swirl, supporting the conclusions from the force data. Supersonic local velocities and increased shock strength were achieved near the leading edge with up-inboard swirl at 35 percent semispan at $M_0 = 0.7$, which contributes to the observed drag increases. The effects of positive swirl are diminished at the 50 percent span station, indicating that the swirl component of the flow is significantly reduced by the inboard portion of the wing which is upstream of the 50 percent span station. This supports the earlier conclusion drawn from the wake-rake data that most of the rotation of the flow is removed by the wing.

Analytical estimates of the surface pressures using a surface panel potential flow computer program capable of including the rotor onset flow are shown in Figure 31.

INTEGRATED WING/NACELLE

Preliminary studies have been made to integrate an over-wing propulsion system installation. An initial attempt at contouring a nacelle to the aerodynamic flow field is shown in Figure 32 and a schematic of a proposed wing/nacelle structural intersection is shown in Figure 33. The aerodynamic contouring was based on the results shown previously plus the flow streamlines ahead of and on the surface of a 25-degree swept wing, as shown in Figure 34. These streamlines were obtained by analysis using a surface panel potential flow computer program. As shown in Figure 32, in the plan-view the propeller and forward nacelle are canted inboard 0.5 degree for alignment with local onset flow and streamlines. The region of the nacelle which passes over the wing upper surface is aligned with the average surface streamline angle. In the profile view, the prop-fan axis alignment was selected after studies by Hamilton Standard found that a 4.5-degree nacelle downtilt angle had excitation factors well within the structural limits of the blades. The excitation factors were evaluated at the extreme operating conditions of high speed-low weight and low speed-high weight. At the nominal cruise condition, the 4.5-degree alignment angle results in a small 1-degree crossflow velocity about the forward part of the nacelle due to upwash and wing angle of attack. However, this upwash increases significantly near the wing leading edge.

The nacelle design shown is a compromise between aerodynamic and mechanical requirements, and therefore does not have extreme streamline contouring. More extensive contouring may be necessary, especially in the profile view, but this will have to be established after more detailed analysis and testing.

CONFIGURATION STUDIES

The fuel savings advantages of a prop-fan propulsion system have been identified by using a Douglas DC-9 Super 80 aircraft (Figure 35) and comparing the calculated performance obtained with a prop-fan propulsion installation to that obtained with the current Pratt and Whitney Aircraft JT8D-209 turbofan engine (Reference 10). Using an actual flying aircraft as a baseline gives a realistic basis from which increments could be calculated for the prop-fan installation, and all engineering aspects of the installation were considered. For these studies, an Allison PD 370-22A turboshaft engine was used to drive an 8-bladed, 800-foot/sec tip speed, Hamilton Standard prop-fan. The PD 370-22A is a derivative of the T701 engine used in helicopters, and a 1985 operational capability was assumed.

Three propulsion system concepts were studied. These are:

Configuration 1 (Figure 36)

- Wing-mounted design with the wing moved forward 95 inches and main landing gear extended 10 inches to provide a 10.5-degree rotation angle.
- Minimum development risk.

Configuration 2 (Figure 37)

- Aft fuselage pylon mount with wing moved rearward 38 inches, main landing gear canted 5 degrees aft, and air-conditioning and 580-gallon belly fuel tank located in forward cargo compartment to satisfy tipover limits.
- Requires development to avoid deep-stall problems associated with the large span extent of the engines and the "T" tail.

Configuration 3 (Figure 38)

- Horizontal tail aft mount with wing moved aft 38 inches and landing gear canted 5 degrees aft.
- Development risk associated with having the horizontal control system affected by the level of propulsion power.

An aerodynamic drag and weight analysis for each of these configurations was conducted so that aircraft mission performance could be calculated. The aerodynamic drag results are shown in Table 1. The table lists the new tail areas required for stability and control and percent drag increments from the DC-9 Super 80 baseline. Drag increments due to the nacelle and pylon are the difference between installing the prop-fan propulsion system and removing the existing JT8D-209 engine. Scrubbing drag increments due to the higher velocities in the propeller slipstream are included. For the wing-mounted configuration, a drag increment was included to account for induced drag and wing profile drag changes due to the prop-fan slipstream flowing over the wing. It was assumed that the other two configurations would not have this increment.

As noted in Table 1, Configuration 3 has the lowest drag because the propulsive support and horizontal tail are combined, thereby reducing the wetted area. The wing-mounted configuration ranks next; the highest drag increment being the wing-induced and profile drag increment which may be reduced by future development testing. Configuration 2 has the highest drag due mainly to the large engine pylon support required.

A summary of the weight increments given as a percent of the takeoff gross weight (TOGW) is shown in Table 2. Configurations 1 and 3 both have an operating weight empty (OWE) about 4.5 percent higher than the DC-9 Super 80, due in part to the heavier propulsion installation. The OWE for Configuration 2 is about 7 percent heavier than the DC-9 Super 80 due to the structure required to support the engines on the aft-mounted pylons.

Offsetting these unfavorable increments is a large 27 percent advantage in cruise specific fuel consumption (SFC, or pounds of fuel burned per hour per pound of thrust). Figure 39 compares the SFC of the prop-fan used in this study and the current JT8D-209.

Using these inputs, mission performance was determined. Conventional reserves were included and the engine was sized at a Mach number for 99 percent maximum specific range and an initial cruise altitude of 31,000 feet after a takeoff at 140,000 pounds gross weight.

The fuel reduction benefits for the three prop-fan configurations for constant altitude cruise at $M_0 = 0.8$ are shown in Figure 40. For a 1000-nautical-mile range, Configuration 3, which had the lowest weight and drag, saved 24 percent in fuel; Configuration 1, which had the same weight but higher drag, saved 22 percent in fuel; Configuration 2, with the highest weight and drag, saved 19 percent in fuel. The performance of Configurations 3, 1, and 2 is reduced from the 27 percent cruise SFC benefit by 3, 5 and 8 percent, respectively, due to the difference in installation effects.

If a mission with the optimum cruise Mach number ($M_0 \approx 0.760$) and a step-cruise altitude is assumed, even larger benefits occur, as shown in Figure 41. Configuration 3 can have a specific range benefit as high as 45 percent. A payload-range curve for the same mission is shown in Figure 42.

FUTURE PLANS

This paper has discussed a limited amount of work that has been done on the installation of the prop-fan propulsion system on a Mach 0.8 cruise aircraft. Studies of prop-fan onset flows, interactions with the wing, and configuration studies have served to scope the magnitude of the aerodynamic problem and have indicated that the installation is feasible and that fuel savings from 20 to 40 percent relative to state-of-the-art engines in service today are realistic. However, to bring the technology to the level where aircraft production would be considered requires more work. Specifically, some of the items that must be considered are the structural integrity of the prop-fan blades at large scale, the gearbox, the prop-fan pitch control, installed propulsion system drag, the engine inlet, and interior noise. Two NASA programs, described below, are addressing some of these problems with assistance from the airframe industry.

NASA is wind tunnel testing a prop-fan powered by an air-driven turbine installed on a supercritical wing (Figure 43). The wing was built to the same coordinates as used in the previous simulator test (References 8 and 9), but at a scale 3.7 times larger. This program will produce an excellent data base for a wing-mounted propulsion system. The data will also be used to evaluate the accuracy of using the simulator concept described earlier. Different nacelle and wing contours are to be investigated to develop the technology for low drag installations of this type.

Cooperative NASA/industry studies are underway to define a testbed configuration to flight test a 10-foot-diameter prop-fan. The rotor can be powered by an Allison T701 turboshaft engine and the nacelle mounted on the wing of a Douglas DC-9 aircraft (Figure 44). This concept is desirable because the primary propulsion system is separate from the prop-fan, the DC-9 is about the right scale for a 10-foot-diameter propeller, and the aircraft is readily available. Engineering analysis has demonstrated that the approach is feasible. The program objectives are to determine the structural integrity of the blades at speeds up to Mach 0.8 and altitudes above 30,000 feet, investigate the acoustic properties on and in the fuselage due to the prop-fan, and evaluate the installed drag of the propulsion system. Flight testing will also solve numerous problems unique to the prop-fan that arise during the program, which will lead to a more successful production program. In addition, subscale low-speed, high-speed, and inlet tests will be conducted prior to the flight tests which will serve to expand the available aerodynamic design data base and determine the agreement between flight and wind tunnel data.

CONCLUSION

A prop-fan propulsion system offers fuel savings of 20 to 40 percent when compared to turbofan propulsion systems flying near $M_0 = 0.8$. As discussed, the aerodynamic installation problems of the prop-fan propulsion package seem manageable, but additional analysis and testing are required to expand the technology data base and develop efficient aircraft designs. This work is leading to prop-fan powered aircraft entering airline service and providing significant reductions in fuel costs, thereby minimizing future increases in ticket prices to the traveling passenger.

REFERENCES

1. Janes All The World's Aircraft 1963-1964, McGraw Hill Book Company, Inc., page 238.
2. Rohrbach, C. and Metzger, F. B., The Prop-Fan - A New Look At Propulsors, AIAA Paper 75-1208, 1975.
3. Rohrbach, C., A Report On The Aerodynamic Design and Wind Tunnel Tests of a Prop-Fan Model, AIAA Paper 76-667, 1976.
4. Mikkelsen, D. C. and Blaha, B. J., Design and Performance of Energy Efficient Propellers for Mach 0.8 Cruise, NASA TM X-73612, 1977.
5. Jeracki, R. J. and Mikkelsen D. C., Wind Tunnel Performance of Four Energy Efficient Propellers Designed for Mach 0.8 Cruise, SAE Paper 790573, 1979.
6. Hess, J. L., The Problem of Three-Dimensional Lifting Potential Flow and Its Solution by Means of Surface Singularity Distribution, Computer Methods in Applied Mechanics and Engineering, Vol. 4, 1974, pages 283-319.
7. Rogallo, V. L., Effects of Wing Sweep on the Upwash at the Propeller Planes of Multiengine Airplanes, NACA TN 2795, 1952.
8. Welge, H. R. and Crowder, J. P., Simulated Propeller Slipstream Effects on a Supercritical Wing, NASA CR 152138, 1978.
9. Bencze, D. P., Smith R. C., Welge, H. R., and Crowder, J. P., Propeller Slipstream Wing Interactions at Mach 0.8, SAE Paper 780997, 1978.
10. Goldsmith, I. M. and Bowles, J. V., Potential Benefits for Prop-Fan Technology on Derivatives of Future Short-to Medium-Range Transport Aircraft, AIAA Paper 80-1090, 1980.

TABLE 1
CONFIGURATION DRAG ANALYSIS

ΔIAS % OF DC-9 SUPER 80 PARASITE DRAG ①

	DC-9-80	CONFIG 1		CONFIG 2		CONFIG 3	
	AREA (FT ²)	AREA (FT ²)	ΔH (%)	AREA (FT ²)	ΔH (%)	AREA (FT ²)	ΔH (%)
WING	1209	1209	—	1209	—	1209	—
HORIZONTAL	313	350	+2.0	392	+3.2	500	+4.6
VERTICAL	161	200	+1.2	215	+1.8	225	+2.2
NACELLE AND PYLON ② (PROP INST - JT8D-209)	—	—	-0.7	—	+5.2	—	-2.0
WING-INDUCED AND PROFILE DRAG ③	—	—	+4.2	—	—	—	—
		TOTAL ΔH (%)					
		6.7		+10.2		+4.8	

- ① SHAPE OF DRAG POLAR AND COMPRESSIBILITY DRAG HELD CONSTANT
② INCLUDES SCRUBBING DRAG AND WING SURFACE COVERED
③ REFERENCE 8, TEST DATA-7 DEG SWIRL

TABLE 2
WEIGHT ANALYSIS

TOGW: 140,000 LB
PAYLOAD: 31,775 LB (22.7% OF TOGW)
PROPELLER DIAMETER: ~ 14.4 FT
RATED SHP: ~ 16,500

	DC-9-80	WING MOUNT CONFIG 1	PYLON MOUNT CONFIG 2	TAIL MOUNT CONFIG 3
WING AREA (FT ²)	1209	1209	1209	1209
HORIZ/VERTICAL TAIL AREA (FT ²)	313/161	350/200	392/215	500/225
WEIGHT (% OF TOGW)				
WING	10.9	11.1	11.0	11.0
HORIZONTAL/VERTICAL	1.4/0.9	1.4/1.1	1.8/1.1	2.0/0.9
NACELLE MOUNTING AND PROPULSION SYSTEM	9.0	10.7	12.1	10.3
OPERATING WEIGHT EMPTY	54.8	59.4	61.6	59.4

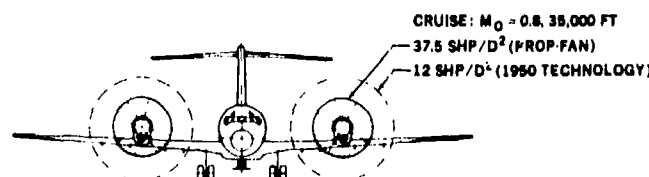
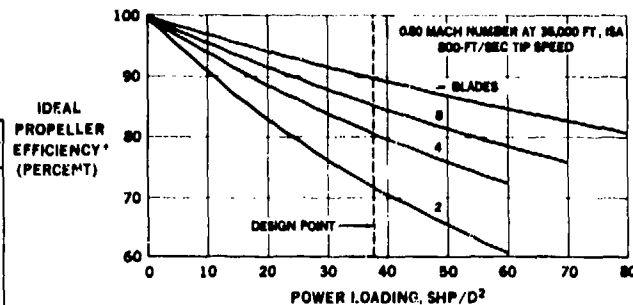


FIGURE 1. EFFECT OF POWER LOADING ON ROTOR DIAMETER



* IDEAL EFFICIENCY INCLUDES AXIAL, SWIRL, AND BLADE TIP LOSSES

FIGURE 2. IDEAL EFFICIENCY AS A FUNCTION OF POWER LOADING AND NUMBER OF BLADES

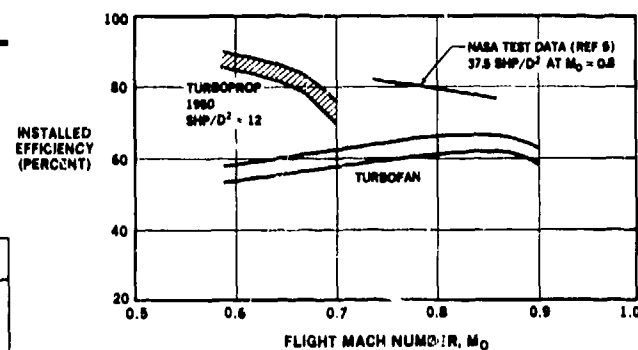


FIGURE 3. PROPULSION SYSTEM EFFICIENCY

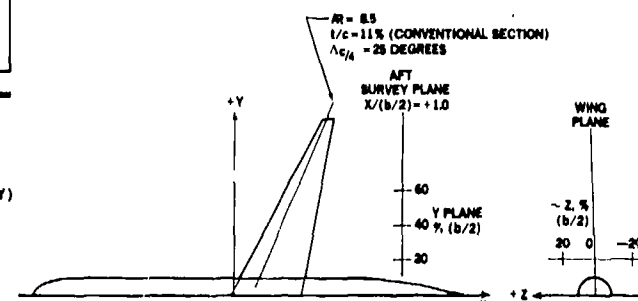
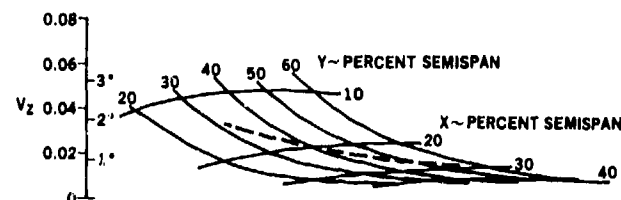
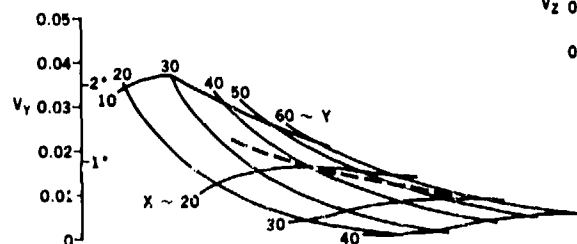
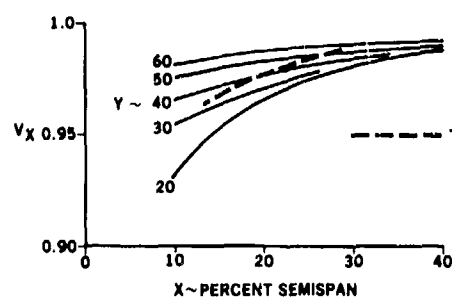


FIGURE 4. SKETCH OF WING BODY AND AFT SURVEY PLANE



X = DISTANCE AHEAD OF WING LEADING EDGE
Y = SPANWISE DIST FROM FUSELAGE C
Z = VERTICAL DIST FROM WING PLANE
ALL VELOCITIES RELATIVE TO FREE STREAM

FIGURE 5. ROTOR FLOW FIELD AHEAD OF THE WING IN THE WING PLANE

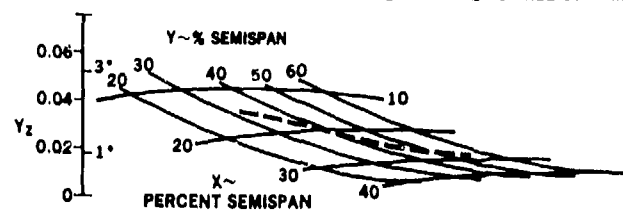
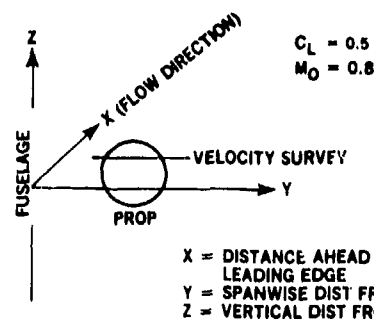
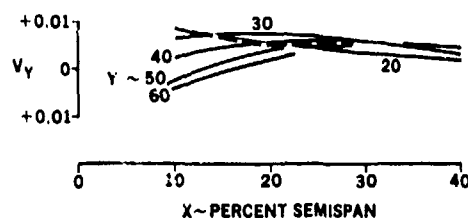
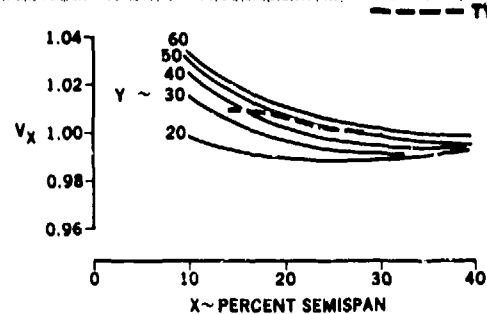


FIGURE 6. ROTOR FLOW FIELD AHEAD OF THE WING 13 PERCENT SEMISPAN ABOVE WING PLANE

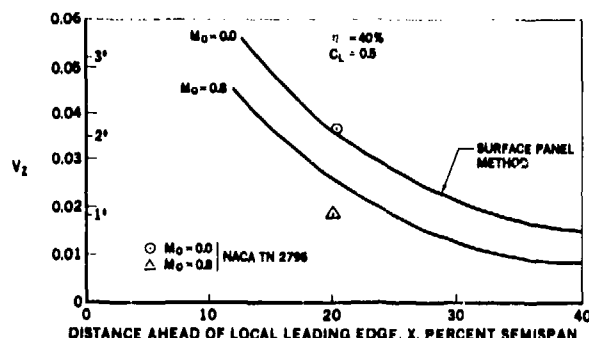


FIGURE 7. MACH NUMBER EFFECT ON UPWASH AHEAD OF WING

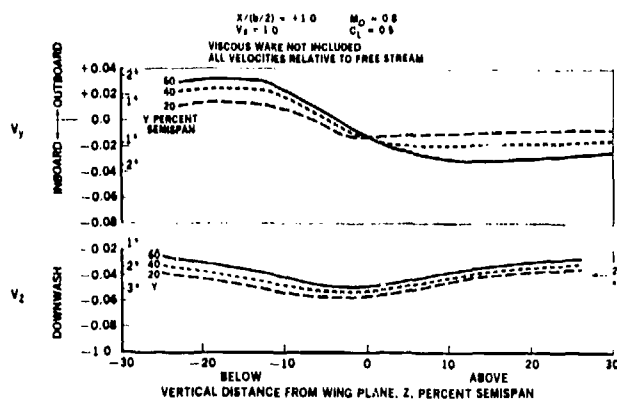


FIGURE 8. FLOW FIELD AFT OF WING - NO FUSELAGE

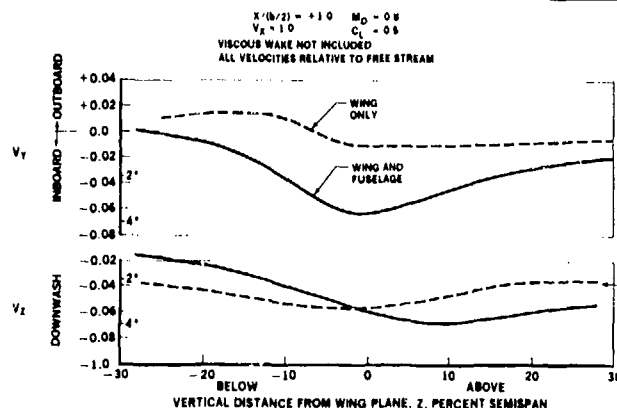


FIGURE 9. EFFECT OF FUSELAGE ON FLOW FIELD AFT OF WING AT 20 PERCENT SEMISPAN

- $M_0 = 0.8$
- $C_L = 0.5$
- WAKE WIDTH IS 5X WING SCALE

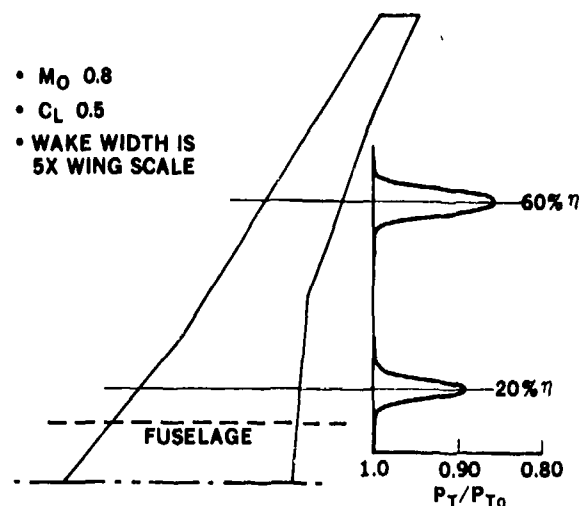


FIGURE 10. SUPERCRITICAL WING WAKE NEAR TRAILING EDGE

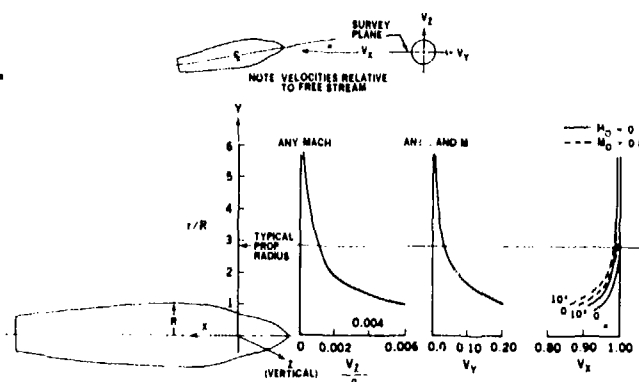


FIGURE 11. FLOW FIELD INDUCED BY A TYPICAL NACELLE

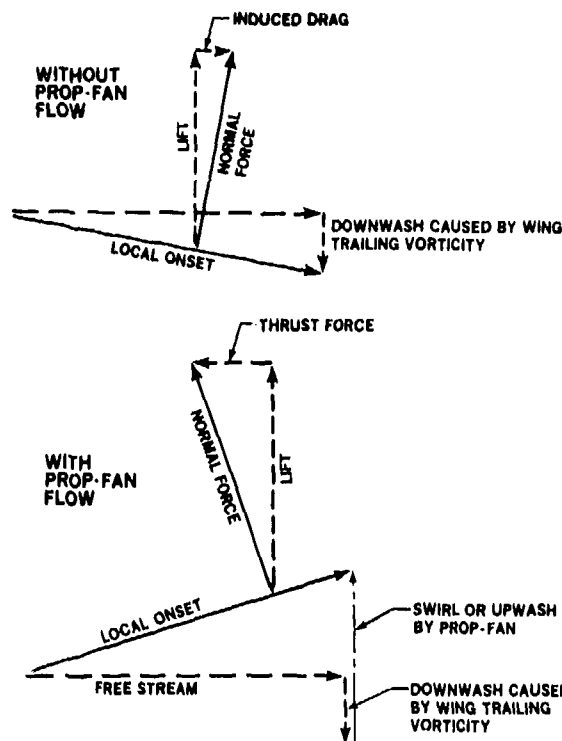


FIGURE 12. EFFECT OF PROP-FAN SWIRL ON AIRFOIL SECTION DRAG

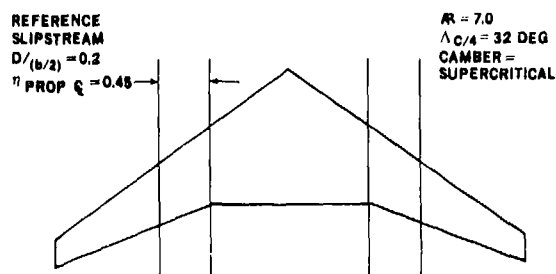


FIGURE 13. WING PLANFORM AND REFERENCE CASE PROP-FAN SLIPSTREAM USED FOR PARAMETRIC INDUCED DRAG STUDIES

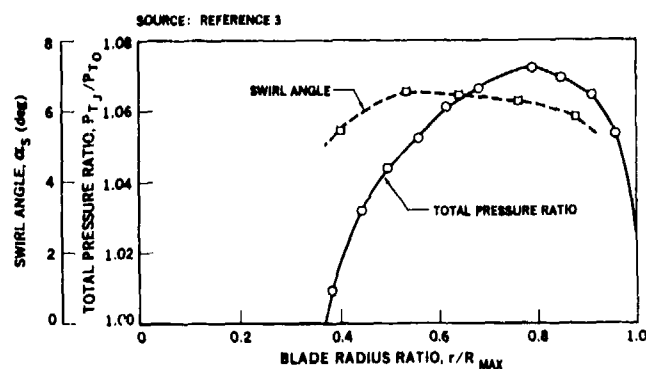


FIGURE 14. NOMINAL SWIRL ANGLE AND PRESSURE RATIO

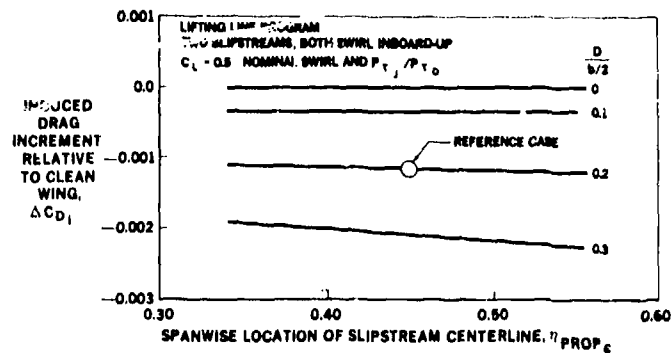


FIGURE 15. EFFECT OF PROP-FAN DIAMETER AND LOCATION ON INDUCED DRAG

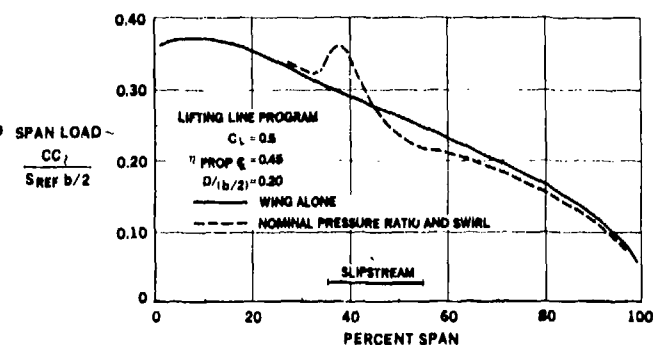


FIGURE 16. EFFECT OF SWIRL AND POWER ON SPAN LOAD DISTRIBUTION

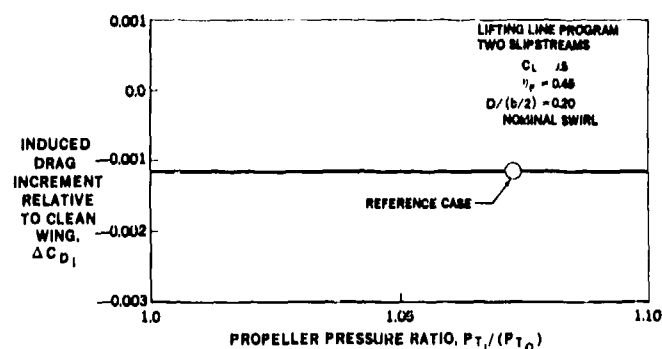


FIGURE 17. EFFECT OF JET PRESSURE RATIO ON INDUCED DRAG

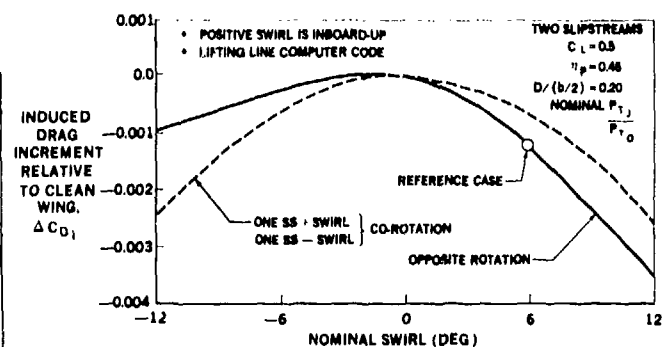


FIGURE 18. EFFECT OF SWIRL DIRECTION ON INDUCED DRAG DETERMINED BY ANALYSIS

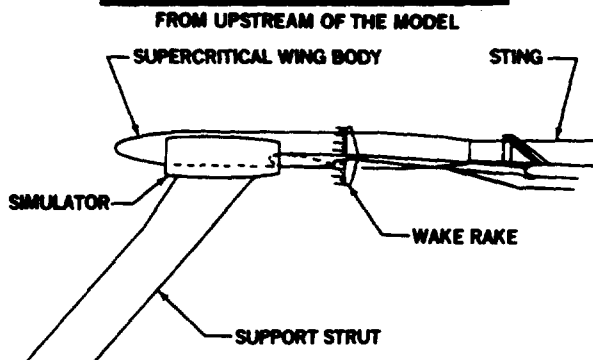


FIGURE 19. PHOTOGRAPH AND SKETCH OF MODEL INSTALLATION

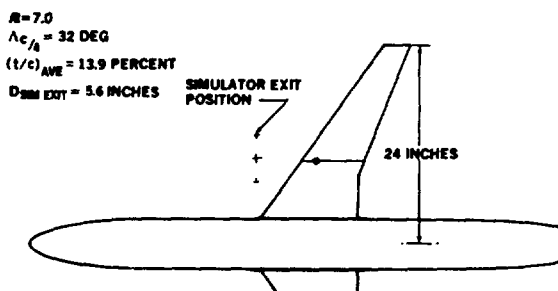


FIGURE 20. DESCRIPTION OF SUPERCritical WING-BODY USED FOR SIMULATOR TEST

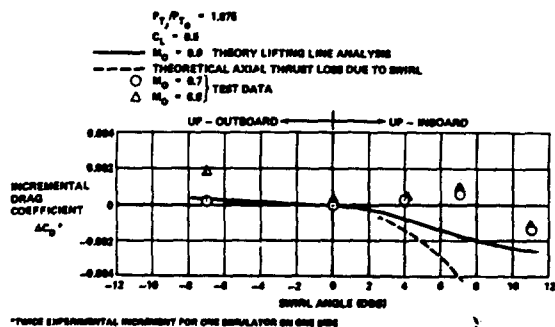


FIGURE 21. COMPARISON OF THEORETICAL AND EXPERIMENTAL SIMULATOR DRAG DATA

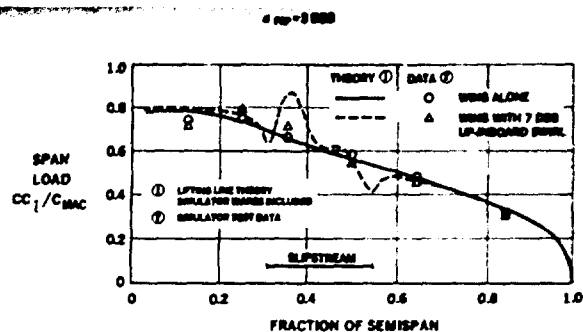


FIGURE 22. COMPARISON OF EXPERIMENTAL AND THEORETICAL SPAN LOAD

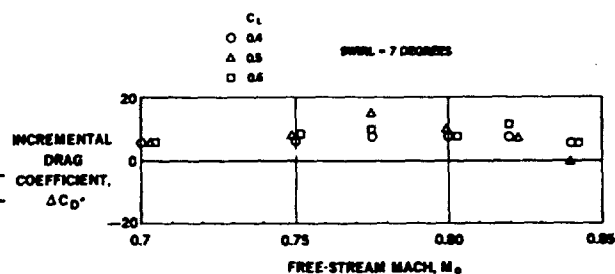


FIGURE 23. INCREMENTAL DRAG VARIATION WITH FREE-STREAM MACH NUMBER

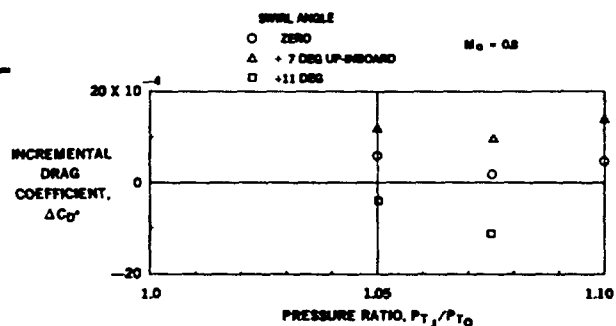


FIGURE 24. DRAG VARIATION WITH SIMULATED PROPELLER PRESSURE RATIO

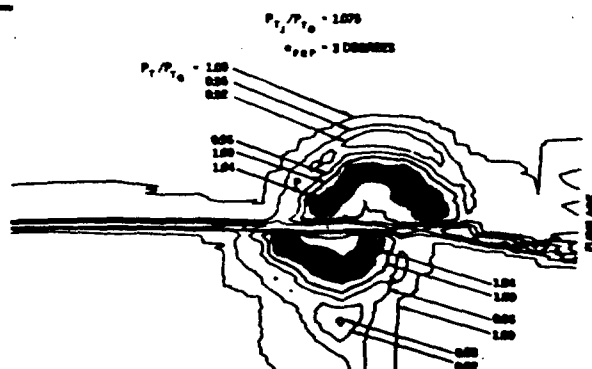


FIGURE 25. WAKE RAKE SURVEY AT $M_0 = 0.8$ WITH ZERO SWIRL

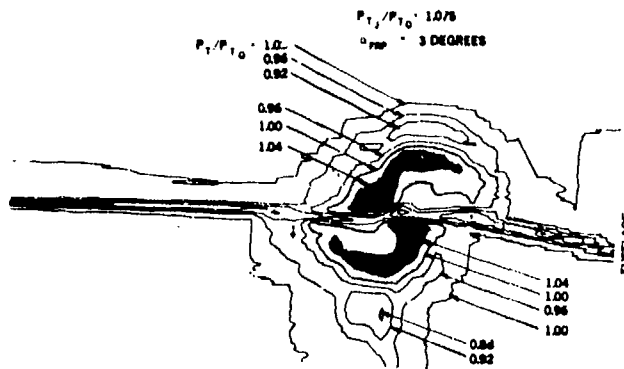


FIGURE 26. WAKE RAKE SURVEY AT $M_0 = 0.8$ AND 7 DEGREES OF SWIRL

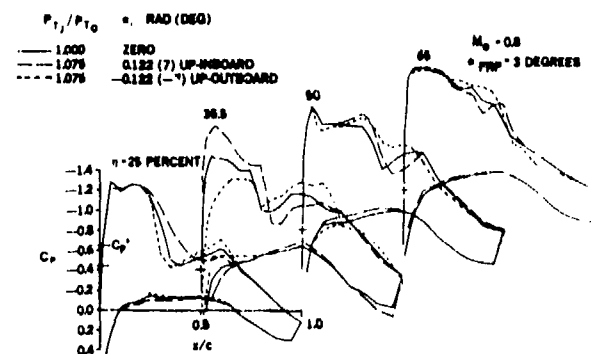


FIGURE 30. WING SURFACE PRESSURE VARIATION DUE TO POWER AND SWIRL AT $M_0 = 0.8$

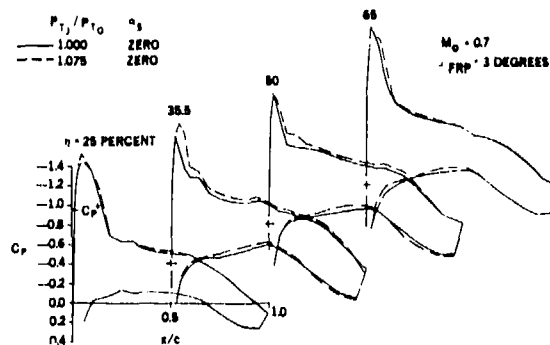


FIGURE 27. WING SURFACE PRESSURE VARIATION DUE TO POWER AT $M_0 = 0.7$

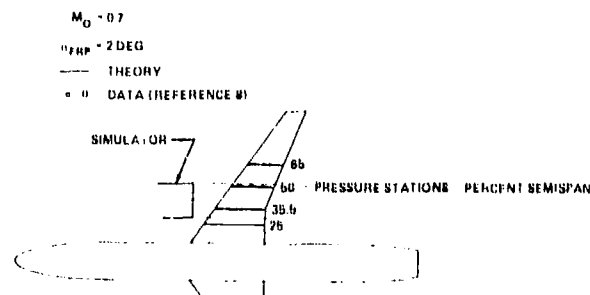


FIGURE 28. WING SURFACE PRESSURE VARIATION DUE TO POWER AT $M_0 = 0.8$

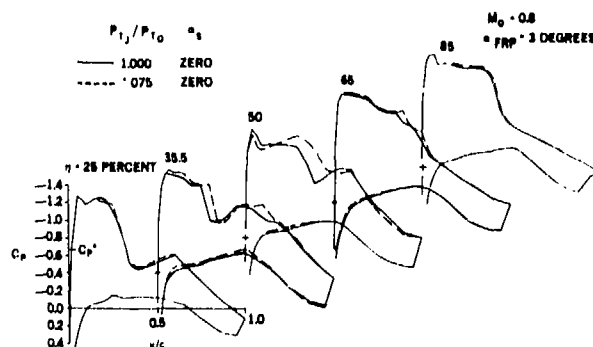
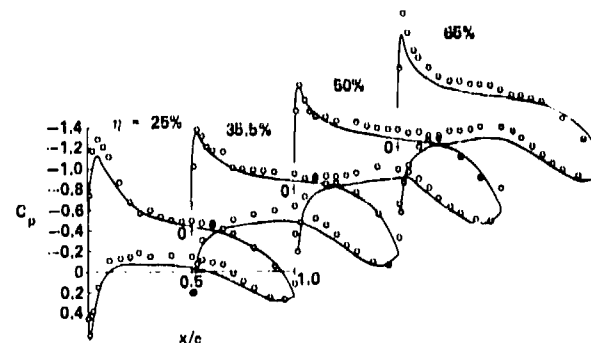


FIGURE 29. WING SURFACE PRESSURE VARIATION DUE TO POWER AND SWIRL AT $M_0 = 0.7$

NOMINAL CONDITIONS

$P_{TJ}/P_{T0} = 1.000$ $\alpha_s = \text{ZERO}$



NOMINAL CONDITIONS

$P_{TJ}/P_{T0} = 1.075$ $\alpha_s = +7 \text{ DEG (UP-INBOARD)}$

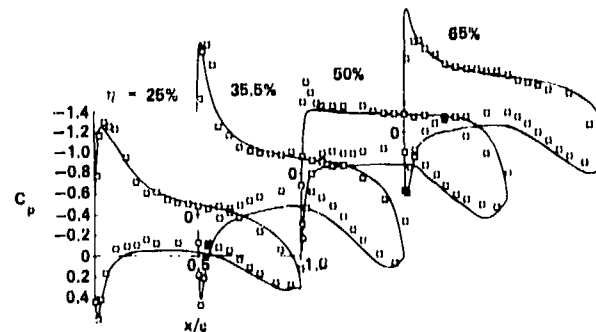


FIGURE 31. COMPARISON OF SIMULATION TEST DATA WITH ADVANCED PANEL METHOD ACCOUNTING FOR PROPFAN POWER EFFECTS

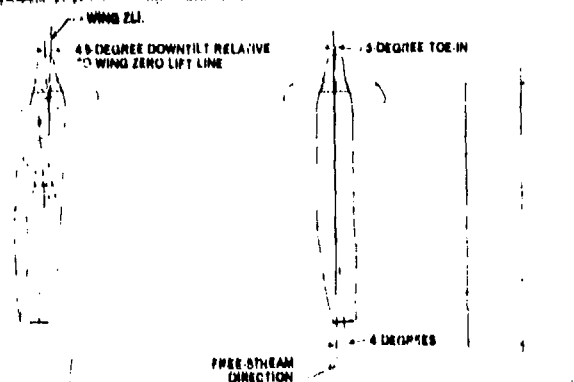


FIGURE 32. INTEGRATED WING/NACELLE/PROP-FAN

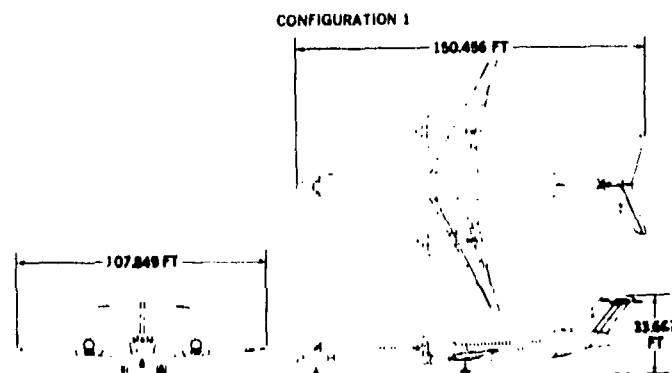


FIGURE 36. WING-MOUNTED PROP-FAN

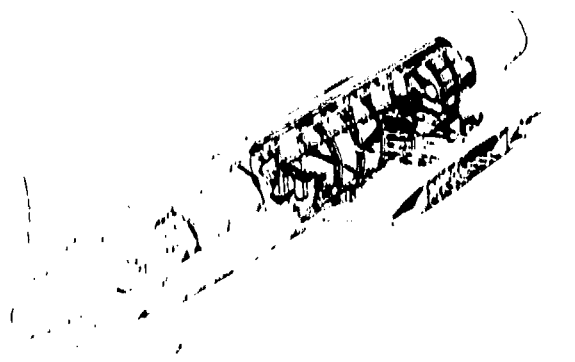


FIGURE 33. SCHEMATIC OF NACELLE-WING STRUT INTERACTION

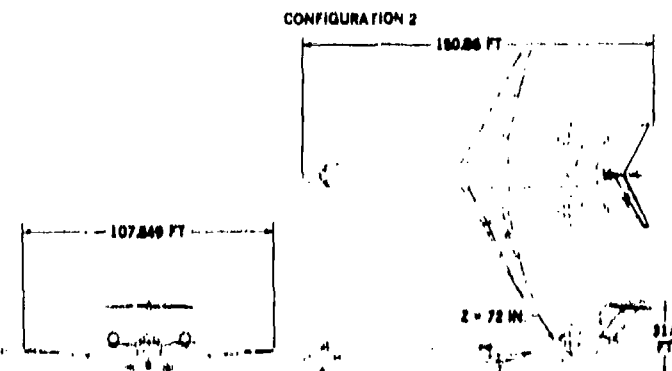


FIGURE 37. AFT FUSELAGE-MOUNTED PROP-FAN

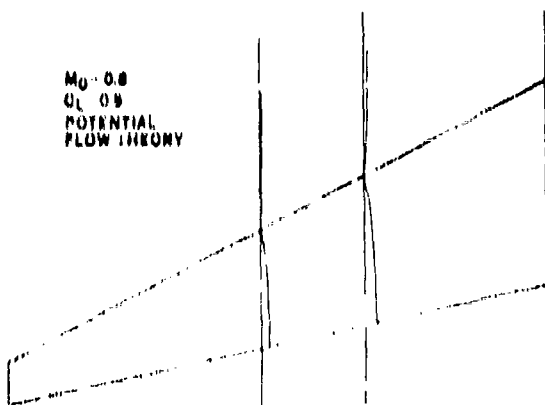


FIGURE 34. UPPER SURFACE STREAMLINES FOR A 20-DEGREE SWEEP WING

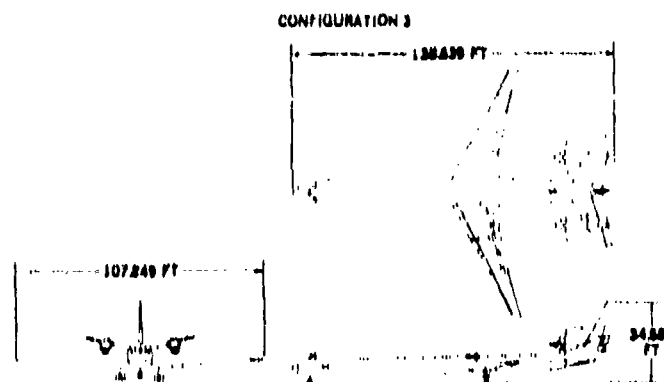


FIGURE 38. HORIZONTAL TAIL-MOUNTED PROP-FAN

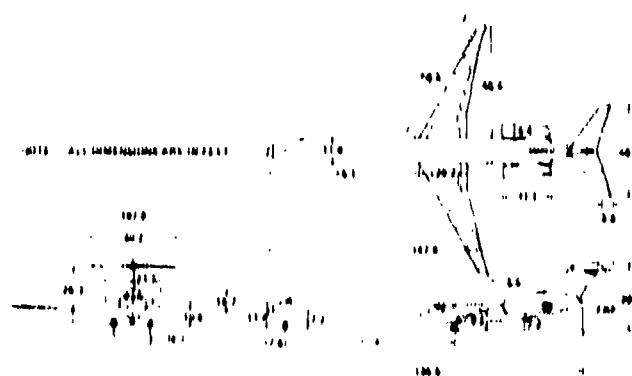


FIGURE 35. MODEL D5 SUPER 80 GENERAL ARRANGEMENT

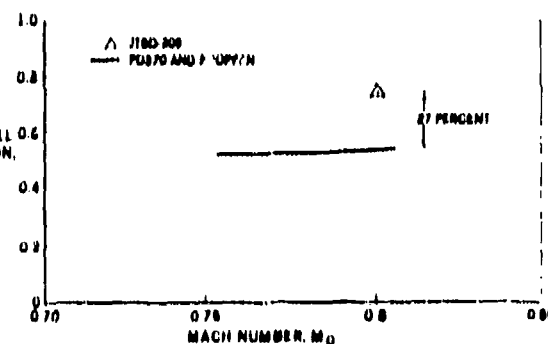


FIGURE 39. INSTALLED FUEL CONSUMPTION

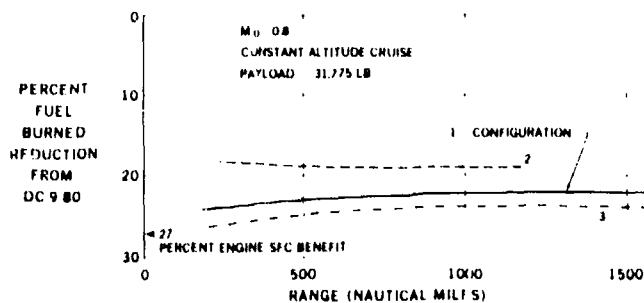


FIGURE 40. FUEL BURNED REDUCTION FOR PROP FAN AS FUNCTION OF RANGE

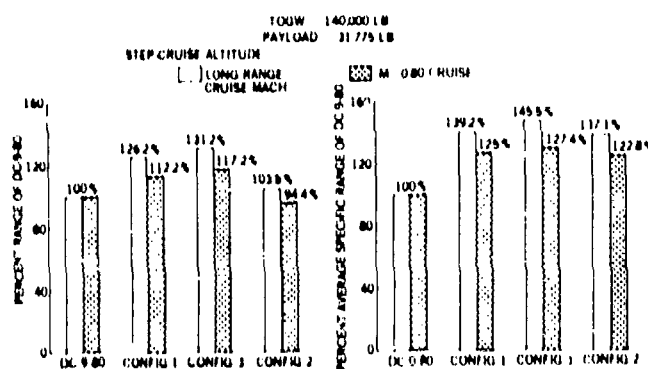


FIGURE 41. RANGE AND SPECIFIC RANGE COMPARISON OF BASE CONFIGURATIONS

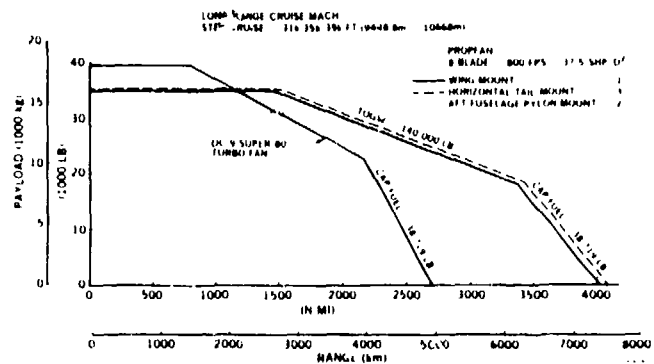


FIGURE 42. PAYLOAD RANGE



FIGURE 43. NASA POWERED PROP FAN TEST INSTALLATION



FIGURE 44. NASA LARGE SCALE DC 9 TESTBED

AIRFRAME-PROPULSION SYSTEM AERODYNAMIC INTERFERENCE PREDICTIONS
AT HIGH TRANSONIC MACH NUMBERS INCLUDING
OFF-DESIGN ENGINE AIRFLOW EFFECTS

by
*R. M. Kulfan and **A. Sigalla
Boeing Commercial Airplane Company
P.O. Box 3707
Seattle, Washington 98124
USA

ABSTRACT

Flow interference between engine nacelles and an airframe has an important effect on the aerodynamic efficiency of all types of aircraft. The performance of airplanes designed for supersonic flight particularly has been affected by adverse interference forces. This has been the case most often at transonic speeds.

This paper emphasizes the transonic speed regime for airplanes at conditions where inlet spillage takes place. Relatively recent availability of appropriate wind-tunnel data has now made it possible to assess available theoretical methods.

The National Aeronautics and Space Administration, NASA, conducted an extensive wind-tunnel test program to evaluate aerodynamic performance penalties associated with propulsion system installation and operation at subsonic through low supersonic speeds. Using those test data, a study to assess the accuracy of analytic methods for predicting transonic engine-airframe interference effects was conducted and forms the content of the paper. Study variables included Mach number, angle of attack, relative nacelle location, and nacelle mass-flow ratio.

Study results included test-theory comparisons of forces as well as induced pressure fields. Prediction capability of induced shock wave strength and locations was assessed. It was found that large interference forces due to engine location and flow spillage occur at transonic speeds; that theory can explain these effects; and that theory, under appropriate conditions, can predict quantitatively these effects.

INTRODUCTION

Flow interference between engine nacelles and the airframe has an important effect on the aerodynamic efficiency of all types of aircraft. The performance of airplanes designed for supersonic flight particularly has been affected by adverse mutual interference forces. This has been the case most often at transonic speeds. These adverse effects often have come as a surprise, being discovered in the course of flight testing at a stage in an airplane program when it was too late to do much about the problem. The reasons for this have been: (1) absence of theoretical methods to help the designer in definition of a configuration that would not exhibit such problems, and (2) difficulty of conducting valid experiments that would warn the designer of potential problems.

Theoretical methods and research testing on this subject, in the past, have focused on the supersonic regime of Mach numbers greater than 1.8. This was primarily because theory was easier to develop for that speed regime, and the testing to verify and enhance the theory was simpler to conduct. Beyond that, and more importantly, engine operation for airplanes designed in that flight regime is such that the flow at the engine nacelle inlet lip is more regular; that is, the mass-flow ratio is near unity. At transonic speeds, theory is more difficult, testing more complicated, and the mass-flow ratios of typical propulsion systems are such that significant spillage takes place. Some of the aerodynamic effects of spillage have been difficult to estimate.

This paper emphasizes the transonic speed regime specifically at conditions where inlet spillage takes place. Availability of appropriate wind-tunnel data has now made it realistically possible to assess available theoretical methods. The aim of the paper is to show how these methods compare with experiment.

The National Aeronautics and Space Administration, NASA, has conducted an extensive wind-tunnel test program to evaluate aerodynamic performance penalties associated with propulsion system installation and operation at subsonic through low supersonic speeds. With these test data in hand, a study to assess the accuracy of analytic methods for predicting transonic engine-airframe interference effects was conducted and forms the contents of this paper.

The wind-tunnel model used to obtain the majority of test data reviewed in this paper is described in section 2. Appropriate information on the experimental conditions is given. A brief description of the theoretical methods that were used for comparison with the experimental data is presented in section 3. Obvious limitations of these methods are listed. Systematic comparisons of theory with experiment are shown in section 4. These comparisons include—

- Isolated wing-body lift, drag, and pitching moment
- Isolated nacelle drag and pressure distributions
- Mutual nacelle interference drag for various nacelle arrangements
- Nacelle interference shock-wave patterns and pressure distributions on the wing lower surface
- Total installed nacelle interference effects on lift, drag, and pitching moments
- Certain jet exhaust effects

Discussion of results is included with these comparisons. A general assessment of the paper, together with suggestions for further work, is summarized in section 5.

- * Senior Specialist Engineer
- ** Technology Chief, New Product Development

2.0 MODEL GEOMETRY AND TEST CONDITIONS

The NASA experimental nacelle-airframe interference program was conducted in the Ames 11- by 11-ft wind tunnel. The wind-tunnel model is shown in figure 1. Basic features and details of the model are summarized in figures 2 and 3.

The wing-body configuration is a 0.024-scale model of the U.S. 1971 SST. The wing-body was sting mounted with a six-component internal strain-gage balance. The left-hand wing had 126 static pressure orifices, 95 on the lower surface and 31 on the upper surface. Two different nacelle geometries were tested. One set of nacelles had sharp inlets, and the second set of nacelles had a slightly blunt inlet lip shape. Investigations reported in this paper concern only the sharp-lip nacelles.

The four individual nacelles were supported just below the wing-body model on individual flow-through stings. The two right-hand nacelles were mounted individually on separate six-component internal strain-gage balances. The left-hand nacelles were pressure instrumented and had 40 static-pressure orifices. The six-component force balances used to support the right-hand nacelles were housed in the thickness of each nacelle. A two-shell flow-through balance, located in each nacelle, used four instrumented flexures located 90 deg apart at two axial locations. The nacelle balances measured the aerodynamic forces on the external surface of the nacelle, plus the forces on a small portion of the internal duct near the inlet. The wind-tunnel data corrections included removal of the estimated skin friction drag on this internal duct area.

The nacelle support system could position the nacelles vertically streamwise, and spanwise relative to the wing-body combination and to each other. The range of achievable nacelle locations is indicated in figure 2. Staggered and nonstaggered arrangements were tested at six different nacelle stations and three different spanwise locations, as shown in figure 4. The support system also provided for independent control and measurement of mass flow through each nacelle by means of a mass-flow control plug and appropriate pressure instrumentation.

Test conditions included:

- Mach numbers: 0.90, 0.98, 1.1, 1.15, 1.2, 1.3, 1.4
- Angle of attack: $\alpha = 0$ to 6 deg
- Mass-flow ratio: MFR = 0.6 to 1.0

Test configurations included:

- Isolated wing-body
- Isolated nacelle
- Four nacelles in various relative positions
- Wing-body plus nacelles in various locations

These tested configurations provided the following measurements of isolated and interference data:

- Isolated wing-body data: measurements on wing-body without the nacelles present
- Isolated nacelle data: measurements on a single nacelle
- Mutual nacelle interference: differences in nacelle measurements with and without the other nacelles being present
- Wing-body interference on the nacelles: differences in nacelle measurements with and without the wing-body being present
- Total wing-body plus nacelle data: sum of wing-body data plus nacelle data
- Spillage interference: differences in measurements on identical configurations with the nacelles spilling according to a specific controlled mass-flow ratio (MFR), and the corresponding data obtained without spillage.

The basic force and pressure data are contained in references 1 and 2, respectively. Complete descriptions of the wind-tunnel model, test conditions, and available test data are given in reference 3.

3.0 DISCUSSION OF THEORETICAL METHODS

This paper shows comparisons of theory with experiment and thus provides a basis for assessment of the value of the theory. A discussion of the theoretical methods used for these comparisons is presented in this section.

3.1 Requirements for Formulation of Theory

The objective is to calculate interference forces and flow fields that occur when engine nacelles are located in proximity to other airplane components. This is to be done at high transonic Mach numbers; that is, from just above Mach 1 to approximately Mach 1.4.

To achieve this objective, the minimum requirements for theory must include:

- Ability to predict the flow field around airplane components in terms of changes in pressures and velocities
- Ability to sum the effects of the various flow field components upon one another
- Ability to predict occurrence of shock waves, their propagation, and their strength in order to determine the consequences of shock-wave-induced forces at transonic Mach numbers

It was desired to assess the effects of engine inlet spillage and jet exhaust plume shape upon interference. An additional requirement for the theory was, therefore, prediction of the flow field around an engine nacelle when either the mass-flow ratio into the inlet was less than unity or when the exhaust jet was not fully expanded.

3.2 Theoretical Methods Used in This Paper

The simplest method that meets some of the above requirements is linear small-perturbation theory for supersonic flow. This method has been developed for the calculation of flow fields around airplane components and has been computerized in many versions. With this method, a study configuration can be broken down into its basic components

(and also into volume and lifting elements) so that the relative flow influences of all these elements can be examined individually. References 4 through 6 describe some of these computerized versions of linear small-perturbation theory.

Small-perturbation theory cannot be used, however, to predict the occurrence, propagation, and location of shock waves. Thus, it could not by itself be used to meet the third objective listed above. A modified form of linear theory that can predict the occurrence and location of shock waves around bodies of revolution was therefore used for the force and moment predictions reported in this paper. This method is described in reference 7. Figure 5 illustrates a typical geometrical representation of a wing-body-nacelle configuration for this modified linear theory program.

The flow around a nacelle at mass-flow ratio less than unity with normal shock spillage contains regions of both subsonic and supersonic flow. Small-perturbation theory, even when modified as in reference 7, cannot predict such flows. Because of this, a more complicated method had to be used for the calculation of the nacelle flow fields at spillage conditions. The method used here is a time marching solution of the Euler equations for two-dimensional or axisymmetric flow. The procedure can compute mixed regions of subsonic and supersonic flow and yield shock wave locations as part of the solution. The method, which was coded for computer use, is described in reference 8.

3.3 Limitations of the Theoretical Methods

In general terms, small-perturbation theory is limited to airplane configurations that are thin and slender. Supersonic small-perturbation theory is also limited to flows that do not contain zones of subsonic flow embedded in supersonic flow.

In practical terms, it is useful to categorize limitations of the theory used in this paper as follows:

- Limitations because of viscosity
- Limitations because of mixed subsonic-supersonic flow
- Limitations because of geometry

The first limitation applies when the actual flow is substantially different from the assumed theoretical attached flow conditions because of large areas of flow separation, vortices, wakes, etc. Criteria can be applied to theoretical predictions, which can tell in advance if occurrence of the above has a high degree of probability. Such criteria, based on experiment, have been presented and discussed in reference 9. An application of these criteria to the type of flow discussed in this paper is shown in section 4.3.

As has been mentioned above, the theory based on solution of the Euler equations can account for mixed subsonic-supersonic flow regions in the vicinity of the nacelles, particularly when normal shock spillage takes place. It was not found feasible, for this study, to allow for mixed subsonic-supersonic flows on other parts of the airplane. It was believed, however, that this limitation would affect predictions primarily in the narrow (but not unimportant) Mach range of 0.95 to 1.05. In general, strong shock waves with downstream subsonic flow will also have an adverse effect on boundary layers and limit theory for the viscous reasons already mentioned.

The small-perturbation theory that has been used here is strictly applicable to all wing-body geometries within the above limitations. Calculation of shock waves and mixed-flowfields is applicable, however, only to nacelle shapes that are axisymmetric. The degree that this limitation would affect overall results should this assumption be violated has not been examined.

In addition, the small-perturbation theory method evaluated for this paper requires introduction of flow images to account for reflection of flow from an adjacent component. In these calculations, complete reflection has been assumed for the nacelle-on-wing interactions. In practice, for some geometric arrangements, partial reflections and refractions take place. Because of this, the theory is limited either to those configurations where the assumption of complete reflections is justified or where there are no reflections at all. The geometric arrangement that is most likely to be affected by this limitation is the situation of a nacelle partly ahead of the leading edge of a swept-wing. Such a case has been analyzed, however, and is reviewed in section 4.3.

3.4 Prediction of Nacelle-Installed Drag

Nacelle-installed drag calculated by the modified linear theory described above uses the superposition approach illustrated in figure 6.

Typically, the nacelle-installed drag is calculated as the sum of the friction drag of the nacelles, the net wave drag, and the lift interference effects.

The net nacelle wave drag includes--

- Nacelle pressure drag
- Nacelle pressures acting on the wing-body volume or thickness
- The wing-body thickness pressures acting on the nacelles
- Mutual nacelle interference

The mutual nacelle interference consists of the effect of the pressure field of a nacelle acting directly on the other nacelles plus the effect of the pressure field reflecting off the wing surface back onto the nacelles.

The lift interference consists of three items:

- The nacelle pressures reflecting off the wing produce an interference lift, ΔC_L . Because of the interference lift, the wing-body incidence required to produce a specified total lift is reduced, which results in a reduction in the wing-body drag-due-to-lift.
- The nacelle pressures acting on the mean lifting surface produce a drag or thrust force.
- The wing lifting pressures produce a buoyancy force on the nacelles.

The accuracy of current analytical methods of evaluating supersonic airplane drag depends on a detailed knowledge of the effective airplane shape. These theoretical methods, at present, represent the flow into the engines and the engine exhaust jets analytically as cylindrical streamtubes extending upstream of the inlet and downstream from the exhaust nozzle exit. However, since the pressure of the exhaust gases at the nozzle exit is generally different from ambient pressure, the jet will tend either to expand or to contract after leaving the nozzle. Additionally, for off-design conditions the engines may spill flow around the inlets. In principle, these deviations of inlet flow and/or jet exhaust from cylindrical streamtubes can result in aerodynamic interference on adjacent nacelle or airframe surfaces.

The effects of engine operating conditions on the surrounding flow field must therefore be considered in the drag calculations. An embedded flow analysis approach is discussed in this paper. In this approach, streamtube shapes are calculated for an isolated nacelle, depending upon the inlet and exit flow conditions. These streamtube shapes are treated as solid pseudo-nacelle shapes in subsequent fully supersonic flow analyses using the modified linear theory. The pseudo-nacelle shapes create pressure fields that can act on adjacent components. The pseudo-nacelles shapes cannot sustain buoyancy forces from these adjacent components. This requires a careful bookkeeping system.

4.0 TEST VERSUS THEORY COMPARISONS

This section contains a number of test versus theory comparisons to illustrate the validity of the theories that were discussed in the previous section. Results are typical of the more extensive comparisons presented in references 10 and 11.

4.1 Application of Theory to Simple Cases

Predicted aerodynamic characteristics of the NASA wind-tunnel model isolated wing-body configuration are compared with the corresponding test data in figures 7 and 8.

Drag predictions at zero lift were obtained as the sum of the volume wave drag calculated by far-field (area-rule) theory plus fully turbulent flow skin-friction drag. These drag predictions agree well with the test data.

The theoretical lift curve slopes also agree reasonably well with the test data. However, theory predicted the aerodynamic center too far aft, particularly at the low supersonic Mach numbers.

The good agreement between theoretical and experimental drag polars in figure 8 indicates that theory should predict the reductions in wing-body drag-due-to-lift associated with the nacelle interference lift (described in section 3.4).

Theoretical predictions of surface pressure distributions and zero-lift drag of the isolated nacelle at a mass-flow ratio of unity (i.e., no spillage) are compared with test data in figure 9.

Theoretical drag predictions agree with the test data at Mach 1.3 and 1.4. Theory overestimates the nacelle drag at Mach 1.2 and below. The Mach 1.15 pressure distribution shows that theory overestimates the expansion (i.e., negative) pressures on the nacelle boattail. This leads to the overestimation of drag at the lower supersonic Mach numbers. The pressure measurement at the first station at both Mach numbers is less than theory. This is probably due to the nacelle actually spilling a small amount of flow at the "mass-flow ratio unity" test condition.

4.2 Application of Theory to Nacelle Inlet Flow Fields

The effect of nacelle spillage (mass-flow ratios as low as 0.7) was investigated in the NASA nacelle-airframe interference test program. The mass flow through each nacelle was varied by a control plug in the flow-through sting supporting the nacelle. At supersonic speeds, a normal shock forms in front of the nacelle and moves progressively upstream as the mass flow through the nacelle is reduced.

Mixed subsonic-supersonic flow analyses were made of the isolated nacelle. The program used a time marching procedure to solve the unsteady two-dimensional "eddy viscosity" Navier-Stokes equations for turbulent flow of a nonconducting fluid. The method is described in reference 8. Viscosity effects were neglected in the analyses. With viscosity being neglected, the mixed-flow analysis program solves the Euler equations.

The calculations made were inviscid and axisymmetric and yield bow shock locations as part of the solution. A schematic of the flow field is shown in figure 10. Results of the computations include bow shock location and shape, flow field streamtubes, definition of subsonic flow regions, and nacelle surface static pressure distributions, as well as detailed flow field information (such as Mach numbers, pressures, velocities) throughout the calculation region.

Calculations first were made for a 5-deg sharp-nose conical pitot inlet to validate the theory. The calculations were made for a freestream Mach number of 1.14 and for mass-flow ratios of 0.64, 0.81, 0.91. Mass-flow ratio equals the ratio of mass-flow rate of the spilling nacelle to the mass-flow rate without spillage.

Computed results are compared with experimental data from reference 12, in figure 11. The conical pitot inlet and the region near the inlet where the detailed flow field analyses were made are shown. Figure 11 also contains comparisons of predicted constant Mach contours with experimental bow shock shapes that were determined from Schlieren pictures. The "bunched" upstream Mach contour lines, which were interpreted as predicted bow shocks, agree well with the test data. The calculations also indicate the presence of a significant region of subsonic flow between the inlet and the detached bow shock. The region of subsonic flow grows rapidly as the mass flow into the nacelle is reduced and more flow is forced to spill around the inlet. Figure 12 compares the predicted and experimental variation of shock standoff distance with mass-flow ratio.

Nacelle surface pressure measurements are compared with the corresponding theoretical predictions in figure 13. Reducing the mass-flow ratio is seen to have significant effect in decreasing the nacelle pressures near the inlet lip. Theoretical predictions agree quite well with test results.

The mixed flow analysis program was then used to calculate the inlet flow field about the NASA-Ames nacelle. Figure 14 shows the calculation mesh and analysis region.

Mach contours and streamtube shapes for flow into and around the nacelle were calculated for different mass-flow ratios and Mach numbers. Figure 15 shows typical results of these calculations.

Figure 16 summarizes the effect of reduced mass flow on the inlet flow field. The subsonic flow region between the detached bow shock and the inlet lip grows dramatically as the Mach number is reduced from 1.4 to 1.15. This figure also shows the location of the nacelle below the wing chord plane corresponding to the NASA-Ames nacelle-airframe wind-tunnel model arrangement. The subsonic flow region is seen to intersect the wing surface at Mach 1.15.

Nacelle theoretical surface pressure distributions were calculated for the forecowl of the NASA nacelle for various amounts of spillage at Mach 1.4 and 1.15. Theoretical pressure distributions are compared with test data in figure 17. The predicted effect of reduced mass flow on the nacelle pressure distributions agrees well with the test data.

Isolated nacelle drag calculations were made for various amounts of spillage. In these drag calculations, it was assumed the effect of spillage on skin friction drag was negligible. The nacelle wave drag with spillage was then calculated by adding the change in forecowl drag due to spillage to the total nacelle wave drag with no spillage. The predicted effect of spillage on isolated nacelle drag, as shown in figure 18, closely matches the test data.

These results indicated that the mixed flow theory program can predict satisfactorily the flow field characteristics around a spilling nacelle.

Predictions of interference pressures near the nacelle were made using the embedded-subsonic-flow analysis approach summarized in figure 19.

In this approach, streamtubes, which were defined by the mixed-flow theory, were analyzed as solid pseudo-nacelle shapes using the supersonic theory. Pressures predicted by these supersonic theory analyses were compared with the corresponding mixed flow theory predictions to assess the accuracy of the approach.

The bow shock shape calculated by the supersonic theory for the nacelle with no spillage agrees well with the mixed-flow theory predictions, as shown in figure 20. The supersonic theory bow shock, however, does "bulge" forward of the mixed flow shock in the region near the inlet lip.

Calculated interference pressures surrounding the nonspilling nacelle are shown in figure 21 for various radial distances from the nacelle. The pressure signatures are quite similar except in the immediate vicinity of the bow shock. The mixed flow theory pressure rise is more gradual than that predicted by the supersonic theory. The more gradual pressure rise is attributed to the relative coarseness of the calculation mesh. These results tend to imply that the supersonic theory predictions of pressures surrounding a nacelle are accurate, provided the flow remains supersonic and the bow shock is of moderate strength.

Calculations were made of pseudo-nacelle geometries to evaluate procedures for using the supersonic theory to predict interference pressures for mass-flow ratios of 0.8 and 0.7. The pseudo-nacelle geometries included:

- Nacelle plus the capture streamtube
- Streamtube shapes surrounding the nacelle over which the flow remains supersonic; three streamtubes at various radial distances were analyzed

The calculated bow shock shapes for these various pseudo-nacelle shapes are compared with the mixed flow theory predictions for the spilling nacelles in figure 22.

The supersonic surrounding streamtubes corresponding to a specified mass-flow ratio all gave similar bow shock shapes and near-field pressure distributions. The capture streamtube results, however, differed from the subsonic surrounding streamtube results.

The shapes of the mixed flow theory bow shock and the supersonic surrounding streamtube bow shock are the same beyond radial distances of approximately two inlet diameters from the centerline. At smaller radial distances, the supersonic surrounding streamtube shock "bulges" forward of the mixed flow theory shock similar to the no-spillage results shown in figure 20.

The bow shocks predicted, using the capture streamtube plus nacelle geometry, fall aft of the corresponding mixed flow theory shocks except very near the nacelle. Here, the supersonic theory shock waves incorrectly bulge forward of the start of the capture streamtube.

Figure 23 compares predicted interference pressure distributions for the spilling nacelles. The figure includes:

- Mixed flow theory results for spilling nacelles
- Supersonic theory predictions using capture streamline plus nacelle
- Supersonic theory predictions using supersonic surrounding streamtube

The mixed flow theory predictions were made using the actual nacelle shape and prescribed boundary conditions to provide the appropriate mass flow into the nacelle. The supersonic theory predictions were obtained from streamtube shapes defined by the mixed flow theory analyses. Inaccuracies in the prescribed streamtube shapes will therefore be reflected in the supersonic theory calculations. The no-spillage predictions of figure 2 implied that the mixed flow theory tended to "smooth" the bow shock over two or three calculation-mesh cell widths. Hence, calculated streamtube shapes will also be overly smoothed. This would result in reduced shock strengths calculated using these shapes.

The previously mentioned differences in predicted bow shock strength are readily apparent in these comparisons. Moderate initial angle changes (approximately 2 deg) would account for the difference between the supersonic theory and the mixed flow theory bow shock strength predictions. Shapes of the pressure distributions computed using the supersonic surrounding streamtubes are similar to the mixed flow theory results. Main features of the flow include a strong shock followed by a rapid expansion behind the shock, which is in turn terminated by a mild shock or flow recompression. Note that results obtained using the capture streamtube-nacelle representation do not give any indication of the strong expansion and mild recompression shock.

The results imply that normal-shock spillage interference can be properly calculated by using the following embedded subsonic flow approach.

1. Use the mixed flow theory to calculate the local flow field characteristics surrounding the spilling nacelle using a fine calculation mesh.
 2. Compute the surrounding streamtube shapes.
 3. Identify a near streamtube over which the flow remains supersonic.
 4. Use this supersonic streamtube shape to calculate the pressure field surrounding the spilling nacelle.
 5. Integration of the spilling nacelles pressure on the wing surface and on adjacent nacelles should provide the interference forces.
- 4.3 Application of Theory to Prediction of Nacelle Interference on Adjacent Airplane Components

Figure 24 contains a comparison of predicted and measured mutual nacelle interference drag for various nacelle stagger arrangements. The mutual nacelle interference is the result of the pressure field of each nacelle pushing on each of the other nacelles. The measured mutual nacelle interference was obtained as the difference in the drag of the nacelles with and without the other nacelles present. Theoretical predictions agree well with test data.

Theoretical nacelle shock-wave patterns and interference pressures on the wing lower surface are compared with test data for one of the aft unstaggered nacelle location in figures 25 and 26. The experimental interference pressures were obtained as the difference in the wing lower surface pressures with and without the nacelles present.

The predicted nacelle bow-shock locations agree well with the experimental shock locations, as indicated by a sudden "jump" in interference pressures, ΔC_p , from zero to a large positive value. Theoretical interference pressure distributions agree reasonably well with the experimental data. The experimental bow-shock strength is less than indicated by the test data. This may be the result of a shock boundary-layer interaction softening this initial sudden pressure rise.

Figure 27 contains a comparison of predicted shock-wave patterns and interference pressure fields with test data for a forward unstaggered nacelle location in which the outboard nacelle is near the wing leading edge. In this nacelle arrangement, the wing experiences not only the bow shocks from the nacelles, but also aft shocks. The aft shocks arise from the flow compression at the aft end of the nacelle where the flow-through sting enters the nacelle shell.

The predicted and measured interference pressures for this wing-body forward nacelle arrangement agree quite well except in local areas near the aft shock and at the most on-board station.

In reference 9 it is shown that flow across a glancing shock wave, in which the flow is deflected in the plane of the wing, will separate if the pressure rise across the shock wave exceeds 50%. Furthermore, it is shown that a local negative pressure field on the wing can amplify the pressure rise across a shock wave.

Theoretical bow shock and aft shock strengths on the wing lower surface are compared with these shock-induced boundary layer separation criteria (ref. 10) in figure 27. The aft shocks are seen to be sufficiently strong to cause boundary layer separation. Indeed, this separation is evident by the discrepancy between the theoretical predictions and test data in the areas near the aft shocks.

Figures 28 and 29 contain experimental and calculated shock wave patterns, and interference pressures on the wing lower surface for conditions in which the nacelles are operating at a mass-flow ratio of approximately 0.8. The theoretical shock-wave patterns for no spillage are also shown for reference. The theoretical predictions are in fair agreement with the test data.

The theoretical calculations for the spillage conditions were made using supersonic theory and pseudo-nacelle geometry consisting of the actual nacelle geometry plus the capture streamtube as inlet extensions. The more accurate supersonic surrounding streamtube method was not used because the previous mixed-flow analyses were restricted to the inlet region only. As a result, the full shapes of the surrounding streamtubes were not defined.

4.4 Installed Nacelle Lift and Drag

Comparisons between theoretical and experimental nacelle lift and drag are shown in figures 30 and 31 for an aft unstaggered nacelle location. The drag comparisons include the net interference on the wing-body, the net interference on the nacelles, and the total nacelle installation drag. The drag and lift predictions agree quite well with the test data.

This aft nacelle location is seen to be a favorable low-drag installation, since at moderate lift coefficients the installed nacelle drag is less than half the isolated nacelle drag level. This favorable effect is primarily due to the reduction in wing-body drag-due-to-lift associated with the nacelle interference lift.

The measured interference lift increment increases with angle of attack, particularly at Mach 1.15. The theoretical interference lift calculations were made at a constant local Mach number equal to the freestream Mach number. The increase in interference lift can be attributed to a reduction in the local Mach number around the nacelles associated with the change in the wing interference pressure fields as angle of attack is increased. This effect is the greatest at very low supersonic Mach numbers.

Similar test versus theory comparisons are shown in figure 32 for a forward nacelle location at Mach 1.4. The theoretical predictions differ significantly from the test data. This difference is believed to be due to two effects: (1) shock-induced separation associated with the strong nacelle aft shocks and (2) influence of the nacelle pressure field affecting the upper surface of the wing. Neither of these effects is included in the theory. However, both theory and test indicate that the nacelle interference effects for this forward location are highly unfavorable. The installed drag increases with angle of attack and approximately doubles the isolated nacelle drag level.

Figures 30, 31, and 32 show that nacelle location can have a powerful effect on the nacelle interference. At the aft nacelle locations, both the interference of the nacelles on the wing-body and the wing-body on the nacelles are favorable. The nacelles in the aft locations produce a substantial level of favorable interference. As the nacelles are moved forward, both of these interference components become unfavorable, which results in considerable unfavorable net interference.

Figure 33 contains comparisons of calculated nacelle interference drag with test data for different mass-flow ratios, i.e., amounts of spillage. The drag of the isolated nacelle, measured at the average mass flow for the nacelles at each nominal test condition, was removed from the corresponding measured total wing-body nacelle drag. Similarly, the theoretical interference drag predictions do not include the calculated isolated nacelle drag.

The effect of spillage on the nacelle interference acting on the wing-body appears to be correctly predicted by the theory.

The effect of spillage on the interference on the nacelles is less than predicted by theory. Consequently, the theoretical effect of spillage on the total nacelle-installed aerodynamic interference drag does not agree very well with the test data.

4.5 Application of Theory to Jet Exhaust Interference

The shape of exhaust plume of a jet engine can provide an additional source of aerodynamic interference. One approach to predicting these interference effects is to represent the jet plume by an equivalent solid body extension. Calculations of aerodynamic interference with and without the solid body extensions would provide an assessment of the jet exhaust interference on the adjacent components of the airplane.

NASA conducted an experimental investigation to verify the concept of representing a jet by an equivalent solid body. The exhaust-nozzle simulation system used in the study is shown in figure 34. Full details of the study are reported in reference 13.

Experimental data from this NASA test program were used to assess the accuracy of the supersonic theory (described in section 3.2) for predicting jet exhaust interference. Theoretical predictions were made of the pressures surrounding the nozzle simulator with the jet shape determined by inviscid theory. Theoretical predictions are compared with test data in figure 34.

Predictions obtained using the inviscid jet shape agree closely with measurements around the actual exhaust jet. These results indicate that the concept of representing a jet plane by a corresponding equivalent solid body shape is valid, and that supersonic theory can predict these effects.

5.0 CONCLUDING REMARKS

Because an extensive experimental data base was made available by NASA, it has been found possible to evaluate the validity of theory as applied to the difficult problem of airframe-propulsion system aerodynamic interference at high transonic Mach numbers including off-design engine mass-flow effects. It was found that practical theoretical methods are now available to address this problem quite satisfactorily. Success was achieved by selecting the simplest applicable theory, examining its inherent limitations, and correcting these limitations selectively and locally.

The configurations examined were limited to wing-body combinations with axisymmetric nacelles. Future work should emphasize departures from axisymmetry in nacelle geometry. To do this, it will first be necessary to carry out experiments, comparable in quality to those used in this paper, with other nacelles. It will then be necessary also to develop corrections to the theory to account for nacelle shapes that are significantly different from those for which the theories used in this paper were developed.

It was not found possible to evaluate the theories used in this paper in the Mach region from 0.95 to 1.05. As the regions of subsonic flow embedded in the main supersonic stream increase in size, procedures that have been shown to work fairly well at Mach 1.05 will eventually fail as Mach number is reduced from that value. Eventually, at Mach numbers less than 0.95, what has been used in this paper should work in principle, but different elemental computer programs will have to be used. The problem now becomes one of supersonic flow pockets in a main subsonic field.

All in all, however, the work presented here has shown that theory can help to understand interference effects of spilling nacelles; and that calculations, using these theories, should help airplane designers avoid nacelle installations that would have high inherent interference drag.



Figure 1. NASA Nacelle-Airframe Interference Wind Tunnel Model

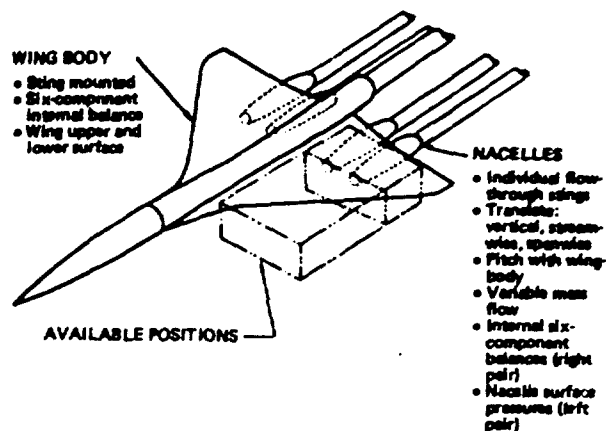


Figure 2. Wind Tunnel Model Features

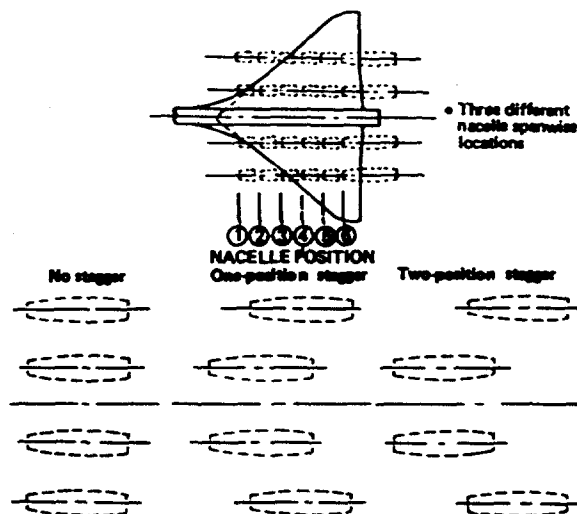
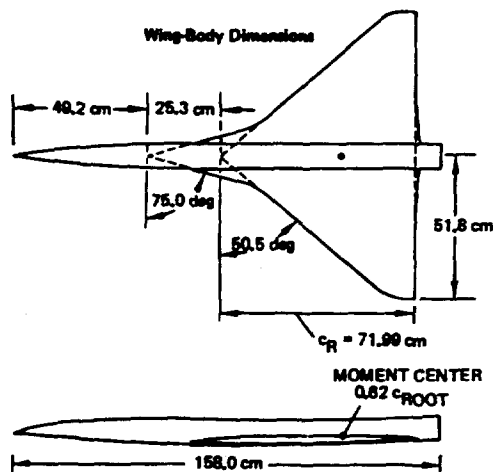


Figure 4. Tested Nacelle Locations

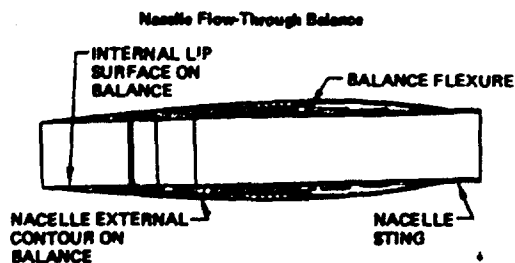
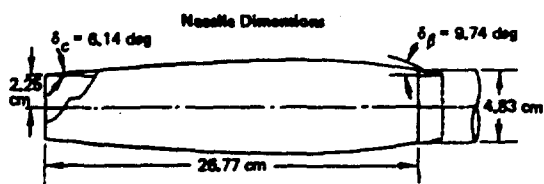


Figure 3. Wind Tunnel Model Dimensions and Details

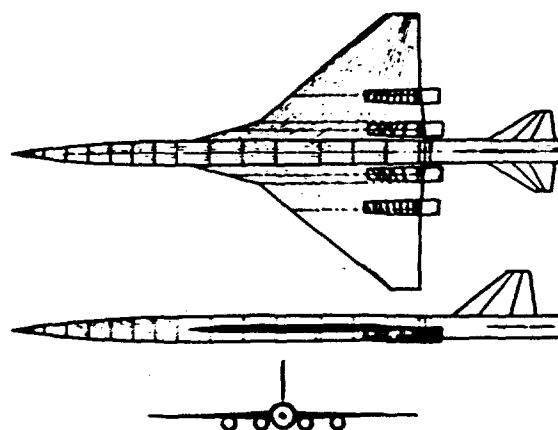


Figure 5. Linearized Supersonic Transport Wind-Tunnel Model Geometry

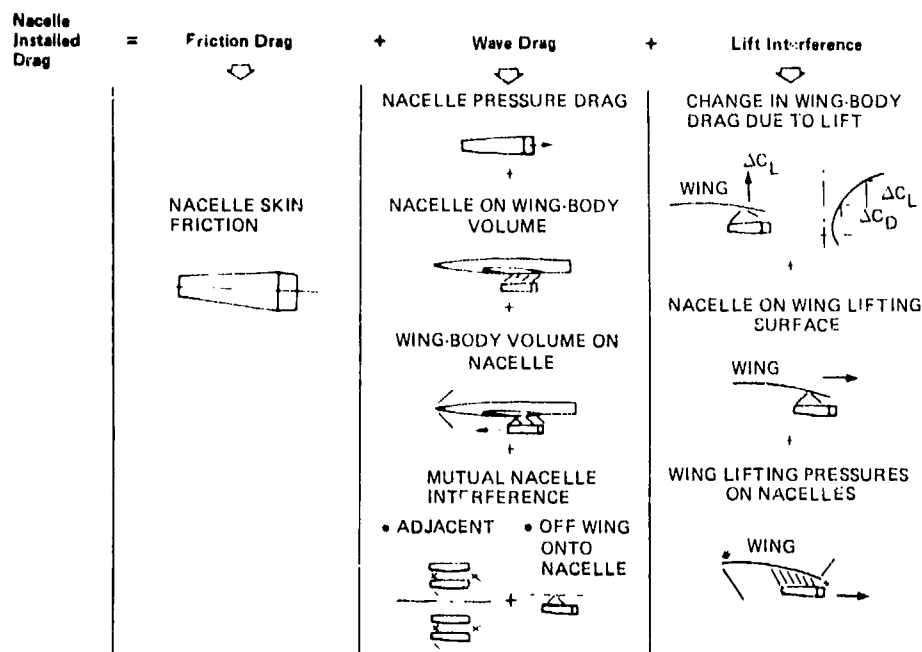


Figure 6. Nacelle Installed Elemental Drag Components

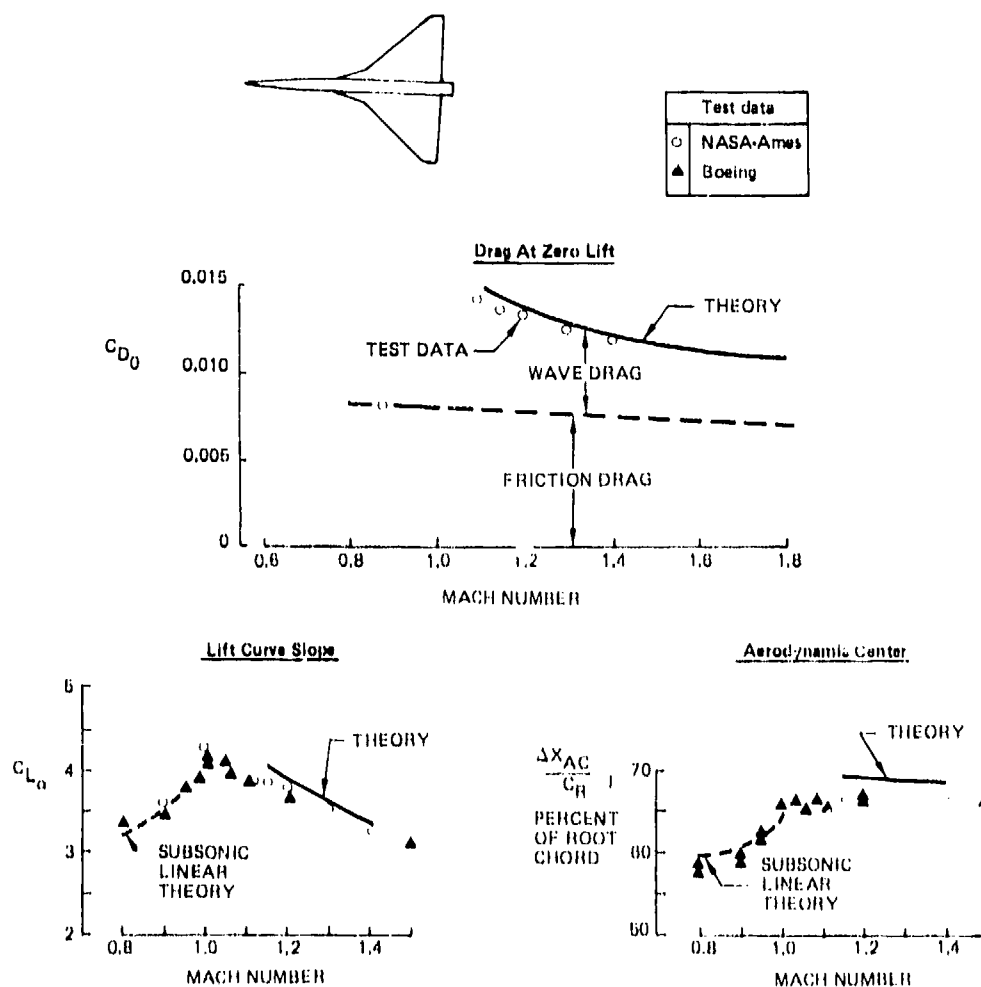


Figure 7. Wing-Body Lift, Drag, and Pitching Moment Comparisons at Zero Lift

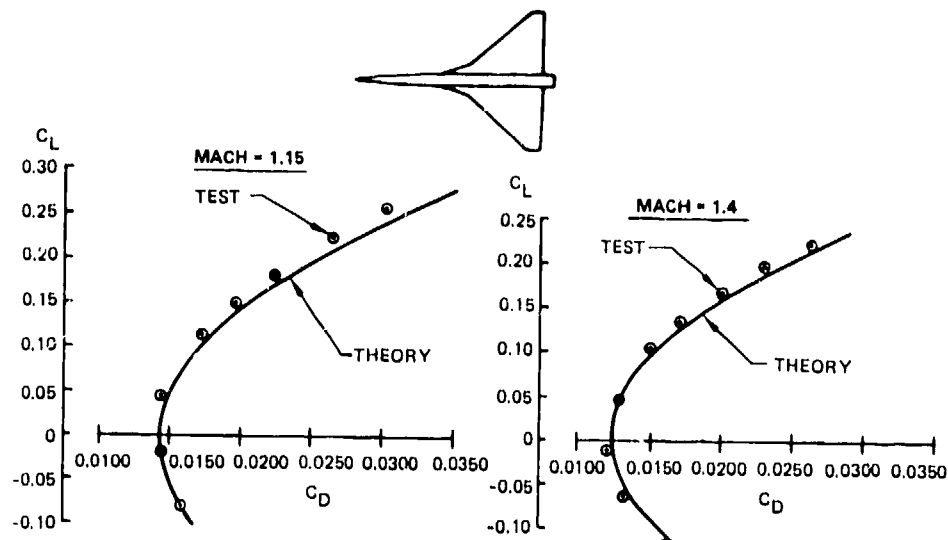


Figure 8. Variation of Wing-Body Drag With Lift

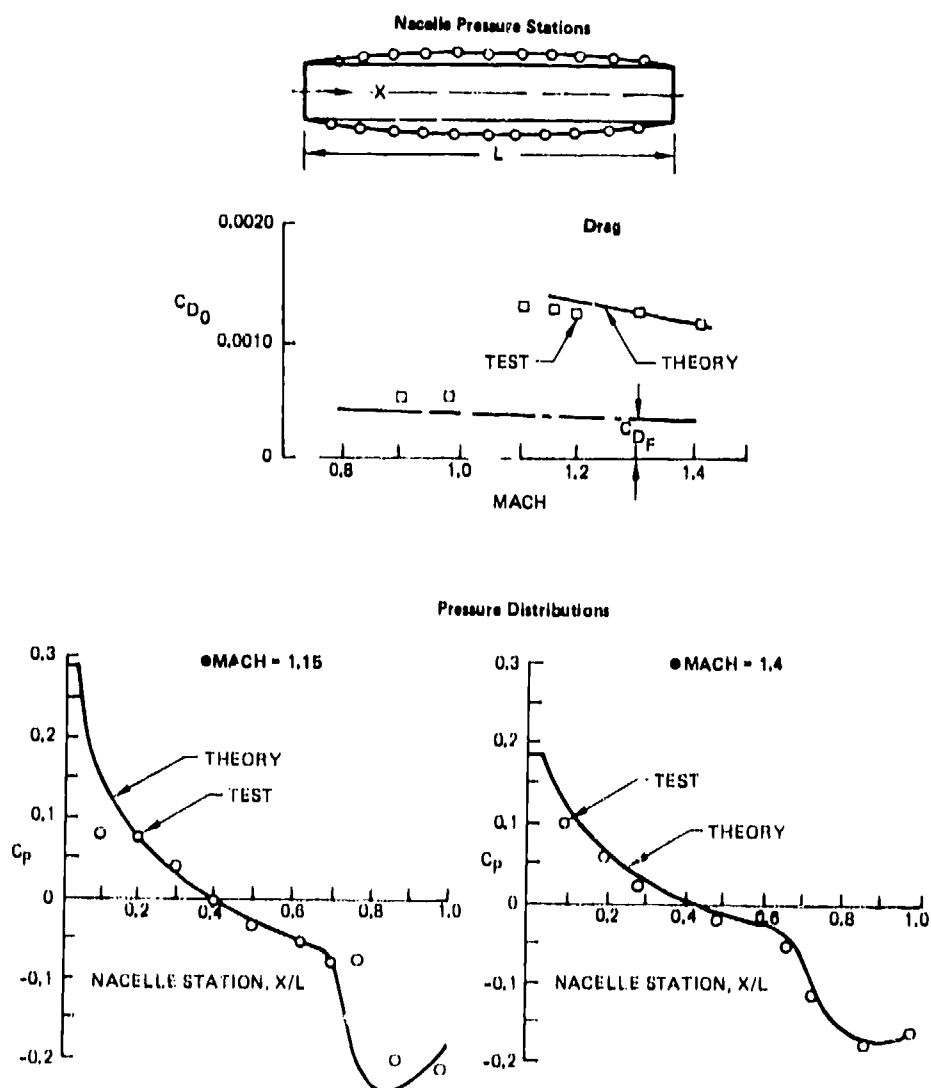


Figure 9. Isolated Nacelle Pressure Distributions and Drag at Zero Angle of Attack and a Mass Flow Ratio of Unity

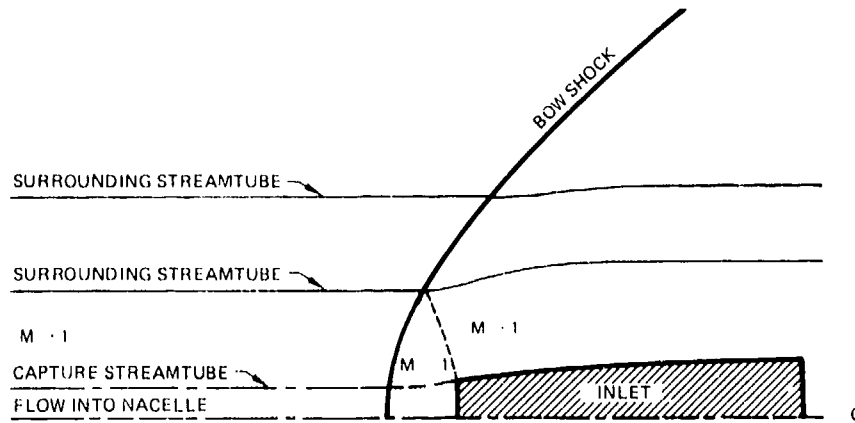


Figure 10. Schematic Diagram of Supersonic Pitot Inlet Flow Field for Mass-Flow Ratio Less Than Unity

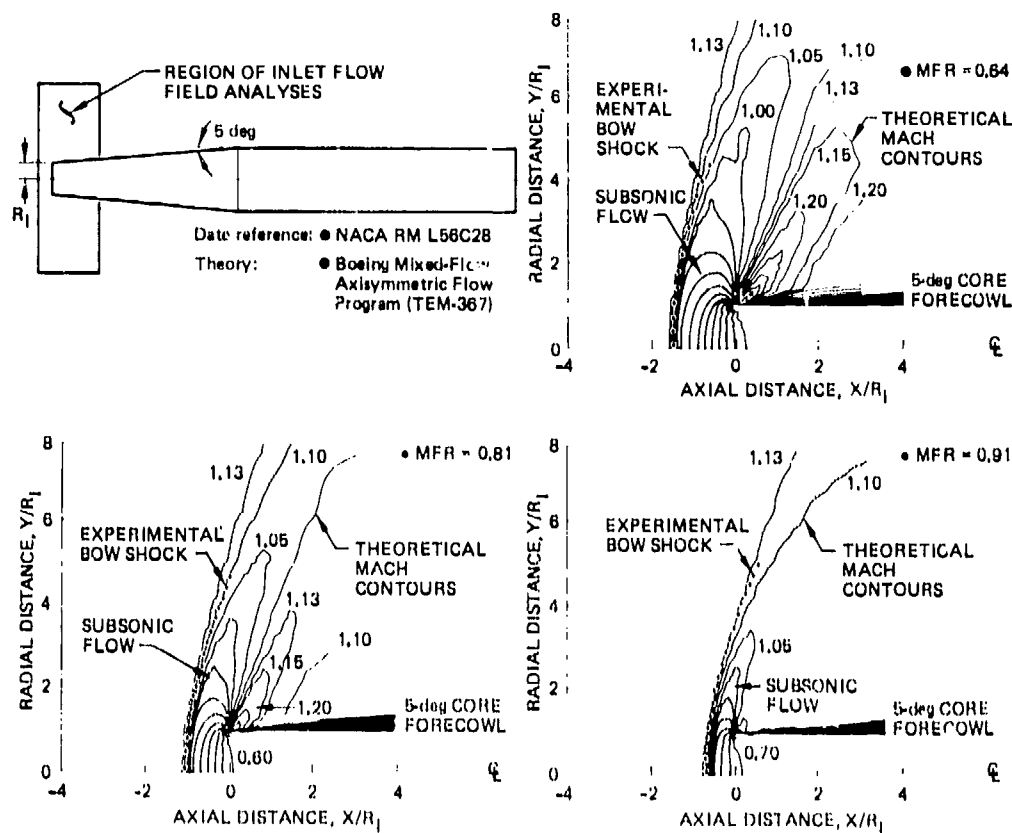


Figure 11. Verification of the Mixed-Flow Theory

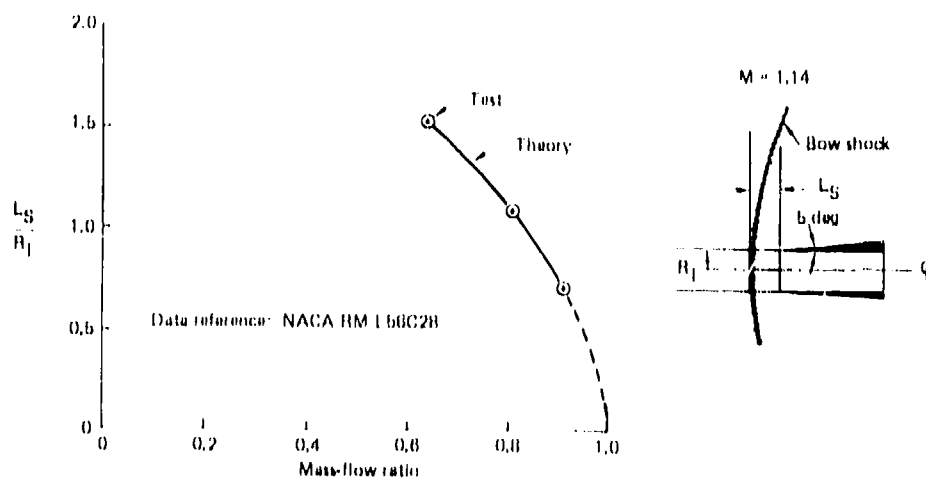


Figure 12. Effect of Mass Flow Ratio on Shock Standoff Distance

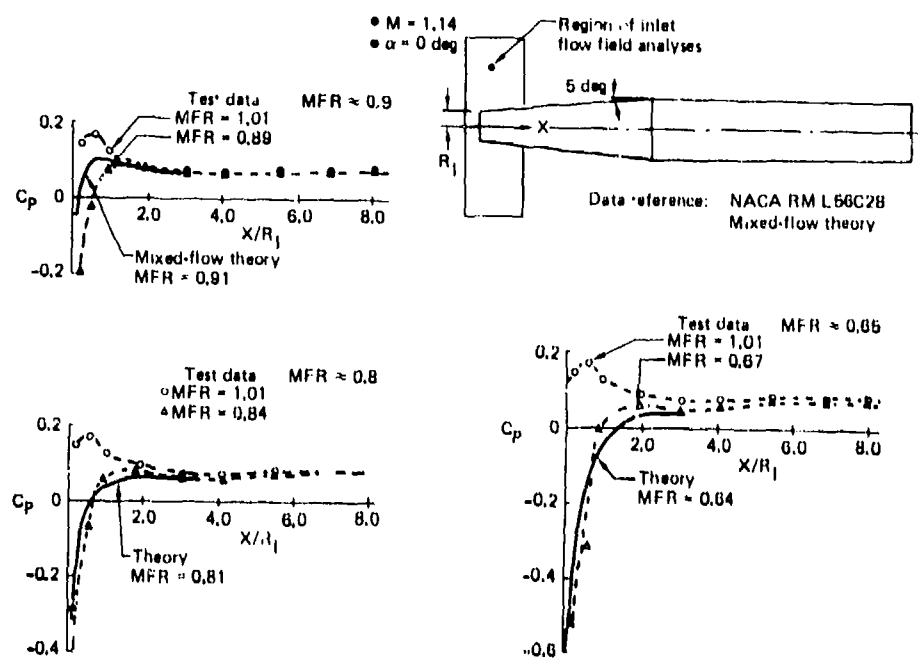


Figure 13. Effect of Mass-Flow Ratio on Conical Inlet Surface Pressures

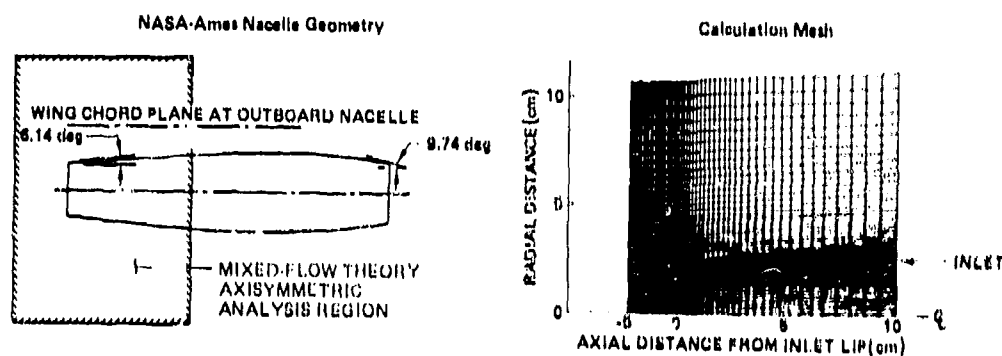


Figure 14. Mixed-Flow Analysis Geometry

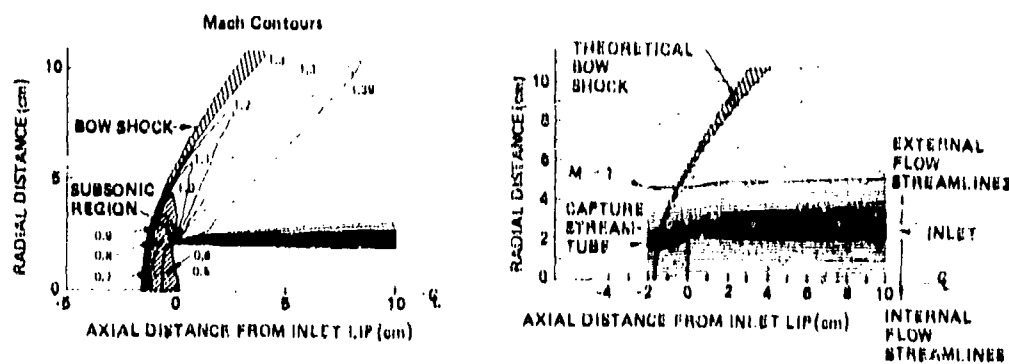


Figure 15. Mixed-Flow Analysis Results at Mach 1.4 and a Mass Flow Ratio of 0.7

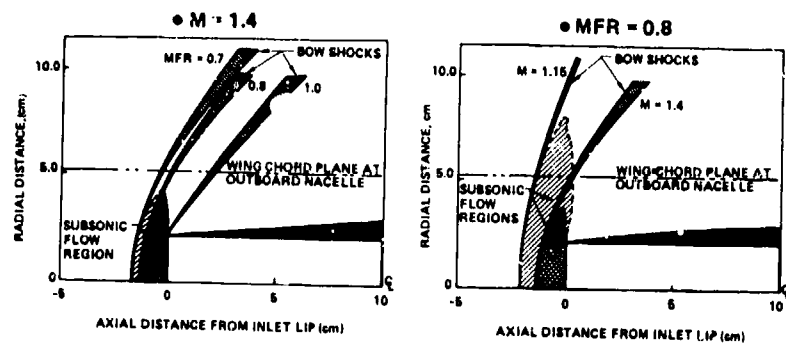


Figure 16. Effect of Spillage on Inlet Flow Field

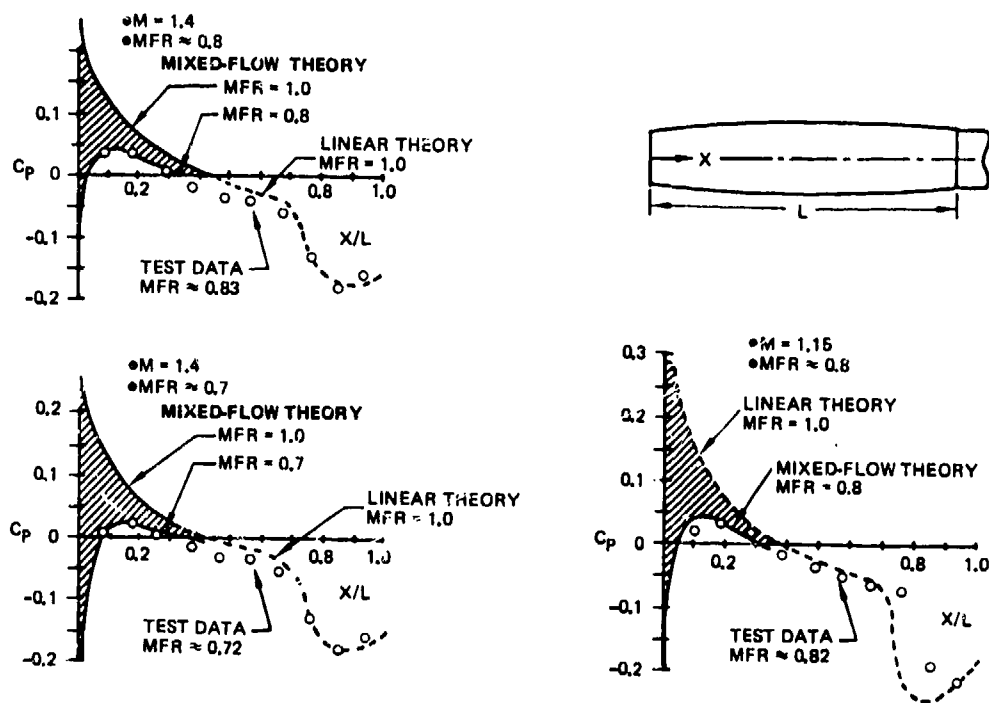


Figure 17. Effect of Spillage on Nacelle Isolated Pressures

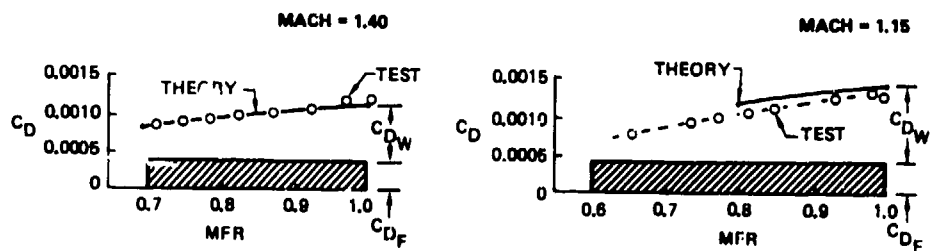
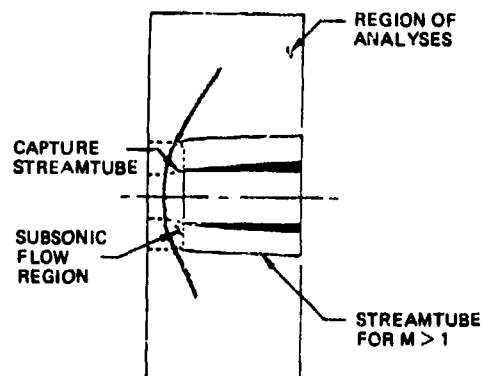


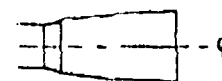
Figure 18. Effect of Spillage on Isolated Nacelle Drag

STEP 1: MIXED-FLOW ANALYSES OF
FLOW FIELD SURROUNDING
INLET

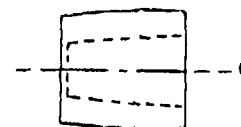


STEP 2: COMPUTE SURROUNDING STREAM-
TUBE SHAPES

• INLET WITH CAPTURE
STREAMTUBE



• $M > 1$ STREAMTUBE



STEP 3: USE SUPERSONIC THEORY TO PREDICT
INTERFERENCE PRESSURES FOR
PSEUDO-NACELLE SHAPES CORRES-
PONDING TO SURROUNDING STREAMTUBES

STEP 4: COMPARE WITH MIXED-FLOW
ANALYSES PRESSURE PREDICTIONS

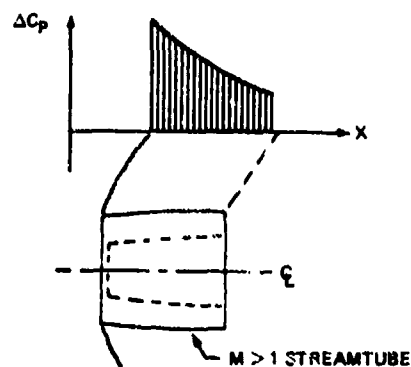


Figure 19. Embedded-Subsonic-Flow Interference Analysis Approach

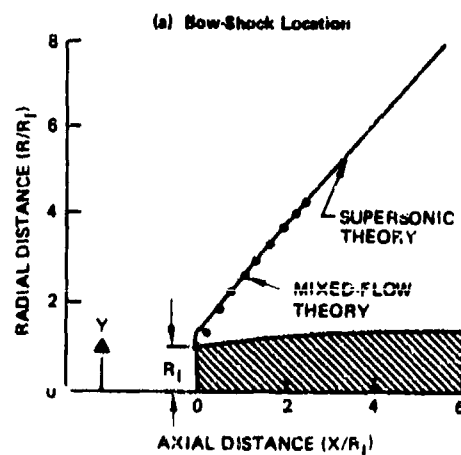


Figure 20. Comparison of Predicted Bow-Shock Characteristics at Mach 1.4 With a Mass-Flow Ratio of Unity

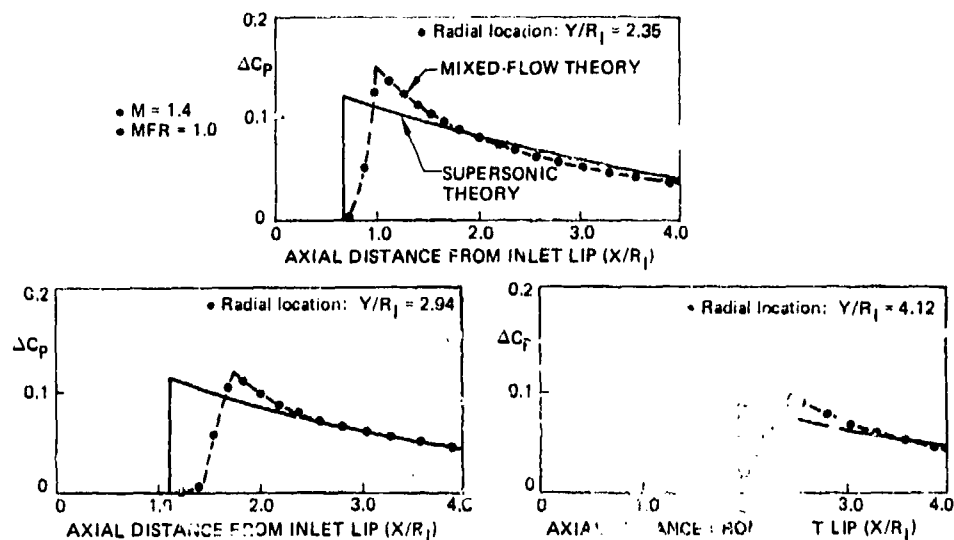


Figure 21. Comparison of Interference Pressures Near a Spilling Nacelle at Mach 1.4

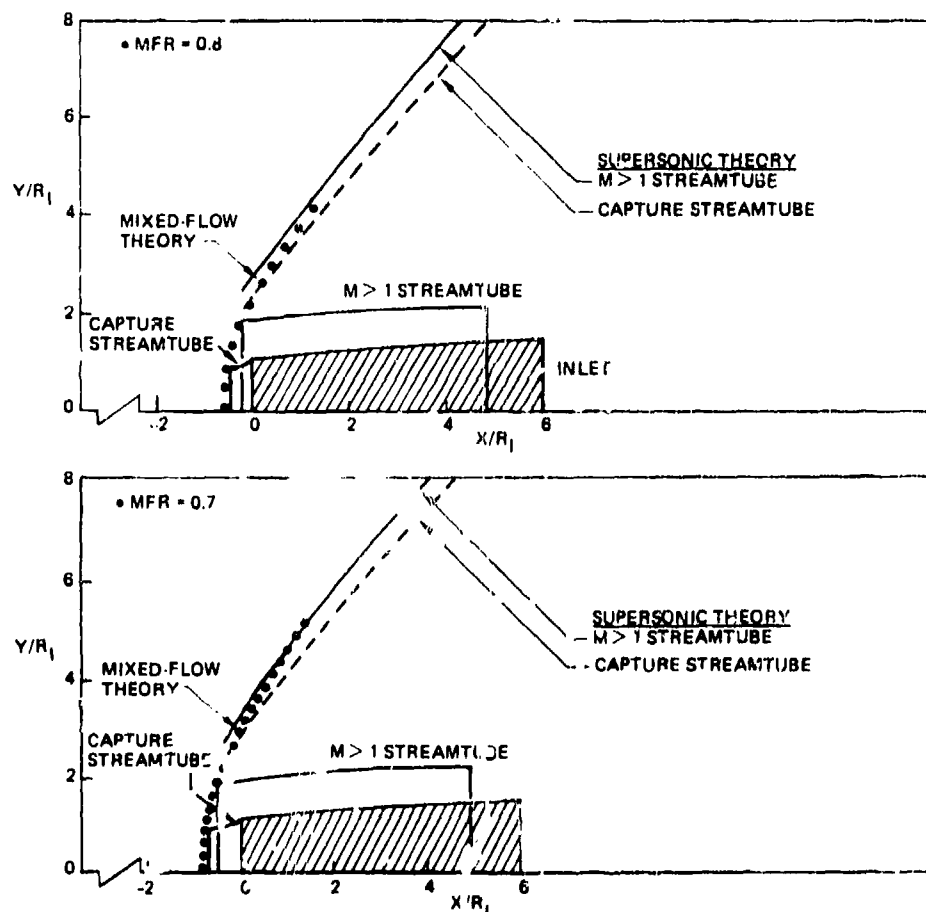


Figure 22. Comparison of Predicted Bow-Shock Shapes for Mass-Flow Ratios of 0.7 and 0.8 at Mach 1.4

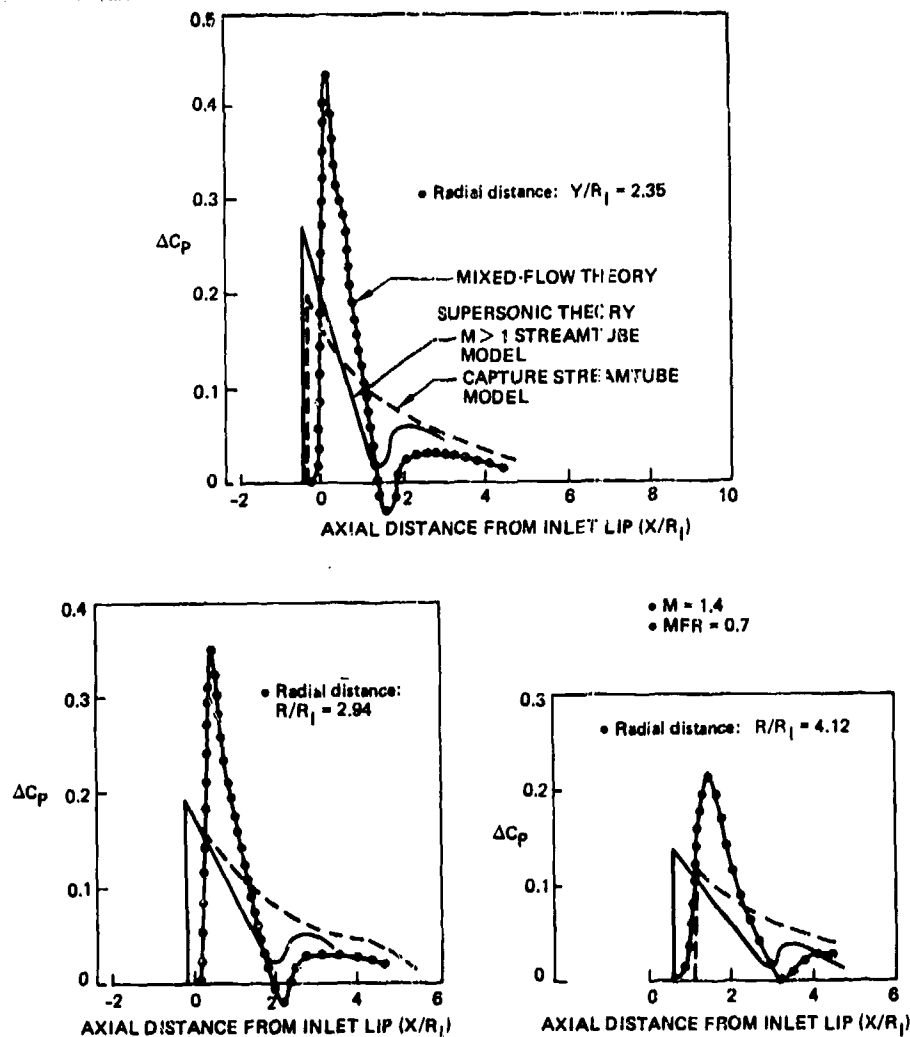


Figure 23. Comparison of Predicted Interference Pressures Around a Spilling Nacelle With a Mass-Flow of 0.7 Mach 1.4

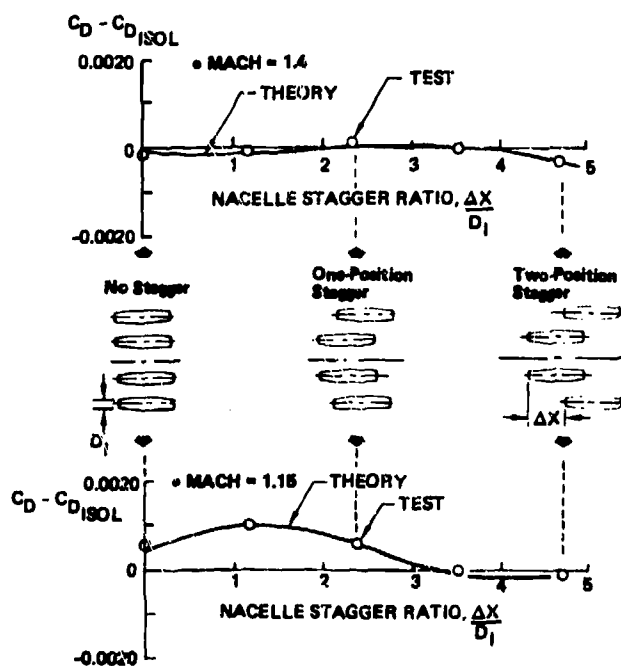


Figure 24. Drag Interference Between Nacelles at Zero Angle of Attack and a Mass Flow Ratio of Unity

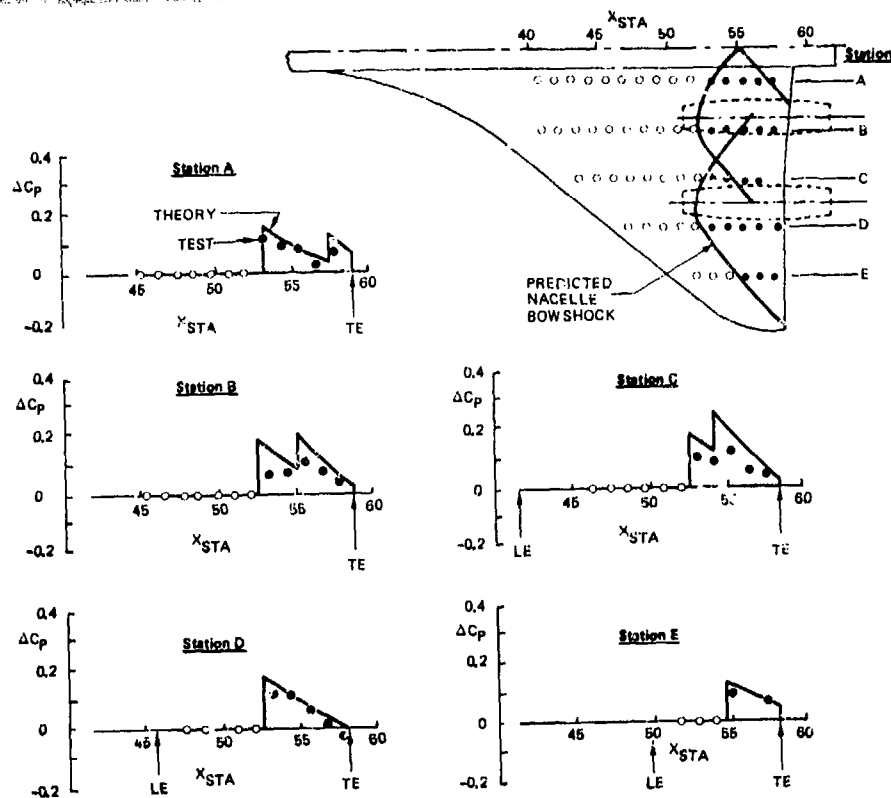


Figure 25. Effect of Nacelles Upon Wing Lower Surface Pressures at Zero Angle of Attack, Mach 1.4, and Mass Flow Ratio of Unity for an Aft Nacelle Location

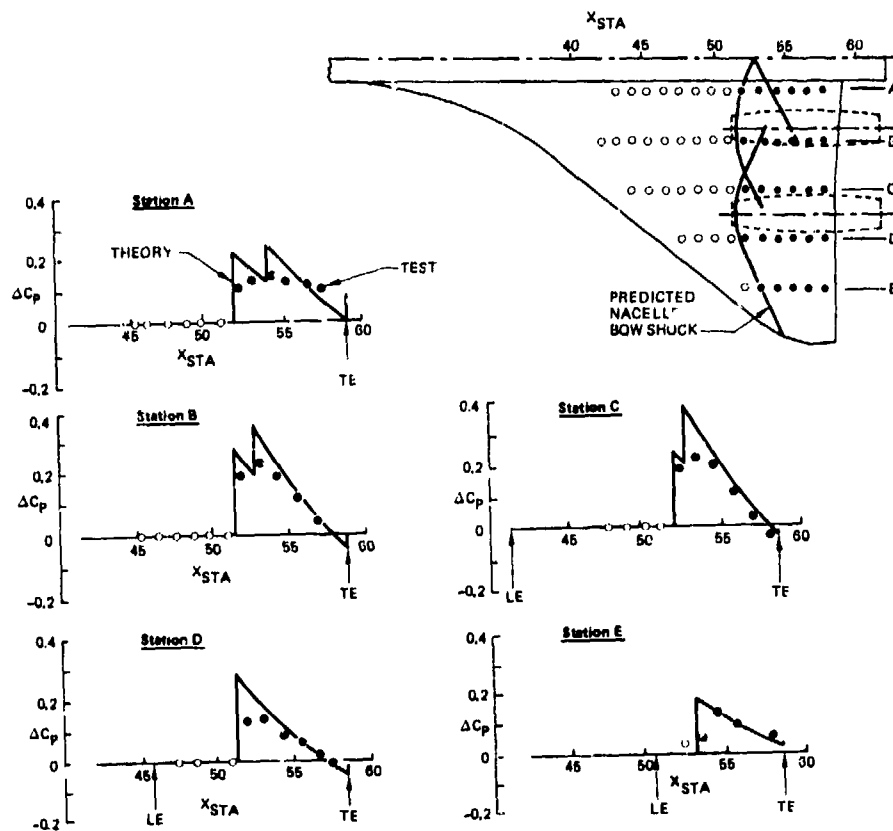


Figure 26. Effect of Nacelles Upon Wing Lower Surface Pressures at Zero Angle of Attack at Mach 1.15 and Mass Flow Ratio on Unity for an Aft Nacelle Location

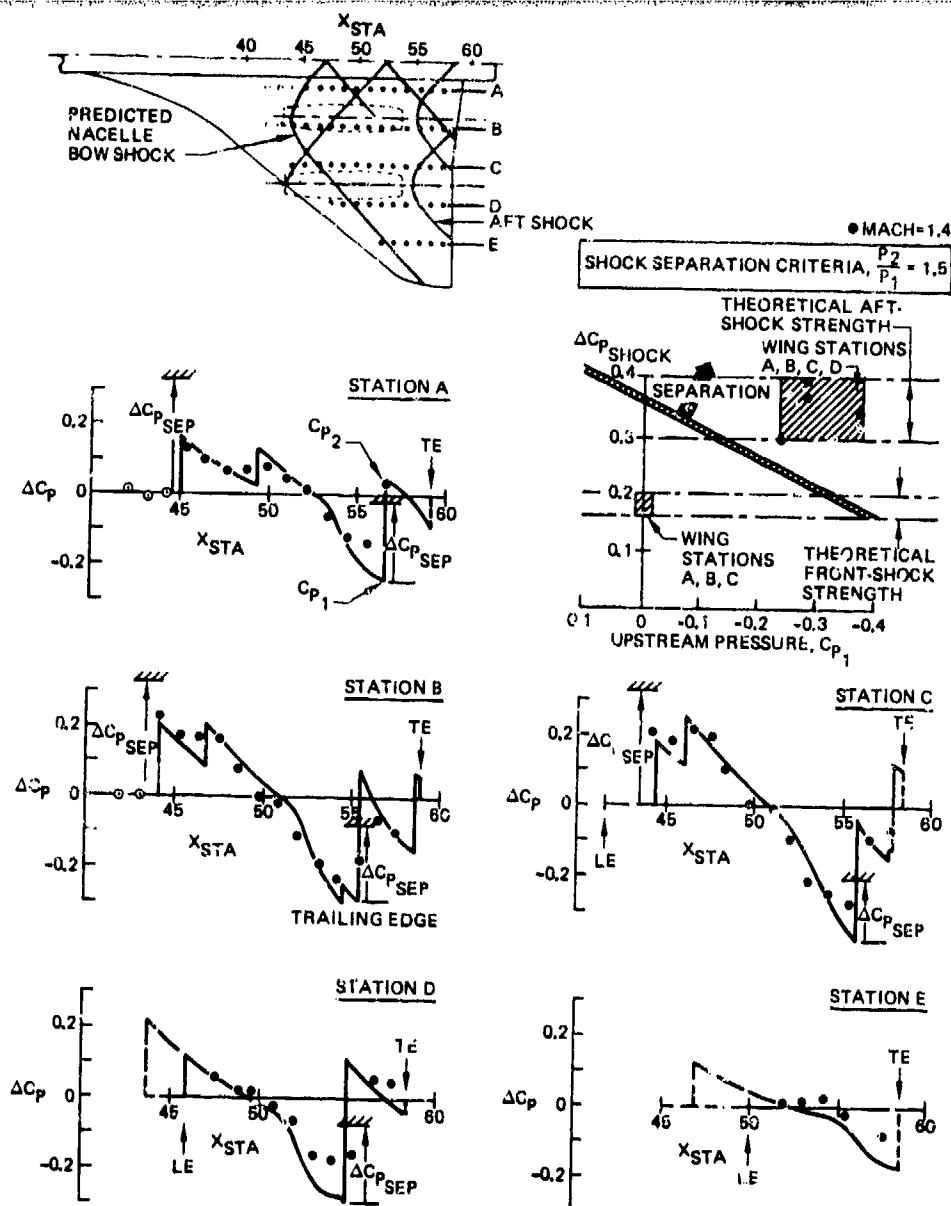


Figure 27. Effect of Nacelles Upon Wing Lower Surface Pressures at Zero Angle of Attack at Mach 1.4 and Mass Flow Ratio of Unity for a Forward Nacelle Location

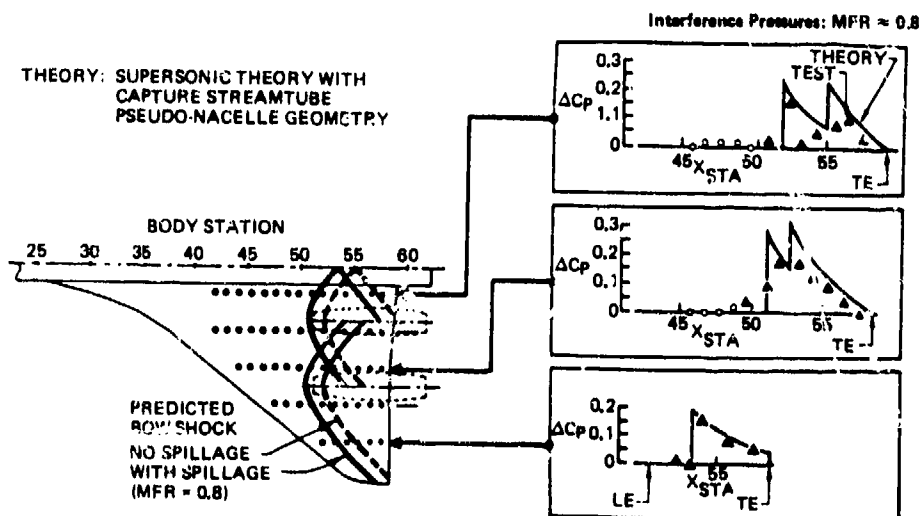


Figure 28. Effect of Normal-Shock Spillage on Isolated Nacelle Pressures and Wing Lower Surface Pressures at Mach 1.4, Zero Angle of Attack, and a Mass Flow Ratio of 0.8

THEORY: SUPERSONIC THEORY WITH
CAPTURE STREAMTUBE
PSEUDO-NACELLE GEOMETRY

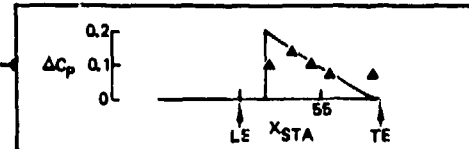
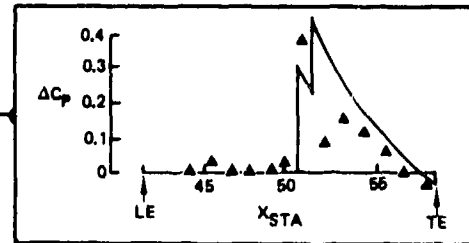
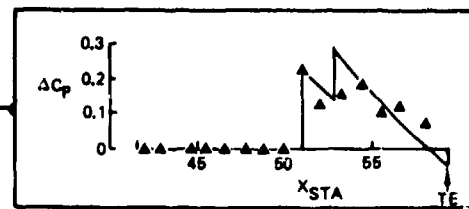
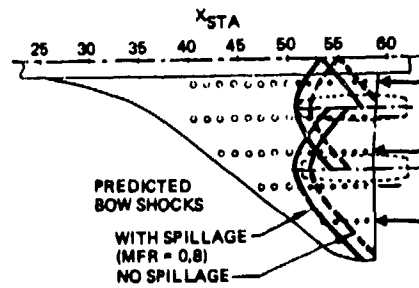


Figure 29. Effect of Normal-Shock Spillage on Isolated Nacelle Pressures and Wing Lower Surface Pressures at Mach 1.15, Zero Angle of Attack, and a Mass Flow Ratio of 0.8

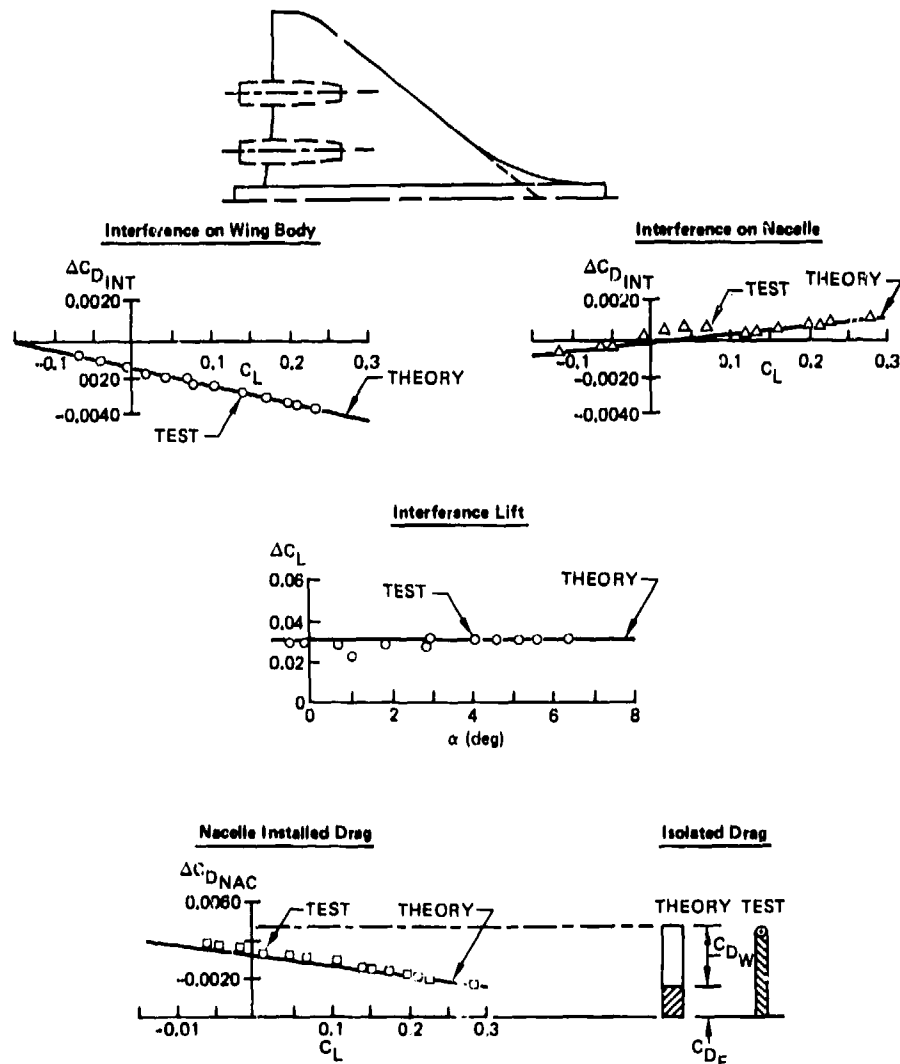


Figure 30. Installed Nacelle Drag for an Aft Nacelle Location at Mach 1.4 and Mass Flow Ratio of Unity

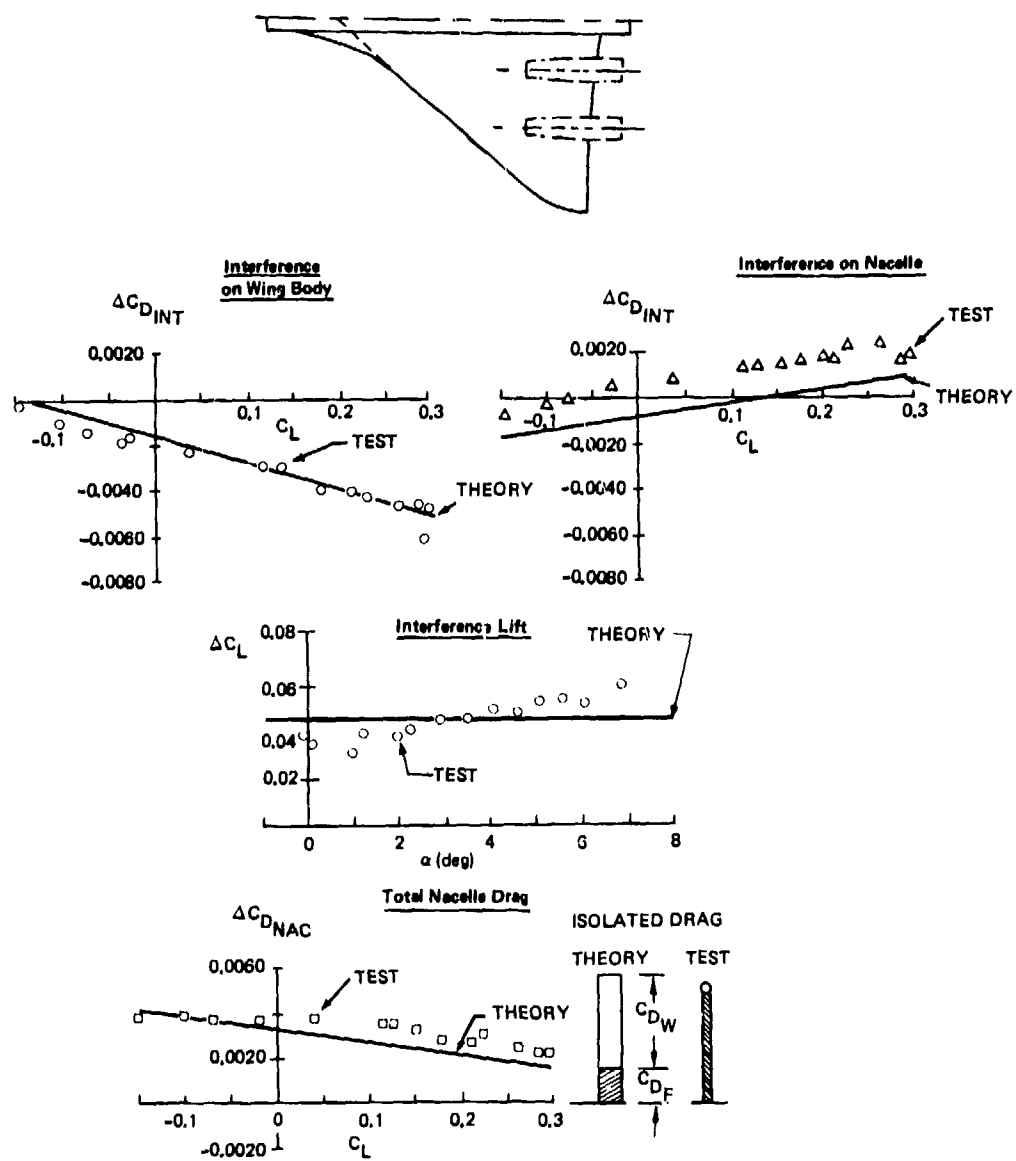


Figure 31. Installed Nacelle Drag for an Aft Nacelle Location at Mach 1.15 and Mass Flow Ratio of Unity

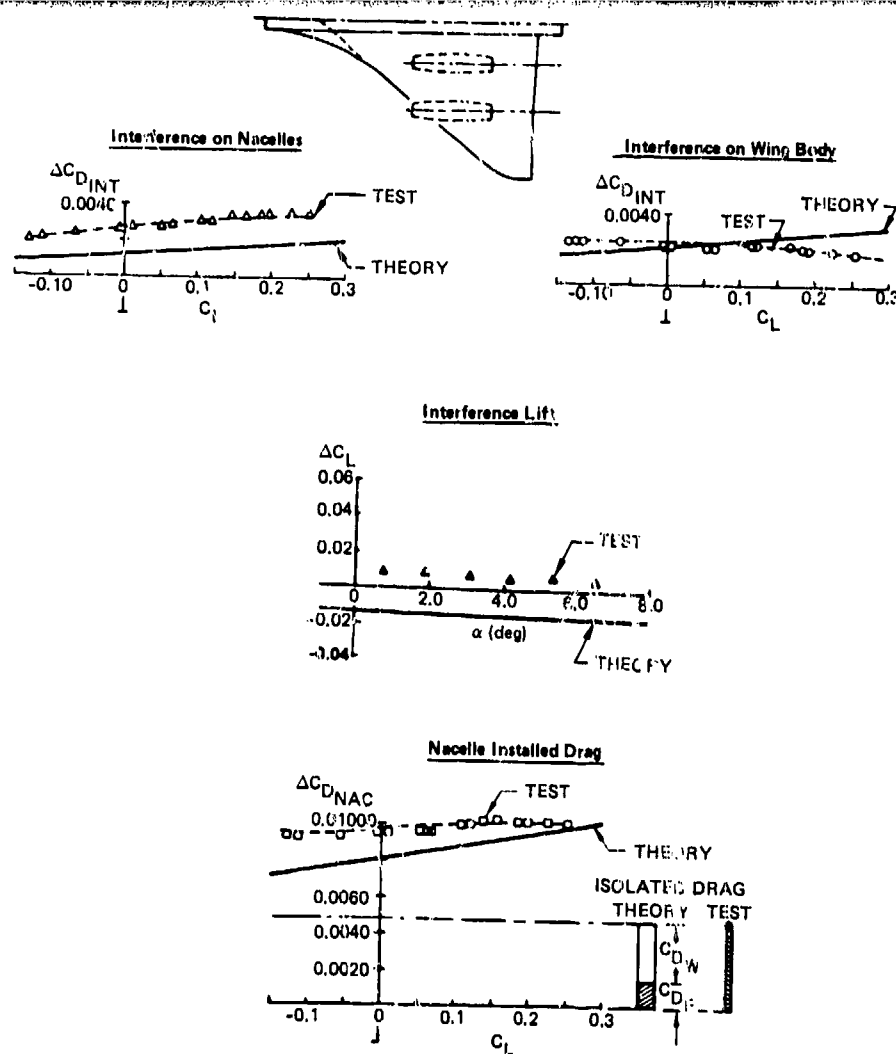


Figure 32. Installed Nacelle Drag for a Forward Nacelle Location at Mach 1.4 and Mass Flow Ratio of Unity

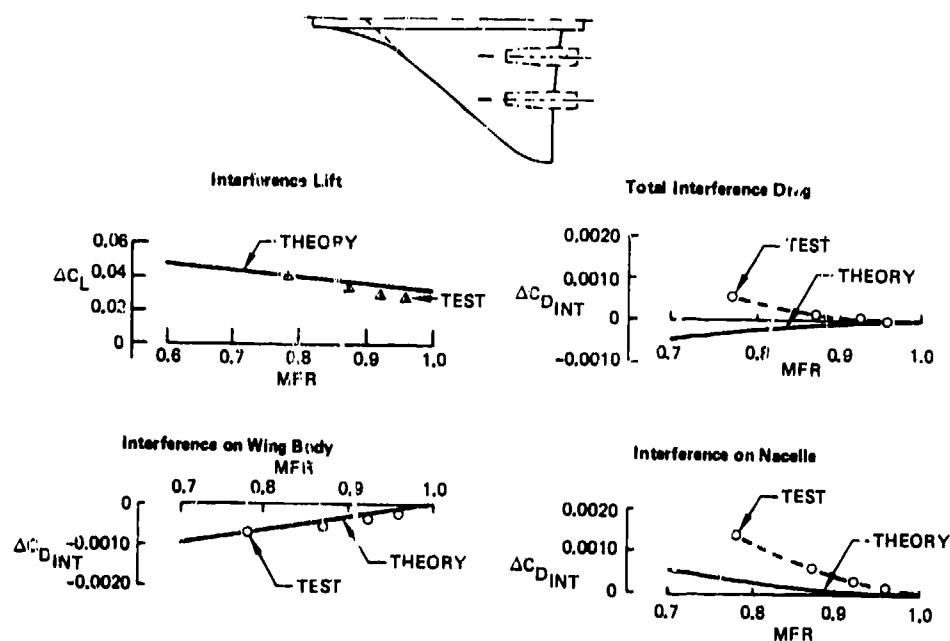


Figure 33. Effect of Normal Shock Spillage on Interference Lift and Drag at Mach 1.4 and Zero Angle of Attack

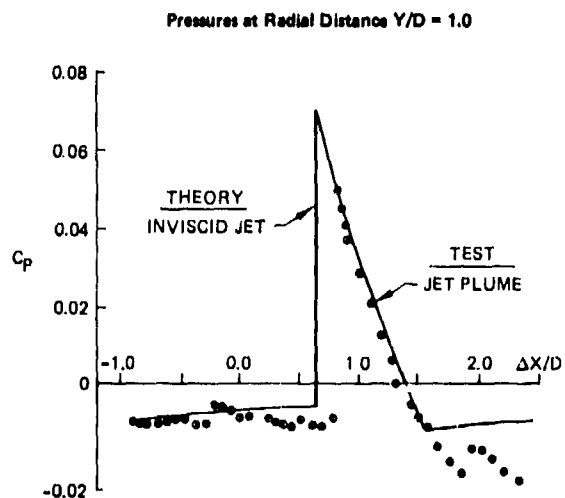
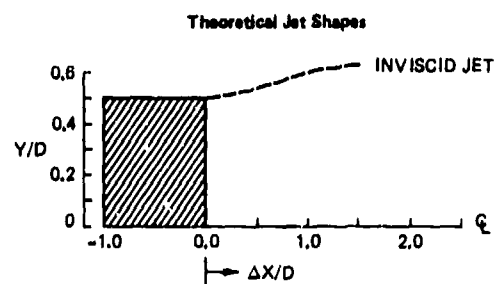
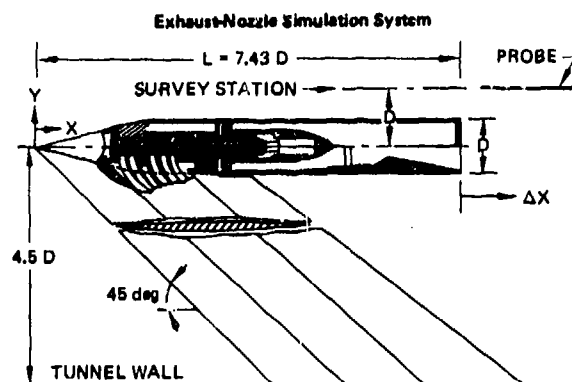


Figure 34. Comparison of Theoretical and Experimental Exhaust Jet Interference Pressures for an Underexpanded Jet ($P_j/P_\infty = 1.093$) at Mach 2.2

REFERENCES

1. Bencze, D. P.; Wind Tunnel Investigation of Nacelle-Airframe Interference at Mach Numbers of 0.90 to 1.4; NASA TMX-62, 489; 1976.
2. Bencze, D. P.; Wind Tunnel Investigation of Nacelle-Airframe Interference at Mach Numbers of 0.9 to 1.4; NASA TMX-73, 149 and 73, 088; 1976.
3. Bencze, D. P.; Experimental Evaluation of Nacelle-Airframe Interference Forces and Pressures at Mach Numbers of 0.9 to 1.4; NASA TMX-3321; March 1977.
4. Carmichael, R. L. and Woodward, F. A.; An Integrated Approach to the Analysis and Design of Wings and Wing-Body Combinations in Supersonic Flow; NASA TN D-3685, October 1966.
5. Woodward, F. A., Tinoco, E. N., and Larsen, J. W., Analysis and Design of Supersonic Wing-Body Combination, Including Flow Properties in the New Field; Part 1—Theory and Applications; NASA 31 CR-73106; 1967.
6. Tinoco, E. N., Johnson, F. T., and Freeman, L. M.; Application of a Higher Order Panel Method to Realistic Supersonic Configurations; AIAA Paper 79-0274; Journal of Aircraft, Vol. 17, No. 1, January 1980, pp. 38-44.
7. Middleton, W. D. and Lundry, J. L.; A System for Aerodynamic Design and Analysis of Supersonic Aircraft:
Part 1—General Description and Theoretical Development; NASA CR-3351
Part 2—User's Manual; NASA CR-3352
Part 3—Computer Program Description; NASA CR-3353
Part 4—Test Cases; NASA CR-3354, September 1980.
8. Peery, K. M. and Forester, C. K.; Numerical Simulation of Multi-Stream Nozzle Flows; AIAA Paper No. 79-1549; July 1979.
9. Kulfan, R. M. and Sigalla, A.; Real Flow Limitations in Supersonic Airplane Design; Journal of Aircraft, Vol. 16, No. 10, pp. 645-658; October 1979.
10. Kulfan, R. M. and Blissell, W. A.; Analysis of Nacelle Transonic Interference Test Data, Section 4.0 of Advanced Concept Studies for Supersonic Vehicles; NASA CR-159244; May 1980.
11. Kulfan, R. M.; Final Report—Advanced Concept Studies for Supersonic Vehicles, Section 4.0; NASA CR—; April 1981.
12. Olstad, W. B.; Transonic-Wind-Tunnel Investigation of the Effects of Lip Bluntness and Shape on the Drag and Pressure Recovery of a Normal-Shock Nose Inlet in a Body of Revolution; NACA RM L56C28; July 1956.
13. Putnam, W. E. and Capone, F. J.; Experimental Determination of Equivalent Solid Bodies to Represent Jets Exhausting into a Mach 2.20 External Stream; NASA TN D-5553; December 1969.

ACKNOWLEDGMENT

This paper is based on work conducted for the Langley Research Center under NASA contract NAS1-14623 and also on work conducted for the Boeing Independent Research and Development program. The authors wish to thank Daniel P. Bencze for providing the data, model definitions, and photographs from the tests he conducted at NASA-Ames Research Center. The authors also wish to thank K. M. Peery, C. E. McFarland, L. J. Runyon, and W. D. Middleton for their efforts in providing the theoretical analyses and for many fruitful discussions.

ROUND TABLE DISCUSSION

DR. GREEN

I hope that our constitutions have withstood the excellent hospitality that we have received from our French hosts and that we still have some reserves of energy left for this final discussion. I believe that this has been a good meeting so far, and I hope the material presented will stimulate a lively and informative Round Table Discussion this afternoon. What I would like to do is use the time available between now and when we leave to review the field as a whole, rather than specifically to review the work that was presented at this meeting. We have amongst us a good proportion of the people in the West who know most about the problems that have been under discussion this week. This gathering of so many eminent propulsion aerodynamics specialists gives us an opportunity today to take stock of the state of our understanding, the weaknesses, the points of contention, and from this discussion to chart some course for the future - to identify the important and most difficult problems now facing us. Part of our discussion will, of course, make reference to the papers that have been presented at this meeting. Those papers, after all, present a number of high points on the terrain, indicating where we stand in the development of particular aspects of the technology. However, I want this Round Table Discussion to focus primarily on the field, rather than specifically on what has been presented at this meeting.

I am going to ask four people with specialist knowledge of the topics that were covered in the four sessions each to review the topic in about 5 minutes. Dr. Richey of the Air Force Wright Aeronautical Laboratories USA will talk to the subject of intakes for military aircraft; Mr. Grieb of Motoren-und Turbinen-Union Germany will talk to the back-end problem: nozzles and afterbodies; Mr. Carter of the Aeronautical Research Association England will discuss the problem of techniques for both civil and military powerplant simulation; and M. Leynaert of ONERA France will review the field of transport aircraft. After that, I would like to open the discussion to the floor and to discuss each of these topics in turn.

What I hope we can do for each of these fields is to achieve some sort of agreement on where we now stand. I am relying on the four specialists to make some statement of our present state of knowledge, and I am relying on people in the audience to disagree with those statements if they think they are incorrect. Silence will be taken as acceptance and the opinions of the specialists will then stand in the written record as the authoritative view of where we now are. I hope this meeting will, in the discussion time, enable us to give the statements of our four speakers the seal of approval or to challenge them and to bring into the open any important areas of disagreement. I would like to ask Dr. Richey to begin. He will talk on the subject of intakes for combat aircraft.

DR. RICHEY

I will give you some of my views on the current state of the art of inlet-airframe integration. (Fig. 1) If we look at the 1970's - a mid-point in that period was the AGARD meeting on Propulsion Installation Effects in Rome in 1974 - you might view that the current state of the art for combat aircraft intakes is that our developments are windtunnel based for the most part. We then flight test to verify the performance and inlet-engine compatibility and do some problem solving in flight. Some good examples have been presented at this meeting, including the work on the Tornado. There is a clear recognition that measuring and assessing instantaneous flow distortion is a correct approach to addressing inlet engine compatibility. This is in view of the fact that the flow out the compressor face flow is unsteady and that an instantaneous distortion index is required. We have seen theoretical analysis techniques emerging, but, as of now, for combat aircraft intakes on supersonic aircraft which tend to be highly manoeuvrable, these theoretical techniques are not strongly used in the design and evaluation of the integrated inlet airframe system.

If we look into the aircraft which could be operational in the 1990's (Fig. 2), we might do a bit of crystal-ball gazing on some of the potential intake design drivers, those characteristics of future aircraft which could have a significant impact on the design of the air intake. There is a potential need for more sustained supersonic capability. Our aircraft today are capable of reaching Mach 2 and above, but not for very long. Fuel usage is high, the drag is high and there is not much sustained supersonic capability in a combat aircraft. There could be more emphasis on this direction, as our uses for combat aircraft change in the future, however, we do not see that we will want to give up any requirements for agility and manoeuvrability that we now have. In fact, there may be more, as the threats become more severe, both ground-based and air-based. Runway denial is a possibility in the future which could lead to requirements for short take off and landing. For the air intake this may require a compatibility with STOL configuration arrangements in terms of reducing or eliminating foreign object damage, being compatible with thrust reversers and their hot gas re-ingestion, and other areas which apply to STOL. Combat aircraft have to carry weapons to the target and thus the aircraft designer has to integrate the aircraft with those weapons. If certain delivery modes are used such as fuselage pointing, aiming, and quick weapons delivery manoeuvres, this could have an impact on aircraft intake design. The final intake design driver is associated with reduced detectability, which could be very important in future aircraft designs. There will be a strong need to reduce the detectability, thereby improving survivability in combat situations. This is certainly an opportunity for unique intake designs and unique inlet-airframe configurations.

From these crystal ball images of potential future drivers - I will not tell you that those will be the only drivers, because they are only based on our view at the present time and the requirements can change very rapidly - we can perhaps derive some new unique opportunities in aircraft intake design. A few of my thoughts are as follows: (Fig. 3) First of all, I believe there is a tremendous potential for computer and theoretically based intake designs to be applied to combat (military) aircraft, using some of the techniques we have seen this afternoon for transport aircraft. I am very encouraged about these theoretical developments for transport aircraft, which M. Leynaert will cover later. I think we need to emphasize the application of advanced computational techniques to combat aircraft, which are more manoeuvrable and operate over a wider range of conditions. I think that there has been some reluctance to use the computer analysis methods in that environment.

As I mentioned earlier, there is perhaps a need and opportunity for extensions to higher supersonic cruise and manoeuvre, more sustained supersonic capability than we now have in combat aircraft. Integration of the inlet and propulsion system with advanced weapons is an area of both concern and opportunity. Perhaps there could be integration of the control system of the inlet or air intake with the control of the vehicle or with the weapon itself. We can look at many unique configurations, and I am sure that there are many inventive people here in this room and amongst your colleagues, who with the requirements set before them, can come up with many unique configurations for more efficiency and wider range of operation.

I will finish up by reminding us of a couple of configurations that we saw on the first day in the paper presented by Mr. Surber. He showed examples of high aspect ratio inlet designs, top mounted inlets and concepts closely integrated with the fuselage. The flow fields of these combat aircraft intakes are interesting to say the least, and these intakes will require a high degree of integration between the propulsion system and the airframe to make them perform effectively and efficiently. In the paper by Mr. Williams there was a good discussion of the very difficult flowfield associated with a top-mounted inlet and the integration with the leading edge extension and wing configurations. If there are benefits to the total aircraft system of these types of inlets, then it is quite a challenge and indeed an opportunity for inlet designers.

DR. GREEN

Thank you very much Dr. Richey. May I now ask Mr. Grieb to review the field of afterbodies and nozzles.

DR. GRIEB

First I would like to make some comments on nozzles. As described in (Fig. 4), the present situation is marked by the application of convergent and convergent/divergent nozzles with various individual designs and subsequent control schemes. So far, the extent of variability of exit and throat areas seems to be rather limited. Evidently, there is a significant trend towards convergent/divergent nozzles. The combination of nozzle and thrust reverser is presently practised in one case on the basis of a very simple convergent short-flap nozzle and a target thrust reverser being also the simplest concept. At least with faired long-flap nozzles favorably shaped afterbodies can be configured.

In my mind, for all nozzles with or without base area, the afterbody drag problem seems to be caused mainly by the normally complicated afterbody configuration of twin-engined aircraft, taking into account also the influences of vertical and horizontal tails, of weapons stations at the fuselage ahead, and last but not least the influence of angles of attack and yaw on the fuselage boundary layer approaching.

Concerning future requirements as well as design and performance aims, considerable attention is being paid to nozzles with thrust vectoring and thrust reverse with respect to manoeuvrability and STOL (Fig. 5). Here the 2-D nozzle concept at first sight seems to be a better starting point than the axisymmetric nozzle as long as the thrust vectoring is limited to the vertical direction. In comparison, axisymmetric nozzles of any design probably form the only base for thrust vectoring in both directions. This might be very attractive in view of super-maneuvrability of the aircraft. However, the combination of sophisticated axisymmetric nozzles with thrust vectoring and thrust reverse will be a very difficult task, all the more since in this case, the simple target thrust reverser would probably not be feasible. All these multi-purpose nozzle concepts will give rise to more or less considerable extra weight and complexity, and I would suggest that aircraft designers should not dream too much of these concepts in view of the effectiveness and the life-cycle cost of the aircraft.

Now some comments on afterbodies. First I should say that I am not an expert in the afterbody aerodynamics and development problems encountered. The experts are sitting in the audience. But, I may be allowed to make some simple comments from an engine designer's point of view (Fig. 6). In my opinion, it is obvious that the design and optimization of afterbodies, at least of twin-engined aircraft, suffers from the fact that flow prediction methods are not yet sufficiently developed, the results gained by wind tunnel testing are often misleading and flight testing does not allow straight identification of afterbody drag. The physical reasons for this rather poor situation are listed here and form a challenge for further theoretical and experimental research on afterbody aerodynamics.

(Fig. 7) Concerning the future situation I realize, on the one hand, that more stringent aircraft requirements as well as advanced nozzle concepts will give great impetus to future R and D work on afterbody aerodynamics. On the other hand, it seems to me that compared with the influence of other aerodynamic and geometric parameters, the choice of a specific nozzle concept is by far not the only decisive contribution to an efficient afterbody.

DR. GREEN

Thank you very much Dr. Grieb. May I now ask Mr. Carter to review the field of techniques.

MR. CARTER

I hope that they get the right viewgraph up this time. I came with a prepared viewgraph because I knew that if it was written in my own fair hand, you wouldn't be able to read it and neither would I. I am sorry if it looks rather long and rather fussy, but I will go through the points, skipping fairly vigorously through them, and then we can come back at a later stage. I also wasn't aware of the fact that these will be kept and used as future evidence against us. I am sure that probably most of us would like to grab our viewgraphs and take them away again.

I have just got two viewgraphs here, the first one is a military one (Fig. 8). I have broken it down on the Chairman's suggestion into what I saw as the present state of the art. This was before this meeting. In general my view was that the scene on the whole is quite promising, but to a large extent we still deal with the military aspect on a rather piecemeal approach. Piecemeal insofar as we test front ends, we test back ends and we find it difficult to test the whole of them together. The piecemeal approach is fairly well documented and handled at the moment. Inlet internal performance, interface methods and dynamic distortion techniques are quite well established now. Inlet spill drag on military configurations is now also apparently well-established by using distorted rear end models with the correct relevant front end portions. These can be done either by momentum traverse or more normally by force measurement for military aircraft. Afterbody performance measurements are currently in hand but in the presence of cold air. Accurate results are difficult to obtain, and I agree entirely with Dr. Grieb that this is a particular area where significant developments can be made.

Through-flow complete models, that we call the aero-force model measurements are well established. On the whole however, I think that we all still find that the process of internal flow calibration is very tedious and very time consuming, very expensive and often somewhat inaccurate. Combining inlets with inlet and exhaust simultaneously represented should be our objectives. Representation of inlets or TPS is beginning to be established, but I would say only-just beginning would be the better emphasis here. The simultaneous representation of inlet and exhaust flows is particularly difficult at present for multi-nozzle or the vectored Pegasus type configurations. So basically, the question is still to be answered, is it really necessary that inlet and exhaust should be simultaneously represented? Future developments on the military side I would see as being (and I am jumping to the bottom of my list for one of the items here) a study of inlet/exhaust mutual interference to demonstrate the need or otherwise of their simultaneous representation. I think that we all feel in our bones, that front ends and back ends, for close coupled configurations must be represented simultaneously but there is no really concrete evidence that has been produced on this that I am aware of. This will be thrown open to the forum.

To summarize the areas of future development then, on the assumption that mutual interference is important, one of our current foremost needs is for a military simulator to provide representative nozzle pressure ratios and inlet flows. If we can have such simulators, will these accept the typical type of engine face distortions which we are going to throw at them? Just as engines dislike distortions, I am quite sure that some of the simulators will dislike them even more, and particularly at high incidence. Equally well, will we be able to calibrate such simulators? I will emphasize here, as a personal view, the need for a short simulator for VTOL Pegasus type installations, where the space in between inlet and exhaust makes it almost an absolute necessity that both should be simultaneously represented, but there is virtually no space in which to do this representation.

Afterbody performance techniques need development, they are currently an extremely difficult technical and practical procedure. There is also development needed, of associated model support systems to produce minimum interference for afterbody work.

This second viewgraph of the civil scene (Fig. 9) is, I am afraid, rather long. I hope that you can just about get it on the screen. On the broad side, viewing the present state of the art, again I would say that in general the position is good. There has been a wide acceptance of the need for high accuracy and correct simultaneous simulation of both inlet and exhaust flows. Relatively, I would think that the state of the art for the civil field is probably more advanced than that of the military, but then the range of the problems is less. Techniques for the internal performance of inlets are now well established, spill drag measurements are fairly well developed both by momentum traverse methods and force methods. Single and twin stream exhaust performance measurements are now readily available on static rigs and external flow rigs. Hot core representation is also provided in certain areas. For complete and half models simultaneous inlet and exhaust flows with TPS are established as are direct twin stream exhaust blow methods, all of which we have heard quite a lot about this past week. The use of ejectors is still developing, just as the arguments for and against ejectors are developing. This work, I would say, with TPS and other simulators, is essentially confined to large wind tunnels, current TPS sizes are dictating model scales and in some cases, are dictating that one must use half models, not because you necessarily want to use a half model, but because the smallest available TPS or other types of simulators really dictate the scale of the model and puts you into a half model situation. The calibration of simulators is developing, and is probably the item which is currently defining the present accuracy limits of testing with simulators.

Summarizing the current limitations, model performance techniques being developed for half and full models are expensive and somewhat inflexible. There is no adequate digested information at present to demonstrate the consistency and repeatability of simulators. I have said that to provoke a little. Simulators are used a lot and calibrated a lot. We get slightly random answers from these. We don't necessarily know whether it is our calibration technique or whether it is the simulator which has got a character of its own which changes daily. Present performance measurements on inlets are invariably isolated. Representation of the curved flow environment of the inlet flow is a subject which worries people. Should we be studying the performance of inlets whilst in the presence of the wing flow, or is it sufficient to do them as isolated items? Present performance measurements on exhaust nozzles are usually isolated but should be made in the presence of the wing. This is possible for discharge coefficient measurements but is very difficult for thrust measurements where interchange of buoyancy forces makes it very difficult to differentiate between drag and force.

Future developments: obviously, there is need for consolidation of the current techniques particularly with TPS and other simulators. Examination of data from simple through-flow representations in comparison with exhaust simulators is needed to optimize the through-flow. We still have a long way to go in defining what are the optimum through flow types of nacelle representation. Calibration of the half model vs the full model techniques and possible tunnel interference with exhaust flows is a subject which is causing some concern. Does the presence of the exhaust flow change the tunnel interference parameters, and in particular, the buoyancy in the tunnel? A metric fuselage and afterbody is an extremely good way of integrating buoyancy forces in a windtunnel and giving the wrong answers.

Development of model support systems for the three engine and rear engine configurations are needed. Forward blade support interference needs development as I feel we are going to have to live with forward supports in the near future. How can these be used without interfering with the answers significantly? Also there is virtually no information on Reynolds number effects on installation performance and again, we would like feedback from the audience on this subject as much of the work discussed at this meeting has been at relatively low Reynolds number for the current civil transports.

In pursuit of that particular item, consideration must be given at this stage to engine representation in cryogenic facilities for Reynolds number effects. I do not anticipate that TPS will be useable here, but maybe the ejector or the blown nozzle will come into its own and will have the advantage that perhaps correct temperature ratio representation will be available by the simple use of normal ambient air in the blowing system against the cryogenic external flow on the models.

Finally, I had a point, which has been answered by Bob Welge very adequately this afternoon, that propellers before they become a reality, and they are becoming a reality, should have the main principles of mutual propeller and wing interference considered along with the special bookkeeping of that work.

DR. GREEN

Thank you Mr. Carter. And now may I ask M. Leynaert for his remarks on the subject of engine installations on transport aircraft.

M. LEYNAERT

The subject of the session IV was the "Installation Aerodynamics of Transport Aircraft". Considering this subject in a broad sense is equivalent to asking "What is the best aircraft solution?" So as not to disagree with everyone, I will answer that all the configurations are "the best one", and go to the next question which is asked by the aircraft manufacturer at a certain definition stage of the aircraft: How to minimize the installation drag?

This question assumes that an ideal wing in clean configuration without any engine has been defined, and an ideal isolated nacelle has been defined, and that we are impressed by the difference:

$$C_D = \text{integrated (wing + nacelle)} - (\text{ideal wing} + \text{ideal nacelle})$$

This is the way in which the various sorts of results have been presented by various speakers. If the engines are at the rear of the fuselage, the wing is to be replaced by the rear fuselage, or by wing and fuselage as a whole. The solution of the problem is based upon three different elements:

- theoretical computations of given configurations. (Inverse solution of optimization conditions does not seem easily conceivable). These calculations have to be carried out either according to the design or off-design conditions.
- wind tunnel testing.
- available aerodynamic test results, among which the importance (not to say the weight...) of AGARD publications should be emphasized; and you have been presented with a great number of them during these sessions.

All these experimental results make it possible to define a first configuration and to give a guideline to computation and testing. The questions concerning these elements can be summarized as follows:

- Theoretical computation problems

Some computations using transonic potential theory do exist at the present time. This is where the greatest progress has been achieved since the last AGARD meeting on this topic. These computations can be applied either to the complete aircraft, or to a detailed analysis of the local flow in the neighborhood of the nacelle. The problem of under-ashing or coupling techniques of the two types of study is, however, where there is still progress to be achieved.

These computations do not include the computation of the two jets of the engine. Some methods have been presented in subsonic flow, but the problem is still to be solved in transonic flow.

The coupling with viscous effects has to be developed and worked upon. The calculation of the viscous effects themselves also needs to make headway. I will simply mention some points which are important in the calculation of a nacelle at incidence:

- . three-dimensional transition of the boundary layer by a laminar separation bubble.
- . three-dimensional shock-boundary layer interaction.
- . separated areas.
- . shear layer of the jet boundary, and coupling with the potential computations.
- Experimental results.
 - . they can be presented for isolated nacelle first, for a definition of inlet or exhaust. Then, what is of interest is the results for either overall performance or very detailed studies of the flow characteristics.
 - . in parallel to the isolated nacelle, there are some results dealing with the installation itself; either optimization results of overall configurations, or local improvement type of results.

As Mr. Carter said, there are already many results available in this particular area, but there are never enough. The technique moves ahead all the time, and we project new specific aircraft configurations with CCV and variable camber of the wing; we talked for instance about prop fans. These projects present some specific aspects which will have to be studied in depth.

To conclude, these overall questions being presented, I hope that certain participants will give their point of view in particular of the key problem of priority. In opposition to what Dr. Green said, I am not really a specialist on all these questions. I have simply had the opportunity to study some particular aspects of certain points, and it will be up to the ladies and gentlemen to really tackle the problem and come to grips with it.

DR. GREEN

Thank you M. Leynaert, and I think here we should acknowledge the efforts of all four speakers. Between them, they have compiled, in effect, a very useful review paper which will appear, including the viewgraphs, in the transcript of this Round Table Discussion that will be printed in the Conference Proceedings.

Now the discussion is open to the floor, and I should like to go through the four areas covered by our speakers one at a time and test with you the points that have been made, starting with Dr. Richey's review of combat aircraft intakes. It seems to me there are two issues of driving importance in the development of combat aircraft intakes - one is performance and the other is the problem of engine/intake compatibility. I took Keith to say that he thinks our understanding of the compatibility problem is acceptable, that we have adequate criteria to tell when our intake is operating satisfactorily, and the problem is really to extend the range of flight conditions over which satisfactory operation is maintained. Is that a view that is accepted around the hall?

DR. COLBOURNE

This problem of compatibility is the one that I wanted to comment upon. We have heard from several authors, myself included, discussion of intake engine compatibility. In particular, the various, ever more sophisticated methods for collecting and processing dynamic pressure distortion data. In addition, we have now had reference to swirl measurements and the suggestion that a representative index could or should be defined (Paper 10). Furthermore, outside this room, there has been the not entirely serious, but perhaps (from past experience), increasingly inevitable call for time-variant swirl measurements. The calculation of these coefficients and their correlation with engine instabilities, I would suggest are engineering approaches to the problem of compatibility, and I would just like to make a plea for a more scientific approach. We should investigate in more detail the physics of the inlet flow interactions with the rotating turbomachinery, and hence understand what fundamental properties really need to be quantified.

DR. GREEN

Could I ask what is in your mind when you say a more scientific approach? Those are fine words, and I use them frequently, but I have to admit that sometimes I don't have a very focussed idea of what line a more scientific approach might follow.

DR. COLBOURNE

This is possibly a plea more to the turbomachinery aerodynamicist rather than the installation aerodynamicist, but he is the one who should, if he hasn't already (and I don't believe he has), gain a better knowledge of exactly how the flows interact.

DR. GREEN

Do you envisage this as a theoretical approach by the turbomachinery man or do you think that he can tackle the problem empirically?

DR. COLBOURNE

I think, first of all anyway, that he has got to attack it empirically, but with due regard to the fundamental effects of variations in the velocities relative to the rotating blades rather than the overall compressor effects.

MR. MOTYCKA

I am glad that you asked the question, because my comment goes just the other way; that is, that I think we must realize that no matter how we deal with inlet/engine compatibility, the odds are very great that the engine will pay a penalty for being supplied with turbulent and distorted air. I would plea for some improvements in inlet technology so that the distortion is reduced or eliminated, particularly during some of these wild manoeuvres that we are looking at in the future aircraft.

DR. GREEN

Could I ask you, as an engine man, a further question on this point? The overall aircraft design problem is surely one of integrating the engine with the intake. The intake man would like to throw you dirty air and have you sort it out in the engine, and you would like perfection from him. What we have to do is strike a balance between the two. Do you have any feel at the moment for how much potential performance is being thrown away when we make this design compromise because of our uncertainties about the compatibility criteria?

MR. MODYKA

There probably is room for improvement in the intake design and comparable improvement in the process of designing the compressor with less conservatism; however, I am not a compressor expert. I do know that the compressor designers have made great improvements in their ability to analyze the effect of distortion on the compressor and that this is also an emerging art. I would like to bring out one thing that we have discovered in the commercial business. Commercial inlets are relatively short, and when you have a separated inlet such as you might have with a high cross wind, or a very high angle of attack, there is very definitely an interaction between the inlet and the fan in this separated wake. The fan can tolerate a fair amount of distortion and tends to work to clean it up. With a very short inlet where you have distortion and the fan close-coupled, talking to each other so to speak, you can take advantage of that favorable interaction. I think that in the military world that advantage should also be explored.

DR. GREEN

That is an interesting point.

MR. GOLDSMITH

Continuing the theme of dynamic distortion measurements - although on the one hand we have heard in Mr. Borg's paper the result of considerable simplification of these type of measurements by using synthesis techniques, we have on the other hand heard from M. Perrier and his ONERA colleagues giving us the results of experience at Dassault which appears on the surface to contradict all the American experience on this subject. Thus M. Perrier is saying, as I understand it, that even with 64 Kulite probes collecting 7 million bits of information in 30 secs of testing, there is still no correlation between any of the peak instantaneous distortion values and the incidence of engine 'coughing'. This is in contrast to the American experience where peak instantaneous distortion measurements based on 40 or 48 probes correlated with engine surging on 90 or 95 % of occasions. Are we back to not understanding this phenomenon or is this French experience an isolated instance?

DR. GREEN

In his review of the subject, Dr. Richey took the view that instantaneous distortion was a satisfactory criterion. That is essentially the American experience, as I understand it: I would like to know the view of the specialists in France. How do they regard the differences between the American experience and their own. I do not see M. Perrier in the room: is there anyone else from France who would like to take up this question?

MR. PERRIER

I would like to make the two following statements:

First: You cannot completely rely on one overall unsteady criteria based on 48 dynamic pressure because the extreme unsteady value can be quite different and at different times and for different flow conditions. One of the main acquisition we obtain of theoretical Navier Stokes direct simulation is that the flow is not well characterized by such approach if you are interested in low level of distortion on long ducts.

Second: When you try to reach better overall performances as Mr. Modycka of P.W. explained and SNECMA and AMD-BA are trying to do, you are to be very cautious on the detail of the unsteady flow and made provision for approximate measurement of unsteady longitudinal vorticity (swirling flow) and transverse vorticity (rolling flows) and mean turbulence.

If you don't make that detailed analysis and choose some simplified unique unsteady distortion index, you will be very disappointed by the correlations for the low level of distortion we consider as a target for the future. But anyway, the past is well established by the U.S. work on unsteady high distortion levels.

M. LEYNAERT

I think that the airframe manufacturer, when turning to test people, will always paint the situation very black, so they have good reasons to ask them to improve their measurement facilities and testing facilities. But what I remember from reading the American papers, and perhaps it can be confirmed for me by a person who was there, is that the instantaneous distortion coefficients give us the possibility of improving the probability of properly predicting the surge limits for the engine. But it doesn't give an absolute and final reply. It cannot promise that the engine is not going to surge at all in this or that condition. The measurements did not indicate that we have reached the limit for surge. I think that what M. Perrier wanted to underline was perhaps inflight testing. He always finds configurations for which the engine has been surging. Even though all distortion coefficients might indicate that in this or that condition the engine should not have surged. It's a matter of probability and may only happen in 5% of the cases.

DR. RICHEY

I agree with the point of view expressed by M. Leynaert. Our inlet-engine compatibility approach gets us pretty close, but there is a probability that there can still be some compressor surges in flight test. But, in the US, and probably the Dassault paper is in general agreement with this, we have found that if you measure instantaneous distortion from an inlet and then set up the proper conditions and settings to the engine, you can determine the major areas where compressor stall will be expected. Through a careful development program and cooperation between engine and airframe designers, there can be then a low probability of compressor stall within the flight regime. Our experience then is that compressor stalls mostly occur when other things are being done to the engine, such as throttle bursts and chops, manoeuvres which are outside the expected envelope, etc. But generally, if you go back to the pure inlet distortion case that the flight test has verified, there is a low probability of stall.

So I am reasonably confident that we generally understand the process, but it is not an exact science, as has been suggested here, to guarantee the elimination of compressor stall. I believe the point is that instantaneous distortion tracking is the best correlator we now have. It needs to be followed rigorously through a development program and can at least minimize the surprises in flight testing.

MR. GRIEB

I would like to make a comment concerning inlet distortions from an engine designer's point of view. In my mind, as long as there is a clear distortion without swirl and without pressure fluctuations, the behavior of a compressor can be predicted fairly accurately. But the combination of pressure distortions with swirl and with severe pressure fluctuations cannot be predicted correctly, all the more since a great number of parameters would be necessary for correctly describing such a complex distortion.

DR. GREEN

I think that I would like to move the discussion along now and consider another aspect of the combat aircraft intake story that Keith Richey laid emphasis on, which is the importance of investing in theoretical methods, the role that advanced theoretical methods can play. I would like some reaction from the audience on this. How far away in time do we think we are from being able to replace our tunnel testing techniques, which are often compromised by their low Reynolds number, with adequate theoretical methods for this very complex type of flow?

MR. GOLDSMITH

I am not going to answer Dr. Green's question, but I would like to support the need for more computational work on engine installations aerodynamics for military aircraft. On the civil aircraft side we did have some nice examples of the correlation between experimental and calculated pressure distributions on wings in the presence of nacelles and on nacelles adjacent to bodies in the work presented by Laughlin in the UK and by the Fokker team. In the military field, however, there appeared to be the usual mixture of incompressible flow solutions for complex shapes or compressible flow solutions for simple shapes that did not match up well with available experimental data. There is a need for more close cooperation between computational and experimental aerodynamicists so that experimental and computational answers are closely aligned. It is possible to set up experiments with axis-symmetric or near two-dimensional duct flows. Would it be a good idea to have an AGARD conference solely on the theme of closely aligned experimental and calculated investigations so that we could really learn the relative merit of various computational schemes?

DR. GREEN

Even for two-dimensional airfoils, we still have discrepancies between computation and experiment: for three-dimensional combat aircraft intakes, the flow can be much more complex and the likelihood of discrepancy will be correspondingly greater.

DR. ROBERTS

Perhaps the reason that experimental people and theoreticians are not talking is because people like John Green keep asking the question, "when can we replace wind tunnels with theory or with computation?". I really think that it is the wrong question to ask. The cost of either experimental work or computational work, in relation to the design risk you take of not having good information from either source is so small that we really shouldn't be worried about replacing one with the other. The real question, as the last speaker pointed out, is: "how soon can we expect, to see the best use of both, and good comparisons between both, working towards the same ends, i.e., removing the design risk?"

DR. GREEN

My apologies to Dr. Roberts: I will rephrase my question, "how soon will it be before computation takes its place along side wind tunnel testing as a fully mature and reliable tool for intake design and development"? It seems we are not yet ready to answer that question, but the point Dr. Roberts makes is worth emphasizing: the costs of computation and wind tunnel R & D are small compared with the costs of rectifying design faults which are only discovered during flight testing.

Are there any other points that you would like to see discussed on the intake side before we leave it, which we shall do very shortly?

DR. RICHEY

Not really, but the comment on the exploitation of computational techniques for combat aircraft intakes here was expressed to the forum as a need and opportunity. That was the point of continuing to emphasize that area. In the U.S. we have run some Navier Stokes calculations on a three-dimensional supersonic inlet using a very fast Cray computer, that computes the flow field through the supersonic region and through the normal shock in mixed compression inlet in less than 20 minutes time per calculation. With advances in both algorithms and computers, it seems to me that this is a fruitful area for continued research.

DR. GREEN

In view of the time, I would like to move on to two of the other areas. Can we turn now to the back end of the military aircraft but continue with the theme we have just been discussing? Again, this is a field which is open to theoretical attack. Is there hope that computational methods can be developed into reliable design tools in the next few years, or do we again face the problem, that, although we can tackle simple configurations with some conviction, we cannot deal with the more important practical problems noted by Mr. Grieb? I am thinking, for example, of the geometrical and aerodynamic complications associated with twin engine configurations, of the problems which arise when the aircraft is flying at high angles of attack and there is aerodynamic interference from tail surfaces as well as separated flow around the base and ahead of it.

I wonder again what the feeling is on the theoretical side? I am looking for an apologist for the theoretical methods in this field, who can offer us some views on the potential applications of theoretical methods and also give us some views on their limitations. The general silence suggests to me that we believe the back-end problem is going to be addressed experimentally for some time to come.

DR. ROBERTS

I think that the problem is really coming down to the size of the computer and the availability of fast memory. The algorithm development is moving along at a pretty fast pace right now. To handle an aft body, especially in a three-dimensional flow, the length scales involved are quite small and to be able to handle it you have to have a huge computer. So, for probably 10 years we are not going to have a computer available, even Cray won't give you everything you want. As far as the algorithms themselves, I think it is a long way there.

DR. GREEN

So, would we accept that backend tactical combat aircraft designs are going to be a matter primarily of development rather than design? That we don't yet understand the physics well enough to have clear design principles and so will have to rely on past experience and 'cut and try'.

DR. ROBERTS

I think that you really need to carry out the numerical work at a high rate of effort, because the codes themselves don't exist right now. You have to have the codes, the technology is on its way. It takes three to five years to get any type of a code into a production capability, so you can't stop now, you have got to keep progressing.

UNIDENTIFIED

To me it seems that the boundary conditions problem is a big one, in the sense that for any numerical method you need boundary conditions to start the problem and whether at the inlet or at the nozzle, these boundary conditions have to be given by the experiment or you have to compute all the engine numerically which is quite a difficult problem, if not impossible. Most of the boundary conditions are totally missing, you cannot have more than a few points when you need perhaps a thousand points to start the problem.

DR. GREEN

Do we believe that it is really necessary to provide the engine information in great detail in order to handle the front or the back-end design problems? It seems to me, admittedly as a layman in this field, that some of the effects that we cannot begin to calculate at the moment are really quite large and gross, and I would expect the detailed aspects of engine performance to be of second order relative to these large uncertainties in the basic external flow.

PROF. RESHOTKO

You have provoked me into some remarks. I am not necessarily going to answer your last question, but I would like to comment on some of the things that I have heard so far. It was sort of agreed in some of the presentations that the front end can be addressed by computation. Yet there was some concern expressed about the rear end because the Cray computers, even when activated, would take a long time to do a case. I think that we are asking different questions on the front and back ends, and maybe the back end is really more amenable to calculation than the front. On the back we are generally asking steady flow questions. We have not identified unsteady effects there that are troublesome for the moment.

There are separations and shock-interactions, jet plume interactions with the aerodynamic surfaces and the like, but we feel that a steady flow result for that would be adequate. When it comes to the front end, the troublesome questions have to do with distortion, time dependent distortion, things that we are not even beginning to look at computationally. Computationally we are trying to define steady-state design points, and steady-state off-design operation. It is going to be a rather long time before inlet computation will address the question of time dependent distortions and things of that sort which seem to be at the root of many of the operational questions. When it comes to the engine we are really in even worse shape because a clear understanding of engine operating problems does require eventually a three-dimensional time-dependent viscous treatment. The people who are working on engine computations are barely able to handle a half stage, not to speak of a whole compressor, with any kind of reliability. So I think that the front end problems particularly relating to inlet-engine integration are for quite a long while going to be handled through testing and experience and development of compatibility techniques through the use of maps, etc., of the time dependent operation of both the inlet and the compressor.

DR. GREEN

There was one paper which referred specifically to the apparently simple problem of Reynolds number effect on afterbodies. It showed that quite a lot of so-called Reynolds number effects found in previous work arose from misinterpretation of the wind tunnel results. The paper highlighted the difficulty of extrapolating from wind tunnel Reynolds numbers to flight, particularly in cases where the trend with Reynolds number appears to be changing as we approach the upper Reynolds number limit of our tunnels. I wonder what the present feeling is about extrapolating from tunnel to flight. Having identified the misleading factors in earlier work, do we now have an acceptable understanding of Reynolds number effects? Is this an area where we could make more use of computational methods?

Each company makes its extrapolation and crosses its fingers and waits for the next guy to produce a paper which says that these results weren't sound results because of some other effect, I suppose.

MR. BRYERS

Speaking about experience full scale to tunnel on the Tornado, we had made some pressure measurements which showed quite good correlation between tunnel and flight. Afterbody base pressure and surface pressures under a ministry contract. I feel that the need actually is also that we ought to be looking at the turbulent aspects on the afterbody with regard to aft end buffet as well, which is a possible problem on the Tornado. Configurations which had the same drag had quite large differences.

DR. GREEN

Thank you, that was a point that was not very much addressed in this meeting. I am conscious of time slipping by. We have strayed into the area of testing techniques. Could we now turn to the points that were made by Mr. Carter, to consider whether his fairly full statement, which will appear in the record of this discussion, constitutes a fair assessment of where we now stand.

MR. SMYTH

I would like to come to the simulation techniques which Mr. Carter was really asking for military aircraft. Now, turbine powered simulators for military aircraft do exist. They are being developed in the United States and are called compact simulators. The technical problems with these simulators arrive from the fact that you have to fulfill an additional requirement of variable nozzle area. This is additional to what we already have on the civil engines, which means you have to simulate the intake flow, the nozzle flow, and also additionally the variable nozzle area. Now to fulfill these requirements, means that you have to return part of the drive air of the turbine after expansion back to the model and out of the windtunnel through the balance system to fulfill these threefold requirements.

In a way similar to the development of turbine-powered simulators for civil high bypass-ratio engines this more complex technique will come someday, but it is a long way to go to get these things working with sufficient accuracy and repeatability.

But they will be coming in any case because they are necessary. This is the next step in the simulators. If you look at future combat aircraft with high angles of attack in low speed flight and with post-stall operation, then there will be strong coupling effects of partially jet-induced supercirculation around the wing influencing the intake flow. You have to simulate intake and nozzle flow at the same time to get the aerodynamic characteristics right.

DR. GREEN

I think that that is an important point. I don't know whether anyone wishes to take issue with it?

Mr. Carter did make the point that the consistency and repeatability of simulators had not been demonstrated adequately. Given the amount of use that is now being made of simulators, particularly on the civil side, I wonder whether people are very happy to have a statement like that written into the record. The people in industry who have to offer performance guarantees to the airline customers must be working on the assumption that their simulators are reasonably adequate at the moment?

MR. SMYTH

If I might just give a very short piece of information there and say, "yes". We have found a reasonably good correlation between low-speed flight test of a transport type of aircraft with model test results, where changes in the nacelle/pylon/wing configuration have produced the same tendencies and magnitudes using turbine simulators. So we have seen that you can get good results. I would like to answer that question that yes, in certain cases adequate, but further work will have to be done. This is the reason for saying: yes, turbine powered simulators have shown to be adequate in these cases. No doubt further work must be done to improve measurement techniques and accuracy.

DR. GREEN

But there is a difference between obtaining good results in one particular case and being confident that your results will always be good. I wonder what Mr. Carter intended when he sowed these doubts in our minds?

MR. CARTER

I think primarily I had in mind that our evidence at the moment are bits of information like that Mr. Smyth has given us. We have a confident feeling, and I think that we wouldn't be in the business at all if we didn't believe in this work that we are doing. The tendency unfortunately has to be that, with the orders of accuracy that we are looking for, the results that you produce for final flight curves from tunnel data for the calibrations in particular, tend to be based on a statistical approach to the work.

With the TPS unit, I defy anyone to go to calibration or test and believe answers based on one or two data points. We all know that there are so many factors, maybe 30 or 40 items which all contribute to the answers which may differ slightly from day to day. You find that you have to go through an almost impossible process to analyze which is the particular faulty item in your measurements, and I am really thinking of calibration in particular here. So, Mr. Smyth and I are thinking very much alike on this. I am quite sure that he wouldn't cross his heart and say that he would believe any one particular result in a test run. He will use the same essentially statistical approach as I feel is necessary. It is simply that it worries me a little that we have made good use of the TPS's, we have made them a working tool and we do believe the answers like Mr. Smyth, but faith is not enough.

No one still, to my mind, has actually demonstrated that some of the discrepancies we may get from point to point in our statistical analysis is due to our calibration technique, as distinct from, does the TPS behave in precisely the same manner from one run to the next run. I was really trying to be provocative rather than going down into posterity in this question - and it was a question, not a statement.

MR. MODYKA

I think that Mr. Carter is well aware that when you use a TPS to do model tests in the wind tunnel, that the force that you are measuring is very close to zero. When you are trying to find a small percentage of a net thrust (which for a half model in 1/20 scale range, is about 50 pounds) and you have a balance that has the capability of measuring 1000 pounds, that trying to get a good reliable number close to zero is very difficult. Perhaps we need some sort of variable capability balance that gets more accurate as it gets close to zero. It is both the balance and the performance of the TPS that must be considered. Besides that, with the higher cost of fuel, the required accuracies are getting smaller and smaller.

DR. HOLDHUSEN

As regards accuracy of TPS calibration, we have a new facility which does not depend upon faired curves as does the facility that Mr. Carter has. We can set any feasible combination of rpm and fan flow independently. Moreover, we can statistically demonstrate repeatability by this method. As regards longterm stability, we ran a program for Mr. Motycka during November through January. At five week intervals, we repeated the basic build three times and came much closer than 1/10th percent to the same average performance curve. The standard error of estimate of all three runs was 0.00079, and we think that, as I mentioned in my talk, this represents a propagation of uncertainty of full-scale performance of one and one-half drag counts if six or eight repeat tests can be afforded. Most of that error is bias error and not scatter error.

DR. GREEN

That is useful information and is the kind of statement I was trying to provoke.

MR. STEPHENSON

I think that in talking about the requirements of flow simulation, we shouldn't lose sight of why we want the flow simulation. There may well be quite different requirements for flow simulation for the civil man to that for the military man. As a civil man I am looking for a good thrust/drag balance and a high accuracy in the drag direction. The military man, as I understand it, is primarily looking for flow simulation over a very broad flight envelope to assess the influence that the intake/exhaust effects can have on the stability and control aspects. My understanding is that he is reasonably happy with the standard of drag accuracy that he is getting from conventional blown nozzle and intake suction techniques and that it is the S & C requirement which demands simultaneous flow representation. For this case it may well be that the TPS approach, adopted for good accuracy by the civil man, may not be the best route for military engine flow simulation.

MR. CARTER

Yes, I think that that is right. When I addressed my doubts, it was related entirely to the civil application as far as accuracy is concerned. The military TPS - I was well aware of the CMAPS work that has been going on. What I have read on that subject tends to frighten me somewhat more in a way. In that application it wasn't only accuracy which was their particular problem, but the actual size of the unit. I am sorry that I am slightly digressing from the point that you have made, but the military application that concerns us is whether it is necessary to represent inlets and exits at the same time. If the answer is yes, then probably, without an available CMAPS, we are going to be forced into the ejector-type arrangement, if anything for this very short, close-coupled inlet and exit work. I don't think that accuracy will be the major feature of designing military TPS, it will be compactness and pressure ratio which will be the major difficulty.

DR. GREEN

I have a question concerning accuracy not of measurement but of our accounting methods. There was some debate in an earlier session about the pressures used for reference and about the definitions used in thrust and drag accounting. I should like to ask Mr. Carter and the audience whether, in this area of powerplant installation, they believe our methods for distinguishing between the forces attributed to the engine and those attributed to the airframe are soundly based.

MR. TIPPER

I'm reporting on Edwardes' view in this respect. He had a long debate with Mr. Harris after Mr. Harris and Mr. Pugh had read their papers. Mr. Edwardes is very concerned about the sensitivity to bookkeeping detail of performance predictions for powerplant changes. Mr. Harris' viewpoint appears to be that he has set up a process through which accurate predictions of full scale thrust minus drag can be made and which avoids various bookkeeping problems. I think that what has not been achieved is the ability to evaluate the consequence of changing the engine or nozzle type except through the kind of carefully constructed test program that Mr. Harris described, but for which there is often neither time nor money. I think that this summarizes Mr. Edwardes' problem which I see as a real one.

Questions by Mr. Edwards
Powerplant Installation Performance and Thrust
Drag Accounting Problems

1.0 INTRODUCTION

In any engine installation there is a need to relate the installed engine performance to the acceptance test performance and possible to a further referee configuration performance.

Whereas the compressor bleed and shaft power offtake effects are well known for turbo-jet and turbo-fan engines, the aerodynamics of the engine as installed on the aircraft compared with the aerodynamics of the test cell installation are not well known. We see a need to define and measure the relevant aerodynamic effects in a manner that will give the most meaningful thrust-drag accounting. We believe the problems we have encountered or are anticipating in doing this are common to many aircraft. I am therefore submitting this note for consideration by the Fluid Dynamics Panel as subject matter for future meetings. At the same time this note provides a better explanation of the thrust-drag accounting method which I attempted to compare with that used by Mr. A.E. Harris and Mr. G. Pugh following their presentations. I would therefore appreciate it if the question "How would you compare your thrust drag accounting method to that proposed in this note?" be entered as a written question to Messrs Harris, Pugh and Carter, and also to Messrs Munnikema, Engelen and Elsenaar, whose paper presented yet another method of thrust/drag accounting.

2.0 STATEMENT OF THE PROBLEMS

The following situation, procedure and problems are common to the installation of two alternate high by-pass ratio turbo-fans on the aft fuselage of the Canadair Challenger executive jet and future variants.

- a) Engine installed performance at sea level and altitude is guaranteed with a "Referee" nozzle configuration that cannot be installed on the Challenger.
- b) The engines are acceptance tested in a test cell using an "Acceptance Test" configuration - different from the "Referee" and again not capable of being installed on the Challenger.
- c) Engines have either been or are planned to be calibrated when installed in the flight nacelle using an isolated nacelle "Open Field" thrust stand.
- d) On our present installation we have experienced as yet unexplained changes in the relationships between engine parameters (N1, N2, ITT) in the above configurations (a, b and c) and the installed configuration on the aircraft.
- e) The effect of installing the nacelle on the aircraft is perhaps the hardest to represent or understand and probably disappears at relatively low forward speeds.

3.0 PROPOSED APPROACH TO DEFINITION AND SOLUTION

- a) Instrumentation to determine: intake recovery (including a few high response transducers), the gross thrust and engine total massflow have been included on flight test nacelles.
- b) Nozzle coefficients have or will be determined over the full range of fan and core pressure ratios using static (no nacelle external flow) exhaust model tests.
- c) It is assumed that the behavior and hence performance of the engine in each configuration and situation (cell, free field or installed on aircraft) is dependent on:

- i Steady state intake recovery of the fan and or core flow independently. Here the effect of turbulence caused by vortices may need consideration.
- ii Forward speed including effective changes due to wind, cell and installation.
- iii The fan and core velocity and discharge coefficients. These must include fan duct losses, core cowl cooling and fan duct leakage.
- iv The effective local static pressure into which the fan and core nozzles discharge.
- v Core cowl scrubbing and pressure drag of an isolated nacelle is accounted as thrust loss. Changes associated with installation on the aircraft or in a test cell must be accounted as interference drag (or installation thrust loss) and by cell thrust corrections respectively
- vi In order to account for the changes in local discharge pressure the nozzle coefficients must be referred to the ratio of total pressure to the local static and the thrust must be determined at the exit plane. This thrust determination must include an application of the ideal choked flow pressure (or the local static if not choked) applied to the geometric nozzle exit area in order to maintain a fixed thrust/drag boundary. The thrust therefore depends upon the velocity and discharge coefficients CV and CD. We take the liberty of assuming that the average exit static pressure is equivalent to the average static pressures measured during nozzle model and full scale calibrations.

4.0 FINAL COMMENT

I believe it is necessary to use a constant thrust-drag geometric boundary to correctly separate the installation effect on drag and engine performance.

When the thrust is determined using the total pressure to ambient static pressure ratio and the installation causes a change in nozzle exit pressure, this is not achieved and changes in thrust which will require more fuel are being assessed as interference drag and may lead to false comparison of configurations.

Response by Mr. Carter

We would not consider it to be necessary or desirable to use a constant thrust-drag geometric boundary for accounting purposes. For complex, by-pass turbo-fan installations the redistribution of the potential thrust between nozzle(s) exit and the infinite fully expanded downstream condition is the major concern. An understanding of this redistribution or in fact the thrust changes at the nozzle(s) exit, whilst being ideally desirable, is not essential nor practicable, unless essential experimental steps in the bookkeeping are missing.

In the work quoted by Mr. Edwardes, the existence of a difference between various ground rig static calibrations on 'referee', 'acceptance' and 'flight' builds, and the flight installation values of N1, N2 and ITT should not be unexpected. If, however, the question is 'how do we determine the installation increment', then our answer would be 'via the appropriate bookkeeping steps'. All establishments have their own variants on the basic bookkeeping theme, but the following steps are necessary:

- A Inlet
Isolated internal performance (recovery, distortion)
Isolated external performance (datum drag, spill drag)
Installed external performance (drag)
- B Exhaust
Isolated T-D (for static and M external flows over engine schedule to obtain (T-D) coefficients and discharge coefficients.
- C Engine ATF
Connected engine test at altitude conditions (thrust coefficients & discharge across the engine schedule).
- D Installation
Turbine powered, blown, or ejector simulation (drag corrected for simulator ATF thrust)
Parallel ATF test of simulator (simulator ATF T/instrumentation cal)
Reference through-flow simulator (datum link if necessary)
Isolated nacelle simulator (installation increment if necessary).

Then in the final bookkeeping:

A gives engine fact input data, spillage drag to correct model inlet flows to real engine flows, and the effects of the inlet installation on these items. C gives the engine brochure performance at correct FNPR, correct internal R No, and zero external stream. B corrects C for uniform external stream effects mainly via core stream mass suppression. D gives the interference drag increment due to nozzle flow relative to the performance that would be assessed via A, B & C. At this point there can be discussion whether a through-flow nacelle datum should be used, or whether an installation increment which includes interference should be used.

But, fundamentally via these experimental routes, the effect of nozzle flows on the environment and the environment on nozzle flows are contained in the total drag bookkeeping without recourse to arbitrary division boundaries.

MESSRS ENGELEN, MUNNIKSMMA, & ELSENAAR

As could be deduced from the final comment of Mr. Edwardes note, his question concerns the split-up of penalties due to engine/airframe integration in thrust and drag terms. To answer the question, how this proposal compares to our thrust minus drag evaluation, knowledge in detail is needed of the engine reference stations, the precise definition of drag and thrust of base line airframe and engine configurations to be used in an accounting procedure. In principal we agree, that steps as described in paragraph 3 of his note will be needed in a thrust minus drag bookkeeping. His main point that engine performances are influenced by the local static pressure around the engine nozzles is correct as long as the nozzle flows are non-choked. This effect is part of the interference, and therefore, may not be excluded from a thrust minus drag optimisation process. It can be understood that from an aircraft manufacturer standpoint, it is important to split up responsibilities with respect to performance prediction along some constant thrust-drag geometric boundary. But, as shown in our paper, induced forces on airframe and engine due to integration cancel to a large part. To our view, a split-up of penalties along a boundary as mentioned is of questionable value for optimizing thrust minus drag.

DR. GREEN

Time is running on, and I think that this is the last issue that we are going to be able to address. Is there anyone from the floor who wishes to make a comment?

MR. HARRIS

I would like to clarify the points that Mr. Tipper has raised. I didn't intend to express the view that it is an intractable problem. The view we express is that if we are looking for installation drag, the accounting can be quite simple. We look for the mass flow and the total pressure and we look at free stream infinity. If you are looking for diagnostic information about discharge coefficients perhaps, or why your drags change in the way they do, then you will have to look at more pressures. But, in our presentation we clearly paralleled the full-scale aircraft in the way that the bookkeeping was done. We particularly looked at the results from the parallel system of accounting and so we don't offer the suggestion it is intractable at all. In reply to Mr. Carter's point on the use of TPS units, I would like to refer again to Paper 25 which showed a very good comparison between the model and the full-scale result. We, on the slender evidence of one comparison, would say that we are finding the right results. We have also recently unearthed one or two other results which parallel the flight results. We are not in a position to publish them today. That is where we stand.

DR. GREEN

I will give Mr. Carter the opportunity to give me a direct answer to a direct question. On the matter of definitions, do you believe our position is satisfactory or unsatisfactory?

MR. CARTER

In the direct answer, yes, I think it is satisfactory.

DR. GREEN

On that joyous note, I should like to bring this session to a close. On behalf of the Programme Committee and my co-chairman on the Committee, Dr. Dunham, from PEP, I would like to thank all the authors who have contributed to this meeting, and also all those who have contributed to this afternoon's Round Table Discussion. I believe overall it has been a very constructive and informative symposium. And now, Dr. Orlik-Ruckemann, Chairman of the Fluid Dynamics Panel, will make some concluding remarks.

DR. ORLIK-RUCKEMANN

It seems like a long time ago, but some of you may recall that in my opening remarks Monday morning, I suggested that we dedicate this meeting to the memory of Dr. von Karman. I think that if von Karman were here this week, he would have been pleased with this symposium. Firstly, it contained a number of excellent technical presentations and some very good discussions, including the one just concluded. Furthermore, by virtue of being the result of a joint effort between two AGARD panels, it confirmed one of von Karman's basic tenets, namely, that the division of AGARD activities into a number of well-defined fields does not have to preclude a joint effort in areas where these fields touch or even overlap. Finally, this symposium demonstrated once again the basic soundness and usefulness of the overall mission of AGARD, providing the opportunities for furthering and developing the international cooperation and at the same time for retaining and strengthening the individual contacts and friendships. I think that von Karman would have approved of this meeting.

Of course, all these nice things do not happen by themselves. There is a lot of effort from a lot of people behind it all. It is now my privilege and my very pleasant duty to recognize some of these people. Firstly, we have Dr. Green of FDP and Dr. Dunham of PEP and their Programme Committee. We owe them our thanks for putting together such an excellent programme and for conducting this symposium so efficiently. We have Mr. Thoulouse, the local coordinator; Mr. Bob Rollins, the Panel Executive; and Mlle Anne-Marie Rivault, who made the necessary practical arrangements, ensuring that all the administrative and logistic elements were functioning smoothly and on time. In this they were expertly assisted by Mme Denise Michaux and Mr. Patrick Sandman, and also the two young ladies who are here. Finally, we had the translation. As you all know, interpreting and trying to keep up with the enthusiastic speakers and discussors is certainly not an easy task. On this occasion we were very fortunate to have with us Mlle Malot, Madame Radisson and Madame Vioche, who tirelessly and efficiently performed this difficult job.

Finally, a few words about some of the future activities being prepared by the Fluid Dynamics Panel. It may be convenient for you to know our plans in advance so that you can start thinking at an early date about your participation or maybe pass this information on to a friend or a colleague. Our next symposium will be on "Fluid Dynamics of Jets with Applications to V/STOL", and will be held in Lisbon, Portugal on the 2 - 5 November of this year. Next spring, we will have two specialist meetings in London, probably in the week of the 17th of May. The topics of these two meetings are "Prediction of Aerodynamic Loads on Rotorcraft" and "Wall Interference in Wind Tunnels". In the fall of 1982 there will be a symposium on "Aerodynamics of Missiles". It will be held in Norway, probably on the 22 - 23 of September. We are also preparing a special course on "Modern Data Analysis Techniques in Noise and Vibration Problems" to be given at VKI in Belgium in December of this year, and a lecture series on "High Angle-of-Attack Aerodynamics" to be presented in Belgium, Germany and the USA in March of 1982. We hope to see you again at some of these activities. With this, I declare this meeting adjourned.

COMBAT AIRCRAFT INTAKES

STATE OF THE ART

- WIND TUNNEL BASED
- FLIGHT TEST VERIFIED
 - PROBLEM SOLVING
- INSTANTANEOUS DISTORTION APPROACH
- EMPHASIS ON $M \approx 2$
- THEORETICAL ANALYSIS EMERGING

SUPERSONIC CONFIGURATION EXAMPLES

- SIDE MOUNTED
 - F15, MIRAGE, TORNADO
- FUSELAGE SHIELDED
 - F16
- WING SHIELDED
 - F18

- GOOD PROGRESS IN 1970s
REF. AGARD ~ ROME 1974
- OPPORTUNITIES IN 80s and 90s

Figure 1

COMBAT AIRCRAFT INTAKES

1990's COMBAT AIRCRAFT

– POTENTIAL INTAKE DESIGN DRIVERS

- MORE SUSTAINED SUPERSONIC
- AGILITY/MANOEUVRABILITY
 - FULL FLIGHT ENVELOPE
- STOL COMPATIBILITY
- WEAPONS INTEGRATION
- REDUCED DETECTABILITY
-
-
-

Figure 2

COMBAT AIRCRAFT INTAKES

NEEDS AND OPPORTUNITIES

- COMPUTER/THEORETICAL BASED DESIGNS
- EXTENSIONS TO HIGHER SUPERSONIC CRUISE AND MANOEUVRE
- WIDE RANGE OF COMBAT AGILITY/MANOEUVRE
- INTEGRATION WITH ADVANCED WEAPONS
- UNIQUE CONFIGURATIONS
 - REDUCED DETECTABILITY
 - STOL & V/STOL
 - MANOEUVRE FREEDOM

Figure 3

NOZZLES FOR MILITARY AIRCRAFT

Present Situation

- Many designs of conv. and conv./div. nozzles applied to various aircraft
- Extent of variability (A_{Throat} , $A_{\text{Exit}}/A_{\text{Throat}}$) rather limited
- Marked trend towards conv./div. nozzles with faired boattail
- Nozzle/thrust reverser arrangement in one case:
Tornado with short-flap conv. nozzle and target type thrust reverser

Figure 4

NOZZLES FOR MILITARY AIRCRAFT

Future Development

- 2D-Nozzles are in principle a good starting point for multi-purpose design with
 - fully variable nozzle contour
 - thrust vectoring (vertical)
 - thrust reverse
- Thrust vectoring vertical *and* horizontal attractive with view to super-maneuvrability
 - only axisymmetric nozzles feasible
- Aircraft weight and life-cycle cost: sensitive to weight and complexity of sophisticated nozzle concepts

Figure 5

AFTERBODIES OF MILITARY AIRCRAFT

Present Situation

- Prediction methods for compressible, viscous flow around afterbodies not yet sufficiently developed
 - influence of jet plume
 - boundary layer separation
 - shock fronts/boundary layer interaction
 - Re-number influence
- Extensive wind tunnel testing as prime development tool necessary, but limited reliability of results
 - wind tunnel calibration problematic
 - Re-numbers too low
- Flight tests do not allow identification of afterbody drag

Figure 6

AFTERBODIES OF MILITARY AIRCRAFT

Future Views

- More stringent requirements on aircraft performance and effectiveness expected
 - careful design of afterbodies with minimum drag mandatory
 - more emphasis on sustained supersonic performance
- Improvement of flow prediction methods important (see Figure 6)
- Advanced multi-purpose nozzle concepts (axisymmetric or 2-D)
(Conv./div., thrust vectoring and reverse)

will cause extra problems with afterbody aerodynamics and design as well as with engine design and installation

Figure 7

MILITARY

Present state of the art

- In general the scene is quite promising but to a large extent is still based on the piecemeal approach.

- Techniques for:
- inlet internal performance, engine face static and dynamic distortion are well established
 - inlet spill drag by force measurements on partial models are satisfactory.
 - afterbody performance measurements in the presence of cold or hot flows are not readily available particularly for fully representative military afterbody shapes at incidence.
 - through-flow complete model measurements corrected for internal forces are satisfactory but calibration of internal force is often time consuming, expensive and inaccurate.
 - complete models with inlet and exhaust simultaneously represented by ejectors or TPS are beginning to be established.

Current limitations

- Accurate definition of internal forces.
- Afterbody performance measurements, with or without live jet suffer inaccuracy and support interference.
- Simultaneous representation of inlet and exhaust flows is difficult, particularly for multi nozzles — is it necessary?

Future developments needed

- Foremost need is for a military simulator providing nozzle pressure ratio and inlet flow. Will these accept typical E.F. distortions at high α ?
- Even more need for a short simulator for VTOL Pegasus type installations with short inlet/exhaust spacing.
- Afterbody performance techniques need development, also associated support systems for minimum interference.
- Study needed of inlet/exhaust mutual interference to demonstrate the need or otherwise of simultaneous representation.

Figure 8

Present state of the art

- In general the position is good. There has been a wide acceptance of the need for high accuracy and correct simultaneous simulation of both inlet and exhaust flows. Relatively, the state of the arts for the civil field is probably more advanced than the military, but the range of the problem is less.

- Techniques for:
- inlet internal performance are well established, spill drag measurements are adequate by pressure and force methods.
 - single and twin stream exhaust performance measurements are readily available on static rigs and external flow rigs. Hot core flows are also provided.
 - for complete and half models simultaneous inlet and exhaust flows with TPS are established, as are direct twin stream exhaust blow methods. Use of ejection is still developing.
This work is essentially confined to large wind tunnels, current TPS sizes are dictating model scales.
 - calibration of simulators is developing and is probably defining the present accuracy limits.

Current limitations

- The model performance techniques being developed for both half and full models are very expensive and somewhat inflexible.
- There is not adequate digested information at present to demonstrate the consistency and repeatability of simulators.
- Present performance measurements on inlets are invariably isolated.
Representation of the curved environment flow due to wing is rarely simulated.
- Present performance measurements on exhaust nozzles are usually isolated *by should* be made in the presence of the wing, this is possible for discharge coefficients but very difficult for thrust (and probably meaningless).

Future developments needed

- Consolidation of current techniques
- Examination of data from simple through-flow representations in comparison with exhaust simulators to optimise through-flow builds.
- Validation of the half model v full model techniques and possible tunnel interference with exhaust flows.
- Development of model support systems for 3 engine and rear engine configurations.
Forward blade support interference development.
- There is virtually no information on Reynolds number effects on installation performance.
- In pursuit of the previous consideration must be given to engine representation in cryogenic facilities.
No TPS here, ejector or blown may have advantages of representation of correct temperature ratios.
- Propellers, before they become reality, the main principles of mutual propeller/wing interference should be considered, as must be the book-keeping.

Figure 9

INSTALLATION AERODYNAMICS OF TRANSPORT AIRCRAFT

- **WHAT IS THE BEST TRANSPORT AIRCRAFT CONFIGURATION?**

Figure 10

HOW TO MINIMISE INSTALLATION DRAG

$$\Delta C_D = \text{integrated (wing + nacelle)} - [\text{ideal wing} + \text{ideal nacelle}]$$

- Theoretical calculations of given configurations -- design/off design
- Wind tunnel tests
- Existing (AGARD) results, as a preliminary guide

Figure 11

THEORETICAL CALCULATIONS

- **Transonic potential flow calculation, applied:**
 - to the complete aircraft
 - to a detailed part of the engine installation
 - improvements in the resolution of the equation
 - coupled with the twin nozzle flow calculation
 - coupled with the viscous effects
- **Viscous flow calculation**
 - 3-D laminar sep. bubble and transition -
 - 3-D shock - B.L. interaction - separate zones -
 - shear layers . . .

EXPERIMENTAL RESULTS

- **Isolated nacelle**
 - Inlet and exhaust design
 - Global performances and detailed flow
- **Installation effects**
 - Optimisation of overall configurations
 - Localised improvements

Figure 12

REPORT DOCUMENTATION PAGE

1. Recipient's Reference	2. Originator's Reference	3. Further Reference	4. Security Classification of Document										
	AGARD-CP-301	ISBN 92-835-0301-5	UNCLASSIFIED										
5. Originator	Advisory Group for Aerospace Research and Development North Atlantic Treaty Organization 7 Rue Ancelle, 92200 Neuilly sur Seine, France												
6. Title	AERODYNAMICS OF POWER PLANT INSTALLATION												
7. Presented at	Ecole Nationale Supérieure de l'Aéronautique et de l'Espace, Complexe Aérospatial de Lespinet, Toulouse, France, 11-14 May 1981.												
8. Author(s)/Editor(s)	Various		9. Date September 1981										
10. Author's/Editor's Address	Various		11. Pages 528										
12. Distribution Statement	This document is distributed in accordance with AGARD policies and regulations, which are outlined on the Outside Back Covers of all AGARD publications.												
13. Keywords/Descriptors	<table border="0"> <tr> <td>Aerodynamics</td> <td>Airframes</td> </tr> <tr> <td>Aircraft engines</td> <td>Engine inlets</td> </tr> <tr> <td>Installing</td> <td>Nozzles</td> </tr> <tr> <td>Fighter aircraft</td> <td>Afterbodies</td> </tr> <tr> <td>Transport aircraft</td> <td>Test procedures</td> </tr> </table>			Aerodynamics	Airframes	Aircraft engines	Engine inlets	Installing	Nozzles	Fighter aircraft	Afterbodies	Transport aircraft	Test procedures
Aerodynamics	Airframes												
Aircraft engines	Engine inlets												
Installing	Nozzles												
Fighter aircraft	Afterbodies												
Transport aircraft	Test procedures												
14. Abstract	<p>Powerplant installations involve complex flows, strongly influenced by viscous effects and often with important aerodynamic interactions between the airframe and propulsion system. The introduction of new vehicle propulsion concepts, and new points of emphasis in aircraft and missile design requirements, provide an expanding range of aerodynamic problems which call for both experimental and theoretical study. It was the purpose of the symposium to survey the current and foreseeable aerodynamic problems in powerplant installation and to review recent work which has improved basic understanding or has enhanced prediction and design methods in this field.</p> <p>The symposium focused on combat and transport aircraft, with five sessions</p> <ul style="list-style-type: none"> I - Combat Aircraft Intakes II - Afterbodies and Nozzles III - Testing and Analysis Techniques IV - Installation Aerodynamics of Transport Aircraft V - Round Table Discussion <p>This symposium was planned by the AGARD Fluid Dynamics Panel with the support of the Propulsion and Energetics Panel which held a simultaneous meeting on "Helicopter Propulsion Systems" at the same meeting site.</p> <p>Papers presented and discussions held at the Fluid Dynamics Panel Symposium held at the Ecole Nationale Supérieure de l'Aéronautique et de l'Espace, Complexe Aérospatial de Lespinet, Toulouse, France, 11-14 May 1981.</p>												

<p>AGARD Conference Proceedings No.301 Advisory Group for Aerospace Research and Development, NATO AERODYNAMICS OF POWER PLANT INSTALLATION Published September 1981 528 pages</p> <p>Powerplant installations involve complex flows, strongly influenced by viscous effects and often with important aerodynamic interactions between the airframe and propulsion system. The introduction of new vehicle propulsion concepts, and new points of emphasis in aircraft and missile design requirements, provide an expanding range of aerodynamic problems which call for both experimental and theoretical study. It was the purpose</p> <p>P.T.O.</p>	<p>AGARD-CP-301</p> <p>Aerodynamics Aircraft engines Installing Fighter aircraft Transport aircraft Airframes Engine inlets Nozzles Afterbodies Test procedures</p>	<p>AGARD Conference Proceedings No.301 Advisory Group for Aerospace Research and Development, NATO AERODYNAMICS OF POWER PLANT INSTALLATION Published September 1981 528 pages</p> <p>Powerplant installations involve complex flows, strongly influenced by viscous effects and often with important aerodynamic interactions between the airframe and propulsion system. The introduction of new vehicle propulsion concepts, and new points of emphasis in aircraft and missile design requirements, provide an expanding range of aerodynamic problems which call for both experimental and theoretical study. It was the purpose</p> <p>P.T.O.</p>	<p>AGARD-CP-301</p> <p>Aerodynamics Aircraft engines Installing Fighter aircraft Transport aircraft Airframes Engine inlets Nozzles Afterbodies Test procedures</p>
<p>AGARD Conference Proceedings No.301 Advisory Group for Aerospace Research and Development, NATO AERODYNAMICS OF POWER PLANT INSTALLATION Published September 1981 528 pages</p> <p>Powerplant installations involve complex flows, strongly influenced by viscous effects and often with important aerodynamic interactions between the airframe and propulsion system. The introduction of new vehicle propulsion concepts, and new points of emphasis in aircraft and missile design requirements, provide an expanding range of aerodynamic problems which call for both experimental and theoretical study. It was the purpose</p> <p>P.T.O.</p>	<p>AGARD-CP-301</p> <p>Aerodynamics Aircraft engines Installing Fighter aircraft Transport aircraft Airframes Engine inlets Nozzles Afterbodies Test procedures</p>	<p>AGARD Conference Proceedings No.301 Advisory Group for Aerospace Research and Development, NATO AERODYNAMICS OF POWER PLANT INSTALLATION Published September 1981 528 pages</p> <p>Powerplant installations involve complex flows, strongly influenced by viscous effects and often with important aerodynamic interactions between the airframe and propulsion system. The introduction of new vehicle propulsion concepts, and new points of emphasis in aircraft and missile design requirements, provide an expanding range of aerodynamic problems which call for both experimental and theoretical study. It was the purpose</p> <p>P.T.O.</p>	<p>AGARD-CP-301</p> <p>Aerodynamics Aircraft engines Installing Fighter aircraft Transport aircraft Airframes Engine inlets Nozzles Afterbodies Test procedures</p>

<p>of the symposium to survey the current and foreseeable aerodynamic problems in powerplant installation and to review recent work which has improved basic understanding or has enhanced prediction and design methods in this field.</p> <p>The symposium focused on combat and transport aircraft, with five sessions</p> <ul style="list-style-type: none"> I - Combat Aircraft Intakes II - Afterbodies and Nozzles III - Testing and Analysis Techniques IV - Installation Aerodynamics of Transport Aircraft V - Round Table Discussion <p>This symposium was planned by the AGARD Fluid Dynamics Panel with the support of the Propulsion and Energetics Panel which held a simultaneous meeting on "Helicopter Propulsion Systems" at the same meeting site.</p> <p>Papers presented and discussions held at the Fluid Dynamics Panel Symposium held at the Ecole Nationale Supérieure de l'Aéronautique et de l'Espace, Complexe Aérospatial de Lespinet, Toulouse, France, 11-14 May 1981.</p> <p>ISBN 92-835-0301-5</p>	<p>of the symposium to survey the current and foreseeable aerodynamic problems in powerplant installation and to review recent work which has improved basic understanding or has enhanced prediction and design methods in this field.</p> <p>The symposium focused on combat and transport aircraft, with five sessions</p> <ul style="list-style-type: none"> I - Combat Aircraft Intakes II - Afterbodies and Nozzles III - Testing and Analysis Techniques IV - Installation Aerodynamics of Transport Aircraft V - Round Table Discussion <p>This symposium was planned by the AGARD Fluid Dynamics Panel with the support of the Propulsion and Energetics Panel which held a simultaneous meeting on "Helicopter Propulsion Systems" at the same meeting site.</p> <p>Papers presented and discussions held at the Fluid Dynamics Panel Symposium held at the Ecole Nationale Supérieure de l'Aéronautique et de l'Espace, Complexe Aérospatial de Lespinet, Toulouse, France, 11-14 May 1981.</p> <p>ISBN 92-835-0301-5</p>
<p>of the symposium to survey the current and foreseeable aerodynamic problems in powerplant installation and to review recent work which has improved basic understanding or has enhanced prediction and design methods in this field.</p> <p>The symposium focused on combat and transport aircraft, with five sessions</p> <ul style="list-style-type: none"> I - Combat Aircraft Intakes II - Afterbodies and Nozzles III - Testing and Analysis Techniques IV - Installation Aerodynamics of Transport Aircraft V - Round Table Discussion <p>This symposium was planned by the AGARD Fluid Dynamics Panel with the support of the Propulsion and Energetics Panel which held a simultaneous meeting on "Helicopter Propulsion Systems" at the same meeting site.</p> <p>Papers presented and discussions held at the Fluid Dynamics Panel Symposium held at the Ecole Nationale Supérieure de l'Aéronautique et de l'Espace, Complexe Aérospatial de Lespinet, Toulouse, France, 11-14 May 1981.</p> <p>ISBN 92-835-0301-5</p>	<p>of the symposium to survey the current and foreseeable aerodynamic problems in powerplant installation and to review recent work which has improved basic understanding or has enhanced prediction and design methods in this field.</p> <p>The symposium focused on combat and transport aircraft, with five sessions</p> <ul style="list-style-type: none"> I - Combat Aircraft Intakes II - Afterbodies and Nozzles III - Testing and Analysis Techniques IV - Installation Aerodynamics of Transport Aircraft V - Round Table Discussion <p>This symposium was planned by the AGARD Fluid Dynamics Panel with the support of the Propulsion and Energetics Panel which held a simultaneous meeting on "Helicopter Propulsion Systems" at the same meeting site.</p> <p>Papers presented and discussions held at the Fluid Dynamics Panel Symposium held at the Ecole Nationale Supérieure de l'Aéronautique et de l'Espace, Complexe Aérospatial de Lespinet, Toulouse, France, 11-14 May 1981.</p> <p>ISBN 92-835-0301-5</p>